

др Светлана Савић-Шевић

**Пријава и документација за реизбор у звање виши
научни сарадник**

ИНСТИТУТ ЗА ФИЗИКУ

Научном већу Института за физику у Београду

Београд, 23. март 2022.

ПРИМЉЕНО:		23. 03. 2022	
Рад.јед.	Б р о ј	Арх.шифра	Прилог
0901	341/1		

ПРЕДМЕТ: Молба за покретање поступка за реизбор звања виши научни сарадник

Молим Научно веће Института за физику да у складу са Правилником о поступку и начину вредновања и квантитативном исказивању научно-истраживачких резултата истраживача покрене поступак за мој реизбор у звање виши научни сарадник.

У прилогу достављам:

1. Мишљење руководиоца пројекта са предлогом чланова комисије
2. Кратку биографију
3. Преглед научне активности
4. Елементе за квалитативну оцену научног доприноса
5. Елементе за квантитативну оцену научног доприноса
6. Списак објављених радова и њихове копије
7. Податке о цитираности радова
8. Копију решења о претходном избору у звање
9. Додатне прилоге

С поштовањем,

Svetlana Savić - Šević

др Светлана Савић-Шевић
виши научни сарадник
Институт за физику у Београду

ПРЕДМЕТ: Мишљење руководиоца лабораторије о реизбору др Светлане Савић-Шевић у звање виши научни

Др Светлана Савић-Шевић је запослена у Лабораторији за квантну и атомску оптику, у оквиру Центра за фотонику. У истраживачком раду бави се израдом и истраживањем нових биополимерних материјала, холографским генерисањем дифракционих решетака и комплексних фотонских наноструктура, њиховом структурном и оптичком анализом, и применом у области сензора, оптичке заштите докумената. Њена област интересовања је и биофизика где се истраживање може се поделити у два правца, 1) примена како класичне, тако и дигиталне холографске интерферометрије у испитивању полимеризације и деформације зубних ткива и 2) проучавање структурних и оптичких особина инсеката (са структуром природног фотонског кристала) као и њиховом биомиметиком.

С обзиром да испуњава све услове предвиђене Правилником о поступку, начину вредновања и квантитативном исказивању научно-истраживачких резултата истраживача МПНТР, сагласан сам са покретањем поступка за реизбор др Светлане Савић-Шевић у звање виши научни сарадник.

За састав комисије за реизбор др Светлане Савић-Шевић у звање виши научни сарадник предлажем:

1. др Дејан Пантелић, научни саветник у пензији, Институт за Физику у Београду
2. др Душан Арсеновић, научни саветник, Институт за Физику у Београду
3. др Сузана Петровић, научни саветник, Институт за нуклеарне науке Винча

др Душан Арсеновић
научни саветник

Руководилац Лабораторије за квантну и атомску оптику

1. БИОГРАФСКИ ПОДАЦИ КАНДИДАТА

Светлана Савић-Шевић рођена је 1962. године у Апатину, где је завршила основну школу, а затим Змај Јовину гимназију у Новом Саду. Дипломирала је на Физичком факултету, смер истраживачки-експериментална физика, Универзитету у Београду 1994. године. Последипломске студије је уписала 1994. године на Физичком факултету Универзитета у Београду – смер квантна оптика. Магистарску тезу под називом “Холографске особине пулулана” је одбранила 1999. године, ментори др Дејан Пантелић и академик порф. др Никола Коњевић. 2007. докторирала је на Физичком Факултету Универзитета у Београду са темом: ”Физичке особине холографских дифракционих решетака на новим дихромираним материјалима”, ментор др Дејан Пантелић.

Запослена је у Институту за физику у Београду од 1994.године. Била је ангажована на домаћим истраживачким, технолошким и иновационим пројектима као и на међународним пројектима.

У периоду 2006. до 2010. године била је ангажована на пројекту "Квантна и оптичка интерферометрија" (Министарство просвете, науке и технолошког развоја Републике Србије 141003, руководилац Бранислав Јеленковић). Од 2011. до 2019. године била је ангажована на пројекту "Генерисање и карактеризација нанофотонских функционалних структура у биомедицини и информатици" (Министарство просвете, науке и технолошког развоја Републике Србије ИИИ 45016, руководилац Бранислав Јеленковић) и пројекту "Холографске методе генерисања специфичних таласних фронтова за ефикасну контролу квантних кохерентних ефеката у интеракцији атома и ласера" (Министарство просвете, науке и технолошког развоја Републике Србије ОИ 171038, руководилац Дејан Пантелић).

У оквиру међународне сарадње учествовала је на пројекту из шестог оквирног пројекта програма FP6 "Reinforcing the Center for quantum and optical metrology" (Европска комисија) у периоду 2006. до 2009. године. Учествовала је и на FP6 пројекту, „World Year of Physics 2005: Activities in Europe“, потпројекту, P.20.02 “Einstein’s thought”, Contract Number 516938, у оквиру Друштва физичара Србије као дела конзорцијума учесника пројекта. У периоду 2008. до 2011. године учесник је COST акције MP0702 - "Towards functional sub-wavelength photonic structures". Учествовала је на билатералном пројекту са Републиком Хрватском у периоду 2016-2017, "Плазмонске структуре великих површина за хемијску и биолошку детекцију" (руководилац Горан Исић). Учествовала је на билатералном пројекту са Републиком Кином у периоду 2019-2021, "Mimetics of insects for sensing and security". (руководилац Бранислав Јеленковић). Такође је учествовала је на билатералном пројекту са Белорусијом у периоду 2020-2021, "Нови региструјући материјали засновани на полимерима и њихове примене у холографији, биофотоници и сезорима" (руководилац Дејан Пантелић).

Априла 2000. године бирана је звање истраживач сарадник, октобра 2007. у звање научни сарадник, маја 2012 у звање виши научни сарадник, септембра 20017 реизбор у звање виши научни сарадник.

Кандидат је у свом досадашњем научном раду објавио укупно 37 радова у међународним часописима категорије M20, са ISI листе, од којих 6 у категорији M21a, 16 у категорији M21, 10 у категорији M22, 5 у категорији M23 и 54 рада у категорији M30.

2. ПРЕГЛЕД НАУЧНЕ АКТИВНОСТИ

Научна активност др Светлане Савић-Шевић је разноврсна и може поделити у више праваца, према проблематици којом се бавила: класична и дигитална холографија, нови холографски материјали и холографске дифракционе решетке, метаматеријали са негативним коефицијентом топлотног ширења, фотонски кристали, биофизика, биомиметика, локализација светлости, структурална карактеризација и анализа нових нано материјала допираних ретким земљама.

Дигитална холографија

Холографија је једно од значајних достигнућа савремене науке и има примену у многим областима: дифракционој оптици, оптичким меморијама, микролитографији, фотонским кристалима. Практичне примене укључују и заштиту докумената и производа, недеструктивно испитивање материјала, а у медицини ендоскопију и томографију.

Прва истраживања Светлане Савић-Шевић односила су се на проблеме дигиталне и оптичке реализације Фуријеовог трансформа и њиховом применом у генерисању и реконструкцији компјутерских холограмима. Анализирано је простирање кохерентног таласног фронта кроз оптички систем који реализује повећану (или умањену) слику Фуријеовог трансформа. Константовано је да постоји читаво област у којој се формира Фуријеов трансформ. Тачније говорећи, постоји само једна Фуријеова равна, али Фуријеов трансформ се формира и у широкој околној зони са добром апроксимацијом. Теоријски подаци су поређени са експериментом у коме је реконструисан компјутерски генерисани холограм. Остварено је повећање Фуријеовог трансформа 10-50 пута. Добијена слика Фуријеовог трансформа је око 50 мм, док је код класичног уређаја око 1 мм.

Кандидат је радио на Виноградовом алгоритму, DFT- применљив за произвољан ред, који је једнак производу узајамно простих множитеља.

Нови холографски материјали и холографске дифракционе решетке

Област истраживања кандидата било је испитивање нових холографских фотоосетљивих материјала. Данас постоји велики број холографских фоторегиструјућих материјала, али ни један не задовољава истовремено све захтеве: високу осетљивост, високу дифракциону ефикасност и резолуциону способност, добру стабилност у односу на околну средину (влага, температура), низак ниво шума. Стога се и данас интензивно ради на проналажењу нових материјала, као и побољшавању особина већ постојећих.

Кандидат је испитивао справљање, наношење и формирање танких фотоосетљивих слојева биополимерних материјала (пулулан и декстран) допираних јонима хрома. Установљене су оптималне методе и услови обраде и развијања експонираних слојева. Проучене су експозиционе и спектралне карактеристике дихромираног пулулана (ДЦП) и декстрана (ДЦД). Посебна пажња је посвећена испитивању зависности дифракционе ефикасности од низа фактора: времена експозиције, дебљине слоја за различите концентрације биополимера и дихромата, просторне учестаности и угла реконструкције. Испитивања су вршена на холографским дифракционим решеткама.

Испитивана је могућност коришћења сензибилизованог пулулана као новог холографског материјала. Фотоосетљиви слојеви су формираны од раствора пулулана у дејонизованој води, сензибилизованог амонијум дихроматом. Материјал је експониран Хе-Не ласером, таласне дужине 543,5 нм. Интерференцијом два таласа формирана је синусна решетка. Константовано је да решетке поседују површински рељеф, те да са повећањем просторне фреквенце опада његова дубина. Испитивана је и зависност дифракционе ефикасности од дебљине пулуланског филма. Резултати су приказани у раду:

Dejan Pantelić, **Svetlana Savić**, Dragica Jakovljević “Dichromated pullulan as a novel photosensitive holographic material”, *Optics Letters*, 23, 807-809, (1998). (M21a, ИФ: 2.951; 3/47)

Експериментално су испитиване динамичке особине дихромираног биополимера током експозиције директним ласерским снопом. Испитивана је дифракциона ефикасност решетке и њена зависност од различитих параметара: концентрације дихромата, густине енергије, густине снаге, просторно-фреквентне учестаности материјала, дебљине слоја. Праћени су ефекти развијања (хемијске обраде) решетке у реалном времену. Константовано је да се фомирају решетке, које дају криве са два максимума што потврђује да су формиране решетке и апсорпционе и фазне (површинско-рељефне). Показано је да су дихромирани биополимери одлични холографски материјали, максимална постигнута дифракциона ефикасност ДЦП и ДЦД решетки је 70 %, дихромирани пулулан и декстран карактеришу се високом просторном учестаношћу, регистровано је око 3000 линија/мм. Резултати су приказани у:

Svetlana Savić, Dejan Pantelić and Dragica Jakovljević “Real-time and postprocessing holographic effects in dichromated pullulan”, *Appl. Optics*, 41, (2002) 4484-4488. (M21 ИФ: 1.515; 16/64).

Мерена је стабилност дифракционих решетки забележених на дихромираном пулулану и декстрану у односу на спољашњу средину. Утврђено је да дифракционе решетке имају одличну стабилност у поређењу са решеткама на дихромираном желатину. Показано је да се профил решетке, после утицаја високе влажности, не мења и дифракциона ефикасност остаје очувана. Дифракциона ефикасност је константна и при деловању УВ зрачења и високе температуре. Дихромиране биополимерне решетке је могуће чувати веома дуг период, без значајнијег опадања њихових карактеристика. Резултати су у раду:

Svetlana Savić-Šević and Dejan Pantelić, “Dichromated pullulan diffraction gratings: influence of environmental conditions and storage time on their properties,” *Appl. Opt.* 46, 287-291 (2007). (M21, ИФ : 1.701; 17/64).

Копирање рељефно фазних холограма је био предмет истраживања. Уобичајен метод копирања холограма штампањем (embossing) састоји се од више корака, а резултира никленом матрицом. Она има ограничен век употребе, услед примене високих притисака и температуре. Од интереса је проналажење трајнијих материјала и једноставнијих метода добијања матрице. Кандидат је дошао на идеју да би материјали који се користе у стоматологији, дентални композити, били добри кандидати, пошто они морају да имају изузетне механичке, хемијске и термалне особине чврстог денталног ткива (дентина и

глеђи). Показано је да су дентални композити одличан материјал за копирање холограма методом штампања. Копија оригиналне полисахаридне решетке је практично идентична оригиналу. Добијена дентална матрица је одличних механичких особина, може да има дебљину од неколико милиметара, што је чини знатно трајнијом од никлене. Резултати истраживања су публиковани у раду:

Svetlana Savić-Šević, Dejan Pantelić, “Relief hologram replication using a dental composite as an embossing tool”, *Optics Express*, 13, 2005. 2747-2754. (M21a, ИФ: 3.764; 2/55)

Предмет истраживања су били рељефно-фазни холограми записани у биополимеру, декстрану, сензибилизованом амонијум дихроматом (ДЦД). Профил дифракционих решетки анализиран је атомским микроскопом (АФМ). Добијени су различити површински профили са просторном учестаношћу од 330 лин/мм, и дубином рељефа од 402 нм. Дихромирани декстран је, захваљујући овим особинама одличан материјал за добијање штампаних холограма. Резултати су објављени у раду:

Svetlana Savić-Šević, Dejan Pantelić, “Biopolymer holographic diffraction gratings”, *Optical Materials*, 30, (2008), 1205-1207 (M21, ИФ :1.519; 54/189)

Проучаване су и запреминске холографске решетке генерисане на дихромираним пулулану. У рефлексионим спектрима уочене су веома ретки мулти-пикови. Утврђено је да су они последица неидеалне структуре запреминске дифракционе решетки. Теоријска анализа и нумеричке симулације су показали да уочено понашање произилази из незнатне рандомизације параметара решетки: рефрактивног индекса, периода решетки, дебљине филма. Нумерички резултати се слажу са експериментом. Резултат је објављен у раду:

S. Savić-Šević, D. Pantelić, V. Damljanović, B. Jelenković, “Bifurcation in reflection spectra of holographic diffraction grating recorded on dicromated pullulan, *Opt. Quant. Electron.* 50, 195, (2018) (M23, ИФ: 1.547)

Фотонски кристали

Последње деценије расте интерес за употребу фотонских кристала као нових материјала који се могу користити у контроли простирања електромагнетних таласа. Фотонски кристали су диелектричне структуре чији је индекс преламања просторно модулисан. Основна карактеристика фотонског кристала је енергетски процеп (band gap) - фреквентни опсег у коме је забрањено простирање електромагнетних таласа у фотонском кристалу. Фотонски кристали имају примене у једно-модним таласоводима, као филтери, сензори, фотонски ласери. Холографска метода последњих година све више се користи у генерисању фотонских кристала. У поређењу са другим методама холографски метод је једноставнији, јефтинији, могу се формирати фотонски кристали великих димензија без нехомогености, даје могућност генерисања различите структуре фотонских кристала помоћу различитих конфигурација снопова.

Као нови материјал за генерисање фотонских материјала уведен је дихромирани пулулан. Генерисане су једнодимензионалне и дводимензионалне фотонске структуре, и

испитивана је могућност њихове примене у области сензора и холографских филтера. Генерисани су фотонски кристали са сложеним нанаометарским структурама и широким енергетским процепима (band gaps).

Холографском методом, у дихромираном пулулану, генерисан је једнодимензионални фотонски кристал. Фотонски кристал генерисан је интерференцијом два таласа супротног смера, формирајући низ равни, паралелних површини субстрата. Добијени су фотонски кристали са забрањеним енергетским процепом у видљивом делу спектра. Показано је да се центар енергетског процепа може померати мењајући концентрацију бихромата, као и мењањем упадног угла реконструишућег снопа. Центар енергетског процепа помера се ка нижим таласним дужинама са повећањем концентрације бихромата, а такође, и са повећањем упадног угла реконструишућег снопа. Центар енергетског процепа може се померати и мењајући експозицију. Спектрално мерење показује да се центар енергетског процепа помера ка већим таласним дужинама са смањењем експозиције. Резултати су презентовани у радовима:

Svetlana Savic-Sevic, Dejan Pantelic, Marko Nikolic, Branislav Jelenkovic “Band-Gap Photonic Structures in Dichromate Pullulan,” *Materials and Manufacturing Processes*, 24: 1127–1129, 2009. (M22, ИФ: 0.968, 18/37)

Svetlana Savić-Šević, “Flexible design of band gaps in the biopolymer photonic crystals,” *Phys. Scr.* T149 (2012) 014073, (M22, ИФ: 1.204)

Испитивана је могућност примене једнодимензионалног фотонског кристала генерисаног у дихромираном пулулану као сензора температуре. Показано је да се загревањем фотонског кристала од собне температуре, 25°C до 100°C, таласна дужина центра енергетског процепа помери за 80 nm. Са повећањем температуре таласна дужина центра енергетског процепа помера се ка нижим таласним дужинама. Процес је реверзибилан, хлађењем таласна дужина центра енергетског процепа помера се ка већим таласним дужинама. Ови резултати су значајни јер показују да се на једноставан начин може добити променљиви (tunable) филтер у оптичком делу спектра, и да се једнодимензионални фотонски кристал у пулулану може користити као сезор температуре. Резултати су у раду:

S. Savic-Sevic, D. Pantelic and B. Jelenkovic “Influence of the Heat Treatment on the Band Gaps in the Biopolymer Photonic Crystals” *Act. Phys. Pol. A* 16 (4) 2009, 645-646. (M23, ИФ: 0.433, 60/71)

Биофизика

Истраживање кандидата у области биофизике може се поделити у два правца: примена холографске интерферометрије у испитивању деформације зубних ткива и проучавање структурних и оптичких особина инсеката (са структуром природног фотонског кристала).

Примена холографске интерферометрије у испитивању деформације зубног ткива

За зубне испуне (пломбе) се користе фотополимеризујући композити. Током полимеризације, композитна пломба се скупља (контрахује) и почиње да делује одређеним притиском на преостало, здраво, зубно ткиво. Дејство контракционе силе се испољава кроз деформацију зуба, која је сасвим мала (2 - 20 микрометара, у зависности од величине зубне шупљине и преосталог ткива). И поред овако мале деформације, прорачуни показују да је резултујући притисак велики (чак и преко 100 Мра - зубно ткиво пуца када је оптерећено притисцима између 40 и 150 Мра). Дакле, контракционе силе могу бити довољно велике да доведу до оштећења зуба или одвајања саме пломбе.

Кандидат се бавио проблемом мерења деформације зуба употребом метода двоекспозиционе холографије. У зубу који се испитује (ин витро) је направљен кавитет, који је испуњен пломбом а затим је постављен у холографски уређај. Снимљен је холограм зуба пре почетка и након полимеризације. Реконструкцијом су добијена два таласа, који су међусобно интерферирали и дали слику где се види зуб са суперпонираним светлим и тамним линијама. Интерференционе линије показују колика је укупна деформација. Максимум деформација је 2 микрометра за кавитет класе I, до 14 микрометара за кавитет МОД класе.

Одређивање унутрашњих напрезања (механичких напона) зубног ткива је захтевало да се направи компјутерски модел зуба. Овакав модел је сада служио да се методом коначних елемената одреде напрезања која дају деформације идентичне онима из експеримента. Израчуната напрезања су између 50 и 100 Мра, у зависности од типа кавитета. Резултати су у раду:

Dejan Pantelić, Larisa Blažić, **Svetlana Savić-Šević**, Bratimir Panić, “Holographic detection of a tooth structure deformation after dental filling polymerization”, *Journal of Biomedical Optics*, 12, (2007) 024026 (M21a, ИФ: 3.084, 3/84)

У ранијем испитивању, деформација зубног ткива је проучавана двоекспозиционом холографском интерферометријом. То је дало могућност мерења укупне деформације, након завршетка процеса полимеризације. Оно што се одиграва у интервалу од укључења до искључења LED лампе, остаје потпуно сакривено. Ради тога је развијен уређај за холографску интерферометрију у реалном времену, који омогућава праћење процеса деформисања зуба од почетка полимеризације, па до краја. Уређај је измењен, јер се холографска плоча налази смештена у стакленој кивети. То омогућава да се комплетан процес хемијске обраде материјала обави без померања холографске плоче. Током поларизације зуб почиње лагано да се деформише. То доводи до промењеног облика рефлектованог таласа, што се види као појава интерференционих линија. Све ово се прати CCD камером тако да се добија филм који у потпуности бележи процес деформације зуба. У експерименту је добијен максимум деформације 11.3 микрометра а израчунато напрезање 40.3 МПа. Резултати су у радовима:

Dejan Pantelić, Larisa Blažić, **Svetlana Savić-Šević**, Branka Murić, Darko Vasiljević, Bratimir Panić, Ilija Belić, “Real-time measurement of internal Stress of dental tissue using holography”, *Optics Express*, 15, (2007), 6823 – 6830. (M21a, ИФ: 4.009, 1/55)

Dejan Pantelić, Darko Vasiljević, Larisa Blažić, **Svetlana Savić-Šević**, Branka Murić, Marko Nikolić, “Biomechanical model produced from light-activated dental composite resins: a holographic analysis,” Phys. Scr. T157 (2013) 014021 (5pp) (M22, ИФ: 1.296)

Користили смо две различите технике полимеризације – једностепену и двостепену. Резултати показују да је двостепени метод бољи јер је деформација мања. Претпоставка је да се након иницијалног осветљавања у зубном полимеру одиграва почетна (тамна) хемијска реакција, која утиче на смањење контракције полимера. Добијено је да је деформација у случају двостепенг метода мања 11% у поређењу са континуалним осветљавањем. Резултати су приказани у раду:

Larisa Blažić, Dejan Pantelić, **Svetlana Savić-Šević**, Branka Murić, Ilija Belić, Bratimir Panić “Modulated photoactivation of composite restoration: measurement of cuspal movement using holographic interferometry,” Laser Med Sci. 26 (2011) 179 - 186. (M21, IF: 2.574, 17/59)

Проучавање структурних и оптичких особина инсеката

Последњих година интензивно се изучавају структурне и оптичке особине инсеката. Њихове структуре су природни фотонски кристали. Посебну пажњу изазивају лептири због своје атрактивне обојености крила. Та обојеност је последица неколико феномена: селективне апсорпције пигмената, расејања, флуоресценције и иридесценције. Посебну пажњу заузима иридесценција која је последица сложене микро и нано- структуре крила лептира.

Предмет истраживања су била две врсте лептира: *Apatura iris* и *A. ilia* и две врсте мољца *Jordanita globulariae* и *Diachrysia chrysitis*. Детаљно је проучавана веза између оптичких особина и микро и нано-структура крила лептира и мољаца. Њихова крила састоје се из великог броја љуспица које су позициониране једна преко друге. Попречни пресек љуспица показује структуру запреминске Брегове решетке. Свака љуспица на површини има велики број бразда које формирају рељефну површинску решетку. Оваква структура крила одговорна је за иридесценцију. Код *Apatura iris* и *A. ilia* мерени максимум рефлективности је око 380 nm са спектралном ширином апроксимативно 50 nm за обе врсте. Угаона селективност је висока и љубичаста иридесцентна боја се види само у угаоном опсегу од 18 степени у оба случаја.

Проучавањем *Jordanita globulariae* показано је да пигмент, расејање и интерференција делују заједно у дво-димензионој таласоводној структури дајући незнатно иридесцентне зелене љуспице. Модел методе коначних елемената (FEM) адекватно описује фотонске особине мољца.

Код мољца *Diachrysia chrysitis* комбинација инетерференција и расејања, које је појачано апсорпцијом, резултују бојом злата на крилима. Кључ механизма је расејање на храпавој унутршњој површини љуспица крила која је повезана са великим повећањем апсорпције у УВ-плавом спектралном опсегу. Нерасејана светлост интерферира и рефлектује се од мулти-слојева љуспица и мембрана. Резултујући спектар је веома сличан спектру злата.

Теорија субталасног расејања површине и повећање локалног интензитета се користе за квантитативно објашњење рефлексионг спектра. Резултати су приказани у радовима:

Dejan Pantelić, Srećko Ćurčić, **Svetlana Savić-Šević**, Aleksandra Korać, Aleksander Kovačević, Božidar Ćurčić and Bojana Bokić “High angular and spectral selectivity of purple emperor (Lepidoptera: *Apatura iris* and *A. ilia*) butterfly wings”, *Optics Express*, 19, (2011) p 5817-26 (M21a, ИФ: 3.753; 5/78)

S. Ćurčić, D. Pantelić, B. Ćurčić, **S. Savić-Šević**, S. Makarov, V. Lačković, M. Labudović-Borović, N. Ćurčić, D. V. Stojanović, “Micro and Nanostructures of Iridescent Wing Scales in Purple Emperor Butterflies (Lepidoptera: *Apatura ilia* and *A. iris*),” *Microscopy research and technique* 75, 968–976 (2012). (M22, ИФ:1.792)

D. Pavlović, **S. Savić-Šević**, B. Salatić, V. Lazović, W. Zhang, D. Zhang, D. Pantelić, “Synergy of interference, scattering and pigmentation for structural coloration of *Jordanita globulariae* moth”, *Soft Matter*, 17, 6477–6485 (2021) (M21, ИФ: 3.679)

D. Pantelić, **S. Savić-Šević**, D. V. Stojanović, S. Ćurčić, A. J. Krmpot, M. Rabasović, D. Pavlović, V. Lazović, V. Milošević, “Scattering-enhanced absorption and interference produce a golden wing color of the burnished brass moth, *Diachrysia chrysitis*,” *Phys. Rev. E* 95, 032405 (2017); (M21, ИФ: 2.366)

Биомиметика

Користећи дихромирани пулулан, генерисане су структуре које имитирају структуру крила лептира. Комбинацијом Брегове решетке и компјутерског форк-холограма генерисана је у дихромираном пулулану структура крила лептира. Резултати су приказани у радовима:

S. Savić-Šević, D. Pantelić, S. Ćurčić, B. Ćurčić, and B. Jelenković “Biologically Inspired Photonic Structures in Dichromated Pullulan“, 13th International Conference on Transparent Optical Networks (ICTON), 2011, Stockholm, Tu.D2.2

Zoran Jakšić, Dejan Pantelić, Milija Sarajlić, **Svetlana Savić-Šević**, Jovan Matović, Branislav Jelenković, Dana Vasiljević-Radović, Srećko Ćurčić, Slobodan Vuković, Vladimir Pavlović, Jelena Buha, Vesna Lačković, Milica Labudović-Borović, Božidar Ćurčić, “Butterfly scales as bionic templates for complex ordered nanophotonic materials: A pathway to biomimetic plasmonics,” *Optical Materials*, 35 1869-1875, (2013) (M21, ИФ: 2.075)

Мољац *Diachrysia chrysitis*, са крилима боје злата, био је инспирација за проучавање новог типа фотонског материјала. То су слојевите фотонске структуре са великом разликом индекса преламања, чији су наизменични слојеви са нано-неравнинама. Теоријска анализа је показала да расејање и интерференција интерагују, повећавајући локално поље унутар слојева и повећавају апсорпцију материјала, нарочито у УВ-плавој области спектра. Теорија је експериментално потвђена генерисањем фотонске стуктуре која добро имитира

структурне и оптичке особине крила мољца. Користећи холографску интерферометрију генерисана је комплексна Брегова решетка у дихромираном пулулану. Наизменични пулулан-ваздух слојеви су одвојени нано-стубићима, а слојеви ваздуха су попуњени са 30-50 nm сферним нано-честицама које доводе до расејања. Такви материјали са великом разликом индекса преламања и нано-расејивачима дају широк спектар са високом рефлективношћу. Боја злата је последица таквих структура.

S. Savić-Šević, D. Pantelić, B. Jelenković, B. Salatić, D. Stojanović, “Golden moth-inspired structures with a synergistic effect of interference, absorption and scattering”, *Soft Matter*, 14, 5595-5603 (2018), (M21, ИФ: 3.899)

Локализација светлости

Током последњих пар деценија локализација светлости привлачи велико интересовање због својих примена у транспорту светлости, код рандом ласера, соларне енергије. Простирање светлости кроз средину са извесном количином неуређености (disorder) локализована је интерференцијом и вишеструким расејањем на рандом структурама што доводи до спречавања простирања светлости. Локализација може бити слаба, позната као кохерентно расејање уназад (coherent backscattering) или јака, тј. Андерсонова локализација, где је простирање светлости потпуно забрањено.

Кохерентно расејање уназад карактерише се повећањем интензитета у тачно одређеном правцу расејања уназад. Оно даје важне информације о средњем слободном путу светлости, густини расејивача и његовим димензијама.

Код конструисања уређаја за мерење кохерентног расејања уназад јавља се проблем јер је ширина угла расејања инверзно пропорционална средњем слободном путу светлости. За материјале са дужином пута од неколико микрометра (код биолошких узорака) угао је веома узак (реда микрорадијана), док је код наноструктурних материјала угао расејања широк (неколико стотина милирадијана). Досадашњи уређаји конструисани су или за мерење широког или уског угла расејања. У овом раду описан је универзални оптички систем који је употребљив за мерења у случајевима и малих и великих углова расејања. Систем је заснован на пројектовању слике расејавајуће површине коришћењем додатног система сочива. Слика се директно пројектује на улазну бленду зумирајућег објектива који је фокусиран на бесконачност. На овај начин, угаони спектар расејаног светла је фокусиран на детекциону површину, омогућавајући обсервацију купе уназад расејане светлости. У оваквој конфигурацији промена видног угла се остварује променљивим увећањем зумирајућег објектива, у зависности да ли је купа расејања уназад велика или мала. Решење конструкције уређаја дато је у раду:

Dejan Pantelić, Svetlana Savić-Šević, Dusan Grujić, “Zoom system for measurement of coherent backscattering of light in micro- and nanomaterials,” *Phys. Scr.* T157 (2013) 014021 (5pp) (M22, ИФ: 1.296)

Кандидат је испитивао кохерентно расејање на комплексним наноструктурама полисахарида које је генерисао комбинацијом холографске методе и нерастварајуће индуковане фазне сепарације (non solvent phase separation). Структура је формирана од наночестица пулулана које су рапоређене на случајан начин, и заробљене између Брегових

слојева пулулана. Мерен је угао расејања и одређен средњи слободан пут светлости. Експериментално је верификовано да је упадна светлост локализована у комплексној структури пулулана. Резултат указује на режим слабе локализације, тј. на кохерентно расејање уназад (coherent backscattering). Резултати су приказани у раду:

Svetlana Savić-Šević, Dejan Pantelić, Dušan Grujić, Branislav Jelenković, “Localization of light in a polysaccharide-based complex nanostructure,” *Opt Quant Electron* (2016) 48, 289, (M22, ИФ: 1.290)

Структурална карактеризација и анализа нових нано материјала допираних ретким земљама

Последњих година Светлана Савић-Шевић се укључила и у истраживања нових нано материјала допираних ретким земљама. Њен допринос првенствено проистиче из потребе за структуралном карактеризацијом ових материјала која се, између осталог, врши и анализом микроскопских слика начињених скенирајућим електронским микроскопом (SEM). Лоцирање, идентификација и анализа репрезентативних микроскопских слика начињених уз претходно одређивање и постављање одговарајућих параметара електронског микроскопа је незаобилан део ових истраживања. Луминесцентне особине нано фосфора заснованих на ретким земљама су веома зависне од величине синтетисаних гранула па је уобичајени део сваког истраживања у овој области анализа и презентација структуралне карактеризације изучаваних узорака.

Значај истраживања нано материјала и њихове примене у индустрији су у развоју и изласку на тржиште оптоелектронских уређаја као што су дисплеји рачунарских монитора, мобилних телефона, таблета и телевизора, као и мерење високих температура безконтактном методом. Обе споменуте примене засноване су на луминесцентним особинама нано материјала допираних ретким земљама.

Из активности кандидата које се односе на структурне и оптичке особине нано материјала допираних ретким земљама до сада је објављени следећи радови у међународним часописима:

M.S. Rabasović, D. Šević, J. Križan, M. Terzić, J. Možina, B.P. Marinković, **S. Savić-Sević**, M. Mitrić, M.D. Rabasović, N. Romčević “Characterization and luminescent properties of Eu³⁺ doped Gd₂Zr₂O₇ nanopowders,” *Journal of Alloys and Compounds* 622 (2015) 292-295 (M 21a)

M.S. Rabasović, D. Šević, J. Križan, M.D. Rabasović, **S. Savić-Šević**, M. Mitrić, M. Petrović, M. Gilić, N. Romčević “Structural properties and luminescence kinetics of white nanophosphor YAG:Dy,” *Optical Materials* 50, 250-255, (2015) (M21)

J. Trajić, M.S. Rabasović, **S. Savić-Šević**, D. Šević, B. Babić, M. Romčević, J.L. Ristić-Djurović, N. Paunović, J. Križan, N. Romčević “Far-infrared spectra of dysprosium doped yttrium aluminum garnet nanopowder,” *Infrared Physics & Technology* 77, 226-229, (2016) (M22)

D. Šević, M. Rabasović, J. Križan, **S. Savić-Šević**, M. Mitrić, M. Gilić, B. Hadžić, N. Romčević, “Characterization and luminescence kinetics of Eu^{3+} doped YVO_4 nanopowders”, *Materials Research Bulletin* 88 121-126, (2017) (M21)

M. Gilic, M. Petrovic, J. Cirkovic, N. Paunovic, **S. Savić-Sevic**, Ž. Nikitovic, M. Romcevic, I. Yahia, N. Romcevic, “Low-temperature photoluminescence of CuSe_2 nano-objects in selenium thin films”, *Processing and Application of Ceramics* 11, 127-135 (2017) (M22)

A. Vlasić, D. Šević, M. S. Rabasović, J. Križan, **S. Savić-Šević**, M.D. Rabasović, M. Mitrić, B. Marinković, M. Nikolić, “Effects of temperature and pressure on luminescent properties of $\text{Sr}_2\text{CeO}_4:\text{Eu}^{3+}$ nanophosphor”, *J. Luminescence* 199, 285-292 (2018) (M21)

M. S. Rabasović, J. Križan, **S. Savić-Šević**, M. Mitrić, M. D. Rabasović, B. Marinković and D. Šević; Orange - reddish light emitting phosphor $\text{GdVO}_4:\text{Sm}^{3+}$ prepared by solution combustion synthesis (SCS), *J. Spectrosc.* 3413864 (2018) (M23)

M. Nikolić, M. S. Rabasović, J. Križan, **S. Savić-Šević**, M. D. Rabasović, B. Marinković, A. Vlasić and D. Šević, Luminescence thermometry using $\text{Gd}_2\text{Zr}_2\text{O}_7:\text{Eu}^{3+}$, *Opt. Quant. Electron.* 50, 258 (2018) (M23)

D. Šević, M. S. Rabasović, J. Križan, **S. Savić-Šević**, M. D. Rabasović, B. Marinković, M. Nikolić, “Effects of temperature on luminescent properties of $\text{Gd}_2\text{O}_3:\text{Er}, \text{Yb}$ nanophosphor”, *Opt. Quant. Electron.* 52, 232 (2020) (M22)

D. Šević, M. S. Rabasović, J. Križan, **S. Savić-Šević**, M. G. Nikolić, B. P. Marinković, M. D. Rabasović, “ $\text{YVO}_4:\text{Eu}^{3+}$ nanopowders: multi-mode temperature sensing technique”; *J. Phys. D: Appl. Phys.* 53, 015106 (2020) (M21)

Графен

Кандидат је учествовао у истраживању графена у интеракцији са фемтосекундним ласером. Уочене су периодичне површинске структуре на вишеструком слоју (10-15 слојева) графена које су нормалне у односу на поларизацију ласера. Мерени период формиране површинске решетке је 70-100 nm, што спада у најмање периоде у поређењу са другим материјалима. Истраживање је приказано у раду:

Angela Beltaos, Aleksander G. Kovačević, Aleksandar Matković, Uroš Ralević, **Svetlana Savić-Šević**, Djordje Jovanović, Branislav M. Jelenković, and Radoš Gajić “Femtosecond laser induced periodic surface structures on multi-layer graphene,” *Journal of Applied Physics* 116, 204306 (2014) (M21)

3. ЕЛЕМЕНТИ ЗА КВАЛИТАТИВНУ ОЦЕНУ НАУЧНОГ ДОПРИНОСА

3.1 Квалитет научних резултата

3.1.1. Научни ниво и значај резултата, утицај научних радова

Др Светлана Савић-Шевић је у свом досадашњем научном раду објавила укупно 37 радова у међународним часописима са ISI листе, од чега 6 категорије M21a, 16 категорије M21, 10 категорије M22 и 5 категорије M23.

У периоду након одлуке Научног већа о предлогу за стицање претходног научног звања, др Светлана Савић-Шевић је објавила 25 радова у међународним часописима са ISI листе. Од тога је 1 рад категорије M21a, 12 радова категорије M21, 8 категорије M22 и 4 рада категорије M23.

У периоду након одлуке Научног већа о предлогу за реизбор научног звања виши научни сарадник, др Светлана Савић-Шевић је објавила 13 радова у међународним часописима са ISI листе. Од тога је 8 радова категорије M21, 2 категорије M22 и 3 рада категорије M23.

Као пет најзначајнијих радова кандидата могу се узети:

1. **S. Savić-Šević**, D. Pantelić, B. Murić, D. Grujić, D. Vasiljević, B. Kolaric, B. Jelenković, “Thermo-osmotic metamaterials with large negative thermal expansion”, *J. Mater. Chem. C*, 9, 8163-8168, (2021)
DOI: 10.1039/d1tc01028j
M21, ИФ: 7.393
2. **S. Savić-Šević**, D. Pantelić, B. Jelenković, B. Salatić, D. V. Stojanović, “Golden moth-inspired structures with a synergistic effect of interference, absorption and scattering”, *Soft Matter*, 14, 5595-5603, (2018)
10.1039/c8sm00683k
M21, ИФ: 3.889
3. D. Pantelić, **S. Savić-Šević**, D. V. Stojanović, S. Ćurčić, A. J. Krmpot, M. Rabasović, D. Pavlović, V. Lazović, V. Milošević, “Scattering-enhanced absorption and interference produce a golden wing color of the burnished brass moth, *Diachrysia chrysis*”, *Phys. Rev. E* 95, 032405 (2017)
DOI: 10.1103/PhysRevE.95.032405
M21, ИФ: 2.366
4. D. Pantelić, S. Ćurčić, **S. Savić-Šević**, A. Korać, A. Kovačević, B. Ćurčić and B. Bokić, “High angular and spectral selectivity of purple emperor (*Lepidoptera: Apatura iris* and *A. ilia*) butterfly wings”, *Optics Express*, 19, 5817-5826 (2011)

M21a, ИФ: 3.753

5. Svetlana Savić-Šević, Dejan Pantelić,

“Relief hologram replication using a dental composite as an embossing tool”,

Optics Express, 13, 2747-2754, (2005)

M21a, ИФ: 3.797

У раду 1. за разлику од до сад публикованих радова на тему материјала са коефицијеном негативног термалног ширења, по први пут уводи се релација између негативног термалног ширења и термо-осмозе. Аутор је генерисао нову класу метаматеријала који се састоји од великог броја вишеслојних нано-мембрана одвојених нано-стубићима, у којим је заробљен ваздух између сваке суседне нано-мембране. Негативно термално ширење се остварује термо-осмозом заробљеног ваздуха кроз веома танке нанослојне мембране. Добила је вредност коефицијеном негативног термалног ширења, који је један од највећих објављених у литератури.

У раду 2. инспирисана мољцем *Diachrysia chrysitis* који има крила боје злата, презентовала нову врсту фотонског материјала, који јако добро имитира структурне и оптичке особине мољца. Користећи холографску интерферометрију направила је комплексну Брагову решетку где су ваздушни слојеви попуњени сферним наночестицама које делују као расејивачи. На основу тих структура успела је да објасни појаву златне боје.

У раду 3. кандидат је дао допринос у експерименталном делу рада и анализи и дискусији резултата.

У раду 4. дала је допринос у експерименталном делу као и у дискусији резултата. Мерила је и анализирала рефлексивне спектре лептира *Apatura iris* и *Apatura ilia*. Показала је да је угаона селективност велика, и да се љубичаста иридисцентна боја види у угаоном опсегу од само 18 степени.

Рад 5. Уобичајен метод копирања холограма штампањем (embossing) састоји се од више корака, а резултира никленом матрицом. Она има ограничен век употребе, услед примене високих притисака и температуре. Од интереса је проналажење трајнијих материјала и једноставнијих метода добијања матрице. Кандидат је дошао на идеју да би материјали који се користе у стоматологији, дентални композити, били добри кандидати, пошто они морају да имају изузетне механичке, хемијске и термалне особине чврстог денталног ткива (дентина и глеђи). Показала је да су дентални композити одличан материјал за копирање холограма методом штампања. Копија оригиналне полисахаридне решетке је практично идентична оригиналу. Добијена дентална матрица је одличних механичких особина, може да има дебљину од неколико милиметара, што је чини знатно трајнијом од никлене. Овај рад је изазвао пажњу и његов приказ и идеје дати су у магазину EuroPhotonics.

3.1.2. Позитивна цитираност научних радова кандидата

При одређивању броја цитата на SCOPUS бази треба водити рачуна о томе да се радови кандидата од 2003 године воде на аутора Светлана Савић-Шевић, а радови пре 2003 на аутора Светлана Савић.

Према бази података SCOPUS на дан 21. 03. 2022. радови кандидатиње који се воде на аутора Светлана Савић-Шевић су цитирани укупано 264 пута, (Хиршов индекс 10), од тога 209 пута без аутоцитата (Хиршов индекс 8).

Према истој бази радови кандидатиње који се воде на аутора Светлана Савић су цитирани укупано 26 пута, (Хиршов индекс 2).

(прилог)

3.1.3. Параметри квалитета часописа

Битан елемент за процену квалитета научних резултата је и квалитет часописа у којима су радови објављени, односно импакт фактор - ИФ. У категорији M21a и M21 кандидат је објавио следеће радове (звездицом се означава број радова након одлуке Научног већа о предлогу за стицање претходног научног звања, а са две звезде након реизбора):

M21a:

3 рада у Optics Express (ИФ: 4,009, СНИП 2.35; ИФ: 3,797, СНИП 2.47; ИФ: 3,753, СНИП: 2.55)

1 рад у Journal of Biomedical Optics (ИФ: 3.084, СНИП: 1.67)

1* рад у Journal of Alloys and Compounds (ИФ: 3.014, СНИП: 1.62)

1 рад у Optics Letters (ИФ: 2.951, СНИП: 1.67)

M21:

1** рад у Journal of Materials Chemistry C (ИФ: 7.393, СНИП: 1.40)

1** рад у Applied Microbiology and Biotechnology (ИФ: 4.813, СНИП: 1.27)

2** рада у Soft Matter (ИФ=3.889, СНИП: 1.01; ИФ: 3.679, СНИП: 1.21)

1** рад у Journal of Physics D: Applied Physics (ИФ: 3.207, СНИП: 1.14)

1** рад у Journal of Luminescence (ИФ: 2.961, СНИП: 1.12)

1 рад у Laser in Medical Science (ИФ: 2.574, СНИП: 1.52)

1* рад у Materials Research Bulletin (ИФ: 2.873, СНИП: 0.96)

1** рад у Physical Review E (ИФ: 2.366, СНИП: 1.08)

1* рад у Current Applied Physics (ИФ: 2.212, СНИП: 1.23)

1* рад у Journal of Applied Physics (ИФ: 2,210, СНИП: 1.30)

2* рада у Optical Materials (ИФ: 2,183, СНИП: 1.24; ИФ: 2,023; СНИП: 1.37)

1 рад у Optical Materials (ИФ: 1,714, СНИП: 1.33)

2 рада у Applied Optics (ИФ: 1.717, СНИП 1.71; ИФ: 1.515, СНИП: 1.99)

Часописи у којима је кандидат објављивао радове су веома цењени у областима којима припадају. Посебно се међу њима истичу: Optics Express и Optics Letters у областима оптике, Journal of Materials Chemistry C и Soft Matter у области науке о материјалима, Applied Optics и Applied Physics у областима примењене физике и оптике. Чињеница да је кандидат објављивао радове у тим часописима указује како на значај, тако и на разноврсност његових истраживања и резултата.

Додатни библиометријски показатељи у вези са објављеним радовима кандидата остварани у периоду након одлуке Научног већа о предлогу за реизбор научног звања виши научни сарадник дати су у доњој табели. Она садржи импакт факторе (ИФ) радова, М бодове радова по српској категоризацији научноистраживачких резултата, као и импакт фактор нормализован по импакту цитирајућег чланка (СНИП). У табели су дате укупне вредности, као и вредности свих фактора усредњених по броју чланака и по броју аутора по чланку.

	ИФ	М	СНИП
Укупно	38.272	83	12.23
Усредњено по чланку	2.944	6.38	0.94
Усредњено по аутору	5.27	11.20	1.67

3.1.4 Степен самосталности и степен учешћа у реализацији радова у научним центрима у земљи и иностранству

Кандидат је водећи аутор 10 радова, на једном раду је једини аутор, други аутор 6 радова, и трећи аутор 6 радова.

На радовима који су објављени у периоду након избора у претходно звање, кандидат је водећи аутор 5 радова, други аутор 4, и трећи аутор 2 рада.

На радовима који су објављени у периоду након одлуке Научног већа о предлогу за реизбор научног звања виши научни сарадник кандидат је водећи аутор 3 рада, други аутор 2 два рада, и трећи аутор 1 рада.

У овим радовима кандидат самостално обавља експериментални рад, од конструисања нових експерименталних поставки, производње узорака, обраде и анализе добијених резултата, писање радова и представљање на конференцијама. Као коаутор доприноси експерименталном раду, обради и интерпретацији добијених резултата. Научне активности представљају оригиналан допринос у областима нових биополимерних холографских материјала (где уводи пулулан и декстран (полисахариде) у холографију), дифракционих решетака, биофизике, генерисању фотонских кристала и комплексних, како уређених, тако и неуређених, наноструктура у органским биополимерима. Генерише нови метаматеријал са високим негативним коефицијенти термалног ширења. Такође, кандидат је покренуо нову област истраживања код нас – биомиметику инсеката.

3.1.5 Награде

Кандидат је са тимом Полимер освојио пето место на Такмичењу за најбољу технолошку иновацију у Србији 2008.године.

Учествовала је на "Nikon International Small World Competition" 2009 и њена фотографија фотонског кристала на дихромираном пулулану под микроскопом ушла је у 100 најбољих на свету.

3.1.6. Елементи применљивости научних резултата

Применљивост научних резултата је разноврсна: производња једно-димензионих и дводимензионих површинских и запреминских дифракционих решетака, у области оптичких филтера и биосензора, у заштити докумената, у неструктивном испитивању материјала. Примењивост научних резултата потврђује и учешће на такмичењу за најбољу технолошку иновацију, конструисан је и направљен прототип ЛЕД лампе за полимеризацију денталних композита.

3.2 Ангажованост у формирању научних кадрова

Кандидат др Светлана Савић-Шевић је ментор при изради докторске дисертације Евгенију Новти, студенту Медицинског факултета у Новом Саду, са одобреном темом "Утицај светлосних водича на својства полимеризационе контракције денталних композитних материјала".

(прилог)

Кандидат је руководио експерименталним делом докторске дисертације "Холографско испитивање деформације зубног патрљка ендодонтски леченог зуба у току припреме за протетичку круну" који је урађен у Институту за физику, др Тање Пушкар са Медицинског факултета у Новом Саду.

(прилог)

Такође, учествовала је екперименталном раду који је везан за холографску интерферометрију и обраду резултата докторске дисертације др Ларисе Блажић са Медицинског факултета у Новом Саду, “Примена светлосних извора са плавим светлосно-емитујућим диодама (ЛЕД) у полимеризацији рестауративних композитних материјала“.

Учествовала је у изради холографских стереограма за магистарску тезу Каролине Мудрински: Проблеми употребе математичке теорије” Поља Галоа” у сфери уметности.
(прилог)

Кандидат је држао предавања студентима Електротехничког факултета у оквиру сарадње Института за Физику и Електротехничког факултета, као и предавања младим истраживачима у Петници.

Активна је на пољу популаризације науке код нас. Учествовала је на првом фестивалу науке са изложбом холограма генерисаних у нашој лабораторији. Такође је учествовала у изради изложбе „Милева Марић и Алберт Ајнштајн кроз простор и време“.

3.3. Нормирање броја коауторских радова, патената и техничких решења

У свим публикованим радовима кандидата су комбинована експериментална истраживања са теоријским и нумеричким симулацијама па се рачунају са пуном тежином у односу на 7 коаутора.

Од 13 радова објављених након претходног реизбора са пуном тежином у односу на број коаутора (до седам) рачуна се 8 радова, остали су нормирани узимајући у обзир њихов број коаутора већи од седам.

Нормирање М бодова кандидатов укупан збир у категоријама М20 умањило је са 99 на 85.38.

3.4. Руковођење пројектима, потпројектима и пројектним задацима

Др Светлана Савић-Шевић је у оквиру пројекта ON171038 "Холографске методе генерисања специфичних таласних фронтова за ефикасну контролу квантних кохерентних ефеката у инеракцији атома и ласера" (2011-2019), финансираном од стране Министарства просвете, науке и технолошког развоја Републике Србије, руководила пројектним задатком "Холографска миметика инсеката".

(прилог)

3.5. Активност у научним и научно-стручним друштвима

Значајне активности и функције кандидата у релевантним научним и научно-стручним Друштвима

Оснивач је и члан Оптичког друштва Србије.

Рецензирање радова у часописима

Кандидат је рецензирао радове за часописе: Micron, Optical and Quantum Electronics, Medicinski pregled.

(прилог)

Кандидат је одржао следеће предавање по позиву:

“Dichromated pullulan: real-time effects and holographic properties”, International Conference Optical Holography and its Applications, 26-29 September 2000 Kiev, Ukraine.

(прилог)

3.6. Утицај научних резултата

Утицајност научних резултата кандидата је наведена у одељцима 3 и 3.1.2 овог документа. Пун списак радова је дат у одељку 5, а подаци о цитираности са интернет странице базе Scopus су дати након списка свих радова кандидата.

3.7 Конкретан допринос кандидата у реализацији радова у научним центрима у земљи и иностранству

Кандидат је значајно допринео у већини радова на којима је аутор или коаутор. Сви радови су урађени у сарадњи са колегама из земље. Др Светлана Савић-Шевић је имала кључни допринос публикацијама на којима је први, други и трећи аутор. У овим радовима кандидат самостално обавља експериментални рад, од конструисања нових експерименталних поставки, производње узорака, обраде и анализе добијених резултата, писања радова и представљање на конференцијама, а такође је учествовао и у комуникацији са рецензентима приликом припреме радова за објављивање. Као коаутор доприноси експерименталном раду, обради и интерпретацији добијених резултата. Научне активности представљају оригиналан допринос у областима нових биополимерних холографских материјала, дифракционих решетака, биофизике, генерисању фотонских кристала и комплексних, како уређених, тако и неуређених, наноструктура у органским биополимерима. Кандидат је увео нови материјал, пулулан, биополимер, у област холографије и фотонских кристала. Такође, кандидат је покренуо нову област истраживања код нас – биомиметику инсеката.

3.8 Уводна предавања на конференцијама и друга предавања

Кандидат је одржао следеће предавање по позиву:

“Dichromated pullulan: real-time effects and holographic properties”, International Conference Optical Holography and its Applications, 26-29 September 2000 Kiev, Ukraine.

(прилог)

Кандидат је одржао предавање “Negative thermal expansion in nanolayered pullulan”, 13th Photonics Workshop, Kopaonik, 8-12 March 2020.

Кандидат је одржао предавање “Origin and biomimicry of golden color in moth”, 12th Photonics Workshop, Kopaonik, 11-14 March 2019.

4. ЕЛЕМЕНТИ ЗА КВАНТИТАТИВНУ ОЦЕНУ НАУЧНОГ ДОПРИНОСА КАНДИДАТА

Остварени резултати у периоду након одлуке Научног већа о предлогу за реизбор научног звања виши научни сарадник:

Категорија	М бодова по раду	Број радова	Укупно М бодова	Укупно нормираних М бодова
M21	8	8	64	53.43
M22	5	2	10	8.57
M23	3	3	9	8.50
M31	3.5	1	3.5	3.50
M34	0.5	12	6	5.48
M52	1.5	2	3	2.57
M61	1.5	1	1.5	1.5
M64	0.2	10	2	1.82
Сума			99	85.38

Поређење са минималним квантитативним условима за избор у звање виши научни сарадник:

Минимални број М бодова		Остварено	Оствар. нормираних
Укупно	50/2	99	85.38
M10+M20+M31+M32+M33+M41+M42	40/2	92.5	79.48
M11+M12+M21+M22+M23+M24	30/2	83	70.5

5. СПИСАК РАДОВА ДР СВЕТЛАНЕ САВИЋ-ШЕВИЋ

5.1 Радови у међународним часописима изузетних вредности (M21a)

Радови објављени након претходног избора у звање (M21a)

1. M.S. Rabasović, D. Šević, J. Križan, M. Terzić, J. Možina, B.P. Marinković, **S. Savić-Sević**, M. Mitrić, M.D. Rabasović, N. Romčević “Characterization and luminescent properties of Eu³⁺ doped Gd₂Zr₂O₇ nanopowders,”

Journal of Alloys and Compounds 622, 292–295 (2015).

ИФ: 3.014

Радови објављени пре претходног избора у звање (M21a)

1. D. Pantelić, S. Ćurčić, **S. Savić-Šević**, A. Korać, A. Kovačević, B. Ćurčić and B. Bokić, “High angular and spectral selectivity of purple emperor (Lepidoptera: Apatura iris and A. ilia) butterfly wings”,

Optics Express, 19, 5817 (2011)

ИФ: 3.753

2. D. Pantelić, L. Blažić, **S. Savić-Šević**, B. Panić,

“Holographic detection of a tooth structure deformation after dental filling polymerization”,

Journal of biomedical optics, 12, 024026 (2007)

ИФ: 3.084

3. D. Pantelić, L. Blažić, **S. Savić-Šević**, B. Murić, D. Vasiljević, B. Panić, I. Belić,

“Real-time measurement of internal Stress of dental tissue using holography”,

Optics Express, 15, 6823-6830 (2007)

ИФ: 4.009

4. **S. Savić-Šević**, D. Pantelić,

“Relief hologram replication using a dental composite as an embossing tool”,

Optics Express, 13, 2747-2754 (2005).

ИФ: 3.797

5. D. Pantelić, **S. Savić**, D. Jakovljević,

“Dichromated pullulan as a novel photosensitive holographic material”,

Optics letters, 23, 807-809 (1998)

ИФ: 2.951

5.2 Радови у врхунским међународним часописима (M21)

Радови објављени након претходног реизбора у звање (M21)

1. **S. Savić-Šević**, D. Pantelić, B. Murić, D. Grujić, D. Vasiljević, B. Kolaric, B. Jelenković;
“Thermo-osmotic metamaterials with large negative thermal expansion”,
J. Mater. Chem. C, 9, 8163–8168 (2021);
ИФ: 7.393

2. D. Pavlović, **S. Savić-Šević**, B. Salatić, V. Lazović, W. Zhang, D. Zhang, D. Pantelić;
“Synergy of interference, scattering and pigmentation for structural coloration of Jordanita globulariae moth”;
Soft Matter, 17, 6477–6485 (2021)
ИФ: 3.679

3. I. Dimkić, S. Stanković, J. Kabić, M. Stupar, M. Nenadić, M. Ljaljević-Grbić, V. Žikić, Lj. Vujisić, V. Tešević, N. Vesović, D. Pantelić, **S. Savić-Šević**, J. Vukojević, S, Ćurčić;
“Bat guano-dwelling microbes and antimicrobial properties of the pygidial gland secretion of a trogliphilic ground beetle against them”,
Applied Microbiology and Biotechnology, 104, 4109-4126, (2020);
ИФ: 4.183

4. D. Šević, M. S. Rabasović, J. Krizan, **S Savić-Šević**, M. G. Nikolić, B. P. Marinković, M. D. Rabasović;
“YVO₄:Eu³⁺ nanopowders: multi-mode temperature sensing technique”;
J. Phys. D: Appl. Phys. 53, 015106 (2020)
ИФ: 3.207

5. **S. Savić-Šević**, D. Pantelić, B. Jelenković, B. Salatić, D. Stojanović;
“Golden moth-inspired structures with a synergistic effect of interference, absorption and scattering”;
Soft Matter, 14, 5595—5603 (2018);
ИФ: 3.889

6. A. Vlasić, D. Šević, M. S. Rabasović, J. Križan, **S. Savić-Šević**, M.D. Rabasović, M. Mitrić, B. Marinković, M. Nikolić;
“Effects of temperature and pressure on luminescent properties of Sr₂CeO₄:Eu³⁺ nanophosphor”;
J. Luminescence **199**, 285-292 (2018);
ИФ: 2.961

7. D. Pantelić, **S. Savić-Šević**, D. V. Stojanović, S. Ćurčić, A. J. Krmpot, M. Rabasović, D. Pavlović, V. Lazović, V. Milošević
“Scattering-enhanced absorption and interference produce a golden wing color of the burnished brass moth, Diachrysia chrysitis”
Phys. Rev. E 95, 032405 (2017);
ИФ: 2.366

8. D. Šević, M. Rabasović, J. Križan, **S. Savić-Šević**, M. Mitrić, M. Gilić, B. Hadžić, N. Romčević,
“Characterization and luminescence kinetics of Eu³⁺ doped YVO₄ nanopowders”, Materials Research Bulletin 88 121–126, (2017)
ИФ: 2.873

Радови објављени након претходног избора у звање (M21)

9. B. Murić, D. Pantelić, D. Vasiljević, **S. Savić-Šević**, B. Jelenković
“Application of tot'hema eosin sensitized gelatin as a potential eye protection filter against direct laser radiation,”
Current Applied Physics 16, 57-62, (2016).
ИФ: 2.212

10. M.S. Rabasović, D. Šević, J. Križan, M.D. Rabasović, **S. Savić-Šević**, M. Mitrić, M. Petrović, M. Gilić, N. Romčević
“Structural properties and luminescence kinetics of white nanophosphor YAG:Dy”
Optical Materials 50, 250–255 (2015).
ИФ: 2.183

11. A. Beltaos, A. Kovačević, A. Matković, U. Ralević, **S. Savić-Šević**, Dj. Jovanović, B. M. Jelenković, and Radoš Gajić
“Femtosecond laser induced periodic surface structures on multi-layer graphene”
Journal of Applied Physics 116, 204306 (2014).
ИФ: 2.210

12. Z. Jakšić, D. Pantelić, M. Sarajlić, **S. Savić-Šević**, J. Matović, B. Jelenković, D. Vasiljević-Radović, S. Ćurčić, S. Vuković, V. Pavlović, J. Buha, V. Lačković, M. Labudović-Borović, B. Ćurčić,
“Butterfly scales as bionic templates for complex ordered nanophotonic materials: A pathway to biomimetic plasmonics,”
Optical Materials 35, 1869–1875 (2013).
ИФ: 2.075

Радови објављени пре претходног избора у звање (M21)

1. L. Blažić, D. Pantelić, **S. Savić-Šević**, B. Murić, I. Belić, B. Panić,
“Modulated photoactivation of composite restoration: measurement of cuspal movement using holographic interferometry,”
Laser med sci. 26, 179 – 186 (2011).
ИФ: 2.311

2. **S. Savić-Šević**, Dejan Pantelić,
“Biopolymer holographic diffraction gratings”,
Optical Materials, 30, 1205-1207 (2008).
ИФ: 1.714

3. **S. Savić-Šević**, D. Pantelić,

“Dichromated pullulan diffraction gratings: influence of environmental conditions and storage time on their properties”

Appl. Optics, 46, 287- 291 (2007).

ИФ: 1.717

4. **S. Savić**, D. Pantelić, D. Jakovljević,

“Real-time and postprocessing holographic effects in dichromated pullulan”,

Appl. Optics, 41, 4484-4488 (2002)

ИФ: 1.515

5.3 Радови у водећим међународним часописима (M22)

Радови објављени након претходног реизбора у звање (M22)

1. D. Šević, M. S. Rabasović, J. Križan, **S. Savić-Šević**, M. D. Rabasović, B. Marinković, M. Nikolić;

“Effects of temperature on luminescent properties of Gd₂O₃:Er,Yb nanophosphor”;

Opt. Quant. Electron. 52, 232 (2020);

ИФ: 2.084

2. M. Gilic, M. Petrovic, J. Cirkovic, N. Paunovic, **S. Savic-Sevic**, Ž. Nikitovic, M. Romcevic, I. Yahia, N. Romcevic,

“Low-temperature photoluminescence of CuSe₂ nano-objects in selenium thin films”,

Processing and Application of Ceramics 11, 127–135 (2017)

ИФ: 1.152

Радови објављени након претходног избора у звање (M22)

3. **S. Savić-Šević**, D. Pantelić, D. Grujić, B. Jelenković,

“Localization of light in a polysaccharide-based complex nanostructure”

Opt Quant Electron 48, 289 (2016)

ИФ: 1.290

4. J. Trajić, M.S. Rabasović, **S. Savić-Šević**, D. Šević, B. Babić, M. Romčević, J.L. Ristić-Djurović, N. Paunović, J. Križan, N. Romčević,

“Far-infrared spectra of dysprosium doped yttrium aluminum garnet nanopowder”

Infrared Physics & Technology 77, 226–229 (2016).

ИФ: 1.713

5. D. Pantelić, **S. Savić-Šević**, D. Grujić,

“Zoom system for measurement of coherent backscattering of light in micro- and nanomaterials,”

Phys. Scr. T157, 014021, 3pp (2013)

ИФ: 1.296

6. D. Pantelić, D. Vasiljević, L. Blažić, **S. Savić-Šević**, B. Murić, M. Nikolić,
“Biomechanical model produced from light-activated dental composite resins: a holographic analysis”

Phys. Scr. T157, 014021, 5pp (2013)

ИФ: 1.296

7. **S. Savić-Šević**,

“Flexible design of band gaps in the biopolymer photonic crystals,”

Phys. Scr. T149, 014073, (3pp) (2012)

ИФ: 1.204

8. S. Ćurčić, D. Pantelić, B. Ćurčić, **S. Savić-Šević**, S. Makarov, V. Lačković, M. Labudović-Borović, N. Ćurčić, D. V. Stojanović,

“Micro and Nanostructures of Iridescent Wing Scales in Purple Emperor Butterflies (Lepidoptera: *Apatura ilia* and *A. iris*),”

Microscopy research and technique 75,968–976 (2012).

ИФ: 1.792

Радови објављени пре претходног избора у звање (M22)

1. **S. Savić-Šević**, D. Pantelic, M. Nikolic, B. Jelenkovic,

“Band-Gap Photonic Structures in Dichromate Pullulan”

Materials and Manufacturing Processes, 24, 1127–1129 (2009).

ИФ: 0.968

2. D. Pantelić, **S. Savić-Šević**, D. Vasiljević, B. Murić, L. Blažić, M. Nikolić, B. Panić, “Holographic measurement of a tooth model and dental composite contraction,”

Materials and Manufacturing Processes, 24, 1142-1146 (2009).

ИФ: 0.968

5. 4 Радови у међународним часописима (M23)

Радови објављени након претходног реизбора у звање (M23)

1. **S. Savić-Šević**, D. Pantelić, V. Damljanović, B. Jelenković;

“Bifurcation in reflection spectra of holographic diffraction grating recorded on dichromated pullulan;

Opt. Quant. Electron. 50, 195, (2018);

ИФ: 1.547

2. M. S. Rabasović, J. Križan, **S. Savić-Šević**, M. Mitrić, M. D. Rabasović, B. Marinković and D. Šević;

Orange - reddish light emitting phosphor $GdVO_4:Sm^{3+}$ prepared by solution combustion synthesis (SCS);

J. Spectrosc., 3413864 (2018);

ИФ: 1.391

3. M. Nikolić, M. S. Rabasović, J. Križan, **S. Savić-Šević**, M. D. Rabasović, B. Marinković, A. Vlasić and D. Šević;

Luminescence thermometry using $Gd_2Zr_2O_7:Eu^{3+}$;

Opt. Quant. Electron. 50, 258 (2018);

ИФ: 1.547

Радови објављени након претходног избора у звање (M23)

4. D. Šević, **S. Savić-Šević**, D. Pantelić, B. Marinković,

“Application of Fourier Pade Approximation in Analysis of Holographic Diffraction Gratings,”

Acta Physica Polonica A, 124, 619-621 (2013).

ИФ: 0.604

Радови објављени пре претходног избора у звање (M23)

1. Т. Пушкар, Д. Васиљевић, Д. Марковић, Д. Јевремовић, Д. Пантелић, **С. Савић-Шевић**, Б. Мурић,

“Формирање тродимензионалног математичког модела зуба методом коначних елемената”

Срп Арк Целок Lek. 138(1-2),19-25 (2010)

ИФ: 0.194

5.5 ЗБОРНИЦИ СА МЕЂУНАРОДНИХ НАУЧНИХ СКУПОВА (M 30)

Зборници објављени након претходног реизбора у звање (M31)

1. **S. Savić-Šević**, B. Salatić, D. Pantelić, B. Jelenković, S. Čurčić, D. Stojanović,

“Optical Properties of Volume Gratings with Nanosphere-Filled Layers-Biomimetics of Moth Structures”

19th International Conference on Transparent Optical Networks (ICTON), 2017, Girona, Spain

Tu.B4.1

Зборници објављени након претходног избора у звање (M31)

2. **S. Savić-Šević**, D. Pantelić, B. Jokić, B. Jelenković

“Holographic Photonic Structures Generated in Dichromated Pullulan”,

15th International Conference on Transparent Optical Networks (ICTON), 2013, Cartagena, Spain, Tu.C5.2

3. **S. Savić-Šević**, D. Pantelić, D. Grujić, B. Jelenković, S. Čurčić, B. Čurčić, D. Stojanović

“Localization of light in photonic crystals of biological origin”,

14th International Conference on Transparent Optical Networks (ICTON), 2012, Coventry, United Kingdom, We.A6.5

Зборници објављени пре претходног избора у звање (M31)

1. **S. Savić-Šević**, D. Pantelić, S. Curčić , B. Ćurčić, and B. Jelenković
“Biologically Inspired Photonic Structures in Dichromated Pullulan“,
13th International Conference on Transparent Optical Networks (ICTON), 2011, Stockholm,
Tu.D2.2

2. **S. Savić Šević**, D. Pantelić, B. Jelenković
“Holographic Photonic Structures Generated in Dichromated Pullulan“,
12th International Conference on Transparent Transparent Transparent Optical Networks
(ICTON), Munich, 2010.We.A2.6

Зборници објављени након претходног избора у звање (M32)

1. D. Pantelić, **S. Savić-Šević**, Z. Jakšić, B. Vasić, B. Jokić, S. Ćurčić, V. Pavlović, V. Lačković, M. Labudović-Borović, D. Stojanović
“Nanophotonics of insects“, Processing, characterisation and application of nanostructured materials and nanotechnology,
the First international conference Nanobelgrade 2012, p 39

Зборници објављени пре претходног избора у звање (M32)

1. D. Pantelić, **S.Savić-Šević**, B. Jelenković, S.Ćurčić, B.Ćurčić
“Holografically generated photonic structures – Analogy to bioinspired structures“,
Second International Workshop Characterization, properties and applications of nanostructured ceramics, polymers and composites, Belgrade 2011.

2. **S. Savic**, Dejan Pantelic, Dragica Jakovljevic
“Dichromated pullulan: real-time effects and holographic properties“
International Conference Optical Holography and its Applications, Kiev, Ukraine, 2000.

Зборници објављени пре претходног избора у звање (M33)

1. V. Damljanovic, **S. Savic-Ševic**, D. Pantelic, B. Jelenkovic
“On the Reflectivity of One-Dimensional Photonic Crystal Realized in Dichromated Pullulan“,
12th International Conference on Transparent Optical Networks (ICTON), Munich, 2010. Mo.P.5

2. **S. Savić Šević**, D. Pantelić, B. Jelenković,
“Holographic 1D Photonic Crystals in Dichromate Pullulan“,
11th International Conference on Transparent Optical Networks (ICTON), 2009, Azores,
We.P.22

3. **S. Savić-Šević**, Dejan Pantelić and Branislav Jelenković,
“Multi-Peak Structure of Photonic Band Gaps on Dichromated Pullulan“,

3rd Mediterranean Winter Conference, ICTON-MW 2009, Angers, FrP.5.

4. **S. Savic-Sevic**, D. Pantelic and B. Jelenkovic

“Influence of the Heat Treatment on the Band Gaps in the Biopolymer Photonic Crystals”
ACTA PHYSICA POLONICA A 16 645-646 (2009)

5. D. Sevic, **S. Savic-Sevic**, D. Pantelic, B. Jelenkovic and B.P. Marinkovic

“Application of Fourier–Padé Approximation in Analysis of Holographic Photonic Crystal Structures”
ACTA PHYSICA POLONICA 116, 647-648 (2009)

6. M.S. Rabasović, D. Šević, M. Terzić, **S.Savić-Šević**, B. Murić, D. Pantelić and B.P. Marinković,
“Measurement of beet root extract fluorescence using TR-LIF technique,”
Acta Phys. Pol., 116, 570-572 (2009).

7. **S. Savić-Šević**, D. Pantelić, B. Jelenković,

“Influence of chemical processing on the band gaps in dichromated pullulan photonic crystals”,
Physical chemistry 2008, Proceedings, Volume II, of the 9th International Conference on
Fundamental and Applied Aspects of Physical Chemistry, pp. 533-535.

8. **S.Savic-Sevic**, D. Pantelic, R. Gajic and G. Isic,

“Holographic Fabrication of Periodic Microstructures in Dichromated Pullulan”
ACTA PHYSICA POLONICA A 112 (5) 079-1082 (2007)

9. D.Pantelic, L.Blazic, **S. Savic-Sevic**, B. Muric, D. Vasiljevic, B. Panic, I. Belic,

“Holographic Measurement of Dental Tissue Contraction and Stress, due to Postpolymerization
Reaction”
ACTA PHYSICA POLONICA A 112 (5) 1157-1160 (2007).

10. S. Savić, D. Pantelić, D. Jakovljević,

“Atmospheric stability of dichromated pullulan holographic gratings”,
Physical chemistry 2002, Proceedings, Volume II, of the 6th International Conference on
Fundamental and Applied Aspects of Physical Chemistry, pp. 535-537.

Зборници објављени након претходног реизбора у звање (M34)

1. **S. Savic-Sevic**, D. Pantelic, B. Jelenkovic;

“Interplay between ordered multilayer structure and randomly distributed nanospheres and
nanopillars in dichromated pullulan increases the width of the photonic bandgap”;
VIII International School and Conference on Photonics, 2021, Belgrade, Serbia, Book of
abstracts, p. 92

2. D. Pavlović, B. Salatić, **S. Savić-Šević**, N. Vesović, D. Pantelić;

“Natural waveguides on *Hoplia argentea* elytra“;

VIII International School and Conference on Photonics, 2021, Belgrade, Serbia, Book of abstracts, p. 99;

3. E. Novta, T. Lainović, **S. Savić-Šević**, D. Grujić, D. Pantelić, L. Blažić;

“Influence of light guide type on dental composite polymerization shrinkage – a holographic and thermographic study“;

VIII International School and Conference on Photonics, 2021, Belgrade, Serbia, Book of abstracts, p. 102;

4. D. Šević, M. S. Rabasović, J. Krizan, **S. Savić-Šević**, M. D. Rabasović, M. Nikolić and B. Marinković;

“Using SOLO software package for classification of temperature dependent luminescence spectra“;

VIII International School and Conference on Photonics, 2021, Belgrade, Serbia, Book of abstracts, p. 171;

5. D. Sević, M. S. Rabasović, J. Krizan, **S. Savić-Šević**, M. D. Rabasović, B. Marinković, M. Nikolić;

“Effects of laser heating on luminescent properties of $Gd_2O_3: Er, Yb$ nanophosphor“;

VIII International School and Conference on Photonics, 2021, Belgrade, Serbia, Book of abstracts, p. 137;

6. **S. Savić-Šević**, D. Pantelić, B. Murić, D. Grujić, D. Vasiljević, B. Kolaric, B. Jelenković;

“Negative thermal expansion of pullulan multilayers“;

VII International School and Conference on Photonics, 2019, Belgrade, Serbia, Book of abstracts, p. 113;

7. D. Šević, M. S. Rabasović, J. Križan, **S. Savić-Šević**, M. D. Rabasović, B. Marinković, M. Nikolić;

“Revealing the optical response of *Stegastes apicalis* fin parts using fluorescence spectroscopy“;

VII International School and Conference on Photonics, 2019, Belgrade, Serbia, Book of abstracts, p. 99;

8. M. Nenadić, A. Krmpot, N. Vesović, M. Rabasović, S. Ćurčić, D. Pavlović, V. Lačković, **S. Savić-Šević**, D. Pantelić;

“Assessment of three microscopic techniques in observing morphology of pygidial glands of ground beetles“;

Electron Microscopy of Nanostructures ELMINA2018 Conference, Belgrade, Serbia, FIRST INTERNATIONAL CONFERENCE ON ELECTRON MICROSCOPY OF NANOSTRUCTURES, Book of Abstracts, p. 252-254.

9. **S. Savić-Šević**, D. Pantelić, V. Damljanović, B. Jelenković,

“Bifurcation in reflection spectra of holographic pullulan diffraction grating“

VI International School and Conference on Photonics, 2017, Belgrade, Serbia, Book of abstracts, p. 90

10. G. Isić, U Ralević, S Aškračić^{1a}, S Graovac, **S Savić-Šević**, A Mikhailov, A Antanovich, A Prudnikau, M Artemyev, I Fabijanić, V Janicki, B Okorn, J Sancho-Parramon, R Gajić
“Film-coupled silver nanoparticles on flat and periodically corrugated aluminium substrates”
VI International School and Conference on Photonics, 2017, Belgrade, Serbia, Book of abstracts, p. 193

11. M. Nikolic, M.S. Rabasovic, J. Krizan, **S. Savić-Sevic**, M.D. Rabasovic, B.P. Marinkovic, A. Vlastic D. Sevic
“Luminescence thermometry using $Gd_2Zr_2O_7:Eu^{3+}$ ”
VI International School and Conference on Photonics, 2017, Belgrade, Serbia, Book of abstracts,

12. **S. Savić-Šević**, D. Pantelić, D. Grujić, B. Jelenković,
“Localization of light in a polysaccharide-based complex nanostructure,”
V International School and Conference on Photonics, 2015, Belgrade, Serbia, Book of abstracts, p. 190.

Зборници објављени након претходног избора у звање (M34)

13. A. Kovačević, S. Petrović, P. Panjan, V. Lazović, D. Peruško, **S. Savić-Šević**, D. Pantelić, B. Jelenković
“Inducing nanoparticles and periodic nanostructures on thin metal films”,
4th International Workshop on Ultrafast Nanooptics (UNO-4), 2015, Bad Durkheim, Book of abstracts, p. 55

14. **S. Savić-Sevic**, D. Pantelic and B. Jelenkovic
“Nanostructures fabricated by combining holographic method and self-assembly”,
IV International School and Conference on Photonics, 2013, Belgrade, Serbia, Book of abstracts, p. 152

15. D. Pantelić, **S. Savić-Šević**, D. Grujić,
“Zoom system for measurement of coherent backscattering of light in micro- and nanomaterials,”
The 3rd International Conference on the Physics of Optical Materials and Devices-ICOM 2012, Belgrade, Serbia, Book of abstracts p. 111.

16. D. Pantelić, D. Vasiljević, L. Blažić, **S. Savić-Šević**, B. Murić, M. Nikolić
“Biomechanical models produced from light-activated dental composite a holographic analysis,” The 3rd International Conference on the Physics of Optical Materials and Devices-ICOM 2012, Belgrade, Serbia, Book of abstracts p. 148.

17. Z. Jakšić, D. Pantelić, M. Sarajlić, S. Savić-Šević, J. Matović, B. Jelenković, D. Vasiljević-Radović, S. Ćurčić, S. Vuković, V. Pavlović,
“Butterfly scales as bionic templates for complex ordered nanophotonic materials”
The 3rd International Conference on the Physics of Optical Materials and Devices-ICOM 2012, Belgrade, Serbia, Book of abstracts p. 131.

Зборници објављени пре претходног избора у звање (M34)

1. **S. Savić-Sevic**, D. Pantelic and B. Jelenkovic,
“Tunability of band gaps in the biopolymer photonic crystals”
III International School and Conference on Photonics, 2011, Belgrade, Serbia, Book of abstracts, p. 137.

2. T. Puskar, D.Vasiljevic, L. Blazic, D. Markovic, **S. Savić-Sevic**, B. Muric, D. Pantelic
“Stress and strain of dental abutment caused by the polymerization shrinkage of dental composite,”
III International School and Conference on Photonics, 2011, Belgrade, Serbia, Book of abstracts, p.118.

3. D. Pantelić, **S. Savić-Šević**, V. Damljanović, B. Jelenković
“Holographic generation of wide bandgap structures”
3rd Mediterranean Conference on Nanophotonics, 2010, Belgrade, Serbia, Book of abstracts, p. 33.

4. V. Damljanović, **S. Savić-Šević**, D. Pantelić, B. Jelenković
“On the appearance of multiple peaks in the reflectivity of one-dimensional photonic crystals”
3rd Mediterranean Conference on Nanophotonics, 2010, Belgrade, Serbia, Book of abstracts, p. 71.

5. D. Pantelić, S. Ćurčić, **S. Savić-Šević**, A. Korać, B. Jelenković, B. Ćurčić
“Photonic properties of the lesser purple emperor butterfly (*Apatura ilia*),
”3rd Mediterranean Conference on Nanophotonics, 2010, Belgrade, Serbia, Book of abstracts, p. 94.

6. **S. Savić-Sevic**, D. Pantelic, B. Jelenkovic
“Influence of the Heat Treatment on the Band Gaps in the Biopolymer Photonic Crystals”
II International School and Conference on Photonics, 2009, Belgrade, Serbia, Book of abstracts, p. 124.

7. D. Sevic, **S. Savić-Sevic**, D. Pantelic, B. Jelenkovic, B. Marinkovic,
“Application of Fourier–Padé Approximation in Analysis of Holographic Photonic Crystal Structures”
II International School and Conference on Photonics, 2009, Belgrade, Serbia, Book of abstracts, p.125

8. M.S. Rabasović, D. Šević, M. Terzić, **S. Savić-Šević**, B. Murić, D. Pantelić, B. Marinković, "Measurement of betanin fluorescence using TR-LIF technique," II International School and Conference on Photonics, 2009, Belgrade, Serbia, Book of abstracts, p. 91.
9. **S. Savić-Sevic**, D. Pantelic, B. Jelenkovic "Optical properties of one-dimensional photonic crystals in dichromated pullulan" 2nd International conference on physics of optical materials and devices, ICOM 2009, Herceg Novi, Montenegro, Book of abstracts, p.125.
10. D. Šević, **S. Savić Šević**, D. Pantelić, B. Marinković, "Application of Fourier-Padé Approximation in Analysis of Materials for Optical Applications", Proc. 2nd International Conference on Physics of Optical Materials and Devices (ICOM 2009), Herceg Novi, Montenegro, Book of Abstracts, p.128.
11. M. Terzić, M. S. Rabasović, D. Ševic, **S. Savić Šević**, B. Murić, D. Pantelić, B. P. Marinković, "Measurement of Laser-Induced Fluorescence of Optical Materials Using a Time-Resolved Spectrometer", Proc. 2nd International Conference on Physics of Optical Materials and Devices (ICOM 2009), Herceg Novi, Montenegro, Book of Abstracts, p.129.
12. B. A. Petruševski, M. Terzić, M. S. Rabasović, D. Šević, **S. Savić Šević**, B. Murić, D. Pantelić, B. P. Marinković, "Measurement of laser-induced fluorescence of molecules using a time-resolved spectrometer," The Second Meeting of COST Action CM0601 Electron Controlled Chemical Lithography-ECCL, 2009, Istanbul, Turkey, Book of abstracts, p. 83.
13. T. Puškar, D. Jevremović, L. Blažić, D. Pantelić, D.Vasiljević, **S. Savić-Šević**, B.Murić "Stress and strain of abutment teeth due to composite core build up shrinkage," 14th Congress of Balkan Stomatological Society, 2009, Varna Bulgaria OP037, Book of abstracts, p. 31.
14. **S. Savić-Šević**, D. Pantelić, M. Nikolić, B. Jelenković, "Band-Gap Photonic Structures in Dichromate Pullulan," Tenth annual conference YUCOMAT, Herceg Novi, Montenegro 2008, Programme and the book of abstracts,
15. D. Pantelić, **S. Savić-Šević**, D. Vasiljević, B. Murić, L. Blažić, M. Nikolić, B.Panić, "Holographic measurement of dental composite contraction" Tenth annual conference YUCOMAT, Herceg Novi, Montenegro 2008, Programme and the book of abstracts, p. 57.
16. **S. Savić-Šević**, D. Pantelić, B. Jelenković,

“Experimental measurement of photonic bands gaps in holographic photonic crystals”,
15th Central European Workshop on Quantum Optics, CEWQO, Belgrade, 2008, Book of Abstracts, p. 89.

17. **S. Savic-Sevic** S, D. Pantelic, R. Gajic, G. Isic, “Holographic Fabrication of Periodic Microstructures in Dichromated Pullulan”, International School and Conference on Optics and Optical Materials-ISCOM, Belgrade 2007, Book of abstracts, p. 130.

18. D. Pantelić, L. Blažić, **S. Savić-Šević**, B. Murić, D. Vasiljević, B. Panić, I. Belić, “Holographic measurement of dental tissue contraction and stress, due to postpolymerization reaction, ”International School and Conference on Optics and Optical Materials-ISCOM, Belgrade 2007, Book of abstracts, p. 74.

19. **S. Savić Šević**, D. Pantelić,
“Biopolymer holographic diffraction gratings”,
ICOM **2006**, International conference on physics of optical materials and devices, book of abstracts, pp. 41

5.6 ЗБОРНИЦИ СКУПОВА НАЦИОНАЛНОГ ЗНАЧАЈА (M50)

Радови објављени након претходног реизбора у звање (M52)

1. D. Šević, A. Vlasić, M. S. Rabasović, **S. Savić-Šević**, M. D. Rabasović, M. Nikolić, B. Murić, B. Marinković, J. Križan;
“Temperature effects on luminescent properties of Sr₂CeO₄:Eu³⁺ nanophosphor: a machine learning approach”;
Tehnika 75, 279-283 (2020)

2. Branka Muric, D. Pantelic, D. Vasiljevic, **S. Savic-Sevic**, B. Jelenkovic
“Application of tot’hema eosin sensitized gelatin film for adaptive microlenses”
Tehnika 72, 787-792 (2017)

5.7 ЗБОРНИЦИ СКУПОВА НАЦИОНАЛНОГ ЗНАЧАЈА (M 60)

Зборници објављени након претходног реизбора у звање (M61)

1. D. Pantelic, S. Curcic, A. Krmpot, D. Stojanovic, M. D. Rabasovic, **S. Savic-Sevic**;
“The Morphological Structures of Some Representatives of the Entomofauna of Serbia as Models in Biomimetics”;
ECOLOGICAL AND ECONOMIC SIGNIFICANCE OF FAUNA OF SERBIA, **171**, 231-250, (2018);

Зборници објављени пре претходног избора у звање (M61)

1. Dejan Pantelić, Svetlana Savić Šević, "Primena holografije i interferometrije u biomedecinskim istraživanjima", XI Kongres fizicara Srbije i Crne Gore, Petrovac na Moru, 3-5 jun, 2004, Zbornik radova, str. 8.1-8.9.

Zbornici objavljeni nakon prethodnog izbora u zvanje (M63)

1. Zoran Jakšić, Dejan Pantelić, Milija Sarajlić, **Svetlana Savić-Šević**, Jovan Matović, Branislav Jelenković, Dana Vasiljević-Radović, Srećko Ćurčić, Slobodan Vuković, Vladimir Pavlović, Jelena Buha

"Design considerations for using butterfly wing scales as biological nanoarchitectural building blocks for plasmonic structures,"

56. konferencija ETRANA, Zlatibor, 11-14 juna 2012, Zbornik radova, MO2.3-1-4.

Zbornici objavljeni pre prethodnog izbora u zvanje (M63)

1. Svetlana Savić-Šević, Dejan Pantelić, "Holografsko generisanje jednodimenzionog fotonickog kristala u dihromiranom pululanu", 52. konferencija ETRANA, Palic, 5-7 juna 2008, Zbornik radova, MO3.3-1-2.

2. Svetlana Savić Šević, Dejan Pantelić "Dvodimenzionalne holografске difrakcione resetke i njihovo kopiranje u kompozitne materijale", 51. konferencija ETRANA, Herceg Novi, 4-8 juna 2007, Zbornik radova, MO4.4.

3. Svetlana Savić Šević, Dejan Pantelić, "Reljefno fazni hologrami zapisani na dihromiranom pululanu", 49. konferencija ETRANA, Budva, 5-7 juna 2005, Zbornik radova, sveska IV, str. 167-169.

4. Dušan Vukić, Marko Živković, Svetlana Savić Šević, Dejan Pantelić, "Projektovanje i izrada holografskog stereograma", 49. konferencija ETRANA, Budva, 5-7 juna 2005, Zbornik radova, sveska IV, str. 164-166

5. Dejan Pantelić, Larisa Blazić, Svetlana Savić Šević, Bratimir Panić "Holografsko merenje deformacije zuba nakon polimerizacije zubne ispune", Kongres metrologa 2005, Zbornik radova, 18.-20. maj 2005, str.266-271

6. Dejan Pantelić, Svetlana Savić Šević, Ilija Belić, Bratimir Panić, "Primena holografskih metoda u ispitivanju mehaničkih deformacija i opterećenja", Jupiter (2005), Zlatibor, Zbornik radova str. 3.64

7. Svetlana Savić Šević, "Razvijanje holografске rešetke na dihromiranom pululanu u realnom vremenu", XLVIII konferencija ETRANA, Čačak, 6-10 juna 2004, Zbornik radova, sveska IV, str. 237-238

8. Svetlana Savić Sević i Dejan Pantelić “Kopiranje površinskih holografskih rešetki u fotopolimernim materijalima”, I Kongres fizicara Srbije i Crne Gore, Petrovac na Moru, 3-5 jun, 2004. Zbornik radova, str. 2.87-2.90
9. Svetlana Savić, Dejan Pantelić “Using dichromated pullulan in holographic products protection”, Applied Physics in Serbia-APS, Belgrade 20002, pp. 179-182
10. Svetlana Savić, Dragica Jakovljević, “Merenje debljine tankih holografskih slojeva”, XLV konferencija ETRANA, Bukovicka Banja, Arandjelovac, Juna 2001, Zbornik radova, sveska IV, str. 314-316
11. Svetlana Savić, Dejan Pantelić, Dragica Jakovljević, “Holografska svojstva dihromiranog dekstrana i njihovo poređenje sa svojstvima dihromiranog pululana”, XLIV konferencija ETRANA, Sokobanja, Juna 2000, Zbornik radova, sveska IV, str. 384-386
12. Svetlana Savić, Dejan Pantelić, Dragica Jakovljević, “Holografske difrakcione rešetke na dihromiranom pululanu”, 10. Kongres fizičara Jugoslavije, Vrnjačka Banja 27-29. Marta 2000, Zbornik radova, knjiga I, str. 119-122
13. Svetlana Savić, Dejan Pantelić, Dragica Jakovljević “Merenje holografskih osobina dihromiranog pululana u realnom vremenu, XLIII konferencija ETRANA, Zlatibor, Septembra 1999, Zbornik radova, sveska IV, str. 217-219
14. Svetlana Savić, Dejan Pantelić, Dragica Jakovljević “Bihromirani pululan- novi holografski materijal”, XLII konferencija za ETRAN, Vrnjačka Banja, 2- 5. Juna 1998, Zbornik radova, sveska IV, str. 425-427
15. Dejan Pantelić, Svetlana Savić “A Simple Optical System with Peculiar Fourier Transform Properties”, XLI konferencija ETRANA, Zlatibor, 3-6. Juna 1997., Zbornik radova, sveska 2, str. 522-525

Zbornici objavljeni nakon prethodnog reizbora u zvađe (M64)

1. D. Pavlovic, **S. Savic-Sevic**, B. Salatic, D. Pantelic,
“Synergy of interference, scattering and pigmentation for structural coloration of *Jordanita globulariae* moth”; *Proc. 15th Photonics Workshop*, March 13-16, 2022, Kopaonik, Book of Abstracts, Oral presentation, p. 54
2. **S. Savic-Sevic**, D. Pantelic, V. Lazovic, B. Jelenkovic;
“Bio-inspired materials with low angle dependence structural colors“;
Proc. 14th Photonics Workshop, March 14-17, 2021, Kopaonik, Book of Abstracts, Oral presentation p. 34;

3. D. Šević, M. S. Rabasović, J. Križan, **S. Savić-Šević**, M. Nikolić, B. Marinković;
“Host effects on luminescent properties of Er, Yb doped nanophosphors“;
Proc. 14th Photonics Workshop, March 14-17, 2021, Kopaonik, Book of Abstracts, Oral presentation p. 24;
4. S. Savić-Šević, D. Pantelic, B. Muric, D. Vasiljevic, B. Kolaric, Branislav Jelenković
“Negative thermal expansion in nanolayered pullulan“
Proc. 13th Photonics Workshop, Kopaonik, 8-12 March 2020, Book of Abstracts, Oral presentation p.42;
5. D. Šević, M. S. Rabasović, J. Križan, **S. Savić-Šević**, M. D. Rabasović, M. Nikolić and B. Marinković;
“Machine learning for laser induced fluorescence spectroscopy“;
Proc. 13th Photonics Workshop, Kopaonik, 8-12 March 2020, Book of Abstracts, Oral presentation p. 18;
6. **S. Savić-Šević**, D. Pantelic, B. Jelenković, B. Salatić, D. V. Stojanović
“Origin and biomimicry of golden color in moth“
Proc. 12th Photonics Workshop, Kopaonik, 11-14 March 2019, Book of Abstracts, Oral presentation, p. ;
7. D. Šević, M. S. Rabasović, J. Križan, **S. Savić-Šević**, M. D. Rabasović, B. Marinković, M. Nikolić;
“Effects of temperature on luminescent properties of Gd₂O₃: Er, Yb nanophosphor“;
Proc. 12th Photonics Workshop, Kopaonik, 11-14 March 2019, Book of Abstracts, Oral presentation, p. 43;
8. D. Šević, M. S. Rabasović, J. Križan, **S. Savić-Šević**, M. Nikolić, B. Marinković, M. D. Rabasović;
“Effects of temperature on luminescent properties of YVO₄:Eu³⁺ nanophosphor“;
Proc. 11th Photonics Workshop, Kopaonik, 11-14 March 2018, Book of Abstracts, Oral presentation, p. 26;
9. Aleksander Kovačević, Suzana Petrović, Marina Lekić, Davor Peruško, Vladimir Lazović, Svetlana Savić-Šević, Borislav Vasić, Branislav Salatić, Radoš Gajić, Dejan Pantelić, Branislav Jelenković;
“Formation of LIPSS on Al/Ti thin metal films by scanning of low-fluence femtosecond beam during cross-directional scanning“;
Proc. 11th Photonics Workshop, Kopaonik, 11-14 March 2018, Book of Abstracts, Oral presentation, p. 34;
10. Marina Lekić, Aleksander Kovačević, Suzana Petrović, Davor Peruško, Vladimir Lazović, Svetlana Savić-Šević, Borislav Vasić, Branislav Salatić, Radoš Gajić, Dejan Pantelić, Branislav Jelenković;
“Formation of LIPSS on Al/Ti thin metal films by scanning of low-fluence femtosecond beam during multi-pass scanning“;

Proc. 11th Photonics Workshop, Kopaonik, 11-14 March 2018, Book of Abstracts, Oral presentation, p. 35

Zbornici objavljeni nakon pretходног избора у звање (M64)

10. Svetlana Savić-Šević, Dejan Pantelić, Dušan Grujić, Branislav Jelenković “Ordered multilayer structure with randomly distributed nanospheres and nanopillars,” Osmo radionica fotonike, Kopaonik, 8-12 marta, 2015, Zbornik apstrakata, p 23.

11. Svetlana Savić-Šević, Dejan Pantelić, Branislav Jelenković “Kompleksne fotonske structure u biopolimeru,” Sedma radionica fotonike, Kopaonik, 10-14 marta, 2014, Zbornik apstrakata, p 2.

12. Svetlana Savić-Šević, Dejan Pantelić, Branislav Jelenković “Hetero-strukture generisane kombinacijom holografske metode i samouredjivanja,” Šesta radionica fotonike, Kopaonik, 4-8 marta, 2013, Zbornik apstrakata, p 19.

13. Svetlana Savić-Šević, Dejan Pantelić, Branislav Jelenković “Температурне особине фотонског кристала,” Peta radionica fotonike, Kopaonik, 10-14 marta, 2012, Zbornik apstrakata, p 42.

14. Дејан Пантелић, Светлана Савић-Шевић, Срећко Ђурчић, Владимир Павловић, Весна Лачковић, Милица Лабудовић-Боровић, “Дифракција у визуелном систему инсеката,” Peta radionica fotonike, Kopaonik, 10-14 marta, 2012, Zbornik apstrakata, p7.

Zbornici objavljeni pre pretходног избора у звање (M64)

1. S. Savic-Sevic, D. Pantelic and B. Jelenkovic “Fotonske structure u pullulanu”, Četvrta radionica fotonike, Kopaonik, 2-6 marta, 2011, Zbornik apstrakata, p21.

2. Srećko Ćurčić, Dejan Pantelić, Božidar Ćurčić, Svetlana Savić-Šević, Slobodan Markov, Vesna Lačković, Milica Labudović-Borović, Nina Ćurčić, Dejan Stojanović, “Mikro i nanostrukture iridescenčnih ljušpica krila leptira prelivača (Lepidoptera: Apatuta Ilia i A. Iris)”, Simpozijum entomologa Srbije 2011, Donji Milovanovac, 21- 25 IX 2011, p.79

3. S. Savic-Sevic, V. Damljanovic, D. Pantelic and B. Jelenkovic, “Fenomen visestrukih maksimuma u refleksionom spektru i sirenja energetskog procepa”, FOTONIKA 2010-teorija i eksperiment u Srbiji, Beograd 2010, Zbornik apstrakata, p24.

4. Tatjana Puškar, D. Vasiljević L. Blažić, D. Pantelić, D. S. Savić-Šević, B. Murić, D. Marković i Ivana Kantardžić “Primena holografske interferometrije za ispitivanje deformacije tvrdih zubnih tkiva prilikom terapije zuba svetlosno polimerizujućim kompozitnim materijalima”, FOTONIKA 2010-teorija i eksperiment u Srbiji, Beograd 2010, Zbornik apstrakata, p3.

5. S. Savic-Sevic, D. Pantelic and B. Jelenkovic "Jednodimenzioni fotonicni kristali u dihromiranom pululanu ," FOTONIKA 2009-teorija i eksperiment u Srbiji, Beograd 2009, Zbornik apstrakata, p24.

6. Darko Vasiljević, Tanja Puškar, Dejan Pantelić, Svetlana Savić-Šević, Branka Murić, Bratimir Panić, "Uprošćeni matematički model zubnog patrljka za analizu deformacija i napona," FOTONIKA 2009-teorija i eksperiment u Srbiji, Beograd 2009, Zbornik apstrakata, p8.

7. Tatjana Puškar, L. Blažić, D. Pantelić, D. Vasiljević, S. Savić-Šević, B. Murić, D. Marković, "Holografska interferometrija u stomatološkoj protetici," XV simpozijum protetičara Srbije, Palić, 12-15. juna 2008, Kratki sadržaji predavanja i postera, p. 44.

6. МАГИСТАРСКЕ И ДОКТОРСКЕ ТЕЗЕ (М 70)

М 72

Holografske osobine pululana

Fizički fakultet, Beograd, (1999)

М 71

Fizičke osobine difrakcionih rešetaka na novim dihromiranim materijalima Fizički fakultet, Beograd, (2007)

Република Србија
МИНИСТАРСТВО ПРОСВЕТЕ,
НАУКЕ И ТЕХНОЛОШКОГ РАЗВОЈА
Комисија за стицање научних звања

Број:660-01-00006/79
27.09.2017. године
Београд

МИНИСТАРСТВО ПРОСВЕТЕ, НАУКЕ И ТЕХНОЛОШКОГ РАЗВОЈА			
ПРИМЉЕНО: 26-10-2017			
Рад.јед.	б р о ј	Арх.шифра	Прилог
р/р/1	1456/1		

На основу члана 22. став 2. члана 70. став 5. и члана 86. ст. 1. и 2. Закона о научноистраживачкој делатности ("Службени гласник Републике Србије", број 110/05 и 50/06 – исправка, 18/10 и 112/15), члана 3. ст. 1. и 3., члана 32. став 1., члана 35. став 2. и члана 40. Правилника о поступку, начину вредновања и квантитативном исказивању научноистраживачких резултата истраживача ("Службени гласник Републике Србије", број 24/16, 21/17 и 38/17) и захтева који је поднео

Инстџиџуџ за физику у Беоџраду

Комисија за стицање научних звања на седници одржаној 27.09.2017. године, донела је

**ОДЛУКУ
О СТИЦАЊУ НАУЧНОГ ЗВАЊА**

Др Свеџлана Савић Шевић

стиче научно звање
Виши научни сарадник
Реизбор

у области природно-математичких наука - физика

О Б Р А З Л О Ж Е Њ Е

Инстџиџуџ за физику у Беоџраду

утврдио је предлог број 179/1 од 07.02.2017. године на седници Научног већа Института и поднео захтев Комисији за стицање научних звања број 198/1 од 13.02.2017. године за доношење одлуке о испуњености услова за реизбор у научно звање **Виши научни сарадник**.

Комисија за стицање научних звања је по претходно прибављеном позитивном мишљењу Матичног научног одбора за физику на седници одржаној 27.09.2017. године разматрала захтев и утврдила да именована испуњава услове из члана 70. став 5. и члана 86. ст. 1. и 2. Закона о научноистраживачкој делатности ("Службени гласник Републике Србије", број 110/05 и 50/06 – исправка, 18/10 и 112/15), члана 3. ст. 1. и 3., члана 32. став 1., члана 35. став 2. и члана 40. Правилника о поступку, начину вредновања и квантитативном исказивању научноистраживачких резултата истраживача ("Службени гласник Републике Србије", број 24/16, 21/17 и 38/17) за реизбор у научно звање **Виши научни сарадник**, па је одлучила као у изреци ове одлуке.

Доношењем ове одлуке именована стиче сва права која јој на основу ње по закону припадају.

Одлуку доставити подносиоцу захтева, именованој и архиви Министарства просвете, науке и технолошког развоја у Београду.

ПРЕДСЕДНИК КОМИСИЈЕ

Др Станислава Стошић-Грујичић,
научни саветник

С. Стошић-Грујичић



Младен Шарчевић

IZJAVA

Ovim izjavljujem da je Svetlana Savić-Šević rukovodila zadatkom „holografska mimetika insekata“, u okviru projekta „Holografske metode generisanja specifičnih talasnih frontova za efikasnu kontrolu kvantnih koherentnih efekata u interakciji atoma i lasera“ (ON171038). U okviru ove teme razvila je holografsku metodu za generisanje nanostrukture sličnih onima kod leptira, koristeći dihromirani pululan kao fotoosetljivi materijal. Ovakvi hologrami imaju zanimljive primene u generisanju specifičnih talasnih frontova.



Dr Dejan Pantelić

Rukovodilac projekta ON171038

Institut za fiziku

УНИВЕРЗИТЕТ У НОВОМ САДУ
МЕДИЦИНСКИ ФАКУЛТЕТ НОВИ САД
НАСТАВНО-НАУЧНО ВЕЋЕ
Број: 05-14/42-2022/4 (41-2022/4-4.1)
Дана: 11. 02. 2022. године
Нови Сад

На основу члана 65. Закона о високом образовању („Сл. гласник РС“ бр. 88/2017, 27/2018-други закон, 73/2018, 67/2019, 6/2020-др. закон, 11/2021-аутентично тумачење, 67/2021 и 67/2021-др. закон), члана 20. ст. 1. *Правила докторских студија Универзитета у Новом Саду* (Сенат Универзитета, бр. 01-134/3 од 25. 02. 2021. године), члана 157. *Статута Медицинског факултета Нови Сад* бр. 02-1260 од 02. 04. 2019. године и члана 44. ст. 1 *Правилника о стицању научног назива доктора наука на Медицинском факултету Нови Сад* од 16. 07. 2021. године и 14. 09. 2021. године-пречишћен текст, на 42. електронској седници Наставно-научног већа, одржаној од 10. 02. 2022. године, од 08 часова до 11. 02. 2022. године, до 14 часова, од укупно 49 чланова са правом одлучивања, од којих је, у наведеном периоду, гласало 39 чланова а није гласало 10 чланова, са 39 гласова „за“ једногласно је донето

РЕШЕЊЕ

Констатује се да је Сенат Универзитета у Новом Саду дао сагласност **Евгенију Новти** за израду докторске дисертације под насловом: „Утицај светлосних водича на својства полимерizacione реакције денталних композитних материјала“.

Др Тијана Лаиновић, научни сарадник (Медицински факултет Нови Сад, Универзитет у Новом Саду) и др Светлана Савић Шевић, виши научни сарадник (Институт за физику Београд), именују се за менторе наведеном кандидату.

Доставити:
-Служби за докторске студије и специјализације
-кандидату
-менторима
-архиви



ПРЕДСЕДНИК НАСТАВНО-НАУЧНОГ ВЕЋА

Проф. др Снежана Бркић, декан

02
Године

Univerzitet u Novom Sadu
Medicinski fakultet Novi Sad
Katedra za stomatologiju
Hajduk Veljkova 3
Novi Sad

01-36/1-2011

POTVRDA

Potvrđuje se da je dr Svetlana Savić-Šević, sa Instituta za fiziku u Beogradu, rukovodila eksperimentom sprovedenim u okviru izrade doktorske disertacije doc. dr Tatjane Puškar sa Medicinskog fakulteta u Novom Sadu. Doktorska disertacija pod naslovom "Holografsko ispitivanje deformacije zubnog patrljka endodontski lečenog zuba u toku pripreme za protetičku krunu", odbranjena je na Medicinskom fakultetu u Novom Sadu 3. jula 2009. godine.

U Novom Sadu, 22.11.2011.g.

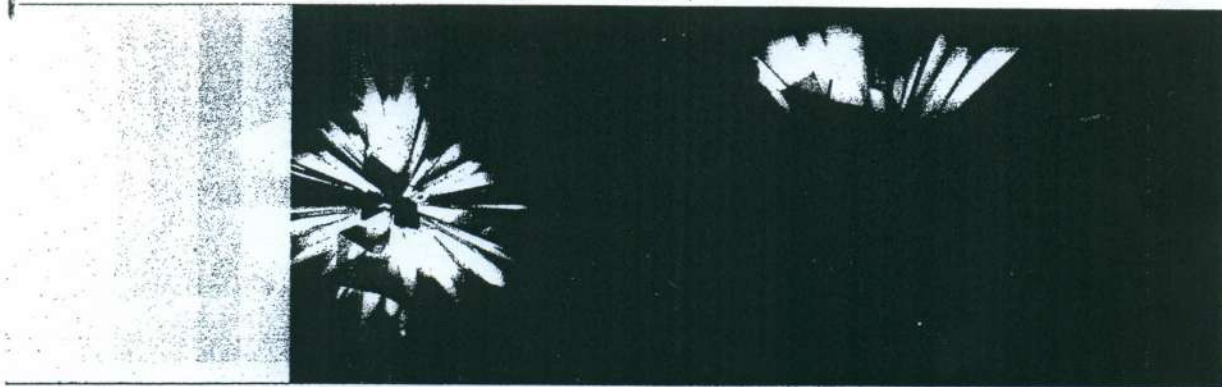


Šef Katedre za stomatologiju

prof. dr Dubravka Marković

Napomena: potvrda se izdaje na lični zahtev dr Svetlane Savić-Šević

Karolina Mudrinski | Konačna polja | 05-17.07.2005.



Dom omladine Beograda

Poetika | Po umetnikovom mišljenju, teorija Galoa predstavlja prevođenje beskonačnog prostora u konačni.

U konačnoj 3D rešetki, preko tablica Galoa se dobijaju skupovi tačaka koji formiraju prave i ravni, čime nastaju neki od mogućih idealnih rasporeda u prostoru.

Na osnovu zakona generisanja, u okviru rešetke se javlja veliki broj asimetričnih oblika, koji su u međusobnoj harmoniji.

Radeći sa tako dobijenim oblicima, umetnik posredstvom intuicije istražuje njihove odnose i forme.

Video | U programu C++, proračunavani su parametri tablice Galoa, na osnovu kojih su generisani oblici i strukture paralelnih ravni.

Napravljena je animacija kao vizuelizacija tako dobijenih formi u okviru 3D rešetke.

Hologrami | Hologram, kao medij koji pruža potpun 3D utisak, pokazao se kao najinteresantiji za vizuelizaciju oblika dobijenih iz teorije Galoa. U laboratoriji za holografiju Instituta za fiziku u Beogradu, specijalno za ovu priliku, konstruisan je uređaj za holografsko snimanje kompjuterski generisanih oblika. Na taj način je umetniku omogućeno da svoju viziju iskaže na potpuno novi način, prvi put u našoj zemlji.

Stručni saradnici | Programerski tim: dr Vojislav Mudrinski, Vedran Radivojkov | Holografski tim: dr Dejan Pantelić, mr Svetlana Savić-Šević, dipl.ing. Dušan Vukić



Karolina Mudrinski | Karolina Mudrinski rođena je u Novom Sadu 1973. godine. Apsolvent je postdiplomskih studija Univerziteta umetnosti u Beogradu, Odsek za digitalnu umetnost, smer totalno digitalno stvaralaštvo. Diplomirala grafiku na Akademiji umetnosti u Novom Sadu, 2000. godine. Do sad je imala preko 20 izložbi u zemlji i inostranstvu.

Adresa | Karolina Mudrinski, Bulevar cara Lazara 49, 21000 Novi Sad (SCG) | tel: 021 63 63 994 | 064 165 81 43
e-mail: kmudrinski@neobee.net

Izabrane samostalne izložbe

2002. Galerija Zlatno oko, Novi Sad- Bilbord prostorna instalacija i video "I Want To Be Your Lucky Star" (Kežman)

2001. Galerija SULUJ, Beograd - Bilbord prostorna instalacija i video "I Want To Be Your Lucky Star" (Kežman)

2000. Galerija Kulturnog centra, Novi Sad- Prostorna instalacija "Thera"

1999. Galerija Doma kulture "Studentski grad", Novi Beograd—grafike i kolaži iz ciklusa Thera

Posebno se zahvaljujem Institutu za fiziku u Beogradu, Milošu Vujanoviću i Predragu Kešelju.



Република Србија
Министарство за науку
и технолошки развој

НАЈБОЉА ТЕХНОЛОШКА НОВАЦИЈА 2008.

Министарство за науку и технолошки
развој Републике Србије,
додељује

ДИПЛОМУ

ТИМУ:

ПОЛИМЕР

за освојено пето место

на Такмичењу за најбољу технолошку иновацију
у Србији 2008. године, у категорији "Корак напред" и одслушане тренинге:

- 1) Резиме: "Слика мог иновативног пословања"
- 2) "Начини продаје иновације и технике преговарања"
- 3) "Како направити видео прилог"

Чланови тима:

Светлана Савић-Шевић

Лариса Блажић

Тамара Панић

Братимир Панић

Бранислав Јеленковић

Илија Мареља

Дејан Пантелић

Милан Минић

У име Министарства за
науку и технолошки развој

Мр Божидар Ђелић, министар

Београд, 23. децембар 2008. године

Република Србија
МИНИСТАРСТВО ПРОСВЕТЕ
И НАУКЕ
Комисија за стицање научних звања

Број:06-00-75/736
09.05.2012. године
Београд

РЕПУБЛИКА СРБИЈА			
ПРОСВЕТА		29-05-2012	
Број	Број	Датум	Страна
0201	237/1		

На основу члана 22. става 2. члана 70. став 6. Закона о научноистраживачкој делатности ("Службени гласник Републике Србије", број 110/05 и 50/06 – исправка и 18/10), члана 2. става 1. и 2. тачке 1 – 4.(прилози) и члана 38. Правилника о поступку и начину вредновања и квантитативном исказивању научноистраживачких резултата истраживача ("Службени гласник Републике Србије", број 38/08) и захтева који је поднео

Инстџиџиџи за физику у Београду

Комисија за стицање научних звања на седници одржаној 09.05.2012. године, донела је

**ОДЛУКУ
О СТИЦАЊУ НАУЧНОГ ЗВАЊА**

Др Свџџџџџџ Савић-Шевић

стиче научно звање
Виши научни сарадник

у области природно-математичких наука - физика

О Б Р А З Л О Ж Е Њ Е

Инстџиџиџи за физику у Београду

утврдио је предлог број 161/1 од 03.02.2012. године на седници научног већа Института и поднео захтев Комисији за стицање научних звања број 204/1 од 28.02.2012. године за доношење одлуке о испуњености услова за стицање научног звања *Виши научни сарадник*.

Комисија за стицање научних звања је по предходно прибављеном позитивном мишљењу Матичног научног одбора за физику на седници одржаној 09.05.2012. године разматрала захтев и утврдила да именована испуњава услове из члана 70. став 6. Закона о научноистраживачкој делатности ("Службени гласник Републике Србије", број 110/05 и 50/06 – исправка и 18/10), члана 2. става 1. и 2. тачке 1 – 4.(прилози) и члана 38. Правилника о поступку и начину вредновања и квантитативном исказивању научноистраживачких резултата истраживача ("Службени гласник Републике Србије", број 38/08) за стицање научног звања *Виши научни сарадник*, па је одлучила као у изреци ове одлуке.

Доношењем ове одлуке именована стиче сва права која јој на основу ње по закону припадају.

Одлуку доставити подносиоцу захтева, именованој и архиви Министарства просвете и науке у Београду.

ПРЕДСЕДНИК КОМИСИЈЕ
др Станислава Стошић-Грујичић,
научни саветник

С. Стошић-Грујичић



МИНИСТАР
Проф. др Жарко Обрадовић

РЕПУБЛИКА СРБИЈА



ФИЗИЧКИ ФАКУЛТЕТ
УНИВЕРЗИТЕТА У БЕОГРАДУ

ДИПЛОМА

О СТЕЧЕНОМ НАУЧНОМ СТЕПЕНУ
ДОКТОРА НАУКА

САВИЋ-ШЕВИЋ (Недељко) СВЕТЛАНА

РОЂЕНА 1. ЈУНА 1962. ГОДИНЕ У АПАТИНУ, РЕПУБЛИКА СРБИЈА, ДАНА 1. ЈУЛА 1999. ГОДИНЕ СТЕКЛА ЈЕ АКАДЕМСКИ НАЗИВ МАГИСТРА ФИЗИЧКИХ НАУКА, А 8. ФЕБРУАРА 2007. ГОДИНЕ ОДБРАНИЛА ЈЕ ДОКТОРСКУ ДИСЕРТАЦИЈУ НА ФИЗИЧКОМ ФАКУЛТЕТУ ПОД НАЗИВОМ „ФИЗИЧКЕ ОСОБИНЕ ХОЛОГРАФСКИХ ДИФРАКЦИОНИХ РЕШЕТАКА НА НОВИМ ДИХРОМИРАНИМ МАТЕРИЈАЛИМА”.

НА ОСНОВУ ТОГА ИЗДАЈЕ ЈОЈ СЕ ОВА ДИПЛОМА О СТЕЧЕНОМ НАУЧНОМ СТЕПЕНУ

ДОКТОРА ФИЗИЧКИХ НАУКА

Редни број из евиденције о издатим дипломама 12 672

У Београду, 6. маја 2008. године

(М. П.)

ДЕКАН

др Љубиша Зековић

РЕКТОР

др Бранко Ковачевић

ICTON 2010 Technical Program

Sunday, June 27

14:00 - 17:00 Registration is open at Technische Universität München

17:00 - 18:00 City tours start at the fish fountain (Fischbrunnen) on Marienplatz

Monday, June 28

7:30 Registration

Opening Ceremony (8:30 - 9:00) Plenary hall

Chair: Norbert Hanik

SESSION Mo.A (9:00 - 10:00) Plenary hall

Plenary

Chair: Hans-Georg Unger

Mo.A.1 European and American research toward next-generation optical access networks (Invited)

9:00 L.G. Kazovsky, C. Popp Larsen, D. Breuer, A. Gavler, M. Popov, K. Wang, G. Jacobsen, E. Weis, C. Lange, S.W. Wong, S-H. Yen, V. Gudla, P. Afshar

Mo.A.2 Optical technologies that enable Green networks (Invited)

9:20 K-I. Sato

Mo.A.3 Micro-nano-photononic device structures: Analysis and applications in communications and sensing (Invited)

9:40 R.M. De La Rue

10:00 - 10:30 Coffee break

10:00 - 10:30 Coffee break

10:00 - 10:30 Coffee break

10:00 - 10:30 Coffee break

SESSION Mo.B1

(10:30 - 12:30) Plenary hall

ICTON I - General I

Chair: Nooya Wada

Mo.B1.1 Advanced modulation formats and digital signal processing for fiber optic communication (Invited)

A. Gorshstein, D. Sadot

Mo.B1.2 Performance of adaptive low-density parity check codes in a low cost spectrally-sliced WDM network (Invited)

S. Sun, M.S. Leeson

Mo.B1.3 Light-by-light polarization control for telecommunication applications (Invited)

J. Fatome, S. Pitois, F. Morin, C. Finot, G. Millot

Mo.B1.4 All-optical RZ-to-NRZ format converters based on nonlinearly and walk-off in optical fibers

P. Honzatko, M. Kersek

Mo.B1.5 All-optical variable delay buffer for next generation optical networks

I. Ashry, H.M.H. Shalaby

Mo.B1.6 Phase-preserving multilevel amplitude regeneration using a modified nonlinear amplifying loop mirror

M. Hierold, T. Roethlingshoefer, K. Sponse, G. Onishchukov, B. Schmauss, G. Leuchs

Mo.B1.7 Red and orange tunable fiber laser

R. Al-Mehrouf, R. Caspary, W. Kowalsky

SESSION Mo.B2

(10:30 - 12:30) Auditorium A

SWP I (WG1)

Chair: Alex Nosich

Mo.B2.1 Homogenization of metamaterials: Parameters retrieval methods and intrinsic problems (Invited)

A. Andryieuski, R. Malureanu, A.V. Lavrinenko

Mo.B2.2 Design, synthesis and photophysical study of fluorophore modified noble metal nanoparticles (Invited)

P. Angelova, N. Kuchukova, G. Dobrikov, I. Petkova, I. Tintchevs, K. Kostova, E. Vauthcy, F. Giorgetti

Mo.B2.3 Thin metamaterials as antireflection coating (Invited)

E. Popov, S. Encci

Mo.B2.4 Designing metamaterials for the optical regime (Invited)

M. Kafesaki, R. Pendu, T. Koschny, N.H. Shen, E.N. Economou, C.M. Soukoulis

Mo.B2.5 Diffractive effects in 1D and 2D gain/loss periodic spatial modulated materials (Invited)

R. Herrero, M. Eotey, K. Staliunas

Mo.B2.6 Metal nanoisland films for the enhancement of the chemical-physical properties of molecular adsorbates (Invited)

E. Giorgetti, G. Margheri, T. Del Rosso, S. Scifini, M. Muniz Miranda, S. Cicchi

12:30 - 14:00 Lunch break

SESSION Mo.C2

(14:00 - 15:55) Auditorium A

SWP II (WG1)

Chair: Anírea Chiappini

Mo.C2.1 From plasmonics to supercontinuum generation: Subwavelength scale devices based on hybrid photonic crystal fibers (Invited)

M. Schmidt, H. Tyagi, H. Lee, N. Granzow, N. Da, M. Peng, L. Woncreader, P. Sio, Russell

SESSION Mo.B3

(10:30 - 12:30) Auditorium B

WAOR I

Chair: Carmen Mas-Machuca

Mo.B3.1 Analysis of traffic engineering information dissemination strategies in PCE-based multi-domain optical networks (Invited)

S. Spadaro, J. Perelló, G. Hernandez-Sola, A. Moreno, F. Agraz, J. Comellas, G. Junyent

Mo.B3.2 Scalable and agnostic optical packet switch subsystem for optical packets with multiple modulation formats and data rates (Invited)

N. Calabretta, W. Wang, T. Dilewig, O. Raz, F. Gomez-Puy, S. Zhang, H. de Waardt, M.J.S. Dronen

Mo.B3.3 A collision-free WDMA strategy for ring MANs to reduce traffic management: A performance optimization study

P. Battiana, I. Pournazeri

Mo.B3.4 Hopfield neural networks for routing in all-optical networks

C.J.A. Bastos-Filho, R.A. Santana, D.R.C. Silva, J.F. Martins-Filho, D.A.R. Chaves

Mo.B3.5 A receiver oblivious WDMA protocol study with propagation delay latency analysis

P. Baziens, P. Pournazeri

Mo.B3.6 Analysis of unbalanced WDM/OCDM transparent optical networks with physical constraints

L.H. Boneni, L. Galidino, F.R. Duran, E. Moschini

Mo.B3.7 Application of network traffic characterization to all-optical networks (Invited)

P.M. Santiago del Rio, J. Ramos, A. Salvador, J.E. López de Vergara, J. Arañiz, A. Cuadrado, M. Cutanda

12:30 - 14:00 Lunch break

SESSION Mo.C3

(14:00 - 16:00) Auditorium B

WAOR II

Chair: Nicola Calabretta

Mo.C3.1 On the physical implementations constraint in OBS networks (Invited)

O. Pedrola, D. Careglio, M. Klinkowski, J. Solé-Pareta

SESSION Mo.B4

(10:30 - 12:25) "Einsäulen" hall

PICAW

Chair: Stefano Taccheo

Mo.B4.1 Interfacing of silicon-on-insulator nanophotonic circuits to the real world (Invited)

L. Wosinski, Z. Wang, Y. Tang

Mo.B4.2 Modelling and optimising planar waveguide devices (Invited)

L. Cahill, T. Clapp

Mo.B4.3 Low-cost optical components based on organic-inorganic hybrids produced using direct UV writing technique (Invited)

R.A.S. Ferreira, C. Vicente, L.R. Xavier, V. Fernandes, L.D. Carlos, P.S. André, E. Pécourato, V. De Zea Bermudez, P. Monteiro, P.V.S. Marques

Mo.B4.4 Analysis and integration of plasmonic wires and rings for VLSI photonics (Invited)

E-H. Lee

Mo.B4.5 Designing wavelength-division-multiplexed optical access networks using reflective photonic components (Invited)

E. Kehayas

Mo.B4.6 Research progress on free-space-wave add/drop multiplexing for WDM optical-interconnect system in packaging (Invited)

S. Ura, K. Kintaka

12:25 - 14:00 Lunch break

SESSION Mo.C4

(14:00 - 15:40) "Einsäulen" hall

MAESI

Chair: Giorgio M. Tosi Beleffi

Mo.C4.1 A techno-economic case-study for an FTTH network deployment (Invited)

I. Tomkos

SESSION Mo.C1

(14:00 - 15:40) Plenary hall

ICTON II - Devices

Chair: Roger Green

Mo.C1.1 Application of trapped pulse amplification in birefringent fibers (Invited)

N. Nishizawa, E. Shimki, K. Itoh

SESSION We.A1

10:30 Plenary hall

CON V – Networks I

Chair: Paulo André

- We.A1.1** Optimizing multi-layered networks towards a transparently optical Internet (Invited)
R.G. Addie, D. Fatseas, M. Zukerman
- We.A1.2** Requirements and limitations of optical interconnects for high-capacity network elements (Invited)
S. Aleksić, N. Fehralović
- We.A1.3** Converged optical networking for packetized bandwidth delivery (Invited)
M. Cvjetić
- We.A1.4** GMPLS energy efficiency scheme for Green photonic networks (Invited)
M. Nazri, M. Warip, I. Glesk, I. Andonovic
- We.A1.5** Optical transparency and network energy efficiency (Invited)
D.C. Kiper, G. Atkinson, S. Korotky
- We.A1.6** Physical layer cryptography in optical networks: A lattice-based approach (Invited)
N. Boudinga, W. Abdallah, M. Hamdi

SESSION We.A2

(8:30 – 10:30)

SWP VII (WG2) Auditorium A

Chair: Katia Gallo

- We.A2.1** Nonlinear optics at the nanoscale (Invited)
C. Sibilia, M. Centini, A. Benedetti
- We.A2.2** Enhanced Raman amplification by hybrid photonic crystals (Invited)
A. Seyedfaraji, V. Ahmadi
- We.A2.3** Exact transparent boundary condition for beam propagation in rectangular domain (Invited)
R.K. Feshchenko, A.V. Popov
- We.A2.4** Silica aerogel in optical fibre devices (Invited)
T.A. Birks, M.D.W. Grogan, L.M. Xiao, M.D. Rollings, R. England, W.J. Wadsworth
- We.A2.5** Plasmonic absorption enhancement in organic photovoltaics (Invited)
B. Maes, A. Abass, H. Shen, P. Bienstman
- We.A2.6** Holographic photonic structures generated in dichromated collulose (Invited)
S. Savić-Šević, D. Pantelić, B. Jelenković

SESSION We.A3

(8:30 – 10:25) Auditorium B

GOWN I

Chair: Prince Anandarajah

- We.A3.1** The impact of receiver sensitivity in the convergence of diverse services over future integrated optical access networks (Invited)
C.P. Tsekrekos, T. Papachristos, I. Tomkos
- We.A3.2** Signal processing techniques for transmission impairments compensation in optical systems (Invited)
J.M.B. Oliveira, L.M. Pessoa, H.M. Saigado, I. Darwazeh
- We.A3.3** Optical technologies for multi-Gbit/s ultra-wireless radio: From the access to the picocell (Invited)
R. Llorens, V. Muriel, M. Beltran
- We.A3.4** 60 GHz radio-over-fiber transmission impairments for broadband wireless signals (Invited)
R. Avó, F. Laurencio, M.C.R. Medeiros
- We.A3.5** On supporting multiple radio channels over a SCM-based distributed antenna system: A feasibility assessment (Invited)
S. Pato, F. Ferreira, F. Monteiro, H. Silva
- We.A3.6** Transparent transportation of digitized microwave environments over 10 Gbps optical networks: Transportation of multi-channel digital broadcast signals
Y. Shoji, Y. Takayama, M. Toyoshima, H. Orita

SESSION We.A4

(8:30 – 10:45) "Einsäulen" hall

Industrial

Chair: Karin Ennser

- We.A4.1** A novel all-optical system of the chaotic encryption for optical networks (Invited)
Y. Ben-Ezra, B.I. Lembrikov, Yu. Yurchenko
- We.A4.2** Monitoring of the transparent fibre infrastructure for FTTx networks: An operator's view (Invited)
A. Ehrhard, H.-M. Foisel, F. Escher, A. Templin, M. Adamy
- We.A4.3** Optical OFDM for the data center (Invited)
Y. Benlachat, R. Bouziane, R.I. Killey, C.F. Berger, P. Milder, R. Koutsoyannis, J.C. Hoe, M. Püschel, M. Glück
- We.A4.4** Impact of topology on layer 2 switched QoS sensitive services (Invited)
B. Puype, G. Verbanck, J. Michielens, M. Moeskops, W. Tavemier, D. Colle, M. Pickavet, P. Demeester
- We.A4.5** Open access networks, the Swedish experience (Invited)
M. Forzati, C. Popp Larsen, C. Mattsson
- We.A4.6** An energy-efficient node interface for optical core networks
C. Donze, A. Morea, O. Rival, B. Berde
- We.A4.7** Standardization in optical access networks: Status and possible directions (Invited)
A. Teixeira

10:30 – 11:00 Coffee break

SESSION We.B1

(11:00 – 12:55) Plenary hall

CON VI – General II

Chair: Moshe Zukerman

- We.B1.1** Queue-based resource management strategy for enabling shared infrastructures over optical networks (Invited)
J.A. Garcia-Espin, X. Hesselbach
- We.B1.2** Algorithms for virtual topology reconfiguration under multi-hour traffic using Lagrangian relaxation and label based approaches (Invited)
F. Aparicio-Pardo, P. Pavon-Marino, N. Skorin-Kapov, B. Garcia-Marrubis, J. Garcia-Ham
- We.B1.3** Multiobjective sparse regeneration placement algorithm in optical networks considering network performance and CAPEX (Invited)
D.A.R. Chaves, C.F.C.L.C. Ayres, R.V.B. Carvalho, H.A. Pereira, C.J.A. Bastos-Filho, J.F. Martins-Filho
- We.B1.4** Investigation of binary modulation implementations for use in wavelength-switched networks (Invited)
J.A. Clarke, C.K. Bramm, V. Bessie, A.D. Ellis
- We.B1.5** De-multiplexing of 107 Gb/s OTDM signal based on pulsed pump optical parametric amplifier
M. Karasek, P. Honzatko

10:30 – 11:00 Coffee break

SESSION We.B2

(11:00 – 12:35) Auditorium A

SWP VIII (WG3)

Chair: George Stanciu

- We.B2.1** Second and third-harmonic generation in disordered quadratic nonlinear media: Application to short-pulse characterization (Invited)
V. Roppo, W. Wang, K. Kalinowski, R. Vilaseca, J. Trull, C. Cojocaru, K. Staliunas, W. Krolikowski, Yu. Kivshar
- We.B2.2** Second-harmonic generation in disordered quadratic media: Role of a ferroelectric domain structure (Invited)
V. Roppo, K. Kalinowski, W. Wang, C. Cojocaru, J. Trull, R. Vilaseca, M. Sauer, W. Krolikowski, Yu. Kivshar
- We.B2.3** Nonlinear optical properties of two-dimensional derivatives (Invited)
D. Alajbeg, M. Stojan, P. Di'ouazzani, M. Benicasse, B. Sraoui
- We.B2.4** Photopolymer recording materials: Characterization, modeling and applications (Invited)
J. T. Chiriac
- We.B2.5** Influence of ultra-ultrafast energy transfer on the properties of nanocrystal quantum dot structures and devices
M. Loni, A.L. Escobedo, W.-T. Chen, V.A. Gerardo, S.J. Byrne, Y.K. Sukko, V. Lesnyak, N. Sazonik

10:25 – 11:00 Coffee break

SESSION We.B3

(11:00 – 12:55) Auditorium B

GOWN II

Chair: Danilo Medeiros

- We.B3.1** Gain and phase in the optical generation of modulated millimetre waves (Invited)
P.M. Jose, S. Rajan, H. Shama, P. Parry, L.F. Poy
- We.B3.2** Figures of merit for microwave photonic phase shifters based on coherent population oscillation slow and fast light effects (Invited)
F. Casili, J. Sanchez-Juaret, D. Sales, J. Capmany
- We.B3.3** Microcavity light scattering based on hybrid systems in quantum dot waveguide (Invited)
Y. Chai, J. Mark
- We.B3.4** Theoretical and experimental study of the linearity of semiconductor optical amplifier-based optical modulator in dual-polarization multiplexed systems (Invited)
R. Olvera, T. Senechal
- We.B3.5** Photonic and microwave signal processing by means of slow and fast light (Invited)
M. Santopostolus, G.G. Somenza

10:45 – 11:15 Coffee break

SESSION We.B4

(11:15 – 12:55) "Einsäulen" hall

Glasses I

Chair: Reinhard Caspary

- We.B4.1** The optical properties of chalcogenide glasses: From measurement to electromagnetic simulation tools (Invited)
H.G. Dantanarayana, A. Vukovic, P. Sewell, Z.G. Lian, D. Furniss, A.B. Seddon, E.A. Romanova, A. Koruyukhov, B. Derkowska, J. Orava, T. Wagner, T.M. Benson
- We.B4.2** Thermal diffusion in chalcogenide glass irradiated by a train of femtosecond laser pulses (Invited)
E. Romanova, A. Koruyukhov, S. Murbach, A. Andonov
- We.B4.3** First-time microwave-synthesis of As₂S₃ chalcogenide glass: With potential for mid-infrared photonics (Invited)
R. Prasad, A.B. Seddon
- We.B4.4** Elaboration of photonic crystal fibers for telecom and mid infrared wavelengths (Invited)
A. Todorov, I. Adam, I. Brilland, Q. Ch. Pham, T. Chertier
- We.B4.5** Study of nonlinear optical properties of Er³⁺- and Yb³⁺-doped oxyfluoride glasses (Invited)
B. Derkowska, Y.L. Wong, D. Furniss, T.M. Benson, A.B. Seddon

Holographic Photonic Structures Generated in Dichromated Pullulan

Svetlana Savić-Šević, Dejan Pantelić, Branislav Jelenković*

Institute of Physics, Pregrevica 118, 11000 Beograd, Serbia

** Tel: (+381-11) 371 3107, Fax: , e-mail: branaj@ipb.ac.rs*

ABSTRACT

Holographic method was used to fabricate volume Bragg gratings, i.e., 1-D photonic crystals, in dichromated pullulan (DCP). Wide and complete band gaps were obtained in transmission spectra of light from the halogen lamp. SEM images of cross sections of DCP film show large voids right under the film surface, followed by regularly spaces bright and dark regions of Bragg grating filled with nano-size air voids. This work presents potentials of DCP as a material for photonic crystals, which so far has not been used for generation of photonic crystals.

Keywords: photonic crystals, band gaps, holograms, polysaccharide.

1. INTRODUCTION

Holography is one of several methods for successful fabrication of photonic crystals [1], but it is the most promising technique in the practical sense. Large areas can be written to produce 3D PC using holographic lithography with significant degree of geometry control (by varying number of interfering beams, their orientation and state of polarization) [1]. Photonic crystals can be constructed as a two or three dimensional lattice, i.e., an extension of Bragg reflector, with a simple holographic recording using a small number of plane waves [2].

Several materials such as dichromated gelatin, polymers with TiO₂, photoresists, sol-gel materials and silver halide emulsions have been used for fabrication of photonic structures using holographic techniques.

In this work we have investigated the optical properties of one-dimensional photonic crystal in dichromated biopolymer. We used the pullulan sensitized with ammonium dichromate (DCP) as recording material [3]. Pullulan is a natural linear polysaccharide, produced from starch by *Aureobasidium pullulans*. It is non poisonous, and easily soluble in water to make clear and viscous solution. So far this material has not been used for generation of photonic crystals. Simple holographic polymerization was done using a single laser beam, exposing DCP to direct and retro-reflecting laser beam which creates a standing wave pattern in the material.

2. EXPERIMENT

Volume gratings are produced using a single laser beam set-up in counter-propagating geometry. DCP is placed in a close contact with the plane mirror and illuminated with the expanded direct and retro-reflected laser beams. Hologram recording was achieved by exposing dichromate pullulan to the single-frequency, diode pumped Nd-YAG laser, at 532 nm, at 20 mW/cm² of optical power, for 10 min. After exposure the material is chemically processed. Processing involves washing the plates in the mixture of water and isopropyl alcohol for 120 seconds, and drying for 120 seconds in pure isopropyl alcohol.

Transmission and reflection spectra of light from halogen lamp with nearly perpendicular incidence on the DCP film were recorded point wise using microscope and fibre coupled Ocean Optics spectrometer. To study morphology of DCP films and investigate surface and volume structures responsible for observed properties of DCP series of SEM images were made and analysed.

3. RESULTS

Figure 1 shows typical transmission spectra of DCP obtained using 20 μm thick film (solid line). The sharp dip in the transmission with nearly 100 % diffraction efficiency indicates formation of volume holograms with appreciable modulation of the refractive index. Although we measured complete band gap in this and not in other directions, it was pretty remarkable to achieve wide and complete band gap by using material of low refractive index. The thick solid line is the $1/\lambda^4$ curve normalized to the experimental transmission spectra, on the blue side of the band gap.

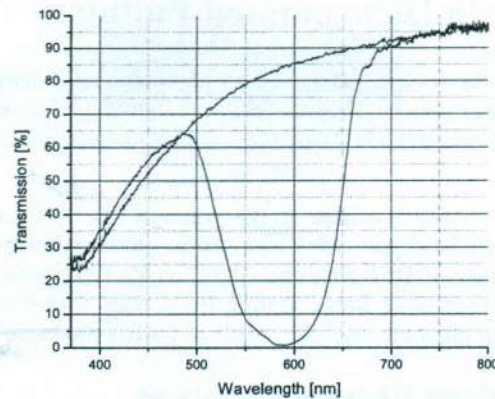


Figure 1. Transmission spectrum of DCP (solid line) and $1/\lambda^4$ fit, normalized to the experiment at 800 nm.

We made series of SEM images along self-induced vertical cracks in DCP. One example is the image in Fig. 2. Volume holograms are formed beneath porous, diffusing surface layer which shows large cracks and voids between them. As seen in the Fig. 2, below this surface layer is a continuous layered structure, with alternating dark and bright regions. The period of layers is of the order of 100 nm, in line with expected spacing of volume Bragg gratings in our DCP film. Volume Bragg gratings have a granular structure with average size below the recording wavelength. Small cracks and voids are also present along the grating layers. We postulate that the $1/\lambda^4$ dependence of the transmission spectrum of Fig. 1. is due to Rayleigh scattering and that a wide bandgap is a consequence of material scattering and Bragg grating.

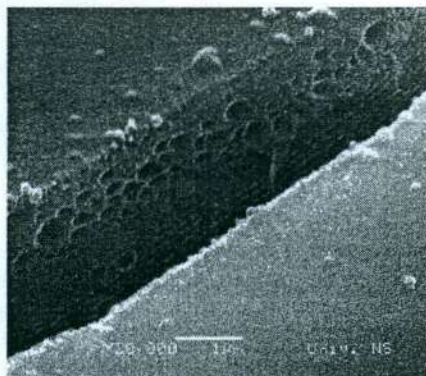


Figure 2. SEM photograph of the DCP around two cracks developed on the on the surface during processing.

4. CONCLUSIONS

We have shown properties of DCP as a new material for holographically generated photonic crystals. Widths of nearly complete band gaps of around 100 nm were obtained. Surface and volume structures, as revealed by SEM photographs, show nano-sized air voids present along layers of Bragg gratings in the volume of DCP. In the small transition region under the surface of the DCP, layers are absent, but large voids are present. In contrast to DCG this material is extremely resistant to humidity. Our results show that DCP is a very promising optical material for photonic crystals. It is also very stable material. We have the layers with holographic structures lasting for more than 10 years under ordinary conditions.

ACKNOWLEDGEMENTS

Work is supported by Serbian Ministry of Science and Technological Development under the project number 141003.

REFERENCES

- [1] D. C. Meisel, M. Wagner, K. Busch, *Phys. Rev. B*, vol. 70, 165104, 2004.
- [2] V. Berger, O. Gauthier-Lafaye, and E. Costard, *J. Appl. Phys.*, vol. 82, 60, 1997.
- [3] S. S. Šević, D. Pantelić, *Appl. Opt.*, vol. 46, 287, 2007.

Y. Sun, M.J. Adams, N. Balkan

- 18 Tu.P.18 Optical characterization of the GaInNAs/GaAs n-type as-grown and annealed modulation doped quantum well structures
O. Donmez, A. Erol, M.C. Arıkan, F. Ungan, E. Kasapoglu, H. San, J. Puustinen, M. Guina
- 19 Tu.P.19 Electronic transport properties of the GaInNAs/GaAs p-type as-grown and annealed modulation doped quantum well structures
A. Erol, F. Sarcan, M. Gunes, M.C. Arıkan, J. Puustinen, M. Guina
- 20 Tu.P.20 Optical and electrical properties of non-intentionally doped InN/GaN and GaN/InN/GaN heterostructures
M. Gunes, O. Donmez, M. Yilmaz, A. Erol, M.C. Arıkan, B. Ulug, A. Ulug, N. Balkan, A.O. Ajagunna, E. Iliopoulos, A. Georgakilas
- 21 Tu.P.21 Analysis and design of novel photonic active devices based on dilute nitrides
G. Calò, D. Alexandropoulos, A. D'Orazio, V. Petruzzelli
- 22 Tu.P.22 Electron transport dynamics in dilute nitrides
N. Vogiatzis, J.M. Rorison
- 23 Tu.P.23 Design considerations for dilute nitride n-i-p-i structure solar cells
B. Royall, N. Balkan, M. Guina, A.J. Smith
- 24 Tu.P.24 Optimum band gap of single and two junction series connected solar cells
O. Kengradomying, J.M. Rorison
- 25 Tu.P.25 FTIR spectroscopy of quantum well infrared photodetectors
F. Nutku, M.Ç. Arıkan, A. Erol, Y. Ergün
- 26 Tu.P.26 Provisioning concepts for the Future Internet IIP initiative
P. Cho'da, J. Gozdecki, M. Kantor, M. Wielgosz, A.R. Pach, K. Wajda, J. Rak

Coffee break (15:35 – 16:00)	Coffee break (15:40 – 16:10)	Coffee break (15:30 – 16:00)	Coffee break (15:25 – 16:00)	Coffee break (15:40 – 16:00)	Coffee break (15:55 – 16:20)
SESSION Tu.D1 (16:00 – 17:40) ICTON VI Chair: Fary Ghassemlooy	SESSION Tu.D2 (16:10 – 17:50) SWP VI (WG3 III) Chair: Pavel Cheben	SESSION Tu.D3 (16:00 – 17:35) GOC I In honor of Fabio Neri Chair: Carmen Mas Machuca	SESSION Tu.D4 (16:00 – 17:40) ESPC I Chair: Katia Gallo	SESSION Tu.D5 (16:00 – 18:00) ICTON-FSO Chair: Roger Green	SESSION Tu.D6 (16:20 – 18:00) PICAW I Chair: Jose Pozo
16:00 Tu.D1.1 Software-defined optical transmission (Invited) W. Freude, R. Schmogrow, B. Nebendahl, D. Hillerkuss, J. Meyer, M. Dreschmann, M. Huebner, J. Becker, C. Koos, J. Leuthold	16:10 Tu.D2.1 Recent developments in the characterisation, modelling and application of photopolymer materials (Invited) J.T. Sheridan	16:00 Tu.D3.1 Energy-efficient IP over WDM networks with data centres (Invited) X. Dong, T. El-Gorashi, J.M.H. Elmirghani	16:00 Tu.D4.1 Photonic crystal and related devices fabricated by CMOS compatible process (Invited) T. Baba	16:00 Tu.D5.1 Free space optical wireless network (Invited) V.W.S. Chan	16:20 Tu.D6.1 Integrated silicon nanophotonics: A solution for computer interconnects (Invited) L. Wosinski, Z. Wang
16:20 Tu.D1.2 Capacity approaching coded modulation in optical communications (Invited) T.H. Lotz, W. Sauer-Greff, R. Urbansky	16:30 Tu.D2.2 Biologically inspired photonic structures in dichromated pullulan (Invited) S. Savia-Savia, D. Pantelias, S. Eurèria, B. Eurèria, B. Jelenkovic	16:20 Tu.D3.2 Network and system architectures for energy-efficient metro and access networks employing reflective photonics (Invited) E. Kehayas, A.M. Clarke, A. Borghesani, K. Vyrsokinos, D.W. Smith, P. Ossieur, D.G. Moodie, R. Jensen, N. Parsons, P.D. Townsend	16:20 Tu.D4.2 InP-based photonic crystal waveguide technology for filtering and sensing applications (Invited) S. Anand, N. Shahid, M. Swillo	16:20 Tu.D5.2 Exploring the potentials of optical-wireless communication using white LEDs (Invited) K.-D. Langer, J. Vubiac, C. Kottke, L. Fernández, K. Habel, A. Paraskevopoulos, M. Wendt, V. Markov	16:40 Tu.D6.2 VLSI photonic interconnection of dielectric and plasmonic nano-wires and devices (Invited) El-Hang Lee
16:40 Tu.D1.3 Optical quantization and coding for 5bit photonic A/D conversion (Invited) T. Konishi, K. Takahashi, H. Matsui, T. Satoh	16:50 Tu.D2.3 Laser-induced micro- and nanostructures at polymer surfaces for applications in cell biology (Invited) J. Heitz, B. Reisinger, S. Yakunin, N. Voelcker, Q. Peng, A.L. Hook, C. Romanin, M. Fahmer	16:40 Tu.D3.3 How to save energy in passive optical networks (Invited) L. Valcarenghi, D. Pham Van, P. Castoldi	16:40 Tu.D4.3 Vector bend sensor on the base of three-core microstructured fiber (Invited) I. Goncharenko, M. Marciniak	16:40 Tu.D5.3 Using tapers for efficient coupling of received FSO-signals into fibres (Invited) E. Leitgeb, S. Stöger, M. Löschnigg	17:00 Tu.D6.3 Agile photonic integrated systems-on-chip enabling WDM terabit networks (Invited) Ch. Kouloumentas, M. Bougioukos, M. Spyropoulou, D. Klonidis, G. Giannoulis, D. Kalavrouziotis, A. Maziotis, P. Gkroumas, D. Apostolopoulos, P. Bakopoulos, A. Poustie, G. Maxwell, K.O. Veltlaus, R. Kaiser, L. Moert, I. Tomkos, H. Avramopoulos
17:00 Tu.D1.4 Filterless optical WDM core networks based on coherent systems (Invited) C. Tremblay, A. Enriquez Castillo, M.P. Bélanger, F. Gagnon	17:10 Tu.D2.4 Oxygen-isotope exchange between CO ₂ and solid Ti ¹⁸ O ₂ (Invited) S. Civiš, M. Ferus	17:00 Tu.D3.4 Introducing optical switching in high-capacity commercial routers (Invited) B. Garcia-Manrubia, P. Pavon-Marino	17:00 Tu.D4.4 Prospects on hollow-core photonic crystal fibers for unconventional fibered laser sources (Invited) R. Jamier, F. Gérôme, G. Humbert, J.-L. Auguste, J.-M. Blondy, F. Benabid	17:00 Tu.D5.4 Auto tracking system for free space optical communications (Invited) R. Ghimire, S. Mohan	17:20 Tu.D6.4 Improved techniques for the design of planar multimode lightwave circuits (Invited) L.W. Cahill, T.V. Clapp
17:20 Tu.D1.5 Passive wide area network solutions: Filterless and semi-filterless optical networks (Invited) J. Chen, S. Khanmohamadi, F. Abtahi,	17:30 Tu.D2.5 Picosecond reading of optically doped azophenylcarbazole (Invited) G. Navickaite, G. Seniutinas, R. Tomašiusas, R. Petruškevičius, V. Getautis	17:20 Tu.D3.5 Hierarchical wireless and optical access networking: Convergence and energy efficiency M.C. Parker, R. Martin, K. Guild, S.D. Walker	17:20 Tu.D4.5 Inhibition of the emission of electromagnetic modes of photonic crystal cavities with a top mirror (Invited) N. Le Thomas, R. Houdré	17:20 Tu.D5.5 Block transmission with frequency domain equalization in the presence of colored noise (Invited) M. Wolf, L. Grobe	17:40 Tu.D6.5 Techniques for embedding non-linear materials in TLM (Invited) H.G. Dantanarayana, X. Meng, P. Sewell, A. Vuković, T.M. Benson

Biologically Inspired Photonic Structures in Dichromated Pullulan

S. Savić-Šević¹, D. Pantelić¹, S. Curčić², B. Čurčić², and B. Jelenković¹

¹Institute of Physics, University of Belgrade, Pregrevica 118, Belgrade, Serbia

²Institute of Zoology, Faculty of Biology, University of Belgrade, Studentski Trg 16, 11000 Belgrade, Serbia

Tel: (381) 11 3713107, e-mail: branaj@ipb.ac.rs

ABSTRACT

We present properties of surface and volume photonic structures generated in Dichromated pullulan (DCP) using holographic technique. Volume Bragg gratings have properties of photonic crystals – wide bandgaps of the order of 100 nm. The bandgap is centered at 560 nm at room temperature, and can be tuned with the substrate temperature to 480 nm at 100 °C. The process is reversible; bandgap goes back to 560 nm if substrate is cooled to 25 °C. Both surface and volume structure of DCP are complex: beneath structured surface there are porous, diffusing surface layer followed by the volume gratings. We have found that such structure resembles structures found in nature. We present a detailed study of wings of two butterfly species *Apatura iris* (Linnaeus, 1758) and *A. ilia* with respect to their optical properties and the relationship of these properties to the microscopic structure of the wing scales. We are presenting also a close analogy between defects on the butterfly wing scales and fork-holograms used to generate vortex beams. We propose using pullulan for generation of butterfly like structures.

Keywords: photonic crystals, holography, biomimetics.

1. INTRODUCTION

Holography offers a way to obtain photonic crystals with wide band gaps in a relatively simple manner. Two or more laser beams interfere and produce intricate structures inside suitable photosensitive materials, thus producing periodic dielectric structures which exhibit properties of photonic crystals [1]. Here we use a dichromated pullulan (DCP) as a holographic material for fabrication of photonic crystals. We show rather complex structure of DCP films, which enables its specific properties as a photonic crystal. In this work special emphasis is on a close relation between advanced optical devices generated holographically and naturally arising structures.

It was shown that very intricate, nanometer-sized structures can be observed on the insect integument and eyes. Butterfly wings possess structures acting as directional and spectral filters, whose behaviour can be described by formalism of photonic structure physics. Depending on habitat vast range of structures was discovered, acting as different types of spectral filters. They can be broad or narrow, UV, visible or infrared, directional. These structures can be used as an inspiration for man-made filters [2]. Compound insect eyes present interesting templates as well [3]. They are each a lenslet array, where ommatidium (together with microlens) is acting as a non-imaging device. On nanometer level each lens is covered with tiny structures providing smooth gradient of equivalent refractive index. As a result, reflection losses are significantly reduced, presenting an interesting inspiration for solar cells with increased efficiency [4].

Special attention will be given to defect structures on *Apatura iris* (Linnaeus, 1758) and *A. ilia* (Denis & Schiffermüller, 1775) butterfly cover scales in males (Lepidoptera: Nymphalidae). It will be shown that these naturally arising patterns are capable of generating vortex beams [5]. However, recent research shows that diffraction of vortex beams on regular apertures produces a distinct pattern. Possibly, diffraction on hexagonally shaped ommatidia might produce a pattern that can be detected by photosensitive cells.

2. PHOTONIC STRUCTURES IN DICHROMATED PULLULAN

DCP was obtained following this preparation procedure. Holographic photosensitive material was prepared by mixing 10 % aqueous solution of pullulan (from Sigma-Aldrich) and 10 % of the ammonium dichromate. DCP solution was stirred and warmed to 50 °C to achieve homogeneity. The solution was coated onto a thoroughly cleaned glass slides placed on the flat horizontal surface. Film was dried overnight under normal laboratory conditions. The thicknesses of the dried layers, was 14 µm. Next, periodic structures in a DCP were fabricated using a single-beam method hologram recording, exposing DCP to a single longitudinal mode, diode pumped Nd-YAG laser, at 532 nm. The laser beam was expanded and pullulan layer was exposed at normal incidence. After propagation through emulsion, the beam was reflected back from a mirror behind the holographic plate. The two counter-propagating beams interfere, creating a standing wave pattern within an emulsion. After the exposure, plates were chemically processed. Processing involves washing the plates in a mixture of water and isopropyl alcohol (3:1 ratio) for 120 seconds, and drying for 60 seconds in pure isopropyl alcohol.

SEM images shows very complex, both surface and volume structures, of DCP. Volume gratings are formed below porous diffusing surface layer, see Fig. 1a. Zoomed images reveals that Bragg gratings are not uniform, they have granular structure, the size of granules being below recording wavelength, Fig. 1b. Such structure enables low index material like pullulan to have properties of photonic crystals. We have measured relatively

wide photonic gaps, of the order of 100 nm. We have also show that it is possible to move this gap towards lower wavelength by increasing temperature of the DCP substrate.

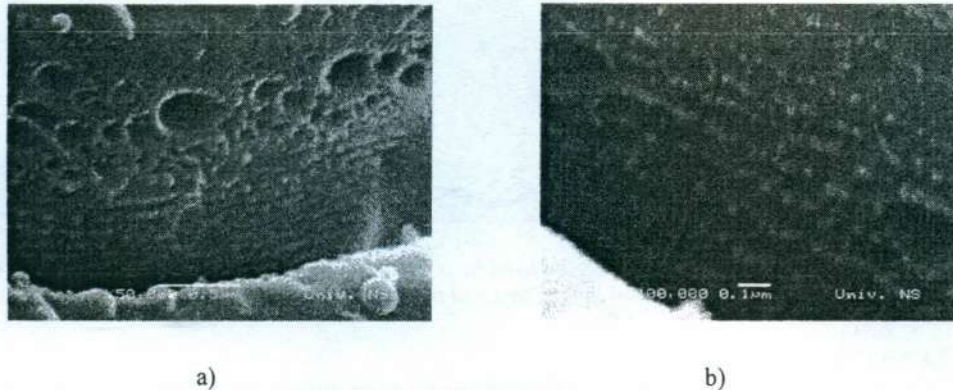


Figure 1: a) and b) SEM images along the vertical crack normal to the surface of DCP.

3. VORTEX PHOTONICS STRUCTURES ON COVER SCALES ON BUTERFLIES

Butterflies, *Apatura iris* and *A. ilia* can be found from Europe to China and are characterized by remarkable purple-UV iridescence present only in males. This is the consequence of ultrastructure of cover scales on dorsal side of their wings. In contrast to many other butterfly species the iridescence is quite narrow, both in spectral (20 nm) and angular distribution (18 degrees). As found by SEM, cover scales are covered with ridges at mutual distance of the order of micrometer, as shown in Figs. 2a and 2b respectively. But zooming further on its upper part shows that each ridge is a multilayer structure, consisting of 5-7 pairs of lamellar projections (Fig. 2c). In fact, the scale structure is a combination of surface relief and Bragg diffraction grating.

We have investigated interesting fork-like structures (see inside the red circle in Fig. 2c) on the butterfly cover scales. It looks as if one ridge splits into two. This bifurcation is not an exceptional feature, since we were able to observe many of them on completely randomly chosen areas of the wing (Figs. 2a and 2b). There can be up to 20 defects on a single cover scale (with approximately $50 \mu\text{m} \times 100 \mu\text{m}$ size). These features are not present in ground scales of the analyzed butterflies. Defects of similar type can be found in literature [6], but there are not as many defects as in the case of *Apatura iris*. Nobody to our knowledge paid any attention to structures like these.

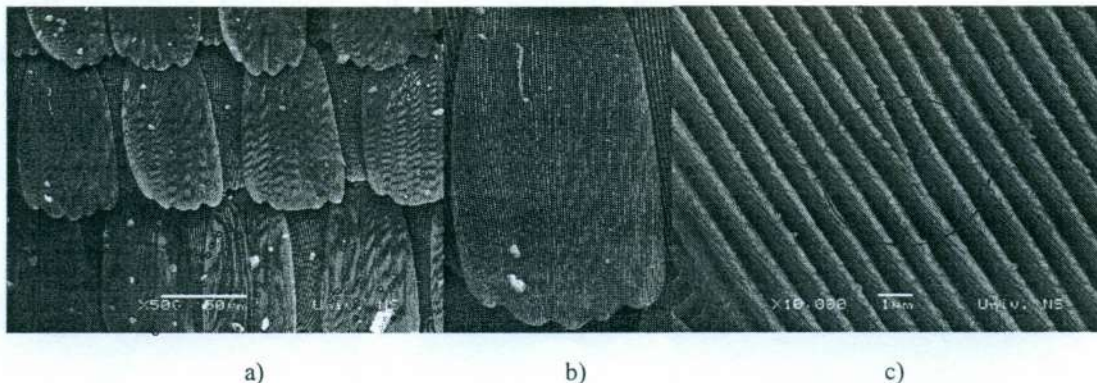


Figure 2: a) SEM image of randomly chosen area of *Apatura iris* butterfly wing. Fork-like defects of the grating are marked by red circles. b) Enlarged leftmost scale from the middle row c) fork-like defect

Now we would like to draw attention to extreme similarity between defects on the butterfly cover scales and so called fork-holograms [5] (Figs. 3a and 3b). They are used to generate vortex beams, a new class of optical beams which are characterized by spiral wavefront with a phase singularity in its centre. They have an additional, orbital angular momentum so interesting in many applications [11].

We have calculated far field distribution from a fork-hologram and *Apatura* defect structure (Figs. 3b and 3c). As can be seen, there is a strong resemblance between the two patterns. Of course, a pattern from a butterfly cover scale is distorted due to non-ideal profile. One advantage of butterfly-like vortex generation is a strong spectral selectivity in contrast to computer-generated hologram.

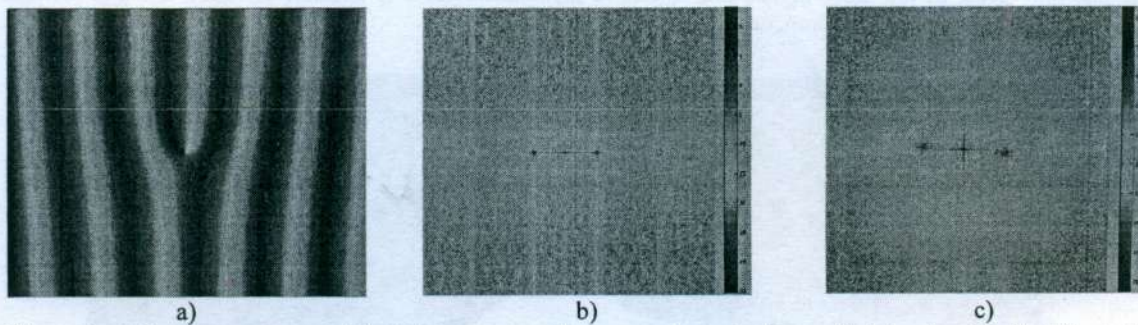


Figure 3: a) Computer-generated fork-hologram used to generate vortex beam. b) Intensity of light diffracted on fork-hologram. c) Intensity of light diffracted from fork-like structure on butterfly wing.

4. CONCLUSIONS

Photonic crystals as volume holograms in DCP were made using simple, single-beam holographic technique. Bandgaps typically between 95 nm and 120 nm wide were generated in a pullulan, material with low index of refraction due to both surface and volume structures of DCP. We have shown a close analogy between images from illuminated DCP films and structures on *Apatura iris* and *A. ilia* butterfly cover scales, as well as analogy between defect in structures their scales and computer-generated fork-holograms. As a combination of surface relief and volume hologram it is amenable for generation by holographic methods. More research is needed in order to see is it just a coincidence or there is an evolutionary advantage of vortex beams generated by fork-like structures.

ACKNOWLEDGEMENTS

Authors acknowledge support by Ministry of education and science of Serbia, under grants 45016, 171038 and 173038.

REFERENCES

- [1] Z. Ye, J. Zheng, D. Liu, S. Pei: "Structures of photonic crystals and band gaps in volume hologram," *Physics Letters A*, vol. 299, pp. 313–317, 2002..
- [2] D. P. Gaillot, *et al.*: Composite organic-inorganic butterfly scales: production of photonic structures with atomic layer deposition, *Phys. Rev. E*, vol. 78, pp. 031922, 2008.
- [3] K.-H. Jeong *et al.*: J. Kim, L. P. Lee, Biologically inspired artificial compound eyes, *Science*, vol. 312, 557-561, 2006.
- [4] C.-H. Sun, *et al.*: Broadband moth-eye antireflection coatings on silicon, *Appl. Phys. Lett.*, vol. 92, 061112, 2008.
- [5] R. K. Tyson, *et al.*, Generation of an optical vortex with a segmented deformable mirror, *Appl. Opt.*, vol. 47, pp. 6300-6306, 2008.
- [6] C. Lawrence, *et al.*: Grazing-incidence iridescence from a butterfly wing, *Appl. Opt.*, vol. 41, pp. 437-441, 2002.
- [7] D. G. Grier: A revolution in optical manipulation, *Nature*, vol. 424, pp. 810-816, 2003.

SCIENTIFIC PROGRAMME

INVITED LECTURERS

PAGE

Lipidic and inorganic nanoparticles for drug delivery, M. Manca, C. Vinci, **Bianca Baroli**

14

Affinity-driven self-assembly nanoparticles and their application for the controlled delivery of therapeutics, **Smadar Cohen**

15

From the idea to the market - the transfer model of a German Research Institute, **Christian Theel**

16

Holografically generated photonic structures – Analogy to bioinspired structures, D. Pantelić, S.Savić-Šević, **Branislav.Jelenković**, S.Čurčić, B.Čurčić

17

Porous ceramics prepared from plasma processed alumina nanopowder, **Eriks Palcevskis**

18

Analysis of new bone formed onto sintered and alginate hydroxyapatite in vivo, A.L. Rossi, J. Werckmann, M. Farina

19

Graphene polymer nanocomposites for optoelectronic applications, **Luca Valentini**

20

ZnO polytypoid nanowires for thermoelectric applications, **Velimir Radmilovic**

21

Novel nanostructured materials for medical applications obtained by electrochemical methods, **V. B. Mišković-Stanković**

22

New compounds synthesized and/or deposited by PLD, MAPLE and LDW for applications in nano-medicine and nano-biology, **Ion N. Mihailescu**

24

Polymer nanocomposites with MWCNT and SiC: characterization, application and risk assessment, **Anita Grozdanov**

25

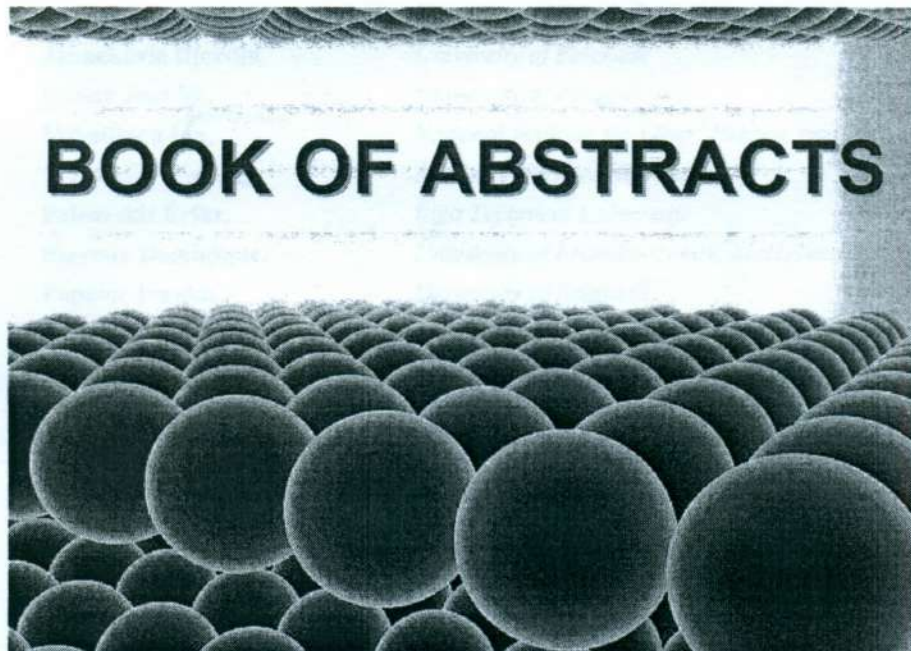
Nanostructuring of biodegradable polymeric matrices for tissue engineering, **Jose Kenny**

27



Second International Workshop

Characterization, properties and applications of nanostructured ceramics, polymers and composites



UNIVERSITY OF BELGRADE
FACULTY OF TECHNOLOGY AND METALLURGY
October 24 - 25, 2011

Program Committee

Chair:

Uskokovic Petar, *University of Belgrade*

Members:

Aleksic Radoslav, *University of Belgrade*
Janackovic Djordje, *University of Belgrade*
Kenny Josè M., *University of Perugia*
Mihailescu Ion, *National Institute for Laser, Plasma, and
Radiation Physics, Bucharest*
Palcevskis Eriks, *Riga Technical University*
Perreux Dominique, *University of Franche-Comté, MaHyTec, Ltd*
Popovic Ivanka, *University of Belgrade*
Radmilovic Velimir, *University of Belgrade*
Ersen Ovidiu, *Institut de Physique et Chimie des
Materiaux de Strasbourg*

Organizing Committee

Chair:

Obradovic Bojana, *University of Belgrade*

Members:

Orlovic Aleksandar, *University of Belgrade*
Petrovic Rada, *University of Belgrade*
Radojevic Vesna, *University of Belgrade*
Stamenkovic Ivan, *University of Belgrade*

Invited lecturers

PROGRAMME

Monday October 24

9.30 – 10.00	Opening session (Ivanka Popovic, Djordje Janackovic, Petar Uskokovic)
10.00 – 10.25	Nanostructuring of biodegradable polymeric matrices for tissue engineering, Jose Kenny
10.25 – 10.50	New compounds synthesized and/or deposited by PLD, c-PLD, MAPLE and LIFT for applications in nano-medicine and nano-biology, Ion Mihailescu
10.50 – 11.15	Non-equilibrium plasmas and their application in nanotechnologies and medicine, Zoran Petrovic
11.15 – 11.30	Coffee break
11.30 – 11.55	Polymer nanocomposites with MWCNT and SiC: characterization, application and risk assessment, Anita Grozdanov
11.55 - 12.20	Novel nanostructured materials for medical applications obtained by electrochemical methods, Vesna Mišković-Stanković
12.20 - 12.45	Graphene polymer nanocomposites for optoelectronic applications, Luca Valentini
12.45 - 13.10	From the idea to the market - the transfer model of a German research institute, Christian Theel
13.10 -13.40	Poster session
13.40-15.00	Lunch break
15.00 - 17.00	Walking tour to the Serbian Academy of Sciences
17.30 - 19.00	Round table: " Biomedical Engineering for Human Health: Priorities, Translation, Education " Joint Session with the Scientific Conference <i>Biomedical Engineering for Human Health</i> , <u>Serbian Academy of Sciences and Arts</u>

**Tuesday
October 25**

9.30 – 9.55	ZnO polytypoid nanowires for thermoelectric applications, Velimir Radmilović
9.55 – 10.20	Affinity-driven self-assembly nanoparticles and their application for the controlled delivery of therapeutics, Smadar Cohen
10.20 - 10.45	Lipidic and inorganic nanoparticles for drug delivery, Bianca Baroli
10.45 – 11.15	Poster session
11.15 – 11.40	Porous ceramics prepared from plasma processed alumina nanopowder, Eriks Palcevskis
11.40 – 12.05	Holographically generated photonic structures – Analogy to bioinspired structures, Branislav Jelenković
12.05 – 12.30	Concluding remarks and closing ceremony

Afternoon – PAC meeting for PAC members

Holographically generated photonic structures – Analogy to bioinspired structures

Dejan Pantelić¹, Svetlana Savić-Šević¹, Branislav Jelenković¹, Srećko Ćurčić², Božidar Ćurčić²

¹Institute of Physics, University of Belgrade, Pregrevica 118, 11080 Zemun, Serbia

²Institute of Zoology, Faculty of Biology, University of Belgrade, Studentski Trg 16, 11000 Belgrade, Serbia

We show a analogy between photonic structures generated holographically in Dichromated pullulan (DCP) and structures found in butterfly wing scales. DCP photonic crystals show wide bandgaps of the order of 100 nm, centered at about 560 nm. SEM images show complex volume structures of DCP: Bragg volume gratings having granular structure, the size of granules being below recording wavelength. Such structure enables low index material like pullulan to have properties of photonic crystals. We compare these structures and those found in *Apatura iris* (Linnaeus, 1758) and *A. ilia* (Denis & Schiffermüller, 1775) butterfly cover scales in males (Lepidoptera: Nymphalidae). We have also observed interesting analogy between defects in periodic structures on the butterfly wing scales (places where one ridge splits into two) and fork-holograms used to generate vortex beams.



Citation overview

Self citations of selected authors are excluded. ✕

[← Back to author details](#)

[↗ Export](#) [🖨 Print](#)

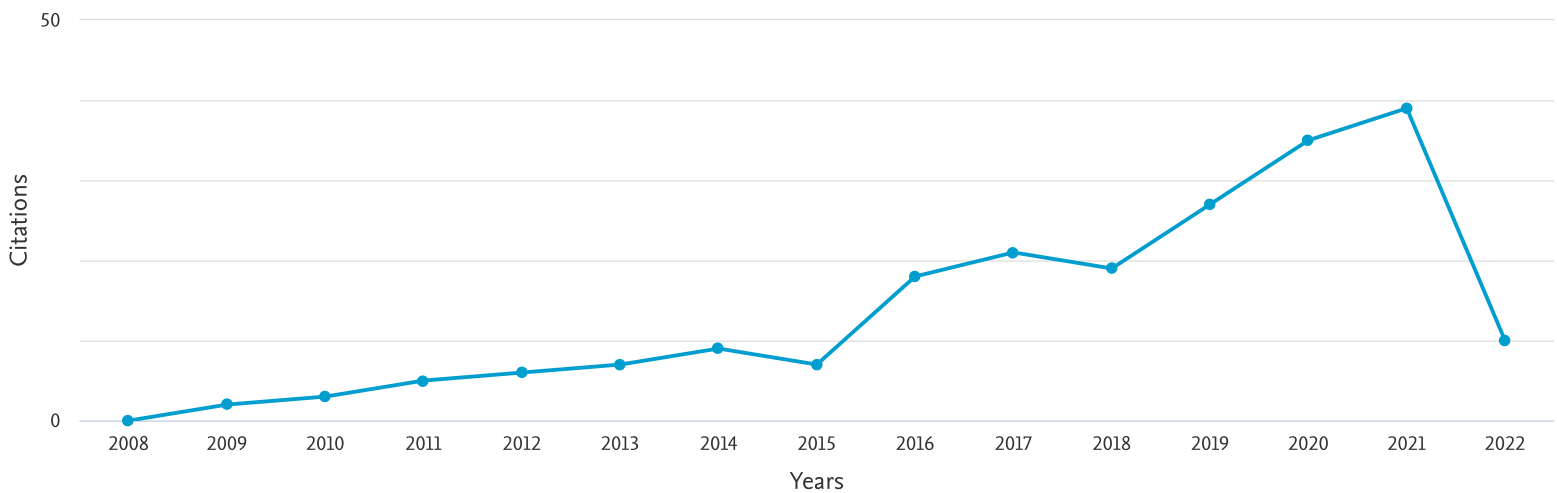
This is an overview of citations for this author.

Author *h*-index : 8 [View *h*-graph](#)

48 Cited Documents from "Savić-Šević, Svetlana N." [+ Add to list](#)

Author ID:23135540700

Date range: to Exclude self citations of selected author Exclude self citations of all authors Exclude citations from books [Update](#)



Sort on: [Date \(newest\)](#)

Page Remove


Documents	Citations	<2008	2008	2009	2010	2011	2012	2013	2014	2015	2016	2017	2018	2019	2020	2021	2022	Subtotal	>2022	Total
<input type="checkbox"/> 1 Thermo-osmotic metamaterials with large negative thermal exp...	2021															1		1	0	1
<input type="checkbox"/> 2 Synergy of interference, scattering and pigmentation for str...	2021																	0		0
<input type="checkbox"/> 3 Effects of temperature on luminescent properties of Gd ₂ ...	2020															3		3		3
<input type="checkbox"/> 4 Bat guano-dwelling microbes and antimicrobial properties of ...	2020															3	1	4		4
<input type="checkbox"/> 5 YVO ₄ :Eu ³⁺ nanopowders: Multi-mode temp...	2020														3	8	2	13		13

Documents			Citations																	Subtotal	Total	
			Total	1	0	2	3	5	6	7	9	7	18	21	19	27	35	39	10	208	0	209
<input type="checkbox"/>	6	Effects of temperature and pressure on luminescent properties...	2018													4	5	4		13		13
<input type="checkbox"/>	7	Luminescence thermometry using Gd ₂ Zr ₂ O...	2018													1	3	1	2	7		7
<input type="checkbox"/>	8	Bifurcation in reflection spectra of holographic diffraction...	2018																	0		0
<input type="checkbox"/>	9	Golden moth-inspired structures with a synergistic effect of...	2018																1	1		1
<input type="checkbox"/>	10	Orange-Reddish Light Emitting Phosphor GdVO ₄ :Sm	2018													2	1	1		4		4
<input type="checkbox"/>	11	Optical properties of volume gratings with nanosphere-filled...	2017																	0		0
<input type="checkbox"/>	12	Characterization and luminescence kinetics of Eu ³⁺	2017										1	2	1	3	1			8		8
<input type="checkbox"/>	13	Scattering-enhanced absorption and interference produce a go...	2017													2			1	3		3
<input type="checkbox"/>	14	Low-temperature photoluminescence of CuSe ₂ nano-o...	2017												2	1	1	1		5		5
<input type="checkbox"/>	15	Far-infrared spectra of dysprosium doped yttrium aluminum ga...	2016										1	2	1	1	2			7		7
<input type="checkbox"/>	16	Localization of light in a polysaccharide-based complex nano...	2016																	0		0
<input type="checkbox"/>	17	Application of tot'hema eosin sensitized gelatin as a potent...	2016										2	2	2				1	7		7
<input type="checkbox"/>	18	Structural properties and luminescence kinetics of white nan...	2015										5	8	2	4	1	5		25		25
<input type="checkbox"/>	19	Characterization and luminescent properties of Eu ³⁺	2015									2	2	4	3	2	1	2		16		16
<input type="checkbox"/>	20	Femtosecond laser induced periodic surface structures on mul...	2014									1	4	2	3	1	7	1	2	21		21
<input type="checkbox"/>	21	Biomechanical model produced from light-activated dental com...	2013																	0		0
<input type="checkbox"/>	22	Zoom system for measurement of coherent backscattering of li...	2013																	0		0
<input type="checkbox"/>	23	Self-assembly of nanostructures by a phase separation in hol...	2013																	0		0
<input type="checkbox"/>	24	Application of fourier-pade approximation in analysis of hol...	2013																	0		0
<input type="checkbox"/>	25	Butterfly scales as bionic templates for complex ordered nan...	2013									2		1		1		1		5		5
<input type="checkbox"/>	26	Localization of light in photonic crystals of biological ori...	2012																	0		0
<input type="checkbox"/>	27	Micro- and nanostructures of iridescent wing scales in purpl...	2012									1		2			2			5		5
<input type="checkbox"/>	28	Flexible design of band gaps in the biopolymer photonic crys...	2012															1		1		1
<input type="checkbox"/>	29	Biologically inspired photonic structures in Dichromated pul...	2011																	0		0
<input type="checkbox"/>	30	High angular and spectral selectivity of purple emperor (Lep...	2011					1	1	1	2	1				1	3	1		11		11
<input type="checkbox"/>	31	Modulated photoactivation of composite restoration: Measur...	2011								1	1	1			1		1		5		5

		Total	1	0	2	3	5	6	7	9	7	18	21	19	27	35	39	10	208	0	209
<input type="checkbox"/>	32 Holographic photonic structures generated in dichromated pul...	2010																	0		0
<input type="checkbox"/>	33 On the reflectivity of one-dimensional photonic crystal real...	2010																	0		0
<input type="checkbox"/>	34 Three dimensional mathematical model of tooth for finite ele...	2010				1										1			2		2
<input type="checkbox"/>	35 Multi-peak structure of photonic band gaps on dichromated pu...	2009																	0		0
<input type="checkbox"/>	36 Holographic 1D photonic crystals in dichromate pullulan	2009																	0		0
<input type="checkbox"/>	37 Band-gap photonic structures in dichromate pullulan	2009																	0		0
<input type="checkbox"/>	38 Holographic measurement of a tooth model and dental composit...	2009				1			2								1		4		4
<input type="checkbox"/>	39 Application of fourier-padé approximation in analysis of hol...	2009							1										1		1
<input type="checkbox"/>	40 Influence of the heat treatment on the band gaps in the biop...	2009																	0		0
<input type="checkbox"/>	41 Measurement of beet root extract fluorescence using TR-LIF t...	2009					1	3	2	1			1		1	1			10		10
<input type="checkbox"/>	42 Biopolymer holographic diffraction gratings	2008				1			1			1				2			5		5
<input type="checkbox"/>	43 Real-time measurement of internal stress of dental tissue us...	2007						1		1		2		1	1				6		6
<input type="checkbox"/>	44 Holographic detection of a tooth structure deformation after...	2007			1				1	1		1		1	1		1		7		7
<input type="checkbox"/>	45 Dichromated pullulan diffraction gratings: Influence of envi...	2007																	0		0
<input type="checkbox"/>	46 Holographic measurement of dental tissue contraction and str...	2007					2	1											3		3
<input type="checkbox"/>	47 Holographic fabrication of periodic microstructures in dichr...	2007																	0		0
<input type="checkbox"/>	48 Relief hologram replication using a dental composite as an e...	2005	1		1	1						1	1		1				5		6

Display: 50  results per page

1

 Top of page

About Scopus

[What is Scopus](#)

[Content coverage](#)

[Scopus blog](#)

[Scopus API](#)

[Privacy matters](#)

Language

[日本語に切り替える](#)

[切换到简体中文](#)

[切换到繁體中文](#)

[Русский язык](#)

Customer Service

[Help](#)

[Tutorials](#)

[Contact us](#)

ELSEVIER

[Terms and conditions](#) ↗ [Privacy policy](#) ↗

Copyright © Elsevier B.V. ↗. All rights reserved. Scopus® is a registered trademark of Elsevier B.V.

We use cookies to help provide and enhance our service and tailor content. By continuing, you agree to the use of cookies.





Citation overview

Self citations of all authors are excluded. ✕

[← Back to author details](#)

[↗ Export](#) [🖨 Print](#)

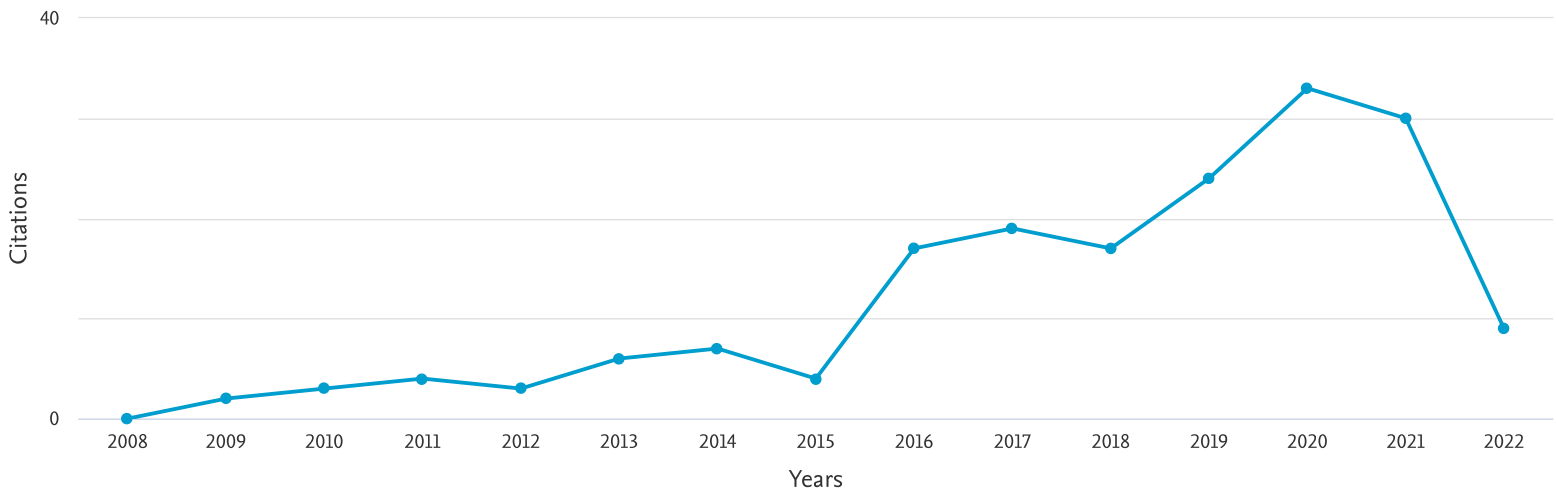
This is an overview of citations for this author.

Author *h*-index : 7 [View *h*-graph](#)

48 Cited Documents from "Savić-Šević, Svetlana N." [+ Add to list](#)

Author ID:23135540700

Date range: to Exclude self citations of selected author Exclude self citations of all authors Exclude citations from books [Update](#)




Sort on:

Page [🗑 Remove](#)

Documents	Citations	<2008	2008	2009	2010	2011	2012	2013	2014	2015	2016	2017	2018	2019	2020	2021	2022	Subtotal	>2022	Total	
<input type="checkbox"/> 1 Thermo-osmotic metamaterials with large negative thermal exp...	2021		1	0	2	3	4	3	6	7	4	17	19	17	24	33	30	9	178	0	179
<input type="checkbox"/> 2 Synergy of interference, scattering and pigmentation for str...	2021																		0		0
<input type="checkbox"/> 3 Effects of temperature on luminescent properties of Gd ₂ ...	2020															2			2		2
<input type="checkbox"/> 4 Bat guano-dwelling microbes and antimicrobial properties of ...	2020															2			2		2
<input type="checkbox"/> 5 YVO ₄ :Eu ³⁺ nanopowders: Multi-mode temp...	2020														3	6	2		11		11

		Total	1	0	2	3	4	3	6	7	4	17	19	17	24	33	30	9	178	0	179
<input type="checkbox"/>	32 Holographic photonic structures generated in dichromated pul...	2010																	0		0
<input type="checkbox"/>	33 On the reflectivity of one-dimensional photonic crystal real...	2010																	0		0
<input type="checkbox"/>	34 Three dimensional mathematical model of tooth for finite ele...	2010				1										1			2		2
<input type="checkbox"/>	35 Multi-peak structure of photonic band gaps on dichromated pu...	2009																	0		0
<input type="checkbox"/>	36 Holographic 1D photonic crystals in dichromate pullulan	2009																	0		0
<input type="checkbox"/>	37 Band-gap photonic structures in dichromate pullulan	2009																	0		0
<input type="checkbox"/>	38 Holographic measurement of a tooth model and dental composit...	2009				1				1							1		3		3
<input type="checkbox"/>	39 Application of fourier-padé approximation in analysis of hol...	2009							1										1		1
<input type="checkbox"/>	40 Influence of the heat treatment on the band gaps in the biop...	2009																	0		0
<input type="checkbox"/>	41 Measurement of beet root extract fluorescence using TR-LIF t...	2009							1	1			1		1	1			5		5
<input type="checkbox"/>	42 Biopolymer holographic diffraction gratings	2008					1		1			1				2			5		5
<input type="checkbox"/>	43 Real-time measurement of internal stress of dental tissue us...	2007						1				2		1	1				5		5
<input type="checkbox"/>	44 Holographic detection of a tooth structure deformation after...	2007			1				1	1		1		1	1		1		7		7
<input type="checkbox"/>	45 Dichromated pullulan diffraction gratings: Influence of envi...	2007																	0		0
<input type="checkbox"/>	46 Holographic measurement of dental tissue contraction and str...	2007					2	1											3		3
<input type="checkbox"/>	47 Holographic fabrication of periodic microstructures in dichr...	2007																	0		0
<input type="checkbox"/>	48 Relief hologram replication using a dental composite as an e...	2005	1		1	1						1	1		1				5		6

Display: 50  results per page1 Top of page

About Scopus

[What is Scopus](#)

[Content coverage](#)

[Scopus blog](#)

[Scopus API](#)

[Privacy matters](#)

Language

[日本語に切り替える](#)

[切换到简体中文](#)

[切换到繁體中文](#)

[Русский язык](#)

Customer Service

[Help](#)

[Tutorials](#)

[Contact us](#)

ELSEVIER

[Terms and conditions](#) ↗ [Privacy policy](#) ↗

Copyright © Elsevier B.V. ↗. All rights reserved. Scopus® is a registered trademark of Elsevier B.V.

We use cookies to help provide and enhance our service and tailor content. By continuing, you agree to the use of cookies.





Citation overview

← Back to author details

Export Print

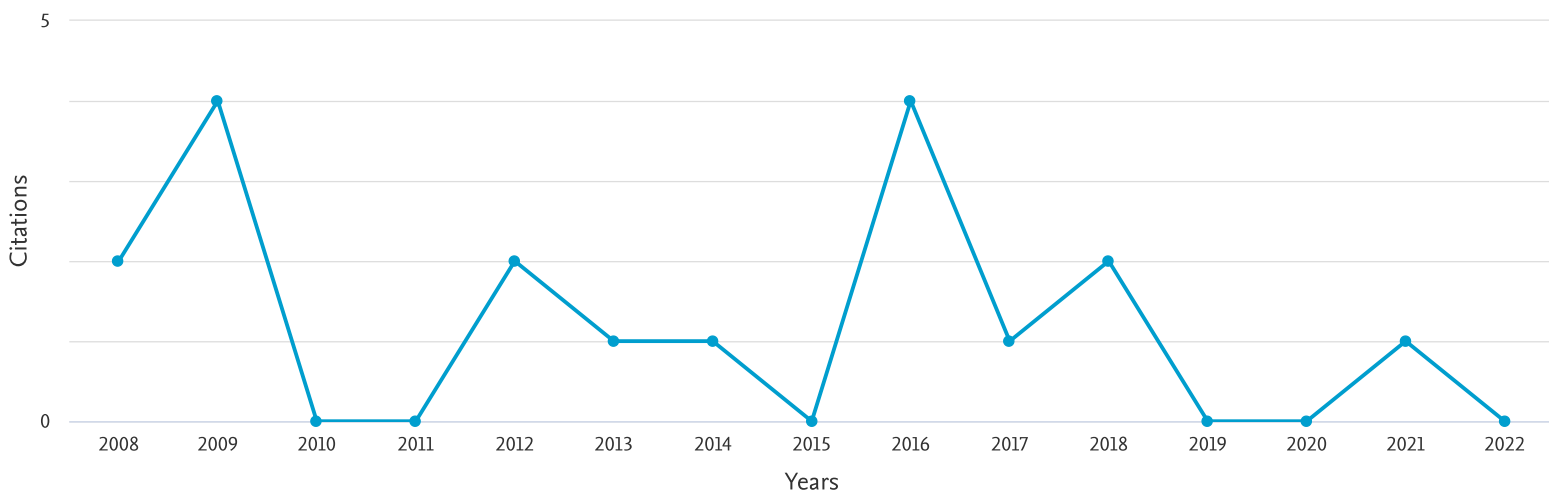
This is an overview of citations for this author.

Author *h*-index : 2 View *h*-graph

2 Cited Documents from "Savić, Svetlana" + Add to list

Author ID:7005859470

Date range: 2008 to 2022 Exclude self citations of selected author Exclude self citations of all authors Exclude citations from books Update



Sort on: Date (newest)

Page Remove

Documents	Citations	<2008	2008	2009	2010	2011	2012	2013	2014	2015	2016	2017	2018	2019	2020	2021	2022	Subtotal	>2022	Total
<input type="checkbox"/> 1 Real-time and postprocessing holographic effects in dichroma...	2002		4	2	2			1	1		2		1					9	0	13
<input type="checkbox"/> 2 Dichromated pullulan as a novel photosensitive holographic m...	1998		4		2			1	1		2	1	1			1		9	0	13

Display: 50 results per page

About Scopus

[What is Scopus](#)

[Content coverage](#)

[Scopus blog](#)

[Scopus API](#)

[Privacy matters](#)

Language

[日本語に切り替える](#)

[切换到简体中文](#)

[切换到繁體中文](#)

[Русский язык](#)

Customer Service

[Help](#)

[Tutorials](#)

[Contact us](#)

ELSEVIER

[Terms and conditions](#) ↗ [Privacy policy](#) ↗

Copyright © Elsevier B.V. ↗. All rights reserved. Scopus® is a registered trademark of Elsevier B.V.

We use cookies to help provide and enhance our service and tailor content. By continuing, you agree to the use of cookies.



Citation overview

The citation overview has been downloaded as a comma separated file (.csv).



< Back to author details

Export Print

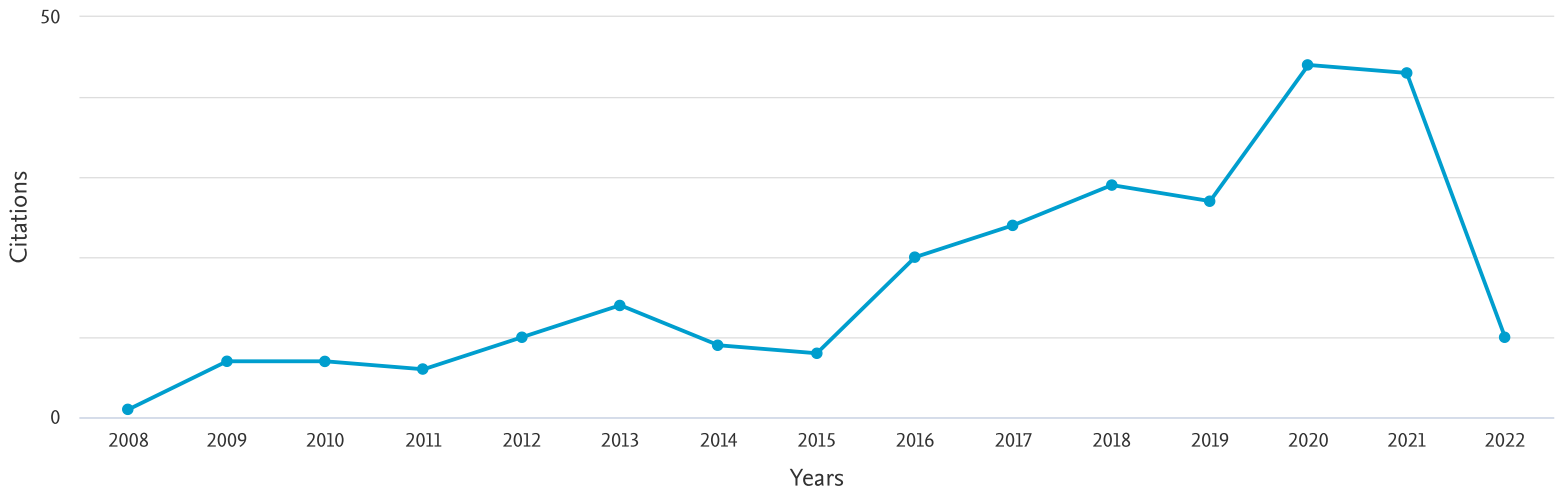
This is an overview of citations for this author.

Author *h*-index : 10 View *h*-graph

48 Cited Documents from "Savić-Šević, Svetlana N." + Add to list

Author ID:23135540700

Date range: 2008 to 2022 Exclude self citations of selected author Exclude self citations of all authors Exclude citations from books Update




Sort on: Date (newest)

Page Remove

Documents	Citations	<2008	2008	2009	2010	2011	2012	2013	2014	2015	2016	2017	2018	2019	2020	2021	2022	Subtotal	>2022	Total
<input type="checkbox"/> 1 Thermo-osmotic metamaterials with large negative thermal exp...	2021															1		1	0	1
<input type="checkbox"/> 2 Synergy of interference, scattering and pigmentation for str...	2021																	0		0
<input type="checkbox"/> 3 Effects of temperature on luminescent properties of Gd ₂ ...	2020															3		3		3
<input type="checkbox"/> 4 Bat guano-dwelling microbes and antimicrobial properties of ...	2020															3	1	4		4

Documents			Citations																	Subtotal	>2022		Total
			Total	5	1	7	7	6	10	14	9	8	20	24	29	27	44	43	10	259	0	264	
<input type="checkbox"/>	5	YVO ₄ :Eu ³⁺ nanopowders: Multi-mode temp...	2020														4	8	2	14		14	
<input type="checkbox"/>	6	Effects of temperature and pressure on luminescent propertie...	2018												1	4	7	4		16		16	
<input type="checkbox"/>	7	Luminescence thermometry using Gd ₂ Zr ₂ O...	2018												1	5	1	2		9		9	
<input type="checkbox"/>	8	Bifurcation in reflection spectra of holographic diffraction...	2018																	0		0	
<input type="checkbox"/>	9	Golden moth-inspired structures with a synergistic effect of..	2018														1	1		2		2	
<input type="checkbox"/>	10	Orange-Reddish Light Emitting Phosphor GdVO ₄ :Sm	2018												1	2	2	1		6		6	
<input type="checkbox"/>	11	Optical properties of volume gratings with nanosphere-filled...	2017																	0		0	
<input type="checkbox"/>	12	Characterization and luminescence kinetics of Eu ³⁺	2017										1	3	1	4	1			10		10	
<input type="checkbox"/>	13	Scattering-enhanced absorption and interference produce a go...	2017										1	1	2		1	1		6		6	
<input type="checkbox"/>	14	Low-temperature photoluminescence of CuSe ₂ nano-o...	2017											2	1	1	1			5		5	
<input type="checkbox"/>	15	Far-infrared spectra of dysprosium doped yttrium aluminum ga...	2016										1	2	1	1	2			7		7	
<input type="checkbox"/>	16	Localization of light in a polysaccharide-based complex nano...	2016																	0		0	
<input type="checkbox"/>	17	Application of tot'hema eosin sensitized gelatin as a potent...	2016										2	2	2			1		7		7	
<input type="checkbox"/>	18	Structural properties and luminescence kinetics of white nan...	2015									6	8	3	4	2	5			28		28	
<input type="checkbox"/>	19	Characterization and luminescent properties of Eu ³⁺	2015								3	2	5	5	2	2	2			21		21	
<input type="checkbox"/>	20	Femtosecond laser induced periodic surface structures on mul...	2014								1	4	2	3	1	7	1	2		21		21	
<input type="checkbox"/>	21	Biomechanical model produced from light-activated dental com...	2013																	0		0	
<input type="checkbox"/>	22	Zoom system for measurement of coherent backscattering of li...	2013																	0		0	
<input type="checkbox"/>	23	Self-assembly of nanostructures by a phase separation in hol...	2013																	0		0	
<input type="checkbox"/>	24	Application of fourier-pade approximation in analysis of hol...	2013																	0		0	
<input type="checkbox"/>	25	Butterfly scales as bionic templates for complex ordered nan...	2013								2		1		1		1			5		5	
<input type="checkbox"/>	26	Localization of light in photonic crystals of biological ori...	2012																	0		0	
<input type="checkbox"/>	27	Micro- and nanostructures of iridescent wing scales in purpl...	2012					1	1	1		2				2				7		7	
<input type="checkbox"/>	28	Flexible design of band gaps in the biopolymer photonic crys...	2012														1			1		1	
<input type="checkbox"/>	29	Biologically inspired photonic structures in Dichromated pul...	2011																	0		0	
<input type="checkbox"/>	30	High angular and spectral selectivity of purple emperor (Lep...	2011				1	3	2	2	1				1	1	3	1		15		15	
<input type="checkbox"/>	31	Modulated photoactivation of composite restoration: Measur...	2011						2	1	1				1			1		6		6	

		Total	5	1	7	7	6	10	14	9	8	20	24	29	27	44	43	10	259	0	264
<input type="checkbox"/>	32 Holographic photonic structures generated in dichromated pul...	2010																	0		0
<input type="checkbox"/>	33 On the reflectivity of one-dimensional photonic crystal real...	2010																	0		0
<input type="checkbox"/>	34 Three dimensional mathematical model of tooth for finite ele...	2010				1										1			2		2
<input type="checkbox"/>	35 Multi-peak structure of photonic band gaps on dichromated pu...	2009																	0		0
<input type="checkbox"/>	36 Holographic 1D photonic crystals in dichromate pullulan	2009																	0		0
<input type="checkbox"/>	37 Band-gap photonic structures in dichromate pullulan	2009																	0		0
<input type="checkbox"/>	38 Holographic measurement of a tooth model and dental composit...	2009				1			2								1		4		4
<input type="checkbox"/>	39 Application of fourier-padé approximation in analysis of hol...	2009							2										2		2
<input type="checkbox"/>	40 Influence of the heat treatment on the band gaps in the biop...	2009																	0		0
<input type="checkbox"/>	41 Measurement of beet root extract fluorescence using TR-LIF t...	2009					1	3	2	1			1		1	1			10		10
<input type="checkbox"/>	42 Biopolymer holographic diffraction gratings	2008					1		2			1				2			6		6
<input type="checkbox"/>	43 Real-time measurement of internal stress of dental tissue us...	2007	1		1	1		1		1		2		1	1				8		9
<input type="checkbox"/>	44 Holographic detection of a tooth structure deformation after...	2007	1		2	1	1		1	1		1		1	1		1		10		11
<input type="checkbox"/>	45 Dichromated pullulan diffraction gratings: Influence of envi...	2007			2	1		1	1			1	1	2			1		10		10
<input type="checkbox"/>	46 Holographic measurement of dental tissue contraction and str...	2007				1	2	1											4		4
<input type="checkbox"/>	47 Holographic fabrication of periodic microstructures in dichr...	2007				1													1		1
<input type="checkbox"/>	48 Relief hologram replication using a dental composite as an e...	2005	3	1	1	1			1			1	1		1		1		8		11

Display: 50  results per page1 Top of page

About Scopus

[What is Scopus](#)

[Content coverage](#)

[Scopus blog](#)

[Scopus API](#)

[Privacy matters](#)

Language

[日本語に切り替える](#)

[切换到简体中文](#)

[切换到繁體中文](#)

[Русский язык](#)

Customer Service

[Help](#)

[Tutorials](#)

[Contact us](#)

ELSEVIER

[Terms and conditions](#) ↗ [Privacy policy](#) ↗

Copyright © Elsevier B.V. ↗. All rights reserved. Scopus® is a registered trademark of Elsevier B.V.

We use cookies to help provide and enhance our service and tailor content. By continuing, you agree to the use of cookies.



International Conference
**Optical Holography and its
Applications**



PROGRAMME

29 – 30 September - 2000

Kyiv, Ukraine

International Conference
Optical Holography and its Applications

29 September

14.30 Optoelectronic device for identification of credit cards

*Leonid I. Muravsky, Yaroslav P. Kulynich, Olexander P. Maksymenko,
Taras I. Voronyak, Volodymyr M. Fitio, Mykhailo V. Shovgenyuk,
G.V. Karpenko Institute of Physics and Mechanics NASU, 5, Naukova str.,
Lviv, Ukraine*

15.00 Volume holographic data storage at IBM

*Geoffrey W. Burr, Hans Coufal, John A. Hoffnagle, C. Michael Jefferson,
Mark Jurich, Brian Marcus, Roger M. Macfarlane, and Robert M. Shelby
IBM Almaden Research Center, D2/K18, 650 Harry Road, San Jose, California
95120*

**15.30 Comparative information characteristics of optical by-bit and volume
holographic memories**

*S.B. Gurevich¹, A.A. Akaev², K.M. Zhumaliev², B.S. Gurevich³,
S.A. Alymkulov², A.A. Sagymbaev²,*

*1 - A.F.Ioffe Physical-Technical Institute, St.Petersburg, Russia, 2 - Institute of
Physics, National Academy of Sciences of Kyrgyzstan, 3 - ELAN Co. St.
Petersburg, Russia.*

**16.00 The reasons of information capacity limitations in volume holographic
memory devices,**

*S.B. Gurevich¹, B.S. Gurevich², K.M. Zhumaliev³, S.A. Alymkulov³,
A.A. Sagymbaev³,*

*1 - A.F.Ioffe Physical-Technical Institute, St.Petersburg, Russia, 2 - ELAN Co.
St. Petersburg, Russia, 3 - Institute of Physics, National Academy of Sciences
of Kyrgyzstan*

**16.30 High-density holographic data storage with random encoded reference
beam**

*V. Markov,
MetroLaser Inc., USA*

International Conference
Optical Holography and its Applications

30 September

10.00 Holographic Imaging by Means of the Effect of Second Harmonic Cross-Correlation of the Wavefields in in the Nonlinear Light-sensitive Material

*Yury N. Denisyuk *) Alessandra Andreoni, Maria Bondani
and Marco A.C. Potenza*

Dipartimento di Scienze Chimiche, Fisiche e Matematiche, Università degli Studi dell'Insubria, 22100 Como and INFN Milano-Università, 20133 Milano, Italy, ph.+(39)031 326225. Fax +(39)031 326230, e-mail: andreoni@fis.unico.it, *) Ioffe Physico-Technical Institute, 194021 St. Petersburg, Russia. ph.+(7)812 2479384 Fax. (7)812 2479384, e-mail: denis@holo.ioffe.rssi.ru, Submit to: Coherent optical effects and holography in linear and non-linear media.

10.30 All-optical actuators based on moving holographic gratings in photosensitive media

Sergey Sarkisov, Department of Physics, Alabama A&M University, 4900 Meridian Street, P.O. Box , 1268, Normal, Alabama 35762, USA,

Michael Curley, Department of Physics, Alabama A&M University, 4900 Meridian Street, P.O. Box, 1268, Normal, Alabama 35762, USA, Aisha Fields, Department of Physics, Alabama A&M University, 4900 Meridian Street, P.O. Box , 1268, Normal, Alabama 35762, USA,

Nikolai Kukhtarev, Department of Physics, Alabama A&M University, 4900 Meridian Street, P.O.Box, 1268, Normal, Alabama 35762, USA

Mykola Kulishov, Adtek Photomask, Montreal, Quebec, Canada.

11.00 Holographic recording in amorphous chalcogenide semiconductor thin films

Janis Teteris,

Institute of Solid State Physics, University of Latvia

11.30 Dichromated pullulan: real-time effects and holographic properties

Svetlana Savic (1), Dejan Pantelic (1), Dragica Jakovljevic(2)

(1) Institute of Physics, Pregrevica 118, 11080 Zemun, Belgrade, Yugoslavia,

(2) Institute of Chemistry, Technology and Metallurgy-Center for Chemistry, Njegoseva 12, 11000 Belgrade, Yugoslavia, Svetlana Savic, Institute of

Physics, Pregrevica 118, 11080 Zemun, Belgrade, Yugoslavia, phone: 381-11-3160-793, fax: 381-11-3162-190, e-mail: savic@phy.bg.ac.yu,

International Conference
Optical Holography and its Applications

12.00 Out Bragg-Plane Angular selectivity of Volume Holographic Grating

V. Markov, A. Khizhnyak, R. Amezquita (a),

MetroLaser Inc., USA, (a) Institute of Applied Optics, Bogota, Colombia.

12.30 Ambient humidity control for maximising replay intensity and resolution in aberration-compensated off-axis holograms of underwater objects

JJ Nebrensky (a), G Craig (b), PR Hobson (a), H Nareid (b), J Watson (b)

Dept. of Electronic and Computer Engineering, Brunel University, Uxbridge, Middlesex UB8 3PH, England; (b) Dept. of Engineering, Aberdeen University, Aberdeen AB24 3UE, Scotland ;

Tel: +44 1895 203199; Fax: +44 1895 272391 e-mail:

j.nebrensky@brunel.ac.uk

13.00 Influence of usage of approximation in diffraction equations on quality of reconstructed from hologram images in digital holography

S. Pasko¹, R. Jozwicki²,

Institute of Micromechanics and Photonics, Warsaw University of Technology, Chodkiewicza 8, 02-525 Warsaw, Poland

13.30 Multiexposure digital holography in multimedia applications

M. Sutkowski, M. Kujawinska,

Institute of Micromechanics and Photonics,

Warsaw University of Technology, ul. Chodkiewicza 8, 02-525 Warsaw, Poland

SUT@MECH.PW.EDU.PL

14.00 Investigation of optical microstructure formation in resist layer of As-S-Se,

Sergey Kostuykevych, Eugen Venger, Petr Shepeliavyi, Vladimir Girnyk, Igor Tverdohleb, Andrey Ivanovski,

Institute of semiconductor physics, NANU, 45, pr. Nauky, Kyiv, Ukraine, 03028

14.30 Analysis of optical arrangements intended for recording of holograms with optically encoded images

S.B. Odínokov, L.A. Bondarev, S.V. Kurakin

Concern "Russian Security Technology", 90, Volokolamskoe Rd., 123424, Moscow, Russia, 007-095-p. 490-48-43, f. 491-35-23

SPIE - The International Society for Optical Engineering

Ukrainian Chapter

Dear Authors: *Svetlana Savic, Dejan Pantelic, Dragica Jakovljevic*

On behalf of the Program and Organizing Committee of the International Conference "*Optical Holography and its Applications*", 28 September - 1 October 2000, it is our pleasure to invite you to present your paper *Dichromated pullulan: real-time effects and holographic properties*, as an invited oral presentation.

Plenary and poster sessions will be held in the Conference Hall of the House of Sciences (Vladimirskay St. 45) 29 September - 1 October 2000.

We will appreciate any information regarding your participation in the Conference "Optical Holography and its Applications" as soon as possible.

SPIE/Ukraine is ready to arrange with the hotel reservation for all participants. You can choose to stay in a downtown hotel(s) (price 85.00 USD to 150.00 USD) or in the Academy of Sciences' hotel (price ~ 65.00 USD). The last one is outside of the city central area, but easy to reach with city transportation system (a block from metro station). Please inform the Organizing Committee your date of arrival and preferred type of hotel.

We hope you will be able to come to Kiev in September and attend the conference.

Best regards and hope to see you in Kiev soon.



Sergey Kostyukevych
Executive Director of SPIE/UKRAINE
Secretary of Program Committee

SPIE-The International Society for Optical Engineering Ukrainian Chapter

Second Announcement
International Conference

Optical Holography and its Applications **28 September -2 October 2000** **Kiev, Ukraine**

The Conference is organized by the Ukrainian Chapter of SPIE, Institute of Applied Optics, Institute of Semiconductor Physics and Institute of Physics of the National Academy of Sciences of Ukraine (Kiev) and under auspice of the Ministry of Education of Ukraine and National Academy of Science of Ukraine. The conference is supported by SPIE/UKRAINE and Ukrainian Physical and Optical Society. The present conference is the fourth meeting on this topic organized in Kiev. Previous meetings were held in Kiev in 1989 (The International UNESCO Seminar "Three-Dimensional Holography: Science, Culture, Education), 1997 and 1999 (International conference Optical Holography and its Applications), and their reports were published in SPIE Proceedings (volume 1238 and 3486) and Journal of Semiconductor Physics, Quantum Electronics and Optoelectronics.

Optical holography is emerging from research laboratories to find wider and more effective applications in different areas of human activity, including engineering, cultural, medical and other applications. This conference will focus on recent advances of holography especially in such areas as, holographic NDT and its practical applications, real-time holography and non-linear recording materials for that.

The topics of particular interest include:

- fundamental properties of 3-D holography
- holographic recording materials and their processing
- holographic interferometry, including non-destructive testing systems and its practical applications in engineering, culture, material study, etc.
- coherent and incoherent optical effects in holography (multi-beam interaction, beam coupling and combining, coherent scattering, image processing, etc.)
- holographic data storage
- optical security elements

Conference Chair: Vladimir Markov, International Center "Institute of Applied Optics," Ukraine

Co-Chair: James D. Trolinger, MetroLaser Inc. USA,

International Advisory and Program Committee:

Prof. Stephen A. Benton, MIT, Cambridge, USA
Prof. Pierre M. Boone, Gent Univ./Inst. of Applied Optics, Belgium
Prof. Mikhail S. Brodin, Inst. of Physics, NAN Ukraine
Prof. Yuri N. Denisyuk, Ioffe Institute, RAN, Russia
Prof. Jean-Marc Fournier, Rowland Inst., Cambridge, USA
Prof. Bert Hesselink, Stanford Univ., USA
Prof. Klaus Hinsch, Oldenburg Univ., Germany
Prof. Roger A. Lessard, Quebec Univ., Canada
Prof. Demetrius Psaltis, Cal.Tech., USA
Prof. Sergey V. Svechnikov, Inst. of Semicond Physics,
Prof. Marat S. Soskin, Inst. of Physics, NAN Ukraine, Kiev
Dr. Dogan Timucin, NASA, USA
Dr. Sergey A. Kostioukevitch, Kiev, Ukraine - Secretary

Organizing Committee:

S.Anokhov, G.Beylin, S. Chaikovskii, A. Chaka, V. Grabovsky, T. Nadeina, A.Savchuk, I.Yavtushenko

Preliminary List of Speakers

1. COMMERCIALIZING OF INNOVATIVE, OPTO-ELECTRONIC TIRE TESTING,
Hans Rottenkolber, Bergweg 47, D-83123 Amerang/Germany
e-mail: rottenkolber.rotech@t-online.de
2. A NEW LASER BASED METHOD OF NON-DESTRUCTIVE TESTING FOR THE DETECTION AND QUANTIFICATION OF HIDDEN CORROSION
John M. Webster, Holographics Inc., USA
Jackie Mew, Robert Topp, University of Portsmouth, UK
3. AMBIENT HUMIDITY CONTROL FOR MAXIMISING REPLAY INTENSITY AND RESOLUTION IN ABERRATION-COMPENSATED OFF-AXIS HOLOGRAMS OF UNDERWATER OBJECTS
JJ Nebrensky (a), G Craig (b), PR Hobson (a), H Nareid (b), J Watson (b)
(a) Dept. of Electronic and Computer Engineering, Brunel University, Uxbridge, Middlesex UB8 3PH, England
(b) Dept. of Engineering, Aberdeen University, Aberdeen AB24 3UE, Scotland
Tel: +44 1895 203199; Fax: +44 1895 272391 e-mail: j.nebrensky@brunel.ac.uk
4. ALL-OPTICAL ACTUATORS BASED ON MOVING HOLOGRAPHIC GRATINGS IN PHOTSENSITIVE MEDIA,
Sergey Sarkisov, Department of Physics, Alabama A&M University, 4900 Meridian Street, P.O.Box , 1268, Normal, Alabama 35762, USA,
Michael Curley, Department of Physics, Alabama A&M University, 4900 Meridian Street, P.O.Box, 1268, Normal, Alabama 35762, USA, Aisha Fields, Department of Physics, Alabama A&M University, 4900 Meridian Street, P.O.Box , 1268, Normal, Alabama 35762, USA,
Nikolai Kukhtarev, Department of Physics, Alabama A&M University, 4900 Meridian Street, P.O.Box, 1268, Normal, Alabama 35762, USA
Mykola Kulishov, Adtek Photomask, Montreal, Quebec, Canada.
5. REAL-TIME HOLOGRAPHY AND SPECTROSCOPY BASED ON REVERSIBLE PHOTBLEACHING IN ORGANIC DYES,
Lantukh Yuri Dmitrievich., Bondarenko Viktor Anatolievich., Ketsle Garry Albertovich, Letuta Sergey Nikolaevich, Pashkevitch Sergey Nikolaevich., 3. Orenburg State University, Institute of Micro- and Nanotechnologies, Pobedy 13, Orenburg, 460352, RUSSIA. E-mail: lantukh@ic.osu.ru,
6. DICHROMATED PULLULAN: REAL-TIME EFFECTS AND HOLOGRAPHIC PROPERTIES,
Svetlana Savic (1), Dejan Pantelic (1), Dragica Jakovljevic(2)
(1) Institute of Physics, Pregrevica 118, 11080 Zemun, Belgrade, Yugoslavia, (2) Institute of Chemistry, Technology and Metallurgy-Center for Chemistry, Njegoseva 12, 11000 Belgrade, Yugoslavia, Svetlana Savic, Institute of Physics, Pregrevica 118, 11080 Zemun, Belgrade, Yugoslavia, phone: 381-11-3160-793, fax: 381-11-3162-190, e-mail: savic@phy.bg.ac.yu. Submit to: Holographic recording materials
7. FEEDBACK-OPTIMIZED HOLOGRAMS RECORDING IN LINBO₃:Fe
Sergiy L. Pavlyuk, Konstantin V. Shcherbin, Serguey G. Odoulov,
Institute of Physics, National Academy of Sciences, Prospekt Nauki 46, 03650 Kiev, Ukraine, Phone: +380 - 44 2650818, Fax: +380 44 2652359, pavluk@iop.kiev.ua, kshcherb@iop.kiev.ua, odoulov@iop.kiev.ua,
Boris Sturman,
International Institute for Nonlinear Studies, Koptyg Ave.1, 630090 Novosibirsk, Russia, sturman@iae.nsk.ru,
Klaus H. Ringhofer, Vlado Kamenov,
Fachbereich Physik der Universitaet, D-49069 Osnabrueck, FRG, ringhofe@uos.de, vlado@physik.uni-osnabrueck.de,
8. GALVANOMAGNETIC PROPERTIES OF PB_{1-x}SN_xTE POLYCRYSTALLINE PRESSED SAMPLES
F.S. Terra, M. Abdel-Rafea, and M. Monir*, Solid State Physics Department, National Research Centre, Dokki, Cairo, Egypt., *Physics Department, Faculty of Science, Cairo University, Cairo, Egypt.
9. HOLOGRAPHIC IMAGING BY MEANS OF THE EFFECT OF SECOND HARMONIC CROSS-CORRELATION OF THE WAVEFIELDS IN IN THE NONLINEAR LIGHT-SENSITIVE MATERIAL,
Yury N.Denisyuk *) Alessandra Andreoni, Maria Bondani, and Marco A.C.Potenza,
Dipartimento di Scienze Chimiche, Fisiche e Matematiche, Universita degli Studi dell Insubria, 22100 Como and INFN Milano-Universita, 20133 Milano, Italy, ph.+(39)031 326225.Fax +(39)031 326230,e-mail:andreoni@fis.unico.it, *) Ioffe Physico -Technical Institute, 194021 St.Petersburg,Russia. ph.+(7)812 2479384 Fax.(7)812 2479384, e-mail:denis_@holo.ioffe.rssi.ru, Submit to: Coherent optical effects and holography in linear and non-linear media.
10. WAVEGUIDE HOLOGRAPHY WITH SURFACE PLASMON MODES,

Guo Ping Wang, Department of Physics, Wuhan University, Wuhan 430072, China., Fax: 86-27-87654569, E-mail: kp_wang@hotmail.com)

11. RELIEF HOLOGRAMS ON SILVER HALIDE MATERIALS: ONE MORE ATTEMPT,
A.N.Timoshenko, Institute of Applied Optics
12. INVESTIGATION OF OPTICAL MICROSTRUCTURE FORMATION IN RESIST LAYER OF AS-S-SE,
Sergey Kostuykevych, Eugen Venger, Petr Shepeliavyi, Vladimir Girnyk, Igor Tverdohleb, Andrey Ivanovski,
13. Holography in real time and protective holographic elements in the securities of Ukraine,
14. V.Komarov, V.Belorus
15. HOLOGRAPHIC RECORDING IN AMORPHOUS CHALCOGENIDE SEMICONDUCTOR THIN FILMS,
Janis Teteris, Institute of Solid State Physics, University of Latvia
16. DYNAMIC PHASE HOLOGRAPHIC MEDIUM WITH DIMERIZABLE ANTHRACENE DERIVATIVES,
Prof. **Vladimir V. Mogilny**, Dr. Yuri V. Gritsai, Belarus State University, Physical Optics Department, F. Skoriny av.,4, Minsk, 220050, Rep. of Belarus. Telephone: (017) 206-62-28, E-mail: mogilny@phys.bsu.unibel.by .
Submit to: Holographic recording materials
17. COHERENT-OPTICAL NDT TECHNIQUES IN SEMI-INDUSTRIAL APPLICATIONS
P.Boone, Gent University, Belgium
18. POLARIZATION HOLOGRAPHIC MEMORY OF SUPERHIGH CAPACITY,
Barbara N. Kilosanidze, Shermazan D. Kakhkhashvili, Optical Research Department, Institute of Cybernetics of the Georgian Academy of Sciences, Sandro Euli str. 5, 380086 Tbilisi, Georgia,
19. COMPARATIVE INFORMATION CHARACTERISTICS OF OPTICAL BY-BIT AND VOLUME HOLOGRAPHIC MEMORIES,
S.B.Gurevich¹, A.A.Akaev², K.M.Zhumaliev², B.S.Gurevich³, S.A.Alymkulov², A.A.Sagymbaev²,
1 - A.F.Ioffe Physical-Technical Institute, St.Petersburg, Russia,
2 - Institute of Physics, National Academy of Sciences of Kyrgyzstan,
3 - ELAN Co. St. Petersburg, Russia.
20. THE REASONS OF INFORMATION CAPACITY LIMITATIONS IN VOLUME HOLOGRAPHIC MEMORY DEVICES,
S.B.Gurevich¹, B.S.Gurevich², K.M.Zhumaliev³, S.A.Alymkulov³, A.A.Sagymbaev³,
1 - A.F.Ioffe Physical-Technical Institute, St.Petersburg, Russia, 2 - ELAN Co. St. Petersburg, Russia, 3 - Institute of Physics, National Academy of Sciences of Kyrgyzstan.
21. NEW PRINCIPLES OF DEVELOPMENT OF ASSOCIATIVE 2D-MEMORIES BASED ON MATRIX-TENSOR EQUIVALENT MODELS,
Vladimir G.Krasilenko, A.E.Nikolsky, V.M.Voloshin, A.V.Zaitsev, Vinnitsa, Ukraine.
22. HIGH-DENSITY HOLOGRAPHIC DATA STORAGE WITH RANDOM ENCODED REFERENCE BEAM
V. Markov, MetroLaser Inc., USA
23. VOLUME HOLOGRAPHIC DATA STORAGE AT IBM
Geoffrey W. Burr, Hans Coufal, John A. Hoffnagle, C. Michael Jefferson, Mark Jurich, Brian Marcus, Roger M. Macfarlane, and Robert M. Shelby
IBM Almaden Research Center, D2/K18, 650 Harry Road, San Jose, California 95120
23. "Out Bragg-Plane" Angular selectivity of Volume Holographic Grating,
V.Markov, A.Khizhnyak, R.Amezquita (a),
MetroLaser Inc., USA,
(a) Institute of Applied Optics, Bogota, Colombia.
24. Single-layer color holograms and their dispersive characteristics,
Gert von Bally (a) A. Timoshenko (b), Vladimir Markov (a), Anatoliy Khizhnyak,
(a) Munster University, Germany
(b) Institute of Applied Optics, Kiev, Ukraine
(c) MetroLaser Inc., USA,
25. BIOMOLECULAR OPTOELECTRONICS WITH BACTERIODOPSIN
A. Lal, J. Trolinger,
MetroLaser Inc., USA.
26. HIGH RESOLUTION OPTICAL PROFILOMETRY,
J. Millerd, N. Brock,
4D Vision Technology, USA.
27. REAL TIME HOLOGRAM COUPLED-LASER CAVITIES WITH MOVING OUTPUT MIRROR
A. Khizhnyak, V. Markov, J. Trolinger,
MetroLaser Inc., USA.
28. **Influence of usage of approximation in diffraction equations on quality of reconstructed from hologram images in digital holography.**

S. Paško¹, R. Józwicki², Institute of Micromechanics and Photonics, Warsaw University of Technology, Chodkiewicza 8, 02-525 Warsaw, Poland

29. Multiexposure digital holography in multimedia applications

M. Sutkowski¹, M. Kujawińska², Institute of Micromechanics and Photonics
Warsaw University of Technology, ul. Chodkiewicza 8, 02-525 Warsaw, Poland

¹ e-mail: sut@mech.pw.edu.pl, fax: +48 (22) 660-86-01

² e-mail: mkzto@mp.pw.edu.pl, fax: +48 (22) 660-86-01

30. "High-capacity holographic memory with ultra-high data transfer rate"

L. Hesselink, S.Orlov, W. Phillips, Stanford University, USA.

31. Optoelectronic device for identification of credit cards

Leonid I. Muravsky, Yaroslav P. Kulynych, Olexander P. Maksymenko, Taras I.Voronyak, Volodymyr M. Fitio, Mykhailo V. Shovgenyuk, G.V. Karpenko Institute of Physics and Mechanics NASU, 5, Naukova str., Lviv, Ukraine.

32. Characterization of fractal surfaces and the angular incidence

M. Lehman, Lisboa 14-A, Col. Juárez, Del. Cuauhtemoc, 06600 Mèxico DF (MEXICO)

Phone: 0052-5566-5472, Fax: 0052-5566-5196, e-mail: mlehman@ole.com

33. An analysis of computer-generated holograms with fractal characteristics

M. Lehman, Lisboa 14-A, Col. Juárez, Del. Cuauhtemoc, 06600 Mèxico DF (MEXICO)

Phone: 0052-5566-5472, Fax: 0052-5566-5196, e-mail: mlehman@ole.com

34. Experimental investigation of solar light coherence

Dmitry V. Panenko, National Taurida V.Vernadsky University, Simferopol, 95007, Ukraine

e-mail: panenko@ccssu.crimea.ua

35. Real-time holography and spectroscopy based on reversible photobleaching in organic dyes

Lantukh Yuri Dmitrievich., Bondarenko Viktor Anatolievich., Ketsle Garry Albertovich, Letuta Sergey Nikolaevich, Pashkevitch Sergey Nikolaevich, Orenburg State University,

Institute of Micro- and Nanotechnologies, Pobedy 13, Orenburg, 460352, RUSSIA.

E-mail: lantukh@ic.osu.ru

The Conference-Colloquium will be held in the capital of Ukraine - in Kiev, which is an important center of scientific research and higher education in Ukraine. More than ten museums, many art galleries and theaters testify Kiev's flourishing cultural life. With its historical buildings, and churches Kiev represents an exciting place to visit.

GENERAL INFORMATION

Location: The Conference will be held in the capital of Ukraine - in Kiev which is an important center of scientific research and education in Ukraine. More than ten museums, many art galleries and theaters testify Kiev's flourishing cultural life. With its historical buildings, churches Kiev represents an exciting place to visit, especially in October.

Language: The official language of the Conference is English.

Registration and Accommodation: The Registration Fees for participants and accompanying persons are US \$ 150 and US \$ 50, respectively. It can be paid in time of registration. The Fee includes: -participation in all scientific sessions at the Conference; -all printed materials of the Conference, including the receiving the Proceedings (after their publishing); - lunches during the Conference; -coffee-breaks at sessions; -transport and accommodation services; main excursion program. The participants of conference should be aware that stay in a hotel is not included in Registration Fees.

Hotel reservation will be made according to the participant's arrival and departure dates.

The Organizing Committee will provide transportation of the participants from the Kiev airport "Borispol" or the Kiev Central railway station.

Attendees should make their own travel arrangement to/from Ukraine.

Facilities: Session rooms will be equipped with a slide and also overhead projectors. Fax, E-mail and Copy machines will be available.

A participant can receive messages at: Fax: +380 (44) 2655430; E-mail: sekret@spie.org.ua.

Visas: In general, both a valid passport and Ukrainian visa are required for entry into Ukraine, however, citizens of the countries having a special agreement with Ukraine don't need visas. A visa may be obtained at Ukrainian Embassy or Consulate.

Social Programs: Excursions to historical, cultural sites of Kiev and sightseeing are planned.

Organizing Committee can also help to arrange an individual scientific or tourist program for participants around Ukraine. The participants are welcome to inform in advance Organizing Committee about their travel plans.

For further information please contact:

Sergey Kostioukevitch, Executive Director of SPIE/UKRAINE, <http://www.spie.org.ua>

Phone: +380 (44) 265-62-05, Fax: +380 (44) 265-54-30, E-mail: sekret@spie-ukr.kiev.ua;

Mailing address: SPIE/UKRAINE. 45, Prospect Nauki, Kiev, 252028, UKRAINE

Dr. Vladimir B. Markov, Head, Applied Optics Group

MetroLaser Inc., 18010 Skypark Circle, Suite 100

Irvine, CA 92614-6428, USA

Phone: (949) 553-0688, Fax. (949) 553-0495, E-mail: vmarkov@metrolaserinc.com

<http://www.metrolaserinc.com>

Thank you for reviewing for Micron

From **Micron**
Sender **em.jmic.0.6c8513.829a147c@editorialmanager.com**
To **Svetlana Savic-Sevic**
Reply-To **Micron**
Date **2020-07-10 12:05**

Message Body

Manuscript Number: JMJC_2020_67R1

Comparative study of nanostructures present in the wing of various orange-coloured Nymphalid butterflies

Arra Abhinay; Harekrushna Sahoo; Monalisa Mishra

Dear Dr Savic-Sevic,

Thank you for reviewing the above referenced manuscript. I greatly appreciate your contribution and time, which not only assisted me in reaching my decision, but also enables the author(s) to disseminate their work at the highest possible quality. Without the dedication of reviewers like you, it would be impossible to manage an efficient peer review process and maintain the high standards necessary for a successful journal.

You will shortly receive a notification from Elsevier's reviewer recognition platform, which provides you with a link to your "My Elsevier Reviews" private profile page, certificates, editor recognition as well as discounts for Elsevier services.

I hope that you will consider Micron as a potential journal for your own submissions in the future.

Kind regards,

Roberto Romani

Receiving Editor

Micron

More information and support

You will find guidance and support on reviewing, as well as information including details of how Elsevier recognises reviewers, on Elsevier's Reviewer Hub: <https://www.elsevier.com/reviewers>

FAQ: How can I reset a forgotten password?
https://service.elsevier.com/app/answers/detail/a_id/28452/supporthub/publishing/kw/editorialmanager/

For further assistance, please visit our customer service site: <https://service.elsevier.com/app/home/supporthub/publishing/>. Here you can search for solutions on a range of topics, find answers to frequently asked questions, and learn more about Editorial Manager via interactive tutorials. You can also talk 24/7 to our customer support team by phone and 24/7 by live chat and email.

In compliance with data protection regulations, you may request that we remove your personal registration details at any time. (Use the following URL: <https://www.editorialmanager.com/jmic/login.asp?a=c>). Please contact the publication office if you have any questions.

Thank You

From **Optical and Quantum Electronics (OQEL)**
Sender **em.oqel.0.5761cb.c318a6ed@editorialmanager.com**
To **Svetlana Savic-Sevic**
Reply-To **Optical and Quantum Electronics (OQEL)**
Date **2017-11-21 11:56**

Message Body

Dear Dr. Savic-Sevic,

Thank you very much for your review of manuscript

OQEL-D-17-00817, "Polarization holographic gratings with high diffraction efficiency recorded in azopolymer PAZO".

We greatly appreciate your assistance.

With kind regards,

Journals Editorial Office

Springer

[medpreg][ID 30909] Primljena recenzija članka

From **SCIndeks Asistent**

To **Svetlana Savić-Šević**

Date **2021-03-14 22:28**

Message Body

Poštovana Svetlana Savić-Šević,

Hvala Vam što ste izradili recenziju članka "Nove tehnike zasnovane na biofotonici – primena u dentalnoj medicini: pregledni rad" za časopis Medicinski pregled. Cenimo Vaš doprinos kvalitetu radova objavljenih u našem časopisu.

Srdačno,
Ljilja Mijatov Ukropina
Univerzitet u Novom Sadu, Medicinski fakultet, Zavod za anatomiju
ljilja.mijatov@gmail.com

Medical Review Society of Physicians of Vojvodina of the Medical Society of Serbia Vase Stajića 9 21000 Novi Sad Tel/fax: +381 21 528 767 Fax: +381 21 521 096 E-mail: dlv@neobee.net http://www.dlv.org.rs/izdavacka_medicenski.htm <http://aseestant.ceon.rs/index.php/medpreg>

Ovaj mejl je poslat sa sistemskog naloga. Ako želite da odgovorite na njega, molimo Vas da koristite sledeću adresu e-pošte:
This e-mail is sent from system account. To reply, please use the following e-mail address:
"Ljilja Mijatov Ukropina"
ljilja.mijatov@gmail.com

Optical Properties of Volume Gratings with Nanosphere-Filled Layers – Biomimetics of Moth Structures

Svetlana Savić-Šević¹, Branislav Salatić¹, Dejan Pantelić¹,
Branja Jelenković¹, Srećko Čurčić², and Dejan Stojanović³

¹ Institute of Physics, University of Belgrade, Pregrnica 118, 11080 Belgrade, Serbia

² Institute of Zoology, University of Belgrade—Faculty of Biology, Studentski Trg 16, 11000 Belgrade, Serbia

³ Institute of Lowland Forestry and Environment, University of Novi Sad,

Antona Cehova 13, 21000 Novi Sad, Serbia

Tel: (381) 62 802 6967, e-mail: savic@ipb.ac.rs

ABSTRACT

A new type of layered photonic structure, whose alternating layers are filled with randomly dispersed nanospheres, is fabricated and its optical properties are experimentally and theoretically analysed. Structures are made on a pullulan doped with chromium ions (dichromated pullulan – DCP) using holography. We found that experimental structures are similar to those observed on wings of the *Diachrysia chrysitis* moth, having layers of overlapping scales. DCP photonic structure has alternating air-pullulan layers, held in place by sparsely separated nano-pillars, and air voids filled with 30 – 60 nm diameter nanospheres which act as scatterers. Theoretical analysis of such structures shows that the scattering and interference interact to enhance the local field within the layers and increase the residual absorption of the material. We compare optical properties of moth scales with properties of structures fabricated in DCP, and calculated from the functional model.

Keywords: holography, photonic structures, nonlinear analysis, bio-mimetics.

1. INTRODUCTION

Nano and micro structures found in insects are increasingly becoming inspiration for fabrications of similar photonic structures because of their unique optical properties [1]. In that respect, butterflies and moths (Lepidoptera) are particularly interesting, due to their intricately nano-patterned wing scales.

There are different methods to imitate natural photonic structures [1], but holography is one of the simplest. It was applied to suitable photo-sensitive materials, such as photoresists [2]. We use interference (holographic) lithography to manufacture Bragg gratings in a home-made dichromated material, based on pullulan [3] (a linear homo-polysaccharide produced by a yeast-like fungus *Aureobasidium pullulans*). In that way, a number of alternating air-pullulan layers, filled with spherical nanoparticles are produced on large substrates. Nano-spheres diffuse the radiation, prevalently in the blue-green part of the spectrum.

Here we show that fabricated structures and their optical properties are similar to those found on wings of the *Diachrysia chrysitis* moth. Their wings are covered with double layer of tiny, overlapping, scales, each individual scale consists of two membranes (laminae) with rough internal surfaces, with roughness between 30 – 50 nm.

We develop theoretical model to describe optical properties of structures with ordered and disordered components, confirming a useful interplay between scattering, local field enhancement, planar waveguiding and interference. From the theoretical point of view, the incoming radiation is treated as being split into scattered and specular components, which are treated separately. Scattered radiation is analyzed by the surface scattering theory [4], supplemented by the intensity enhancement mechanism in planar layers [5]. The specular component interferes on a multilayer structure and is calculated using transfer matrix method [6].

2. FABRICATION OF DCP VOLUME HOLOGRAPHIC GRATING

Diffraction gratings with spherical inclusions are fabricated by combination of holographic method (top-down technique) and non-solvent-induced phase separation (bottom-up technique) [7]. The whole process goes in several steps: (1) preparation of DCP film on a glass plate (2) film exposure using a laser (3) development of exposed film (4) immersion in a non-solvent bath (isopropyl) at room temperature, and (5) drying in closed vessel.

In the first step, DCP was prepared by mixing 8% aqueous solution of pullulan (from Sigma-Aldrich) and 45% of the ammonium dichromate (by weight of pullulan). The solution was coated onto a clean glass slide in a horizontal position and the film was dried overnight under normal laboratory conditions. Dry DCP film is yellowish and transparent.

The film was exposed at normal incidence using a single longitudinal mode, diode pumped Nd YAG laser, at 532 nm. After propagation through the emulsion, beam was reflected back from a mirror behind the DCP plate. The two counter-propagating beams interfere to create a standing wave pattern and grating within an emulsion. The interference pattern consists of planes parallel to the substrate surface with spacing $d = \lambda/2n$,

where λ is the wavelength of the laser source and $n = 1.47$ is the refractive index of DCP. During exposure, hexavalent chromium ion Cr^{+6} is photo-reduced to trivalent Cr^{+3} , which covalently cross-links with pullulan molecules in the areas of constructive interference. Cross-linking hardens the pullulan, creating a solubility difference between exposed and unexposed regions.

DCP plate was chemically processed after exposure. Mixture of water and isopropyl alcohol (3:1 ratio) was used as a developer, which dissolves unexposed material. After two minutes, developer was replaced with pure isopropyl-alcohol used to dehydrate the DCP film. Finally, material is dried in closed vessel.

3. MODEL FOR SCATTERING FROM DIFFRACTION GRATINGS WITH NANOPARTICLES

Here we outline a theory of volume gratings with subwavelength, nanometer sized spherical inclusions (schematically shown in Fig. 1a) – details can be found in [8]. Under these assumptions, scalar surface-scattering theory is applicable, which predicts splitting of the incident light into two components: one, regular, propagating as if the surface is perfectly flat, and the other diffusely scattered (haze) – see Fig. 1b. Scattering effectively reduces Fresnel reflection and transmission coefficients according to [4]:

$$T_H(\lambda) = T_0 \left[1 - \exp \left(- \left[\frac{2\pi\sigma}{\lambda} (n_i \cos \phi_i - n_t \cos \phi_t) \right]^2 \right) \right] \quad (1)$$

$$R_H(\lambda) = R_0 \left[1 - \exp \left(- \left[\frac{4\pi\sigma}{\lambda} n_i \cos \phi_i \right]^2 \right) \right] \quad (2)$$

where T_0 and R_0 are the transmittance and the reflectance of a perfectly flat surface respectively, λ is the vacuum wavelength, ϕ_i and ϕ_t are the angles of incidence and refraction, n_i and n_t are corresponding refractive indices, while σ is the surface RMS roughness. Calculation, based on Eqs. (1) and (2), shows that between 1% and 3% of incident radiation is scattered at each interface, depending on the wavelength and assuming normal angle of incidence ($\phi_i = 0$), RMS roughness $\sigma = 20$ nm and the refractive index of pullulan $n_i = 1.47$. As expected, short wavelengths are scattered more than long. The scattered light has a tendency to be trapped inside chitin layers, in a manner similar to textured solar cells. Local field enhancement due to scattering and fraction of the incident radiation escaping the layer are calculated based on formulas in [5].

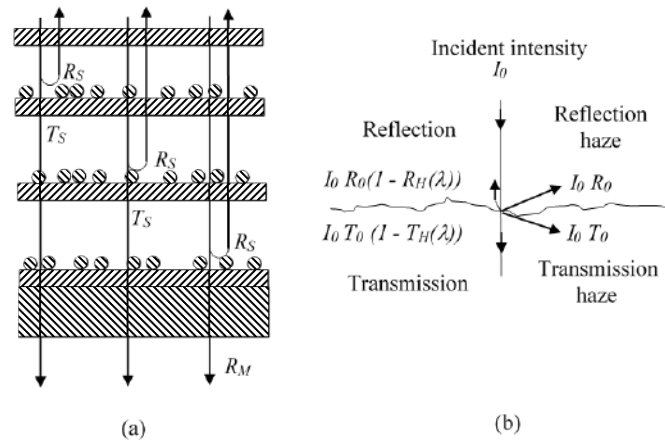


Figure. 1: (a) Schematic presentation of a diffraction grating with nano-sized particles; (b) Incident radiation is divided into specular component and haze.

4. PROPERTIES OF LAYERED SCATTERING STRUCTURES

In this section we compare morphology and optical properties of structures on moth's scales and fabricated photonic structures in DCP. And also present results of theoretical model that calculates transmission and reflection from similar structures, taking into account interference and scattering on multiple layers and nano particles.

Morphology of the moth scales and DCP grating were investigated using high resolution field emission scanning electron microscopes (Mira FEGSEM, manufactured by Tescan). Moth wing is covered with overlapping layers of scales, which produce a volume structure. Each scale has rough internal surfaces with a number of spherical inclusions (Fig. 2a). A DCP grating has a similar structure. It is layered too, with nano-spheres filling the space between the layers (Fig. 2b).

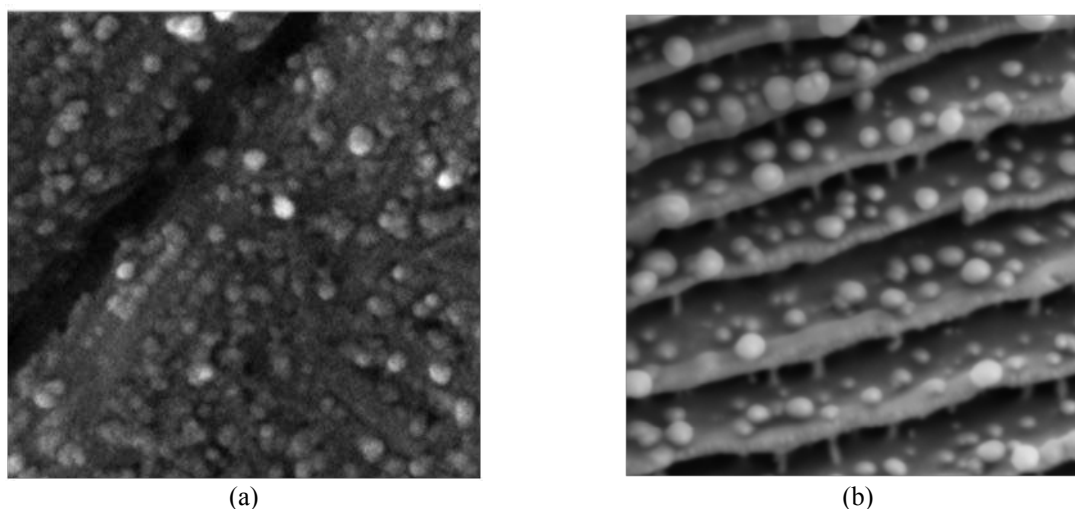


Figure 2. FEGSEM image of: (a) Internal surface of the *D. chrysitis* wing scale;
(b) Internal structure of a DCP grating.

Measured transmission and reflection spectra of the *D. chrysitis* wings and the DCP grating are presented in Figs. 3a and 3b. The maximum of reflection peaks between 500 – 550 nm. Transmission increases in the near infrared.

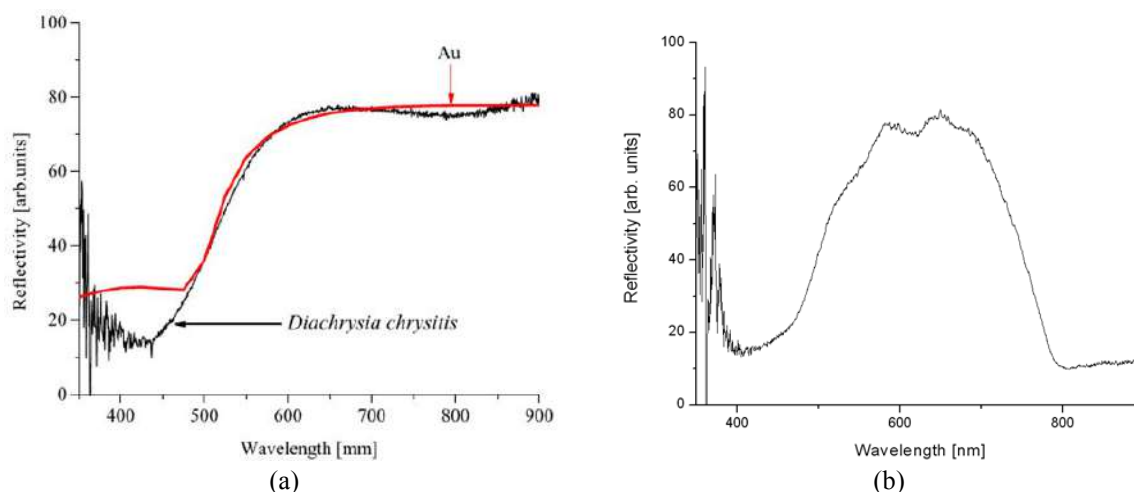


Figure 3. Experimentally recorded reflection spectra of (a) the *D. chrysitis* wing (compared to spectrum of metallic gold) and (b) the DCP grating.

In Fig. 4 we present a reflection spectrum using transfer matrix method for several values of RMS roughness. By comparing the averaged spectrum with the experimentally recorded one agreement is qualitatively good.

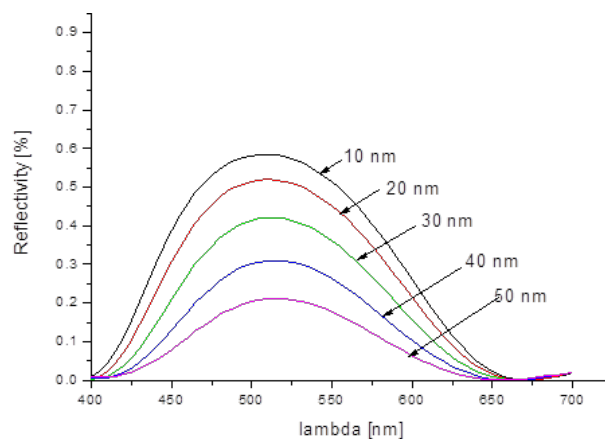


Figure 4. Reflectance spectrum of a model calculated by transfer matrix method with scattering effects included. Family of curves presents spectra for rough surface RMS ranging from 10 – 50 nm.

5. CONCLUSIONS

We have shown that peculiar, natural photonic structure can be reproduce by using relatively simple method of holographic lithography. Fabricated photonic structures exhibit similar morphology and optical properties as structures on scales on wings of *Diachrysia chrysitis* moth. Measured optical reflection spectra and calculated by finite element method, applied to the model simulating a multi-layers with nan-sizes particles in between, have shown good agreement between the two.

ACKNOWLEDGEMENTS

Authors like to acknowledge financial support from projects ON171038 and III45016 of the Ministry of Education, Science and Technological Development of the Republic of Serbia.

REFERENCES

- [1] O.Karthaus *ed.*: *Biomimetics in Photonics*, CRC Press (2013).
- [2] R. H. Siddique, R. Hünig, A. Faisal, U. Lemmer, and H. Hölscher: Fabrication of hierarchical photonic nanostructures inspired by Morpho butterflies utilizing laser interference lithography, *Optical Materials Express* 5, 996-1005 (2015).
- [3] S. Savić-Šević and D. Pantelić: Dichromated pullulan diffraction gratings: Influence of environmental conditions and storage time on their properties, *Applied Optics* 46, 287-291 (2007).
- [4] D. Domine, F.-J. Haug, C. Battaglia, and C. Ballif: Modeling of light scattering from micro- and nanotextured surfaces, *J. Appl. Phys* 107, 044504:1-8 (2010).
- [5] E. Yablonovich and G. D. Cody: Intensity enhancement in textured optical sheets for solar cells, *IEEE Trans. Electron Devices* 29, 300 (1982).
- [6] J. Springer, A. Porube, and M. Vanacek: Improved three-dimensional optical model for thin film silicon solar cells, *J. Appl. Phys.* 96, 5329 (2004).
- [7] Y. Wang et al.: Phase-separation-induced micropatterned polymer surfaces and their applications, *Adv. Funct. Mater.* 15, 655-663 (2005).
- [8] D. Pantelić *et al.*: Scattering-enhanced absorption and interference produce a golden wing color of the burnished brass moth, *Diachrysia chrysitis*, *Phys. Rev. E* 95, 032405 (2017).

Research Article

Orange-Reddish Light Emitting Phosphor $\text{GdVO}_4:\text{Sm}^{3+}$ Prepared by Solution Combustion Synthesis

M. S. Rabasovic ¹, J. Krizan ², S. Savic-Sevic ¹, M. Mitric ³, M. D. Rabasovic ¹,
B. P. Marinkovic ¹ and D. Sevic ¹

¹Institute of Physics, University of Belgrade, P.O. Box 68, Pregrevica 118, 11080 Belgrade, Serbia

²AMI d.o.o, Ptuj, Slovenia

³Vinca Institute of Nuclear Science, University of Belgrade, P.O. Box 522, 11001 Belgrade, Serbia

Correspondence should be addressed to D. Sevic; sevic@ipb.ac.rs

Received 12 December 2017; Accepted 16 April 2018; Published 2 May 2018

Academic Editor: Damien Boyer

Copyright © 2018 M. S. Rabasovic et al. This is an open access article distributed under the Creative Commons Attribution License, which permits unrestricted use, distribution, and reproduction in any medium, provided the original work is properly cited.

The gadolinium vanadate doped with samarium ($\text{GdVO}_4:\text{Sm}^{3+}$) nanopowder was prepared by the solution combustion synthesis (SCS) method. After synthesis, in order to achieve the full crystallinity, the material was annealed in air atmosphere at 900°C . Phase identification in the postannealed powder samples was performed by X-ray diffraction, and morphology was investigated by high-resolution scanning electron microscopy (SEM). Photoluminescence characterization of the emission spectrum and time-resolved analysis have been performed using the tunable laser optical parametric oscillator excitation and the streak camera. Several strong emission bands in the Sm^{3+} emission spectrum were observed, located at 567 nm ($^4\text{G}_{5/2}-^6\text{H}_{5/2}$), 604 nm ($^4\text{G}_{5/2}-^6\text{H}_{7/2}$), and 646 (654) nm ($^4\text{G}_{5/2}-^6\text{H}_{9/2}$), respectively. The weak emission bands at 533 nm ($^4\text{F}_{3/2}-^6\text{H}_{5/2}$) and 706 nm ($^4\text{G}_{5/2}-^6\text{H}_{11/2}$) and a weak broad luminescence emission band of VO_4^{3-} were also observed by the detection system. We analyzed the possibility of using the host luminescence for two-color temperature sensing. The proposed method is improved by introducing the temporal dependence in the line intensity ratio measurements.

1. Introduction

Many investigations have been devoted to rare earth orthovanadates RVO_4 ($R = \text{Sc}, \text{Y}, \text{La}, \text{Gd}, \text{or Lu}$) (see [1–4] and references therein). Gadolinium vanadate (GdVO_4) is a very important host for the luminescence of rare earth activators which find applications in the high-power solid state lasers, X-ray medical radiography, energy-saving fluorescent lamps, artificial production of light, other display devices [5–11], and temperature sensing [4]. Phosphors based on gadolinium compounds play an important role because the Gd^{3+} ion ($4f^7$) has its lowest excited level at relatively high energy, which is due to the stability of the half-filled shell ground state [6]. The $\text{GdVO}_4:\text{Sm}$ nanopowder is an efficient orange-reddish light emitting material due to a strong absorption of ultraviolet light by GdVO_4 and

efficient energy transfer from vanadate groups (VO_4^{3-}) to dopants (Sm^{3+}).

In this paper, we present the results of experimental investigation of Sm^{3+} -doped GdVO_4 nanopowders, prepared by the solution combustion synthesis (SCS) method [12, 13].

Simplicity and low cost are the main characteristics of this process. Phase identification in the postannealed powder samples was performed by X-ray diffraction, and morphology was investigated by high-resolution scanning electron microscopy (SEM). The main aim of this study is time-resolved analysis of luminescence properties of $\text{GdVO}_4:\text{Sm}^{3+}$ nanopowders. The possibility for $\text{GdVO}_4:\text{Sm}^{3+}$ usage in phosphor thermometry was analyzed in [4], where temperature determination of sensing calibration curves was based on intensity ratios of luminescence of samarium lines. Here, we have taken a different approach. First, we use intensity

ratio of the host and samarium line luminescence emissions (two-color thermometry). This new approach to the ratio-metric luminescence thermometry was proposed recently, using TiO_2 nanopowders doped with Eu^{3+} [14] and Sm^{3+} [15], Zn_2SiO_4 doped with Mn^{2+} [16], and $\text{Eu}^{3+} \text{Gd}_2\text{Ti}_2\text{O}_7$ doped with Eu^{3+} [17]. So, this concept, used in our study, provides high relative sensitivities by itself. However, the method presented here is further improved by introducing the temporal dependence in the luminescence intensity ratio measurements, as proposed in [18], providing even more increased sensitivity.

2. Experimental

2.1. Synthesis. GdVO_4 nanopowder doped with samarium ions was prepared by the solution combustion method, as described in [12, 13]. Stoichiometric quantities of starting chemicals $\text{Sm}(\text{NO}_3)_3$, $\text{Gd}(\text{NO}_3)_3 \cdot 6\text{H}_2\text{O}$, and NH_4VO_3 with the purity of 99.99% were chosen to obtain the Sm^{3+} concentration in GdVO_4 of 1 at.% ($\text{Gd}_{1-0.01}\text{Sm}_{0.01}\text{VO}_4$). The used chemicals and ammonium nitrate (NH_4NO_3) were purchased from ABCR, and urea ($(\text{NH}_2)_2\text{CO}$) from Sigma-Aldrich. The dry mixture of 0.134 g (0.4 mmol) of $\text{Sm}(\text{NO}_3)_3$, 18.05 g (40 mmol) of $\text{Gd}(\text{NO}_3)_3 \cdot 6\text{H}_2\text{O}$, and 4.676 g (40 mmol) of NH_4VO_3 was combined with the mixture of 4.8 g (60 mmol) of ammonium nitrate and 3.003 g (50 mmol) of urea which were used as organic fuels. The prepared starting reagents were combusted with the flame burner at approximately 500°C , yielding a voluminous foamy powder in an intensive exothermic reaction. After the solution combustion synthesis, the nanopowder was annealed for 2 hours, in air atmosphere, at 900°C . Annealing has an effect on increasing the grain size of the nanopowders, and it is widely used to achieve the higher emission intensity.

2.2. Instruments and Measurements. The structure of the nanopowder was verified by X-ray diffraction analysis, using a Philips PW 1050 instrument, with Ni filtered $\text{Cu} \cdot \text{K}_{\alpha 1,2}$ radiation ($\lambda = 0.15405 \text{ nm}$). X-ray diffraction measurements were done at room temperature over the 2θ range of $10\text{--}90^\circ$ with a scanning step width of 0.05° and a counting time of 8 s per step. The morphology of nanopowders and the size of crystallites were determined by high-resolution scanning electron microscopy (SEM) equipped with a high-brightness Schottky field emission gun (FEGSEM, TESCAN) operating at 4 kV. Photoluminescence (PL) studies reported in this work were performed using an optical parametric oscillator (Vibrant OPO), as described in [12, 13]. The output of the OPO can be continuously tuned over a spectral range from 320 nm to 475 nm. Time-resolved streak images of the emission spectrum excited by the OPO system were collected by using a spectrograph (SpectraPro 2300i) and recorded with a Hamamatsu streak camera (model C4334). All streak camera operations were controlled by the HPD-TA (High Performance Digital Temporal Analyzer) software. We used a homemade temperature control system for luminescence measurements presented here.

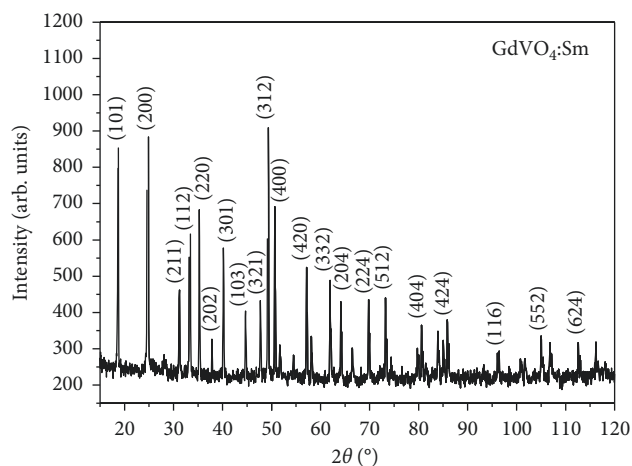


FIGURE 1: The XRD patterns of the $\text{GdVO}_4\text{:Sm}$ nanopowder with respective Miller indices.

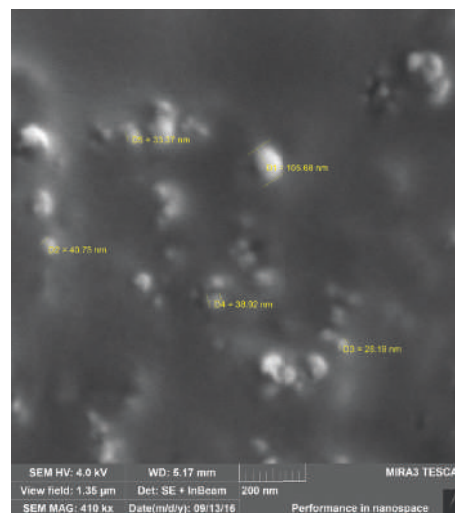


FIGURE 2: The SEM image of the $\text{GdVO}_4\text{:Sm}$ nanopowder annealed at 900°C .

3. Results

3.1. XRD and SEM Study. In order to know the structural properties and differences in the phase purities of the prepared $\text{GdVO}_4\text{:Sm}$ nanopowder, XRD analysis was recorded and is presented in Figure 1. XRD confirmed the successful formation of the pure-phase GdVO_4 powder with the $I4_1/amd$ space group (JCPDS Card no. 86-0996). Ionic radius of the Sm^{3+} ion (0.964 \AA) is a slightly larger than that of Gd^{3+} ion (0.938 \AA), which indicates that Sm^{3+} could be successfully incorporated into the GdVO_4 host lattice by substituting Gd^{3+} without changing the tetragonal zircon type structure of GdVO_4 [9]. The particle size and morphology of the $\text{GdVO}_4\text{:Sm}$ nanopowder annealed at 900°C were characterized by SEM (Figure 2). Some particles are agglomerated as clusters; however, individual spherical-shaped particles are also visible and labeled in Figure 2. The average grain size, D , was estimated by the Scherrer equation, $D = K\lambda/\beta \cos \theta$, where K is a constant related to

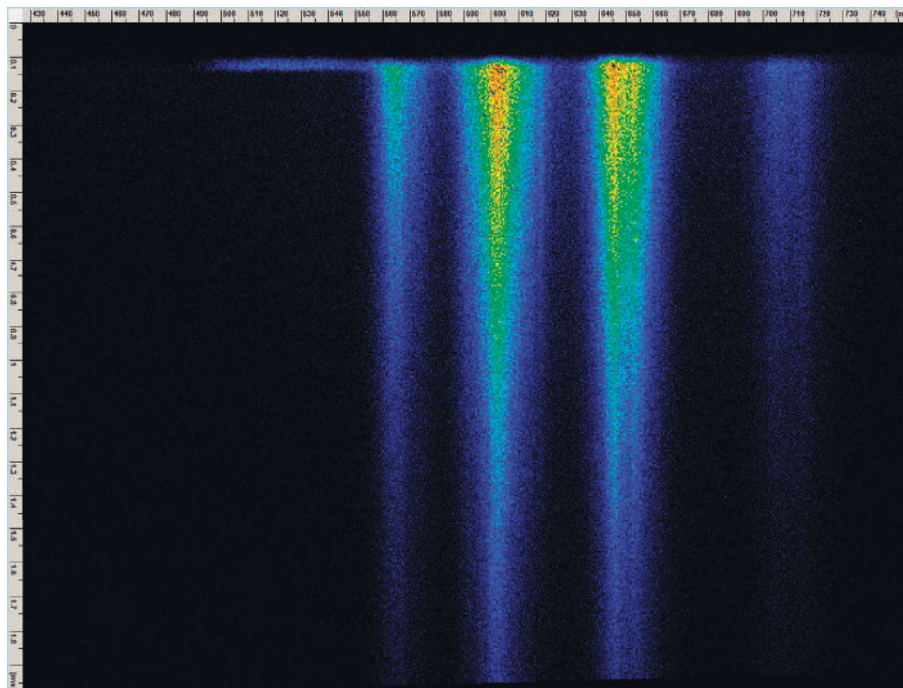


FIGURE 3: The streak image of the photoluminescence spectrum of $\text{GdVO}_4:\text{Sm}^{3+}$ nanoposphor (OPO excitation at 330 nm).

the shape of the crystallite and is approximately equal to unity, we used $K = 0.89$ as in [19], λ is the X-ray wavelength (0.15405 nm), and θ and β are the diffraction angle and full width at half maximum (FWHM, in radians) of the corresponding peak, respectively. The strongest peaks (2θ) from XRD were used to calculate the average crystallite size (D) in the $\text{GdVO}_4:\text{Sm}$ nanopowder. The estimated particle size is about 43 nm. The SEM image (Figure 2) reveals that sizes of individual particles of nanopowders are between 30 nm and 105 nm, which is in agreement with the calculated averaged result from XRD.

3.2. Photoluminescence and Lifetime Analysis. The streak image of the time-resolved photoluminescence spectrum of the $\text{GdVO}_4:\text{Sm}^{3+}$ nanopowder using the 330 nm excitation is presented in Figure 3. Horizontal scale of the streak image corresponds to wavelength, and the vertical scale shows development of spectra in time. Images are presented in pseudocolor, where different colors mean different optical intensities.

Spectral characteristics of luminescence emission intensities of the synthesized $\text{GdVO}_4:\text{Sm}^{3+}$ (1 at.%) nanopowder sample are shown in Figure 4. The spectrum was obtained by integrating in time the spectral image acquired by the streak camera in the photon counting mode, with the time scale of 5 ms, at the excitation of 330 nm.

It could be seen in Figure 4 that the $\text{GdVO}_4:\text{Sm}$ nanopowder sample have comparable luminescence emission intensities in green, orange, and red regions. All those emission bands correspond to the transitions from excited energy level ${}^4\text{G}_{5/2}$ of Sm^{3+} ion to ${}^6\text{H}_{5/2}$ (~567 nm), ${}^6\text{H}_{7/2}$ (602 nm), ${}^6\text{H}_{9/2}$ (646 and 654 nm), and ${}^6\text{H}_{11/2}$ (~706 nm) level, respectively. The strong emission of Sm^{3+} is due to efficient energy transfer from the VO_4^{3-} group to Sm^{3+} ion

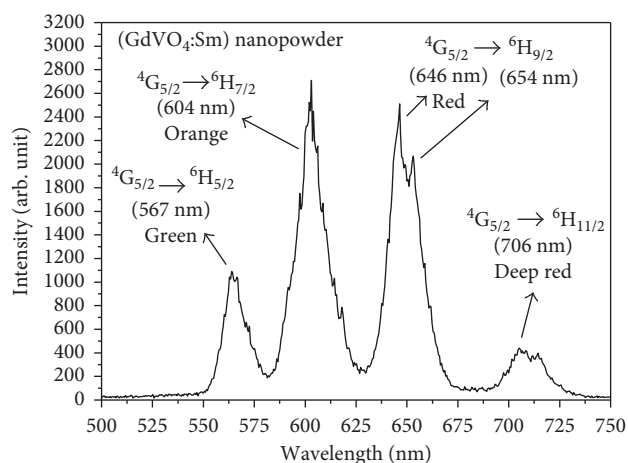


FIGURE 4: The photoluminescence (PL) emission spectrum of our $\text{GdVO}_4:\text{Sm}$ nanopowder sample (OPO excitation at 330 nm).

in the $\text{GdVO}_4:\text{Sm}^{3+}$ sample. However, the deep red emission of these samples is almost on the end of the region of human eye color sensitivity, so the small influence of this emission on the color chromaticity coordinates of $\text{GdVO}_4:\text{Sm}^{3+}$ is expected. The transitions at 604 and 646 nm have relatively higher emission intensities over the other transitions causing an orange-reddish emission from the Sm^{3+} .

Fluorescence lifetime analysis for the $\text{GdVO}_4:\text{Sm}^{3+}$ nanopowder has also been performed, and the obtained result is presented in Figure 5. We present the fluorescence lifetime analysis for the most intense emission peak (${}^4\text{G}_{5/2} \rightarrow {}^6\text{H}_{7/2}$) in Sm^{3+} ion. Luminescence decay curve is well fitted using a double-exponential function. The average luminescence lifetime can be determined by the following formula [20–24]:

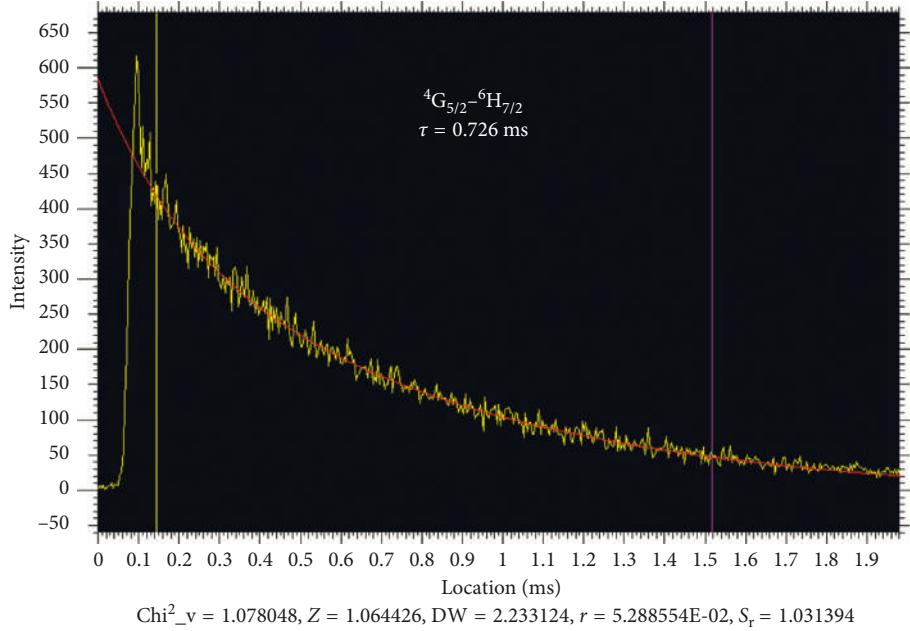


FIGURE 5: The luminescence decay curve for the ${}^4G_{5/2}$ - ${}^6H_{7/2}$ transition in Sm^{3+} ion fitted by a double-exponential decay.

$$\tau = \frac{(A_1 \tau_1^2 + A_2 \tau_2^2)}{(A_1 \tau_1 + A_2 \tau_2)}, \quad (1)$$

where A_1 and A_2 denote the amplitudes of respective decay components and τ_1 and τ_2 are fluorescence lifetime components contributing to the average lifetime. The obtained result for average lifetime for Sm^{3+} ion is 0.726 ms. It is found that our result for lifetime of Sm^{3+} ion in the GdVO_4 nanopowder is longer in comparison with 0.66 ms [20], 0.55 ms [25], and 0.42 ms [6]. It is well known that the luminescent lifetime of rare earth ion is influenced by the structure of the host, the rare earth located sites (on the surface or bulk) of the host, defects, and impurity [26]. The defect and impurity may act as quenching centers and reduce luminescent lifetime.

The double-exponential decay behavior of the activator is frequently observed when the excitation energy is transferred from the donor [6]. The energy transfer is not the main cause of the deviation from the single-exponential behavior of the decay curve since the energy transfer from the VO_4^{3-} groups to Sm^{3+} ions mainly influences the rise time of the decay curve [27]. The streak image of $\text{GdVO}_4:\text{Sm}^{3+}$ nanopowder luminescence with a time scale of 100 μs is shown in Figure 6. In this time scale, the host luminescence and weak samarium line at 533 nm (${}^4F_{3/2}$ - ${}^6H_{5/2}$), barely discernible and not denoted in Figures 3 and 4, are easily identified. In our measurements, all luminescence bellow 500 nm is cut off by the optical filter used for blocking the OPO excitation. The spectral shape of host luminescence, detected by us only above 500 nm, is similar to spectra presented in [1, 9, 28]. The GdVO_4 luminescence is ascribed to the VO_4^{3-} group. Calculated lifetime of host luminescence of 2.82 μs agrees well with the time-resolved analysis provided in [28]. Moreover, as we have shown in the next subsection, this luminescence is gradually quenched by

raising the temperature, which means that it is not measuring error caused by stray light of laser excitation.

The estimated rise time of samarium luminescence shown in Figure 6 is negligible for effects of interest. For used time scale, it is determined mainly by the instrumental response. So, the multiexponential behavior should be ascribed to the absorbed impurities, which lead to the defects and the quenching centers [27, 29]. Decay kinetics behavior depends also on the number of different luminescent centers [20, 27]. If rare earth ions occupy several different sites in host lattices, they can generate several different luminescent centers which lead to a multiexponential behavior [29]. Tian et al. [30] explained that, in Dy^{3+} -doped bulk $\text{GdVO}_4:\text{Dy}$ phosphors, the energy transfers mainly happen between Dy^{3+} ions [31, 32]. In the case of nanoparticles, the energy transfer starting from the luminescent level can be more complicated, since the defects, which can act as quenching centers, in nanoparticles are more plenteous than those in bulk phosphors [29, 31, 33]. Due to the defects produced during the preparation process and trace impurities contained in the raw materials, the samples necessarily have quenching centers (traps) with very low concentrations. When the excited luminescent center is in the vicinity of the trap, the excited energy could be transferred easily to the trap from which it is lost nonradiatively [33]. As a result, decay time should become short. In our case, longer lifetime of 0.726 ms may be due to the better crystallization and less defects, which reduces the nonradiative probability and results in the longer lifetimes.

3.3. Temperature Sensing Using $\text{GdVO}_4:\text{Sm}$ Nanophosphor. Recently, the new concept of using the host luminescence for the fluorescence intensity ratio method was introduced (see [14–17] and references therein). In our study, the method is

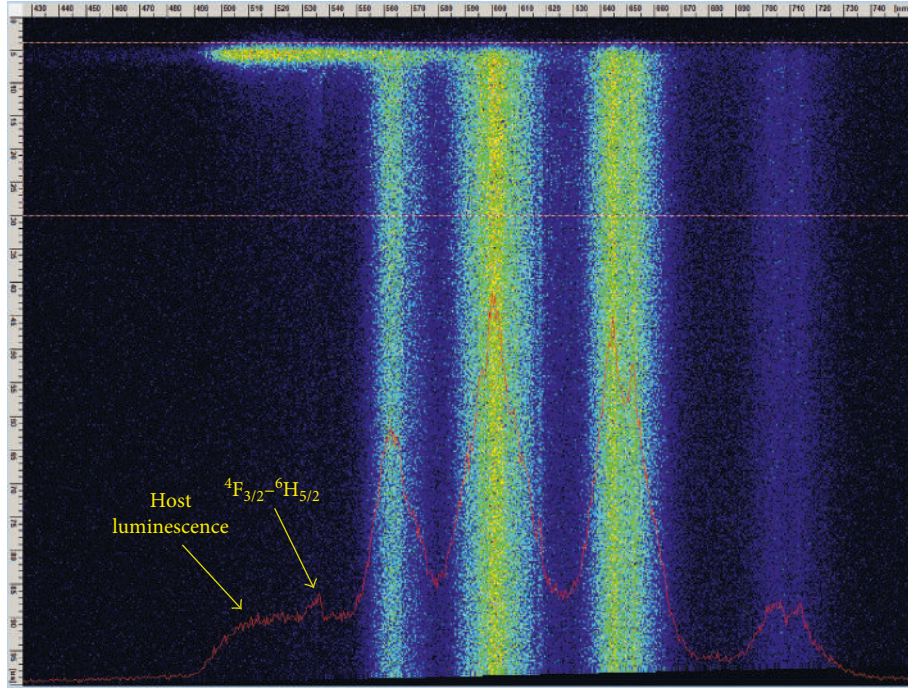


FIGURE 6: The streak image of the GdVO₄:Sm nanopowder. The time scale of 100 μ s was adjusted for analysis of rise time of samarium lines and detection of fast host luminescence emission (OPO excitation at 330 nm).

improved by introducing the temporal dependence in the intensity ratio measurements, as proposed in [18]. Namely, it is possible to increase the sensitivity of the curve of intensity ratio between the host and samarium luminescence if an appropriately selected part of temporal evolution is used in calculation. We used the streak camera to prove the concept. The real application of this method will be based on using the gated CCD cameras and appropriate bandwidth filters for selecting the emission region of interest.

The luminescence spectra of the GdVO₄:Sm nanopowder were measured at various temperatures, using the OPO excitation at 330 nm and the streak camera. For calculation of intensity ratio, the narrow bands (5 nm) of host luminescence around 520 nm and the samarium line at 602 nm were used and integrated in time from their beginning. However, we varied gating times for end of signal integration. In order to apply the intensity ratio method in thermometry, it is required to fit a calibration function of analyzed thermophosphor. Based on considerations in [34, 35], we decided to use the simple empirical equation for fitting the calculated intensity ratios of experimental data: $IR(T) = A + C \cdot e^{-T/\alpha}$ [34, 35], where T is the temperature in K and empirical A , C , and α are the constants obtained through fitting of measured data. The results are shown in Figure 7.

It could be seen in Figure 7 that the intensity ratio between the host luminescence band centered at 520 nm and the line at 602 nm increases with decreasing the gate time of the signal. However, decreasing the gate time decreases the integrated signal intensity, so we did not use delays smaller than 30 μ s.

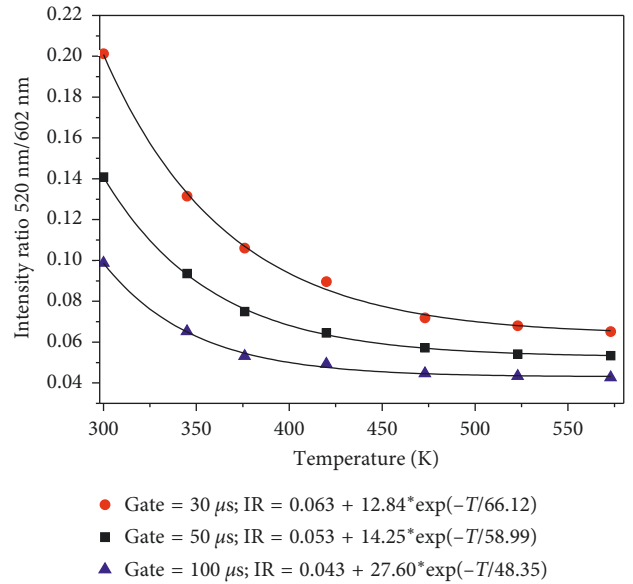


FIGURE 7: The temperature sensing calibration curve of the GdVO₄:Sm³⁺ nanopowder sample.

The absolute thermal sensitivity, S_a , of the intensity ratio method is defined as the rate at which IR changes with the temperature:

$$S_a = \left| \frac{dIR}{dT} \right|. \quad (2)$$

The relative thermal sensitivity, S_r , of the intensity ratio method S_r is determined using the following formula:

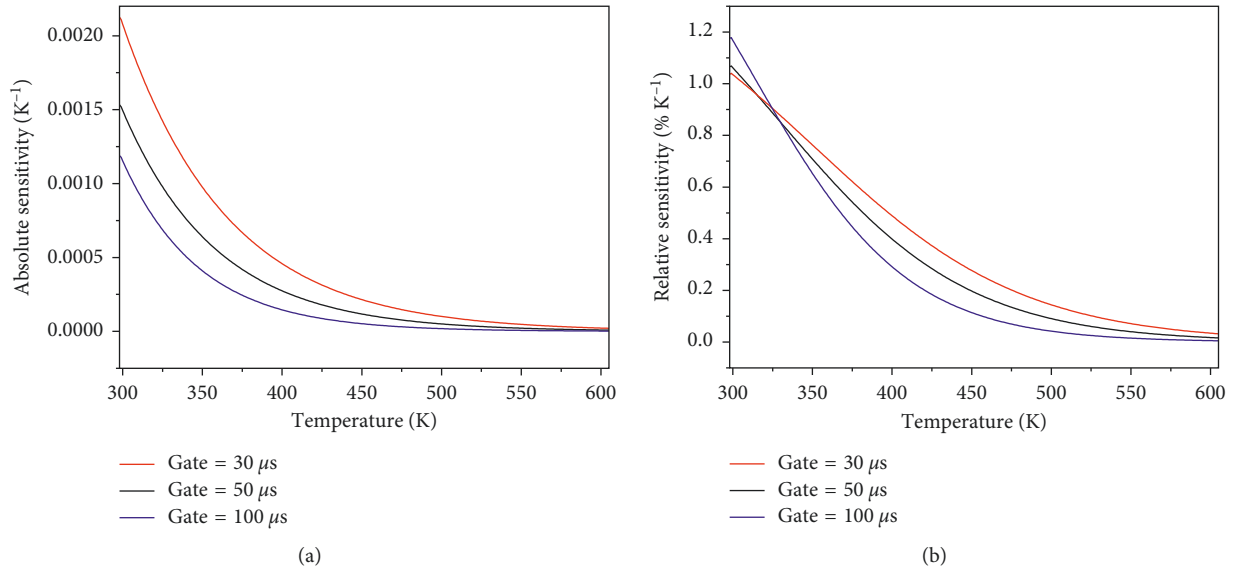


FIGURE 8: (a) Absolute sensitivity and (b) relative sensitivity of GdVO₄:Sm³⁺ nanophosphor as a function of temperature.

$$S_r = \left| \frac{1}{IR} \frac{dIR}{dT} \right|. \quad (3)$$

Absolute and relative temperature sensitivities of GdVO₄:Sm³⁺ nanophosphor are shown in Figure 8. The best sensitivity is obtained by the gate time of 30 μs. We estimate that this kind of temperature sensing is useful up to 500 K, where the calculated intensity ratio values stop increasing and the curve flattens, resulting in small sensitivity, even for the optimal gate time of 30 μs (see Figures 7 and 8). The proposed method provides better sensitivity than that reported in [4] for the same nanophosphor.

The CIE (Commission Internationale de l'Éclairage, 1931) chromaticity coordinates of GdVO₄:Sm³⁺ are presented in Figure 9. It could be seen that the GdVO₄:Sm³⁺ sample shows the orange-reddish luminescence color, and the chromaticity coordinates at room temperature are $x = 0.5963$ and $y = 0.3989$. Denoted points correspond to the temperature range from 300 K up to 673 K. The CIE diagram shows that the luminescence intensities corresponding to the last two points, 623 K and 673 K (350°C and 400°C), are obviously measured with high uncertainty, and they were not included in fitting the temperature sensing calibration curves of GdVO₄:Sm³⁺.

4. Conclusion

The time-resolved analysis of GdVO₄:Sm³⁺ nanophosphor luminescence was conducted. The estimated lifetime of the most prominent optical emission of samarium from the ⁴G_{5/2} level is 0.726 ms. The host luminescence was also identified. Lifetime of host luminescence is 2.82 μs. The rise time of samarium luminescence is estimated as negligible for effects that are here of interest.

We have shown that, for the analyzed GdVO₄:Sm³⁺ material, the temperature sensing based on ratio of intensities of the host luminescence and the samarium line

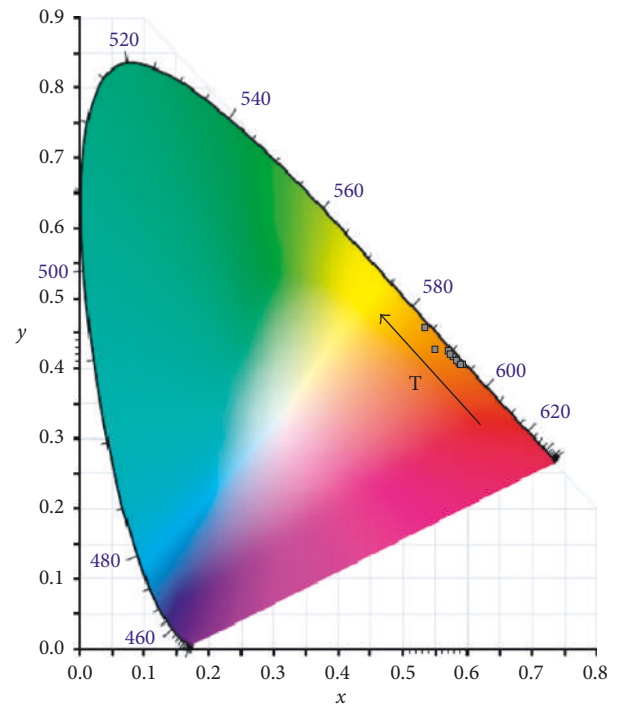


FIGURE 9: The CIE chromaticity diagram of emission spectra of 1 mol% GdVO₄:Sm³⁺. Denoted points correspond to the temperature range from 300 K up to 673 K.

is useful up to 500 K. The used method was improved by introducing the temporal dependence in the ratio measurements. Our analysis shows that the gating time of 30 μs is optimal for acquiring the integrated luminescence intensity.

By using the CIE chromaticity diagram of emission spectra, it has been shown that this GdVO₄:Sm³⁺ nanophosphor material (chromaticity coordinates $x = 0.596$, $y = 0.398$) can be used for development of orange-reddish light emitting

optical devices. We also plotted the temperature dependency of CIE chromaticity coordinates for this nanopowder.

In summary, results of all our analyses prove that the Sm^{3+} -doped GdVO_4 nanopowder prepared by a simple and low-cost solution combustion synthesis method is an appropriate material for light-emitting optoelectronic devices and remote temperature sensing.

Conflicts of Interest

The authors declare that they have no conflicts of interest.

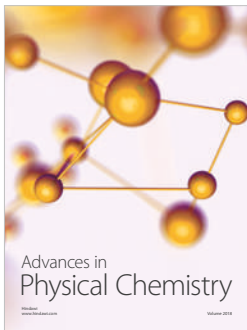
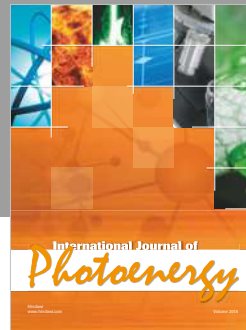
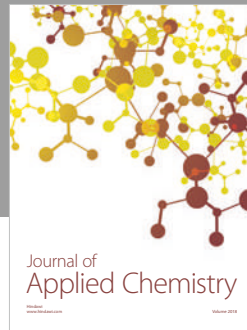
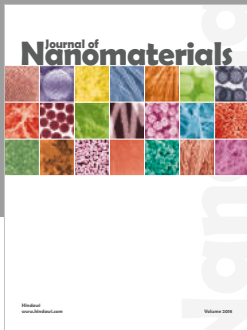
Acknowledgments

This work was financially supported within the projects of Ministry of Education, Science and Technological Development of the Republic of Serbia (OI171020).

References

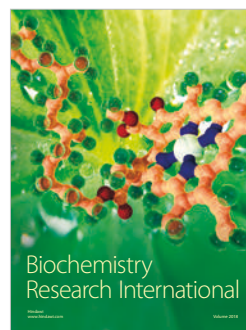
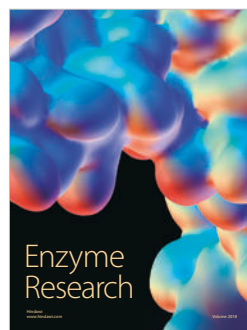
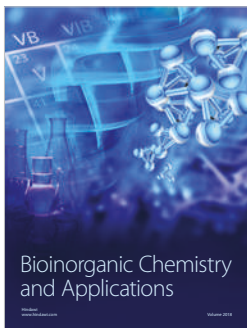
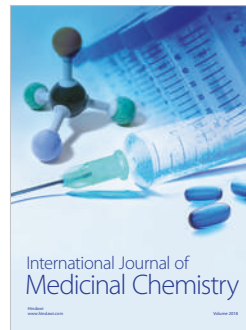
- [1] M. Anitha, P. Ramakrishnan, A. Chatterjee, G. Alexander, and H. Singh, "Spectral properties and emission efficiencies of GdVO_4 phosphors," *Applied Physics A: Materials Science & Processing*, vol. 74, no. 2, pp. 153–162, 2012.
- [2] Z. Hou, P. Yang, C. Li et al., "Preparation and Luminescence Properties of $\text{YVO}_4:\text{Ln}$ and $\text{Y}(\text{V}, \text{P})\text{O}_4:\text{Ln}$ ($\text{Ln} = \text{Eu}^{3+}, \text{Sm}^{3+}, \text{Dy}^{3+}$) nanofibers and microbelts by sol-gel/electrospinning process," *Chemistry of Materials*, vol. 20, no. 21, pp. 6686–6696, 2008.
- [3] D. J. Jovanovic, Z. Antic, R. M. Krsmanovic et al., "Annealing effects on the microstructure and photoluminescence of Eu^{3+} -doped GdVO_4 powders," *Optical Materials*, vol. 35, no. 10, pp. 1797–1804, 2013.
- [4] M. G. Nikolic, D. J. Jovanovic, V. Đorđević, Z. Antic, R. M. Krsmanovic, and M. D. Dramicanin, "Thermographic properties of Sm^{3+} -doped GdVO_4 phosphor," *Physica Scripta*, vol. T149, p. 014063, 2012.
- [5] S. Kaowphong, N. Chumha, P. Nimmanpipug, and S. Kittiwachana, "Nanosized GdVO_4 powders synthesized by sol-gel method using different carboxylic acids," *Rare Metals*, 2016.
- [6] X. Li, M. Yu, Z. Hou et al., "One-dimensional $\text{GdVO}_4:\text{Ln}^{3+}$ ($\text{Ln} = \text{Eu}, \text{Dy}, \text{Sm}$) nanofibers: electrospinning preparation and luminescence properties," *Journal of Solid State Chemistry*, vol. 184, no. 1, pp. 141–148, 2011.
- [7] H. Xin, L. X. Lin, J. H. Wu, and B. Yan, "Hydrothermal synthesis and multi-color photoluminescence of $\text{GdVO}_4:\text{Ln}^{3+}$ ($\text{Ln} = \text{Sm}, \text{Dy}, \text{Er}$) sub-micrometer phosphors," *Journal of Materials Science: Materials in Electronics*, vol. 22, no. 9, pp. 1330–1334, 2011.
- [8] F. Zheng, W. Wang, and P. Yang, " $\text{GdVO}_4:\text{Ln}^{3+}$ ($\text{Ln} = \text{Sm}, \text{Dy}$, and Er) microstructures: solvothermal and luminescent properties," *Optoelectronics and Advanced Materials: Rapid Communications*, vol. 5, no. 6, pp. 596–599, 2011.
- [9] Y. Liu, G. Liu, J. Wang, X. Dong, and W. Yu, "Reddish-orange-emitting and paramagnetic properties of $\text{GdVO}_4:\text{Sm}^{3+}/\text{Eu}^{3+}$ multifunctional nanomaterials," *New Journal of Chemistry*, vol. 39, no. 11, pp. 8282–8290, 2015.
- [10] Y. K. Voron'ko, A. A. Sobol', V. E. Shukshin, A. I. Zagumennyi, Y. D. Zavartsev, and S. A. Kutovoi, "Raman spectroscopic study of structural disordering in YVO_4 , GdVO_4 , and CaWO_4 crystals," *Physics of the Solid State*, vol. 51, no. 9, pp. 1886–1893, 2009.
- [11] A. A. Kaminskii, O. Lux, H. Ghee et al., "Low-temperature stimulated Raman scattering spectroscopy of tetragonal GdVO_4 single crystals," *Physica Status Solidi B*, vol. 251, no. 5, pp. 1045–1062, 2014.
- [12] M. S. Rabasovic, D. Sevic, J. Krizan et al., "Structural properties and luminescence kinetics of white nanopowder $\text{YAG}:\text{Dy}$," *Optical Materials*, vol. 50, pp. 250–255, 2015.
- [13] M. S. Rabasović, D. Sević, J. Krizan, M. D. Rabasović, and N. Romcević, "Annealing effects on luminescent properties of Eu^{3+} doped $\text{Gd}_2\text{Zr}_2\text{O}_7$ nanopowders," *Science of Sintering*, vol. 47, no. 3, pp. 269–272, 2015.
- [14] M. G. Nikolic, Z. Antic, S. Culubrk, J. M. Nedeljkovic, and M. D. Dramicanin, "Temperature sensing with Eu^{3+} doped TiO_2 nanoparticles," *Sensors and Actuators B: Chemical*, vol. 201, pp. 46–50, 2014.
- [15] M. D. Dramicanin, Z. Antic, S. Culubrk, S. P. Ahrenkiel, and J. M. Nedeljkovic, "Self-referenced luminescence thermometry with Sm^{3+} doped TiO_2 nanoparticles," *Nanotechnology*, vol. 25, no. 48, p. 485501, 2014.
- [16] V. Lojpur, M. G. Nikolic, D. Jovanovic, M. Medic, Z. Antic, and M. D. Dramicanin, "Luminescence thermometry with $\text{Zn}_2\text{SiO}_4:\text{Mn}^{2+}$ powder," *Applied Physics Letters*, vol. 103, no. 14, p. 141912, 2013.
- [17] V. Lojpur, S. Čulubrk, and M. D. Dramicanin, "Radiometric luminescence thermometry with different combinations of emissions from Eu^{3+} doped $\text{Gd}_2\text{Ti}_2\text{O}_7$ nanoparticles," *Journal of Luminescence*, vol. 169, pp. 534–538, 2016.
- [18] M. Alden, A. Omrane, M. Richter, and G. Särner, "Thermographic phosphors for thermometry: a survey of combustion applications," *Progress in Energy and Combustion Science*, vol. 37, no. 4, pp. 422–461, 2011.
- [19] B. K. Grandhe, V. R. Bandi, K. Jang, S. Ramaprabhu, S.-S. Yi, and J.-H. Jeong, "Enhanced red emission from $\text{YVO}_4:\text{Eu}^{3+}$ nano phosphors prepared by simple co-precipitation method," *Electronic Materials Letters*, vol. 7, no. 2, pp. 161–165, 2011.
- [20] S. Tang, M. Huang, J. Wang, F. Yu, G. Shang, and J. Wu, "Hydrothermal synthesis and luminescence properties of $\text{GdVO}_4:\text{Ln}^{3+}$ ($\text{Ln} = \text{Eu}, \text{Sm}, \text{Dy}$) phosphors," *Journal of Alloys and Compounds*, vol. 513, pp. 474–480, 2012.
- [21] N. Shanta Singh, R. S. Ningthoujam, M. Niraj Luwang, S. Dorendrajit Singh, and R. K. Vatsa, "Luminescence, lifetime and quantum yield studies of $\text{YVO}_4:\text{Ln}^{3+}$ ($\text{Ln}^{3+} = \text{Dy}^{3+}, \text{Eu}^{3+}$) nanoparticles: concentration and annealing effects," *Chemical Physics Letters*, vol. 480, no. 4–6, pp. 237–242, 2009.
- [22] G. Z. Li, Z. L. Wang, M. Yu, Z. W. Quan, and J. Lin, "Fabrication and optical properties of core-shell structured spherical $\text{SiO}_2@\text{GdVO}_4:\text{Eu}^{3+}$ phosphors via sol-gel process," *Journal of Solid State Chemistry*, vol. 179, no. 8, pp. 2698–2706, 2006.
- [23] H. Wang, M. Yu, C. K. Lin, and J. Lin, "Core-shell structured $\text{SiO}_2@\text{YVO}_4:\text{Dy}^{3+}/\text{Sm}^{3+}$ phosphor particles: Sol-gel preparation and characterization," *Journal of Colloid and Interface Science*, vol. 300, no. 1, pp. 176–182, 2006.
- [24] M. Yu, J. Lin, and J. Fang, "Silica spheres coated with $\text{YVO}_4:\text{Eu}^{3+}$ layers via sol-gel process: a simple method to obtain spherical core-shell phosphors," *Chemistry of Materials*, vol. 17, no. 7, pp. 1783–1791, 2005.
- [25] X. He, L. Zhang, G. Chen, and Y. Hang, "Crystal growth and spectral properties of $\text{Sm}:\text{GdVO}_4$," *Journal of Alloys and Compounds*, vol. 467, no. 1–2, pp. 366–369, 2009.
- [26] V. Sudarsan, F. C. J. M. van Veggel, R. A. Herring, and M. Raudsepp, "Surface Eu^{3+} ions are different than "bulk" Eu^{3+}

- ions in crystalline doped LaF_3 nanoparticles,” *Journal of Materials Chemistry*, vol. 15, no. 13, pp. 1332–1342, 2005.
- [27] G. Jia, Y. Song, M. Yang, Y. Huang, L. Zhang, and H. You, “Uniform $\text{YVO}_4:\text{Ln}^{3+}$ (Ln = Eu, Dy, and Sm) nanocrystals: solvothermal synthesis and luminescence properties,” *Optical Materials*, vol. 31, no. 6, pp. 1032–1037, 2009.
- [28] J. Leppert, S. Peudenier, E. Bayer, B. C. Grabmaier, and G. Blasse, “Time resolved emission spectroscopy of gadolinium vanadate ceramics ($\text{GdVO}_4:\text{Bi}^{3+}$),” *Applied Physics A Solids and Surfaces*, vol. 59, no. 1, pp. 69–72, 1994.
- [29] F. He, P. P. Yang, N. Niu et al., “Hydrothermal synthesis and luminescent properties of $\text{YVO}_4:\text{Ln}^{3+}$ (Ln = Eu, Dy, and Sm) microspheres,” *Journal of Colloid and Interface Science*, vol. 343, no. 1, pp. 71–78, 2010.
- [30] Y. Tian, B. Chen, B. Tian et al., “Size-dependent energy transfer and spontaneous radiative transition properties of Dy^{3+} ions in the GdVO_4 phosphors,” *Journal of Nanoparticle Research*, vol. 15, no. 6, pp. 1757–1767, 2013.
- [31] B. N. Tian, B. J. Chen, Y. Tian et al., “Concentration and temperature quenching mechanisms of Dy^{3+} luminescence in $\text{BaGd}_2\text{ZnO}_5$ phosphors,” *Journal of Physics and Chemistry of Solids*, vol. 73, no. 11, pp. 1314–1319, 2012.
- [32] H. Zhong, X. P. Li, R. S. Shen et al., “Spectral and thermal properties of Dy^{3+} -doped NaGdTiO_4 phosphors,” *Journal of Alloys and Compounds*, vol. 517, pp. 170–175, 2012.
- [33] W. P. Zhang, P. B. Xie, C. K. Duan et al., “Preparation and size effect on concentration quenching of nanocrystalline $\text{Y}_2\text{SiO}_5:\text{Eu}$,” *Chemical Physics Letters*, vol. 292, no. 1-2, pp. 133–136, 1998.
- [34] M. D. Rabasovic, B. D. Muric, V. Celebonovic, M. Mitric, B. M. Jelenkovic, and M. G. Nikolic, “Luminescence thermometry via the two-dopant intensity ratio of $\text{Y}_2\text{O}_3:\text{Er}^{3+}, \text{Eu}^{3+}$,” *Journal of Physics D: Applied Physics*, vol. 49, no. 48, p. 485104, 2016.
- [35] D. Ananias, C. D. S. Brites, L. D. Carlos, and J. Rocha, “Cryogenic nanothermometer based on the MIL-103 (Tb, Eu) metal-organic framework,” *European Journal of Inorganic Chemistry*, vol. 2016, no. 13-14, pp. 1967–1971, 2016.



Hindawi

Submit your manuscripts at
www.hindawi.com



Scattering-enhanced absorption and interference produce a golden wing color of the burnished brass moth, *Diachrysia chrysitis*

Dejan Pantelić,^{1,*} Svetlana Savić-Šević,¹ Dejan V. Stojanović,² Srećko Ćurčić,³ Aleksandar J. Krmpot,¹ Mihailo Rabasović,¹ Danica Pavlović,¹ Vladimir Lazović,¹ and Vojislav Milošević¹

¹*Institute of Physics, University of Belgrade, Pregrevica 118, 11080 Zemun, Belgrade, Serbia*

²*Institute of Lowland Forestry and Environment, University of Novi Sad, Antona Čehova 13, 21000 Novi Sad, Serbia*

³*Institute of Zoology, University of Belgrade—Faculty of Biology, Studentski Trg 16, 11000 Belgrade, Serbia*

(Received 3 November 2016; published 8 March 2017)

Here we report how interference and scattering-enhanced absorption act together to produce the golden wing patches of the burnished brass moth. The key mechanism is scattering on rough internal surfaces of the wing scales, accompanied by a large increase of absorption in the UV-blue spectral range. Unscattered light interferes and efficiently reflects from the multilayer composed of the scales and the wing membranes. The resulting spectrum is remarkably similar to the spectrum of metallic gold. Subwavelength morphology and spectral and absorptive properties of the wings are described. Theories of subwavelength surface scattering and local intensity enhancement are used to quantitatively explain the observed reflectance spectrum.

DOI: [10.1103/PhysRevE.95.032405](https://doi.org/10.1103/PhysRevE.95.032405)

I. INTRODUCTION

Fascinating “inventions” of evolution have been discovered in a large number of recent studies dealing with the biophysics of living creatures. In that respect, insects are an excellent research subject due to their diversity and abundance.

Biophotonics of insects is a particularly active subject which aims to explain function and imitate intricate micro- and nanostructures on their bodies. Several studies present a comprehensive overview of the current research [1–3]. Surprising results are still being published, such as the photonic system of a Saharan silver ant, enabling radiative dissipation of heat, directly through the IR atmospheric window [4]. This and a number of other studies suggest that nature has developed many technologies which can be used to solve everyday problems, if successfully imitated [5,6].

Optical photonic structures in the living world are diverse and have been classified by Land [7], based on their biological function, including tapeta (light-path doubling or image forming), camouflage, display, optical filters (e.g., corneal nipples of insect compound eyes), and anatomical accidents (features whose optical properties have no obvious biological function, e.g., mother-of-pearl in some mollusks).

More specifically, the biophotonics of Lepidoptera draws much attention, mostly due to the attractiveness of butterflies. Much less is known about moths (suborder Heterocera), which represent a group of Lepidoptera, characterized by the wings mostly having drab colors (gray or brown), and feathery or saw-edged antennae (vs club-shaped in butterflies). While moths are more numerous than butterflies, the number of structural coloration studies is significantly smaller. Only attractive and conspicuous moth species were explored, such as the Madagascan sunset moth [8]. The lack of interest is, possibly, due to the simpler wing-scale structure of moths, compared to really complex features present on the scales of day flying butterflies (e.g., Bragg gratings or photonic crystals).

Golden wing patches are prominent features of some noctuid moths. The patches might be just small marks as in *Autographa jota* (Linnaeus, 1758) and *A. bractea* (Denis & Schiffermüller, 1775), or large areas, as in *Diachrysia balluca* Geyer, 1832. The physics behind the golden moth color was previously analyzed using the diffraction theory of Stratton-Silver-Chu [9] in the case of *Thysanoplusia orichalcea* (Fabricius, 1775) (previously included in the genus *Trichoplusia* McDunnough, 1944) (Noctuidae family). However, a correspondence between theory and experimentally recorded spectra was qualitative, probably due to approximations of the mathematical formalism.

Other insects with a golden cuticle do exist, such as *Chrysin aurigans* (Rothschild & Jordan, 1894) (Coleoptera: Scarabaeidae) [10], whose broadband metallic reflection is due to a chirped Bragg mirror within the cuticle. Some species have a tunable color, which depends on atmospheric humidity [11] or stressful events [12], enabling the insects to change the color from red to golden.

Rothschild *et al.* [13] found that carotenoid pigments may also contribute to golden metallic areas of Danainae butterfly pupae. Similar results were obtained by Taylor [14] and Neville [15]. In contrast, Steinbrecht *et al.* [16] proved that golden reflections of *Euploea core* (Cramer, 1780) (Lepidoptera: Nymphalidae) pupae have an entirely physical nature. They showed that reflectance spectra of the cuticle (possessing multiple endocuticular thin alternating layers) and metallic gold are very similar, with a characteristic edge at 450–550 nm. The authors also emphasize that the carotenoids in the epidermis cannot contribute to the color effects because the cuticle practically does not transmit yellow light at all.

Scattering from an irregular surface is a secondary mechanism of structural coloration—interference and diffraction being dominant ones. For example, lycaenid butterflies (in particular, subfamily Polyommatae) scatter light from the internal, pepper-pot-like, Bragg layers (having holes of 100 nm average diameter). The wing-scale laminae are almost hollow and permit the blue radiation to escape [17]. Pieridae can also be mentioned due to the nanobeads (pigment granules), which fill the space between the laminae [18], where the scattering

*pantelic@ipb.ac.rs

and fluorescence extend the reflection spectrum [19,20]. Scattering in the living world is sometimes accompanied by light trapping, as in diatoms [21]. This seems to be a significant mechanism for efficient light harvesting in photosynthetic organisms.

Here we describe how several optical mechanisms interact to produce the golden wing color of the burnished brass moth, *Diachrysia chrysitis* (Linnaeus, 1758). We have studied spectral properties of the golden wing patches, as well as the internal and external ultrastructure of the wing scales and wing membranes. It was found that the scattering from irregular internal surfaces of each scale suppresses the UV-blue reflection, while interference efficiently reflects the red-infrared spectral range. A theoretical model is proposed, which combines interference and scattering from the scale laminae. The finite element method (FEM) is used to confirm the trapping and local intensity enhancement of light inside the laminae, while the modified transfer matrix method is used to calculate the reflection spectrum.

II. OPTICAL PROPERTIES AND STRUCTURE OF *D. CHRYSITIS* WING

The burnished brass moth (*D. chrysitis*; shown in Fig. 1) is a common species of the Noctuidae family (Insecta: Lepidoptera). It inhabits temperate climates in the Palearctic region [22]. *D. chrysitis* is a remarkable moth with big, golden (sometimes brassy-green) areas on each forewing. The wingspan is 28–35 mm, while the length of each forewing is 16–18 mm [23]. The burnished brass moth is usually found in marshy areas or in slightly moist forb communities. The larvae feed on plants such as *Urtica* spp., *Lamium* spp., or *Cirsium* spp. [24]. The moth flies from May to October depending on the location. It flies regularly in dusk, and was seen visiting flowers of various plants. Sometimes it can be noticed during the day, even sucking nectar. The species is widespread in Serbia [25].

It is supposed that irregular golden patches in the forewings of *D. chrysitis* are an example of disruptive coloring, as an excellent way of hiding oneself by breaking up the body contours [26]. Additionally, it was also postulated that specular



FIG. 1. Burnished brass moth (*D. chrysitis*) with golden areas on its forewings.

reflection of the sun's rays may imitate the glittering of dew droplets. Even more, it seems that the wing color is optimized to efficiently reflect the yellowish light of the sun. As a dusk species, the moth may emit a signal in the IR spectral range from the golden patches, which might be used as a signal for intraspecific recognition. Anatomical accidents seem unlikely because metallic areas on *D. chrysitis* forewings form species-specific patterns [27].

From the optical point of view, the most prominent features of the studied moth are golden-color wing patches, as seen in Fig. 1. The corresponding wing spectra were recorded in reflection using a fiber optic spectrometer (manufactured by Ocean Optics, HR2000CG-UV-NIR), with a 400- μm core diameter fiber. A halogen lamp was used as a light source, and spectra were referenced to a standard white surface. The light collection angle was limited by the numerical aperture of the fiber ($\text{NA} = 0.22$, which is equivalent to an angular range of $\pm 12.7^\circ$), positioned such that an approximately 40- mm^2 area is observed. This means that the spectra of individual scales are integrated both angularly and across the wing surface. This fact was accounted for in the numerical simulations.

The spectrum of *D. chrysitis* is broad, with a cutoff wavelength at approximately 500 nm. Its exact shape slightly depends on the angle between light source, wing, and detector. There is a close similarity with the spectrum of metallic gold, as shown in Fig. 2. The specular reflectance spectrum of gold is taken tabulated from Ref. [28], where it is treated as a reference standard.

Optical reflection microscopy of the *D. chrysitis* forewing reveals an almost uniform, intense golden sheen as shown in Fig. 3(a). In contrast, reflection from individual scales is yellowish, with occasional red and green bands, presented in Fig. 3(b). Overlapped scales show increased reflection and color bands, as can be observed in the same image. If observed in transmission, an individual scale in air [see Fig. 3(c)] is quite transparent, with a slight residual absorption. By immersing

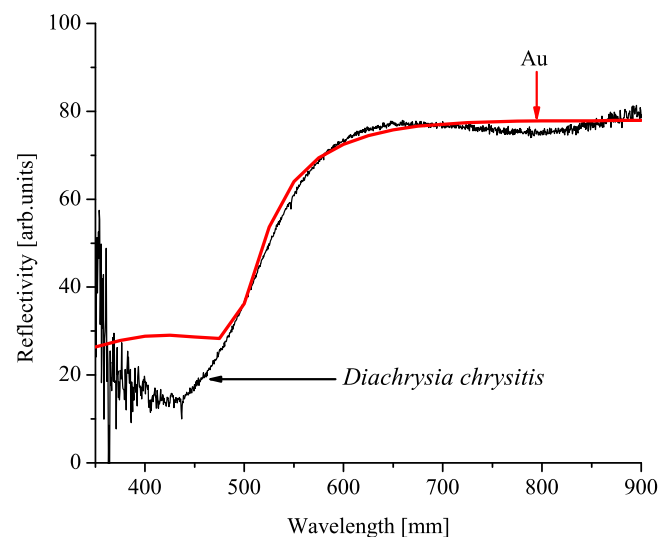


FIG. 2. Spectral reflectance of metallic gold (red curve) and golden wing patch of *D. chrysitis* forewings (black curve). Reflectance of *D. chrysitis* is scaled to emphasize the similarity with the gold.

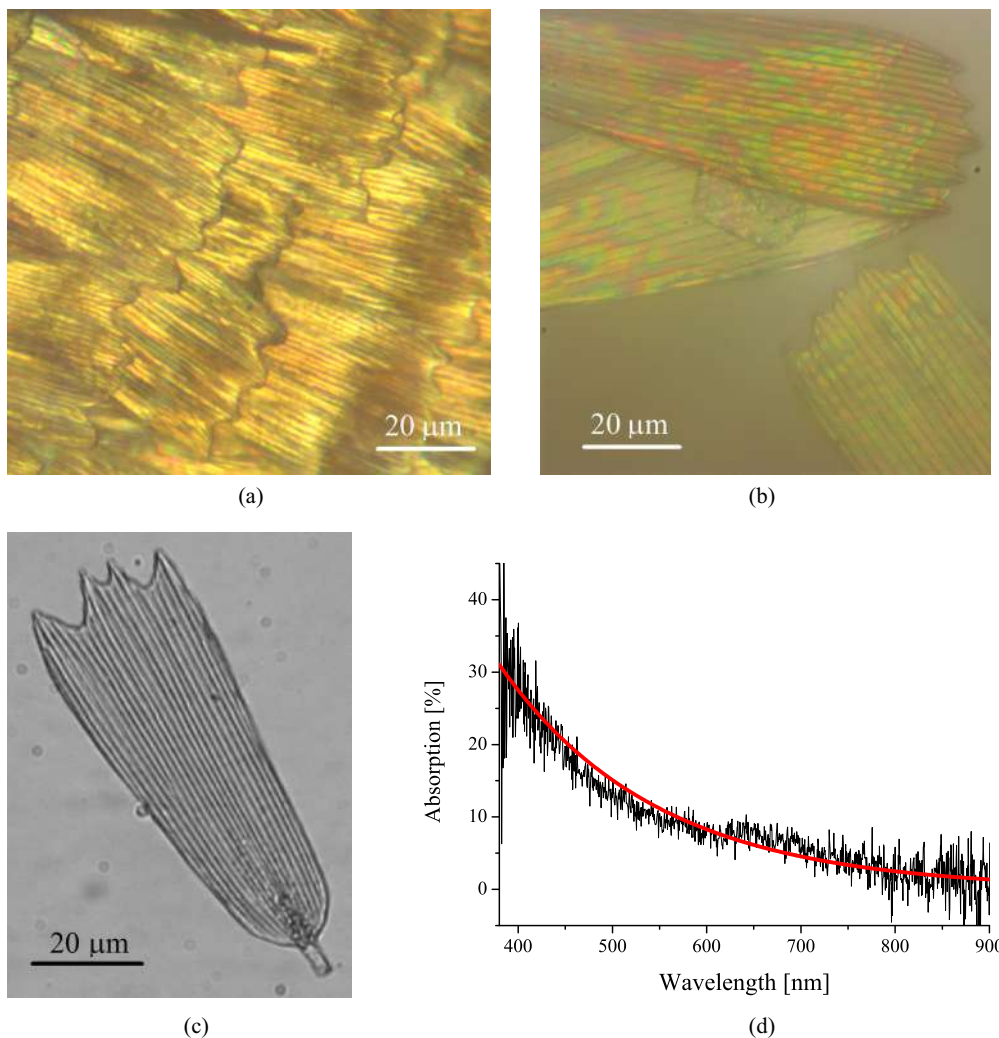


FIG. 3. Optical microscope images of *D. chrysitis*: (a) Scales on the forewing showing the uniformly golden reflection. (b) A microscope reflection image of two individual, overlapped scales. (c) A transmission image of an individual scale in air. (d) Absorption spectrum of a single scale placed in an immersion oil (black line) and the corresponding exponential fit (red line).

the scale in an index matching liquid (manufactured by Cargile, series A, with the certified refractive index 1.5700 ± 0.0002) Fresnel reflection was suppressed. We measured the absorption spectrum [Fig. 3(d)], which is very similar to that of melanin [29], showing exponential decrease from the UV to the IR part of the spectrum. We were able to estimate the value of the absorption coefficient α (or the imaginary part of the complex index of refraction $k = \alpha\lambda/4\pi$), and use it in further calculations. We have found that k ranges between 0.081 (at 380 nm) and 0.0013 (at 800 nm).

A field-emission gun scanning electron microscope (FEGSEM) was used to study the fine anatomy of the moth scales. The *D. chrysitis* forewing possesses a number of overlapping scales [as in Fig. 4(a)], but we were not able to see a difference between cover and ground scales. At higher magnification, as in Fig. 4(b), we can see that the upper lamina is ornamented with very thin lamellar ridges (separated by approximately $1.8 \mu\text{m}$). They are connected with herringbone shaped cross ribs, which constitute a subwavelength diffraction grating with the period of roughly 150 nm. A dual wing membrane seems to be an important optical component, too.

Its thickness is of the order of 500 nm and contains a number of 300-nm diameter, randomly dispersed, hemispherical protuberances [see inset in Fig. 4(a)].

Individual scales were prepared for scanning electron microscopy by the double transfer method, which was begun by detaching a scale with a low-surface-energy adhesive (adhesive layer of “Post-it” sticky note), followed by the transfer to a high-surface-energy tape (conductive carbon). By that means, the original scale orientation was preserved. Figure 5 shows one of the partially destroyed scales and its internal and external laminae structures. We see that the external side of the upper lamina (the one facing outwards) is strongly patterned, as explained above, while its internal surface is very irregular, with linear grooves directly beneath the ridges. The external side of the lower lamina (the one facing the wing membrane) is smooth, while its internal surface is completely irregular, similar to nanometer-sized “pebbles,” with a diameter less than 60 nm.

We have observed a strong autofluorescence of scales, which is enough for nonlinear (NL) fluorescence microscopy. We used a nonlinear microscope for laser processing and

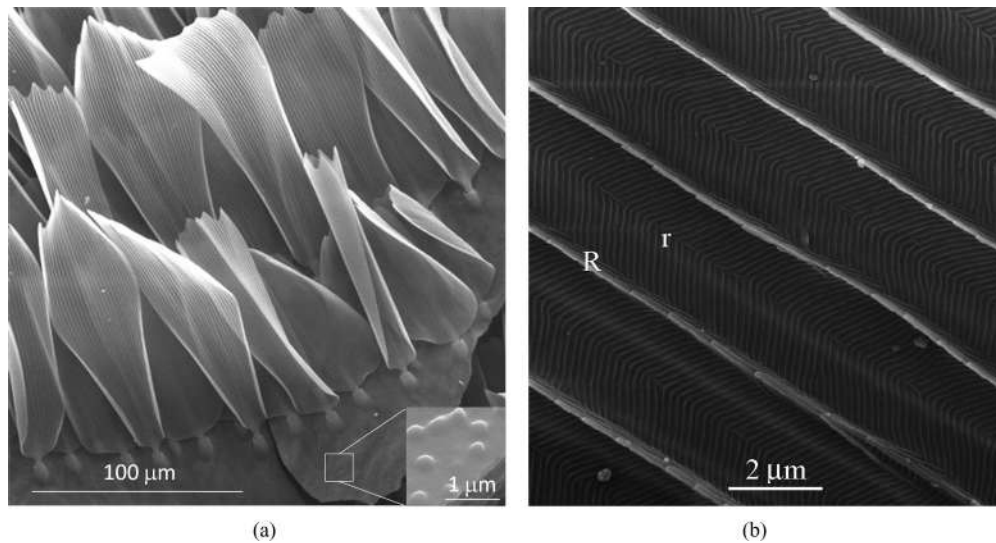


FIG. 4. (a) Scales of *D. chrysitis* in their natural position on the wing. The inset shows the enlarged part of the wing membrane with 300-nm-diameter protuberances. (b) Enlarged image of a single scale, showing lamellar ridges (R) and herringbone shaped cross ribs (r).

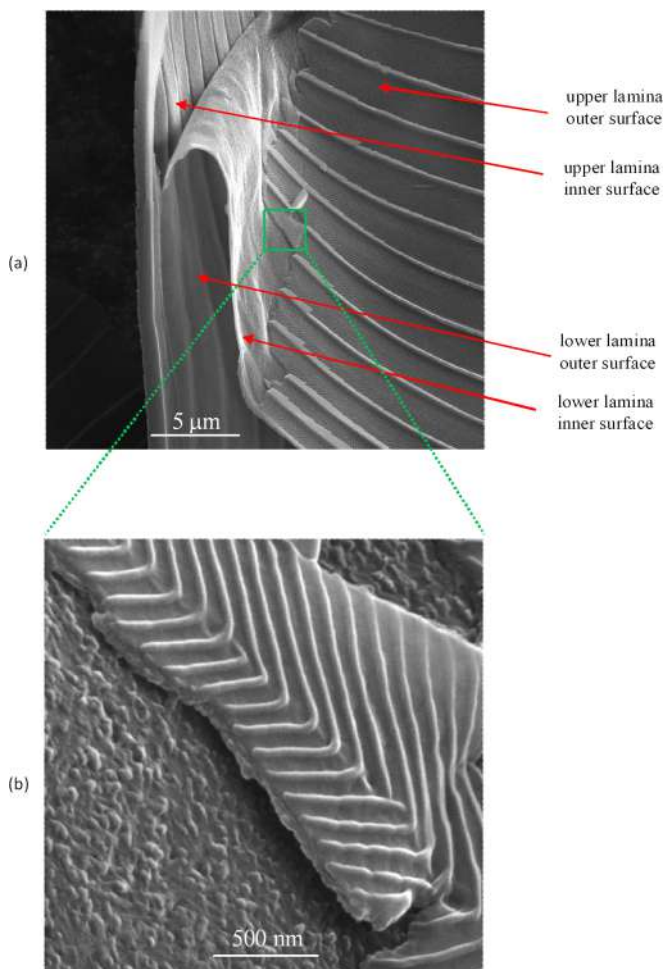


FIG. 5. FEGSEM images of a single *D. chrysitis* scale at two different magnifications. (a) This image reveals the internal and external structure of a single scale. (b) Enlarged zone of a scale showing rough internal surfaces.

cutting, too, which turned out to be a good tool for exposing otherwise hidden features. The beam power was increased above the threshold level and software was modified to enable drawing arbitrary shapes using vector images. At 840 nm and ~ 100 fs pulse length we were cutting moth chitinous structures with as low as a few milliwatts of laser power. However, continuous wave (cw) radiation at the same wavelength required an order of magnitude higher power. It was interesting that the laser-cut lines were rather irregular in the case of *D. chrysitis*, in contrast to scales of other lepidopteran species, which produced clear, well defined, lines.

To further reveal the cross-sectional geometry of *D. chrysitis* moth scales, we cut them as explained above. A SEM image of a laser-cut scale is shown in Fig. 6. The internal space of the scale is not visible due to the welding of the upper and lower laminae, but we were able to estimate the thickness of the scale at 300 nm, and the height of the ridge at 400 nm. Based on the scanning electron microscope images we are able to draw a general scheme of an individual scale as presented in Fig. 7.

We emphasize that the external features of the wing scale (such as the distance between the ridges) can be measured accurately from FEGSEM images, because they are recorded at normal incidence. Other characteristics, such as laminae thickness, are more complicated to quantify due to difficulty in determining the exact relative position of the scale and the scanning electron microscope optics (see Fig. 6, where the scale is partially lifted from the substrate). In such cases, measurements were performed using external features as a reference—e.g., lamina thickness was determined at approximately 75 nm by observing that it is approximately one half of the distance between the cross ribs (150 nm). Anyway, such measurements served just as a starting point for a wing-scale model.

Variability of the moth scales is another source of uncertainty. We recorded a number of SEM images, measured relevant features at several positions, and were able to find that they vary between 15% and 20% (depending on the measured characteristics).

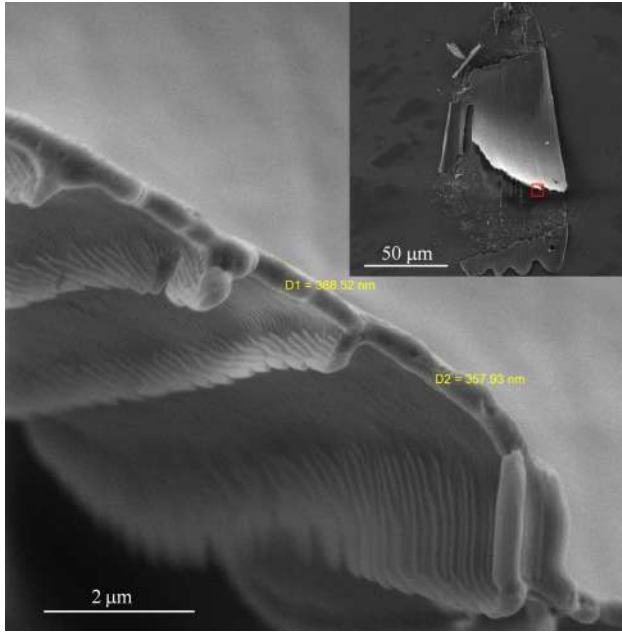


FIG. 6. A cross-sectional image of a femtosecond-laser-cut *D. chrysis* wing scale. The image of the whole, laser-cut scale is shown in the inset.

III. OPTICAL MODELING OF THE *D. CHRYSITIS* WING SCALES

The transparency of *D. chrysis* scales and the apparent simplicity of their internal and external structure pose a problem in explaining the golden wing color. We show that all the wing components (a double layer of scales and a wing membrane, possibly also the pigmented scales on the wing underside) work together to produce the final effect. Several features operate synergistically: slight absorbance of each scale, scattering on internal scale surfaces, interference of light within the scale, reflection of light from the wing membrane, and diffraction on the upper lamina grating.

We first demonstrate that the scattering on the internal scale surfaces leads to significant dispersal of incident light. As shown in Fig. 5, the internal scale surfaces are highly irregular, with the root mean squared (RMS) roughness estimated between 10 and 30 nm. The wavelength of the incident visible light (inside material) is much larger than the roughness and

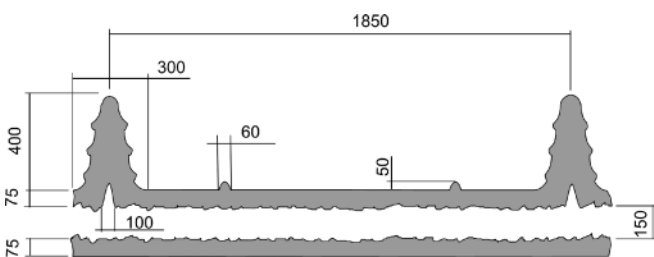


FIG. 7. A dimensional scheme of a *D. chrysis* scale cross section. All dimensions (expressed in nanometers) are estimated from SEM images and vary across the scales. Due to the variability of features in the living world, uncertainty of all the dimensions is between 15% and 20%.

the widely used scalar surface-scattering theory [30,31] is applicable. Under these circumstances, the light is split into two parts: one, regular, propagating as if the surface is perfectly flat, and the other diffusely scattered (haze).

Quantitatively, both components are described relative to transmittance T_0 and reflectance $R_0 = 1 - T_0$ of an ideally flat surface, when Fresnel equations hold. Accordingly, the haze transmittance $T_H(\lambda)$ and reflectance $R_H(\lambda)$ of a rough surface are described by [31]

$$T_H(\lambda) = T_0 \left(1 - \exp \left\{ - \left[\frac{2\pi\sigma}{\lambda} (n_i \cos \phi_i - n_t \cos \phi_t) \right]^2 \right\} \right), \quad (1)$$

$$R_H(\lambda) = R_0 \left\{ 1 - \exp \left[- \left(\frac{4\pi\sigma}{\lambda} n_i \cos \phi_i \right)^2 \right] \right\}, \quad (2)$$

where T_0 and R_0 are the transmittance and the reflectance of a perfectly flat surface, respectively; λ is the wavelength in vacuum; ϕ_i and ϕ_t are the angles of incidence and refraction; n_i and n_t are corresponding refractive indices; σ is the surface RMS roughness.

A simple calculation, based on Eqs. (1) and (2), shows that between 1% and 3% of incident radiation is scattered at each interface, depending on the wavelength and assuming normal angle of incidence ($\phi_i = 0$), RMS roughness $\sigma = 20$ nm, and the refractive index of chitin $n_i = 1.57$. As expected, short wavelengths are scattered more than long ones. The scattered light has a tendency to be trapped inside chitin layers, in a manner similar to textured solar cells [32]. It was shown in [33] that the local light intensity is increased by $2n^2$, and absorption by $4n^2$, where n is the refractive index. This was verified for the *D. chrysis* moth by using the finite element method (FEM) with periodic boundary conditions, applied to the model simulating a double layer of scales, as shown in Fig. 8(a). The corresponding electromagnetic field distributions can be seen in Fig. 8(b) showing the strong electromagnetic field enhancement.

Local field enhancement due to scattering is accompanied by increased absorption as predicted by the model described in [33]. We made slight modifications to correctly describe the scales of *D. chrysis*.

The change of the beam cross section is ignored due to the thinness of the scales. This is justified by the following arguments: Assume that the angle of divergence is $\theta = 40^\circ$ and scale laminae thickness is $D = 75$ nm; then the beam spread is defined by $2Dtg(\theta/2) = 55$ nm. This is insignificant for a beam width of approximately 7 mm, as used in our spectral measurement. The surface absorption was disregarded, too, because the residual melanin is expected to be distributed inside the laminae.

Under these assumptions, the absorption A_{int} inside the planar layer can be described by

$$A_{int} = \frac{4n^2 T_{inc}}{T_{esc} + 4n^2 \alpha l}, \quad (3)$$

where α is absorption coefficient, n is the refractive index, I_{inc} is incident light intensity, l is the layer thickness, and T_{inc} is a fraction of light transmitted through the interface. T_{esc} is an

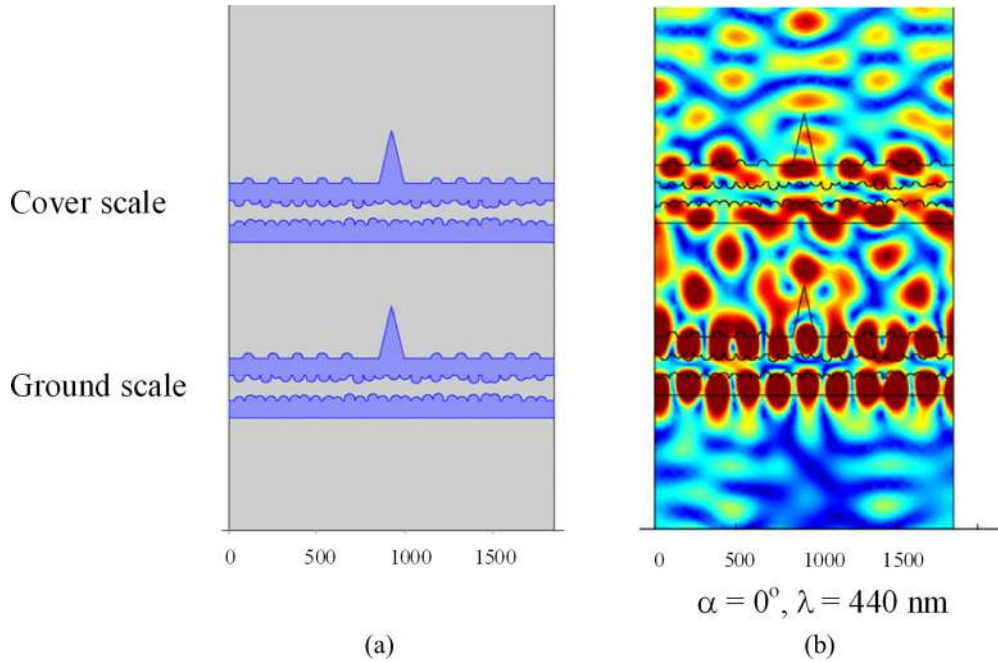


FIG. 8. (a) Geometry of the FEM model. (b) Intensity enhancement at 440 nm wavelength. The electromagnetic field is enhanced both in the ground and cover scales. Calculations were performed assuming that the angle of incidence is $\alpha = 0$ and there is no absorption.

average transmission factor of the escaping radiation, due to partial (Fresnel) transmission at the interface. According to the same model, fraction of the incident radiation escaping the layer is described by

$$F_{\text{esc}} = \frac{T_{\text{inc}} T_{\text{esc}}}{T_{\text{esc}} + 4n^2 \alpha l}. \quad (4)$$

Now we have tools to treat the problem of the golden coloration of the burnished brass moth. Its geometry includes two layers of scales and two wing membranes as shown in Fig. 9(a). It is assumed that the outside surfaces of the scales are flat, which is strictly true only for the lower lamina. The upper lamina is structured with two gratings. The coarse one

will produce diffraction orders which will be treated similarly during the propagation through the scales, the only difference being the angle of incidence. The dense grating is incapable of generating any propagating modes and will not enter the calculations. The inside scale surfaces are rough with RMS roughness of 10–30 nm, and the wing membranes are treated as flat. Fresnel reflection and transmission will be taken into account at flat surfaces, while rough surfaces will also include haze in reflection and transmission as schematically shown in Fig. 9(b). In the latter case, haze $R_H(\lambda)$ and $T_H(\lambda)$ diminish Fresnel coefficients R_0 and T_0 by the amounts $R_0 R_H(\lambda)$ and $T_0 T_H(\lambda)$. The resulting transmission and reflection coefficients are described by $R_0 - R_0 R_H(\lambda)$ and $T_0 - T_0 T_H(\lambda)$.

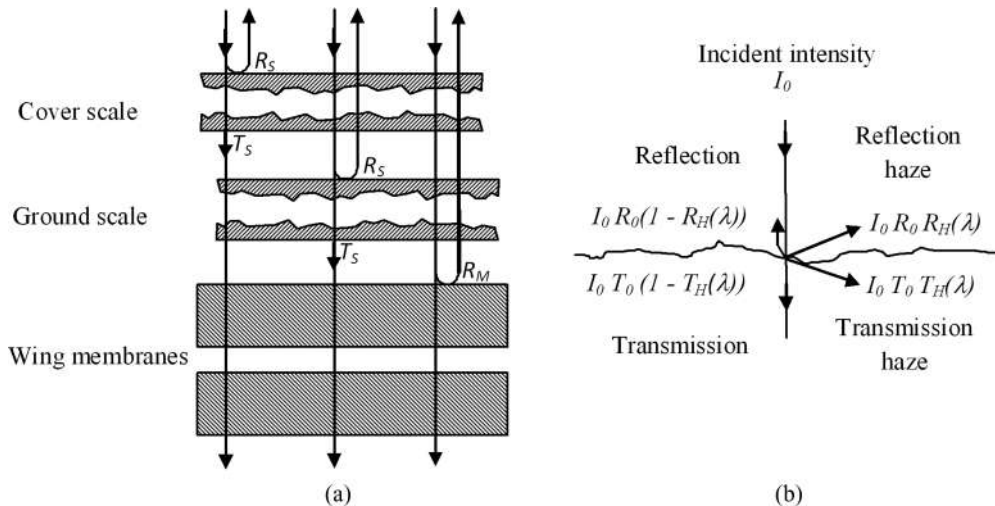


FIG. 9. (a) Geometry of the model used to simulate the wing of *D. chrysitis*. R_S and R_M are reflectance of a scale and a wing membrane, respectively. T_S is a transmittance of a single scale. (b) Reflection and transmission through the interface, as treated in a model. Incident intensity I_0 is split into four components: Fresnel reflectance (R_0), Fresnel transmittance (T_0), reflection haze (R_H), and transmission haze (T_H).

TABLE I. Numerical values of the parameters used for modeling optical reflection from *D. chrysitis* moth scales.

Parameter	Meaning	Value
N	Refractive index of chitin	1.57
α_0	Melanin absorption parameter, Eq. (5)	0.23 (1/nm)
A	Melanin absorption parameter, Eq. (5)	90 (nm)
λ_0	Melanin absorption parameter, Eq. (5)	380 (nm)
σ	RMS surface roughness	30 (nm)

The interference problem will be solved for an individual wing scale, as well as for the wing membranes, but not for the wing as a whole. This is a reasonable assumption, because the relative distances between the scales and the wing membrane are highly variable and the resulting effect is averaged across the wing surface. As a consequence, the resulting reflection spectral intensities of scales and membranes will be incoherently added.

Optical parameters of the model were estimated from the measurements performed on the scale embedded in an immersion liquid ($n = 1.57$), as described in the previous section. Therefore, the refractive index was taken to be 1.57 (consistent with the results published in [34]). According to the same study [34], the refractive index dispersion is less than 4% within the wavelength range of interest (380–900 nm) and the resulting effects were found to be insignificant. The coefficient of absorption α was modeled with an exponential function (assuming that the residual pigment is most probably melanin):

$$\alpha = \alpha_0 \exp\left(-\frac{\lambda - \lambda_0}{A}\right). \quad (5)$$

All parameters of the model are summarized in Table I.

Finding the exact solution to the multilayer interference is a problem requiring numerical tools. Here we adopt the transfer matrix method, described and used in [35] to analyze light scattering and trapping in silicon thin film solar cells. We divide incident light into two components: a scattered one, which is mostly absorbed and diffused, and an unscattered one, which interferes in wing scales and wing membranes. For the unscattered component we apply a transfer matrix method, where scattering from subwavelength rough surfaces is treated as a wavelength-dependent correction for Fresnel coefficients.

Reflection and transmission from a single scale are treated coherently using the transfer matrix method. As a result, the spectral reflectance R_S and transmittance T_S were found. Similarly, the reflection from the double wing membrane was treated coherently (with the resulting reflectance R_M). Scattering from the wing membrane was not included in calculations due to the sparsity and large dimensions of scattering inclusions (as illustrated in Fig. 4). The resulting spectrum of the wing as a whole is composed of three components: one which is reflected from the cover scales, the other reflected from the ground scales, and the final one due to the wing membranes. We combine them incoherently, because the mutual position between scales and membranes is stochastic and highly variable. The final reflected spectral

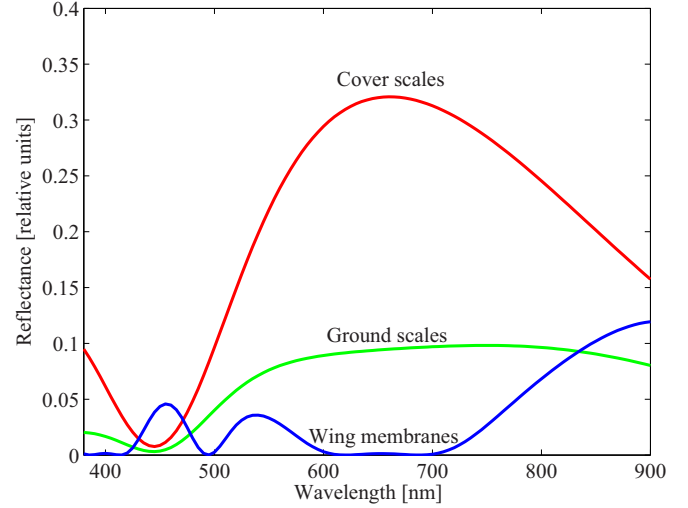


FIG. 10. Contributions of wing membranes, cover scales, and ground scales to the resulting wing spectrum. They are calculated using the transfer matrix method and normalized to the intensity of the incident light before being transmitted through the layers.

distribution of the whole wing is thus

$$R = R_S + T_S R_S T_S + T_S^2 R_M T_S^2. \quad (6)$$

The first term corresponds to the reflection from the cover scale, the second to the transmission through the cover scale, followed by the reflection from the ground scale and return path through the cover scale. The third term describes transmission through the cover and ground scales, followed by the reflection from the wing membrane, and return path through both layers of the scales. The calculated contribution of each term to the final spectrum is shown in Fig. 10 (normalized to the intensity of light before being transmitted through the layers).

Spectral contributions of wing components significantly depend on their geometry, i.e., scale laminae and wing membrane thicknesses. For some combination of dimensional parameters, even a single scale can quite faithfully reproduce an experimentally recorded spectrum (as in Fig. 11). However, there are slight modulations within the whole spectral range, due to thin film interference effects. They disappear when spatial and angular averaging is included, as further explained. As explained above, losses are much higher inside the blue-UV spectral range, as can be seen in Fig. 11. According to Eqs. (3) and (4), most of the light energy is absorbed, and the rest of the radiation is scattered. It is interesting to note that a significant amount of radiation is transmitted through the wing membranes (green curve in Fig. 11). However, the UV component of transmitted radiation is efficiently absorbed by the dark, pigmented scales, on the wing underside.

There is an important word of caution. In order to get a consistently golden wing color, the dimensional and optical parameters of each individual scale should be kept within quite tight tolerances—a task completely impossible in the living world. It is more realistic to expect significant variability of all the parameters. Thus they were varied in our simulations (according to the normal distribution) within $\pm 15\%$ of the values producing fit in Fig. 11. The angle of incidence was also

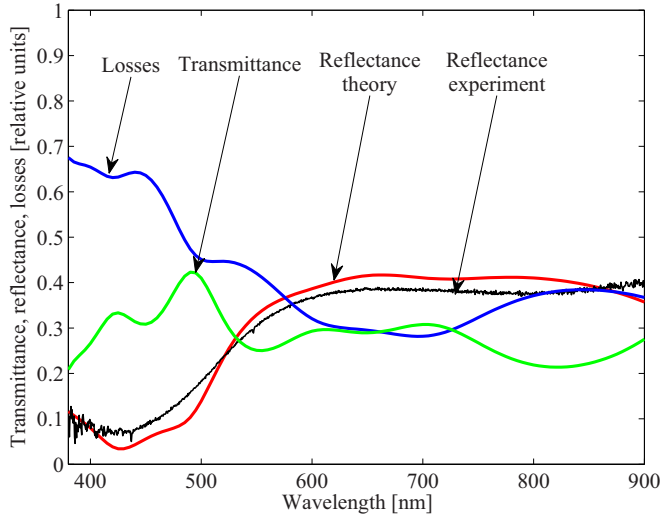


FIG. 11. A spectral reflectivity (red curve) of a *D. chrysitis* moth wing, calculated by the transfer matrix method is shown. The corresponding experimental curve (black curve) is added for reference. Losses (due to scattering and absorption, blue curve) and the wing transmittance (green curve) are displayed, too.

allowed to fluctuate within $\pm 20^\circ$, which imitates variability of scale orientations.

As a result, 100 different spectra were calculated (for clarity, only 25 of them are displayed in Fig. 12 as light blue curves). They were consequently averaged, in agreement with our experimental procedure where the light is collected from the wing area and within an angular range (the resulting curve is shown in blue). By comparing the calculated spectrum with the experimentally recorded one (red curve in the same figure), agreement appears remarkably good, except for the radiation above 800 nm.

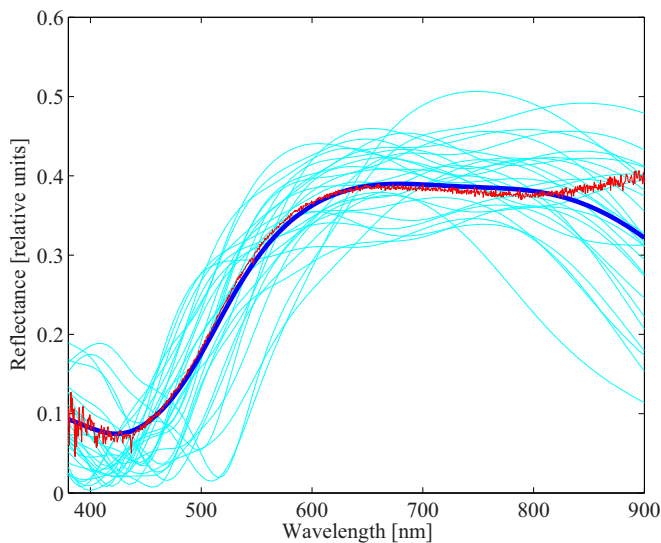


FIG. 12. Spectral averaging of light reflected from *D. chrysitis* wing, calculated by the transfer matrix method which includes scattering and local field enhancement. Light blue curves are individual spectra, blue curve is the averaged spectrum, and the red curve is the experimentally recorded spectrum.

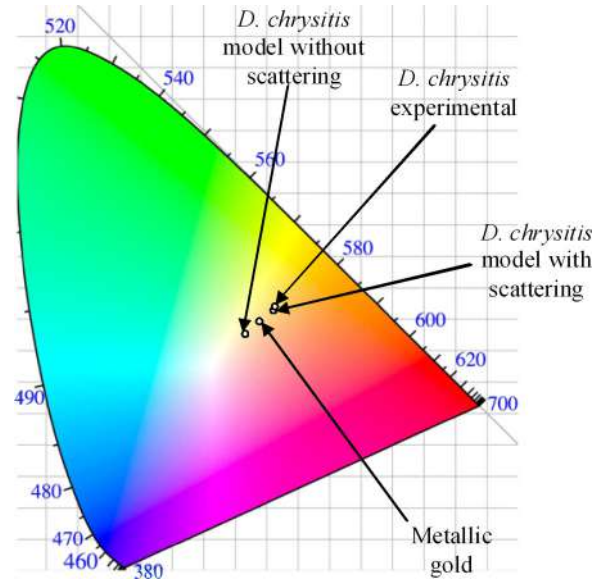


FIG. 13. CIE color coordinates of metallic gold and *D. chrysitis* forewing golden patches, with and without scattering.

The final shape of the spectrum is influenced by the layer thicknesses and the RMS surface roughness. They collectively influence the final calculated spectrum, but in general terms we have observed that increased thickness shifts the spectrum towards the red, while increased roughness depletes the blue part of the spectrum and decreases overall reflectivity.

All the computations are based on a transfer-matrix code, developed in [36] (declared free to use and made public at the URL provided therein). The program was modified by including scattering and local field enhancement effects [as defined by Eqs. (1)–(4)].

IV. DISCUSSION AND CONCLUSIONS

In contrast to most other lepidopteran species, each and every wing structure of *D. chrysitis* plays a certain role in iridescent color production. The same goes for the optical mechanisms—interference, diffraction, absorption, and surface scattering. They seem to be intricately intertwined in a synergistic manner—by omitting any of them, a significant change of the spectral profile would result. To demonstrate the fact, we calculated the resulting spectrum without taking into account scattering-enhanced absorption. As expected, reflection in the UV-blue spectral range is not attenuated. The corresponding CIE color coordinate testifies that the resulting color is whitish, as presented on a CIE 1931 diagram (Fig. 13). For reference, we have also displayed points corresponding to metallic gold, experimentally recorded spectrum, and full simulation of *D. chrysitis* wing. It is obvious that without scattering, the color coordinate would approach the achromatic center of the diagram—i.e., the wing will have only a slight coloration. It is interesting to note that the moth wing looks “yellow” than the gold.

As noted before, scattering stimulates confinement of light and increases the intensity by the $2n^2$ factor. It seems that the ground scale layer further amplifies the confinement [see Fig. 8(b)]. One possible explanation is that the cover scales

diffuse the incoming light, while the ground scales additionally disperse it and make it amenable for wave guiding within the layer.

Angular variability of *D. chrysitis* wing coloration is noticeable, and the golden color is observable within the $\pm 20^\circ$ from the specular direction. Beyond that, the color abruptly changes from golden to brown-gray. However, within the specular range, dependence of the reflected spectrum is slight for several reasons. On one hand, it results from irregular internal surfaces of the scale laminae and irregular mutual position of scales in ground and cover layers. The other reason is that the reflectivity at air-chitin interfaces is almost constant between 0° and 30° , as predicted by Fresnel equations. Therefore, the overall shape of the spectrum is not altered, but slightly shifted with the angle of incidence. Coarse diffraction grating on the upper lamina additionally diminishes angular dependence. From whichever direction light enters the scale, at least one of the diffraction orders is being reflected. This is what gives the notable stability of the optical effect with respect to the illumination direction (within the stated angular range).

We have not observed polarization sensitivity of the described reflection spectra, even though it certainly exists at the single wing-scale level. If observed macroscopically, across the whole wing, polarization effects cancel out due to strong variability of individual scale orientations with respect to incident radiation.

It is also interesting to note that the scales from brown-gray and golden areas of the wing have very similar morphology if observed under the scanning electron microscope. The most important difference is optical: while the golden area scales are almost transparent, the others contain a significant amount of absorbing pigment which leads to suppression of the specular component in the brown wing regions. Also, the brown scales are flatter, while the golden ones are slightly curled.

Calculations, according to Eqs. (3) and (4), have shown that approximately 70% of incoming radiation at 380 nm is scattered. Forty percent of the scattered component is absorbed, while the rest is uniformly dispersed all over the full solid angle. At the other end of the spectrum (above 800 nm), only 20% of light is scattered, without being absorbed to any significant extent. As a whole, the spectrum of unabsorbed light is quite flat from UV to IR. Its contribution to the wing

reflection is really small, because it is dispersed over the 4π solid angle, while the reflected light is concentrated around the specular direction.

A dual wing membrane is densely covered with nanosized spherical inclusions, conveniently situated, just beneath the scales. It seems that this could be an additional mechanism to scatter light back through the layer of scales. Transmission of the membranes is high and light further propagates to underside scales. They are gray, most probably due to melanin, which will further absorb the UV-blue part of the spectrum. In the red-infrared range, melanin absorbance is insignificant, and scales are again capable of reflecting light back through all the previous layers. This might account for the increased reflectivity in the infrared, which is not predicted by the theory described in the previous section.

Insects with golden body parts are rare and interesting from the biological point of view. The roles of the golden color may be diverse and are related mostly to possible defense mechanisms. We suppose that in *D. chrysitis* the golden forewing patches may appear to predators as warning and/or they can facilitate the conspecific recognition [15].

To summarize: All the structures—cover and ground scales, wing membranes, and underside wing scales—contribute to the golden wing color of the burnished brass moth. Interference, scattering, and absorption enhancement are optical mechanisms responsible for the effect. In short, interference on the scales produces a broad reflection spectrum with a peak in the green part of the spectrum. The blue part of the spectrum is absorbed due to scattering-enhanced absorption on a residual pigment. The red part of the spectrum is transmitted to the wing membrane, where it reflects, goes back through the scales, and combines with the reflection from the scales. The resulting spectrum is strongly attenuated below 520 nm, being almost flat up to 800 nm. The forewings of the *D. chrysitis* moth seem to be a remarkable, finely tuned, optical filter.

ACKNOWLEDGMENTS

This research was supported by Projects No. ON171038, No. III45016, and No. ON173038 funded by the Ministry of Education, Science and Technological Development of the Republic of Serbia.

-
- [1] J. Sun, B. Bhushan, and J. Tong, Structural coloration in nature, *RSC Adv.* **3**, 14862 (2013).
 - [2] J. Zi, B. Dong, T. Zhan, and X. Liu, in *Bioinspiration: From Nano to Micro Scales*, edited by X. Y. Liu (Springer, Berlin, 2012), pp. 275–329.
 - [3] T. Starkey and P. Vukusic, Light manipulation principles in biological photonic systems, *Nanophotonics* **2**, 289 (2013).
 - [4] N. N. Shi, C.-C. Tsai, F. Camino, G. D. Bernard, N. Yu, and R. Wehner, Keeping cool: Enhanced optical reflection and radiative heat dissipation in Saharan silver ants, *Science* **349**, 298 (2015).
 - [5] O. Karthaus, *Biomimetics in Photonics* (CRC Press, Boca Raton, FL, 2013).
 - [6] Z. Gan, M. D. Turner, and M. Gu, Biomimetic gyroid nanostructures exceeding their natural origins, *Sci. Adv.* **2**, e1600084 (2016).
 - [7] M. F. Land, The physics and biology of animal reflectors, *Prog. Biophys. Mol. Biol.* **24**, 75 (1972).
 - [8] S. Yoshioka, T. Nakano, Y. Nozue, and S. Kinoshita, Coloration using higher order optical interference in the wing pattern of the Madagascan sunset moth, *J. R. Soc., Interface* **5**, 457 (2008).
 - [9] D. J. Brink, J. E. Smith, M. E. Lee, and A. Möller, Optical diffraction by the microstructure of the wing of a moth, *Appl. Opt.* **34**, 6049 (1995).
 - [10] M. Hernández-Jiménez, D. E. Azofeifa, E. Libby, C. Barboza-Aguilar, Á. Solís, L. Arce-Marenco, I. García-Aguilar, A. Hernández, and W. E. Vargas, Qualitative correlation between structural chirality through the cuticle of *Chrysina aurigans* scarabs and left-handed circular polarization of the reflected light, *Opt. Mater. Express* **4**, 2632 (2014).

- [11] F. Liu, B. Q. Dong, X. H. Liu, Y. M. Zheng, and J. Zi, Structural color change in longhorn beetles *Tmesisternus isabellae*, *Opt. Express* **17**, 16183 (2009).
- [12] J. P. Vigneron, J. M. Pasteels, D. M. Windsor, Z. Vártesy, M. Rassart, T. Seldrum, J. Dumont, O. Deparis, V. Lousse, L. P. Biró, D. Ertz, and V. Welch, Switchable reflector in the Panamanian tortoise beetle *Charidotella egregia* (Chrysomelidae: Cassidinae), *Phys. Rev. E* **76**, 031907 (2007).
- [13] M. Rothschild, B. Gardiner, and R. Mummery, The role of carotenoids in the “golden glance” of danaid pupae (Insecta: Lepidoptera), *J. Zool.* **186**, 351 (1978).
- [14] R. L. Taylor, The metallic gold spots on the pupa of the monarch butterfly, *Entomol. News* **75**, 253 (1964).
- [15] A. C. Neville, Metallic gold and silver colours in some insect cuticles, *J. Insect Physiol.* **23**, 1267 (1977).
- [16] R. A. Steinbrecht, W. Mohren, H. K. Pulker, and D. Schneider, Cuticular interference reflectors in the golden pupae of danaine butterflies, *Proc. R. Soc. London, Ser. B* **226**, 367 (1985).
- [17] B. D. Wilts, H. L. Leertouwer, and D. G. Stavenga, Imaging scatterometry and microspectrophotometry of lycaenid butterfly wing scales with perforated multilayers, *J. R. Soc., Interface* **6**, S185 (2009).
- [18] N. I. Morehouse, P. Vukusic, and R. Rutowski, Pterin pigment granules are responsible for both broadband light scattering and wavelength selective absorption in the wing scales of pierid butterflies, *Proc. R. Soc. London, Ser. B* **274**, 359 (2007).
- [19] D. G. Stavenga, S. Stowe, K. Siebke, J. Zeil, and K. Arikawa, Butterfly wing colours: Scale beads make white pierid wings brighter, *Proc. R. Soc. London, Ser. B* **271**, 1577 (2004).
- [20] S. M. Luke, P. Vukusic, and B. Hallam, Measuring and modelling optical scattering and the colour quality of white pierid butterfly scales, *Opt. Express* **17**, 14729 (2009).
- [21] X. Chen, C. Wang, E. Baker, and C. Cun, Numerical and experimental investigation of light trapping effect of nanostructured diatom frustules, *Sci. Rep.* **5**, 11977 (2015).
- [22] A. Hille, M. A. Miller, and S. Erlacher, DNA sequence variation at the mitochondrial cytochrome oxidase I subunit among pheromotypes of the sibling taxa *Diachrysia chrysitis* and *D. tutti* (Lepidoptera: Noctuidae), *Zool. Scr.* **34**, 49 (2005).
- [23] A. Seitz, *The Macrolepidoptera of the World. A Systematic Description of the Known Macrolepidoptera. I Section. 3. Volume: The Palearctic Noctuidae. Plates* (Verlag des Seitz'schen Werkes, Stuttgart, 1914).
- [24] G. S. Robinson, P. R. Ackery, I. J. Kitching, G. W. Beccalon, and L. M. Hernández, *HOSTS—a Database of the World's Lepidopteran Hostplant* (Natural History Museum, London, 2010).
- [25] D. V. Stojanović and S. B. Čurčić, The diversity of noctuid moths (Lepidoptera: Noctuidae) in Serbia, *Acta Zool. Bulg.* **63**, 47 (2011).
- [26] M. Boardman, R. R. Askew, and L. M. Cook, Experiments on resting site selection by nocturnal moths, *J. Zool.* **172**, 343 (1974).
- [27] I. Svensson, P. Douwes, and B. O. Stille, Are *Diachrysia chrysitis* (L.) and *D. tutti* (Kostrowicki) different species? (Lepidoptera: Noctuidae), *Insect Syst. Evol.* **20**, 15 (1989).
- [28] A. D. Rakic, A. B. Djuricic, J. M. Elazar, and M. L. Majewski, Optical properties of metallic films for vertical-cavity optoelectronic devices, *Appl. Opt.* **37**, 5271 (1998).
- [29] D. G. Stavenga, H. L. Leertouwer, T. Hariyama, H. A. De Raedt, and B. D. Wilts, Sexual dichromatism of the damselfly *Calopteryx japonica* caused by a melanin-chitin multilayer in the male wing veins, *PLoS One* **7**, e49743 (2012).
- [30] H. Davies, The reflection of electromagnetic waves from rough surface, *Proc. IEE-Part IV: Inst. Monogr.* **101**, 209 (1954).
- [31] D. Domine, F.-J. Haug, C. Battaglia, and C. Ballif, Modeling of light scattering from micro- and nanotextured surfaces, *J. Appl. Phys.* **107**, 044504 (2010).
- [32] Y. A. Akimov, W. S. Koh, S. Y. Sian, and S. Ren, Nanoparticle-enhanced thin film solar cells: Metallic or dielectric nanoparticles? *Appl. Phys. Lett.* **96**, 073111 (2010).
- [33] E. Yablonovich and G. D. Cody, Intensity enhancement in textured optical sheets for solar cells, *IEEE Trans. Electron Devices* **29**, 300 (1982).
- [34] H. L. Leertouwer, B. D. Wilts, and D. G. Stavenga, Refractive index and dispersion of butterfly chitin and bird keratin measured by polarizing interference microscopy, *Opt. Express* **19**, 24061 (2011).
- [35] J. Springer, A. Porube, and M. Vanacek, Improved three-dimensional optical model for thin film silicon solar cells, *J. Appl. Phys.* **96**, 5329 (2004).
- [36] J. Junesch, T. Sannomiya, and A. B. Dahlin, Optical properties of nanohole arrays in metal-dielectric double films prepared by mask-on-metal colloidal lithography, *ACS Nano* **6**, 10405 (2012). Transfer matrix code can be found in <http://adahlin.com/onewebmedia/TransferMatrix3.m>.



Cite this: *Soft Matter*, 2021, 17, 6477

Synergy of interference, scattering and pigmentation for structural coloration of *Jordanita globulariae* moth

Danica Pavlović,^a Svetlana Savić-Šević,^a Branislav Salatić,^a Vladimir Lazović,^a Wang Zhang,^b Di Zhang^b and Dejan Pantelić^a

Structural and pigment colorations are omnipresent in insects, producing a range of colors for camouflage, warning, mimicry and other strategies necessary for survival. Structural coloration has attracted a lot of attention due to its significance in biophotonics, biomimetics and even esthetic appeal. The coupling of structural and pigment colorations has been largely unnoticed. Herein we show how pigments, scattering and interference work together in two-dimensional waveguiding structures to produce the coloration of *Jordanita globulariae* (Huebner, 1793), a moth whose forewings sparkle with slightly iridescent green scales. We show that subwavelength structures scatter and couple light into a concave multilayered structure to enhance the absorption of pigments. A finite element method (FEM) model, adequately describing the photonic properties of *J. globulariae*, was developed based on the nanoscale architecture of the insect's wing scales. The principle of absorption enhanced by scattering and waveguiding is present in many insect species and might be imitated to tailor the spectral properties of optical devices.

Received 29th January 2021,
Accepted 25th May 2021

DOI: 10.1039/d1sm00157d

rsc.li/soft-matter-journal

1. Introduction

Animals produce colors in two fundamentally different ways: by pigments and structurally. Most animals have pigmentary coloration that is based on the selective absorption of a certain range of wavelengths. However, the most intense and brightest colors are structural. They result from the interaction of light with micro- and nanostructures comparable with visible wavelengths.¹

Pigment coloration is prevalent, except for blue and green, which seem to be rare, but nonetheless can be found in some vertebrates,² the most notable being the green coloration of frogs.³ The same is true for insects, whose blue-green colors can be produced by bile pigments such as pterobilin, phorbabilin and sarpodobilin. Some butterfly species have a bluish- or greenish-pigmented hue obtained by bile pigments (seen in two Papilionidae genera: *Papilio* and *Graphium*). Pigmented blue has not been found in other insects.⁴ Structural coloration seems to be an alternative, evolutionarily developed, way to generate shiny, pronounced shades of arbitrary colors, including blues and greens.

There are many different studies and advanced techniques dealing with structural coloration.^{5,6} The genesis of green coloration is particularly interesting because of its significance in camouflage. Structural green sometimes arises solely from photonic structures^{7,8} or due to color mixing within concave structures (as in the wing scales of some Papilionidae species (Lepidoptera) and Cicindelidae (Coleoptera)).^{9,10} It is worth noting that green may be a result of the color-mixing of structural blue and pigmentary yellow.^{11,12}

Such a peculiar coloration is even more interesting if it is found on the wings of moths (Heterocera: Lepidoptera). Moths are mostly nocturnal, and therefore, generally drab in color (brown or grey). However, there are some moth species that possess attractive coloration such as the tropical Madagascan sunset moth.¹³ There is also a whole group of colorful, day-flying moths of the Zygaenidae family. The majority of zygaenids are tropical, but they are nevertheless quite well represented in temperate regions. The species *Jordanita globulariae* (subfamily Procrinae) caught our attention because of the dull, slightly iridescent green coloration of its forewings.

In this study we reveal the structure and function of the scales of the *Jordanita globulariae* moth through morphological characterization, spectral measurement and numerical simulation. The synergistic operation of structure and pigments is analyzed. We also discuss the role of this particular coloration in the moth's lifestyle.

^a Institute of Physics Belgrade, Pregrevica 18, 11080 Zemun, Belgrade, Serbia.
E-mail: danica.pavlovic@ipb.ac.rs

^b State Key Lab of Metal Matrix Composite, Shanghai Jiao Tong University, 800 Dongchuan Road, Shanghai 200240, China

2. Materials and methods

2.1 Specimen details

Jordanita globulariae (Fig. 1) is a day-flying moth (fam. Zygaenidae, subfam. Procridinae). The species is widespread from the Iberian Peninsula in the west to the Urals in the east of Europe. The forewing's length is 10.5–17 mm in males and 7.7–10.1 mm in females. It flies during the sunny days from May to August, usually in limestone pastures.¹⁴ Larvae are fed on species from the genera *Centaurea* L., *Cirsium* and *Globularia* L. On very hot days, the moth usually perches on flowers and other vegetation. Males occasionally fly at night.¹⁵ Adults of this moth have green forewings, while the hind ones are grey-brown. When at rest, the hindwings are completely obscured under the green forewings, enabling the insect to hide in foliage. Several species within this family have similar morphological characteristics [e.g. *Adscita statices* (Linnaeus, 1758)]. We had three, conserved and pinned *J. globulariae* specimens at our disposal, collected during May and June of 2011 on Mt. Fruška Gora, near the city of Novi Sad, Serbia (leg. D. Stojanović).

2.2 Microscopy and spectroscopy

Field-emission gun scanning electron microscope (FEGSEM) (MiraSystem, TESCAN) was used to study the fine anatomy of the moth scales. Dried insect forewings were mounted and sputter-coated with 5–10 nm of Au/Pd in preparation for SEM. We used an Au/Pd target because it has a smaller grain size and it is the recommended metal coating for a wide range of sample types.

Individual scales were prepared for SEM by the double transfer method: a scale was detached with a low-surface-energy adhesive ("Post-it" sticky note), followed by transfer to a high-surface-energy tape (conductive carbon). In this way, the original scale orientation was preserved. During this process some of the scales were mechanically broken, revealing the inner structure and cross section of the scales.



Fig. 1 *Jordanita globulariae* with structurally green dorsal sides of the forewings.

Optical characteristics of the wings and scales were analyzed on a trinocular microscope MET104 (Colo Lab Experts) with a Plan Achromatic POL Polarizing objective lens (10X/20X/40X).

To record reflectance spectra, we used a fiber optic spectrometer (Ocean Optics, HR2000CG-UV-NIR) with a 400 μm core diameter fiber. A halogen lamp was used as a light source and spectra were referenced to a standard white surface. Angular variation of the reflectance spectra was measured with a stationary sample illuminated by the light source at normal incidence. The spectrometer fiber was rotated within the angular range from 10° to 50° .

2.3 Optical modeling

A finite element method (FEM) was used to model the interaction of visible light with wing pigmented scale nanostructures. The model is two-dimensional because it saves computation time, which was approximately 20 min on our PC. It would be difficult to model the exact shape of photonic structures that are certainly not spherical, but somewhat irregular, rather oval and elongated along one axis (Fig. 2(b) and 3(a)). Thus, a 2D model (which is equivalent to a 3D infinite cylinder) is a satisfactory approximation, as the photonic structure studied here departs significantly from cylindrical only at its edges. The arrayed structure of wing scales is modeled using one unit cell with periodic boundary conditions. Perfectly matched layers (PMLs) are placed above and below the structure in order to minimize any reflected signal. In the model, the average mesh size was manually set to one-fifth

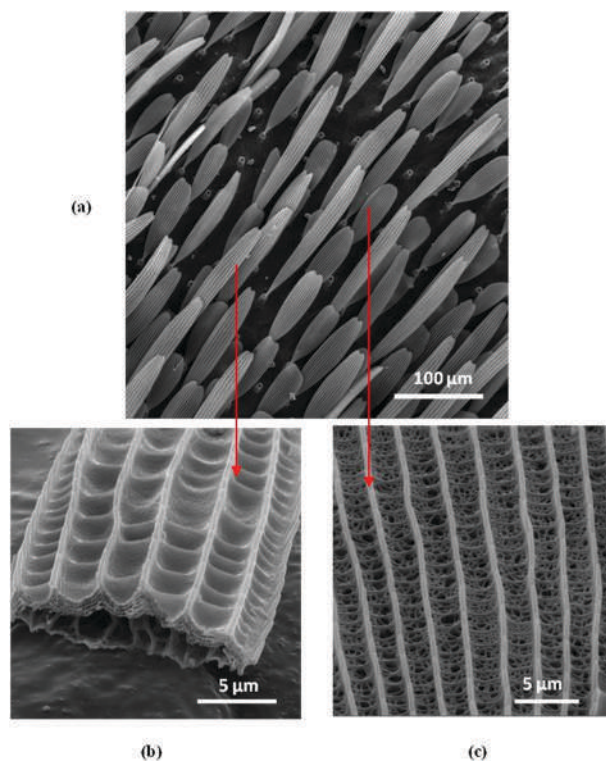


Fig. 2 (a) A SEM image of the *J. globulariae* forewing with two types of scales. Magnified SEM images of: (b) a long scale covered with several cup-shaped dips and (c) a short scale with a random, sponge-like structure.

of the minimum incident wavelength, which was 400 nm in our case. However, mesh density was adaptively adjusted to correctly model the tiniest structures of the model. To create a numerical simulation, it is necessary to know the complex refractive index of the biological structure. It is difficult to know the exact value, but we found that modest variation ($\Delta n \sim \pm 0.03$) of the refractive index has only a slight impact on simulations. The real part of the complex refractive index was taken from the literature: $n = 1.57$.^{16,17}

The extinction coefficient was determined experimentally by measuring the transmission of light through the structure and applying Beer–Lambert's law. We assumed that the structures analyzed here had a subwavelength size and could be regarded within the effective medium approximation. Imaginary part k of the refractive index was 0.011 at 400 nm, 0.019 at 500 nm and 0.01 at 800 nm.

3. Results

3.1 Morphological and optical analysis of *J. globulariae* wing structures

The dorsal side of *J. globulariae* forewings is covered with scales that seem to be randomly distributed (Fig. 2(a)). The scales are either long with a regular internal architecture (Fig. 2(b)), or short with an irregular, sponge-like structure (Fig. 2(c)).

Long scales (with characteristic dimensions of approximately $20 \mu\text{m} \times 150 \mu\text{m}$) seem to be more elaborate. At higher magnification (Fig. 3(a)), we can see that their upper lamina is ornamented with thin, lamellar ridges (separated by approximately $3 \mu\text{m}$) connected by cross ribs. Together, ridges and cross ribs produce a sequence of concave dips (cup-like structures, $0.5\text{--}3 \mu\text{m}$ deep) whose surface has a large number of tiny pores ($20\text{--}50 \text{ nm}$). The interior of the whole scale is hollow, supported by large, $1.5 \mu\text{m}$ high, trabeculae (Fig. 3(a)) connecting the upper and lower lamina (which is irregular, single-layered and about 100 nm thick).

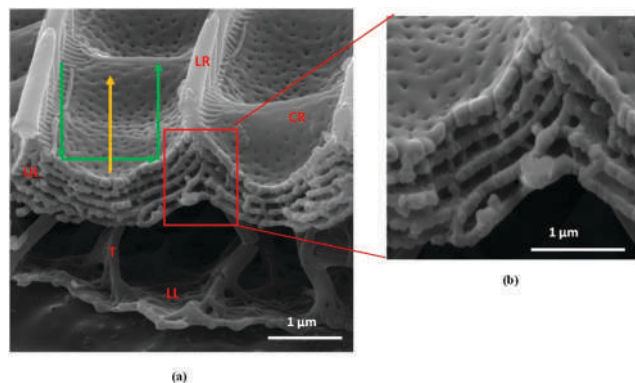


Fig. 3 SEM image of *J. globulariae* long wing-scale structure. (a) A cross section of the scale showing concave, multilayered upper lamina and single-layer lower lamina separated by trabeculae (LR – lamellar ridges; CR – cross ribs; T – trabeculae; UL – upper lamina; LL – lower lamina). Green and yellow arrows indicate different wavelengths for radiation hitting the structure at its center or its edges. (b) A concave multilayer of the upper lamina with five chitin layers.

The cross section of the scale (Fig. 3(b)) shows the concave upper lamina with five chitin layers whose thickness is approximately 110 nm . They are mutually separated by tiny, pillar-like structures, producing 90 nm -thin, air-filled, voids. This arrangement will be further considered as a curved multilayer serving as a specific, spectrally selective, filter.

On the other hand, short scales (whose approximate size is $40 \mu\text{m} \times 80 \mu\text{m}$) are quite different. They are almost hollow, filled with an intricate, irregular, sponge-like structure (Fig. 4(a) and (b)), but surface ridges and cross ribs can be seen as well.

From an optical point of view, the green color of the insect is diffuse, dim and slightly iridescent (Fig. 1) – *i.e.* we were able to observe a significant color shift only for large, almost grazing, angles of observation. If observed through an optical microscope, long scales reflect, while short ones absorb light (Fig. 5). If the image of a long scale is further magnified (inset in Fig. 5), a number of discrete blue-green and yellow dots can be seen.

Comparing SEM and optical images, we can see accurate matching between the morphology of long scales and the observed optical pattern. It is well known that the spectral reflection of a layered structure is influenced by the distance between the layers, the refractive index and the angle of incidence. In this case, reflection is strongly affected by the concave shape of the layers. We can see that light falling on the center of the concavity has a different angle of incidence compared to off-center zones. This is why we observe differently colored spots in the inset of Fig. 5. Macroscopically, colors are mixed to produce the insect's green color.

Apart from structural coloration, scales are slightly pigmented, as can be seen from the transmission optical image (Fig. 6(a) – scales were immersed in an index matching fluid to suppress Fresnel reflections). Interestingly, the long (structurally colored) scale has significantly higher (0.25) absorption than the short (nonstructural) one (0.16).

Absorption is much higher in the blue part of the spectrum and decreases towards the green-red part (as can be seen in Fig. 6(b)). We found that the average coefficient of absorption is between $0.35 \text{ 1}/\mu\text{m}$ in the blue part of the spectrum and $0.1 \text{ 1}/\mu\text{m}$ in the red. All the above facts signify that the effect of pigments cannot be disregarded, as we will further show.

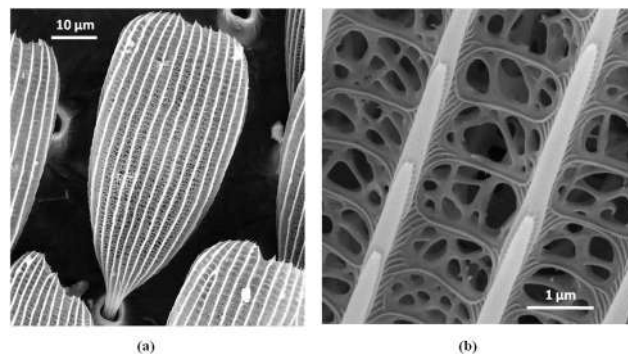


Fig. 4 SEM images of (a) a short wing scale of *J. globulariae* and (b) its hollow, sponge-like internal structure.

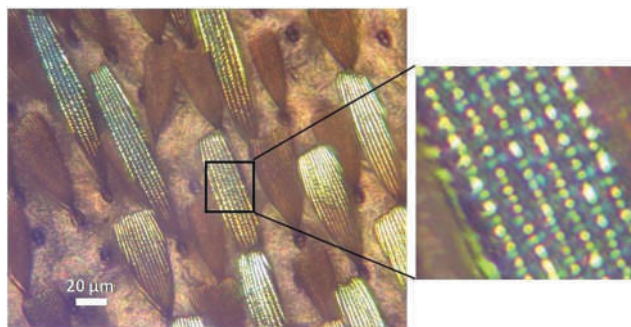
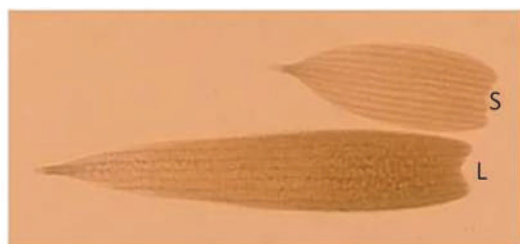
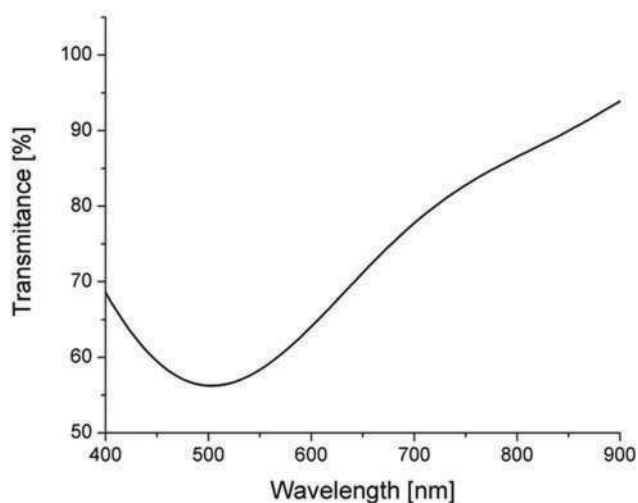


Fig. 5 Optical micrograph of *J. globulariae* wing scales. An enlarged part of a structurally colored one is shown on the right (with yellow and blue-green dots).



(a)



(b)

Fig. 6 *J. globulariae* moth: (a) Transmission optical image of long (L) and short (R) scales. (c) Transmittance spectrum of the long, structurally colored scale.

We measured the angular variation of the spectrum by rotating the detector (spectrometer fiber) and keeping the wing and illuminator positions fixed. Illumination was at normal incidence with respect to the wing. The reflection was recorded within the angular range of 10–50 degrees. Under these conditions we observed a slight spectral shift of 40 nm (Fig. 7(a)). This corresponds to the perception of unsaturated green color,

irrespective of the angle of observation. As a final remark, we emphasize that the spectrum fits nicely into the spectrum of foliage (Fig. 7(b)), enabling the insect to hide effectively in its natural environment.

3.2 Optical modeling of *J. globulariae* wing scales

Here we present an optical model of structurally colored scales (Fig. 8(a)) designed to simulate all the characteristic features observed in SEM images (Fig. 3):

- concave dip (1.5 μm radius) with five chitin layers, 110 nm thick, and refractive index 1.57;
- layers separated by (20 nm × 90 nm) producing 90 nm air spaces;
- outer surface with a number of 10 nm-diameter holes.

On this basis, we will establish a link between the architecture and the optical response of wing scales.

In a simplified model and before going into more detail, we will approximate the structure with a collection of Bragg gratings with different orientations. According to Bragg's law:

$$\lambda = 2nd \cos \theta \quad (1)$$

where λ is the wavelength of multilayer reflectance maximum, d is the grating period, n is the effective refractive index of the grating, and θ is the angle of incidence of radiation. Observe that the incident plane wave irradiates the concave structure within the range of angles – 0 degrees in the center and 50 degrees at the edges. At the center of a concave dip (angle of incidence $\theta = 0^\circ$) the Bragg wavelength can be estimated at 520 nm (assuming a grating period of 200 nm and an effective refractive index of 1.3). Towards the edge, the Bragg resonance drops to 370 nm. Due to only five Bragg layers, the reflection maxima are broad (Fig. 8(b)) and the resulting spectra cover the UV-blue part of the spectrum.

We can conclude that, without an additional mechanism, *J. globulariae* wings will evenly reflect visible light, making the insect appear to be bluish. Absorption alone is not enough to modify the reflection spectrum due to the thinness of individual scales and small amount of pigment (Fig. 6). In the following we will prove that scattering amplifies absorption in accordance with the theory of Yablonovitch described in ref. 18. It was shown that rough surfaces amplify the radiation intensity within planar layers by $2n^2$ factor, where n is the refractive index of the material. This leads to increased absorption of up to $4n^2$ times compared to ideally flat layers. For chitinous structures of scales ($n = 1.57$), absorption may thus increase up to 9.9 times.

The Yablonovitch theory is universally applicable to layers of any thickness, as it is based on the basic laws of radiation. For subwavelength multilayer structures, as is the case here, the effects of evanescent waves certainly lead to radiation being redistributed among the layers. However, the total thickness of all layers taken together is significantly larger than the wavelength and the radiation stays entrapped and waveguided. Here we add that the theory is limited to randomly distributed (Lambertian) incoming radiation. This is usually the case for the environmental, solar, irradiation omnipresent in most natural surroundings. We have previously used the theory to

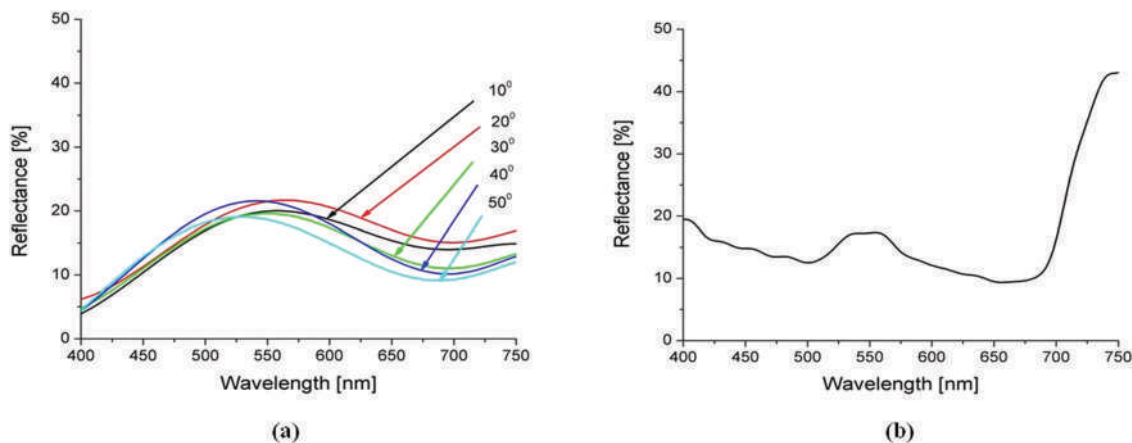


Fig. 7 (a) A slight angular variation (within a 10–50° range) of the *J. globulariae* wing reflectance spectrum. (b) A reflectance spectrum of the green leaves of Hibiscus.

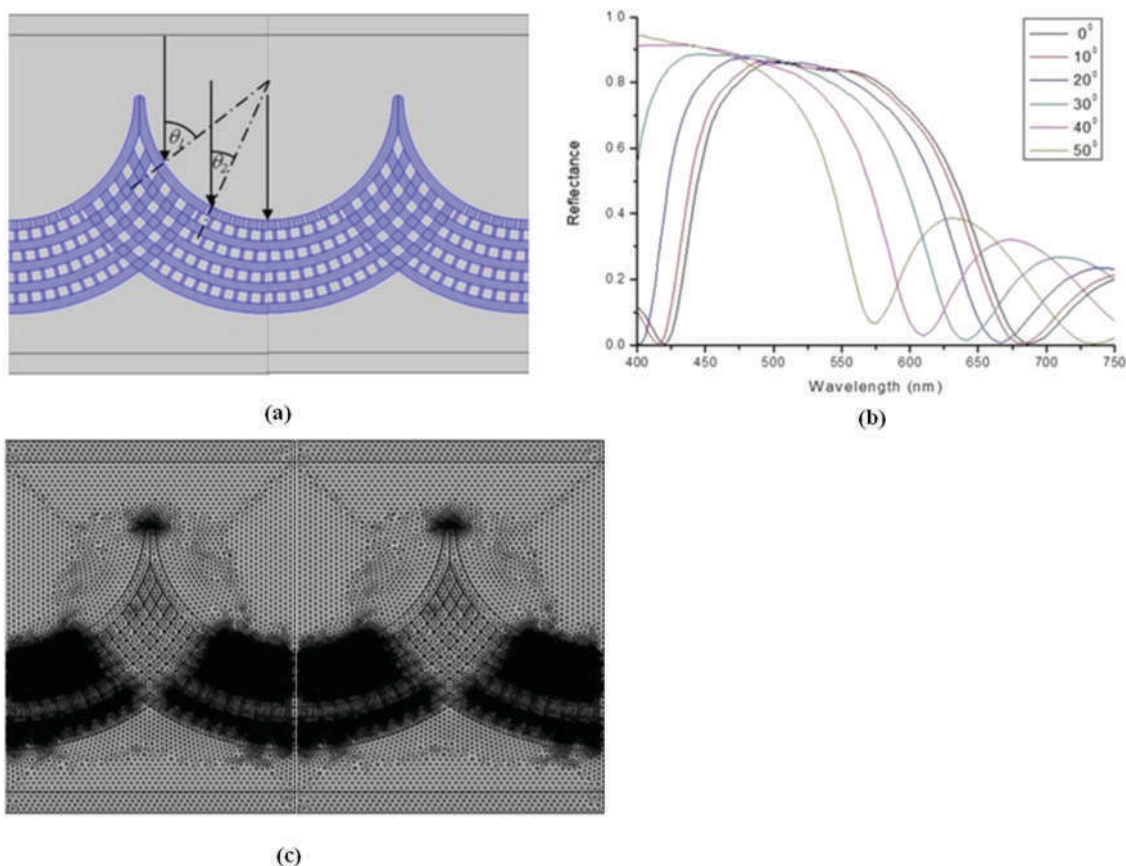


Fig. 8 (a) Geometry of a concave multilayer model used in FEM. Arrows indicate the radiation direction and θ is the angle of incidence. (b) Strong spectral shift for different angles of incidence. (c) A model, depicted in (a), is adaptively meshed for correct FEM analysis of the smallest features.

explain a golden coloration of rather simple wing scales of *Diachrysis chrysitis* moths.¹⁹

In the case of *J. globulariae* wing scales, scatterers are numerous and include nanometer scale pits on the surface, nanopillars between the layers and many of the other defects of otherwise regular structures. The whole problem is too

complicated to be analyzed analytically because it includes the effects of scattering on subwavelength structures, spectrally dependent absorption, waveguiding and radiation localization, as well as interference effects on a very specific concave Bragg grating. This is why we had to use FEMs to calculate the reflection spectrum of the scales. A model in Fig. 8(a) was

adaptively meshed (*i.e.* finer structures were meshed more densely – Fig. 8(c)) in order to obtain the correct results.

First, we calculated the electromagnetic intensity distribution (square of the amplitude) without taking into account absorption (Fig. 9(a)). We clearly observed the localization of the field within the concave Bragg structure due to wave-guided modes. They were introduced into the structure because of scattering on subwavelength structures (pillars and pits) in accordance with the Yablonovitch theory. Resulting spectra are wide and independent on the angle of incidence (Fig. 9(b)).

If absorption is introduced into the model, in accordance with the characteristics of real scales, we can clearly see that waveguided modes are strongly absorbed (Fig. 9(c)) and the resulting spectra are narrowed (Fig. 9(d)) and independent on the angle of illumination, to match those observed experimentally (Fig. 7(a)). This is in stark contrast to the completely flat Bragg grating – its reflectance is very high (up to 90%) but its angular dependence is significant (the shift is larger than 150 nm).

It seems that natural evolution has brought about a nicely balanced set of features: concave structures to induce angular insensitivity of coloration, residual pigments to absorb light and subwavelength structures to enhance scattering and waveguiding. As a result, *J. globulariae* becomes quite inconspicuous within its environment.

We can note that theoretical spectra have a number of local minima and maxima, resulting from a very complex structure with many resonances (Fig. 9(b) and (d)). In reality, the resulting spectrum is obtained by reflection from a large number of scales. They are not identical, and the resonances are averaged to produce a smooth curve as in Fig. 7(a).

To further refine the model, we sliced a spherical multilayer into 8 planar cross-sections and approximated each one as a collection of cylindrical layers (as shown in Fig. 10(a)). Due to symmetry of the structure, there were only 4 different sections (designated 1–4 in Fig. 10(a)) to which we applied an FEM technique in the manner described above. By averaging spectral distributions of all cross sections, we obtained the resulting spectrum in Fig. 10(b), which is comparable to the experimentally recorded curves in Fig. 7(a).

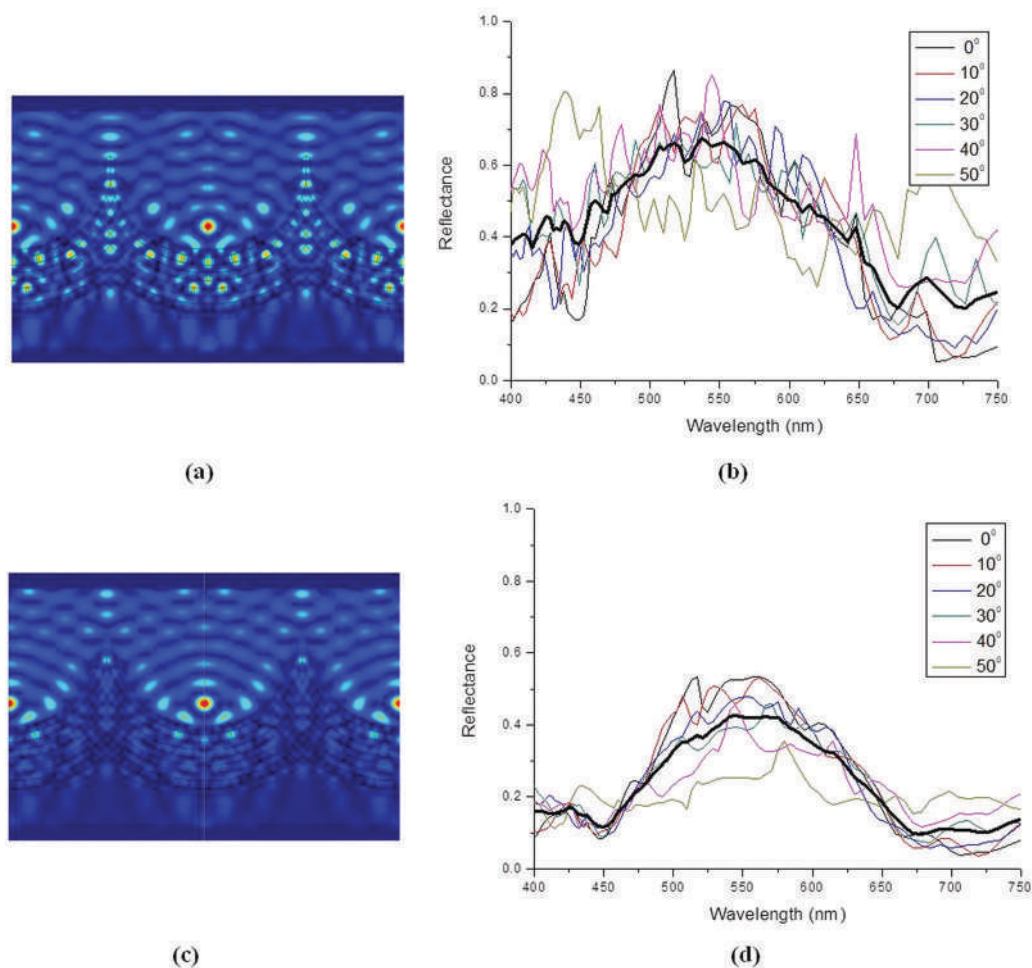


Fig. 9 (a) Strong localization of the electromagnetic field ($\lambda = 479$ nm) inside the structure (WITHOUT pigmentation taken into account), and (b) the corresponding spectra at different angles of incidence. (c) Absorption of a localized electromagnetic field ($\lambda = 479$ nm) inside the structure (WITH pigmentation taken into account), and (d) the corresponding spectra at different angles of incidence.

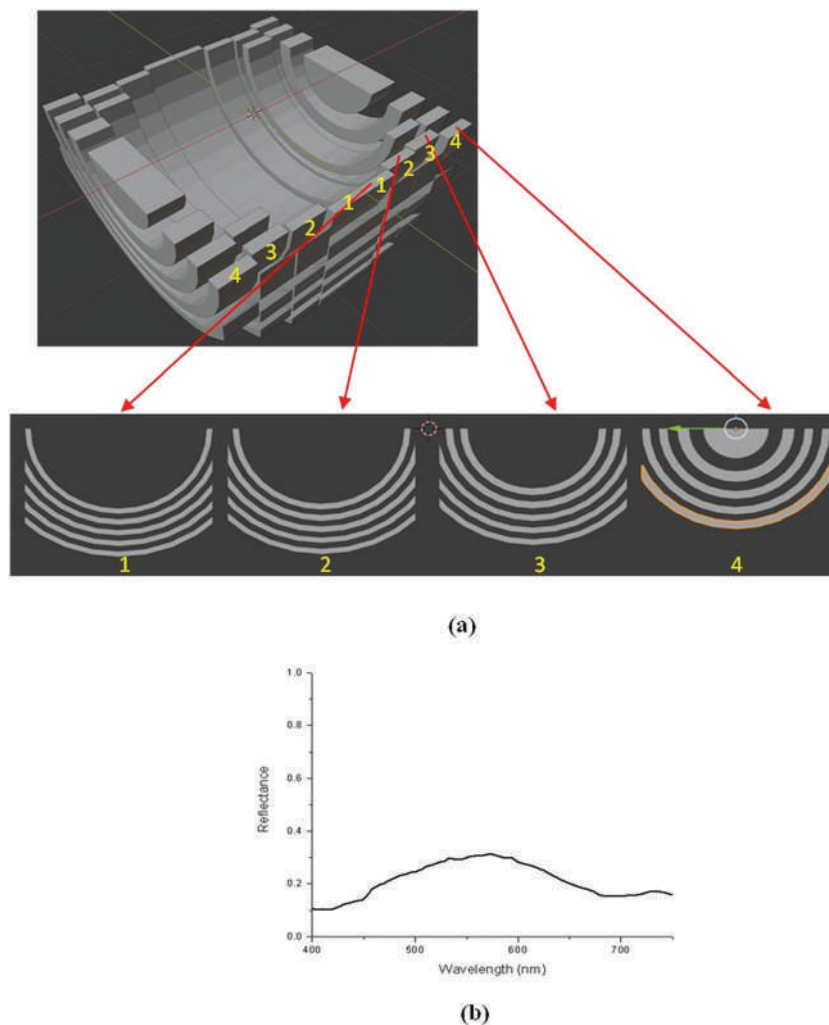


Fig. 10 (a) A characteristic multilayer dip of *J. globulariae* wing scale is modeled as a collection of cylindrical cross-sections designated by numbers 1–4. (b) The resulting spectral distribution, obtained by angular averaging spectra of cross-sections 1–4.

4. Discussion

We have shown that the wings of the *J. globulariae* moth possess a set of structural features that produce a slightly iridescent (*i.e.* observable only at grazing incidence) green structural color. This is important for a day-flying insect to remain unseen on the green background of vegetation. To do this, wings evolved with low angular variation and reflectance comparable to that of green surroundings.

Similar structural coloration was also observed in other insects. It was found that *Papilio palinurus* produces its green coloration as a result of color mixing between reflected and retroreflected light from a concave multilayer structure.¹⁰ There, the effects of scattering and pigmentation were not analyzed, and the coloration was explained solely by the multilayer interference.

The question of adequate modeling is an important (and still open) problem for understanding the interaction of light with biophotonic structures. Three-dimensional modeling is extremely demanding, with respect to execution time and

memory requirements. Massively parallel computers are used with computational time of the order of several hours (for a single 3D geometry and single wavelength) and tens (even hundreds) of gigabytes of working memory.⁷

Overall architecture of *J. globulariae* structures is variable – ranging from almost spherical to cylindrical, with several layers and a number of randomly distributed nano-pillars and holes. Such complexity is beyond the capability of most computers. Even the fastest ones are incapable of calculating irregular, stochastically distorted, nano-patterned geometries on a reasonable timescale. Here, we used 2D, cylindrical models of essentially three-dimensional structures. This is quite sufficient for oblong structures, while for those closer to spherical symmetry, a dip was sectioned in order to make the approximation more adequate. Anyway, optical microscopy (Fig. 5) shows that the overall optical effect is quite tolerant to random variation of size, shape and nanostructure. The computational results presented here confirm that slightly absorbing nanostructures restrict the radiation to the green-red part of the spectrum

(compare Fig. 9(b) and (d)) in accordance with the theory of absorption enhancement by scattering.

The role of pigments was analyzed in ref. 20. The authors described the *Eudocima materna* moth whose cover scales act as an interference mirror (not the multilayer one), while ground scales are strongly pigmented. For certain angles of observation, cover scales mirror the incoming radiation, thereby making underlying pigmented scales invisible. For other angles, radiation is redirected by the mirror scales outside the viewing direction, making the underlying pigmented scales visible. Again, interference, scattering and absorption are not interlinked and enhanced.

A somewhat different analysis of the interplay between wing coloration and visual pigments was performed in ref. 21. It was found that additional visual pigment in the photoreceptors of Lycaenidae is well tuned to the characteristic structural coloration of butterflies within this family.

A good overview of photonic structures has been given in ref. 22. The authors remark that green pigments are absent in butterfly wing scales and analyze blackness and fluorescence enhancement caused by structures.

Structures at all dimensional scales are included and work in synergy to produce the coloration of *J. globulariae*. At the molecular level, dark pigments (melanin) are needed to selectively absorb the blue part of the spectrum. However, in this particular insect there is only a small amount of pigment, which is not enough to significantly absorb the blue part of the spectrum as shown in Fig. 9(b). Therefore, nanoscales, pillars, pits and other subwavelength structures are necessary to preferentially scatter blue light and enhance its absorption. Micron-sized concave multilayers selectively filter the red part of the spectrum while making it angularly independent.

On a higher scale (in the order of hundreds of micrometers and millimeters), the wing as a whole must be accounted for. Our model shows that the reflectivity of a single structural scale is in the order of 40% (Fig. 9(d)). However, the reflectivity of the wing is much lower (20–25%, Fig. 7) as a result of sparse scale population, attenuation by nonstructural scales and the wing membrane. The resulting value corresponds well to the reflectivity of vegetation, making the insect almost invisible in its environment. We have calculated the CIE xy color coordinates of the green leaves of *Hibiscus*.^{23,24} *J. globulariae* and our model show how well nature has “adjusted” the insect to the environment (Fig. 11). Here, a CIE diagram is used as a simple way to compare complex spectra, not as a measure of human color perception, which is certainly quite different compared to that of insects.

For reference, we have shown the color coordinates of a model without scattering and absorption. In this case, the insect's color would have been blue, making it highly visible.

In this paper we had no space to analyze the “nonstructural” scales, but it seems that there are structural effects too. By looking closely at Fig. 6(a), we can see that the absorption of a nonstructural scale is lower than that of the structural one, yet it is highly absorbing on the wing (Fig. 5). It seems that scattering enhances the absorption of the rather hollow structure of a “nonstructural” scale as well.

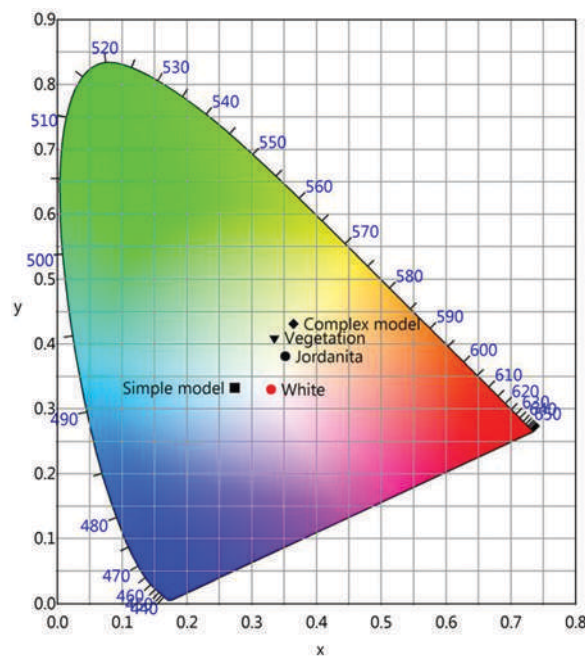


Fig. 11 A CIE diagram showing the xy chromatic coordinates of vegetation, *J. globulariae* and a complex model (concave layer with scattering structures and absorption). Coordinates of achromatic white and a simple, flat, layer model have been shown for reference.

From a biological point of view, the color green usually has a cryptic role in insects,^{25–27} providing very effective camouflage among leaves. This greenish color, which is not highly reflective, indicates a primary defensive role in *J. globulariae*. Slight iridescence and color contrast, which are very important in communication between species, further speak in favor of the protective role of such an optical signal.²⁸

On the other hand, species of this family (including *J. globulariae*) also possess a chemical defense mechanism. All Zygaenidae¹⁵ contain hydrogen cyanide (HCN), taken from plants or synthesized from plant glucose.²⁹ Therefore, they are poisonous or, at least, distasteful to potential predators. Sending a warning is another reason why the species of this family may have such coloration. The color green becomes highly visible during feeding on flowers¹⁴ when it acquires its second, aposematic role.³⁰ Other examples are also known among Lepidoptera where warning and camouflage coloration are not contradictory.³¹ We can therefore assume that the role of *J. globulariae* can be cryptic, when resting, hidden in leaves, and aposematic, during nectar feeding.

In most moths, the dorsal side of the front wings is visible during rest.³² Given that all Zygaenidae are diurnal species, evolution has ensured that they have structural coloration only on the dorsal surface of their forewings.¹⁵

5. Conclusion

This paper reveals the delicate combination of interference, scattering, absorption and color mixing, all working together,

to facilitate the survival of *J. globulariae*. The fine tuning of many structural factors, from submicron to macroscopic levels, is amazing and its imitation provides a new way to control the spectral content of light.

Conflicts of interest

There are no conflicts to declare.

Acknowledgements

The authors acknowledge funding provided by the Institute of Physics, Belgrade, through a grant from the Ministry of Education, Science and Technological Development of the Republic of Serbia and the Science and Technology Development Program – Joint Funding of Development and Research Projects of the Republic of Serbia and the People's Republic of China: Mimetics of insects for sensing and security, No. I-2. DP acknowledges support from L'Oréal-UNESCO "For Women in Science". We express our gratitude to Dejan Stojanović from the Institute of Lowland Forestry and Environment, Novi Sad, Serbia, who donated *J. globulariae* specimens from his insect collection.

References

- 1 J. Sun, B. Bhushan and J. Tong, *RSC Adv.*, 2013, **3**, 14862–14889.
- 2 J. T. Bagnara, P. J. Fernandez and R. Fujii, *Pigment Cell Res.*, 2007, **20**, 14–26.
- 3 C. Taboada, A. E. Brunetti, M. L. Lyra, R. R. Fitak, A. F. Soverna, S. R. Ron, M. G. Lagorio, C. F. B. Haddad, N. P. Lopes, S. Johnsen, J. Faivovich, L. B. Chemes and S. E. Bari, *Proc. Natl. Acad. Sci. U. S. A.*, 2020, **117**, 18574–18581.
- 4 P. Simonis and S. Berthier, How nature produces blue color. in *Photonic Crystals – Introduction*, ed. A. Massaro, Applications and Theory, InTech, Rijeka, 2012, pp. 3–24.
- 5 P. Kaspar, D. Sobola, P. Sedlák, V. Holcman and L. Grmela, *Microsc. Res. Tech.*, 2019, **82**, 2007–2013.
- 6 D. Sobola, S. Talu, P. Sadvovsky, N. Papez and L. Grmela, *Adv. Electr. Electron. Eng.*, 2017, **15**, 569–576.
- 7 K. Michielsen, H. De Raedt and D. G. Stavenga, *J. R. Soc., Interface*, 2010, **7**, 765–771.
- 8 B. D. Wilts, K. Michielsen, J. Kuipers, H. De Raedt and D. G. Stavenga, *Proc. R. Soc. B*, 2012, **279**, 2524–2530.
- 9 S. Berthier, *Iridescences, les couleurs physiques des insectes*, Springer Science & Business Media, 2007.
- 10 P. Vukusic, J. R. Sambles and C. R. Lawrence, *Nature*, 2000, **404**, 457.
- 11 D. L. Fox, *Animal biochromes and structural colours: physical, chemical, distributional & physiological features of coloured bodies in the animal world*, University of California Press, 1976.
- 12 D. G. Stavenga, M. A. Giraldo and H. L. Leertouwer, *J. Exp. Biol.*, 2010, **213**, 1731–1739.
- 13 S. Yoshioka, T. Nakano, Y. Nozue and S. Kinoshita, *J. R. Soc., Interface*, 2008, **5**, 457–464.
- 14 K. A. Efetov and G. M. Tarmann, *Forester Moths: The genera Theresimima Strand, 1917, Rhagades Wallengren, 1863, Jordanita Verity, 1946, and Adscita Retzius, 1783 (Lepidoptera: Zygaenidae, Procridinae)*, Apollo Books, 1999.
- 15 C. M. Naumann, G. M. Tarmann and W. G. Tremewan, *The Western Palaearctic Zygaenidae (Lepidoptera)*, Apollo Books, 1999.
- 16 N. N. Shi, C. C. Tsai, F. Camino, G. D. Bernard, N. Yu and R. Wehner, *Science*, 2015, **349**, 298–301.
- 17 H. L. Leertouwer, B. D. Wilts and D. G. Stavenga, *Opt. Express*, 2011, **19**, 24061.
- 18 E. Yablonovitch and G. D. Cody, *IEEE Trans. Electron Devices*, 1982, **29**, 300–305.
- 19 D. Pantelić, S. Savić-Šević, D. V. Stojanović, S. Curčić, A. J. Krmpot, M. Rabasović, D. Pavlović, V. Lazović and V. Milošević, *Phys. Rev. E*, 2017, **95**, 032405.
- 20 J. L. Kelley, N. J. Tatarnic, G. E. Schröder-Turk, J. A. Endler and B. D. Wilts, *Curr. Biol.*, 2019, **29**, 2919–2925.
- 21 Z. Bálint, K. Kertész, G. Piszter, Z. Vértesy and L. P. Biró, *J. R. Soc., Interface*, 2012, **9**, 1745–1756.
- 22 L. P. Biró and J. P. Vigneron, *Laser Photonics Rev.*, 2011, **5**, 27–51.
- 23 C. Buschmann and E. Nagel, *Int. J. Remote Sens.*, 1993, **14**, 711–722.
- 24 C. Buschmann, S. Lenk and H. K. Lichtenthaler, *Isr. J. Plant Sci.*, 2012, **60**, 49–64.
- 25 F. Liu, H. Yin, B. Dong, Y. Qing, L. Zhao, S. Meyer, X. Liu, J. Zi and B. Chen, *Phys. Rev. E: Stat., Nonlinear, Soft Matter Phys.*, 2008, **77**, 1–4.
- 26 A. R. Parker, D. R. McKenzie and M. C. J. Large, *J. Exp. Biol.*, 1998, **201**, 1307–1313.
- 27 D. G. Stavenga, Surface Colors of Insects: Wings and Eyes, in *Functional Surfaces in Biology. Little Structures with Big Effects*, ed. S. N. Gorb, Springer, The Netherlands, 2009, vol. 1, 285–306.
- 28 P. Vukusic, J. R. Sambles, C. R. Lawrence and R. J. Wootton, *Proc. R. Soc. B*, 1999, **266**, 1403–1411.
- 29 O. Niehuis, S. H. Yen, C. M. Naumann and B. Misof, *Mol. Phylogenet. Evol.*, 2006, **39**, 812–829.
- 30 C. Wiklund and B. Sillen-Tullberg, *Evolution*, 1985, **39**, 1155.
- 31 K. L. Prudic, A. K. Skemp and D. R. Papaj, *Behav. Chem. Ecol.*, 2007, **18**, 41–46.
- 32 N. P. Kristensen, *Handbook of Zoology, Vol. IV, Part 3.: Lepidoptera: Moths and Butterflies. Morphology, Physiology, and Development*, Walter DeGruyter Press, Berlin, 2004.

COMMUNICATION



Cite this: *J. Mater. Chem. C*, 2021, 9, 8163

Received 5th March 2021,
Accepted 6th June 2021

DOI: 10.1039/d1tc01028j

rsc.li/materials-c

Thermo-osmotic metamaterials with large negative thermal expansion

Svetlana Savić-Šević,^a Dejan Pantelić,^a Branka Murić,^a Dušan Grujić,^a
Darko Vasiljević,^a Branko Kolaric^{ab} and Branislav Jelenković^a

Negative thermal expansion (NTE) is important for compensation of thermal dilatation effects and has significant applications in high-precision devices and instruments. Several materials with intrinsic negative expansion exist but are chemically complex, difficult to manufacture and their thermal expansion coefficients (TECs) are small, typically in the order of $10^{-5}/\text{K}$ – $10^{-6}/\text{K}$. Here we present a metamaterial with a large NTE, with TEC in the order of $10^{-3}/\text{K}$, enabled by thermo-osmosis of entrapped air molecules through a multitude of nanometer-thin layers. We have generated this material by holographically patterning a biopolymer (dichromated pullulan). The presented manufacturing process is quite simple and capable of generating large-area NTE materials. The concept of achieving (NTE) through thermo-osmosis is universal and can be extended to many other polymers. Our research, for the first time, introduces a relation between NTE and thermo-osmosis.

Introduction

All materials change their dimensions with temperature due to thermally dependent interatomic distances.¹ This behavior is quantified by linear (α_l) or volumetric (α_V) thermal expansion coefficients (TEC):

$$\alpha_l = \frac{1}{l} \frac{dl}{dT} \quad \text{and} \quad \alpha_V = \frac{1}{V} \frac{dV}{dT} \quad (1)$$

where dl and dV are length l and volume V changes induced by temperature difference dT , respectively.² Almost all materials expand upon heating and the thermal expansion coefficient is thus positive (PTEC). Organic materials and polymers usually have a larger coefficient of thermal expansion (PTEC greater than $10^{-4}/\text{K}$) than inorganic materials (such as metals and ceramics with PTEC of about $10^{-6}/\text{K}$).³

Materials with negative thermal expansion coefficients (NTECs) are expensive, rare (except water between 273 K–277 K) and their chemical composition is very specific.^{4,5} One of the main goals of NTE research is finding materials with large NTECs to compensate PTECs. In materials associated with a magnetic, ferroelectric or charge-transfer phase transition a large NTE has been discovered and such materials are used as thermal-expansion compensators.⁶

The development of a material with a large NTEC is possible by designing special structures made of several constituents.^{7,8} For example, origami structures, consisting of a bi-material's 2D or 3D lattices, enable tailoring metamaterials with novel mechanical properties, including a wide range of PTECs and NTECs.⁹ Such NTE materials have important applications for the control of the thermal expansion of materials. They allow adjustment of the thermal expansion of composites and can be used in microchip devices,¹⁰ as dental fillings,¹¹ in optical and electronic devices,¹² for fasteners¹³ and as coating materials.¹⁴ However, such materials have a complex geometry difficult to manufacture.

Many methods have been used to fabricate metamaterials: laser interference lithography,¹⁵ electron-beam lithography,¹⁶ direct laser writing,¹⁷ and focused-ion beam (FIB),¹⁸ to mention just a few. Metamaterials can be fabricated from different substances including photoresists,¹⁹ semiconductors,²⁰ and metals.²¹ Holographic methods stand out as being capable of producing one-, two- and three-dimensional periodic metamaterials. Large areas can be fabricated simply and cheaply in a matter of minutes.

Here we describe a holographic method for generation of mechanical metamaterials with simple architecture and high NTECs, much higher than those of the other materials we found in the available literature. Pullulan, a biological polysaccharide, is used as a base material, which is further sensitized and holographically patterned at the nanoscale. Structural, optical and mechanical properties of the resulting metamaterial are studied, its NTEC measured and a thermo-mechanical model, explaining NTE behavior, presented. We also disclose a new physical mechanism behind such unusual behavior.

^a Institute of Physics, University of Belgrade, Pregrevica 118, Zemun 11080, Serbia.
E-mail: savic@ipb.ac.rs

^b MNM Group, Department of Physics, UMONS, Mons, Belgium

Holographic generation of mechanical metamaterial

Doped pullulan is a home-made holographic photosensitive material used throughout this research to manufacture layered metamaterial and analyze its thermo-mechanical behavior. Pullulan is a linear polysaccharide produced from the yeast-like fungus *Aureobasidium pullulans*. The material is composed of maltotriose units connected by α -D-1,6-glycoside linkages²² and can be photosensitized with chromium ions to produce dichromated pullulan (DCP)²³ as a transparent, thermo-stable film. Properties of DCP films as holographic material–surface gratings, its diffraction efficiency, copying and environmental stability—were previously investigated.^{24,25}

DCP film was prepared by mixing an 8% aqueous solution of pullulan and 30% ammonium dichromate, which was poured on a flat glass plate. After drying, a thin film was placed in the holographic setup to produce a volume Bragg grating.²⁶ To do that, the laser beam from a single-frequency, a diode pumped Nd-YAG laser, at 532 nm, was expanded to expose the pullulan film at normal incidence. A mirror was set behind the film and a volume Bragg grating was recorded inside the DCP film by interference of two counter propagating beams. The interference pattern is responsible for generation of a large number of alternating DCP and air layers, parallel to the substrate. After exposure, the pullulan film was chemically processed by washing the plate in a mixture of water and isopropanol, followed by drying in pure isopropanol. Finally, the grating is slowly and fully dried in a closed vessel.

The resulting hologram is about 10 μm thick and has a complex structure, as shown in Fig. 1. On the nanoscopic level, the structure is characterized by approximately fifty Bragg layers. They are mutually separated and supported by nanopillars with a diameter of up to 50 nm, enabling the mechanical stability of the whole structure.

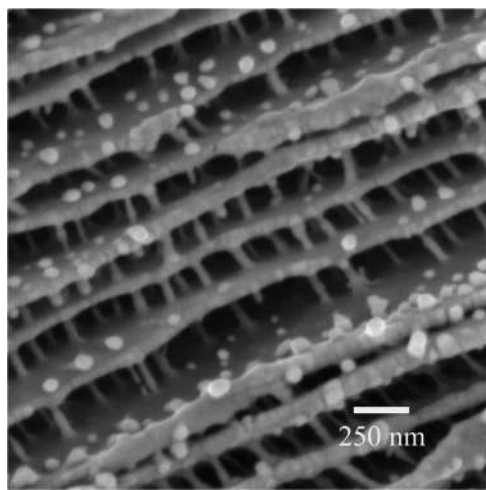


Fig. 1 A cross-section of pullulan metamaterial (recorded using a scanning electron microscope) showing pullulan layers separated by nanopillars.

The metamaterial acts as a selective reflector in the specific band of wavelengths in accordance with the Bragg's law:

$$\lambda = 2(n_a l_a + n_p l_p) \quad (2)$$

where l_a and l_p are the thicknesses of the air and pullulan layers (both about 100 nm), and refractive indices $n_a = 1$ and $n_p = 1.45$, respectively. A Bragg maximum (as defined in eqn (2)) depends on thermal variation of refractive indices and layer thicknesses. Thus, the spectral shift as a function of temperature can be found by taking the first derivative of eqn (2):

$$\frac{d\lambda}{dT} = 2 \left(l_a \frac{dn_a}{dT} + n_a \frac{dl_a}{dT} + l_p \frac{dn_p}{dT} + n_p \frac{dl_p}{dT} \right) \quad (3)$$

This optical property of the DCP metamaterial was measured in a heating/cooling cycle. The sample was heated and cooled using a Peltier element (controlling temperature between 295 K and 323 K) and the reflection spectra of the white light from the halogen lamp were recorded using a fiber type spectrometer. A thermocouple was embedded within the sample to obtain accurate measurement of the temperature. As can be seen in Fig. 2a, the reflectance peaks are blue-shifted from 580 nm to 535 nm during heating, exhibiting a negative spectral shift of 45 nm for a positive temperature difference of +25 K (equivalent to 1.8 nm K⁻¹). Upon temperature decrease, a spectral maximum returns close to its initial position. Spectral shift vs. temperature, for the whole heating–cooling cycle, shows characteristic hysteresis, as in Fig. 2b. The hysteresis effects are inherent to many natural phenomena. In our case, we assume that hysteresis is a consequence of the nonlinear viscoelastic behaviour of the polymer,²⁷ i.e. pullulan nanopillars, with temperature. Upon heating, air diffuses through membranes and escapes into the surrounding environment, lowering the pressure inside the multilayer. Outside pressure then compresses the layers until a new mechanical equilibrium is achieved. Due to the compression of the layers, the pullulan nanopillars are bent. It is assumed that at higher temperatures the viscoelasticity of the pillars slightly decreases. Thanks to the capability to creep,²⁷ after strain due to pressure, the pillars return to their initial state, with a slightly lower temperature than the initial one.

Thermal behavior of optical systems is typically explained by thermal expansion and thermal variation of the refractive indices (as in eqn (3)). In the following, we will show that these mechanisms cannot account for the large and negative spectral shift.

First, we experimentally determined the linear TEC of a pure, unstructured DCP film. A circular, freestanding DCP membrane was produced, clamped at its perimeter, and its central zone was heated with the laser beam. The temperature of the film was measured using a thermal camera, while the resulting thermal bending was measured using digital holographic interferometry. The linear expansion coefficient was calculated from the recorded interferogram, Fig. 3, and found to be $\alpha_{\text{DCP}} = 8.8 \times 10^{-5}/\text{K}$, which is in agreement with the values obtained for other polysaccharides.^{28,29}

Now we can calculate spectral shift of the Bragg maximum using eqn (3). The thermo-optic coefficient of air (dn_a/dT)³⁰ is

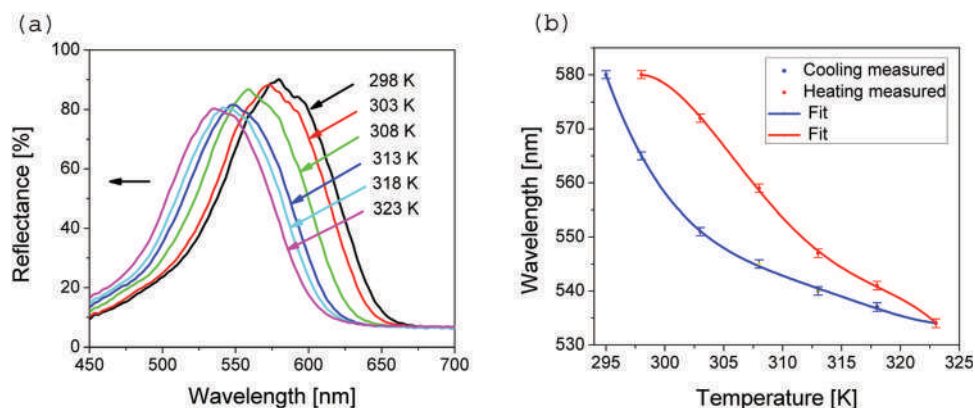


Fig. 2 (a) Reflectance spectra of DCP metamaterial during heating and (b) spectral peak shift during a heating and cooling cycle.

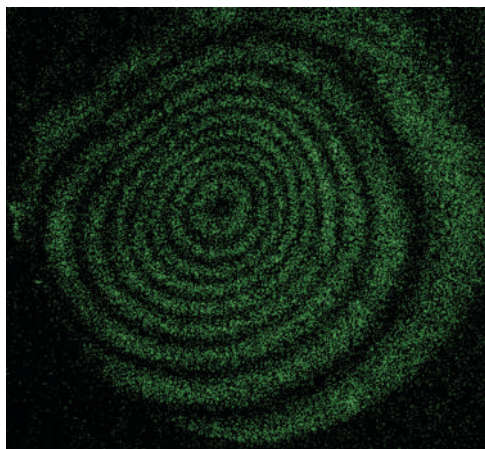


Fig. 3 Interferogram of the thermal bending of the DCP film.

very small and the first term in eqn (3) can be neglected. Additionally, thicknesses of air and pullulan layers are almost the same $l_a = l_p = l$ and eqn (3) can be simplified:

$$\frac{d\lambda}{dT} = 2 \left(n_a \frac{dl}{dT} + l \frac{dn_p}{dT} + n_p \frac{dl}{dT} \right) \quad (4)$$

In a linear approximation dilatation $dl = \alpha l T$ (see eqn (1)) and finally:

$$\frac{d\lambda}{dT} = 2l \left(\frac{dn_p}{dT} + \alpha(n_p + n_a) \right) \quad (5)$$

We were not able to measure the thermo-optic coefficient of DCP, and we assumed the largest thermo-optical coefficient recorded up to now, $dn/dT = -5 \times 10^{-4}/K$.³¹

By including these values of thermal constants dn/dT and α_{DCP} into eqn (5), together with the value of the layer thickness $l = 118$ nm and refractive indices of air and pullulan, we have found that the expected temperature shift of the Bragg peak is $d\lambda/dT = -0.07$ nm K^{-1} . This value is much lower than the one recorded experimentally, $d\lambda/dT = -1.8$ nm K^{-1} , and classical thermal effects fail to explain the very large NTEC.

As shown above, while the change in the DCP film thermal expansion is small, the thickness variation of air layers must be the main contributor to the overall metamaterial contraction. From the experimentally observed spectral shift and a temperature change of +25 K, the calculated change in air layer thickness (using eqn (2)) is -22 nm. Knowing that there are fifty Bragg layers, the total thickness change is $dl = -1.1$ μ m. Knowing that the initial thickness of the material is $l = 10$ μ m, we estimate (using eqn (1)) that the linear thermal expansion coefficient of DCP metamaterial is $\alpha_{DCPm} = -4.4 \times 10^{-3}/K$. This value is quite large, compared to values of NTEC, available in the literature. The results presented here have been verified in a series of experiments on many different samples. We have found that the behaviour of pullulan metamaterial is the same, confirming a negative thermal expansion with NTEC of the order $10^{-3}/K$.

Thermo-osmotic mechanism of negative thermal expansion

As explained above, negative and large TEC cannot be explained by usual and simple thermal effects (thermal dilatation and refractive-index variation). In this section, the peculiar behavior of DCP metamaterial is explained through thermo-osmosis,³² a process defined as fluid or gas diffusion through a membrane due to a temperature gradient.^{32,33} This phenomenon was found in many areas from biology³⁴ to energy harvesting.³⁵

We should note that the pullulan layers are very thin (about 100 nm) and their mutual separation is of the same order of magnitude. In such a small volume, only a small number of air molecules are entrapped between the pullulan layers (the mean path length of air molecules is 67 nm under normal conditions)³⁶ and molecules diffuse through the layers, depending on the temperature difference between the layer and their environment. In a thermal equilibrium, a net flow of molecules between the layer and the environment is zero. If the temperature of the layer rises, more molecules escape the layer, lowering the pressure inside the layer. The resulting pressure difference compresses the layers, supported only by tiny nanopillars (Fig. 1).

Diffusion through permeable membranes is described by Fick's law,³⁷ which determines the diffusive flux per unit area Φ as a function of pressure p_0 and membrane thickness l :

$$\Phi = \frac{Pp_0}{l} \quad (6)$$

where P is membrane permeability, which is an intrinsic property of the material.

Effects of temperature on gas permeability were previously analyzed.^{38,39} For gases, the temperature-dependence of permeability is defined according to the Arrhenius relationship:

$$P = P_0 \exp\left(-\frac{E_p}{RT}\right) \quad (7)$$

where P_0 is a constant (a kinetic frequency factor), R is the gas constant, and E_p is the activation energy for permeation. According to the above equation the gas permeability increases with temperature.

For simplicity of the further analysis, we will explore a single membrane separating a closed compartment from the surrounding air environment; see Fig. 4.

We suppose that the environment is a thermal reservoir with infinite capacity at constant temperature T_0 and pressure p_0 . If a compartment with a membrane is at temperature T_1 and pressure p_1 , we have a flux Φ_1 of molecules diffusing out of the compartment into the environment and flux Φ_0 of particles flowing from the environment into the compartment, *i.e.* by combining eqn (6) and (7):

$$\Phi_0 = \frac{P_0}{l} p_0 \exp\left(-\frac{E_p}{RT_0}\right) \quad (8)$$

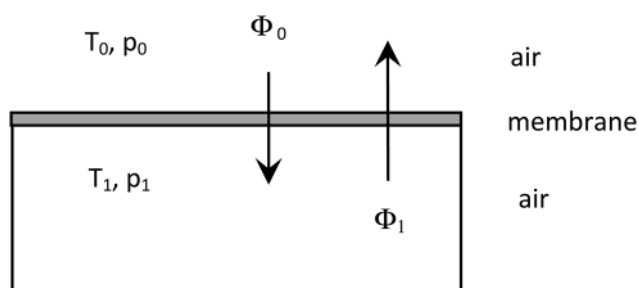


Fig. 4 Compartment with a single membrane, where T and p are temperatures and pressures, while Φ are fluxes.

$$\Phi_1 = \frac{P_1}{l} p_0 \exp\left(-\frac{E_p}{RT_1}\right) \quad (9)$$

Due to the temperature difference between the compartment and its external environment, ingoing and outgoing fluxes are not equal any more, and there is a net molecular flow. Suppose that the temperature inside the compartment is larger than that of the surrounding air, molecules will leak out and reduce the pressure p_1 inside the compartment. The resulting pressure difference will exert a mechanical force on the membrane and compress it until a new equilibrium is reached, *i.e.* when $\Phi_1 = \Phi_0$. From eqn (8) and (9) we can easily find that this will happen when:

$$p_1 = p_0 \exp\left(-R \left(\frac{1}{T_0} - \frac{1}{T_1}\right) \frac{E_p}{R}\right) \quad (10)$$

As stated before, this pressure difference is compensated by the mechanical resistance of nanopillars to compression.

In the case of DCP metamaterial, we have a number of pullulan membranes stacked one above the other and separated by tiny nanopillars. Air is gradually leaking from one layer to another until it goes out to the atmosphere. Air leakage is a process that takes some time, before thermo-mechanical equilibrium is reached.

Dependence of pressure p_1 on temperature was calculated from eqn (10) and is shown in Fig. 5(a). The activation energy of air permeation through the polysaccharide membrane is about 40 kJ mol^{-1} .⁴⁰ The graph shows that p_1 decreases with increasing temperature of the pullulan layers. Based on this dependence, Fig. 5(b) and (c) show the dependence of pressure p_1 on the measured time to achieve a new equilibrium state and the dependence of pressure p_1 on the air layer thickness, respectively.

Discussion and conclusions

We have shown that the proposed thermo-osmotic mechanism explains well all the experimentally recorded properties of the pullulan NTE metamaterial. However, there are other, less obvious mechanisms that could contribute to the negative thermal expansion, most notably the effect of air humidity.

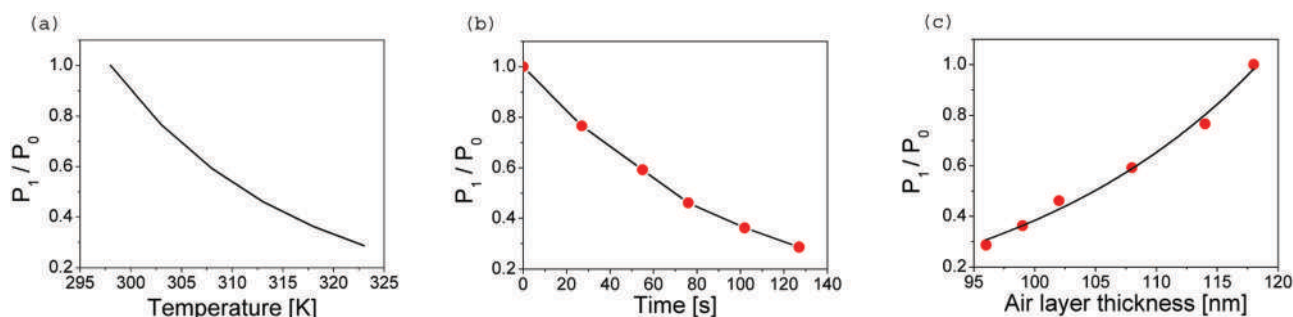


Fig. 5 Ratio of the pressure inside and outside of the compartment as a function of (a) DCP temperature, (b) time needed to reach a new equilibrium state, and (c) air layer thickness. The points on graphs (b) and (c) correspond to experimentally measured values.

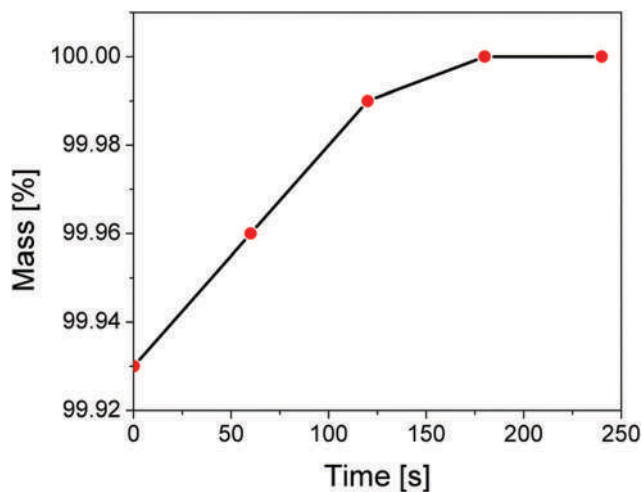


Fig. 6 The change of mass of DCP metamaterial in time due to humidity.

To test if pullulan absorbs water from the air we performed a simple gravimetric experiment with an analytical balance. First, the DCP metamaterial was measured under normal laboratory conditions, it was then heated to 373 K for 45 min, to eliminate moisture, and measured again. After that, the sample was kept under normal laboratory conditions and the mass was measured every hour until it reached its original value, see Fig. 6. It can be seen that the change of mass, caused by moisture, is only 0.07%. Bearing in mind that pullulan does not form the gel, and does not swell significantly, we conclude that the influence of moisture on the pullulan structure is negligible.

As a final proof of diffusion of air through pullulan layers and the corresponding thermo-osmosis, as a dominant mechanism, we placed the pullulan metamaterial in a vacuum chamber, at the pressure of 4×10^{-2} Pa, for 45 minutes. During that time, entrapped air diffused out of the pullulan layers. The reflection spectra measured immediately after the sample was removed from the vacuum and placed back to the normal atmospheric conditions, were shifted towards lower wavelengths. This shift was caused by the air pressure compressing the layers due to the large pressure difference between the inside ($p \sim 0$ Pa) and outside of the metamaterial ($p_{\text{atm}} \sim 100\,000$ Pa). Following the prolonged stay in the atmosphere the air diffuses into the layers, equilibrating pressures and expanding the material as evidenced by the spectral shift, see Fig. 7.

It is also important to note that when the temperature excised a certain maximum value (higher than 383 K) the DCP metamaterial loses its NTE properties. We believe that in this case there are no more air molecules entrapped within the pullulan layers, and the pressure difference is large enough to break the pullulan nanopillars, which otherwise will sustain the mechanical integrity of the whole structure. Bear in mind that all the mentioned effects (dilatation, thermo-optical, and humidity) are simultaneously present, but nevertheless our experiments show that the thermo-osmosis is a dominant one, which converts an ordinary PTE into an NTE material. Without diffusion, a pressure of entrapped air between the pullulan

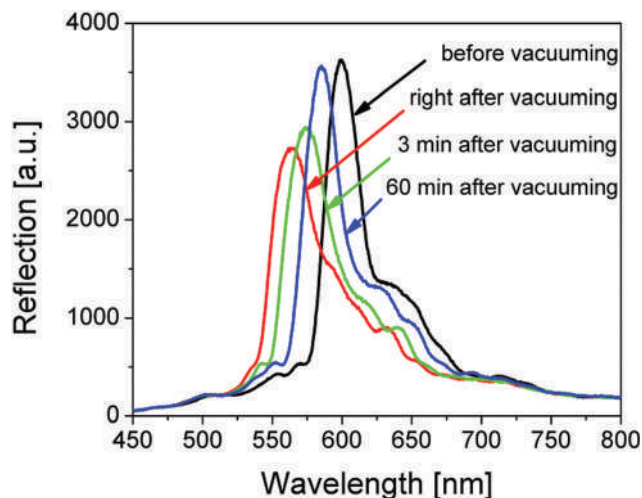


Fig. 7 Reflectance before and after vacuuming and exposing to air.

multilayers will follow the temperature variation—increasing upon heating, and decreasing upon cooling. This will turn the pullulan multilayer into a positive thermal expansion material, in contrast to what we observed experimentally.

Regarding the thermo-osmotic process, we emphasize the simplicity of the presented model, which very well describes the complex phenomenon responsible for NTE. First of all, the pullulan layers have a stochastic distribution of thicknesses, size and position of nanopillars, which is difficult to take into account in the model. Also, the mechanical properties of materials at the nanoscale level can be quite different, compared to those of the bulk. Additionally, for such thin layers, air cannot be treated as continuum and more complex effects come into play, such as thermophoresis and thermoconvection. In our case, the situation is further complicated by extremely small (100 nm) separation between the layers when the number of entrapped molecules is correspondingly small. This means that losing a single molecule from the layer significantly reduces the pressure. In spite of this, the proposed model is able to explain the most distinctive properties of the system: negative thermal expansion and the corresponding optical properties.

In conclusion, we have found that holographically patterned dichromated pullulan is a new mechanical metamaterial with a large NTE of $\alpha_{\text{DCPm}} = -4.4 \times 10^{-3}/\text{K}$ in a temperature range between 295 K and 323 K. Our investigations are in this temperature range because most of the practical interests and potential applications of organic devices are around room temperature. We show that it is simple to fabricate a stable and durable material using the holographic technique. Our explanation of the mechanism that converts an ordinary positive thermal expansion material into an NTE material is based on thermo-osmosis of the air molecules through the pullulan nanolayers. Dependence of the optical response on temperature of the pullulan metamaterials was investigated. The reflection spectra show a blue shift with increasing temperature, which originates from the contraction of air nanolayers due to the thermo-osmosis of the air molecules through the pullulan nanolayers.

The proposed mechanism can be applied to various holographic structures and materials, as well as to different gases and temperature ranges. We have performed the same measurements using holographically patterned dextran (another polysaccharide) and found NTE, too. While pullulan is linear, dextran has a branching structure but shows the same behavior as pullulan, and the reflectance peaks are blue-shifted during heating. Our multilayer design is simple and the proposed mechanism is useful for surfaces of arbitrary size. We have shown that experimental results can be explained by simple relationships, in the nanoscale, linking the structures, mechanical and optical properties, and temperature-response. The disclosed mechanism is universal and opens a range of possibilities to construct engineered materials with tailored negative thermal expansion.

Conflicts of interest

There are no conflicts to declare.

Acknowledgements

The authors acknowledge funding provided by the Institute of Physics Belgrade, through the grant by The Ministry of Education, Science, and Technological Development of the Republic of Serbia. B. Kolaric acknowledges support from the F.R.S-FNRS.

Notes and references

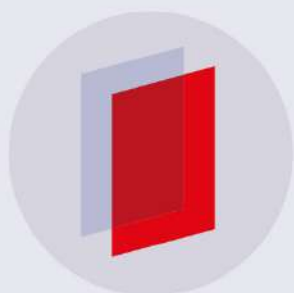
- 1 K. Takenaka, *Front. Chem.*, 2018, **6**, 267.
- 2 J. P. Attfield, *Front. Chem.*, 2018, **6**, 371.
- 3 R. Lakes, *J. Mater. Sci. Lett.*, 1996, **15**, 475–477.
- 4 M. Szafranski, *J. Mater. Chem. C*, 2013, **1**, 7904–7913.
- 5 H. Liu, J. Chen, X. Jiang, Z. Pan, L. Zhang, Y. Rong, Z. Lin and X. Xing, *J. Mater. Chem. C*, 2017, **5**, 931–936.
- 6 K. Takenaka, Y. Okamoto, T. Shinoda, N. Katayama and Y. Sakai, *Nat. Commun.*, 2017, **8**, 14102.
- 7 L. Cabras, M. Brun and D. Misseroni, *Proc. Natl. Acad. Sci. U. S. A.*, 2019, **475**, 20190468.
- 8 J. Qu, M. Kadic, A. Naber and M. Wegener, *Sci. Rep.*, 2017, **7**, 40643.
- 9 E. Boatti, N. Vasios and K. Bertoldi, *Adv. Mater.*, 2017, **29**, 1700360.
- 10 J. Chen, L. Hu, J. Deng and X. Xing, *Chem. Soc. Rev.*, 2015, **44**, 3522–3567.
- 11 A. Versluis, W. Douglas and R. Sakaguchi, *Dent. Mater.*, 1996, **12**, 290–294.
- 12 R. Bastait, G. Rodrigues, P. Jetteur, P. Hagedorn and A. Preumont, *Smart Mater. Struct.*, 2012, **21**, 064004.
- 13 O. Sigmund and S. Torquato, *J. Mech. Phys. Solids*, 1997, **45**, 1037–1067.
- 14 A. Sanson and J. Chen, *Front. Chem.*, 2019, **7**, 284.
- 15 Y. Zhou, X. Y. Chen, Y. H. Fu, G. Vienne, A. I. Kuznetsov and B. Luk'yanchuk, *Appl. Phys. Lett.*, 2013, **103**, 123116.
- 16 E. Almeida, O. Bitton and Y. Prior, *Nat. Commun.*, 2016, **7**, 12533.
- 17 M. S. Rill, C. Plet, M. Thiel, I. Staude, G. von Freymann, S. Linden and M. Wegener, *Nat. Mater.*, 2008, **7**, 543–546.
- 18 C. Enkrich, F. Pérez-Willard, D. Gerthsen, J. Zhou, T. Koschny, C. M. Soukoulis, M. Wegener and S. Linden, *Adv. Mater.*, 2005, **17**, 2547–2549.
- 19 D.-Y. Kang, W. Lee, D. Kim and J. H. Moon, *Langmuir*, 2016, **32**, 8436–8441.
- 20 T. K. Kormilina, E. A. Stepanidenko, S. A. Cherevko, A. Dubavik, M. A. Baranov, A. V. Fedorov, A. V. Baranov, Y. K. Gun'ko and E. V. Ushakova, *J. Mater. Chem. C*, 2018, **6**, 5278–5285.
- 21 X. Zheng, W. Smith, J. Jackson, B. Moran, H. Cui, D. Chen, J. Ye, N. Fang, N. Rodriguez, T. Weisgraber and C. M. Spadaccini, *Nat. Mater.*, 2016, **15**, 1100–1107.
- 22 Y. Enomoto-Rogers, N. Lio, A. Takemura and T. Iwata, *Eur. Polym. J.*, 2015, **66**, 470–477.
- 23 D. Pantelic, S. Savic and D. Jakovljevic, *Opt. Lett.*, 1998, **15**, 807–809.
- 24 S. Savic-Sevic and D. Pantelic, *Appl. Opt.*, 2007, **46**, 287–291.
- 25 S. Savic-Sevic and D. Pantelic, *Opt. Express*, 2005, **13**, 2747–2754.
- 26 S. Savic-Sevic, D. Pantelic, B. Jelenkovic, B. Salatic and D. V. Stojanovic, *Soft Matter*, 2018, **14**, 5595–5603.
- 27 G. Strobl, *The Physics of Polymers*, Springer-Verlag, Berlin Heidelberg, 2007.
- 28 M. Wada and Y. Saito, *J. Polym. Sci., Part B: Polym. Phys.*, 2001, **39**, 168–174.
- 29 V. Ramiah and D. A. I. Goring, *J. Polym. Sci., Part C: Polym. Symp.*, 1965, **11**, 27–48.
- 30 B. Edlen, *Metrologia*, 1966, **2**, 71–80.
- 31 T. Handa, H. Tahara, T. Aharen and Y. Kanemitsu, *Sci. Adv.*, 2019, **5**, eaax0786.
- 32 K. G. Denbigh and G. Raumann, *Proc. R. Soc. London, Ser. A*, 1952, **210**, 377–387.
- 33 K. G. Denbigh, *Nature*, 1949, **163**, 60.
- 34 W. Große, *Aquat. Bot.*, 1996, **54**, 101–110.
- 35 A. P. Straub, N. Y. Yip, S. Lin, J. Lee and M. Elimelech, *Nat. Energy*, 2016, **1**, 1–6.
- 36 S. G. Jennings, *J. Aerosol Sci.*, 1988, **19**, 159–166.
- 37 N. Gontard, R. Thibault, B. Cuq and S. Guilbert, *J. Agric. Food Chem.*, 1996, **44**, 1064–1069.
- 38 C. G. Biliaderis, A. Lazaridou and I. Arvanitoyannis, *Carbohydr. Polym.*, 1999, **40**, 29–47.
- 39 N. Acharya, P. Yadav and Y. Vijay, *Indian J. Pure Appl. Phys.*, 2004, **42**, 179–181.
- 40 L. A. El-Azzami and E. A. Grulke, *J. Polym. Sci., Part B: Polym. Phys.*, 2007, **45**, 2620–2631.

PAPER

YVO₄:Eu³⁺ nanopowders: multi-mode temperature sensing technique

To cite this article: D Sevic *et al* 2019 *J. Phys. D: Appl. Phys.* **53** 015106

View the [article online](#) for updates and enhancements.



IOP | ebooks™

Bringing you innovative digital publishing with leading voices to create your essential collection of books in STEM research.

Start exploring the collection - download the first chapter of every title for free.

YVO₄:Eu³⁺ nanopowders: multi-mode temperature sensing technique

D Sevic^{1,3}, M S Rabasovic¹, J Krizan², S Savic-Sevic¹, M G Nikolic¹,
B P Marinkovic¹ and M D Rabasovic¹

¹ Institute of Physics Belgrade, University of Belgrade, Serbia

² Ami DOO, Ptuj, Slovenia

E-mail: sevic@ipb.ac.rs

Received 18 May 2019, revised 14 September 2019

Accepted for publication 1 October 2019

Published 15 October 2019



Abstract

In this paper we study several temperature sensing techniques using the same thermographic phosphor: luminescence intensity ratio, lifetime, rise time. Moreover, we analyze some recently presented techniques, based on host luminescence intensity ratio method and delayed gate intensity ratio technique. We have selected YVO₄:Eu³⁺ nano powder as an appropriate material for this study, because it has easily detectable luminescence rise time and host luminescence. The material was prepared using simple solution combustion synthesis. The time resolved analysis of emission spectra was achieved using the streak camera system. We present a very detailed analysis of measured lifetimes and rise times of all emission lines and their temperature dependence. We propose a multi-mode temperature sensing technique based on the concept of luminescence detection part of the temperature sensor capable of switching between several measurements modes to obtain the best sensitivity in desired range of operation.

Keywords: temperature sensing, phosphors, optical properties, luminescence, time-resolved optical spectroscopy

(Some figures may appear in colour only in the online journal)

1. Introduction

Thermographic phosphors offer many advantages for temperature measurement compared to other methods [1–10]. Optical thermometry is very accurate, contactless method of remote sensing. Moreover, it is conceptually simple. There are several ways to use phosphors for thermometry purposes. Spectroscopy techniques are usually employed to remotely measure effects of temperature on phosphors photoluminescence. The most common method is based on intensity ratio of two, appropriately selected, spectral peaks of thermophosphor. The method is called fluorescence intensity ratio (FIR). The second commonly used method is based on phosphor luminescence lifetime. This technique needs to measure only one spectral peak. Some phosphors have temperature dependent

luminescence rise time sufficiently long to be of practical use for thermometry. Many thermophosphors offer the possibilities for two promising modifications of the FIR method. First, using of host luminescence instead of one of the two dopant luminescence peaks for intensity ratio calculations could improve the sensitivity or overall characteristics of the FIR basic, in regard of simplicity and reliability [11–15]. Another possible improvement of the sensitivity could be achieved by proper selection of the time frame for calculating the intensity ratio [3, 15, 16].

Aim of this study is to compare the before mentioned thermometry techniques using the same nanophosphor. Our previous studies of europium, dysprosium or samarium doped hosts implied that, among the nanophosphors analyzed in [15–21], only Yttrium Vanadate (YVO₄) doped with europium ions (YVO₄:Eu³⁺) offers the long enough luminescence rise time, in microsecond domain, to be of practical use for thermometry. Nano phosphors Y₂O₃ [8, 22–24], SrY₂O₄ [25] and

³ Author to whom any correspondence should be addressed.

BaY₂ZnO₅ [26] are also used for temperature measurements based on rise time.

It is well known fact that absorption and excitation times are typically in femtosecond domain, see [8]. The detected long rise time of some ⁵D₀ emission lines is related to the specific energy transfer mechanism of analyzed nanophosphor. A detailed time resolved luminescence analysis of optical emission presented in this paper will provide an insight into energy transfer mechanism of YVO₄:Eu³⁺.

Studies of structural and luminescent characteristics of YVO₄:Eu³⁺ phosphors, including various methods of synthesis, are reported in [27–50] and references therein. Compared with other oxide luminescence compounds such as Y₂O₃, YVO₄ has lower formation energy and higher crystallinity, which makes it easier to form regular morphology and shows higher luminous efficiency [27].

Transitions from the ⁵D₀ state, from which most of europium luminescence comes, have a slow decay. Lifetimes of slow decay lines of europium doped YVO₄ are measured and reported in many publications. The luminescence intensity of ⁵D₀-⁷F₂ transition is the most intensive, so it is usually used for europium luminescence lifetime measurements [42, 48, 51, 52]. However, there are not so many publications regarding any europium doped host, where measured lifetimes of europium fast decay transitions or rise times of slow decay transitions [23, 25, 26, 35, 51, 53] are provided. To the best of our knowledge, the results of measurements of the rise time of transitions from the ⁵D₀ state and lifetime of fast decay transitions from the ⁵D₁ state of YVO₄:Eu³⁺ phosphors are only presented in [19], measured only at the room temperature and [35] measured at and below room temperature. In this work we will focus on temperature dependency of YVO₄:Eu³⁺ luminescence, not analyzed in our previous papers.

2. Experimental procedures

Europium doped YVO₄ nanophosphor was efficiently prepared using a solution combustion synthesis (SCS) method [54]. The structure of synthesized Y_{0.98}VO₄:Eu_{0.02}³⁺ material has been confirmed and characterized in our earlier publication [19], using x-ray powder diffraction (XRD), scanning electron microscope (SEM), Raman and photoluminescence (PL) techniques. The average grain size of about 51 nm was estimated by the Scherer equation.

As an excitation source for photoluminescence measurements we used the optical parametric oscillator (Vibrant OPO), continuously tunable over a spectral range from 320 nm to 475 nm. The emission spectra and luminescence lifetimes and rise time of synthesized nanopowders were analyzed using the streak camera system. The camera is equipped with the spectrograph. The details of our experimental setup can be found in [16, 19]. The part of experimental setup for luminescence measurement as a function of temperature is described in [55].

3. Results and discussion

3.1. Optical properties

The streak images of time resolved photoluminescence spectrum of YVO₄:Eu³⁺ material are presented in figure 1. It was shown that optical spectral properties reported for YVO₄:Eu³⁺ in the literature remain the same for GdVO₄:Eu³⁺ as well [56]. Excitation spectra of VO₄ groups are very similar for both phosphors. This fact is explained, proved in detail and generalized for rare earth doped vanadates in [57–60]. Moreover, it was shown in [57–61] that absorption of VO₄³⁻ group shifts to longer wavelengths with increasing temperature, and that it could be used for improved temperature sensing characteristics [57–60].

In [38, 46, 49, 50, 56–60, 62] it was shown that the VO₄ excitation spectra consist of a strong absorption band between 250 and 350 nm, corresponding to the charge transfer from O₂₋ to the central vanadium ion V⁵⁺ of vanadate VO₄³⁻ groups. So, it should be pointed out that the excitation of Eu³⁺ ion is basically caused by energy transfer from vanadate groups to Eu³⁺ ion. Due to the weak intensities of *f–f* transitions of Eu³⁺ ions compared with that of VO₄³⁻ ion, these transition lines often have not been observed in measured excitation spectra, or simply neglected in many publications. In our work [16] we showed that it is possible to exploit the direct excitation of europium for temperature and pressure sensing purposes.

However, there is another interesting phenomenon regarding the direct excitation of europium. It is discovered and explained for the first time in [57]. As described there, excitation spectra with respect to the characteristic excitations of Eu³⁺ ions from ⁷F₀, ⁷F₁ and ⁷F₂ states to ⁵D₂ state are temperature dependent, so the phenomenon could be used for temperature measurements. Further, it is explained that beside temperature quenching, another factor that affects the emission intensity is the population of the initial state for the excitation. Namely, the populations between ⁷F₀, ⁷F₁ and ⁷F₂ states of Eu³⁺ ions follow Boltzmann distribution due to their appropriate energy gaps [57]. Thus, with increasing temperature, the population of the ground state ⁷F₀ as the initial state of 395 nm excitation decreases because of the thermally populating of high energy levels (⁷F₁ and ⁷F₂), leading to the decreasing of response intensity for excitation at 395 nm [57]. Because of the relatively weak measured signal of optical response of europium excited at this wavelength in our present experimental setup, we declined of further analysis of this mode of operation for temperature sensing.

We have used the excitation at 330 nm, which is slightly on right-hand side from the excitation peak of YVO₄:Eu³⁺ on wavelength scale. As usual, the streak image is presented in pseudocolor. Note that, because of streak camera automatic lookup table (LUT) for generating pseudocolor which is nice to eye, the luminescence intensities on different streak images should not be compared visually. The Eu transitions

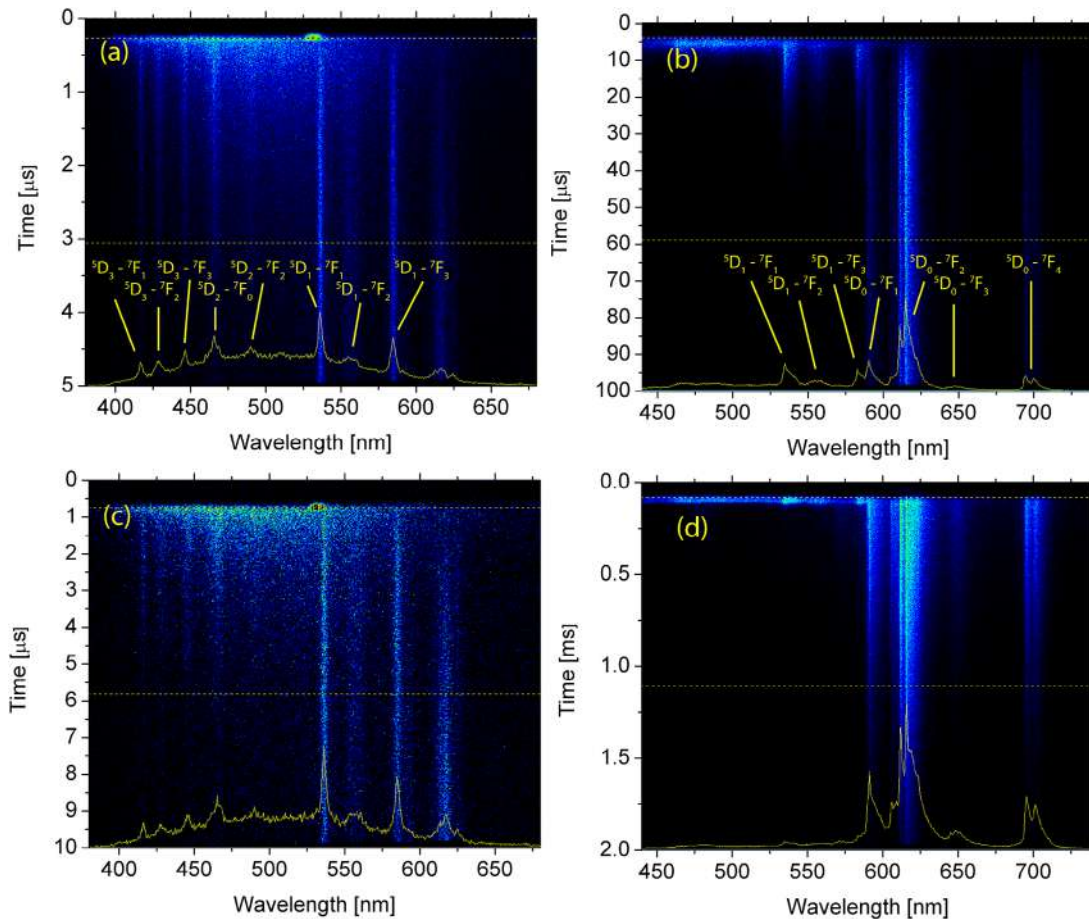


Figure 1. Streak images of photoluminescence spectrum of $\text{YVO}_4:\text{Eu}^{3+}$ nano phosphor. Time ranges of acquired spectral streak images are (a) $5 \mu\text{s}$, (b) $100 \mu\text{s}$, (c) $10 \mu\text{s}$ and (d) 2ms . Spectral line profiles (yellow curves) are integrated-in-time as marked by dashed yellow lines. OPO excitation is at 330nm .

are denoted in figure 1 according to [51, 63]. Because we use OPO blocking filter, host optical emission is measured only above 400nm , showing wide luminescence band up to about 550nm . The host emission of similar spectral shape is presented and analyzed in [31, 35, 41]. It could be seen in figure 1 that the host emission, compared to europium transitions, has very fast decay. The observed host emission is also of very short duration in [35]. The slow decay transitions observable in figure 1, originating from $^5\text{D}_0$ level, are well explained in literature and their detailed description can be found in our previous work [19]. In this study, we have conducted the time resolved analysis for all transitions which are identified in figure 1.

Looking at streak image presented in figure 1(a) or (c) it could be estimated that the raising edges of optical emissions of YVO_4 host and of lines originating from transitions from $^5\text{D}_3$, $^5\text{D}_2$ and $^5\text{D}_1$ europium levels are almost instantaneous and that the lifetimes of host emission and transitions from $^5\text{D}_3$ and $^5\text{D}_2$ are very short. Figure 1(b) implies that the lifetime of transitions from $^5\text{D}_1$ level and rise time of transitions from $^5\text{D}_0$ level are in the microsecond domain. Figure 1(d)

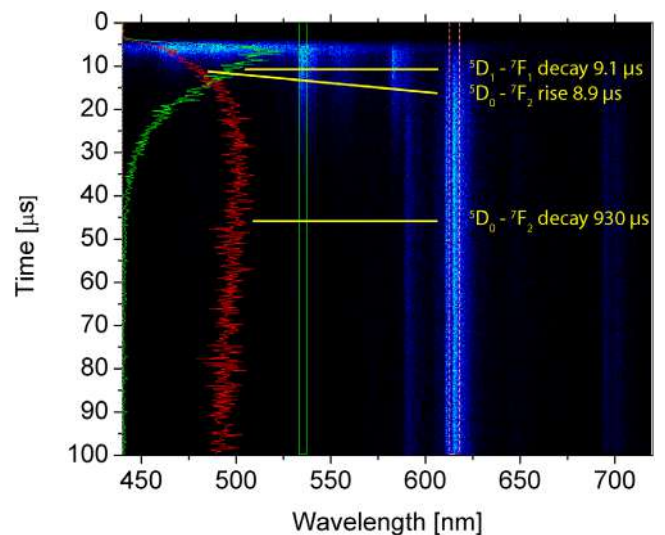
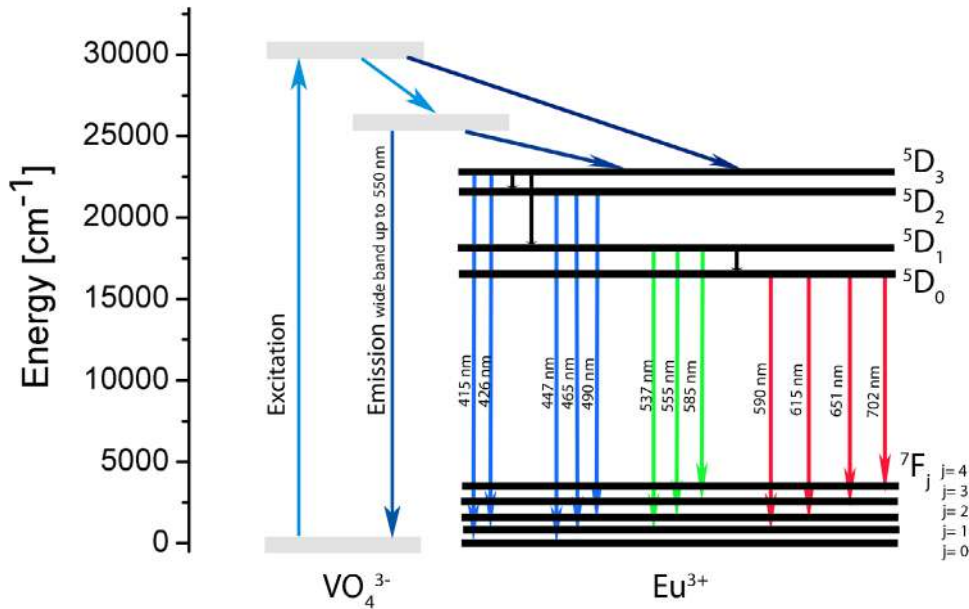


Figure 2. Temporal responses of optical emission of two europium lines in $\text{YVO}_4:\text{Eu}^{3+}$ nano phosphor, shown as projections on time axis, integrated in spectral range marked as green for $^5\text{D}_1-^7\text{F}_1$ transition (green curve) and dashed red for $^5\text{D}_0-^7\text{F}_2$ transition (red curve).

Table 1. Values of lifetimes of detected $\text{YVO}_4:\text{Eu}^{3+}$ transitions measured at room temperature, excited at 330 nm. The rise time of $^5\text{D}_0$ transitions is 8.9 μs .

Transition	$^5\text{D}_3-^7\text{F}_1$	$^5\text{D}_3-^7\text{F}_2$	$^5\text{D}_3-^7\text{F}_3$	$^5\text{D}_2-^7\text{F}_0$	$^5\text{D}_2-^7\text{F}_2$	$^5\text{D}_1-^7\text{F}_1$	$^5\text{D}_1-^7\text{F}_2$	$^5\text{D}_1-^7\text{F}_3$	$^5\text{D}_0-^7\text{F}_1$	$^5\text{D}_0-^7\text{F}_2$	$^5\text{D}_0-^7\text{F}_3$	$^5\text{D}_0-^7\text{F}_4$	YVO_4 host
Wavelength (nm)	416	428	446	465	490	537	556	584	591	615	648	693	Up to 550 nm
Lifetime (μs)	2.2			2.7			9.1			930			2

**Figure 3.** Schematic view of $\text{YVO}_4:\text{Eu}^{3+}$ energy transfer processes.

shows that the lifetime of transitions from $^5\text{D}_0$ level is in millisecond domain.

General shapes of temporal response of optical emissions of fast decay $^5\text{D}_1-^7\text{F}_1$ transition and slow decay $^5\text{D}_0-^7\text{F}_2$ transition of $\text{YVO}_4:\text{Eu}^{3+}$ nano phosphor are illustrated in figure 2. The rise component of $^5\text{D}_0-^7\text{F}_2$ transition and the decay component of $^5\text{D}_1-^7\text{F}_1$ transition look almost mirrored, implying that there is an energy transfer mechanism between them. The phenomenon that the rise time of europium slow decay $^5\text{D}_2$ luminescence is similar to the lifetime of fast decay $^5\text{D}_1$ emission was observed long ago [53]; and analyzed in detail, including energy transfer, in [35]. The explanation of energy transfer between the host YVO_4 and Eu^{3+} ions is also provided in [32].

To check the presumption that the rise times of fast decay transitions can be considered as instantaneous, we have used the time scales of streak camera even shorter than 5 μs .

We have concluded that, at the present time, rise times of fast decay transitions of $\text{YVO}_4:\text{Eu}^{3+}$ are not of any practical use for temperature sensing. The only measurable rise time is of $^5\text{D}_0$ transitions; it is 8.9 μs . We have calculated the rise time according to Ranson equation [23, 24].

The values of lifetimes of $\text{YVO}_4:\text{Eu}^{3+}$ transitions detected in our study, measured at room temperature, excited at 330nm, are presented in table 1. We also made preliminary estimations of temperature dependences of lifetimes of transitions from YVO_4 host and $^5\text{D}_3$ and $^5\text{D}_2$ levels. We concluded

that lifetime measurements of $^5\text{D}_3$ and $^5\text{D}_2$ transitions are not so appropriate for temperature sensing, because of small signal intensities compared to intensities of luminescence of $^5\text{D}_0$ and $^5\text{D}_1$ transitions. The host luminescence is more rapidly quenched by temperature than europium transitions, providing possibility of improved sensitivity in physiological temperature range. The integrated-in-time host luminescence signal strength is quite satisfactory for intensity ratio calculations. On the other hand, measuring the host luminescence lifetime with temperature raise, although possible, showed itself to us as unreliable at the present time. However, with some improvements in detection, the lifetime of host could be of interest for temperature sensing in physiological temperature range.

Based on our estimations of shape of temporal response and time durations of luminescence of host and of europium transitions shown in figures 1 and 2, we propose the schematic view of $\text{YVO}_4:\text{Eu}^{3+}$ energy transfer processes presented in figure 3.

3.2. Temperature sensing using luminescence intensity ratio with variable delayed gating

Luminescence intensity ratio technique is based on measuring the intensities of two emission lines in luminescence spectra of thermographic phosphors. The temperature is calculated by the emission intensity ratio of these two lines. Many problems

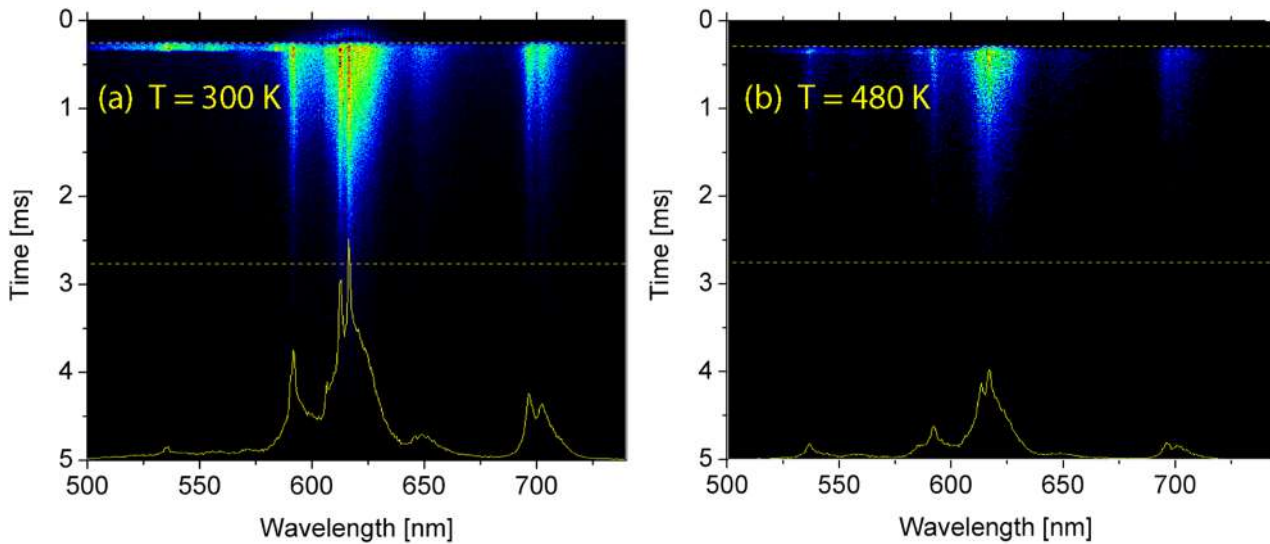


Figure 4. Streak images of photoluminescence spectra of $\text{YVO}_4:\text{Eu}^{3+}$ and their integrated-in-time (time range marked by yellow dashed line) spectral line profiles (yellow curves): (a) $T = 300\text{ K}$, (b) $T = 480\text{ K}$, selected for illustration of FIR analysis.

regarding measuring errors, optical condition deviations and excitation power fluctuation are eliminated in this way. Two closely spaced energy levels of rare earth ion, which are thermally coupled, are usually selected for temperature sensing. Small energy gap between these two levels allows the upper level to be populated from the lower level by thermalization. The upper level becomes more populated as the temperature increases and hence the fluorescence from this level gradually increases. Relative population between two levels, ${}^5\text{D}_1$ level (I_1) and ${}^5\text{D}_0$ level (I_0), IR, follows Boltzmann type population distribution given by [1, 2]:

$$\text{IR} = \frac{I_1}{I_0} = C \cdot \exp\left(-\frac{\Delta E}{kT}\right) \quad (1)$$

where k is the Boltzmann constant, $k = 0.69503476(63)\text{ cm}^{-1}\text{ K}^{-1}$, C is a constant and ΔE is the energy gap between two excited levels, in case analyzed here, between ${}^5\text{D}_1$ and ${}^5\text{D}_0$ europium levels.

Instruments for measuring luminescence often detect small signals, even when there is no emission, because of detector dark currents, etc. Moreover, spectrograph stray light introduces error in measured intensity of a signal. Therefore, another constant, A , should be introduced to equation (1), to account for the finite value of IR at low temperatures [14]:

$$\text{IR} = A + C \cdot \exp\left(-\frac{\Delta E}{kT}\right). \quad (2)$$

It should be noted that ΔE corresponds to energy gap between two excited states only in the case of measuring the intensity ratio in conventional way, i.e. without any gate delay in our study. However, when we introduce the delay for gating of measured signals, using ΔE from equation (2) for an estimation of energy gap of excited levels would be quite misleading, although it can be well exploited for fitting the temperature calibration curve. The same holds for calculating the intensity ratio between optical emissions of the host and the selected europium line.

The spectral line intensities from the ${}^5\text{D}_0$ and ${}^5\text{D}_1$ transitions depend on two physical processes. The first process is the thermalization of the ${}^5\text{D}_1$ level with rising temperature, where the energy difference to populate the ${}^5\text{D}_1$ level from the ${}^5\text{D}_0$ level is fully covered by phonons. The second process is nonradiative quenching of the ${}^5\text{D}_0$ and ${}^5\text{D}_1$ levels through the charge transfer state. Both processes can be recognized by the analysis of integrated-in-time profiles of luminescence spectra in figure 4. Namely, the intensity ratio between the lines at 537 nm and 618 nm increases with temperature. However, both lines are thermally quenched. Again, because of streak camera automatic LUT, comparison of luminescence intensities should be not done simply by looking at images.

In our study the intensity ratio method has been improved by introducing the temporal dependence in the intensity ratio measurements, as proposed in [3]. We have implemented this method in [15, 16] where we have shown that it is possible to increase the sensitivity of temperature calibration curve if appropriately selected part of luminescence temporal evolution is used in calculation.

To determine the temperature calibration curves, the luminescence spectra of $\text{YVO}_4:\text{Eu}^{3+}$ nano phosphor were measured at various temperatures, using OPO excitation at 330 nm and the streak camera. For calculation of intensity ratio in a usual way the narrow bands (5 nm) of europium luminescence around 537 nm and around 618 nm were used integrated in time from their beginning. Then, to improve the temperature sensitivity of the FIR method, we have varied the gating times for beginning of 618 nm signal in-time-integration. In this way, because smaller portion of falling 618 nm luminescence signal was integrated, the intensity ratio was increased in favor of 537 nm signal, following the general increase of ratio of 537 nm and 618 nm signals with temperature.

Here, the thermalization and quenching through charge transfer both have significant influence on the fluorescence intensity ratio (FIR). This means that the measured results cannot be simply fitted to the Boltzmann distribution. To

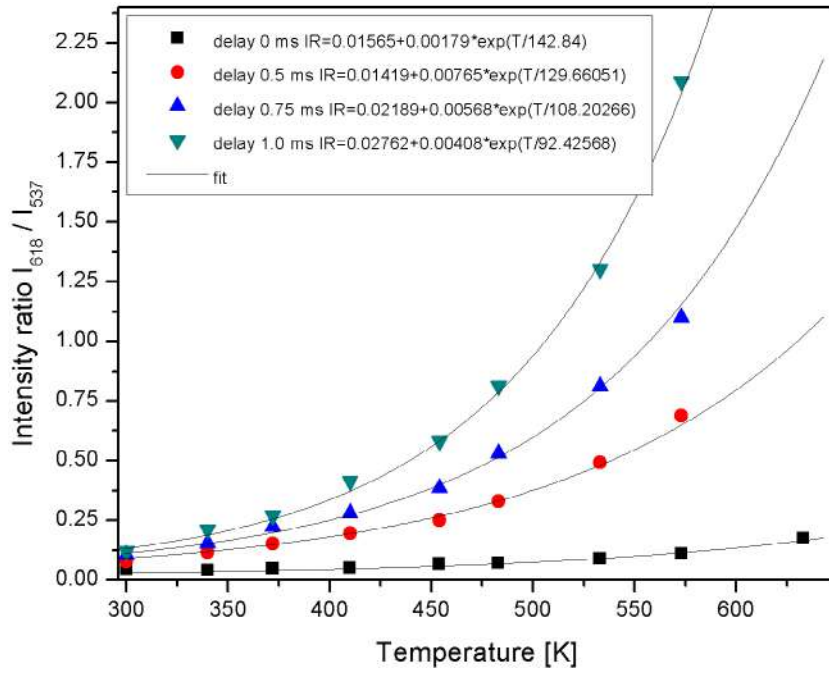


Figure 5. Temperature sensing calibration curve of YVO₄:Eu³⁺ nanopowder sample.

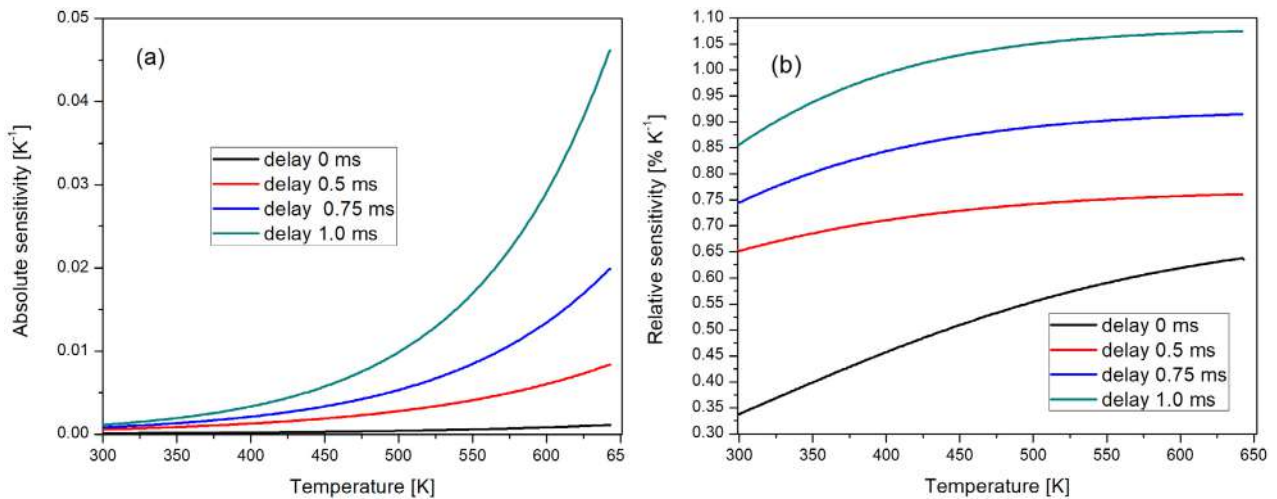


Figure 6. (a) Absolute and (b) relative sensitivities of YVO₄:Eu³⁺ nanopowder as the functions of temperature shown in figure 4.

implement the fluorescence intensity ratio method in thermometry it is necessary to fit a calibration function of analyzed thermophosphor. Based on considerations in [15, 16, 55, 64] we decided to use the simple empirical equation for fitting the calculated intensity ratios of experimental data: $IR(T) = A + C \cdot e^{-T/\alpha}$, where T is temperature in K, and A , C and α are empirical constants obtained through fitting of measured data. In principle, for temperature sensing, it is enough to determine the temperature calibration sensing curve, no further knowledge regarding the underlying physics is necessary [65]. The results are shown in figure 5, where delay of 0 ms corresponds to the FIR, the usual way of calculating the intensity ratio.

It could be seen in figure 5 that intensity ratio increases with increasing the gate delay time of signal. However, increasing the gate delay time decreases the integrated signal intensity, so we refrained from using delays longer than 1 ms.

The absolute thermal sensitivity S_a of the intensity ratio method is defined as the rate at which IR changes with the temperature:

$$S_a = \left| \frac{dIR}{dT} \right|. \quad (3)$$

The relative thermal sensitivity of the intensity ratio method S_r is determined using formula:

$$S_r = \left| \frac{1}{IR} \frac{dIR}{dT} \right|. \quad (4)$$

Absolute sensitivity is of a small or no use for comparison of different samples. We will provide its values here for comparison of the improvements of various FIR methods used with the same sample.

Absolute and relative temperature sensitivities of YVO₄:Eu³⁺ nanopowder are shown in figure 6. Best

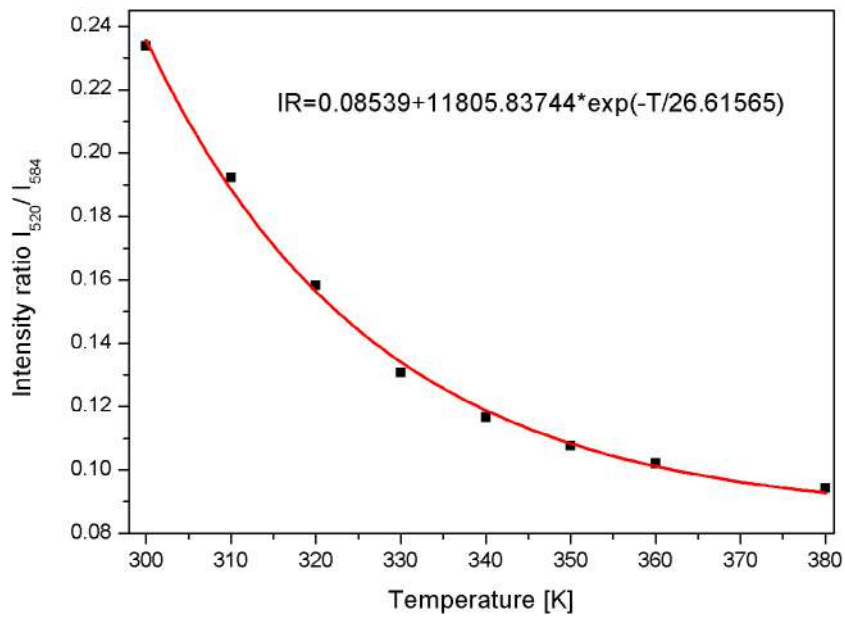


Figure 7. The temperature sensing calibration curve, calculated as intensity ratio of host luminescence and ${}^5D_2-{}^7F_3$ transition (584 nm).

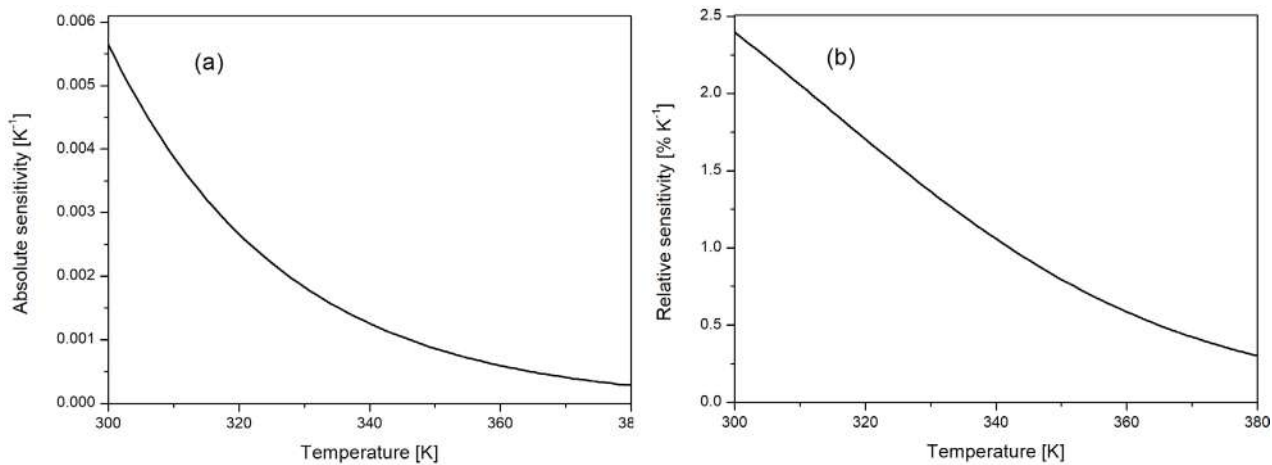


Figure 8. (a) Absolute and (b) relative sensitivities of $YVO_4:Eu^{3+}$ nanopowder as the function of temperature shown in figure 7.

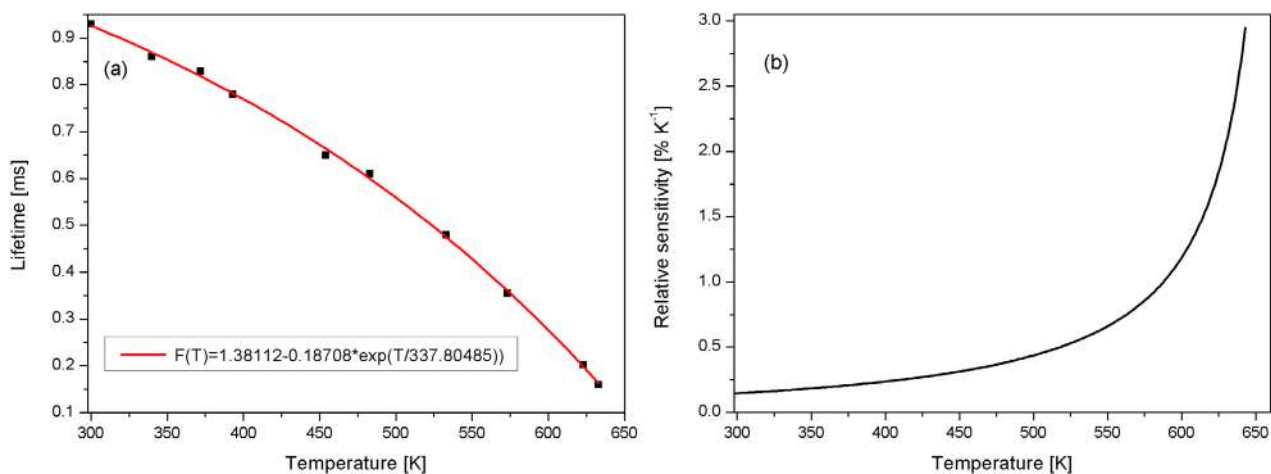


Figure 9. (a) Luminescence lifetime temperature dependence of $YVO_4:Eu^{3+}$ nano phosphor and (b) its relative sensitivity.

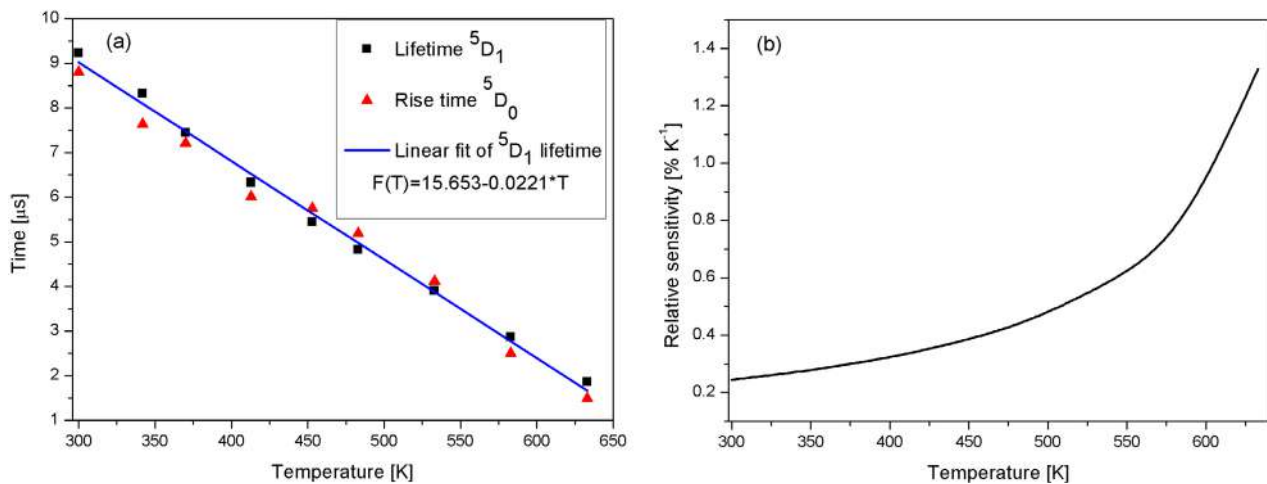


Figure 10. (a) Temperature calibration curve of luminescence lifetime of 5D_1 and rise time of 5D_0 transitions of $YVO_4:Eu^{3+}$ nano phosphor and (b) the relative sensitivity of temperature calibration curve based on fit 5D_1 lifetime.

sensitivity is obtained by gate time of 1 ms. We estimate that this kind of temperature sensing is useful up to about 650 K, where intensities of both measured signals become too low for reliable calculating.

3.3. Temperature sensing using luminescence intensity ratio between YVO_4 host and europium $^5D_1-^7F_2$ transition

Our measurements show that the host luminescence, although much weaker than emission from 5D_1 and 5D_0 transitions, is easily detected. Its emission is in the wide band, so its integration could be done in a wider spectral range (we used a band of 10 nm). Host luminescence is rapidly quenched with temperature. We have determined the temperature sensing calibration curve, presented in figure 7, as intensity ratio of host luminescence and $^5D_2-^7F_3$ transition (584 nm). The line at 584 nm is prominent and it has no overlap with the host luminescence, see figure 1. We see that the sensitivity in physiological temperature range is greatly improved; however, the sensing range is reduced to about 380 K.

Absolute and relative sensitivities of $YVO_4:Eu^{3+}$ nanopowder are shown in figure 8. Compared to sensitivities of other temperature sensing curves of this nano phosphor shown in figures 6, 9 and 10, we see that this method offers the best sensitivity in physiological range of temperatures.

3.4. Luminescence lifetime temperature dependency

All transitions from the same level have the same lifetime, so it is usual practice for estimation of decay time to use the line with highest intensity of luminescence. To determine the temperature sensing calibration curve we used the most prominent europium spectral line at 618 nm. Analysis presented in [11] confirms that it is possible to use the same form of empirical equation for fitting the lifetime experimental data as we have used for fitting the intensity ratio, namely: $F(T) = A + C \cdot e^{-T/\alpha}$, [15, 16, 55, 64], where T is temperature in K, and A , C and α are empirical constants obtained through fitting of measured data. The temperature sensing calibration curve is shown in figure 9. For our sample of $YVO_4:Eu^{3+}$ nano

Table 2. The sensing characteristics of various temperature sensing modes.

Sensing mode	Quality of sensing at temperature (K)		
	300–340	340–500	500–650
Intensity ratio	Poor	Between poor and good	Good
Intensity ratio with delayed gating	Good	Good	Good
Intensity ratio using host	Excellent	Good up to 380	No signal
Slow decay lifetime	Poor	Good	Excellent
Slow decay rise time/ fast decay lifetime	Poor	Good	Fairly excellent

phosphor the method is reliable up to 650 K. The sensitivity increases by temperature raising.

3.5. Luminescence rise time temperature dependency

Temperature dependence of luminescence lifetime of 5D_1 and rise time of 5D_0 transitions of $YVO_4:Eu^{3+}$ nano phosphor and the relative sensitivity of temperature calibration curve based on fit 5D_1 lifetime are shown in figure 10.

In this range of temperatures, the rise time dependence is linear, similarly as observed in [22, 23, 25]. Moreover, it seems that it is the same if we use decay of 537 nm line, or rise time of 618 nm line. The choice would be dependent on which signal is overall stronger and easier to analyze for a given sample. It should be also mentioned that, instead of measuring the rise time, the measured time of achieving the signal maximum at 618 nm could be efficiently used for temperature measurements [22, 25, 66].

3.6. Multi-mode temperature sensing technique

Comparing temperature sensing characteristics of $YVO_4:Eu^{3+}$, shown in figures 5–10, we conclude that europium lines intensity ratio method, the luminescence lifetime method and rise time method offer the same sensing range. Lifetime and rise

Table 3. The sensing characteristics of various hosts doped with Eu^{3+} .

Host	Sensing range (K)	Relative sensitivity (% K^{-1})	Reference
YVO_4	300–650	0.2–2.9	This work
YVO_4	300–650	0.33–0.63	This work, FIR
YVO_4	300–650	2.4–2.9	This work, optimal sensing mode
$\text{Gd}_2\text{Zr}_2\text{O}_7$	300–650	0.4–0.92	[21]
Sr_2CeO_4	300–400	1.0–2.4	[16]
YNbO_4	300–720	0.3–2.6	[67, 68]
Gd_2O_3	300–800	0.25–3.25	[69]
Lu_2O_3	300–800	0.3–0.33	[70]
$\text{Gd}_2\text{Ti}_2\text{O}_7$	300–420	0.3–0.95	[14]
TiO_2	300–530	0.12–2.3	[11]
GdAlO_3	300–750	0.3–2.9	[71]
YBO_3	330–760	0.3–1.8	[72]

time methods have improved sensitivity on higher temperatures. Delayed gating of intensity ratio method provides improved sensitivity. The sensing characteristics of various temperature sensing modes are summarized in table 2. The luminescence detection part of the temperature sensor should be capable of switching between several measurements modes, so the best sensitivity could be obtained in desired range of operation.

Comparison of temperature sensing characteristics of various hosts doped with Eu^{3+} is presented in table 3. The values of relative sensitivity are usually used for comparison purposes between various materials because relative sensitivity is much better performance indicator than absolute sensitivity. We can see that only $\text{Gd}_2\text{O}_3:\text{Eu}^{3+}$ has slightly better value of maximal relative sensitivity and higher sensing range. Some of hosts listed in table 3 have similar but slightly inferior performances compared to $\text{YVO}_4:\text{Eu}^{3+}$. Other hosts are obviously inferior. We conclude that performance of $\text{YVO}_4:\text{Eu}^{3+}$ nano phosphor analyzed here is more than satisfactory. However, it seems that analysis of multi-mode technique applied to the $\text{Gd}_2\text{O}_3:\text{Eu}^{3+}$ nano phosphor could be a worthy effort.

4. Conclusions

In this paper we have analyzed the several temperature sensing techniques using the $\text{YVO}_4:\text{Eu}^{3+}$ nanopowder. The material was prepared by simple solution combustion synthesis method. We have showed that, for analyzed $\text{YVO}_4:\text{Eu}^{3+}$ material, the temperature sensing techniques based on ratio of intensities of two lines, lifetime or rise time are useful up to 650 K. We have obtained sensitivity improvement of the intensity ratio method by simulating the delayed gating of integrating-in-time intensity of one of spectral lines. If the YVO_4 host luminescence is used in intensity ratio method, the sensitivity in physiological temperature range is greatly improved; however, the sensing range is reduced to about 380 K.

So, our analysis shows that remote temperature sensor based on of $\text{YVO}_4:\text{Eu}^{3+}$ nano phosphor has good sensitivity not only in the physiological temperature range but also for the higher temperatures that are of interest when monitoring the thermal behavior of electronic devices and engines. The luminescence detection part of the temperature sensor should

be capable of switching between several measurements modes in order to obtain the best sensitivity in desired range of operation. We have proved the proposed concept by using the streak camera. Real application should be based on less expensive equipment.

Beside luminescence kinetics of slow decay transitions we also estimated rise times and lifetimes of fast decay transitions and the host luminescence. The rise times of fast decay transitions and host luminescence is estimated as negligible for effects that are here of interest. At the present time, the lifetimes of luminescence of fast decay transitions, $^5\text{D}_3$ and $^5\text{D}_2$, and the host are also too small to be of interest. However, with some improvements in detection, the lifetime of host could be of interest for temperature sensing in physiological temperature range.

Acknowledgment

This work was financially supported by Ministry of Education, Science and Technological Development of the Republic of Serbia under Project OI171020.

ORCID iDs

D Sevic  <https://orcid.org/0000-0002-7206-6370>
M S Rabasovic  <https://orcid.org/0000-0002-4882-8080>
J Krizan  <https://orcid.org/0000-0003-4195-8322>
S Savic-Sevic  <https://orcid.org/0000-0002-6406-0745>
B P Marinkovic  <https://orcid.org/0000-0002-6904-6360>
M D Rabasovic  <https://orcid.org/0000-0002-9235-4388>

References

- [1] Jaque D and Vetrone F 2012 *Nanoscale* **4** 4301–26
- [2] Brites C D S, Lima P P, Silva N J O, Millan A, Amaral V S, Palacio F and Carlos L D 2012 *Nanoscale* **4** 4799–829
- [3] Aldén M, Omrane A, Richter M and Särner G 2011 *Prog. Energy Combust. Sci.* **37** 422–61
- [4] Allison S W and Gillies G T 1997 *Rev. Sci. Instrum.* **68** 2615–50
- [5] Goss L P, Smith A and Post M E 1989 *Rev. Sci. Instrum.* **60** 3702–6

- [6] Heyes A L 2009 *J. Lumin.* **129** 2004–9
- [7] Gentleman M M and Clarke D R 2004 *Surf. Coat. Technol.* **188–9** 93–100
- [8] Khalid A H and Kontis K 2008 *Sensors* **8** 5673–744
- [9] Wade S A, Collins S F and Baxter G W 2003 *J. Appl. Phys.* **94** 4743–56
- [10] Wade S A, Forsyth D I and Grattan K T V 2001 *Rev. Sci. Instrum.* **72** 3186–90
- [11] Nikolic M G, Antic Z, Culubrk S, Nedeljkovic J M and Dramicanin M D 2014 *Sens. Actuators B* **201** 46–50
- [12] Dramicanin M D, Antic Z, Culubrk S, Ahrenkiel S P and Nedeljkovic J M 2014 *Nanotechnology* **25** 485501
- [13] Lojpur V, Nikolic M G, Jovanovic D, Medic M, Antic Z and Dramicanin M D 2013 *Appl. Phys. Lett.* **103** 141912
- [14] Lojpur V, Culubrk S and Dramicanin M D 2016 *J. Lumin.* **169** 534–8
- [15] Rabasovic M S, Krizan J, Savic-Sevic S, Mitric M, Rabasovic M D, Marinkovic B P and Sevic D 2018 *J. Spectrosc.* **2018** 3413864
- [16] Vlastic A, Sevic D, Rabasovic M S, Krizan J, Savic-Sevic S, Rabasovic M D, Mitric M, Marinkovic B P and Nikolic M G 2018 *J. Lumin.* **199** 285–92
- [17] Rabasovic M S, Sevic D, Krizan J, Terzic M, Mozina J, Marinkovic B P, Savic Sevic S, Mitric M, Rabasovic M D and Romcevic N 2015 *J. Alloys Compd.* **622** 292–5
- [18] Rabasovic M S, Sevic D, Krizan J, Rabasovic M D, Savic-Sevic S, Mitric M, Petrovic M, Gilic M and Romcevic N 2015 *Opt. Mater.* **50** 250–5
- [19] Sevic D, Rabasovic M S, Krizan J, Savic-Sevic S, Mitric M, Gilic M, Hadzic B and Romcevic N 2017 *Mater. Res. Bull.* **88** 121–6
- [20] Rabasovic M S, Krizan J, Gregoric P, Rabasovic M D, Romcevic N and Sevic D 2016 *Opt. Quantum Electron.* **48** 163
- [21] Nikolic M G, Rabasovic M S, Krizan J, Savic-Sevic S, Rabasovic M D, Marinkovic B P, Vlastic A and Sevic D 2018 *Opt. Quantum Electron.* **50** 258
- [22] Khalid A H and Kontis K 2009 *Meas. Sci. Technol.* **20** 025305
- [23] Allison S W, Goedeke S M, Cates M R, Hollerman W A, Eldridge J I and Bencic T J 2005 *Oak Ridge National Laboratory Report No.* 123055
- [24] Ranson R M, Evangelou E and Thomas C B 1998 *Appl. Phys. Lett.* **72** 2663–4
- [25] Lojpur V, Antic Z and Dramicanin M D 2014 *Phys. Chem. Chem. Phys.* **16** 25636–41
- [26] Li X, Wei X, Qin Y, Chen Y, Duan C and Yin M 2016 *J. Alloys Compd.* **657** 353–7
- [27] Liu R, Liu L and Liang Y 2018 *Opt. Mater. Express* **8** 1686
- [28] Riul A, Justino L G and Caiut J M A 2017 *Nanotechnology* **28** 235601
- [29] Xie D, Peng H, Huang S, You F, Zhang X and Wang G 2015 *Mater. Lett.* **157** 307–10
- [30] Huong T T, Phuong H T, Vinh L T, Khuyen H T, Anh T K and Minh L Q 2016 *J. Sci.* **1** 295–300
- [31] Shirmane L, Feldmann C and Pankratov V 2017 *Physica B* **504** 80–5
- [32] Ningthoujam R S, Singh L R, Sudarsan V and Singh S D 2009 *J. Alloys Compd.* **484** 782–9
- [33] Huignard A, Gacoin T and Boilot J-P 2000 *Chem. Mater.* **12** 1090–4
- [34] Huignard A, Buissette V, Laurent G, Gacoin T and Boilot J-P 2002 *Chem. Mater.* **14** 2264–9
- [35] Riwozki K and Haase M 2001 *J. Phys. Chem. B* **105** 12709–13
- [36] Bhatkar V B 2013 *Int. J. Eng. Sci.* **2** 426–32
- [37] Georgescu S, Cotoi E, Voiculescu A M and Toma O 2008 *Rom. Rep. Phys.* **60** 947–55
- [38] Park W J, Jung M K, Masaki T, Im S J and Yoon D H 2008 *Mater. Sci. Eng.* **146** 95–8
- [39] Sanson A, Giarola M, Rossi B, Mariotto G, Cazzanelli E and Speghini A 2012 *Phys. Rev. B* **86** 214305
- [40] Thakur S and Gathania A K 2015 *J. Electron. Mater.* **44** 3444–9
- [41] Grandhe B K, Bandi V R, Jang K, Ramaprabhu S, Yi S-S and Jeong J-H 2011 *Electron. Mater. Lett.* **7** 161–5
- [42] Chang Y-S, Huang F-M, Tsai Y-Y and Teoh L-G 2009 *J. Lumin.* **129** 1181–5
- [43] Han R, Hu R and Chen K 2009 *Opt. Mater.* **32** 329–33
- [44] Yan-bo Q, Xiao-feng L, Qiang Z, Dan-ping C, Ye-wen W and Wen-bo M 2010 *Mater. Lett.* **64** 1306–8
- [45] Yu M, Lin J, Wang Z, Fu J, Wang S, Zhang H J and Han Y C 2002 *Chem. Mater.* **14** 2224–31
- [46] Matos M G, de Faria E H, Rocha L A, Calefi P S, Ciuffi K J, Nassar E J, Hugo V and Sarmento V 2014 *J. Lumin.* **147** 190–5
- [47] Kumari P, Baitha P K and Manam J 2015 *Indian J. Phys.* **89** 1297–306
- [48] Shanta Singh N, Ningthoujam R S, Niraj Luwang M, Dorendrajit Singh S and Vatsa R K 2009 *Chem. Phys. Lett.* **480** 237–42
- [49] Saltarelli M, Matos M G, de Faria E H, Ciuffi K J, Rocha L A and Nassar E J 2015 *J. Sol-Gel Sci. Technol.* **73** 283–92
- [50] Saltarelli M, Luz P P, Matos M G, de Faria E H, Ciuffi K J, Calefi P S, Rocha L A and Nassar E J 2012 *J. Fluoresc.* **22** 899–906
- [51] Chambers M D, Rousseve P A and Clarke D R 2009 *J. Lumin.* **129** 263–9
- [52] Chang Y-S, Lin H-J, Chai Y-L and Li Y-C 2008 *J. Alloys Compd.* **460** 421–5
- [53] Darwent J R, Flint C D and O’Grady P J 1986 *Chem. Phys. Lett.* **127** 547–50
- [54] Krizan J, Mazaj M, Kaucic V, Bajsic I and Mozina J 2014 *Acta Chim. Slov.* **61** 608–14
- [55] Rabasovic M D, Muric B D, Celebonovic V, Mitric M, Jelenkovic B M and Nikolic M G 2016 *J. Phys. D: Appl. Phys.* **49** 485104
- [56] Anitha M, Ramakrishnan P, Chatterjee A, Alexander G and Singh H 2002 *Appl. Phys. A* **74** 153–62
- [57] Zhou S, Duan C, Yin M, Zhang S and Wang C 2019 *J. Alloys Compd.* **784** 970–4
- [58] Zhou S, Duan C and Han S 2018 *Dalton Trans.* **47** 1599–603
- [59] Zhou S, Duan C, Yin M, Liu X, Han S, Zhang S and Li X 2018 Optical thermometry based on cooperation of temperature-induced shift of charge transfer band edge and thermal coupling *Opt. Express* **26** 27339–45
- [60] Zhou S, Duan C and Wang M 2017 *Opt. Lett.* **42** 4703–6
- [61] Nikolic M G, Jovanovic D J and Dramicanin M D 2013 *Appl. Opt.* **52** 1716–24
- [62] Shao B, Zhao Q, Guo N, Jia Y, Lv W, Jiao M, Lu W and You H 2013 *CrystEngComm* **15** 5776–83
- [63] Binnemans K 2015 *Coord. Chem. Rev.* **295** 1–45
- [64] Ananias D, Brites C D S, Carlos L D and Rocha J 2016 *Eur. J. Inorg. Chem.* **2016** 1967–71
- [65] Culubrk S, Lojpur V, Ahrenkiel S P, Nedeljkovic J M and Dramicanin M D 2016 *J. Lumin.* **170** 395–400
- [66] Dramicanin M D 2016 *Methods Appl. Fluoresc.* **4** 042001
- [67] Đacanin L R, Dramicanin M D, Lukic-Petrovic S R, Petrovic D M and Nikolic M G 2013 *Radiat. Meas.* **56** 143–6
- [68] Đacanin L R, Lukic-Petrovic S R, Petrovic D M, Nikolic M G and Dramicanin M D 2014 *J. Lumin.* **151** 82–7
- [69] Nikolic M G, Al-Juboori A Z, Djordjevic V and Dramicanin M D 2013 *Phys. Scr.* **T157** 014056
- [70] Lojpur V, Antic Z, Krsmanovic R, Medic M, Nikolic M G and Dramicanin M D 2012 *J. Serb. Chem. Soc.* **77** 1735–46
- [71] Lojpur V, Culubrk S, Medic M and Dramicanin M D 2016 *J. Lumin.* **170** 467–71
- [72] Lu Z, Zhongmin C, Xiantao W, Min Y and Yonghu C 2017 *J. Rare Earths* **35** 356–60



Bat guano-dwelling microbes and antimicrobial properties of the pygidial gland secretion of a trogliphilic ground beetle against them

Ivica Dimkić¹ · Slaviša Stanković¹ · Jovana Kabić¹ · Miloš Stupar¹ · Marija Nenadić¹ · Milica Ljaljević-Grbić¹ · Vladimir Žikić² · Ljubodrag Vujisić³ · Vele Tešević³ · Nikola Vesović¹ · Dejan Pantelić⁴ · Svetlana Savić-Šević⁴ · Jelena Vukojević¹ · Srećko Ćurčić¹

Received: 7 November 2019 / Revised: 26 January 2020 / Accepted: 23 February 2020
© Springer-Verlag GmbH Germany, part of Springer Nature 2020

Abstract

Bat guano is an important source of microbial diversity in caves and can be a source of potential pathogens. *Laemostenus (Pristonychus) punctatus* is a guanophilic ground beetle species, which pygidial gland secretion exhibits action against pathogenic and other microbes. The distribution and diversity of microbes in bat guano from a karstic cave were determined in this study. Additionally, antimicrobial activity of the pygidial gland secretion of *L. (P.) punctatus* against guano-dwelling microbes was tested; minimal inhibitory concentration (MIC) and chemical composition of the secretion were analyzed. In total, 63 different bacterial species and 16 fungal morphotypes were isolated from guano samples by the cultivation method and confirmed using phenotypic characterization and molecular identification. There was a difference in the composition of certain microorganisms between the sampling points (cave locations) and between the guano layers. The largest number of bacterial isolates belongs to the genera *Lysinibacillus* and *Paenibacillus*, while *Pseudomonas* species were highly abundant at the innermost sampling point. For the guanophilic fungi, the majority are ascomycetes, with *Penicillium* and *Aspergillus* as the most dominant genera. *Meyerozyma guilliermondii* was the only yeast species found in the guano samples. The most sensitive isolates were *Enterococcus eurekaensis* (MIC 0.007 mg/mL) and *Escherichia fergusonii* (MIC 0.028 mg/mL). The most sensitive fungal isolates were *M. guilliermondii*, *Penicillium expansum*, and *Trichoderma harzianum* (MIC 0.15 mg/mL). This study opens a new possibility for better understanding of ecological relations between microorganisms and trogliphilic ground beetles and for detailed investigations of morpho-anatomical aspects of pygidial glands.

Keywords Microbial diversity · Bat guano · Karstic cave · *Laemostenus (Pristonychus) punctatus* · Pygidial glands

Electronic supplementary material The online version of this article (<https://doi.org/10.1007/s00253-020-10498-y>) contains supplementary material, which is available to authorized users.

✉ Ivica Dimkić
ivicad@bio.bg.ac.rs

¹ University of Belgrade - Faculty of Biology, Studentski Trg 16, Belgrade 11000, Serbia

² Department of Biology and Ecology, University of Niš - Faculty of Science and Mathematics, Višegradska 33, Niš 18000, Serbia

³ University of Belgrade - Faculty of Chemistry, Studentski Trg 12-16, Belgrade 11000, Serbia

⁴ University of Belgrade - Institute of Physics, Pregrevica 118, Belgrade 11080, Serbia

Introduction

Caves represent nutritionally deficient environments, where energy sources and nutrients generally enter in the form of atmospheric gases, as aromatic and polyaromatic compounds from the ground or through water sources. Bat guano is the most important energy source in caves in temperate climates (Poulson and Lavoie 2000). The main sources of microorganisms, although widespread in caves, are usually guano, excrements from other animals and carcasses of animals (Barton 2006; Mulec 2008). In addition to fur-borne bat microorganisms, guano is an important source of microorganisms in caves. Bacterial species identified in guano samples mainly belong to the family *Enterobacteriaceae*, although species from the families

Pseudomonadaceae and *Enterococcaceae* have been identified as well (Di Bella et al. 2003). Jurado et al. (2010) reported the presence of a large number of pathogenic and opportunistic bacteria in caves. Bat guano can serve as a vector for the transmission of diseases between humans and animals (Borda et al. 2014; Vandžurová et al. 2013). Micromycetes (the mycobiota), together with other microorganisms, primarily bacteria, cyanobacteria, and algae, form an integral part of the cave microbiota. Guanophilic fungi are an ecological group of fungi which inhabit guano. They are very common in caves (Barton 2006). Since bat guano can represent a source of potential human and animal pathogens, such as *Pseudogymnoascus destructans* and *Histoplasma capsulatum*, guanophilic fungi were extensively studied in recent years (Medellin et al. 2017; Rocha-Silva et al. 2014). Guano is an important source of microbial aerosolization in caves and thus a threat to human and bat health (Julg et al. 2008). Research of microbial diversity in caves could be of particular importance for determining potential biohazards, especially because interest in cave tourism is increasing nowadays.

Laemostenus (Pristonychus) punctatus (Dejean, 1828) (*Coleoptera: Carabidae*) is an epigeal and sub-lapidicolous ground beetle species, very often trogliphilic and guanophilic, found in caves, burrows of mammals, and artificial hypogean habitats in the southern part of its range (Casale 1988). In the older literature, it was considered a subspecies of the closely related *Laemostenus (Pristonychus) terricola* (Herbst, 1784) (Casale 1988). The range of *L. (P.) punctatus* includes mainly the Balkan Peninsula, but also extends northwards to Slovakia (Casale 1988). It has been reported from caves in eastern, southeastern, and southwestern Serbia (Ćurčić et al. 2007). This predatory beetle mostly feeds in caves on small invertebrates living in guano (Nešić et al. 2008). Trogliphilic populations of the species are more abundant compared to epigeal ones (Nenadić et al. 2017), most likely due to the almost constant environmental conditions in caves throughout the year. *L. (P.) punctatus* is adapted to environmental conditions via production of a secretion mixture by paired pygidial exocrine glands composed of two sets of secretory lobe aggregations, collecting canals, reservoirs, and efferent ducts, which probably serve to protect the beetle from predators (Blum 1981; Nenadić et al. 2016, 2017). Besides the defensive role against predators, the secretion of *L. (P.) punctatus* has also shown an antimicrobial potential (Nenadić et al. 2016, 2017). Recently, chemical composition of the beetle's secretion has been identified using dichloromethane as the extraction chemical (Vesović et al. 2015). The antibacterial and antifungal action of the beetle's secretion against human microbial pathogens (Nenadić et al. 2016) and its antifungal effect against cave-dwelling micromycetes (Nenadić et al. 2017) were recently determined. During biospeleological research conducted in a karstic cave near the city of Niš in southeastern Serbia

(Ogoreliška Pećina Cave), it has been observed that the abundance of *L. (P.) punctatus* is surprisingly high compared to any other invertebrate species inhabiting the same cave or any other cave in Serbia. This suggests that one of the reasons for its high abundance could be that the beetle has certain mechanisms which protect it from pathogenic microbes inhabiting guano situated on the cave floor.

Although morphology of the pygidial glands of *L. (P.) punctatus* has been recently elucidated (Nenadić et al. 2016), nothing is known about their detailed anatomy and ultrastructure. There is therefore a need to obtain better insight into internal structures of the glands using available novel microscopic techniques. A combination of several modern microscopic techniques (scanning electron microscopy (SEM), focused ion beam (FIB) microscopy, and fluorescence microscopy) was used to investigate the pygidial gland system in some ground beetles of the subfamily *Brachininae* (*Brachinus* spp., *Pheropsophus* spp., and *Aptinus* spp.), which possess a similar, but evolutionarily more developed and more complex pygidial glands than the one occurring in *Platyninae*, to which *L. (P.) punctatus* belongs (Di Giulio et al. 2015). Use of fluorescence microscopy without labeling is possible in carabidology due to the autofluorescence of resilin in the cuticular structures of individuals. This phenomenon is very important in morphological and optical analyses of various cuticular structures in ground beetles (e.g., genitalia) (Rabasović et al. 2015). Within the family *Carabidae*, the two-photon excitation fluorescence (TPEF) modality of nonlinear microscopy (NLM) was applied in order to examine and determine *Pheggomisetes*, a specific trechine genus, primarily on the basis of anatomy (Vrbica et al. 2018). Cuticle and certain types of tissues, such as connective tissue (due to the presence of collagen) (Jiang et al. 2011) and muscle tissue (due to the presence of myosin) (Ibrahim et al. 2015; Wallace et al. 2008), the most dominant components of the pygidial gland structures of ground beetles, have a possibility of autofluorescence. Thus, the TPEF modality of NLM can be applied to investigate the morphology of these structures, especially different anatomical aspects of them, both in ground beetles and other insects.

The aims of the current study were (i) to give for the first time an inventory of microbial communities associated with bat guano in a karstic cave from southeastern Serbia (Ogoreliška Pećina Cave); (ii) to evaluate culturable communities and explore the potential of the pygidial gland secretion of *L. (P.) punctatus* against selected bacteria and micromycetes from the same microenvironment using the traditional cultivation approach; (iii) to conduct chemical analysis of the secretion using methanol extraction; and (iv) to report the first detailed data on morphoanatomy of the pygidial glands of *L. (P.) punctatus* using SEM and the TPEF modality of NLM.

Material and methods

Microbial diversity of the Ogoreliška Pećina Cave

Guano samples (each of approximately 8–20 g) were collected in the Ogoreliška Pećina Cave from five different sampling points and two layers (top and bottom layers) followed the protocol described by Ogórek et al. (2016) and Newman et al. (2018). Collection of guano samples was allowed by the Ministry of Agriculture and Environmental Protection of the Republic of Serbia (Permission No. 353-01-2588/2016-17). One sampling point was in the middle part of each cave section. The average thickness of the guano layers was approx. around 6 cm. Samples of guano layers were collected at top and bottom depths of 0.5 and 4 cm, respectively. Names of isolates were given after the cave sampling points and layers of guano where samples were isolated (Supplementary Table S1). Bat guano taken from each sampling site and layer (1 g) was suspended in sterile saline solution (9 mL) and then shaken three times vigorously for 20 min in an Erlenmeyer flask (250 mL), with a 5-min interval of resting between shakings. For differential bacterial growth, R2 minimal medium (bioMérieux, Marcy-l'Étoile, France), and Gibco Luria-Bertani medium (LB) (Thermo Fisher Scientific, Waltham, USA) were used for growing at 25 °C for 48 h. Also, samples were thermally inactivated at 80 °C for 10 min and further grown on LB at room temperature for 48 h. For isolation of fungi, samples from the same batch were plated using serial dilution on potato dextrose agar (PDA) (LAB M Ltd., Heywood, UK), malt extract agar (MEA) (LAB M Ltd., Heywood, UK) and dichloran (18%) glycerol agar (DG18) (LAB M Ltd., Heywood, UK) and incubated at 25 °C. After a 7-day incubation period, the number of colony-forming units (CFUs) per 1 g of guano was calculated as the average from replicates of all used nutrient media.

Preliminary identification of bacterial isolates was performed using phenotypic characterization (morphological observations, Gram staining, and catalase assay). The obtained guanophilic fungal isolates were identified based on macroscopic cultural characteristics of 7-day-old colonies and morphological characteristics of reproductive structures, respectively. Reproductive structures were observed by light microscopy using a Zeiss Axio Imager M.1 microscope equipped with the AxioVision Release 4.6 software (Carl Zeiss AG, Oberkochen, Germany). Preliminary identification of micromycetes was performed using the following identification keys: Raper and Fennel (1965), Pitt (1979), Watanabe (2002), and Samson et al. (2010). To verify identifications based on morphology, molecular identification was applied for selected isolates. The total DNA of bacterial strains was extracted from an overnight bacterial culture incubated at 30 °C in LB with shaking at 180 rpm. Single-spore fungal isolates were grown on MEA for 7 days at 25 °C. After

incubation, mycelium (approx. 100 mg) was harvested and suspended in 200 µL of sterile distilled water. Total genomic DNA extraction for all fungal isolates was performed using the ZR Fungal/Bacterial DNA MiniPrep KIT, according to the protocol of the manufacturer (Zymo Research, Irvine, USA).

Primers used to amplify the regions of specific genes, as well as their corresponding PCR profiles (Jovčić et al. 2009; Kim et al. 2003; O'Donnell and Cigelnik 1997; Roe et al. 2011; White et al. 1990), are listed in Supplementary Table S2. The amplification of all the regions was performed in final volumes of 25 µL, as described by Dimkić et al. (2013) and Savković et al. (2016). The PCR conditions for amplification of bacterial DNA were as follows: an initial denaturation step at 94 °C for 5 min; 30 cycles consisting of a denaturation step of 30 s at 94 °C, primer annealing at 50 °C for 1 min and extension at 72 °C for 30 s; and one last cycle of extension at 72 °C for 7 min. The PCR conditions for amplification of fungal DNA were as follows: one cycle of denaturation at 94 °C for 4 min; 30 cycles of denaturation at 94 °C for 30 s, annealing at 55 °C for 50 s, and extension at 72 °C for 50 s; and one final cycle of extension at 72 °C for 10 min. All PCR products were purified using the QIAquick PCR Purification KIT/250 (QIAGEN GmbH, Hilden, Germany) according to the manufacturer's protocol. Purified PCR products were sequenced commercially using Sanger dideoxy sequencing or chain-termination method with universal primers (Macrogen Inc., Amsterdam, the Netherlands). The obtained sequences were analyzed for homology with gene sequences deposited in the GenBank database through the National Center for Biotechnology Information (NCBI) via the Basic Local Alignment Search Tool (BLAST) search for nucleotides (cutoff value for BLAST hits was 99% of similarity). All sequences were aligned using the ClustalW multiple sequence alignment in the BioEdit program (ver. 7.1.3.0) (Hall 1999). In loci with duplications or transversions, corrections were made according to the reference strain sequences. Phylogenetic trees were constructed in MEGA 7 (Kumar et al. 2016) using the neighbor-joining method with Kimura's two-parameter nucleotide substitution model (Kimura 1980) for bacterial sequences and the maximum likelihood method based on Tamura's three-parameter model (Tamura et al. 2013) for fungal sequences. The trees are drawn to scale, with branch lengths measured in the relative number of substitutions per site. All positions containing gaps and missing data were eliminated. Additionally, the obtained bacterial sequences were grouped based on the layer of guano samples and the cave section. Within each group, the sequences were clustered into bacterial classes based on similarity of the BLAST results and the Ribosomal Database Project (RDP) classifier (cutoff value for BLAST and RDP classifier results was each 99% of similarity).

Bacterial and fungal sequences were submitted to the NCBI database under the GenBank submission numbers

SUB6039655 and SUB6046415, respectively. GenBank accession numbers were received for bacterial strains (MN197930-MN198090), as well as for fungal species based on the ITS region (MN206946-MN206972) and the β -tubulin gene (under BankIt number 2248777) (MN233612-MN233631) (Supplementary Tables S3 and S4).

Collection and handling of ground beetle specimens

Adult individuals (41 specimens of both genders) of *L. (P.) punctatus* were collected manually during November of 2017 from the guano situated on the floor of the Ogorelička Pećina Cave, village of Sićevo, near Niš, Svrljiške Planine Mts., southeastern part of Serbia. Collection of the ground beetle was allowed by the Ministry of Agriculture and Environmental Protection of the Republic of Serbia (Permission No. 353-01-2588/2016-17). Beetles were gathered at five sampling points, which correspond to sampling points of guano. Insects were collected from a defined surface with a high amount of guano at each sampling point. Collection time was not limited and lasted approximately 2 h (in average 25 min per sampling point). Detected environmental conditions within the cave sections and the number of collected adult beetles are shown in Supplementary Table S5. Live ground beetles were transported and kept in cool portable plastic boxes for a few days before taking samples of the pygidial gland's content. We maintained constant temperature of 10 °C, total darkness, and moist soil conditions using soil from the collecting site. The beetles were fed on earthworms and springtails collected from the Ogorelička Pećina Cave. After analyses, dry pinned beetle specimens were deposited in the collection of the Institute of Zoology, University of Belgrade - Faculty of Biology, Belgrade, Serbia (Supplementary Fig. S1).

Chemical extraction and analyses

Preparation of samples for gas chromatography-mass spectrometry (GC-MS) was performed in the laboratory at room temperature. Specimens of *L. (P.) punctatus* were milked into a 12-mL glass vial with absolute methanol (0.5 mL) for 5 min. The beetles were stimulated to discharge pygidial gland secretions by squeezing the abdomens against the wall of a vial containing extraction solvent. To eliminate the effects of composition-altering oxidation and degradation of compounds, GC-MS was performed immediately after sampling. The amount of discharged pygidial gland secretion was measured on a Sartorius Model 2405 analytical balance with 0.001 mg resolution (Sartorius Group, Göttingen, Germany). Weight of the vial was measured on the analytical balance prior to (empty vial) and after discharging the pygidial gland secretion (with the secretion inside). The difference in weight

represented the total amount of secretion released by the analyzed beetle species.

The GC and GC-MS analyses were performed in the splitless mode. A 7890A GC system (Agilent Technologies, Santa Clara, USA) equipped with a 5975C inert XL EI/CI mass selective detector (MSD) and a flame ionization detector (FID) (Agilent Technologies, Santa Clara, USA) connected by capillary flow technology through a two-way splitter were used for analyses. The injection volume was 1 μ L, the injector temperature was 240 °C and the transfer line temperature was 280 °C. The carrier gas (He) flow rate was 2.0 mL/min at 40 °C (constant pressure mode). Temperature of the HP-INNOWax column (30 m length, 0.32 mm i.d., 0.25 μ m film thickness) (Agilent Technologies, Santa Clara, USA) was programmed linearly in a range of 40–240 °C at a rate of 10 °C/min, with a final 10-min hold. The FID temperature was 300 °C. The EI mass spectra (70 eV) were acquired in a range of 40–550 *m/z*, and the ion source temperature was 230 °C for all analyses. Library search and mass spectral deconvolution and extraction were performed at the Faculty of Chemistry, University of Belgrade database containing 4951 spectra and commercially available NIST11 and Wiley07 libraries containing approximately 500,000 spectra using the NIST Automated Mass Spectral Deconvolution and Identification System (AMDIS) software (ver. 2.70) (Kind 2003). Relative percentages of identified compounds were computed from corresponding peak areas from a GC-FID chromatogram.

Antimicrobial assays

Preparation of samples for antimicrobial analyses was performed in the laboratory at room temperature. To eliminate the effects of composition-altering oxidation and degradation of compounds, antimicrobial analyses were performed immediately after sampling. The broth microdilution method of Ristivojević et al. (2016) was used in the antibacterial assay to determine the minimum inhibitory concentration (MIC) and minimum bactericidal concentration (MBC) for the secretion obtained from the pygidial glands of *L. (P.) punctatus* specimens. A modified microdilution technique (Daouk et al. 1995; Hänel and Raether 1988) was used in the antifungal assay. Final tested concentration of the secretion was in a range of 0.007–0.225 mg/mL for 12 selected bacterial species and in a range of 0.1–1 mg/mL for the five most common isolated fungal species. Concentration of the solvent (methanol) was 10%. Two-fold serial dilutions of the secretion were made with Luria-Bertani (LB) broth and Malt Extract Broth (MEB) in 96-well microtiter plates. In addition to a negative control (bacterial and fungal growth control) and a sterility control, the antibiotic streptomycin (in concentration range of 0.0063–0.2 mg/mL)

and the commercial fungicide nystatin (in a concentration range of 0.1–1 mg/mL) were used as positive controls. Each well, except in the case of the sterility control, was inoculated with 20 μ L of bacterial culture (1×10^6 CFU/mL, suspensions were adjusted to McFarland 0.5 standard turbidity), reaching a final volume of 200 μ L. Conidia and yeast cells in the case of *Meyerozyma guilliermondii* were washed from the surface of agar slants with sterile saline (0.85%) containing 0.1% Tween 20 (v/v). In order to prepare inocula, conidia/cell suspensions were adjusted with sterile saline (0.85%) to a concentration of approximately 1.0×10^5 in a final volume of 100 μ L per well in 96-well microtiter plates. The plates were incubated at 30 °C for 24 h and at 25 °C for 72 h for bacterial and fungal growth, respectively. Spectrophotometric bacterial growth readings were performed using a microplate reader (Multiskan FC Microplate Photometer, OD 570 nm, Thermo Fisher Scientific, Waltham, USA), after which 22 μ L of resazurin (resazurin sodium salt ($C_{12}H_6NNaO_4$)) (TCI, Zwijndrecht, Belgium), at a final concentration of 0.675 mg/mL, was added to each well and the microtiter plates were incubated at 30 °C for two additional hours. Following incubation, the resazurin color change reaction was observed. The MIC values were determined as indicated by no change in color, while MBCs were obtained by sub-culturing the test dilutions from each well without color change on agar plates and incubating them for 24 h. The lowest concentration showing no bacterial growth was defined as the MBC value. In the case of the tested fungal species, MIC values of the secretion were determined as the lowest used concentration without visible growth detected with a binocular microscope. Further, minimum fungicidal concentrations (MFCs) were determined by serial sub-cultivation (2 μ L) into microtiter plates each containing 100 μ L of MEB. The lowest concentration with no detected visible fungal growth was defined as the MFC, indicating 99.5% killing of the original inoculum. The results were expressed in mg/mL.

SEM and TPEF modality of NLM analyses

Preparation of tissues

Pygidial glands of *L. (P.) punctatus* were first isolated and tissue of the glands was then dehydrated through a series of ethanol solutions of increasing concentrations (30, 50, 70, 90, and 100%). The structures were stored in 100% ethanol at 4 °C before SEM recording. In order to obtain a detailed insight into morphology of the pygidial glands of *L. (P.) punctatus*, the TPEF modality of NLM was used for visualization. After isolation, the pygidial glands were stored in concentrated glycerol.

Experimental setup and procedure

Scanning electron microscope images were obtained with a field emission gun scanning electron microscope (MIRA3 FEGSEM, Tescan, Brno, Czech Republic) in the high-vacuum mode at an acceleration voltage of 15 kV. The electron beam current was between 750.18 pA and 1.40 nA, depending on imaging conditions, while pressure in the column was around 127.19×10^{-3} Pa. The samples were coated with gold/palladium to make them conductive for SEM analyses.

Two-femtosecond lasers were used for the TPEF modality of NLM of all samples: a Ti-sapphire laser (76-MHz repetition rate, within the tuning range of 700–1000 nm) (Mira 900-F, Coherent, Santa Clara, USA) pumped by a 10-W laser (Verdi V10, Coherent, Santa Clara, USA) at 532 nm, and (as a secondary source of excitation) a 1040-nm Yb KGW femtosecond laser (GLX-Yb) (Time-Bandwidth Products AG, Schlieren, Switzerland). A Plan Apochromat microscope objective (20×0.8 , 500 μ m field of view) (Carl Zeiss, Jena, Germany) was used for sample imaging. Galvanometric scanning mirrors (Cambridge Technology 6215H, Cambridge, USA) were used for raster-scanning. Recordings were performed at different power settings (80–150 mW), depending on the sample. An EOS 50D digital camera (Canon, Tokyo, Japan) was used for adjustment and classical transmission microscopy. VolView 3.4 open-source software (Kitware, Inc., Clifton Park, USA) was used for 3D visualization of a set of slices.

Results

Microbial diversity of the studied cave

Bacterial diversity

In total, 220 bacterial isolates were originally obtained from the guano samples, but 161 isolates were selected for further identification based on their biochemical and morphological characteristics. We preliminarily identified 117 isolates as Gram-positive bacteria, nine isolates as Gram-negative bacteria, while 35 isolates exhibited a variable Gram reaction. A positive catalase reaction was shown by 119 isolates, while 42 isolates showed a negative reaction. The obtained and purified isolates were divided into three groups, depending on the different isolation method and media applied. Isolates that showed growth after incubation at 80 °C were placed in the group of thermal inactivation (designated T); the oligotrophic group (designated O) contains isolates that grew on depleted substrates; and the third group was the LB growth group of isolates (without a prefix).

Further identification of the selected isolates involved amplification and sequencing of the 16S rRNA gene. The

conducted BLAST analysis of 161 isolates yielded 135 Gram-positive and 26 Gram-negative members of the phyla *Actinobacteria*, *Firmicutes*, and *Proteobacteria*. Dendrograms with phylogenetic relationships of isolates and reference strains were divided into two groups, depending on the Gram reaction (Figs. 1 and 2). Only one of each representative bacterial species among all identified isolates was placed on the dendrograms for a better and easier presentation.

Within the Gram-positive bacteria group (Fig. 1), we identified 26 strains of *Viridibacillus arvi*; 13 strains of *Bacillus mycoides*; 10 strains of *Lysinibacillus parvivoronicapiens*; nine strains of *Bacillus simplex*; seven strains of *Paenibacillus odorifer*; six strains of *Bacillus thuringiensis*; five strains of *Enterococcus faecalis*, *Staphylococcus epidermidis*, and *Paenibacillus polymyxa*; four strains of *Bacillus toyonensis*; three strains of *Brevibacterium frigoritolerans* and *Psychrobacillus psychrodurans*; two strains of *Paenibacillus wynnii*, *Paenibacillus taichungensis*, *Paenibacillus anaericanus*, *Sporosarcina globispora*, *Sporosarcina aquimarina*, *Bacillus amyloliquefaciens*, and *Bacillus mojavensis*; and one strain of *Lysinibacillus macrolides*, *Lysinibacillus contaminans*, *Lysinibacillus sphaericus*, *Lysinibacillus mangiferihumi*, *Rhodococcus jialingiae*, *Rhodococcus cerastii*, *Staphylococcus aureus*, *Staphylococcus caprae*, *Staphylococcus arlettae*, *Paenibacillus peoriae*, *Paenibacillus ginsengisoli*, *Paenibacillus amyolyticus*, *Micrococcus yunnanensis*, *Microbacterium hydrocarbonoxydans*, *Bacillus subtilis*, *Bacillus cereus*, *Bacillus weihenstephanensis*, *Bacillus pumilus*, *Bacillus clausii*, *Bacillus eiseniae*, *Bacillus bataviensis*, *Bacillus oceanisediminis*, *Bacillus soli*, *Bacillus endoradicis*, and *Enterococcus eurekensis*.

Within the group of Gram-negative bacteria (Fig. 2), we identified three strains of *Pseudomonas brenneri* and *Serratia proteamaculans*; two strains of *Pseudomonas putida*, *Comamonas jiangduensis*, and *Citrobacter freundii*; and one strain of *Serratia quinivorans*, *Buttiauxella noackiae*, *Citrobacter gillenii*, *Escherichia fergusonii*, *Kluyvera intermedia*, *Brevundimonas bullata*, *Pseudomonas oryzae*, *Pseudomonas miguelae*, *Pseudomonas fragi*, *Pseudomonas psychrophila*, *Pseudomonas mucidolens*, *Pseudomonas donghuensis*, *Pseudomonas monteillii*, and *Pseudomonas helmanticensis*.

By the selected methods of cultivation and identification, a total of 63 different bacterial species were isolated from the guano samples. Thirty-three different bacterial species were isolated within the thermal inactivation group, 28 within the LB group, and 23 within the oligotrophic group. The isolated bacterial species partly overlapped using different cultivation methods. When the thermal inactivation method was used, most of the isolated bacteria belonged to *Paenibacillus* and *Sporosarcina* sporulating bacteria, while some nonsporulating species of the genera *Pseudomonas*, *Micrococcus*, and

Microbacterium were also obtained by this method of cultivation. Within the LB group, most of the isolated bacteria belonged to the genera *Bacillus* and *Lysinibacillus*, and representatives of *L. contaminans*, *L. mangiferihumi*, *L. macroides*, *B. subtilis*, *B. eiseniae*, *B. pumilus*, *B. clausii*, and *B. bataviensis* were isolated only within this group. Within the group of oligotrophic bacteria, representatives of the species *B. bullata*, *C. freundii*, *C. gillenii*, *K. intermedia*, *L. sphaericus*, and *E. fergusonii* were characteristic. All of the analyzed sequences were identified as members of five bacterial classes: α -*Proteobacteria*, β -*Proteobacteria*, γ -*Proteobacteria*, *Actinobacteria*, and *Bacilli*. The results showed that bacteria of the *Bacilli* class have the highest diversity and prevalence according to identified number of species, regardless of their count, in the cultured microbial community, in both of the examined guano layers and in different parts of the cave's premises. The number of species collected per each bacterial class in the two guano layers is shown in Fig. 3a. In the upper guano layer, *Bacilli* were represented by less species (75%) than in the lower layer (88.6%), while more cultured species from γ -*Proteobacteria* and *Actinobacteria* were present in the upper layer. Members of α -*Proteobacteria* and β -*Proteobacteria* had comparable number of identified species. *Bacilli* were also prevalent at all sampling points, as shown in Fig. 3b. The highest bacterial richness was observed at the second (24 bacterial species) and last (26 bacterial species) sampling points. At the first and third sampling points, somewhat fewer species were recorded (20 and 19 species, respectively), while the fourth point had the lowest bacterial richness (13 species) (Supplementary Table S3).

Fungal diversity

In total, 67 fungal isolates were obtained at all sampling points. After identification of macro- and micromorphological features, 29 at first glance different morphotypes were sent for ITS and β -tubulin gene sequencing. Fungi were identified on the basis of homology of the obtained sequences with reference strains from the GenBank database, thereby confirming the identification based on morphological features (Fig. 4). A total of 16 fungal morphotypes were isolated from the tested guano samples (Supplementary Table S4). The majority of fungi were ascomycetes (87.5%). *Mucor racemosus*, *Peniophora lycii*, and *M. guilliermondii* were the only *Mucoromycotina*, basidiomycete, and ascomycetous yeast species in the analyzed samples, respectively. The largest group of guanophilic fungi in the Ogorelička Pečina Cave consisted of members of the genera *Penicillium* and *Aspergillus* (25%), both represented with four identified species (*P. citrinum*, *P. sanguifluum*, *P. expansum* and *P. purpurogenum* (teleomorph *Talaromyces*

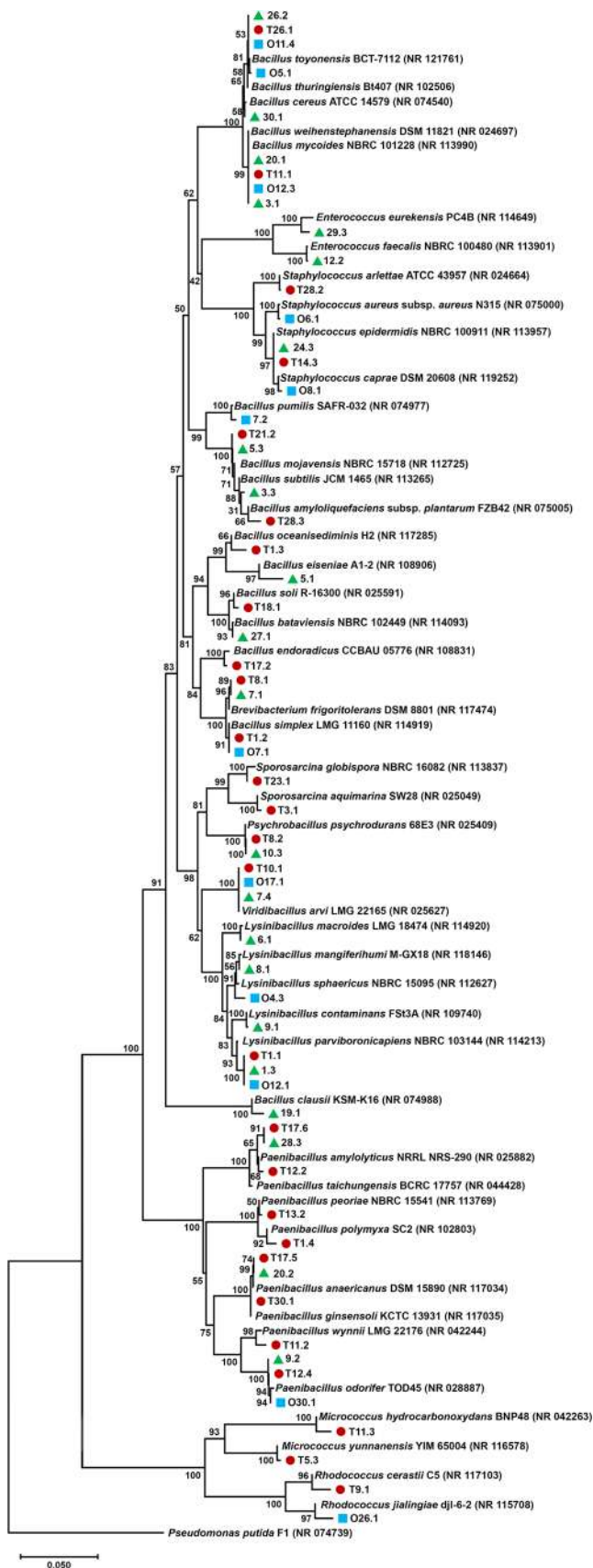


Fig. 1 Neighbor-joining phylogenetic tree based on 16S rRNA sequences (1500 bp) showing relationship of the representative Gram-positive isolates from the bat guano. Distances were calculated using Kimura's two-parameter model. *P. putida* was used as an outgroup. Red circles represent strains from the thermal inactivation group; blue squares, strains from the oligotrophic group; and green triangles, strains from the LB group

purpurogenus); and *A. flavus*, *A. aureolatus*, *A. pallidofulvus* and *A. creber*). *A. creber* and *Cosmospora viridescens* were isolated only from the upper guano layer (Supplementary Table S1), and both were documented only at the innermost sampling point (Supplementary Table S4). *Humicola grisea* was also isolated at the same sampling point. Apart from that, no other significant differences of fungal distribution were observed between the examined guano layers. The highest fungal diversity (75% of all identified species) was documented at the innermost sampling point, followed by the fourth sampling point (68.8%). The highest isolation frequency (100%) was recorded for *M. guilliermondii*, *P. citrinum*, and *Trichoderma harzianum*. These species were documented in both guano layers at all sampling points in the Ogorelička Pečina Cave. Among all *Penicillium* species, *P. citrinum* was the most common isolated fungal species. Apart from lower diversity in general, the highest concentrations of fungal propagules detected at the fourth (on MEA growth medium) and second (on DG18 growth medium) sampling points were 7146.2 and 6384.61 CFU/g, respectively. The lowest fungal concentration was recorded in the lower layer at the first sampling point on DG18 (286.73 CFU/g). In all examined parts of the cave's premises and on all media used for fungal isolation, a significantly higher fungal concentration was recorded in the upper guano layer than in the lower one (Fig. 5).

Occurrence and abundance of *L. (P.) punctatus* in the investigated cave

The largest number of adult specimens of *L. (P.) punctatus* was collected in the Ogorelička Pečina Cave in total darkness, at sampling points 2 (relative atmospheric humidity 86%, air temperature 15 °C) and 3 (relative atmospheric humidity 90%, air temperature 13.8 °C) (12 and 11 individuals, respectively) (Supplementary Table S5).

Total amount of discharged pygidial gland secretion of *L. (P.) punctatus* and its chemical composition

The total amount of the discharged pygidial gland secretion from 41 specimens of the tested ground beetle species was 0.189 ± 0.001 mg. The amount of discharged secretion per one beetle specimen was 0.005 ± 0.001 mg.

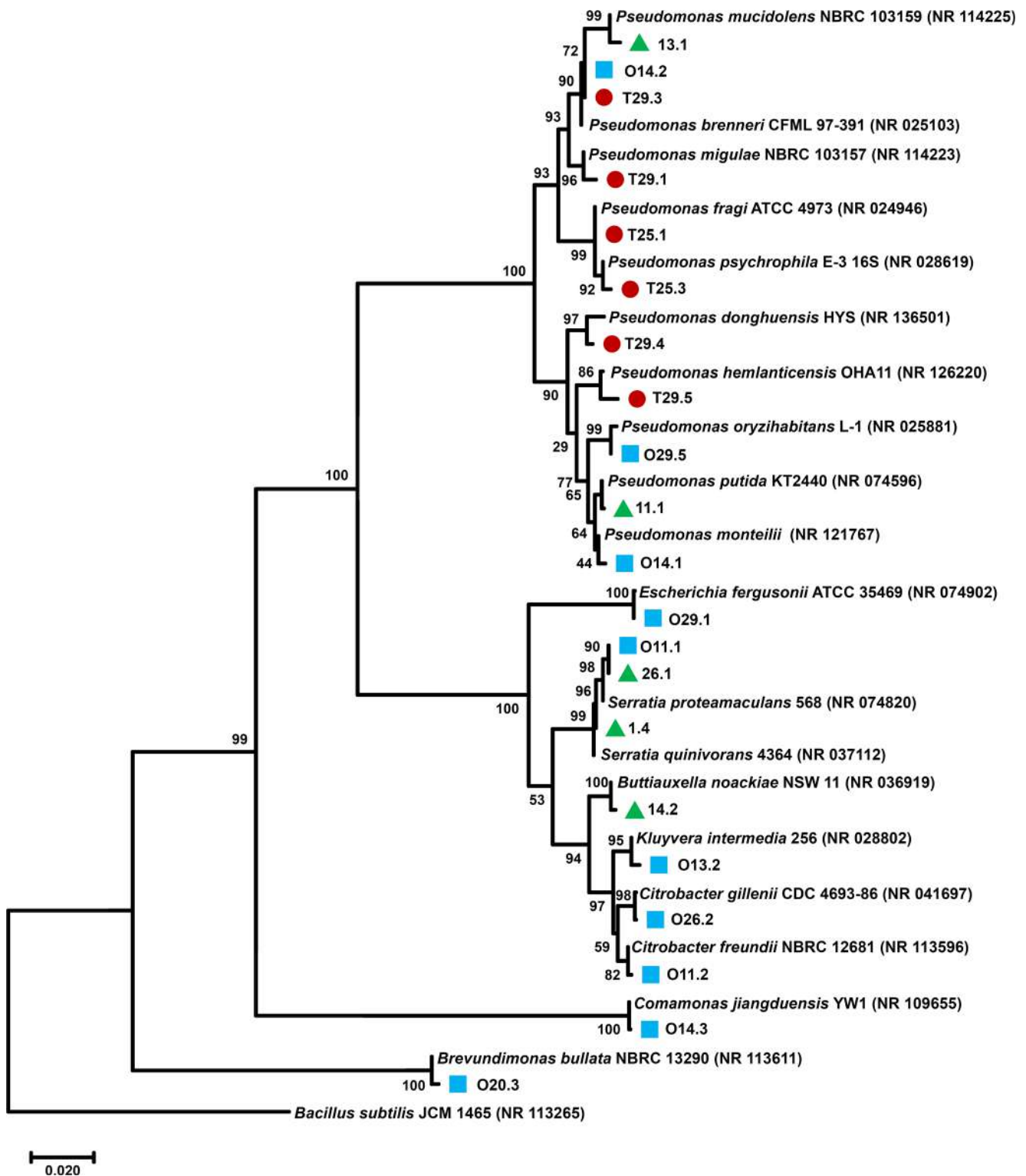


Fig. 2 Neighbor-joining phylogenetic tree based on 16S rRNA sequences (1500 bp) showing relationship of the representative Gram-negative isolates from the bat guano. Distances were calculated using Kimura's two-parameter model. *B. subtilis* was used as an outgroup.

Red circles represent strains from the thermal inactivation group; blue squares, strains from the oligotrophic group; and green triangles, strains from the LB group

Concentration of the secretion dissolved in absolute methanol was 0.063 mg/ml. The experiment was repeated three

times during a short period of time in order to confirm validity of the results.

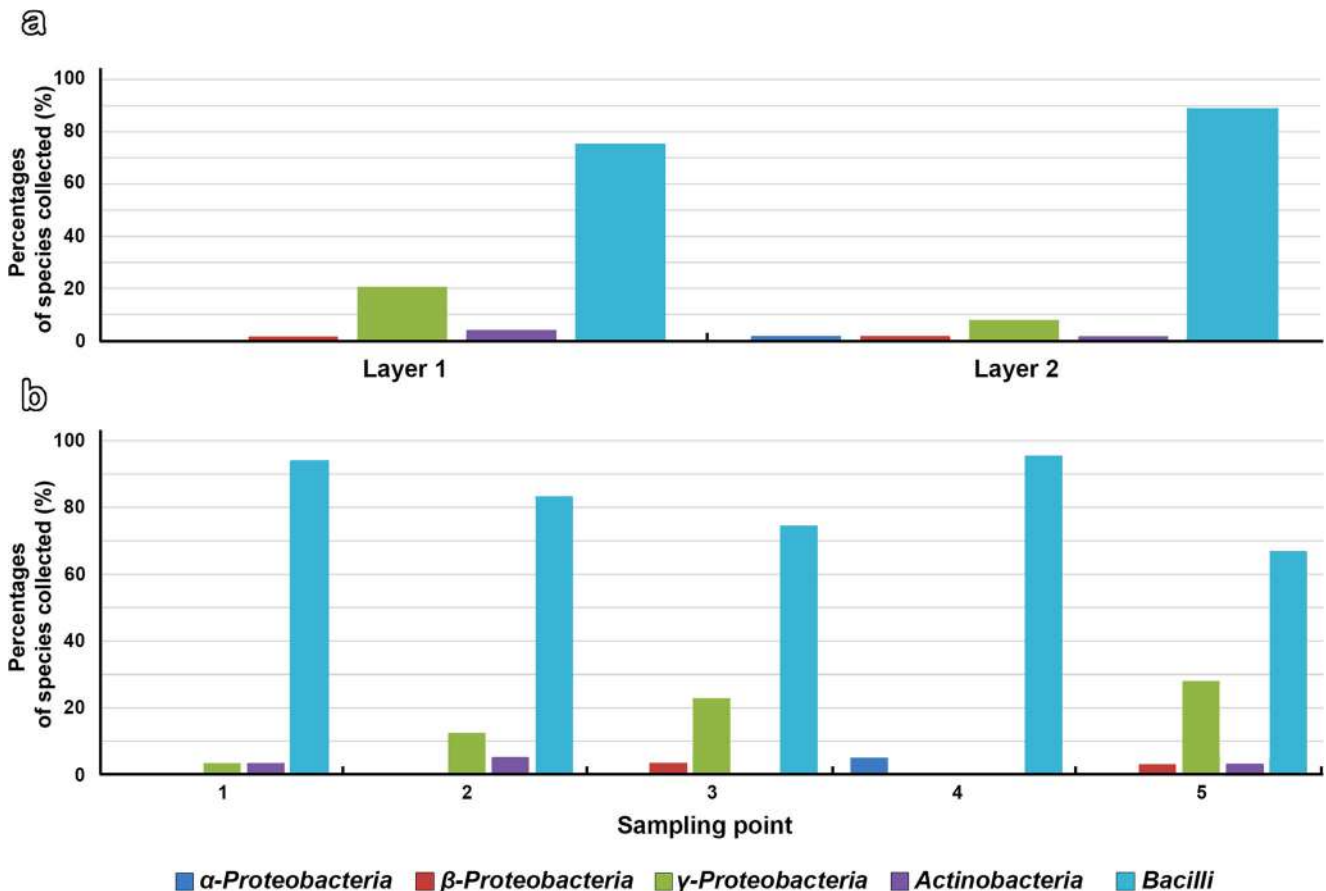


Fig. 3 Percentages of species collected per bacterial class depending on guano layers (a) and sampling points (b). Relative distribution was obtained by statistical and phylogenetic analysis of their 16S rRNA sequence. Layer 1, upper guano layer; layer 2, lower guano layer

Chemical analysis yielded a total of four detected and identified compounds from the methanol extract of the pygidial gland secretion of *L. (P.) punctatus*: one alkane, two low molecular weight carboxylic acids, and one ester. Major components of the secretion are undecane (58.9%) and dodecyl acetate (36.7%), followed by acetic (2.5%) and formic (1.9%) acids (Supplementary Fig. S2; Table 1).

Antimicrobial effect of the pygidial gland secretion of *L. (P.) punctatus* against guano-dwelling microbes

In the initial testing, 12 of the most common Gram-positive isolates (*E. faecalis* 3.2; *E. eurekaensis* 29.3; *R. jialingiae* O26.1; *M. yunnanensis* T5.3; *B. thuringiensis* 26.2; *B. cereus* 30.1; *L. sphaericus* O4.3; *P. polymyxa* T21. 1; *V. arvi* T26.2; *B. frigoritolerans* 7.1; *S. aureus* O6.1; and *S. epidermidis* 24.3) and five Gram-negative isolates (*E. fergusonii* O29.1; *P. putida* 11.1; *C. freundii* O11.3; *S. proteamaculans* O11.1; and *K. intermedia* O13.2) were chosen from all of the cave's sampling points. On the basis of initial testing using the well diffusion method (data not shown), 12 of the most sensitive bacterial strains were selected for further testing using the MIC assay technique. Isolates

E. faecalis, *B. frigoritolerans*, *S. aureus*, *S. epidermidis*, and *K. intermedia* were the most resistant in the initial testing of antibacterial activity of the secretion, so they were excluded from further analyses. The results obtained in testing antibacterial activity of the secretion, spectrophotometrically measured at OD 570 nm, are shown in Supplementary Fig. S3. As the final confirmation of spectrophotometric readings, we used the resazurin reaction of MIC and MBC values (Table 2). The most sensitive bacterial isolate was *E. eurekaensis* (with the lowest MIC value, namely, 0.007 mg/mL), and at the same time, it possessed antibiotic resistance to streptomycin at the highest tested concentration. Other Gram-positive isolates generally also showed higher susceptibility, between 0.056 and 0.113 mg/mL for the majority of them (the most resistant were *B. cereus* and *P. polymyxa*), compared to Gram-negative ones. Interestingly, among all the tested Gram-negative isolates, *E. fergusonii* showed a marked sensitivity to the secretion (0.028 mg/mL), almost twice as high as sensitivity to the tested antibiotic. On the other hand, the pygidial gland secretion of *L. (P.) punctatus* had a weaker effect on the tested fungal strains than on the bacterial strains. Lower MIC and MFC values were achieved against *M. guilliermondii*, *P. expansum*, and *T. harzianum*, with fungistatic and

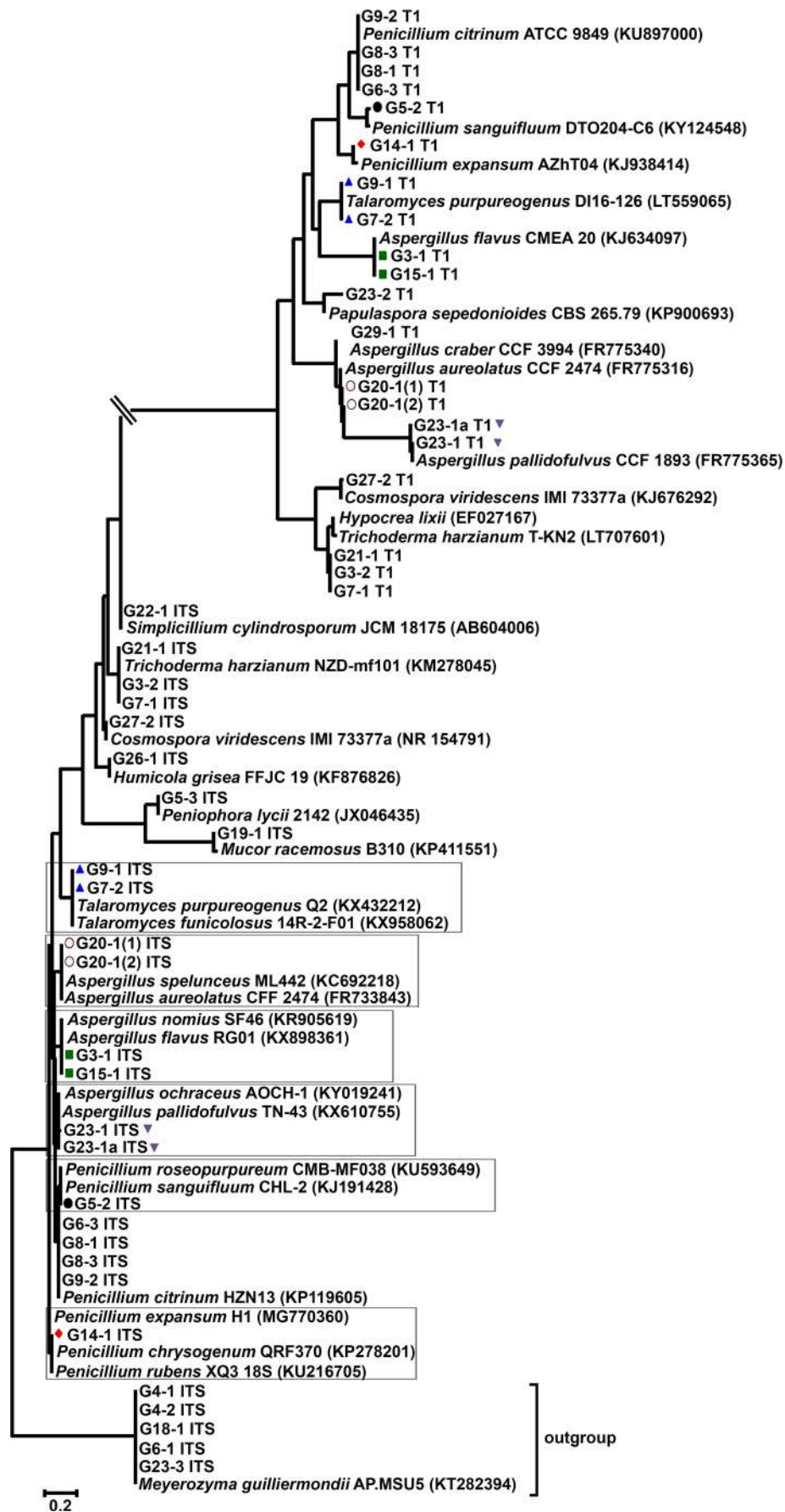


Fig. 4 Maximum likelihood phylogenetic tree based on the ITS region and β -tubulin gene (T1) as ultimate confirmation of species status. Distances were calculated using Tamura's three-parameter model. A group of strains belonging to *M. guilliermondii* was used as an outgroup. Framed squares show all unidentified species at the ITS level, in contrast to confirmation by sequencing the β -tubulin gene

fungicidal action in the concentration range of from 0.15 to 0.30 mg/mL. The highest MIC and MFC values were scored for *P. citrinum* (0.3 and 0.6 mg/mL, respectively). This isolate also proved to be the most resistant in nystatin treatment.

Morphology and anatomy of the pygidial glands of *L. (P.) punctatus*

Spherical secretory lobes of variable diameter (average value of 200 μ m) are present in a large number (approximately 50–60 per gland) (Figs. 6, 7a, b, and 8a; Supplementary Files S1 and S2). In the TPEF modality of NLM images, these are of circular form in cross section (Fig. 8b). Diameter of a randomly selected single radial collecting canal (Fig. 7c) is approximately 16.19 μ m. Tracheoles are in close connection with the pygidial gland system, especially with radial collecting canals (Figs. 7b and 8a). The main collecting canal (Figs. 6, 7f, and 8c) connects secretory lobes with a reservoir in the reservoir's concave zone called the hilum, positioned in its middle part (Fig. 6; Supplementary Files S3 and S4). The length of the main collecting canal is 10–15 mm, while its diameter is about 120 μ m (Fig. 8d). The muscle-coated reniform reservoir is

Table 1 Chemical composition of methanol extract of the pygidial gland secretion of *L. (P.) punctatus* analyzed by GC-FID and GC-MS

Peak	t_R (min) ^a	Compound	Relative percentage (%) ^b
1	3.91	Undecane	58.9
2	8.80	Acetic acid	2.5
3	9.54	Formic acid	1.9
4	14.22	Dodecyl acetate	36.7

t_R retention time

^a Obtained from GC-MS data on HP-INNOWax capillary column

^b Percentages calculated from GC-FID peak areas

about 1.1 mm in diameter (Fig. 7d) and shows a fine regular parallel arrangement of muscle fibers (Fig. 7e). The thickness of its muscle wall is about 130 μ m (Fig. 8e). The secretion of the pygidial glands is transported from the reservoir to an efferent duct (Fig. 7d), through which it is discharged to the outside via an opening (Fig. 6). No morphological or anatomical differences of glandular structure were observed between the sexes.

Discussion

Microbial distribution and diversity of cave guano samples

Of the 63 different bacterial species detected using three methods of cultivation, only some of them overlapped using

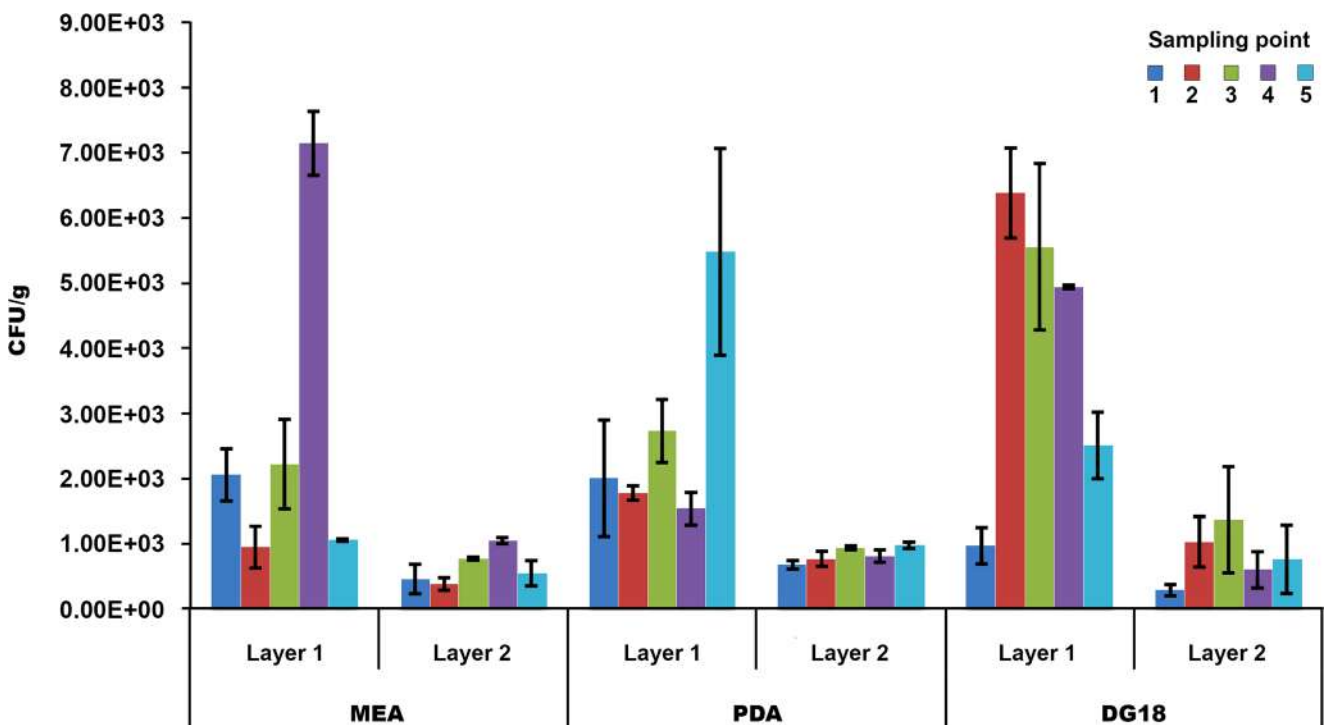


Fig. 5 Fungal density (CFU/g) documented on media used (MEA, PDA, DG18) at all sampling points in both guano layers. Layer 1, upper guano layer; layer 2, lower guano layer

Table 2 Minimum inhibitory concentration (MIC), minimum bactericidal concentration (MBC) and minimum fungicidal concentration (MFC) (mg/mL) of the pygidial gland secretion of *L. (P.) punctatus* compared to a positive control (streptomycin/nystatin)

No.	Strain name	<i>L. (P.) punctatus</i> pygidial gland secretion		Streptomycin/nystatin	
		MIC	MBC/MFC	MIC	MBC/MFC
1	<i>Enterococcus eurekensis</i> 29.3	0.007	0.113	–	–
2	<i>Rhodococcus jialingiae</i> O26.1	0.056	0.113	0.050	0.200
3	<i>Micrococcus yunnanensis</i> T5.3	0.113	0.225	0.200	–
4	<i>Bacillus thuringiensis</i> 26.2	0.056	0.225	–	–
5	<i>Bacillus cereus</i> 30.1	0.225	–	0.025	0.200
6	<i>Lysinibacillus sphaericus</i> O4.3	0.056	0.113	–	–
7	<i>Paenibacillus polymyxa</i> T21.1	0.225	–	0.013	0.025
8	<i>Viridibacillus arvi</i> T26.2	0.113	0.225	0.006	0.013
9	<i>Escherichia fergusonii</i> O29.1	0.028	0.225	0.050	0.200
10	<i>Pseudomonas putida</i> 11.1	0.225	–	0.200	–
11	<i>Citrobacter freundii</i> O11.3	0.225	–	–	–
12	<i>Serratia proteamaculans</i> O11.1	0.225	–	0.200	–
13	<i>Meyerozyma guilliermondii</i> G13-4	0.15	0.30	0.05	0.05
14	<i>Aspergillus flavus</i> G3-1	0.22	0.30	0.05	0.25
15	<i>Penicillium citrinum</i> G5-1	0.30	0.60	0.50	1.00
16	<i>Penicillium expansum</i> G14-1	0.15	0.30	0.50	0.75
17	<i>Trichoderma harzianum</i> G3-2	0.15	0.30	0.25	0.75

– not determined at the maximum concentration tested

different methods of cultivation, indicating that these methods proved to be adequate for testing the diversity of sporulating and oligotrophic bacteria. The oligotrophic method of selection made it possible to isolate bacterial species (slow growers and less abundant) which in plating on a rich nutrient medium would be suppressed by other, more dominant heterotrophic bacterial species. Although the thermal inactivation method made isolation of sporulating bacteria possible, some nonsporulating species from the genera *Pseudomonas* and *Micrococcus* were also obtained. Suzina et al. (2004) indicated that certain nonsporulating bacteria, ones such as *Pseudomonas* spp. and *Micrococcus* spp., under unfavorable environmental conditions can form specialized structurally complex resting cells, which are important for the state of constitutive dormancy. In the same research, it was shown that these resting cells included cyst-like cells, which were characterized by a thickened or a multiprofiled cell wall (CW), typically made up of a layer of preexisting CW and one to three de novo synthesized murein layers, and by the presence of large intramembrane particles. Additionally, there was a difference in the composition of certain species between the sampling points. At the first two sampling points, a greater number of bacteria from the genera *Lysinibacillus* and *Paenibacillus* occurred, while there were fewer members of these genera at the last three sampling points. Bacteria from the phylum *Actinobacteria* were detected only at the first two sampling points and at the last, innermost sampling point. At the last

sampling point, the highest percentage of members of the class γ -*Proteobacteria* was observed, among which the highest diversity was of *Pseudomonas* species. Bacteria of the genus *Pseudomonas* can prevail in certain guano micro-environments, probably due to their tolerance to different physical conditions and metabolic diversity (Mulec et al. 2002). The great diversity of bacterial species in the cave's guano can also be explained by structure of the Ogorelička Pečina Cave, proximity to its entrance in the case of the first two sampling points, or high humidity in the cave's inner part in the case of the last sampling point. The identified bacteria coincide with the previously described composition of bacterial communities in caves. Examination of a cave in Dunhuang (Gansu Province, China) revealed the presence of bacteria from different genera, among which the most prominent members were from the genera *Bacillus* and *Paenibacillus* (Ma et al. 2015). Analysis of microbial diversity in the Fairy Cave (Colorado, USA) showed species of the phylum *Actinobacteria* to be predominant, followed by bacteria of the phylum *Firmicutes*, and classes of α -*Proteobacteria*, β -*Proteobacteria*, and γ -*Proteobacteria* (Barton 2006). In the present case, however, the composition of certain bacterial species deviates from the results obtained in earlier examinations of guano samples (De Mandal et al. 2015; Di Bella et al. 2003). In the light of those results (De Mandal et al. 2015; Di Bella et al. 2003), a higher abundance of *Chloroflexi*, *Actinobacteria*, and *Proteobacteria* was

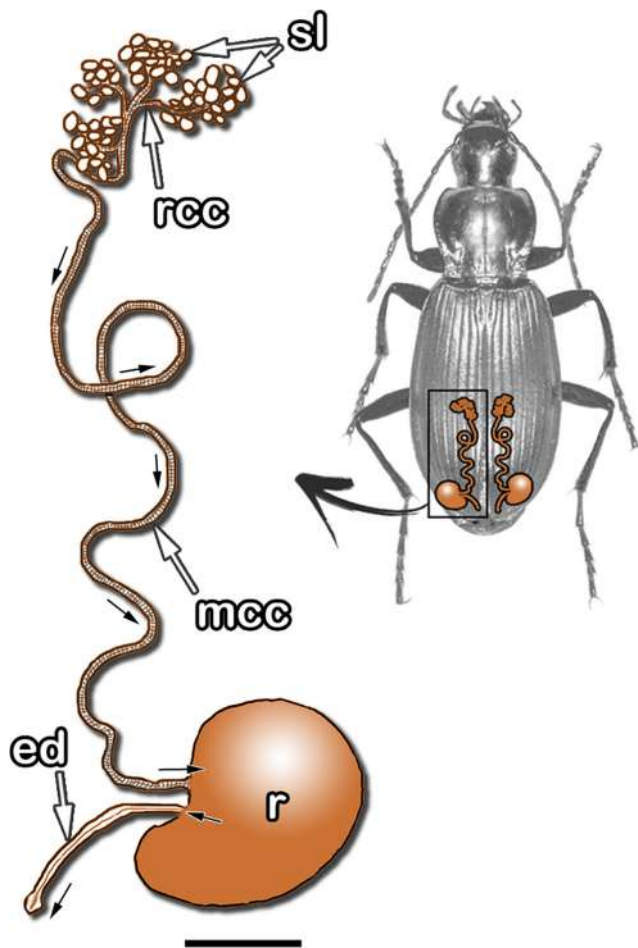


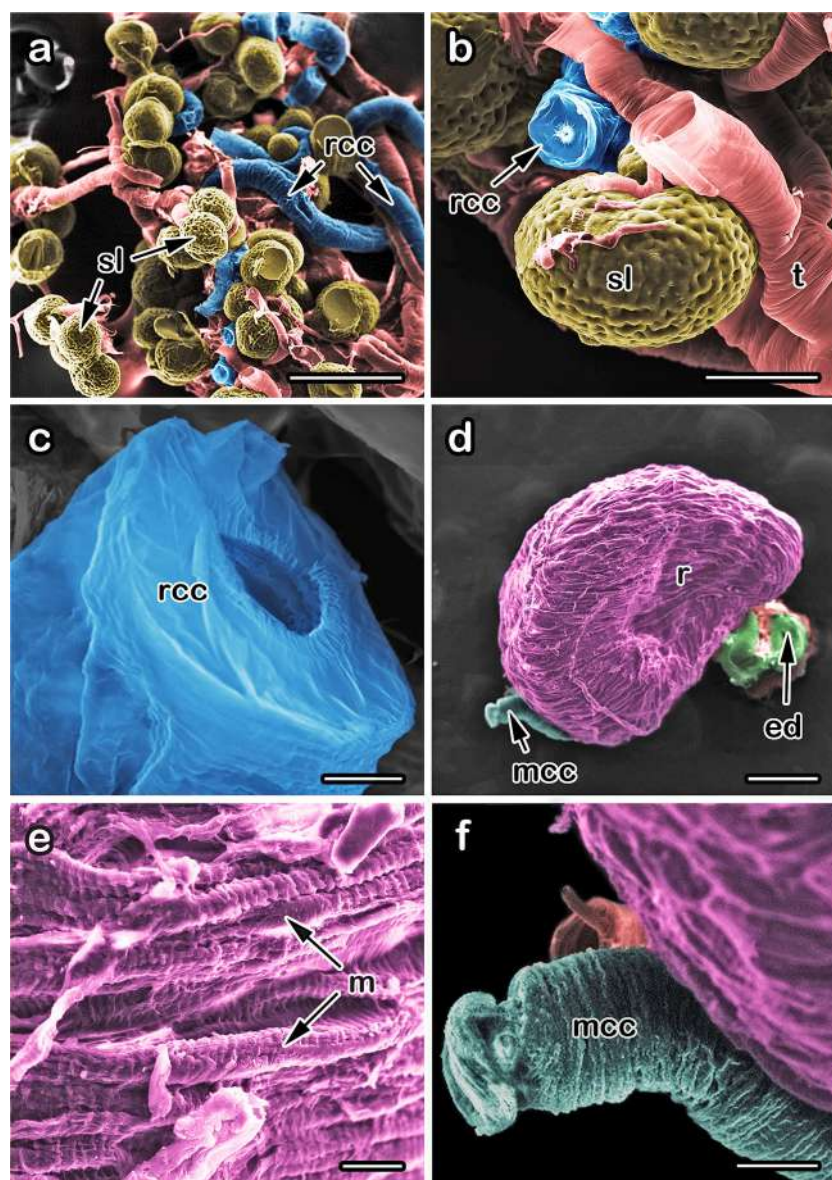
Fig. 6 Schematic depiction of location (right) and general morphology (left) of the pygidial glands of *L. (P.) punctatus*. sl cluster of secretory lobes with radial collecting canals (rcc); mcc main collecting canal, r reservoir, ed efferent duct. Small black arrows show direction of secretion flow. Scale 1 mm

expected to be present. The reason for this deviation probably lies in the chosen method of cultivation of bacterial isolates, which does not provide a realistic picture of the environment's diversity (Hugenholz et al. 1998) as metagenomic analysis does. A large number of bacteria observed in natural habitats have not yet been successfully cultivated in laboratory conditions. Our methods were selected for the isolation of potential antagonists and their further testing. The resulting differences in bacterial populations between guano layers were expected due to different conditions between the layers. In the upper guano layer, a higher percentage of aerobic, heterotrophic bacterial species (*Pseudomonas* spp., *Bacillus* spp.) and a higher percentage of enterobacteria (*Citrobacter* spp., *Kluyvera* spp., and *Escherichia* spp.) were observed. In the lower guano layer, facultative anaerobic and oligotrophic bacterial species (*Paenibacillus* spp., *Lysinibacillus* spp., and *Staphylococcus* spp.) were mainly present. In a study of the microbial diversity of guano samples from Romanian caves,

smaller number of bacteria and lower bacterial diversity (without the presence of coliform bacteria) were detected in deeper layers of guano than in the guano surface (Borda et al. 2014).

Concerning fungal distribution, the total of 16 identified species indicates that moderate fungal diversity occurs in guano samples from the Ogorelička Pečina Cave. Published data on the diversity of guanophilic fungi in other European caves are rather scarce. A moderate diversity of guanophilic fungi was reported in other European caves, especially in caves of Slovakia: in the Ardovská and Domica Caves (Nováková et al. 2005), as well as in the Harmanecká and Driny Caves (Ogórek et al. 2016). By way of contrast, high diversity of guanophilic fungi was reported by Nieves-Rivera et al. (2009) for three caves in southwestern Puerto Rico, where the presence of 50 different species was recorded. Differences in fungal diversity reported in various investigations of guano samples are due to use of different isolation and cultivation methods, different numbers of samples examined, and different environmental factors in the caves. The obtained results concerning the density of fungal spore concentration either correspond with the data presented by Ogórek et al. (2016) for the Harmanecká (3498.3 CFU/g) and Driny (4720.1 CFU/g) Caves in Slovakia, or else the density in the current study is higher. It should be emphasized that the highest fungal concentration was documented on the DG18 medium (6384.61 CFU/g, sampling point 2, upper guano layer). To our knowledge, this medium has not so far been used for isolation of guanophilic fungi, and the results obtained with it suggest xerophilic preferences of some isolates. Nevertheless, the highest fungal diversity was documented at the last, innermost sampling point (75% of all identified species), using the non-selective PDA medium (5447.78 CFU/g), which could point to the existence of optimal conditions for the majority of guanophilic fungi detected in the present study. The results of our qualitative analyses of fungi correspond with previously published data on the guanophilic mycobiota in other cave systems worldwide. The fungal isolates recorded in our research to have the highest isolation frequency, namely, isolates of *M. guilliermondii*, *P. citrinum*, and *T. harzianum*, were also found in guano samples from other caves previously investigated. Nováková et al. (2005) reported the presence of *T. harzianum* and *P. citrinum* in guano samples from the Domica Cave in Slovakia. *T. harzianum* was also documented in stone samples from the Niedźwiedzia Cave in Poland (Ogórek et al. 2013). Ulloa et al. (2006) found *M. guilliermondii* in guano samples collected in the Juxtaluaca Cave (Guerrero, Mexico). However, fungi with lower isolation frequency were also recorded in studies dealing with cave guano microbiology. Porca et al. (2011) isolated *M. racemosus* from the Castañar Cave in Spain, while Vanderwolf et al. (2016) reported the

Fig. 7 SEM images of the pygidial glands of *L. (P.) punctatus*. **a** Cluster of grouped secretory lobes (sl) and radial collecting canals (rcc). **b** Single secretory lobe (sl) and radial collecting canal (rcc) intertwined with tracheoles (t). **c** Cross section of radial collecting canal (rcc). **d** Reservoir (r) with main collecting canal (mcc) and efferent duct (ed). **e** Fine structure of reservoir muscle fibers (m). **f** Part of main collecting canal (mcc). Scales: 200 μm (**a** and **d**), 50 μm (**b** and **f**), 20 μm (**e**), and 10 μm (**c**)



presence of *C. viridescens* in two caves in Canada: Grotte de la Baie de la Tour and Grotte du lac Maloin. *A. flavus* was documented in guano samples from the Domica Cave in Slovakia (Nováková 2009) and several caves in Puerto Rico (Nieves-Rivera et al. 2009).

Occurrence and abundance of *L. (P.) punctatus* in the cave

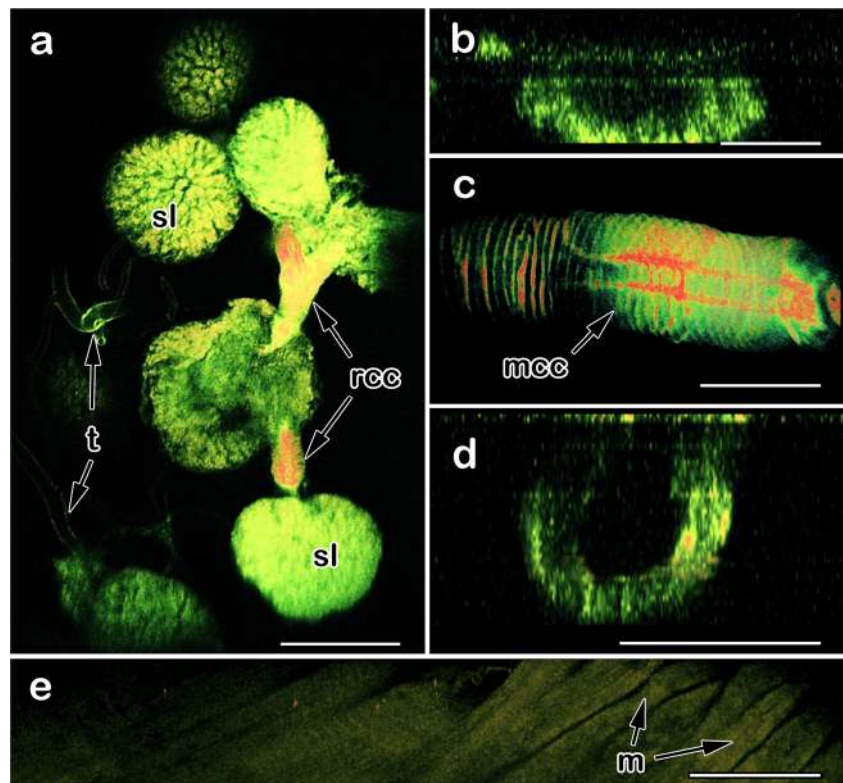
Environmental factors favorable for the occurrence and abundance of *L. (P.) punctatus* in the investigated cave included the presence of total darkness, relative atmospheric humidity between 86 and 90%, and air temperature between 13.8 and 15 °C. Lower air temperatures (below 13.8 °C) and higher relative atmospheric humidity (greater than 90%) seem to be unfavorable for the beetle's existence in the cave. Moreover,

its abundance was lowest in the innermost part of the cave (last cave section) and highest in its middle part (second and third cave sections) (50–70 m from the entrance).

Chemical characterization of the pygidial gland secretion of *L. (P.) punctatus*

The pygidial gland secretion of *L. (P.) punctatus* was previously analyzed using dichloromethane as an extraction chemical (Vesović et al. 2015). There are numerous differences between the results of previous research (Vesović et al. 2015) and those of the current study. Firstly, the number of identified components in the secretion is not the same: 13 compounds were reported in previous research (Vesović et al. 2015), while only four compounds are recorded in the present study. The most dominant compound in both the

Fig. 8 TPEF modality of NLM images of the pygidial glands of *L. (P.) punctatus*. **a** Part of a cluster of grouped secretory lobes (sl) and radial collecting canals (rcc) intertwined with tracheoles (t). **b** Cross section of secretory lobe. **c** Part of main collecting canal (mcc). **d** Cross section of main collecting canal. **e** Cross section of part of reservoir's muscle wall with visible muscle fibers (m). Scales: 200 μm (a), 130 μm (d), 120 μm (c), and 100 μm (b and e)



previous study and the present research was undecane (40.4% vs. 58.9%, respectively), followed by dodecyl acetate (34.2% vs. 36.7%, respectively). Using different extraction method, Vesović et al. (2015) reported that the content of formic acid in the secretion was 19.4%, compared to only 1.9% in the present study. Conversely, the share of acetic acid in the secretion was 0.6% in the previous study (Vesović et al. 2015), while was 2.5% in the current research. Vesović et al. (2015) identified an additional nine compounds (oleic, palmitic, stearic and caproic acids, decyl acetate, undecyl acetate, 1-dodecanol, 9-methyltetracosane, and 7-hexyldocosane) but were not detected using a methanol extract of the secretion. Four out of five of the secretion's most abundant components extracted by dichloromethane (undecane, dodecyl acetate, formic, and acetic acids) were also identified by extraction using absolute methanol. The only compound expected to be found in the secretion but not identified in the current study was 9-methyltetracosane. In the study of Vesović et al. (2015), the concentration of this compound in the secretion was 2.6% (even greater than that of acetic acid). The reason for such qualitative differences between the two studies is most likely connected with the type of extracting solvent. To be specific, dichloromethane as a standard chemical for extracting chemical components from various secretions of arthropods seems to be better than absolute methanol for this purpose because most of the minor components of the secretion (below 1%) are not detected using the latter solvent. Methanol was used as the extraction solvent in the present study because it is the solvent

best suited for testing the antimicrobial potential of arthropod secretions (Ilić et al. 2018; Stanković et al. 2016). It is also frequently used as a solvent in analyzing the chemical composition of such secretions (Clark 2009), especially for species having polar short-chain organic acids in their secretions. Additionally, it is recommended that the same solvent be used in all analyses.

Antimicrobial action of the pygidial gland secretion of *L. (P.) punctatus* against guano-dwelling microbes

The in vitro antibacterial assay demonstrated that the pygidial gland secretion of the ground beetle species *L. (P.) punctatus* possesses a significant level of antibacterial activity, mostly against Gram-positive isolates. Results of a previous study on the antibacterial potential of the pygidial gland secretion of *L. (P.) punctatus* (Nenadić et al. 2016) indicated that this secretion has moderate antibacterial activity against human pathogens. *Listeria monocytogenes*, *Enterobacter cloacae*, *Pseudomonas aeruginosa*, *S. aureus*, and *Salmonella typhimurium* showed moderate resistance to the secretion of *L. (P.) punctatus* at (MIC value of 2.2 mg/mL) (Nenadić et al. 2016). The same research also confirmed high MIC values for *B. cereus* (2.2 mg/mL), which were much higher than the MIC values obtained in our study (0.225 mg/mL). On the other hand, *E. fergusonii* in this study showed significant sensitivity to the secretion (MIC value of 0.028 mg/mL), while in the study of Nenadić et al. (2016), *E. coli* was inhibited with an

MIC value of 3.7 mg/mL. Additionally, *Micrococcus flavus* was a highly resistant strain (MIC value of 4.3 mg/mL), as shown by Nenadić et al. (2016), in comparison with our guanophilic *M. yunnanensis* isolate, which showed greater susceptibility (0.113 mg/mL).

In vitro antifungal testing indicated a fungistatic and fungicidal potential of the pygidial gland secretion of *L. (P.) punctatus* against selected guano-dwelling isolates. Fungal isolates already cited as components of the cave-dwelling mycobiota with mass sporulation and small conidia or cells (as in the case of *M. guilliermondii*) were chosen to investigate the antifungal potential of the pygidial gland secretion of the ground beetle *L. (P.) punctatus* against fungi from the cave's guano. In the case of *P. citrinum* and *T. harzianum*, the lower obtained MIC and MFC values suggested that the secretion has a stronger antifungal potential than the commercial fungicide nystatin. Antifungal activity of the pygidial gland secretion of *L. (P.) punctatus*, not only against cave-dwelling *Penicillium* and *Trichoderma* species but also against clinical isolates and laboratory strains, has already been proven by Nenadić et al. (2016, 2017), but in significantly higher concentrations than in the present study. It should be emphasized that investigations on the antimicrobial potential of ground beetle secretions are scarce.

Analysis of chemical composition of the secretion indicates the existence of variable organic components (some of them belonging to the group of fatty acids) such as formic, acetic, palmitic, and oleic acids, in a low percentage (Lečić et al. 2014; Vesović et al. 2015). It can be assumed that the presence of such compounds can be responsible for the secretion's antimicrobial potential (Nenadić et al. 2016). This assertion is apparently confirmed by the low level of cytotoxicity of the secretion (Nenadić et al. 2018).

Concerning ecological conditions, which are stable and suitable in the Ogorelička Pečina Cave throughout the year in terms of temperature and humidity, and due to significant deposits of the bat guano, the cave's population of trogliphilic *L. (P.) punctatus* is particularly abundant. As reported by Casale (1988), the beetle is not strictly hypogean (trogliphilic and guanophilic) and can be located in habitats above the soil surface too. We also report a great richness of microorganisms in this cave. However, the exact understanding of ecological relationship between *L. (P.) punctatus* and microorganisms living in the bat guano cannot be established at this point with certainty due to the fact that we estimated only a small portion of microbial composition of the bat guano. Due to limitation of the used conventional methods, we cannot give an estimate of the actual microbial taxa richness in the bat guano analyzed. Currently, we can only assume that chemical products of the pygidial glands of *L. (P.) punctatus* might additionally contribute to general allomonic role, by possessing a considerable antimicrobial activity against some of the microorganisms in microbiota of their natural environment. That potential secondary (i.e.,

antimicrobial) role of the pygidial gland secretion might be particularly significant in the stationary (pupal) stage of post-embryonic development of ground beetles (Giglio et al. 2009). However, we still cannot confirm with certainty that the pygidial gland secretion is being used for this purpose in the habitat.

In the future, studies such as ours will open possibilities of further research on ecological relationships between the analyzed and other trogliphilous and guanophilous ground beetle species and microbes from the same habitat.

Morphological characterization of the pygidial glands of *L. (P.) punctatus*

Previous investigations of morphology and anatomy of the pygidial glands of *L. (P.) punctatus* (Forsyth 1972; Nenadić et al. 2016), studies in which conventional light microscopy (LM) was applied proved to be insufficient for detailed observations of these structures. A more complete investigation of the ultrastructure and anatomy of these organs was conducted in the present study using SEM and the TPEF modality of NLM.

Compared to SEM and the TPEF modality of NLM, LM is less satisfactory because it provides insight only into simple external morphology and allows conducting measurements of certain exterior structures (Forsyth 1972; Nenadić et al. 2016). The undeniable fact is that SEM is the most suitable microscopic method for observing external morphology of the pygidial glands of *L. (P.) punctatus*, since it provides detailed insight into form of the reservoir and yields the most information about the external appearance of other glandular structures (e.g., diameter, thickness and detailed structure of radial collecting canals of the secretory lobes and efferent ducts). On the other hand, the TPEF modality of NLM proved to be the most appropriate method in examining internal structure of the glands (e.g., shape, diameter and dimensions of internal structures of reservoirs, secretory lobes, collecting canals and efferent ducts; arrangement of muscle fibers) without prior preparation of the tissues, thereby providing additional three-dimensional information about the analyzed structures. Acquiring three-dimensional cross sections without preparation and cutting of tissues, their staining and labeling, as well as obtaining diameters and other dimensions of inner microstructures of the observed pygidial gland system are significant advantages of the TPEF modality of NLM over SEM and conventional LM. On the basis of all the advantages/disadvantages of the three microscopy techniques applied so far in analyzing structure of the pygidial glands in *L. (P.) punctatus*, it can be asserted that the combination of SEM and the TPEF modality of NLM provide the most detailed information about the morphology and anatomy of these biological structures.

Acknowledgments We are grateful to Dr. Saša Stanković (University of Niš - Faculty of Science and Mathematics, Niš, Serbia), who helped us in

field research. The assistance of Marina Todosijević, B.Sc., in secretion measuring is acknowledged.

Author contributions All authors contributed to the study conception and design. Material preparation, data collection, and analysis were performed by Ivica Dimkić, Jovana Kabić, Marija Nenadić, Miloš Stupar, Ljubodrag Vujisić, Svetlana Savić-Šević, Vladimir Žikić, and Nikola Vesović. The first draft of the manuscript was written by Ivica Dimkić, Jovana Kabić, Miloš Stupar, Marija Nenadić, Milica Ljaljević Grbić, and Srećko Čurčić, and all authors commented on previous versions of the manuscript. Funding acquisition: Slaviša Stanković, Jelena Vukojević, Dejan Pantelić, Vele Tešević, Srećko Čurčić. Supervision: Ivica Dimkić, Slaviša Stanković, Milica Ljaljević Grbić, and Srećko Čurčić. All authors read and approved the final manuscript.

Funding information The work was financially supported by the Serbian Ministry of Education, Science and Technological Development (Grants Nos. ON173026, ON173032, ON173038, III43001, ON172053, III45016, and ON171038). This study was additionally funded jointly by the Serbian Ministry of Education, Science and Technological Development and the Ministry of Science and Technology of the People's Republic of China (Grant "Mimetics of Insects for Sensing and Security," I-2).

Compliance with ethical standards

Conflict of interest The authors declare that they have no conflict of interest.

Ethical approval All applicable international, national, and/or institutional guidelines for the care and use of animals were followed.

References

- Barton HA (2006) Introduction to cave microbiology: a review for the non-specialists. *J Cave Karst Stud* 68(2):43–54
- Blum MS (1981) Chemical defenses of arthropods. Academic Press, New York
- Borda DR, Năstase-Bucur RM, Spînu M, Uricariu R, Mulec J (2014) Aerosolized microbes from organic rich materials: case study of bat guano from caves in Romania. *J Cave Karst Stud* 76(2):114–126
- Casale A (1988) Revisione degli *Sphodrina* (Coleoptera, Carabidae, Sphodrini). Monografie V. Regional Museum of Natural Science, Turin
- Clark VC (2009) Collecting arthropod and amphibian secretions for chemical analyses. In: Zhang W, Liu H (eds) Behavioral and chemical ecology. Nova Science Publishers, Hauppauge, pp 1–46
- Čurčić SB, Brajković MM, Čurčić BPM (2007) The carabids of Serbia. Monographs, volume 11. Institute of Zoology, Faculty of Biology, University of Belgrade, Committee for Karst and Speleology, Serbian Academy of Sciences and Arts, Department of Conservation Biology, Vegetation- and Landscape Ecology, Faculty of Life Sciences, University of Vienna & UNESCO MAB Committee of Serbia, Belgrade-Vienna, Serbia-Austria
- Daouk KD, Dagher MS, Sattout JE (1995) Antifungal activity of the essential oil of *Origanum syriacum* L. *J Food Prot* 58:1147–1149
- De Mandal S, Zothansanga AKP, Bisht SS, Senthil KN (2015) First report of bacterial community from a bat guano using Illumina next-generation sequencing. *Genom Data* 4:99–101
- Di Bella C, Piraino C, Caracappa S, Fornasari L, Violani C, Zava B (2003) Enteric microflora in Italian *Chiroptera*. *J Mt Ecol* 7:221–224
- Di Giulio A, Muzzi M, Romani R (2015) Functional anatomy of the explosive defensive system of bombardier beetles (Coleoptera, Carabidae, Brachininae). *Arthropod Struct Dev* 44:468–490
- Dimkić I, Živković S, Berić T, Ivanović Ž, Gavrilović V, Stanković S, Fira Đ (2013) Characterization and evaluation of two *Bacillus* strains, SS-12.6 and SS-13.1, as potential agents for the control of phytopathogenic bacteria and fungi. *Biol Control* 65(3):312–321
- Forsyth DJ (1972) The structure of the pygidial defence glands of *Carabidae* (Coleoptera). *Trans Zool Soc Lond* 32:249–309
- Giglio A, Brandmayr P, Dalpozzo R, Sindona G, Tagarelli A, Talarico F, Brandmayr TZ, Ferrero EA (2009) The defensive secretion of *Carabus lefebvrei* Dejean 1826 pupa (Coleoptera, Carabidae): gland ultrastructure and chemical identification. *Microsc Res Tech* 72(5):351–361
- Hall TA (1999) BioEdit: a user-friendly biological sequence alignment editor and analysis program for Windows 95/98/NT. *Nucleic Acids Symp Ser* 41:95–98
- Hänel H, Raether W (1988) A more sophisticated method of determining the fungicidal effect of water-insoluble preparations with a cell harvester, using miconazole as an example. *Mycoses* 31(3):148–154
- Hugenholtz P, Goebel BM, Pace NR (1998) Impact of culture-independent studies on the emerging phylogenetic view of bacterial diversity. *J Bacteriol* 180(18):4765–4774
- Ibrahim A, Hage CH, Souissi A, Leray A, Hélot L, Souissi S, Vandembunder B (2015) Label-free microscopy and stress responses reveal the functional organization of *Pseudodiptomus marinus* copepod myofibrils. *J Struct Biol* 191:224–235
- Ilić B, Dimkić I, Unković N, Ljaljević-Grbić M, Vukojević J, Vujisić L, Tešević V, Stanković S, Makarov S, Lučić L (2018) Millipedes vs. pathogens: defensive secretions of some julids (*Diplopoda: Julida*) as potential antimicrobial agents. *J Appl Entomol* 142:775–791
- Jiang X, Zhong J, Liu Y, Yu H, Zhuo S, Chen J (2011) Two-photon fluorescence and second-harmonic generation imaging of collagen in human tissue based on multiphoton microscopy. *Scanning* 33:53–56
- Jovčić B, Begović J, Lozo J, Topisirović L, Kojić M (2009) Dynamics of sodium dodecyl sulfate utilization and antibiotic susceptibility of strain *Pseudomonas* sp. ATCC19151. *Arch Biol Sci* 61:159–165
- Julg B, Elias J, Zahn A, Koppen S, Becker-Gaab C, Bogner J (2008) Bat-associated histoplasmosis can be transmitted at entrances of bat caves and not only inside the caves. *J Travel Med* 15:133–136
- Jurado V, Laiz L, Rodriguez-Nava V, Boiron P, Hermosin B, Sanchez-Moral S, Saiz-Jimenez C (2010) Pathogenic and opportunistic microorganisms in caves. *Int J Speleol* 39:15–24
- Kim JJ, Kim SH, Lee S, Breuil C (2003) Distinguishing *Ophiostoma ips* and *Ophiostoma montium*, two bark beetle-associated sapstain fungi. *FEMS Microbiol Lett* 222:187–192
- Kimura M (1980) A simple method for estimating evolutionary rates of base substitutions through comparative studies of nucleotide sequences. *J Mol Evol* 16:111–120
- Kind T (2003) Automated mass spectral deconvolution and identification system (AMDIS). www.amdis.net. Accessed 27 December 2019
- Kumar S, Stecher G, Tamura K (2016) MEGA7: molecular evolutionary genetics analysis version 7.0 for bigger datasets. *Mol Biol Evol* 33(7):1870–1874
- Lečić S, Čurčić S, Vujisić L, Čurčić B, Čurčić N, Nikolić Z, Anđelković B, Milosavljević S, Tešević V, Makarov S (2014) Defensive secretions in three ground-beetle species (*Insecta: Coleoptera: Carabidae*). *Ann Zool Fenn* 51:285–300
- Ma Y, Zhang H, Du Y, Tian T, Xiang T, Liu X, Feng H (2015) The community distribution of bacteria and fungi on ancient wall paintings of the Mogao Grottoes. *Sci Rep* 5:7752
- Medellin RA, Wiederholt R, Lopez-Hoffman L (2017) Conservation relevance of bat caves for biodiversity and ecosystem services. *Biol Conserv* 211:45–50
- Mulec J (2008) Microorganisms in hypogean: examples from Slovenian karst caves. *Acta Carsol* 7(1):153–160

- Mulec J, Zalar P, Hajna NZ, Rupnik M (2002) Screening for culturable microorganisms from cave environments (Slovenia). *Acta Carsol* 31(2):177–187
- Nenadić M, Soković M, Glamočlija J, Ćirić A, Perić-Mataruga V, Tešević V, Vujisić L, Todosijević M, Vesović N, Ćurčić S (2016) Antimicrobial activity of the pygidial gland secretion of the trogliphilic ground beetle *Laemostenus (Pristonychus) punctatus* (Dejean, 1828) (*Insecta: Coleoptera: Carabidae*). *Bull Entomol Res* 106:474–480
- Nenadić M, Ljaljević-Grbić M, Stupar M, Vukojević J, Ćirić A, Tešević V, Vujisić L, Todosijević M, Vesović N, Živković N, Ćurčić S (2017) Antifungal activity of the pygidial gland secretion of *Laemostenus punctatus* (*Coleoptera: Carabidae*) against cave-dwelling micromycetes. *Sci Nat* 104:52
- Nenadić M, Soković M, Calhelha RC, Ferreira ICFR, Ćirić A, Vesović N, Ćurčić S (2018) Inhibition of tumour and non-tumour cell proliferation by pygidial gland secretions of four ground beetle species (*Coleoptera: Carabidae*). *Biologia* 73(8):787–792
- Nešić D, Pavićević D, Zatezalo A, Mijatović M, Grubač B (2008) Rezultati kompleksnih istraživanja Ogoreličke pećine. *Zaštita Prirode* 59:51–66
- Newman MM, Kloepper LN, Duncan M, McInroy JA, Kloepper JW (2018) Variation in bat guano bacterial community composition with depth. *Front Microbiol* 9:914
- Nieves-Rivera ÁM, Santos-Flores CJ, Dugan FM, Miller TE (2009) Guanophilic fungi in three caves of southwestern Puerto Rico. *Int J Speleol* 38(1):61–70
- Nováková A (2009) Microscopic fungi isolated from Domica cave system (Slovak karst National Park, Slovakia). A review. *Int J Speleol* 38(1):71–82
- Nováková A, Elhottová D, Křišťůfek V, Lukešová A, Hill P, Kováč L, Mock A, Luptačík P (2005) Feeding sources of invertebrates in the Ardovska Cave and Domica Cave systems – preliminary results. In: Tajovský K, Schlaghamerský J, Pižl V (eds) Contributions to soil zoology in Central Europe. Institute of Soil Biology of the Czech Academy of Sciences, České Budějovice, pp 107–112
- O'Donnell K, Cigelnik E (1997) Two divergent intragenomic rDNA ITS2 types within a monophyletic lineage of the fungus *Fusarium* are nonorthologous. *Mol Phylogenet Evol* 7:103–116
- Ogórek R, Lejman A, Matkowski K (2013) Fungi isolated from Niedźwiedzia cave in Kletno (lower Silesia, Poland). *Int J Speleol* 42(2):161–166
- Ogórek R, Dyląg M, Kozak B, Višnovska Z, Tančinová D, Lejman A (2016) Fungi isolated and quantified from bat guano and air in Harmanecká and Driny Caves (Slovakia). *J Cave Karst Stud* 78(1):41–49
- Pitt JI (1979) The genus *Penicillium* and its teleomorphic state *Eupenicillium* and *Talaromyces*. Academic Press, London
- Porca M, Jurado V, Martin-Sanchez MP, Hermonis B, Bastian F, Alabouvette C, Saiz-Jimenez C (2011) Aerobiology: an ecological indicator for early detection and control of fungal outbreaks in caves. *Ecol Indic* 11:1594–1598
- Poulson TL, Lavoie KH (2000) The trophic basis of subsurface ecosystems. In: Wilkens H, Culver DC, Humphreys WF (eds) Ecosystems of the world, Subterranean ecosystems, vol 30. Elsevier, Amsterdam, pp 231–249
- Rabasović MD, Pantelić DV, Jelenković BM, Ćurčić SB, Rabasović MS, Vrbica MD, Lazović VM, Ćurčić BPM, Krmpot AJ (2015) Nonlinear microscopy of chitin and chitinous structures: a case study of two cave-dwelling insects. *J Biomed Opt* 20:016010
- Raper BK, Fennel DI (1965) The genus *Aspergillus*. The Williams and Wilkins company, Baltimore
- Ristivojević P, Dimkić I, Trifković J, Berić T, Vovk I, Milojković-Opsenica D, Stanković S (2016) Antimicrobial activity of Serbian propolis evaluated by means of MIC, HPTLC, bioautography and chemometrics. *PLoS One* 11:e0157097
- Rocha-Silva F, Figueiredo SM, Silveira TT, Assunção CB, Campolina SS, Pena-Barbosa JP, Rotondo A, Caligionne RB (2014) Histoplasmosis outbreak in Tamboril cave—Minas Gerais state, Brazil. *Med Mycol Case Rep* 4:1–4
- Roe AD, Rice AV, Coltman DW, Cooke JE, Sperling FA (2011) Comparative phylogeography, genetic differentiation and contrasting reproductive modes in three fungal symbionts of a multipartite bark beetle symbiosis. *Mol Ecol* 20:584–600
- Samson RA, Houbraken J, Thrane U, Frisvad JC, Andersen B (2010) Food and indoor fungi. CBS-KNAW Fungal Biodiversity Centre, Utrecht
- Savković Ž, Unković N, Stupar M, Franković M, Jovanović M, Erić S, Šarić K, Stanković S, Dimkić I, Vukojević J, Grbić ML (2016) Diversity and biodeteriorative potential of fungal dwellers on ancient stone stela. *Int Biodeterior Biodegradation* 115:212–223
- Stanković S, Dimkić I, Vujisić L, Pavković-Lučić S, Jovanović Z, Stević T, Sofrenić I, Mitić B, Tomić V (2016) Chemical defence in a millipede: evaluation and characterization of antimicrobial activity of the defensive secretion from *Pachyulus hungaricus* (Karsch, 1881) (*Diplopoda, Julida, Julidae*). *PLoS One* 11:e0167249
- Suzina NE, Mulyukin AL, Kozlova AN, Shorokhova AP, Dmitriev VV, Barinova ES, Mokhova ON, Duda VI (2004) Ultrastructure of resting cells of some non-spore-forming bacteria. *Microbiology* 73(4): 435–447
- Tamura K, Stecher G, Peterson D, Filipiński A, Kumar S (2013) MEGA6: molecular evolutionary genetics analysis version 6.0. *J Mol Evol* 30: 2725–2729
- Ulloa M, Lappe P, Aguilar S, Park H, Pérez-Mejía A, Toriello C, Taylor LM (2006) Contribution to the study of the mycobiota present in the natural habitats of *Histoplasma capsulatum*: an integrative study in Guerrero, Mexico. *Rev Mex Biodivers* 77:153–168
- Vanderwolf KJ, Malloch D, Ivanova VN, McAlpine FD (2016) Lack of cave-associated mammals influences the fungal assemblages of insular solution caves in eastern Canada. *J Cave Karst Stud* 78(3): 198–207
- Vandžurová A, Bačkor P, Javorský P, Pristaš P (2013) *Staphylococcus nepalensis* in the guano of bats (*Mammalia*). *Vet Microbiol* 164: 116–121
- Vesović N, Ćurčić S, Vujisić L, Nenadić M, Krstić G, Perić-Mataruga V, Milosavljević S, Antić D, Mandić B, Petković M, Vučković I, Marković Đ, Vrbica M, Ćurčić B, Makarov S (2015) Molecular diversity of compounds from pygidial gland secretions of cave-dwelling ground beetles (*Insecta: Coleoptera: Carabidae*): the first evidence. *J Chem Ecol* 41:533–539
- Vrbica M, Petrović A, Pantelić D, Krmpot A, Rabasović M, Pavlović D, Jovanić S, Guéorguiev B, Goranov S, Vesović N, Antić D, Marković Đ, Petković M, Stanisavljević L, Ćurčić S (2018) The genus *Pheggomisetes* Knirsch, 1923 (*Coleoptera: Carabidae: Trechinae*) in Serbia: taxonomy, morphology and molecular phylogeny. *Zool J Linnean Soc* 183:347–371
- Wallace SJ, Morrison JL, Botting KJ, Kee TW (2008) Second-harmonic generation and two-photon-excited autofluorescence microscopy of cardiomyocytes: quantification of cell volume and myosin filaments. *J Biomed Opt* 13:064018
- Watanabe T (2002) Soil and seed fungi. Morphologies of cultured fungi and key to species. CRC Press, London
- White TJ, Bruns T, Lee S, Taylor J (1990) Amplification and direct sequencing of fungal ribosomal RNA genes for phylogenetics. In: Innis MA, Gelfand DH, Sninsky JJ, White TJ (eds) PCR protocols: a guide to methods and applications. Academic Press, New York, pp 315–322

Bifurcation in reflection spectra of holographic diffraction grating recorded on dichromated pullulan

Svetlana Savić-Šević¹ · Dejan Pantelić¹ · Vladimir Damljanović¹ · Branislav Jelenković¹

Received: 6 November 2017 / Accepted: 3 April 2018
© Springer Science+Business Media, LLC, part of Springer Nature 2018

Abstract Volume diffraction gratings were created holographically on a dichromated pullulan (polysaccharide doped with chromium). Specific and very rare multi-peak structure in the reflection spectra is observed. It was found that multiple peaks are consequence of non-ideal structure of volume diffraction grating. Theoretical analysis and numerical simulations confirm that the observed behavior arise from a slight randomness of grating parameters: refractive index, grating period, film thickness. The results of calculation are in agreement with experimental results.

Keywords Holographic diffraction grating · Reflection spectra · Bifurcation · Polysaccharide

1 Introduction

Reflection volume hologram gratings, fabricated using a single-beam method, usually have only one Bragg peak in the spectrum. Wang et al. (2006) noted the appearance of multiple peaks in the spectrum of volume diffraction grating recorded in dichromated gelatin, phenomenon that looks like bifurcation within the Bragg plateau. We also observed bifurcation phenomena in the reflection spectrum of diffraction gratings recorded in dichromated pullulan (DCP), which is a polysaccharide doped with chromium. Compared to dichromated gelatin, the DCP material is simpler to prepare and process, it is weakly sensitive to humidity, thus retaining high resolution and diffraction

This article is part of the Topical Collection on Focus on Optics and Bio-photonics, Photonica 2017.

Guest Edited by Jelena Radovanovic, Aleksandar Krmpot, Marina Lekic, Trevor Benson, Mauro Pereira, Marian Marciniak.

✉ Svetlana Savić-Šević
savic@ipb.ac.rs

¹ Institute of Physics, University of Belgrade, Pregrevica 118, 11080 Zemun, Belgrade, Serbia

efficiency (Pantelic et al. 1998; Savic et al. 2002; Savić-Šević and Pantelic 2007). The typical number of peaks in the spectrum is between two and four. We have extended the research presented in (Wang et al. 2006) by taking into account that the grating parameters depend also on x, y coordinates.

In order to understand multi-peak structure of diffraction gratings, experimental results were compared with theory. The corresponding model investigates effects of several important parameters: absorption of radiation within the photosensitive layer, non-uniform thickness of layers, refractive index modulation and non-uniform spatial period of the grating. Reflection spectra of volume Bragg gratings were calculated using method of characteristic matrix (Born and Wolf 1980). Our model suggests that multi peak structures are produced by uneven modulation of Bragg layers inside the volume hologram. The results of calculation are in agreement with experimental results. Such behavior of reflection spectra is important for effect of broadening bandgaps of photonic crystals. Understanding mechanism of their formations and appearance can help us to establish standard procedure for fabrications of such spatially non uniform volume gratings.

2 Fabrication and optical characterization of volume holographic gratings

The results presented below were obtained by the following preparation procedure for DCP. Holographic photosensitive material was prepared by mixing 10% aqueous solution of pullulan (from Sigma–Aldrich) and 10% of the ammonium dichromate. DCP solution was stirred and warmed to 50 °C to achieve homogeneity. The solution was coated onto a thoroughly cleaned glass slides placed on the flat horizontal surface. Film was dried overnight under normal laboratory conditions. The thicknesses of the dried layers, was 14 μm .

The experimental setup is shown in Fig. 1. Periodic structures in a DCP were fabricated using a single-beam method schematically shown in Fig. 1a. Hologram recording was achieved by exposing DCP to a single longitudinal mode, diode pumped Nd-YAG laser (Verdi) at 532 nm. The laser beam was expanded and pullulan layer was exposed at normal incidence with 200 mW/cm^2 of optical power, for 120 s. After propagation through emulsion, the beam was reflected back from a mirror behind the holographic plate. The two counter-propagating beams interfere, creating a standing wave pattern within an emulsion.

Plates were chemically processed, after the exposure. Processing involves washing the plates in a mixture of water and isopropyl alcohol (3:1 ratio) for 120 s, and drying for 60 s in pure isopropyl alcohol. Periodic structure formed below the surface during the processing is revealed in cross-sectional view of the DCP grating, Fig. 2.

To measure reflection, and transmission spectra, of the DCP, light from the halogen lamp was collimated and directed onto the DCP plate using set-ups given in Fig. 1b, c, respectively. Spectra were measured using fiber type spectrometer (Ocean Optics).

The photonic structure obtained under usual experimental conditions looks uniform, as in Fig. 3a. However, magnified part of the same sample shows that the structure is not ideally uniform across the layer of the DCP, Fig. 3b. In Fig. 3c we show several transmission spectra of the same DCP grating. Spectra were measured using the microscope attached to the spectrometer, as schematically presented in Fig. 1c. Transmission spectra were measured at several positions and each spectrum corresponds to area which is approximately 50 μm in diameter, with 1 mm distance between two adjacent areas.

Fig. 1 Experimental setup for **a** generating holographic diffraction gratings in DCP; and for measuring reflection and transmission spectra **b** macroscopically; and **c** microscopically

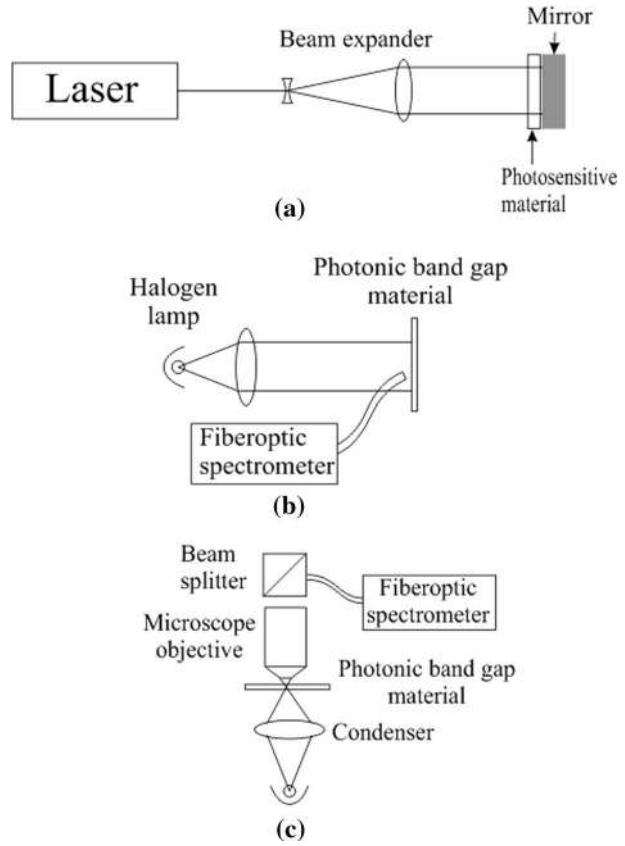
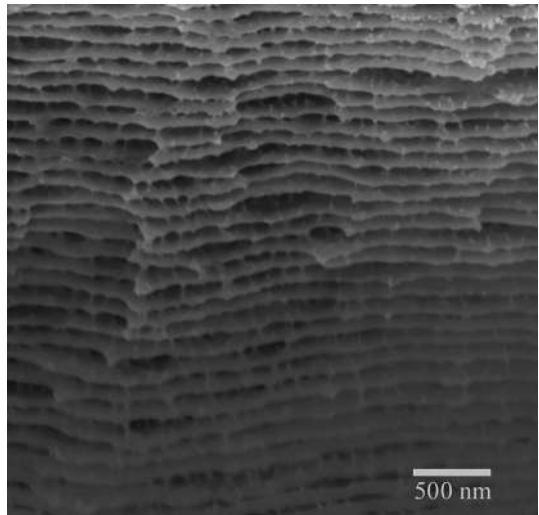


Fig. 2 SEM picture of the cross-section of DCP volume diffraction grating



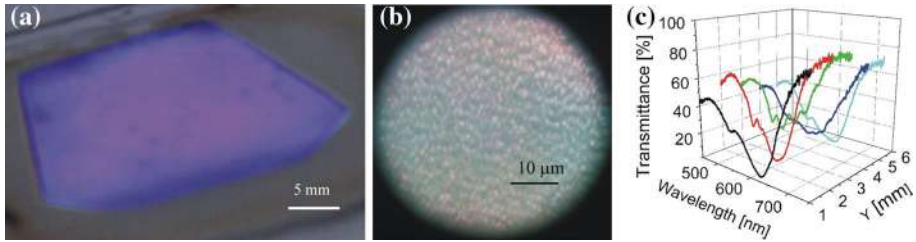


Fig. 3 **a** Image of the DCP sample, the scale bar is 5 mm; **b** zoomed part of the image **a** obtained using $\times 40$ objectives, and microscopic set-up shown in Fig. 1c. The scale bar is 10 μm ; **c** transmission spectra obtained from different areas (each of diameter of 50 μm) of the DCP sample, with 1 mm distance between two adjacent areas

3 Numerical simulations

We have calculated reflection spectra of a volume Bragg gratings by the method of characteristic matrix (Born and Wolf 1980). First, we approximated the refractive index variation along the direction perpendicular to the DCP surface, with a function whose mathematical expression is as follows (Wang et al. 2006, 2008; Liu and Zhou 1994):

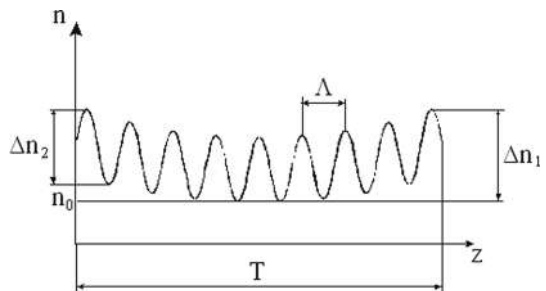
$$n(z) = n_0 + \Delta n_1 \exp(-\alpha_g T) \operatorname{ch} \left\{ \alpha_g \left[(N - j + 1)\Lambda - \frac{z}{M_j} \right] \right\} + \Delta n_2 \exp(-\alpha_g T) \cos \left(\frac{2\pi \times z}{\Lambda \times M_j} \right) \tag{1}$$

Graphical presentation of the function is given in Fig. 4. As can be seen from Eq. (1), z -dependence of the refractive index $n(z)$ incorporates three terms. The first one is the average refractive index of the material n_0 , indicated by the dashed line in Fig. 4.

The second term describes the effects of attenuation of two counter-propagating beams leading to global variation of the refractive index Δn_1 (described by hyperbolic cosine). The last term describes a sinusoidal modulation (with amplitude Δn_2) of the index of refraction. Additional parameters are: α_g —absorption coefficient, T —the material thickness, Λ —grating period, N —the number of grating layers. We assume that the grating period is not constant, due to uneven expansion of the material during processing. Instead, each period of the grating (defined by parameter j ; $1 \leq j \leq N$) is slightly changed, as defined by random variable M_j :

$$M_j = 1.262 - \frac{0.26}{N - 1} j + \frac{R_j}{45} \tag{2}$$

Fig. 4 Refractive index variation of a Bragg grating recorded in DCP, used in theoretical calculations



where R_j is a random number with Gaussian statistics, zero mean value and the standard deviation of 1.5. Variation of the layer thickness is small, however, consequences on optical properties are significant, leading to the band gap broadening.

With the above assumptions, the method of characteristic matrix produces rapidly oscillating spectra. This is different from experimentally recorded smooth spectra. Therefore, we had to modify the theoretical model. In previous research (Wang et al. 2006), it was assumed that grating parameters vary only along z-axis (i.e. depth of material). As we have found from microscope images (Fig. 3b, c) transmission or reflection spectra depend on the location on the material surface (x and y coordinates). This means that the grating parameters depend on x, y coordinates too. The resulting spectrum (as measured by any finite aperture optical device) is an average value of many spectra integrated along the aperture.

Therefore, we introduced an additional random factor $r_{k,j}$ into Eq. (2):

$$M_j \rightarrow M_j + \frac{r_{k,j}}{45} = 1.262 - \frac{0.26}{N-1}j + \frac{R_j}{45} + \frac{r_{k,j}}{45} \quad (3)$$

here $r_{k,j}$ is also Gaussian random number with mean value 0 and standard deviation of 1.5. The meaning of other parameters is the same as in Eq. (2).

First we use Eq. (2) to calculate spectrum by the characteristic matrix method. This calculation is repeated several times giving typically reflection spectra with 2, 3 and 4 peaks. The following values for parameters were used: $n_0=1.45$, $\Lambda=184$ nm, $N=78$, $\Delta n_1 \exp(-\alpha_g T) = \Delta n_2 \exp(-\alpha_g T) = 0.08$, $T=14$ μm , and $\alpha_g = 0.02(\mu\text{m})^{-1}$ (measured value). Then we fixed R_j and generate arrays $r_{k,j}$ where k is from 1 to 15 and j from 1 to 78. These way k different spectra were calculated and the result is obtained by averaging individual spectra.

The results of the model given in (Wang et al. 2006) show that appearance of multi peak band gap can be due to uneven spatial modulation of interference pattern recorded inside the material. There are two reasons for uneven modulation, irregular swelling of material during processing, and attenuation of radiation inside the emulsion.

The results of our calculations are shown in Fig. 5. We can see that for different variations of layer thickness after processing, different number of peaks appear. Since differences in the variations in the layer thickness are exclusively due to presence of random parameter with Gaussian distribution, we can assign appearance of peaks to this parameter, which is in agreement with (Wang et al. 2006).

Results presented in the upper row in Fig. 5, calculated assuming that thickness of layers varies (middle row) according to Eq. (2), contain noise-like, rapidly oscillating part. The bottom row in Fig. 5 presents resulting spectra obtained by lateral averaging defined by Eq. (3). Averaging over spectrums from several neighboring points eliminates rapidly oscillating part. In the bottom row of Fig. 5 we compare reflection spectra obtained experimentally using set-up shown in Fig. 1b (black dotted curves) and by numerical simulation (red solid curves). The results of calculation are in agreement with experimental results.

4 Discussion of fabrication of structured band gaps in DCP

Structured reflection spectra under the usual chemical processing are very rare [0.5% probability (Wang et al. 2006)]. In order to investigate how special techniques in processing volume holograms lead to more frequent appearance of structured reflection spectra, we prepared 250 samples of DCP photonic crystals with different concentration of ammonium

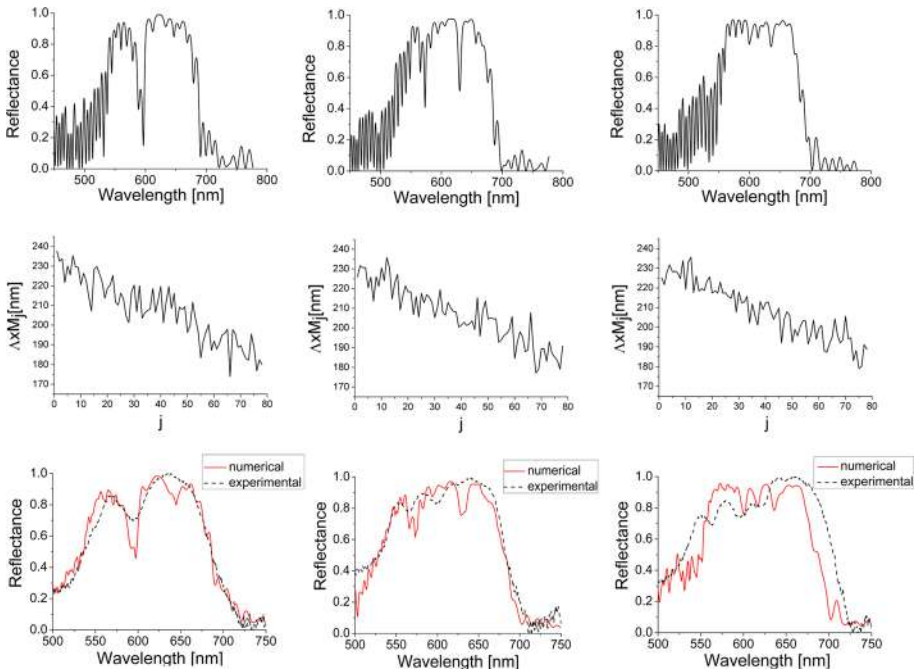


Fig. 5 Calculated reflection spectra of photonic structures in DCP showing multiple peaks as result of the layer thickness variation (upper row). Layer thickness variation (middle row). Averaged results taking into account the different thickness variation of layers in adjacent lateral regions of the film (red solid curve) and reflection spectra obtained experimentally (black dotted curve) using set-up shown in Fig. 1b (bottom row). (Color figure online)

dichromate (from 10 to 50% by weight of pullulan), different thickness of DCP (6–30 μm) and use various chemical processing. Samples were developed in mixture of water and isopropyl alcohol. We noticed that probability of obtaining multi peak and wider band gap photonic crystals is higher (although by only a few percent), by increasing the water to isopropyl ratio. If water to isopropyl ratio is 3:1 or more, analysis of our samples shows that probability of obtaining two peak photonic crystals is about 10 and 1.5% for three or more peaks.

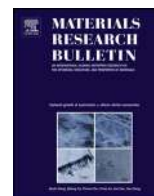
5 Conclusions

In this paper we investigated bifurcation in the reflection spectra of the holographic DCP gratings. Volume holograms in DCP were made using simple, single-beam holographic technique. Although these types of diffraction spectra of volume hologram are usually rare, there are exact ways to increase the frequency of appearance of multi peak structure by using certain techniques in processing of DCP, as described in Sect. 2. Our simulation model suggests that multi peak structures are produced by uneven modulation of interference pattern inside the volume hologram. In addition, smoothness of reflectivity function is due to the difference in layer thickness in neighboring regions of the grating.

Acknowledgements This work was funded by the Ministry of Education, Science and Technological Development of the Republic of Serbia, under Grants Number OI 171038 and III 45016.

References

- Born, M., Wolf, E.: Principles of Optics. Pergamon, New York (1980)
- Liu, D., Zhou, J.: Nonlinear analysis for a reflection hologram. *Opt. Commun.* **107**, 471–479 (1994)
- Pantelić, D., Savić, S., Jakovljević, D.: Dichromated pullulan as a novel photosensitive holographic material. *Opt. Lett.* **23**, 807–809 (1998)
- Savić, S., Pantelić, D., Jakovljević, D.: Real-time and postprocessing holographic effects in dichromated pullulan. *Appl. Opt.* **41**, 4484–4488 (2002)
- Savić-Šević, S., Pantelić, D.: Dichromated pullulan diffraction gratings: influence of environmental conditions and storage time on their properties. *Appl. Opt.* **46**, 287–291 (2007)
- Wang, Z., Liu, D., Zhou, J.: Investigation of a peculiar bifurcation phenomenon in diffraction spectra of volume holograms. *Opt. Lett.* **31**, 3270–3272 (2006)
- Wang, Z., Zhai, T., Zhao, R., Liu, D.: The influence of asymmetric expansion properties and random fluctuation on the bandwidth of a hologram. *J. Opt. A Pure Appl. Opt.* **10**, 085205 (2008)



Characterization and luminescence kinetics of Eu^{3+} doped YVO_4 nanopowders



D. Sevic^{a,*}, M.S. Rabasovic^a, J. Krizan^b, S. Savic-Sevic^a, M. Mitric^c, M. Gilic^a, B. Hadzic^a, N. Romcevic^a

^a Institute of Physics, University of Belgrade, Serbia

^b Ami DOO, Ptuj, Slovenia

^c Vinča Institute of Nuclear Science, University of Belgrade, P.O. Box 522, 11001 Belgrade, Serbia

ARTICLE INFO

Article history:

Received 7 November 2016

Received in revised form 28 November 2016

Accepted 19 December 2016

Available online 21 December 2016

Keywords:

Phosphors

Optical properties

Luminescence

Time – resolved optical spectroscopy

ABSTRACT

In this paper we describe the synthesis and characterization of the $\text{YVO}_4:\text{Eu}^{3+}$ nanopowder. The material was prepared using simple solution combustion synthesis. X-ray powder diffraction (XRD), scanning electron microscope (SEM), Raman and photoluminescence (PL) techniques were used to confirm and characterize the prepared material. The time resolved analysis of emission spectra was achieved by using the streak camera system. Beside luminescence lifetime of slow decayed transitions we also measured their rise time and lifetime of fast decayed transitions. We also determined the excitation spectra of this nano material. Results of our analysis prove that $\text{YVO}_4:\text{Eu}^{3+}$ nanopowder is appropriate material for various optoelectronic devices.

© 2016 Elsevier Ltd. All rights reserved.

1. Introduction

Yttrium Vanadate (YVO_4) phosphors doped with europium ions (Eu^{3+}), $\text{YVO}_4:\text{Eu}^{3+}$ are vastly investigated and have found many applications, see [1–10] and references therein. Various methods of synthesis and studies of structural and luminescent characteristics of nano phosphors based on $\text{YVO}_4:\text{Eu}^{3+}$ are reported in [1,2,10–20].

In this study, nanopowders $\text{YVO}_4:\text{Eu}^{3+}$ were efficiently prepared using a Solution Combustion Synthesis (SCS) method [21,22]. The main characteristics of this process are simplicity and low cost. Moreover, it is possible to tune the size and morphology of particles. The structure of prepared materials has been confirmed and characterized using X-ray powder diffraction (XRD), scanning electron microscope (SEM), Raman and photoluminescence (PL) techniques. The excitation and emission spectra and luminescence lifetimes and rise time of synthesized nanopowders were analyzed by using the streak camera system. PL spectra were obtained at different excitation wavelengths using Optical Parametric Oscillator and 532 nm laser line. Transitions from the $^5\text{D}_0$ state, from which most of europium luminescence comes, are slow decayed. Lifetimes of slow decayed lines of europium doped YVO_4 are measured and reported in many publications. However, there are

not so many publications where results regarding lifetimes of fast decayed transitions or rise times of slow decayed transitions [23–26] of europium are provided. In this study, beside luminescence lifetime of slow decayed transitions from the $^5\text{D}_0$ state, we also measured their rise time and lifetime of fast decayed transitions from the $^5\text{D}_1$ state. The luminescence rise time measurements can be used for high temperature remote thermometry [24,25].

This paper is continuation of our previously published works regarding europium atom, where some other hosts were also used [21,27].

2. Experimental procedures

2.1. The preparation of samples

Europium doped YVO_4 nanopowders were prepared, as described in [21,22]. Stoichiometric quantities of starting chemicals $\text{Y}(\text{NO}_3)_3 \cdot 6\text{H}_2\text{O}$, NH_4VO_3 , NH_4NO_3 , $\text{Eu}(\text{NO}_3)_3 \cdot 6\text{H}_2\text{O}$ with the purity of 99.99% were chosen to obtain the Eu^{3+} concentration in YVO_4 of 2 mol%. The listed chemicals were purchased from ABCR and urea, $(\text{NH}_2)_2\text{CO}$, from Sigma-Aldrich. The dry mixture of 15.32 g (40 mmol) of $\text{Y}(\text{NO}_3)_3 \cdot 6\text{H}_2\text{O}$, 4.676 g (40 mmol) of NH_4VO_3 and 0.357 g (0.8 mmol) of $\text{Eu}(\text{NO}_3)_3 \cdot 6\text{H}_2\text{O}$ was combined with the mixture of 4.8 g (60 mmol) of ammonium nitrate and 3.003 g (50 mmol) of urea which were used as organic fuels. The prepared

* Corresponding author.

E-mail address: sevic@ipb.ac.rs (D. Sevic).

starting reagents were combusted with the flame burner at approximately 500 °C, yielding the voluminous foamy pink powder in intensive exothermic reaction. After the solution combustion synthesis, the nanopowder was annealed for 2 h in air atmosphere at 1200 °C. The annealing of material is needed to achieve optimal optical characteristics of synthesized material.

2.2. Experimental details

X-ray diffraction measurements were done at room temperature over the 2θ range of 10–90° with a scanning step width of 0.05° and a counting time of 8 s per step. We used a Philips PW 1050 instrument, with Ni filtered Cu $K_{\alpha 1,2}$ radiation ($\lambda = 0.15405$ nm). The nanopowders were also observed by scanning electron microscopy (SEM).

The Raman spectra in a spectral range from 100 to 900 cm^{-1} , in back scattering geometry, were obtained by the micro-Raman Jobin Yvon T64000 spectrometer, equipped with a nitrogen cooled charge-coupled device detector. Our Raman setup uses the continuous laser excitation at 532 nm.

As an excitation source for photoluminescence measurements we used the output of the Optical Parametric Oscillator (Vibrant OPO), continuously tunable over a spectral range from 320 nm to 475 nm. To better discern the Raman lines from the luminescent ones in obtained spectra we also measured the luminescence response of synthesized $\text{YVO}_4:\text{Eu}^{3+}$ using the second harmonic of our OPO pumping Nd:YAG laser at 532 nm.

Time-resolved streak images of the luminescence response of $\text{YVO}_4:\text{Eu}^{3+}$ excited by our OPO system were acquired by Hamamatsu streak camera. The camera is equipped with the spectrograph. The details of our acquisition system can be found in [21]. We also used Ocean Optics 2000 spectrometer. Measurements presented here are obtained at room temperature.

3. Results and discussion

3.1. Structure

XRD pattern of our sample of $\text{YVO}_4:\text{Eu}^{3+}$ nanopowder is shown in Fig. 1. Observed peaks are in good agreement with the published results [11,16] and JCPDS card 17-0341. The diffractogram shown in Fig. 1. proves that monophased sample is crystallized, and that its nature is tetragonal. The fact that doping of Eu^{3+} into YVO_4 material does not change the crystalline structure is proved by the lack of

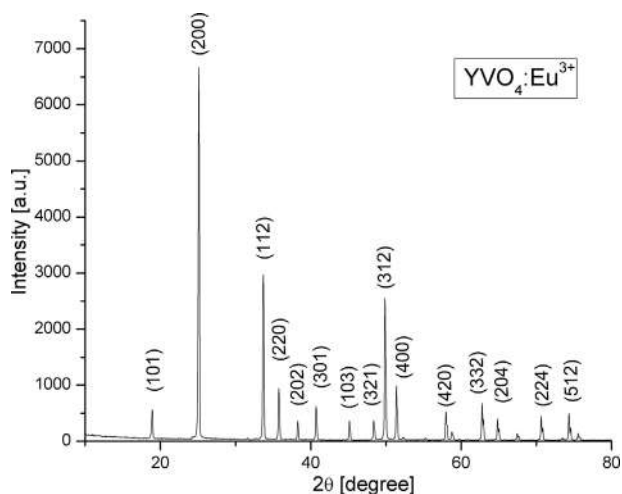


Fig. 1. XRD profile of $\text{YVO}_4:\text{Eu}^{3+}$ nano phosphor prepared by solution combustion method, with respective Miller indices.

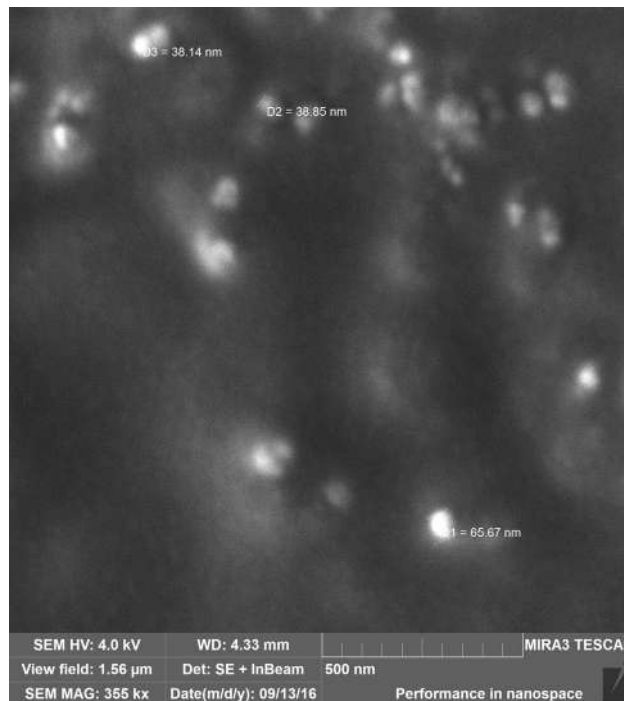


Fig. 2. SEM image of $\text{YVO}_4:\text{Eu}^{3+}$ nano phosphor prepared by solution combustion method.

any additional peaks. The average grain size, D , was estimated by the Scherrer equation, $D = K\lambda/\beta\cos\theta$, where K is a constant related to the shape of the crystallite and is approximately equal to unity, we used $K=0.89$, the same as in [11], λ is the X-ray wavelength (0.15405 nm), θ and β are the diffraction angle and Full Width at Half Maximum (FWHM, in radians) of the corresponding peak. Using θ and β of two most intense diffraction peaks for calculation, we obtained the average grain size of about 51 nm.

The representative SEM image of our sample of $\text{YVO}_4:\text{Eu}^{3+}$ material is presented in Fig. 2. The SEM micrograph confirms the previously calculated average size of the prepared YVO_4 material doped with Eu^{3+} . The SEM image of the material shows the irregular crystallite size distribution. The agglomerated grains could be also noticed. The particles with dimensions from 37 nm to over 70 nm could be observed in Fig. 2. Effects of particle size on the luminescence of $\text{YVO}_4:\text{Eu}$ nanocrystals are studied in detail in [7]. The size of particles, just after the synthesis, is about 6 nm. It was observed, that, with increasing the annealing temperature, the grain sizes increase. The annealing temperature of 1200 °C was chosen to obtain optimal luminescence response of synthesized material.

3.2. Raman spectroscopy

The Raman spectrum of $\text{YVO}_4:\text{Eu}^{3+}$ nanopowder phosphor is presented in Fig. 3. The peaks corresponding to Raman spectrum of YVO_4 material are marked on graph, by their shift in cm^{-1} . However, there are some other peaks on diagram. Our analysis of excitation spectra of $\text{YVO}_4:\text{Eu}^{3+}$ (Section 3.3.1) shows that our sample, if excited at 532 nm with average laser power comparable with power of excitation laser used in our Raman measurements, provides luminescence response similar in intensity with Raman spectrum of the sample. The existence of luminescence response of europium ions hosted in YVO_4 excited at 532 nm was also reported in [7,12]. Time resolved analysis, using streak camera and pulsed OPO laser excitation (of 5 ns duration), shows that these peaks are

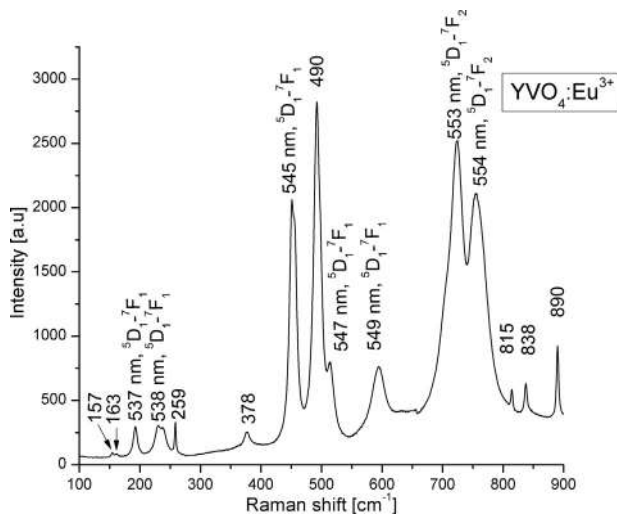


Fig. 3. Raman spectrum of $\text{YVO}_4:\text{Eu}^{3+}$ nano phosphor prepared by solution combustion synthesis. Peaks which are due to luminescence response of the sample are also denoted.

undoubtedly luminescent in nature, because their duration is in microsecond domain (Section 3.3.2, see Fig. 7). Peaks which are due to luminescence response of the sample are also denoted in Fig. 3, by their wavelength in nm. These relatively small, fast decayed luminescence responses of the sample could be observed in our Figs. 6 and 7 and in [17,23,27,28].

We have detected the external modes of Raman spectra at low vibrational frequencies, $B_{1g}(1)$ at 157 cm^{-1} and $E_{g2}(2)$ at 163 cm^{-1} . Internal modes are also observed, B_{2g} at 259 cm^{-1} , $A_{1g}(1)$ at 378 cm^{-1} , $B_{1g}(3)$ at 490 cm^{-1} , $B_{1g}(4)$ at 815 cm^{-1} , $E_g(5)$ at 838 cm^{-1} and $A_{1g}(2)$ at 890 cm^{-1} .

The positions of Raman peaks observed by us are in a good agreement with published results [9–11,29–33]. These peaks, detected in our measurements, imply strong interactions between the atoms, arising mainly from the stretching and bending of the shorter metal-oxygen bonds within the anionic groups [10,11,34]. The similarity of our spectrum with published spectra of undoped samples proves that crystal structure was not disturbed by doping material with europium.

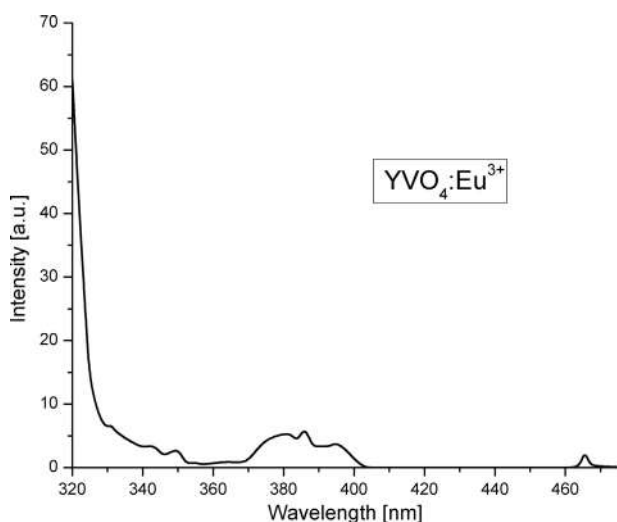


Fig. 4. Excitation spectrum of $\text{YVO}_4:\text{Eu}^{3+}$ nano phosphor, corresponding to 619 nm emission.

3.3. Optical properties

3.3.1. Luminescence excitation and emission spectra

The excitation spectrum of $\text{YVO}_4:\text{Eu}^{3+}$ nano phosphor, corresponding to 619 nm emission, is shown in Fig. 4. As excitation source we used our OPO (320–475 nm) and the emission spectra were recorded using a step of 2 nm. The broad band up to 350 nm corresponds to strong absorption of light by YVO_4 host and charge transfer from host to Eu dopant [2,12,18]. The narrow lines observed in the 350–475 nm range refer to direct excitation of Eu (intra-4f transitions) [12]. Our aim, when recording the excitation spectra, was to include the wavelengths of direct excitation of Eu. The similar excitation spectra are presented in [8,16,19,20,32]. The small peak at about 350 nm, visible in Fig. 4, could be seen only in one of the excitation spectra presented in [20].

To complete the analysis of $\text{YVO}_4:\text{Eu}^{3+}$ nano phosphor excitation, we also recorded, using additionally Ocean Optics 2000 spectrometer, the emission spectrum when 532 nm laser line is used for excitation, see Fig. 5. Because both our spectrographs (used for luminescence measurements) have not enough stray light rejection for 532 nm excitation, the part of the spectrum near 532 nm was omitted from the diagram. We have investigated the existence of luminescence response of europium ions hosted in YVO_4 excited at 532 nm because of encountered problems in our analysis of Raman spectra. Compared to the main luminescence emission this emission is of relatively small intensity. The emission, making problems in our Raman spectroscopy, is due to transitions from 5D_1 state. Because we did not measure the emission for excitation wavelengths between 475 nm and 532, this peak, even smaller than peak on 466 nm, is not included on diagram in Fig. 4. This weak emission is due to $^7F_0-^6D_1$ transition [12].

The streak image of time resolved photoluminescence spectrum of $\text{YVO}_4:\text{Eu}^{3+}$ material using the 320 nm excitation is presented in Fig. 6. As usual, the streak image is presented in pseudocolor. The Eu transitions are denoted in Fig. 6 according to [23,35]. The slow decayed transitions observable in Fig. 6, originating from 5D_0 level, are well explained in literature and their detailed description can be found in our previous work [21].

Let us add that the emission spectrum shown in Fig. 6, is similar to spectra presented in [11,17,19,20,28,32]. The fast decayed lines (538 nm and 587 nm) shown in Fig. 6, are detected in [14,15,17,32]. The transitions between $^5D_1-^7F_2$ states are barely discernible in

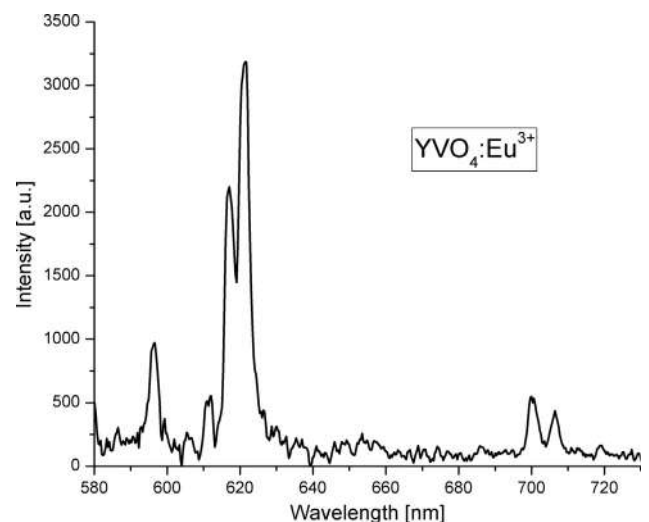


Fig. 5. Emission spectrum of $\text{YVO}_4:\text{Eu}^{3+}$ nano phosphor excited at 532 nm. The horizontal and vertical scales are adapted for better visualization of luminescence emission.

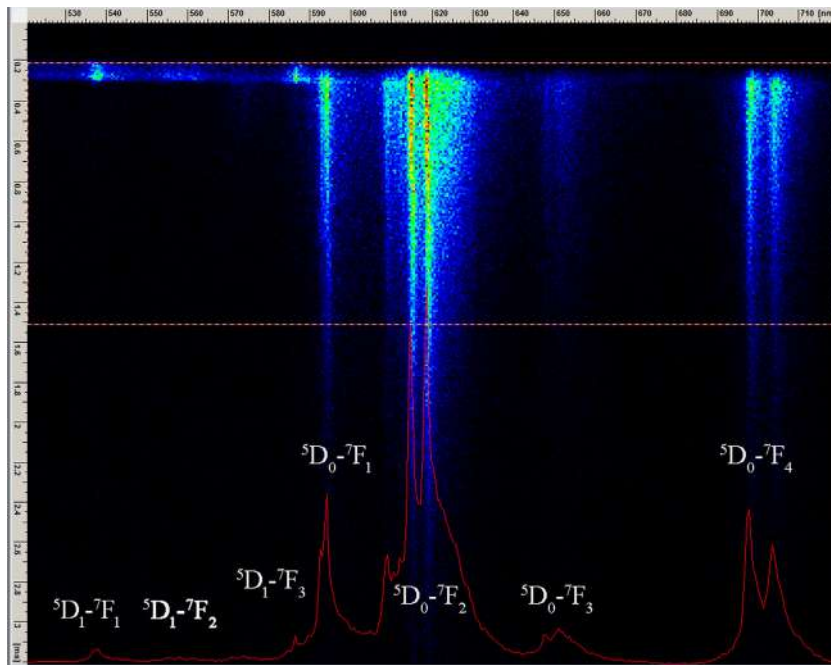


Fig. 6. Streak image of photoluminescence spectrum of $\text{YVO}_4:\text{Eu}^{3+}$ nano phosphor. OPO excitation is at 320 nm.

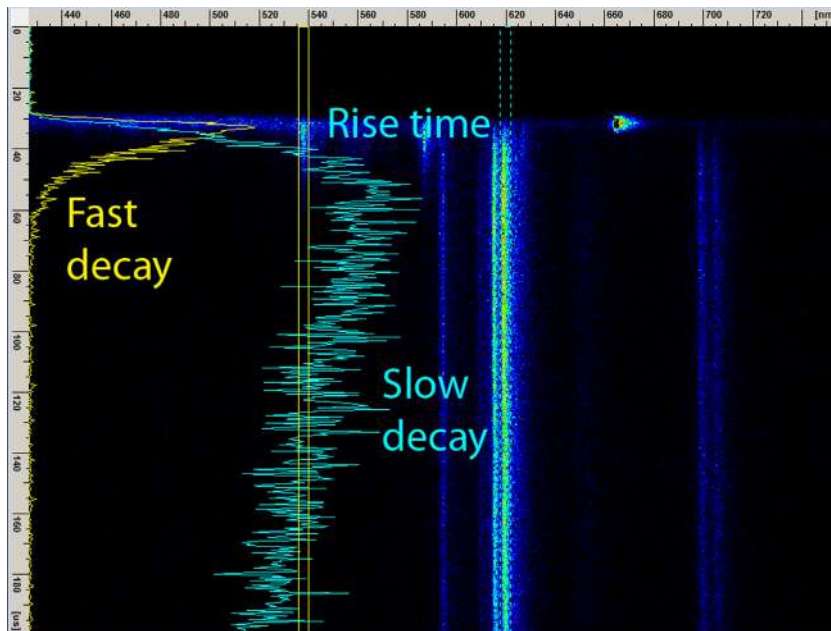


Fig. 7. Streak image of photoluminescence spectrum of $\text{YVO}_4:\text{Eu}^{3+}$ nano phosphor with the time range of 200 μs tuned for analysis of rise time of slow decayed transitions and lifetime of fast decayed transitions. OPO excitation is at 330 nm (its second harmonic generated by diffraction grating is visible on 660 nm).

Fig. 6. They are slightly better visible in Fig. 7. These transitions are clearly observed in [15].

The transitions from $^5\text{D}_1$ visible in region below 550 nm are relatively smaller and we didn't detect these lines in our previous experiments regarding $\text{Gd}_2\text{Zr}_2\text{O}_7:\text{Eu}^{3+}$ [21,27]. However, in our present measurements of $\text{YVO}_4:\text{Eu}^{3+}$ nano phosphor we have clearly detected the line at 538 nm, see Fig. 6.

3.3.2. Lifetime and rise time analysis

We conducted the time resolved analysis for transitions which are identified in Fig. 6. The transitions are characterized by emission peaks at 538 nm and 587 nm (fast decayed, from the level

$^5\text{D}_1$), 594 nm, 609 nm, 615 nm, 619 nm 699 nm and 704 nm wavelengths (slow decayed, from the level $^5\text{D}_0$). The streak image of photoluminescence spectrum of $\text{YVO}_4:\text{Eu}^{3+}$ nano phosphor with the time range of 200 μs tuned for analysis of rise time of slow decayed transitions and lifetime of fast decayed transitions is shown in Fig. 7.

We obtained that the lifetimes of transitions from the level $^5\text{D}_1$ are about 8.7 μs and from the level $^5\text{D}_0$ the lifetimes are about 0.93 ms. For the fast decay it is similar as reported in [23], where transition from $^5\text{D}_1$ level has a fast decay with the lifetime of about 10.2 μs , while the decays of peaks which belong to $^5\text{D}_0$ have the lifetime of about 1.5 ms. Other references provide the values of fast

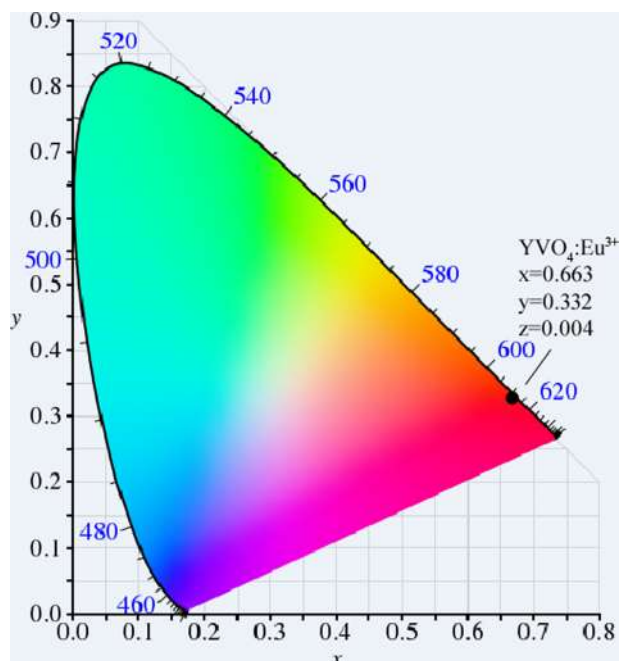


Fig. 8. The CIE chromaticity diagram of emission spectra of Eu doped YVO₄ nanopowder.

[28] and slow [12,15,19,20,38] decay time more or less similar to our result. Decay curve of the most intensive ⁵D₀–⁷F₂ transition is usually used for europium luminescence lifetime measurements [23,36].

We calculated the rise time according to Ranson equation [24,39]. We obtained that the rise time of luminescence of our sample of YVO₄:Eu³⁺ for the ⁵D₀–⁷F₂ line is about 8.1 μs. The phenomenon that the rise time of slow decayed luminescence is similar to the lifetime of fast decayed transition was observed long ago [26] (interestingly enough, there are only a few references regarding the europium rise time since then). It could be concluded that these time periods are related to energy transfer from host to Eu dopant. Schematic diagram of the energy transfer between the host YVO₄ and Eu³⁺ ions and explanation is provided in [2], however, without measuring the rise time. The nice explanation and diagram of decay pathways in Eu³⁺, (although for different host, Ca₂Gd₈Si₆O₂₆), including the measured rise time, is presented in [23].

Rise time of luminescence of many phosphors, including Eu, is temperature dependent, so it is possible to use this phenomenon for remote high temperature sensing [24].

3.3.3. CIE chromaticity coordinates

The chromaticity coordinate values, CIE 1931, were calculated for our sample of YVO₄:Eu³⁺ and presented in Fig. 8. By using the CIE diagram, it is easy to see that our sample of YVO₄:Eu³⁺ red phosphor, combined with appropriate green and blue phosphors, maximizes the area of the color gamut compared to red phosphors based on other hosts described in [27,40–44]. The nano phosphor studied in our paper has similar chromaticity coordinates as materials analyzed in [10,17,45].

4. Conclusions

In this paper we described the synthesis and characterization of the YVO₄:Eu³⁺ nanopowder. Solution combustion synthesis method was used to prepare the analyzed material. The structure of prepared material has been verified and characterized using

X-ray powder diffraction (XRD), scanning electron microscope (SEM), Raman and photoluminescence (PL) techniques. The excitation and emission spectra and luminescence kinetics of synthesized nanopowders were analyzed by using the streak camera system. PL spectra were obtained at different excitation wavelengths. Beside luminescence kinetics of slow decayed transitions we also measured their rise time and lifetime of fast decayed transitions. To the best of our knowledge, the detailed luminescence time resolved analyses of both slow decayed (including their rise time) and fast decayed transitions of the YVO₄:Eu³⁺ nano powder, provided by using the streak camera system, are first presented here. Measured values of rise time of luminescence emission of lines originating from transitions from ⁵D₀ level could be used for remote temperature sensing. YVO₄:Eu³⁺ nanopowder maximizes the area of the color gamut in CIE diagram. So, results of our analysis prove that YVO₄:Eu³⁺ nanopowder prepared by a simple and low cost process is appropriate material for various optoelectronic devices.

Acknowledgement

This work was financially supported within the Projects Ministry of Education, Science and Technological Development of the Republic of Serbia under Projects III45003 and OI171020.

References

- [1] L. Shirmane, C. Feldmann, V. Pankratov, to appear in: *Physica B: Physics of Condensed Matter*, 10.1016/j.physb.2016.10.007.
- [2] R.S. Ningthoujam, L.R. Singh, V. Sudarsan, S.D. Singh, *J. Alloys Compd.* 484 (2009) 782–789.
- [3] A. Huignard, T. Gacoin, J.-P. Boilot, *Chem. Mater* 12 (2000) 1090–1094.
- [4] A. Huignard, V. Buisette, G. Laurent, T. Gacoin, J.-P. Boilot, *Chem. Mater* 14 (2002) 2264–2269.
- [5] K. Riwotzki, M. Haase, *J. Phys. Chem. B* 102 (1998) 10129–10135.
- [6] V.B. Bhatkar, *Int. J. Eng. Sci. Inn. Tech.* 2 (2013) 426–432.
- [7] S. Georgescu, E. Cotoi, A.M. Voiculescu, O. Toma, *Rom. Rep. Phys.* 60 (2008) 947–955.
- [8] W.J. Park, M.K. Jung, T. Masaki, S.J. Im, D.H. Yoon, *Mater. Sci. Eng.* 146 (2008) 95–98.
- [9] A. Sanson, M. Giarola, B. Rossi, G. Mariotto, E. Cazzanelli, A. Speghini, *Phys. Rev. B* 86 (2012) 214305.
- [10] S. Thakur, A.K. Gathania, *J. Electronic Materials* 44 (10) (2015) 3444–3449.
- [11] B.K. Grandhe, V.R. Bandi, K. Jang, S. Ramaprabhu, S.-S. Yi, J.-H. Jeong, *Electron. Mater. Lett.* 7 (2) (2011) 161–165.
- [12] Y.-S. Chang, F.-M. Huang, Y.-Y. Tsai, L.-G. Teoh, *J. Lumin.* 129 (2009) 1181–1185.
- [13] R. Han, R. Hu, K. Chen, *Opt. Mater.* 32 (2009) 329–333.
- [14] Q. Yan-bo, L. Xiao-feng, Z. Qiang, C. Dan-ping, W. Ye-wen, M. Wen-bo, *Mater. Lett.* 64 (2010) 1306–1308.
- [15] M. Yu, J. Lin, Z. Wang, J. Fu, S. Wang, H.J. Zhang, Y.C. Han, *Chem. Mater* 14 (2002) 2224–2231.
- [16] M.G. Matos, E.H. de Faria, L.A. Rocha, P.S. Calefi, K.J. Ciuffi, E.J. Nassar, V. Hugo, V. Sarmiento, *J. Lumin.* 147 (2014) 190–195.
- [17] P. Kumari, P.K. Baitha, J. Manam, *Indian J. Phys.* 89 (2015) 1297–1306.
- [18] N. Shanta Singh, R.S. Ningthoujam, M. Niraj Luwang, S. Dorendrajit Singh, R.K. Vatsa, *Chem. Phys. Lett.* 480 (2009) 237–242.
- [19] M. Saltarelli, M.G. Matos, E.H. de Faria, K.J. Ciuffi, L.A. Rocha, E.J. Nassar, *J. Sol-Gel Sci. Technol.* 73 (2015) 83–292.
- [20] M. Saltarelli, P.P. Luz, M.G. Matos, E.H. de Faria, K.J. Ciuffi, P.S. Calefi, L.A. Rocha, E.J. Nassar, *J. Fluoresc.* 22 (2012) 899–906.
- [21] M.S. Rabasovic, D. Sevic, J. Krizan, M. Terzic, J. Mozina, B.P. Marinkovic, S. Savic Sevic, M. Mitric, M.D. Rabasovic, N. Romcevic, *J. Alloys Compd.* 622 (2015) 292–295.
- [22] J. Krizan, M. Mazaj, V. Kaucic, I. Bajsic, J. Mozina, *Acta Chim. Slov.* 61 (2014) 608–614.
- [23] M.D. Chambers, P.A. Rousseve, D.R. Clarke, *J. Lumin.* 129 (2009) 263–269.
- [24] S.W. Allison, S.M. Goedeke, M.R. Cates, W.A. Hollerman, J.I. Eldridge, T.J. Bencic, Oak Ridge National Laboratory Report No 123055, (2005) (Published through SciTech Connect, 03/24/2005).
- [25] X. Li, X. Wei, Y. Qin, Y. Chen, C. Duan, M. Yin, *J. Alloys Compd.* 657 (2016) 353–357.
- [26] J.R. Darwent, C.D. Flint, P.J. O'Grady, *Chem. Phys. Lett.* 127 (1986) 547–550.
- [27] M.S. Rabasovic, J. Krizan, P. Gregorcic, M.D. Rabasovic, N. Romcevic, D. Sevic, *Opt. Quantum Electron.* 48 (2016) 163.
- [28] D.-K. Kim, W. Kang, *Korean Chem. Soc.* 25 (2004) 1859–1862.
- [29] Yu.K. Voron'ko, A.A. Sobol', V.E. Shukshin, A.I. Zagumennyi, Yu. D. Zavartsev, S. A. Kutovoi, *Phys. Solid State* 51 (2009) 1886–1893.

- [30] B.M. Jin, S. Erdei, A.S. Bhalla, F.W. Ainger, *Material Research Bulletin* 30 (1995) 1293–1300.
- [31] S.A. Miller, H.H. Caspers, H.E. Rast, *Phys. Rev.* 168 (1968) 964–969.
- [32] B. Shao, Q. Zhao, N. Guo, Y. Jia, W. Lv, M. Jiao, W. Lu, H. You, *CrystEngComm* 15 (2013) 5776–5783.
- [33] A. Jayaraman, G.A. Kourouklis, G.P. Espinosa, A.S. Cooper, L.G. Van Uitert, *J. Phys. Chem. Solids* 48 (1987) 755–759.
- [34] Z.C. Ling, H.R. Xia, W.L. Liu, H. Hand, X.Q. Wang, S.Q. Sun, D.G. Ran, L.L. Yu, *Mater. Sci. Eng. B* 128 (2006) 156–160.
- [35] K. Binnemans, *Coord. Chem. Rev.* 295 (2015) 1–45.
- [36] Y.-S. Chang, H.-J. Lin, Y.-L. Chai, Y.-C. Li, *J. Alloy Compd.* 460 (2008) 421–425.
- [38] N. Shanta Singh, R.S. Ningthoujam, M. Niraj Luwang, S. Dorendrajit Singh, R.K. Vatsa, *Chem. Phys. Lett.* 480 (2009) 237–242.
- [39] R.M. Ranson, E. Evangelou, C.B. Thomas, *Appl. Phys. Lett.* 72 (1998) 2663–2664.
- [40] C.A. Rao, P.R.V. Nannapaneni, K.V.R. Murthy, *J. Sci. Res.* 5 (2013) 1–11.
- [41] C.A. Rao, P.R.V. Nannapaneni, K.V.R. Murthy, *Adv. Mater. Lett.* 4 (2013) 207–212.
- [42] I.P. Sahu, D.P. Bisen, N. Brahme, R.K. Tamrakar, *J. Radiat. Res. Appl. Sci.* 8 (2015) 104–109.
- [43] I.P. Sahu, D.P. Bisen, N. Brahme, *J. Radiat. Res. Appl. Sci.* 8 (2015) 381–388.
- [44] W. Lu, Y. Jia, W. Lv, Q. Zhao, H. You, *J. Lumin.* 147 (2014) 159–162.
- [45] P.C. de Sousa Filho, T. Gacoin, J.-P. Boilot, R.I. Walton, O.A. Serra, *J. Phys. Chem. C* 119 (2015) 24062–24074.



Effects of temperature and pressure on luminescent properties of $\text{Sr}_2\text{CeO}_4:\text{Eu}^{3+}$ nanophosphor



A. Vlastic^a, D. Sevic^{a,*}, M.S. Rabasovic^a, J. Krizan^b, S. Savic-Sevic^a, M.D. Rabasovic^a, M. Mitric^c, B.P. Marinkovic^a, M.G. Nikolic^a

^a Institute of Physics Belgrade, University of Belgrade, P.O. Box 68, Pregrevica 118, 11080 Belgrade, Serbia

^b AMI, d. o. o, Ptuj, Slovenia

^c Vinca Institute of Nuclear Science, University of Belgrade, P. O. Box 522, 11001 Belgrade, Serbia

ARTICLE INFO

Keywords:

Photoluminescence
Time resolved analysis
Thermographic phosphor
High pressure sensing

ABSTRACT

In this paper we describe the synthesis and characterization of the $\text{Sr}_2\text{CeO}_4:\text{Eu}^{3+}$ nanopowder and possibilities of its application for temperature and high pressure sensing. The material was prepared using simple solution combustion synthesis. X-ray powder diffraction (XRD), scanning electron microscope (SEM) and photoluminescence (PL) techniques have been used to confirm and characterize the prepared material. Time resolved analysis of emission spectra was achieved by using the streak camera system. Measured lifetime values of luminescence emission and the intensity ratios of spectral lines were used for determining the calibration curves for remote temperature sensing. We have analyzed sensitivity improvement of the intensity ratio method by using a temporal evolution of emission lines and simulation of delayed gating of one of them. Pressure effects on optical properties of $\text{Sr}_2\text{CeO}_4:\text{Eu}^{3+}$ nanophosphor are also investigated.

1. Introduction

Thermographic phosphors are widely used in many applications [1–10]. They typically consist of a ceramic host and rare-earth dopant. These materials are structurally stable regarding various parameters, including temperature, pressure, magnetic field, electromagnetic radiation. The temperature dependency of their luminescence is used for remote temperature sensing. For obvious reasons, non contact measurements have many advantages. The luminescence lifetime is usually used for determining the temperature in a point; and the ratio of intensities of two spectral lines is often used for surface (2D) temperature measurements [3,5]. Mechanical influences on nanophosphor photoluminescence are also vastly investigated [9–13].

Strontium Cerium Oxide (Sr_2CeO_4) phosphors doped with europium ions (Eu^{3+}), $\text{Sr}_2\text{CeO}_4:\text{Eu}^{3+}$ are thoroughly investigated and several applications have been found. As pointed out in [14], emission color change in a wide range of temperatures proves a great potential of $\text{Eu}^{3+}:\text{Sr}_2\text{CeO}_4$ nanocrystals for industrial applications, particularly in nanothermometric technology. Moreover, additional application possibilities for this material are provided by the fact that the samples with different grain sizes are characterized by various luminescence colors [14]. The possibility of application of this nanophosphor in single-color and two-color fluorescence thermometry techniques in temperature

range of 303–523 K has been proposed in [15]. In [16] it was shown that the Eu^{3+} doped Sr_2CeO_4 phosphors emitting white light (by combining blue, green and red emissions) has potential applications not only in the fields of lamps and display devices under 280 nm excitation, but also in the field of LEDs under near UV (350 nm) excitation. Recently, paper considering $\text{Sr}_2\text{CeO}_4:\text{Eu}^{3+}$ as a source of anti-stokes white light generated under near infrared excitation was published [17]. Various methods of synthesis and studies of structural and luminescent characteristics of nanophosphors based on $\text{Sr}_2\text{CeO}_4:\text{Eu}^{3+}$ or nondoped Sr_2CeO_4 are reported in [14–24], and references therein.

In this study, $\text{Sr}_2\text{CeO}_4:\text{Eu}^{3+}$ nanopowders were efficiently prepared using a Solution Combustion Synthesis (SCS) method [25,26]. The main characteristics of this process are simplicity and low cost. Moreover, it is possible to tune the size and morphology of particles. The structure of prepared materials has been confirmed and characterized using X-ray powder diffraction (XRD), scanning electron microscope (SEM) and photoluminescence (PL) techniques. The excitation and emission spectra, luminescence lifetimes and rise time of synthesized nanopowders were analyzed by using the streak camera system. PL spectra were obtained at different excitation wavelengths using Optical Parametric Oscillator (OPO). Continuous excitation at 405 nm was achieved by a laser diode. The most of europium luminescence comes from slow decay transitions from the $^5\text{D}_0$ state. Lifetimes of the slow decay lines

* Corresponding author.

E-mail address: sevic@ipb.ac.rs (D. Sevic).

are measured and reported in many publications. However, there are not many publications providing results regarding lifetimes of fast decay transitions, or rise times of slow decay transitions [27–31] of europium. In this study, we have estimated the lifetime and the rise time of europium transitions from the 5D_1 and 5D_0 states. Beside the lifetime, the luminescence rise time measurements [32] can be used for high temperature remote thermometry [2,28,30,31] as well. However, the uncertainty of these measurements is relatively high.

In our recent publication [33] we have shown that $Sr_2CeO_4:Eu^{3+}$ made by solution combustion synthesis could be used as a red phosphor. Now we study the possibility of using the synthesized $Sr_2CeO_4:Eu^{3+}$ for temperature measurements. We analyze the temperature effects on the intensity ratio of europium lines and their photoluminescence lifetime. We estimate a possible sensitivity improvement of the intensity ratio method by using the temporal evolution of emission lines, as proposed in [3]. Pressure effects on optical properties of $Sr_2CeO_4:Eu^{3+}$ nanophosphor are also investigated and, to the best of our knowledge, firstly presented in detail here. Our research followed the approach of simultaneous analysis of temperature dependencies and mechanical influences on nanophosphor photoluminescence [9,10].

2. Experimental procedure

2.1. The preparation of samples

Europium doped Sr_2CeO_4 nanopowders were prepared by solution combustion method, similarly as described in [25,26]. Stoichiometric quantities of starting chemicals $Sr(NO_3)_2$, $5CH_4N_2O$, $Ce(NO_3)_3 \cdot 6H_2O$, and $Eu(NO_3)_3 \cdot 6H_2O$ with the purity of 99.99% were chosen to obtain the Eu^{3+} concentration in Sr_2CeO_4 of 2.5 at% ($Sr_{2-0.05}Eu_{0.05}CeO_4$). The used chemicals were purchased from ABCR, and urea, $(NH_2)_2CO$, from Sigma-Aldrich. The dry mixture of 10.32 g (48.75 mmol) of $Sr(NO_3)_2$, 15.015 g (250 mmol) of CH_4N_2O , 10.86 g (25 mmol) of $Ce(NO_3)_3 \cdot 6H_2O$ and 0.558 g (1.25 mmol) of $Eu(NO_3)_3 \cdot 6H_2O$ was combined with the mixture of 4.8 g (60 mmol) of ammonium nitrate and 3.003 g (50 mmol) of urea which were used as organic fuels. The prepared starting reagents were combusted with the flame burner at approximately 500 °C, yielding a voluminous foamy pink powder in an intensive exothermic reaction. After the solution combustion synthesis, the nanopowder was annealed for 2 h, in air atmosphere, at 900 °C. The annealing of the material is needed to achieve optimal optical characteristics of synthesized material.

2.2. Experimental details

X-ray diffraction measurements were done at room temperature using a Philips PW 1050 instrument, with Ni filtered $Cu K_{\alpha 1,2}$ radiation ($\lambda = 0.15405$ nm). The structure of nanopowders was also observed by a high resolution scanning electron microscope (SEM) equipped with a high brightness Schottky Field Emission gun (FEGSEM, TESCAN) operating at 4 kV. The samples were coated with gold/palladium to make them conductive for SEM analysis.

As an excitation source for photoluminescence measurements we used the output of the Optical Parametric Oscillator (Vibrant OPO), continuously tunable over a spectral range from 320 nm to 475 nm. Laser pulse duration is about 5 ns, at a repetition rate of 10 Hz. Time-resolved streak images of the luminescence response of $Sr_2CeO_4:Eu^{3+}$ nanopowder excited by the OPO system were acquired by Hamamatsu streak camera equipped with a spectrograph.

Excitation spectrum of $Sr_2CeO_4:Eu^{3+}$ was acquired using Fluorolog SPEX. For temperature and pressure dependent measurements we also used Ocean Optics USB2000 and AVANTES AvaSpec 2048TEC USB2 spectrometers and continuous laser diode excitation at 405 nm. The experimental setup for luminescence measurement as a function of temperature is described in [34].

High pressure was achieved using Membrane Diamond Anvil Cell (MDAC) manufactured by BETSA (France), with a 300 μm culet diameter (the culet is the tiny facet at the very bottom of faceted gemstones, added to protect the fragility of the pointed tip). Principle of operation of Diamond Anvil Cell (DAC) is based on the fact that very high pressures can be obtained by reasonable mechanical forces if tips of diamond anvils have small surface area, because obtained pressure equals the ratio of mechanical force versus surface area of culet. The measured sample is placed between the tips of opposite anvils, which are tightened by mechanical force. On earlier models, the necessary mechanical force pushing the anvils to each other was obtained by tightening screw. In the case of membrane DAC used here, the force on the piston pushing the upper anvil is generated by pressurized helium, which presses a circular membrane. This solution enables fine control and adjustment of the force applied to the anvils. In order to get the uniform distribution of pressure on the sample the transmitting fluid should be used. The metal gasket is often used to prevent the leakage of this fluid. The shape of gasket is formed by pressing it between two opposed anvils of the MDAC, first without the sample. Then, the gasket with the sample, pressure transmitting fluid and a small ruby sphere is compressed by the same anvils. The diamond anvils are optically transparent, so the optical measurements of pressurized sample are possible. We used the sample in the form of powder and a 4:1 mixture of methanol and ethanol as a pressure transmitting medium. The pressure was determined from the redshift of the ruby R1 line.

3. Results and discussion

3.1. Structure

XRD pattern of our of $Sr_2CeO_4:Eu^{3+}$ nanopowder sample is shown in Fig. 1. Observed peaks are in good agreement with the published results [14–24] and ICSD card 50-0115. The XRD pattern, shown in Fig. 1, proves the good crystallinity of our sample. The lack of any significant additional peaks confirms that doping the material with Eu^{3+} did not change the crystalline structure of Sr_2CeO_4 . The X-ray Line Profile Fitting Program (XFIT) with a Fundamental Parameters convolution approach to generating line profiles [35] was used for the calculation of both the crystallite size and the microstrain parameter of the synthesized powder. Three most intense peaks were included in the fitting procedure, and the obtained values for crystallite size and microstrain are 114.0 nm and 0.14%, respectively.

The representative SEM image of our sample of $Sr_2CeO_4:Eu^{3+}$ material is presented in Fig. 2. The SEM image confirms the previously calculated average size of the prepared material. The image of the

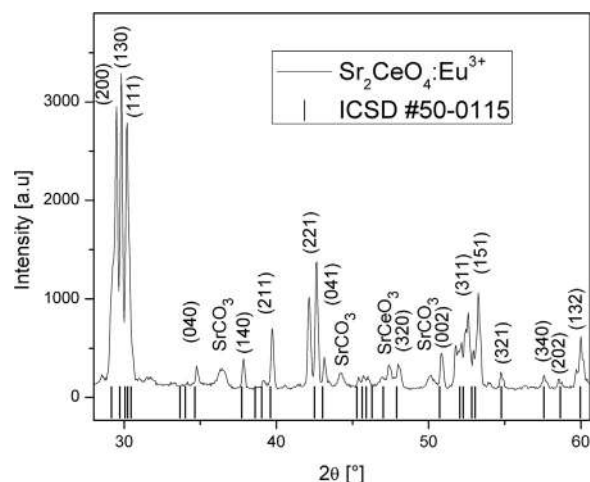


Fig. 1. XRD profile of $Sr_2CeO_4:Eu^{3+}$ nano phosphor prepared by solution combustion method, with respective Miller indices for prominent peaks.

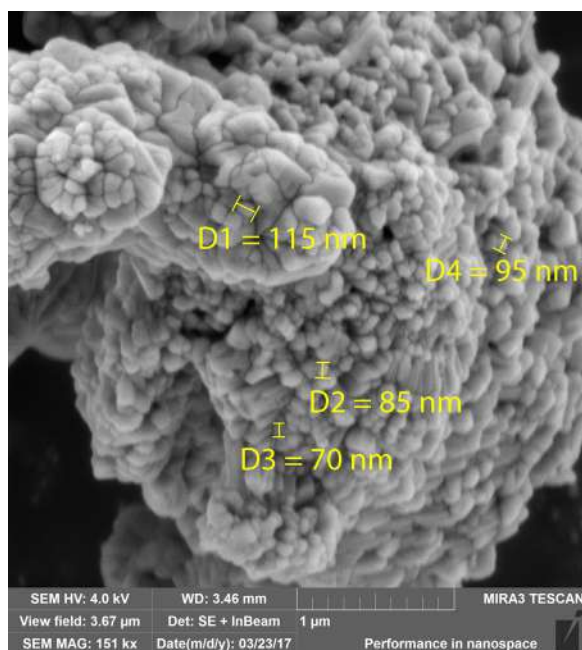


Fig. 2. SEM image of $\text{Sr}_2\text{CeO}_4:\text{Eu}^{3+}$ nano phosphor prepared by solution combustion method.

synthesized material shows the irregular crystallite size distribution. The agglomerated grains can be also noticed. The particles with dimensions from 67 nm to over 120 nm can be easily observed in Fig. 2. Effects of annealing temperatures on particle size and thus resulting overall influence on the luminescence of $\text{Sr}_2\text{CeO}_4:\text{Eu}^{3+}$ nanocrystals are studied in detail in [14,18]. It was observed that with increasing the annealing temperature the grain sizes also increase. The annealing temperature of 900 °C was chosen to obtain optimal luminescence response of synthesized material.

3.2. Optical properties

3.2.1. Luminescence excitation and emission spectra

The excitation spectrum of $\text{Sr}_2\text{CeO}_4:\text{Eu}^{3+}$ nano phosphor, corresponding to the 614 nm emission, is shown in Fig. 3. The wide band, up to about 400 nm, corresponds to a strong absorption of light by the Sr_2CeO_4 host and a charge transfer from host to Eu dopant [14–18,23]. Narrow peaks, at higher wavelengths, come from the direct excitation of europium. The peaks are denoted by corresponding europium transitions. The similar excitation spectra are presented in [14–19].

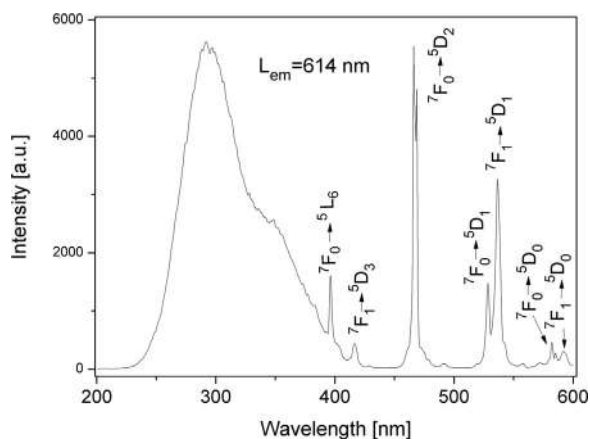


Fig. 3. Excitation spectrum of $\text{Sr}_2\text{CeO}_4:\text{Eu}^{3+}$ nano phosphor, corresponding to the 614 nm emission.

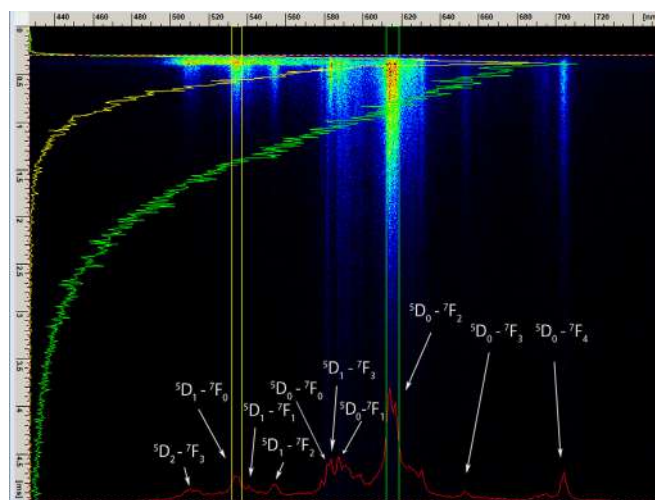


Fig. 4. Streak image of the photoluminescence spectrum of $\text{Sr}_2\text{CeO}_4:\text{Eu}^{3+}$ nanophosphor. (OPO excitation at 330 nm).

The streak image of the time resolved photoluminescence spectrum of the $\text{Sr}_2\text{CeO}_4:\text{Eu}^{3+}$ using the 330 nm excitation is presented in Fig. 4. Horizontal scale of streak image corresponds to wavelength, vertical scale shows development of spectra in time. Images are presented in pseudocolor, where different colors mean different optical intensities. The Eu transitions are denoted in Fig. 4, according to [27,36]. The slow decay transitions originating from $^5\text{D}_0$ state, are well explained in literature and their detailed description can be found in our previous work [25]. Positions of the different $^5\text{D}_0 - ^7\text{F}_J$ transitions are located so that the distance between a J and the J+1 line increases with increasing J value. Transition $^5\text{D}_0 - ^7\text{F}_1$ is very close to the $^5\text{D}_0 - ^7\text{F}_0$ transition [36]. The weak $^5\text{D}_0 - ^7\text{F}_0$ transition, which is forbidden by both electric and magnetic dipole selection rules in the case of the free ion, occurs due to a weak J mixing by the crystalline field [37]. Magnetic dipole transition like $^5\text{D}_0 - ^7\text{F}_1$ are allowed by the Laporte selection rule, but their intensities are weak and comparable to those of the induced electric dipole transitions [36]. The fast decay transitions from $^5\text{D}_2$ and $^5\text{D}_1$ are also denoted in Fig. 4. The $^5\text{D}_1 - ^7\text{F}_3$ transition (583 nm), located closely between the $^5\text{D}_0 - ^7\text{F}_0$ (582 nm) and the $^5\text{D}_0 - ^7\text{F}_1$ (587 nm) transitions is easy to identify on the time resolved image. Its time integrated peak has a comparable intensity to the intensities of peaks originating from nearby $^5\text{D}_0$ levels (see the line profile denoted by a red curve in Fig. 4). The luminescence spectra presented in publications usually do not have the time resolution, so it is hard to guess which transitions are short lived. Streak image presented in Fig. 4. shows clearly that the $^5\text{D}_1 - ^7\text{F}_3$ transition has a much higher intensity and a much shorter lifetime than nearby transitions from $^5\text{D}_0$ state.

3.2.2. Lifetime and rise time analysis

We conducted the time resolved analysis for transitions which are identified in Fig. 4. The streak image of photoluminescence spectrum of $\text{Sr}_2\text{CeO}_4:\text{Eu}^{3+}$ nanophosphor with the time range of 200 μs is shown in Fig. 5. The time range in Fig. 5. was selected to get a clear visual impression of time development of luminescence signals at their beginning and to enable a rough estimate of rise time of all transitions shown in Fig. 4. To obtain the more precise values of rise time we had to use streak camera time range of 5 μs .

We obtained that the lifetime of the level $^5\text{D}_1$ is about 0.21 ms and the level $^5\text{D}_0$ lifetime is about 0.78 ms. For the fast decay the lifetime is much longer than reported for other hosts in [27,32], where transitions from $^5\text{D}_1$ level have a fast decay with the order of lifetime of about 10 μs . Other references [14,20,33] provide the values of slow decay time of $\text{Sr}_2\text{CeO}_4:\text{Eu}^{3+}$ nanophosphor more or less similar to our result. Decay curve of the most intensive $^5\text{D}_0 - ^7\text{F}_2$ transition is usually used for

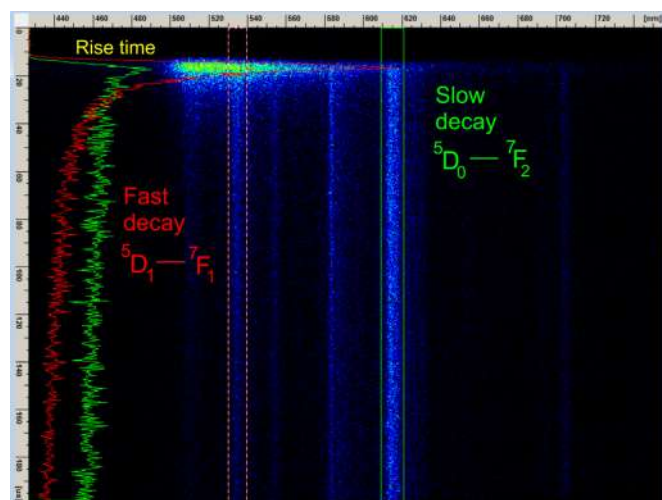


Fig. 5. Streak image of photoluminescence spectrum of $\text{Sr}_2\text{CeO}_4:\text{Eu}^{3+}$ nanoporphor with the time range of 200 μs tuned for analysis of rise time of all transitions. (OPO excitation at 330 nm.).

europium luminescence lifetime measurements [26].

In [32] we have proved that our experimental setup is capable of detecting fast rise times. We calculate the rise time according to Ranson equation [38,39]. $\text{YVO}_4:\text{Eu}^{3+}$ nanoporphor has clearly detectable rise time of slow decay transitions [32], for the ${}^5\text{D}_0 - {}^7\text{F}_2$ line it is about 8.1 μs . This relatively long luminescence rise time is related to energy transfer mechanism in $\text{YVO}_4:\text{Eu}^{3+}$ nanoporphor and it is useful for practical considerations. Our measurements of $\text{Sr}_2\text{CeO}_4:\text{Eu}^{3+}$ nanoporphor show that the luminescence rise time of ${}^5\text{D}_0 - {}^7\text{F}_2$ line of 0.39 μs is too short to be of practical use if cost effective equipment is to be used. So, it seems to us that for temperature sensing based on photoluminescence rise time measurements the other europium doped hosts, for example Yttrium orthovanadate $\text{YVO}_4:\text{Eu}^{3+}$, would be more appropriate.

3.2.3. The temperature dependency of intensity ratio of spectral lines

The luminescence of samples was measured both using pulsed (OPO) and continuous excitation. The measured luminescence spectra of Eu^{3+} doped Sr_2CeO_4 at various temperatures are presented in Fig. 6.

The spectral line intensities from the ${}^5\text{D}_0$ and ${}^5\text{D}_1$ transitions depend on two physical processes. The first process is the thermalization of the ${}^5\text{D}_1$ level with rising temperature, where the energy difference to populate the ${}^5\text{D}_1$ level from the ${}^5\text{D}_0$ level is fully covered by phonons. The second process is nonradiative quenching of the ${}^5\text{D}_0$ and ${}^5\text{D}_1$ levels through the charge transfer state. Configuration coordinate model,

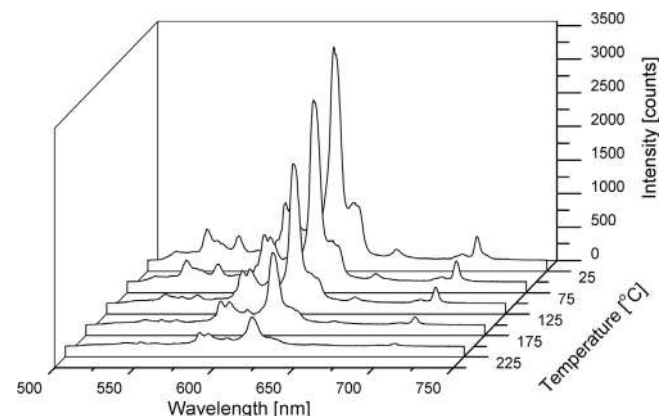


Fig. 6. Luminescence spectra of Eu^{3+} doped Sr_2CeO_4 at various temperatures. (Continuous laser diode excitation at 405 nm).

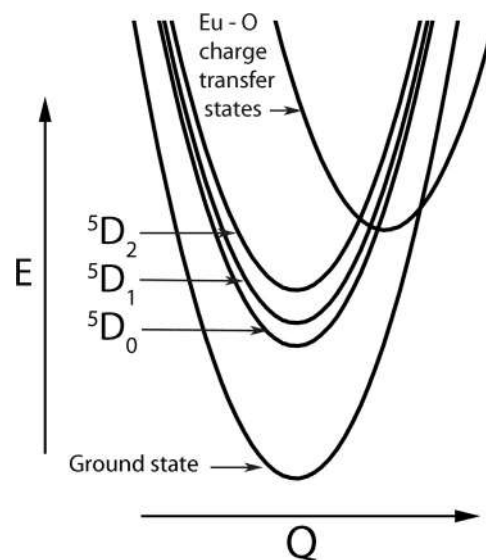


Fig. 7. Configuration coordinate model of $\text{Sr}_2\text{CeO}_4:\text{Eu}^{3+}$ nanoporphor relevant for understanding the temperature dependency of intensity ratio of spectral lines.

based on the same line of thought as presented in [15], is shown in Fig. 7. The $\text{Eu}^{3+} - \text{O}_2$ charge transfer state intersects not only with the europium ground state but also with three excited states, ${}^5\text{D}_2$, ${}^5\text{D}_1$ and ${}^5\text{D}_0$. By increasing the sample temperature the electrons in the ${}^5\text{D}_0$ state are thermally pushed to the crossover point and nonradiatively go to the ground state via the charge transfer state. Regarding the ${}^5\text{D}_1$ state, part of electrons go the same path as described for ${}^5\text{D}_0$ state. However, part of them go only to the ${}^5\text{D}_0$ level via charge transfer state. This explains why is ${}^5\text{D}_1$ state more rapidly quenched by temperature than ${}^5\text{D}_0$ state. So, the thermalization and quenching through charge transfer both have significant influence on the fluorescence intensity ratio (FIR). This means that the measured results cannot be simply fitted to the Boltzmann distribution. However, in order to apply the intensity ratio method in thermometry, it is required to calculate and fit a calibration function of analyzed potential thermophosphor. Based on considerations in [34,40], we decided to use the simple empirical equation for fitting the calculated intensity ratios of experimental data: $IR(T) = A + C \cdot e^{-T/\alpha}$, [34,40], where T is temperature in K, and empirical A , C and α are constants obtained through fitting of measured data.

The absolute thermal sensitivity S_a of the intensity ratio method is defined as the rate at which IR changes with the temperature:

$$S_a = \left| \frac{dIR}{dT} \right| \quad (1)$$

The relative thermal sensitivity of the intensity ratio method S_r is determined using formula:

$$S_r = \left| \frac{1}{IR} \frac{dIR}{dT} \right| \quad (2)$$

The temperature sensing calibration curve, shown in Fig. 8, was determined by calculating intensity ratio of photoluminescence spectral peaks at 614 nm and 537 nm. The calculation was repeated for all spectra, measured at different temperatures, first for increasing, then for decreasing temperatures. This kind of temperature sensing is useful up to 400 K, where the calculated intensity ratio values stop increasing and curve flattens beyond reasonable fitting.

3.2.4. Improved sensitivity of intensity ratio method based on temporal analysis

As proposed in [3], it is possible to improve the sensitivity of the intensity ratio method by using the temporal evolution of emission

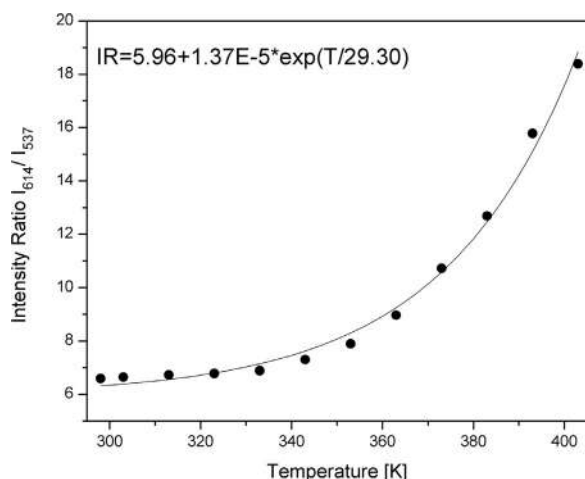


Fig. 8. Temperature sensing calibration curve of $\text{Sr}_2\text{CeO}_4:\text{Eu}^{3+}$ nanophosphor. (Continuous laser diode excitation at 405 nm).

lines. If integrated-in-time intensity of one of the signals is recorded with delayed gate, the additional temperature dependence is introduced in intensity ratio calculation. Namely, at low temperatures where emission lifetime is long the small gate delay of one of the signals will have relatively small effect on intensity ratio. However, at higher temperatures where the lifetime is short, the delayed gate will give rise to an increased signal difference. Moreover, this method of recording the signal with gated delay offers an efficient solution for minimizing or eliminating the effects of host luminescence, overlapping of emission from thermally coupled levels, and stray light originating from other intense transitions or from the laser excitation.

The method is illustrated in Fig. 9. The use of streak camera proves the concept, real application will be based on gated CCD cameras and appropriate bandwidth filters for selecting the emission lines. For calculation of intensity ratio the line at 614 nm is used integrated in time from its beginning, and line at 537 nm is integrated in time with various delays.

Temperature sensing calibration curves of $\text{Sr}_2\text{CeO}_4:\text{Eu}^{3+}$ nanophosphor for various delays of gating the signal at 537 nm are shown in Fig. 10.

It could be seen in Fig. 10 that intensity ratio between lines at 614 nm and 537 nm increases with increasing the gate delay of signal at 537 nm. However, increasing the delay decreases the integrated signal

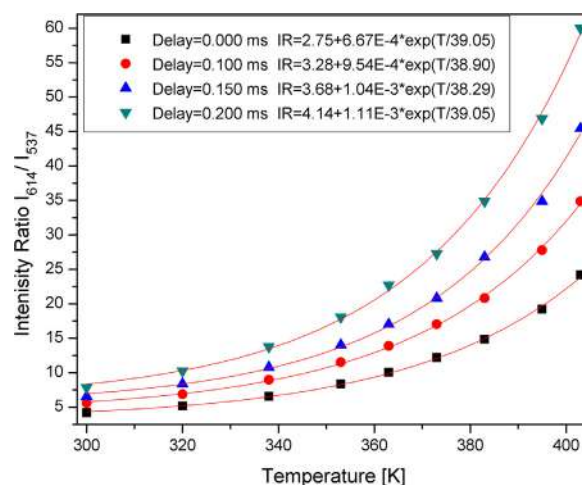


Fig. 10. Temperature sensing calibration curves of $\text{Sr}_2\text{CeO}_4:\text{Eu}^{3+}$ nanophosphor, for various delays of gating the signal at 537 nm. (Pulsed laser excitation at 330 nm).

intensity, so we didn't use delays larger than 200 μs . The host luminescence and other emission not belonging to europium lines at 537 nm and 614 nm spoil the temperature sensitivity. However, they last up to 100 μs , so their influence is eliminated for delays higher than 100 μs . Absolute and relative temperature sensitivities of $\text{Sr}_2\text{CeO}_4:\text{Eu}^{3+}$ nanophosphor are shown in Fig. 11. Increased sensitivity obtained by delayed gate of 537 nm emission is obvious from Fig. 11. It should be pointed out that continuous laser excitation at 405 nm pumps mainly the europium directly, resulting with much better elimination of host emission. However, the emission is generally weaker when europium is excited directly.

We have shown that continuous laser excitation provides satisfactory results. Increased sensitivity could be obtained by much more complex measurements technique presented here.

3.2.5. Luminescence lifetime temperature dependency

The temperature sensing calibration curve, shown in Fig. 12, was determined by calculating lifetime of spectral line at 614 nm. When the temperature was increased higher than 200 $^\circ\text{C}$ the intensity of measured spectra become too low to achieve reliable calculation of luminescence lifetime. Analysis presented in [41] shows that the temperature dependence of intensity ratio and luminescence lifetime, for the ideal

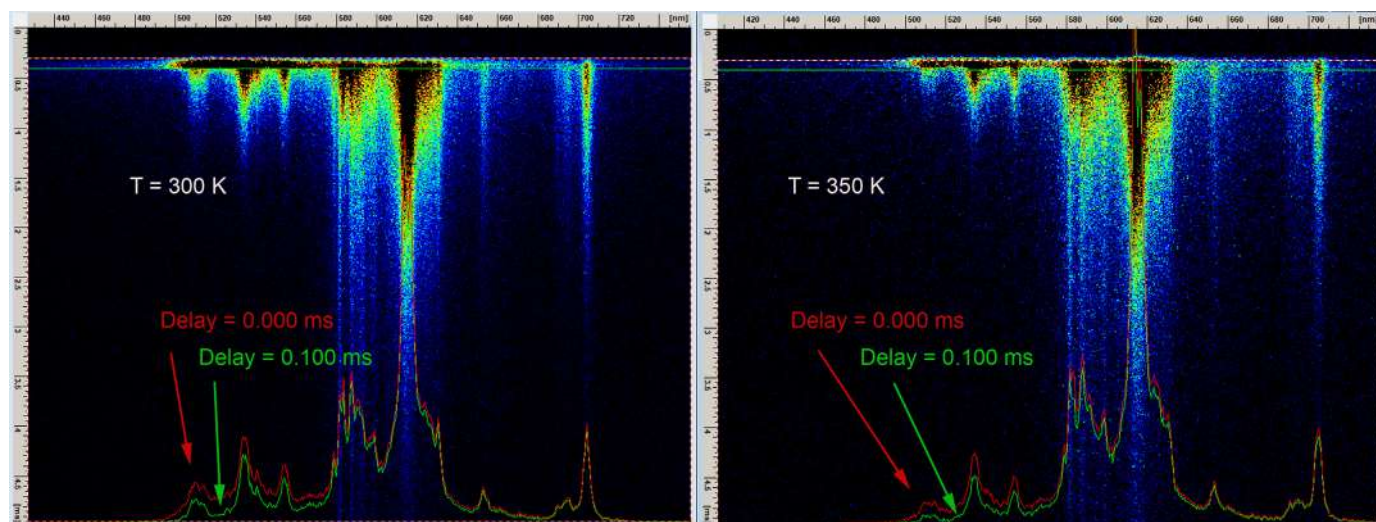


Fig. 9. Streak images of optical emission of $\text{Sr}_2\text{CeO}_4:\text{Eu}^{3+}$ at room temperature (left) and at 80 $^\circ\text{C}$ (right). Pulsed laser excitation is at 330 nm. The red profile corresponds to time integration of the whole signal, the green one to integration gated after 100 μs delay.

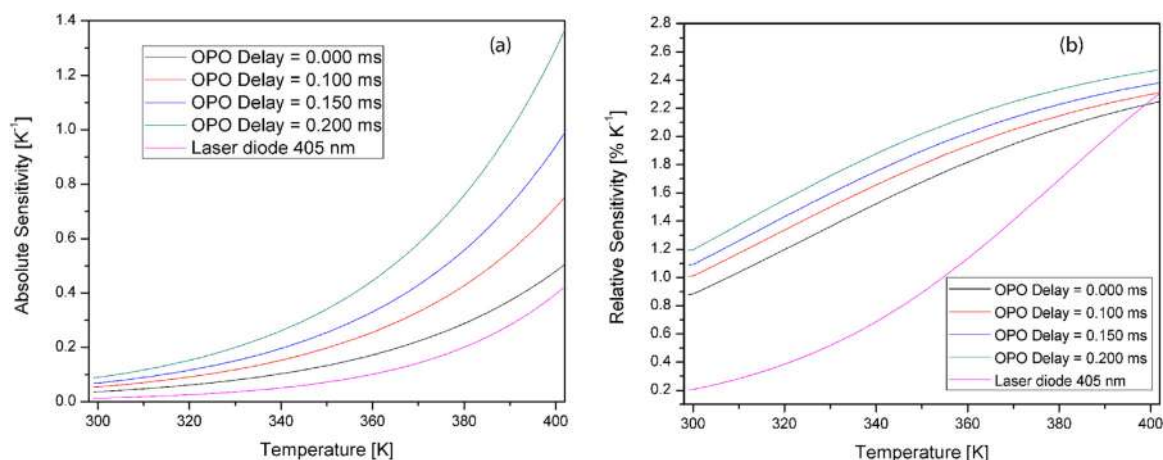


Fig. 11. (a) Absolute and (b) relative sensitivity of $\text{Sr}_2\text{CeO}_4:\text{Eu}^{3+}$ nanophosphor as a function of temperature.

case, differ only in magnitude by a certain factor. So, we will use the same form of empirical equation for fitting the lifetime experimental data as we used for fitting the intensity ratio, namely: $F(T) = A + C e^{-T/\alpha}$, [34,40], where T is temperature in K, and A , C and α empirical constants obtained through fitting of measured data.

In [42] europium hosted in PMMA matrix was used for lifetime based temperature sensing, in a range between 0 and 70 °C, with reported lifetimes between 0.28 ms and 0.4 ms. Temperature sensitive europium probes, excited at 405 nm, are described in [43], where reported lifetimes are in the range between 0.15 ms and 0.7 ms, corresponding to the same temperature sensing range as in [42], between 0 and 70 °C. In [44] the sensed temperature range is between 10 and 50 °C, measured lifetimes are between 0.12 ms and 0.35 ms. It seems that europium, hosted in another medium like PMMA, provides lesser sensing range with better sensitivity. Compared to our results of intensity ratio method, the luminescence lifetime method offers increased sensing range, because only the most intensive europium line at 614 nm is used for temperature sensing calibration curve determination. The intensity ratio calculations become unreliable when the intensity of the line at 537 nm turned out to be too small due to temperature increasing. Our measurements show that sensor based on $\text{Sr}_2\text{CeO}_4:\text{Eu}^{3+}$ nanophosphor covers not only the physiological temperature range but also the higher temperatures that are of interest when monitoring the thermal behaviour of electronic devices. Compared to other hosts doped with europium, TiO_2 [41], Gd_2O_3 [45], YNbO_4 , [46] and Lu_2O_3 [47], including references therein, it is easy to notice that there is usual trade-off between the sensitivity and sensing range, so the optimal host could be selected based on desired sensing range.

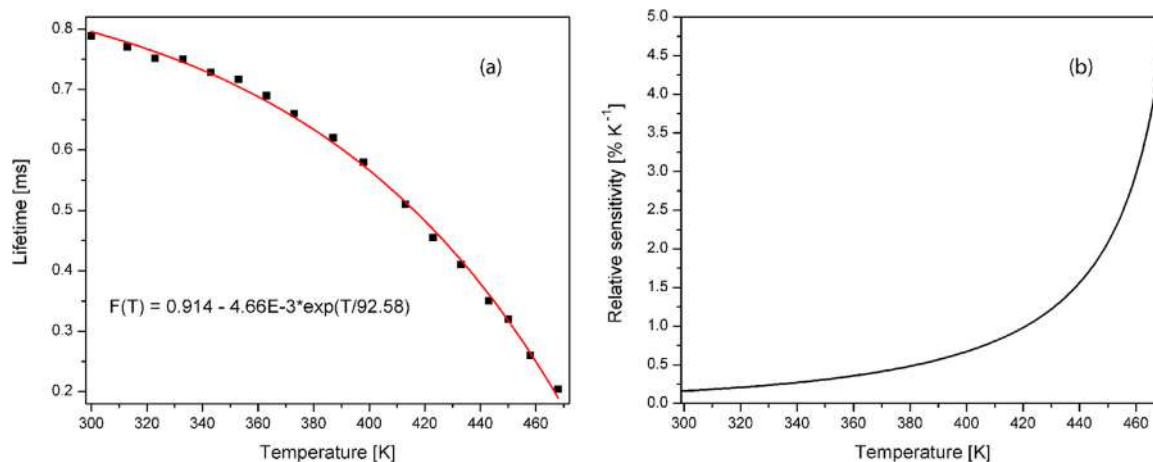


Fig. 12. Luminescence lifetime temperature dependence of $\text{Sr}_2\text{CeO}_4:\text{Eu}^{3+}$ nano phosphor and its relative sensitivity.

Methods for temperature sensing based on fluorescence intensity ratio and lifetime are not sensitive, regarding errors, to fluctuations in excitation intensity and light collection efficiency [3]. Moreover, if the lifetime of the used nanophosphor (measured here between 0.2 ms and 0.78 ms) is much longer than the laser pulse (5 ns), evaluation error could be neglected [3]. So, we conclude that measurement errors mostly originate from the fitting procedures and least-square errors in extracting the temperatures from the calibration curve [3]. For all presented methods, the relative errors are smaller than 3% in the whole measuring range and below 1% for temperatures above 350 K.

3.2.6. The high pressure effects on $\text{Sr}_2\text{CeO}_4:\text{Eu}^{3+}$ photoluminescence

The spectral responses were measured at various pressures in order to analyze the high pressure effects on photoluminescence emission of $\text{Sr}_2\text{CeO}_4:\text{Eu}^{3+}$ nanophosphor. Luminescence spectra of Eu^{3+} doped Sr_2CeO_4 at various pressures are shown in Fig. 13. To check the existence of hysteresis, the spectral measurements were performed successively, first for increasing and then for decreasing pressure.

It is well known that rare earth ions are highly sensitive to local symmetry. Any change in the symmetry is observable in their luminescence spectra [48]. In the paper by Zhang et al. [49] dependencies between the phase transitions of the crystal structure induced by pressure and the changes in the luminescence spectrum of the Eu^{3+} ion are explained. It was shown in [49] that the red shift rate and relative intensity ratio of emissions vary along with increasing pressure. Namely, the red shift of emissions can be ascribed to the expansion of the f orbit of the Eu^{3+} ; and the relative intensity ratio variation of emissions is attributed to the change of crystal field due to the phase

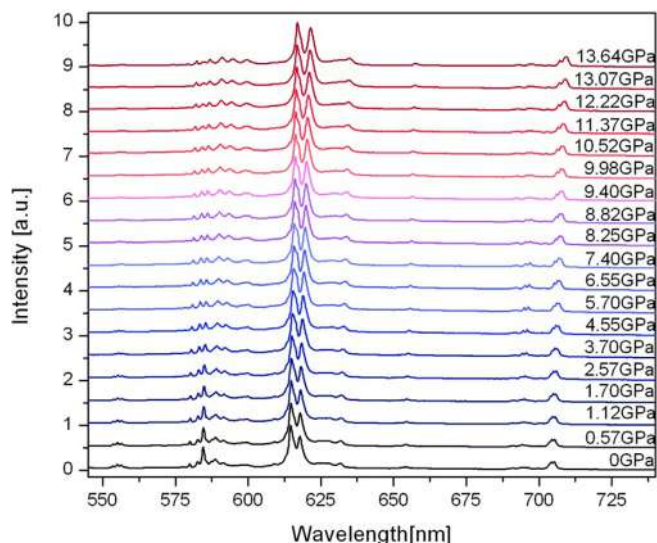


Fig. 13. Luminescence spectra of Eu^{3+} doped Sr_2CeO_4 at various pressures. (Continuous laser diode excitation at 405 nm).

transition.

Changes and deformations of luminescence spectrum which imply phase transitions are easily identified in Fig. 3 in [49]. Fig. 13. shows that, in presented pressure range, there are no such deformations of

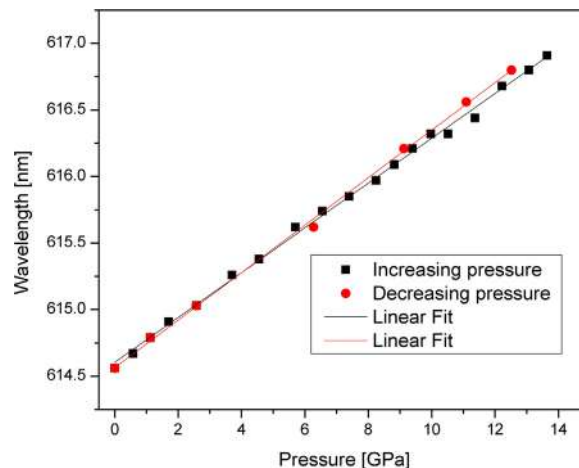


Fig. 15. Pressure induced shift in wavelength of the highest intensity peak, at 614.56 nm at atmospheric pressure.

$\text{Sr}_2\text{CeO}_4:\text{Eu}^{3+}$ luminescence spectrum. This means that our sample didn't undergo the phase transition.

Our measurements show that after decompression the luminescence spectrum of $\text{Sr}_2\text{CeO}_4:\text{Eu}^{3+}$ is completely restored. Other publications show similar results for different host matrixes [13,50].

Pressure induced change in the crystal lattice parameters also disturb the position of energy levels [11–13,49–51]. The variation of

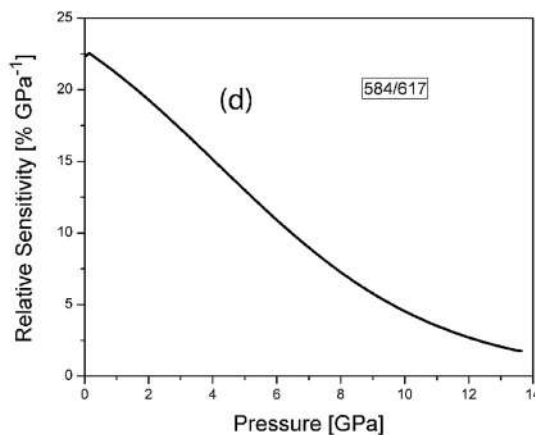
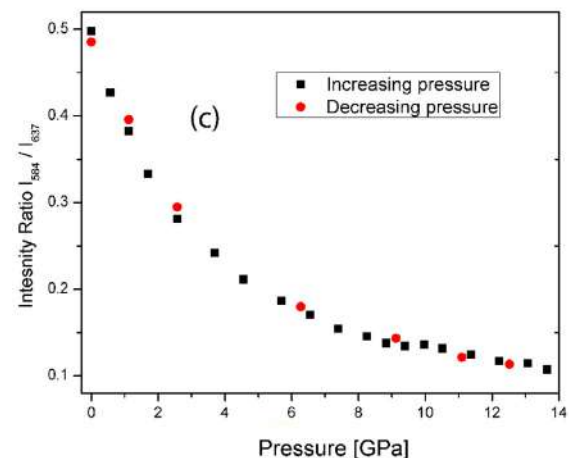
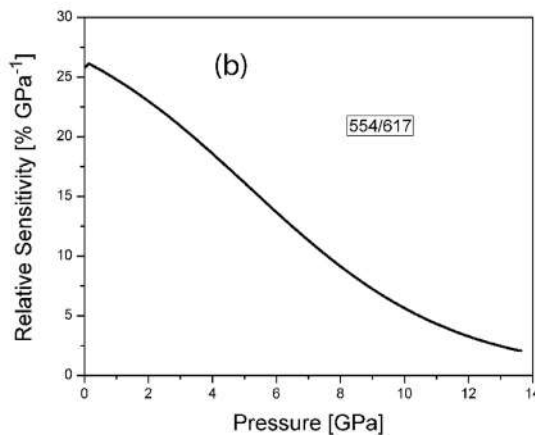
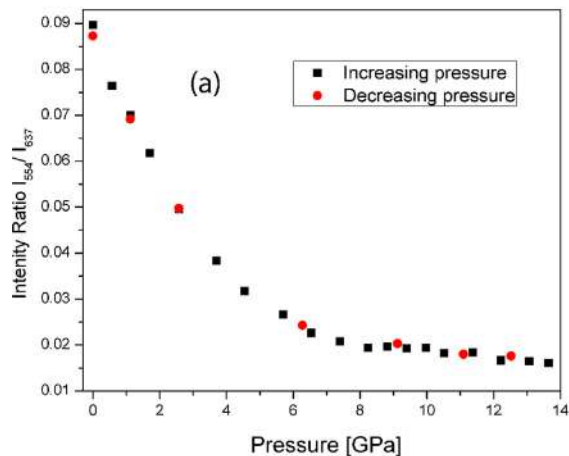


Fig. 14. High pressure sensing calibration curves of $\text{Sr}_2\text{CeO}_4:\text{Eu}^{3+}$ nanophosphor. (a) Intensity ratio I_{554}/I_{637} . (b) Its relative sensitivity. (c) Intensity ratio I_{584}/I_{614} . (d) Its relative sensitivity. (Continuous laser diode excitation at 405 nm.).

energy of 5D_1 and 5D_0 levels and change of charge transfer region position leads to a rise in probability for non-radiative transitions. The applied pressure predominantly affects 5D_1 level, as can be seen in Fig. 13. A slight variation in the intensity of the most prominent $^5D_0 \rightarrow ^7F_2$ transition lines can also be observed in Fig. 13. The intensity ratios of intensities of emission lines from 5D_1 and 5D_0 states are shown in Fig. 14. Exact positions of luminescence peaks used for calculating the intensity ratios are at 554.2 nm, 584.52 nm and 617 nm at atmospheric pressure. The observed decrease of intensity ratio with rising pressure is also due to greater dependence of non-radiative transitions from 5D_1 state. The values for both compression and decompression of sample are displayed in the Fig. 14. The hysteresis is negligible, which means the repeatability is good. For intensity ratio of lines at 584 nm and 637 nm, the reliable part of curve is from 0 GPa up to 10 GPa (for intensity ratio of lines at 554 nm and 637 nm the reliable part of curve is up to 8 GPa), which opens the possibility for using the material as a pressure sensor.

Another method of sensing pressure is based on measuring the pressure induced red shift in wavelength of appropriately selected, usually highest intensity peak. Pressure induced shift in wavelength of the highest intensity peak of $Sr_2CeO_4:Eu^{3+}$ luminescence (614.56 nm at atmospheric pressure) is shown in Fig. 15. The proposed method is very usable, with almost linear curve, for high pressures up to 14 GPa. Red-shift rate was estimated to be about $0.17 \text{ nm} \times \text{GPa}^{-1}$. The rate is the same for other emission lines from 5D_0 state, and for $^5D_0 \rightarrow ^7F_1$ it is about $0.096 \text{ nm} \times \text{GPa}^{-1}$.

To the best of our knowledge, there are no published results regarding using of $Sr_2CeO_4:Eu^{3+}$ nanophosphor for pressure sensing. Compared to the other materials doped with the Eu^{3+} ions, Sr_2CeO_4 provides similar pressure sensing range in terms of unambiguousness as $ZrGeO_4$ [11], $LaPO_4$ [12], $GdVO_4$ [13] and TiO_2 [50]. Y_2O_3 host offers much wider unambiguous pressure sensing range [49]. Under unambiguous we mean the fact that one luminescence intensity ratio corresponds to only one pressure. So, it seems that Sr_2CeO_4 is quite promising for making devices for remote pressure sensing.

To estimate errors of pressure sensing in our study the similar line of thought holds as for temperature sensing methods. For intensity ratio method relative errors are smaller than 8% in pressure range up to 10 GPa. For method of sensing pressure based on measuring the pressure induced red shift in wavelength of highest intensity peak the relative error is below 2% for the whole measured range (up to 14 GPa).

4. Conclusion

In this paper we described the synthesis and characterization of the $Sr_2CeO_4:Eu^{3+}$ nanopowder. Beside luminescence kinetics of slow decay transitions we also estimated their rise time and lifetime of fast decay transitions. Measured values of lifetime of luminescence emission of lines originating from transitions from 5D_0 level and intensity ratios of two spectral lines were used for determining the calibration curves for remote temperature sensing. We have showed that, for analyzed $Sr_2CeO_4:Eu^{3+}$ material, the temperature sensing based on ratio of intensities of two lines is useful up to 400 K, while sensing based on lifetime of spectral line at 614 nm could be used up to 460 K. We have obtained sensitivity improvement of the intensity ratio method by simulating the delayed gating of acquiring the intensity of one of spectral lines. The using of streak camera proved the proposed concept. The real application will be based on gated cameras and appropriate bandwidth filters for selecting the emission lines. Also, we have analyzed the effects of pressure on photoluminescence response of synthesized material. To the best of our knowledge, this analysis is first presented here. Results of all our analyses prove that $Sr_2CeO_4:Eu^{3+}$ nanopowder prepared by a simple and low cost solution combustion synthesis method is appropriate material for remote temperature and pressure sensing and for various other optoelectronic devices.

Acknowledgement

This work was financially supported within the Projects of Ministry of Education, Science and Technological Development of the Republic of Serbia OI171020, ON171038 and III45016.

References

- [1] D. Jaque, F. Vetrone, *Nanoscale* 4 (2012) 4301–4326.
- [2] C.D.S. Brites, P.P. Lima, N.J.O. Silva, A. Millan, V.S. Amaral, F. Palacio, L.D. Carlos, *Nanoscale* 4 (2012) 4799–4829.
- [3] M. Aldén, A. Omrane, M. Richter, G. Särner, *Prog. Energy Combust. Sci.* 37 (2011) 422–461.
- [4] S.W. Allison, G.T. Gillies, *Rev. Sci. Instrum.* 68 (1997) 2615–2650.
- [5] L.P. Goss LP, A.A. Smith, M.E. Post ME, *Rev. Sci. Instrum.* 60 (1989) 3702–3706.
- [6] A.L. Heyes, *J. Lumin.* 129 (2009) 2004–2009.
- [7] M.M. Gentleman, D.R. Clarke, *Surf. Coat. Technol.* 188–189 (2004) 93–100.
- [8] A.H. Khalid, K. Kontis, *Sensors* 8 (2008) 5673–5744.
- [9] S.A. Wade, S.F. Collins, G.W. Baxter, *J. Appl. Phys.* 94 (2003) 4743–4756.
- [10] S.A. Wade, D.I. Forsyth, K.T.V. Grattan, *Rev. Sci. Instrum.* 72 (2001) 3186–3190.
- [11] R. Rao, T. Sakuntala, S.N. Achary, A.K. Tyagi, *J. Appl. Phys.* 106 (2009) (123517-1-5).
- [12] Z. Zhi, Z. Jian, D. Zejun, *J. Rare Earths* 28 (2010) 254–257.
- [13] C.C. Zhang, Z.M. Zhang, R.C. Dai, Z.P. Wang, J.W. Zhang, Z.J. Ding, *J. Phys. Chem. C* 114 (2010) 18279–18282.
- [14] M. Stefanski, L. Marciniak, D. Hreniak, W. Strek, *Mater. Res. Bull.* 76 (2016) 133–139.
- [15] L. Shi, H. Zhang, C. Li, Q. Su, *RSC Adv.* 1 (2011) 298–304.
- [16] K. Suresh, N.V. Poornachandra Rao, K.V.R. Murthy, *Bull. Mater. Sci.* 37 (2014) 1191–1195.
- [17] M. Stefanski, M. Lukaszewicz, D. Hreniak, W. Strek, *J. Chem. Phys.* 146 (2017) (104705-1-7).
- [18] M. Stefanski, L. Marciniak, D. Hreniak, W. Strek, *J. Chem. Phys.* 142 (2015) (184701-1-7).
- [19] X. Yang, Z. Shao, H. Ru, *J. Mater. Sci. Technol.* 32 (2016) 1066–1070.
- [20] T. Grzyb, A. Szczeszak, J. Rozowska, J. Legendziewicz, S. Lis, *J. Phys. Chem. C* 116 (2012) 3219–3226.
- [21] C.A. Rao, P. Rao, V. Nannapaneni, K.V.R. Murthy, *Adv. Mater. Lett.* 4 (2013) 207–212.
- [22] B.W.R. Kumar, K.V.R. Murthy, B.S. Rao, M. Shaik, *Int. J. Sci. Innov. Discov.* 1 (2011) 145–150.
- [23] C.A. Rao, P.R.V. Nannapaneni, K.V.R. Murthy, *J. Sci. Res.* 5 (2013) 1–11.
- [24] J. Gomes, A.M. Pires, O.A. Serra, *Quim. Nova* 27 (2004) 706–708.
- [25] M.S. Rabasovic, D. Sevic, J. Krizan, M. Terzic, J. Mozina, B.P. Marinkovic, S. Savic Sevic, M. Mitric, M.D. Rabasovic, N. Romcevic, *J. Alloy. Compd.* 622 (2015) 292–295.
- [26] J. Krizan, M. Mazaj, V. Kaucic, I. Bajsic, J. Mozina, *Acta Chim. Slov.* 61 (2014) 608–614.
- [27] M.D. Chambers, P.A. Rousseve, D.R. Clarke, *J. Lumin.* 129 (2009) 263–269.
- [28] S.W. Allison, S.M. Goedeke, M.R. Cates, W.A. Hollerman, J.I. Eldridge, T.J. Bencic, Oak Ridge National Laboratory Report No 123055, 2005. (Published through SciTech Connect, 03/24/2005).
- [29] X. Li, X. Wei, Y. Qin, Y. Chen, C. Duan, M. Yin, *J. Alloy. Compd.* 657 (2016) 353–357.
- [30] J.R. Darwent, C.D. Flint, P.J. O'Grady, *Chem. Phys. Lett.* 127 (1986) 547–550.
- [31] A.H. Khalid, K. Kontis, *Meas. Sci. Technol.* 20 (2009) (025305-1-9).
- [32] D. Sevic, M.S. Rabasovic, J. Krizan, S. Savic-Sevic, M. Mitric, M. Gilic, B. Hadzic, N. Romcevic, *Mater. Res. Bull.* 88 (2017) 121–126.
- [33] M.S. Rabasovic, J. Krizan, P. Gregoric, M.D. Rabasovic, N. Romcevic, D. Sevic, *Opt. Quantum Electron.* 48 (2016) 163.
- [34] M.D. Rabasovic, B.D. Muric, V. Celebonovic, M. Mitric, B.M. Jelenkovic, M.G. Nikolic, *J. Phys. D: Appl. Phys.* 49 (2016) (485104-1-6).
- [35] R.W. Cheary, A. Coelho, A fundamental parameters approach to X-ray line-profile fitting, *J. Appl. Crystallogr.* 25 (1992) 109–121.
- [36] K. Binnemans, *Coord. Chem. Rev.* 295 (2015) 1–45.
- [37] Y. Dwivedi, S.C. Zilio, *Opt. Express* 21 (2013) 4717–4727.
- [38] S.W. Allison, S.M. Goedeke, M.R. Cates, W.A. Hollerman, J.I. Eldridge, T.J. Bencic, Oak Ridge National Laboratory Report No 123055, 2005. (Published through SciTech Connect, 03/24/2005).
- [39] R.M. Ranson, E. Evangelou, C.B. Thomas, *Appl. Phys. Lett.* 72 (1998) 2663–2664.
- [40] D. Ananias, C.D.S. Brites, L.D. Carlos, J. Rocha, *Eur. J. Inorg. Chem.* 2016 (2016) 1967–1971.
- [41] M.G. Nikolic, Z. Antic, S. Culubrk, J.M. Nedeljkovic, M.D. Dramicanin, *Sens. Actuators B* 201 (2014) 46–50.
- [42] J. Yu, L. Sun, H. Peng, M.L.J. Stich, *J. Mater. Chem.* 20 (2010) 6975–6981.
- [43] S.M. Borisov, O.S. Wolfbeis, *Anal. Chem.* 78 (2006) 5094–5101.
- [44] H.S. Peng, M.L.J. Stich, J.B. Yu, L.N. Sun, L.H. Fischer, O.S. Wolfbeis, *Adv. Mater.* 22 (2010) 716–719.
- [45] M.G. Nikolic, A.Z. Al-Juboori, V. Đordjevic, M.D. Dramicanin, *Phys. Scr.* T157 (2013) (014056-1-5).
- [46] Lj.R. Đačanin, M.D. Dramicanin, S.R. Lukic-Petrovic, D.M. Petrovic, M.G. Nikolic, *Radiat. Meas.* 56 (2013) 143–146.
- [47] V. Lojpur, Z. Antic, R. Krsmanovic, M. Medic, M.G. Nikolic, M.D. Dramicanin, *J. Serb. Chem. Soc.* 77 (2012) 1735–1746.
- [48] G. Blasse, B.C. Grabmaier, *Luminescent Materials*, Springer Verlag, Berlin, 1994.
- [49] J. Zhang, H. Cui, P. Zhu, C. Ma, X. Wu, H. Zhu, Y. Ma, Q. Cui, *J. Appl. Phys.* 115 (2014) 023502.
- [50] Z. Zhao, Q.G. Zeng, Z.M. Zhang, Z.J. Ding, *J. Lumin.* 122–123 (2007) 862–865.
- [51] S. Surendra Babu, P. Babu, C.K. Jayasankar, Th Troster, W. Sievers, G. Wortmann, *J. Phys.: Condens. Matter* 18 (2006) 1927–1938.



Effects of temperature on luminescent properties of Gd₂O₃:Er, Yb nanophosphor

D. Šević¹ · M. S. Rabasović¹ · J. Križan² · S. Savić-Šević¹ · M. D. Rabasović¹ · B. P. Marinković¹ · M. G. Nikolić¹

Received: 8 October 2019 / Accepted: 7 April 2020
© Springer Science+Business Media, LLC, part of Springer Nature 2020

Abstract

In this study we analyze nano powder Gd₂O₃ doped with Er³⁺ and Yb³⁺. Material was synthesized by simple and efficient solution combustion method. The nano phosphor was optically excited at 980 nm by using pulsed laser diode. We have obtained time resolved upconversion luminescence spectra of nano powder samples of Gd₂O₃:Er,Yb using a streak camera and analyzed temperature dependence of erbium optical line emission intensities. The possibilities of using Gd₂O₃:Er,Yb for temperature sensing were analyzed by means of luminescence intensity ratio method. We show that synthesized Gd₂O₃:Er,Yb material is useful for temperature measurements up to 550 K.

Keywords Photoluminescence · Thermographic phosphor · Laser spectroscopy · Combustion synthesis

1 Introduction

There is a growing interest in recent years for luminescence upconverting (UC) materials (Zhao et al. 2019; Gavrilovic et al. 2016; Ang et al. 2011). Using of upconversion nanoparticles provides many advantages compared to using of conventional phosphors. The effects of autofluorescence and of stray excitation light are inherently removed. Moreover, signal-to-noise ratio is notably improved.

The optical thermometry is widely used to remotely measure the temperature. There are several techniques of temperature sensing by using the thermographic phosphors, analyzed by us in (Sevic et al. 2020); they are based on intensity ratio, lifetime or rise time of luminescence. However, the luminescence intensity ratio (LIR) based temperature sensing is

This article is part of the Topical Collection on Advanced Photonics Meets Machine Learning.

Guest edited by Goran Gligoric, Jelena Radovanovic and Aleksandra Maluckov.

✉ D. Šević
sevic@ipb.ac.rs

¹ Institute of Physics Belgrade, University of Belgrade, Belgrade, Serbia

² AMI D.O.O, Ptuj, Slovenia

most commonly used and will be analyzed here. The technique is based on calculating the optical emission intensity variations of thermally coupled transitions, measured at different temperatures. Literature survey shows that the Er^{3+} ion is a prevalently used for the LIR based temperature sensing with UC phosphors (Li X. et al. 2016; Li L. et al. 2016; Avram et al. 2018; Du et al. 2017; Du et al. 2018; Dong et al. 2007; Xu et al. 2012; Liu et al. 2016; Santos et al. 1999; Wang et al. 2015; Manzani et al. 2017; Singh et al. 2009; Krizan et al. 2014).

The luminescence temperature dependence of downconverting materials is exhaustively analyzed in literature (Goss et al. 1989; Feist et al. 1999; Heyes 2009; Cates et al. 2002; Eldridge et al. 2012). The detailed analyses of thermographic phosphors are provided in review papers (Allison et al. 1997; Alden et al. 2011; Brites et al. 2012; Jaque and Vetrone 2012; Khalid and Kontis 2008). Studies of sensing of temperature using UC materials doped with Er, Yb could be found in (Li X. et al. 2016; Li L. et al. 2016; Avram et al. 2018; Du et al. 2017; Du et al. 2018; Dong et al. 2007; Xu et al. 2012; Liu et al. 2016; Santos et al. 1999; Wang et al. 2015; Manzani et al. 2017; Singh et al. 2009; Krizan et al. 2014).

The aim of this study is analysis of potentials of using the $\text{Gd}_2\text{O}_3:\text{Er}^{3+}, \text{Yb}^{3+}$ for temperature measurements. Gd_2O_3 host doped with Er and Yb was prepared by simple and cost effective process. There are various improvements of nano phosphor materials in regard the luminescent efficiency (Li et al. 2017; May et al. 2018; Ou et al. 2018; Su et al. 2019; Xing et al. 2017; Zhang et al. 2019). However, due to appropriately positioned erbium transition lines, $\text{Gd}_2\text{O}_3:\text{Er}^{3+}, \text{Yb}^{3+}$ is a very good candidate for luminescence intensity ratio based remote temperature sensing.

This is not our first study about Gd_2O_3 host. Analysis of temperature effects on $\text{Gd}_2\text{O}_3:\text{Er}^{3+}, \text{Yb}^{3+}$, using continuous excitation, was presented in (Krizan et al. 2014). The pulsed laser excitation, used in this study, has some advantages compared to continuous excitation in regard of local heating of material. The luminescence temperature dependence of the Gd_2O_3 host doped with Eu was also analyzed before (Nikolic et al. 2013).

2 Experimental procedures

The Solution Combustion Synthesis (SCS) method, explained in detail in (Krizan et al. 2014), was used to prepare the studied nano phosphor.

Stoichiometric quantities of starting chemicals $\text{Gd}(\text{NO}_3)_3 \cdot 6\text{H}_2\text{O}$, $\text{Er}(\text{NO}_3)_3 \cdot 5\text{H}_2\text{O}$ and $\text{Yb}(\text{NO}_3)_3 \cdot 5\text{H}_2\text{O}$ with the high purity were chosen to obtain the Er concentration of 2.0 at.% and Yb concentration of 0.5 at.% in $\text{Gd}_2\text{O}_3:\text{Er}, \text{Yb}$ ($\text{Gd}_{1.95}\text{Er}_{0.04}\text{Yb}_{0.01}\text{O}_3$).

For solution combustion synthesis we have used the dry mixture of 14.67 g (32.5 mmol = 195/6 mmol) of $\text{Gd}(\text{NO}_3)_3 \cdot 6\text{H}_2\text{O}$, 0.296 g (0.667 mmol = 4/6 mmol) of $\text{Er}(\text{NO}_3)_3 \cdot 5\text{H}_2\text{O}$ and 0.075 g (0.167 mmol = 1/6 mmol) of $\text{Yb}(\text{NO}_3)_3 \cdot 5\text{H}_2\text{O}$, combined with the mixture of 1 g of β -alanine and 5 g of urea which were used as organic fuels.

Pulsed laser diode excitation at 980 nm was used to acquire the photoluminescence emission spectra of $\text{Gd}_2\text{O}_3:\text{Er}^{3+}, \text{Yb}^{3+}$ nano phosphor. The optical emission of analyzed samples was detected by using the streak camera system, used and explained in (Sevic et al. 2020; Vlastic et al. 2018). The detailed explanation of the setup for temperature measurements is provided in (Rabasovic et al. 2016).

A high resolution scanning electron microscope (SEM) equipped with a high brightness Schottky Field Emission gun (FEGSEM, TESCAN) operating at 4 kV was used to check the structure of studied nano phosphor.

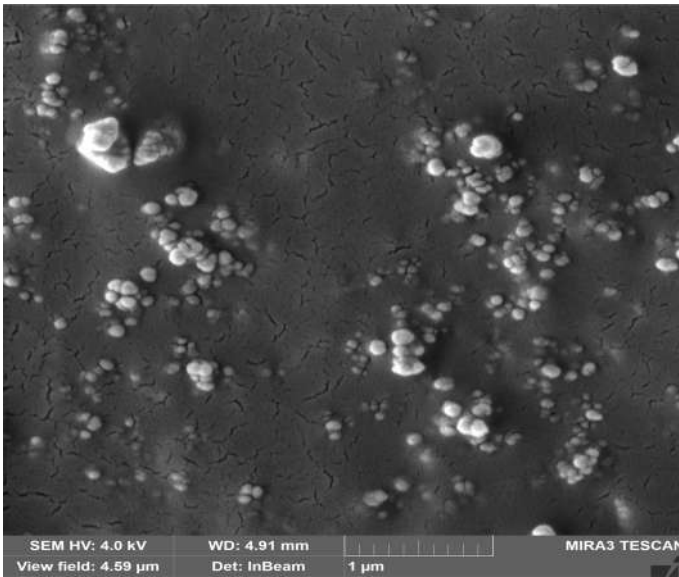


Fig. 1 SEM image of $\text{Gd}_2\text{O}_3:\text{Er}^{3+},\text{Yb}^{3+}$ nano phosphor prepared by SCS method

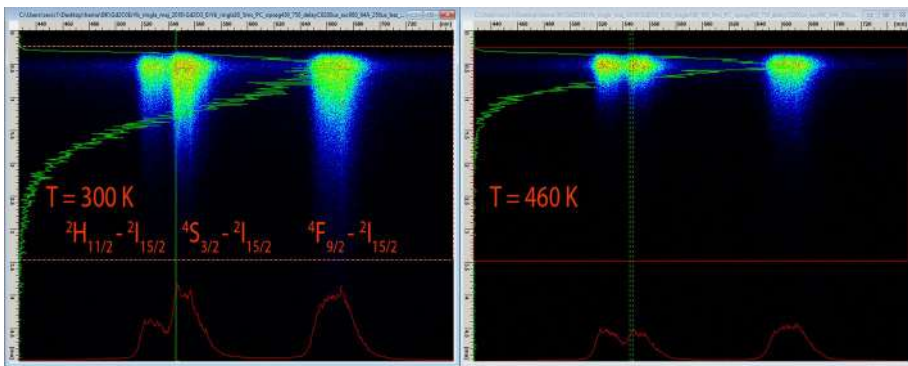


Fig. 2 Time-resolved luminescence spectra of $\text{Gd}_2\text{O}_3:\text{Er}^{3+},\text{Yb}^{3+}$ at two temperatures. Pulsed laser diode excitation is at 980 nm

3 Results and discussion

The representative SEM image of the synthesized $\text{Gd}_2\text{O}_3:\text{Er}^{3+},\text{Yb}^{3+}$ nano material, see Fig. 1, shows the agglomerated grains and particles with dimensions from 50 nm to over 100 nm.

The photoluminescence emission of $\text{Gd}_2\text{O}_3:\text{Er}^{3+},\text{Yb}^{3+}$ was measured over the temperature range 300–660 K. To get the general impression of luminescence temperature dependence, time-resolved luminescence spectra of $\text{Gd}_2\text{O}_3:\text{Er}^{3+},\text{Yb}^{3+}$ at two temperatures are displayed in Fig. 2. The emission band centered at 528 nm originates from ${}^2\text{H}_{11/2} \rightarrow {}^2\text{I}_{15/2}$ transition, the emission band at 553 nm originates from ${}^4\text{S}_{3/2} \rightarrow {}^2\text{I}_{15/2}$

transition, and the emission bands at 670 nm originates from ${}^4F_{9/2} \rightarrow {}^2I_{15/2}$ transition of Er^{3+} ion.

Luminescence quenching, i.e. decreasing of luminescence quantum yield at increasing concentrations of dopants in phosphors is a well known phenomenon. Literature survey (Lojpur et al. 2013; Li X. et al. 2016; Li L. et al. 2016; Avram et al. 2018; Du et al. 2017; Du et al. 2018; Dong et al. 2007; Xu et al. 2012; Liu et al. 2016; Santos et al. 1999; Wang et al. 2015; Manzani et al. 2017; Singh et al. 2009) shows that concentrations of dopants in our work are too small in regard the concentration quenching phenomenon, so it was neglected.

Concentration effects on luminescence intensities of Er transitions were analyzed in (Lojpur et al. 2013). It was shown that by varying the concentration of Yb, it is possible to vary the intensity and lifetime ratio of green and red component of luminescence (color tuning). By decreasing the Yb concentration the ratio between the green and red component increases in favor of the green component, emitted at two Er transitions, namely ${}^2H_{11/2} \rightarrow {}^2I_{15/2}$ and ${}^4S_{3/2} \rightarrow {}^2I_{15/2}$ transitions.

At the room temperature, the sample of $\text{Gd}_2\text{O}_3:\text{Er},\text{Yb}$ analyzed in this work has similar intensities and lifetimes (in order of about 0.7 ms, measured from data obtained by streak image shown in Fig. 2) of green and red component of luminescence. So, in regard of using of this material for remote temperature sensing, the dopant concentrations could be considered as optimal.

Integrated-in-time luminescence spectra of $\text{Gd}_2\text{O}_3:\text{Er}^{3+},\text{Yb}^{3+}$ at several temperatures are shown in Fig. 3. We see that for temperatures above 550 K the measured signal gets weak and impractical for reliable analysis.

Based on our estimations of shape of spectral response and time durations of luminescence of erbium transitions shown in Fig. 2, we propose the schematic view of $\text{Gd}_2\text{O}_3:\text{Er}^{3+},\text{Yb}^{3+}$ energy transfer processes presented in Fig. 4.

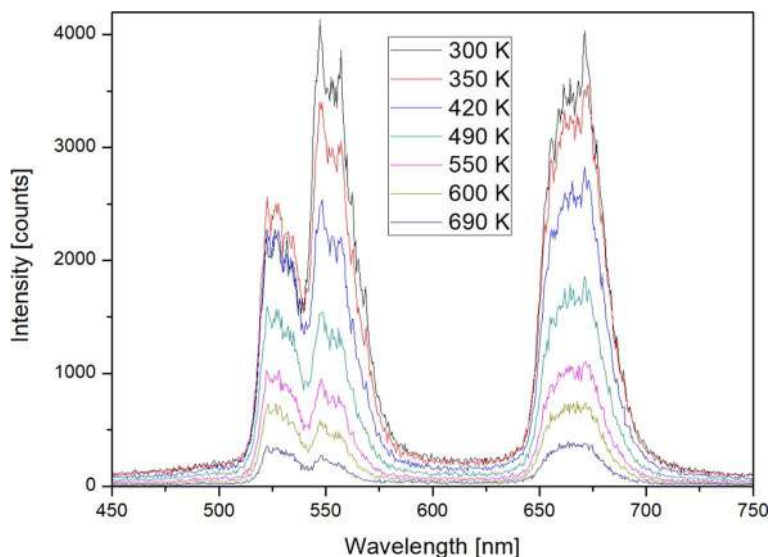
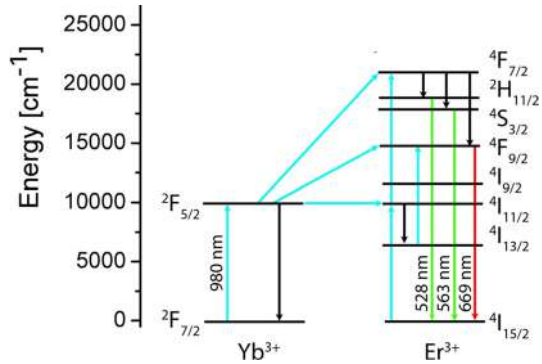


Fig. 3 Luminescence spectra of $\text{Gd}_2\text{O}_3:\text{Er}^{3+},\text{Yb}^{3+}$ at several temperatures. Pulsed laser diode excitation is at 980 nm

Fig. 4 Schematic view of $Gd_2O_3:Er^{3+},Yb^{3+}$ energy transfer processes



Looking at Figs. 2 and 3 it is easily noticed that luminescence intensity ratio between lines at 528 nm and 553 nm is temperature dependent. It is well known that the luminescence intensity ratio is independent on small variations of laser excitation energy or optical gain of acquisition system (Brites et al. 2012; Jaque and Vetrone 2012). Two emission lines, with a small energy gap between them, are mostly chosen to implement the temperature sensing. The higher energy level becomes more populated with increasing of temperature by thermalization effects from the lower energy level. In this way, relative intensity of higher level, in regard the lower level, gradually increases by temperature increase.

Ratio of intensities of two levels, IR , is determined by Boltzmann-type population distribution given by (Brites et al. 2012; Jaque and Vetrone 2012; Đačanin et al. 2014; Nikolic et al. 2018):

$$IR = \frac{I_{31}}{I_{21}} = C \exp\left(-\frac{\Delta E}{kT}\right) \tag{1}$$

where k is the Boltzmann constant, $k=0.695\ 034\ 76(63)\ \text{cm}^{-1}\ \text{K}^{-1}$ and ΔE is the energy gap between two excited levels.

However, as explained in (Lojpur et al. 2016; Sevic et al. 2020) another constant, A , should be introduced to Eq. (1), to account for the finite value of IR at low temperatures:

$$IR = \frac{I_{31}}{I_{21}} = A + C \exp\left(-\frac{\Delta E}{kT}\right) \tag{2}$$

Figure 5 shows temperature sensing calibration curve based on luminescence intensity ratio of two Er emission lines, at 528 nm and 553 nm. Being of strong intensity and closely located, these two lines satisfy all criteria for choosing them for LIR method. Estimated value of the energy gap is $\Delta E=728\ \text{cm}^{-1}$. It is obtained by fitting the sensing calibration curve by Eq. (2). Our estimation of the energy gap is similar to results presented in (Li X. et al. 2016; Li et al. 2016; Avram et al. 2018; Du et al. 2017; Du et al. 2018; Dong et al. 2007; Xu et al. 2012; Liu et al. 2016; Santos et al. 1999; Wang et al. 2015; Manzani et al. 2017; Singh et al. 2009). We have discarded the measured points above 550 K to avoid large fitting errors.

The rate at which IR changes with the temperature defines the absolute thermal sensitivity, S :

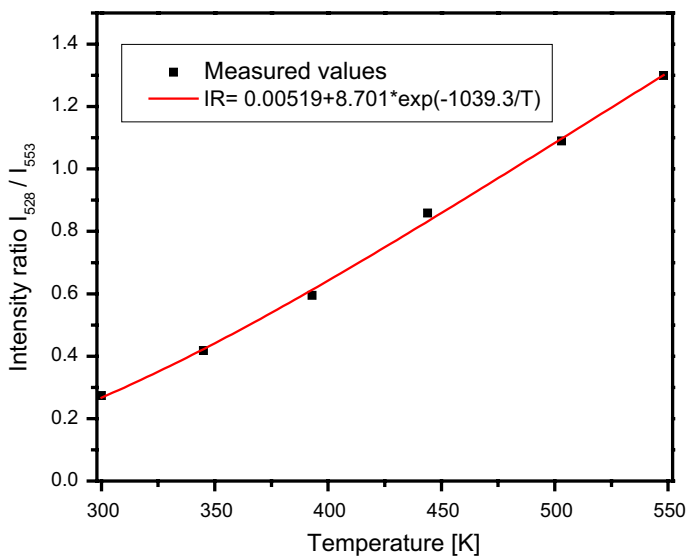


Fig. 5 Temperature sensing calibration curve of $\text{Gd}_2\text{O}_3:\text{Er},\text{Yb}$, using intensity ratio of two Er emission lines, at 553 nm and 529 nm. Experimental points are denoted by black squares and fitted temperature calibration curve is denoted by red line

$$S = \left| \frac{dIR}{dT} \right| \quad (3)$$

The absolute thermal sensitivity is of a small practical use for comparison purposes, so, we use the relative thermal sensitivity, S_r , defined by Eq. (3):

$$S_r = \left| \frac{1}{IR} \frac{dIR}{dT} \right| \quad (4)$$

Figure 6 shows the relative sensitivity curve, calculated by Eq. (4). Looking at the Fig. 6 we see that the relative sensitivity is highest at room temperature, its value is $1.18\% \text{ K}^{-1}$, and its lowest value is about $0.35\% \text{ K}^{-1}$ at 550 K.

Comparing the results presented here and in (Krizan et al. 2014), we see that the temperature sensing calibration curves look very similar, only slightly in favor of pulsed excitation because of somewhat better intensity ratio. However, the pulsed excitation offers possibility for using the luminescence lifetime for temperature sensing, providing grounds for multi-mode temperature sensing described in (Sevic et al. 2020).

4 Conclusion

We have studied the possibilities of using $\text{Gd}_2\text{O}_3:\text{Er}^{3+},\text{Yb}^{3+}$ for remote temperature sensing. Analyzed samples were fabricated by simple and low-cost Solution Combustion Synthesis (SCS) method. We have used the pulsed laser excitation because it has some advantages compared to continuous excitation in regard of local heating of material. Erbium spectral lines at 528 nm (${}^2\text{H}_{11/2} \rightarrow {}^2\text{I}_{15/2}$ transition) and 553 nm (${}^4\text{S}_{3/2} \rightarrow {}^2\text{I}_{15/2}$ transition)

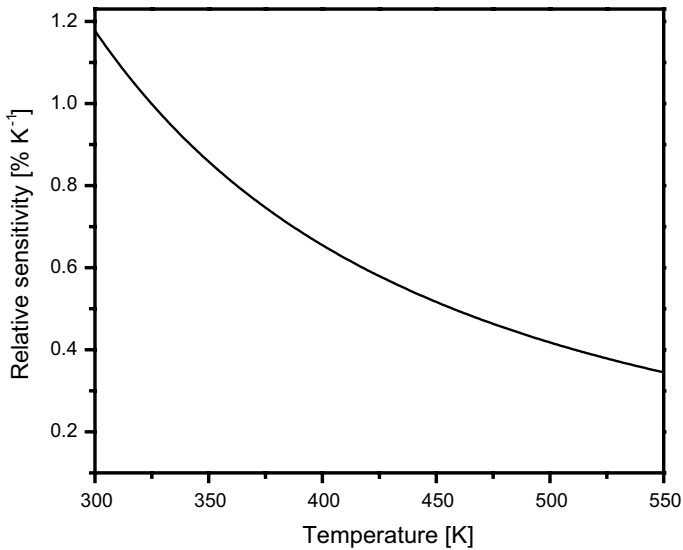


Fig. 6 Relative sensitivity curve as the function of temperature for $\text{Gd}_2\text{O}_3:\text{Er,Yb}$

were selected for implementation of luminescence intensity ratio method for temperature measurements. Our analysis shows that synthesized $\text{Gd}_2\text{O}_3:\text{Er,Yb}$ material is useful for temperature measurements up to 550 K, with relative sensitivity of $1.18\% \text{ K}^{-1}$ at room temperature. With increasing the temperature the relative sensitivity decreases up to $0.35\% \text{ K}^{-1}$ at 550 K. In our future work we will analyze prospects of using the erbium optical emission lifetime for temperature sensing.

Acknowledgements This work was financially supported within the Projects of Ministry of Education, Science and Technological Development of the Republic of Serbia OI171020.

References

- Alden, M., Omrane, A., Richter, M., Särner, G.: Thermographic phosphors for thermometry: A survey of combustion applications. *Prog. Energy Combust. Sci.* **37**, 422–461 (2011)
- Ang, L.Y., Lim, M.E., Ong, L.C., Zhang, Y.: Applications of upconversion nanoparticles in imaging, detection and therapy. *Nanomedicine* **6**, 1273–1288 (2011)
- Allison, S.W., Gillies, G.T.: Remote thermometry with thermographic phosphors: Instrumentation and applications. *Rev. Sci. Instrum.* **68**, 2615–2650 (1997)
- Avram, D., Tiseanu, C.: Thermometry properties of Er, Yb– $\text{Gd}_2\text{O}_3\text{S}$ microparticles: dependence on the excitation mode (cw versus pulsed excitation) and excitation wavelength (980 nm versus 1500 nm). *Methods Appl. Fluoresc.* **6**, 025004 (2018)
- Brites, C.D.S., Lima, P.P., Silva, N.J.O., Millan, A., Amaral, V.S., Palacio, F., Carlos, L.D.: Thermometry at the nanoscale. *Nanoscale* **4**, 4799–4829 (2012)
- Cates, M.R., Allison, S.W., Jaiswal, S.L., Beshears, D.L.: YAG:Dy and YAG:Tm Fluorescence above 1400. Oak Ridge National Laboratory, Report ORNL/TM-2002/71 (2002)
- Dong, B., Liu, D.P., Wang, X.J., Yang, T., Miao, S.M., Li, C.R.: Optical thermometry through infrared excited green upconversion emissions in $\text{Er}^{3+}\text{-Yb}^{3+}$ codoped Al_2O_3 . *Appl. Phys. Lett.* **90**, 181117 (2007)

- dos Santos, P.V., de Araujo, M.T., Gouveia-Neto, A.S., MedeirosNeto, J.A., Sombra, A.S.B.: Optical Thermometry Through Infrared Excited Upconversion Fluorescence Emission in Er- and Er–Yb -doped Chalcogenide Glasses. *IEEE J. Quantum Electron.* **35**, 395–399 (1999)
- Du, P., Deng, A.M., Luo, L., JaeYu, J.S.: Simultaneous phase and size manipulation in NaYF₄:Er³⁺/Yb³⁺ upconverting nanoparticles for a non-invasion optical thermometer. *New J. Chem.* **41**, 13855–13861 (2017)
- Du P., Yu J.S.: Synthesis of Er(III)/Yb(III)-doped BiF₃ upconversion nanoparticles for use in optical thermometry. *Microchimica Acta* **185**, 237–1–8 (2018)
- Đačanin, LjR, Lukić-Petrović, S.R., Petrović, D.M., Nikolić, M.G., Dramićanin, M.D.: Temperature quenching of luminescence emission in Eu³⁺- and Sm³⁺-doped YNbO₄ powders. *J. Lumin.* **151**, 82–87 (2014)
- Eldridge, J.I., Jenkins, T.P., Allison, S.W., Wolfe, D.E., Jordan, E.H.: Development of YAG:Dy Thermographic Phosphor Coatings for Turbine Engine Applications, 58h International Instrumentation Symposium San Diego, CA, 5–8, (2012)
- Feist, J.P., Heyes, A.L., Choy, K.L., Su, B.: Phosphor Thermometry for High Temperature Gas Turbine Applications. *Proceedings of IEEE*; **6.1** (1999)
- Gavrilovic, T.V., Jovanovic, D.J., Smits, K., Dramicanin, M.D.: Multicolor upconversion luminescence of GdVO₄:Ln³⁺/Yb³⁺(Ln³⁺ = Ho³⁺, Er³⁺, Tm³⁺, Ho³⁺/Er³⁺/Tm³⁺) nanorods. *Dyes Pigm.* **126**, 1–7 (2016)
- Goss, L.P., Smith, A.A., Post, M.E.: Surface thermometry by laser-induced fluorescence. *Rev Sci. Instrum* **60**, 3702–3706 (1989)
- Heyes, A.L.: On the design of phosphors for high-temperature thermometry. *J. Lumin.* **129**, 2004–2009 (2009)
- Jaque, D., Vetrone, F.: Luminescence nanothermometry. *Nanoscale* **4**, 4301–4326 (2012)
- Khalid, A.H., Kontis, K.: Thermographic phosphors for high temperature measurements: principles, current state of the art and recent applications. *Sensors* **8**, 5673–5774 (2008)
- Krizan, J., Mazaj, M., Kaucic, V., Bajsic, I., Mozina, J.: Synthesis of Er- and Yb-doped Gadolinium Oxide Polymorphs and Influence of Their Structures on Upconversion Properties. *Acta Chim. Slov.* **61**, 608–614 (2014)
- Li, X., Song, Y., Yang, Y., Mi, C., Liu, Y., Yu, F., Liu, L., Zhang, J., Li, Z.: Structure and Optical Thermometry Characterization of Er³⁺/Yb³⁺ Co-Doped BaGd₂CuO₅. *J. Nanosci. Nanotechnol.* **16**, 3542–3546 (2016)
- Li, D., Qin, W., Zhang, P., Wang, L., Lan, M., Shi, P.: Efficient luminescence enhancement of Gd₂O₃:Ln³⁺ (Ln = Yb/Er, Eu) NCs by codoping Zn²⁺ and Li⁺ inert ions. *Optical Materials Express* **7**, 329 (2017)
- Li, L., Zheng, L., Xu, W., Liang, Z., Zhou, Y., Zhang, Z.: Cao W (2016) Optical thermometry based on the red upconversion fluorescence of Er³⁺ in CaWO₄:Yb³⁺/Er³⁺ polycrystalline powder. *Opt. Lett.* **41**, 1458–1461 (2016)
- Liu, L., Qin, F., Lv, T., Zhang, Z., Cao, W.: Accurate thermometry based on the red and green fluorescence intensity ratio in NaYF₄:Yb, Er nanocrystals for bioapplication. *Optics Letters* **41**, 4664–4667 (2016)
- Lojpur, V., Čulubrk, S., Dramićanin, M.D.: Ratiometric luminescence thermometry with different combinations of emissions from Eu³⁺ doped Gd₂Ti₂O₇ nanoparticles. *J. Lumin.* **169**, 534–538 (2016)
- Lojpur, V., Ahrenkiel, P., Dramićanin, M.D.: Color-tunable up-conversion emission in Y₂O₃:Yb³⁺, Er³⁺ nanoparticles prepared by polymer complex solution method. *Nanoscale Res. Lett.* **8**, 131 (2013)
- Manzani D., Petrucic J. F. da S., Nigoghossian K., Cardoso A.A., Ribeiro S.J.L.: A portable luminescent thermometer based on green upconversion emission of Er³⁺/Yb³⁺ co-doped tellurite glass. *Scientific Reports* 7:41596 (2017) DOI: 10.1038/srep41596
- May, P.S., Baride, A., Hossan, M.Y., Berry, M.: Measuring the Internal Quantum Yield of Upconversion Luminescence for Ytterbium-Sensitized Upconversion Phosphors Using the Ytterbium(III) Emission as an Internal Standard. *Nanoscale* **10**, 17212–17226 (2018)
- Nikolic, M.G., Al-Juboori, A.Z., Djordjevic, V., Dramicanin, M.D.: Temperature luminescence properties of Eu³⁺-doped Gd₂O₃ phosphors. *Phys. Scr.* **T157**, 014056–1–14065 (2013)
- Nikolic, M.G., Rabasovic, M.S., Krizan, J., Savic-Sevic, S., Rabasovic, M.D., Marinkovic, B.P., Vlastic, A., Sevic, D.: Luminescence thermometry using Gd₂Zr₂O₇:Eu³⁺. *Opt Quant Electron.* **50**, 1–8 (2018)
- Ou, Q., Zhang, Y., Wang, Z., Yuwono, J.A., Wang, R., Dai, Z., Li, W., Zheng, C., Xu, Z.-Q., Qi, X., Duhm, S., Medhekar, N.V., Zhang, H., Bao, Q.: Strong Depletion in Hybrid Perovskite p–n Junctions Induced by Local Electronic Doping. *Adv. Mater.* **30**, 1705792 (2018)
- Rabasovic, M.D., Muric, B.D., Celebonovic, V., Mitric, M., Jelenkovic, B.M., Nikolic, M.G.: Luminescence thermometry via the two-dopant intensity ratio of Y₂O₃:Er³⁺, Eu³⁺. *J. Phys. D: Appl. Phys.* **49**(485104), 1–6 (2016)
- Sevic D, Rabasovic M.S., Krizan J., Savic-Sevic S., Nikolic M.G., Marinkovic B.P., Rabasovic M.D., “YVO₄:Eu³⁺ nanopowders: multi-mode temperature sensing technique”, *J. Phys. D: Appl. Phys.* **53**, 015106–1–10 (2020)

- Singh, S.K., Kumar, K., Rai, S.B.: Er³⁺/Yb³⁺ codoped Gd₂O₃ nano-phosphor for optical thermometry. *Sensors and Actuators A* **149**, 16–20 (2009)
- Su L., Fan X., Yin T., Wang H., Li Y., Liu F., Li J., Zhang H., and Heping Xie.: *Inorganic 2D Luminescent Materials: Structure, Luminescence Modulation, and Applications*. *Adv. Optical Mater.* 1900978 (2019)
- Vlasic, A., Sevic, D., Rabasovic, M.S., Krizan, J., Savic-Sevic, S., Rabasovic, M.D., Mitric, M., Marinkovic, B.P., Nikolic, M.G.: Effects of temperature and pressure on luminescent properties of Sr₂CeO₄:Eu³⁺ nanophosphor. *J. Lumin.* **199**, 285–292 (2018)
- Wang, X., Liu, Q., Bu, Y., Liu, C.-S., Liua, T., Yan, X.: Optical temperature sensing of rare-earth ion doped phosphors. *RSC Adv.* **5**, 86219–86236 (2015)
- Xing C., Xie Z., Liang Z., Liang W., Fan T., Ponraj J.C., Dhanabalan S.C., Fan D., Zhang H.: 2D Nonlayered Selenium Nanosheets: Facile Synthesis, Photoluminescence, and Ultrafast Photonics. *Adv. Optical Mater.* 1700884 (2017)
- Xu, W., Gao, X., Zheng, L., Wang, P., Zhang, Z., Cao, W.: Optical Thermometry through Green Upconversion Emissions in Er³⁺/Yb³⁺-Codoped CaWO₄ Phosphor. *Appl. Phys. Express* **5**, 072201 (2012)
- Zhang, Y., Chang-Keun Lim, C.-K., Dai, Z., Yu, G., Haus, J.W., Zhang, H., Prasad, P.N.: Photonics and optoelectronics using nano-structured hybrid perovskite media and their optical cavities. *Phys. Rep.* **795**, 1 (2019)
- Zhao, Y., Wang, X., Zhang, Y., Li, Y., Yao, X.: Optical temperature sensing of up-conversion luminescent materials: Fundamentals and progress. *J. Alloy. Compd.* (2019). <https://doi.org/10.1016/j.jallcom.2019.152691>

Publisher's Note Springer Nature remains neutral with regard to jurisdictional claims in published maps and institutional affiliations.



Cite this: *Soft Matter*, 2018, 14, 5595

Golden moth-inspired structures with a synergistic effect of interference, absorption and scattering

Svetlana Savić-Šević,^a Dejan Pantelić,^a Branislav Jelenković,^a Branislav Salatić^a and Dejan V. Stojanović^b

We describe a new type of photonic material inspired by a *Diachrysia chrysitis* moth, whose nano-structured wings exhibit a prominent golden color. This is a layered photonic structure with a large refractive index contrast, whose alternating layers are rough at the nanoscale level. Theoretical analysis shows that the scattering and interference interact to enhance the local field within the layers and increase the absorption of the material, particularly in the UV–blue part of the spectrum. Theory is experimentally verified using holographically manufactured Bragg gratings in the dichromated-pullulan (DCP). Alternating air-pullulan layers are produced and held in place by sparsely separated nano-pillars. Air voids are filled with 20–100 nm diameter spherical nanoparticles which act as scatterers. Such materials, with a high refractive index contrast and nano-scale scatterers, are important for achieving large reflectance and a broad spectrum, with scattering as an additional mechanism for spectral control.

Received 2nd April 2018,
Accepted 1st June 2018

DOI: 10.1039/c8sm00683k

rsc.li/soft-matter-journal

Introduction

Natural nanotechnology still surpasses the technological achievements of our civilization. This is most evident, even visible by the naked eye, in the world of insects whose structural colors constantly amaze keen observers. The shiny blue colors of *Morpho* butterflies,¹ the violet tints of *Apatura iris* (Linnaeus, 1758) and *Apatura ilia* (Denis & Schiffermüller, 1775) butterflies,² the green colors of beetles (*Coleoptera*),³ or the yellow-greens of certain bugs (Hemiptera),⁴ are marvels of natural nanotechnology. They are produced quickly, effortlessly and in huge amounts, during the short lifecycle of insects.

Structural colors in nature mostly have a spectral distribution within a rather limited wavelength range and produce well defined colors – typically blues and greens. In spite of that, certain insects reflect light in a wide spectral range, resulting in silvery,⁵ gold⁵ or bronze⁶ colors. Such broad spectral distributions are usually caused by chirped Bragg gratings, but color mixing⁷ or local spectra averaging⁸ can be found in certain insect species.

The richness of insect structures provides a constant inspiration for researchers to look for new ways of imitating natural optics and photonics structures.^{9,10} There are quite a number of techniques used for biomimetics of photonic structures and a

good overview is given in the paper of Butt *et al.*¹¹ Certain techniques are complex, slow and expensive, such as the one using focused Ga⁺ ion beam chemical vapor deposition to manufacture free-standing butterfly-type structures with 80 nm resolution.¹² Other methods are simpler and use natural structures as templates for directly copying into other materials, such as TiO₂.¹³ That is why industrial-scale production methods of simple biomimetic surfaces were developed, such as layer-by-layer spraying.¹⁴

Holography and interference methods stand out for their capability to generate complex, large-area photonic structures cheaply and efficiently.¹⁵ Several laser beams interfere in a suitable photo-sensitive material: polymer dispersed liquid crystals,¹⁶ photoresists,¹⁷ dichromated gelatin¹⁸ or silver-halide emulsions.¹⁹ After chemical processing, nanostructures are generated, whose minimum dimension is limited by the wavelength of light. This method was used to create *Morpho*-butterfly-like structures on a photoresist.²⁰

We were inspired by the Burnished brass moth, *Diachrysia chrysitis* (Linnaeus, 1758), whose wing scales and membranes represent a layered structure with rough surfaces. Here we see that several optical effects – interference, scattering and absorption⁸ – cooperate to produce the golden wing color. Other insects^{7,10} or their fossilized remnants²¹ were found with a similar type of structure, resulting in the same, rather broad, reflection spectra.

In this paper we propose a new class of photonic materials characterized by layers with irregular, rough surfaces, residual absorption and high refractive index contrast. From the theoretical

^a Institute of Physics, University of Belgrade, Pregrevica 118, 11080 Zemun, Serbia.
E-mail: savic@ipb.ac.rs

^b Institute of Lowland Forestry and Environment, University of Novi Sad, Antona Čehova 13, 21000 Novi Sad, Serbia

point of view, such structures exhibit a useful interplay between scattering, local field enhancement, planar waveguiding and interference. As a result, radiation is reflected in a broad spectral range. We use a transfer matrix method²² and surface scattering theory²³ with associated intensity enhancement²⁴ to theoretically explain the observed optical properties.

As a proof of concept, we used holography (interference lithography) to pattern a pullulan – a linear homo-polysaccharide produced by the yeast-like fungus *Aureobasidium pullulans*. Pullulan was photo-sensitized by doping with chromium ions – we named the resulting material dichromated pullulan (DCP).²⁵ After exposure and simple chemical processing, the material exhibited just what we needed: a number of pullulan layers densely covered with randomly dispersed nano-spheres. The layers are separated by nano-scale pillars and the space between them is void. The resulting spectrum is wide and closely resembles the spectra of metallic gold and *D. chrysitis* moth wings.

Properties of the *Diachrysia chrysitis* moth wing and its holographically generated analogue

D. chrysitis is an attractive insect with large, golden-color patches covering its fore wings (Fig. 1a). The wings are covered with scales which are almost transparent if observed individually. However, in their natural position on the wing (Fig. 1b), wing membranes, ground and cover scales act together to produce the resulting color.⁸ The spectrum is wide and visually closely corresponds to the color of gold.

From the morphological point of view, the wings have the standard structure of the vast majority of Lepidoptera

(Fig. 1c), with two wing membranes (approximately 1 μm thick) covered ventrally and dorsally with two layers of scales (cover and ground). There are actually six distinct layers because each scale has two, air-spaced, laminae (air layers and laminae are 100 nm thick, each). The ventral side of the wing is not of much interest here, because wing-scales are pigmented, strongly attenuate the radiation and are incapable of reflecting a significant amount of light. All layers are structured: wing membranes have a number of hemispherical protuberances, the external surfaces of scales' upper laminae have a regular grating structure (Fig. 2a), while their internal surfaces are rough (Fig. 2b and c).

In order to imitate the optical characteristics of *D. chrysitis*, it is necessary to manufacture the layered structure having rough surfaces. We did that by holographically generating Bragg grating inside the dichromated pullulan – a homemade material produced by sensitization of pullulan with ammonium dichromate.

Diffraction gratings with spherical inclusions are fabricated by combination of the holographic method (top-down technique) and non-solvent-induced phase separation (bottom-up method).^{26–28} The whole process involves several steps:

- (1) preparation of a DCP film on a glass plate,
- (2) film exposure using a laser,
- (3) chemical development,
- (4) desiccation in a non-solvent bath at room temperature, and
- (5) drying in a closed vessel.

In the first step, the DCP is prepared by mixing 8% aqueous solution of pullulan (purchased from Sigma-Aldrich) and 45% of ammonium dichromate (by weight of pullulan). The solution

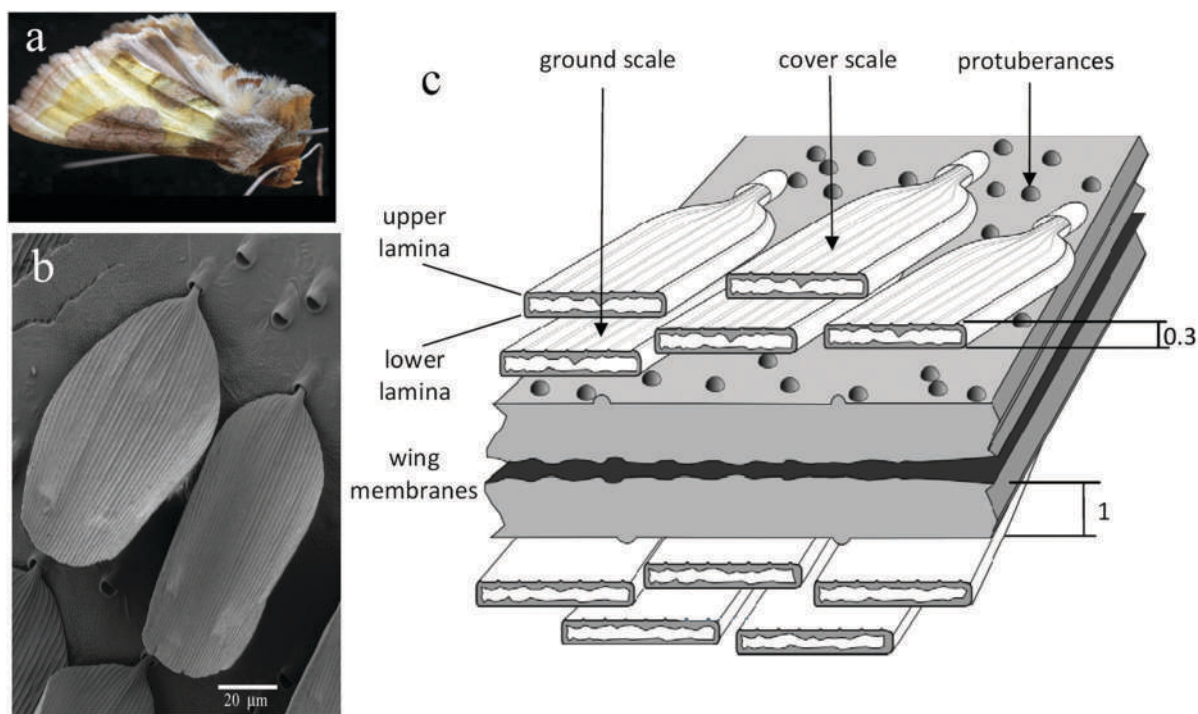


Fig. 1 (a) *Diachrysia chrysitis* moth. (b) Wing scales on the wing membrane of *D. chrysitis* moth, observed under a scanning electron microscope. (c) A scheme of the *D. chrysitis* wing's. The whole structure is cross-sectioned to display rough internal surfaces of wing scales. Dimensions are in μm .

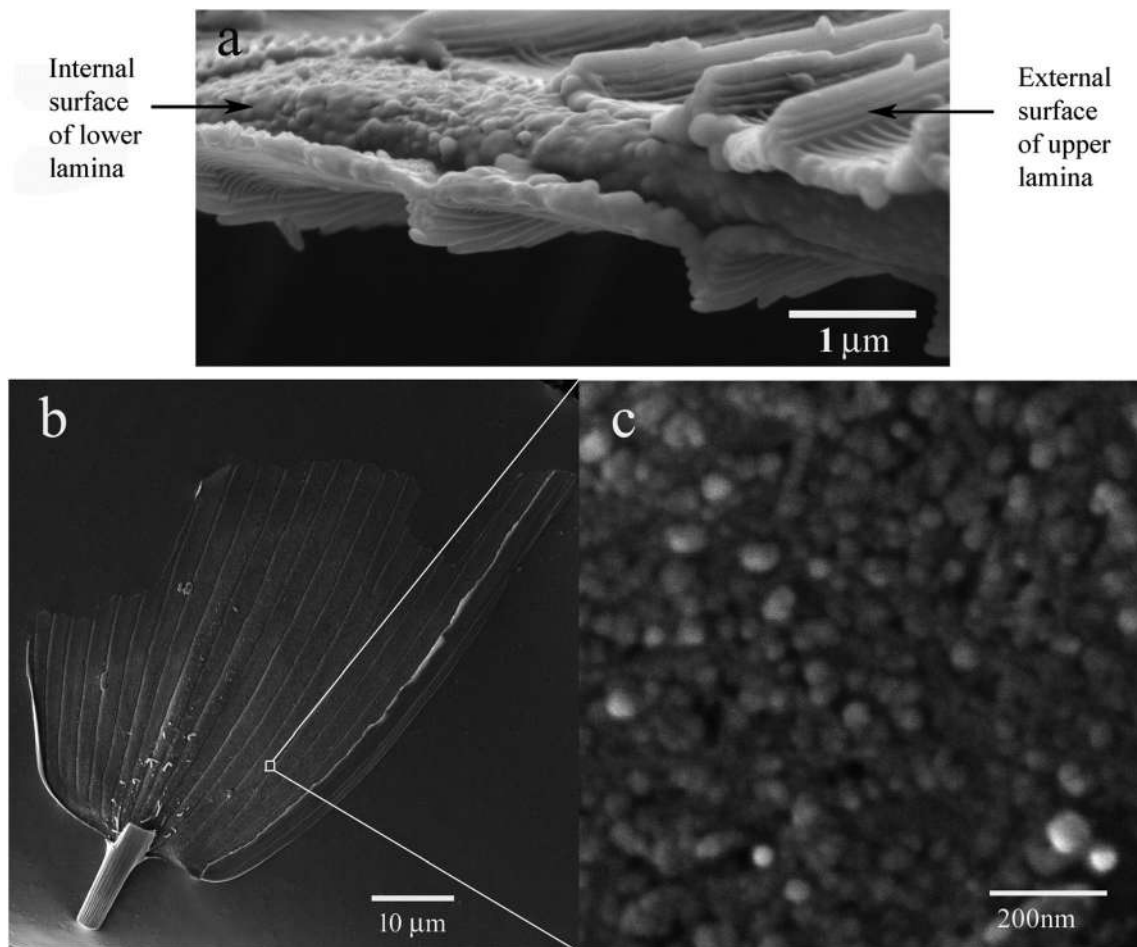


Fig. 2 (a) A broken and folded *D. chrysitis* scale revealing simultaneously the external grating-like structure and internal random structure. (b) Wing scale of *D. chrysitis* with intentionally removed lower lamina. (c) Enlarged portion of the image in (b) showing the rough internal surface in more detail.

was coated onto a clean glass slide in a horizontal position and the film was dried overnight under normal laboratory conditions. The resulting DCP film is 10 μm thick, yellowish, transparent and photosensitive.

The dried film is exposed at normal incidence using a single longitudinal mode, diode-pumped Nd-YAG laser, at 532 nm. After propagation through the film, the laser beam is back-reflected from a mirror behind the DCP plate. Two counter-propagating beams interfere to create a standing wave pattern consisting of parallel planes with spacing equal to $\lambda/2n$ (λ is the wavelength of the laser and n is the refractive index, which is 1.45 for pullulan²⁹).

The DCP plate was further chemically processed using a mixture of water and isopropyl alcohol (ratio 3 : 1 respectively). Treatment lasted for two minutes, followed by pure isopropyl-alcohol dehydration. Finally, the material is fully dried in a closed vessel.

The morphology of the resulting DCP grating was investigated using a high resolution field emission gun scanning electron microscope (FEGSEM). A number of DCP layers with a spacing of about 135 nm and a similar thickness are visible.

The space between them is void and they are supported and separated by tiny pillars (Fig. 3a and b). The layers are covered with nano-sized spherical particles distributed according to the Weibull distribution³⁰ (Fig. 3c), which exhibits maximum at 45 nm and mean at 55 nm (maximum and mean are different due to the asymmetry of the distribution).

There is a complex mechanism leading to the generation of structures in the DCP, which is based on pullulan's solubility in water and insolubility in isopropyl alcohol. During exposure, hexavalent chromium ion Cr^{6+} is photo-reduced to trivalent Cr^{3+} , which covalently cross-links with pullulan molecules in exposed areas. Cross-linking hardens the pullulan making it insoluble in water. This causes a solubility difference between exposed and unexposed regions.

After exposure, the DCP grating is chemically processed using a mixture of water and isopropyl alcohol as a developer. The unexposed regions (areas of destructive interference) are chemically unaffected and are dissolved in the developer. In contrast, areas of constructive interference are not dissolved during development, as a consequence of hardening by cross-linking. As a result, solid DCP layers are produced. At this stage,

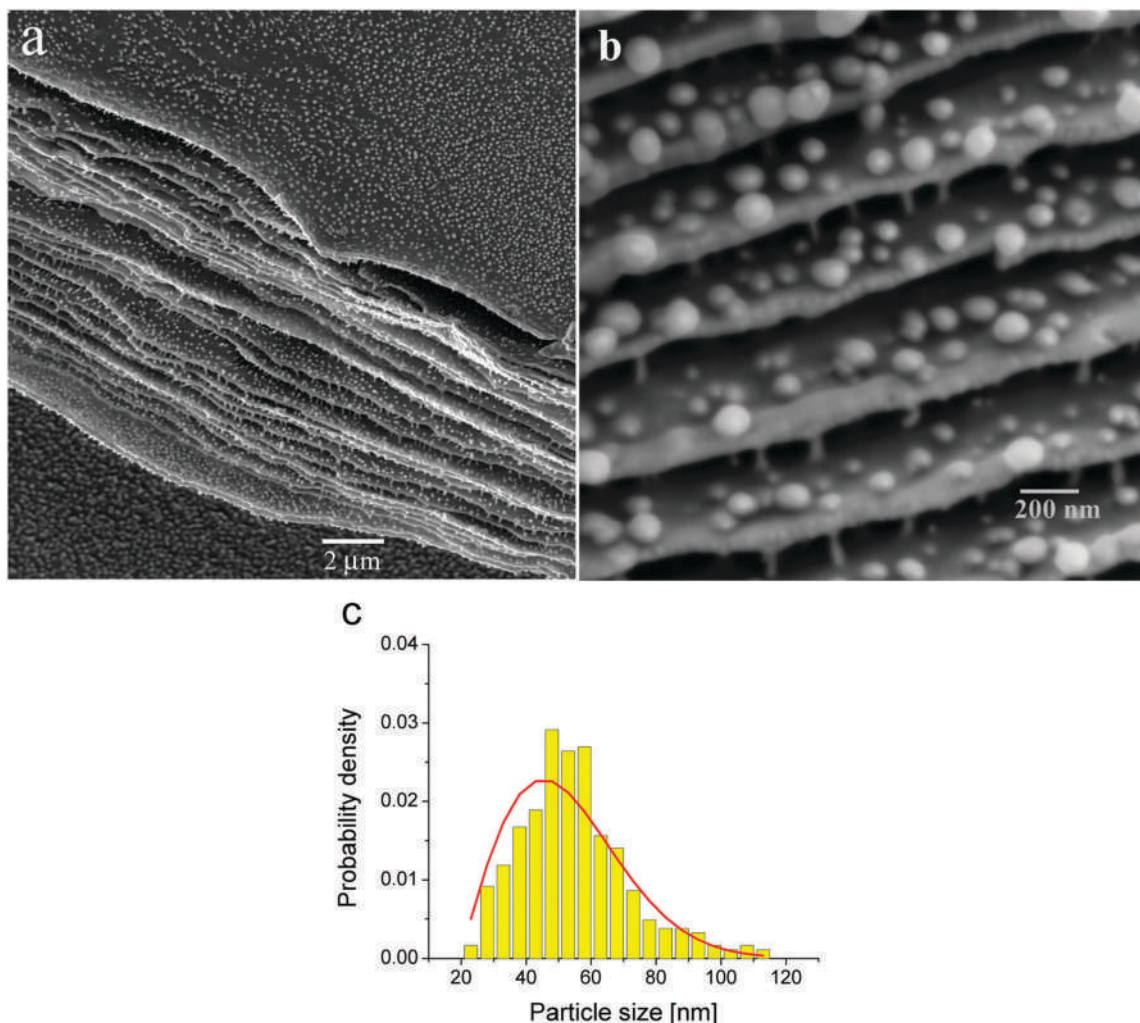


Fig. 3 (a) FEGSEM image of a cross-section of the DCP grating. Particle density is 58 ± 12 particles μm^{-2} . (b) Enlarged portion of a DCP grating with nano-spheres of average size 55 ± 17 nm. (c) Size distribution of nanospheres between DCP layers (yellow bar chart) and the corresponding Weibull distribution (red line). Distribution maximum is at 45 nm and its mean is at 55 nm.

the developer with dissolved pullulan remains trapped between solid layers. The processing is finished by immersing the DCP in pure isopropyl alcohol, which removes water and forces dissolved pullulan to aggregate into nanoparticles (as a result of non-solvent phase separation).

Fig. 4a shows the DCP sample displaying a golden color. On the microscopic level, color variation is detected (see differently colored dots in Fig. 4b), which means that the macroscopically observed color results from local spectra mixing. Transmission and reflection spectra, Fig. 4c and d, respectively, were measured using a spectrometer (Ocean Optics) attached to an optical microscope. The reflection spectrum of DCP is quite similar to that of *D. chrysitis*.⁸ Both spectra are broad with a cut-off wavelength of approximately 500 nm, visually corresponding to a golden color. However, the maximum reflectance R of DCP is significantly higher ($R \approx 0.6$), compared to *D. chrysitis* ($R \approx 0.4$). This is due to the much larger number of layers in the DCP (40) vs. only 6 in *D. chrysitis*. In both cases,

the reflectance is enhanced by the high refractive index contrast between air and material.

Theoretical analysis of the optical properties

Here we present a theoretical analysis of photonic structures characterized by regularly spaced layers with irregular surfaces and a large refractive index contrast. We treat structures as Bragg gratings, schematically shown in Fig. 5a, with scattering and internal field enhancement effects taken into account.

We first demonstrate that the scattering on the internal grating surfaces leads to significant dispersal of incident light. The wavelength of the incident visible light (inside material) is much larger than the scatterers and, widely used, scalar surface-scattering theory^{23,31} is applicable to determine the amount of scattered radiation.

Under these circumstances, the incident light is split into two parts: one, regular, propagating as if the surface is perfectly flat, and the other diffusely scattered (haze), see Fig. 5b.

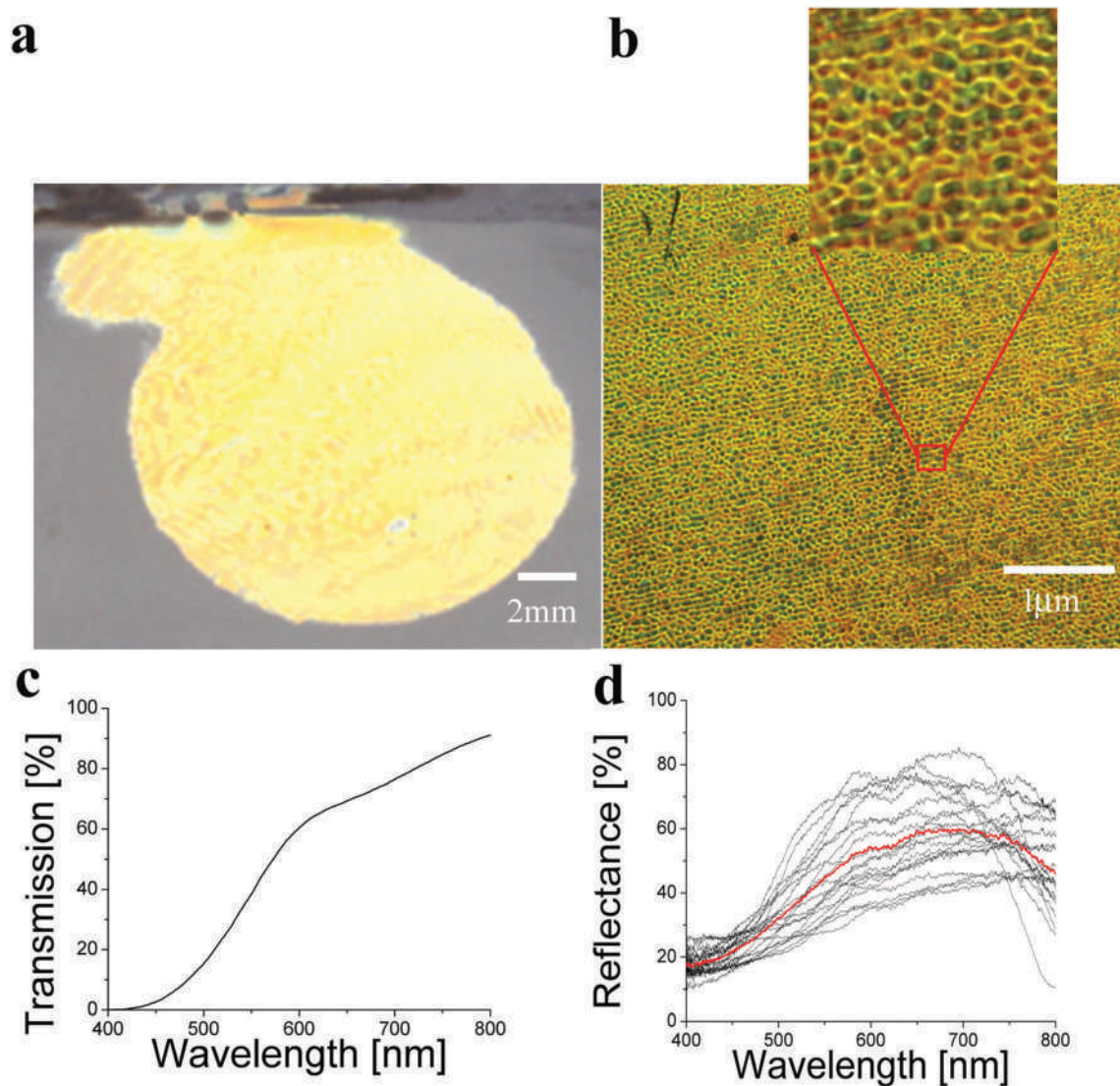


Fig. 4 (a) Golden appearance of the DCP layer. (b) Reflection from the DCP layer recorded under the reflection microscope. (c) Transmission spectrum of unexposed, chemically unprocessed dichromated pullulan, showing the strong absorption in the blue–green part of the spectrum. This spectrum is quite uniform across the sample. (d) Experimentally recorded reflection spectra of the DCP grating recorded at several positions. Individual, local, spectra (black curves) were recorded under the optical microscope and averaged (red curve).

Regularly propagating light obeys classical Fresnel reflection/transmission laws and “sees” the material as a volume Bragg grating. The haze and the regular component are described relative to transmittance T_0 and reflectance $R_0 = 1 - T_0$ of an ideally flat surface (assuming that the Fresnel equations hold). Accordingly, the haze transmittance $T_H(\lambda)$ and reflectance $R_H(\lambda)$ of a rough surface are described by:^{2,3}

$$T_H(\lambda) = T_0 \left[1 - \exp \left(- \left[\frac{2\pi\sigma}{\lambda} (n_i \cos \phi_i - n_t \cos \phi_t) \right]^2 \right) \right] \quad (1)$$

$$R_H(\lambda) = R_0 \left[1 - \exp \left(- \left[\frac{4\pi\sigma}{\lambda} n_i \cos \phi_i \right]^2 \right) \right] \quad (2)$$

where T_0 and R_0 are the transmittance and the reflectance of a perfectly flat surface, respectively, λ is the wavelength of light

under vacuum, ϕ_i and ϕ_t are the angles of incidence and refraction, n_i and n_t are the corresponding refractive indices, while σ is the root mean square (RMS) roughness of the surface.

We have computed the intensity of scattering for materials within the RMS range of several tens of nano-meters, and shown them in Fig. 6a and b. The intensity of transmitted haze does not depend on whether it comes from a high or low refractive index medium, Fig. 6a. In contrast, the intensity of reflected haze depends on the side from which the radiation comes, Fig. 6b. By comparing Fig. 6a and b, it is obvious that the scattering is 4–5 times stronger in transmission, compared to reflection. For both reflected and transmitted radiation, haze is much stronger at shorter wavelengths (as in Rayleigh scattering). As can be seen in Fig. 6 the intensity of scattering is much higher inside the blue–UV spectral range.

On the other hand, scattered radiation excites planar waveguide modes of Bragg layers. It was verified by the finite element

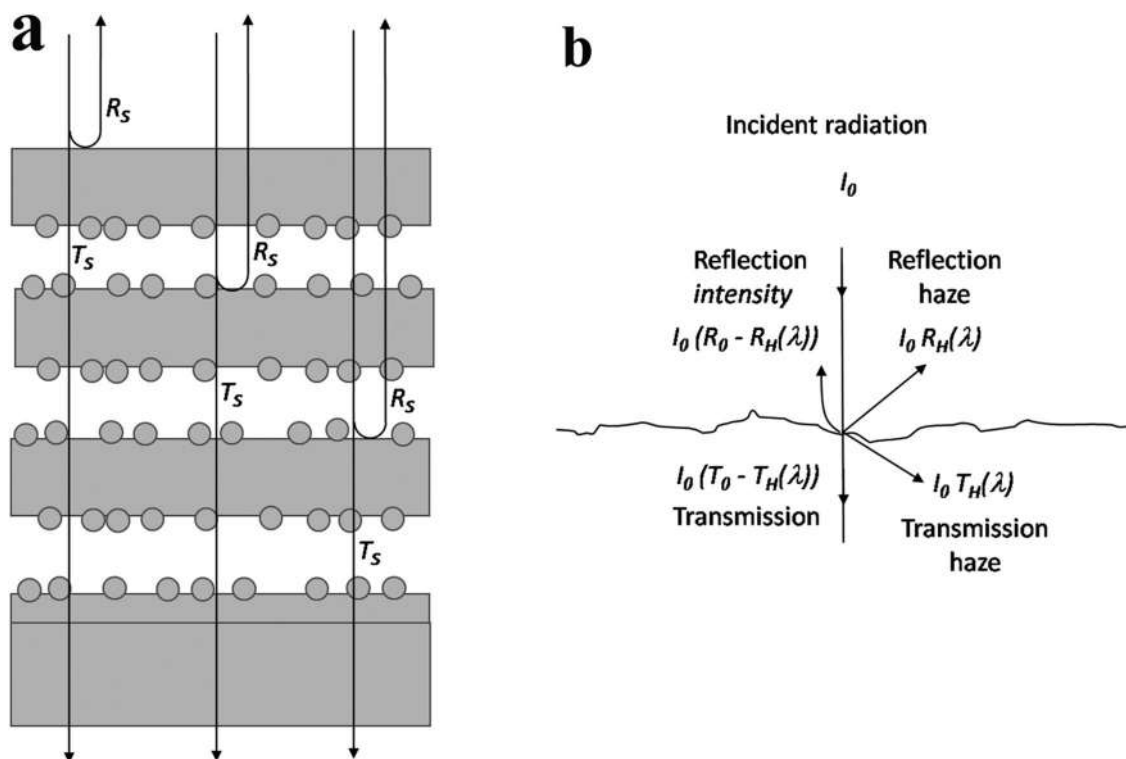


Fig. 5 (a) Scheme of a DCP diffraction grating with nano-sized particles. R_s and T_s are specular reflection and transmission coefficients, corrected for scattering effects. (b) Incident radiation is divided into specular and haze components.

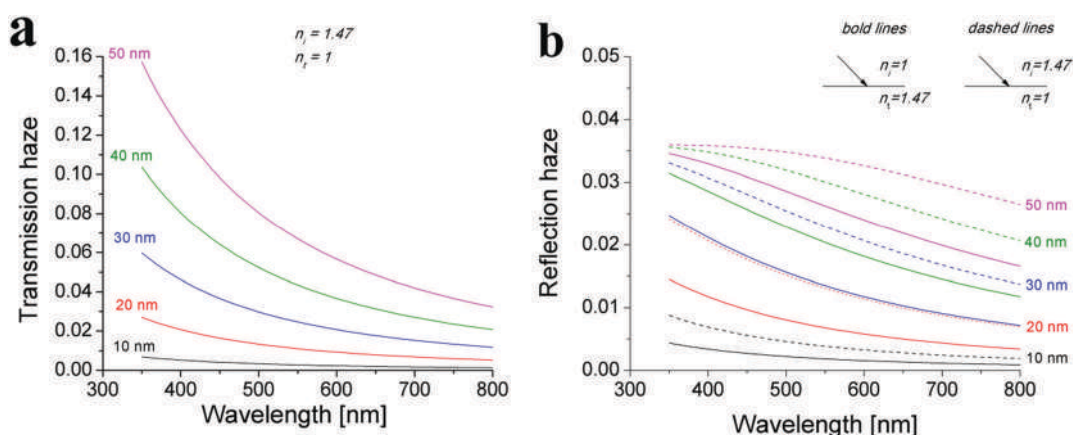


Fig. 6 Spectral dependence of haze from an interface with RMS roughness (ranging from 10 nm to 50 nm) as a parameter: (a) transmission and (b) reflection (in this case haze depends on whether light comes from the high index (dashed curves) or low index material (bold lines)). Haze was calculated for a single surface between air and pullulan.

method (FEM) applied to the DCP structure with a layer thickness of 135 nm, an air space of 130 nm and a refractive index of 1.45. The roughness was simulated using nanoparticles of 55 nm diameter (see Fig. 7a). Periodic boundary conditions were used in a simulation, and perfectly matching layers were positioned above and below the grating. Fig. 7b shows excited planar modes at the resonant wavelength, under the assumption that there is no absorption. It is interesting to note that by redistributing the spheres, the overall modal structure remains almost the same, with a possible slight shift

of the wavelength of planar modes. By reducing the number of particles, the planar modes gradually disappear, as the system approaches the pure multilayer geometry (without any inclusions).

So far, all the calculations have been done assuming non-absorbing materials. In reality this cannot be neglected. Calculations show that absorption efficiently suppresses the modes (Fig. 7c) and influences the diffraction efficiency, as predicted by the model developed by Yablonoich and Cody.²⁴

The FEM method cannot account for the stochastic nature of scattering surfaces. It would be possible to run many

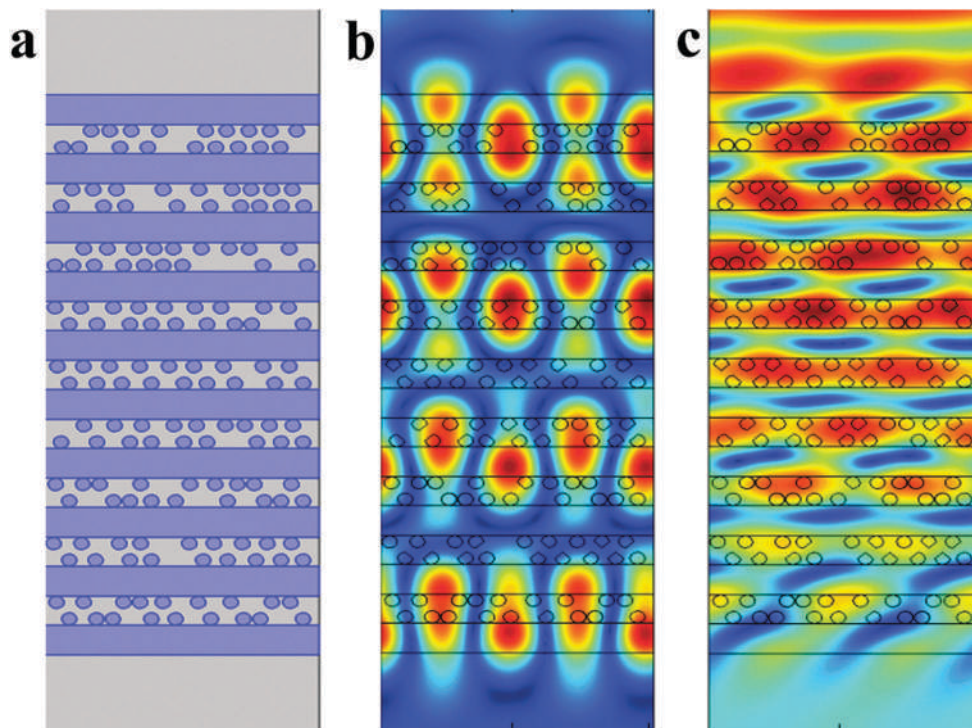


Fig. 7 (a) A geometry of the FEM model. (b) Intensity of electro-magnetic field at the resonance wavelength. Calculation were performed assuming that the angle of incidence is $\alpha = 0$, wavelength 624 nm and there is no absorption. (c) Field distribution with absorption included in the model. Parameters are the same as in (b).

variations of the same model with different surface profiles (but the same RMS) and then average the results. However, this would be very time consuming, and periodic boundary conditions would still introduce periodic repetition of spherical particle arrangements. To efficiently model this type of interaction we modified a transfer matrix method (TMM) to calculate the reflectance of the Bragg grating. This is a well known technique used to calculate the propagation of electromagnetic (EM) waves in a multilayer medium. Fresnel equations are used to establish the matrix relation between the EM field at the beginning and end of each layer.³² The resulting EM field of the whole structure is obtained as a result of matrix multiplication of matrices corresponding to individual layers. Scattering was accounted for by simply correcting the Fresnel reflection coefficient by subtracting the intensity of scattered radiation. Absorption losses, due to scattering, were calculated using the theory of Yablonoich and Cody.²⁴ TMM software, developed by Junesch *et al.*³³ and made publicly available, was modified to account for scattering enhanced absorption. Further details can be found in the previous publication.⁸

We used parameters corresponding to pullulan diffraction gratings recorded in our experiments: 40 layers with 135 nm thickness and 130 nm air space, refractive index $n_i = 1.45$. The RMS roughness was calculated from the statistics of nanosphere size and their surface distribution, as determined from a series of FEGSEM images (two of them can be seen in Fig. 3). We found that the average particle size is $55 \text{ nm} \pm 17 \text{ nm}$ and their density is $58 \pm 12 \text{ particles } \mu\text{m}^{-2}$ (corresponding to the

average distance of $131 \pm 14 \text{ nm}$). The associated RMS roughness is calculated by averaging integral of the square of the surface profile over the interval L and taking a square root of the result. The resulting RMS roughness is $34.4 \pm 16.4 \text{ nm}$.

There is an important word of caution: in order to get a golden wing color, the dimensional and optical parameters of each individual layer should be kept within quite tight tolerances – a condition completely impossible to satisfy in the real world. It is more realistic to expect significant variability of all the parameters. We have chosen to vary the most important ones – RMS roughness and layer thickness within $\pm 30\%$ (according to the normal distribution). The particular value of $\pm 30\%$ was chosen in accordance with the large variability of particle size ($\pm 30\%$) and their surface density ($\pm 20\%$). The angle of incidence was also allowed to fluctuate within ± 10 degrees – thus imitating the finite angular range of the incident radiation.

As a result, 160 different spectra were calculated. Each individual spectral curve is irregular with multiple peaks, corresponding to irregularities in the volume grating structure. Individual spectra were averaged – corresponding to natural spectral averaging by the detecting instrument or an observer. Our calculations have shown that the best fit of the experimentally recorded spectrum is obtained assuming that the surface roughness is 45 nm. This is larger than the 34.4 nm RMS roughness, found from FEGSEM images, but still within the uncertainty interval of $\pm 16.4 \text{ nm}$. The resulting curve is shown in red color in Fig. 8, together with several individual

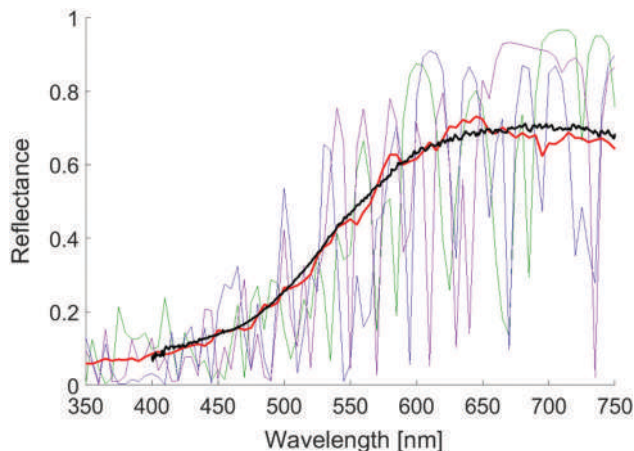


Fig. 8 Reflectance spectrum of a model in Fig. 7(a) calculated by transfer matrix method with scattering effects included (red curve). 160 individual spectra were calculated to represent natural variability of the grating (three of them can be seen in violet, green and blue color). The final reflectance spectrum (red curve) was calculated by averaging individual spectra. Experimentally recorded spectrum of DCP is shown for reference (black curve).

spectra (violet, blue and green color). The theoretical spectrum appears noisy because the finite number of individual spectral curves (used in the calculation) cannot completely make the resulting curve smooth. By comparing the averaged spectrum with the experimentally recorded one (black curve in Fig. 8), agreement appears quite good.

Discussion and conclusions

As far as we know, DCP is the only material capable of artificially introducing spherical nano-particles inside the Bragg grating, thus well imitating wing-scales of the *Diachrysis chrysitis* moth. Both pullulan (Fig. 3b) and butterfly's wing (Fig. 2c) possess a number of layers with rough internal surfaces (RMS roughness between 20 and 100 nm). The result is the same: strong suppression of radiation reflected in the UV–blue part of the spectrum. In this spectral range, light is strongly scattered by the rough surfaces and guided through the planar layers. Even a small amount of absorption is being enhanced by the increased path length.

It is interesting to discuss the mechanisms of nanoparticle formation both in *D. chrysitis* and DCP. In the case of *D. chrysitis* moth, we are not able to describe the exact mechanism of wing scale structure growth, because it was beyond this study. However, it is known that the wing scales are dead remnants of cells, whose main constituent is chitin (a natural polysaccharide). Chitin production and excretion are the result of a complicated biochemical process.³⁴ Additionally, according to Saranathan *et al.*³⁵ and Dinwiddie *et al.*,³⁶ wing-scale structures are produced by the complex growth of the cellular plasma membrane and intracellular smooth endoplasmic reticulum. The process is highly unpredictable as supported by the significant body of literature devoted to the, so called, cellular noise.³⁷ It was found that even genetically identical cells express random variation of

their properties, such as size, structure or protein level. In the case of DCP, we proposed the non-solvent induced phase separation as the main process behind the pullulan nano-sphere particle formation, as fully described in the main body of the paper.

In conclusion, we have created a peculiar kind of volume diffraction grating, where the nano-spherical particles are introduced between the grating layers. It was created through a combination of the holographic method (top-down technique) and non-solvent-induced phase separation (bottom-up method). The bangap is strongly influenced by the scattering and light intensity enhancement inside the grating layers. Large size gratings can be fabricated simply and quickly (in a few minutes). It was found that the DCP grating has excellent mechanical and environmental stability.

Such multilayer materials might be of interest in solar energy collection to selectively absorb the most energetic photons of UV–blue light, while reflecting unusable long wavelength radiation.^{38,39}

Conflicts of interest

There are no conflicts to declare.

Acknowledgements

The authors express their gratitude to the Ministry of Education, Science and Technological Development of the Republic of Serbia for supporting this research through projects ON171038, III45016, III43002.

References

- 1 S. Berthier, *Photonique des Morphos*, Springer Science & Business Media, 2010.
- 2 D. Pantelić, S. Čurčić, S. Savić-Šević, A. Korać, A. Kovačević, B. Čurčić and B. Bokić, *Opt. Express*, 2011, **19**, 5817.
- 3 H. Arwin, T. Berlind, B. Johs and K. Järrendahl, *Opt. Express*, 2013, **21**, 22645.
- 4 D. Azofeifa, H. Arguedas and W. Vargas, *Opt. Mater.*, 2012, **35**, 175.
- 5 C. Campos-Fernández, D. Azofeifa, M. Hernández-Jiménez, A. Ruiz-Ruiz and W. Vargas, *Opt. Mater. Express*, 2011, **1**, 85.
- 6 M.-N. Wu, C.-Y. Chen and W. Pan, *AIP Adv.*, 2015, **5**, 127227.
- 7 J. P. Vigneron, M. Ouedraogo, J.-F. Colomer and M. Rassart, *Phys. Rev. E: Stat. Phys., Plasmas, Fluids, Relat. Interdiscip. Top.*, 2009, **79**, 021907.
- 8 D. Pantelić, S. Savić-Šević, D. Stojanović, S. Čurčić, A. Krmpot, M. Rabasović, D. Pavlović, V. Lazović and V. Milošević, *Phys. Rev. E*, 2017, **95**, 032405.
- 9 O. Karthaus, *Biomimetics in photonics*, CRC Press, 2013.
- 10 J. P. Vigneron, M. Rassart, C. Vandembem, V. Lousse, O. Deparis, L. Biró, D. Dedouaire, A. Cornet and P. Defrance, *Phys. Rev. E: Stat. Phys., Plasmas, Fluids, Relat. Interdiscip. Top.*, 2006, **73**, 041905.

- 11 H. Butt, A. Yetisen, D. Mistry, S. A. Khan, M. U. Hassan and S. H. Yun, *Adv. Opt. Mater.*, 2016, **4**, 497.
- 12 K. Watanabe, K. Kanda, Y. Haruyamaet, T. Kaito and S. Matsui, *J. Vac. Sci. Technol., B*, 2005, **23**, 570.
- 13 X. Liu, S. Zhu, D. Zhang and Z. Chen, *Mater. Lett.*, 2010, **64**, 2745.
- 14 K. Krogman, R. Cohen, P. Hammond, M. Rubner and B. Wang, *Bioinspiration Biomimetics*, 2013, **8**, 045005.
- 15 M. Campbell, D. Sharp, M. Harrison, R. Denning and A. Turberfield, *Nature*, 2000, **404**, 53.
- 16 M. Escuti, J. Qi and G. Crawford, *Opt. Lett.*, 2003, **28**, 522.
- 17 Y. Miklyaev, D. Meisel, A. Blanco and G. von Freymann, *Appl. Phys. Lett.*, 2003, **82**, 1284.
- 18 R. Ma, J. Xu and W. Tam, *Appl. Phys. Lett.*, 2006, **89**, 081116.
- 19 M. H. Kok, R. Ma, J. C. W. Lee, W. Y. Tam, C. T. Chan and P. Sheng, *Phys. Rev. E: Stat. Phys., Plasmas, Fluids, Relat. Interdiscip. Top.*, 2005, **72**, 047601.
- 20 R. H. Siddique, R. Hünig, A. Faisal, U. Lemmer and H. Hölscher, *Opt. Mater. Express*, 2015, **5**, 996.
- 21 M. McNamara, D. Briggs, P. Orr, S. Wedmann, H. Noh and H. Cao, *PLoS Biol.*, 2011, **9**, e1001200.
- 22 J. Springer, A. Porube and M. Vanacek, *J. Appl. Phys.*, 2004, **96**, 5329.
- 23 D. Domine, F.-J. Haug, C. Battaglia and C. Ballif, *J. Appl. Phys.*, 2010, **107**, 044504.
- 24 E. Yablonovich and G. Cody, *IEEE Trans. Electron Devices*, 1982, **ED-29**, 300.
- 25 S. Savić Šević and D. Pantelić, *Appl. Opt.*, 2007, **46**, 287.
- 26 N. Kasoju, N. Hawkins, O. Pop-Georgievski, D. Kubies and F. Vollrath, *Biomater. Sci.*, 2016, **4**, 460.
- 27 E. Piacentini, D. Shanthana Lakshmi, A. Figoli, E. Drioli and L. Giorno, *J. Membr. Sci.*, 2013, **448**, 190.
- 28 S. Aruna, P. Binsy, E. Richard and B. Basu, *Appl. Surf. Sci.*, 2012, **258**, 3202.
- 29 A. Kaya, X. Du, Z. Liu, J. Lu, J. Morris, W. Glasser, T. Heinze and A. Esker, *Biomacromolecules*, 2009, **10**, 2451.
- 30 Z. Fang, B. Patterson and M. Turner, *Mater. Character.*, 1993, **31**, 177.
- 31 H. Davies, *Proc. IEEE*, 1954, **101**, 209.
- 32 B. Wolf, *Principles of Optics*, Pergamon, 1980.
- 33 J. Junesch, T. Sannomiya and A. B. Dahlin, *ACS Nano*, 2012, **6**, 10405.
- 34 H. Merzendorfer and L. Zimoch, *J. Exp. Biol.*, 2003, **206**, 4393.
- 35 V. Saranathan, C. O. Osuji, S. G. J. Mochrie, H. Noh, S. Narayanan, A. Sandy, E. R. Dufresne and R. O. Prum, *PNAS*, 2010, **107**, 11676.
- 36 A. Dinwiddie, R. Null, M. Pizzano, L. Chuong, A. Leigh Krup, H. E. Tan and N. H. Patel, *Dev. Biol.*, 2014, **392**, 404.
- 37 I. Johnston, B. Gaal, R. Pires das Neves, T. Enver, F. Iborra and N. Jones, *PLoS Comput. Biol.*, 2012, **8**, e1002416.
- 38 J. Nagel and M. Scarpulla, *Opt. Express*, 2010, **18**, 139.
- 39 N. Dahan and J. Greffet, *Opt. Express*, 2012, **20**, 530.



Low-temperature photoluminescence of CuSe₂ nano-objects in selenium thin films

Martina Gilić^{1,*}, Milica Petrović¹, Jovana Ćirković², Novica Paunović¹,
Svetlana Savić-Sević¹, Željka Nikitović¹, Maja Romčević¹, Ibrahim Yahia³,
Nebojša Romčević¹

¹Institute of Physics Belgrade, University of Belgrade, Pregrevica 118, Belgrade, Serbia

²The Institute for Multidisciplinary Research, University of Belgrade, Belgrade, Serbia

³Nano-Science and Semiconductors Labs., Physics Department, Faculty of Education, Ain Shams University, Roxy, Cairo, Egypt

Received 8 December 2016; Received in revised form 28 March 2017; Accepted 17 May 2017

Abstract

Thin films of CuSe₂ nanoparticles embedded in selenium matrix were prepared by vacuum evaporation method on a glass substrate at room temperature. The optical properties of the films were investigated by photoluminescence spectroscopy ($T = 20\text{--}300\text{ K}$) and UV-VIS spectroscopy ($T = 300\text{ K}$). Surface morphology was investigated by scanning electron microscopy. The band gap for direct transition in CuSe₂ was found to be in the range of 2.72–2.75 eV and that for indirect transition is in the range of 1.71–1.75 eV determined by UV-VIS spectroscopy. On the other hand, selenium exhibits direct band gap in the range of 2.33–2.36 eV. All estimated band gaps slightly decrease with the increase of the film thickness. Photoluminescence spectra of the thin films clearly show emission bands at about 1.63 and 2.32 eV at room temperature, with no shift observed with decreasing temperature. A model was proposed for explaining such anomaly.

Keywords: chalcogenides, thin films, optical properties, spectroscopy, SEM

I. Introduction

Selenides of copper (Cu-Se) exist in many phases and structural forms: i) stoichiometric forms, such as CuSe (klockmannite), Cu₂Se_x, CuSe₂ (marcasite), α -Cu₂Se (bellidoite), Cu₃Se₂ (umangite), Cu₅Se₄ (athabaskite), Cu₇Se₄ etc., as well as ii) non-stoichiometric forms, such as Cu_{2-x}Se (berzelianite). All those phases can be classified into several crystallographic forms (monoclinic, cubic, tetragonal, hexagonal, etc.). Copper selenide is a semiconductor with p-type conductivity, and has numerous applications in various devices, such as solar cells [1–3], photo detectors [4], optical filters [5], microwave shielding [6], thermoelectric converters [7], etc. Photovoltaic cells and Schottky diodes are also based on these metal chalcogenide compounds [8,9]. CuSe₂ is a superconductor at low temperatures with a transition temperature $T_C \sim 2.4\text{ K}$ [10], and has a weak ferro-

magnetic response below 31 K [11,12]. CuSe₂ is widely used as a precursor material for CuInSe₂ (CIS) and Cu(In,Ga)Se₂ (CIGS) preparation, suitable for highly efficient photovoltaic elements [13]. Also, CuSe₂ is used as a typical anion conductor and significant Cu-Se alloys targets for the preparation of CIGS/CIS thin film solar cells in RF magnetic sputtering [14].

Possible application of Cu-Se strongly depends on its optical properties. Despite the numerous publications of the optical properties of Cu-Se thin films, the estimated value of band gap of Cu-Se is not well defined. Cu-Se has both direct and indirect transitions, so the presence of both band gaps, direct and indirect, can be observed. Literature data are quite controversial: direct allowed transitions are reported to have corresponding band gap in the range of 2 to 3 eV, and indirect band gap between 1.1 and 1.5 eV [15–18]. The indirect band gap being near the optimum value for solar cell applications makes this material capable of potentially offer a high efficiency of conversion. However, Cu-Se nanoparticles

*Corresponding author: tel: +381 11 3713 036,
fax: +381 11 3713 052, e-mail: martina@ipb.ac.rs

have been reported to possess a direct band gap of 4 eV and indirect one of 1.87 eV [19]. The reasons of such variation in band gaps could lie in the sharp cut off of the wavelength with the spectral transmittance instead of the slow increase, the presence of large number of dislocations, wide range of stoichiometric deviation and quantum confinement effect.

In our previous report [20], we prepared Cu-Se thin films of three different thicknesses by vacuum evaporation technique using Mo boat onto glass substrate at room temperature, and investigated their structural properties. XRD and far-infrared spectroscopy revealed the presence of CuSe_2 nanocrystals in predominant Se films.

The objective of this research was to determine optical properties of Cu-Se thin films, using UV-VIS and low-temperature photoluminescence spectroscopy, and to investigate how the film thickness could influence the band gap value and photoluminescence properties. SEM analysis was also performed in order to get information about the morphology of the obtained Cu-Se thin films.

II. Experimental

Thin films were obtained by evaporating commercially high purity CuSe powder (99.99%) supplied from Aldrich Company. The powder was deposited onto highly pre-cleaned glass substrates with use of Mo boat. The procedure was done in a high-vacuum environment with typical background pressures of 3 mPa. The deposition rate, 10 nm/s, was monitored by quartz crystal thickness monitor - FTM4, Edwards and the final films thicknesses was found to be 56 nm, 79 nm and 172 nm for the films labelled as F-55, F-80 and F-170, respectively [20].

SEM imaging was done using scanning electron microscope equipped with a high brightness Schottky field emission gun (FEGSEM, TESCAN) operating at 4 kV. The samples were coated with gold/palladium to make them conductive.

The UV-VIS diffuse reflectance and transmittance spectra were recorded in the wavelength range of 300–1000 nm on a Shimadzu UV-2600 spectrophotometer equipped with an integrated sphere. The diffuse reflectance and transmittance spectra were measured relative to a reference sample of BaSO_4 .

Photoluminescence measurements on various temperatures ($T = 20\text{--}300\text{ K}$) were obtained by Jobin-Yvon U1000 spectrometer, equipped with RCA-C31034A photomultiplier with housing cooled by Peltier element, amplifiers and counters. The 488 nm laser line of argon laser was used as excitation source.

III. Results and discussion

3.1. SEM analyses

Scanning electron microscopy (SEM) images were obtained for the Cu-Se thin films deposited on glass substrate in order to study the surface morphology and

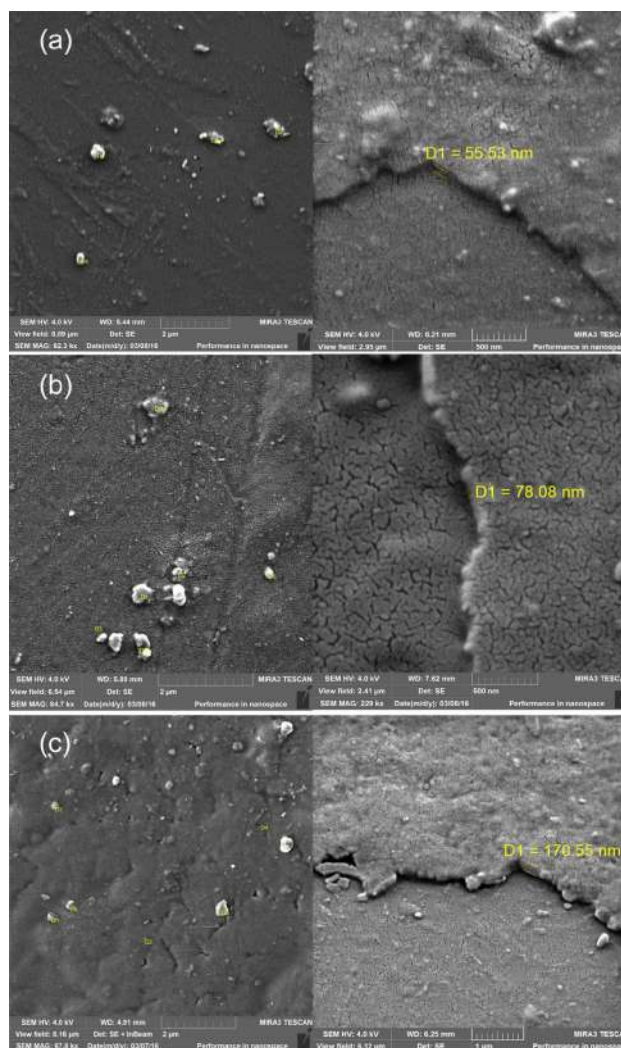


Figure 1. Top view and tilted SEM micrographs of films: a) F-55, b) F-80 and c) F-170

agglomeration of the samples.

Top view and tilted micrographs of the thin films are presented in Fig. 1. From the top view micrographs it can be observed that the surface of the samples is relatively uneven and rather rough, with presence of cracks and voids. Formation of the Cu-Se thin films most probably proceed unevenly, in the form of islands which later grew into agglomerates. Agglomerated clusters of few hundreds nanometers in diameter are distributed non-uniformly along the surface and form the structure consisting of CuSe_2 nanocrystals in predominant Se matrices. In order to determine the film thicknesses, the samples were tilted at 30° . The thicknesses estimated by SEM are: $\sim 56\text{ nm}$, $\sim 78\text{ nm}$ and $\sim 171\text{ nm}$ for the films F-55, F-80 and F-170, respectively. The thickness values estimated by SEM analysis match the ones obtained during the preparation of thin films.

3.2. UV-VIS spectroscopy

In Fig. 2 diffuse reflectance R and transmittance T spectra of the thin films samples in the wavelength range 300–1000 nm (4.13–1.24 eV) on room temperature (T

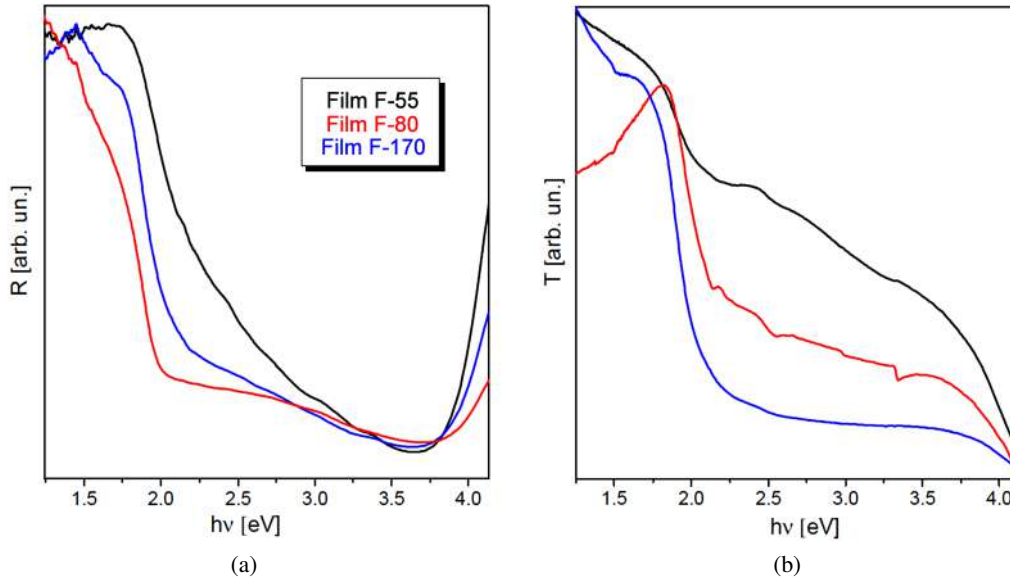


Figure 2. Diffuse reflectance, R (a), and transmittance, T (b) spectra

= 300 K) are presented. As it can be seen, the transmittance increases with decrease in the film thickness, which is not the case for reflectance. This is typical for films with high electrical conductivity and implies a reflection coefficient nearing 1 for films with metallic conductivity.

In this study we used the Tauc plot for the determination of the optical band gap from diffuse reflectance measurements. The determination of band gap in semiconductors is significant for obtaining the basic solid state physics. The relation expression proposed by Tauc, Davis and Mott [21–23] is the following:

$$\alpha \cdot h \cdot \nu = A (h \cdot \nu - E_g)^{1/n} \quad (1)$$

where h is the Planck’s constant, A is the transition probability constant depending on the effective mass of the charge carriers in the material, E_g is the band gap, $h \cdot \nu$ is the photon energy and α is the absorption coefficient which is defined as the relative rate of decrease in light intensity along its propagation path, i.e. a property of a material that defines the amount of light absorbed by it. The value of n denotes the nature of the transition. In case of direct transitions n equals $1/2$ and $3/2$ for allowed and forbidden transitions, respectively. As for indirect transitions, n equals 2 and 3 for allowed and forbidden transitions, respectively. Since CuSe exhibits both direct and indirect allowed transitions, $n = 1/2$ and $n = 2$.

Then, the acquired diffuse reflectance spectra are converted to Kubelka-Munk function [24]:

$$\alpha = \frac{(1 - R)^2}{2R} \quad (2)$$

So using this function, a plot of $(\alpha \cdot h \cdot \nu)^{1/n}$ against $h \cdot \nu$ is obtained. The energy band gap is determined by extrapolating the linear portion of $(\alpha \cdot h \cdot \nu)^{1/n}$ vs. $h \cdot \nu$

to the energy axis at $(\alpha \cdot h \cdot \nu)^{1/n} = 0$. The intercept of these plots on the energy axis gives the energy band gap. Such plots are given in Fig. 3. Direct transitions (left part of Fig. 3) reveal band gap for both selenium and CuSe₂, while indirect transitions (right part of Fig. 3) reveal band gap for CuSe₂ only.

The experimentally determined values of energy gaps for CuSe₂ show slight decrease with film thickness and their values range from 2.75 to 2.72 eV for direct transitions, and from 1.75 to 1.71 eV in case of indirect transitions. The estimated band gaps for selenium follow the same trend with film thickness and range between 2.33 and 2.36 eV. The estimated band gap positions for each sample are given in Table 1. The difference in the film thicknesses causes the small difference in band gaps in the second decimal place and they follow the well-established trend, the smaller the thickness, the wider the band gap is. Also, their values are quite wider than the ones that can be found in literature [7,16,25–33].

Table 1. Estimated band gap energies of thin films determined with UV-VIS spectroscopy

	F-55	F-80	F-170
CuSe ₂ direct transition [eV]	2.75	2.74	2.72
CuSe ₂ indirect transition [eV]	1.75	1.72	1.71
Se direct transition [eV]	2.36	2.34	2.33

Broad range of energy band gap values for Cu-Se can be found in literature. For direct transitions those values are usually between 2 and 3 eV. Bari *et al.* [25] obtained the value of 2.51 eV for the sample with thickness of 150 nm, and with the increase of film thickness they reported the decrease of band gap width. Grozdanov [26], Garcia *et al.* [16] and Sakr *et al.* [27] obtained the value of 2.33, 2.13–2.38 and 2.74 eV, respectively. The latter is very similar to the results obtained in this paper. Rajesh *et al.* [28] got a diversity of band gaps ranging from

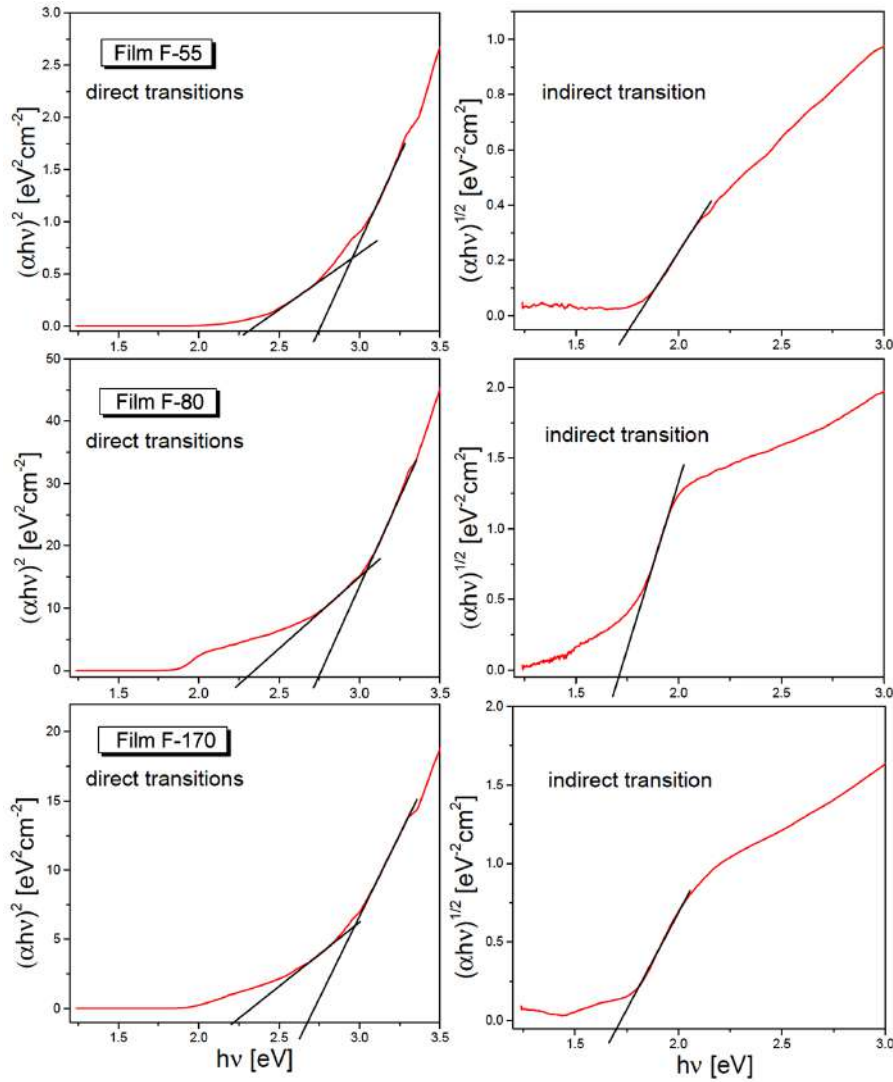


Figure 3. Dependence of $(\alpha \cdot h \cdot \nu)^2$ on photon energy ($h \cdot \nu$) – left side, and dependence of $(\alpha \cdot h \cdot \nu)^{1/2}$ on photon energy ($h \cdot \nu$) – right side

1.95 (the thickest film) to 3.70 eV (the thinnest film). However, for indirect transitions they received less attention. Garcia *et al.* [16] obtained values in the range 1.22–1.34 eV, whereas the value obtained by Bhuse *et al.* [7] is about 1.4 eV. Our values (~1.7 eV) are bigger than the reported in literature. According to our opinion, the larger indirect band gap values are due to quantum confinement effect [29,30] whereby the electrons are localized in individual crystallites, and due to specific border conditions between CuSe₂ nanoparticles and selenium matrix.

For the pure selenium, the direct band gap was reported to be about 2 eV for the bulk [31,32] and 2.20–2.06 for the thin films of thickness 130–290 nm [33]. Our films are thinner than the ones mentioned in the literature and it is not surprising that we obtained wider band gap values, about 2.3 eV. The film F-170 has the thickness between 130 and 290 nm, but the higher value in band gap is the result of specific border conditions between selenium matrix and CuSe₂ nanoparticles. We presume that CuSe₂ nanoparticles directly influence the

band gap of predominant selenium, and vice versa.

The Urbach energy is also analysed. Urbach rule states that the optical absorption coefficient α just below the band edge in insulators and semiconductors varies exponentially with the incident photon energy [34]:

$$\alpha = \alpha_0 \exp\left(\frac{h \cdot \nu}{E_U}\right) \quad (3)$$

where α_0 is a constant and characteristic parameter of the material, $h \cdot \nu$ is incident photon energy, and the term E_U which is the width of the exponential tail is called Urbach energy. The Urbach energy represents the width of defect states in the band gap. Figure 4 shows $\log \alpha$ as a function of incident photon energy for the film F-170, as a representative one. By extrapolating the linear part of the plot and with use of Equation 3, the Urbach energy can be determined as the inverse of the slope and α_0 from the intercept of extrapolated plot. From the slope and inception of extrapolated plot it was determined that E_U is 0.32 eV and α_0 is 3.02 cm⁻¹.

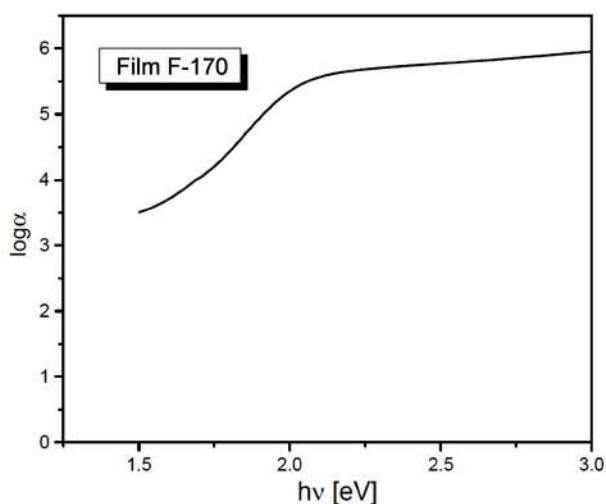


Figure 4. Logarithmic dependence of the absorption coefficient on the photon energy for F-170 film

3.3. Photoluminescence spectroscopy

Photoluminescence (PL) spectra can be used for investigating the possible outcomes of photo-induced electrons and holes in a semiconductor, since photoluminescence emission results from the recombination of free charge carriers. There are two types of photoluminescence phenomenon according to its attributes and formation mechanism: the band-to-band photoluminescence and the excitonic photoluminescence [35–37]. The band-to-band PL spectrum regards the separation situation of photo-generated charge carriers. The excitonic PL spectrum, however, cannot directly reflect the separation situation of photo-induced carriers. If discrete energy levels are present in the band gap, these may dominate the optical spectrum. PL measurements then yield information about the energetic positions of the electronic states in the gap. Such localized states can originate from various types of imperfections like vacancies, interstitial atoms, atoms at surfaces and grain boundaries. However, it is often difficult to determine the exact position and origin of these states.

Photoluminescence spectra of thin films on various temperatures are presented in Fig. 5. The spectra are rather complex, thus for their analysis the deconvolution method had to be employed. Two typical resolved spectra are presented in Fig. 6 (on 20 K and room temperature), and the deconvolution of the others is done in the same manner. Each spectrum is characterized with 5 bands. Band-to-band photoluminescence dominates the room temperature spectra. The band in red area at ~ 1.6 eV is clearly seen. According to the UV-VIS results (see previous chapter), we can attribute this mode to band-to-band transition for indirect transition in CuSe_2 . In green area, a broad band is observed at ~ 2.3 eV which originates from direct transitions in selenium (also see prev. chapter). Due to Stokes shift, the obtained positions are a bit lower than the ones obtained by UV-VIS spectroscopy. Between these two bands there are three defect modes at 2.1 eV, 1.9 eV and

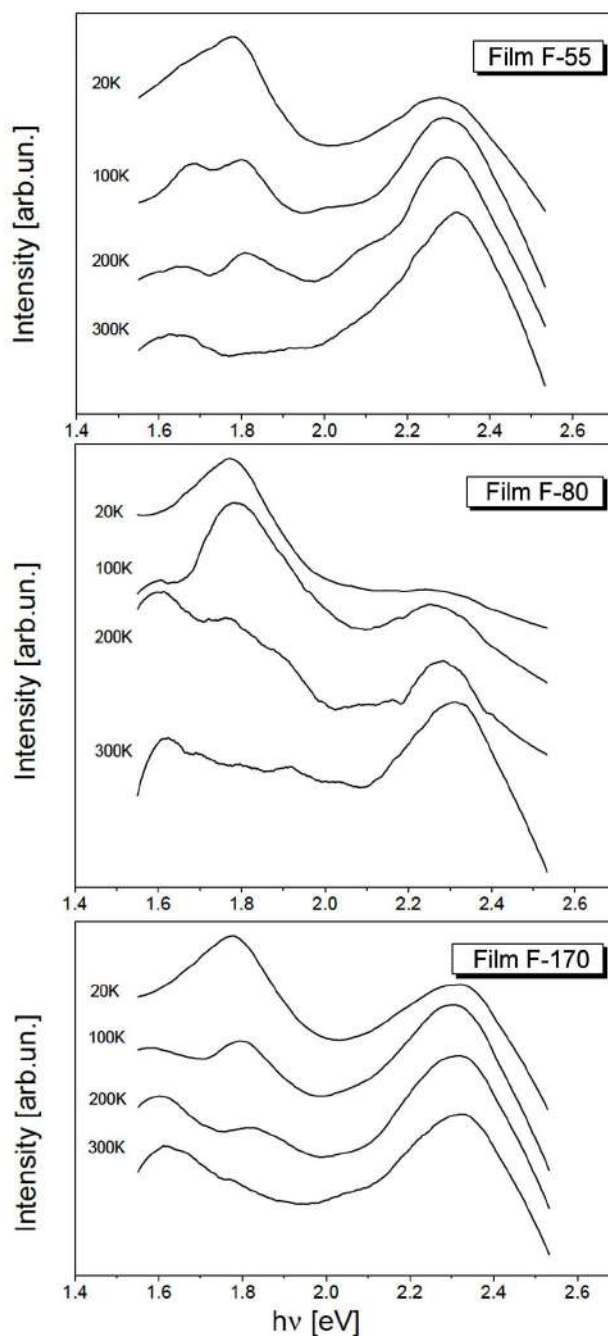


Figure 5. Photoluminescence spectra of thin films at various temperatures: a) F-55, b) F-80 and c) F-170

1.8 eV, which are of small intensity on room temperature. Lowering the temperature, the band at ~ 1.8 eV increases its intensity, and becomes the dominant one at 20 K. According to literature data [32] this band is attributed to selenium defect mode – negative U-centre. This mode is expected to appear at 0.5 eV from the band edges. Another two defect modes, at 2.1 and 1.9 eV, are attributed to the defect modes of CuSe_2 , according to the work of Urmila *et al.* [38]. In their work they obtained bands at 2.1, 1.9 and 1.5 eV in PL spectrum of Cu_7Se_4 thin film. They concluded that there is nonradiative transition from conduction band to defect levels with energies 2.1, 1.9 and 1.5 eV and from these lev-

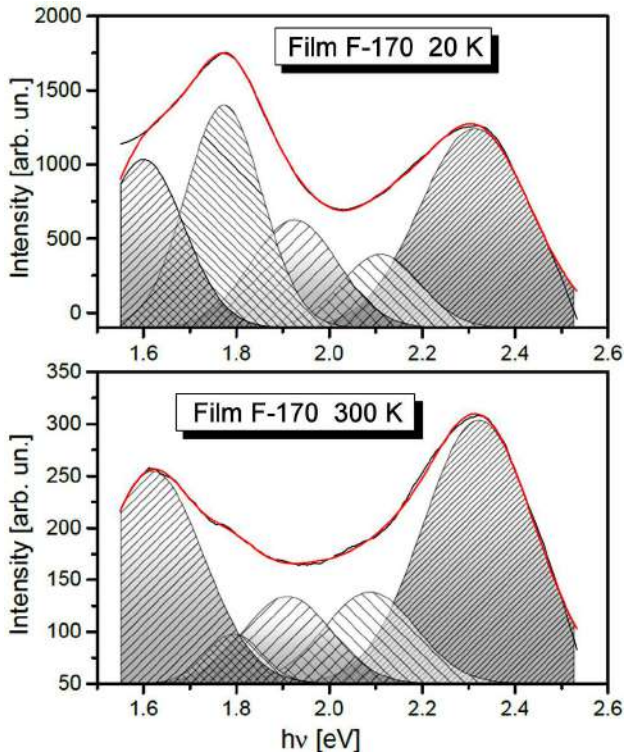


Figure 6. Typical resolved photoluminescence spectra of thin films F-170: a) on 20 K and b) room temperature

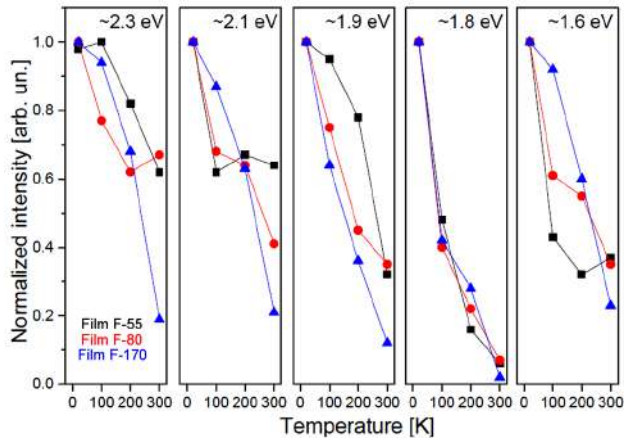


Figure 7. Temperature dependence of PL emission bands intensities, normalized on the most intensive ones (black squares – film F-55, red circles – film F-80, blue triangles – film F-170)

els radiative transitions occurred to valence band. The values 2.1 and 1.9 eV match the band positions we obtained in this work, thus we can assign these bands to defect modes in CuSe_2 . Due to predominant phase of selenium, these bands are hidden by the bands originated from selenium and cannot be observed without the deconvolution method. Chong [39] in his work also obtained a PL band at ~ 2.16 eV without assigning it to any transition. In all spectra, the uprise of peak intensity with lowering temperature is observed, Fig. 7. The intensities have their maximum values at the lowest temperature (20 K) and show decrease with rising temperature. The most radical decrease is observed for the band

at ~ 1.8 eV, which intensity drops to $\sim 40\%$ at 200 K, and only to $\sim 6\%$ at room temperature.

Temperature dependence of PL emission band positions is shown in Fig. 8. Let us discuss the band position of indirect transitions of CuSe_2 . At the room temperature, there are differences on the second decimal place for films of different thicknesses, the same as observed when analysing UV-VIS spectra. The same trend is observed on 20 K. If the shift of this band with temperature is analysed for each film, it can be noticed the temperature invariance, i.e. small non-monotonous differences in positions on the second decimal place. This is in contradiction with the expected red shift, characteristic for the semiconductors. The temperature invariance is observed for other bands as well. There is a question that needs to be answered: why the PL measurements show no shift with increasing temperature, instead of the conventional red shift characteristic for the semiconductors? A model proposed by Shen *et al.* [40] explains those discrepancies. It involves surface electron accumulation as a result of severe band bending in nanorods. However, the same trend was observed in thin film samples (including ours), whose curvature-less surface does not support a spatial charge separation such as in 1D nanostructures. Wei *et al.* [41] gave more exact explanation of this phenomenon in their work. They began the analysis by making difference between E_{PL} and E_g :

$$E_{PL}(n, T) = E_g(n, T) + E_{F_n}(n, T) - E_{F_p}(n, T) \quad (4)$$

where E_{F_n} and E_{F_p} are the electron and hole quasi-Fermi levels measured from the bottom of conduction band and the top of valence band, respectively. So the temperature dependence of the band gap shift is the competition between the lattice dilation dE_g/dT on the one hand, and the sum $(dE_{F_n}/dT - dE_{F_p}/dT)$ on the other hand. The former results in the conventional red shift of the band gap with increasing temperature and the latter gets the blue shift. The resulting shift depends

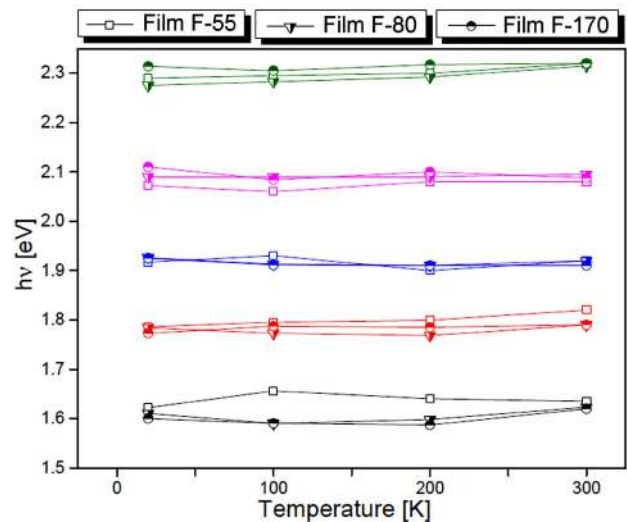


Figure 8. Temperature dependence of photoluminescence emission bands positions

on the magnitude of these two contributions. Usually when the electron density n is high, the thermal response in the material is governed by electronic rather than photonic interactions, the sum ($dE_{Fn}/dT - dE_{Fp}/dT$) becomes dominant thus the blue shift of E_{PL} is observed. However, if these two contributions are of the same magnitude, it will result in no shift with changing temperature, as in case of our samples.

PL emission bands positions as a function of film thicknesses are presented in Fig. 9. It is common knowledge that as the confining dimension decreases, typically in nanoscale, the energy spectrum turns to discrete so the band gap of a semiconductor becomes size dependent. For one-dimensional confinement (film thickness), the quantization energies increase when the size along the confinement direction decreases [42,43]. In an amorphous or structurally disordered film, the imperfection in the film causes the bands of localized states to get broaden and a band gap reduction may occur due to the Urbach edge [44]. If we observe the shift of the band at ~ 1.6 eV, which corresponds to indirect transitions in CuSe_2 , we can see the blue shift with decreasing size, as being expected. On the other hand, the band at ~ 2.3 eV which corresponds to direct transitions in Se, we can see no size dependence with the band position. The reason of this behaviour lies in specific composition of our films, i.e. CuSe_2 nano-objects embedded in selenium matrix. The particles of CuSe_2 are small enough to react on the size reduction, but the selenium matrix the amorphous effect becomes dominant.

As it can be seen from the above, the temperature changes do not affect the band gap. The size changes, i.e. the reduction of film thickness affects the band gap only on a second decimal place. Thus, we can state that the low cost technique of vacuum evaporation gives us the opportunity to produce quality, stable thin films

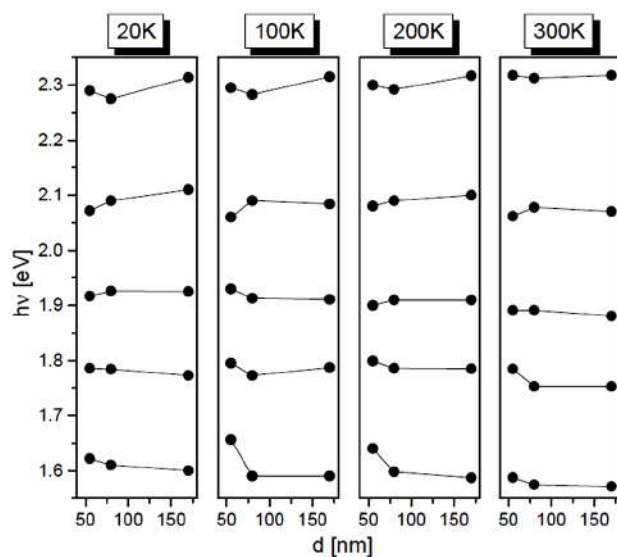


Figure 9. PL emission bands positions dependence of film thicknesses

suitable for further applications in heterojunction solar cells and photo detectors.

IV. Conclusions

Cu-Se thin films of three different thicknesses, obtained by vacuum evaporation technique on glass substrate, underwent through photoluminescence investigation along with UV-VIS measurements and SEM analysis. Reflectance measurements revealed values for both direct and indirect band gap: ~ 2.7 and 1.7 eV, respectively for CuSe_2 and ~ 2.3 eV for Se. The existence of indirect band gap in CuSe_2 at this value, little wider than in literature, is confirmed by photoluminescence measurements. A band at ~ 1.8 eV, registered by PL measurements at low temperatures, is attributed to defect level of selenium – negative U-center. In this paper we proved that simple and low-cost technique as vacuum evaporation is capable of producing high-quality thin films.

Acknowledgements: This work is supported by Serbian Ministry of Education, Science and Technological Development under Project III45003.

References

1. T.P. Hsieh, C.C. Chuang, C.S. Wu, J.C. Chang, J.W. Guo, W.C. Chen, "Effects of residual copper selenide on CuInGaSe_2 solar cells", *Solid State Electron.*, **56** (2011) 175–178.
2. M. Singh, J. Jiu, T. Sugahara, K. Suganuma, "Thin-film copper indium gallium selenide solar cell based on low-temperature all-printing process", *ACS Appl. Mater. Interfaces*, **6** (2014) 16297–16303.
3. J.H. Scofield, A. Duda, D. Albin, B.L. Ballard, P.K. Predecki, "Sputtered molybdenum bilayer back contact for copper indium diselenide-based polycrystalline thin-film solar cells", *Thin Solid Films*, **260** (1995) 26–31.
4. S. Lei, A. Sobhani, F. Wen, A. George, Q. Wang, Y. Huang, P. Dong, B. Li, S. Najmaei, J. Bellah, G. Gupta, A.D. Mohite, L. Ge, J. Lou, N.J. Halas, R. Vajtai, P. Ajayan, "Ternary $\text{CuIn}_7\text{Se}_{11}$: Towards ultra-thin layered photodetectors and photovoltaic devices", *Adv. Mater.*, **45** (2014) 7666–7737.
5. G. Juska, V. Gulbinas, A. Jagminas, "Transient absorption of copper selenide nanowires of different stoichiometry", *Lith. J. Phys.*, **50** (2010) 233–239.
6. C. Levy-Clement, M. Neumann-Spallart, S.K. Haram, K.S.V. Santhanam, "Chemical bath deposition of cubic copper (I) selenide and its room temperature transformation to the orthorhombic phase", *Thin Solid Films*, **302** (1997) 12–16.
7. V.M. Bhuse, P.P. Hankare, K.M. Garadkar, A.S. Khomane, "A simple, convenient, low temperature route to grow polycrystalline copper selenide thin films", *Mater. Chem. Phys.*, **80** (2003) 82–88.
8. S.Y. Zhang, C. Fang, Y. Tian, K. Zhu, B. Jin, Y. Shen, J. Yang, "Synthesis and characterization of hexagonal CuSe nanotubes by templating against trigonal Se nanotubes", *Cryst. Growth Des.*, **6** (2006) 2809–2813.
9. H.M. Pathan, C.D. Lokhande, D.P. Amalnerkar, T. Seth, "Modified chemical deposition and physico-chemical

- properties of copper (I) selenide thin films”, *Appl. Surf. Sci.*, **211** (2003) 48–56.
10. Y. Takana, N. Uchiyama, S. Ogawa, N. Mori, Y. Kimishima, S. Arisawa, A. Ishii, T. Hatano, K. Togano, “Superconducting properties of $\text{CuS}_{2-x}\text{Se}_x$ under high pressure”, *Physica C: Superconduct.*, **341-348** (2000) 739–740.
 11. G. Krill, P. Panissod, M.F. Lapiere, F. Gautier, C. Robert M.N. Eddine, “Magnetic properties and phase transitions of the metallic CuX_2 dichalogenides ($X = \text{S}, \text{Se}, \text{Te}$) with pyrite structure”, *J. Phys. C*, **9** (1976) 1521–1533.
 12. M. Kontani, T. Tutui, T. Moriwaka, T. Mizukoshi, “Specific heat and NMR studies on the pyrite-type superconductors CuS_2 and CuSe_2 ”, *Physica B*, **284** (2000) 675–676.
 13. R.R. Pai, T.T. John, M. Lakshimi, K.P. Vijayakumar, C.S. Kartha, “Observation of phase transitions in chemical bath deposited copper selenide thin films through conductivity studies”, *Thin Solid Films*, **473** (2005) 208–212.
 14. N.H. Kim, S. Oh, W.S. Lee, “Non-selenization method using sputtering deposition with a CuSe_2 target for CIGS thin film”, *J. Korean Phys. Soc.*, **61** (2012) 1177–1180.
 15. P. Hankare, A. Khomane, P. Chate, K. Rathod, K. Garadkar, “Preparation of copper selenide thin films by simple chemical route at low temperature and their characterization”, *J. Alloys Comp.*, **469** (2009) 478–482.
 16. V. Garcia, P. Nair, M. Nair, “Copper selenide thin films by chemical bath deposition”, *J. Cryst. Growth*, **203** (1999) 113–124.
 17. O. Arellano-Tanori, M. Acosta-Enriquez, R. Ochoa-Landin, R. Iniguez-Palomares, T. Mendivil-Reynoso, M. Flores-Acosta, S. Castillo, “Copper-selenide and copper-telluride composites powders sintetized by ionic exchange”, *Chalcogenide Lett.*, **11** (2014) 13–19.
 18. A. Jagminas, R. Juskenas, I. Gailiute, G. Statkute, R. Tomasinas, “Electrochemical synthesis and optical characterization of copper selenide nanowire arrays within the alumina pores”, *J. Cryst. Growth*, **294** (2006) 343–348.
 19. D. Patidar, N.S. Saxena, “Characterization of single phase copper selenide nanoparticles and their growth mechanism”, *J. Cryst. Growth*, **343** (2012) 68–72.
 20. M. Gilic, M. Petrovic, R. Kostic, D. Stojanovic, T. Barudzija, M. Mitric, N. Romcevic, U. Ralevic, J. Trajic, M. Romcevic, I. Yahia, “Structural and optical properties of CuSe_2 nanocrystals formed in thin solid Cu-Se film”, *Infrared Phys. Techn.*, **76** (2016) 276–284.
 21. J. Tauc, R. Grigorovici, A. Vancu, “Optical properties and electronic structure of amorphous germanium”, *Phys. Status Solidi*, **15** (1966) 627–637.
 22. J. Tauc, *Optical Properties of Solids*, F. Abeles ed. North Holland, 1972.
 23. E. Davis, N. Mott, “Conduction in non-crystalline systems V. Conductivity, optical absorption and photoconductivity in amorphous semiconductors”, *Philos. Mag.*, **22** (1970) 903–922.
 24. P. Kubelka, F. Munk, “Ein Beitrag zur Optik der Farbanstriche”, *Zeits F. Teckn. Physik.*, **12** (1931) 593–601.
 25. R. Bari, V. Ganesan, S. Potadar, L. Patil, “Structural, optical and electrical properties of chemically deposited copper selenide films”, *Bull. Mater. Sci.*, **32** (2009) 37–42.
 26. I. Grozdanov, “Electroconductive copper selenide films on transparent polyester sheets”, *Synthetic Metals*, **63** (1994) 213–216.
 27. G. Sakr, I. Yahia, M. Fadel, S. Fouad, N. Romcevic, “Optical spectroscopy, optical conductivity, dielectric properties and new methods for determining the gap states of CuSe thin films”, *J. Alloys Comp.*, **507** (2010) 557–562.
 28. D. Rajesh, R. Chandrakanth, C. Sunandana, “Annealing effects on the properties of copper selenide thin films for thermoelectric applications”, *IOSR J. Appl. Phys.*, **4** (2013) 65–71.
 29. G. Hodes, A. Albu-Yayor, F. Decker, P. Motisuke, “Three-dimensional quantum-size effect in chemically deposited cadmium selenide films”, *Phys. Rev. B*, **36** (1987) 4215–4221.
 30. V. García, M. Nair, P. Nair, R. Zingaro, “Chemical deposition of bismuth selenide thin films using N,N-dimethylselenourea”, *Semicond. Sci. Technol.*, **12** (1997) 645–653.
 31. S. Kasap, J.B. Frey, G. Belev, O. Tousignant, H. Mani, L. Laperriere, A. Reznik, J.A. Rowlands, “Amorphous selenium and its alloys from early xeroradiography to high resolution X-ray image detectors and ultrasensitive imaging tubes”, *Phys. Status Solidi*, **246** (2009) 1794–1805.
 32. M. Benkheldir, *Defect Levels in Amorphous Selenium Bandgap*, Katholieke Universiteit Leuven, PhD Thesis 2006.
 33. M. Singh, K. Bhahada, Y. Vijay, “Variation of optical band gap in obliquely deposited selenium thin films”, *Indian J. Pure Appl. Phys.*, **43** (2005) 129–131.
 34. F. Urbach, “The long-wavelength edge of photographic sensitivity and of the electronic absorption of solids”, *Phys. Rev.*, **92** (1954) 1324.
 35. F.B. Li, H.Z. Li, “Photocatalytic properties of gold/gold ion-modified titanium dioxide for wastewater treatment”, *Appl. Catal. A*, **228** (2002) 15–27.
 36. P. Kumar, K. Singh, “Wurtzite ZnSe quantum dots: Synthesis, characterization and PL properties”, *J. Opto. Biomed. Mater.*, **1** (2009) 59–69.
 37. J.G. Yu, Y.R. Su, B. Cheng, “Template-free fabrication and enhanced photocatalytic activity of hierarchical macro-/mesoporous titania”, *Adv. Funct. Mater.*, **17** (2007) 1984–1990.
 38. K. Urmila, N. Asokan, B. Pradeep, “Photoluminescence study of copper selenide thin films”, *AIP Conf. Proc.*, **1391** (2011) 770–772.
 39. W.S. Chong, “Synthesis and characterization of copper selenide nanoparticles via emulsion technique”. A project report submitted to the Department of Chemical Science Faculty of Science, Universiti Tunku Abdul Rahman, In partial fulfilment of requirements for the degree of Bachelor of Science (Hons) Chemistry, May 2011.
 40. C.H. Shen, H.Y. Chen, H.-W. Lin, S. Gwo, A.A. Klochikhin, V.Y. Davydov, “Near-infrared photoluminescence from vertical InN nanorod arrays grown on silicon: Effects of surface electron accumulation layer”, *Appl. Phys. Lett.*, **88** (2006) 253104.
 41. P. Wei, S. Chattopadhyay, F. Lin, C. Hsu, S. Jou, J. Chen, P. Huang, H. Hsu, H. Shih, K. Chen, L. Chen, “Origin of the anomalous temperature evolution of photoluminescence peak energy in degenerate InN nanocolumns”, *Opt. Express*, **17** (2009) 11690–11697.
 42. S.V. Gaponenko, *Optical Properties of Semiconductor Nanocrystals*, Cambridge University Press, Cambridge, 1998.
 43. A. Shik, *Quantum Wells: Physics and Electronics of Two-*

- Dimensional Systems*, World Scientific, Singapore, 1997.
44. S.G. Tomlin, E. Khawaja, G.M.K. Thutupalli, “The optical properties of amorphous and crystalline germanium”, *J. Phys. C*, **9** (1976) 4335–4347.

Luminescence thermometry using $\text{Gd}_2\text{Zr}_2\text{O}_7:\text{Eu}^{3+}$

M. G. Nikolic¹ · M. S. Rabasovic¹ · J. Krizan² · S. Savic-Sevic¹ · M. D. Rabasovic¹ ·
B. P. Marinkovic¹ · A. Vlastic¹ · D. Sevic¹ 

Received: 15 October 2017 / Accepted: 5 June 2018 / Published online: 12 June 2018
© Springer Science+Business Media, LLC, part of Springer Nature 2018

Abstract In this paper we study the possibility of using the synthesized nanopowder samples of $\text{Gd}_2\text{Zr}_2\text{O}_7:\text{Eu}^{3+}$ for temperature measurements by analyzing the temperature effects on its photoluminescence. The nanopowder was prepared by solution combustion synthesis method. The photoluminescence spectra used for analysis of $\text{Gd}_2\text{Zr}_2\text{O}_7:\text{Eu}^{3+}$ nano phosphor optical emission temperature dependence were acquired using continuous laser diode excitation at 405 nm. The temperature dependencies of line emission intensities of transitions from $^5\text{D}_0$ and $^5\text{D}_1$ energy levels to the ground state were analyzed. Based on this analysis we use the two lines intensity ratio method for temperature sensing. Our results show that the synthesized material can be efficiently used as thermographic phosphor up to 650 K.

Keywords Photoluminescence · Thermographic phosphor · Laser spectroscopy · Combustion synthesis

1 Introduction

Phosphor thermometry is a non-contact technique that uses photoluminescence to remotely measure the temperature. Being a non-contact technique it has many advantages compared to conventional contact ones. Thermographic phosphors are materials that are synthesized in such a way that their structural stability regarding various parameters including the

This article is part of the Topical Collection on Focus on Optics and Bio-photonics, Photonica 2017.

Guest Edited by Jelena Radovanovic, Aleksandar Krmpot, Marina Lekic, Trevor Benson, Mauro Pereira, Marian Marciniak.

✉ D. Sevic
sevic@ipb.ac.rs

¹ Institute of Physics Belgrade, University of Belgrade, Belgrade, Serbia

² AMI d.o.o, Ptuj, Slovenia

temperature, pressure, magnetic field, electromagnetic radiation could be obtained. They typically consist of a ceramic host and rare-earth dopant. These materials are widely used in many applications. The temperature dependencies of their various luminescence characteristics are used for temperature sensing (Goss et al. 1989; Feist et al. 1999; Heyes 2009; Gentleman and Clarke 2004; Cates et al. 2002; Eldridge et al. 2012). The comprehensive reviews of the topic could be found in (Allison and Gillies 1997; Alden et al. 2011; Brites et al. 2012; Jaque and Vetrone 2012; Khalid and Kontis 2008). Study of luminescence sensing of temperature in pyrochlore zirconate materials could be found in (Gentleman and Clarke 2005).

This paper is extension of previous work regarding $\text{Gd}_2\text{Zr}_2\text{O}_7:\text{Eu}^{3+}$ nanopowder, presented in (Rabasovic et al. 2015). Recently, we have begun research of the potentials of using rare earth doped nano powders as temperature and high pressure sensors (Vlasic et al. 2018; Rabasovic et al. 2018). Europium doped nano powders are now investigated intensively for remote temperature sensing, using various hosts: TiO_2 (Nikolic et al. 2014), Gd_2O_3 (Nikolic et al. 2013), YNbO_4 , (Đačanin et al. 2013, 2014), Lu_2O_3 (Lojpur et al. 2012), $\text{Gd}_2\text{Ti}_2\text{O}_7$ (Lojpur et al. 2016), $\text{Sr}_2\text{CeO}_4:\text{Eu}^{3+}$ (Vlasic et al. 2018), including references therein. Here, we study the possibility of using the synthesized nanopowder samples of $\text{Gd}_2\text{Zr}_2\text{O}_7:\text{Eu}^{3+}$ for temperature measurements. The analysis is based on two lines intensity ratio method for temperature sensing. To the best of our knowledge, this kind of a study of the thermographic potentials of $\text{Gd}_2\text{Zr}_2\text{O}_7:\text{Eu}^{3+}$ nanomaterial, prepared by simple and cost effective process, is firstly presented in this paper.

The studied nanopowder material was prepared by solution combustion synthesis (SCS) method and its structural characteristics were confirmed by SEM images and XRD analysis (Rabasovic et al. 2015). The $\text{Gd}_2\text{Zr}_2\text{O}_7:\text{Eu}^{3+}$ material received the renewed interest recently, regarding the infrared (Mitric et al. 2018) and Raman (Krizan et al. 2017) spectroscopy studies.

2 Experimental procedures

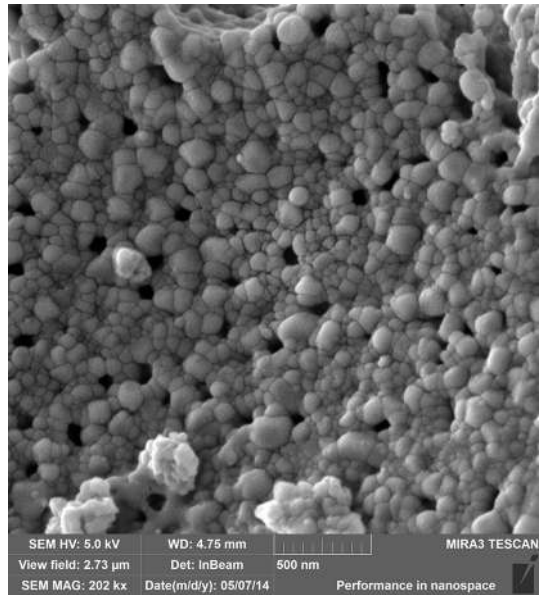
In our experiments luminescence of samples were measured both using pulsed and continuous excitation (Rabasovic et al. 2015). Pulsed excitation was necessary for lifetime measurements (Rabasovic et al. 2015). For temperature measurements using two lines intensity ratio we decided to use continuous excitation due to larger acquisition count rates compared to pulsed excitation.

The photoluminescence spectra used for analysis of $\text{Gd}_2\text{Zr}_2\text{O}_7:\text{Eu}^{3+}$ nano phosphor optical emission temperature dependence were acquired using continuous laser diode excitation at 405 nm and Ocean Optics spectrometer USB2000. The detailed explanation of the setup is provided in (Rabasovic et al. 2016). The structure of nanopowders was observed by high resolution scanning electron microscope (SEM) equipped with a high brightness Schottky Field Emission gun (FEGSEM, TESCAN) operating at 4 kV.

3 Results and discussion

The representative SEM image of our sample of $\text{Gd}_2\text{Zr}_2\text{O}_7:\text{Eu}^{3+}$ material is presented in Fig. 1. The detailed structural study, including the XRD, of the material from which our sample was taken is provided in (Rabasovic et al. 2015). The detailed time resolved

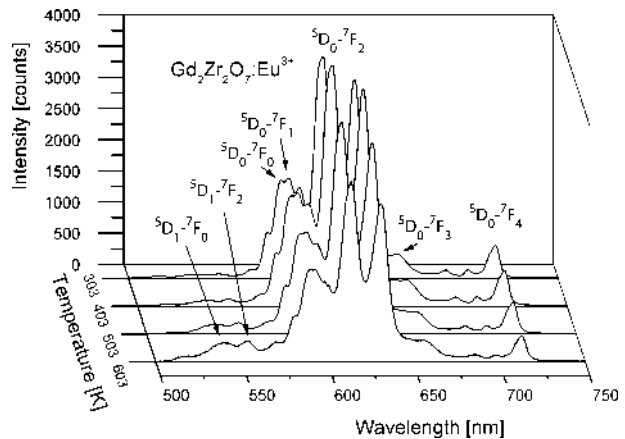
Fig. 1 SEM image of $\text{Gd}_2\text{Zr}_2\text{O}_7:\text{Eu}^{3+}$ nano phosphor prepared by SCS method



analysis of emission spectra under pulsed excitation is also provided in (Rabasovic et al. 2015). The obtained lifetimes from $^5\text{D}_0$ level are about 1.5 ms. XRD analysis confirmed that sample was crystallized in fluorite (F) type structure (space group $\text{Fm}\bar{3}\text{m}$). The image of the synthesized material, see Fig. 1, shows the irregular crystallite size distribution. Particles with dimensions from 50 nm to over 100 nm are easily discernible. The agglomerated grains could be also noticed.

Photoluminescence spectra of Eu^{3+} doped $\text{Gd}_2\text{Zr}_2\text{O}_7$ were recorded over the temperature range 300–700 K, with a step of 20 K. In order to make the image clear, only spectra with the temperature distance of 100 K are displayed in Fig. 2. The emission band at 537 nm corresponds to $^5\text{D}_1 \rightarrow ^7\text{F}_1$, the emission band at 553 nm corresponds to $^5\text{D}_1 \rightarrow ^7\text{F}_2$, and the emission bands at 580, 592, 614 and 631 nm, 654 and 713 nm correspond to the

Fig. 2 Luminescence spectra of Eu^{3+} doped $\text{Gd}_2\text{Zr}_2\text{O}_7$ at several temperatures (continuous laser diode excitation at 405 nm)



$^5D_0 \rightarrow ^7F_1$, $^5D_0 \rightarrow ^7F_2$, $^5D_0 \rightarrow ^7F_3$, $^5D_0 \rightarrow ^7F_4$ transitions of Eu³⁺ ions, respectively. To minimize the effects of host luminescence we used excitation at 405 nm, where europium optical response to direct excitation is still good.

Fluorescence intensity ratio technique is based on monitoring the two emission lines in luminescence spectra of thermographic phosphors. The temperature is calculated by the emission intensity ratio of these two lines. Many problems regarding measuring errors, optical condition deviations and excitation power fluctuation are eliminated in this way. Two closely spaced energy levels of rare earth ion, which are thermally coupled, are usually selected for temperature sensing. Small energy gap between these two levels allows the upper level to be populated from the lower level by thermalization. The upper level becomes more populated as the temperature increases and hence the fluorescence from this level gradually increases. Relative population between two levels, IR , follows Boltzmann-type population distribution given by (Brites et al. 2012; Jaque and Vetrone 2012; Đaćanin et al. 2014):

$$IR = \frac{I_{31}}{I_{21}} = C \exp\left(-\frac{E_{32}}{kT}\right) \quad (1)$$

where k is the Boltzmann constant, $k=0.695\ 034\ 76(63)\ \text{cm}^{-1}\ \text{K}^{-1}$ and E_{32} is the energy gap between two excited levels.

However, in fluorescence measurements, instruments frequently detect small signals, even when there is no emission, because of detector dark currents, etc. Moreover, spectrograph stray light introduces error in measured intensity of a signal. Therefore, another constant, A , should be introduced to Eq. (1), to account for the finite value of IR at low temperatures (Lojpur et al. 2016):

$$IR = \frac{I_{31}}{I_{21}} = A + C \exp\left(-\frac{E_{32}}{kT}\right) \quad (2)$$

We have analyzed the temperature sensing calibration curves based on various combinations of ratios of measured intensities of two europium optical emission lines. The lines should be from different energy levels, of strong intensity and close proximity of their upper levels on energy diagram, so the thermalization effect will be effective. After preliminary analysis of all obtained spectra, the $^5D_1 \rightarrow ^7F_2$ (553 nm) and $^5D_0 \rightarrow ^7F_2$ (614 nm) transitions were selected to be used to obtain values in the intensity ratio method.

The dependences of $^5D_1 \rightarrow ^7F_2$ and $^5D_0 \rightarrow ^7F_2$ emission line intensities of Eu³⁺ doped Gd₂Zr₂O₇ as a function of temperature are shown in Fig. 3. We have used the band of about 2 nm to integrate areas of peaks, thus alleviating the various measurements problems. The intensity of the europium $^5D_1 \rightarrow ^7F_2$ emission line slightly increases from 300 to 600 K and then decreases. The intensity of the $^5D_0 \rightarrow ^7F_2$ emission line was reduced almost three times in the same temperature interval. Line intensity measurements are sensitive, regarding errors, to variations of laser excitation power and light detection efficiency. Our repeated measurements (not presented for clarity purposes in Fig. 3) prove the good repeatability and very low hysteresis which is a good characteristic of this material for applicability in temperature measurement.

Temperature dependence of the intensity ratio of two Eu emission lines, at 553 and 614 nm, is shown in Fig. 4. Temperature sensing calibration curve was fitted using Eq. (2). Because of small signal intensity we discarded the measured points above 650 K. Calculated value for the energy gap, $E_{32}=1787.9987\ \text{cm}^{-1}$, is in good agreement with the europium energy level positions $E_{553}-E_{614}=1746\ \text{cm}^{-1}$ (Dieke 1968; Binnemans 2015).

Fig. 3 Measured intensity-temperature dependencies of two Eu emission lines, at 553 and 614 nm, for Eu^{3+} doped $Gd_2Zr_2O_7$

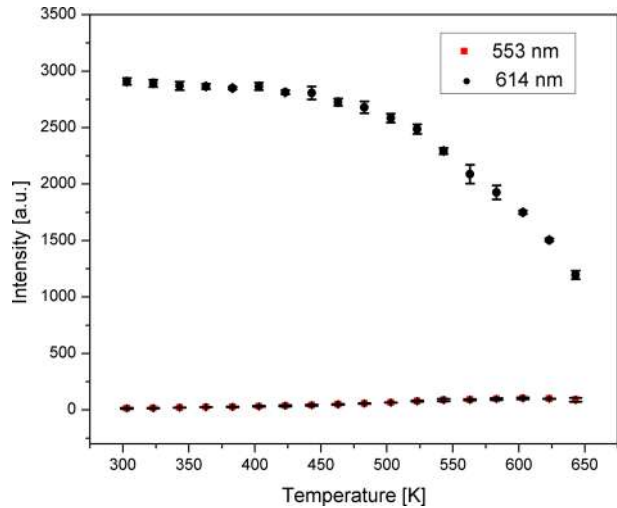
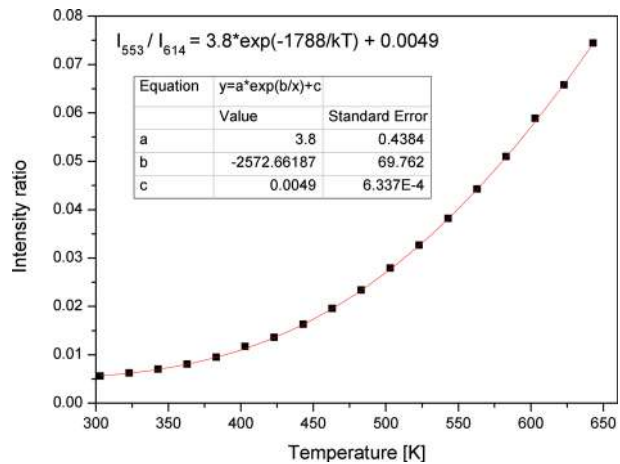


Fig. 4 Temperature dependence of the intensity ratio of two Eu emission lines, at 553 and 614 nm, for Eu^{3+} doped $Gd_2Zr_2O_7$. Experimental points are denoted by black squares and fitted temperature calibration curve is denoted by red line



The absolute thermal sensitivity, S , is defined as the rate at which IR changes with the temperature:

$$S = \left| \frac{dIR}{dT} \right| \tag{3}$$

The relative thermal sensitivity, Sr , is given by:

$$Sr = \left| \frac{1}{IR} \frac{dIR}{dT} \right| \tag{4}$$

Absolute sensitivity [calculated according to Eq. (3)] and relative sensitivity [calculated according to Eq. (4)] curves as the function of temperature are presented in Fig. 5. Relative sensitivity is highest around 425 K and its value is $0.92\% K^{-1}$, and is lowest value is about

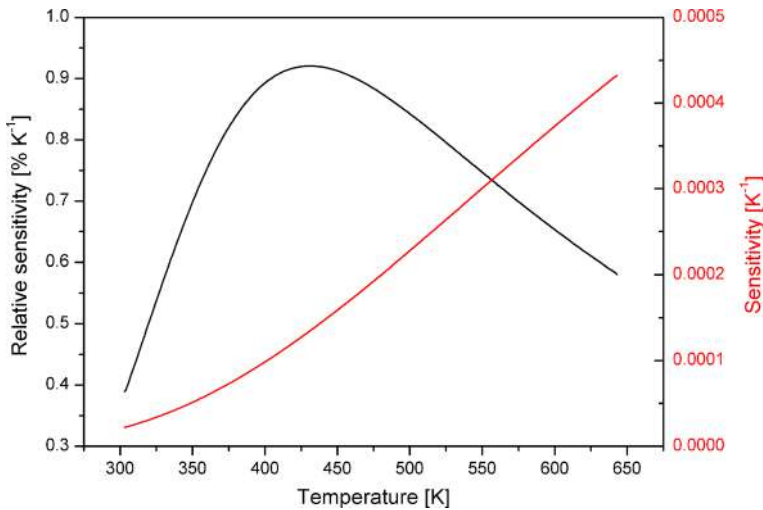


Fig. 5 Absolute and relative sensitivity curves as the function of temperature for Eu^{3+} doped $\text{Gd}_2\text{Zr}_2\text{O}_7$

$0.4\% \text{ K}^{-1}$ at 303 K, proving that this material could be used as a good temperature sensor within the studied temperature range.

Table 1 shows comparison of temperature sensing characteristics of various hosts doped with Eu^{3+} . The relative sensitivity is much better indicator than absolute sensitivity for comparison purposes between various materials. Comparing temperature sensing characteristics of various hosts doped with europium, presented in Table 1, it is easy to notice that there is usual trade-off between the sensitivity and sensing range, so the optimal host could be selected based on desired sensing range.

Methods for temperature sensing based on fluorescence intensity ratio are not sensitive, regarding errors, to variations of laser excitation power and light detection efficiency (Alden et al. 2011). So, using the same line of reasoning as in (Vlasic et al. 2018) we conclude that measurement errors mostly originate from the fitting procedures and least-square errors in extracting the temperatures from the calibration curve (Alden et al. 2011). For presented measurements the relative errors are smaller than 5% in the whole measuring

Table 1 Comparison of temperature sensing characteristics of various hosts doped with Eu^{3+}

Host	Sensing range (K)	Rel. sensitivity ($\% \text{ K}^{-1}$)		References
		Min	Max	
$\text{Gd}_2\text{Zr}_2\text{O}_7$	300–650	0.4	0.92	This work
Sr_2CeO_4	300–400	1	2.4	Vlasic et al. (2018)
YNbO_4	300–720	0.3	2.6	Đaćanin et al. (2013), Đaćanin et al. (2014)
Gd_2O_3	300–800	0.25	3.25	Nikolic et al. (2013)
Lu_2O_3	300–800	0.3	0.33	Lojpur et al. (2012)
$\text{Gd}_2\text{Ti}_2\text{O}_7$	300–420	0.3	0.95	Lojpur et al. (2016)
TiO_2	300–530	0.12	2.3	Nikolic et al. (2014)

range and below 2% for temperatures above 350 K. For used Ocean Optics spectrometer with 12 bit resolution, the estimated resolution of temperature measurements is about 7 K. However, aim of our work is to prove the concept of using the $\text{Gd}_2\text{Zr}_2\text{O}_7:\text{Eu}^{3+}$ nanoposphor for thermometry. So, the estimated resolution of our measurements is, before all, the characteristics of our equipment, not of the analyzed phosphor.

4 Conclusion

In this paper we have analyzed the temperature effects on photoluminescence of nanopowder samples of $\text{Gd}_2\text{Zr}_2\text{O}_7:\text{Eu}^{3+}$. The nanopowder was prepared by solution combustion synthesis (SCS) method. After plotting and analyzing the temperature sensing calibration curves based on various combinations of two europium optical emission lines, we selected the spectral lines at 553 and 614 nm to be used for temperature measurements. Our results show that the synthesized material can be efficiently used as thermographic phosphor up to 650 K. Relative sensitivity is highest around 425 K and its value is $0.92\% \text{ K}^{-1}$, its lowest value is about $0.4\% \text{ K}^{-1}$ at 303 K, and it is $0.76\% \text{ K}^{-1}$ at 643 K. Comparing these results with characteristics of other state-of-the-art materials, we prove that this material could be used as a good temperature sensor within the studied temperature range.

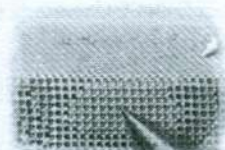
Acknowledgements This work was financially supported within the Projects of Ministry of Education, Science and Technological Development of the Republic of Serbia OI171020, OI171038 and III45016.

References

- Alden, M., Omrane, A., Richter, M., Särner, G.: Thermographic phosphors for thermometry: a survey of combustion applications. *Prog. Energy Combust. Sci.* **37**, 422–461 (2011)
- Allison, S.W., Gillies, G.T.: Remote thermometry with thermographic phosphors: instrumentation and applications. *Rev. Sci. Instrum.* **68**, 2615–2650 (1997)
- Binnemans, K.: Interpretation of europium(III) spectra. *Coord. Chem. Rev.* **295**, 1–45 (2015)
- Brites, C.D.S., Lima, P.P., Silva, N.J.O., Millan, A., Amaral, V.S., Palacio, F., Carlos, L.D.: Thermometry at the nanoscale. *Nanoscale* **4**, 4799–4829 (2012)
- Cates, M.R., Allison, S.W., Jaiswal, S.L., Beshears, D.L.: YAG:Dy and YAG:Tm Fluorescence Above 1400 C. Oak Ridge National Laboratory, Report ORNL/TM-2002/71 (2002)
- Dieke, G.H.: Spectra and Energy Levels of Rare Earth Ions in Crystals. Interscience Publishers, New York (1968)
- Đačanin, L.R., Lukić-Petrović, S.R., Petrović, D.M., Nikolić, M.G., Dramićanin, M.D.: Temperature quenching of luminescence emission in Eu^{3+} - and Sm^{3+} -doped YNbO_4 powders. *J. Lumin.* **151**, 82–87 (2014)
- Đačanin, L.R., Dramićanin, M.D., Lukić-Petrović, S.R., Petrović, D.M., Nikolić, M.G.: Eu^{3+} doped YNbO_4 phosphor properties for fluorescence thermometry. *Radiat. Meas.* **56**, 143–146 (2013)
- Eldridge, J.I., Jenkins, T.P., Allison, S.W., Wolfe, D.E., Jordan, E.H.: Development of YAG:Dy thermographic phosphor coatings for turbine engine applications. In: 58th International Instrumentation Symposium San Diego, CA, June 5–8 (2012)
- Feist, J.P., Heyes, A.L., Choy, K.L., Su, B.: Phosphor thermometry for high temperature gas turbine applications. In: Proceedings of IEEE; 6.1 (1999)
- Gentleman, M.M., Clarke, D.R.: Concepts for luminescence sensing of thermal barrier coatings. *Surf. Coat. Technol.* **188–189**, 93–100 (2004)
- Gentleman, M.M., Clarke, D.R.: Luminescence sensing of temperature in pyrochlore zirconate materials for thermal barrier coatings. *Surf. Coat. Technol.* **200**, 1264–1269 (2005)
- Goss, L.P., Smith, A.A., Post, M.E.: Surface thermometry by laser-induced fluorescence. *Rev. Sci. Instrum.* **60**, 3702–3706 (1989)

- Heyes, A.L.: On the design of phosphors for high-temperature thermometry. *J. Lumin.* **129**, 2004–2009 (2009)
- Jaque, D., Vetrone, F.: Luminescence nanothermometry. *Nanoscale* **4**, 4301–4326 (2012)
- Khalid, A.H., Kontis, K.: Thermographic phosphors for high temperature measurements: principles, current state of the art and recent applications. *Sensors* **8**, 5673–5774 (2008)
- Krizan, G., Gilic, M., Ristic-Djurovic, J.L., Trajic, J., Romcevic, M., Krizan, J., Hadzic, B., Vasic, B., Romcevic, N.: Raman spectroscopy and electron-phonon coupling in Eu^{3+} doped $\text{Gd}_2\text{Zr}_2\text{O}_7$ nanopowders. *Opt. Mater.* **73**, 541–544 (2017)
- Lojpur, V., Čulubrk, S., Dramićanin, M.D.: Ratiometric luminescence thermometry with different combinations of emissions from Eu^{3+} doped $\text{Gd}_2\text{Ti}_2\text{O}_7$ nanoparticles. *J. Lumin.* **169**, 534–538 (2016)
- Lojpur, V., Antic, Z., Krsmanovic, R., Medic, M., Nikolic, M.G., Dramićanin, M.D.: Thermographic properties of Eu^{3+} and Sm^{3+} doped Lu_2O_3 nanophosphor. *J. Serb. Chem. Soc.* **77**, 1735–1746 (2012)
- Mitric, J., Krizan, J., Trajic, J., Krizan, G., Romcevic, M., Paunovic, N., Vasic, B., Romcevic, N.: Structural properties of Eu^{3+} doped $\text{Gd}_2\text{Zr}_2\text{O}_7$ nanopowders: far-infrared spectroscopy. *Opt. Mater.* **75**, 662–665 (2018)
- Nikolic, M.G., Antic, Z., Culubrk, S., Nedeljkovic, J.M., Dramićanin, M.D.: Temperature sensing with Eu^{3+} doped TiO_2 nanoparticles. *Sens. Actuators B* **201**, 46–50 (2014)
- Nikolic, M.G., Al-Juboori, A.Z., Djordjevic, V., Dramićanin, M.D.: Temperature luminescence properties of Eu^{3+} -doped Gd_2O_3 phosphors. *Phys. Scr.* (2013). <https://doi.org/10.1088/0031-8949/2013/T157/014056>
- Rabasovic, M.S., Krizan, J., Savic-Sevic, S., Mitric, M., Rabasovic, M.D., Marinkovic, B.P., Sevic, D.: Orange-reddish light emitting phosphor $\text{GdVO}_4:\text{Sm}^{3+}$ prepared by solution combustion synthesis (SCS). *J. Spectrosc.* (2018). <https://doi.org/10.1155/2018/3413864>
- Rabasovic, M.D., Muric, B.D., Celebonovic, V., Mitric, M., Jelenkovic, B.M., Nikolic, M.G.: Luminescence thermometry via the two-dopant intensity ratio of $\text{Y}_2\text{O}_3:\text{Er}^{3+}$, Eu^{3+} . *J. Phys. D Appl. Phys.* (2016). <https://doi.org/10.1088/0022-3727/49/48/485104>
- Rabasovic, M.S., Sevic, D., Krizan, J., Terzic, M., Mozina, J., Marinkovic, B.P., Savic-Sevic, S., Mitric, M., Rabasovic, M.D., Romcevic, N.: Characterization and luminescent properties of Eu^{3+} doped $\text{Gd}_2\text{Zr}_2\text{O}_7$ nanopowders. *J. Alloys Compd* **622**, 292–295 (2015)
- Vlasic, A., Sevic, D., Rabasovic, M.S., Krizan, J., Savic-Sevic, S., Rabasovic, M.D., Mitric, M., Marinkovic, B.P., Nikolic, M.G.: Effects of temperature and pressure on luminescent properties of $\text{Sr}_2\text{CeO}_4:\text{Eu}^{3+}$ nanophosphor. *J. Lumin.* **199**, 285–292 (2018)

UNIVERZITET U BEOGRADU
Institut za fiziku



Konferencija
Sedma radionica fotonike
(2014)

Zbornik apstrakata



PHOTONICS
CENTER

Kopaonik, 10.-14.3.2014.

Konferencija **Sedma radionica fotonike 2014**

ZBORNIK APSTRAKATA

Kopaonik 10-14.3.2014.

Izdaje

Institut za fiziku Univerziteta u Beogradu

Za izdavača

dr Aleksandar Belić, direktor

Urednici

dr Aleksander Kovacević

dr Dragan Lukić

Tiraž

100 primeraka

ISBN 978-86-82441-39-7

Štampa

Razvojno-istraživački centar,
Tehnološko-metalurškog fakulteta u Beogradu
Karnegijeva 4, Beograd

CIP - Каталогизација у публикацији
Народна библиотека Србије, Београд

CIP

535(048)

681.7(048)

66.017/.018(048)

КОНФЕРЕЦИЈА радионица фотонице (7 ; 2014 ; Копаноник)

Zbornik apstrakata / Konferencija Sedma radionica fotonike (2014), Kopaonik,
10.-14.3.2014. ;[urednici Aleksander Kovacević, Dragan Lukić]. - Beograd : Institut za fiziku,
2014 (Beograd : Razvojno-istraživački centar grafičkog inženjerstva TMF). - XI, 52 str. :ilustr;
25 cm

Na vrhu nasl. str.: Univerzitet u Beogradu. - Apstrakti na srp. i engl. jeziku. - Tekst ćir. i lat. -

Tiraž 100. - Reč urednika: str. VII. - Registar.

ISBN 978-86-82441-39-7

a) Оптика - Апстракти b) Оптоелектроника - Апстракти c) Технички материјали - Апстракти
COBISS.SR-ID 205669644

Programski i organi

dr Aleksandar Krr
Odbora)

dr Aleksander Ko
Zbornika i Sajta)

dr Dragan Lukić, vi

Akademik dr Branis

Sponzori Konferenc

Ministarstvo prosv

Optičko društvo Srb

„Senzor Infiz“ d.o.c

Kompleksne fotonske strukture u biopolimeru

Svetlana Savić-Šević, Dejan Pantelić, Branislav Jelenković

Institut za fiziku, Univerzitet u Beogradu, Pregrevica 118, 11080 Zemun, Srbija

Kontakt: S. Savić-Šević (savic@ipb.ac.rs)

Apstrakt. Kompleksne fotonske strukture generisane su u biopolimeru. Kao biopolimer korišćen je polisaharid, pululan, dopiran jonima hroma. Strukture su formirane kombinacijom holografske metode i fazne separacije. Holografskom metodom formirana je zapreminska refleksiona rešetka. U eksperimentu je korišćen jednomodni Nd-YAG laser, talasne dužine 532 nm. Ekspozirani slojevi su hemijski obrađeni.

Fotonske strukture su karakterisane korišćenjem visoko rezolucionog skenirajućeg elektronskog mikroskopa sa elektronskim topom Šotkijevog tipa. Formirane su linearne i sferne (onion-like) višeslojne Bregove strukture. U Bregovim ravnima zarobljene su šuplje sfere pululana koje su formirane u procesu fazne separacije u toku hemijske obrade materijala.

Sa ciljem optičke karakterizacije ovih kompleksnih struktura mereni su transmisioni spektri korišćenjem spektrometra.

Optimiza

Peda

Apstrakt. Je određivanje sastav zemlje. Karakteri ovako neprozirne potrebno ispitati predstavljamo fib da se može kori različitim gustina

Merna glava vode uvek ulazi Hidrofon je po t laku izmenu men je moguće menje hidrofona. Razv rezonantnog pik predloženi fiber membrane, pode optičkih vlakana razvijenoj proces

UNIVERZITET U BEOGRADU
Institut za fiziku



Konferencija
Osma radionica fotonike (2015)

Zbornik apstrakata



Kopaonik, 8.-12.3.2015.

Konferencija **Osmo radionica fotonike 2015**
ZBORNİK APSTRAKATA
Kopaonik 8-12.3.2015.

Izdaje
Institut za fiziku Univerziteta u Beogradu

Za izdavača
dr Aleksandar Belić, direktor

Urednik
dr Dragan Lukić

Tiraž
100 primeraka

ISBN 978-86-82441-41-0

Štampa
Razvojno-istraživački centar,
Tehnološko-metalurškog fakulteta u Beogradu
Karnegijeva 4, Beograd

CIP - Каталогизacija y publikaciji
Narodna biblioteka Srbije, Beograd

CIP

535(048)
681.7(048)
66.017/.018(048)

КОНФЕРЕЦИЈА Радионица фотонике (8 ; 2015 ; Копаник)
Zbornik apstrakata / Konferencija Osmo radionica fotonike (2015),
Kopaonik, 8.-12. 3. 2015. ; [urednik Dragan Lukić]. - Beograd : Institut za fiziku,
2015 (Beograd : Razvojno-istraživački centar grafičkog inženjerstva TMF). - XII,
46 str. : ilustr. ; 25 cm

Na vrhu nasl. str.: Univerzitet u Beogradu. - Apstrakti na srp. i engl.
jeziku. - Tiraž 100. - Reč urednika: str. VII. - Registar.

ISBN 978-86-82441-41-0 (broš.)

a) Оптика - Апстракти b) Оптоелектроника - Апстракти c) Технички
материјали - Апстракти

COBISS.SR-ID 213633292

Ordered multilayer structure with randomly distributed nanospheres and nanopillars

Svetlana Savić-Šević, Dejan Pantelić, Dušan Grujić, Branislav Jelenković

Institute of Physics, University of Belgrade, Pregrevica 118, 11080 Zemun, Belgrade, Serbia

Contact: Svetlana Savić-Šević (savic@ipb.ac.rs)

Abstract. Complex nanostructures with interesting properties for photonic applications received great attention [1]. Here we present structures having both ordered and disordered components, integrated into novel photonic structure. Photonic structure consisting of ordered multilayer grating and randomly distributed nanospheres and nanopillars is fabricated through a combination of holographic method and non-solvent induced phase separation in a polysaccharide-based material. We show that the interplay between regularity and irregularity significantly increases the width of the photonic bandgap, which can be wide about two hundred nanometers. The resulting photonic material has properties of both ordered photonic crystals (band gap and high reflectivity) and disordered structures (weak localization, as a precursor to Anderson localization).

Photonic structures are recorded in Pullulan, a linear homo-polysaccharide produced by micro-organisms (*Aureobasidium pullulans*) [2], doped with ammonium dichromate - (DCP). Multilayer structures were fabricated as a volume Bragg reflection grating using a simple counter-propagating beam configuration. DCP was exposed with a single longitudinal mode, diode pumped Nd-YAG laser, at 532 nm.

The morphology of the resulting photonic structure was investigated using a high resolution scanning electron microscope equipped with a high brightness Schottky Field Emission gun (FEGSEM).

REFERENCES

- [1] W. G. Bae, H. N. Kim, D. Kim, S. H. Park, H. E. Jeong, K. Y. Suh, *Adv. Mater.* **26**, (2014) 675–700.
- [2] V. Prajapati, G. Jani, and S. Khanda, *Carbohydr. Polymers* **95**, (2013) 540–549.

**The 3rd International Conference on the Physics
of Optical Materials and Devices**

BOOK OF ABSTRACTS

Editors: Dr. Miroslav Dramićanin
Dr. Bruno Viana

Publisher: Agencija FORMAT, Belgrade

Print run: 250 copies

ISBN: 978-86-7306-116-0

August 2012, Belgrade, Serbia

ICOM 2012

**The 3rd International Conference on the Physics
of Optical Materials and Devices**

BOOK OF ABSTRACTS

Belgrade, Serbia
September 3rd – September 6th, 2012

ZOOM SYSTEM FOR MEASUREMENT OF COHERENT BACKSCATTERING OF LIGHT IN MICRO AND NANOMATERIALS

Dejan Pantelić, Svetlana Savić-Šević, Dušan Grujić

Institute of Physics, University of Belgrade, Pregrevica 118, 11080 Zemun, Belgrade, Serbia, pantelic@ipb.ac.rs

Coherent backscattering is a process observed in physical systems with certain amount of disorder. Systems can be either completely random (like clouds or milk) or regular with slight randomness. This is an interference phenomenon inherent for any type of waves – from electrons and sound to light. It is characterized by increased intensity in exact backscattering direction. Coherent backscattering was observed in many optical materials (artificial or natural) and gives important information about mean free path of light, density of scatterers and their dimensions.

Devices for measurement of backscattering are simple in principle, but rather demanding from the experimental point of view [1]. The main problem is that the width of backscattering cone is inversely proportional to mean free path length of light. For materials with path-length of the order of several micrometers (like in biological tissues) the cone is very narrow (of the order of microradian), while for nanostructured materials backscattering cone can be quite wide (several hundreds of milliradians). In that respect present systems are either constructed for observation of wide [2] or narrow backscattering cones [3].

Here we report on the universal system which can be used both for low and high backscattering angles. The system is based on imaging the scattering surface using an additional lens system. Image is directly projected into entrance pupil of a zoom lens (Canon 17 – 85 mm) which is focused at infinity and functions as a Fourier lens. In this way angular spectrum of scattered light is focused on the detection surface, making observation of backscattering cone possible. In this configuration, variable magnification of a zoom lens changes the angular field of view, depending on whether the backscattering cone is large or small. Light is detected on a 15.1 Mega pixel CMOS chip of a Canon EOS 50D camera.

Helium-neon laser (633 nm) was used as a light source in a polarization preserving configuration. The laser beam was expanded, its polarization changed to circular, before entering the non-polarizing beam-splitter. Scattered radiation was collected by previously described optical system, and detected by the camera. All ghost reflections from optical components were blocked and we were able to observe clear backscattering pattern. The sample was mounted on the motorized stage, which was used to slightly move the sample during exposure in order to average the speckle.

We observed and measured backscattering cones (both wide and narrow) of a range of samples: milk, skin, Teflon, barium-sulphate, artificial photonic structures, etc.

- [1] D. S. Wiersma, M. P. van Albada, A. Lagendijk, *Rev. Sci. Instrum.* 66 (1995) 5473 – 5476.
- [2] P. Gross, M. Störzer, S. Fiebig, M. Clausen, G. Maret, C. M. Aegerter, *Rev. Sci. Instrum.* 78 (2007) 033105.
- [3] Y. L. Kim, Y. Liu, R. K. Wali, H. K. Roy, V. Backman, *Appl. Opt.* 44 (2005) 366 – 377.

M. Zorin^a, Yu. L. Kopylov^c

^a Moscow, Russian Federation,
^b Moscow, Russian Federation,
^c Fryazino branch, 1
 k215@ire216.msk.su

ometry structure combine
 optical nonlinearity, etc, and
 data processing. The main
 of preparation and low cost.
 red polycrystalline films of
 some fields for possible
 (lowest order) of TADPH
 and harmonic generation was
 for p- and s-polarization at
 54 nm, pulse duration 30 ns,
 e. It was found from angle
 m point group of symmetry
 The intensity of the second
 e film increases from room
 tion at this temperature to
 r phase transition.

manufacturing of electron –
 TADPH films are used for
 This convertor we called as
 mal vision system based on
 linear optical properties and

Sh. Sh. Nabiev, S. M. Nikiforov,
 u Electronica. V.10, №6 (1983)

B. A. Chayuanov, Akusticheskiy

BUTTERFLY SCALES AS BIONIC TEMPLATES FOR COMPLEX ORDERED NANOPHOTONIC MATERIALS

Zoran Jakšić^a, Dejan Pantelić^b, Milija Sarajlić^a, Svetlana Savić-Šević^b, Jovan Matović^c,
 Branislav Jelenković^b, Dana Vasiljević-Radović^a, Srećko Ćurčić^d, Slobodan Vuković^a,
 Vladimir Pavlović^e

^aInstitute of Chemistry, Technology and Metallurgy, University of Belgrade, Njegoševa
 12, 11000 Belgrade, Serbia, jaksa@nanosys.ihtm.bg.ac.rs

^bInstitute of Physics, University of Belgrade, Zemun, Serbia, dejan.pantelic@ipb.ac.rs

^cInstitute of Sensors and Actuator Systems, Vienna University of Technology,
 Floragasse 7/ E366, A 1040 Vienna, Austria, Jovan.Matovic@tuwien.ac.at

^dUniversity of Belgrade, Faculty of biology, Department of Invertebrate zoology and
 entomology, Studentski trg 16, 11000 Belgrade, Serbia

^eUniversity of Belgrade, Faculty of agriculture, Department of Agricultural
 Engineering, Nemanjina 6, 11080 Zemun, Belgrade, Serbia

Biological structures can be extremely intricate [1], exceeding man-made nanostructures in complexity, form and function. Up to now researchers were mostly investigating physical (optical, acoustical, mechanical) properties of insect exoskeletons – the question is how to utilize them. One research direction is to mimic nature by artificially generating biomimetic structures [2]. Another possibility is to utilize biological material itself, where new properties are achieved by additional functionalization [3].

Recently we have analyzed photonic properties of the nanostructured scales on the wings of *Apatura ilia* and *A. iris* butterflies [4, 5]. Their intricate nanometer-sized features produce remarkable UV-blue iridescence, spectrally and directionally narrow. An extremely wide variability of butterfly scale forms, shapes and sizes is observed [6]. In this paper we propose a possible use of butterfly scales as templates for ordered 2D or 3D nanophotonic materials, with complexity not easily reproducible by conventional micro/nanofabrication methods. Nanocompositing is utilized to impart novel properties [7]. We show that one is thus able to achieve functionalities seldom if ever met in nature, like a combination of plasmonic behavior with bionic functions, but also other functions like enhanced light localization, light- and plasmon waveguiding and general metamaterial behavior. We present our theoretical analysis including preliminary calculations, as well as initial experimental verification. As an example, we consider a possibility to produce structures with extraordinary optical transmission [8] in a simple manner and at a fraction of the cost and necessary engineering efforts compared to the conventional methods. We conclude that bionic approach offers potentials for vast expansion of the nanophotonic and nanoplasmonic material toolbox.

[1] P. Vukusic, J. R. Sambles, *Nature*, 424, 6950 (2003) 852-855.

[2] M. Kolle, P. M. Salgard-Cunha, M. R. J. Scherer, F. Huang, P. Vukusic, S. Mahajan, J. J. Baumberg, U. Steiner, *Nature Nanotechnology*, 5, (2010) 511-515.

[3] N. L. Garrett, P. Vukusic, F. Ogrin, E. Sirotkin, C. P. Winlove, J. Moger, *J. Biophotonics*, 2 (2009) 157-166.

[4] D. Pantelić, S. Ćurčić, S. Savić-Šević, A. Korać, A. Kovačević, B. Ćurčić, B. Bokić, *Opt. Express* 19 (2011) 5817-5826.

[5] S. Ćurčić, D. Pantelić, B. Ćurčić, S. Savić-Šević, S. Makarov, V. Lačković, M. Labudović-Borović, N. Ćurčić, D. Stojanović, *Microsc. Res. Tech.* (2012) doi: 10.1002/jemt.22021

[6] A. L. Ingram, A. R. Parker, *Phil. Trans. Royal Soc. B.* 363 (2008) 2465-2480.

[7] Z. Jakšić, J. Matovic, *Materials*, 3 (2010) 165-200.

[8] T. W. Ebbesen, H. J. Lezec, H. F. Ghaemi, T. Thio, P. A. Wolff, *Nature*, 391, 6668 (1998) 667-669.



Far-infrared spectra of dysprosium doped yttrium aluminum garnet nanopowder



J. Trajić^{a,*}, M.S. Rabasović^a, S. Savić-Šević^a, D. Šević^a, B. Babić^b, M. Romčević^a, J.L. Ristić-Djurović^a, N. Paunović^a, J. Križan^c, N. Romčević^a

^a Institute of Physics, University of Belgrade, Pregrevica 118, 11080 Belgrade, Serbia

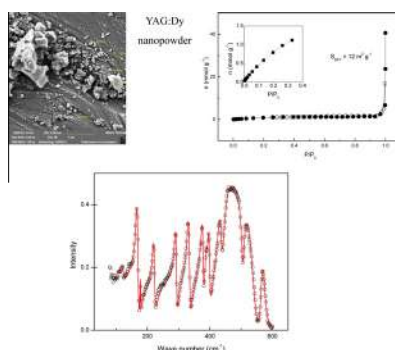
^b Vinca Institute of Nuclear Sciences, University of Belgrade, 11001 Belgrade, Serbia

^c AMI, d.o.o., Ptuj, Slovenia

HIGHLIGHTS

- YAG:Dy nanopowder was produced by Solution Combustion Synthesis (SCS) method.
- Powders are composed by well-defined and separated nanoparticles.
- Some particles are agglomerated but there are also separated particles.
- The dielectric function was modeled by the Maxwell–Garnet formula.
- Optical phonon confinement is registered.

GRAPHICAL ABSTRACT



ARTICLE INFO

Article history:

Received 20 April 2016

Revised 8 June 2016

Accepted 9 June 2016

Available online 9 June 2016

Keywords:

$Y_3Al_5O_{12}$

Dy^{3+}

Nanopowders

Light absorption and reflection

ABSTRACT

The solution combustion synthesis was used to prepare nanopowders of yttrium aluminum garnet (YAG) and YAG doped with dysprosium ions, Dy^{3+} , (YAG:Dy). The morphology, specific surface area, texture, and optical properties of the prepared materials were studied by the means of scanning electron microscopy (SEM), nitrogen adsorption method, and far-infrared spectroscopy at room temperature in the spectral region between 80 and 600 cm^{-1} . It was established that all the examined samples were microporous. The Maxwell–Garnet formula was used to model dielectric function of YAG and YAG:Dy nanopowders as mixtures of homogenous spherical inclusions in air.

© 2016 Elsevier B.V. All rights reserved.

1. Introduction

Importance of yttrium aluminum garnet, $Y_3Al_5O_{12}$, commonly abbreviated as YAG, arises from its high chemical stability as well as excellent optical and high-temperature mechanical properties [1]. It is a ceramic material with a cubic garnet crystallographic

structure whose thermal expansion is isotropic, whereas its optical properties are homogeneous, without birefringence effects [2,3]. Over the last five decades the structural properties of YAG were the subject of numerous studies, which proved its technological relevance and led to its use in a broad range of applications. For example, YAG has found its role as a host material in solid-state lasers of different kinds, luminescence materials, and scintillators [4–6].

Two prospective applications particularly draw attention toward trivalent dysprosium-activated optical materials. Namely,

* Corresponding author.

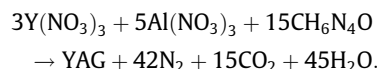
E-mail address: jelena@ipb.ac.rs (J. Trajić).

if the phonon energy of host matrix is low, these materials could be an alternative to praseodymium-doped optical amplifiers used in the second telecommunication window [7]. The second promising area of application, the solid-state lasers operating in the visible part of the spectrum [8], is based on the blue and yellow emissions originating from ${}^4F_{9/2}$ level of Dy^{3+} . These emissions are much more probable than the non-radiative relaxation to the next lower energy level, ${}^6F_{3/2}$, that corresponds to large energy gap of approximately 7500 cm^{-1} . Consequently, relatively high phonon energy of yttrium aluminum garnet presents YAG crystal as a prospective host material for dysprosium ions [9].

We used solution combustion synthesis (SCS) method to prepare nanopowder samples of YAG and YAG doped with 2 mol% Dy. Optical properties of the samples were analyzed by far-infrared spectroscopy (FIR), whereas nitrogen adsorption method was employed to examine specific surface area and texture. The dielectric function of the nanopowders was modeled using the Maxwell–Garnet formula.

2. Samples preparation and characterization

The SCS method used to prepare the YAG and YAG:Dy nanopowder samples was performed in several steps. Yttrium oxide (Y_2O_3) and aluminum oxide (Al_2O_3) of 99.99% purity was purchased from the NOAH Technologies. The oxides were dissolved in HNO_3 followed by the addition of carbohydrazide to the solution of aluminum nitrate and yttrium nitrate:



Good reactivity of the raw materials provided absence of the intermediate phases, e.g., YAM ($Y_4Al_2O_9$) or YAP ($YAlO_3$), in the obtained YAG powder. The YAG:Dy samples were produced by doping YAG host with Dy^{3+} ions using the concentration of 2 mol%. Further, YAG:Dy nanopowder was annealed in the air atmosphere at $1300\text{ }^\circ\text{C}$ with the aim to obtain full crystallinity [10].

The morphology of the prepared YAG and YAG:Dy nanopowders was examined using a high resolution scanning electron microscope (SEM) equipped with the high brightness Schottky Field Emission gun (FEGSEM, TESCAN) operating at 4 kV. In order to provide conductivity of the samples needed for SEM analysis, the samples were coated with gold/palladium. The SEM images of our YAG and YAG:Dy samples are given in Fig. 1. The powders are composed of well-defined and separated nanoparticles,

clusters, and agglomerated particles. The size of individual spherical particles is in the range of about 30–50 nm. The spherical shape of particles is of great importance because it provides lower light scattering and brighter luminescence performance [11].

3. Results and discussion

3.1. Adsorption isotherms – BET experiments

The analyzer Surfer (Thermo Fisher Scientific, USA) was used to examine YAG and YAG:Dy nanopowders.

The dependences of the adsorbed amount of N_2 on the relative pressure, P/P_0 , at the temperature of $-196\text{ }^\circ\text{C}$, i.e., the nitrogen adsorption isotherms, for the YAG and YAG:Dy samples are given in Fig. 2. The adsorptions at low relative pressures, given in the graph inserts, indicate that there are micropores on the particle surfaces. According to the IUPAC classification pores are classified as macropores (pore width above 50 nm), mesopores (pore width 2–50 nm) and micropores (pore width below 2 nm) [12]. At the same time, non-limiting adsorption at high P/P_0 , was found to correspond to non-rigid aggregates of particles giving rise to slit-shaped pores [13]. Note that these conclusions are in agreement with the SEM images given in Fig. 1, which show that our samples contain agglomerated as well as separated particles. The separated particles are found to be spherical with the diameter of approximately 40 nm. The specific surface areas calculated by the BET equation, S_{BET} , are found to be $5\text{ m}^2\text{ g}^{-1}$ and $12\text{ m}^2\text{ g}^{-1}$ for the YAG and YAG:Dy samples, respectively. Since the radius of Dy^{3+} ion of 0.1167 nm is larger than the radius of Y^{3+} ion, which is 0.1159 nm, it comes as no surprise that the presence of Dy led to increase of the overall specific surface of particles. Also, dopants introduce defects into the structure of the material which results in different charge on the particle surface when doped and undoped are compared. This charge on the particle surface leads to differences in packaging particles and their greater or lesser agglomeration, which on the other hand have significant role on the porosity and specific surface area. Incorporated dopants have a tendency to concentrate at the surface of nanomaterials. All these have significant role on the increasing of the specific surface area.

3.2. Far-infrared spectroscopy

The far-infrared measurements were carried out with the BOMEM DA – 8 FIR spectrometer. The wave number range between 80 and 600 cm^{-1} was covered with the DTGS pyroelectric detector.

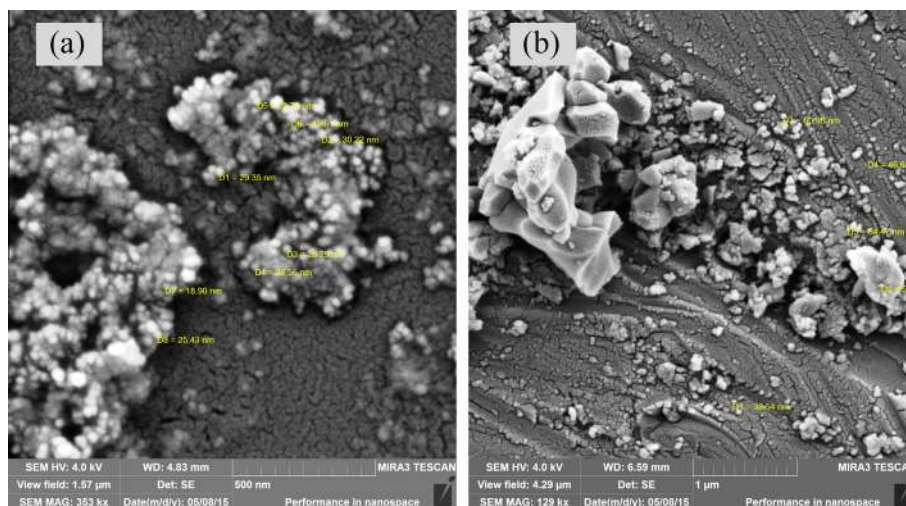


Fig. 1. SEM micrographs. The micrographs of YAG and YAG:Dy nanopowders are given in part (a) and (b), respectively.

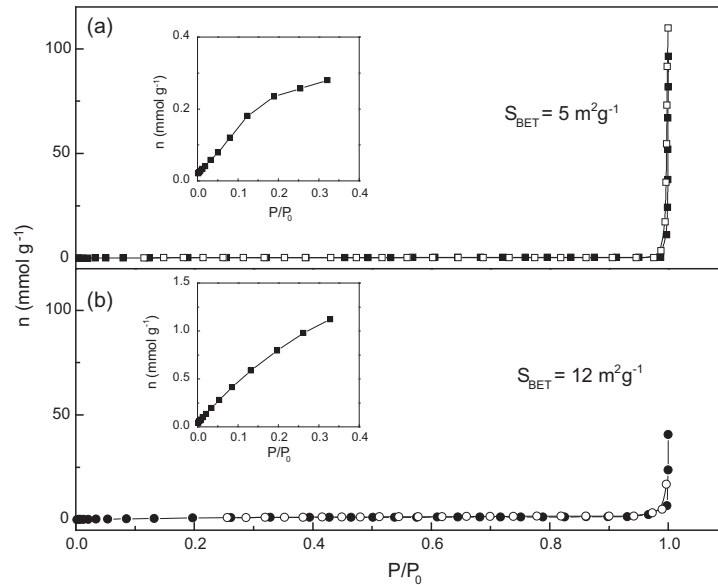


Fig. 2. Nitrogen adsorption isotherms. The amount of adsorbed N_2 given as a function of the relative pressure is shown in graphs (a) and (b) for YAG and YAG:Dy nanopowders, respectively. Solid symbols correspond to adsorption, whereas open symbols represent desorption. The shapes of the curves around zero are enlarged in the inserts.

If the visible light wavelength, λ , is much larger than the characteristic size of semiconducting nanoparticles, d , i.e., if $\lambda \gg d$, the heterogeneous composite of nanoparticles with the dielectric function ε_2 distributed in a medium with the dielectric constant ε_1 can be treated as a homogeneous medium and effective medium theory is applicable. The effective dielectric permittivity of such a mixture can be modeled by a number of mixing models [14]. We chose the Maxwell–Garnet model since our samples are well defined and separated nanosized spherical grains. Consequently, the predicted effective permittivity of the mixture becomes [15]:

$$\varepsilon_{\text{eff}} = \varepsilon_1 + 3f\varepsilon_1 \frac{\varepsilon_2 - \varepsilon_1}{\varepsilon_2 + 2\varepsilon_1 - f(\varepsilon_1 - \varepsilon_2)}, \quad (1)$$

where spheres of permittivity ε_2 were taken to occupy a volume fraction f as well as to be randomly located in a homogeneous environment characterized with ε_1 . In the considered nanopowders, nanoparticles are situated in air, therefore $\varepsilon_1 = 1$. To determine the dielectric function of the nanoparticles, i.e., ε_2 , we used the plasmon–phonon interaction model [16]:

$$\varepsilon_2(\omega) = \varepsilon_\infty \left(\prod_{k=1}^n \frac{\omega_{LOk}^2 - \omega^2 + i\gamma_{LOk}\omega}{\omega_{TOk}^2 - \omega^2 + i\gamma_{TOk}\omega} - \frac{\omega_p^2}{\omega(\omega - i\tau^{-1})} \right) \quad (2)$$

where ε_∞ is the bound charge contribution and it is assumed to be a constant, ω_{TOk} and ω_{LOk} are the transverse and longitudinal frequencies, γ_{TOk} , and γ_{LOk} are their dampings, ω_p is the plasma frequency and τ is the free carrier relaxation time. The first term in Eq. (2) is the lattice contribution, whereas the second term corresponds to the Drude expression for the free carrier contribution to the dielectric constant.

The measured and calculated far-infrared spectra of YAG and YAG:Dy nanopowders, in the spectral range between 80 and 600 cm^{-1} , at room temperature are shown in Fig. 3. The experimental data are depicted by circles, whereas the solid lines are used to draw the calculated spectra obtained by the fitting procedure based and the model defined by Eqs. (1) and (2). The best fit parameters corresponding to YAG and YAG:Dy nanopowders are given in Table 1. The values corresponding to the YAG single crystal are taken from [17].

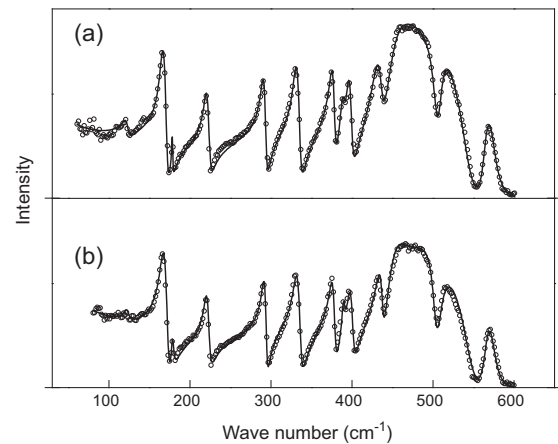


Fig. 3. Far-infrared reflection spectra of YAG nanopowder (a) and YAG:Dy nanopowder (b) at room temperature. The experimental data are represented by circles. The solid lines are the calculated spectra obtained with the parameter values given in Table 1 and the fitting procedure based on the model given by Eqs. (1) and (2).

YAG crystallizes in the cubic structure, it has the symmetry of O_h^{10} - $Ia3d$ space group, and eight molecules of $Y_3Al_5O_{12}$ per primitive unit cell. Out of the ninety-eight theoretically predicted Brillouin zone center modes that correspond to the O_h structure in the YAG group, $3A_{1g} + 5A_{2g} + 8E_g + 14T_{1g} + 14T_{2g} + 5A_{1u} + 5A_{2u} + 10E_u + 18T_{1u} + 16T_{2u}$, only the eighteen T_{1u} modes are IR-active [19]. Further, out of these eighteen theoretically predicted IR-active modes, fourteen are visible in the experimental and modeled far-infrared reflectivity spectra of the YAG and YAG:Dy nanopowders, and in the data corresponding to the YAG single crystal retrieved from literature, see Fig. 3 and Table 1. The bands at around 430, 453, 477, 510 and 566 cm^{-1} represent the characteristic metal–oxygen vibrations, which are in our example Y–O and Al–O. Our data are in agreement with the previous reports regarding single crystals [18,19] as well as with the results on nanocrystals of YAG [20,21]. The peaks located in the vicinity of 477, 510 and 566 cm^{-1} are the asymmetric stretching vibrations, whereas the peak at approximately 453 cm^{-1} is the symmetric vibration

Table 1

Best fit parameters of far-infrared spectra of YAG single crystal, YAG nanopowder and YAG:Dy nanopowder.

	YAG single crystal	YAG nanopowder	YAG:Dy nanopowder	Vibrations
ω_{TO} (cm ⁻¹)	122	122	122	T (+T _d) translations of tetrahedral and dodecahedral cation
	165	165	163	T _d translations of dodecahedral cation
	180	178	178	T _d (+T) translations of tetrahedral and dodecahedral cation
	221	220	219	T _d translations of dodecahedral cation (translations of cations in YO ₃ and AlO ₄)
	291	290	289.5	T ₀
	327	330	328	T translations of tetrahedral cation
	375	375	373	R libration of tetrahedral cation
	390	388.5	389	T ₀ translations of octahedral cation
	396	399.5	396	R libration of tetrahedral cation
	432	431	431	T ₀ translations of octahedral (translations + libration) cations in AlO ₆ and AlO ₄
	453	447	444	v ₂ symmetric
	477	465	465	v ₄ symmetric
	510	508	507	v ₄
	566	563	564	v ₄ (symmetric and asymmetric stretching of Al–O in octahedrons)
	ω_p (cm ⁻¹)	220	190	220
τ (cm ⁻¹)	0.001	0.002	0.035	–
f	1	0.96	0.80	–

of Al–O bond in the octahedral arrangement of garnet structure. The four lowest energy peaks correspond to the translation and vibration of cations in different coordination – tetrahedral, octahedral and dodecahedral [22]. The peaks around 165, 220, 375 and 396 cm⁻¹ have been attributed to the translator motion of Y³⁺ ions within the distorted cube that has eight oxygen ions at its vertices, as well as to the heavy mixing of the translational, rotational, and v₃ mode of the (AlO₄) unit.

Differences in the structure of YAG single crystal and YAG nanopowder cause changes in the phonon frequencies. Namely, decrease in the crystallite size causes optical phonon confinement. The influence of doping of YAG by Dy³⁺ on the spectral properties and lattice vibrations is not significant. Compared to the spectra of YAG single crystal and YAG nanopowder, there are no new phonon modes corresponding to the YAG:Dy nanopowder; however, further decrease of phonon frequencies is registered. Since Dy³⁺ ions are by 0.69%, larger than Y³⁺ ions, substitution of Y³⁺ with Dy³⁺ leads to further distortion of the cubic cell, and consequently to the shift of characteristics frequencies toward lower frequencies, as can be seen in Fig. 3 and Table 1.

The values of filling factors were determined from the analysis of reflection spectra. The main volume fraction, f , obtained as the best fit parameter estimation, is listed in Table 1. These results are consistent with the results obtained by the BET experiment described in Section 3.1. Namely, high values of the filling factor are associated with the existence of micropores.

4. Conclusions

Due to their prospective application in optical amplifiers for the second telecommunication window and solid-state lasers that operate in the visible part of the spectrum, properties of the YAG:Dy nanopowder were investigated and compared to those corresponding to the YAG nanopowder and YAG single crystal. The nanopowders were synthesized by the solution combustion synthesis technique and the samples were analyzed by the scanning electron microscopy, nitrogen adsorption method as well as by the far-infrared spectroscopy. The measured far-infrared spectra were in complete agreement with the modeled spectra obtained with the Maxwell–Garnet formula, plasmon–phonon interaction model, and fitting procedure. It was determined that the Dy doped as well as non-doped YAG nanopowders are microporous. Spherical, well-defined and separated nanoparticles as well as agglomerated particles were detected. The far-infrared measurements revealed that the YAG nanopowder has lower phonon

frequencies than the YAG single crystal as well as that doping of YAG by Dy³⁺ does not have significant influence on the spectral properties and lattice vibrations. However, the doping caused further decrease of phonon frequencies, with respect to the frequencies that correspond to the YAG single crystal and YAG nanopowder.

Acknowledgment

This work was supported by the Serbian Ministry of Education, Science and Technological Development under Project III45003.

References

- [1] Ji-Guang Li, Takayasu Ikegami, Jong-Heun Lee, Toshiyuki Mori, *J. Am. Ceram. Soc.* 83 (4) (2000) 961–963.
- [2] L. Wen, X. Sun, Z. Xiu, S. Chen, Chi-Tay Tsai, *J. Eur. Ceram. Soc.* 24 (2004) 2681–2688.
- [3] J.W.G.A. Vrolijk, J.W.M.M. Willems, R. Metselaar, *J. Eur. Ceram. Soc.* 6 (1990) 47–51.
- [4] Y. Fujimoto, T. Yanagida, H. Yagi, T. Yanagidani, V. Chani, *Opt. Mater.* 36 (2014) 1926–1929.
- [5] C.R. Varney, D.T. Mackay, S.M. Reda, F.A. Selim, *J. Phys. D Appl. Phys.* 45 (2012) 015103–015106.
- [6] A. Senyshyn, L. Vasylechko, *Acta Phys. Pol., A* 124 (2013) 329–335.
- [7] B. Cole, L.B. Shaw, P.C. Pureza, R. Mossadegh, J.S. Sanghera, I.D. Aggarwal, *J. Non-Cryst. Solids* 256–257 (1999) 253–259.
- [8] A. Kaminskii, U. Hommerich, D. Temple, J.T. Seo, K.-I. Ueda, S. Bagayev, A. Pavlyulk, *Jpn. J. Appl. Phys., Part 2: Lett.* 39 (3A/B) (2000). L208–11.
- [9] M. Klimczak, M. Malinowski, J. Sarnecki, R. Piramidowicz, *J. Lumin.* 129 (2009) 1869–1873.
- [10] M.S. Rabasovic, D. Sevic, J. Krizan, M.D. Rabasovic, S. Savic-Sevic, M. Mitric, M. Petrovic, M. Gilic, N. Romcevic, *Opt. Mater.* 50 (2015) 250–255.
- [11] Joo-Yun Chong, Yuelan Zhang, Brent K. Wagner, Zhitao Kang, *J. Alloys Compd.* 581 (2013) 484–487.
- [12] K.S.W. Sing, D.H. Everett, R.A.W. Haul, L. Moscou, R.A. Pierotti, J. Rouquerol, et al., *Pure Appl. Chem.* 57 (4) (1985) 603–619.
- [13] S. Lowell, J.E. Shields, M.A. Thomas, M. Thommes, *Characterization of Porous Solids and Powders: Surface Area, Pore Size and Density*, Kluwer Academic Publishers, Dordrecht Netherlands, 2004. 44.
- [14] K. Karkkainen, A. Saviola, K. Nikoskinen, *IEEE Trans. Geosci. Remote Sens.* 39 (5) (2001) 1013–1018.
- [15] J.C.M. Garnett, *Trans. R. Soc. Vol. CCIII* (1904) 385–420.
- [16] I.J. Uhanov, *Opt. svojstva poluprovodnikov*, Nauka, Moskva (1977).
- [17] S. Kostić, Z.Ž. Lazarević, V. Radojević, A. Milutinović, M. Romčević, N.Ž. Romčević, A. Valčić, *Mater. Res. Bull.* 63 (2015) 80–87.
- [18] J.P. Hurrel, P.S. Porto, I.F. Chang, S.S. Mitra, R.P. Bauman, *Phys. Rev.* 173 (1968) 851–856.
- [19] G.A. Slack, D.W. Oliver, R.M. Chrenko, S. Roberts, *Phys. Rev.* 177 (1969) 1308–1314.
- [20] Z.H. Chen, Y. Yang, Z.G. Hu, J.-T. Li, S.L. He, *J. Alloys Compd.* 433 (2007) 328–331.
- [21] E. De la Rosa, L.A. Díaz-Torres, P. Salas, A. Arredondo, J.A. Montoya, C. Angeles, R.A. Rodríguez, *Opt. Mater.* 27 (2005) 1793–1799.
- [22] A.M. Hofmeister, K.R. Campbell, *J. Appl. Phys.* 72 (1992) 638–646.

Femtosecond laser induced periodic surface structures on multi-layer graphene

Angela Beltaos,^{a)} Aleksander G. Kovačević, Aleksandar Matković, Uroš Ralević, Svetlana Savić-Šević, Djordje Jovanović, Branislav M. Jelenković, and Radoš Gajić
Institute of Physics, University of Belgrade, Pregrevica 118, 11080 Belgrade, Serbia

(Received 29 July 2014; accepted 18 November 2014; published online 26 November 2014)

In this work, we present an observation of laser induced periodic surface structures (LIPSS) on graphene. LIPSS on other materials have been observed for nearly 50 years, but until now, not on graphene. Our findings for LIPSS on multi-layer graphene were consistent with previous reports of LIPSS on other materials, thus classifying them as high spatial frequency LIPSS. LIPSS on multi-layer graphene were generated in an air environment by a linearly polarized femtosecond laser with excitation wavelength λ of 840 nm, pulse duration τ of ~ 150 fs, and a fluence F of ~ 4.3 – 4.4 mJ/cm². The observed LIPSS were perpendicular to the laser polarization and had dimensions of width w of ~ 30 – 40 nm and length l of ~ 0.5 – 1.5 μ m, and spatial periods Λ of ~ 70 – 100 nm ($\sim \lambda/8$ – $\lambda/12$), amongst the smallest of spatial periods reported for LIPSS on other materials. The spatial period and width of the LIPSS were shown to decrease for an increased number of laser shots. The experimental results support the leading theory behind high spatial frequency LIPSS formation, implying the involvement of surface plasmon polaritons. This work demonstrates a new way to pattern multi-layer graphene in a controllable manner, promising for a variety of emerging graphene/LIPSS applications. © 2014 AIP Publishing LLC. [<http://dx.doi.org/10.1063/1.4902950>]

I. INTRODUCTION AND BACKGROUND

Graphene, a two-dimensional crystal of carbon atoms in a hexagonal lattice, has been attracting much attention in the research community since its discovery in 2004¹ as a unique new material with outstanding electronic,² optical,³ and mechanical⁴ properties. Being an ultra-thin, strong, transparent, flexible conductor, graphene has excellent potential for a wide variety of applications, such as solar cells.^{5,6} In addition to single-layer graphene, multi-layer graphene has also been important for fundamental studies and applications, such as investigations of its electronic and magneto-optical properties,^{1,7,8} second harmonic generation,⁹ Q-switching and mode-locking of lasers,¹⁰ and patterning/lithography.¹¹

For many graphene applications, the ability to pattern or structure it in a controllable manner is very important, e.g., in transparent electrodes, field effect transistors, chem/biosensors, and energy devices.^{12,13} So far, patterned structures have been achieved on graphene using several chemical and physical techniques mainly classified by lithography, soft lithography, and direct laser writing.^{12,13} Parallel periodic structures have been produced on graphene by self-assembly onto patterned substrates,¹⁴ multi-beam interference,¹⁵ and strain-based techniques,^{16,17} and have applications in, for example, nanoscale electronic devices.¹⁶ In general, various patterning techniques are required to meet the needs of different graphene applications.¹²

Another patterning method, which has not yet been explored for graphene, involves laser irradiation and produces nanostructures known as “laser-induced periodic surface structures” (LIPSS). LIPSS are parallel periodic

structures, also known as “surface ripples,” classified by their spatial period (centre-to-centre distance between neighbouring parallel structures), and should not be confused with nanoribbons, being ultrathin strips of material.

The occurrence of LIPSS has long been known and studied (since 1965¹⁸) on a wide variety of other materials, including metals, semiconductors, and dielectrics^{19–22} and has many applications in fields such as photonics, plasmonics, and optoelectronics.²³ For example, LIPSS applications include the modification of a material’s optical, electrical, or wetting properties, structural colours, absorptance enhancement, antireflective films, biomedical applications, and optofluidics applications.

The technique of producing LIPSS offers a number of advantages useful for applications:²³ *simplicity*, *wide applicability*, and *low cost*—neither additional materials (as in lithography) nor laser scanning (as in direct writing) are required, and patterning can be done under normal ambient conditions in a quick one-step process; *high resolution*—capable of sub-wavelength nanostructuring; and *controllability*—the LIPSS orientation depends on the beam polarization direction, while the period can be varied by the laser wavelength, incidence angle, or effective refractive index of the interface between the material and surrounding medium.^{23–26}

LIPSS are typically formed on a material surface by a linearly polarized pulsed laser beam at normal incidence,²³ with orientation depending on the polarization of the incident beam.^{19,27,28} The resulting spatial period (Λ) is either on the order of the laser wavelength (λ) in low spatial frequency LIPSS (LSFL) or significantly smaller than λ ($\Lambda < \lambda/2$) in high spatial frequency LIPSS (HSFL).¹⁹ For application purposes, smaller spatial periods (HSFL) are desirable, and much research is devoted to minimize the LIPSS spatial

^{a)}abeltaos@ualberta.ca

period. For example, spatial periods as little as $\Lambda \approx 70\text{--}90\text{ nm}$ ($\lambda/10$) have been reported in an air environment on titanium by Bonse *et al.*¹⁹ HSFL are fabricated using femtosecond irradiation,^{19,23} and have been observed mostly on transparent materials.^{27,28} The underlying process of the formation of LIPSS is not completely understood, with debate in the literature and different theories proposed. Generally, the formation is described by the interference of the incident laser beam with a surface wave, such as a laser-excited surface plasmon polariton (SPP), leading to a spatial periodic energy distribution on the material surface.^{21,29–32} Second harmonic generation³³ and self-organization³⁴ effects have also been proposed.

Single or multi-layer graphene's high transparency and ability to be patterned or ablated with a pulsed laser in the femtosecond regime^{12,35} make it a desirable material for HSFL formation. In addition, SPPs in graphene are in a new emerging field,³⁶ and their existence has been recently experimentally demonstrated.³⁷ SPPs in multi-layer graphene systems have also been investigated.^{36,38} All of these properties, along with its high potential for applications, make graphene a promising candidate for the formation of LIPSS, while at the same time, the advantages of the LIPSS fabrication technique would be very useful in the applications of graphene. As an example, one potential application of graphene LIPSS could be the fabrication of graphene nanoribbons, with the advantages of mass production of nanoribbons in a quick, simple, cost-effective manner, with controllable dimensions and orientation via the laser parameters. Since LIPSS have never been observed before on graphene, the immense opportunities for new applications are apparent through the known applications of patterned graphene and the known applications of LIPSS on other materials, as mentioned above.

In this work, we present an observation of LIPSS on graphene. LIPSS on multi-layer graphene were induced by femtosecond laser irradiation. The samples and structures were analyzed using Raman spectroscopy, optical microscopy, atomic force microscopy (AFM), and scanning electron microscopy (SEM). The results were compared to previous reports on other materials.

II. EXPERIMENT

Sample preparation and characterization: Graphene samples of $\sim 3\text{--}15$ layers were prepared from kish graphite (NGS Naturgraphit GmbH) on transparent quartz substrates (Edmund Optics) by the standard micromechanical exfoliation technique,¹ and located on the substrates by optical microscopy. Characterization of the samples was performed by Raman Spectroscopy at room temperature using Micro Raman Chromex 2000 and TriVista TR557 Raman systems, each with a frequency doubled Nd^{3+} : YAG laser as an excitation source at a wavelength of $\lambda = 532\text{ nm}$. In both systems, a $50\times$ or a $40\times$ microscope objective was used, and the laser power on the sample was $\sim 1\text{--}2\text{ mW}$, preventing sample degradation. Acquisition times of the micro-Raman spectra were $150\text{--}900\text{ s}$ with a spectral resolution of $\sim 2\text{ cm}^{-1}$. Sample thickness was determined by a combination of Raman

spectroscopy, optical microscopy in transmission mode,³⁹ and AFM (details described below).

Laser interaction: Femtosecond laser beam interaction with the samples was performed in an air environment using the setup shown in Figure 1. The source of the beam ($\lambda = 840\text{ nm}$ wavelength, $\tau \approx 150\text{ fs}$ pulse duration, $\nu = 76\text{ MHz}$ repetition rate) was a Coherent Mira 900 Ti:Sapphire system. The beam power and exposure time were varied for the experiments. The beam was focused onto the samples using a focusing lens, while the position of the beam on the sample was monitored using a light microscope. The femtosecond laser experiments were performed in transmission mode, i.e., the samples were irradiated from below with the beam first passing through the transparent substrate and then irradiating the back of the sample at normal incidence. The wavelength was confirmed to be unchanged by passing through the quartz substrate and sample using an Ocean Optics HR2000CG-UV-NIR fiber-optic spectrometer.

Characterization of laser-induced structures: After the interaction, the samples were characterized by AFM and SEM. AFM measurements were done using an NTEGRA prima in the tapping mode under ambient conditions. The SEM measurements were done using a Tescan MIRA3 field emission gun SEM, with electron energies of $1\text{--}2\text{ kV}$. Sample preparation for the SEM measurements was performed in two different ways, coated with $\sim 5\text{ nm}$ of gold (higher resolution) and uncoated. SEM measurements were generally performed after all the other experiments, in order to avoid potential electron beam damage of the samples^{40,41} and/or because of the gold coating on top, which restricted further experimentation.

III. RESULTS AND DISCUSSION

The experiment as described above was performed on selected graphene samples of $3\text{--}5$ layers and $\sim 10\text{--}15$ layers. Figure 2 shows examples of a 15-layer graphene sample (Figs. 2(a) and 2(b)) and a 5-layer graphene sample (Figs. 2(c) and 2(d)) before (left) and after (right) femtosecond laser interaction. Raman spectroscopy and optical transmission microscopy, the methods used for sample characterization and thickness determination, are represented in Fig. 3(a), and Figs. 3(b) and 3(c), respectively. The occurrence of the G, G', and 2D peaks in the Raman spectrum in Fig. 3(a) shows the presence of graphene. The shape of the 2D peak indicates the number of layers and a relatively small (or lack of) D-peak

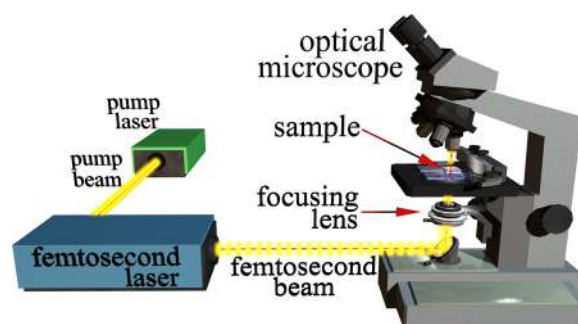


FIG. 1. Schematic of the femtosecond laser interaction set-up.

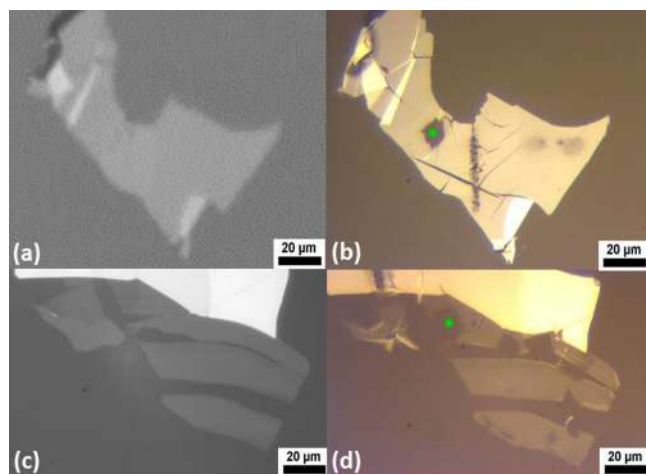


FIG. 2. Optical microscope images of (a) and (b) 15-layer graphene, and (c) and (d) 5-layer graphene samples before (left) and after (right) laser interaction. The green dots mark regions ablated for $t = 4$ min ($N \approx 1.8 \times 10^{10}$) of irradiation by a beam of $F \approx 4.3\text{--}4.4$ mJ/cm².

indicates the presence of good quality (or defect-free) graphene.^{42,43} Analysis of the optical microscope images in transmission mode (Figs. 3(b) and 3(c)) allows us to calculate the number of layers¹ based on the amount of absorption of transmitted light through the sample as compared to the substrate (each layer absorbing $\sim 2.3\%$ (Ref. 39)).

In the optical microscope images of the samples after laser interaction (Figs. 2(b) and 2(d)), the areas of interaction for various fluences and exposure times are seen as dark spots on the sample, which range from disordered graphene to completely ablated regions, as shown in previous work.³⁵

The laser fluence (F) was varied from ~ 1 to 6 mJ/cm², while exposure time (t) was varied from 1 s to 4 min. Analysis of the various regions of interaction in SEM showed that clearly defined parallel nanostructures (LIPSS) consistently formed in the ablated regions of the 10–15 layer samples (Figs. 4(a) and 4(b)) for laser fluences slightly above the multi-layer graphene ablation threshold of 4.2 mJ/cm² (as found in Ref. 35 using N values similar to this work of $N = 1.5 \times 10^8\text{--}1.8 \times 10^{10}$. Incubation effects and the dependence of N on the threshold were not investigated.) whereas

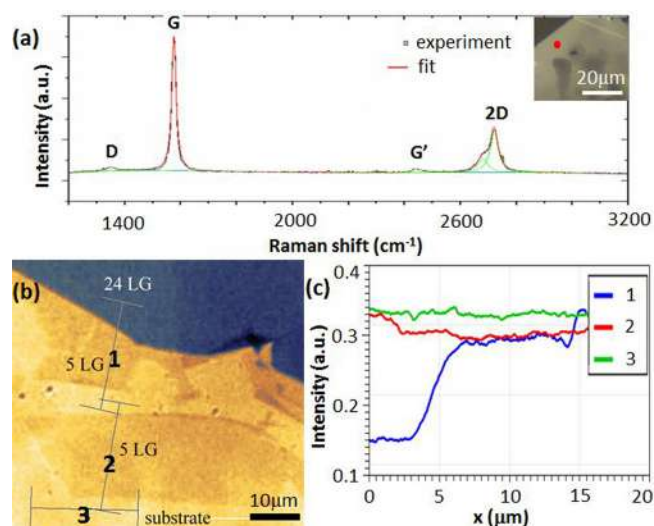


FIG. 3. (a) Micro-Raman spectrum of a 14-layer graphene sample. Inset: Optical microscope image, where the red dot indicates the position of the Raman measurement on a non-interacted area of the sample. (b) Transmission optical image of a 5-layer graphene (5 LG) sample, adjacent to a 24-layer flake (24 LG). The intensity of transmitted light for profile lines 1, 2, and 3 is shown in (c) in blue, red, and green, respectively.

structures were not found for fluences below this threshold. The obtained structures were perpendicular to the laser polarization used in the interaction (Fig. 4(c)). Our results are consistent with previous observations of LIPSS on other materials, which are generally formed at fluences slightly above the damage threshold and perpendicular to the laser polarization.^{23,35} Repeated experiments showed that the most clearly defined and intact LIPSS on multi-layer graphene were produced using the parameters $F \approx 4.3\text{--}4.4$ mJ/cm² and $t = 4$ min (corresponding to number of laser shots (N) of $\sim 1.8 \times 10^{10}$). The green dot in Fig. 2(b) shows an ablated region using these parameters.

Using the same experimental parameters on the thinner samples of 3–5 layers (Fig. 2(d))—green dot did not lead to the occurrence of LIPSS. Even by decreasing the fluence and exposure time to $F = 3.2$ mJ/cm² and $t = 2$ min ($N = 9 \times 10^9$), LIPSS were still not observed on these samples, as shown in the comparison SEM images of Figure 5.

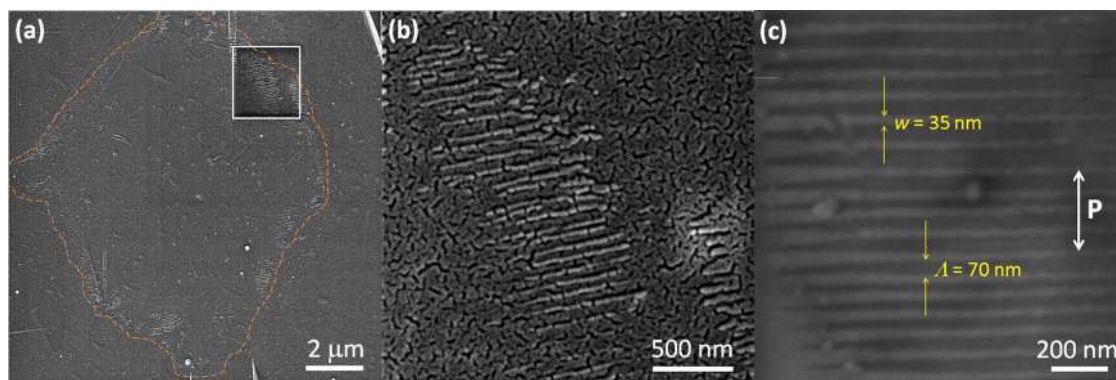


FIG. 4. SEM images of LIPSS observed on multi-layer graphene coated with a gold layer of ~ 5 nm: (a) ablated region due to laser interaction marked by orange dashed line. The white square shows where LIPSS were found, with a zoomed in image shown in part (b); (c) typical obtained LIPSS, showing width w and period Λ of the nanostructures and the polarization direction (P) of the laser used in the interaction.

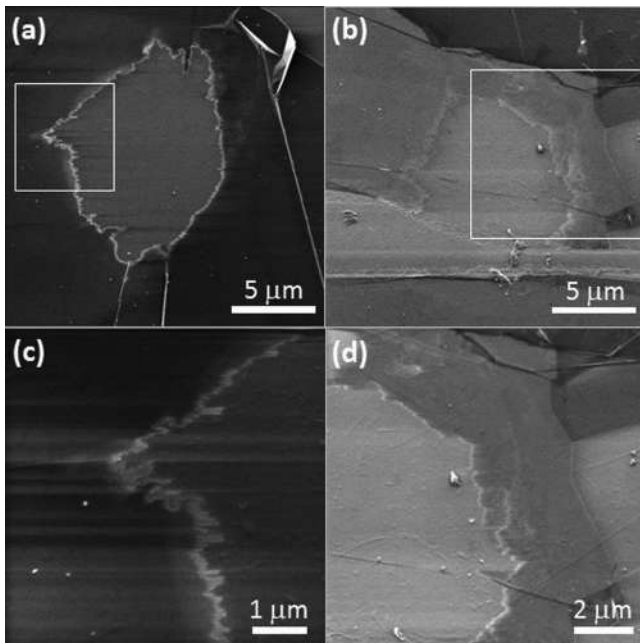


FIG. 5. Comparison SEM images of 15-layer graphene (left panel) and 5-layer graphene (right panel) samples. Ablated regions are shown in (a) and (b), where the white squares indicate the area examined in the corresponding larger image below in (c) and (d). The SEM images were taken without gold on the sample.

Parallel structures can be clearly seen at the edge of the ablated region of a 15-layer sample (Figs. 5(a) and 5(c)) but not on a 5-layer sample (Figs. 5(b) and 5(d)) for the same SEM parameters. Further studies are required to determine the ablation threshold of these thinner graphene samples and hence the laser interaction parameters for LIPSS formation.

The LIPSS on multi-layer graphene were further analyzed using AFM as shown in Figure 6. The structures were found in the ablated regions of the samples irradiated with a laser fluence of $F \approx 4.3\text{--}4.4 \text{ mJ/cm}^2$ (Fig. 6(a)), usually in the peripheral area attached to the surrounding sample (Fig. 6(b)), and occasionally in the central area as well (Fig. 6(c)). A close-up phase image of the structures is shown in Fig. 6(d), in which it can be seen that the LIPSS were surrounded by

dense nanostructures. Height profiles of the LIPSS (Fig. 6(e)) were obtained from which the spatial period (Λ) and width (w) of the structures were measured and found to be $\Lambda \approx 70\text{--}100 \text{ nm}$ and $w \approx 35 \pm 5 \text{ nm}$. The height profiles (Fig. 6(e)) also showed that the LIPSS were less than or equal to the height of the surrounding sample, with some variation due to surface roughness as shown in the 3D height map of Fig. 6(f). Aside from these variations, the height of the structures was relatively constant along their length, with a sudden decrease where they were truncated, as represented in Fig. 6(f). Typical measured values of the height of the structures were $\sim 1\text{--}2 \text{ nm}$ less than the sample height, corresponding to ablation of 3–6 layers of graphene, which indicates why structures were not observed for the thinner samples.

The width and period of the LIPSS as measured by AFM were also confirmed by SEM measurements (as in Fig. 4(c)). In addition, from the SEM measurements, the lateral dimensions of length (l) and range (r) of the structures were obtained. The structures typically spanned a range as large as the ablated region, $r \approx 4.5\text{--}5 \mu\text{m}$, and the length varied from $l \approx 0.5$ to $1.5 \mu\text{m}$ (Fig. 7(a)). The variation in length of structures often displayed a wave-like behaviour (Fig. 7(b)).

To investigate the formation of LIPSS on the 10–15 layer samples, the exposure time was significantly decreased to $\sim 16\text{--}20 \text{ s}$ ($N \approx 1.2 \times 10^9\text{--}1.5 \times 10^9$), while the laser fluence was kept at $F \approx 4.4 \text{ mJ/cm}^2$. The shorter exposure time led to a much smaller area of the ablated region,³⁵ as shown in Fig. 8(a). The existence of structures at the edges of these regions was confirmed by AFM as shown in Figures 8(a) and 8(b). The structures were much less clearly defined than those with longer exposures, and were wider ($w \approx 55\text{--}85 \text{ nm}$), shorter ($l \approx 80\text{--}200 \text{ nm}$), and farther apart ($\Lambda \approx 115\text{--}120 \text{ nm}$) (Fig. 8(c)). As before, these structures were perpendicular to the laser polarization.

Discussion: For our incident wavelength of $\lambda = 840 \text{ nm}$, the measured spatial periods of $\sim 70\text{--}100 \text{ nm}$ correspond to $\sim \lambda/8\text{--}\lambda/12$, classifying the LIPSS as HSFL with periods amongst the smallest ever reported.¹⁹ For comparison, on bulk graphite, LIPSS with periods of 110–800 nm were found.²² The spatial period has been shown to decrease by

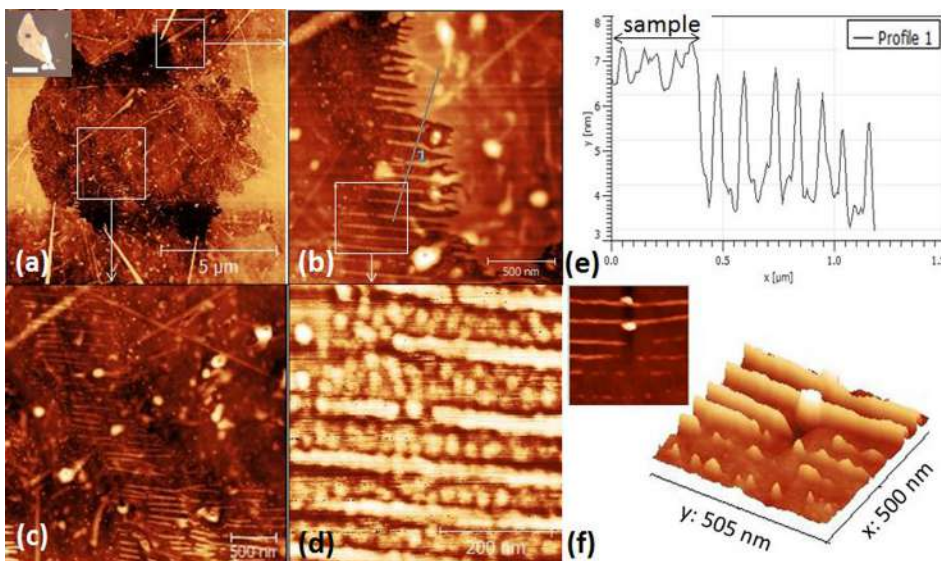


FIG. 6. AFM analysis of LIPSS on multi-layer graphene: (a) Ablated region of the sample. Inset: optical image of the sample where the ablated region can be seen as a black dot (scale bar of inset is $40 \mu\text{m}$). White squares represent areas where structures were found, corresponding to (b) and (c), respectively; (d) phase image of the structures, zoomed in from the white square in (b); (e) height profile corresponding to the profile line "1" in (b); (f) 3D height map of structures, with inset showing corresponding 2D image.

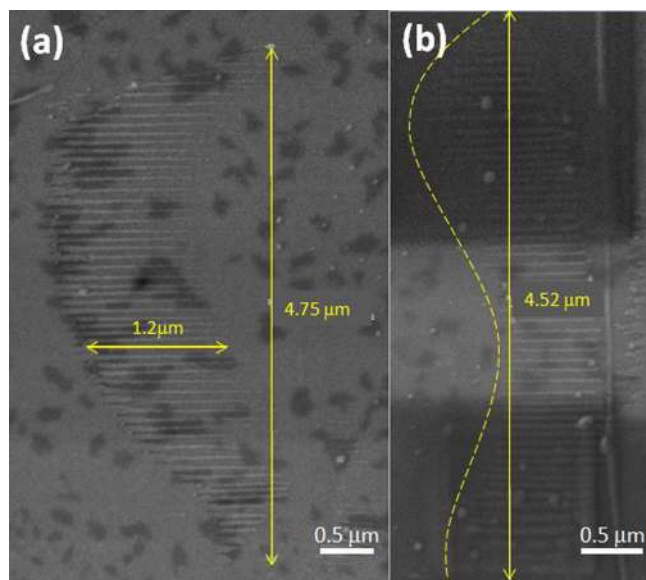


FIG. 7. SEM images showing the lateral dimensions of the LIPSS on multi-layer graphene coated with a gold layer of ~ 5 nm: (a) range and length; (b) variations in length, marked by the yellow dashed curve. Black squares are due to SEM charging, while black dots are due to ambient contamination.

increasing the number of laser shots N .^{19,21,23,44,45} Our observations of LIPSS with larger periods for smaller N also agree with this phenomenon. Various effects of the laser fluence have been reported in the literature, with an increase in fluence resulting sometimes in an increase in period⁴⁴ and sometimes a decrease in period.²⁴ Here, we have observed HSFL using orders of magnitude lower values of F and higher N than typical values on other materials,¹⁹ which is possible due to the thinness of multi-layer graphene that allows for a lower ablation threshold.³⁵ Therefore, our results coincide with a decrease in period for higher N and lower F values, also suggesting a reason for the smaller observed periods. In addition, reports have shown that HSFL with wavelengths significantly smaller than the laser wavelength are found, as in our case, on transparent materials, in the

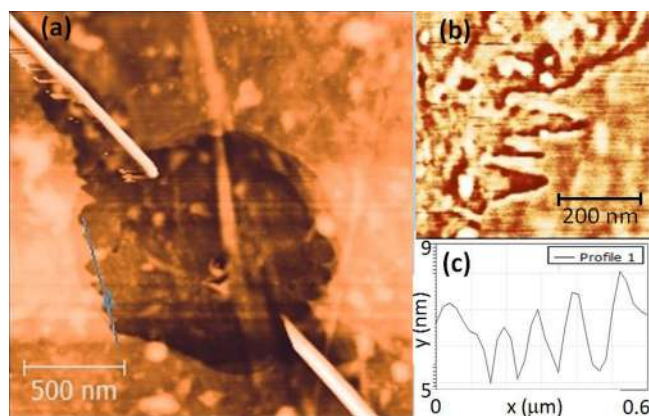


FIG. 8. AFM analysis of LIPSS on multi-layer graphene with reduced laser exposure time: (a) ablated region; structures are seen around the peripheral area; (b) phase image of structures; (c) height profile corresponding to the profile line "1" in (a).

femtosecond regime, and around the peripheral area of ablated regions.^{23,27–29} The latter effect is due to the Gaussian beam profile of the laser, and studies have even shown a transition from LSFL in the high-intensity central ablated region to HSFL around the lower-intensity edges.³⁴ In our case, this effect was not observed, as the central region was mainly ablated in the higher intensity area of the laser beam.

The very small observed periods in our study as compared with other materials could be explained by following an SPP model³² of LIPSS formation. While the origin of LSFL is typically described as the interference of the incident laser light with surface plasmons at the material-medium interface,^{21,29–31} the origin of HSFL has been described as two SPPs propagating in opposite directions with interference effects leading to a reduced period equal to even fractions of the laser wavelength.³² This is plausible for our results, since the measured spatial periods of $\Lambda \approx 70, 80, 90,$ and 100 nm are within error of ~ 5 nm ($\sim 5\%$) to $\lambda/12 = 70$ nm, $\lambda/10 = 84$ nm, and $\lambda/8 = 105$ nm, and because SPPs on graphene with varying wavelengths and interference effects have also been reported.^{36,38} Graphene is known to have SPPs with strong confinement and low loss, leading to wavelengths much smaller than that of the incident light,³⁶ and in a multi-layer system, the wavelength is predicted to be smaller as compared to single-layer graphene.³⁸

Some studies have related the decrease in spatial period with increase in N to be due to the positive feedback of the SPP model,²⁹ a process which results in HSFL densely covered with nanostructures. A reduced period is expected by this model due to a change of effective refractive index at the air-material interface when the nanostructures develop on the surface, affecting SPP propagation. Also, a wave-like variation in height/length of the HSFL coincides with the spatial periodic energy distribution density suggested by this model. These effects are consistent with our observations, indicating further evidence for the SPP model of the formation of LIPSS on multi-layer graphene.³²

IV. CONCLUSION

In this work, we observed laser induced periodic surface structures (LIPSS) on multi-layer graphene. Using a femtosecond laser, LIPSS perpendicular to the laser polarization with length ~ 0.5 – 1.5 μm and width $\sim 35 \pm 5$ nm were induced on 10–15-layer graphene in an air environment. The measured spatial periods were ~ 70 – 100 nm ($\sim \lambda/8$ – $\lambda/12$), amongst the smallest periods ever reported for LIPSS on other materials. The spatial period and width of the LIPSS were shown to decrease for an increased number of laser shots. The incident laser beam parameters used for the fabrication of LIPSS were $\lambda = 840$ nm, $F \approx 4.3$ – 4.4 mJ/cm^2 , and $N \approx 1.8 \times 10^{10}$. Using the same parameters, a comparison was made with thinner graphene samples of 3–5 layers, on which LIPSS were not observed. Our results on multi-layer graphene are consistent with previous experimental findings of LIPSS on other materials. Specifically, HSFL were observed in the femtosecond regime, on a transparent material, in the peripheral of laser-ablated regions, and with the

effect of a smaller spatial period for a higher number of laser shots. The observed HSFL are also consistent with a surface plasmon polariton model of LIPSS formation.

Through this work, we have demonstrated the patterning of graphene in a new controllable way (the width, period, and orientation are controlled using the laser parameters) by using the LIPSS technique that is well-known for other materials. The discovery of graphene LIPSS displays a fundamental property of graphene, placing it into the known field of LIPSS and giving insight into the physics of this unique material and the intriguing LIPSS formation process. Thus, our results have opened up the possibility for graphene LIPSS applications and research, laying the groundwork to build on for further studies in this direction.

ACKNOWLEDGMENTS

The authors would like to thank Miloš Bokorov (Faculty of Science, University of Novi Sad, Novi Sad, Serbia) for preliminary SEM measurements, and Dejan Pantelić (Institute of Physics, University of Belgrade, Belgrade, Serbia) for helpful discussions. This work was supported by the Ministry of Science (Republic of Serbia) under the projects OI171005, III45016, and III45018.

- ¹K. S. Novoselov, A. K. Geim, S. V. Morozov, D. Jiang, Y. Zhang, S. V. Dubonos, I. V. Grigorieva, and A. A. Firsov, *Science* **306**, 666 (2004).
- ²N. M. R. Peres, *Rev. Mod. Phys.* **82**(3), 2673 (2010).
- ³K. F. Mak, L. Ju, F. Wang, and T. F. Heinz, *Solid State Commun.* **152**(15), 1341 (2012).
- ⁴C. Lee, X. Wei, J. W. Kysar, and J. Hone, *Science* **321**(5887), 385 (2008).
- ⁵K. S. Novoselov, V. I. Falko, L. Colombo, P. R. Gellert, M. G. Schwab, and K. Kim, *Nature* **490**, 192 (2012).
- ⁶F. Bonaccorso, Z. Sun, T. Hasan, and A. C. Ferrari, *Nature Photon.* **4**, 611 (2010).
- ⁷M. Koshino and T. Ando, *Phys. Rev. B* **77**(11), 115313 (2008).
- ⁸J. Hass, W. A. De Heer, and E. H. Conrad, *J. Phys.: Condens. Matter* **20**(32), 323202 (2008).
- ⁹A. Y. Bykov, T. V. Murzina, M. G. Rybin, and E. D. Obraztsova, *Phys. Rev. B* **85**, 121413 (2012).
- ¹⁰J. L. Xu, X. L. Li, J. L. He, X. P. Hao, Y. Z. Wu, Y. Yang, and K. J. Yang, *Appl. Phys. Lett.* **99**, 261107 (2011).
- ¹¹Y. Zhou, Q. Bao, B. Varghese, L. A. L. Tang, C. K. Tan, C. Sow, and K. P. Loh, *Adv. Mater.* **22**, 67 (2010).
- ¹²J.-Y. Hong and J. Jang, *J. Mater. Chem.* **22**, 8179 (2012).
- ¹³J. Feng, W. Li, X. Qian, J. Qi, L. Qi, and J. Li, *Nanoscale* **4**(16), 4883 (2012).
- ¹⁴T. Kaplas and Y. Svirko, *Carbon* **70**, 273 (2014).
- ¹⁵Y. Li, Y. Li, W. Shi, S. Chen, G. Zhang, Z. Liu, Q. Sun, J. Tian, Y. Xu, and Y. Chen, *Int. J. Nanomanuf.* **8**(3), 221 (2012).
- ¹⁶W. Bao, F. Miao, Z. Chen, H. Zhang, W. Jang, C. Dames, and C. N. Lau, *Nat. Nanotechnol.* **4**(9), 562 (2009).
- ¹⁷A. Capasso, E. Placidi, H. F. Zhan, E. Perfetto, J. M. Bell, Y. Gu, and N. Motta, *Carbon* **68**, 330 (2014).
- ¹⁸M. Birnbaum, *J. Appl. Phys.* **36**, 3688 (1965).
- ¹⁹J. Bonse, J. Krüger, S. Höhm, and A. Rosenfeld, *J. Laser Appl.* **24**(4), 042006 (2012).
- ²⁰G. Dumitru, V. Romano, H. P. Weber, M. Sentis, and W. Marine, *Appl. Phys. A* **74**(6), 729 (2002).
- ²¹M. Huang, F. Zhao, Y. Cheng, N. Xu, and Z. Xu, *ACS Nano* **3**(12), 4062 (2009).
- ²²E. V. Golosov, A. A. Ionin, Y. R. Kolobov, S. I. Kudryashov, A. E. Ligachev, S. V. Makarov, Y. N. Novoselov, L. V. Seleznev, D. V. Sinityn, and A. R. Sharipov, *Phys. Rev. B* **83**(11), 115426 (2011).
- ²³A. Y. Vorobyev and C. Guo, *Laser Photon. Rev.* **7**(3), 385 (2013).
- ²⁴E. V. Golosov, A. A. Ionin, Y. R. Kolobov, S. I. Kudryashov, A. E. Ligachev, Y. N. Novoselov, L. V. Seleznev, and D. V. Sinityn, *J. Exp. Theor. Phys.* **113**(1), 14 (2011).
- ²⁵T. Y. Hwang and C. Guo, *J. Appl. Phys.* **108**(7), 073523 (2010).
- ²⁶A. Y. Vorobyev and C. Guo, *J. Appl. Phys.* **104**(6), 063523 (2008).
- ²⁷M. Rohloff, S. K. Das, S. Höhm, R. Grunwald, A. Rosenfeld, J. Krüger, and J. Bonse, *J. Appl. Phys.* **110**(1), 014910 (2011).
- ²⁸Q. Wu, Y. Ma, R. Fang, Y. Liao, Q. Yu, X. Chen, and K. Wang, *Appl. Phys. Lett.* **82**(11), 1703 (2003).
- ²⁹A. Y. Vorobyev, V. S. Makin, and C. Guo, *J. Appl. Phys.* **101**(3), 034903 (2007).
- ³⁰J. Bonse, A. Rosenfeld, and J. Krüger, *J. Appl. Phys.* **106**(10), 104910 (2009).
- ³¹J. E. Sipe, J. F. Young, J. S. Preston, and H. M. Van Driel, *Phys. Rev. B* **27**(2), 1141 (1983).
- ³²V. S. Makin, R. S. Makin, A. Y. Vorobyev, and C. Guo, *Tech. Phys. Lett.* **34**(5), 387 (2008).
- ³³D. Dufft, A. Rosenfeld, S. K. Das, R. Grunwald, and J. Bonse, *J. Appl. Phys.* **105**(3), 034908 (2009).
- ³⁴J. Reif, *Laser-Surface Interactions for New Materials Production*, Springer Series in Materials Science Vol. 130, edited by A. Miotello and P. Ossi (Springer, Berlin, 2010), pp. 19–41.
- ³⁵A. Beltaos, A. Kovačević, A. Matković, U. Ralević, Dj. Jovanović, and B. Jelenković, *Phys. Scr.* **2014**(T162), 014015 (2014).
- ³⁶Y. V. Bludov, A. Ferreira, N. M. R. Peres, and M. I. Vasilevskiy, *Int. J. Mod. Phys. B* **27**(10), 1341001 (2013).
- ³⁷J. Chen, M. Badioli, P. Alonso-González, S. Thongrattanasiri, F. Huth, J. Osmond, M. Spasenović, A. Centeno, A. Pesquera, P. Godignon, A. Z. Elorza, N. Camara, F. J. García de Abajo, R. Hillenbrand, and F. H. Koppens, *Nature* **487**(7405), 77 (2012).
- ³⁸B. Wang, X. Zhang, F. J. García-Vidal, X. Yuan, and J. Teng, *Phys. Rev. Lett.* **109**(7), 073901 (2012).
- ³⁹R. R. Nair, P. Blake, A. N. Grigorenko, K. S. Novoselov, T. J. Booth, T. Stauber, N. M. R. Peres, and A. K. Geim, *Science* **320**, 1308 (2008).
- ⁴⁰D. Teweldebrhan and A. A. Balandin, *Appl. Phys. Lett.* **94**, 013101 (2009).
- ⁴¹I. Childres, L. A. Jauregui, M. Foxe, J. Tian, R. Jalilian, I. Jovanovic, and Y. P. Chen, *Appl. Phys. Lett.* **97**, 173109 (2010).
- ⁴²A. C. Ferrari, J. C. Meyer, V. Scardaci, C. Casiraghi, M. Lazzeri, F. Mauri, S. Piscanec, D. Jiang, K. S. Novoselov, S. Roth, and A. K. Geim, *Phys. Rev. Lett.* **97**, 187401 (2006).
- ⁴³D. Graf, F. Molitor, K. Ensslin, C. Stampfer, A. Jungen, C. Hierold, and L. Wirtz, *Nano Lett.* **7**, 238 (2007).
- ⁴⁴Y. Yang, J. Yang, L. Xue, and Y. Guo, *Appl. Phys. Lett.* **97**(14), 141101 (2010).
- ⁴⁵J. Bonse and J. Krüger, *J. Appl. Phys.* **108**(3), 034903 (2010).

Journal of Applied Physics is copyrighted by the American Institute of Physics (AIP). Redistribution of journal material is subject to the AIP online journal license and/or AIP copyright. For more information, see <http://ojps.aip.org/japo/japcr/jsp>



Characterization and luminescent properties of Eu^{3+} doped $\text{Gd}_2\text{Zr}_2\text{O}_7$ nanopowders



M.S. Rabasovic^{a,*}, D. Sevic^a, J. Krizan^b, M. Terzic^c, J. Mozina^b, B.P. Marinkovic^a, S. Savic-Sevic^a, M. Mitric^d, M.D. Rabasovic^a, N. Romcevic^a

^a Institute of Physics, University of Belgrade, Serbia

^b Faculty for Mechanical Engineering, University of Ljubljana, Slovenia

^c Faculty of Science, University of Novi Sad, Serbia

^d Vinča Institute of Nuclear Science, University of Belgrade, P.O. Box 522, 11001 Belgrade, Serbia

ARTICLE INFO

Article history:

Received 11 September 2014

Received in revised form 7 October 2014

Accepted 13 October 2014

Available online 22 October 2014

Keywords:

Phosphors

Optical properties

Luminescence

Time-resolved optical spectroscopies

ABSTRACT

Nanopowders based on gadolinium zirconium oxide ($\text{Gd}_2\text{Zr}_2\text{O}_7$) doped by europium ions (Eu^{3+}) were successfully prepared using a flame combustion method. This material is suitable for various optical devices. The structure of prepared materials has been confirmed and characterized using X-ray powder diffraction (XRD), scanning electron microscope (SEM) and photoluminescence (PL) techniques. The luminescence properties of synthesized nanopowders were characterized by emission spectra and luminescence lifetimes by using the streak camera system. PL spectra were obtained at three different excitation wavelengths (Optical Parametric Oscillator (OPO) at 360 nm, laser diode at 365 nm and Ar laser line at 514.5 nm). The strong emission lines at 611 nm and 630 nm corresponding to the ${}^5\text{D}_0 \rightarrow {}^7\text{F}_2$ long lived transition could be used as a new red light source in optical devices.

© 2014 Elsevier B.V. All rights reserved.

1. Introduction

Rare earth zirconates ($\text{Re}_2\text{Zr}_2\text{O}_7$) have been identified as the attractive candidates for TBC (thermal barrier coatings) applications, high temperature heating devices and host materials for luminescence applications [1]. Their crystal structure is stable in high temperature, oxidizing environments and because they emit intense, visible emission. There are two kinds of different crystal structures for $\text{Re}_2\text{Zr}_2\text{O}_7$, as the pyrochlore structure, and the fluorite structure [2]. Among them, gadolinium zirconate ($\text{Gd}_2\text{Zr}_2\text{O}_7$) stand out as a material with a distinctively low thermal conductivity and high phase stability [3]. The strong fluorescent properties of the $\text{Gd}_2\text{Zr}_2\text{O}_7$ may make it excellent candidate for potential photoactive materials [4].

Rare earth ions have been extensively employed as activators for various phosphors and other organic and inorganic luminescent materials [5]. Europium as a solid-solution chromophore dopant is explored for measuring temperature in pyrochlore zirconates [6]. Also Eu^{3+} ions within the configuration $[\text{Xe}] 4f^6$ doped compound in different host lattice are found to give a rise to the strong luminescence emitting bright red light. That material shows typical f-f transitions of only europium ions. It is known that luminescence is

relatively independent to the host crystal field in trivalent rare earth ions because the optically active 4f electrons of the ions are shielded from the rest of ions by the outer 5s and 5p shells [7]. According to the selection rules of lanthanide ions, magnetic dipole (MD) transitions are allowed and electric dipole (ED) transitions are forbidden. However, ED transitions are possible. They are very sensitive to the environments of crystal fields and could be completely absent or very intense [8]. In the case of Eu^{3+} ions, most or all of the luminescence usually comes from the ${}^5\text{D}_0$ state, which is a single level and this avoids the convolution of overlapping emission peaks from different levels [9]. An example of a hypersensitive transition is the ${}^5\text{D}_0 \rightarrow {}^7\text{F}_2$ of Eu^{3+} ions.

In this work, we provide the optical structure characterization of europium ions doped gadolinium zirconate particles. The Gd^{3+} ions do not have the capacity to give out visible light. Due to the similar ionic radius and valence state of Gd and Eu ions, europium could easily replace the Gd^{3+} without lattice distortion. We also investigate photoluminescence spectra as well as lifetime analysis by using a streak camera.

2. Experimental procedures

2.1. The preparation of samples

The combustion method has been used for the synthesis of Eu^{3+} doped $\text{Gd}_2\text{Zr}_2\text{O}_7$ nanopowders. Starting chemicals $\text{Gd}(\text{NO}_3)_3 \cdot 6\text{H}_2\text{O}$, $\text{Zr}(\text{NO}_3)_2 \cdot \text{H}_2\text{O}$,

* Corresponding author. Tel.: +381 113713131.

E-mail address: majap@ipb.ac.rs (M.S. Rabasovic).

$\text{Eu}(\text{NO}_3)_3 \cdot 6\text{H}_2\text{O}$ with the purity of 99.99% were purchased from ABCR, Gd_2O_3 (99.9%) from the NOAH Technologies and urea $(\text{NH}_2)_2\text{CO}$ from Sigma–Aldrich.

Europium doped cubic $\text{Gd}_2\text{Zr}_2\text{O}_7$ nanopowders were prepared by Solution Combustion Synthesis (SCS) method. The flame combustion process is the most frequently used due to the simplicity and low cost of the synthesis procedures and also due to the possibility of tailoring the size and morphology of particles. After the synthesis, the nanopowder was annealed in air atmosphere at 1200°C for 2 h. The morphology analysis of the synthesized materials indicates the irregular crystallite size distribution and existence of agglomerated grains which are in the submicron size. The annealing of material is needed in order to achieve the full crystallinity. The Eu^{3+} concentration in $\text{Gd}_2\text{Zr}_2\text{O}_7$ was 2 mol%.

2.2. Experimental details

X-ray diffraction measurements were obtained on a Philips PW 1050 instrument, using Ni filtered $\text{Cu K}_{\alpha 1,2}$ radiation. Measurements were done at room temperature over the 2θ range of $10\text{--}90^\circ$ with a scanning step width of 0.05° and a counting time of 8 s per step. The morphology of nanopowders and the size of crystallites synthesized by SCS method were examined by scanning electron microscopy (SEM).

Photoluminescence (PL) studies reported in this work were performed at room temperature using three different excitation sources: Argon laser at 514.5 nm , laser diode at 365 nm , and Optical Parametric Oscillator (OPO) at 360 nm . The output of the OPO can be continuously tuned over a spectral range from 320 nm to 475 nm . PL spectrum excited by Ar laser line at 514.5 nm was measured using a Jobin–Yvon model U-1000 monochromator with a conventional photocounting system. The spectrum obtained by the laser diode excitation at 365 nm was recorded on an Ocean Optics USB4000 spectrometer.

Time-resolved streak images of the fluorescence spectrum excited by OPO system were acquired by Hamamatsu streak camera system (model C4334-01) and the HPD-TA (High Performance Digital Temporal Analyzer) streak camera control software. The software provides advanced analysis of streak images. Fluorescence lifetime fitting analysis was carried out using the TA-Fit program.

3. Results and discussion

3.1. Structure

Structures of synthesized $\text{Gd}_2\text{Zr}_2\text{O}_7$ doped by europium ions powders were identified by XRD pattern as is shown in Fig. 1. The diffractogram confirms that monophased sample that is crystallized in fluorite type structure (space group $\text{Fm}\bar{3}\text{m}$) was obtained and all of the observed diffraction peaks are indexed according to this space group (Fig. 1). There is no evidence of the presence of pyrochlore phase (crystallizes in space group $\text{Fd}\bar{3}\text{m}$), which is characterized by the occurrence of “superlattice” and additional peaks at 2θ angle of about 29° , 37° and 44.7° . The Eu^{3+} ions could replace the Gd^{3+} site in lattice due to the same valence state and similar ionic radii between Eu^{3+} and Gd^{3+} that, for the coordination number 8, have values of 0.1066 nm and 0.1053 nm , respectively. Absence of any additional peaks (see Fig. 1) that could

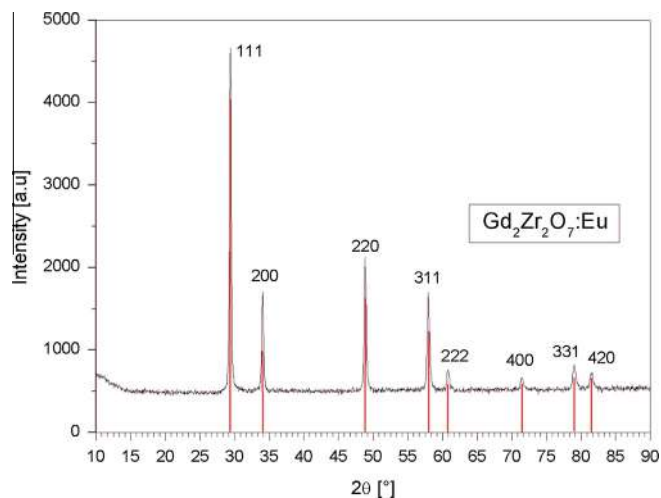


Fig. 1. XRD pattern recorded on $\text{Gd}_2\text{Zr}_2\text{O}_7:\text{Eu}$ material.

belong to Eu_2O_3 , ZrO_2 or Gd_2O_3 phases is the first evidence that doping of Eu^{3+} into $\text{Gd}_2\text{Zr}_2\text{O}_7$ material does not change the crystalline structure.

Microstructure characterization of $\text{Gd}_2\text{Zr}_2\text{O}_7:\text{Eu}$ material was carried out by SEM and selected images are presented in Fig. 2 (a and b). The size of cubic $\text{Gd}_2\text{Zr}_2\text{O}_7$ material doped with Eu^{3+} given by Hu et al. [4] was of about 200 nm . The morphology of the nanopowder in Fig. 2(a and b) demonstrates the structure particles with dimensions from 50 nm (Fig. 2(a)) to over 100 nm (Fig. 2(b)), so, the agglomerated particles were melted together by sintering process.

3.2. Optical properties

3.2.1. Fluorescence emission spectra

The photoluminescence emission spectra of $\text{Gd}_2\text{Zr}_2\text{O}_7$ doped by europium ions obtained at room temperature under the excitations at 365 nm and 514.5 nm are presented in Fig. 3. A several recognizable fluorescence bands can be seen in emission spectra (Fig. 3) over the visible region from 580 nm to 720 nm wavelength range.

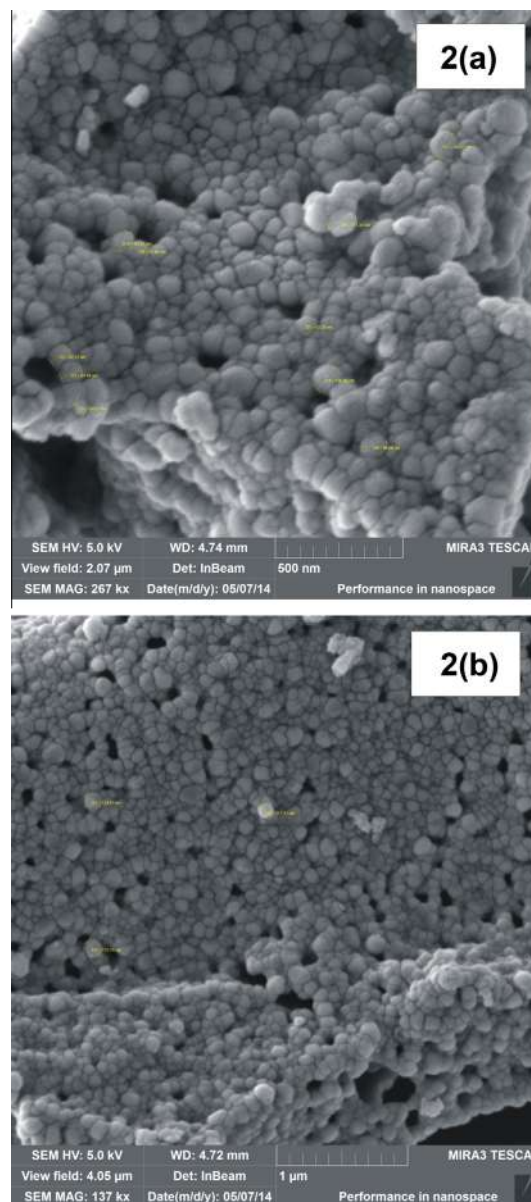


Fig. 2. SEM micrographs of $\text{Gd}_2\text{Zr}_2\text{O}_7:\text{Eu}$ material.

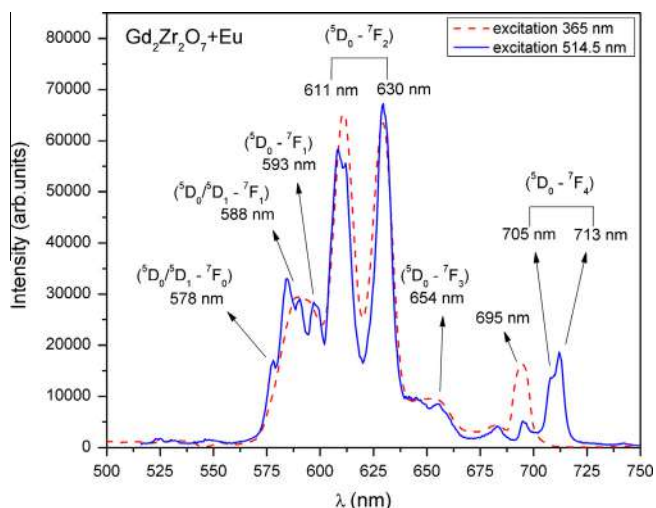


Fig. 3. Luminescence emission spectra of $\text{Gd}_2\text{Zr}_2\text{O}_7$ doped by Eu ions immediately after synthesis. The excitation wavelengths are 365 nm and 514.5 nm.

A pronounced peak at about 611 nm on the spectrum is in accordance with expectation based on the existence of f-f transitions that are responsible for luminescence in trivalent rare earth ions (Eu^{3+}) [7]. The most intense peaks are resolved between 610 and 635 nm, which are caused by forced electronic dipole transitions between ${}^5\text{D}_0$ - ${}^7\text{F}_2$ states. Its intensity is hypersensitive to the variation of the local structure environment of the Eu^{3+} . The emissions between 580 nm and 610 nm are due to magnetic dipole allowed ${}^5\text{D}_0$ - ${}^7\text{F}_1$ transition and its intensity hardly changes with the local structure symmetry of the Eu^{3+} ions. That transition does not depend on the site symmetry at which europium is situated. The ratio between the electric dipole and the magnetic dipole is a measure of the site symmetry in which europium is situated [10].

Transition from ${}^5\text{D}_1$ level has a fast decay with the lifetime of about 10.2 μs , while the decays of peaks which belong to ${}^5\text{D}_0$ have

the lifetime of about 1.5 ms [9]. The transitions from ${}^5\text{D}_1$ situated in region below 550 nm are very fast and we cannot detect these lines in our emission spectrum in Fig. 3. The peaks at wavelengths of 578 nm and 585 nm in Fig. 3 are formed by overlapping the upper levels ${}^5\text{D}_0$ and ${}^5\text{D}_1$ showing double – exponential decay. It should be noted that spectrograph used for measuring the 514.5 nm excitation has much better wavelength resolution than spectrograph used in the case of 365 nm excitation, so some of the differences of spectra presented in Fig. 3 are caused by different spectral resolutions of used acquisition systems.

3.2.2. Time resolved measurements

In the time resolved fluorescence measurements reported here, the luminescence emission was collected in the reflective mode. The fluorescence emission is collected using a Spectrograph (SpectraPro 2300i) and Hamamatsu streak camera (C4334-01). Streak camera is designed to measure ultra-fast light events with a resolution up to 15 ps. The fundamental advantage of the streak scope is its two dimensional nature, enabling the acquiring of the temporal evolution of laser induced phenomena [11,12].

The streak image of the fluorescence emission spectrum of Eu doped in $\text{Gd}_2\text{Zr}_2\text{O}_7$ is presented in Fig. 4. The grayscale image is presented in pseudocolor, where different intensities are coded as different colors. For image shown in Fig. 4, the spectrograph diffraction grating of 50 lines/mm was selected, covering a 330 nm spectral range (horizontal axis) with the resolution of about 0.5 nm. The streak camera has the overall spectral range from 200 nm to 850 nm. The streak image is acquired in photon counting mode of operation with 1000 expositions and saved in .img format which contains all relevant information of the image. Further processing is accomplished by HPD-TA (High Performance Digital Temporal Analyzer) software installed on computer.

To take the streak image in the time frame of interest, it is required to set the proper delay time on digital delay generator (Stanford DG 535) that triggers the streak camera. The vertical axis in Fig. 4 corresponds to the plasma development in time domain of 5 ms. These results provide a good insight into the development of

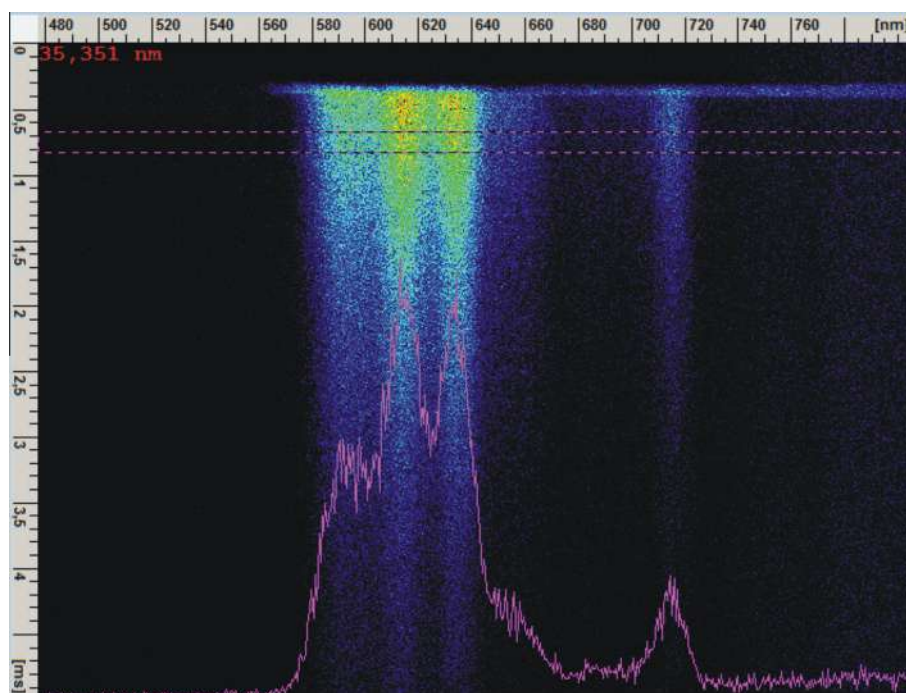


Fig. 4. Streak image of Eu doped in $\text{Gd}_2\text{Zr}_2\text{O}_7$ fluorescence spectra. OPO excitation is at 360 nm. The wavelength range (horizontal axis) is 330 nm. The time range (vertical axis) is 5 ms.

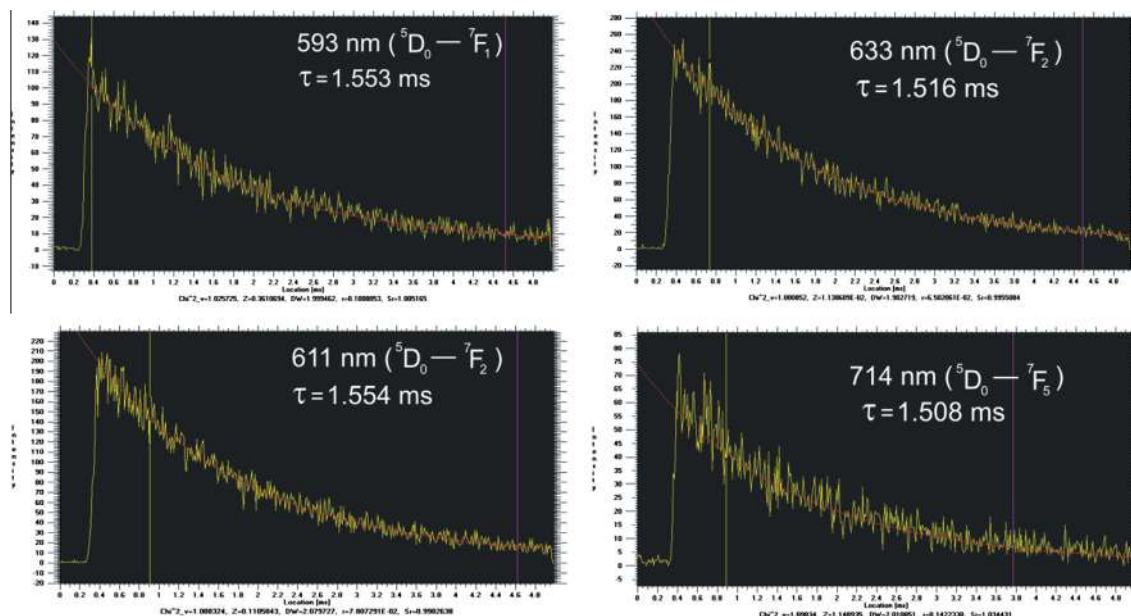


Fig. 5. Luminescence decay curves for four transitions fitted by single exponential decay.

fluorescence emission in time. Our time resolved measurements can be accomplished in the time range from 1 ns to 10 ms. The start of the fluorescence emission which can be seen in Fig. 4 is delayed for 0.3 ms regarding the beginning of the vertical (time) axis.

3.2.3. Decay curve and decay time

We conducted the fluorescence lifetime analysis for four transitions which are identified in Fig. 4. These are emission peaks at 593 nm, 611 nm, 633 nm and 714 nm wavelengths. The line at 613 nm ($^5D_0-^7F_2$) is the most prominent in emission spectrum with a high intensity and narrow full-width at half maximum (FWHM). That is the only one electric dipole allowed transition of the observed transitions. Namely, f–f transitions arising from forced electric dipole are parity forbidden and become partially allowed when the ion is situated at the low symmetry site. Therefore, europium trivalent ions occupy such lattices for nonsymmetric center causing very intensive $^5D_0-^7F_2$ transition. Because of that, the lifetime of f–f transitions lasts long, in millisecond range, so we tuned the time scale of streak camera accordingly.

Fluorescence decay and fitted curve of 593 nm ($^5D_0-^7F_1$), 611 nm ($^5D_0-^7F_2$), 633 nm ($^5D_0-^7F_2$) and 713 nm ($^5D_0-^7F_4$) transitions under the excitation at 360 nm are shown together in Fig. 5. All curves demonstrate almost perfect single – exponential decay. Fluorescence line profiles are selected from time resolved streak image shown in Fig. 5 using the integration process for radiative transitions in regions: (590,6–593,2 nm) at 593 nm, (608–612 nm) for line at 611 nm, (631,4–635,5 nm) at 633 nm and (713,38–716,99 nm) at 714 nm.

The obtained lifetimes are 1.553 ms, 1.554 ms, 1.516 ms and 1.508 ms for lines 593 nm, 611 nm, 630 nm and 713 nm, respectively (Fig. 5). Decay curve of the most prominent $^5D_0-^7F_2$ transition of the doped Eu^{3+} ions in different host materials has been chosen for lifetime measurements by many authors [7,9]. That is because the presence of the Eu^{3+} environment is unique in accordance with the crystal structure and decay mechanism for that transition is a single decay component between Eu^{3+} ions only. Our lifetime results are very similar with the Chambers et al. [9]. The lifetime τ is related to the radiative and nonradiative transition rates. Decrease of the lifetime could be caused by the increasing of the nonradiative transitions or by formation of the second phase [7].

4. Conclusions

In this paper we describe the synthesis and characterization of the $\text{Gd}_2\text{Zr}_2\text{O}_7:\text{Eu}$ nano powder, material suitable for various optical devices. Results of our analysis show that $\text{Gd}_2\text{Zr}_2\text{O}_7:\text{Eu}$ nano powder is appropriate for TBC (thermal barrier coatings) applications, high temperature heating devices and as a host material for luminescence applications. To the best of our knowledge, the detailed fluorescence lifetime analysis of the $\text{Gd}_2\text{Zr}_2\text{O}_7:\text{Eu}$ nano powder, provided by using the streak camera system, is first presented here. Our lifetime analysis of europium trivalent ion doped in the $\text{Gd}_2\text{Zr}_2\text{O}_7$ confirms that this red light material is suitable for many optical applications and fabrication of various optical devices.

Acknowledgements

This work was financially supported within the Projects Ministry of Education, Science and Technological Development of the Republic of Serbia OI 171020 and Bilateral Project Serbia – Slovenia #651-03-1251/2012-09/03.

References

- [1] J. Wu, X. Wei, N.P. Padture, P.G. Klemens, M. Gell, E. Garcia, P. Miranzo, M.I. Osendi, *J. Am. Ceram. Soc.* 85 (12) (2002) 3031–3035.
- [2] Y.H. Lee, H.S. Sheu, J.P. Deng, H.-C.I. Kao, *J. Alloys Comp.* 487 (2009) 595–598.
- [3] L. Wang, J.I. Eldridge, S.M. Guo, *Scripta Mater.* 69 (2013) 674–677.
- [4] K.-J. Hu, Z.-G. Liu, J.-Y. Wang, T. Wang, J.-H. Ouyang, *Mater. Lett.* 89 (2012) 276–278.
- [5] I.E. Kolesnikov, D.V. Tolstikova, A.V. Kurochkin, A.A. Manshina, M.D. Mikhailov, *Opt. Mater.* (2014) (in press).
- [6] M.M. Gentleman, D.R. Clarke, *Surf. Coat. Technol.* 200 (2005) 1264–1269.
- [7] Y.-S. Chang, H.-J. Lin, Y.-L. Chai, Y.-C. Li, *J. Alloys Comp.* 460 (2008) 421–425.
- [8] M.H.V. Werts, *Sci. Prog.* 88 (2) (2005) 101–131.
- [9] M.D. Chamber, P.A. Rousseve, D.R. Clarke, *J. Luminesc.* 129 (2009) 263–269.
- [10] A. Patra, E. Sominska, S. Ramesh, Yu. Koltypin, Z. Zhong, H. Minti, R. Reisfeld, A. Gedanken, *J. Phys. Chem. B* 103 (1999) 3361–3365.
- [11] D. Sevic, M.S. Rabasovic, B.P. Marinkovic, *IEEE Trans. Plasma Sci.* 39 (11) (2011) 2782.
- [12] M.S. Rabasovic, D. Sevic, M. Terzic, B.P. Marinkovic, *Nucl. Instrum. Meth. B* 279 (2012) 16–19.



Butterfly scales as bionic templates for complex ordered nanophotonic materials: A pathway to biomimetic plasmonics



Zoran Jakšić^{a,*}, Dejan Pantelić^b, Milija Sarajlić^a, Svetlana Savić-Šević^b, Jovan Matović^c, Branislav Jelenković^b, Dana Vasiljević-Radović^a, Srećko Ćurčić^d, Slobodan Vuković^a, Vladimir Pavlović^e, Jelena Buha^f, Vesna Lačković^g, Milica Labudović-Borović^g, Božidar Ćurčić^d

^a Centre of Microelectronic Technologies and Single Crystals, Institute of Chemistry, Technology and Metallurgy, University of Belgrade, Njegoševa 12, 11000 Belgrade, Serbia

^b Institute of Physics, University of Belgrade, Pregrevica 118, 11080 Zemun, Serbia

^c Institute of Sensors and Actuator Systems, Vienna University of Technology, Floragasse 7/E366 A, 1040 Vienna, Austria

^d University of Belgrade, Faculty of Biology, Institute of Zoology, Studentski Trg 16, 11000 Belgrade, Serbia

^e University of Belgrade, Faculty of Agriculture, Dept. Agricultural Engineering, Nemanjina 6, 11080 Zemun, Belgrade, Serbia

^f EMPA, Swiss Federal Laboratories for Materials Science and Technology, Überlandstrasse 129, 8600 Dübendorf, Switzerland

^g University of Belgrade, Faculty of Medicine, Institute of Histology and Embryology, Višegradska 26, 11000 Belgrade, Serbia

ARTICLE INFO

Article history:

Available online 30 April 2013

Keywords:

Nanophotonics
Plasmonics
Biomimetics
Nanocomposites
Butterfly scales

ABSTRACT

In this paper we propose a possible use of butterfly scales as templates for ordered 2D or 3D nanophotonic materials, with complexity not easily reproducible by conventional micro/nanofabrication methods. Functionalization through laminar nanocompositing is utilized to impart novel properties to the biological scaffold. An extremely wide variability of butterfly scale forms, shapes, sizes and fine structures is observed in nature, many of them already possessing peculiar optical properties. Their nanophotonic functionalization ensures a large choice of forms and functions, including enhanced light localization, light and plasmon waveguiding and general metamaterial behavior, to mention a few. We show that one is able to achieve a combination of plasmonics and bionics, resulting in functionalities seldom if ever met in nature. As an illustration we have analyzed the photonic properties of the nanostructured scales on the wings of Purple Emperor butterflies *Apatura ilia*, *Apatura iris* and *Sasakia charonda*. Their intricate nanometer-sized structures produce remarkable ultraviolet-blue iridescence, spectrally and directionally narrow. We present our analysis of their plasmonic/nanophotonic functionalization including preliminary calculations and initial experimental results. As a simple example, we used radiofrequency sputtering to produce nanoaperture-based plasmonic structures at a fraction of the cost and necessary engineering efforts compared to the conventional top-down methods. We conclude that the described pathway to biomimetic plasmonics offers potentials for significant expansion of the nanophotonic and nanoplasmonic material toolbox.

© 2013 Elsevier B.V. All rights reserved.

1. Introduction

Plasmonics is playing an ever increasing role in contemporary photonics, nanophotonics, nanosciences and physical sciences generally. Propagation of surface plasmons polaritons (SPPs) has been proposed as the operating principle of a new generation of ultrafast and ultra-compact electronics, merging the density of contemporary integrated circuits with extreme speeds of all-optical photonic devices [1]. Plasmonics also represents the basis of modern adsorption-based ultrasensitive, label-free chemical and biological sensors. Last but not least, plasmonics opens a pathway toward optical metamaterials with electromagnetic properties surpassing

those of ordinary materials, thus opening a door to novel phenomena and novel principles of operation, even opening the new field of transformation optics [2].

Basically plasmonics is based on artificial 1D, 2D or 3D ordered metal-dielectric superlattices with subwavelength dimensions (subwavelength plasmonic crystals) – or, more generally, nanostructures containing parts with both positive and negative values of relative dielectric permittivity ϵ . The frequency dispersion of the negative ϵ parts is most often described by Drude or Lorentz model. Plasmonic structures support the formation of SPP electromagnetic waves that are evanescent in the directions perpendicular to the surface. Due to the highly nonlinear spectral dispersion of plasmonic materials SPP waves may have extremely large values of wavevector, i.e. their wavelengths are often much smaller than in vacuum at the identical frequency, reaching down to tens of nanometers at optical frequencies [3]. A wealth of different modes may

* Corresponding author. Tel.: +381 11 2628 587, mobile: +381 64 3257 897; fax: +381 11 2182 995.

E-mail address: jaksa@nanosys.ihtm.bg.ac.rs (Z. Jakšić).

appear in such structures, including those with superluminal group velocities, slow light and negative group velocities. These modes may be tailored by the design of plasmonic nanostructures.

One of the large obstacles toward a more widespread use of nanoplasmonic structures and devices is the complexity of their fabrication. Typically the dimensions of their building blocks should be much smaller than the operating wavelengths, and, as mentioned above, the wavelengths themselves in plasmonic structures are much shorter than those of visible light in vacuum. This leaves one with a need to fabricate ordered nanostructures in the range of tens of nanometers and smaller. While such a task is relatively straightforward for 1D structures, the ultrathin film deposition technologies being mature and well developed, this is not the case with 2D and even less with 3D structures.

A source of the most complex forms man has ever encountered is biology, living organisms being a wealth of intricate structures with an infinity of variations. Ordered structures with characteristic dimensions in the micrometer and nanometer range and with a plethora of different properties are readily found in living organisms. However such structures nevertheless cannot be harvested and straightforwardly utilized in plasmonics, and indeed, as far as the authors of this text know, until now man has not encountered biological plasmonic structures. However, one can always adopt bionic approach, where one of the possibilities is to use a biological pattern as a template for the fabrication of artificial nanostructures [4]. Thus it obviously occurs that one could utilize the intricacy of the structural traits of biological forms to obtain biomimetic/bionic structures for plasmonics.

In optics, a wealth of different shapes and forms with a plethora of optical functionalities is met in zoological structures, and especially within the insect world [5]. A large diversity of optical nanostructures is met among butterflies (order Lepidoptera), where an extremely wide variability of butterfly scale forms, shapes, sizes and fine structures is observed [6]. This leads to various optical effects that can be observed. A bionic use of iridescent butterfly scales as a biological platform for sensing was reported in [7], where *Morpho* butterfly scales were used as low-thermal-mass resonator for infrared detection. Another example is the use of butterfly scales for sensing with highly selective vapour response [8]. Metallization of butterfly scales was utilized to obtain naturally inspired substrates for biochemical analysis utilizing surface enhanced Raman spectroscopy [9].

In this work we propose the use of butterfly scales for bionic structures for nanoplasmonics. To this purpose we analyze the applicability of nanostructured scales of *Apatura ilia* (Denis and Schiffermüller, 1775), *Apatura iris* (Linnaeus, 1758) and *Sasakia charonda* (Hewitson, 1863) butterflies [10–12]. We theoretically and experimentally consider the possibility to functionalize the scales utilizing the deposition of plasmonic materials, thus obtaining a biological–nonbiological hybrid with plasmonic functionality.

2. Material and method

We consider a specific case of the Purple Emperor (*A. iris*), Lesser Purple Emperor (*A. ilia*), and Great Purple Emperor (*S. charonda*). Their wings show a variety of optical effects, one of which is angle-dependent iridescence, i.e. high angular and spectral selectivity [10]. A similar situation is naturally occurring in many other Lepidoptera species [6], where the observed color strongly depends on the mutual position of the light source, the butterfly wing and the observer. In Fig. 1 orange or brown¹ color of the dorsal side of the wings of male *A. ilia* butterfly can be seen from all angles, while



Fig. 1. Example of directional iridescence in *A. ilia* butterfly. (The overall appearance and pattern of iridescence of *A. iris* and *Sasakia Charonda* is similar to *A. ilia*).

purple iridescence is seen only from some specific and rather well defined positions. The position of the butterfly when making the photograph shown in Fig. 1 was so adjusted to show angular iridescence on the right fore and hind wings only. Thus the left fore and hind wings appear orange-brownish, while the right fore and hind ones are with purple hue, although the color of both pairs of wings is actually identical.

Let us consider first the microstructure of the wings of the Purple Emperor (*A. iris*) butterflies we analyzed. When observed by scanning electron microscope (SEM) they show scale-like structures that completely cover their surface. Each scale is a small plate-like structure and they are arranged on the wings like tiles on the roof (Fig. 2). Two types of scales on the dorsal side of both the fore and hind wings exist – cover and ground scales. Iridescence is observed only in the former ones.

Finer examination (Fig. 3) shows that the cover scales in the case of *A. ilia*, *A. iris* and *S. charonda* butterflies [10,11,13] possess a series of parallel ridges which behave like a surface-relief diffraction grating. The ridges have a very intricate structure resembling a stack of slanted lamellas. Each pair of ridges is connected by cross ribs, thus forming a network of submicrometer holes.

The cross section of an *A. ilia* scale as seen under transmission electron microscope (Fig. 4) shows dimensional relations between the characteristic features. Ridges are separated by a distance of 1 μm , 50 nm-thick lamellas are separated by a distance of 100 nm, the ventral surface of the scale is separated from the ridges of the dorsal side of the scale by a distance of 2 μm , while the characteristic dimensions of the bottom holes (width–length) are 400–600 nm.

Our approach can be described as follows. We observed that there is a structural and geometrical similarity between the structure of the *Apatura* and *Sasakia* butterfly cover scales and the extraordinary optical transmission (EOT) aperture arrays [14], as well as the designer (spoof) plasmon structures [15]. All of these exhibit 2D ordered subwavelength hole arrays. As an illustration, Fig. 5 shows a comparison of an SEM image of an *A. ilia* cover scale (Fig. 5a) with a 2D array plasmonic crystal with EOT functionality (Fig. 5b). The similarity of the fine structures is apparent. However, it is only geometrical and does not extend to materials and compositions. The essential difference is that the scales are all-dielectric, while EOT and spoof plasmon structures are metal-dielectric.

Our idea was to deposit an ultrathin layer of plasmonic metal onto the scales of *A. ilia*, thus imparting plasmonic functionality to them and effectively turning them into a 2D subwavelength plasmonic crystal. In this manner EOT/spoof plasmon structure is obtained in a straightforward way without a need to fabricate

¹ For interpretation of color in Fig. 1, the reader is referred to the web version of this article.

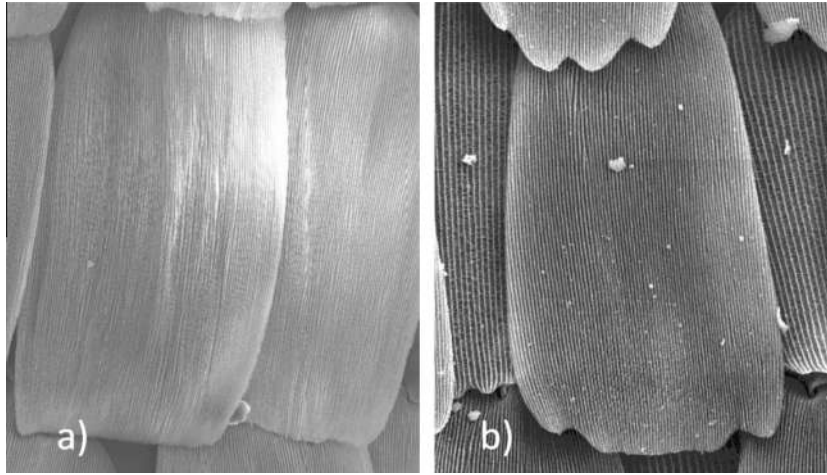


Fig. 2. Scales of (a) *S. charonda* and (b) *A. iris* as seen under SEM.

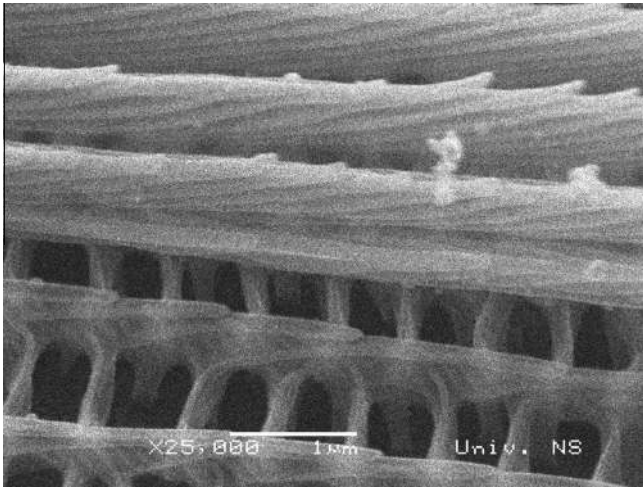


Fig. 3. Higher magnification SEM image of an *A. ilia* scale.

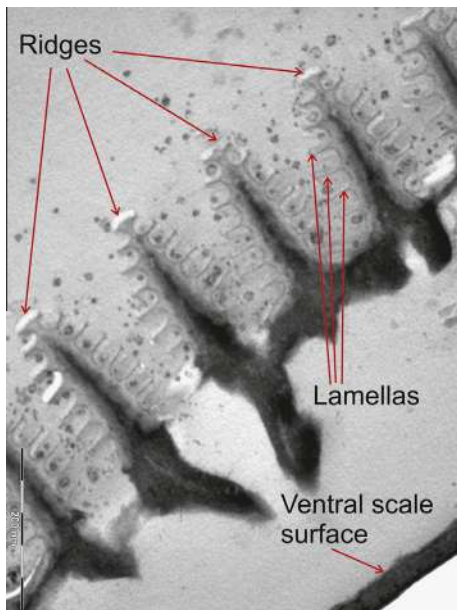


Fig. 4. Transmission electron microscope image of the cross section of *A. ilia* butterfly scale.

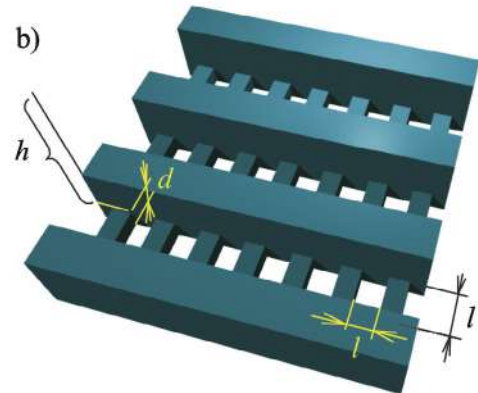
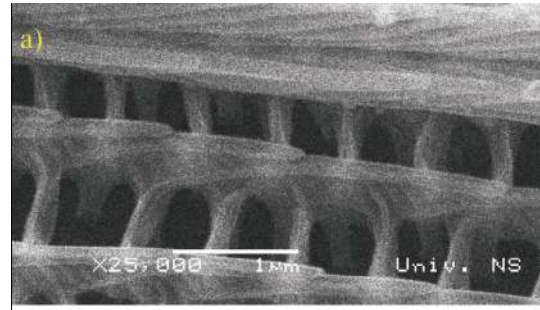


Fig. 5. (a) SEM image of a detail of *A. ilia* cover scale; (b) simplified rendering of a 2D EOT structure; l is the characteristic dimension of an aperture (equal to side length for square openings and hole diameter for circular openings), d is the metal layer thickness, and h is the distance from the observation point to the surface.

ordered arrays of subwavelength holes, replacing the expensive submicrometer photolithography process by simple and relatively inexpensive thin film deposition.

3. Calculation

We performed a rule-of-thumb calculation of the achievable performance for a natural structure (schematically shown in Fig. 5b), covered by a metal film about 40 nm thick. It is well known that metal layer permittivity may be described by the Drude model

$$\epsilon_1 = 1 - \frac{\omega_p^2}{\omega^2} \quad (1)$$

where ω_p is the plasma frequency and ω is the angular frequency of the incident radiation. The peak wavelength can be assessed by considering the EOT array as a 2D diffractive grating enabling coupling of propagating photons, thus the in-plane wave vector of surface plasmons is

$$k_x = \frac{\omega}{c} \sin \theta \pm 2m\pi/a \quad (2)$$

where a is the lattice constant (the distance between the neighboring holes), θ is the incident angle, and m is an integer. Since the transmission peak wavelength is $\lambda_{peak} = 2\pi/k_x$

$$\lambda_{peak} = \frac{a}{m} \sqrt{\frac{\epsilon_1(\lambda_{peak})\epsilon_2}{\epsilon_1(\lambda_{peak}) + \epsilon_2}} \quad (3)$$

and thus λ_{peak} is straightforwardly determined from the implicit Eq. (3). Here ϵ_1 and ϵ_2 denote the real and the imaginary part of the complex permittivity, respectively.

The transmission coefficient may be approximately calculated using the generalized Ohm's law approach. This method is presented in [16] and may be shortly described as an approximation for optical parameters of nonhomogeneous thin films in the case when the quasistatic approximation is not applicable, but the inhomogeneity length scale is much smaller than the wavelength, albeit not smaller than the skin depth. In that case the transmission coefficient can be calculated as

$$T = \frac{16p^2|u_m^2(1 + u_h v_h)|^2}{|C_1 C_2|^2} \quad (4)$$

$$\begin{aligned} C_1 &= u_h - pu_h + (1+p)(1 - iu_h)u_m - i(1-p)u_m^2 \\ C_2 &= (i + u_m)(u_m v_h - 1) + p(i - u_m)(u_m v_h + 1) \end{aligned} \quad (5)$$

where u and v are effective Ohmic parameters, the subscript m denotes their value in metal, the subscript h denotes the value in the holes, while p is the ratio of hole surface to the whole sample surface (the filling factor of the quasi-two-dimensional nanocomposite).

The effective Ohmic parameters are given as

$$u_h = \frac{k \operatorname{tg}(2hk) - \gamma \sqrt{\xi^2 - k^2}}{k + \gamma \sqrt{\xi^2 - k^2} \operatorname{tg}(2hk)} \quad (6)$$

$$v_h = \frac{\sqrt{\xi^2 - k^2} \operatorname{tg}(2hk) + k\gamma}{\sqrt{\xi^2 - k^2} - k\gamma \operatorname{tg}(2hk)} \quad (7)$$

$$u_m = -ctg(hk) \quad (8)$$

$$\gamma = \tanh \left[\left(\frac{d}{2} - h \right) \sqrt{\xi^2 - k^2} \right] \quad (9)$$

where $\xi = 3.68/l$ is the eigenvalue for the basic mode for a cylindrical waveguide, k is the wavevector, h is the distance from the surface, l is the hole characteristic dimension (diameter for round holes and side length for square holes) and d is the metal layer thickness that must be larger than the skin depth in metal.

Finally, the resonant transmission coefficient of a subwavelength EOT structure can be calculated as

$$T = 4|u_m|/|1 + u_m^2| \quad (10)$$

Fig. 6 shows the functional dependence between the characteristic dimension a and the approximate position of the peak wavelength for gold, as calculated according to (3). The spectral dependence of the real and the imaginary part of the relative dielectric permittivity of gold has been taken from [17].

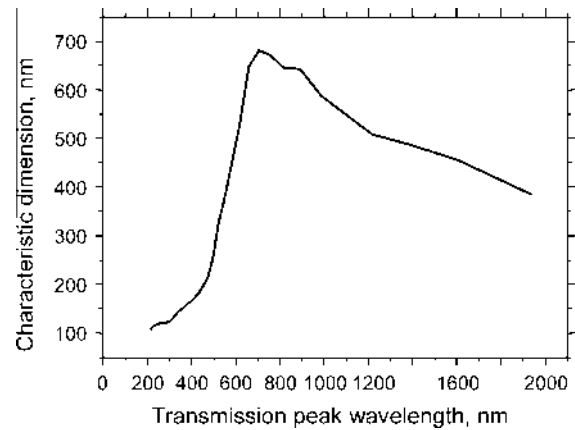


Fig. 6. Characteristic dimension a of a nanoaperture array in gold slab versus peak wavelength.

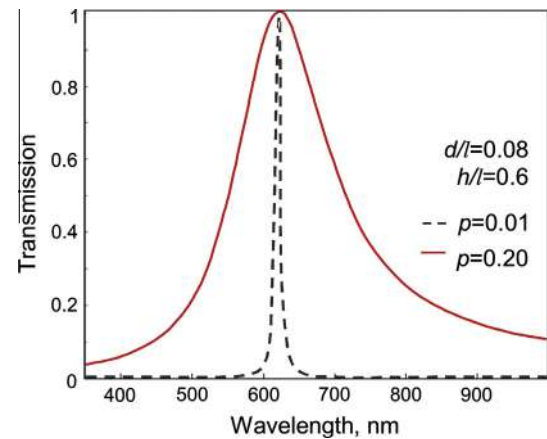


Fig. 7. Calculated spectral transmission peak of an EOT array with square matrix of nanoapertures with a characteristic dimension of $l = 0.5 \mu\text{m}$.

Fig. 7 shows the extraordinary transmission peak calculated approximately according to the above analytical approach. The calculation was done for a lattice constant $a = 1 \mu\text{m}$, the ratios $d/l = 0.08$, $h/l = 0.6$. It can be seen that the transmission peak is narrower for smaller number of nanoholes on the surface.

4. Experimental

We considered plasmonic functionalization of butterfly scales using radiofrequent sputtering. Regarding materials, it is possible to sputter different plasmonic materials including common plasmonic metals like gold, silver, chromium, etc., or alternative plasmonic materials like transparent conductive oxides. For our experiments we chose gold.

The first step was immobilization of scales to a substrate surface. For the substrate we used single-side polished single-crystalline silicon wafers, 10 cm diameter, thickness 525 μm , n-type. Epoxy resin was used to fix the samples to the surface. We considered two different approaches to scale preparation. One was to retain a sample cut from the desired area of a butterfly wing and to glue it by epoxy to the silicon surface. The other approach was to first place the wing sample on an auxiliary surface to serve as an intermediary substrate (e.g. microscopic glass slide) and to transfer scales from the wing to this auxiliary surface using a weak adhesive or an electrostatic force. Thus prepared intermediary

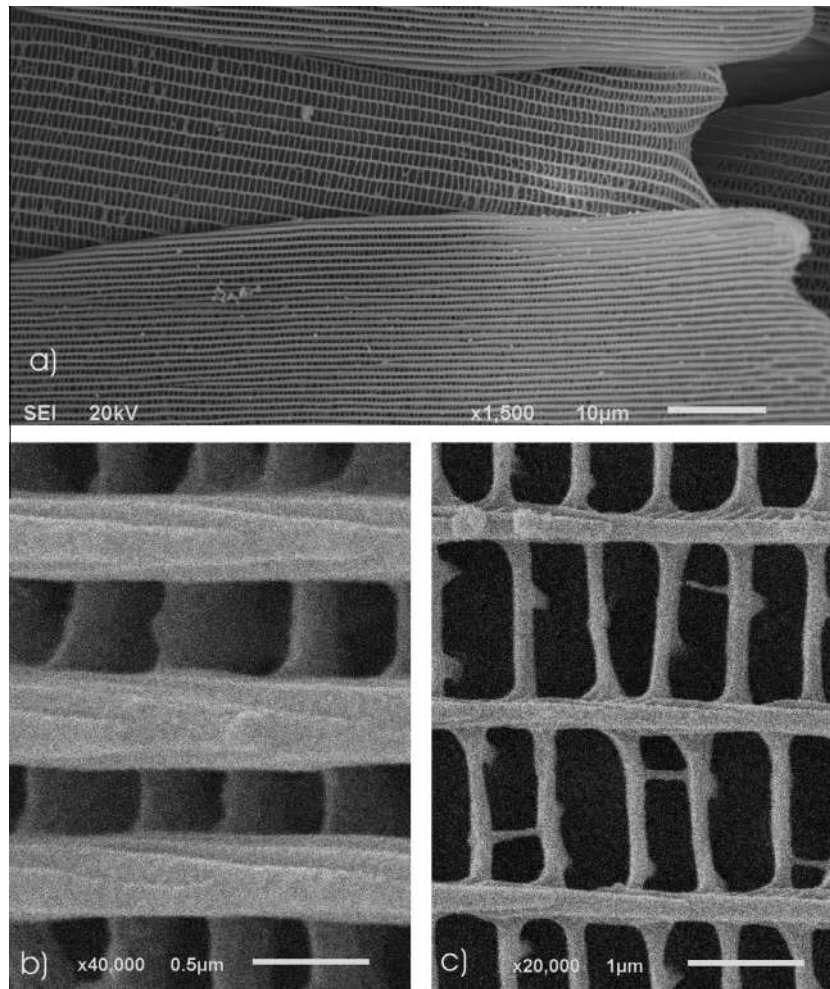


Fig. 8. SEM micrographs of *A. ilia* wing scales after 32 nm of gold has been deposited over them. (a) overall pattern of the scales; (b) details of a covering scale; (c) details of an underlying scale.

surface is brought into contact with the final substrate covered with epoxy resin. Due to adhesive effect the scales stick to the final surface and remain on it. In both cases the cover scales are turned in the same direction as was their original position on the wing and they even retain their tiled arrangement. However, since complete scales are used, together with their base plates and even with the

underlying wing structure, the prepared samples are convenient for observation in reflected spectrum only.

Sputtering was done at a base pressure of $p_0 = 2.6 \times 10^{-5}$ Pa, with argon sputtering pressure $p_{sp} = 0.67$ Pa. The applied radiofrequent power was $P = 0.5$ kW at a frequency of 13.56 MHz, non-magnetronic. The target voltage was 2200 V, and the distance

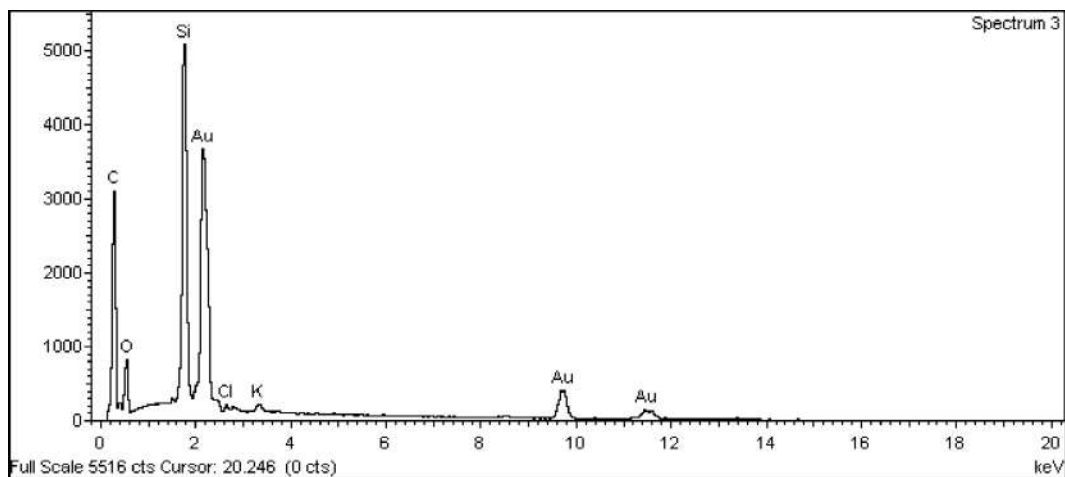


Fig. 9. Energy-dispersive X-ray spectrum of an *A. ilia* sample with 32 nm thick sputtered layer.

target-substrate was $d = 6.35$ cm. Sputtering was performed at room temperature. Several different thicknesses of gold layers was deposited onto different butterfly scale samples. Gold layers of about 11 nm were sputtered after 20 s, 22 nm after 40 s, and 32 nm after 2×30 s, with a pause of 10 min to avoid overheating and damaging the biological samples.

We performed SEM analysis of the sputtered samples in order to check if their morphology and structure has been damaged or modified, since this would effectively render our approach useless for bio-templating. As an example, Fig. 8a shows the overall pattern of the scales on an *A. ilia* wing with 32 nm gold, where the cover scales with pronounced ridges are interleaved with the underlying scales characterized by much thinner structure. Fig. 8b shows a detail of one of the cover scales, and Fig. 8c represents the structure of an underlying ground scale. It is readily observed that the complexity and precision of starting butterfly tissue is fully retained and that no damages whatsoever occurred during the gold deposition process.

Further we performed energy-dispersive X-ray spectroscopy (EDS) analysis of the bio-templated samples. Fig. 9 shows an EDS diagram of our sample with 32 nm thick sputtered layer showing that its main constituent after sputtering is indeed gold. Other constituents, expectedly, include organic carbon and oxygen as constituents of the organic template, as well as silicon stemming from the substrate.

Visual observation of *A. ilia* wings before and after processing shows that the deposited gold layer decreases their reflection, the more so the thicker the layer is. At first sight this may appear paradoxical, since the deposition of highly reflective metal actually decreases reflection, but if we observe our approximate calculation results shown in Fig. 7 (the curve for $p = 0.20$), we see that a reflection dip (corresponding to the transmission peak in Fig. 7) is indeed expected.

Fig. 10 shows measured UV–vis reflection spectra of our bio-templated samples. The measurement was performed under an angle of 45° to the wing surface, from the direction normal to the larger ridges in the covering scales. It is seen that a wide dip in the measured reflection appears. Counter-intuitively at a first glance, the measured reflectance decreases proportionally to the thickness of the deposited gold. Actually this is a natural consequence of increasingly plasmonic behavior of the whole structure. If we consider the dependence in Fig. 7, we observe that a dip in reflectance should correspond to the presented peak in transmittance. The wavelength position of the measured reflectance dip is approximately between 420 nm and 520 nm.

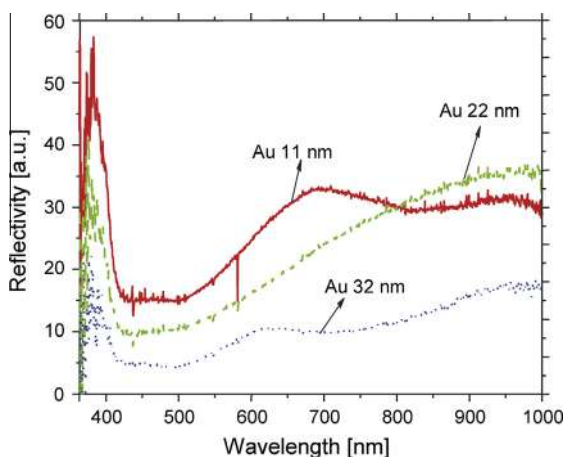


Fig. 10. Measured UV–vis reflection spectra of *A. ilia* scales with plasmonic functionalization using gold layers of different thickness.

Qualitatively this behavior corresponds to the one predicted by our rule-of-thumb calculations, where a reflection dip also appears, exactly corresponding to the transmission peak. The calculated reflection dip is positioned at approximately 600 nm and is narrower than the measured one (the calculated width being dependent on the filling factor of the nanocomposite p). Such behavior is expected, since the generalized Ohm's law approach itself is only approximate to begin with, while at the same time neither the shape of the apertures in the simplified model (squares) corresponds to the real ones (elongated rectangles), nor does the incident angle (45° instead of 90°). Finally, the measurements are actually performed with two types of interleaved scales, the cover and the ground scales, each of which has different geometry.

If we observe carefully the cover and ground scale structure in Fig. 8b and c, we see that the characteristic dimensions of some apertures are smaller than 500 nm and consequently their corresponding transmission peak/reflection dip wavelengths move to the left in Fig. 6. Actually the geometry shows significant variations both within a single scale and among different ones, as one could expect from the living tissue. A real reflectance spectrum will be a superposition of these slightly different geometries, resulting in the spectrum widening. The increased wavelength width of the dips of the spectra of experimental structures thus represents a logical consequence of the real geometry of the scales. This variety actually represents an advantage, since one can choose among a wide range of different structures and parameters.

5. Conclusion

The functionalization of butterfly scales as bio-templates by metal/plasmonic material ensures a relatively straightforward fabrication of complex plasmonic structures that are difficult or impossible to produce by conventional top-down methods and opens a pathway toward biomimetic plasmonics. We considered a possibility to fabricate 2D plasmonic crystals with nanoaperture arrays using butterfly scales and functionalization by lamellar nanocompositing. To this purpose we first did a simplified calculation to assess the obtainable photonic properties of the biological–nonbiological hybrid and then performed experiments using radio-frequency sputtering of gold layers with different thicknesses to prove the concept. Our SEM analysis has shown that the original geometry of the biological tissue of *A. ilia* is remarkably well preserved after plasmonic functionalization by sputtering of gold, thus proving the concept of bio-templating for plasmonic/metamaterial purposes. Depending on the particular wing area where they have been harvested and on the species of Lepidoptera used, the basic biological nanostructures show different dimensions and properties. Obviously a large range of different plasmonic structures can be obtained, their electromagnetic behavior may be very rich and the method itself leaves room for different optimizations and can be thus used for different purposes. We conclude that bionic approach offers potentials for vast expansion of the nanophotonic and nanoplasmonic material toolbox.

Acknowledgments

This work was supported by the Serbian Ministry of Education, Science and Technological Development through the Projects TR32008, III45016, OI171038, OI173038 and III41002.

References

- [1] E. Ozbay, Plasmonics: merging photonics and electronics at nanoscale dimensions, *Science* 311 (2006) 189.
- [2] H. Chen, C.T. Chan, P. Sheng, Transformation optics and metamaterials, *Nat. Mater.* 9 (2010) 387.

- [3] S.A. Maier, *Plasmonics: Fundamentals and Applications*, NY: Springer Science+Business Media, New York, 2007.
- [4] J. Matovič, Z. Jakšić, *Bionic (Nano)Membranes Biomimetics – Materials, Structures and Processes. Examples, Ideas and Case Studies*, in: P. Gruber, D. Bruckner, C. Hellmich, H-B. Schmiedmayer, H. Stachelberger, I.C. Gebeshuber (Eds.), Springer, Berlin, 2011, pp. 9–24.
- [5] P. Vukusic, J.R. Sambles, Photonic structures in biology, *Nature* 424 (2003) 852.
- [6] AL. Ingram, AR. Parker, A review of the diversity and evolution of photonic structures in butterflies incorporating the work of John Huxley (The Natural History Museum, London from 1961 to 1990), *Phil. Trans. Royal Soc. B: Biol. Sci.* 363 (2008) 2465.
- [7] AD. Pris, Y. Utturkar, C. Surman, WG. Morris, A Vert, S. Zalyubovskiy, T. Deng, HT. Ghiradella, RA. Potyrailo, Towards high-speed imaging of infrared photons with bio-inspired nanoarchitectures, *Nat. Photonics* 6 (2012) 195.
- [8] RA. Potyrailo, H. Ghiradella, A. Vertiatichikh, K. Dovidenko, JR. Cournoyer, E. Olson, *Morpho* butterfly wing scales demonstrate highly selective vapour response, *Nat. Photonics* 1 (2007) 123.
- [9] NL. Garrett, P. Vukusic, F. Ogrin, E. Sirotkin, CP. Winlove, J. Moger, Spectroscopy on the wing: naturally inspired SERS substrates for biochemical analysis, *J. Biophotonics* 2 (2009) 157.
- [10] D. Pantelić, S. Čurčić, S. Savić-Šević, A. Korać, A. Kovačević, B. Čurčić, B. Bokić, High angular and spectral selectivity of purple emperor (*Lepidoptera: Apatura iris* and *Apatura ilia*) butterfly wings, *Opt. Express* 19 (2011) 5817.
- [11] S.B. Čurčić, D.V. Pantelić, B.P. Čurčić, S.N. Savić-Šević, S.E. Makarov, V.B. Lačković, M.M. Labudović-Borović, N.B. Čurčić, D.V. Stojanović, Micro- and nanostructures of iridescent wing scales in purple emperor butterflies (*Lepidoptera: Apatura ilia* and *Apatura iris*), *Microsc. Res. Tech.* 75 (2012) 976.
- [12] A. Masui, GC. Bozano, A. Floriani, Guide to the butterflies of the palearctic region: nymphalidae Part 4: Subfamily Apaturinae, *Omnes Artes* (2011).
- [13] J. Matejková-Plšková, S. Shiojiri, M. Shiojiri, Fine structures of wing scales in *Sasakia charonda* butterflies as photonic crystals, *J. Microsc.* 236 (2009) 88–93.
- [14] T.W. Ebbesen, H.J. Lezec, H.F. Ghaemi, T. Thio, P.A. Wolff, Extraordinary optical transmission through sub-wavelength hole arrays, *Nature* 391 (1998) 667.
- [15] JB. Pendry, L. Martá-n-Moreno, FJ. Garcia-Vidal, Mimicking surface plasmons with structured surfaces, *Science* 305 (2004) 847.
- [16] A.K. Sarychev, V.A. Podolskiy, A.M. Dykhne, V.M. Shalaev, Resonance transmittance through a metal film with subwavelength holes, *IEEE J. Quant. Electr.* 38 (2002) 956.
- [17] PB. Johnson, RW. Christy, Optical constants of the noble metals, *Phys. Rev. B* 6 (1972) 4370.



Structural properties and luminescence kinetics of white nanophosphor YAG:Dy



M.S. Rabasovic^{a,*}, D. Sevic^a, J. Krizan^b, M.D. Rabasovic^a, S. Savic-Sevic^a, M. Mitric^c, M. Petrovic^a, M. Gilic^a, N. Romcevic^a

^a Institute of Physics, University of Belgrade, P.O. Box 68, Pregrevica 118, 11080 Belgrade, Serbia

^b AMI, d. o. o., Ptuj, Slovenia

^c Vinca Institute of Nuclear Science, University of Belgrade, P.O. Box 522, 11001 Belgrade, Serbia

ARTICLE INFO

Article history:

Received 23 October 2015

Received in revised form 3 November 2015

Accepted 3 November 2015

Available online 6 November 2015

Keywords:

Y₃Al₅O₁₂

Dy³⁺

Nanopowders

Phosphor

Lifetime

ABSTRACT

Dysprosium (Dy³⁺ ions) doped YAG nanopowders were prepared by the solution combustion synthesis (SCS) method and undoped yttrium aluminum garnet (YAG, Y₃Al₅O₁₂) single crystal was grown by the Czochralski technique. The structure of the prepared materials has been confirmed and characterized using X-ray powder diffraction (XRD), scanning electron microscope (SEM), Raman and photoluminescence (PL) spectroscopy. PL spectra were acquired using Optical Parametric Oscillator (OPO) excitation tuned at 350 nm. Several emission bands in Dy³⁺ emission spectrum were observed in the blue (470–500 nm), yellow (560–600 nm), red (660–685 nm) and infra-red (750–780 nm) regions, corresponding to ⁴F_{9/2}–⁶H_{15/2}, ⁴F_{9/2}–⁶H_{13/2}, ⁴F_{9/2}–⁶H_{11/2}, ⁴F_{9/2}–(⁶H_{9/2} + ⁶H_{11/2}) transitions in the 4f levels of Dy³⁺ ions, respectively. By using the Commission Internationale de l'Eclairage (CIE) chromaticity diagram of emission spectra it has been shown that this material can be used as a source of a white light. The result of lifetime analysis of the ⁴F_{9/2} level in dysprosium ion has been reported, as well.

© 2015 Elsevier B.V. All rights reserved.

1. Introduction

Yttrium Aluminum Garnet (YAG) is a well-known crystalline material with many interesting optical and mechanical properties. It has a cubic garnet crystallographic structure with isotropic thermal expansion and homogeneous optical properties without birefringence effects [1,2]. Due to the structural properties of YAG, it is widely used as a host in solid state lasers, luminescence materials and scintillators [3,4].

Rare earth ions luminescence has been extensively used in applications as the active ions in phosphors for development of flat panel displays, plasma display panels (PDPs), thin film electroluminescent devices (TFEL), white light emitting diode (LED). Trivalent rare-earth ions have a partially filled 4f shell that is well shielded by 5s² and 5p⁶ orbitals. The 4f–4f inner-shell transitions in trivalent rare-earth ions allow the expression of features such as high luminescence yield, narrow emission line, and long decay time constant. Because of this, most rare-earth elements are doped into many light emitting materials and laser materials [5,6].

Due to its high optical transparency (it remains transparent through the whole visible region), YAG is ideal for studying of rare

earth ions in both diluted and concentrated form. As the size of lanthanide ions decreases with the increase of atomic number, $r(La) \gg r(Lu)$, single rare earth garnets exist only for rare-earth ions with at least seven 4f electrons. Others, with less than seven 4f electrons, can replace just a certain percentage of Y³⁺ ions. The electronic structure of dysprosium is $1s^2 2s^2 2p^6 3s^2 3p^6 4s^2 3d^{10} 4p^6 5s^2 4d^{10} 5p^6 6s^2 4f^{10}$ – 10 of 14 possible electrons in the last 4f shell. So, the structure Dy₃Al₂(AlO₄)₃ is indeed possible. If we look at the size of Y³⁺ and Dy³⁺, the difference is only 0.69%, the radius of Dy³⁺ ion is 1.167 Å and radius of Y³⁺ ion (1.159 Å) as is depicted in Fig. 1(a).

Structural and optical properties of YAG and Nd:YAG single crystals have been analyzed previously using XRD, Raman and IR spectroscopy [7]. Nd:YAG single crystal is a well-known lasing material for more than 30 years. Now, we have extended our research to YAG:Dy phosphors. When the Dy³⁺ ions are incorporated in the host crystal field with wide band gap, the visible emission of these ions manifolds mainly in the blue and yellow spectral regions. The energy level scheme of Dy³⁺ ions in YAG phosphor is presented in Fig. 1(b). The investigations regarding the ratio of blue and yellow transition of the Dy³⁺ ions indicate that the lightly doped samples should be considered for the production of the white light emission [8,9].

The aim of this paper is to present the results of experimental investigation of Dy³⁺ doped YAG nanopowders, annealed at

* Corresponding author.

E-mail address: majap@ipb.ac.rs (M.S. Rabasovic).

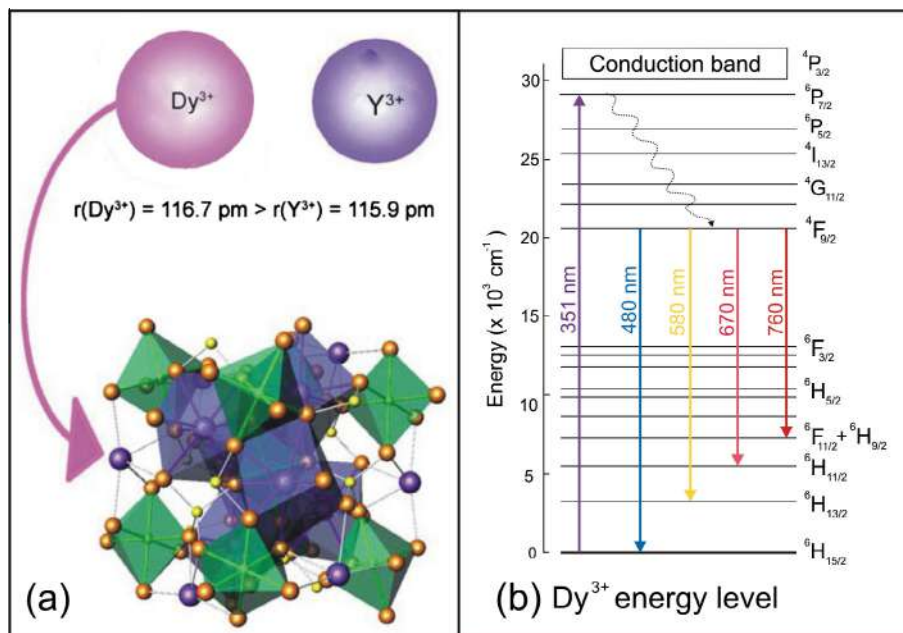


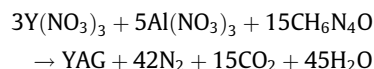
Fig. 1. (a) YAG:Dy atomic structure. Dy³⁺ is substituted in Y³⁺ sites. (b) The energy level scheme of Dy³⁺ ions.

1300 °C. YAG:Dy nanopowder was prepared by the solution combustion synthesis (SCS) method [10]. We also study time-resolved luminescence properties and differences in the visible and near IR spectral range of the YAG single crystal and dysprosium doped YAG nanopowders. The CIE chromaticity coordinates were calculated from the luminescence spectra in order to confirm the possibility of application of synthesized YAG:Dy material as the white light source.

2. Experimental procedures

2.1. The preparation of samples

Measurements were performed on samples of YAG single crystal and YAG nanopowder doped with Dysprosium ions (2 mol%). The YAG single crystal was grown by the Czochralski technique, using a MSR 2 crystal puller controlled by a Eurotherm [11]. YAG:Dy nanopowder was produced by Solution Combustion Synthesis (SCS) method. Yttrium oxide (Y₂O₃) and aluminum oxide (Al₂O₃) are used as starting materials (all 99.99%). These samples were purchased from NOAH Technologies. Synthesis was made by dissolving the oxides in HNO₃. After that a solution of carbohydrate is added to a solution of aluminum nitrate and yttrium nitrate:



Due to good reactivity of raw materials, no intermediate phases such as YAM (Y₄Al₂O₉) or YAP (YAlO₃) coexists in the obtained yttrium aluminum garnet (YAG or Y₃Al₅O₁₂) powder. After synthesis, YAG host is doped with Dy³⁺ ions at the 2 mol% concentration. In second step, in order to achieve the full crystallinity, YAG:Dy nanopowder was annealed in air atmosphere at 1300 °C.

Phase identification in the post-annealed powder samples were performed by X-ray diffraction (Philips PW 1050 instrument) using Ni filtered Cu K_{α1,2} radiation ($\lambda = 0.15405 \text{ nm}$). X-ray diffraction measurements were done at room temperature over the 2θ range of 10–90° with a scanning step width of 0.05° and a counting time of 8 s per step.

2.2. Experimental setup

The Raman spectra in a spectral range from 100 to 900 cm⁻¹, in back scattering geometry, were obtained by the micro-Raman Jobin Yvon T64000 spectrometer, equipped with a nitrogen cooled charge-coupled device detector. As the excitation source we used the 532 nm laser.

The morphology of the YAG:Dy nanopowders were investigated by high resolution scanning electron microscope (SEM) equipped with a high brightness Schottky Field Emission gun (FEGSEM, TESCAN) operating at 4 kV. The samples were coated with gold/palladium to make them conductive, for SEM analysis.

Photoluminescence (PL) studies reported in this work were performed at room temperature using Optical Parametric Oscillator (Vibrant OPO) tuned at 350 nm as excitation source. Time-resolved streak images of the emission spectrum excited by OPO system are collected by using a spectrograph (SpectraPro 2300i) and recorded with a Hamamatsu streak camera (model C4334). All streak camera operations are controlled by the HPD-TA (High Performance Digital Temporal Analyzer) software. The HPD-TA software also provides advanced analysis of streak images. Fluorescence lifetime fitting analysis was carried out using the TA-Fit program.

3. Results and discussion

The X ray diffraction patterns of Dy:YAG nanopowder and YAG single crystal samples are shown in Fig. 2. For both samples, the characteristic diffraction peaks corresponding to YAG phase are easy to see. The diffraction peak at 67.30° is noticed only for YAG single crystal sample. For the YAG single crystal sample all diffraction peaks are assigned to YAG phase and no other phase can be observed in the pattern. However, several diffraction peaks corresponding to other phases appear at YAG:Dy diffraction pattern. They are labeled with blue arrows (YAlO₃, perovskite) and green arrows (α - Al₂O₃, corundum). Existence of these impurities implies that the sample didn't turn into garnet phase completely. But the main difference between the two spectra is the fact that the YAG:Dy nanopowder diffraction peaks are slightly shifted

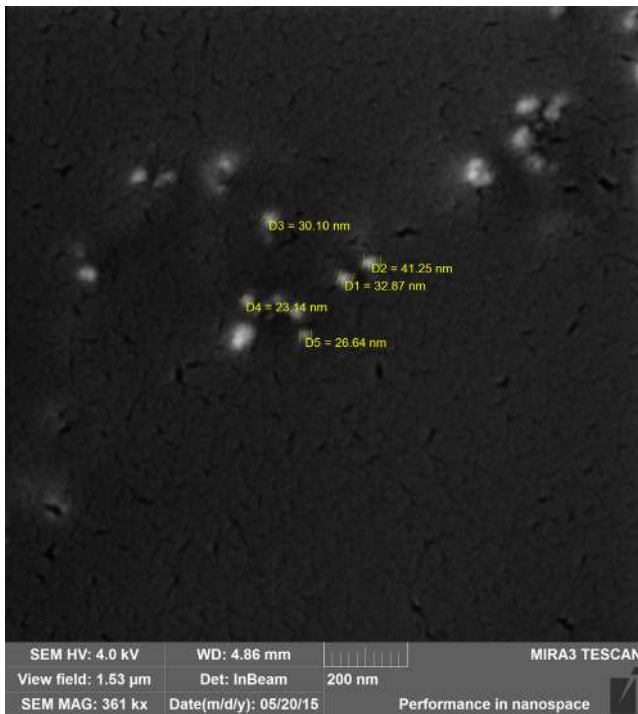


Fig. 4. SEM micrographs of material.

Dy³⁺ ion to ⁶H_{15/2} (blue ~485 nm), ⁶H_{13/2} (yellow ~580 nm) and ⁶H_{11/2} (red ~680 nm) and (⁶H_{9/2} + ⁶H_{11/2}) (~760 nm) level, respectively. The blue and yellow regions are the prominent. The last two lines, belonging to red and IR region, are also perceptible. On magnified curve corresponding to undoped YAG single crystal, luminescence band peaks are clearly observed at ~647 and ~680 nm, see Fig. 6. It is interesting to note that the position as well as the shape of this emission band in single crystal coincides with corresponding parameters for cerium doped YAG single crystals in ref. [23].

The (blue) ⁴F_{9/2}–⁶H_{15/2} transition is mainly magnetic dipole (MD) transition, which hardly varies with the crystal field strength around Dy³⁺ ions, while the (yellow) ⁴F_{9/2}–⁶H_{13/2} transition belongs to a hypersensitive transition ($\Delta L = 2$ and $\Delta J = 2$), which is forced

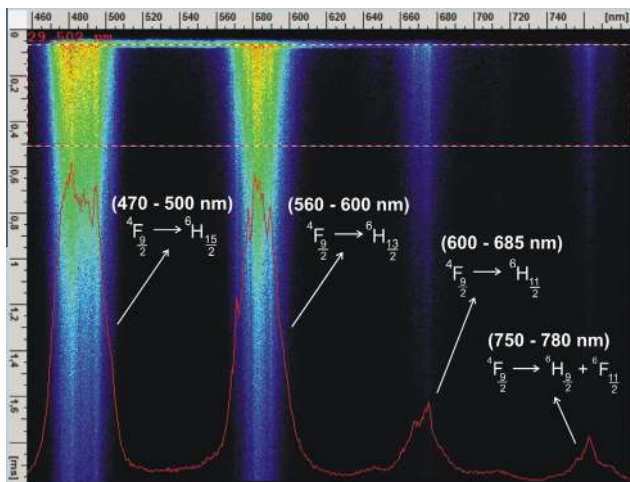


Fig. 5. Streak image of photoluminescence spectrum of Dy³⁺ doped YAG nanopowder. OPO excitation is at 350 nm. The wavelength range (horizontal axis) is 330 nm. The time range (vertical axis) is 2 ms.

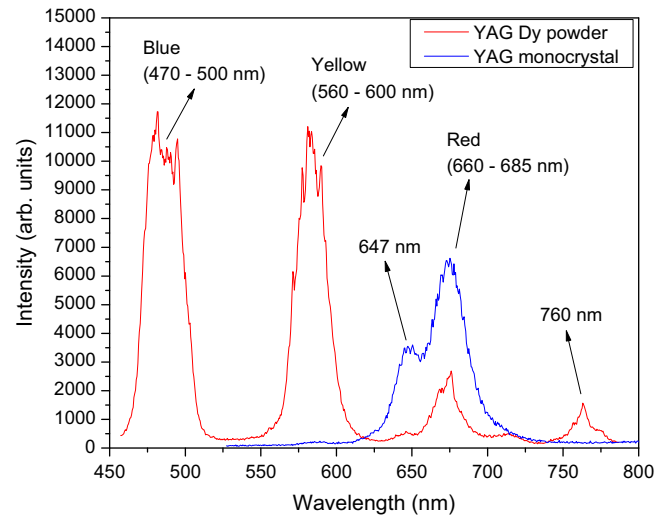


Fig. 6. The PL spectra of the YAG:Dy nanopowder annealed at 1300 °C and YAG single crystal integrated along time axis. The spectra were obtained by using the OPO excitation at 350 nm. Much weaker optical response of YAG single crystal is presented magnified about forty times so the shapes of spectra could be compared.

electric dipole (ED) transition and is strongly influenced by the chemical environment surrounding Dy³⁺ ions. As a consequence, the YAG:Dy phosphor could be good source of the white light, depending on the ratio between these two transitions [8]. Factors which influence the yellow-to-blue intensity ratio (Y/B) in Dy³⁺ ions were investigated in ref. [24]. The intensity of these two emission bands depend on the host composition, doping concentration and excitation wavelength [25]. More precisely, the intensity ratio between these two transitions is a measure of the site symmetry where Dy³⁺ ions are situated. The emission spectra of rare earth ions almost remain the same in different hosts, but the luminescent efficiency, chemical stability and durability depend on physical properties of the hosts [25].

Using the time-resolved streak images of YAG:Dy nanopowder luminescence, we have conducted the luminescence lifetime analysis for the most intensive transition ⁴F_{9/2}–⁶H_{15/2}. For optimal concentration of 2 mol%, the vertical profile curve obtained from streak image demonstrates almost perfect single exponential decay. At the samples with low doped Dy³⁺ ions, the decay curve is a single exponential because then the effects between optically active ions are minimized. For higher concentrations the decay curve has to be bi-exponential as is explained in Raju et al. [22]. The luminescence decay and fitted curve of the ⁴F_{9/2} level are presented in Fig. 7. The obtained lifetime of 0.870 ms agrees well with the published results corresponding to 2 mol% Dy concentration [26].

The usefulness of synthesized YAG:Dy phosphor is examined by calculating the CIE chromaticity coordinates, presented in Fig. 8. White light can be obtained by a suitable mixture of the blue¹ and yellow transitions of the Dy³⁺ ions. It is evident from Fig. 8 that the calculated color coordinates of YAG:Dy phosphors are located in the white light region of that color space. Therefore, the color coordinates for 2 mol% YAG:Dy phosphor (x,y) = (0.353,0.362) are very close to ideal white emission color (0.313,0.329) coordinate [27]. However, it should be noted that there are some weaknesses of using this material: low absorption of the excitation photons (forbidden f–f transitions) and slightly too high energy of the excitation transitions even when using the so-called UV-LEDs.

¹ For interpretation of color in Fig. 8, the reader is referred to the web version of this article.

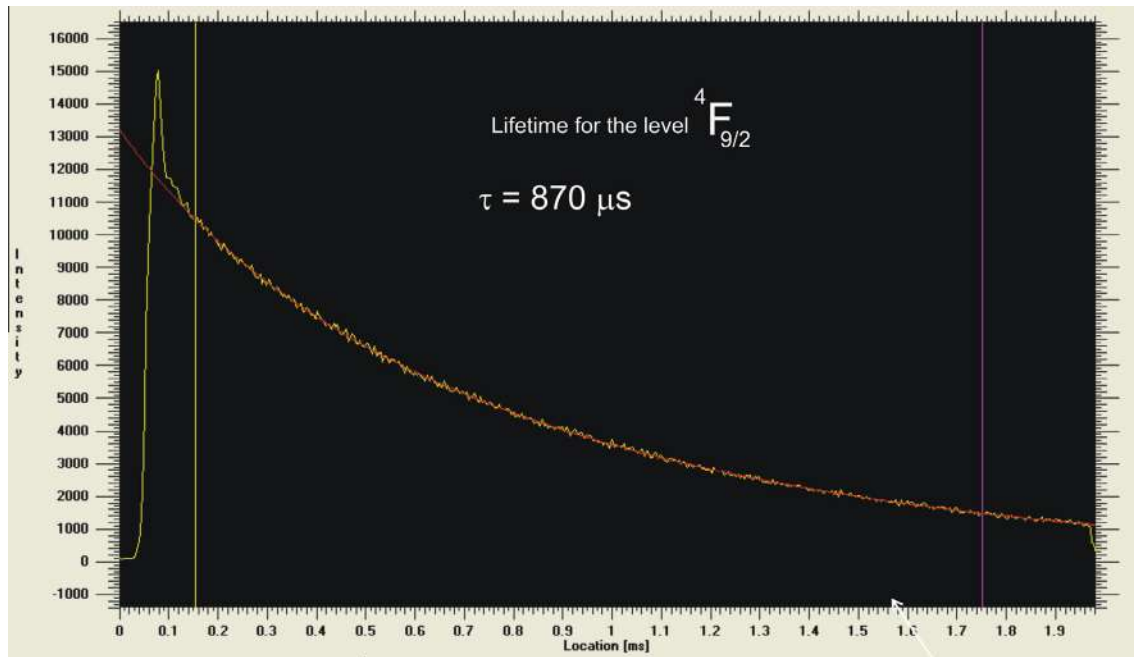


Fig. 7. Luminescence decay curve fitted by single exponential decay.

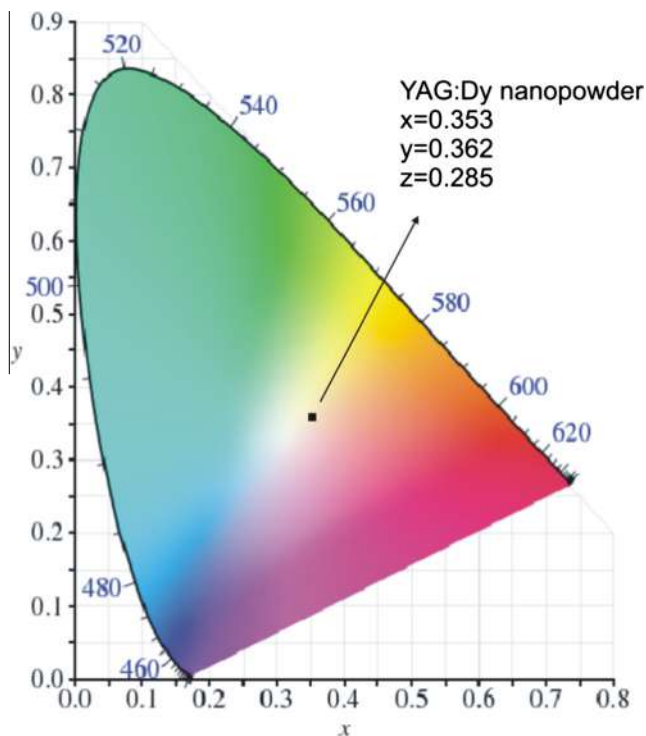


Fig. 8. The CIE chromaticity diagram of emission spectra of 2 mol% YAG:Dy.

4. Conclusion

- We have presented the new results of experimental investigation of Dy^{3+} doped YAG nanopowders, synthesized by solution combustion method and annealed at $1300\text{ }^\circ\text{C}$. Their structural and optical properties were compared with undoped yttrium aluminum garnet (YAG, $\text{Y}_3\text{Al}_5\text{O}_{12}$) single crystal grown by the Czochralski technique.

- We also study time-resolved luminescence properties and differences in the visible and near IR spectral range of the YAG single crystal and dysprosium doped YAG nanopowders.
- The structure of the prepared materials has been confirmed and characterized using X-ray powder diffraction (XRD), scanning electron microscope (SEM), Raman and photoluminescence (PL) spectroscopy.
- Several emission bands in Dy^{3+} emission spectrum were observed in the blue (470–500 nm), yellow (560–600 nm), red (660–685 nm) and infra-red (750–780 nm) regions, corresponding to ${}^4\text{F}_{9/2}-{}^6\text{H}_{15/2}$, ${}^4\text{F}_{9/2}-{}^6\text{H}_{13/2}$, ${}^4\text{F}_{9/2}-{}^6\text{H}_{11/2}$, ${}^4\text{F}_{9/2}-({}^6\text{H}_{9/2}+{}^6\text{H}_{11/2})$ transitions in the $4f$ levels of Dy^{3+} ions, respectively.
- By using the CIE chromaticity diagram of emission spectra it has been shown that this 2 mol% YAG:Dy phosphor material $(x,y) = (0.353,0.362)$ can be used as a source of a white light.
- The decay curve and lifetime analysis of the ${}^4\text{F}_{9/2}$ level in dysprosium ion have also been reported.

Acknowledgements

This work was financially supported within the Projects Ministry of Education, Science and Technological Development of the Republic of Serbia III45003, OI171020 and Bilateral Project Serbia – Slovenia (2014–2015) No. 451-03-3095/2014-09/30.

References

- [1] L. Wen, X. Sun, Z. Xiu, S. Chen, Chi-Tay Tsai, J. Eur. Ceram. Soc. 24 (2004) 2681–2688.
- [2] J.W.G.A. Vrolijk, J.W.M.M. Willems, R. Metselaar, J. Eur. Ceram. Soc. 6 (1990) 47–51.
- [3] Y. Fujimoto, T. Yanagida, H. Yagi, T. Yanagidani, V. Chani, Opt. Mater. 36 (2014) 1926–1929.
- [4] C.R. Varney, D.T. Mackay, S.M. Reda, F.A. Selim, J. Phys. D Appl. Phys. 45 (2012) 015103–015106.
- [5] Y.-C. Li, Y.-H. Chang, Y.-F. Lin, Y.-S. Chang, Yi-J. Lin, J. Alloys Compd. 439 (2007) 367–375.
- [6] B. Grobelna, P. Bojarski, B. Kuklinski, A.A. Kubicki, A. Synak, Opt. Mater. 34 (2011) 103–108.

- [7] S. Kostić, Z. Lazarević, M. Romčević, V. Radojević, A. Milutinović, G. Stanišić, M. Gilić, *Phys. Scr. T.* 162 (2014) 014026.
- [8] G.R. Dillip, B. Ramesh, C.M. Reddy, K. Mallikarjuna, O. Ravi, S.J. Dhoble, S.W. Joo, B. Deva Prasad Raju, *J. Alloys Compd.* 615 (2014) 719–727.
- [9] M.R.N. Soares, M.J. Soares, A.J.S. Fernandes, L. Rino, F.M. Costa, T. Monteiro, *J. Mater. Chem.* 21 (2011) 15262.
- [10] M.S. Rabasović, D. Šević, J. Križan, M. Terzić, J. Možina, B.P. Marinković, S. Savić Šević, M. Mitrić, M.D. Rabasović, N. Romčević, *J. Alloys Compd.* 622 (2015) 292–295.
- [11] S. Kostic, Z.Ž. Lazarevic, V. Radojevic, A. Milutinovic, M. Romcevic, N.Ž. Romcevic, A. Valcic, *Mater. Res. Bull.* 63 (2015) 80–87.
- [12] A. Lukowiak, R.J. Wiglusz, M. Maczka, P. Gluchowski, W. Srek, *Chem. Phys. Lett.* 494 (2010) 279.
- [13] R.A. Buchanan, K.A. Wickersheim, J.J. Pearson, G.F. Herrman, *Phys. Rev. A* 159 (1967) 245.
- [14] Y.F. Chen, P.K. Lim, S.J. Lim, Y.J. Yang, L.J. Hu, H.P. Chiang, W.S. Tse, *J. Raman Spectrosc.* 34 (2003) 882.
- [15] M.C. Klein, F. Hache, D. Ricard, C. Flytzanis, *Phys. Rev. B* 42 (1990) 11123.
- [16] G. Gouadec, Ph. Colomban, *Prog. Cryst. Growth Charact. Mater.* 53 (2007) 1.
- [17] A. Chopelas, *Phys. Chem. Miner.* 38 (2011) 709.
- [18] A. Misra, H.D. Bist, M.S. Navati, R.K. Thareja, J. Narayan, *Mat. Sci. Eng.* B79 (2001) 49.
- [19] A. Potdevin, G. Chadeyron, D. Boyer, B. Caillier, R. Mahiou, *J. Phys. D Appl. Phys.* 38 (2005) 3251–3260.
- [20] Joo-Yun Chong, Yuelan Zhang, Brent K. Wagner, Zhitao Kang, *J. Alloys Compd.* 581 (2013) 484–487.
- [21] Z. Boruc, B. Fetlinski, M. Malinowski, S. Turczynski, D. Pawlak, *Opt. Mater.* 34 (2012) 2002–2007.
- [22] G.S.R. Raju, H.C. Jung, J.Y. Park, J.W. Chung, B.K. Moon, J.H. Jeong, Se-Mo Son, J. H. Kim, *J. Optoelectr. Adv. Mat.* 12 (6) (2010) 1273–1278.
- [23] C.R. Varney, S.M. Reda, D.T. Mackay, M.C. Rowe, F.A. Selim, *AIP Adv.* 1 (2011) 042170.
- [24] Q. Su, H. Liang, C. Li, H. He, Y. Lu, J. Li, Y. Tao, *J. Lumin.* 122–123 (2007) 927–930.
- [25] G.R. Dillip, S.J. Dhoble, B.D.P. Raju, *Opt. Mater.* 35 (2013) 2261–2266.
- [26] Y. Zhou, J. Lin, M. Yu, S. Wang, *J. Alloys Compd.* 375 (2004) 93–97.
- [27] https://en.wikipedia.org/wiki/Illuminant_D65.

Localization of light in a polysaccharide-based complex nanostructure

Svetlana Savić-Šević¹ · Dejan Pantelić¹ · Dušan Grujić¹ ·
Branislav Jelenković¹

Received: 6 November 2015 / Accepted: 7 April 2016 / Published online: 19 April 2016
© Springer Science+Business Media New York 2016

Abstract An experimentally study of the coherent light scattering from disordered photonic structure is presented. We have measured the light localization length for a complex disordered multilayer system, which we have prepared by holography. The structure consisting of pullulan nanoparticles arranged in a random manner and confined between Bragg layers. The width of backscattering cone indicates a weak localization regime.

Keywords Weak localization · Backscattered cone · Photonic multilayer structure · Disorder · Polysaccharide

1 Introduction

During the past few decades, localization of light has great interest because of their applications, such as in light transport (Wiersma et al. 1997; Wiersma 2013), random lasers (Liu et al. 2014) and solar energy (Pratesi et al. 2013). Transport of light through a disordered medium can be localized by interference and multiple scattering from random structures, halting its propagation. Under the Ioffe-Regel criterion (John 1984), localization is either weak, known as coherent backscattering (when $l \sim \lambda$), or strong—Anderson localization (for $kl \leq 1$), where λ denotes laser wavelength, l is the mean free path and k is

This article is part of the Topical Collection on Advances in the Science of Light.

Guest Edited by Jelena Radovanovic, Milutin Stepic, Mikhail Sumetsky, Mauro Pereira and Dragan Indjin.

✉ Svetlana Savić-Šević
savic@ipb.ac.rs

¹ Institute of Physics, University of Belgrade, Pregrevica 118, Zemun, Belgrade 11080, Serbia

the wave number. Weak localization is a precursor to Anderson localization (Segev et al. 2013) where transport of light is a complete halt.

Coherent backscattering has been observed experimentally and studied in powders of gallium arsenide (Wiersma et al. 1997), aqueous suspensions of polystyrene particles (Wolf and Maret 1985; van Albada and Lagendijk 1985), liquid crystals (Strangi et al. 2006), animals (Jordan et al. 2014), cold atoms (Jendrzejewski et al. 2012) and in many other materials.

In this paper we have investigated backscattering of light in periodically ordered and disordered structure. We have measured the backscattered cone of light from He–Ne laser by polysaccharide-based complex nanostructure, generated by combining holography and non solvent phase separation (Li and Han 2011). Photonic structure consists of periodic ordered solid multilayer with alternately periodic multilayer of random arranged sphere, i.e. of Bragg layers filled with polydisperse nanoparticles arranged in a random way. To the best of our knowledge, results of back scattering measurements of complex structure proposed in this paper have not been published before.

2 Fabrication of photonic structures

Polysaccharide, pullulan, sensitized with ammonium dichromate (DCP-dichromated pullulan) was used as recording material (Pantelić et al. 1998; Savić et al. 2002; Savić-Šević and Pantelić 2007). Pullulan is linear homo-polysaccharide that is produced by microorganisms of the *Aureobasidium pullulans* type (*Pullularia pullulans*) (Prajapati et al. 2013).

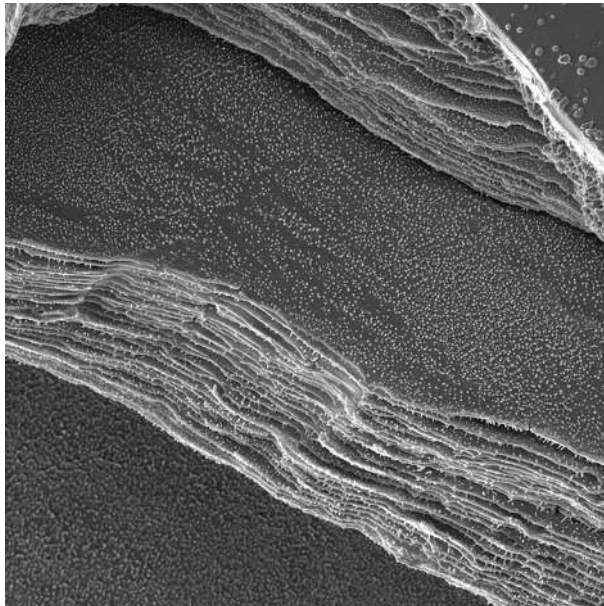


Fig. 1 FEGSEM image of internal structure of DCP grating

Photonic structures were fabricated as a volume Bragg reflection grating using a simple counter-propagating beam configuration. DCP was exposed with a single longitudinal mode, diode pumped Nd-YAG laser, at 532 nm. After exposure, grating was chemically processed in a developer. The resulting Bragg layers, upon phase separation, is filled with polydisperse, almost spherical nanoparticles arranged in a random way.

The morphology of the resulting photonic structure was investigated using a high resolution scanning electron microscope equipped with a high brightness Schottky Field Emission gun (FEGSEM). Internal structure of the DCP sample, with a number of regularly spaced Bragg layers (200 nm periods), is shown in Fig. 1. It could be seen that the Bragg grating is filled with polydisperse, almost spherical nanoparticles, with average diameter of 60 nm, arranged in a random way. Nanoparticles of pullulan are formed during phase separation.

3 Weak localization of light

Coherent light which is incident on random media is multiply elastic scattered, before exit in random direction, causing constructive interference of waves traveling in opposite directions, Fig. 2a. These randomly distributed rays interfere with each other results in enhancement of the reflected intensity (coherent back scattering) within a narrow cone with angular width (van der Mark et al. 1988),

$$W \approx \frac{0.7\lambda}{2\pi l} \tag{1}$$

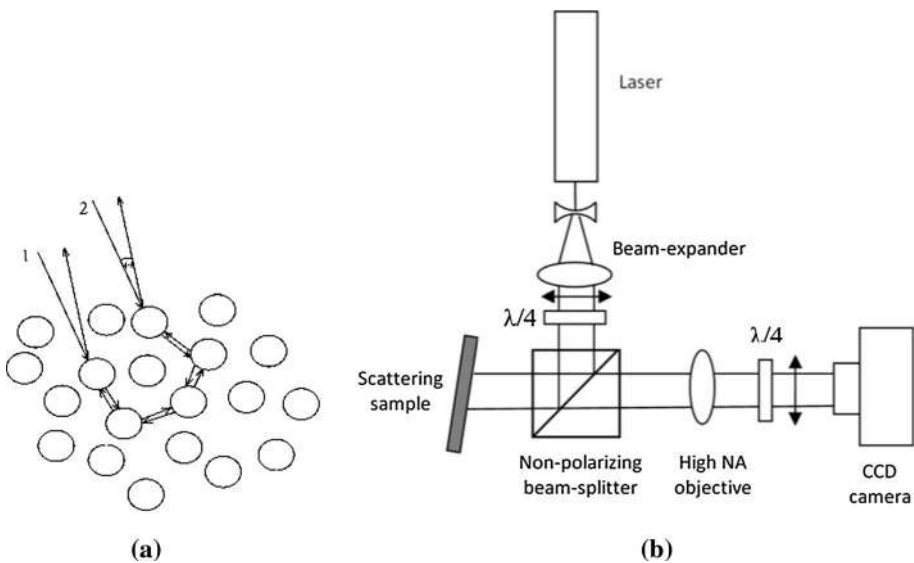


Fig. 2 a Coherent backscatter showing interference between counter-propagating light paths, b experimental setup

We have measured the backscattered light cone and determined the mean free path l of light in DCP structure by using the setup with circularly polarized light (Wiersma et al. 1995), schematically shown in Fig. 2b.

A He–Ne laser (633 nm) was used as a light source. The laser beam was expanded, and its polarization changed to circular, before entering the non-polarizing beam splitter. The spatial distribution of backscattered light is detected on a CMOS camera (15.1 mega pixel resolution, Canon EOS 50D), while speckle averaging was performed by vibrating the sample using electric motor. Clear backscattering signal is detected, obtained by averaging multiple camera exposures, as seen in Fig. 3 (down).

The value of the mean free path is calculated from angular width of the coherent backscattering peak, Fig. 3 (top). The full width at half maximum of the backscattering cone is $W = 77$ mrad, the value for the mean free path of light in DCP structure is $l = 0.9$ μm and $kl = 8.5$. This value indicates a weak localization regime (John 1984).

4 Conclusion

In conclusion, we investigated coherent backscattering by polysaccharide-based complex nanostructure. The structure, generated by holography, has pullulan nanoparticles, arranged in a random manner, and confined between DCP Bragg layers. We have measured the

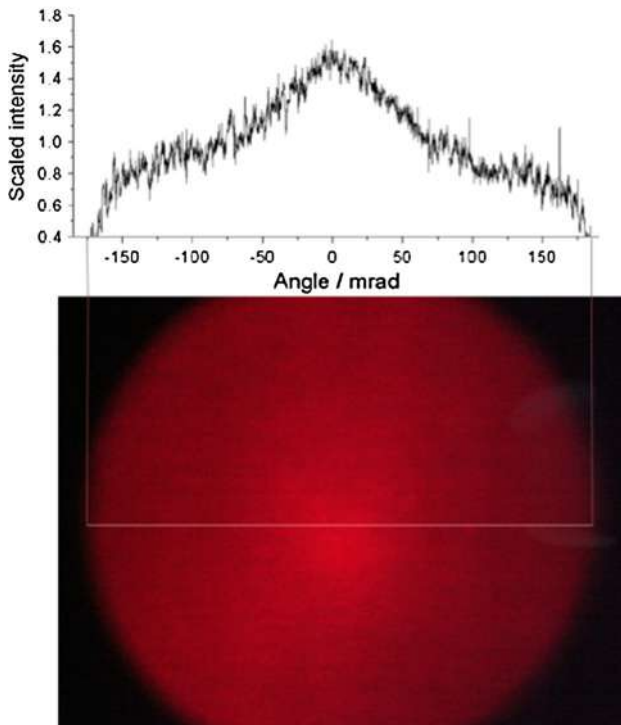


Fig. 3 Angular distribution of the backscattered light (top) and two dimensional image of backscattering obtained by averaging multiple camera exposures (down)

backscattered light cone and determined the mean free path of light in structure. It is verified experimentally that incident light is localized in disordered DCP photonic structures. The results indicate a weak localization regime.

Acknowledgments This work was funded by the Ministry of Education, Science and Technological Development of the Republic of Serbia, under Grants Nos. OI 171038 and III 45016.

References

- Jendrzewski, F., Müller, K., Richard, J., Date, A., Plisson, T., Bouyer, P., Aspect, A., Josse, V.: Coherent backscattering of ultracold atoms. *Phys. Rev. Lett.* **109**, 195302 (2012)
- John, S.: Electromagnetic absorption in a disordered medium near a photon mobility edge. *Phys. Rev. Lett.* **53**, 2169–2172 (1984)
- Jordan, T.M., Partridge, J.C., Roberts, N.W.: Disordered animal multilayer reflectors and the localization of light. *J. R. Soc. Interface* **11**, 20140948 (2014)
- Li, X., Han, Y.: Tunable wavelength antireflective film by non-solvent-induced phase separation of amphiphilic block copolymer micelle solution. *J. Mater. Chem.* **21**, 18024–18033 (2011)
- Liu, J., García, P.D., Ek, S., Gregersen, N., Suhr, T., Schubert, M., Mørk, J., Stobbe, S., Lodahl, P.: Random nanolasing in the Anderson localized regime. *Nat. Nanotechnol.* **9**, 285–289 (2014)
- Pantelić, D., Savić, S., Jakovljević, D.: Dichromated pullulan as a novel photosensitive holographic material. *Opt. Lett.* **23**, 807–809 (1998)
- Prajapati, V., Jani, G., Khanda, S.: Pullulan: an exopolysaccharide and its various applications. *Carbohydr. Polym.* **95**, 540–549 (2013)
- Pratesi, F., Burresi, M., Riboli, F., Vynck, K., Wiersma, D.S.: Disordered photonic structures for light harvesting in solar cells. *Opt. Exp.* **21**, 460–468 (2013)
- Savić, S., Pantelić, D., Jakovljević, D.: Real-time and postprocessing holographic effects in dichromated pullulan. *Appl. Opt.* **41**, 4484–4488 (2002)
- Savić-Šević, S., Pantelić, D.: Dichromated pullulan diffraction gratings: influence of environmental conditions and storage time on their properties. *Appl. Opt.* **46**, 287–291 (2007)
- Segev, M., Silberberg, Y., Christodoulides, D.: Anderson localization of light. *Nat. Photon.* **7**, 197–204 (2013)
- Strangi, G., Ferjani, S., Barna, V., De Luca, A., Versace, C., Scaramuzza, N., Bartolino, R.: Random lasing and weak localization of light in dye-doped nematic liquid crystals. *Opt. Exp.* **14**, 7737–7744 (2006)
- van Albada, M.P., Lagendijk, A.: Observation of weak localization of light in a random medium. *Phys. Rev. Lett.* **55**, 2692–2695 (1985)
- van der Mark, M.B., van Albada, M.P., Lagendijk, A.: Light scattering in strongly scattering media: multiple scattering and weak localization. *Phys. Rev. B* **37**, 3575–3592 (1988)
- Wiersma, D.: Disordered photonics. *Nat. Photon.* **7**, 188–196 (2013)
- Wiersma, D.S., van Albada, M.P., Lagendijk, A.: An accurate technique to record the angular distribution of backscattered light. *Rev. Sci. Instrum.* **66**, 5473–5476 (1995)
- Wiersma, D., Bartolini, P., Lagendijk, A., Righini, R.: Localization of light in a disordered medium. *Nature* **390**, 671–673 (1997)
- Wolf, P.E., Maret, G.: Weak localization and coherent backscattering of photons in disordered media. *Phys. Rev. Lett.* **55**, 2696–2699 (1985)



Serbian Academy of Sciences and Arts

Book of abstracts

PHOTONICA2015

the Fifth international school and conference on photonics

& COST actions: MP1204, BM1205 and MP1205

& the Second international workshop "Control of light and matter waves propagation and localization in photonic lattices"

24 August – 28 August 2015

Belgrade, Serbia

Editors

Suzana Petrović, Goran Gligorić and Milutin Stepić

Vinča Institute of Nuclear Sciences, Belgrade, Serbia

Belgrade, 2015

This work was supported by the Serbian Ministry of Education and Science through project III 45005. D.S. is grateful to the Italian Ministry of Foreign Affairs-Science and Technology Cooperation for a Travel Grant to visit CNR-IFN.

REFERENCES

- [1] J. F. Galisteo-Lopez et al., *Adv. Mater.* 23, 30 (2011).
- [2] J. Joannopoulos et al., *Molding the flow of light*, Princeton University Press (2011).
- [3] P. Jiang, M. J. McFarland, *J. Am. Chem. Soc.* 126, 13778 (2004).
- [4] P. Jiang et al., *Chem. Mater.* 11, 2132 (1999).
- [5] A. Chiappini et al, *J. Non-Cryst. Solids* 355, 1167 (2009).

Localization of light in a polysaccharide-based complex nanostructure

S. Savić-Šević, D. V. Pantelić, D. Ž. Grujić and B. M. Jelenković

Institute of Physics, University of Belgrade, Pregrevica 118, 11080 Zemun, Belgrade, Serbia
e-mail: savic@ipb.ac.rs

Complex nanostructures are interesting research topic, due to remarkable properties for photonic applications [1]. Photonic structures are generated by many methods. Holographic method [2] has several advantages: it is simple and fast, capable of producing one-, two- and three- dimensional periodic nanostructures over a large area. We combine the holographic method with non-solvent induced phase separation to generate complex photonic structures.

Polysaccharide sensitized with ammonium dichromate was used as recording material. Photonic structures were fabricated as a volume Bragg reflection grating recorded with the single-frequency, diode pumped Nd-YAG laser, at 532 nm. After exposure, grating was chemically processed in a developer. The resulting Bragg layers, upon phase separation, is filled with polydisperse, almost spherical nanoparticles arranged in a random way.

We investigated optical bandgap properties in the complex nanostructure, as a measure of the photon confinement in the layer, and we have measured the backscattered light cone and determined the mean free path of light in structure. The width of backscattering cone indicates a weak localization regime.

REFERENCES

- [1] W. G. Bae et al., *Adv. Mater.* 26, 675 (2014).
- [2] M. Birnkrant et al., *Nano Lett.* 7, 3128 (2007).

REFERENCES

- [1] Y. Liu et al., *Opt. Las. Technol.* 12, 947 (2010)
- [2] A. N. Chumakov et al., *Phys. Scr.* T167, 114016 (2014)

Transparent

T. Tomašević-Ilić¹

¹Center for Solid State

Liquid phase exfoliation and subsequent deposition of few-layer graphene compatible with us exfoliated from gra dimethylacetamide exfoliated in a wa surfactant-based pr that our films exfol transmittance comp step for GS exfol properties of graph atomic force micr measurements. Ou conductive films coating technology

This work is supported by the Serbian Ministry of Education, Science and Technological Innovation Project through Projects N

REFERENCES

- [1] K. R. Paton et al.
- [2] H. K. Kim et al.
- [3] F. Bonaccors
- [4] M. Lotya et al.

Flexible design of band gaps in the biopolymer photonic crystals

This content has been downloaded from IOPscience. Please scroll down to see the full text.

2012 Phys. Scr. 2012 014073

(<http://iopscience.iop.org/1402-4896/2012/T149/014073>)

View [the table of contents for this issue](#), or go to the [journal homepage](#) for more

Download details:

IP Address: 147.91.1.45

This content was downloaded on 01/12/2016 at 14:49

Please note that [terms and conditions apply](#).

You may also be interested in:

[Holographic imaging of 3D objects on dichromated polymer systems](#)

Guylain Lemelin, Anne Jourdain, Gurusamy Manivannan et al.

[FDTD analysis of photonic quasicrystals with different tiling geometries and fabrication by single-beam computer-generated holography](#)

G Zito, B Piccirillo, E Santamato et al.

[Fabrication and application of holographic Bragg gratings in lithium niobate channel waveguides](#)

J Hukriede, D Runde and D Kip

[Methylene-blue sensitized dichromated gelatin](#)

Jianhua Zhu, Guangxing Dong, Xiaowei Guo et al.

[Effective volume holographic structures based on organic–inorganic photopolymer nanocomposites](#)

O V Sakhno, L M Goldenberg, J Stumpe et al.

[Holograms preparation using commercial fluorescent benzyl](#)

V Dorantes-García, A Olivares-Pérez, M J Ordoñez-Padilla et al.

[Graded photonic crystals by optical interference holography](#)

Chunrui Han and Wing Yim Tam

[Diffraction efficiency measurement in photorefractive thick volume holograms](#)

I de Oliveira and J Frejlich

[Hologram demultiplexer of a waveguide communication system with wavelength-division multiplexing](#)

A L Dmitriev

Flexible design of band gaps in the biopolymer photonic crystals

S Savić-Šević

Institute of Physics, University of Belgrade, Pregrevica 118, 11080 Zemun, Serbia

E-mail: savic@ipb.ac.rs

Received 31 August 2011

Accepted for publication 23 November 2011

Published 27 April 2012

Online at stacks.iop.org/PhysScr/T149/014073

Abstract

One-dimensional photonic crystals (PC) are fabricated in dichromate-sensitized biopolymer as volume holograms. The flexibility of the PC band gap (BG) parameters was investigated. The spectral position of a BG can be varied by changing the exposure for two concentrations of sensitizer during the fabrication process. The spectral measurements show that the BG centre shifts towards longer wavelengths with decreasing exposure and concentration of the sensitizer. A tuning of the position of the BG for about 120 nm was obtained.

PACS numbers: 42.70.Qs, 42.40.Eq, 42.70.Ln

(Some figures may appear in colour only in the online journal)

1. Introduction

Photonic crystals are dielectric materials that exhibit band gaps (BGs) in which electromagnetic wave propagation is forbidden [1]. Several photonic BG materials, such as dichromated gelatin [2, 3], polymers with TiO₂ [4] and photoresists [5, 6] have been used for the fabrication of photonic structures using holographic techniques. Here, we report the fabrication of photonic crystals using optical holography. One-dimensional (1D) periodic structures, i.e. holographic volume gratings, were fabricated by using a single-beam method. Volume gratings have been created by standing waves formed in holographic material by two-beam interference of an incident laser beam.

Tunability of the photonic crystals (PC) BG during the fabrication of the 1D PC in dichromate biopolymer was investigated. We used pullulan sensitized with ammonium dichromated pullulan (DCP) as recording material [7–9]. Pullulan is a natural linear polysaccharide, produced by a fungus *Aureobasidium pullulans*. It is non-poisonous and easily soluble in water making a clear and viscous solution [10].

We found that the position of the BG can be tuned by changing the exposure and concentration of the dichromate. Spectral measurements show that the BG centre shifts towards longer wavelengths with decreasing exposure and concentration of dichromate. The tuning is a consequence of the different amounts of swelling of photosensitive material.

An efficient tuning of the position of the BG for about 120 nm is obtained. These results are important as they present a convenient way to move the centre wavelength of the BG of the photonic crystal, thus making holographic filters for different spectral ranges.

2. The sample preparation

Holographic photosensitive material was prepared by an 8% aqueous solution of pullulan (Sigma). Ammonium dichromate was added and the mixture was stirred at 50 °C to achieve homogeneity. Two concentrations of ammonium dichromate were used in our experiments: 5 and 30% by weight of pullulan. Solutions are coated onto clean glass slides in the horizontal position. Films were dried under normal laboratory conditions. The dried DCP layers were about 15 μm thick.

3. Fabrication of biopolymer photonic crystals

1D periodic structures, i.e. Bragg gratings, in a DCP, were fabricated using a single-beam method. To minimize vibrations, the experimental setup for the recording of holograms was assembled on an optical table placed on the large concrete block, suspended on vibration-damping supports. Hologram recording was achieved by exposing DCP by a single-frequency, diode-pumped Nd-YAG laser, at 532 nm. The radius of the laser beam was expanded

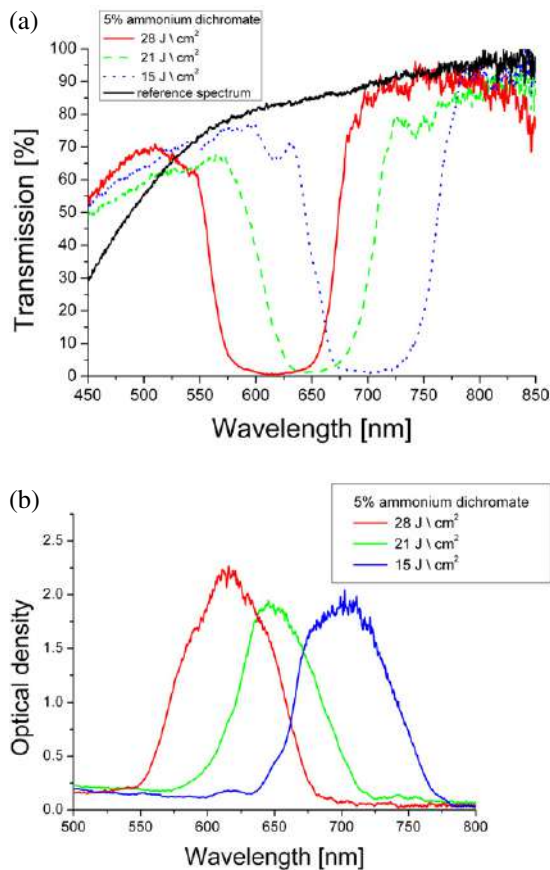


Figure 1. Transmission (a) and optical density (b) for the DCP sample with 5% concentration of ammonium dichromate for three different energy densities of the recording beam: 15, 21 and 28 J cm^{-2} .

and the pullulan layer was exposed at normal incidence. After propagation through the emulsion, the laser beam was reflected back from the mirror behind the holographic plate. The two counter-propagating beams interference creates a standing wave pattern and the hologram within an emulsion. The interference pattern consists of planes parallel to the substrate surface with the spacing $d = \lambda/2n$, where λ is the wavelength of the laser source and n is the refractive index. For DCP, $n = 1.44$, and the space between the two adjacent constructive planes was calculated to be 184 nm.

After exposure, the plates were chemically processed. Processing involves washing the plates in a mixture of water and isopropyl alcohol (in the ratio 3 : 1) for 120 s, and drying for 60 s in pure isopropyl alcohol.

4. Tunability of the band gaps during grating fabrication

The transmission (reflection) spectra of PC directly show their band structures. Spectra were measured using a microscope attached to a spectrometer. The spectral position of a BG was varied by changing the exposure for two concentrations of dichromate during the fabrication process.

Figure 1 shows the transmission spectra and optical densities of DCP PC with 5% ammonium dichromate for three different energy densities of the recording beam: 15, 21 and 28 J cm^{-2} .

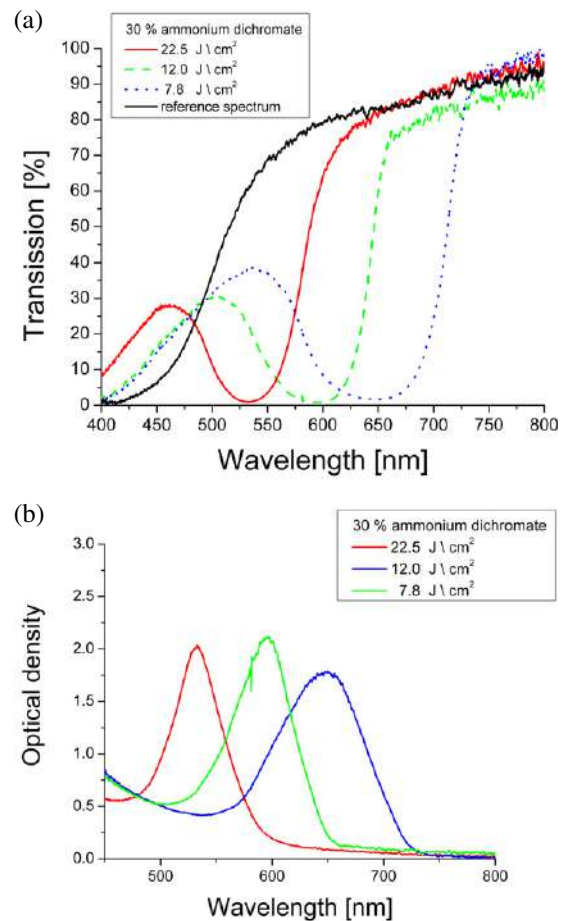


Figure 2. Transmission (a) and optical density (b) for the DCP sample with 30% concentration of ammonium dichromate for three different energy densities of the recording beam: 7.8, 12 and 22.5 J cm^{-2} .

The transmission gaps for 5% ammonium dichromate were centred at about 615, 650 and 700 nm for different energy densities of the recording beam: 15, 21 and 28 J cm^{-2} , respectively. The bandwidths of gaps were about 110 nm. The centre wavelength of the PC BG was shifted by about 85 nm towards the shorter wavelengths by raising the exposure from 15 to 28 J cm^{-2} .

Figure 2 shows the transmission spectra and optical densities of DCP PC with 30% ammonium dichromate for three different energy densities of the recording beam: 7.8, 12 and 22.5 J cm^{-2} .

The transmission gaps for 30% ammonium dichromate were centred at about 530, 600 and 650 nm, for energy density of the recording beam: 7.8, 12 and 22.5 J cm^{-2} , respectively. The bandwidths of gaps were between 70 and 115 nm. The centre of the wavelength of the PC was shifted by about 120 nm towards the shorter wavelength by raising the exposure from 7.8 to 22.5 J cm^{-2} .

It can be seen from figures 1 and 2 that the position of the BG can be tuned by changing the exposure and concentration of ammonium dichromate. The tuning is a consequence of the different amounts of swelling of photosensitive material for different exposures and concentrations of ammonium dichromate. Our results show that by increasing the exposure and concentration of ammonium dichromate, the BG is shifted towards shorter wavelengths.

5. Conclusion

We have produced BG photonic structure in dichromate-sensitized biopolymer using the holographic recording method. It has been shown that the BG position can be tuned by varying the exposure and concentration of ammonium dichromate during the fabrication. These results are important since they present a convenient way to move the centre wavelength of the BG of the photonic crystal, thus making holographic filters for different spectral ranges.

Acknowledgment

This work was supported by the Ministry of Education and Science of the Republic of Serbia under project grant numbers ON171038 and III45016.

References

- [1] Busch K, Lolkes S, Wehrspohn R B and Foll F 2003 *Photonic Crystals: Advance in Design, Fabrication and Characterization* (Weinheim: Wiley)
- [2] Ma R, Xu J and Tam W Y 2006 *Appl. Phys. Lett.* **89** 081116
- [3] Ye Z, Zheng J, Liu D and Pei S 2002 *Phys. Lett. A* **299** 313
- [4] Sharp D T, Campbell M, Dedman E, Harrison M, Denning R G and Tuberfield A J 2002 *Opt. Quantum Electron.* **34** 3
- [5] Ohira T, Segawa T, Nagai K, Utaka K and Nakao M 2002 *Japan. J. Appl. Phys.* **41** 1085
- [6] Miklyaev Y, Meisel D, Blanco A and Freymann G 2003 *Appl. Phys. Lett.* **82** 1284
- [7] Pantelić D, Savić S and Jakovljević D 1998 *Opt. Lett.* **23** 807
- [8] Savić S, Pantelić D and Jakovljević D 2002 *Appl. Opt.* **41** 4484
- [9] Savić-Šević S and Pantelić D 2007 *Appl. Opt.* **46** 287
- [10] Sano T, Uemura Y and Furuta A 1976 *US Patent Specification* 3960685

Biomechanical model produced from light-activated dental composite resins: a holographic analysis

This content has been downloaded from IOPscience. Please scroll down to see the full text.

2013 Phys. Scr. 2013 014021

(<http://iopscience.iop.org/1402-4896/2013/T157/014021>)

View [the table of contents for this issue](#), or go to the [journal homepage](#) for more

Download details:

IP Address: 147.91.1.41

This content was downloaded on 01/12/2016 at 14:39

Please note that [terms and conditions apply](#).

You may also be interested in:

[Computed-tomography scan-based finite element analysis of stress distribution in premolars restored with composite resin](#)

I Kantardži, D Vasiljevi, L Blaži et al.

[Holography-techniques and applications](#)

I Weingartner

[Microwave holographic interferometry](#)

V M Ginsburg, V M Meschankin, G I Ruhkman et al.

[Holographic interferometry in engineering practice](#)

I K Leadbetter

[A Method for Detecting Microstructure Deformation in Diffuse Objects by Holographic Interferometry](#)

Kiyofumi Matsuda and Jumpei Tsujiuchi

[Finite Element Analysis of Viscoelasticity of Test Pieces for Tactile Sensor](#)

Subaru Kudo, Yuuichi Akiba, Ryoji Aoyagi et al.

[Comparative study of nanomechanical properties of cements used in teeth restoration](#)

M S Peluccio, C Bignardi, S Lombardo et al.

[Effects of Er, Cr:YSGG laser irradiation on external adaptation of restorations in caries-affected cavities](#)

Mateus Rodrigues Tonetto, Matheus Coelho Bandéca, Alvaro Henrique Borges et al.

[Wavefront buffer memory for holographic interferometry](#)

Evelin Weidner, Gilles Pauliat and Gérald Roosen

Biomechanical model produced from light-activated dental composite resins: a holographic analysis

Dejan Pantelić¹, Darko Vasiljević¹, Larisa Blažić², Svetlana Savić-Šević¹, Branka Murić¹ and Marko Nikolić³

¹ Photonics Center, Institute of Physics, University of Belgrade, Belgrade, Serbia

² Vojvodina Clinic of Dentistry, Faculty of Medicine, University of Novi Sad, Novi Sad, Serbia

³ Laboratory for Radiation Chemistry and Physics, Vinca Institute of Nuclear Sciences, University of Belgrade, Belgrade, Serbia

E-mail: darko@ipb.ac.rs

Received 25 August 2012

Accepted for publication 18 December 2012

Published 15 November 2013

Online at stacks.iop.org/PhysScr/T157/014021

Abstract

Light-activated dental composites, commonly applied in dentistry, can be used as excellent material for producing biomechanical models. They can be cast in almost any shape in an appropriate silicone mold and quickly solidified by irradiation with light in the blue part of the spectrum. In that way, it is possible to obtain any number of nearly identical casts. The models can be used to study the behavior of arbitrary structure under mechanical loads. To test the technique, a simple mechanical model of the tooth with a mesio–occluso–distal cavity was manufactured. Composite resin restoration was placed inside the cavity and light cured. Real-time holographic interferometry was used to analyze the contraction of the composite resin and its effect on the surrounding material. The results obtained in the holographic experiment were in good agreement with those obtained using the finite element method.

PACS numbers: 42.40.Kw, 42.40.My, 87.85.G–, 87.85.J–

(Some figures may appear in color only in the online journal)

1. Introduction

Bio-mechanical structures are frequently modeled in order to study their functionality and properties when loaded. Models can be either mechanical (in hardware) or digital (in software). Even though contemporary computers are capable of modeling complicated structures, mechanical models are still closer to reality—especially if biological (anatomical) structures are analyzed.

Bio-mechanical models can be directly produced from computer-aided design (CAD) drawings or computer aided tomography (CAT) and magnetic resonance imaging (MRI) images [1, 2] using rapid prototyping [3, 4]. Models are usually made from plastic materials (e.g. acrylonitrile butadiene styrene) [5] or composites (glass fiber epoxy) [6]. In order to analyze internal stresses, photo-elastic techniques are used. Replicas of various biological structures are made from

epoxy resin and polycarbonate- [7] or methacrylate- [8] based substances.

Mechanical models can be fabricated using alternative materials provided they are readily available, have useful mechanical properties and can be easily molded. In that respect, light-curing dental composite resins seem to be good candidates [9]. These are paste-like substances composed of three essential components: a resin-based polymer matrix, a photo-initiator (usually camphorquinone) and a filler (hard material particles). After irradiation with blue light (with the spectrum centered at 474 nm), a polymerization reaction is initiated, transforming composite resin to a solid state [10]. When cured, dental composite resin is a hard material, imitating dentin and enamel, with regard to modulus of elasticity, hardness, color and translucency [11, 12].

Once produced, models are mechanically loaded in order to study their deformation. Deformation can be measured in

various ways: using transducers [13], photo-elasticity [7, 8], and speckle or holographic interferometry [14], just to name a few techniques.

Holographic interferometry seems to be well suited to analysis in biomechanics, due to its ability to observe arbitrary, irregular objects in three dimensions. It is very sensitive—capable of measuring micron and submicron deformations.

The goal of our research was to use holography to analyze the behavior of a mechanical model made of dental composite resin. To test the model, we decided to analyze the problem of polymerization shrinkage that accompanies the polymerization reaction during setting of composite resin restoration. Light-induced polymerization, which follows composite resin insertion, leads to material contraction and transfer of mechanical stress to cavity walls, which may result in coronal deformation, post-operative sensitivity, microfractures and microleakage due to failure of tooth-restoration adhesive interfaces [15].

2. Mechanical model manufacturing using composite resins

The tooth model with simplified geometry representing a class II mesio-occluso-distal (MOD) cavity was produced. Such geometry enabled reliable comparison of the experimental results with finite element method (FEM) calculations. Thus, predictions of finite element analysis could be verified and internal stress distribution calculated.

Firstly, a template was made of aluminum and impressed into Elite HD (Zhermack, Italy) addition-type silicone impression material (which guaranteed accuracy of the order of $1.5\ \mu\text{m}$ [16]). The composite resin (Gradia direct anterior A2—manufactured by GC Dental Products Corp., Japan) was inserted in increments of 2 mm into the mold and cured (Smartlite PS, Dentsply, USA). Insertion of an equal amount of composite resin was obtained by weighing the material portions before placement. After finishing a light-curing procedure, the composite resin was extracted and the same silicone mold was used over and over for further production of the models.

The MOD cavity models were placed in the aluminum holders and rigidly attached using the dental plaster (Marmorock 20; Dr Böhme & Schöps, GmbH, EN 26873/ISO 6873, class IV-green). In this way, they could be inserted into the experimental setup, with the stability required in holography. Models had to be silver painted in order to record high-contrast interference fringes (PX-20(L), Mitsubishi Pencil Co. Ltd). Otherwise, the light would penetrate deep into the model with back-scatter from inside the material. The correlation between the wavefront reflected from the mechanical loaded model and its holographic image (in an unloaded state) would then be lost. As a result, the contrast of the resulting interference pattern would become extremely low. It should be noted that the paint layer was so thin that it could not influence the mechanical properties of the model as a whole.

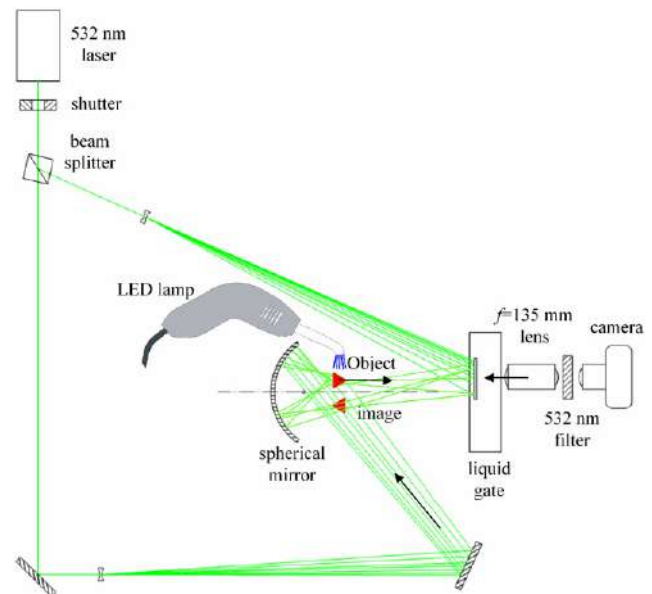


Figure 1. Real-time holography setup. Red triangles in the figure represent the object and its inverted mirror image.

3. Real-time holography measurements

Real-time-holographic interferometry has previously been used in biomechanical research [17, 18]. The hologram of an object in its initial, unperturbed state was recorded. After hologram reconstruction, electromagnetic waves emanated from the three-dimensional holographic image and reflected from the object interfered. If an object were mechanically loaded, interference fringes would appear, indicating an amount of deformation.

The real-time, split-beam holographic setup was used (figure 1). The laser beam (532 nm wavelength, 80 mW power) was divided into an object and a reference component. The object beam illuminated the tooth model, while the reference beam illuminated the photosensitive (holographic) plate. The photosensitive material was placed in a container with glass walls (so-called liquid gate) and used to perform wet chemical processing without disturbing the hologram (*in situ*).

A spherical mirror was used to produce an image of the back of the model. In this manner we could simultaneously observe both the sides, giving us a complete picture of the deformation field. This is particularly important when investigating asymmetrical objects or asymmetrical loads. The interference pattern was recorded using a CCD camera, by observing through the liquid gate. In order to enlarge the image, the lens (135 mm focal length) was placed between the liquid gate and the camera. An interference filter was used to block polymerization light (470 nm) and transmit the laser light (532 nm) used in the holographic experiment.

The measurements were performed as follows. The MOD cavity of the tooth model was bulk filled with the composite resin and placed inside the holographic setup. For each cavity, the material was weighed in order to ensure placement of an equal amount. The holographic plate (green-sensitive VRP-M type, manufactured by Slavich, Russia) was loaded in the

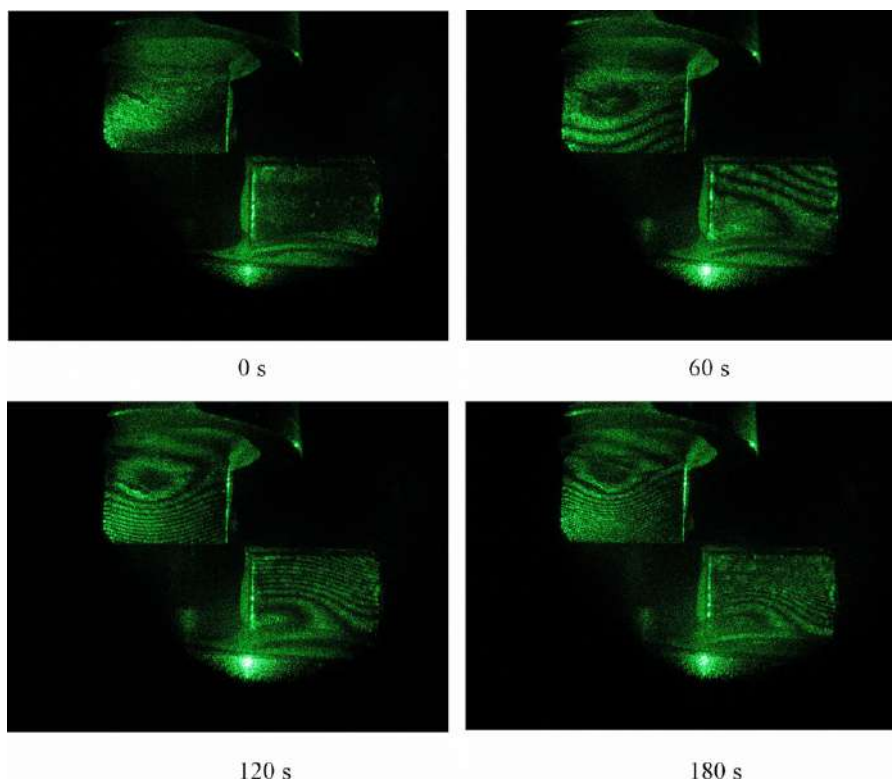


Figure 2. Sequence of holographic interferograms, recorded at 60 s intervals. The model itself is on the right, while its image in a spherical mirror is on the left, turned upside down.

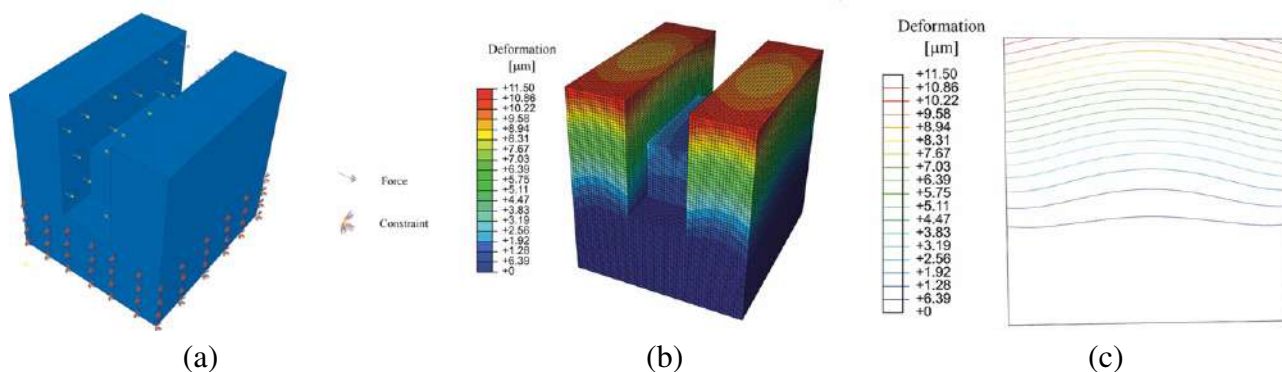


Figure 3. (a) FEM model with constraints (marks at the bottom of the model) and forces (arrows), (b) three-dimensional deformation field calculated using FEM and (c) lines of equal deformation on the external wall of the model—compare them to experimentally recorded interference patterns in previous figures.

liquid gate filled with distilled water. The photosensitive material was left in the gate for several minutes, in order to swell the gelatin layer. Exposure was made by opening the laser beam shutter for 1 s. The liquid gate was emptied, and the developer (Ilford ID-11) was poured in. After 30 s of development, the developer was poured out. Several distilled water baths followed, in order to thoroughly wash the film. This completed the hologram process recording. The final water bath was left inside the liquid gate, and the hologram was observed through the water.

The light polymerization of the composite resin restoration was initiated by the LED light source positioned directly above the model. The resulting contraction of the composite resin induced the deformation of the model and the reflected wavefront was distorted. The interference between the reflected and the holographically ‘frozen’ wavefronts produced dark and bright fringes.

At the beginning of the polymerization, fringes appeared at the top of the external cavity wall. During polymerization, fringes floated downwards to the bottom of the model and their number increased. After 3 min the interference pattern stabilized, indicating that the polymer was cured. The sequence of images was recorded (using a CCD camera at 1 frame s^{-1}) corresponding to the temporal variation of the interference pattern (four out of 140 images are shown in figure 2). The number of interference maxima gave information on the total deformation at any particular object point.

In order to test the reproducibility of the model making and the analysis, the holographic procedure was repeated on five identical tooth models. They were produced using the same type of composite resin and utilizing the same silicone mold. The holographic experiment was repeated for each model. Every time practically the same interference pattern was seen on the model surface.

4. Finite element analysis of the model

It is important to point out that the deformation measurement was just the starting point for the calculation of internal stress using the finite element method. The digital geometric model of the object under investigation was constructed. The model was meshed, directions of forces and pressures were defined and boundary conditions were given in accordance with the experiment (see figure 5(a)).

The mechanical structure under investigation was simple, and the construction of the digital model was straightforward. It had 242 576 nodes in 228 520 brick (linear hexahedral) elements and was constrained at its base (see figure 3(a)). Uniform pressure was applied to all free surfaces of the MOD cavity. The elasticity modulus of the dental composite used in this research (Gradia direct anterior) was 5.2 GPa and its Poisson's ratio was 0.22, according to [19].

The pressure reproducing the measured deformation was determined (see figures 3(b) and (c)). It could be seen that the numerical results matched the experimentally recorded interference pattern (figure 2).

5. Discussion and conclusion

In this work, we detected an effect of the composite resin restoration polymerization contraction on the surrounding structure. From a dental practitioner's point of view, the whole method was a good approximation to the real therapeutic procedure. Performing the testing procedure was easy, since the inserted restoration of an uncured composite resin adhered well to the model (made of cured composite resin). The molds and the restorations were made from the same composite resin in order to obtain a totally maintained interface between the tooth model and the composite restoration during light-induced polymerization. Such an interface represented the same pattern used while restoring a cavity preparation in an everyday dental practice; composite resin material is inserted in a portion, while every increment adheres to a previous one.

When a composite restoration is cured inside the model of a MOD cavity, accompanying contraction is transferred to the cavity walls expressed as a deformation. In a clinical surrounding, where a gap might develop between a tooth and restorative material, the free surface of a composite resin plays an important role in stress relief, decreasing its impact on the surrounding structure. The flow capacity of restoration with debonding is increased and the resulting deformation of cavity walls cannot be detected completely. That is why it is expected that the method presented would give more accurate insight into the stresses transferred to the bounded tooth structure while performing the restorative procedure.

We showed that dental composite resins could be effectively used for the manufacture of mechanical models. A great number of dental composite resins are available on the market, with a range of mechanical properties, which can be matched to a particular application. Using the silicone mold, an almost arbitrary number of identical casts could be manufactured. This can be particularly important in biomechanics, where collecting of biological samples is time consuming and raises ethical questions. In addition,

there is great variability between biological specimens, making it difficult to perform the same measurement under the same conditions. Coupled with holographic interferometry, reproducible and reliable results were obtained regarding deformation and stress measurement. Anyway, small structures (teeth, small bones) could be effectively produced, at quite reasonable cost.

The method described in this paper is particularly suited to studying various dental procedures, such as composite resin polymerization techniques and strategies, loading of teeth and dental implants. The findings obtained could help dental practitioners choose therapeutic procedures that are most favorable for patients.

Acknowledgment

This research was funded by the Serbian Ministry of Education and Science under contract numbers III 45016 and OI 171038.

References

- [1] Undt G, Wild K, Reuther G and Ewers R 2000 MRI-based stereolithographic models of the temporomandibular joint: technical innovation *J. Cranio-Maxillofacial Surg.* **28** 258–63
- [2] Kantardžić I, Vasiljević D, Blažič L and Tasić M 2012 Computed-tomography scan based finite element analysis of stress distribution in premolars restored with composite resin *Phys. Scr.* **T149** 014075
- [3] Ready J F and Farson D F 2001 *Handbook of Laser Materials Processing* (Orlando, FL: Laser Institute of America) pp 541–81
- [4] Steen W M 2003 *Laser Material Processing* (London: Springer) pp 279–99
- [5] Sanghera B, Naique S, Papaharilaou Y and Amis A 2001 Preliminary study of rapid prototype medical models *Rapid Prototyping J.* **7** 275–84
- [6] Katz D M, Blatcher S and Shelton J C 1998 Quantification of holographic fringe data: comparison of intact and implanted femurs *Med. Eng. Phys.* **20** 114–23
- [7] Shuster M, Sherman D, Siegmund A, Narkis M, Jennewein C M and Eyerer P 1996 Stress distribution in and around a spherically ended fiber embedded in a polymer matrix *Polym. Compos.* **17** 568–77
- [8] Cehreli M, Duyck J, De Cooman M, Puers R and Naert I 2004 Implant design and interface force transfer: a photoelastic and strain-gauge analysis *Clin. Oral Implant. Res.* **15** 249–57
- [9] Moszner N and Salz U 2006 *Composites for dental restoratives Polymers for Dental and Orthopedic Applications* ed S W Shalaby and U Salz (Baton Range, FL: CRC Press/Taylor and Francis) pp 13–69
- [10] Cook W D 1982 Spectral distribution of dental photopolymerization sources *J. Dent. Res.* **61** 1436–8
- [11] Delfino C S, Pfeifer C S C, Braga R R, Youssef M N and Turbino M L 2009 Shrinkage stress and mechanical properties of photoactivated composite resin using the argon ion laser *Appl. Phys. B* **96** 79–84
- [12] Lee Y K and Powers J M 2007 Color changes of resin composites in the reflectance and transmittance modes *Dent. Mater.* **23** 259–64
- [13] Jantarat J, Panitvisai P, Palamara J E A and Messer H H 2001 Comparison of methods for measuring cuspal deformation *J. Dent.* **29** 75–82
- [14] Shahar R and Weiner S 2007 Insights into whole bone and tooth function using optical metrology *J. Mater. Sci.* **42** 8919–33

- [15] Blažić L, Pantelić D, Savić-Šević S, Murić B, Belić I and Panić B 2011 Modulated photoactivation of composite restoration—measurement of cuspal movement using holographic interferometry *Lasers Med. Sci.* **26** 179–86
- [16] Verran J, Rowe D L and Boyd R D 2003 Visualization and measurement of nanometer dimension surface features using dental impression materials and atomic force microscopy *Int. Biodeterioration Biodegradation* **51** 221–8
- [17] Ko K, Erickson R, Schmidt T and Webster J 2005 Holographic interferometry of cerebral pulsations *Surg. Neurol.* **63** 118–22
- [18] Gesualdi M R R, Mori M, Muramatsu M, Liberti E A and Munin E 2007 Phase-shifting real-time holographic interferometry applied to load transmission evaluation in dried human skull *Appl. Opt.* **46** 5419–29
- [19] Sorrentino R, Aversa R, Ferro V, Auriemma T, Zarone F, Ferrari M and Apicella A 2007 Three-dimensional finite element analysis of strain and stress distributions in endodontically treated maxillary central incisors restored with different post, core and crown materials *Dent. Mater.* **23** 983–93

PAPER

Zoom system for measurement of coherent backscattering of light in micro- and nanomaterials

D Pantelić, S Savić-Šević and D Grujić

Published 15 November 2013 • 2013 The Royal Swedish Academy of Sciences

Physica Scripta, Volume 2013, T157

pantelic@ipb.ac.rs

Institute of Physics, University of Belgrade, Pregrevica 118, 11080 Zemun, Belgrade, Serbia

Received 18 August 2012

Accepted 12 December 2012

Published 15 November 2013

D Pantelić *et al* 2013 *Phys. Scr.* **2013** 014020

<http://dx.doi.org/10.1088/0031-8949/2013/T157/014020>

Buy this article in print

Abstract

We report on an optical system capable of detecting backscattering cones within a wide angular range—from less than mrad up to 500 mrad. It is based on an intermediate optical system placed between the sample and the CCD camera equipped with a $5 \times$ zoom objective. The theory of operation is explained and experimental results are presented.

Export citation and abstract

BibTeX

RIS

1. Introduction

Coherent backscattering is a process observed in physical systems with a certain amount of disorder. Systems can be either completely random (like clouds or milk) or regular with slight randomness. This is an interference phenomenon inherent for any type of wave—from electrons and sound to light. It is characterized by increased intensity in the exact backscattering direction. Coherent backscattering has been observed in many optical materials (artificial or natural) and gives important information about the mean free path of light, the density of scatterers and their dimensions.

Devices for the measurement of backscattering are simple in principle, but rather demanding from the experimental point of view [1]. The main problem is that the width of the backscattering cone is inversely proportional to the mean free path length of light. For materials with path lengths of the order of several micrometers (as in biological tissues) the cone is very narrow (of the order of microradians), while for nanostructured materials the backscattering cone can be quite wide (several hundreds of milliradians). In that respect, present systems are constructed for the observation of either wide [2] or narrow backscattering cones [3].

There are several experimental techniques for the detection of backscattered radiation. One of them is based on the angular scanning of a detector around the scattering sample. The technique is accurate but rather slow. An improvement is based on using many discrete detectors, in which case there is no need for mechanical scanning. However, the cost of such a system is high and there is the problem of achieving the same electrical response from all detectors. Another

method is to use CCD array detectors and imaging optics, where the detection speed is significantly improved. However, a calibration procedure is needed to correct for variation of Fresnel losses inside the imaging system. None of those systems are capable of detecting both wide and narrow backscattering cones, thus significantly reducing their general utility.

Here we report on the universal system that can be used for both low and high backscattering angles. The system is based on imaging the scattering surface using an additional lens system. The image is directly projected into the entrance pupil of a zoom lens that is focused at infinity. In this way, the angular spectrum of scattered light is focused on the detection surface, making observation of the backscattering cone possible. In this configuration, the variable magnification of a zoom lens changes the angular field of view, depending on whether the backscattering cone is large or small. Light is detected on a 15.1 mega pixel resolution CMOS camera.

2. Principle of operation

In a classical imaging system for detection of backscattered radiation, the scattering sample is far from the entrance pupil of the imaging lens. Therefore, the angular range of scattered radiation is severely limited by the aperture diaphragm (figure 1 (a)). Also the magnification of the system is constant.

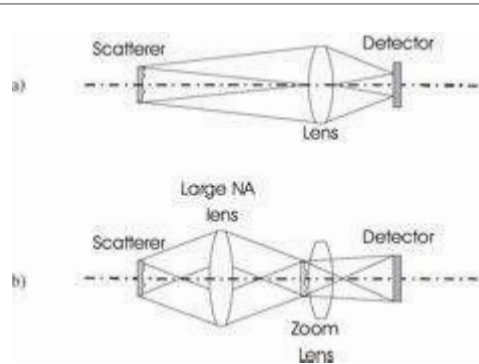
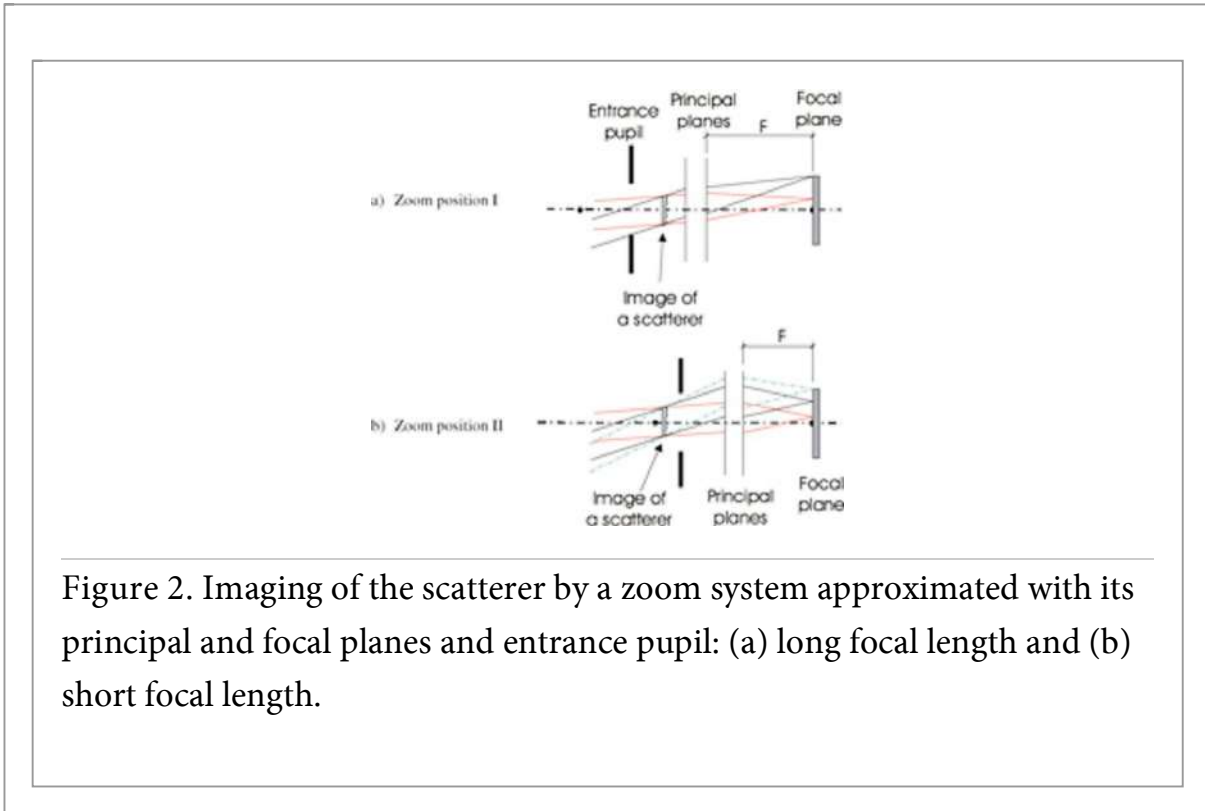


Figure 1. Schematic representation of (a) a classical imaging system for detection of backscattered radiation and (b) a zoom system for detection of backscattered radiation.

The solution is to produce a real image of the scatterer (by an additional optical imaging system) and project it directly into the entrance pupil (figure 1(b)) of a lens in front of the detection plane. If a zoom lens is used before the detector then we have a variable magnification system, whose operation can be best understood by replacing a zoom lens by a set of principal and focal planes and an entrance pupil (figure 2).



Two zoom positions are presented in figure 2. The first zoom position is one with long focal length (figure 2(a)) in which a small angular range is observed on the whole detection area. The second zoom position is one with short focal length (figure 2(b)) in which a large scattering cone is projected on the detector surface. As can be seen, no matter how we change the focal length of a zoom lens, the image of a scatterer always stays close to the entrance pupil, thus significantly increasing the angular acceptance of the system. In this way, we have a system capable of observing both large and small scattering cones.

3. Experimental realization

The experimental configuration is schematically presented in figure 3. A helium–neon laser (10 mW at 633 nm) was used as the light source in a polarization preserving configuration. The laser beam was expanded, and its polarization changed to circular, before entering the non-polarizing beam splitter. Scattered radiation was collected by placing an additional objective that projected a real image of the scatterer into zoom objective (Canon EF-S 17–85 mm 1:4-5.6 IS USM) of a CCD camera (Canon EOS 50D). All ghost reflections from optical components were blocked and we were able to observe a clear backscattering pattern. The sample was mounted on a motorized rotation stage, which was used to slightly move the sample during exposure in order to average the speckle.

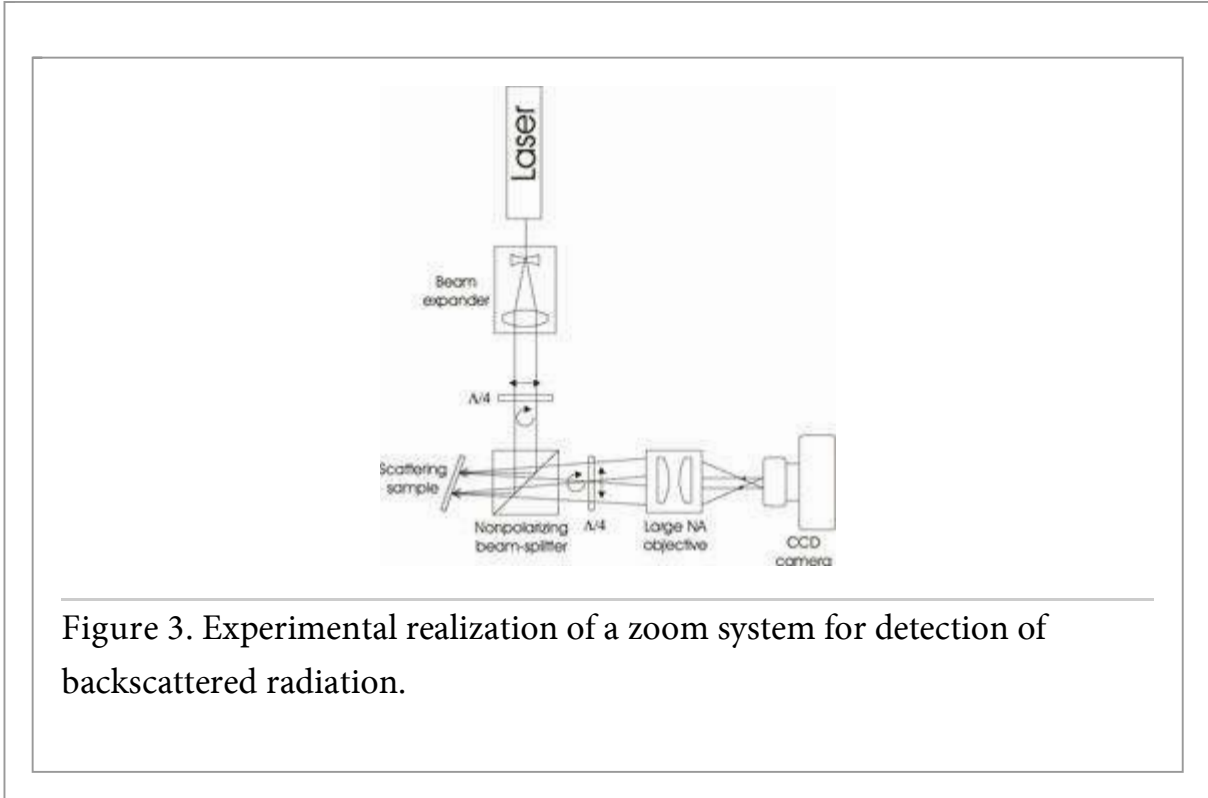
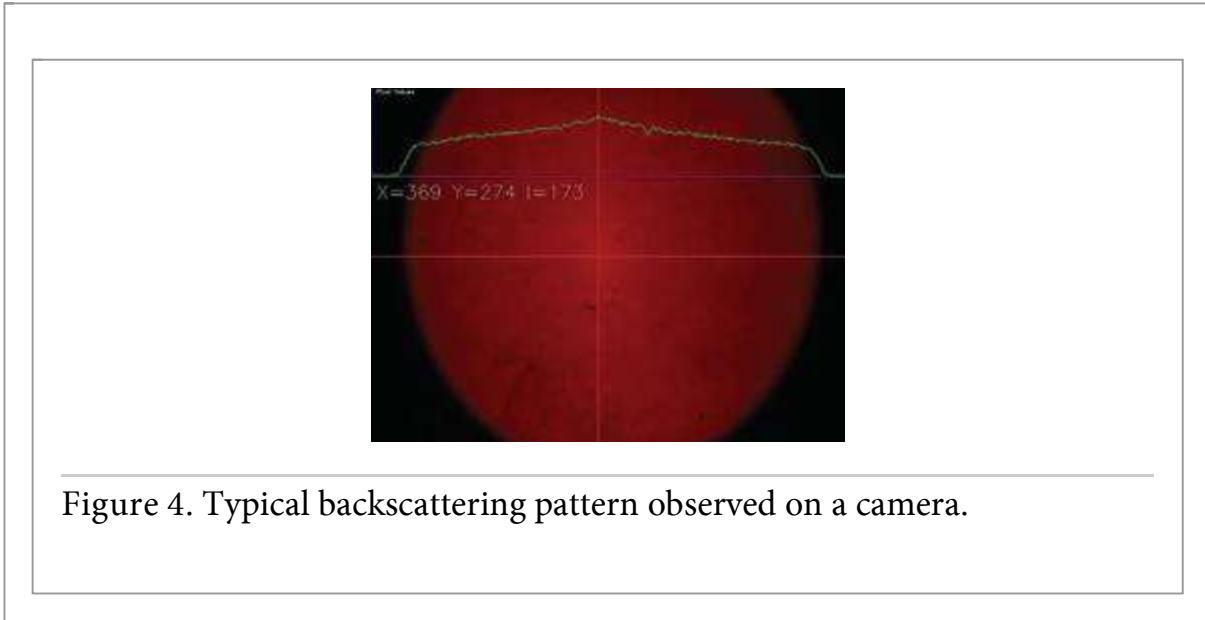


Figure 3. Experimental realization of a zoom system for detection of backscattered radiation.

It was necessary to correct the detected intensities for Fresnel losses inside the optical system preceding the CCD chip. This was done by replacing the scattering sample with a mirror. Its angular position was controlled by a motorized rotation stage. Thus, we were able to record correspondence between the angle of incidence and the detected intensity. This was further used to correct the backscattering measurement results.

We observed and measured the backscattering cones (both wide and narrow) of a range of samples: milk, skin, Teflon, barium sulfate, artificial photonic structures, butterfly and moth wings, etc. A typical backscattering pattern is shown in figure 4.



conclusions

We have described, constructed and tested a zoom system for backscattered radiation detection. It was used to observe both wide and narrow backscattering cones of various biological and artificial samples. The system is easy to construct and use, under the condition that ghost reflections are eliminated.

Acknowledgments

We express our gratitude to the Serbian Ministry of Education and Science for supporting this work through grant numbers III45016 and ON171038.

References

1. Iersma D S, van Albada M P and Agendij A 1995 *Rev. Sci. Instrum.* 5473
CrossRef <http://dx.doi.org/10.103/1.114071>
2. Gross P, Strer M, Iebig S, Lausen M, Maret G and Aegerter M 2007 *Rev. Sci. Instrum.* 033105
CrossRef <http://dx.doi.org/10.103/1.2712943>

Export references:

BibTeX

RIS

R d

R A AR E

herent bacscattering of turbid samples containing large Mie spheres

bservation of coherent bacscattering factor of three in a numerical experiment

ow to mae the 'real image' more real

omparison of the 'glory' with coherent bacscattering of light in turbidmedia

bservation of coherent bacscattering of light by coldatoms

lux conservation in coherent bacscattering and wea localiation of light

Localization of Light in Photonic Crystals of Biological Origin

Svetlana Savić-Šević¹, Dejan Pantelić¹, Dušan Grujić¹, Branislav Jelenković^{1*}, Srećko Ćurčić²,
Božidar Ćurčić², Dejan Stojanović³

¹*Institute of Physics, University of Belgrade, Pregrevica 118, 11080 Zemun, Belgrade, Serbia*

²*Institute of Zoology, Faculty of Biology, University of Belgrade, Studentski Trg 16, 11000 Belgrade, Serbia*

³*Fruška Gora National Park, Zmajev Trg 1, 21208 Sremska Kamenica, Serbia*

*Corresponding author's e-mail: branaj@ipb.ac.rs

ABSTRACT

Structures similar to those found on butterfly wings were produced holographically on thin layers of dichromated pullulan. Light propagation and scattering is studied in these nanometre periodic structures, and in the wings of Lepidoptera (moths and butterflies). We have found that the width of photonic band-gaps in each case is influenced by light localization (either weak or strong), due to certain amount of disorder. We have also measured experimentally characteristics of backscatter signal (amplitude and angular width) on wings of *Apatura ilia* butterfly as well as on *Diachrysia chrysitis* and *Autographa bractea* noctuid moths. It was found that both spectral and scattering characteristics of the artificial material could mimic those found in butterflies and moths.

1. INTRODUCTION

Photonic structures are frequently found in living organisms, especially in insects [1]. The evolution produces intricate patterns which generate iridescent coloration by physical mechanisms like interference, diffraction or scattering. The final result is better adaptation of an organism to its environment through crypsis, aposematism or mimicry.

Photonic crystals introduce photonic band-gap, thus significantly altering spectral properties of the material. It was thought that high refractive index modulation is a necessary condition for achievement of wide band gaps. However, disorder in photonic crystals significantly widens the band gap even for materials with low refractive index. Indeed, insects are an excellent example of such behavior – the refractive index of insect chitin (the main constituent of integument) is rather low (of the order of 1.5), but the band-gap can be rather wide, as in *Morpho* butterflies [2].

Disordered photonic crystals are an interesting research topic, due to interesting possibility of weak or strong (Anderson) light localization [3]. In that respect measurement of coherent backscattering is important as it gives information on the mean free path of light [4]. This enables estimation of the fulfilment of Ioffe-Regel criterion ($k \cdot l < 1$ where k is wave-number and l is mean free path) as a border between strong and weak localization.

We have previously analyzed optics and biological significance of nanometer size structures on the wings of *Apatura ilia* (Denis & Schiffermüller, 1775) and *A. iris* (Linnaeus, 1758) butterflies [5]. In the present paper we intend to investigate the contribution of backscattering and localization to overall optical properties of *Apatura ilia* and two interesting species of moths (*Autographa bractea* (Denis & Schiffermüller, 1775) and *Diachrysia chrysitis* (Linnaeus, 1758)).

Apatura ilia butterfly is an interesting insect whose wings show, angularly and spectrally rather limited, UV-purple iridescence (Fig. 1a). On the other hand *Autographa bractea* and *Diachrysia chrysitis* are moths exhibiting patches with golden color (Figs. 2a and 3a). We have measured their wide backscattering cones which are very close to Ioffe-Regel criterion, but still in the weak localization zone.

2. EXPERIMENTAL SETUP

We have built a setup for measurement of backscattered radiation. Unpolarized HeNe laser (633 nm wavelength) was used as a light source. Laser beam was transmitted through a combination of a linear polarizer and a quarter-wave plate in order to produce circularly polarized light. The sample was irradiated and observed through non-polarizing beam-splitter. A second wave plate and linear polarizer were placed in scattered beam. Condenser was used to efficiently couple the scattered radiation into entrance pupil of a camera (Canon EOS 50D with zoom objective 17-85 mm). In this way we were able to observe backscattering cone with different magnifications and resolution.

We used milk and Teflon (PTFE) for calibration purposes as it is known that they possess a narrow backscattering peak (bellow the resolution of our camera at low magnification) and behaves as Lambert scatterer (Fig. 4a). Barium sulphate reflectance standard was also used as a material with wide backscattering cone (see Fig. 4b), due to short mean free path.



Figure 1: a) *Apatura ilia* butterfly; b) *A. ilia* backscattering cone.



Figure 2: a) *Diachrysia chrysitis*; b) *D. chrysitis* backscattering cone



Figure 3: a) *Autographa bractea*; b) *A. bractea* backscattering cone.

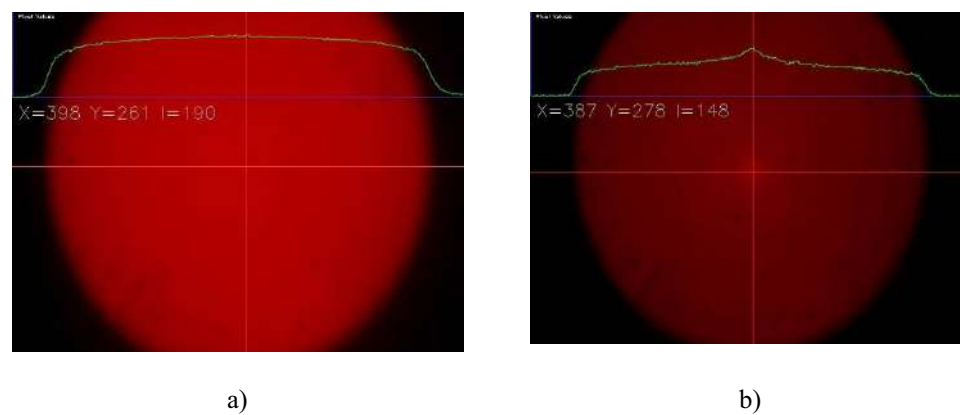


Figure 4. Backscattering cone of: a) milk, b) barium sulphate ($BaSO_4$).

We have found that the backscattering cone of *Apatura ilia* and *Diachrysia chrysitis* (Figs. 1b and 2b) is significantly wider compared to barium-sulphate (see Fig. 5). By fitting experimental results to theory we have found that the mean free path is approximately 200 nm (In terms of Ioffe-Regel criterion $k l$ product is 2), in

contrast to 400 nm for barium sulphate, which is the same as in the case of *Autographa bractea* (Figs. 3b and 4b). As can be seen, for *A. ilia* and *D. chrysis* scattering is quite close to Anderson localization.

This seems to be consistent with the anatomy of scales which cover wings of lepidoptera. Photonic structures are a combination of volume Bragg and surface relief grating and examination under scanning electron microscope reveals numerous defects and disorder [6]. Judging by the width of backscattering cone and mean free path, light is “expelled” from the butterfly wings for two reasons: band-gap produced by regular structures and weak localization due to disorder.

In order to mimic structure of butterfly scales we used volume holography to generate Bragg gratings and direct laser writing to superpose surface relief grating. Dichromated pullulan was used as a photosensitive material. Depending on exposure and chemical processing we are able to manufacture photonic structures whose color ranges from purple to golden, just like in previously described insects. Scattering properties artificial material are almost the same as in insects.

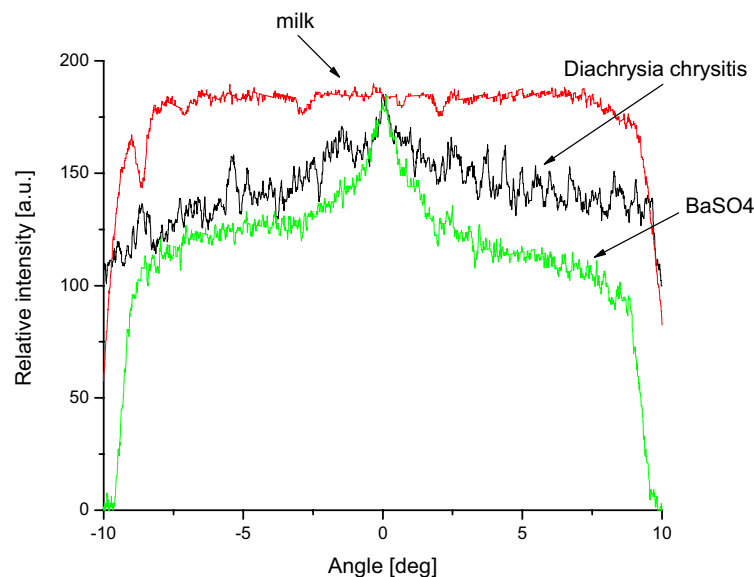


Figure 5. Comparison of backscattering cones of milk (identical to teflon), barium sulphate and *Diachrysis chrysis*.

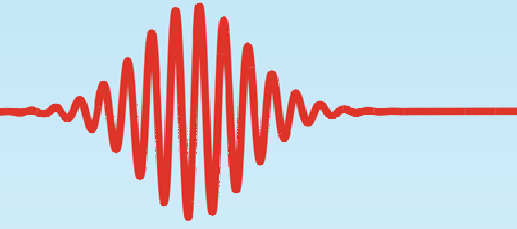
3. CONCLUSIONS

We have measured the coherent backscattering on the wings of three insects exhibiting iridescent coloration. The width of backscattering cone indicates that the mean free path of light is rather short (between 200 and 400 nm depending on the species). It looks that the interplay between band-gap and localization results in characteristic color of insects. We have succeeded in mimicking biological structures using holography.

REFERENCES

- [1] S. Berthier, *Iridescences – The Physical Colors of Insects*, (2007) Springer Science + Business Media, LLC
- [2] S. Yoshioka, S. Kinoshita, Wavelength-selective and anisotropic light-diffusing scale on the wing of the *Morpho* butterfly, *Proc. R. Soc. Lond. B*, 271 (2004), p. 581-587
- [3] T. Schwartz, G. Bartal, S. Fishman, M. Segev, Transport and Anderson localization in disordered two-dimensional photonic lattices, *Nature*, 446 (2007), p. 52–55
- [4] D. S. Wiersma, P. Bartolini, A. Lagendijk, R. Righini, Localization of light in a disordered medium, *Nature*, 390 (1997), p. 671 - 673
- [5] D. Pantelić, S. Čurčić, S. Savić-Šević, A. Korać, A. Kovačević, B. Čurčić, B. Bokić, High angular and spectral selectivity of Purple Emperor (*Lepidoptera*: *Apatura iris* and *A. ilia*) butterfly wings, *Opt. Express* 19, (2011) p. 5817-5826
- [6] S. B. Čurčić, D. V. Pantelić, B. P.M. Čurčić, S. N. Savić-Šević, S. E. Makarov, V. B. Lačković, M. M. Labudović-Borović, N. B. Čurčić, D. V. Stojanović, Micro- and nanostructures of iridescent wing scales in purple emperor butterflies (*Lepidoptera*: *Apatura ilia* and *A. iris*), to be published in *Microscopy Research and Technique*, DOI: 10.1002/jemt.22021.

UNO-4



4th International Workshop on Ultrafast Nanooptics

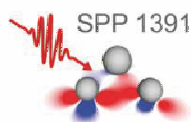
collocated with

**COST Action MP1403 - Nanoscale Quantum Optics - Work Group Meeting
Nonlinearities and Ultrafast Processes in Nanostructured Media**



October 18-22, 2015

Bad Dürkheim



Scope and Aim

We cordially welcome you in Bad Dürkheim to the *4th International Workshop on Ultrafast Nanooptics (UNO-4)* collocated with the regular Meeting of Work Group 2 on *Nonlinearities and Ultrafast Processes in Nanostructured Media* of the COST Action MP1403 on *Nanoscale Quantum Optics*. In addition, this workshop serves as the final meeting of the DFG priority program 1391 *Ultrafast Nanooptics* and will follow the successful previous versions of this international workshop.

The aim of *Ultrafast Nanooptics* is the combination of nanooptics and ultrafast laser spectroscopy, a rapidly evolving field in physics and neighboring disciplines. As in the past, this workshop is dedicated to facilitate the exchange of knowledge between the two up to now rather separate fields of research and shall stimulate the interaction of different groups working in these research areas. 11 invited speaker together with 23 contributed talks and 25 posters will present and discuss the recent advances in this emerging fields. Topics will cover both theoretical and experimental aspects of nonlinearities and ultrafast processes in plasmonic nanostructures.

The COST action MP1403 on *Nanoscale Quantum Optics* serves as European platform to enhance networking and research collaboration in the rapidly evolving field of quantum nanooptics that has substantial overlap with the topics covered in the UNO workshop series. Actually, half of the workshop is dedicated to the COST work group meeting on *Nonlinearities and Ultrafast Processes in Nanostructured Media*.

The image shows two handwritten signatures in black ink. The signature on the left is 'W. Pfeiffer' and the signature on the right is 'M. Aeschlimann'. Both are written in a cursive, flowing style.

Walter Pfeiffer and Martin Aeschlimann

Workshop Program

Sunday, October 18, 2015

17:00 – 21:00 Arrival and Registration at Bad Dürkheim Kurpark-Hotel
from 19:00 *SOCIAL GATHERING AND BUFFET SUPPER*

Monday, October 19, 2015

7:45 *BREAKFAST*

8:50 **Opening remarks**

Session 1

9:00 Martin Aeschlimann
(University of Kaiserslautern, Germany)
Priority program 1391 on Ultrafast Nanooptics - Résumé

9:25 Walter Pfeiffer
(Bielefeld University, Germany)
**Future developments and information about the
COST action 1403 on Nanoscale Quantum Optics**

9:50 *F. Süßmann, L. Seiffert, S. Zherebtsov, V. Mondes, J. Stierle,
M. Arbeiter, J. Plenge, P. Rupp, C. Peltz, A. Kessel, S. A. Trushin,
B. Ahn, D. Kim, C. Graf, E. Rühl, M.F. Kling, T. Fennel*
(MPI Garching, LMU Munich, Univ. Rostock, FU Berlin, Germany &
POSTECH Pohang, Korea)
**Field propagation-induced directionality of CEP-controlled
photoemission from nanospheres**

10:15 *COFFEE BREAK*

Session 2

11:00 Mark I. Stockman – invited
(Georgia State University, USA)
**Condensed matter in ultrafast and
superstrong fields: attosecond phenomena**

11:50 Lara Wimmer, Georg Herink, Oliver Karnbach,
Sergey Yalunin, Claus Ropers
(University of Göttingen, Germany)
THz near-field streaking at metal nanotips

Monday, October 19, 2015

12:15 *S. H. Chew, A. Gliserin, J. Schmidt, S. Nobis, H. Bian, E. Krauss, P. Geisler, F. Schertz, M. Kübel, B. Hecht, U. Kleineberg*
(LMU Munich, Univ. Würzburg, Surface-Concept GmbH, Germany)

Laser intensity effects in carrier-envelope phase-tagged time of flight-photoemission electron microscopy

12:30 LUNCH

Session 3

14:00 *Ulrich Höfer - invited*
(University of Marburg, Germany)

Ultrafast dynamics of electrons in topological surface and metal/organic interface states

14:50 *D. Kilbane, A. K. Mahro, S. Mathias, G. Spektor, L. Gal, M. Orenstein, B. Frank, S. Ristock, H. Giessen, F. Meyer zu Heringdorf, M. Aeschlimann*
(Univ. Kaiserslautern, Univ. Stuttgart, Univ. Duisburg-Essen, Germany & Technion, Israel)

Near-field imaging of the dynamics of plasmonic vortices

15:15 COFFEE BREAK

Session 4

16:00 *Daniel Podbiel, Philip Kahl, Bettina Frank, Harald Giessen, Frank Meyer zu Heringdorf*
(Univ. Stuttgart, Univ. Duisburg-Essen, Germany)

Plasmoemission: emission of electrons in a strong plasmonic field

16:25 *Carsten Reinhardt, Tobias Birr, Tim Fischer, Urs Zywiets, Boris Chichkov*
(Laser Zentrum Hannover e.V., Germany)

Ultrafast interactions of surface plasmon polaritons

16:50 *E. Oesterschulze, C. Gonzalez, M. Hartelt, D. Bayer, E. Ilin, M. Aeschlimann*
(Univ. Kaiserslautern, Germany)

Mie scattering probe for polarization resolved investigation of surface plasmons

Monday, October 19, 2015

- 17:15 *Ralf Vogelgesang, Martin Esmann, Simon F. Becker, KyungWan Yoo, Heiko Kollmann, Jan Vogelsang, Jörg Robin, Benedek J. Nagy, Péter Dombi, Daniel Rosenkranz, Manuela Schiek, Petra Groß, NamKyoo Park, Christoph Lienau*
(Univ. Oldenburg, Germany & Seoul Nat. Univ., Korea & Wigner Res. Centr., Hungary)
Plasmonic nanofocusing: Gap plasmons, light scattering spectroscopy and electron generation
- 17:40 **Poster Session**
- 19:00 DINNER
- 21:00 **Informal Discussion**

Tuesday, October 20, 2015

7:45 BREAKFAST

Session 5

9:00 Hayk Harutyunyan - invited
(Emory University, USA)
Controlling the generation of hot electrons in hybrid plasmonic nanostructures

9:50 Heiko Linnenbank, Yevgen Grynko, Jens Förstner, Stefan Linden
(Univ. Bonn, Univ. Stuttgart, Univ. Paderborn, Germany)
Ultrafast nonlinear response of hybrid dielectric/plasmonic nanoantennas

10:15 COFFEE BREAK

Session 6

11:00 Melanie Müller, Lutz Waldecker, Roman Bertoni, Thomas Vasileiadis, Vasily Kravtsov, Markus Raschke, Alexander Paarmann,
Ralph Ernstorfer - invited
(FHI Berlin, Germany & University of Colorado, USA)
Photocurrents and structural dynamics in nanomaterials probed by femtosecond electron pulses

11:50 J. Kern, A. Trügler, I. Niehues, J. Ewering, R. Schmidt,
R. Schneider, S. Najmaei, A. George, J. Zhang, J. Lou,
U. Hohenester, S. Michaelis de Vasconcellos, R. Bratschitsch
(Univ. Münster, Germany & Univ. Graz, Austria & Rice University, USA)
Nanoantenna-enhanced light-matter interaction of atomically thin WS₂

12:15 Dominik Differt, Matthias Hensen, Walter Pfeiffer
(Bielefeld University, Germany)
Time reversal versus adaptive optimization for spatiotemporal nanolocalization in a random nanoantenna

12:40 LUNCH

Session 7

14:00 Shinya Koshihara - invited, Keiki Fukumoto, Ken Onda
(Tokyo Institute of Technology, JST-CREST, KEK, JST-PRESTO, Japan)
Visualization of ultrafast electron dynamics using time-resolved photoemission electron microscopy

Tuesday, October 20, 2015

- 14:50 *Thomas Pertsch, Carsten Rockstuhl*
(Univ. Jena, KIT, Germany)
**Nonlinear optical nano-antennas and nano-resonators
from Lithium Niobate**
- 15:15 *Alfred J. Meixner, Anke Horneber, Frank Wackenhut, Xiao Wang
and Dai Zhang*
(University of Tübingen, Germany)
**Interplay of plasmon and exciton decay excited
by ultrashort laserpulses**
- 15:40 *Malte Großmann, Alwin Klick, Christoph Lemke, Ahnaf Zillohu,
Jacek Fiotowski, Jacob Kjelstrup-Hansen, Mady Elbahri, Franz Faupel,
Horst-Günter Rubahn, and Michael Bauer*
(University of Kiel, Germany & Univ. of Southern Denmark, Denmark)
**Light-triggered Control of Plasmonic Refraction and Group Delay by
Photochromic Molecular Switches**
- 16:30 EXCURSION
- 19:00 DINNER
- 21:00 **Informal Discussion**

Wednesday, October 21, 2015

07:45 *BREAKFAST*

Session 8

8:50 Opening Remarks:
COST action MP 1403 – Nanoscale Quantum Optics - WG2 Meeting
Nonlinearities and Ultrafast Processes in Nanostructured Media

9:00 Steven Cundiff - *invited*
(University of Michigan, USA)
Two Dimensional Coherent Spectroscopy of Epitaxial Quantum Dots

9:50 Markus Krecik, Marten Richter
(TU Berlin, Germany)
Proposal of using nanoplasmonics and coherent two-dimensional spectroscopy to dissect secular and non secular relaxation processes

10:15 COFFEE BREAK

Session 9

11:00 Giulio Cerullo - *invited*
(Politecnico di Milano, Italy)
Tracking ultrafast energy flow in plasmonic nanostructures

11:50 Markus Betz
(TU Dortmund, Germany)
Active plasmonics with surface acoustic waves

12:15 Polina Lisinetskaya, Roland Mitric
(University of Würzburg, Germany)
Simulation and control of light propagation in ultrasmall noble-metal cluster arrays

12:40 LUNCH

Session 10

14:00 Javier García de Abajo - *invited*
(ICFO-Institut de Ciències Fòniques, Spain)
Graphene plasmonics

14:50 Harald Giessen, Bettina Frank, Simon Ristok, Liwei Fu,
Grisha Spektor, Philip Kahl, Frank Meyer zu Heringdorf,
Deirdre Kilbane, Martin Aeschlimann
(Univ. Stuttgart, Univ. Duisburg-Essen, Univ. Kaiserslautern, Germany)
Short-range surface plasmonics and its (sub-)femtosecond dynamics

Wednesday, October 21, 2015

15:15 COFFEE BREAK

Session 11

- 16:00 Stephen K. Gray - invited
(Argonne National Laboratory, USA)
Optically-Induced Entanglement in Hybrid Quantum Dot/Plasmonic Systems
- 16:50 Alberto Comin, Richard Ciesielski, Alexander Bouhelier, Achim Hartschuh
(LMU München, Germany & Univ. de Bourgogne, France)
Coherent control in single plasmonic nanostructures
- 17:15 Daniela Wolf, Thorsten Schumacher, Markus Lippitz
(University of Bayreuth, Germany)
Shaping the nonlinear near-field
- 17:40 **Poster Session**
- 19:00 *DINNER*
- 21:00 **COST: Work Group 2 Discussion**

Thursday, October 22, 2015

07:45 *BREAKFAST*

Session 12

9:00 *M. Ethis de Corny, N. Chauvet, L. Olgeirsson, S. Waterman, M. Jeannin, G. Nogues, S. Huant, A. Bouhelier, J. Sharma, E. Dujardin, G. Bachelier - invited*

(Univ. Joseph Fourier, Univ. Bourgogne, CEMES - CNRS, France)

Nonlinear responses in plasmonic nanostructures

9:50 *Jeremy Butet, Kuang-Yu Yang, Gabriel Bernasconi, Olivier J. F. Martin*
(EPFL, Switzerland)

Second harmonic generation in plasmonic nanostructures: multiresonant nanoantennas and eigenmodes

10:15 *COFFEE BREAK*

Session 13

11:00 *Thomas Durt - invited*

(Institut Fresnel, Ecole Centrale de Marseille, France)

The photon wave function: a bridge from Maxwell to Schroedinger, and beyond

11:50 *Martin Aeschlimann, Tobias Brixner, Benjamin Frisch, Bert Hecht, Bernhard Huber, Matthias Hensen, Christian Kramer, Enno Krauss, Walter Pfeiffer, Martin Piecuch, Philip Thielen*

(Univ. Kaiserslautern, Univ. Würzburg, Bielefeld Univ., Germany)

Coherent and long-range plasmon-assisted energy transfer between two plasmonic nanoantennas

12:15 *Armin Feist, Katharina E. Echternkamp, Jakob Schauss, Sergey V. Yalunin, Sascha Schäfer, Claus Ropers*

(University of Göttingen, Germany)

Coherent electron-light interaction in an ultrafast electron microscope

12:40 *Closing Remarks*

13:00 *LUNCH*

END OF WORKSHOP and WORK GROUP MEETING / DEPARTURE

Program Overview

4 th International Workshop on Ultrafast Nanooptics				
COST MP1403 – WG2 Meeting – Nonlinearities and Ultrafast Processes				
Time	Sunday	Monday 19.10.	Tuesday 20.10.	Wednesday 21.10.
8:50		Opening Remarks		Thursday 22.10
9:00		M. Aeschlimann SPP Résumé	H. Harutyunyan Emory Univ., USA	G. Bachelier Institute Néel, France
9:25		W. Pfeiffer Developments & COST-1403	<i>Hot electrons in hybrid nanostructures</i>	<i>Nonlinear Response in nanostructures</i>
9:50		L. Seiffert Univ. Rostock, Germany	H. Linnenbank Univ. Bonn, Germany	J. Butet EPFL, Switzerland
10:15		Coffee Break	Coffee Break	
11:00		M. I. Stockman Georgia State Univ., USA	R. Ernstorfer FHI, Germany	T. Durt Institute Fresnel, France
		<i>Attosecond phenomena</i>	<i>Dynamics probed by fs electron pulses</i>	<i>The photon wave function</i>
11:50		L. Wimmer Univ. Göttingen, Germany	I. Niehues Univ. Münster, Germany	M. Hensen Bielefeld Univ., Germany
12:15		S. H. Chew LMU Munich, Germany	W. Pfeiffer Bielefeld Univ., Germany	K. Echterkamp Univ. Göttingen, Germany
12:40		Lunch	Lunch	Lunch
14:00		U. Höfer Univ. Marburg, Germany	S. Koshihara Tokyo Inst. Tech., Japan	Departure
		<i>Dynamics in topological states</i>	<i>Visualization of electron dynamics</i>	
14:50		D. Kilbane Univ. Kaiserslautern, Germany	T. Pertsch Univ. Jena, Germany	
15:15		Coffee break	A. Meixner Univ. Tübingen, Germany	
16:00		F. Meyer zu Heringdorf Univ. Duisburg, G.	M. Bauer Univ. Kiel, Germany	
16:25		C. Reinhardt LZH, Germany	Excursion	
16:50		E. Oesterschulze Univ. Kaiserslautern, Ger.		
17:15		R. Vogelgesang Univ. Oldenburg, Germany		
17:40		Poster Session		Poster Session
18:00	Arrival and Registration			
19:00	Buffet Supper	Dinner	Dinner	Dinner
		Informal discussion	Informal discussion	20:00 COST: Work group discussion

Abstracts of oral Presentations *(in chronological order)*

Field propagation-induced directionality of CEP-controlled photoemission from nanospheres

F. Süßmann^{1,2}, L. Seiffert⁷, S. Zherebtsov^{1,2}, V. Mondes³, J. Stierle¹, M. Arbeiter⁷, J. Plenge³,
P. Rupp^{1,2}, C. Peltz⁷, A. Kessel¹, S.A. Trushin¹, B. Ahn^{4,5}, D. Kim^{4,5}, C. Graf³,
E. Rühl³, M.F. Kling^{1,2,4,6}, and T. Fennel⁷

¹ *Max-Planck Institut für Quantenoptik, D-85748 Garching, Germany*

² *Physik Department, Ludwig-Maximilians-Universität München, D-85749 Garching, Germany*

³ *Physical Chemistry, Freie Universität Berlin, D-14195 Berlin, Germany*

⁴ *Physics Department, POSTECH, Pohang, Kyungbuk 790-784, Republic of Korea*

⁵ *Max Planck Center for Attosecond Science, Pohang, Kyungbuk 790-784, Republic of Korea*

⁶ *J.R. Macdonald Laboratory, Physics Department, Kansas-State University, Manhattan, KS, USA*

⁷ *Institut für Physik, Universität Rostock, D-18059 Rostock, Germany*

Near-fields of non-resonantly laser-excited nanostructures enable strong localization of ultrashort light fields and have opened novel routes to fundamentally modify and control electronic strong-field processes [1, 2]. Harnessing spatiotemporally tunable near-fields for the steering of sub-cycle electron dynamics may enable ultrafast optoelectronic devices and unprecedented control in the generation of attosecond electron and photon pulses. Here we utilize unsupported sub-wavelength dielectric nanospheres to generate near-fields with adjustable structure and study the resulting strong-field dynamics via photoelectron imaging [3]. We demonstrate field propagation induced tunability of the emission direction of fast recollision electrons up to a regime, where non-linear charge interaction effects become dominant in the acceleration process. Our analysis supports that the timing of the recollision process remains controllable with attosecond resolution by the carrier-envelope phase, indicating the possibility to expand near-field mediated control far into the realm of high-field phenomena.

[1] M. Krüger et al., *Nature* **475**, 78-81 (2011)

[2] S. Zherebtsov et al., *Nature Phys.* **7**, 656-662 (2011)

[3] F. Süßmann et al., *Nat. Commun.* **6**, 7944 (2015)

Condensed matter in ultrafast and superstrong fields: attosecond phenomena

Mark I. Stockman

Center for Nano-Optics, Georgia State University, 29 Peachtree Center Ave, Atlanta, GA 30303, USA

We present a new class of phenomena in condensed matter optics when a strong optical field $\sim 1-3$ V/Å adiabatically (reversibly) changes a solid within optical cycle [1-7]. Such a pulse drives ampere-scale currents in dielectrics and controls their properties, including optical absorption and reflection, extreme UV absorption, and generation of high harmonics [8] in a non-perturbative manner on a 100-as temporal scale. Applied to a metal, such a pulse causes an instantaneous and reversible loss of the metallic properties. We will also discuss our latest theoretical results on graphene that in a strong ultrashort pulse exhibits unique behavior [9, 10]. New phenomena are predicted for buckled two-dimensional solids, silicene and germanine [11]. These are fastest phenomena in optics unfolding within half period of light. They offer potential for petahertz-bandwidth signal processing, generation of high harmonics on a nanometer spatial scale, etc.

- [1] M. Durach et al., Phys. Rev. Lett. **105**, 086803 (2010).
- [2] M. Durach et al., Phys. Rev. Lett. **107**, 086602 (2011).
- [3] A. Schiffrin et al., Nature 493, **70** (2013).
- [4] M. Schultze et al., Nature 493, **75** (2013).
- [5] V. Apalkov, and M. I. Stockman, Phys. Rev. B **88**, 245438 (2013).
- [6] V. Apalkov, and M. I. Stockman, Phys. Rev. B **86**, 165118 (2012).
- [7] F. Krausz, and M. I. Stockman, Nat. Phot. **8**, 205 (2014).
- [8] T. Higuchi, M. I. Stockman, and P. Hommelhoff, Phys. Rev. Lett. **113**, 213901 (2014).
- [9] H. K. Keldar, V. Apalkov, and M. I. Stockman, Phys. Rev. B **90**, 085313 (2014).
- [10] H. K. Keldar, V. Apalkov, and M. I. Stockman, Phys. Rev. B **91**, 045439 (2015).
- [11] H. K. Keldar, V. Apalkov, and M. I. Stockman, Phys. Rev. B **92**, 045413 (2015).

THz near-field streaking at metal nanotips

Lara Wimmer, Georg Herink, Oliver Karnbach, Sergey Yalunin, Claus Ropers

IV. Physical Institute, Georg-August University Göttingen, Friedrich-Hund-Platz 1, 37077 Göttingen

We present a streaking experiment at single metal nanotips with ultrashort terahertz (THz) transients and femtosecond near-infrared (NIR) pulses. The photoelectrons are emitted by the NIR pulses and accelerated in the THz-induced near-field at the tip apex. The high localization and enhancement of the THz near-field allow for a direct mapping of the near-field strength onto the electron kinetic energy. The characteristic parameters of the near-field are determined by numerical simulations.

Laser intensity effects in carrier-envelope phase-tagged time of flight-photoemission electron microscopy

S. H. Chew¹, A. Gliserin¹, J. Schmidt¹, S. Nobis¹, H. Bian¹, E. Krauss², P. Geisler²,
F. Schertz³, M. Kübel¹, B. Hecht², U. Kleineberg¹

¹ *Faculty of Physics, Ludwig-Maximilians-Universität München, 85748 Garching, Germany*

² *Nano-Optics and Biophotonics Group, Experimentelle Physik 5, Physikalisches Institut,
Universität Würzburg, Würzburg D-97074, Germany*

³ *Surface Concept GmbH, Staudingerweg 7, 55128 Mainz, Germany*

A time of flight-photoemission electron microscope is combined with a single-shot stereographic above-threshold ionization phase meter for studying attosecond control of electrons in tailored plasmonic nanostructures spatially and energetically via a carrier-envelope phase tagging technique. Recent carrier-envelope phase-resolved measurements of gold nanoparticles on gold plane and surface roughness from a gold film show an apparent carrier-envelope phase modulation with a period of π . This modulation is found to originate from an intensity dependence of the photoelectron spectra and the carrier-envelope phase measurement rather than from an intrinsic carrier-envelope phase dependence, which is supported by a correlation of this modulation with intensity fluctuations of our laser on a time scale of hundreds of milliseconds to seconds. We suggest intensity tagging should be taken into account in future phase-tagged experiments in order to detect small CEP-dependence from supported nanostructures.

Ultrafast dynamics of electrons in topological surface and metal/organic interface states

Ulrich Höfer

Department of Physics, Philipps University of Marburg, Germany

Electron transfer processes at surfaces and interfaces play a crucial role in diverse fields of materials sciences. In this talk I will discuss surfaces of three-dimensional topological insulators and interfaces between metals and organic semiconductors. Time-resolved two-photon photoemission (2PPE), a method that combines femtosecond pump-probe techniques with photoelectron spectroscopy, can provide detailed information about the ultrafast dynamics of electrons excited into surface and interface-specific states of these systems. For investigations of metal/organic interfaces, PTCDA/Ag(111) has proven to be an excellent model system. It will be shown that the interface state, located between the Fermi level of the metal and the molecular LUMO of this and related systems, can efficiently mediate the electron transfer between the metal and the organic semiconductor. Three-dimensional topological insulators belong to a new class of materials which are characterized by an insulating bulk and a metallic topological surface state (TSS). The most remarkable properties of the TSS are its Dirac-cone-like energy dispersion and its chiral spin texture in k space which incorporates a protection against electron backscattering. It will be shown that mid-infrared pump pulses permit a direct excitation of the unoccupied TSS of Sb_2Te_3 across the Dirac point. The optical coupling leads to an asymmetric transient population of the TSS in momentum space which in turn reflects a macroscopic electric surface current. By observing the decay of the asymmetric population with time-delayed UV probe pulses, we directly access the dynamics of the long-lived photocurrent and its topologically protected property.

Near-field imaging of the dynamics of plasmonic vortices

D. Kilbane¹, A. K. Mahro¹, S. Mathias¹, G. Spektor², L. Gal², M. Orenstein², B. Frank³, S. Ristock³,
H. Giessen³, F. Meyer zu Heringdorf⁴, M. Aeschlimann¹

¹ *Physics Department and Research Centre OPTIMAS, University of Kaiserslautern, Germany*

² *Department of Electrical Engineering, Technion, Haifa, Israel*

³ *Fourth Physics Institute and Research Center SCoPE, University of Stuttgart, Germany*

⁴ *Faculty of Physics and CENIDE, University of Duisburg-Essen, Germany*

Depending on the spin angular momentum of circularly polarized light, and the geometry of the illuminated metallic structure we can shape plasmonic near fields to form a vortex - a rotational flow around a phase singularity [1]. By combining interferometric time-resolved two photon photoemission and photoemission electron microscopy (ITR-2PPE PEEM) [2,3] we perform near-field imaging of plasmonic vortices. A broadband ultrashort pulse laser excites and probes the plasmonic dynamics with 100 as time step and 40 nm spatial resolution. Here we observe the spatiotemporal evolution of vortices in plasmonic Archimedes spirals (PAS) and vortex lenses (PVL).

- [1] C.-D. Ku, W.-L. Huang, J.-S. Huang and C.-B. Huang, *IEEE Photon. J.* **5** 4800409 (2013)
- [2] A. Kubo, K. Onda, H. Petek, Z. Sun, Y. S. Jung and H. K. Kim, *Nano Lett.* **5** 1123 (2005)
- [3] M. Bauer, C. Wiemann, J. Lange, D. Bayer, M. Rohmer and M. Aeschlimann, *Appl. Phys. A* **88** 473 (2007)

Plasmoemission: emission of electrons in a strong plasmonic field

Daniel Podbiel¹, Philip Kahl¹, Bettina Frank², Harald Giessen², Frank Meyer zu Heringdorf¹

¹ *Faculty of Physics and CENIDE, University of Duisburg-Essen, 47048 Duisburg, Germany*

² *4th Physics Institute and Research Center SCoPE, University of Stuttgart, 70550 Stuttgart, Germany*

Observing surface plasmon polaritons (SPPs) in a photoemission electronmicroscope (PEEM) is possible via nonlinear photoemission if ultra-short laser pulses (<20fs) of a suitable wavelength are directed onto the surface of a plasmonic material. We study the time-resolved propagation and interaction of SPPs by means of a direct conceptual visualization of the SPPs in a "normal incidence geometry". This experimental setup allows us to observe transient phenomena that exist for only a few femtoseconds during the coherent interaction of the ultrashort SPP pulses. In focusing structures for SPPs we find an unexpected time-signature of the nonlinear photoemission signal at the focus point that must be explained by emission of electrons from the SPP alone. The energy distribution of these 'plasmoelectrons' shows that the SPP fields are sufficiently high to make nonlinear photoemission pathways of higher orders the dominant contribution to the PEEM signal.

Ultrafast interactions of surface plasmon polaritons

Carsten Reinhardt, Tobias Birr, Tim Fischer, Urs Zywietz, Boris Chichkov

Laser Zentrum Hannover e.V., Hollerithallee 8, 30419 Hannover, Germany

We present studies on ultrafast interactions of multiple coherently excited surface plasmon-polaritons (SPPs) and light beams in nanoparticle and waveguiding systems and on plane metal films. SPPs are excited by local scattering of laser light on surface nanostructures consisting of polymeric or metallic ridges, grooves, and nanoparticles. SPP interaction and scattering effects are investigated by temporally resolved leakage radiation microscopy. The interference of SPPs inside dielectrically-loaded SPP waveguides as well as the interference of SPPs with additional light fields is used for tracking the propagation of ultrashort SPP pulses excited by 60 fs laser pulses at a central wavelength of 800 nm. We demonstrate ultrafast scattering of propagating SPPs on regions of metal films pumped by additional laser pulses. In a time-delay pump-probe experiment it is shown that this SPP scattering occurs on the time scale of the pulse duration. Additionally, the interactions of coherently excited SPPs and light beams in complex dielectric waveguides and with laser printed isolated spherical metallic or silicon nanoparticles are demonstrated. Coherent control of SPP and light interactions further allows for the construction of ultrafast low-power SPP switches, transistors, and all-optical gate structures. Results on cascading of these plasmonic elements are presented and an all-plasmonic half adder is demonstrated.

Mie scattering probe for polarization resolved investigation of surface plasmons

E. Oesterschulze¹, C. Gonzalez², M. Hartelt², D. Bayer², E. Ilin¹, M. Aeschlimann²

¹ *University of Kaiserslautern, Physics and Technology of Nanostructures, Physics Department,
Erwin Schrödinger Strasse 46, D-67663 Kaiserslautern*

² *University of Kaiserslautern, Department of Physics and Research Center OPTIMAS,
Erwin Schrödinger Strasse 46, D-67663 Kaiserslautern*

We present a cantilever based near field probe with integrated Mie scattering dielectric silicon dioxide microsphere (MSDM) for near-field optical imaging as well as femtosecond spectroscopy applications. In contrast to the state of the art transmissive near-field probes, the MSDM reveals a transmission of almost unity known from far-field microscopy configuration. For proper handling the microsphere is integrated at the apex of a conventional pyramidal aperture tip carried by an atomic force microscopy cantilever. It proved to be mechanically robust during the scanning process even if operating it in the contact mode. The spherical symmetry provides on one hand a well defined mechanical contact point with the sample irrespective of its inclination angle to the sample surface. On the other hand, the symmetry of the device preserves the polarization of light proving to be useful for the investigation of the polarization dependent behavior of plasmonic nanostructures. The device has also shown to be able to be an excellent tool for the study of surface plasmons on Au thin films when measuring the dispersion relation of SPPs, bringing results with an excellent agreement with similar experiments performed with PEEM. The high transmission combined with low dispersion renders spectroscopic investigations on the femtosecond time scale with a moderate lateral resolution. Moreover, second autocorrelation experiments on a BBO-crystal reveals a time resolution well below 100fs at 190nm spatial resolution.

Plasmonic nanofocusing: Gap plasmons, light scattering spectroscopy and electron generation

Ralf Vogelgesang¹, Martin Esmann¹, Simon F. Becker¹, KyungWan Yoo^{1,2}, Heiko Kollmann¹,
Jan Vogelsang¹, Jörg Robin¹, Benedek J. Nagy³, Péter Dombi³, Daniel Rosenkranz¹,
Manuela Schiek¹, Petra Groß¹, NamKyoo Park², Christoph Lienau¹

¹ Carl von Ossietzky Universität, Oldenburg, Germany

² Seoul National University, Seoul, Korea

³ Wigner Research Centre for Physics, 1121 Budapest, Hungary

Apertureless scattering-type scanning near-field optical microscopy (SNOM) conventionally operates with some form of modulation and demodulation technique to eliminate the overwhelmingly strong far-field optical signal background. Such an approach renders SNOM *spectroscopy* a relatively slow, serial measurement technique. To establish parallel, multi-channel SNOM spectroscopy, a very promising approach is the concept of nanofocusing in single crystalline metallic tapers [1,2]. Surface plasmon polaritons are excited on a grating coupler and result in strongly confined near-fields at the taper apex without much background excitation of surrounding volumes.

We apply nanofocusing SNOM to spectrally resolve the field distribution around individual plasmonic rod antennas. An AFM image of chemically grown rods is acquired simultaneously with maps of the intensity scattered in different wavelength intervals. These maps exhibit a pronounced intensity pattern with spatially confined minima at the rod ends.

Initial characterization of the SNOM taper was done by measuring optical transmission approach curves over a gold film in combination with a k -space imaging technique [3]. At very small tip-sample separation the transmitted intensity sharply increases. Numerical simulations attribute this feature to the formation of an intense gap-mode between tip and sample, which is laterally confined to a length scale proportional to the geometric mean of the gap separation and the effective apex radius [4]. Hence, this extremely short ranged interaction has the potential to further improve the spectroscopic imaging resolution of nanofocusing SNOM down to the single nanometer regime.

Finally, we present photoelectron emission from the apex of a gold taper illuminated with few-cycle near-infrared laser pulses [5]. Compared to direct apex illumination, we find a fifty-fold increase in electron yield. Point-projection microscopic imaging of Ag-nanowires is performed and spatial localization of the electron emission to a nanometer-sized region is demonstrated.

References

- [1] M.I. Stockman, PRL **93**, 137404 (2004).
- [2] S. Schmidt et al., ACS Nano **6**, 6040 (2012).
- [3] M. Esmann et al., BJ Nano **4**, 603 (2013).
- [4] P. Johansson, PRB **58**, 10823 (1998).
- [5] J. Vogelsang, et al., Nano Lett., **15**, 4685 (2015)

Controlling the generation of hot electrons in hybrid plasmonic nanostructures

Hayk Harutyunyan

Department of Physics, Emory University, 400 Dowman Dr, Atlanta, GA 30322, USA

The interaction of light and matter in noble metal nanosystems is governed by the collective oscillation of their conduction electrons, called surface plasmons. After excitation, these resonances experience ultrafast damping through radiative and non-radiative losses, i.e. absorption. The latter occurs through coupling to electronic inter- and intraband transitions in the metal, creating a highly non-thermal distribution of hot electrons. The electron population then decays through electron–electron interactions, creating thermalized hot electron distribution within a few hundred femtoseconds, followed by a further relaxation via electron–phonon scattering on the timescale of a few picoseconds. In the spectral domain, these processes can be observed by tracking the changes of the plasmonic resonance of the nanostructure due to the modification of the dielectric constant of the metal at different timescales. In this talk I will discuss strategies of enhancing hot electron generation in plasmonic hot spots and will show how their ultrafast response can be controlled both in temporal and spectral domain. I will present our recent results on hot electron generation in metal/oxide nanostructures and show how the geometry, the composition of the nanostructure and the excitation wavelength can drastically influence the ultrafast dynamics. The ability to enhance and control the generation of energetic electrons through specifically designed plasmonic nanostructures can be used in applications where hot electron generation is beneficial, such as in solar photocatalysis, photodetectors and nonlinear devices.

Ultrafast nonlinear response of hybrid dielectric/plasmonic nanoantennas

Heiko Linnenbank¹, Yevgen Grynko², Jens Förstner³, Stefan Linden¹

¹ *Physikalisches Institut Universität Bonn, Nußallee 12, Bonn, Germany*

² *Physikalisches Institut Universität Stuttgart, Pfaffenwaldring 57, Stuttgart, Germany*

³ *FG Theoretische Elektrotechnik Universität Paderborn, Warburger Straße 100, Paderborn, Germany*

An important goal of the project “Ultrafast nonlinear optical response of metallic nanostructures: Collective effects and hybrid materials” is to boost the intrinsic nonlinear response of dielectric nanoparticles by employing the huge local field enhancement inherent to plasmonic nanostructures. To characterize the nonlinear response of the hybrid structures consisting of metallic nanoantennas and dielectric nanoparticles the technique of second harmonic generation spectroscopy is employed. For this purpose a frequency tunable femtosecond light source is developed. This light source is based on optical parametric generation and amplification with a double-pass geometry in a single macroscopic lithium niobate crystal. The device delivers more than two watts of tunable near-infrared radiation at 42 MHz repetition rate with pulse durations down to 200 fs. By combining the results of linear extinction measurements and SHG spectroscopy it is revealed that an increase of the SHG efficiency of plasmonic nanoantennas is obtained by filling their feed gaps with a dielectric nanoparticle. However, this enhancement of the SHG signal is independent of the nonlinear properties of the dielectric nanoparticles. Our experiments show that the intrinsic nonlinear response of plasmonic nanoantennas is several orders of magnitude higher than that of nonlinear dielectric nanoparticles and can be further boosted by employing double resonant nanoantenna geometries. To gain a deeper understanding of double resonant plasmonic nanostructures, plasmonic nanostructures are investigated which are resonant for the second harmonic light only. We observe an enhancement of the second harmonic efficiency even in the absence of resonances for the pump light. This property can be understood in the framework of the anharmonic oscillator model. Furthermore this study indicates that the general symmetry selection rules for second harmonic generation can be also applied to plasmonic nanostructures.

Photocurrents and structural dynamics in nanomaterials probed by femtosecond electron pulses

Melanie Müller¹, Lutz Waldecker¹, Roman Bertoni¹, Thomas Vasileiadis¹, Vasily Kravtsov²,
Markus Raschke², Alexander Paarmann¹, Ralph Ernstorfer¹

¹ *Fritz-Haber-Institut, Faradaweg 4-6, 14195 Berlin, Germany*

² *University of Colorado, Boulder, USA*

We report a novel concept for femtosecond point-projection microscopy (fsPPM) and femtosecond low-energy electron diffraction (fsLEED) utilizing laser-triggered electron emission from metal nanotips as pulsed electron source, delivering either divergent or collimated femtosecond single-electron wave packets in the sub-kV energy range. Due to the large scattering cross-section of low-energy electrons and their high sensitivity to electric fields, such electrons represent sensitive probes for the investigation of ultrafast currents and electric fields in nanoobjects as well as of atomic structure in low-dimensional materials with femtosecond time resolution. We demonstrate the visualization of ultrafast photo-induced currents in III-V semiconductor nanowires [1]. To further advance the temporal and spatial resolution in fsPPM, we realized plasmon-driven sub-10 femtosecond electron emission from a gold nanotip as femtosecond electron point source. Electron emission is triggered by the optical near field at the tip apex after laser excitation and subsequent nanofocusing of a surface plasmon polariton [2]. Structural dynamics in nanoscale materials, in particular few-layer semiconducting transition metal dichalcogenides and gold nanoparticles, are investigated with femtosecond transmission electron diffraction [3].

- [1] M. Müller et al., *Nature Communications* **5**, 5292 (2014).
- [2] S. Berweger et al., *J. Phys. Chem. Lett.* **3**, 945 (2012).
- [3] L. Waldecker et al., *J. Appl. Phys.* **117**, 044903 (2015).

Nanoantenna-enhanced light-matter interaction of atomically thin WS₂

J. Kern¹, A. Trügler², I. Niehues¹, J. Ewering¹, R. Schmidt¹, R. Schneider¹, S. Najmaei³, A. George³, J. Zhang³, J. Lou³, U. Hohenester², S. Michaelis de Vasconcellos¹, R. Bratschitsch¹

¹ *Institute of Physics and Center for Nanotechnology, University of Münster, 48149 Münster, Germany*

² *Institute of Physics, University of Graz, 8010 Graz, Austria*

³ *Department of Mechanical Engineering and Material Science, Rice University, Houston, Texas 77005, USA*

Atomically-thin transition metal dichalcogenides (TMDCs) are promising two-dimensional materials for optical and opto-electronic devices, because they exhibit an optical band gap in the visible regime. Monolayers absorb more than 10% of the light at their excitonic resonance and show photoluminescence. However, the absorption length of TMDC monolayers is extremely short and the photoluminescence quantum yield of 10^{-3} is low. Therefore, strategies are needed to optimize the light-matter interaction. We present a hybrid system consisting of a plasmonic nanoantenna and atomically-thin WS₂ layer [1]. The antennas are single-crystalline gold nanorods, functionalized by a molecular layer. The nanorods are drop-cast onto a monolayer of tungsten disulphide (WS₂), which was grown by chemical vapor deposition (CVD) on SiO₂/Si substrate. Whereas the PL emission from the WS₂ monolayer alone shows no polarization dependence and is homogenous across the flake, a clear enhancement is observed at the position of the nanoantennas. By matching both excitation and emission polarization an overall PL enhancement of up to 11 is observed. The fact that the PL intensity strongly depends on the excitation as well as emission polarization indicates that absorption as well as emission are increased. This effect is due to the enhanced optical near-field created by the longitudinal plasmon resonance of the nanoantenna. The tailored hybrid nanoantenna-monolayer system lights the way to efficient photodetectors, solar cells, light emitting and conceptually new valleytronic devices based on two-dimensional materials.

- [1] J. Kern, A. Trügler, I. Niehues, J. Ewering, R. Schmidt, R. Schneider, S. Najmaei, A. George, J. Zhang, J. Lou, U. Hohenester, S. Michaelis de Vasconcellos, and R. Bratschitsch, *ACS Photonics* **2**, 1260 (2015).

Time reversal versus adaptive optimization for spatiotemporal nanolocalization in a random nanoantenna

Dominik Differt, Matthias Hensen, Walter Pfeiffer

Fakultät für Physik, Universität Bielefeld, Universitätsstr. 25, 33615 Bielefeld, Germany

Spatiotemporal nanolocalization of ultrashort pulses in a random scattering nanostructure via time reversal and adaptive optimization is studied for two positions separated by only a tenth of the wavelength. The nanostructure is composed of core-shell nanoparticles placed randomly surrounding the target positions. The time reversal scheme achieves selective nanolocalization only by chance if the incident radiation can couple efficiently to dipolar local modes interacting with the target/emitter particle. Even embedding the structure in a reverberation chamber fails improving the nanolocalization. In contrast, the adaptive optimization reliably yields nanolocalization of the radiation and allows a highly selective excitation of either target position. This demonstrates that random scattering structures are interesting multi-purpose optical nanoantennas to realize highly flexible spatiotemporal optical near-field control.

Visualization of ultrafast electron dynamics using time-resolved photoemission electron microscopy

Shinya Koshihara¹, Keiki Fukumoto², Ken Onda³

¹ *Tokyo Institute of Technology*

² *Tokyo Institute of Technology, JST-CREST and KEK, JAPAN*

³ *Tokyo Institute of Technology and JST-PRESTO*

We constructed a TR-PEEM with 180fs and 90nm time and spatial resolutions, respectively. This compact facility makes possible to directly image the photo-generated electron dynamics in semiconductor on nm and fs scales. Carrier transport properties relating to device performance, carrier lifetime, drift velocity and mobility, are investigated.

Nonlinear optical nano-antennas and nano-resonators from Lithium Niobate

Thomas Pertsch¹, Carsten Rockstuhl²

¹ *Institute of Applied Physics, Abbe Center of Photonics, Friedrich-Schiller-Universität Jena,
Max-Wien-Platz 1, 07743 Jena, Germany*

² *Institute of Theoretical Solid State Physics, Institute of Nanotechnology, Karlsruhe Institute of Technology,
Wolfgang-Gaede-Strasse 1, 76131 Karlsruhe, Germany*

The notion of nano-antennas has altered our perception how to tame light. In most cases, nano-antennas are made from metallic structures to induce a resonant response at one or multiple wavelengths while being able to enhance light-matter-interactions. Here, we exploit nano-antennas to enhance the nonlinear optical response. For this purpose, the nano-antennas are in most cases supported by LiNbO₃; being a strong $\chi^{(2)}$ -nonlinear material. To harvest the potential of optical nanoantennas, it is required to have means at hand to tune their optical response. On the one hand, quantifying the response in terms of multipole moments allows to tailor how the nano-antenna scatters light. On the other hand, the near field enhancement and the efficient conversion of energy at multiple wavelengths are other criteria. In this contribution, we demonstrate the applicability of such methodology, both in theory and experiment, to study optical nano-antennas that enhance the nonlinear response from LiNbO₃. For this purpose, isolated metallic nano-antennas are of interest whose geometry is tuned. We also consider nano-antennas to be embedded into an optical environment that enforces their optical response. An example is the surrounding of an electric dipolar nanoantennas with an annular metallic grating. Here, the grating serves to enhance the local field in the central antenna. In the cause of time it has been appreciated that optical nano-resonators can be also made directly from LiNbO₃. The material possesses a high permittivity, which allows inducing strong resonances in spherical or cylindrical objects. Moreover, periodically patterning the material at length scales comparable to the wavelength allows to take advantage of multiply coherently scattered light. This enables the exploitation of photonic crystal effects to observe a notable nonlinear response. An overview across our activities in the last years in the context of this stream of research will be presented.

Interplay of plasmon and exciton decay excited by ultrashort laser pulses

Alfred J. Meixner, Anke Horneber, Frank Wackenhut, Xiao Wang and Dai Zhang

Institute of Physical and Theoretical Chemistry, University of Tübingen, Germany

Gold nanostructures (or nanoantennas) exhibit usually strong plasmon resonances, depending on their geometry and on the coupling of particles which influence significantly their emission properties. While scattering of coupled plasmonic systems has been in the focus during the last years studies of the photoluminescence (PL) emission of gold nanostructures excited by ultrashort laser pulses depends also on band-structure of these materials is by far less common. We will report on our recent studies aiming at a deeper insight the interplay between plasmons and excitons of gold nanostructures. In particular, we have investigated the linear and non-linear PL emission from various plasmonic systems like nanoparticles, sharp tips and nanotriangles [1-3] excited with radially or azimuthally polarized 100 fs laser pulses in combination with either diffraction limited confocal optical microscopy or tip enhanced scanning near-field optical microscopy.

- [1] P. Reichenbach, A. Horneber, D. A. Gollmer, A. Hille, J. Mihaljevic, C. Schäfer, D. P. Kern, A. J. Meixner, D. Zhang, M. Fleischer and L. M. Eng, “Nonlinear optical point light sources through field enhancement at metallic nanocones,” *Opt. Express* **22**, 15484 (2014).
- [2] A. Horneber, A. L. Baudrion, P. M Adam, A. J. Meixner and D. Zhang, “Compositional-asymmetry influenced non-linear optical processes of plasmonic nanoparticle dimers,” *Physical chemistry chemical physics : PCCP* **15**, 8031 (2013).
- [3] A. Horneber, K. Braun, J. Rogalski, P. Leiderer, A. J. Meixner and D. Zhang, “Nonlinear optical imaging of single plasmonic nanoparticles with 30 nm resolution,” *PCCP* **17**, 21288 (2015).

Light-triggered Control of Plasmonic Refraction and Group Delay by Photochromic Molecular Switches

Malte Großmann¹, Alwin Klick¹, Christoph Lemke¹, Ahnaf Zillohu², Jacek Fiutowski³,
Jacob Kjelstrup-Hansen³, Mady Elbahri², Franz Faupel²,
Horst-Günter Rubahn³, and Michael Bauer¹

¹ *Institute for Experimental and Applied Physics, University of Kiel, Germany*

² *Faculty of Engineering, NanoSYD, University of Kiel, Germany*

³ *Mads Clausen Institute, NanoSYD, University of Southern Denmark, Denmark*

Photochromic molecules have been successfully used in the past to achieve reversible control of optical transmission [1] and plasmonic damping [2] at metal-dielectric interfaces. In this paper we provide experimental evidence that in the same manner also the propagation of surface plasmon polaritons (SPP) can be steered. Switchable metal-dielectric interfaces are prepared from a gold substrate coated with polystyrene films doped with spiropyrans. Changes in the SPP dispersion relation at illumination with light of different wavelength are measured using photoemission electron microscopy [3] evidencing a substantial and reversible switching of SPP group and phase velocity [4]. The results imply the realization of nonvolatile plasmonic switching units providing new and complex functionalities. Based on this concept we realize a switchable plasmonic lens as a first demonstrator for potential applications. Reversible focus control is experimentally demonstrated yielding changes of about 5% of the total focal length.

- [1] M. Jamali, M. Keshavarz Hedayati, B. Mozooni, M. Javaherirahim, R. Abdelaziz, A. Usman Zillohu, M. Elbahri, *Adv. Materials* **23** (2011), 4243.
- [2] R.A. Pala, K.T. Shimizu, N.A. Melosh, M.L. Brongersma, *Nano Letters* **8** (2008), 1506.
- [3] C. Lemke, T. Leißner, A. Klick, J. Fiutowski, J. W. Radke, M. Thomaschewski, J. Kjelstrup-Hansen, H.-G. Rubahn, M. Bauer, *Appl. Phys. B* **116** (2013), 585.
- [4] M. Großmann, A. Klick, C. Lemke, J. Falke, M. Black, J. Fiutowski, A. Goszczak, E. Sobolewska, A. Usman Zillohu, M. Keshavarz Hedayati, H.-G. Rubahn, F. Faupel, M. Elbahri, and M. Bauer, *ACS Photonics* **2**, (2015), 1327.

Two Dimensional Coherent Spectroscopy of Epitaxial Quantum Dots

Steven Cundiff

University of Michigan, 450 Church St., Ann Arbor, MI USA

Two-dimensional coherent spectroscopy has the ability to make size resolved measurements in an inhomogeneously broadened ensemble of nano-objects where the inhomogeneous distribution of resonance energies arises from the size fluctuations of the objects [1]. This ability results from correlating the frequencies during two time periods, via a two-dimensional Fourier transform. This concept will be used to make measurements on “natural” quantum dots, which occur in thin quantum wells due to intrinsic well-width fluctuations, and used to measure the size the dependence of the exciton-phonon and exciton-exciton interaction [2]. It will then be used to study InAs self-organized quantum dots, which display biexcitonic side bands. The results show that the biexciton binding energy appears to be independent of dots size within the inhomogeneous distribution, whereas single dot studies showed significant variation. By using a pre-pulse to coherently prepare the ensemble, clear Rabi oscillations are observed for the individual size groups. The results show that both ground-state to excitation and excitation to biexciton Rabi oscillations are occurring simultaneously due the use of broadband pulses.

- [1] S.T Cundiff, J. Opt. Soc. Am. B **29**, A69-A81 (2012).
- [2] G. Moody, M.E. Siemens, A.D. Bristow, X. Dai, D. Karaiskaj, A.S. Bracker, D. Gammon, S.T. Cundiff, Phys. Rev. B **83**, 115324 (2011).
- [3] G. Moody, R. Singh, H. Li, I.A. Akimov, M. Bayer, D. Reuter, A.D. Wieck, A.S. Bracker, D. Gammon, S.T. Cundiff, Phys. Rev. B , 041304(R) (2013).

Proposal of using nanoplasmonics and coherent two-dimensional spectroscopy to dissect secular and non secular relaxation processes

Markus Krecik, Marten Richter

*Institut für Theoretische Physik, Nichtlineare Optik und Quantenelektronik, Technische Universität Berlin,
Hardenbergstr. 36 EW 7-1, 10623 Berlin, Germany*

Relaxation or coherence conversion caused by system bath interaction, like electron-phonon interaction, is often described sufficiently by secular processes and the Markovian approximation. Only conversion processes, where the involved excitonic populations or coherences are nearly resonant, are included in secular processes. For many treatments, non-secular process can be often neglected. However interesting Non-Markovian signatures potentially involve secular as well as non secular processes. The dissection and study of non secular and secular processes is routinely carried out in theory, however the identification of a pure non secular experimental observable was pending. This is especially important for testing various Non-Markovian theories. We suggest an experimental signal, which we includes only contributions from non secular processes in an idealized case. We use a combination of coherent spectroscopy and nanoplasmonics to detect non secular relaxation processes in a quantum dot. The optical pulses at the quantum dot are dynamically controlled by the nanoplasmonic structure, to have either a vanishing field or field gradient at the quantum dot position. This results in a control of optical selection rules, which we use to detect Liouville pathways including only non secular processes with coherent spectroscopy. This will open the door to study and test nonsecular processes in experiments against e.g. elevated Non-Markovian theories. Furthermore we also discuss the robustness of the protocol to error in the dynamical control of optical selection rules.

Tracking ultrafast energy flow in plasmonic nanostructures

Giulio Cerullo

*Dipartimento di Fisica, Politecnico di Milano, Piazza L. da Vinci 32, 20133 Milano, Italy
IFN-CNR, Italy*

A very recent novel branch of plasmonics is aimed at the investigation of the nonlinear optical phenomena taking place in metal nanostructures (NS), and which can be exploited for a new generation of devices with application to all-optical switching and sensing. To address the challenging task of designing such nonlinear nanoplasmonic devices, it is necessary to quantitatively understand and model the nonlinear optical phenomena taking place on the ultrafast timescale in metallic NS, which occur on a hierarchy of timescales, ranging from tens of fs to hundreds of ps. An ultrashort pump pulse impinging on the NS excites free electrons in a non-thermal distribution, with an excess energy per unit volume that is subsequently rapidly released, by electron–electron scattering, to the thermalized electronic population, heating it up to a higher temperature. Subsequently, electron–phonon scattering causes the electronic gas to cool down and the lattice to increase its temperature, until a long-living equilibrium temperature is achieved. A much slower phonon–phonon scattering process causes the excess energy originally delivered to the nano-object to flow into the environment. If the timescale of the lattice heating is much shorter than the period of mechanical vibrational modes of the NS, coherent oscillations can be launched which modulate the extinction of the nanostructure. The period and damping of these oscillations provide information on the geometrical properties, the speed of sound and the Young modulus at the nanoscale. This presentation will introduce several examples of ultrafast spectroscopy of metal nanostructures, from thin films to metal-dielectric heterostructures, individual colloidal and lithographed nanoparticles finally and self-assembled supracrystals.

Active plasmonics with surface acoustic waves

Markus Betz

Experimentelle Physik 2, TU Dortmund, Germany

In my talk, I will discuss the impact of coherent surface acoustic waves (SAWs) on plasmonic devices. These high-frequency mechanical distortions can be driven all-electrically using conventional radio-frequency electronics. In a first step, we demonstrate a SAW driven converter of light into surface plasmon polaritons. In essence, an otherwise unstructured metal thin film is deformed by surface-bound acoustic waves traveling on a piezoelectric substrate underneath. This spatially periodic corrugation enables to overcome the wavevector mismatch between free-space radiation and surface-bound electro-magnetic modes. This concept is demonstrated for gold thin films on a LiNbO₃ chip. In particular, interdigital transducers generate ~500 MHz surface acoustic waves of ~1 nm surface ripple on the substrate and the deposited metal film. For near-infrared light of 950 nm wavelength we observe a 0.01% efficiency for the excitation of surface plasmon polaritons. As a next step, we explore the influence of radio-frequency SAWs travelling across a commensurable, static gold grating. Such a structure constitutes a paradigm for a pre-defined injector for surface plasmon polaritons. Here, the electro-mechanically induced, dynamic surface deformation strongly modulates the launcher's coupling characteristics on sub-nanosecond timescales. The modulation of the efficiency is as large as 2% and is monitored in real time with a stroboscopic technique utilizing SAWs synchronized to an optical pulse train.

Simulation and control of light propagation in ultrasmall noble-metal cluster arrays

Polina Lisinetskaya, Roland Mitric

Julius-Maximilians Universität Würzburg, Sanderring 2, Würzburg, Germany

We present a theoretical approach for simulation of light propagation in nanosized noble-metal cluster arrays. Within the approach the array is represented by a Hamiltonian with the coupling elements calculated based on transition dipole moments for arrays with well-separated subunits and transition charges in the opposite case. The proposed approach is applied to simulation of absorption spectra and electron dynamics in Ag^{3+} arrays and in porphyrin-based Ag^4 arrays. Additionally, a possibility of optimal control of light propagation in a T-shaped structure consisting of ultrasmall silver clusters is investigated.

Graphene plasmonics

Javier García de Abajo

*ICFO-Institut de Ciències Fotoniques, The Barcelona Institute of Science and Technology,
08870 Castelldefels (Barcelona), Spain*

Graphene plasmons have recently attracted much attention because of their excellent electrical tunability and extreme sub-wavelength confinement, which enable applications such as fast light modulation, improved biosensing, and quantum optics in robust solid-state environments. In this presentation, we review recent theoretical and experimental advances in these directions and explore further possibilities, such as sensing at the single-molecule level, electrical detection of single plasmons, and ultrafast transient plasmonic phenomena.

Short-range surface plasmonics and its (sub-)femtosecond dynamics

Harald Giessen¹, Bettina Frank¹, Simon Ristok¹, Liwei Fu¹, Grisha Spektor², Philip Kahl³,
Frank Meyer zu Heringdorf³, Deirdre Kilbane⁴, Martin Aeschlimann⁴

¹ *4th Physics Institute and Research Center SCoPE, University of Stuttgart, Germany*

² *Technion, Haifa, Israel*

³ *Department of Physics, University of Duisburg-Essen, Germany*

⁴ *Department of Physics, Technical University of Kaiserslautern, Germany*

We use single crystalline gold flakes on atomically flat silicon substrates to generate ideally suitable metals for plasmon propagation. By electrochemical means, the thickness is tunable from a few tens to over 100 nm. Using sub-20 fs laser pulses around 800 nm, we excite surface plasmons, whose dynamics can be observed using time-resolved two-photon excitation electron emission (PEEM).

Plotting the dispersion of surface plasmons in a thin gold slab on silicon, one finds that excitation at 800 nm can lead to extreme wavelength reduction due to the dispersion slope of over five. Using focused ion beam for cutting rings with appropriate periodicity into the samples (see left image), we can excite concentric surface plasmons that create a nanofocus of only 60 nm width for 800 nm excitation. Using Archimedean spirals with broken n-fold radial symmetry, it is possible to excite surface plasmons with angular orbital momentum on the gold flakes. This leads in case of 4-fold symmetry to cloverleaf-type nanofoci on the order of 100 nm, which rotate during four optical cycles by 360 degrees.

Using two-pulse experiments with a subwavelength-stabilized Michelson interferometer, it is possible to observe the dynamics of the surface patterns with a (sub-)femtosecond resolution, thus giving insight into the dynamics of the nanofocus formation as well as on the plasmonic spin-orbit coupling.

Optically-Induced Entanglement in Hybrid Quantum Dot/Plasmonic Systems

Stephen K. Gray

Center for Nanoscale Materials, Argonne National Laboratory, Argonne, Illinois 60439, USA

Quantum dynamics calculations are carried out on model Hamiltonians corresponding two, three, and four quantum dot systems interacting with a dissipative, plasmonic system that is subjected to ultrafast laser pulses. We show how the pulses can be used to create multiple entanglements among the dots from an initially cold systems.

Coherent control in single plasmonic nanostructures

Alberto Comin¹, Richard Ciesielski¹, Alexander Bouhelier², Achim Hartschuh¹

¹ *Ludwig-Maximilians-Universitaet Muenchen Department Chemie and CeNS*

² *Laboratoire Interdisciplinaire Carnot de Bourgogne, CNRS UMR 6303,
Université de Bourgogne, Dijon 21078, France*

In this contribution we present a new way to visualise coherent control of plasmonic resonances in single metal nanostructures with sub-diffraction dimensions. The approach makes use of the extremely high localisation accuracy that can be achieved in far-field nanoscopy. Here we apply it to the detection of the position of the second harmonic generation (SHG) and non-linear photoluminescence from gold nanostructures. Due to the high signal levels and their temporal stability the center-of-mass of these signals can be tracked with sub-nanometer resolution. We demonstrate that the center-of-mass can be controlled within a single nanostructure by chirping the spectral phase of the excitation pulse. We attribute this to the control of the interference of plasmonic resonances with different spatial profiles within the laser spectrum.

Shaping the nonlinear near-field

Daniela Wolf, Thorsten Schumacher, Markus Lippitz

Experimental Physics III, University of Bayreuth, Universitaetsstrasse 30, D-95440 Bayreuth, Germany

Linear scattering and absorption of plasmonic nanoparticles and their assemblies have led to a wealth of application in metamaterials and nanooptics. Almost any desired field distribution can be realized by well-chosen arrangements of multiple particles. While the shaping of fields around nanostructures is widely studied, the influence of the field inside nanostructures is often overlooked. The linear field distribution inside the structure taken to the third power causes third-harmonic generation, a nonlinear optical response of matter. Here we demonstrate how this simple fact can be used to shape complex fields around already a single particle alone. We employ this scheme to switch the third-harmonic emission from a single point source to two spatially separated but coherent sources, as in Young's double slit assembly. We envision applications as diverse as coherently feeding antenna arrays or optical circuits and optical spectroscopy of spatially extended electronic states.

Nonlinear responses in plasmonic nanostructures

M. Ethis de Corny¹, N. Chauvet¹, L. Olgeirsson¹, S. Waterman¹, M. Jeannin¹, G. Nogues¹, S. Huant¹, A. Bouhelier², J. Sharma³, E. Dujardin³, G. Bachelier¹

¹ *Institut Néel, CNRS – Université Joseph Fourier, 25 rue des Martyrs, Grenoble, France*

² *LICB, CNRS – Université de Bourgogne, 9 Av. A. Savary, Dijon, France*

³ *CEMES, CNRS, 29 Rue Jeanne Marvig, Toulouse, France*

Transferring the concepts of nonlinear optics down to the nanoscale is highly desirable for practical applications, but it suffers from the intrinsic weakness of the nonlinear responses. In this context, plasmonics is foreseen to play a major role thanks to the associated field enhancement and spatial tailoring of the near-field maps. For example, two photon luminescence (TPL) has been widely used at the single particle level to infer the field localization at the nanoscale, becoming a key tool for investigating the plasmonic antennas. Thought, as we have recently demonstrated, this technique fails in providing a clear view on another popular nonlinear response, the second harmonic generation (SHG). Using a specific particle geometry (a gold nanoprism with a triangular base) we will evidence the main differences between SHG and TPL but also between the two mechanisms involved in the SHG process. In addition, we will discuss different strategies to enhance the nonlinear efficiency and show how double resonance condition (resonance at the fundamental and the harmonic frequency) can be achieved using aluminum nanostructures. We will present our latest results obtained on a new experimental and simulation platform we have developed at the Néel Institute.

Second harmonic generation in plasmonic nanostructures: multiresonant nanoantennas and eigenmodes

Jeremy Butet, Kuang-Yu Yang, Gabriel Bernasconi, Olivier J. F. Martin

*Nanophotonics and Metrology Laboratory (NAM), Swiss Federal Institute of Technology Lausanne (EPFL),
1015, Lausanne, Switzerland*

During this presentation, we provide a full understanding of the mechanisms that lead to SHG in multiresonant plasmonic structures. By combining experiments on aluminum plasmonic nanostructures with surface integral equation simulations, we have investigated the SHG modulation from double resonant nanoantennas (DRAs) with a broad variety of geometries emphasizing the role played by the mode coupling in the nonlinear conversion enhancement. In a second part, we will show that SHG can also provide information on the underlying modes supported by a given plasmonic nanostructure. Indeed, a combination of modes at the fundamental frequency can generate SH waves supported by modes that cannot be excited at the fundamental frequency, the so called dark modes. SHG can then be used to measure the radiation pattern of those dark modes. If the fundamental frequency matches a resonance of the structure, the high field enhancement will yield a high SHG. Additionally, if the SH frequency matches another higher frequency mode, the SH emission will be stronger and thus more easily measurable as in the case of the DRAS. This will be very useful for the design of practical applications as nonlinear plasmonic sensing.

The Photon Wave Function: a bridge from Maxwell to Schroedinger, and beyond

Thomas Durt

*Institu Fresnel, Ecole Centrale de Marseille, France
COST 1403: WG leader: Coherence at the Nanoscale.*

When few photons are present, the photon wave function is a useful tool for understanding as well as exploring the predictions of QED. In certain circumstances (for instance when the state of light is coherent in the sense of Glauber), it is formally nearly equivalent to a classical, Maxwell field, but in other circumstances it exhibits a surprising behaviour. For instance, during the process of spontaneous emission of light by an excited atom, the photon wave function slightly violates Einsteinian causality, in accordance with Hegerfeldt's theorem. Our goal is to give an overview of these topics, and to discuss related departures from the Fermi golden rule that were never observed so far but constitute an exciting challenge for experimentalists.

Coherent and long-range plasmon-assisted energy transfer between two plasmonic nanoantennas

Martin Aeschlimann¹, Tobias Brixner^{2,3}, Benjamin Frisch¹, Bert Hecht⁴,
Bernhard Huber^{2,3}, Matthias Hensen⁵, Christian Kramer^{2,3}, Enno Krauss⁴,
Walter Pfeiffer⁵, Martin Piccuch¹, Philip Thielen^{1,7}

¹ *Fachbereich Physik and Research Center OPTIMAS, University of Kaiserslautern,
Erwin-Schrödinger-Str. 46, 67663 Kaiserslautern, Germany*

² *Institut für Physikalische und Theoretische Chemie, Universität Würzburg, Am Hubland, 97074 Würzburg, Germany*

³ *Röntgen Research Center for Complex Material Systems (RCCM), Universität Würzburg,
Am Hubland, 97074 Würzburg, Germany*

⁴ *Nano-Optics and Bio-Photonics Group, Department of Experimental Physics 5, Universität Würzburg,
Am Hubland 97074 Würzburg, Germany*

⁵ *Fakultät für Physik, Universität Bielefeld, Universitätsstr. 25, 33615 Bielefeld, Germany*

⁷ *Graduate School of Excellence Materials Science in Mainz,
Gottlieb-Daimler-Str. 47, 67663 Kaiserslautern, Germany*

Short-range coherent energy transfer dynamics e.g. in light harvesting complexes and their implications from a control systems perspective has been discussed vividly. Here, the long-range energy transfer mechanism between two coupled plasmonic whispering gallery nanoantennas [1] in an elliptical cavity [2] is investigated by optical excitation with (shaped) sequences of ultrashort pulses centered at 800 nm. Only one gold antenna is excited selectively when the structure is illuminated under grazing incidence. Plasmon-enhanced time-resolved photoemission microscopy [3] detected at both nano-antennas reveals periodic energy transfer on a micrometer length scale in the hybridized antenna-cavity system. Exposing single quantum emitters to the antenna-induced field enhancement these systems might serve for future applications involving weak, or even strong, interaction of well-separated single quantum systems.

[1] E. J. R. Vesseur et al., *Nano Lett.* **9**, 3147-3150 (2009)

[2] D. T. Schoen et al., *Nano Lett.* **13**, 188-193 (2013)

[3] M. Aeschlimann et al., *Science* **333**, 1723-1726 (2011)

Coherent electron-light interaction in an ultrafast electron microscope

Armin Feist, Katharina E. Echternkamp, Jakob Schauss, Sergey V. Yalunin,
Sascha Schäfer, Claus Ropers

4th Physical Institute - Solids and Nanostructures, Friedrich-Hund-Platz 1, 37077 Göttingen, Germany

We implemented the first ultrafast transmission electron microscope (UTEM) [1] based on a laser pump/electron probe technique that operates with a nanoscale laser-driven photocathode. Here, we employ the advanced beam properties of the UTEM to study quantum coherent electron-light interactions. In our experiments, a tightly focused, pulsed electron beam traverses the optically excited near-field of a nanostructure. The spatial confinement of the near-field allows for an otherwise forbidden coupling between the free electrons and photons, leading to strongly modulated electron kinetic energy spectra. Field strength dependent Rabi oscillations in the sideband population reveal the quantum coherence of the process [2]. Free propagation over a few mm will reshape the electron wave function into a train of attosecond pulses, in principle allowing for the study of attosecond phenomena in electron microscopy. In an advanced experiment, we control the free electron momentum superposition states with two spatially separated interaction sites, in some analogy to the Ramsey method for atomic clocks.

[1] A. H. Zewail, *Science* 328, **187** (2010).

[2] A. Feist, K. E. Echternkamp, J. Schauss, S. V. Yalunin, S. Schäfer, and C. Ropers, *Nature* **521**, 200-203 (2015).

Abstracts of Poster Presentations (sorted by poster number)

#	Presenting Author	Title
1	<i>Felix Becker</i>	Nanoantenna supported thermionic current injection in metal-insulator-metal junctions
2	<i>Markus Betz</i>	Quantum interference control of electrical currents in GaAs microstructures: physics and spectroscopic applications
3	<i>Tobias Birr</i>	Ultrafast surface plasmon-polariton logic gates and half-adder
4	<i>Soo Hoon Chew</i>	Current progress on probing and control of near-field dynamics using photoemission electron microscopy
5	<i>Benjamin Frisch</i>	Coherent and long-range plasmon-assisted energy transfer between two plasmonic nanoantennas
6	<i>Cristian González</i>	Investigation of the dispersion relation of SPPs with Mie scattering probes in the optical and near infrared range
7	<i>Bernhard Huber</i>	Anderson localization of light in randomly nanotextured layers as a new paradigm for the design of highly efficient thin-film absorbers
8	<i>Dan-Nha Huynh</i>	Ultrafast sum-frequency and second-harmonic generation in plasmonic nanostructures
9	<i>Alwin Klick</i>	Amplitude and phase of surface plasmon polaritons excited at step edges
10	<i>Aleksander Kovačević</i>	Inducing nanoparticles and periodic nanostructures on thin metal films by low-fluence femtosecond beam
11	<i>Martin Lehr</i>	Time of flight momentum microscopy of plasmon assisted photoemission
12	<i>Polina Lisinetskaya</i>	Methods for simulation of light propagation in small metal cluster arrays
13	<i>Anna-Katharina Mahro</i>	Time- and space-resolved imaging of gold nanostructures
14	<i>Martin Piecuch</i>	MANTIS – A novel XUV-IR pump probe photoemission scheme for the investigation of attosecond dynamics
15	<i>Daniel Podbiel</i>	Exploring Plasmoemission of Electrons in NI-PEEM
16	<i>Simon Ristok</i>	Bottom-up synthesis of large area single-crystalline atomically flat gold flakes with single crystalline silver cubes as single quantum emitter nanoantennas
17	<i>Carsten Rockstuhl</i>	Nonlinear optical plasmonic nanoantennas from Lithium Niobate
18	<i>Benjamin Schröder</i>	Nanotip surface plasmons: real-space imaging using EELS and grating-coupled nonlinear photoemission
19	<i>Thorsten Schumacher</i>	The optimal antenna for nonlinear spectroscopy of weakly and strongly scattering nanoobjects
20	<i>Martin Silies</i>	Light localization in disordered nanostructures - Giant fluctuations of Second Harmonic and electron emission
21	<i>Vladimir Smirnov</i>	Suppression of radiative damping and enhancement of second harmonic generation in bull's eye nanoantennas
22	<i>Judith Specht</i>	Applications of nanoplasmonics: Full quantum statistics of many emitter spasers and spin dependent reconstruction scheme of exciton wave functions
23	<i>Philip Thielen</i>	Long-Lived Coherence in the Metal-Organic-Hybrid Cobalt/Alq ₃
24	<i>Felicitas Walter</i>	Controlling the excitation of localized plasmonic resonances by strong near-field coupling
25	<i>Xiao Wang</i>	Plasmon and exciton decay in nanostructures excited with ultrashort pulses formed by cylindrical vector laser beams

Poster 1:

Nanoantenna supported thermionic current injection in metal-insulator-metal junctions

Felix Becker¹, Detlef Diesing², Dominik Differt¹, Adelheid Godt³, Ingo Heesemann³,
Matthias Hensen¹, Walter Pfeiffer¹ and Christian Strüber⁴

¹ *Molekül- und Oberflächenphysik, Fakultät für Physik, Universität Bielefeld, 33615 Bielefeld, Germany*

² *Surface Dynamics Group, Fakultät für Chemie, Universität Duisburg-Essen, 45141 Essen, Germany*

³ *Organic Chemistry and Polymer Chemistry, Fakultät für Chemie, Universität Bielefeld, 33615 Bielefeld, Germany*

⁴ *Quantum Optics and Laser Science Research Group, Imperial College London, SW7 2AZ London, GB*

In the interaction of intense laser pulses with nanostructures or optical antennas the electron emission is commonly discussed in the context of multi-photon processes [1] and strong field phenomena [2-5]. The latter process facilitates the opportunity to implement the scheme of “lightwave electronics” [6], in which electronic motion is coherently steered by the electric field itself. Although this scheme is studied at the metal-vacuum interface of nanostructures, it is not yet demonstrated for electrons remaining inside a nanodevice.

Few-cycle laser pulse injected currents in metal-insulator-metal junctions might fill this gap. Recently, it has been shown that plasmonic resonances at structural defects on the top electrode of the heterosystem facilitate the injection of charge carriers above the tunnel barrier of the oxide [7]. Here, we demonstrate the prearranged injection of charge carriers by exploiting the near field enhancement of gold nanoparticle antennas on the top electrode. In contrast to multi-photon and strong field interaction, we identify strongly localised thermionic emission as the dominating process for current injection. Experimental evidence for the transition from multi-photon excitation to thermionic emission is supported by finite-difference time-domain simulations and time-resolved calculations of the excited electronic distribution function. Time-resolved heat diffusion calculations of the electron gas model the spacial temperature distribution and thus the transient thermionic injection current. The results serve as an onset to overcome incoherent obstacles on the way to coherently controlled nanodevices on the sub-femtosecond time scale.

[1] J. Lehmann et al., Phys. Rev. Lett. **85**, 2921–2924 (2000)

[2] R. Bormann et al., Phys. Rev. Lett. **105**, 147601 (2010)

[3] P. Dombi et al., Opt. Express **18**, 24206–24212 (2010)

[4] M. Krüger et al., Nature **475**, 78–81 (2011)

[5] B. Piglosiewicz et al., Nature Photon. **8**, 37-42 (2014)

[6] E. Goulielmakis et al., Science **317**, 769-775 (2007)

[7] D. Differt et al., Appl. Phys. Lett. **101**, 111608 (2012)

Poster 2:

Quantum Interference Control of Electrical Currents in GaAs Microstructures: Physics and Spectroscopic Applications

E. Sternemann¹, C. Ruppert¹, T. Jostmeier¹, S. Thunich¹, R. Podzimski², H.T. Duc²,
T. Meier², M. Betz¹

¹ *Experimentelle Physik 2, TU Dortmund, Germany*

² *Fachbereich Physik, Universität Paderborn, Germany*

We present a comprehensive study of coherently controlled charge currents in electrically contacted GaAs microdevices. Currents are generated all-optically by phase-related femtosecond pulse pairs (fundamental/second harmonic) and are often linked to the third order optical nonlinearity. Here, we first focus on elevated irradiances where absorption saturation and ultimately the onset of Rabi oscillations contribute to the optical response. In particular, we identify clear departures of the injected current from the third order response. Theoretical simulations for the coherently controlled current based on the semiconductor Bloch equations agree well with the experimental trends. We then move on to investigate spectroscopic applications of the quantum interference control technique. In particular, we implement a versatile scheme to analyze the phase structure of femtosecond pulses. It relies on phase-sensitive current injection driven by two time-delayed portions of the pulse pair. Most strikingly, the group velocity dispersions of both the fundamental and second harmonic components can be unambiguously determined from a simple Fourier transform of the resulting current interferogram. Finally, we aim to use femtosecond pulse pairs to demonstrate a theoretically proposed scheme for all-optical current detection in thin GaAs membranes. However, we find the signal to be superimposed by second harmonic generation related to the electric field inducing the current. As a result, the currents' signature cannot be unambiguously identified.

Poster 3:

Ultrafast surface plasmon-polariton logic gates and half-adder

Tobias Birr, Urs Zywietz, Parva Chhantyal, Tim Fischer, Boris Chichkov, Carsten Reinhardt

Laser Zentrum Hannover e.V., Hollerithallee 8, 30419, Hannover, Germany

In 1965, Moore verbalized his law about doubling of the packing density of circuits in electronic devices. However, this downsizing combined with an increase of operational speed is facing physical limits. On the other hand, optical fibers are used since decades but they have much bigger dimensions than electronic devices and are still using electronic front and back ends. Solving this mismatch would offer the possibility to strongly increase computational capacities. One possibility is the use of surface plasmon-polaritons as carriers of information. For this purpose several groups recently investigated the properties of different plasmonic structures in terms of the usage as plasmonic logic elements. These published approaches contain limitations since either random structures have been used or the system under consideration suffers from severe damping leading to extremely short propagation lengths. In this work, dielectric plasmonic waveguides are used for the construction of logic gates for near infrared light. They were investigated experimentally regarding their efficiency depending on their geometrical properties. These measurements, obtained by leakage radiation microscopy, have been compared with FDTD simulations of the same structures. The results were used to design plasmonic half adders which functionality has been demonstrated experimentally. These investigations are an important step in the development of optical technologies which could lead to a next photonic era.

Poster 4:

Current progress on probing and control of near-field dynamics using photoemission electron microscopy

S. H. Chew^{1,2}, A. Gliserin^{1,2}, J. Schmidt^{1,2}, S. Nobis^{1,2}, H. Bian^{1,2}, E. Krauss³, P. Geisler³,
F. Schertz⁴, M. Kübel^{1,2}, B. Hecht³, U. Kleineberg^{1,2}

¹ *Faculty of Physics, Ludwig-Maximilians-Universität München, 85748 Garching, Germany*

² *Max-Planck-Institut für Quantenoptik, 85748 Garching, Germany*

³ *Nano-Optics and Biophotonics Group, Experimentelle Physik 5, Physikalisches Institut,
Universität Würzburg, Würzburg D-97074, Germany*

⁴ *Surface Concept GmbH, Staudingerweg 7, 55128 Mainz, Germany*

Here we present the concept of carrier-envelope phase-tagged time of flight-photoemission electron microscopy and the recent experimental results. We discuss the laser intensity effects on the current phase-resolved measurements of gold nanoparticles on gold plane and surface roughness from a gold film. The apparent carrier-envelope phase modulation with a period of π is found to originate from an intensity dependence of the photoelectron spectra and the phase potato rather than from an intrinsic carrier-envelope phase dependence. We propose next steps such as the implementation of intensity tagging and improved plasmonic sample to probe and control near-field dynamics from supported nanostructures.

Poster 5:

Coherent and long-range plasmon-assisted energy transfer between two plasmonic nanoantennas

Martin Aeschlimann¹, Tobias Brixner^{2,3}, Benjamin Frisch¹, Bert Hecht^{3,4}, Bernhard Huber²,
Matthias Hensen⁵, Christian Kramer², Enno Krauss⁴, T. Löber⁷, Walter Pfeiffer⁵,
Martin Piccuch¹ and Philip Thielen^{1,6}

¹ *Fachbereich Physik and Research Center OPTIMAS, University of Kaiserslautern,
Erwin-Schrödinger-Str. 46, 67663 Kaiserslautern, Germany*

² *Institut für Physikalische und Theoretische Chemie, Universität Würzburg, Am Hubland, 97074 Würzburg, Germany*

³ *Röntgen Research Center for Complex Material Systems (RCCM), Universität Würzburg,
Am Hubland, 97074 Würzburg, Germany*

⁴ *Nano-Optics and Bio-Photonics Group, Department of Experimental Physics 5, Universität Würzburg,
Am Hubland 97074 Würzburg, Germany*

⁵ *Fakultät für Physik, Universität Bielefeld, Universitätsstr. 25, 33615 Bielefeld, Germany*

⁶ *Graduate School of Excellence Materials Science in Mainz, Gottlieb-Daimler-Str. 47, 67663 Kaiserslautern*

⁷ *Nano-Structuring-Centre, Erwin-Schrödinger-Str. 13, 67663 Kaiserslautern*

Hybridization of localized plasmonic resonances and propagating surface plasmon-polaritons (SPP) facilitates to combine the benefits of two worlds: Longevity and coherent light concentration. This combination has recently been demonstrated in random plasmonic resonators [1]. Here, we present experimental and theoretical results on a prearranged system that allows long-distance ($> 2\lambda_0$) coupling between two plasmonic nanoantennas [2] mediated by an extended SPP mode in an elliptic all-metallic cavity [3]. The system, qualitatively described by three coupled differential equations, is prepared on single crystalline gold flakes [4] allowing plasmonics on atomically flat surfaces. First experiments on temporal dynamics of plasmonic excitation with time-resolved PEEM confirm the coherent back and forth transfer of energy between widely separated nanoantennas. Moreover, we show theoretically that the system obeys the phenomenon of impedance matching: By tuning the dissipation of the cavity it is possible to periodically switch on the excitation at one antenna while the opposite antenna remains dark. Besides applications of the here presented system in long-range routing of plasmonic excitations the cavities might even serve for interesting experiments involving quantum systems coupled to incorporated nanoantennas.

[1] M. Aeschlimann et al., *Science* 333, 1723-1726 (2011)

[2] E. J. R. Vesseur et al., *Nano Lett.* 9, 3147-3150 (2009)

[3] D. T. Schoen et al., *Nano Lett.* 13, 188-193 (2013)

[4] X. Wu et al., *Cryst. Res. Technol.* 50, 595–602 (2015)

Poster 6:

Investigation of the dispersion relation of SPPs with Mie scattering probes in the optical and near infrared range

C. González¹, M. Hartelt¹, D. Bayer¹, M. Aeschlimann¹, E. Ilin², E. Oesterschulze²

¹ *Department of Physics and Research Center OPTIMAS, University of Kaiserslautern,
Erwin Schroedinger Str. 46 D-67663, Kaiserslautern*

² *Department of Physics, Physics and Technology of Nanostructures, University of Kaiserslautern,
Erwin Schroedinger Str. 46 D-67663, Kaiserslautern*

We present a cantilever based near field probe with integrated Mie scattering dielectric silicon dioxide microsphere (MSDM) for near-field optical imaging as well as femtosecond spectroscopy applications. In contrast to the state of the art transmissive near-field probes, the MSDM reveals a transmission of almost unity known from far-field microscopy configuration. For proper handling the microsphere is integrated at the apex of a conventional pyramidal aperture tip carried by an atomic force microscopy cantilever. It proved to be mechanically robust during the scanning process even if operating it in the contact mode. The spherical symmetry provides on one hand a well defined mechanical contact point with the sample irrespective of its inclination angle to the sample surface. On the other hand, the symmetry of the device preserves the polarization of light proving to be useful for the investigation of the polarization dependent behavior of plasmonic nanostructures. The device has also shown to be able to be an excellent tool for the study of surface plasmons on Au thin films when measuring the dispersion relation of SPPs, bringing results with an excellent agreement with similar experiments performed with PEEM . The high transmission combined with low dispersion renders spectroscopic investigations on the femtosecond time scale with a moderate lateral resolution. Moreover, second autocorrelation experiments on a BBO-crystal reveals a time resolution well below 100 fs at 191 nm spatial resolution.

Poster 7:

Anderson localization of light in randomly nanotextured layers as a new paradigm for the design of highly efficient thin-film absorbers

Martin Aeschlimann¹, Tobias Brixner^{2,3}, Dominik Differt⁴, Ulrich Heinzmann^{4,5}, Matthias Hensen⁴, Bernhard Huber², Christian Kramer², Florian Lükermann^{4,5}, Pascal Melchior¹, Walter Pfeiffer⁴, Martin Piecuch¹, Christian Schneider¹, Helmut Stiebig^{4,5}, Christian Strüber⁶, and Philip Thielen^{1,7}

¹ *Fachbereich Physik and Research Center OPTIMAS, Technische Universität Kaiserslautern, Erwin-Schrödinger-Str. 46, 67663 Kaiserslautern, Germany*

² *Institut für Physikalische und Theoretische Chemie, Universität Würzburg, Am Hubland, 97074 Würzburg, Germany*

³ *Röntgen Research Center for Complex Material Systems (RCCM), Universität Würzburg, Am Hubland, 97074 Würzburg, Germany*

⁴ *Fakultät für Physik, Universität Bielefeld, Universitätsstr. 25, 33615 Bielefeld, Germany*

⁵ *Institut für Innovationstransfer an der Universität Bielefeld, Universitätsstr. 25, 33615 Bielefeld, Germany*

⁶ *Quantum Optics and Laser Science Group, Imperial College London, London SW7 2AZ, UK*

⁷ *Graduate School of Excellence Materials Science in Mainz, Gottlieb-Daimler-Str. 47, 67663 Kaiserslautern, Germany*

Unraveling the localization mechanisms of light in disordered nanostructures is of great interest in a number of applications, including photovoltaics and thermoelectrics. The efficient use of natural resources and physical constraints in photovoltaic devices require thin but efficient absorbers. Although already exploited in commercial devices, the enhancement mechanism for devices with nanotextured interfaces is still subject to debate. Here, we demonstrate the existence of localized photonic states in nanotextured amorphous silicon layers as used in commercial thin-film solar cells using coherent light scattering and coherent two-dimensional nanoscopy [1]. Resonant absorption in these Anderson localized photonic modes accounts for enhanced absorption in the long-wavelength cutoff region giving rise to interesting opportunities for future highly effective absorber layer designs based on this localization mechanism.

- [1] M. Aeschlimann, T. Brixner, D. Differt, U. Heinzmann, M. Hensen, C. Kramer, F. Lükermann, P. Melchior, W. Pfeiffer, M. Piecuch, C. Schneider, H. Stiebig, C. Strüber, and P. Thielen, *Nature Photon.* **9**, 663 (2015).

Poster 8:

**Ultrafast sum-frequency and second-harmonic generation
in plasmonic nanostructures**

Dan-Nha Huynh¹, Matthias Moferdt¹, Christian Matyssek¹, Christian Wolff³, Kurt Busch²

¹ *Humboldt-Universität zu Berlin, Institut für Physik, Newtonstr. 15, 12489 Berlin, Germany*

² *Max-Born-Institut, Max-Born-Str. 2A, 12489 Berlin, Germany*

³ *School of Mathematical and Physical Sciences, University of Technology Sydney, NSW 2007 Ultimo, Australia*

Optical second-order nonlinear spectroscopy has been a subject of investigations for over two decades [1,2]. Nevertheless, its theoretical understanding is still emerging. Based on a hydrodynamic description, featuring nonlinear as well as nonlocal characteristics, we present time-domain computations of three-wave-mixing signals, in particular second-harmonic and sum-frequency signals, from plasmonic nanoantennas.

- [1] J. E. Sipe, V. C. Y. So, M. Fukui, and G. I. Stegeman. Phys. Rev. B, **21**:4389–4402, May 1980.
- [2] J. A. Maytorena, W. L. Mochán, and B. S. Mendoza. Phys. Rev. B, **57**:2580–2585, Jan 1998.

Poster 9:

Amplitude and phase of surface plasmon polaritons excited at step edges

Alwin Klick¹, Sergio de la Cruz², Malte Großmann¹, Hauke Beyer¹, Jacek Fiutowski³,
Horst-Günter Rubahn³, Eugenio R. Mendez², Michael Bauer¹

Institute of Experimental and Applied Physics, University of Kiel, Leibnizstr. 19, 24118 Kiel, Germany

*División de Física Aplicada, Centro de Investigación Científica y de Educación Superior de Ensenada,
Carretera Ensenada-Tijuana No. 3918, Ensenada 22860, BC, Mexico*

Mads Clausen Institute, University of Southern Denmark, NanoSYD Alsion 2, 6400 Sønderborg, Denmark

We present a combined theoretical and experimental study on the laser-induced excitation of surface plasmon polaritons (SPPs) at defined step edges representing one of the most basic light-SPP coupling geometries. The calculations are performed within an integral equation approach for the solution of two-dimensional scattering problems [1], whereas in the experimental part we utilized two-photon photoemission electron microscopy (2P-PEEM) [2]. Analysis of the data provides information on the laser-SPP coupling efficiency of the step edges and the phase of the excited SPP. As an important parameter determining the coupling efficiency we identify the ratio between step height H and excitation wavelength λ . For specific values of H/λ a substantial suppression of light-SPP coupling is observed. At the same time the phase of the SPP undergoes an overall shift by π . Based on the calculations it is possible to assign the changes in coupling efficiency and phase to the interference of incident and reflected laser field in the presence of the step edge.

[1] De la Cruz, S. et al., *Physica Status Solidi (B)* **249(6)**, (2012)

[2] Lemke, C. et al., *Applied Physics B* **116** (2013)

Poster 10:

Inducing nanoparticles and periodic nanostructures on thin metal films by low-fluence femtosecond beam

Aleksander G. Kovačević¹, Suzana Petrović², Peter Panjan³, Vladimir Lazović¹, Davor Peruško²,
Svetlana Savić-Šević¹, Dejan Pantelić¹, Branislav M. Jelenković¹

¹ *Institute of Physics, University of Belgrade, Pregrevica 118, 11080 Belgrade, Serbia*

² *Institute for Nuclear Sciences Vinča, University of Belgrade, PO Box 522, 11001 Belgrade, Serbia*

³ *Institute Jožef Štefan, Jamova cesta 39, 1000 Ljubljana, Slovenia*

In many fields, like semiconductor technology, optics, chemistry, mechanics, magnetism, electricity, the applications of thin films play an important role. Various types of coatings for protection, diffusion barriers, filtering, reflection/antireflection, sensing, waveguiding, decorative and other purposes are just some to mention. Structuring of thin films can enhance their characteristics. From the other side, nanoparticles are of great interest due to their position between bulk materials and atomic/molecular structures. The interaction of femtosecond laser beam with thin films can have various outcomes, in which the generation of nanoparticles and of surface periodic structures gains more interest. We have used low-fluence femtosecond beam of various wavelengths and exposures to thin film samples: Al on Si, CrVN, multilayer Al/Ti on Si and multilayer Ni/Pd on Si. Having excellent mechanical characteristics (wearing, corrosion resistance), some samples have prospective applications in holography. The exposures yielded the generation of nanoparticles and the formation of periodic surface structures (LIPSS). The processes of liquid or solid-state dewetting could be responsible for regrouping of generated nanoparticles and nanoparticle clusters, while LIPSS is most probably induced by the occurrence of the surface plasmon polariton. The presence of the sublayer, depending on its optical characteristics, strongly influences both the shape and the quality of the LIPSS.

Acknowledgements: This work has been supported by the Ministry of Science of the Republic of Serbia with projects OI171005 and III45016, as well as by COST action MP1403.

Poster 11:

Time of flight momentum microscopy of plasmon assisted photoemission

Martin Lehr¹, Karina Bley², Nicolas Vogel², Hans-Joachim Elmers¹

¹ *Johannes Gutenberg-University Mainz, Staudingerweg 7, D-55099 Mainz*

² *Friedrich-Alexander University Erlangen-Nürnberg, Haberstraße 9a, D-91058 Erlangen*

The photoemission properties of a Au nano triangular array have been investigated using a time-of-flight-momentum microscope (ToF-PEEM), equipped with a state-of-the-art Surface Concept delay line detector (DLD). The nano triangular array has been fabricated by deposition of a gold film on a self-assembled colloidal sphere structure. The triangles can be resonantly excited by Ti:sapphire femtosecond laser pulses. The sample is illuminated from the backside at normal incidence. The dependence of the electron momentum distribution on the light polarization has been investigated. The energy spectra of the emitted electrons show unexpectedly high energies of up to 4 eV.

Poster 12:

Methods for simulation of light propagation in small metal cluster arrays

Polina Lisinetskaya, Alexander Humeniuk, Roland Mitrić

Institut für Physikalische und Theoretische Chemie, Universität Würzburg, Emil-Fischer-Str. 42, 97074 Würzburg

We present a theoretical approach for the simulation of the optical response and electric field propagation in ordered arrays constructed of small noble-metal clusters including the effect of a support. In such systems the size of an array subunit is comparable or larger than the separation between neighboring subunits. In order to describe the interaction between individual constituents we use the transition charge method. The electronic population dynamics in the array under an external laser pulse action is simulated by numerical integration of the time-dependent Schrödinger equation with the coupled array Hamiltonian. The results are employed to represent each subunit of the array by a system of time-dependent partial point charges and the spatio-temporal electric field distribution is evaluated by means of classical electrodynamics methods. The time-dependent partial charges are determined based on the stationary partial and transition charges obtained in the framework of the ab initio TDDFT. In order to treat large arrays constructed of many constituents the approximate self-consistent iterative approach presented in [1] is modified to include transition-charge-based interaction between subunits. The developed methods are used to study the optical response of Ag_3^+ arrays, to control the light propagation in a T-shaped structure constructed of seven Ag_8 clusters, and to simulate the spatio-temporal electric field distribution in a ring constructed of ten porphyrin- Ag_4 subunits under the action of circularly-polarized laser pulse.

[1] P. Lisinetskaya and R. Mitrić, Phys. Rev. B **89**, 035433, 2014.

Poster 13:

Time- and space-resolved imaging of gold nanostructures

Anna-Katharina Mahro¹, Deirdre Kilbane¹, Pascal Melchior¹, Stefan Mathias²,
Martin Aeschlimann¹

¹ *Department of Physics and Research Centre OPTIMAS, University of Kaiserslautern,*

Erwin-Schrödinger-Straße 46, 67663 Kaiserslautern, Germany

² *Georg-August-Universität Göttingen, I.Physikalisches Institut, Friedrich Hund Platz 1, 37077 Göttingen, Germany*

Knowledge of fundamental light-matter interactions such as the local response of nanostructures to incident light is necessary for designing plasmonic devices. This response is determined on the nanometer scale (below the diffraction limit of light). We therefore use a photoemission electron microscope (PEEM) to image the near-field distribution. To gain information about the local response of our gold nanostructures, we apply phase and time resolved two photon photoemission techniques. We use a phase-stabilized Mach-Zehnder-interferometer based on Pancharatnam phase [1,2] in combination with a broadband ultrashort pulse laser and PEEM. This setup provides a temporal precision in the pump-probe delay of 30 as thus allowing the dynamics of plasmon excitations in different nanostructures to be compared in real time. Under resonant excitation the phase-resolved autocorrelations from these nanostructures contain information about their local response.

[1] S. Pancharatnam, Proc. Indian Natl. Sci. Acad., A **44**, 247-262 (1956)

[2] M.U. Wehner et al., Opt. Lett. **22**, 1455-1457 (1997)

Poster 14:

MANTIS – A novel XUV-IR pump probe photoemission scheme for the investigation of attosecond dynamics

M. Piecuch¹, M. Aeschlimann¹, S. Mathias²

¹ *University of Kaiserslautern and Research Center OPTIMAS, Kaiserslautern, Germany*

² *Georg-August-Universität Göttingen, I. Physikalisches Institut, Göttingen, Germany*

Reconstruction of attosecond beating by interference of two-photon transitions (RABITT) is a powerful and well-established method for attosecond pulse characterization. Furthermore the method proved to be very useful for the investigation and the understanding of phase shifts in core-level photoemission spectra. However, as RABITT makes use of the energy comb of high-harmonics in an attosecond pulse train (APT), one collects multiple overlapping photoemission spectra, which renders the interpretation and investigation of phase shifts in valence-band spectroscopy a hard task. Here we present an extension of the RABITT scheme (named MANTIS) by combining it with a method derived from 2D-spectroscopy. We combine the APT with two IR-laser pulses and use the concept of phase cycling to select specific coherence pathways which results in clean high-resolution phase resolved photoemission spectra. We show that this method will open up a new and powerful route to study attosecond dynamics in atoms, molecules and materials.

Poster 15:

Exploring plasmoemission of electrons in NI-PEEM

Daniel Podbiel¹, Philip Kahl¹, Bettina Frank², Harald Giessen², Frank-J. Meyer zu Heringdorf¹

¹ *Faculty of Physics and Center for Nanointegration CENIDE, University of Duisburg-Essen, 47057 Duisburg, Germany*

² *4th Physics Institute and Research Center SCoPE, University of Stuttgart, 70550 Stuttgart, Germany*

We use time-resolved normal-incidence photoemission electron microscopy (NI-PEEM) to study surface plasmon polariton (SPP) propagation, interference, and focussing. We analyzed the probing contrast in NI-PEEM and found that it is caused by the in-plane component of the SPPs electric field. We demonstrate that the measurement signatures in NI-PEEM (arising due to time-integration) can be easily explained with the help of ‘space-time’ diagrams. From an analysis of the signatures we can conclude that SPP-induced emission of electrons, referred to as ‘plasmoemission’, is governed by the out of-plane component of the SPPs electric field. To achieve higher plasmoemission yields, we studied focussing of SPPs at a Fresnel-type grating coupler as well as in circular grating couplers. At the focus points of circular grating couplers multiplasmon plasmoemission processes up to an order of six could be observed. Furthermore an SPP-induced material transport occurs, and leads to the formation of nanostructures, at which localized electron emission take place. Kinetic energy spectra of the emitted electrons indicate a transition into a different electron emission regime.

Poster 16:

Bottom-up synthesis of large area single-crystalline atomically flat gold flakes with single crystalline silver cubes as single quantum emitter nanoantennas

Simon Ristok, Bettina Frank, Harald Gießen

*University of Stuttgart, 4th Physics Institute and Research Center SCoPE,
Pfaffenwaldring 57, 70569 Stuttgart, Germany*

When using quantum emitters such as NV centers in diamond, quantum dots, or dye molecules as effective photon sources, it is often necessary to control certain characteristics of the emitted radiation, e.g., the emission rate and direction. A promising approach is the coupling of the emitters to a plasmonic nanoantenna. In this work, we fabricate plasmonic nanopatch antennas using exclusively bottom-up methods. The antennas consist of silver nanocubes which are positioned over the atomically flat surface of a gold microplate. Both Ag nanocubes and Au microplates are single-crystalline and are separated by a dielectric polymer spacing layer. The plasmonic resonance of the antennas can be tuned by varying the size of the Ag nanocubes and the thickness of the spacing layer. The further steps include the embedding of fluorescent dye molecules into the gap of the nanopatch antenna, followed by fluorescence enhancement and lifetime measurements. Investigating this system can help us understanding the prerequisites to expand the range of emitters also to NV centers and quantum dots.

Poster 17:

Nonlinear optical plasmonic nanoantennas from Lithium Niobate

Carsten Rockstuhl¹, Thomas Pertsch²

¹ *Institute of Theoretical Solid State Physics, Institute of Nanotechnology, Karlsruhe Institute of Technology, Wolfgang-Gaede-Strasse 1, 76131 Karlsruhe, Germany*

² *Institute of Applied Physics, Abbe Center of Photonics, Friedrich-Schiller-Universität Jena, Max-Wien-Platz 1, 07743 Jena, Germany*

Optical nanoantennas, or photonic nanostructures in more general, can be used to shape the propagation characteristics of light as well as its localization. Both aspects can be controlled to a notable extent spectrally selective. This renders photonic nanostructures ideal candidates to mediate and to enhance nonlinear optical effects and to enhance the interaction of light with quantum emitters at the nanoscale. Here, we report in a comprehensive manner on our contributions to the field of optical nanoantennas, both dielectric and metallic, their tunability, and their ability to affect nonlinear processes. We are interested in LiNbO₃ as the nonlinear material. Nonlinear processes in such material tend to be enhanced when considering two distinguished scenarios. First, nanoantennas themselves can be combined in a suitable manner with LiNbO₃. Second, the resonant photonic nanostructure itself is made from LiNbO₃. When considering nanoantennas as additional elements to enhance the nonlinear processes, we studied on the one hand metallic disc antennas. Their resonant response is reinforced when surrounded by annular metallic gratings and light is much better localized and enhanced. On the other hand, metallic nanowires with a suitably chosen termination have been considered. Using such material platform allows to tune multiple resonances independent to each other, being a prerequisite to drive parametric nonlinear processes highly efficient. When considering resonant photonic nanostructures made from LiNbO₃, we studied isolated nanoparticles or nanowires but also photonic crystal based architectures. The work is done both experimentally and theoretically/numerically. The methodology developed in our work will be presented at the poster. The methodology had also been used to study problems in the context of ultrafast nanooptics in close collaboration with other partners from the SPP. An overview across these collaborations will be presented as well.

Poster 18:

Nanotip surface plasmons: real-space imaging using EELS and grating-coupled nonlinear photoemission

Benjamin Schröder¹, Murat Sivis¹, Thorsten Weber², Sergey V. Yalunin¹, Thomas Kiel⁴, Christian Matyssek⁴, Reiner Bormann¹, Felix von Cube², Stephan Irsen³, Kurt Busch⁵, Stefan Linden², Sascha Schäfer¹, Claus Ropers¹

¹ *4th Physical Institute – Solids and Nanostructures, University of Göttingen,
Friedrich-Hund-Platz 1, Göttingen, Germany*

² *Physikalisches Institut, Rheinische Friedrich-Wilhelms-Universität Bonn, Nußallee 12, Bonn, Germany*

³ *Electron Microscopy and Analytics, Center of Advanced European Studies and Research,
Ludwig-Erhard-Allee 2, Bonn, Germany*

⁴ *Institut für Physik, Humboldt-Universität zu Berlin, Newtonstraße 15, Berlin, Germany*

⁵ *Max-Born-Institut, Max-Born-Straße 2A, Berlin, Germany*

In this contribution, we present our latest results concerning the excitation of surface plasmon polaritons (SPPs) on metal nanotips. First, SPPs on a straight conical gold taper are imaged and spectrally analyzed by electron energy loss spectroscopy within a scanning transmission electron microscope. We observe standing wave patterns which are ascribed to reflections of the SPPs at the apex of the taper. The experimental findings are in a very good agreement with numerical computations and analytical calculations. In a second experiment, SPPs are excited with a resonant grating coupler on the shaft of a gold tip and accompanied photoemission is measured and analyzed. In our setup, we use a modified field-emitter gun assembly to control the electrostatic environment around nanotip and demonstrate that grating excitation remotely triggers multiphoton photoemission from the nanometer size apex.

Poster 19:

The optimal antenna for nonlinear spectroscopy of weakly and strongly scattering nanoobjects

Thorsten Schumacher¹, Matthias Brandstetter¹, Daniela Wolf¹, Kai Kratzer², Mario Hentschel², Harald Giessen², Markus Lippitz¹

¹ *Experimental Physics III, University of Bayreuth, Universitaetsstrasse 30, D-95440 Bayreuth, Germany*

² *4th Physics Institute and Research Center SCoPE, University of Stuttgart, Pfaffenwaldring 57, D-70550 Stuttgart, Germany*

³ *Max Planck Institute for Solid State Research, Heisenbergstrasse 1, D-70569 Stuttgart, Germany*

Optical nanoantennas, i.e., arrangements of plasmonic nanostructures, promise to enhance the light-matter interaction on the nanoscale. Especially nonlinear optical spectroscopy of single nanoobjects would profit from such an antenna, as nonlinear optical effects are already weak for bulk material, and become almost undetectable for single nanoobjects. We investigate the design of optical nanoantennas for transient absorption spectroscopy in two different cases: the mechanical breathing mode of a metal nanodisc and the quantum-confined carrier dynamics in a single CdSe nanowire. In the latter case, an antenna with a resonance at the desired wavelength optimally increases the light intensity at the nanoobject. In the first case, the perturbation of the antenna by the investigated nanosystem can not be neglected and off-resonant antennas become most efficient.

Poster 20:

Light localization in disordered nanostructures - giant fluctuations of second harmonic and electron emission

Martin Silies¹, Manfred Mascheck¹, Pascal Melchior², Slawa Schmidt¹, David Leipold³, Heiko Kollmann¹, Kokoro Kitamura⁵, Takashi Yatsui⁴, Motoicho Ohtsu⁴, Erich Runge³, Martin Aeschlimann², Christoph Lienau¹

¹ *Institute of Physics and Center of Interface Science, University of Oldenburg, D-26129 Oldenburg, Germany*

² *Department of Physics, University of Kaiserslautern, D-67663 Kaiserslautern, Germany*

³ *Institut für Physik, Technische Universität Ilmenau, D-98684 Ilmenau, Germany*

⁴ *School of Engineering, University of Tokyo, 113-8656 Tokyo, Japan*

⁵ *Department of Mechanical, Electrical and Electronic Engineering, Shimane University, Shimane 690-8504 Japan*

Localization of light as an ubiquitous phenomena occurs in all kinds of disordered materials including randomly arranged arrays of dielectric or metallic scatterers. However, a direct comparison of the localization in dielectric and metallic samples for the same dimensions of the scattering particles is lacking. Here, we measure the localization of near-infrared light and of localized surface plasmons in randomly arranged dielectric and metallic nanoneedles of the same length, diameter and density. Coherent, ultra-broadband Second Harmonic microscopy and ultrashort, multi-photon photoemission electron microscopy are used to probe the spatial and temporal mode distribution in both ZnO and Au-coated ZnO needle arrays. Intensity fluctuations of the SH for the dielectric and of the multi-photon-induced electron emission for the metal-covered needles are taken as an indicator for the localization of electric and plasmonic fields within the arrays. Additionally, by using interferometric autocorrelation techniques, life times of several femtoseconds of the photon and the plasmon mode are measured, therefore exhibiting the central characteristics for weak localization of light in an array of randomly distributed dielectric and metallic scatterers.

Poster 21:

Suppression of radiative damping and enhancement of second harmonic generation in bull's eye nanoantennas

Juemin Yi¹, Vladimir Smirnov¹, Xianji Piao², Jiho Hong², Heiko Kollmann¹, Wei Wang¹,
Petra Groß¹, Ralf Vogelgesang¹, Namkyoo Park², Christoph Lienau¹

¹ *Institute of Physics and Center of Interface Science, Carl von Ossietzky Universität Oldenburg,
D-26129 Oldenburg, Germany*

² *Photonic Systems Laboratory, School of Electrical Engineering, Seoul National University, 151-742 Seoul, Korea*

We report a drastic enhancement of the damping time of surface plasmon polaritons in bull's eye nanostructures to more than 35 fs. This is achieved by tailoring the groove depth and by enlarging the coherence length of the confined plasmon field to more than 10 μm . Experimentally, this is demonstrated by probing the plasmon dynamics at the field level using broadband spectral interferometry. The experimental results are supported by numerical simulations performed using finite element method. We demonstrate that the nanoantennas allow us to efficiently confine the incident field inside the central aperture of the bull's eye structure and to tailor its local optical nonlinearity by varying the aperture geometry. In particular we achieve a 50-time enhancement in second harmonic generation efficiency by replacing the central circular hole with an annular ring structure. This allows us to demonstrate the efficient localization of long-lived SPP fields inside nanoapertures by interferometric frequency-resolved autocorrelation (IFRAC). Such a light localization in a nanoresonator with high quality factor has high potential for sensing and coherent control of light-matter interactions on the nanoscale.

Poster 22:

Applications of nanoplasmonics: Full quantum statistics of many emitter spasers and spin dependent reconstruction scheme of exciton wave functions

Judith Specht, Michael Gegg, Markus Krecik, Andreas Knorr, Marten Richter

*Institut für Theoretische Physik, Nichtlineare Optik und Quantenelektronik, Technische Universität Berlin,
Hardenbergstr. 36, EW 7-1, 10623 Berlin, Germany*

The spatial confinement and control of electromagnetic excitations on a subwavelength scale plays a key role in nanooptics and quantum plasmonics. Optically active (hybrid) systems composed of several coupled constituents are promising candidates for optoelectronic applications. Nanoplasmonic emitters allow for an electric field localization below the diffraction limit. For instance, there is a need for externally pumped nanoscale sources of different plasmon statistics. The considered composite system consists of a metal nanoparticle driven by a gain medium formed of externally pumped quantum emitters, e.g., quantum dots or dye molecules. We study the spaser using a non-perturbative, numerically exact solution of the full quantum statistics of the multi quantum emitter - cavity laser problem. This way, the statistical properties of plasmon generation and exciton distribution can be accessed and different operating regimes are characterized for varying numbers of quantum emitters. As a possible application of localized nanooptical fields, we propose a quantum state tomography protocol for reconstructing the hybrid wave functions of coupled quantum emitters, now extended to the case including different spin states of the quantum emitters. To achieve this, a four-wave mixing technique is combined with field localization supplied by nanoplasmonic structures together with pulse-shaped fields. Therefore, one pulse of the pulse sequence applied to the hybrid system is localized at a specific quantum emitter and its polarization is controlled. We study a system composed of two coupled semiconductor quantum dots which form new, delocalized exciton states due to Förster resonance energy transfer between the two quantum emitters. Applying the suggested reconstruction scheme to coherent two-dimensional spectra allows to investigate the internal structure of the interacting single-exciton and two-exciton states and to explore their spin dependent properties.

Poster 23:

Long-lived coherence in the metal-organic-hybrid Cobalt/Alq₃

M. Aeschlimann¹, T. Brixner^{2,3}, M. Cinchetti¹, N. Haag¹, M. Hensen⁴, B. Huber²,
C. Kramer², W. Pfeiffer⁴, M. Piecuch¹, C. Schneider¹, B. Stadtmüller¹ and P. Thielen^{1,5}

¹ *Fachbereich Physik and Research Center OPTIMAS, Technische Universität Kaiserslautern,
Erwin-Schrödinger-Str. 46, 67663 Kaiserslautern, Germany*

² *Institut für Physikalische und Theoretische Chemie, Universität Würzburg, Am Hubland, 97074 Würzburg, Germany*

³ *Röntgen Research Center for Complex Material Systems (RCCM), Universität Würzburg,
Am Hubland, 97074 Würzburg, Germany*

⁴ *Fakultät für Physik, Universität Bielefeld, Universitätsstr. 25, 33615 Bielefeld, Germany*

⁵ *Graduate School of Excellence Materials Science in Mainz,
Gottlieb-Daimler-Str. 47, 67663 Kaiserslautern, Germany*

In order to exploit the great potential of hybrid metalorganic interfaces for future applications, an understanding of where and how charge transport takes place is crucial. Here we investigate the coherent electron dynamics in optically pumped (400 nm) molecular states of the metalorganic complex tris(8-hydroxyquinolinato)aluminium (Alq₃) [1] deposited on a Cobalt surface by means of time-resolved photoemission spectroscopy. We observe a coherence signal in interferometric autocorrelation traces when probing the excited-state manifold of Alq₃ with 800nm laser pulses. Desorption of the molecules down to one monolayer is achieved by heating of the sample, determining that the observed molecular feature originates from the first monolayer of Alq₃. In two-dimensional nanoscopy spectra [2], two excited electronic states are identified with an energy spacing of about 77 meV. Their linewidth is 11 meV and 48 meV, respectively, corresponding to coherence lifetimes of about 370 fs and 87 fs. Measuring the kinetic energy of the photoelectrons, these features exist over the entire accessible energy range of about one eV. We explain the observed features by long-lived coherent excited states of the adsorbate that decay among others via coupling to excited electrons in the substrates giving rise to a photoemission signal that depends linearly on the 800 nm laser intensity. The appearance of such narrow spectral features indicates that electronic excitations in an individual adsorbate state can be surprisingly long-lived and thus can play an important role in determining charge transfer efficiencies at the metal-hybrid interface.

[1] S. Steil, N. Großmann, M. Laux, A. Ruffing, D. Steil, M. Wiesenmayer, S. Mathias, O.L.A. Monti, M. Aeschlimann, *Nature Physics* **9**, 242 – 274 (2013).

[2] M. Aeschlimann, T. Brixner, A. Fischer, C. Kramer, P. Melchior, W. Pfeiffer, C. Schneider, C. Strüber, P. Tuchscherer, D. V. Voronine, *Science* **333**, 1723 (2011).

Poster 24:

**Controlling the excitation of localized plasmonic resonances
by strong near-field coupling**

Franziska Zeuner, Felicitas Walter, Thomas Zentgraf

University of Paderborn, Department of Physics, Warburger Str. 100, 33098 Paderborn, Germany

A direct control of the light-matter interaction and therefore the modification of the light propagation is a major challenge in optical research. In particular the weak interaction of light with active materials requires propagation distances of at least several wavelengths. Plasmonic nanostructures on the other side have shown the potential to strongly interact with light and generate high optical density of states. Here, we demonstrate how a coherent excitation of orthogonal eigenmodes in a plasmonic meta-atom can be controlled by a strong near-field coupling effect. The excitation of strongly coupled plasmonic modes allows therefore to utilize noninterfering far-field excitation of different polarization at the same time. We will show how the excitation of normal modes in the coupled system can be used to obtain a coherent control of the localized plasmon modes without having the problem with the short life time of the plasmonic system or the interference of the excitation beam. For our demonstration we utilize the strong nonlinearities in plasmonic system to detect the excitation strength of the localized plasmons by the emission of the third-harmonic signal in a particular polarization state. By introducing a phase shift into two orthogonal excitation beams we are able to control the excitation which build up by the coupling of different nanorods within the unit-cell of the material. Our results give a more complete understanding of the linear and nonlinear optical properties of collective excitations in strongly coupled metallic meta-atoms and metamaterials and demonstrate the potential of utilizing the near-field coupling for coherent processes.

Poster 25:

Plasmon and exciton decay in nanostructures excited with ultrashort pulses formed by cylindrical vector laser beams

Xiao Wang, Anke Horneber, Frank Wackenhut, Dai Zhang, Alfred J. Meixner

Institute of Physical and Theoretical Chemistry, University of Tübingen, Germany

Noble metal nanostructures, such as gold or silver nano spheres and nano rods, exhibit strong plasmon resonances in the visible spectral range, which influence significantly their photoluminescence (PL) emission properties. While scattering of coupled plasmonic systems has been in the focus during the last years, PL emission of nanostructures excited by ultrashort laser pulses depends also on the band-structure of these materials. Here we present our recent studies aiming at a deeper insight into the interplay between plasmons and excitons of gold nanostructures. In particular, we have investigated the linear and non-linear PL emission from various plasmonic systems like nanoparticles, sharp tips and nanotriangles [1-4] excited with radially or azimuthally polarized 100 fs laser pulses in combination with either diffraction limited confocal optical microscopy or tip enhanced scanning near-field optical microscopy. Furthermore, we are extending our studies to other nanoscale systems, such as the exciton decay in semiconductor nanowires excited by ultrashort focused cylindrical vector ultrashort laser pulses.

- [1] F. Wackenhut, A. V. Failla, A. J. Meixner, *J. Phys. Chem. C*, **117**, 17870 (2013).
- [2] P. Reichenbach, A. Horneber, D. A. Gollmer, A. Hille, J. Mihaljevic, C. Schäfer, D. P. Kern, A. J. Meixner, D. Zhang, M. Fleischer and L. M. Eng, *Opt. Express* **22**, 15484, (2014).
- [3] A. Horneber, A. L. Baudrion, P. M. Adam, A. J. Meixner and D. Zhang, *PCCP* **15**, 8031, (2013).
- [4] A. Horneber, K. Braun, J. Rogalski, P. Leiderer, A. J. Meixner and D. Zhang, *PCCP* **17**, 21288, (2015).

**Participants (alphabetical) of
4th International Workshop on Ultrafast Nanooptics (UNO-4)
and
COST MP1403 – Nanoscale Quantum Optics – Work Group Meeting (WG2)**

	Last name	First name	Email
1.	Aeschlimann	Martin	ma@physik.uni-kl.de
2.	Ai	Qi	q.ai@pi4.uni-stuttgart.de
3.	Azzaroli	Nicolò	azzaroli@lens.unifi.it
4.	Bachelier	Guillaume	guillaume.bachelier@neel.cnrs.fr
5.	Becker	Felix	fbecker@physik.uni-bielefeld.de
6.	Betz	Markus	mbetz@ph.tum.de
7.	Birr	Tobias	t.birr@lzh.de
8.	Bratschitsch	Rudolf	Rudolf.Bratschitsch@uni-muenster.de
9.	Brixner	Tobias	brixner@phys-chemie.uni-wuerzburg.de
10.	Busch	Kurt	kurt.busch@physik.hu-berlin.de
11.	Butet	Jeremy	jeremy.butet@epfl.ch
12.	Cerullo	Giulio	giulio.cerullo@polimi.it
13.	Chew	Soo Hoon	SooHoon.Chew@physik.uni-muenchen.de
14.	Comin	Alberto	alberto.comin@cup.uni-muenchen.de
15.	Cundiff	Steven	cundiff@umich.edu
16.	Durt	Thomas	thomas.durt@fresnel.fr
17.	Echternkamp	Katharina	echternkamp@ph4.physik.uni-goettingen.de
18.	Eckstein	Andreas	andreas.eckstein@physics.ox.ac.uk
19.	Ernstorfer	Ralph	ernstorfer@fhi-berlin.mpg.de
20.	Frank	Bettina	b.frank@pi4.uni-stuttgart.de
21.	Frisch	Benjamin	bfrisch@physik.uni-kl.de
22.	García de Abajo	Javier	javier.garciadeabajo@icfo.es
23.	Giessen	Harald	giessen@physik.uni-stuttgart.de
24.	González	Cristian	cagonza6@gmail.com
25.	Gray	Stephen	gray@anl.gov
26.	Gui	Lili	l.gui@pi4.uni-stuttgart.de
27.	Hartelt	Michael	hartelt@physik.uni-kl.de
28.	Harutyunyan	Hayk	hayk.harutyunyan@emory.edu
29.	Hensen	Matthias	mhensen@physik.uni-bielefeld.de
30.	Hentschel	Mario	m.hentschel@physik.uni-stuttgart.de
31.	Höfer	Ulrich	hoefer@physik.uni-marburg.de
32.	Huber	Bernhard	bernhard.huber@phys-chemie.uni-wuerzburg.de
33.	Humeniuk	Alexander	alexander.humeniuk@gmail.com
34.	Huynh	Dan-Nha	dhuynh@physik.hu-berlin.de
35.	Kilbane	Deirdre	dkilbane@physik.uni-kl.de
36.	Klick	Alwin	klick@physik.uni-kiel.de
37.	Koshihara	Shin-ya	skoshi@cms.titech.ac.jp
38.	Kovacevic	Aleksander	Aleksander.Kovacevic@ipb.ac.rs
39.	Lehr	Martin	lehrm@uni-mainz.de
40.	Leipold	David	david.leipold@tu-ilmenau.de

	Last name	First name	Email
41.	Lienau	Christoph	christoph.lienau@uni-oldenburg.de
42.	Linden	Stefan	linden@physik.uni-bonn.de
43.	Linnenbank	Heiko	h.linnenbank@pi4.uni-stuttgart.de
44.	Lippitz	Markus	markus.lippitz@uni-bayreuth.de
45.	Lisinetskaya	Polina	polina.lisinetskaya@fu-berlin.de
46.	Mahro	Anna-Katharina	akmahro@physik.uni-kl.de
47.	Meixner	Alfred J.	alfred.meixner@uni-tuebingen.de
48.	Meyer zu Heringdorf	Frank	meyerzh@uni-due.de
49.	Niehues	Iris	iris.niehues@uni-muenster.de
50.	Oesterschulze	Egbert	oester@physik.uni-kl.de
51.	Pertsch	Thomas	thomas.pertsch@uni-jena.de
52.	Pfeiffer	Walter	pfeiffer@physik.uni-bielefeld.de
53.	Piecuch	Martin	piecuch@rhrk.uni-kl.de
54.	Podbiel	Daniel	daniel.podbiel@stud.uni-due.de
55.	Ragnoni	Elena	ragnoni@physik.uni-siegen.de
56.	Razinskas	Gary	grazinskas@physik.uni-wuerzburg.de
57.	Reinhardt	Carsten	c.reinhardt@lzh.de
58.	Richter	Marten	mrichter@itp.tu-berlin.de
59.	Rockstuhl	Carsten	carsten.rockstuhl@uni-jena.de
60.	Runge	Erich	Erich.Runge@TU-Ilmenau.de
61.	Schnedermann	Christoph	christoph.schnedermann@chem.ox.ac.uk
62.	Schröder	Benjamin	schroeder@ph4.physik.uni-goettingen.de
63.	Schumacher	Thorsten	thorsten.schumacher@uni-bayreuth.de
64.	Schuster	Cosima	cosima.schuster@dfg.de
65.	Schwarz	Felix	felix.schwarz@tu-ilmenau.de
66.	Seiffert	Lennart	lennart.seiffert@uni-rostock.de
67.	Silies	Martin	martin.silies@uni-oldenburg.de
68.	Smirnov	Vladimir	vladimir.smirnov@uni-oldenburg.de
69.	Specht	Judith	specht@itp.tu-berlin.de
70.	Staude	Isabelle	isabelle.staude@uni-jena.de
71.	Stockman	Mark	mstockman@gsu.edu
72.	Thielen	Philip	thielen@physik.uni-kl.de
73.	Vogelgesang	Ralf	ralf.vogelgesang@uni-oldenburg.de
74.	Wang	Xiao	xiao.wang@uni-tuebingen.de
75.	Wimmer	Lara	wimmer@ph4.physik.uni-goettingen.de
76.	Wolf	Daniela	daniela.wolf@uni-bayreuth.de
77.	Zhan	Jinxin	jinxin.zhan@uni-oldenburg.de

Application of Fourier–Pade Approximation in Analysis of Holographic Diffraction Gratings

D. SEVIC*, S. SAVIC-SEVIC, D. PANTELIC AND B. MARINKOVIC

Institute of Physics, University of Belgrade, Zemun Pregrevica 118, P.O. Box 68, 11080 Belgrade, Serbia

(Received February 24, 2012; in final form July 9, 2013)

The diffraction gratings, fabricated in our laboratory, were presented and analyzed by atomic force microscopy in earlier publications. In this paper we apply the Fourier–Pade approximation on our data previously analyzed by fast Fourier transform, proving advantages of using the Fourier–Pade approximation for spectral analysis of structural properties of some optical materials.

DOI: [10.12693/APhysPolA.124.619](https://doi.org/10.12693/APhysPolA.124.619)

PACS: 02.30.Mv, 02.30.Nw, 42.40.Eq

1. Introduction

Fast Fourier transform (FFT) is widespread tool in spectral analysis, primarily because of its computational efficiency and a steady convergence as a function of increasing the sequence length. In this paper a method based on the Fourier transform and Pade approximants [1, 2] is investigated for analysis of holographic diffraction gratings. Pade approximants are often used to accelerate the convergence of a slowly converging sequence. Namely, for a power series

$$F_n(z) = \sum_{k=0}^N c_k z^k \quad (1)$$

of order N in the variable z (real or complex) with coefficients c_k , the Padé approximant is a rational fraction $P_m(z)/Q_n(z)$, which approximates the fully converged values of the function $F_n(z)$. If we let $z = e^{-jkn}$, then Eq. (1) calculates discrete Fourier transform (DFT), so the Pade method could be used to improve spectral resolution of DFT. The method is usually called the Fourier–Pade (FP) approximation.

In this analysis we applied Fourier–Pade approximation on data acquired by atomic force microscopy (AFM) scans of diffraction grating investigated in earlier papers [3, 4]. We recently used FP for analysis of holographic photonic crystal structures [5]. All obtained results proved advantages of using FP for spectral analysis of structural properties of optical materials instead of FFT. Our calculation of FP is efficiently implemented as a C code. The computer running time of calculating FP is only slightly longer than by evaluating the FFT.

2. Analyzed samples

The diffraction gratings fabricated in our laboratory were analyzed by AFM. Figure 1 shows a zoomed part of sinusoidal shaped grating recorded in dextran sensitized with ammonium dichromate (DCD) [3] (left side of figure). The AFM greyscale image is usually presented in

pseudocolor, where different profile heights are coded as different colors. A corresponding one-dimensional profile is also shown in Fig. 1 (right side).

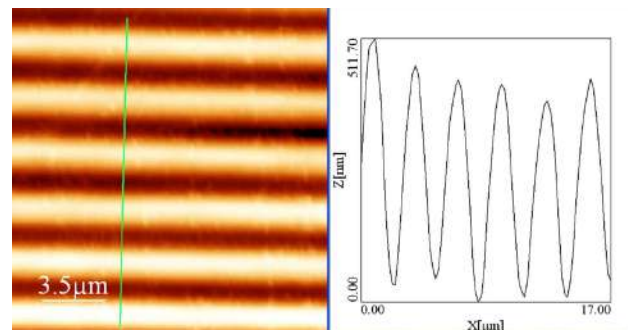


Fig. 1. The zoomed part of AFM image of DCD surface relief diffraction grating with sinusoidal profile (left) and its line profile (right).

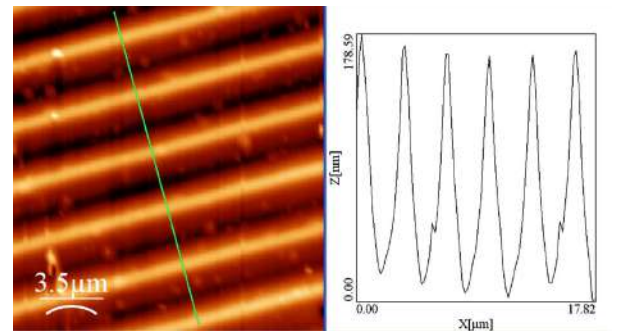


Fig. 2. The zoomed part of AFM image of DCD surface relief diffraction grating with non-sinusoidal profile (left) and its line profile (right).

Non-sinusoidal DCD profile grating and its line profile are shown in Fig. 2.

Figure 3 shows a saw-tooth shaped dental polymer (Herculite xrv) grating and its line profile. The grating was made by copying dichromate sensitized pullulan (DCP) grating into dental composite [4].

*corresponding author; e-mail: sevic@ipb.ac.rs

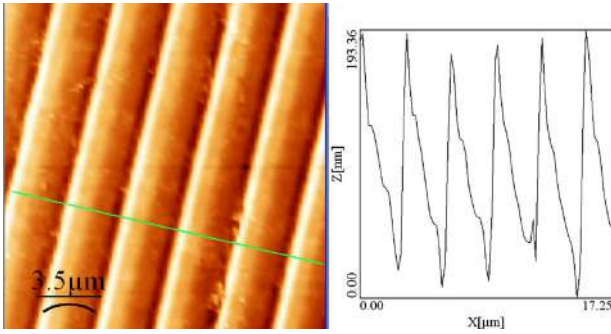


Fig. 3. The zoomed part of AFM image of dental composite (Herculite xrv) diffraction grating (left) and its line profile (right).

3. Analysis of diffraction grating structures using FP

Two-dimensional (2D) Pade approximation is not separable, so calculating the 2D FP is very demanding [1, 2, 5]. Fortunately, diffraction grating structures which are of interest here have directional structure, so we will use the Pade approximation to enhance one-dimensional Fourier analysis of line profiles. The Fourier transform of line profile of the surface relief shown in Fig. 1 is calculated and presented in Fig. 4. Zero frequency (DC)

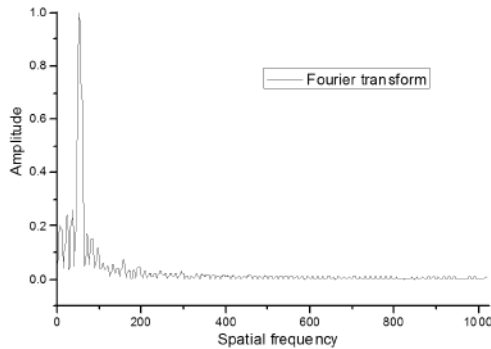


Fig. 4. Fourier transform of line profile of surface relief shown in Fig. 1.

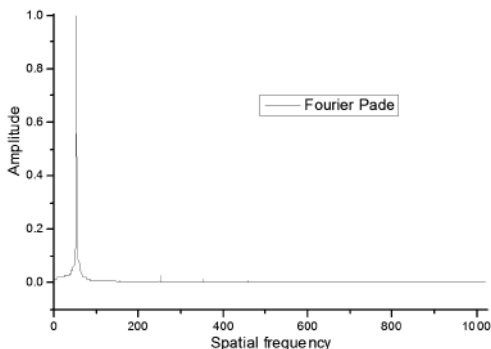


Fig. 5. Fourier-Pade approximation of line profile of surface relief shown in Fig. 1.

component is removed by subtracting the average value of the sequence from every point. FP of the same data is calculated and presented in Fig. 5. AFM images analyzed here are 256×256 , so lengths of analyzed line profiles are up to about $\sqrt{2 \times 256}$. To enhance resolution, the Fourier transform of 2048 points is used. The Fourier spectra of real valued data are symmetrical, so only one half of the spectra are presented. Spatial frequency is in the range 0 to π and is scaled to 1024 points. Sinusoidal component is easy to discern even in Fig. 4, although there is a lot of “ringing” in FT spectrum. Fundamental sinusoidal component is much more pronounced in FP spectrum. Advantages of using the FP for structural analysis are obvious.

The Fourier transform of line profile of the nonsinusoidal surface relief shown in Fig. 2 is calculated and presented in Fig. 6. DC component is, again, removed. FP of the same data is calculated and presented in Fig. 7. Fundamental components are possible to notice in Fig. 6, but not clearly. Fundamental components are much clearer on FP spectrum, Fig. 7. Components at about 280, 395, and 420 are visible only on FP spectrum. In this case, FP provides much better spectral analysis. However, it should be noted that aforesaid components could be numerical effects caused by the fact that line profile is not orthogonal to the horizontal axis of AFM image. Then,

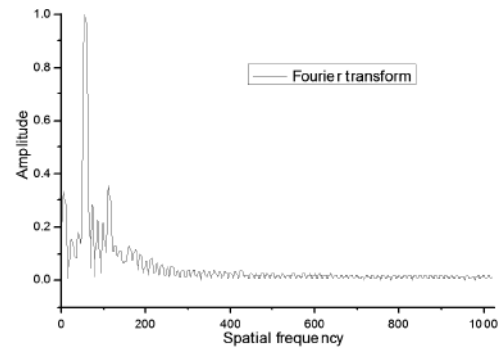


Fig. 6. Fourier transform of line profile of nonsinusoidal surface relief shown in Fig. 2.

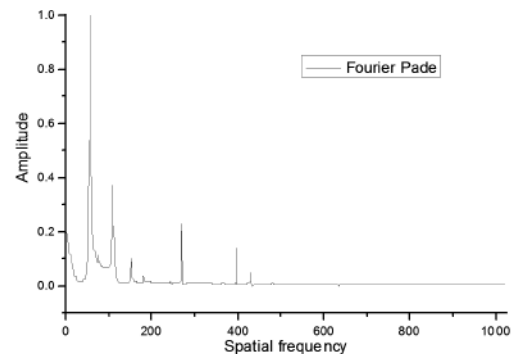


Fig. 7. Fourier-Pade approximation of line profile of nonsinusoidal surface relief shown in Fig. 2.

the values of the line profile are interpolated through orthogonally sampled points of AFM image.

The Fourier transform of line profile of the saw-tooth shaped surface relief shown in Fig. 3 is calculated and presented in Fig. 8. DC component is, again, removed. FP of the same data is calculated and presented in Fig. 9. Saw-tooth sequence has plenty of components which are not quite possible to identify in Fig. 8. Components are easier to identify on FP spectrum, Fig. 9. FP analysis provides enhanced insight into spatial frequency characteristics of diffraction grating structures.

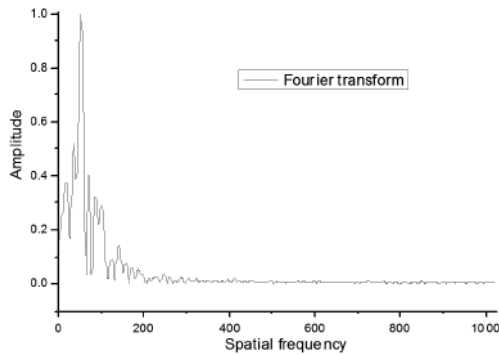


Fig. 8. Fourier transform of line profile of saw-tooth shaped surface relief shown in Fig. 3.

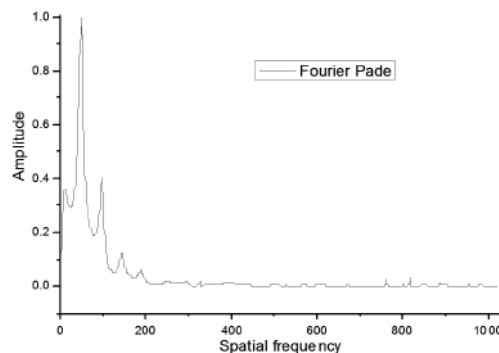


Fig. 9. Fourier–Pade approximation of line profile of saw-tooth shaped surface relief shown in Fig. 3.

It should be commented here that although with such superior performance, as presented in this study, FP is not widely used as FFT. There are several reasons for this. First of all, as already mentioned, the FFT is the

most popular tool for spectral analysis because of its simplicity of using and availability. The Fourier–Pade approximation is not so simple to use, moreover, it is not available as application software. Computational complexity of length- N FFT is of order of $(N \log N)$ arithmetic operations, while FP requires several orders of magnitude larger number of operations, depending on the rate of its convergence for the specific case. However, for relatively short one-dimensional data sequences analyzed in this paper, the computer running time of calculating FP is just slightly longer than when computing the FFT.

4. Conclusion

In this paper a method based on the Fourier transform and Pade approximants is investigated for structural analysis of diffraction gratings fabricated in our laboratory. Compared to the conventional use of the Fourier transform, structural analysis of fabricated samples is enhanced by better spatial frequency resolution provided by the Fourier–Pade approximation. Spectral components which are just discernible in the Fourier spectrum are more pronounced when using the Fourier–Pade approximation. We implemented computing of the Fourier–Pade approximation as a C code.

Acknowledgments

The work has been done within the projects OI 171020, OI 171038 and III45016 financed by the Ministry of Education and Science, Republic of Serbia.

References

- [1] M.F. Calaghan, D.J. Larkman, J.V. Hajnal, *Magn. Res. Med.* **54**, 1490 (2005).
- [2] Dz. Belkic, *Nucl. Instrum. Methods Phys. Res. A* **471**, 165 (2001).
- [3] S. Savic-Sevic, D. Pantelic, *Opt. Mater.* **30**, 1205 (2008).
- [4] S. Savic-Sevic, D. Pantelic, *Opt. Expr.* **13**, 2747 (2005).
- [5] D. Sevic, S. Savic-Sevic, D. Pantelic, B. Jelenkovic, B.P. Marinkovic, *Acta Phys. Pol. A* **116**, 647 (2009).

Micro- and Nanostructures of Iridescent Wing Scales in Purple Emperor Butterflies (Lepidoptera: *Apatura ilia* and *A. iris*)

SREĆKO B. ĆURČIĆ,^{1*} DEJAN V. PANTELIĆ,² BOŽIDAR P.M. ĆURČIĆ,¹ SVETLANA N. SAVIĆ-ŠEVIĆ,² SLOBODAN E. MAKAROV,¹ VESNA B. LAČKOVIĆ,³ MILICA M. LABUDOVIĆ-BOROVIĆ,³ NINA B. ĆURČIĆ,⁴ AND DEJAN V. STOJANOVIĆ⁵

¹*Institute of Zoology, Faculty of Biology, University of Belgrade, Studentski Trg 16, 11000 Belgrade, Serbia*

²*Institute of Physics, University of Belgrade, Pregrevica 118, 11080 Zemun, Serbia*

³*Institute of Histology and Embryology, Faculty of Medicine, University of Belgrade, Višegradska 26, 11000 Belgrade, Serbia*

⁴*Geographical Institute "Jovan Cvijić", Serbian Academy of Sciences and Arts, Đure Jakšića 9, 11000 Belgrade, Serbia*

⁵*Fruška Gora National Park, Zmajev Trg 1, 21208 Sremska Kamenica, Serbia*

KEY WORDS *Apatura ilia* and *A. iris*; Purple Emperor butterflies; SEM; TEM; wing scale morphology

ABSTRACT *Apatura ilia* (Denis and Schiffermüller, 1775) and *A. iris* (Linnaeus, 1758) are fascinating butterflies found in the Palaearctic ecozone (excepting the north of Africa). The wings of these insects are covered with a great number of two types of scales positioned like roof tiles. Type I scales are on the surface, while type II scales are situated below them. The structural color of the type I scales is recognized only on the dorsal side of both the fore and hind wings of the males of the aforementioned species. Both types of scales are responsible for pigment color of the wings, but iridescence is observed only in the type I scales. The brilliant structural color is due to a multi-layer structure. The features of the scales, their dimensions and fine structure were obtained using scanning electron microscopy. Cross sections of the scales were then analyzed by transmission electron microscopy. The scales of the “normal” and *clytie* forms of *A. ilia* have a different nanostructure, but are of the same type. A similar type of structure, but with a different morphology, was also noticed in *A. iris*. The scales of the analyzed species resemble the scales of tropical *Morpho* butterflies. *Microsc. Res. Tech.* 75:968–976, 2012. © 2012 Wiley Periodicals, Inc.

INTRODUCTION

The diurnal representatives of the order Lepidoptera (butterflies) are thought to be very attractive insects. Iridescence features are present in numerous butterfly species, and in particular those inhabiting the tropics (Garrett et al., 2009; Matejková-Plšková et al., 2009; Prum et al., 2006; Shawkey et al., 2009; Srinivasarao, 1999; Vukusic, 2006; Vukusic and Sambles, 2003; Vukusic et al., 1999). Some butterflies are mimetic, camouflaged, and therefore unattractive and invisible to potential predators. Others have visible aposemy and therefore have warning coloration. Sexual dimorphism is present in some taxa, like in the *Apatura* species.

Apart from structural coloration, pigment coloration is also present in the butterfly species. Coloration in butterflies is due to several physical effects. Selective absorption and fluorescence are the consequence of the chemical properties of chitin and various pigments. On the other hand, interference, diffraction, and scattering produce coloration due to the micro- and nanostructure of the cuticle. Structural color investigations in butterflies have been intensive and diverse in the last period (Ghiradella, 1989, 1991, 1998; Ghiradella et al., 1972). The following features are the most interesting in these studies: the optical properties of scales and their nanostructure (Birø et al., 2007; Han et al., 2009; Srinivasarao, 1999; Vártesy et al., 2006), diffraction

and interference in butterflies (Vukusic et al., 1999), ultraviolet reflection (Imafuku et al., 2002), brightness (Stavenga et al., 2004) and blackness of butterfly scales (Vukusic et al., 2004), fluorescence (Vukusic and Hooper, 2005), coherent scattering-induced structural color of scales (Prum et al., 2006), light scattering and absorption of scales (Morehouse et al., 2007), possible role of scales in artificial material manufacturing (Kertész et al., 2008), measuring and modeling of the optical properties of scales (Luke et al., 2009), and optical reflectors in butterflies (Vukusic et al., 2009). The coloration of the ventral side of the wings originated from pigments and is not structural.

The species *Apatura ilia* (Denis and Schiffermüller, 1775) includes a total of six subspecies and is represented by two phenotype forms: *ilia* or “normal” form (the darker one) and *clytie* (the lighter one) (Higgins and Riley, 1970). The presence of these forms depends on the type of habitat and climate (Lafranchis, 2004;

*Correspondence to: Srećko Ćurčić, Institute of Zoology, Faculty of Biology, University of Belgrade, Studentski Trg 16, 11000 Belgrade, Serbia. E-mail: srecko@bio.bg.ac.rs

Received 2 December 2011; accepted in revised form 13 January 2012

Contract grant sponsor: Serbian Ministry of Education and Science; Contract grant numbers: ON173038, ON171038, III45016, III41002, III47007, III43002.

DOI 10.1002/jemt.22021

Published online 6 March 2012 in Wiley Online Library (wileyonlinelibrary.com).

Tolman and Lewington, 1997). It was proven that the “normal” form of the species is present in cooler regions, where larval development is generally longer. On the other hand, the form *clytie* is found in warmer habitats, where the larvae develop faster. These forms are treated as two distinctive subspecies by some authors (Jakšić, 2003). The so-called “normal” form of the Lesser Purple Emperor (*Apatura ilia*) is very similar to the Purple Emperor (*A. iris*). These are distinguishable by the underside wing pattern and by the extra eye spot on the dorsal side of the fore wing. The form *clytie* of *Apatura ilia* is generally common as well. This form has more extensive pale markings on the upper side of the wings that are yellow or buff, not white. It is very similar to the Freyer’s Purple Emperor (*Apatura metis* Freyer, 1829).

The species *Apatura iris* (Linnaeus, 1758) comprises four subspecies. The dorsal side of the wings in males has violet reflection.

The occurrence of iridescence in *Apatura* spp. is known, but insufficiently studied (Han et al., 2008; Vértsey et al., 2007). The authors analyzed the phenomenon in *Apatura ilia* f. *clytie* (Han et al., 2008), but very rarely in the “normal” form of the species (Vértsey et al., 2007). Until very recently, *Apatura iris* has not been studied at all. In our previous article, we started a study of its optical properties and this article is an in-depth analysis of biological significance of submicron structures of *Apatura* spp. (Pantelić et al., 2011).

Apatura species are characterized by the basic pigment color and intensive iridescence in the UV region of the spectrum. The males of *Apatura* spp. have iridescent color on the dorsal side of the wings. The role of this characteristic is probably in the intrasexual communication between males (i.e., territorial behavior of the butterflies), rather than intersexual communication and attraction (Silberglied, 1984). The male individuals of *Apatura* species can be easily noticed by the wing iridescence in their habitats. The flight behavior of the male *Apatura iris* was recently studied, and it consisted mainly of conspecific and patrol flights within the continuum from perching to patrolling (Page, 2010). The daily aggregation of males at favored landmark sites from around midday was observed as well (Page, 2010). The structural color of the wings in males is visible in their flight. The iridescence of the wings is noticeable at certain angles during wing movements. During flight, the color of the dorsal side of the wings changes from violet-blue to brownish.

Two types of scales are present on the dorsal side of the wings of the *Apatura ilia* form *clytie* (Han et al., 2008). These scales cover the wing surface like tiles on a roof. Each of the scales possesses parallel ridges. About 1,200 ridges per millimeter are situated on the surface of the first type of scale. On the second type, there are about 700 ridges per millimeter. Cross ribs connect adjacent ridges. Type I scales are iridescent, while type II are not. The ventral side of the wings is without iridescence. The second type of scale is mostly situated ventrally, but is also present dorsally on the wings, below type I scales. The iridescent effect of the scales is caused by the presence of the first type of scale (Han et al., 2008). From the transverse section of the first type of scale, we can see that they are composed of multilayer-structured ridges. Each ridge comprises

about 10 cuticle layers mutually separated by an air layer. The cuticle layers are thicker than the air layers. The mentioned structures enable the structural coloration of the wings due to Bragg diffraction.

The article presents full information on wing scale micro- and nanostructures related to wing color in the given species, as well as in both forms of *Apatura ilia* observed by high resolution scanning electron microscopy (SEM) and transmission electron microscopy (TEM).

Analyzed Species

The species considered herein belong to the subfamily Apaturinae, family Nymphalidae, of butterflies. These butterflies are of medium to large dimensions (wingspan 50–70 mm). The thorax is massive and the wings are strong. The genus *Apatura* Fabricius, 1807 comprises a total of four species, among which three are present in Europe: *Apatura ilia*, *A. iris*, and *A. metis*. Sexual dimorphism is clearly noticeable. The dorsal side of the male wings of *Apatura* butterflies is of violet-blue iridescent hue. This hue is caused by optical interference (Pantelić et al., 2011). Additional difference between the sexes is found in the structure of their fore legs that are larger in females, with five tarsomeres, while in males there are three tarsomeres.

***Apatura ilia* (Denis and Schiffermüller, 1775) (Fig. 1a).**

Total Distribution. Inhabits the areas of Central and Southern Europe, the Caucasus Mountains, the southern part of the Urals, south-western Kazakhstan, and north-eastern China.

Short Description. Wingspan: 50–60 mm. “Normal” form: the dorsal side of the fore wings has a well-defined eye-shaped spot. Both dorsal and ventral sides of the hind wings have a slightly curved white strip each. Ventral side of the fore wings: the cell has two two-point shaped black spots. Form *clytie*: the dorsal side of the fore wings: orange postdiscal strip not prolonged to the apex. Dorsal side of the hind wings: postdiscal row of points well developed, without pale points. Ventral side of the hind wings: postdiscal points well distinguished, the lower one being eye-shaped, blue. Females are usually bigger, with elongated white spots. Their iridescence was not observed.

Flight Period. Two generations per year exist in southern regions—May–June and August–September, but only one in northern areas—July (Higgins and Riley, 1970; Lafranchis, 2004; Tolman and Lewington, 1997).

***Apatura iris* (Linnaeus, 1758) (Fig. 1b).**

Total Distribution. Lives in Central Europe, north-western Kazakhstan, southern Urals, Amur region, north-eastern China, and Korea.

Short Description. Wingspan: 58–70 mm. The dorsal side of the fore wings is without eye-shaped spots. Both dorsal and ventral sides of the hind wings have a straight white strip each. Ventral side of the fore wings: the cell has two compact black spots. The female is usually bigger, without iridescence, with extended white spots on dorsal side of the wings.

Flight Period. May–June and August–September. Two generations per year in southern and one in northern parts of Europe (Higgins and Riley, 1970; Lafranchis, 2004; Tolman and Lewington, 1997).

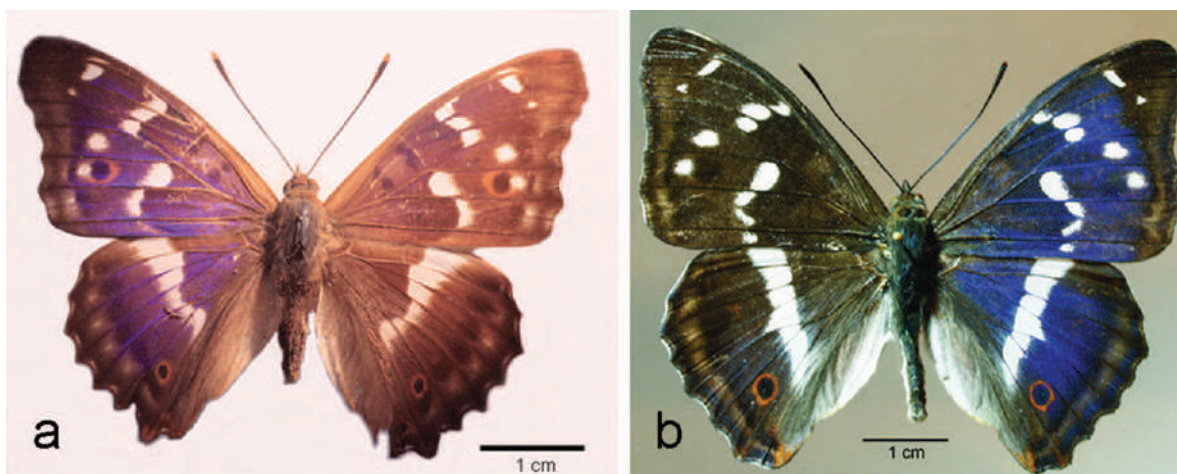


Fig. 1. The Purple Emperor butterfly species analyzed. Optical microscopy images of body habitus of "normal" form of *Apatura ilia* (Denis and Schiffermüller, 1775) (a) and of *A. iris* (Linnaeus, 1758) (dorsal views) (b). [Color figure can be viewed in the online issue, which is available at wileyonlinelibrary.com.]

MATERIALS AND METHODS

Data Collection

Specimens of the species *Apatura ilia* and *A. iris* were used for fine morphological investigations of the wings. Both species were collected from the Balkan Peninsula: *Apatura ilia* ("normal" form)—Mt. Fruška Gora, northern Serbia (July 2009, leg. D. Stojanović), and *A. iris*—Mt. Stara Planina, south-eastern Serbia (July 2009, leg. D. Stojanović). The butterflies were killed by pressing their thorax between the fingertips. The specimens were kept in entomological boxes belonging to the collection of the Institute of Zoology, Faculty of Biology, University of Belgrade (Figs. 1a and 1b).

SEM Procedure

Two specimens of *Apatura ilia* and two specimens of *A. iris* were rinsed by diethyl ether to obtain a clear surface of the wings. The wings of the males were cut to form squares with a surface of 1 mm². This was followed by dehydration to get dry samples. These were fixed on test-beds and subsequently covered with gold. The prepared samples were analyzed using a tungsten-filament scanning electron microscope (JSM-6460LV, JEOL, Tokyo, Japan). During the microscopy, a 20-kV voltage was used.

TEM Procedure

The wings were cut into small pieces. The tissue was fixed by immersion in 3% solution of glutaraldehyde in 0.1 mol/dm³ cacodylic buffer (pH = 7.4) over night at +4°C. The cacodylic buffer was prepared as an aqueous solution of cacodylic acid sodium salt trihydrate (C₂H₆AsO₂Na × 3 H₂O). Thereafter, the tissue samples were carefully rinsed with cacodylic buffer and postfixated in 1% solution of osmium tetroxide (OsO₄) in 0.1 mol/dm³ cacodylic buffer for 1 h at +4°C. The tissue was then rinsed in cacodylic buffer and incubated over night at +4°C in a 4.8% aqueous solution of uranyl acetate.

The tissues were dehydrated in graded ethanol aqueous solutions. First, 50% ethanol was used for 5 min at room temperature. Thereafter, the tissues were treated

with 70% ethanol for 30 min at +4°C, and with 96% ethanol (Gram, Belgrade, Serbia) for 30 min at +4°C. Afterward, 100% ethanol (Zorka Pharma, Sabac, Serbia) was applied three times for 10 min at room temperature. The tissues were then cleared by propylene oxide (C₃H₆O; SERVA 33715, Heidelberg, Germany) twice for 10 min at room temperature. During the procedure, the tissues were continuously and completely immersed into the described chemicals. Potential air drying of tissues was avoided with special caution. Ethyl alcohol solutions of 50% and 70% were made from 100% ethanol.

After the dehydration procedure, the samples were embedded in a four-component embedding medium made of: (i) epoxy embedding medium (Fluka Chemika 45345, Buchs, Germany), (ii) dodecyl succinic anhydride (C₁₆H₂₆O₃; Fluka Chemika 45346), (iii) Epon hardener methyl nadic anhydride (C₁₀H₁₀O₃; Fluka Chemika 45347), and (iv) Epon hardener accelerator *n*-benzyl dimethylamine [C₆H₅-CH₂-N(CH₃)₂; Agar Scientific R1062b, Stansted, United Kingdom]. Embedding of the tissue through polymerization of the medium was done at +60°C for 36–48 h.

The blocks of embedded tissue were sectioned by an ultramicrotome (Leica Ultracut UCT, Vienna, Austria). First, semithin 1-μm-thick sections were cut, stained with toluidine blue, and analyzed by an Olympus BX41 microscope (Olympus GmbH, Hamburg, Germany). All the slides were photo-documented by an Olympus C—5060 ADU wide zoom camera and the Olympus DP-soft Image Analyzer programme (Olympus GmbH).

Thereafter, the ultrathin sections were sampled from chosen representative areas. The ultrathin sections were treated with uranyl acetate [(CH₃COO)₂UO₂ × 2 H₂O] and lead citrate [Pb₃(C₆H₅O₇)₂ × 3 H₂O], and were analyzed by TEM (Fei Morgagni 268D transmission electron microscope, Eindhoven, The Netherlands). The transmission electron microscope was equipped with a MegaViewIII Soft Imaging System digital camera (Olympus Soft Imaging Solutions GmbH, Münster, Germany).

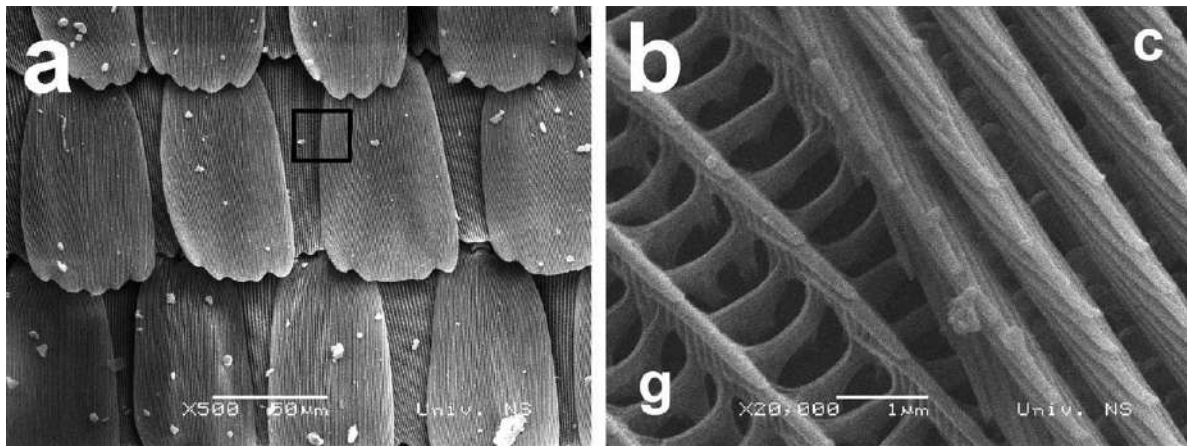


Fig. 2. SEM images of scales of upper surface of wing of *Apatura ilia* (dorsal view) at lower (a) and higher magnifications (b). The parts of cover (c) and ground scales (g) are marked by a rectangle and enlarged (b).

RESULTS

Location, General and Fine Structure, and Morphometric Measurements of Scales in *Apatura ilia*

We recognized two types of scales on the dorsal side of both the fore and hind wings of the “normal” form of *Apatura ilia*. All the scales are positioned like roof tiles and possess parallel ridges covering the entire dorsal side. Type I scales (cover scales) are on the surface, and type II scales (ground scales) are situated below them. The type I scales are ~ 104 – $112 \mu\text{m}$ long and 53 – $58 \mu\text{m}$ wide (Fig. 2a). Han et al. (2008) reported that the type I scales in the *clytie* form of *Apatura ilia* are larger— $150 \mu\text{m}$ long and $60 \mu\text{m}$ wide. The type I scales are responsible for the violet-blue iridescence of *Apatura ilia* (Pantelić et al., 2011). Iridescent violet-blue can be seen on the whole dorsal wing surface in males and is observed in narrow angular range. These scales are pale brown, with melanin, reflecting violet-blue iridescence on their surfaces. The ones in white spots of the wings are almost the same in shape and structure except the color, which is transparent and lustrous white due to lack of pigment. The type II scales are pigmented, but without reflective effects. Their apical border mostly has five projections.

The ridges on the type I scales are mutually closer (about 680 nm) than the same structures on the scales of type II (distance 1.23 – $1.35 \mu\text{m}$). The ridges of the type I scales are $0.50 \mu\text{m}$ wide, while the ridges situated on the type II scales are $0.27 \mu\text{m}$ wide. About 1,500 ridges are present per millimeter on the surface of the type I scales (vs. about 1,200 ridges per millimeter in the form *clytie*), while there are about 700 ridges per millimeter on the surface of the type II scales (like in the form *clytie*; Han et al., 2008). Each pair of ridges from the type II scale is connected by cross ribs (Fig. 2b). Lamellae on the ridges of the type I scales are dorsally subtriangular, overlap, and form the multilayer structure responsible for iridescence (Fig. 2b; Pantelić et al., 2011). Lamellae exist dorsally on the ridges of the type II scales as well, but these are subcylindrical, slightly widened basally, only partly

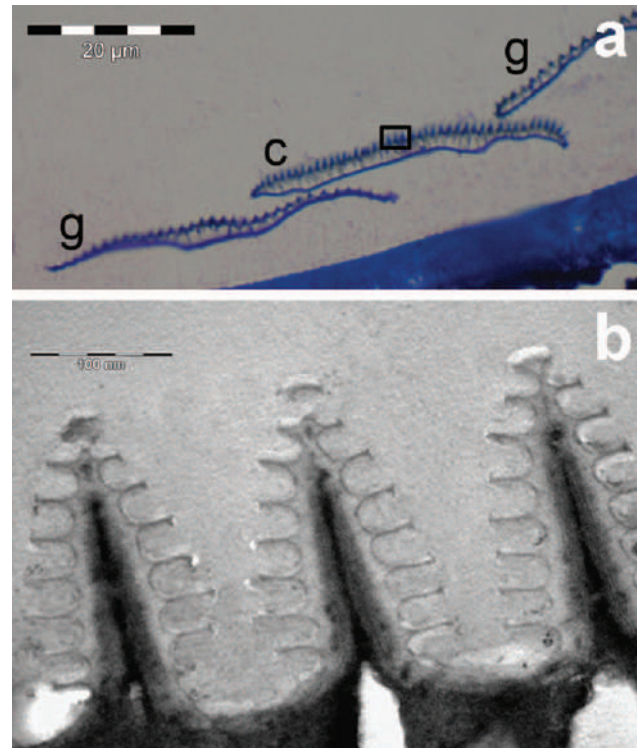


Fig. 3. Images of cross sections through wing scales in *Apatura ilia*. Optical microscopy image of semithin cross section through cover (c) and ground scales (g) (a). The lamellae are marked by a rectangle. TEM image of ultrathin cross section through longitudinal ridges of the cover scale, showing lamellae on the ridges (b). One-fifth of the whole scale line = 100 nm . [Color figure can be viewed in the online issue, which is available at wileyonlinelibrary.com.]

overlap, and do not produce structural coloration. The lamellae on the ridges of the type I scales of the “normal” form of *Apatura ilia* in lateral view have a visible multilayer structure, are conifer-like in cross section, with six-seven pairs of straight lateral projections widened distally, and are triangularly pointed (Figs. 3a and 3b). The whole interior of the ridges of

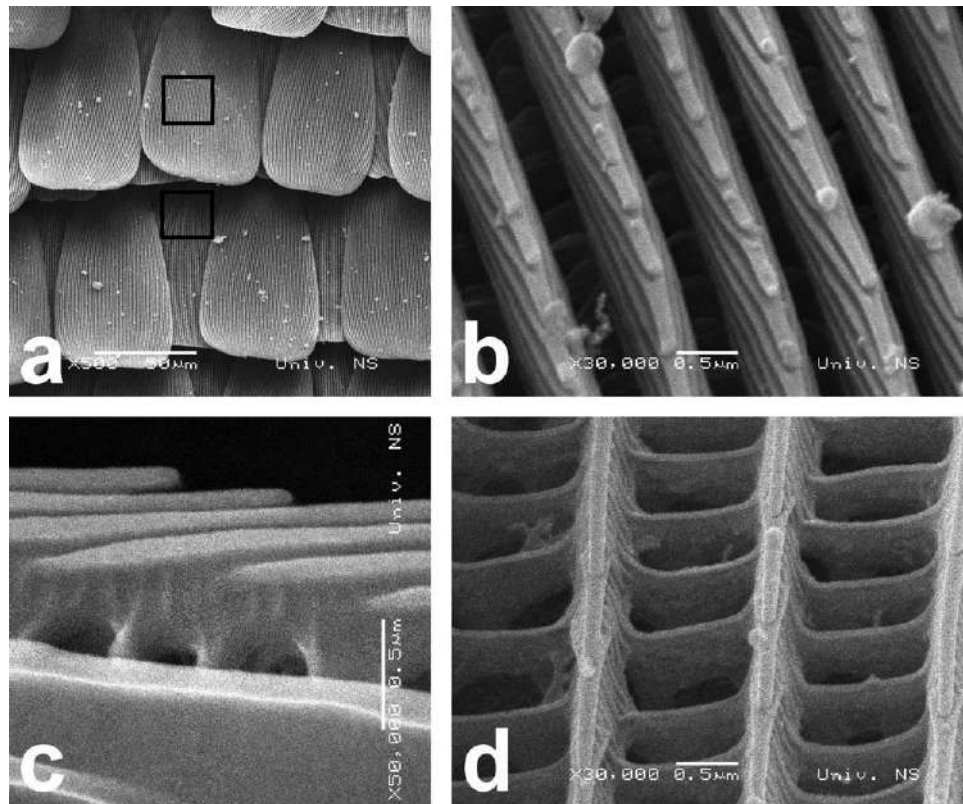


Fig. 4. SEM images of scales of upper surface of wing of *Apatura iris*. SEM image of scales of the upper surface of wing (dorsal view) (a). The parts of cover and ground scales are marked by rectangles. SEM images of lamellae of the cover scale in dorsal (b) and lateral views (c). SEM image of surface of ground scale (dorsal view) (d).

the type I scales is with a dark pigment and strongly melanized (Fig. 3b). The ventral wing surface is virtually flat, but small ridges are apparent on the lower surface, as seen in its cross section.

The micrographs of the TEM-photographed cross sections of the “normal” and *clytie* forms of *Apatura ilia* show clear distinctions between them: the lamellae of the “normal” form are higher, widening basally, with six/seven pairs of lateral projections; the lamellae of form *clytie* are lower, almost subparallel, with five/six pairs of lateral projections (Han et al., 2008; present study). The abovementioned morphological differences supported by the ecological preferences, other existing morphological differences, and our data provide additional support to the view that these forms may even be two distinct subspecies.

The type I scales of both forms of *Apatura ilia* have a role in iridescence due to their denser microscopic structure in comparison to the type II scales (Pantelić et al., 2011). The type I scales are numerous in the iridescent areas of the wings. There are no such scales on the pairs of female wings and on the non-iridescent areas of male wings, so that the color of these wings does not change when viewed from different angles. Type II scales are present both on the dorsal (below the type I scales) and ventral sides of the wings. They do not have iridescent features, but possess pigments.

Location, General and Fine Structure, and Morphometric Measurements of Scales in *Apatura iris*

Two types of scales are situated on the dorsal side of both the fore and hind wings in *Apatura iris* males. The scales here also look like roof tiles. They have parallel ridges situated dorsally. Analyzing the dorsal side of both wings in males, we registered type I scales (cover scales) on the surface with type II scales (ground scales) below them. The type I scales have a role in the violet-blue iridescence effects of *Apatura iris* (Pantelić et al., 2011). Iridescent violet-blue can be seen on the whole dorsal wing surface in males and is observed in narrow angular range. These scales are brown, with melanin, reflecting violet-blue iridescence on their surfaces. The ones in white spots of the wings are almost the same in shape and structure except the color, which is transparent and lustrous white due to lack of pigment. The type II scales are pigmented, but do not produce iridescence. The type I scales are ~ 95–100 μm long and 55–61 μm wide, somewhat shorter than in *Apatura ilia* (Fig. 4a). Their apical border is mostly straight or with three projections. The ridges on the scales are mutually closer (distance of about 820 nm vs. 680 nm in *A. ilia*) than the ridges on the scales of type II (distance 1.23–1.46 μm). The ridges of the type I scales are 0.53 μm broad (vs. 0.50 μm in *Apatura ilia*), while the ridges on type II scales are 0.18 μm



Fig. 5. TEM image of ultrathin cross section through longitudinal ridges of the cover scale in *Apatura iris*, showing lamellae on the ridges. One-fifth of the whole scale line = 100 nm.

TABLE 1. Character differences between the scales of the analyzed Purple Emperor and Morpho butterfly species

Morphological character	<i>Apatura ilia</i>	<i>A. iris</i>	<i>Morpho</i> spp.
Type I scale length (μm)	104–150	95–100	200–220
Type I scale width (μm)	53–60	55–61	85–108
Shape of apical border of the scale I	Mostly with five projections	Straight/with three projections	Straight/rounded
Distance between ridges on the type I of scale (nm)	680	820	450–1,000
Distance between ridges on the type II of scale (μm)	1.23–1.35	1.23–1.46	—
Width of a ridge on the type I of scale (μm)	0.50	0.53	0.45–0.78
Width of a ridge on the type II of scale (μm)	0.27	0.18	—
Type I scale ridge period	1,200–1,500/mm	1,200/mm	1,400–2,000/mm
Type II scale ridge period	700/mm	630/mm	—
Shape of lamellae of the type I of scale	Higher/of the same height, triangular/almost subparallel, somewhat narrowed sub-basally	Lower, triangular, not narrowing basally	Much higher, gradually narrowing distally, almost subparallel, not narrowing basally
Number of lateral lamellar projections of the type I of scale	Six/seven pairs	Five/six pairs	Five-twelve pairs
Shape of lateral lamellar projections of the type I of scale	Widened distally, straight	Not widened distally, bent	Not widened distally, straight
Degree of melanization of interior of the ridge of the type I of scale	More expressed	Less expressed	More expressed

The ranges of single measurements are presented (Berthier, 2010; Prum et al., 2006; Srinivasarao, 1999; Vukusic et al., 1999; present study).

wide (vs. 0.27 μm in *A. ilia*). About 1,200 ridges are present per millimeter on the surface of the type I scales (vs. 1,200–1,500 ridges per millimeter in *A. ilia*), while about 630 ridges per millimeter exist on the surface of the type II scales (vs. 700 ridges per millimeter in *A. ilia*). The lamellae on the ridges of the type I scales are subtriangular (dorsal view), overlap, and form the multilayer structure responsible for the iridescent color (Figs. 4b and 4c; Pantelić et al., 2011). Each pair of ridges from the type II scales is connected by cross ribs (Fig. 4d). The lamellae on the ridges of the

type II scales are subcylindrical (dorsal view), widened only basally, just partly lying one on another. They are not iridescent. The lamellae on the ridges in cross section exhibit a multilayer structure (lateral view), conifer-like, with five/six pairs of bent lateral projections that are not dilated distally, triangularly pointed (Fig. 5). Only basal part of the ridge interior of the type I scales is with a dark pigment. The ridges are therefore less melanized (Fig. 5). The ventral wing surface is virtually flat, but small ridges are apparent on the lower surface, as seen in its cross section. The geometry of

the microscopic structure of the *A. iris* wing scale resembles that in *A. ilia*.

Presence, number, color, and position of both types of scales in *Apatura iris* are similar to ones in *Apatura ilia*, as listed in the last paragraph of the previous heading.

DISCUSSION

Apart from the differences between *Apatura ilia* and *A. iris* observed by SEM that are listed in the previous chapter, the following differences between the mentioned species were additionally registered in the structures visible in micrographs done by TEM. The lamellae of *Apatura ilia* are higher/of the same height, triangular/almost subparallel, somewhat narrowed sub-basally, with

six/seven pairs of straight lateral projections widened distally; the lamellae of *Apatura iris* are lower, triangular, not narrowed basally, with five/six pairs of bent lateral projections that are not widened distally. Furthermore, the type I scales of both species look somewhat different in the degree of melanization (occurrence of a dark pigment in the ridge interiors; Table 1). Additionally, character differences between the scales of the analyzed Purple Emperor butterfly species and tropical *Morpho* species (where scale iridescence is noticeable as well) are listed in Table 1 (Berthier, 2010; Prum et al., 2006; Srinivasarao, 1999; Vukusic et al., 1999; present study).

The type I scales in both analyzed butterfly species show iridescent effects due to their denser microscopic structure in comparison to the type II scales (Pantelić et al., 2011). The type I scales have a superficial position on the dorsal side of both the fore and hind wings in males, and they are present there in great abundance. The result of this is the occurrence of violet-blue brilliance in the areas of the wings. Females lack such scales and these are not registered on the ventral side of both wing pairs in males. Therefore, no optical effects are present in females and on the ventral surface of male wings. Type II scales totally cover the ventral side of the wings, and lie below the type I scales on the dorsal side of the wings. The color of the type II scales has pigment origin.

Additionally, lamellae are not present along the whole type I scale length in either species. The proximal-most part of the scale I has ridges, but lamellae are missing and appear subproximally. Therefore, we can say that iridescent effects may be produced by most of the surface of the dorsal scales, but not by the whole scales. Furthermore, the cross ribs with pigment granules are absent in this area as well. The proximal-most parts of the type I scales are covered by distal-most parts of the scales of the same type, and are not responsible for the color of the wings. On the other hand, both lamellae and cross ribs exist in the distal-most parts of the scales (Fig. 6). These parts are not covered by other scales and their color is both of structural and pigment origin.

Additional differences were registered between two analyzed *Apatura* species. The greater part of the sur-

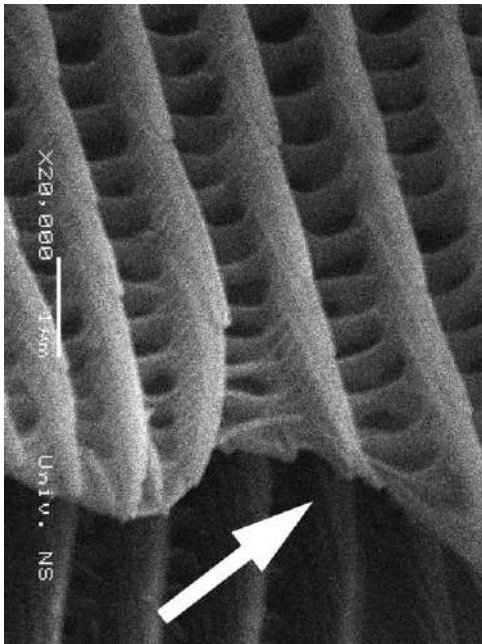


Fig. 6. SEM image of distal-most part of cover scale in *Apatura ilia* (dorsal view), as indicated by an arrowhead.

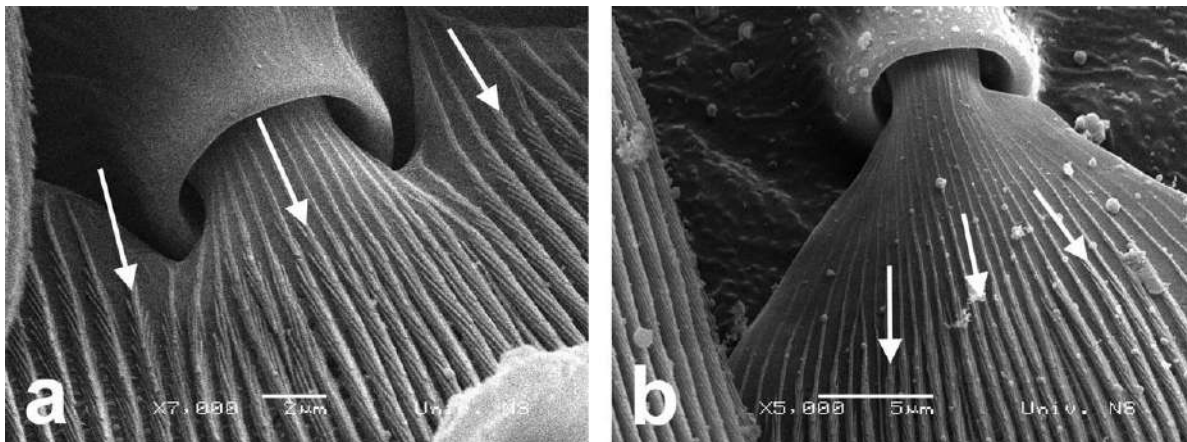


Fig. 7. SEM images of proximal parts of cover scales in *Apatura ilia* (a) and *A. iris* (dorsal views) (b). Places of lamellar appearance are indicated by arrowheads.

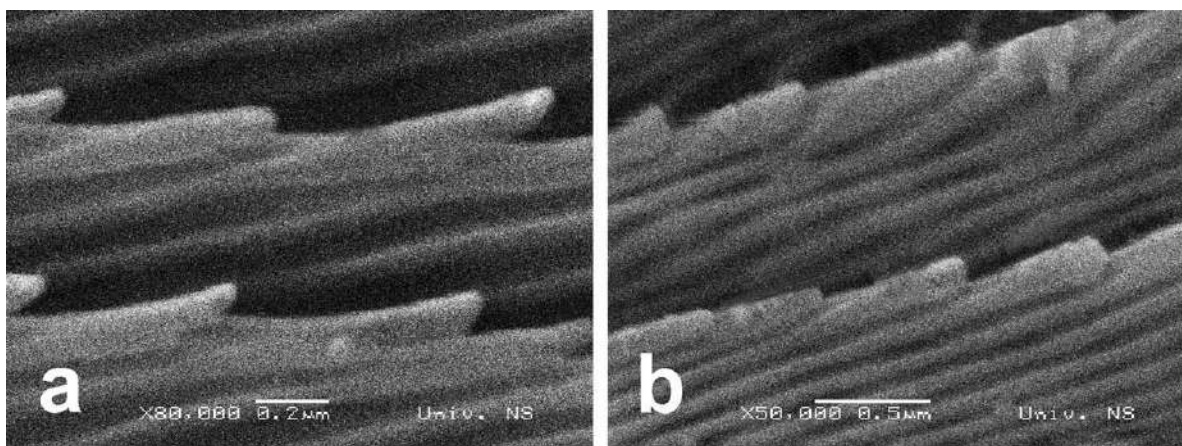


Fig. 8. SEM images of lamellae of cover scales in *Apatura ilia* (a) and *A. iris* (dorsolateral views) (b).

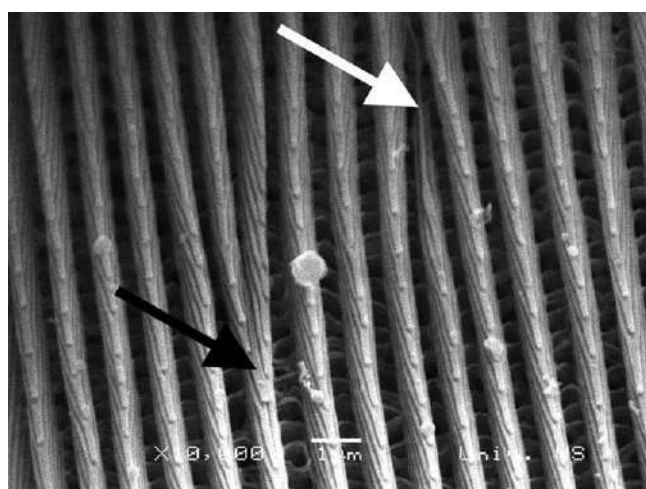


Fig. 9. SEM image of fusion (black arrowhead) and appearance of lamellae (white arrowhead) in cover scale of *Apatura iris* (dorsal view).

face of the type I scale is covered with lamellae in *Apatura ilia* (starting closer to the proximal edge of the scale; Fig. 7a) in comparison to *A. iris* (appearing somewhat distally from the mentioned point; Fig. 7b). Iridescence effects of *Apatura ilia* may be produced by the greater surface of the type I scales as compared with *A. iris*. Lamellae are somewhat elevated distally in *Apatura ilia*, while almost straight distally in *A. iris* (Figs. 8a and 8b). Both lamellae and cross ribs exist on the ventral wing side and they are like those in the type II scale. They cover the whole upper surface of the scales.

Some lamellar rows may be fused in some cases in both analyzed species, looking like dislocation in a crystal (Fig. 9). This may be a developmental defect. Additionally, certain lamellar rows appear distant from the subproximal part of the scale toward its distal end (Fig. 9). These features could be manifestations of intraspecific polymorphism.

The ventral side of the scales is mostly smooth in both species, but distally with ridges and weakly expressed cross ribs (Fig. 10). Sometimes the mentioned structures are visible laterally on the ventral side of the scales as well.

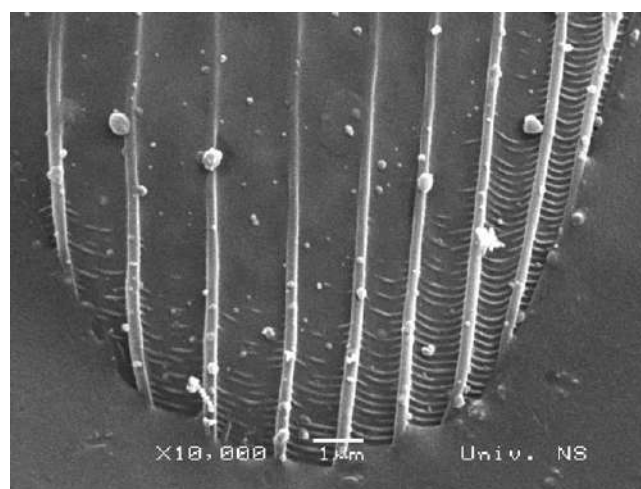


Fig. 10. SEM image of apical part of cover scale in wing of *Apatura iris* (ventral view).

The difference between the *Apatura* and *Morpho* species is partly due to different orientations of butterfly scales with respect to wing membrane. In *Apatura* butterflies, the scales are strongly inclined, while in *Morpho* butterflies the scales are parallel to the membrane.

CONCLUSIONS

The brilliant iridescent color in some male butterflies enables long-range communication between members of the species. Micro- and nanostructures are presumably responsible for this coloration and it is to a lesser extent of pigment origin. It seems that intrasexual communication between males is the reason for the brilliant coloration in male butterflies (Silberglied, 1984). The wing iridescence in the two analyzed butterfly species serves for both threat and movement of rival males from locations (Page, 2010). This phenomenon is visible in flight or at rest with opened wings.

The photonic type nanostructures consisted of chitin, occurring in the butterfly wing scales of the male

individuals of the species *Apatura ilia* and *A. iris*, were investigated by both SEM and TEM.

Although males of *Apatura ilia* have an iridescent violet-blue color of wings dorsally arising from the both micro- and nanostructures and a yellowish-brown color produced by pigments on the wings ventrally, the males of *A. iris* have a similar iridescent color on the dorsal side of the wings and a brownish color on the ventral side.

The system producing structural color comprises ridges of the type I scales bearing lamellae. The architecture of the scales is complex—they possess numerous alternating lucent (air) and dense (cuticle) layers.

The SEM micrographs show that there are two types of scales on the dorsal side of the wings in males in both species, while only type I scales are responsible for the structural color of the wings. The type II scales play a role in the creation of the pigment-originated brownish color.

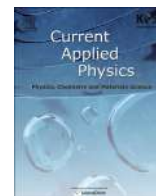
Iridescence is observed in a quite narrow angular range in both analyzed Purple Emperor species (18 degrees for both species), while it is much greater in other previously studied butterfly species. The spectral width of iridescence is small (around 50 nm FWHM for both analyzed *Apatura* species), but it is much greater in *Morpho* butterflies inhabiting the tropics (Pantelić et al., 2011).

ACKNOWLEDGMENTS

The authors owe their gratitude to Mr. Miloš Bokorov (Faculty of Science, University of Novi Sad, Novi Sad, Serbia) for help in preparing SEM photographs. The study was financially supported by the Serbian Ministry of Education and Science (Projects Nos. ON173038, ON171038, III45016, III41002, III47007, and III43002).

REFERENCES

- Berthier S. 2010. *Photonique des morphos*. Paris: Springer-Verlag France. 214 p.
- Biró LP, Kertész K, Vértessy Z, Márk GI, Bálint Z, Lousse V, Vigneron J-P. 2007. Living photonic crystals: Butterfly scales—Nanostructure and optical properties. *Mater Sci Eng C* 27:941–946.
- Garrett NL, Vukusic P, Ogrin F, Sirotkin E, Winlove CP, Moger J. 2009. Spectroscopy on the wing: Naturally inspired SERS substrates for biochemical analysis. *J Biophotonics* 2:157–166.
- Ghiradella H. 1989. Structure and development of iridescent butterfly scales: Lattices and laminae. *J Morphol* 202:69–88.
- Ghiradella H. 1991. Light and colour on the wing: Structural colours in butterflies and moths. *Appl Opt* 30:3492–3500.
- Ghiradella H. 1998. Hairs, bristles, and scales. In: Locke M, editor. *Microscopic anatomy of invertebrates*, Vol. 11A: Insecta. New York: Wiley-Liss. pp. 257–287.
- Ghiradella H, Aneshansley D, Eisner T, Silberglied RE, Hinton HE. 1972. UV reflection of male butterfly: Interference colour caused by thin-layer elaboration of wing scales. *Science* 178:1214–1217.
- Han Z, Wu L, Qiu Z, Guan H, Ren L. 2008. Structural colour in butterfly *Apatura ilia* scales and the microstructure simulation of photonic crystal. *J Bionic Eng Suppl* 5:14–19.
- Han Z, Wu L, Qiu Z, Ren L. 2009. Microstructure and structural colour in wing scales of butterfly *Thaumantis diores*. *Chin Sci Bull* 54:535–540.
- Higgins LG, Riley ND. 1970. *A field guide to the butterflies of Britain and Europe*. London: Collins. 380 p.
- Imafuku M, Hirose Y, Takeuchi T. 2002. Wing colours of *Chrysozephyrus* butterflies (Lepidoptera; Lycaenidae): Ultraviolet reflection by males. *Zool Sci* 19:175–183.
- Jakšić P. 2003. *Red data book of Serbian butterflies*. Lepidoptera: Hesperioidea and Papilionoidea. Belgrade: Institute for Nature Conservation of Serbia. 198 p.
- Kertész K, Molnár G, Vértessy Z, Koós AA, Horváth ZE, Márk GI, Tapasztó L, Bálint Z, Tamáska I, Deparis O, Vigneron J-P, Biró LP. 2008. Photonic band gap materials in butterfly scales: A possible source of “blueprints”. *Mater Sci Eng B* 149:259–265.
- Lafranchis T. 2004. *Butterflies of Europe*. New field guide and key. Paris: Diatheo. 350 p.
- Luke SM, Vukusic P, Hallam B. 2009. Measuring and modelling optical scattering and the colour quality of white pierid butterfly scales. *Opt Express* 17:14729–14743.
- Matejková-Plšková J, Shiojiri S, Shiojiri M. 2009. Fine structures of wing scales in *Sasakia charonda* butterflies as photonic crystals. *J Microsc* 236:88–93.
- Morehouse NI, Vukusic P, Rutowski R. 2007. Pterin pigment granules are responsible for both broadband light scattering and wavelength selective absorption in the wing scales of pierid butterflies. *Proc R Soc Lond B Biol Sci* 274:359–366.
- Page RJC. 2010. Perching and patrolling continuum at favoured hill-top sites on a ridge: A mate location strategy by the Purple Emperor butterfly *Apatura iris*. *Entomol Rec J Var* 122:61–70.
- Pantelić D, Čurčić S, Savić-Sević S, Korać A, Kovačević A, Čurčić B, Bokić B. 2011. High angular and spectral selectivity of Purple Emperor (Lepidoptera: *Apatura iris* and *A. ilia*) butterfly wings. *Opt Express* 19:5817–5826.
- Prum RO, Quinn T, Torres RH. 2006. Anatomically diverse butterfly scales all produce structural colours by coherent scattering. *J Exp Biol* 209:748–765.
- Shawkey MD, Morehouse NI, Vukusic P. 2009. A protean palette: Colour materials and mixing in birds and butterflies. *J R Soc Interface* 6:S221–S231.
- Silberglied RE. 1984. Visual communication and sexual selection among butterflies. In: Vane-Wright RI, Ackery PE, editors. *The biology of butterflies*. Symposium of the Royal Society of London, No. 11. London: Academic Press. pp. 207–223.
- Srinivasarao M. 1999. Nano-optics in the biological world: Beetles, butterflies, birds, and moths. *Chem Rev* 99:1935–1961.
- Stavenga DG, Stowe S, Siebke K, Zeil J, Arikawa K. 2004. Butterfly wing colours: Scale beads make white pierid wings brighter. *Proc R Soc Lond B Biol Sci* 271:1577–1584.
- Tolman T, Lewington R. 1997. *Collins field guide. Butterflies of Britain and Europe*. London: HarperCollins Publishers. 320 p.
- Vértessy Z, Bálint Z, Kertész K, Vigneron J-P, Lousse V, Biró LP. 2006. Wing scale microstructures and nanostructures in butterflies—Natural photonic crystals. *J Microsc* 224:108–110.
- Vértessy Z, Kertész K, Bálint Z, Molnár G, Eros M, Biró LP. 2007. SEM and TEM investigations in the scales of the European nymphalid butterfly *Apatura ilia* dark and light phenotypes. In: Tapasztó L, editor. *BioPhot Workshop 2007. Complexity and Evolution of Photonic Nanostructures in Bioorganisms: Templates for Materials Science (BioPhot)*, Workshop 6, Budapest, Hungary, 24–25 September 2007. Abstract Book. Budapest: Research Institute for Technical Physics and Materials Science. pp. 14–15.
- Vukusic P, Hooper I. 2005. Directionally controlled fluorescence emission in butterflies. *Science* 310:1151.
- Vukusic P. 2006. Structural colour in Lepidoptera. *Curr Biol* 16:R621–R622.
- Vukusic P, Kelly R, Hooper I. 2009. A biological sub-micron thickness optical broadband reflector characterized using both light and microwaves. *J R Soc Interface* 6:S193–S201.
- Vukusic P, Sambles JR. 2003. Photonic structures in biology. *Nature* 424:852–855.
- Vukusic P, Sambles JR, Lawrence CR. 2004. Structurally assisted blackness in butterfly scales. *Proc R Soc Lond B Biol Sci Suppl* 271:S237–S239.
- Vukusic P, Sambles JR, Lawrence CR, Wootton RJ. 1999. Quantified interference and diffraction in single *Morpho* butterfly scales. *Proc R Soc Lond B Biol Sci* 266:1403–1411.



Application of tot'hema eosin sensitized gelatin as a potential eye protection filter against direct laser radiation



Branka D. Muric^{*}, Dejan V. Pantelic, Darko M. Vasiljevic, Svetlana N. Savic-Sevic, Branislav M. Jelenkovic

Institute of Physics, University of Belgrade, Pregrevica 118, 11080 Zemun, Serbia

ARTICLE INFO

Article history:

Received 7 July 2015

Received in revised form

11 September 2015

Accepted 25 September 2015

Available online 9 October 2015

Keywords:

Microstructure fabrication

Laser safety

Eye protection

Polymers

Optical properties

Filter

Damage

ABSTRACT

The optical limiting properties of tot'hema and eosin sensitized gelatin layer (short TESHG) under continuous second harmonic Nd:YAG laser light were investigated. In contrast to classical eye protection filters the microlens formation and carbonization in TESHG are the main mechanisms for eye protection from direct laser radiation. Results have shown that safety goggles made on TESHG can protect the eye from up to 10 W of incident laser power. Filters for other wavelengths can be manufactured by varying the sensitizer.

© 2015 Published by Elsevier B.V.

1. Introduction

The growing number of laser applications requires development of materials which protect against laser radiation. Special attention is dedicated to eye protection, due to focussing power of the eye lens. It is well known the eye lens produces high intensities at the retina surface [1–7] potentially leading to permanent vision impairment. Different parts of the eye can be damaged, depending on the laser wavelength and intensity. UV light (<400 nm) and part of IR light (>1400 nm) damage the cornea and the eye lens, while light at wavelengths between 400 nm and 1400 nm endanger the retina, which is the most sensitive part of eye [1–7].

The usual method of eye protection is based on different types of filters, (absorption, reflection, interference, or polarization) inside goggles or protective windows [8–11]. The majority of safety filters are plastic materials which protect human eye from scattered or otherwise diffusely reflected laser light. Some manufacturers offer glass-based filters, either as absorption or thin-film interference devices. A good quality laser eye protection goggles are

characterized by a very small transmission for particular laser wavelength, and high transmission of visible light. According to European laser eye protection standards EN 207 [12] and EN 208 [13] a laser goggle must be able to protect the user for a minimum of 5 s (CW laser) or 50 pulses (pulsed laser) of direct laser radiation. The maximum permissible exposure (MPE), measured at the cornea of the human eye, is the highest laser power density or energy density that is considered safe for a given wavelength and exposure time [14]. In all cases, the protection level is limited by the laser energy absorbed within the material. Above certain threshold, the material absorbs enough energy to be melted and punctured, letting the full laser power to pass-through.

Here we report on the material exhibiting three different protective mechanisms. At low powers, absorption reduces the intensity of transmitted radiation below the MPE. In the intermediate range, microlens is produced which diverges the radiation, again reducing the eye irradiance below the MPE. Finally, at high powers the material carbonizes rather than melting, thus making the irradiated zone opaque.

This paper investigates the optical limiting behaviour of tot'hema and eosin Y sensitized gelatin layer (short TESHG) as well as possible application as an eye protection filter against high-power direct laser beams. The tot'hema is a mixture of Fe(II)-, Mn(II)-

^{*} Corresponding author.

E-mail address: muric@ipb.ac.rs (B.D. Muric).

and Cu(II) gluconates used in medicine for curing iron deficiencies. Eosin is an organic dye with absorption maximum about 532 nm, used in medicine, too. Previously, we have shown that TESHG is an excellent optical material [15,16]. The microlens formation and dye bleaching occur simultaneously during laser exposure. Although the TESHG layer is initially coloured due to presence of eosin and tot'hema, after irradiation with a 532 nm laser the dye bleaches leaving an irradiated layer with completely transparent microlenses. The process of microlenses formation is thermal as we have verified using a thermal camera [17]. The protection mechanism of the TESHG layer is based on microlenses formation during the laser irradiation. The layer carbonization at higher laser power additionally protects an eye. As a result of all mentioned processes the TESHG layer was able to reduce 10 W (CW operation at 532 nm) direct laser beam to the safe level.

The TESHG layer is chemically stable (under the normal laboratory conditions), elastic [18] and not very sensitive to scratches and tearing. However, it is slightly sticky and dust and fingerprints may collect on the surface. In practice, the laser goggles require sandwiching of TESHG between two transparent plastic plates (such as thin polycarbonate). This enables mechanical protection of the filter and goggle cleaning. Additional advantages of TESHG such as easy manufacturability, low cost, non-toxicity and stability, make this layer very interesting for eye protection applications.

2. Material and methods

The layers were prepared as described in our previous papers [15,16]. The 5 g of gelatin powder (Gelatin from bovine skin gel strength ~225 g Bloom, Type B, Sigma) was swelled in 100 ml deionised water for 60 min. The gelatin is heated for 10 min in a water bath (Vela™, Cole Parmer) at 50 °C, with stirring. In order to prevent crystallization of the layer and keep elasticity, 1 g of sodium chloride (puriss. p.a. were purchased from Sigma–Aldrich) was added together with the 20 ml of tot'hema oral solution (Laboratoire Innotech International, France). At the end 0.3 ml of 1% water solution of eosin Y (5 wt.% in H₂O, Sigma–Aldrich) is supplemented. Eosin Y enhances absorption of TESHG layer at 532 nm. The TESHG solution is then centrifuged (Cole Parmer at 3400 rpm/min) for 30 min in order to remove impurities. In the next step the 10 ml of TESHG solution is poured onto a precisely levelled and well-cleaned 2 mm thick polycarbonate (lexan) plate. The layer is dried in the dark, in relatively stable laboratory conditions. After drying, TESHG layer thickness of 1 mm was obtained. The thickness of each deposited layer is an average of measurements at eight different points with a digital micrometre. The resulting layer is very elastic and sticky, and can be easily peeled and transferred to another substrate.

Protection filter prepared by adhering 1 mm thick layers of TESHG on both sides of 2 mm thick transparent lexan plate was positioned 20 mm in front of a 5 mm diameter aperture, as shown in Fig. 1. The

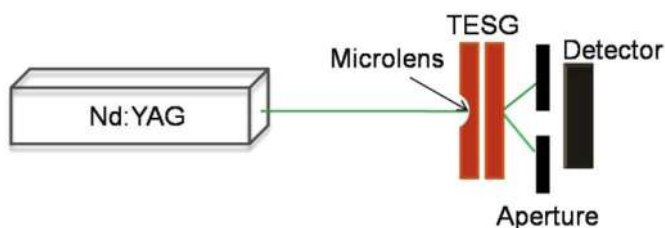


Fig. 1. Experimental setup: The transmitted power of CW laser light operating at 532 nm after passing an optical filter (made of a lexan plate sandwiched between two TESHG layers) and aperture were measured by a power meter.

aperture is simulating the human pupil which normally opens about 2 mm in daylight, and 7 mm in the dark [19]. This configuration is analogous to laser protective goggles placed in front of eyes.

A 10 W, 532 nm Nd:YAG laser was used (Verdi V-10 manufactured by Coherent Inc.) to test the protective properties of TESHG. The beam diameter was 2.3 mm. Transmitted laser power was measured by OPHIR power meter (NOVA II) with a photometric head placed close to the aperture (see Fig. 1). The laser power used to test TESHG filter was varied between 100 mW and 10 W. Transmission spectra of TESHG were analysed by a fibre-type spectrometer (Ocean Optics) with a tungsten-halogen light as illumination source. The morphology of the TESHG layer and a plastic protective layer were investigated using a high resolution scanning electron microscope equipped with a high brightness Schottky field emission gun (FESEM).

3. Results and discussions

3.1. Power limiting and protective properties of TESHG

At the beginning, we would like to emphasize the difference between TESHG layer and classical plastic absorptive filters. TESHG layer and one plastic filter were exposed with direct Nd:YAG laser beam at 532 nm wavelength, and power of 100 mW. After less than a second the plastic layer was perforated, as shown in Fig. 2a. In the case of TESHG layer, after 10 s exposure, the microlens is formed (see Fig. 2b). The scanning electron microscopy images of a perforated hole and TESHG microlens are shown in Fig. 2c and d, respectively. Important characteristic of the TESHG layer is its property to bleach under the laser beam action. The bleaching (photochemical transition of eosin dye from pink to colourless state) and microlens formation occurs simultaneously during laser irradiation. The increased transmission due to bleaching is compensated by expansion of the laser beam by a microlens. As a result the irradiation level behind the microlens is constant. This is very important since bleaching prevents the layer overheating (within certain power levels) and perforating. The pink colour of TESHG layer is due to eosin, but otherwise the visibility through the 1 mm thick layer is good.

3.1.1. A generic eye model and protection mechanism

To illustrate the eye protection principle, a generic model of the human eye is constructed (Fig. 3) and ray tracing is used to calculate the beam propagation through the eye [20,21]. In the case when the laser beam enters an unprotected eye (see Fig. 3a) the radiation is focused on the retina (0.17 mm spot diameter). The power density is high and retinal damage is possible.

If a protective filter, with the microlens (created under the influence of the beam) is placed in front of the eye the situation is changed. A microlens is an additional optical component between the laser beam and the human eye. It expands the beam, and only a small fraction of the radiation goes through the pupil of an eye. Even more, the radiation is not tightly focused (Fig. 3b) as in the previous situation (Fig. 3a). According to ray tracing calculation, the resulting spot on retina has 2.01 mm diameter, which is about 12 times larger compared to the direct laser beam spot size. As can be seen in Fig. 3b there are two effects— one is reduction of the amount of light transmitted through the eye pupil and another is increased size of the focused spot. The overall reduction of power density is approximately six orders of magnitude.

As we can see in Fig. 4 the protection mechanism is determined by the laser power and exposure time.

According to Fig. 4, the absorption of laser light dominates up to the laser power of 50 mW, and it doesn't affect the protective layer.

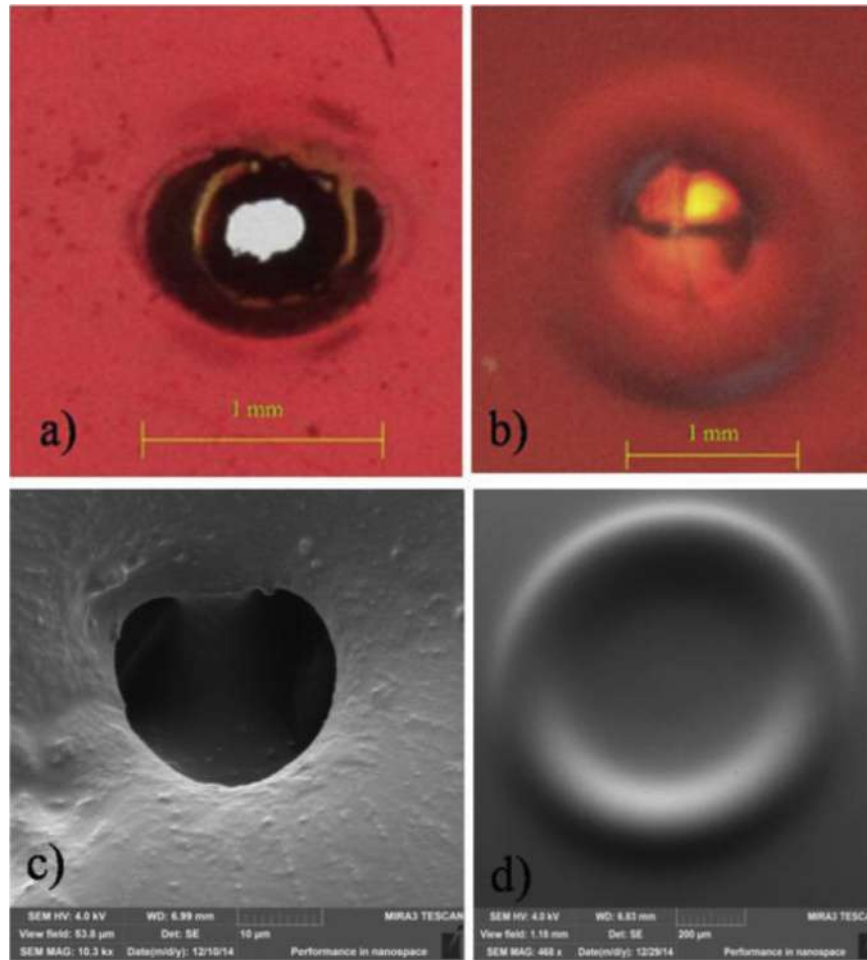


Fig. 2. Effects of the laser radiation on the layers of plastic protective material (a, c) and TEG (b, d). Images a) and b) are recorded using an optical microscope, and c) and d) are recorded using a field-emission gun scanning electron microscope.

Within this power range TEG is linear absorber for both CW and pulsed radiation, since the mechanism of laser material interaction is of thermal nature [17]. The microlens formation starts above 50 mW after certain irradiation period (see middle section in Fig. 4).

The laser beam diverges through the microlens. The significantly reduced energy density then reaches the second layer deposited on other side of a lexan plate, which absorbs the attenuated laser beam. Above 600 mW of laser power the protection layer starts to carbonize (right section in Fig. 4). The layer carbonization produces a localized opaque black area which further blocks the laser beam.

In order to investigate if the TEG layer can be used as an eye protection filter, the laser power behind the TEG filter was measured for different laser powers using the experimental setup from Fig. 1. The output power density after the filter (E) was calculated according to expression: $E = P/A$, where P is the measured laser power after the filter. The aperture area ($A = 19.6 \text{ mm}^2$) corresponds to 5 mm diameter, used in our experiments.

It has to be emphasized that for laser powers above 50 mW, TEG layer goes through a sequence which starts with the absorption, continues with the microlens formation and ends with the carbonization (see Fig. 4). The duration of each part of a sequence depends on the laser power, but the transmitted power density trough the filter is always well below MPE (see Fig. 5). Since the basic mechanism is thermal, overall effect depends only on the average laser power, no matter whether the beam is pulsed or continuous. For the first 150 ms, the intensity of transmitted radiation is constant, even at the maximum measured input laser power of 9.6 W (see Fig. 5). Additionally, for shorter times MPE is higher (for 1 ms MPE is 0.01 W/cm^2 , while for $1 \mu\text{s}$, MPE is 0.8 W/cm^2). After the first 150 ms, the power density oscillates, but always

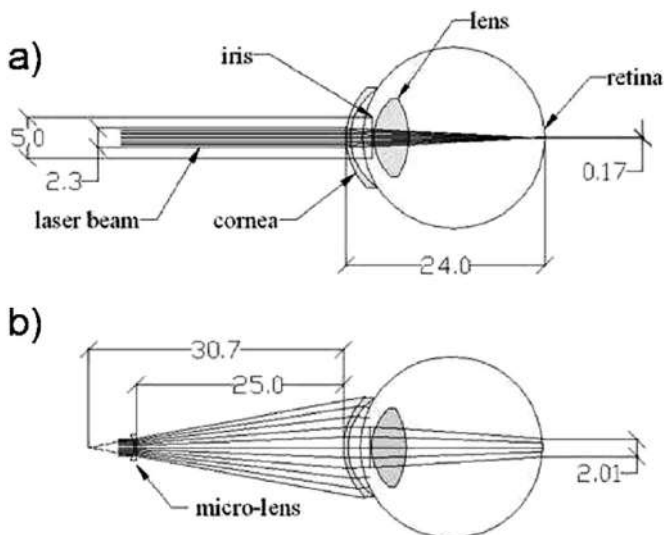


Fig. 3. The laser beam focussing by: (a) the unprotected eye (b) the eye protected with microlens forming filter. All dimensions are in millimeters.

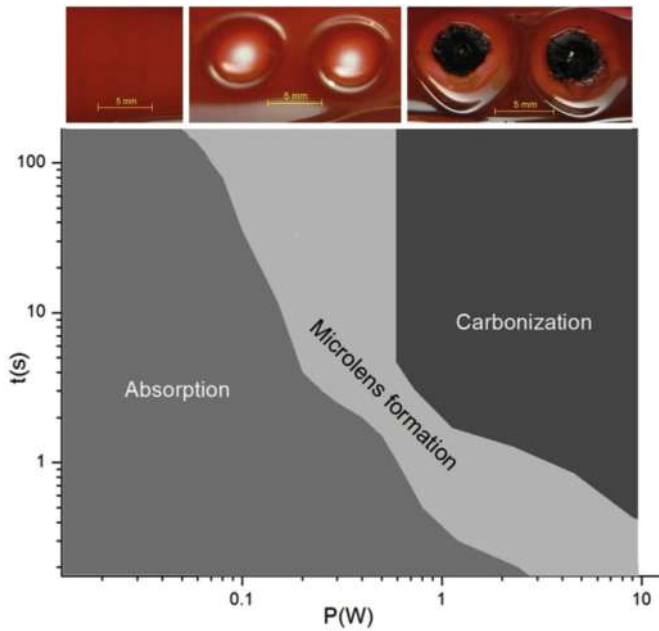


Fig. 4. The influence of the laser power (for the second harmonic Nd:YAG laser) and irradiation time on the protection mechanism of TESG filter. Note the logarithmic scale on both axes. Three photographs above the graph depict appearance of the TESG layer at different laser powers.

stays significantly below MPE (as a consequence of stochastic nature of carbonization). The reduction of output power density (0.017 mW/cm^2 – 0.34 mW/cm^2) is approximately six orders of magnitude compared to the input laser power density (1.5 W/cm^2 – 49 W/cm^2). We emphasize that output power density is always far below MPE during 7 s of exposure – although standards require period of 5 s.

3.1.2. TESG laser goggles

To demonstrate TESG filter capabilities, we made laser protective eyewear by modifying welder's goggles (see Fig. 6). The protection level can be controlled by flipping the front set of TESG filters. When the front filter set is up, the goggles offer lower

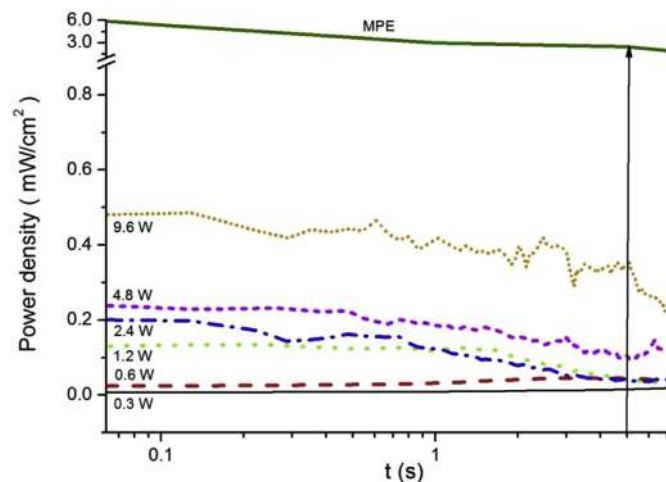


Fig. 5. Power density measured after the TESG filter vs. exposure time for different Nd:YAG laser input powers. Five measurements were made for each input laser power and the average values are shown. Note the break on the ordinate and logarithmic scale on abscissa. Numbers inside the diagram indicate input laser power.

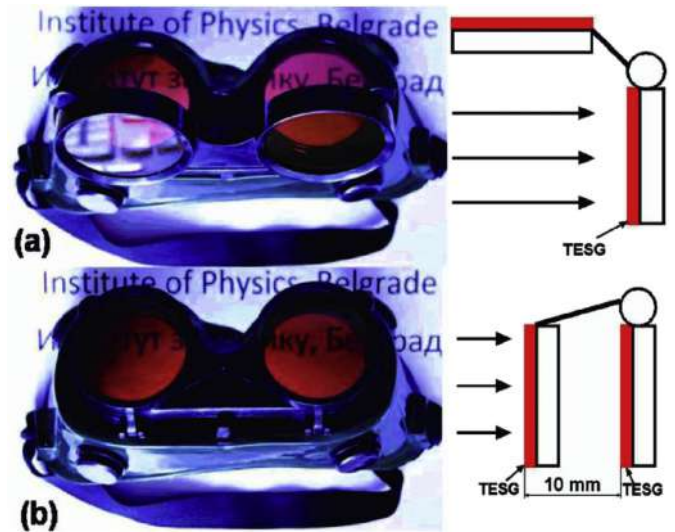


Fig. 6. Photograph of eye-protection goggles with TESG layers on both movable and stationary pair of filters of the commercial welder goggles: (a) when the first set of filters is lifted – goggles are suitable for adjustment of laser beam and (b) with both filters protecting from direct light exposure. Insets on the right schematically show the filter arrangement.

protection level but allow one to see the beam and adjust the laser. If both layers are used, goggles efficiently protect from direct laser beam exposure.

The transmitted laser power density (after 5 s) vs. input laser power density was recorded (Fig. 7). One curve is for a TESG filter and another one for laser goggles. In both cases output power density is well below MPE. Compared to TESG filter, goggles offer better protection (by about two orders of magnitude) due to 10 mm distance between two TESG layers (see Fig. 6).

Additionally, the transmission of the visible light (using white LED lamp as a light source) through TESG and commercial THORLABS LG10 glasses was also measured. Fig. 8 shows that transparency of TESG goggles is comparable with commercial THORLABS LG10.

In Fig. 9 we present a transparency of TESG goggles as a function of wavelength for one and two TESG layers. As can be seen, the 532 nm Nd:YAG laser beam transmission is very small.

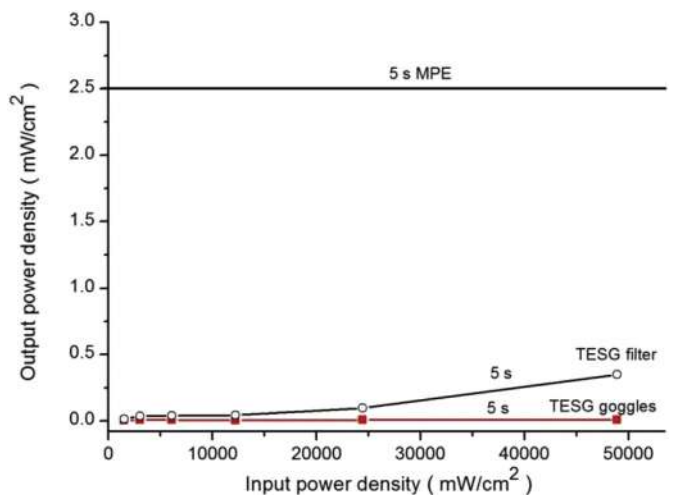


Fig. 7. Output laser power density (after 5 s) vs. input power density for TESG filter and goggles.

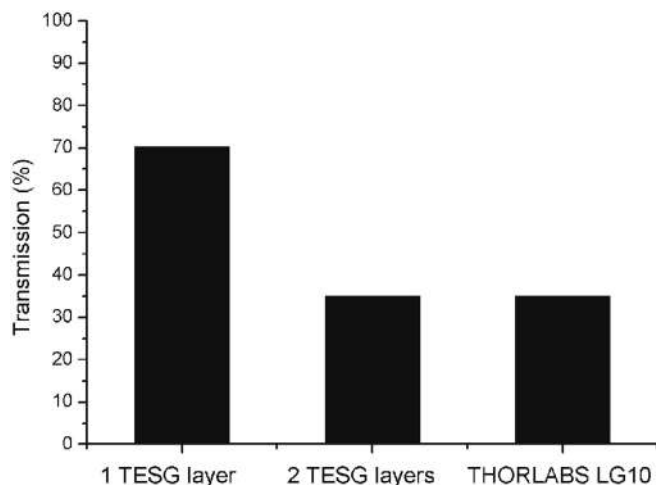


Fig. 8. Visible light transmission for TESG goggles (one or two layers) and THORLABS LG10 goggles. The transmission is almost the same for two layers and THORLABS LG10, while it is doubled for a single TESG layer.

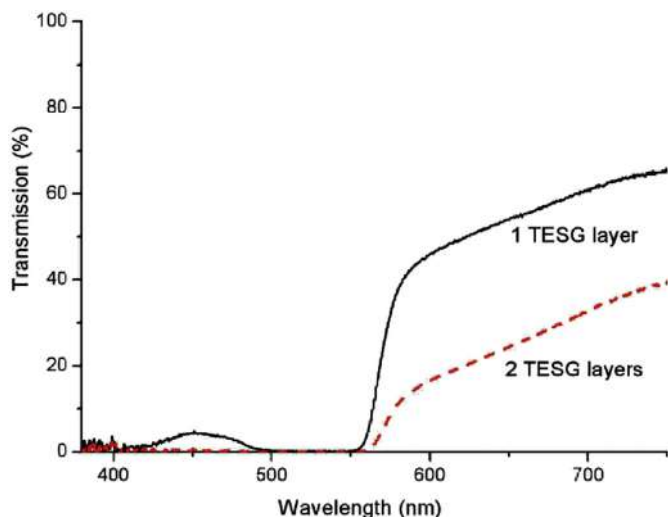


Fig. 9. Transmission spectra of TESG goggles (for one or two sets of TEG filters). The increase of transmission around 450 nm for single TEG layer is related to transmission properties of TEG. The amount of light transmitted around 450 nm decreases with increasing the layer thickness [15].

Spectral transparency depends on the TEG layer thickness, concentrations of eosin and tot'hema, and number of layers. Increasing the number of layers increases the total thickness of the filter, and thus reduces its transmission (see Fig. 9). However, even single layer thickness can't be increased more due to decreasing of visible light transmission.

As we already mentioned TEG layer is very easy to produce from cheap and environmentally friendly materials making it very interesting for production of laser goggles and large-area filters. Additionally, if TEG layer is damaged, it can easily be replaced. To demonstrate the effectiveness of TEG goggles we show the sequence of images during the 30 s irradiation time (Fig. 10).

Supplementary video related to this article can be found at <http://dx.doi.org/10.1016/j.cap.2015.09.014>.

Laser-induced microlenses and carbonization are universally applicable for protection against the laser radiation. Our

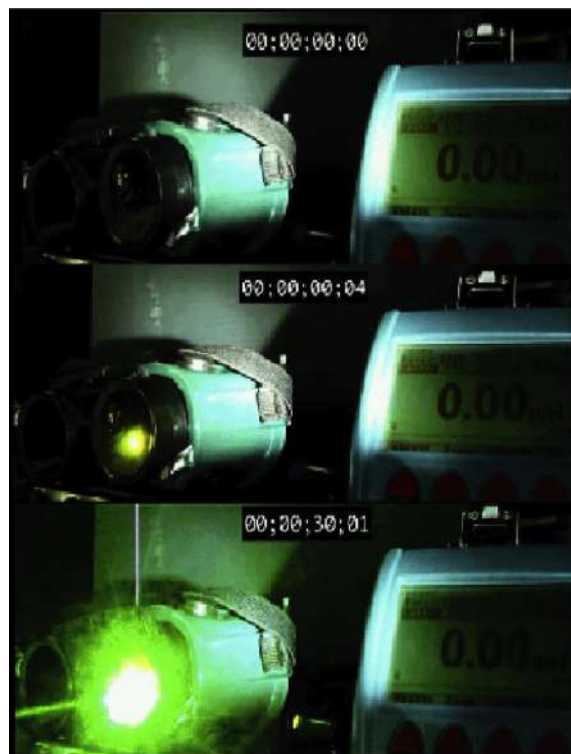


Fig. 10. Laser goggles irradiated with 10 W 532 nm Nd:YAG laser: Sequence of images corresponding to moment just before the laser was turned on (0 s), 4 s and 30 s (see the Supplementary Information).

preliminary results show that the protection wavelength can be tailored by using various sensitizing dyes. As a test, we replaced eosin Y with naphthol green B, and obtained an 800 nm protective layer, capable of withstanding 2 W of femto-second radiation.

4. Conclusions

Optical limiting properties of tot'hema eosin sensitized gelatin (TESG) were investigated. It was demonstrated that TEG can be used as a protection filter against the second harmonic Nd:YAG laser beam. The laser protection mechanism is based on microlens formation and layer carbonization. A simple, cheap and effective protection goggles are tested and used in laboratory environment. The results are demonstrating that protective goggles based on two single layer filters made of TEG can be used for the eye protection from 10 W of direct laser beam power.

According to our preliminary results the transmission spectral range of the TEG can be easily tuned to any part of the spectrum, by choosing the appropriate organic dye as sensitizer. Because the interaction of the TEG with laser radiation is based on a purely thermal mechanism the filter use can be extended to any laser type.

Optical and protective properties of TEG layer depend on its thickness and chemical composition (tot'hema and eosin concentrations). These were found experimentally as a compromise between the visible light transmission and protective properties against the highest power laser at our disposal (10 W at 532 nm). For protection against even higher power lasers, systematic research will be needed to establish the relation between the layer thickness, chemical composition and its protective properties.

Nevertheless, it has to be emphasized that approving TEG filters for universal eye protection requires additional measurements related to exposure to lasers of ultrashort pulse duration and of different wavelengths.

Acknowledgements

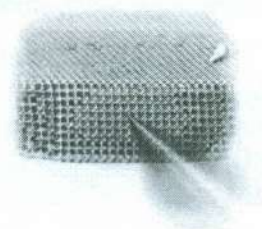
This paper was written as a part of research supported by the Ministry of Education, Science and Technological Development of the Republic of Serbia under grants ON 171038 and III 45016.

References

- [1] A. Schirmacher, *Med. Laser Appl.* 25 (2010) 93–98.
- [2] M. Chen, C. Li, Xu Mai, W. Wang, S. Ma, Y. Xia, *Opt. Laser Technol.* 39 (2007) 214–218.
- [3] M.J. Grout, *Opt. Mater.* 14 (2000) 155–160.
- [4] Y. Liu, J. Zhou, X. Zhang, Z. Liu, X. Wan, J. Tian, T. Wang, Y. Chen, *Carbon* 47 (2009) 3113–3121.
- [5] E. Sutter, A. Schirmacher, *Opt. Laser Technol.* 33 (2001) 255–258.
- [6] E. Buckley, *J. SID* 18 (2010) 944–951.
- [7] D.H. Sliney, R.W. Wajnant, M.N. Ediger (Eds.), *Electro-optics Handbook*, McGraw-Hill, New York, 1993 (chap. 23).
- [8] M. Lenner, C. Spielmann, *Appl. Opt.* 44 (2005) 3532–3539.
- [9] M. Lenner, C. Spielmann, *Appl. Phys. B* 78 (2004) 689–692.
- [10] J. Krüger, M. Lenzner, S. Martin, M. Lenner, C. Spielmann, A. Fiedler, W. Kautek, *Appl. Surf. Sci.* 208–209 (2003) 233–237.
- [11] C.H. Lee, B. Bihari, R. Filler, B.K. Manda, *Opt. Mater.* 32 (2009) 147–153.
- [12] EN 207: 2009 Personal eye-protection equipment—Filters and eye-protectors against laser radiation (laser eye-protectors).
- [13] EN 208: 2009 Personal eye-protection—Eye-protectors for adjustment work on lasers and laser systems (laser adjustment eye-protectors).
- [14] American National Standards Institute, “Safe Use of Lasers,” Standard Z-136.1, ANSI, New York, 1986.
- [15] B. Murić, D. Pantelić, D. Vasiljević, B. Panić, *Opt. Mater.* 30 (2008) 1217–1220.
- [16] B.D. Murić, D.V. Pantelić, D.M. Vasiljević, B.M. Panić, *Appl. Opt.* 46 (2007) 8527–8532.
- [17] B. Murić, D. Pantelić, D. Vasiljević, B. Panić, B. Jelenković, *Appl. Opt.* 48 (2009) 3854–3859.
- [18] B. Murić, D. Pantelić, D. Vasiljević, B. Zarkov, B. Jelenković, S. Pantović, M. Rosić, *Phys. Scr.* T157 (2013) 014018 (4pp).
- [19] D.A. Atchison, C.C. Girgenti, G.M. Campbell, J.P. Dodds, T.M. Byrnes, A.J. Zele, *Clin. Exp. Optom.* 94 (2011) 545–548.
- [20] A.V. Goncharov, M. Nowakowski, M.T. Sheehan, C. Dainty, *Opt. Express* 16 (2008) 1692–1703.
- [21] D.A. Atchinson, G. Smith, *Optics of the Human Eye*, Butterworth-Heinemann, Oxford, 2000.

UNIVERZITET U BEOGRADU

Institut za fiziku



Konferencija
**Šesta radionica fotonike
(2013)**

Zbornik apstrakata



**Photonics
center**

Kopaonik, 04.-08.3.2013.

Konferencija **Šesta radionica fotonike 2013**
ZBORNİK APSTRAKATA
Kopaonik 04-08.3.2013.

Izdaje

Institut za fiziku Univerziteta u Beogradu

Za izdavača

dr Aleksandar Belić, direktor

Urednici

dr Aleksander Kovacević
dr Dragan Lukić

Tiraž

100 primeraka

ISBN 978-86-82441-35-9

Štampa

Razvojno-istraživački centar,
Tehnološko-metalurškog fakulteta u Beogradu
Karnegijeva 4, Beograd

CIP - Каталогизација у публикацији
Народна библиотека Србије, Београд

535(048)
681.7(048)
66.017/.018(048)

КОНФЕРЕНЦИЈА радионица фотонице (6 ; 2013 ; Копеоник)

Zbornik apstrakata / Konferencija Šesta radionica fotonike (2013), Kopaonik, 04.-08.3.2013. ;
[urednici Aleksander Kovacević, Dragan Lukić]. - Beograd : Institut za fiziku, 2013
(Beograd : Razvojno-istraživački centar grafičkog inženjerstva TMF). - X, 36 str. : ilustr. ; 25 cm

Na vrhu nasl. str.: Univerzitet u Beogradu. -

Apstrakti na srp. i engl. jeziku. - Tekst ćir. i lat. - Tiraž 100. - Reč urednika: str. V. - Registar.

ISBN 978-86-82441-35-9

a) Оптика - Апстракти b) Оптоелектроника - Апстракти c) Технички материјали - Апстракти
COBISS.SR-ID 197041164

CIP

Programski i organi

dr Dragan Lukić,
(urednik Zbornika)

dr Aleksander Kov
(Sajta)

mr Bojana Bokić,
(Zbornika)

dr Aleksandar Krmj

Akademik dr Brani

Sponzori Konferenc

Ministarstvo za nau

„Senzor Infiz“ d.o.o

„Kristal Infiz“ d.o.o

„Optela Infiz“ d.o.o

raciju pigmentnih

y D. Dramićanin

radu, pp 522,

spektroskopije, poput malignog od zdravog rvanja bili su izmereni 15 uzorka nevusa i 22 ilmer fluorescentnom intervalu talasne dužine e dobijaju simultanim razlike talasnih dužina spektri su dalje bili l Component Analysis išćeni za obučavanje ikacionog modela za a postoje veoma jasne osnovu kojih se može ma klasifikacije.

Hetero-strukture generisane kombinacijom holografske metode i samouređivanjaSvetlana Savić-Šević¹, Dejan Pantelić¹, Bojan Jokić², Branislav Jelenković¹

(1) Institut za fiziku, Univerzitet u Beogradu, Pregrevica 118, 11080 Zemun, Srbija

(2) Tehnološko-metalurški fakultet, Univerzitet u Beogradu, Karnegijeva 4, 11120 Beograd, Srbija

Kontakt: S. Savić-Šević (savic@ipb.ac.rs)

Apstrakt. Kombinacijom holografske metode i samouređivanja generisane su hetero-strukture u polisaharidu, pululanu, dopiranom jonima hroma. Koristeći holografski metod, interferencijom dva suprotno propagirajuća talasa jednomodnog Nd-YAG lasera, talasne dužine 532 nm, formirane su višeslojne zapreminske refleksione Bregove rešetke. Eksponirani slojevi su hemijski obrađeni.

Fotonske strukture su karakterisane korišćenjem visoko-rezolucionog skenirajućeg elektronskog mikroskopa sa elektronskim topom Šotkijevog tipa. Formirane su hetero-strukture koje se sastoje od dve različite višeslojne strukture koje su međusobno povezane tranzicionim slojem. Gornji višeslojni deo sastoji se od niza sfera pululana poređanih duž Bregovih ravni. Sfere, nalik perlama u nizu, su dimenzija oko 30 nm. Donji višeslojni deo sastoji se od sfera pululana dimenzija oko 70 nm koje su zarobljene Bregovim ravnima. Tranzicioni sloj sastoji se od linearnih tubula dužine oko 150 nm, i širine oko 20 nm.

Bregova rešetka formirana je holografskom metodom, a sfere pululana su nastale u procesu fazne separacije u toku hemijske obrade materijala.

Da bismo optički okarakterisali hetero-strukture, merili smo transmisionu spektre koristeći spektrometar.

Holographic detection of a tooth structure deformation after dental filling polymerization

Dejan Pantelić

Institute of Physics
Pregrevica 118
11080 Zemun, Belgrade
Serbia
E-mail: pantelic@phy.bg.ac.yu

Larisa Blažić

University of Novi Sad
Faculty of Medicine
Dental Clinic
Hajduk Veljkova 12
21000 Novi Sad
Serbia

**Svetlana Savić-Šević
Bratimir Panić**

Institute of Physics
Pregrevica 118
11080 Zemun, Belgrade
Serbia

Abstract. An experimental technique to reveal the effects of dental polymer contraction is established to choose the most appropriate polymerization technique. Tooth deformation following a dental filling polymerization is analyzed using double-exposure holographic interferometry. A caries-free, extracted human molar is mounted in dental gypsum and different cavity preparations and fillings are made on the same tooth. Dental composite fillings are polymerized by an LED light source especially designed for this purpose. Holographic interferograms are made for occlusal (class I), occlusomesial (class II), and mesioocclusodistal (class II MOD) cavities and fillings. Maximum interspal deformation ranges from 2 μm for the class I cavity to 14 μm for the MOD class cavity. A finite element method (FEM) is used to calculate von Mises stress on a simplified tooth model, based on experimental results. The stress varies between 50 and 100 MPa, depending on the cavity type. © 2007 Society of Photo-Optical Instrumentation Engineers. [DOI: 10.1117/1.2714056]

Keywords: holography; interferometry; biomechanics; dental composites.

Paper 06046RR received Mar. 3, 2006; revised manuscript received Nov. 22, 2006; accepted for publication Nov. 27, 2006; published online Mar. 12, 2007.

1 Introduction

Polymerization shrinkage of dental composites is still a cause of serious clinical problems such as loss of bonding between composite and a tooth, or microfractures of a tooth tissue, both resulting in premature dental filling failure.¹ In addition, stress caused by polymerization contraction may also cause postoperative sensitivity.² It is difficult to directly measure stress induced by dental composite contraction, as it is distributed inside the tooth. Instead, the resulting deformation of a tooth surface is measured and the stress is estimated.

The current research is performed in several directions. One deals with linear and volumetric contraction of pure composite layers (outside the dental cavity).³⁻⁷ The second, clinically more relevant approach focuses on measuring tooth deformation induced by the composite inside the dental cavity. Changes in tooth structure and the resulting cuspal deflection⁸⁻¹¹ due to polymerization shrinkage are detected by several measurement techniques: microscopy,¹² strain gauges,¹³ interferometry,¹⁴ and photoelasticity.^{15,16}

The third, computational, approach analyzes both deformation and the resulting stress, using the finite element method¹⁷⁻²⁰ (FEM). This is essentially a computer simulation that gives detailed information about shrinkage stresses, but does not take into consideration specific differences in human teeth which vary considerably in their coronal morphology and mechanical properties.²¹ Therefore, the same results for numerical and experimental studies cannot be expected, because the total shrinkage and the resulting stress are depen-

dent on the cavity shape, tooth tissue structure, and the properties of the composite material, bonding system, and polymerization process.

As can be seen, a method connecting experimental measurements of dental deformation with numerical calculation of internal stress is necessary. First, complete deformation field should be measured, and then the FEM should be applied to determine stress inside the tooth.

Holography offers a solution to the problem of the deformation field measurement. In particular, laser interferometry by holography is a nondestructive method for measurement of mechanical deformations of different structures and materials. Deformation is seen as a system of dark and bright fringes superposed on the 3-D holographic image. The fringes are maps of the investigated structure deformation and represent an extremely sensitive picture of displacements caused by mechanical stress.

Holographic interferometry was used previously to investigate various dental tissues or dental implants.²²⁻²⁶ To our knowledge, this paper is the first holographic study of a complete tooth deformation field induced by dental composite shrinkage. The holographic interferometry method was used (*in vitro*) to determine the total deformation at any point of the tooth surface. Based on experimental data, the resulting stress was calculated using the FEM.

2 Method

Caries-free extracted human third molars were used. They were kept in a saline solution at 4°C to preserve their biological and mechanical properties. Just before measurement, the

Address all correspondence to Dejan Pantelic, Lasers and Optoelectronics, Institute of Physics, Pregrevica 118, 11080 Zemun, Belgrade, Serbia; Tel: 381 11 3160793; Fax: 381 11 3162190; E-mail: pantelic@phy.bg.ac.yu



Fig. 1 Tooth mounted in dental gypsum in an inclined position.

tooth was mounted in an inclined position using dental gypsum, in a manner shown in Fig. 1. After drying, a good mechanical contact between the tooth and gypsum was obtained, enabling stability during holographic measurements.

Standard cavity preparations and restorations were made (class I, class II, and class II MOD) and the configuration is shown schematically in Figs. 2(a)–2(c). They were cut using a diamond coated burr attached to the water-cooled air turbine. Each cavity was prepared for dental composite placement by the “Prompt L Pop” adhesive system according to the manufacturer’s (3M ESPE, Seefeld, Germany) instruction. Consequently, the cavities were filled in one increment (bulk tech-

nique) with a commercially available dental composite resin “Filtek Z 250” (3M ESPE, Seefeld, Germany).

Dental composite resin was polymerized by an LED light source, specially designed for research purposes. LED diodes (42 of them in total, with 10 mW of optical output power, each) were mounted on the hemispherical holder [Figs. 3(a) and 3(b)]. The light source produced an evenly illuminated circular spot (more than 1 cm in diameter) at the center of a sphere where the tooth was placed, illuminated, and a dental filling was polymerized. This enabled contactless operation, in contrast to commercial devices, where the LED lamp tip should be in complete contact with dental polymer.

Operation without contact is important in holographic research, where extreme mechanical stability is required. Additionally, possible heat transfer from the LED to the tooth is negligible, because LEDs dissipate only a small amount of heat and the tooth is 30 mm from the lamp.

The tooth surface must be painted to improve fringe visibility in the resulting holographic interferogram.^{26,27} A paint layer must be thin, but opaque to laser radiation and capable of drying fast. A silver marker [PX-20(L) produced by Mitsubishi Pencil Co. Ltd.] served this purpose perfectly.

Double-exposure holograms were produced using a simple split beam setup (Fig. 4) with 10-mW power, 632.8-nm wavelength HeNe laser. The LED lamp was positioned above the tooth to induce polymerization. The first holographic exposure (of 5-s duration) was made before polymerization. The LED lamp was turned on for the time period necessary to induce complete polymerization. Subsequently, the LED source was turned off and the second holographic exposure (5 s) was made. Therefore, two holographic images were recorded on the same holographic photosensitive material (silver halide glass plate, Agfa 8E75HD).

Following the standard chemical processing (development, fixing, bleaching, and drying), the hologram plate was returned to its original position and prepared for reconstruction and analysis. On reconstruction two coherent images were seen—one corresponding to the undeformed and the other to the deformed state of the tooth. Interference of these two

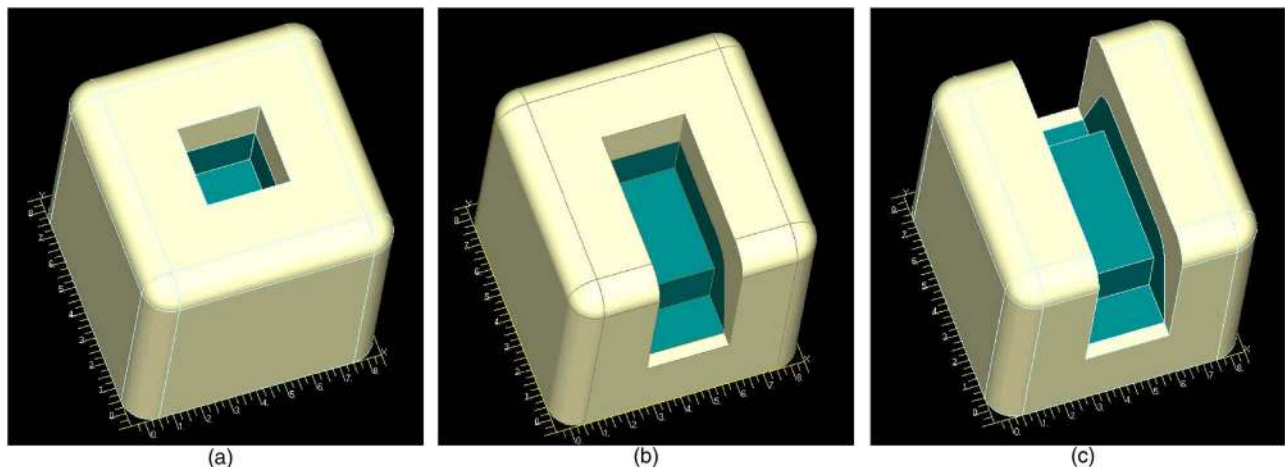


Fig. 2 Standard dental cavity configurations: (a) class I, (b) class II, and (c) class II MOD.

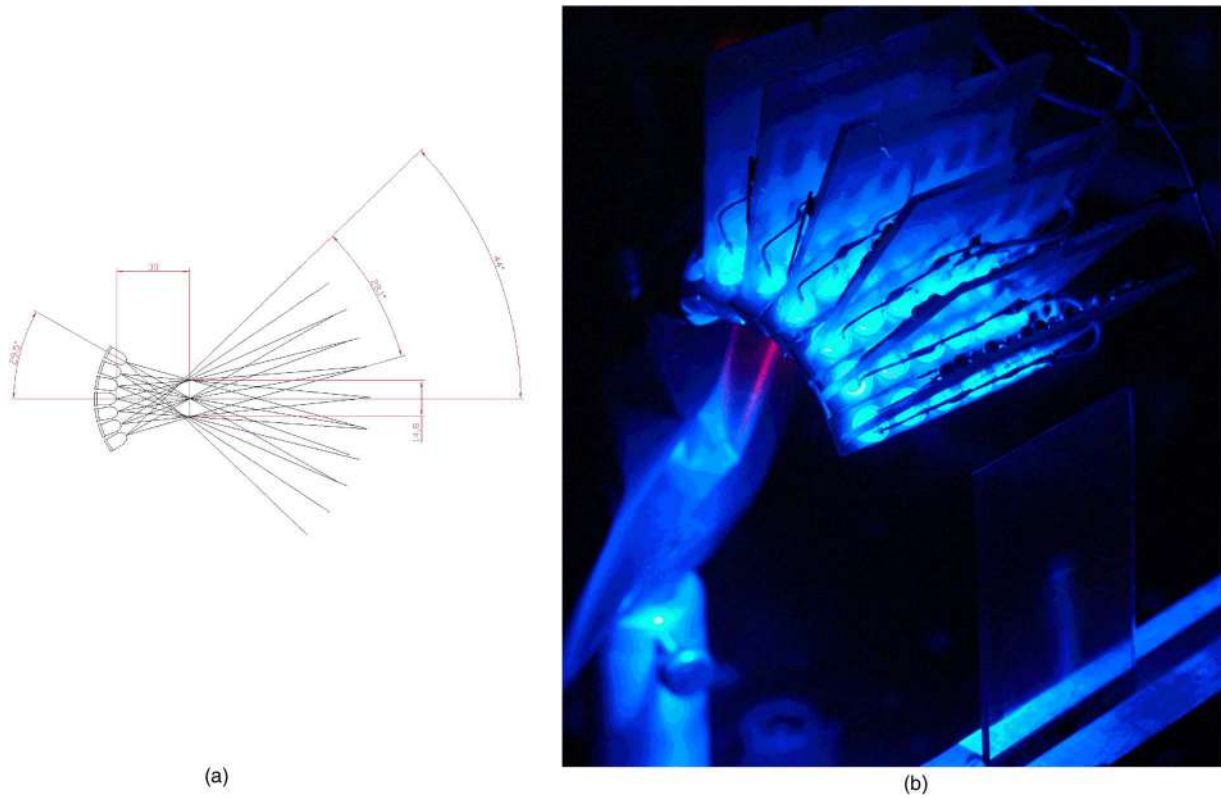


Fig. 3 LED lamp used during experiments produces even illumination on a circle with more than 1 cm diameter: (a) technical drawing with dimensions in millimeters and (b) photograph of an LED lamp.

images produces a series of dark and bright fringes—an interferogram.

The holographic interferogram was made first for the occlusal cavity (class I), and then the same procedure was

repeated for the occlusomesial cavity (class II) and the mesioocclusodistal cavity (class II MOD). All cavities were made in the same tooth specimen by gradually increasing the cavity dimension from class I to class II MOD type.

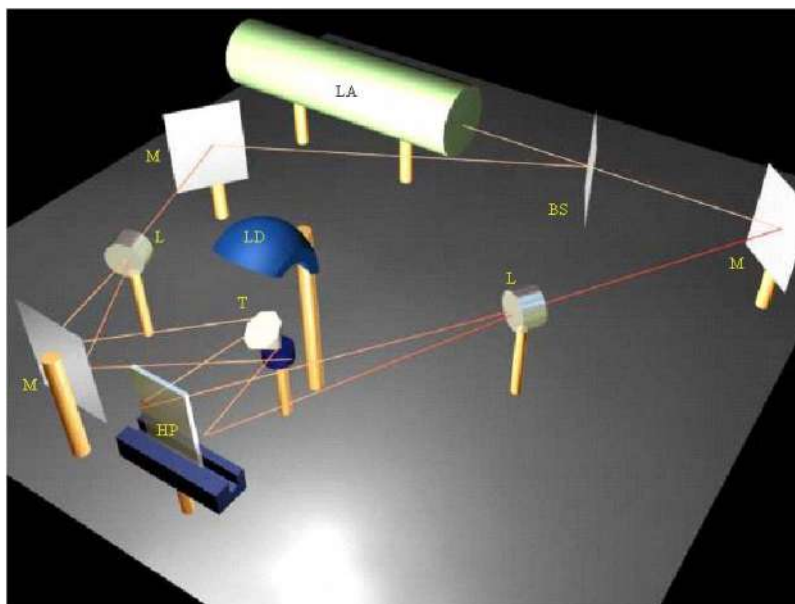


Fig. 4 Holographic interferometry setup: LA, laser; BS, beamsplitter; M, mirror; L, diverging lens (pinhole filter); HP, holographic plate; T, tooth; LD, LED lamp.

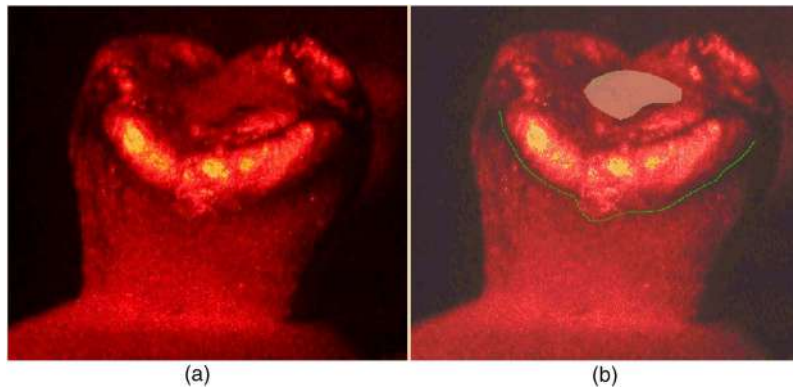


Fig. 5 Tooth hologram reconstruction of (a) class I cavity and (b) class I cavity with contour lines drawn (numbers designate deformation in micrometers).

3 Results of Holographic Measurements

As a general conclusion, it was found that a larger volume of composite material (due to a larger cavity) induced more strain. Photographs show a series of interferograms obtained for occlusal cavity [class I, Figs. 5(a) and 5(b)], occlusomesial cavity [class II, Figs. 6(a) and 6(b)], and mesioocclusodistal cavity (class II MOD, Figs. 7(a) and 7(b)). Figures 5(a), 6(a), and 7(a) are the original photographs, while in Figs. 5(b), 6(b), and 7(b) dark fringes are emphasized by lines with numbers indicating the corresponding deformation in micrometers (i.e., deformation is constant along each line or fringe).

Obviously, number of fringes increases with an increased cavity size. An occlusal cavity produced only one, barely visible, fringe at the tooth cusp [Figs. 5(a) and 5(b)]. Fringe number increases to 7 for the occlusomesial cavity [Figs. 6(a) and 6(b)], and for mesioocclusodistal cavity [Figs. 7(a) and 7(b)], 12 fringes are visible. Knowing the wavelength of the

laser radiation (633 nm), it was concluded that maximum deflections range from, approximately, 1 (class I cavity) to 7 μm (class II MOD cavity).

In our experiment, we could see only one side of a tooth, while the other was completely invisible. It can be assumed that roughly the same deformation was produced on the hidden side, since a tooth is almost symmetrical with respect to the mesiodistal line, and cavities were also intentionally drilled symmetrically (see Fig. 1). Therefore, the resulting intercusp movement ranges from 2 to 14 μm (double of what was observed on one side of the tooth).

4 Mechanical Model and Finite Element Calculation of Mechanical Stress

The FEM is a powerful tool in dentistry. However, its results should be treated more as an estimate, rather than an exact

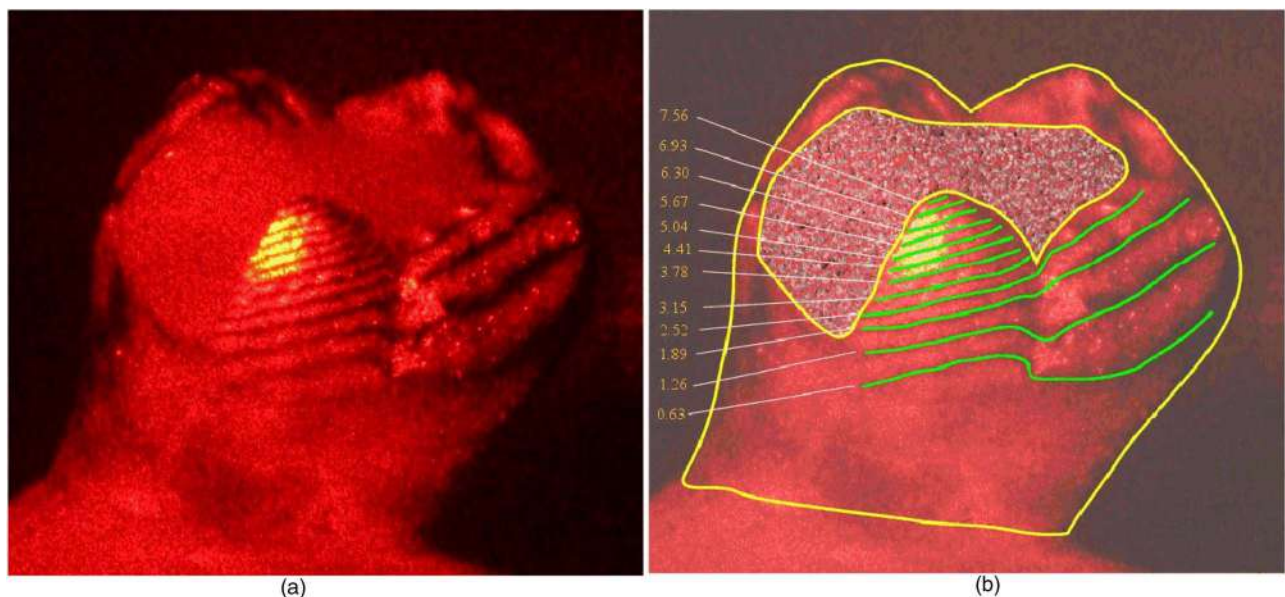


Fig. 6 Tooth hologram reconstruction of (a) class II cavity and (b) class II cavity with contour lines drawn (numbers designate deformation in micrometers).

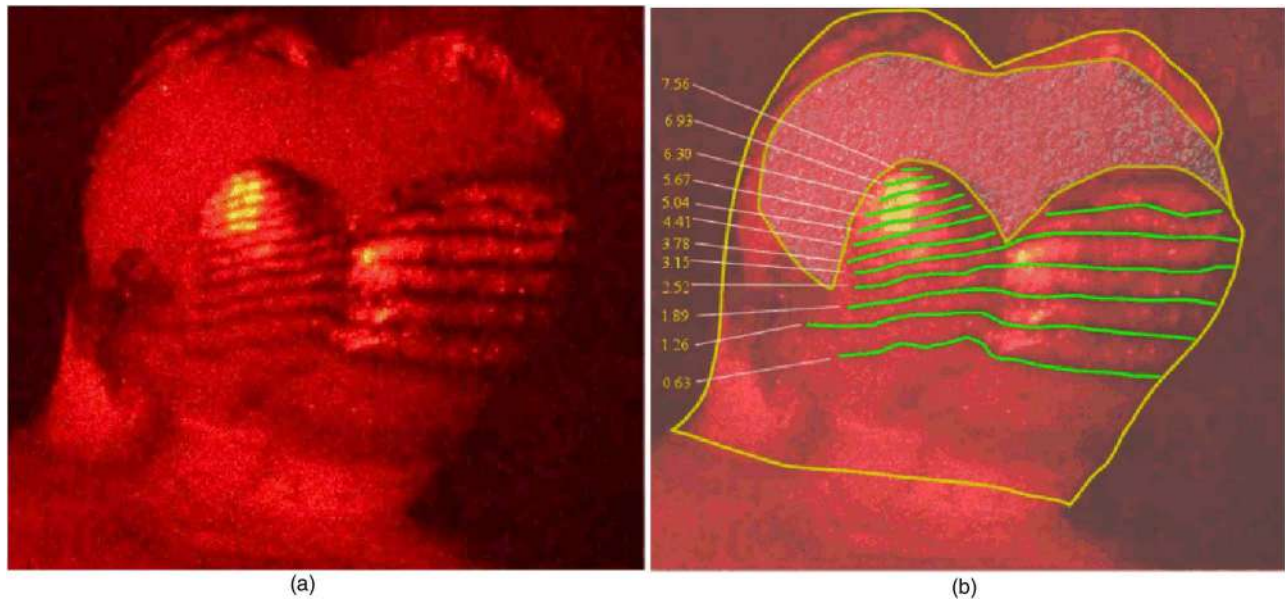


Fig. 7 Tooth hologram reconstruction of (a) class II MOD cavity and (b) class II MOD cavity with contour lines drawn (numbers designate deformation in micrometers).

picture of the actual stress distribution inside the dental tissue. This is due to natural variability in properties of teeth, differences in characteristics of dental polymers, and because of approximations made during modeling and calculation.

Teeth were previously modeled in many ways, and stress and strain were calculated. Two-dimensional (2-D) and 3-D models were constructed by approximating a tooth with a cylinder²⁸ or a parallelepiped.¹⁷ More realistic mechanical models were obtained by computerized tomography²⁹ (CT) or laser scanning of a real tooth.³⁰

In general, results obtained by approximating a tooth^{17,28} are quite similar to more comprehensive models.^{18,30} Stress distributions are comparable and numerical values of maximum von Mises stress are roughly the same.

Therefore, a simplified tooth model was developed, similar to one described in Ref. 17. The tooth was approximated, as shown in Fig. 8, with a cube made of enamel [Young's modulus 60 GPa, Poisson's ratio 0.3 (Ref. 17)], with its interior composed of dentin [Young's modulus 15 GPa, Poisson's ratio 0.31 (Ref. 17)]. It was assumed that materials are linear and isotropic, as usually accepted in the literature.³⁰ Interfaces between dental filling, dentine, and enamel were treated as rigid. Mesh was refined up to 19,089 nodes, and 11,526 10-point tetrahedral elements to test the model for convergence.

The bottom surface of a parallelepiped was rigidly constrained, so that the model actually approximates a tooth cusp. This was reasonable since the stress is only slightly transferred to the tooth root, as shown in FEM study of Ausiello et al.³⁰

Different types of cavities were made in a digital model [Figs. 2(a)–2(c)] and analyzed using the FEM. It is known that dental composite contracts volumetrically and isotropically. We have, therefore, assumed that the composite exerts constant pressure on the cavity walls.

The exact value of the pressure exerted by the composite on the cavity walls is not known. Therefore, the pressure on

the cavity sides was varied until the deformation of the model matched that observed experimentally. This is an iterative procedure that starts with an arbitrarily chosen value of the cavity internal pressure. A resulting deformation field is calculated using the FEM and deflections are compared to the holographic interferogram. If the difference between the model and experiment is unacceptably high, internal pressure is changed and model recalculated. The procedure is repeated until experiment and theory are within the measurement uncertainty (of the order of one interference fringe— $0.633 \mu\text{m}$). Luckily, this is achieved in 5 to 10 iterations, making the procedure not too time consuming. The resulting deformation patterns, shown in Figs. 9(a)–9(c), compare well with experi-

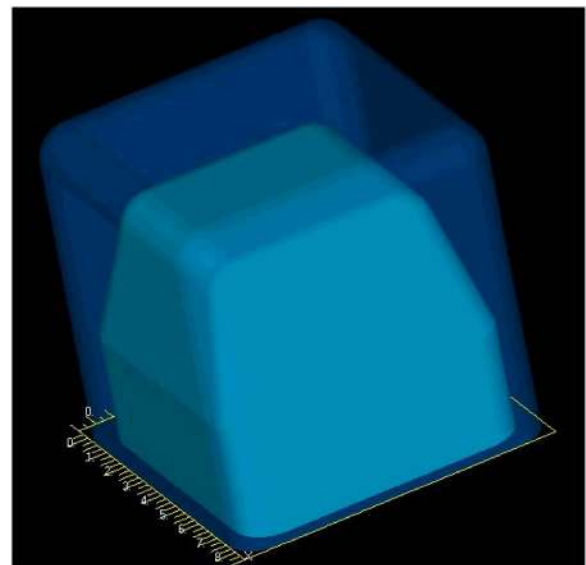


Fig. 8 Simplified mechanical model of a tooth.

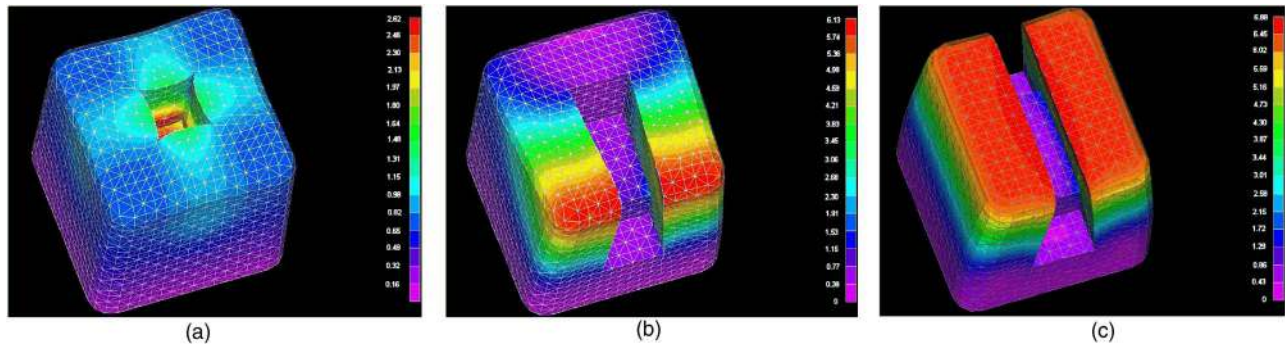


Fig. 9 Tooth deformation as calculated by the FEM for the cases of (a) a class I cavity, (b) a class II cavity, and (c) a class II MOD cavity. Colored contours represent deformation in micrometers (as shown in the bar on the right side of the figure).

mentally recorded deformation fields [Figs. 5–7]. Related von Mises internal stress was calculated for each cavity type [Figs. 10(a)–10(c)].

We found that the maximum von Mises internal stress varies from 50 to 100 MPa, depending on the cavity type. It was the highest in the case of class I cavity, lower in the class II type, and the lowest in the MOD cavity. Note that the preceding calculations produce only “the order of magnitude” of stress. A more exact model would require tomographic tooth analysis.

The stress obtained in our research (50 to 100 MPa), agrees with literature data.^{18,31} It reaches a rather high value, if compared to mechanical strength of dentin (40 to 140 MPa, see Refs. 32 and 33) and enamel (11.5 to 95 MPa, see Refs. 32 and 34). Therefore, we can conclude that there is a real danger of damaging dental tissues. Luckily, areas of high stress are localized to cavity edges [as can be seen in Figs. 10(a)–10(c)] and may cause confined effects (microcracking, composite debonding).

5 Discussion and Conclusions

Tooth tissues have microscopic features (the so-called prisms in enamel, with approximately 5 μm diameter and 2 to 4 μm microtubules in dentin) that strongly scatter and diffract light, as shown in many research papers.^{35–38} During polymerization, a tooth is subjected to deformation of up to 14 μm (as we found holographically), which is large compared to dimen-

sions of dental microstructures. This necessarily induces major changes in the profile of a back-scattered light wave.

In double-exposure holography, two significantly different wavefronts produce interference fringes with very high density—well above the resolving power of a detection system (camera or eye). This is exactly what we have in our experiment: wavefronts before and after polymerization are quite different. The final outcome is that fringes become practically invisible.

To verify the assumption that polymerization contraction induces internal changes of dentin and enamel, we made double-exposure tooth interferogram without polymerization. Between exposures, the tooth was deliberately translated (without deformation). As a result, fringes with high-contrast were obtained after processing. Thus, we can conclude that if a tissue is not deformed, high-contrast fringes are obtained. If it is deformed, the interference pattern vanishes due to internal distortion of dental microstructures.

The purpose of this paper was to introduce holography as a measurement method for the tooth deformation field, due to composite polymerization contraction. It was found that the number and shape of the resulting interference fringes depend on the particular tooth and dental cavity design. In general, total deformation was the smallest at the tooth root and the largest at its cusp. We found that total intercusp displacement is between 2 and 14 μm , which is comparable to a numerical study¹⁸ where the calculated deformation was 10 to

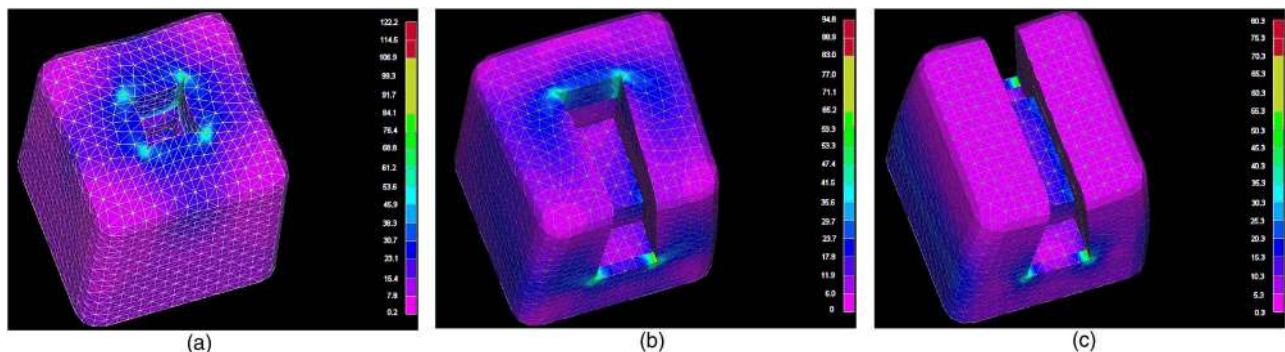


Fig. 10 Von Mises stress distribution in a tooth with a (a) class I cavity, (b) class II cavity, and (c) class II MOD cavity. Colored contours represent stress in megapascals (as shown in the bar on the right side of the figure).

20 μm . The strain due to setting of composite restoration was quantified previously by measuring cuspal movement,^{12,36,39} with similar experimental results.

The resulting stress was calculated using the FEM applied to the simplified tooth model. Correspondence with measurements was established, and the resulting maximum stress was estimated between 50 and 100 MPa. To achieve more exact picture of dental stress, tomographic methods should be used.

Finally, holographic interferometry has indirectly indicated that there are alterations in internal structure of dental tissues caused by polymerization contraction of composite material. This was verified by the almost total absence of an interference pattern in the case of an unpainted tooth surface.

Acknowledgments

This work was supported by the Serbian Ministry of Science and Environmental Protection under the Contract No. 141003.

References

1. D. Tantbiroj, A. Versluis, M. R. Pintado, R. DeLong, and W. H. Douglas, "Tooth deformation patterns in molars after composite restoration," *Dent. Mater.* **20**, 535–542 (2004).
2. N. J. M. Opdam, F. J. M. Roeters, A. J. Feilzer, and E. H. Verdonshot, "Marginal integrity and postoperative sensitivity in class 2 resin composite restoration in vivo," *J. Dent.* **26**, 555–562 (1998).
3. C. Alvarez-Gayosso, F. Barcelo-Santana, J. Guerrero-Ibarra, G. Saez-Espinola, and M. A. Canseco-Martinez, "Calculation of contraction rates due to shrinkage in light-cured composites," *Dent. Mater.* **20**, 228–235 (2004).
4. R. L. Sakaguchi, B. D. Wiltbank, and N. C. Shah, "Critical configuration analysis of four methods of measuring polymerization shrinkage strain of composites," *Dent. Mater.* **20**, 388–396 (2004).
5. J. H. Lai and A. E. Johnson, "Measuring polymerization shrinkage of photo-activated restorative materials by a water-filled dilatometer," *Dent. Mater.* **16**, 172–176 (1993).
6. C. L. Davidson, A. J. De Gee, and A. J. Feilzer, "True linear polymerization shrinkage of unfilled resin and composites determined with a linometer," *Dent. Mater.* **9**, 11–14 (1993).
7. E. A. Fogleman, M. T. Kelly, and W. T. Grubbs, "Laser interferometric method for measuring linear polymerization shrinkage in light cured dental restoratives," *Dent. Mater.* **18**, 324–330 (2002).
8. R. H. Kuijs, W. M. M. Fennis, C. M. Kreulen, M. Barink, and N. Verdonshot, "Does layering minimize shrinkage stresses in composite restorations?" *J. Dent. Res.* **82**, 967–971 (2003).
9. N. Martin, N. M. Jedyakiewicz, and D. F. Williams, "Cuspal deflection during polymerization on composite lutes of ceramic inlays," *J. Dent.* **27**, 29–36 (1999).
10. B. E. Causton, B. Miller, and J. Sefton, "The deformation of cusps by bonded posterior composite restorations: an in-vitro study," *Br. Dent. J.* **159**, 397–400 (1985).
11. G. J. Pearson and S. M. Hegarty, "Cusp movement of molar teeth with composite filling materials in conventional and modified MOD cavities," *Br. Dent. J.* **166**, 162–165 (1989).
12. A. A. Suliman, D. B. Boyer, and R. S. Lakes, "Cusp movements in premolars resulting from composite polymerization shrinkage," *Dent. Mater.* **9**, 6–10 (1993).
13. N. Meredith and D. J. Setchell, "In vitro measurement of cuspal strain and displacement in composite restored teeth," *J. Dent.* **25**, 331–337 (1997).
14. A. A. Suliman, D. B. Boyer, and R. S. Lakes, "Interferometric measurement of cusp deformation of teeth restored with composite," *J. Dent. Res.* **72**, 1532–1536 (1993).
15. Y. Kinomoto and M. Torii, "Photoelastic analysis of polymerization contraction stresses in resin composite restoratives," *J. Dent.* **26**, 165–171 (1998).
16. C. P. Ernst, G. R. Meyer, K. Klöcker, and B. Willershausen, "Determination of polymerization shrinkage stress by means of a photoelastic investigation," *Dent. Mater.* **20**, 313–321 (2004).
17. H. Ensaff, D. M. O'Doherty, and P. H. Jacobsen, "The influence of the restoration-tooth interface in light cured composite restorations: a finite element analysis," *Biomaterials* **22**, 3097–3103 (2001).
18. A. Versluis, D. Tantbiroj, M. R. Pintado, R. DeLong, and W. H. Douglas, "Residual shrinkage stress distributions in molars after composite restoration," *Dent. Mater.* **20**, 554–564 (2004).
19. P. Hubsch, J. Middleton, and J. Knox, "The influence of cavity shape on the stresses in composite dental restorations: a finite element study," *Comput. Methods Biomech. Biomed. Eng.* **5**, 343–349 (2002).
20. M. Barink, P. C. Van der Mark, W. M. Fennis, R. H. Kuijs, C. M. Kreulen, and N. Verdonshot, "A three dimensional finite element model of the polymerization process in dental restorations," *Biomaterials* **24**, 1427–1435 (2003).
21. J. Jantararat, P. Panitvisai, J. E. A. Palamara, and H. Messerh, "Comparison of methods for measuring cuspal deformation in teeth," *J. Dent.* **29**, 75–82 (2001).
22. A. Wesson, G. R. Goldstein, and A. Schulman, "Flexion characteristics of fixed partial denture frameworks tested by using elapsed-time holographic interferometry," *J. Prosthet. Dent.* **60**, 308–310 (1988).
23. R. J. Van Straten, L. M. Hitge, W. Kalk, and J. Schenk, "A study of acrylic resin denture base material distortion using computer-aided holographic interferometry," *Int. J. Prosthodont* **4**, 577–585 (1991).
24. P. R. Wedendal and H. I. Bjelkhagen, "Dental holographic interferometry in vivo utilizing a ruby laser system I. Introduction and development of methods for precision measurements on the functional dynamics of human teeth and prosthodontic appliances," *Acta Odontol. Scand.* **32**, 131–145 (1974).
25. P. R. Wedendal and H. I. Bjelkhagen, "Dental holographic interferometry in vivo utilizing a ruby laser system. II. Clinical applications," *Acta Odontol. Scand.* **32**, 345–356 (1974).
26. P. R. Wedendal and H. I. Bjelkhagen, "Dynamics of human teeth in function by means of double pulsed holography: an experimental investigation," *Appl. Opt.* **13**, 2481–2485 (1974).
27. D. Fried, R. E. Glena, J. D. B. Featherstone, and W. Seka, "Nature of light scattering in dental enamel and dentin at visible and near-infrared wavelengths," *Appl. Opt.* **34**, 1278–1285 (1995).
28. B. Kahler, A. Kotousov, and K. Borkowski, "Effect of material properties on stresses at the restoration-dentin interface of composite restorations during polymerization," *Dent. Mater.* **22**, 942–947 (2006).
29. N. Verdonshot, W. M. M. Fennis, R. H. Kuijs, J. Stolk, C. M. Kreulen, and N. H. J. Creugers, "Generation of 3-D finite element models of restored human teeth using micro-CT techniques," *Int. J. Prosthodont* **14**, 310–315 (2001).
30. P. Ausiello, A. Apicella, C. L. Davidson, and S. Rengo, "3D-finite element analyses of cusp movements in a human upper premolar, restored with adhesive resin-based composites," *J. Biomech.* **34**, 1269–1277 (2001).
31. P. Ausiello, A. Apicella, and C. L. Davidson, "Effect of adhesive layer properties on stress distribution in composite restorations—a 3D finite element analysis," *Dent. Mater.* **18**, 295–303 (2002).
32. M. Giannini, C. J. Soares, and R. M. de Carvalho, "Ultimate tensile strength of tooth structures," *Dent. Mater.* **20**, 322–329 (2004).
33. P. A. Miguez, P. N. R. Pereira, P. Atsawasuwan, and M. Yamauchi, "Collagen cross-linking and ultimate tensile strength in dentin," *J. Dent. Res.* **83**, 807–810 (2004).
34. E. B. De Las Casas, T. P. M. Cornacchia, P. H. Gouvea, and C. A. Cimini, Jr., "Abfraction and anisotropy-effects of prism orientation on stress distribution," *Comput. Methods Biomech. Biomed. Eng.* **6**, 65–73 (2003).
35. J. R. Zijp, J. J. ten Bosch, and R. A. J. Groenhuis, "HeNe-laser light scattering by human dental enamel," *J. Dent. Res.* **74**, 1891–1898 (1995).
36. R. E. Walton, W. C. Outhwaite, and D. F. Pashley, "Magnification—an interesting optical property of dentin," *J. Dent. Res.* **55**, 630–642 (1976).
37. W. J. O'Brien, "Fraunhofer diffraction of light by human enamel," *J. Dent. Res.* **67**, 484–486 (1988).
38. R. Schilke, J. A. Lisson, O. Baus, and W. Geurtsen, "Comparison of the number and diameter of dentinal tubules in human and bovine dentine by scanning electron microscopic investigation," *Arch. Oral Biol.* **45**, 355–361 (2000).
39. A. A. Suliman, D. B. Boyer, and R. S. Lakes, "Polymerization shrinkage of composite resins: comparison with tooth deformation," *J. Prosthet. Dent.* **71**, 7–12 (1994).

Modulated photoactivation of composite restoration: measurement of cuspal movement using holographic interferometry

Larisa Blažić · Dejan Pantelić · Svetlana Savić-Šević ·
Branka Murić · Ilija Belić · Bratimir Panić

Received: 10 March 2009 / Published online: 23 March 2010
© Springer-Verlag London Ltd 2010

Abstract The purpose of this research was to investigate the influence of modulated photoactivation on cuspal movement. Eight class II MOD composite restorations were analyzed under various photoactivation protocols in a real-time manner using holographic interferometry. During the first photoactivation protocol, the composite restoration was illuminated for 200 s continuously. In the second protocol, the polymerization lamp was first turned on for 5 s, then turned off for 120 s, and again turned on for a final 195 s. In both protocols, radiant exposure was the same. A significant decrease ($p < 0.05$) in cuspal deflection was found for two-step irradiation (average value of total cuspal deflection was $5.03 \pm 0.62 \mu\text{m}$) compared to continuous irradiation (average value of total cuspal deflection was $5.95 \pm 0.65 \mu\text{m}$). The two-step photoactivation protocol was found preferable, since it resulted in a significantly lower cuspal deflection (11% lower, compared to the continuous illumination).

Keywords Composite restoration · Photoactivation · Cuspal movement · Holographic interferometry

Introduction

Dental resin composites are widely employed in contemporary restorative procedures. Due to their superior esthetics, accompanied with improved physical and mechanical properties, these materials are also accepted as a replacement for the traditional amalgam restorations in posterior dentition [1].

Most clinical problems associated with the posterior resin composite restorations can be related to the polymerization contraction. Mechanical stresses generated in resin composite due to contraction are transmitted to the surrounding tooth tissues via an adhesive layer. Negative effects of stresses may result in: cracks and crazes inside enamel and dentin, cuspal movement (coronal deformation), postoperative sensitivity, and marginal gap formation [1–5]. All factors mentioned may compromise the restoration longevity leading to pre-mature restoration failure.

Different solutions have been recommended in order to prevent the problems inherent to polymerization contraction, such as modified filler particle interfaces, cavity lining with flowable composite, and employment of non-shrinking resins [6–8]. There is also a possibility to decrease the polymerization reaction rates and consecutive mechanical stresses transferred to the cavity walls. This is achieved by decreasing an irradiance of a light source or by using different photoactivation protocols [9–11]. In the last case, intensity of the light source is altered (modulated) during polymerization in a controlled fashion. In that respect, several methods were suggested, such as “soft start”, “ramp”, “pulse activation”, or “two-step” [10–14]. Regardless of the name, the underlying principle is the same: initial cure is performed at lower irradiance, lowering the polymerization rate (and contraction stresses). This is followed by a curing period of higher irradiance in order

L. Blažić (✉)
Faculty of Medicine, Clinic of Dentistry of Vojvodina,
University of Novi Sad,
Hajduk Veljkova 12,
21000 Novi Sad, Serbia
e-mail: larisa@eunet.rs

D. Pantelić · S. Savić-Šević · B. Murić · I. Belić · B. Panić
Institute of Physics,
Pregrevica 118,
11080 Belgrade, Zemun, Serbia

to complete polymerization. It has been reported that modulated photoactivation regimes improve the quality of marginal integrity, increasing the flexural modulus and flexural strength [14, 15]. On the contrary, many researchers did not find benefit from modulated photoactivation due to decreasing the final conversion and mechanical properties, or absence of stress reduction in the clinical situation [10, 16–18]. Therefore, there is still a standing debate regarding positive impacts of the modulated photoactivation protocols on the resin composite restorations.

Characterization and measurement of polymerization contraction were performed in a number of experimental and numerical studies [19–22]. To our knowledge, there were no studies that performed real-time characterization of cuspal movement under various illumination schemes. The aim of the current study was to apply holographic interferometry to the problem of modulated photoactivation-induced cuspal movement, thereby providing a real-time measurement of tooth deformation that accompanies the light polymerization of a bonded composite restoration. We used real-time holographic interferometry to measure deformation and cuspal deflection of dental tissues, from the very beginning to the end of polymerization. Two photoactivation protocols were used: a one-step (continuous) and a two-step (modulated). The research hypothesis is that the cuspal deflection (and shrinkage stress) are lower for the two-step photoactivation protocol compared to the one-step illumination [11].

Materials and methods

Methods

Deformation of a tooth structure was directly monitored by using real-time holographic interferometry. Holography is based on dividing an incident laser beam into two (using beam splitter). One (called the object beam) is expanded by a diverging lens and used to illuminate an object. Radiation reflected from the object under investigation falls on the photographic plate. The other beam (called the reference) is expanded too, and used to illuminate directly the same photographic plate. The interference pattern between the object and the reference beam is recorded on a photosensitive material (a glass plate coated with a special photosensitive layer, which we will refer to as a "holographic plate" from this point on).

After chemical processing, the holographic plate contains complete information about all three dimensions of the object (referred to as the "hologram"). The information is reconstructed by illuminating a hologram with the reference beam (while blocking the object beam), i.e., an observer sees the object entirely in three dimensions.

In holographic interferometry, the object beam is not blocked, meaning that the observer sees both the original object and its holographic image simultaneously. If there is no relative movement of either object or hologram, two identical wavefronts are produced. If the object is mechanically disturbed (moved or deformed) the wavefront changes its profile. However, a wavefront reconstructed from the hologram is "frozen", having the profile corresponding to the initial state of the object. Now we have two slightly different optical waves, which interfere. The result is seen as a series of dark and bright fringes superimposed on the object. Period, shape, and orientation of the fringes give information about movement of the object under investigation.

Sample preparation

Eight, sound, surgically extracted lower third molars of similar anatomy and dimensions ($9.89 \pm 0.45 \times 11.15 \pm 0.70$ mm) were used throughout this investigation. They were free from hypoplastic defects and cracks on visual examination and cleaned by hand instruments and pumicing. The teeth were disinfected in 0.5% chloramine for 15 days, and stored for less than 6 months in a 0.9% saline solution at 4°C until the start of the experiment. Just before the experiment, each tooth was mounted in a specially constructed holder in an inclined position using dental gypsum (Marmorock 20; Dr. Böhme & Schöps, GmbH, EN 26873/ ISO 6873, Class IV-green) in a manner shown in Fig. 1. This enabled good mechanical contact between the tooth and the gypsum and excellent mechanical stability, which is necessary for holographic measurements [2]. The angulation of the samples was 5–10° (due to differences in the teeth geometry) to the long axis of the tooth in a bucco-lingual direction. An inclined position was selected to obtain maximum illumination of the tooth during polymerization.

Standardized Class 2 Mesio-Occlusal-Distal (MOD) cavities (the occlusal preparation was 4 mm wide and 3 mm deep, with the approximal boxes 2 mm apical to the cavity floor), were prepared in each tooth using a water-

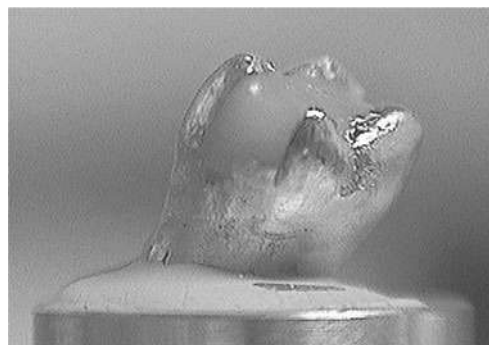


Fig. 1 Tooth sample mounted in a dental gypsum

cooled turbine and a diamond-coated bur. A 1-mm bevel was prepared at the enamel margins of the approximal boxes to maximize composite-enamel bonding. The cavity preparations were rinsed for 10 s with an air water spray and then gently air-dried. The composite restorations were adhesively bonded to the cavity walls with non-rinsing adhesive system (Adper Prompt L Pop 3M ESPE, Dental Products, St. Paul, MN), which was applied to the tooth surface and rubbed with moderate pressure for 15 s. A gentle stream of air was directed at the tooth to thoroughly spread the adhesive into a thin film. The tooth was positioned in the experimental setup and illuminated for 20 s. All of the cavities in the present study were restored in bulk with the resin-based composite (Filtek P 60 (A3 shade), 3M ESPE, Dental Products, St. Paul, MN), specifically designed for posterior teeth. The occlusal, mesial, and distal surfaces of the restoration were carved to approximate a tooth anatomy. Before starting the illumination of the restoration, each tooth sample had to be painted with a thin, opaque layer of paint (PX-20(L), Mitsubishi Pencil Co. Ltd.) to improve fringe visibility in the resulting holographic interferogram [2].

Each individual tooth was analyzed twice: employing the one-step (continuous) and the two-step (modulated) photoactivation mode. In order to ensure consistency in the restoration volumes, the mass of every tooth was measured on an analytical balance before the first restoration was placed. The resin composite restoration was removed (by an experienced dentist), between two consecutive measurements, making an effort to produce the same cavity dimensions and shape. Diamond instruments in a high-speed handpiece with water spray were used to remove the restorations and the adhesive remnants. Every tooth sample was weighted again after the removal of the first restoration. We found the differences in tooth masses were negligible (of the order of several mg, or 0.2%). After the restoration removal, each cavity was examined under the 10X magnification for the presence of the resin composite and the adhesive system remnants. Before insertion of the second resin composite restoration, the adhesive bonding procedure was applied in the same manner as described previously.

The research protocol was reviewed and approved by the Review Board of the School of Dentistry, Faculty of Medicine, University of Novi Sad.

Experimental procedure

The experimental setup is shown schematically in Fig. 2. A frequency-doubled Nd-YAG laser (manufactured by Light-wave Electronics) with 400-mW power, 532-nm wavelength, and 1-km coherence length, was used as a source of coherent radiation. The beam was split into object and

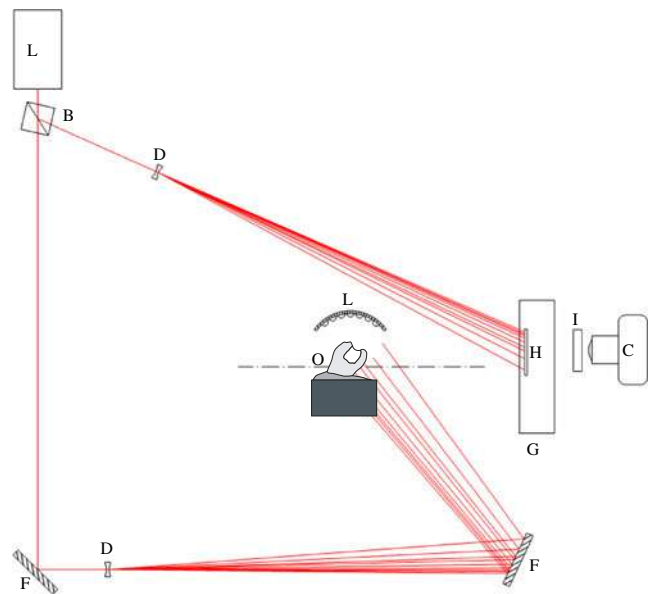


Fig. 2 Setup for real-time hologram recording of a tooth during composite restoration polymerization. *L* laser, *B* beam splitter, *D* diverging (beam expanding) lens, *F* beam folding mirror, *G* liquid gate, *H* hologram, *I* 532-nm interference filter, *C* CCD camera, *L* experimental LED lamp, *O* tooth mounted in an aluminum holder

reference using a beam splitter. The object beam was used to illuminate the tooth samples mounted in the aluminum holder using the dental gypsum. The reference beam illuminated the holographic plate, which was placed in a liquid gate container with glass walls, where complete chemical processing could be done without moving the photosensitive material. With this, we were able to keep the plate motionless. The whole setup was mounted on the vibrationally isolated table to exclude all external mechanical disturbances.

The composite restorations were cured by an LED light source especially designed for research purposes (Fig. 3). The experimental LED light source was constructed by using LEDs (Hosfelt Electronics, Inc, USA), with a maximum emitted radiation at 480 nm. The single diode was encapsulated in a clear plastic case and powered by a 20-mA constant current source emitting approximately 10 mW of optical power within the 30° angle. In order to produce power density suitable for polymerization, 42 diodes were used and placed in the spherically shaped (30-mm radius) aluminum holder, as described in the previous paper [2]. The angle of the light incidence was within the -45° , $+45^\circ$ range. As a consequence, we were able to obtain almost uniform light distribution on a circular area of 20-mm diameter. In order to establish an irradiance of the experimental LED curing light, the optical power was measured and 80 mW/cm² irradiance was calculated by dividing the optical power by the illuminated area. The distance between the LED device and the tooth sample was

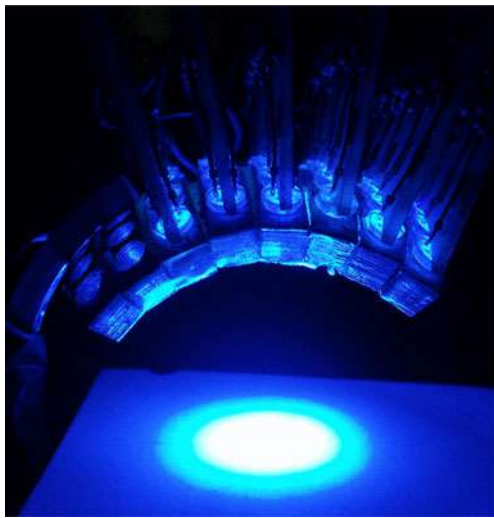


Fig. 3 Photograph of the experimental LED curing unit

30 mm, enabling a contactless curing procedure, which is important in holography where extreme mechanical stability is required. The construction of the experimental LED curing device guaranteed that light energy was transferred without losses inherent in a commercial LED light source with a light guide (Fig. 4). Operating around 470 nm, the experimental LED light source could be used for efficient curing of dental composite resins. The spectral distribution was recorded using a fiber optic spectrometer manufactured by Ocean Optics Inc. (Fig. 5).

The sequence of the photoactivation protocols was assigned in an alternating manner. The resin composite restorations were placed in the cavities in bulk, and light-cured over the entire restoration (mesial box, occlusal isthmus, and distal box). If the first restoration in the tooth sample was cured by the one-step photoactivation mode, the first restoration in the next sample was cured by the two-step photoactivation mode. We thus eliminated the possible systematic effects due to the restoration removal and filling the same tooth again.

Two different photoactivation protocols were employed: the one-step mode and the two-step mode. During the one-step photoactivation mode, the restorations were continuously illuminated for 200 s. In the two-step photoactivation

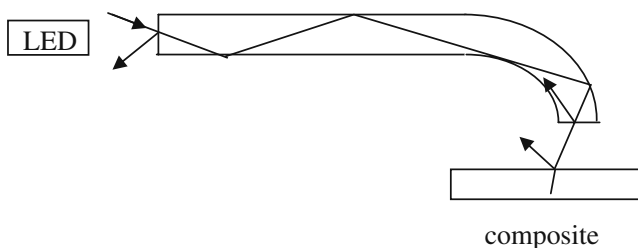


Fig. 4 Losses due to the light guide

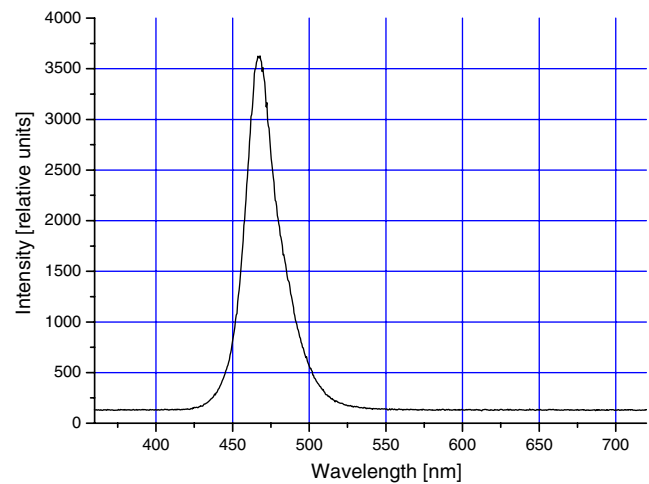


Fig. 5 The spectrum distribution for the experimental LED curing unit

mode, a 5-s light exposure was followed by a 120-s without light exposure, and then the polymerization was completed with a 195-s illumination. A 120-s delay between the first and final illumination was selected in an attempt to relieve the contraction stress through a viscous flow (before the material becomes predominantly rigid) [11]. Radiant exposure for both of the polymerization protocols was 16 J/cm^2 .

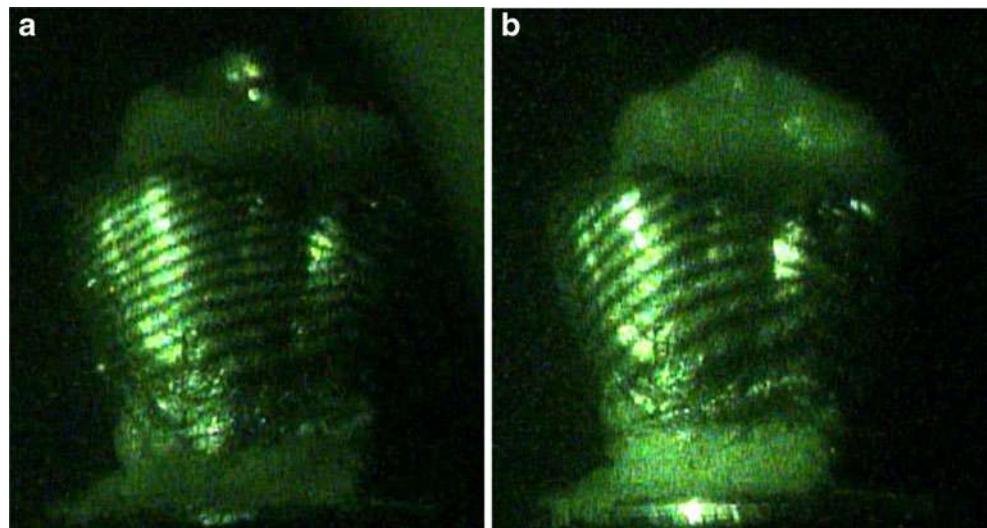
The completely prepared (mounted and filled) tooth sample was placed in the holographic setup directly beneath the experimental LED curing unit. The holographic plate was mounted in a liquid gate. The first laser-light exposure (lasting 2 s) was made before the polymerization, and the plate was consequently developed (2 min). This ended the process of the hologram recording.

To reconstruct the hologram, the laser beam was turned on again. Both the tooth and its holographic image could be observed through the hologram plate (liquid gate). Two wavefronts interfere: the one emerging from the tooth itself and the second reconstructed from the hologram. Initially, both the wavefronts were identical. After turning on the LED light source, the resin composite started contracting. The tooth deformed, which was seen as dark and bright interference fringes. The resulting interference pattern was recorded using a CCD camera. An interference filter at 532 nm was used to separate useful interference patterns from the polymerization light. The signal was digitized, saved on a PC, and further analyzed.

Results

The tooth deformation was seen as a series of dark and bright fringes (see Fig. 6a and b) in a resulting hologram. The fringes were easily interpreted as cuspal deflection, by multiplying their number on the tooth surface by $0.576 \mu\text{m}$.

Fig. 6 Interference pattern seen on the tooth surface after completing the illumination: the one-step technique (a), and the two-step technique (b). The distance between two consecutive bright (dark) fringes corresponds to deformation of $0.576 \mu\text{m}$



At the very start of the photoactivation (illumination), there were no fringes seen on the hologram. This signified that the deformation was negligible. In the one-step photoactivation protocol, the first fringe appeared on a tooth cusp after 10–15 s. It traveled down towards the gingival third of the tooth surface. More fringes followed, so that there were between 7 and 12 fringes present by the end of the illumination. The cuspal deflection, as a function of time, is presented in Fig. 7a (for the continuous photoactivation protocol). There were eight curves in total, corresponding to the each tooth in this study. In one case, we had accidentally prolonged measurement after the illumination phase was over. We observed that contraction continued to a certain extent—a fact we attributed to the post-polymerization reaction.

In the two-step photoactivation protocol, only one fringe appeared during a 120-s pause (after the first (5-s) illumination phase). Upon the start of the second illumination phase (which lasts for a 195 s), the fringes immediately started flowing across the tooth surface in the same manner

as it was in the continuous case (Fig. 7b). There was no delay between the start of the second illumination phase and the fringe movement. The reason was that during a 120-s pause, the polymerization reaction was initiated and the tooth contracted to a certain degree (one fringe). Continuation of the illumination only speeded up the contraction. An important difference was that at the end of the illumination, there were fewer fringes (1–3 less), compared to the continuous photoactivation protocol (see Fig. 7a and b). The cuspal deflection curves for the continuous and the two-step photoactivation were averaged and are shown on the same graph (Fig. 7c).

Standard *t* test was applied to our results (Table 1). Analysis showed that the average value of total cuspal deflection in the one-step case was $5.95 \pm 0.65 \mu\text{m}$, while in the two-step technique deflection was $5.03 \pm 0.62 \mu\text{m}$. The results are statistically significant, according to $p < 0.05$ criterion (in our case $p = 0.0017$, meaning that the probability of obtaining such difference by pure chance was 0.0017). An effect size (as measured by Cohen's *d* [23])

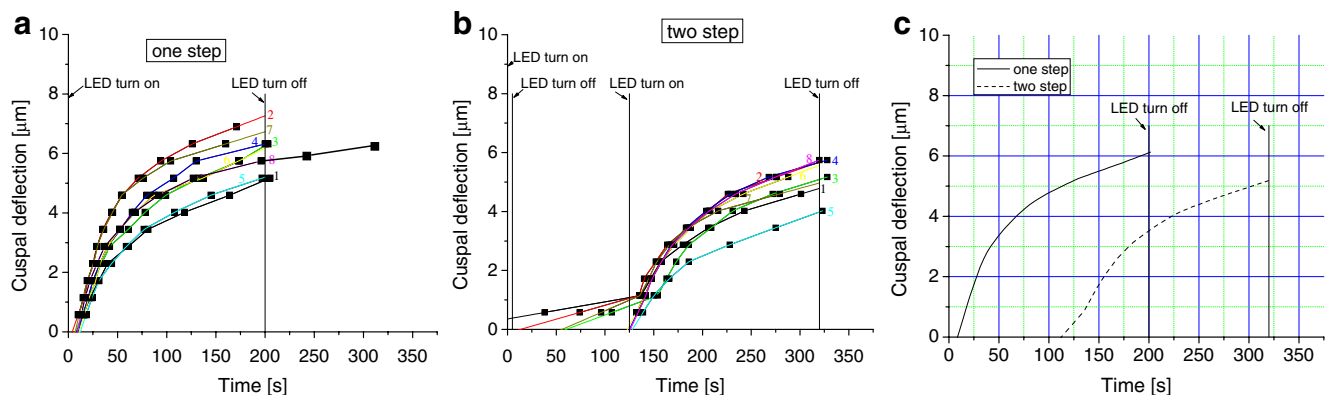


Fig. 7 Number of the fringes in a hologram as a function of the illumination time in: **a** the one-step polymerization, each curve corresponding to one tooth (one tooth was observed after the

illumination was terminated), **b** the two-step polymerization, each curve corresponding to one tooth, and **c** averaged curves of the one-step and the two-step polymerization

Table 1 Statistical analysis of eight teeth samples. *t* test was performed with paired two-sample for means (one-tail)

	One-step	Two-step
Mean	5.95 μm	5.03 μm
Variance	0.65 μm	0.62 μm

$p=0.00171193$ (*t*test)

was 1.55, signifying that the difference between the one- and the two-step technique was large (Cohen's *d* greater than 0.8 is regarded as large effect [23]). On average, 11% lower cuspal deflection was found for the two-step irradiation protocol if compared to the continuous one. The larger deflection in the continuous case, thus, became obvious. Our experimental results confirmed the hypothesis.

The polymerization contraction and resulting stresses transferred to cavity walls were higher for the continuous illumination, regardless of the photoactivation protocol employed on the tooth sample throughout the investigation.

We noted that several fringes had started propagating from a gingival third of the teeth surface. They appeared much later, during the polymerization procedure, and we attributed them to the polymerization contraction at the very bottom of the cavity.

As can be seen in Fig. 7a and b, the slope of the curves indicates that the polymerization would continue to contract dental tissue, even after the illumination was complete. This was supported by one of our measurements (which was performed accidentally, by simply forgetting to turn off the camera). Since the investigation of the post-polymerization reaction was not the aim of this paper, we did not perform any further measurements in that direction.

By extrapolating the experimental data (using the exponential function; see Fig. 8a and b), we found that the deformation of the tooth due to the light-induced curing would be, on average, completed after 155 s following the

end of the illumination for the continuous photoactivation. In the two-step process, recordable changes in the tooth structure would be complete in 135 s, following the end of the illumination. After that time interval, the further deformation would be less than one-quarter of the interference fringe (0.144 μm), which we regarded as insignificant.

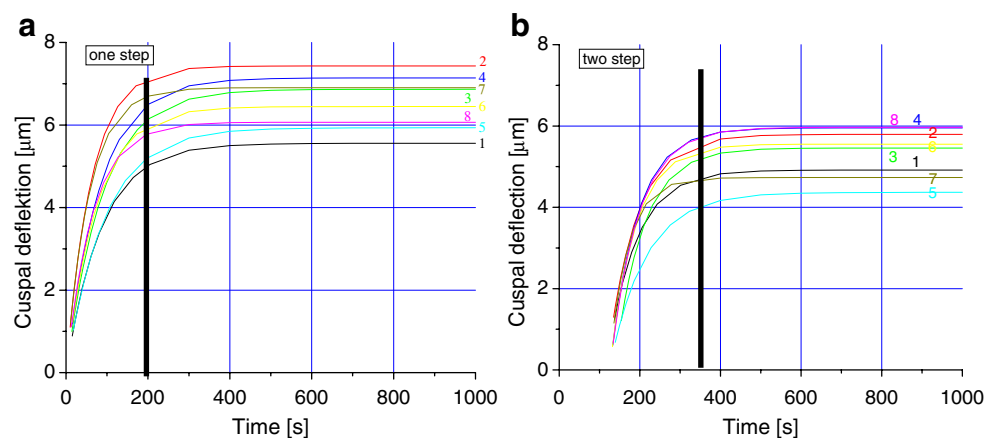
The displaced cusps did not recover after the light illumination was complete. Within the limitations of the present investigation, we concluded that the tooth structure deformation was permanent.

Discussion

During a light-curing procedure, a resin composite is transformed from a viscous-plastic state to a rigid-elastic state. At the beginning of the polymerization, contraction of the composite is compensated by its viscous flow. Some time after the start of illumination, the viscous flow is reduced, and stresses are transferred to the tooth structures. This happens when the composite reaches its gel point. To reduce the stress, the resin composite should have enough time to flow, and relieve contraction forces. In this respect, it is understood that a variety of modulated photoactivation regimes decrease the polymerization rate and, consequently, the contraction stress [10–13].

An adequate light energy is needed to completely cure the resin composite [24]. Throughout the present research, the radiant exposure was 16 J/cm², which is sufficient to complete the polymerization procedure [13, 25, 26]. It was shown that the radiant exposure is the only thing that matters for a proper light-curing [27]. A light source with a less than “optimal” irradiance (although there is no consensus on an adequate irradiance) can give effective polymerization employing longer curing times. In the present research, the total energy density remained constant throughout both of the photoactivation protocols. Required

Fig. 8 Extrapolation of the cusp-deflection measurements, signifying that contraction continued for several minutes after the illumination had ended: **a** the one-step technique and **b** the two-step technique. The vertical bar signifies the moment when the illumination was turned off



radiant exposure was achieved by increasing the exposure time (200 s) under conditions of lower irradiance, which seems too long compared to modern photoactivation protocols. On the contrary, the high irradiance light-curing units of today promote shorter exposure times, which are more convenient for the dental practitioner as well as the patient, but the polymerization contraction is larger. Therefore, the light-curing procedure should be performed slowly with low irradiance, which permits the flow necessary to minimize the effects of polymerization contraction.

It is our opinion that the two-step procedure does not prolong the whole procedure significantly (just several minutes), but the benefit is important (considerably reduced polymerization stress), which will certainly influence a longevity of the composite restoration.

Holographic interferometry represents an extremely sensitive tool for deformation detection. The method presented allows highly precise real-time monitoring of dimensional changes due to light-induced polymerization of the composite restoration [2]. Therefore, the significant difference in cuspal deflection under the different illumination regimes was found (Table 1).

When the light-curing procedure was completed, the number of interferometric fringes was not reduced. This signifies that there was no debonding of the composite restoration. If debonding did occur, then this would produce a reverse motion, and the number of fringes would decrease accordingly. Thus, we hypothesize that the real-time holography, apart from the tooth-deformation monitoring, may offer direct detection of the moment debonding occurs.

The light intensity is the highest at the surface of the restoration and decreases in deeper parts. The bottom of the composite restoration, which is furthest from the light source, will reach the gel point later than the surface. As a consequence, the stress will be relieved (by flow) more efficiently in deeper parts of the material [28]. As noted previously, the fringes first appeared on the cusp and traveled towards the gingival third of the tooth surface. In the later stages of curing, few of them appeared in the gingival third and very slowly traveled upwards, confirming polymerization reaction at the cavity base.

Cuspal deflection curves (Fig. 7a and b) indicate that the polymerization process was not over by the end of illumination. They are slanted, suggesting that the polymerization process continued, even when the illumination had finished. The post-curing contraction should be attributed to the remaining free radicals. Double bonds in the composite continued to react, and the deformation continued. Therefore, the deformation takes place even in the post-curing period, and cuspal movement may occur over a period of time. Our results indicated that slow cuspal movement persisted for several minutes after the light was

turned off, which closely agrees with the literature [29]. The extrapolation of the fringes appeared in a “dark cure” period (Fig. 8a and b), which suggested that the mechanical loading of a restored tooth should be limited during the first several minutes after the restoration has been placed.

Conclusions

In conclusion, the real-time holographic investigation of cuspal movement during polymerization of the composite restoration may give an extremely detailed insight into deformation of the tooth structure. An experimental LED light-curing unit with low irradiance, but on sufficient exposure, generated two different fringe patterns during the one-step and two-step light-curing protocols. The tested hypothesis that cuspal deflection is lower for the two-step photoactivation protocol compared to the one-step illumination was validated by the results. The current study has also shown a persistence of cuspal movement when the curing procedure was over, indicating that the polymerization process lasted after finishing illumination.

Acknowledgments This work was supported by the Serbian Ministry of Science and Technological Development under Contract No. 141003. We thank the 3M Representation Office in Belgrade, Serbia, for providing the dental adhesive system and the composite.

References

1. Sarret DC (2005) Clinical challenges and the relevance of materials testing for posterior composite restorations. *Dent Mater* 21:9–20
2. Pantelić D, Blažić L, Savić-Šević S, Panić B (2007) Holographic detection of a tooth structure deformation after dental filling polymerization. *J Biomed Opt* 12:024026–024027
3. Tantbirojn D, Versluis MR, Pintado R, De Long R, Douglas WH (2004) Tooth deformation patterns in molars after composite restoration. *Dent Mater* 20:535–542
4. Tielmans M, Compere Ph, Geerts SO, Lamy M, Limme M, De Moor RJG, Delme KIM, Bertrand MF, Rompen E, Nammour S (2007) Comparison of microleakages of photo-cured composites using three different light sources: halogen lamp, LED and argon laser; an in vitro study. *Lasers Med Sci*. doi:10.1007/s 10103-007-0504-4
5. Marzouk MA, Ross JA (1989) Cervical enamel crazings associated with occluso-proximal composite restorations in posterior teeth. *Am J Dent* 2:333–337
6. Condon JR, Ferracane JL (1998) Reduction of composite contraction stress through non-bonded microfiller particles. *Dent Mater* 14:256–260
7. Miguez PA, Pereira PNR, Foxton RM, Walter R, Nunes MF, Swift EJ Jr (2004) Effects of flowable resin on bond strength and gap formation in class I restorations. *Dent Mater* 20:839–845
8. Eick JD, Kotha SP, Chappelow CC, Kilway KV, Giese GJ, Glaros AG, Pinzino CS (2007) Properties of silorane-based dental resins and composite containing a stress-reducing monomer. *Dent Mater* 23:1001–1017

9. Silikas N, Eliades G, Watts DC (2000) Light intensity effects on resin-composite degree of conversion and shrinkage strain. *Dent Mater* 16:292–296
10. Lu H, Stansbury JW, Bowman CN (2005) Impact of curing protocol on conversion and shrinkage stress. *J Dent Res* 84:822–826
11. Lim BS, Ferracane JL, Sakaguchi RL, Condon JR (2002) Reduction of polymerization contraction stress for dental composites by two-step light activation. *Dent Mater* 18:436–444
12. Kubo S, Yokota H, Yokota H, Hayashi Y (2004) The effect of light curing modes on the microleakage of cervical resin composite restorations. *J Dent* 32:247–254
13. Cunha LG, Alonso RCB, Pfeifer CSC, Correr-Sobrinho L, Ferracane JL, Sinhoreti MAC (2007) Modulated photoactivation methods: influence on contraction stress, degree of conversion and push-out bond strength of composite restoratives. *J Dent* 35:318–324
14. YoshikawaT BMF, Tagami J (2001) A light curing method for improving marginal sealing and cavity wall adaptation of resin composite restorations. *Dent Mater* 17:359–366
15. Mehl A, Hickel R, Kunzelman KH (1997) Physical properties and gap formation of light-cured composites with and without “soft-start” polymerization. *J Dent* 25:321–330
16. Asmussen E, Peutzfeldt A (2003) Two-step curing: influence on conversion and softening of a dental polymer. *Dent Mater* 19:466–470
17. Soh MS, Yap AU (2004) Influence of curing modes on crosslink density in polymer structures. *J Dent* 32:321–326
18. Friedl KH, Schmalz G, Hiller KA, Markl A (2000) Marginal adaptation of Class V restorations with and without “soft-start” polymerization. *Oper Dent* 25:26–32
19. Ausiello P, Apicella C, Davidson CL, Rengo S (2001) 3D-finite element analyses of cusp movements in human upper premolar restored with adhesive resin-based composites. *J Biomech* 34:1269–1277
20. Barink B, Van der Mark PC, Fennis WM, Kuijs RH, Kreulen CM, Verdonchot N (2003) A three-dimensional finite element model of the polymerization process in dental restorations. *Biomaterials* 24:1427–1435
21. Versluis A, Tantbirojn MR, Pintado R, De Long WH, Douglas WH (2004) Residual shrinkage stress distributions in molars after composite restoration. *Dent Mater* 20:554–564
22. Magne P (2007) Efficient 3D finite-element analysis of dental restorative procedures using micro-CT data. *Dent Mater* 23:539–548
23. Cohen J (1988) *Statistical power analysis for the behavioral sciences*, 2nd edn. Lawrence Erlbaum Associates Ltd., Hillsdale
24. Emami N, Soderholm KJM, Benglund LA (2003) Effect of light power density variations on bulk curing properties of dental composites. *J Dent* 31:189–196
25. Vandewalle KS, Ferracane JL, Hilton TJ, Erickson RL, Sakaguchi RL (2004) Effect of energy density on properties and marginal integrity of posterior resin composite restorations. *Dent Mater* 20:96–106
26. Loguercio AD, Reis A, Schroeder M, Balducci VA, Ballester RY (2004) Polymerization shrinkage: effects of boundary conditions and filling technique of resin composite restorations. *J Dent* 32:459–470
27. Musanje L, Darwell BW (2003) Polymerization of resin composite restorative materials: exposure reciprocity. *Dent Mater* 19:531–541
28. Kinomoto Y, Torii M (1998) Photoelastic analysis of polymerization contraction stresses in resin composite restorations. *J Dent* 26:165–171
29. Ratih DN, Palamara JEA, Messer HH (2007) Dentinal fluid flow and cuspal displacement in response to resin composite restorative procedures. *Dent Mater* 23:1405–1411

Real-time and postprocessing holographic effects in dichromated pullulan

Svetlana Savić, Dejan Pantelić and Dragica Jakovljević

Experimental results concerning both real-time and postprocessing (after-development) behavior of a novel photosensitive material, dichromate-sensitized pullulan (DCP), are investigated. The exposure mechanism and possibilities for controlling holographic grating properties are discussed. We have shown that it is possible to maximize the diffraction efficiency of interference gratings after development by controlling diffraction efficiency in real time. Stronger real-time effects of DCP compared with those of dichromated gelatin are achieved. © 2002 Optical Society of America

OCIS codes: 090.2900, 050.1950.

1. Introduction

Lack of optimal recording material causes most of the limitations of today's holographic techniques and applications. Therefore further progress in holography depends on developing new types of holographic recording media.

A significant group of holographic materials is doped with dichromate. Gelatin is one of the best materials for recording holograms with respect to diffraction efficiency and recording resolution.¹⁻⁴ However, it has poor environmental stability and low sensitivity.⁵ Other dichromate materials, such as poly(vinyl alcohol) (DC-PVA),⁶⁻⁸ cellulose triacetate (DCCTA),⁹ pectin,¹⁰ gum arabic,¹⁰ and starch,¹⁰ are also good materials for recording holograms.

Recently, we discovered that pullulan¹¹ (polysaccharide polymer of linear structure) sensitized with ammonium dichromate (dichromate-sensitized pullulan; DCP) possess good holographic properties. The material has useful characteristics such as good environmental stability, simple fabrication, high diffraction efficiency, and high resolution. We also found the existence of strong surface-relief modulation.¹²

Some holographic applications require real-time recording materials. It has been shown that it is feasible to use dichromate materials in real-time holographic configurations such as double-exposure holography, generation of phase-conjugate wave fronts, edge enhancement, character recognition, and image subtraction. Dichromated gelatin (DCG), DC-PVA, and DCCTA as real-time holographic recording materials have been studied by several researchers.^{6-9, 13, 14}

The most important material parameters are diffraction efficiency, resolution, linearity of the recording, and spectral and exposure sensitivity. These parameters for DCP film have been determined experimentally.

In practice, knowledge of the maximum diffraction efficiency of the grating is required. The experiments in real time allow us to study several parameters that can affect the diffraction efficiency of the recorded grating. It is difficult to obtain dichromate materials of consistent quality. A number of variables, such as temperature, humidity, and concentration of ammonium dichromate during preparation, affect the quality of the material. Variations in the characteristics of the dichromate materials necessitate real-time monitoring of the diffraction efficiency growth during recording. In this paper we discuss possibilities for controlling holographic grating properties.

2. Dichromate-Sensitized Pullulan Layer Preparation and Processing

Sensitization of pullulan is possible by addition of a photopolymerizable monomer such as acrylamide, acrylic acid, or methacrylic acid.¹¹ We have sensitized

S. Savić (savic@phy.bg.ac.yu) and D. Pantelić are with Institute of Physics, Pregrevica 118, 11080 Zemun, Belgrade, Yugoslavia. D. Jakovljević is with Institute of Chemistry, Technology and Metallurgy-Center for Chemistry, Njegoševa 12, 11000 Belgrade, Yugoslavia.

Received 15 November 2001; revised manuscript received 18 April 2002.

0003-6935/02/224484-05\$15.00/0

© 2002 Optical Society of America

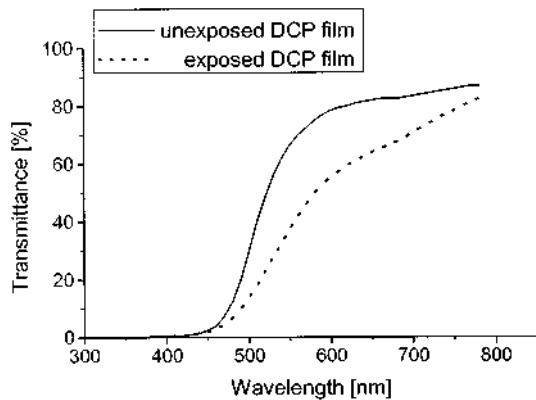


Fig. 1. Transmittance spectra of DCP film.

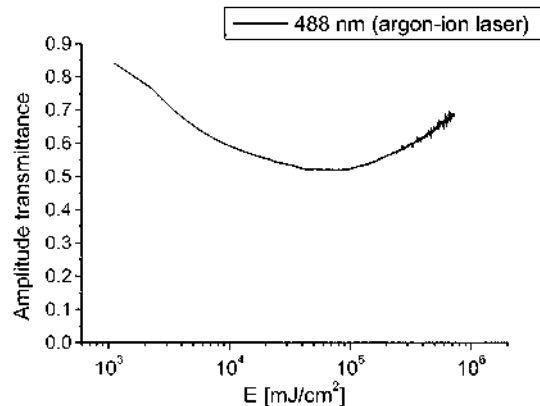


Fig. 2. Real-time amplitude transmittance of DCP film versus energy density.

pullulan with ammonium dichromate. Various concentrations of ammonium dichromate were tested from 10% to 75% by weight of pullulan. DCP samples were prepared by mixing of ammonium dichromate and pullulan solution. It was found that an 8% aqueous solution of pullulan (Sigma; average molecular weight, 200,000) gives the best results. DCP solution was stirred and warmed to 40 °C to achieve homogeneity. The solution was then coated onto clean glass slides in a horizontal position. The film was dried overnight under normal laboratory conditions (22–24 °C; relative humidity, ≈40–60%). The thickness of the dried DCP layer was 20 μm.

The convenient characteristic in the production of DCP films is the fact that the solution of pullulan is stable for a long period without showing any sign of deterioration or polymerization. Also, pullulan is completely soluble in water without producing gel.

The exposed plate was washed with a mixture of 60% isopropanol and 40% water for 2 min (pure water destroys the cross linking produced by light exposure) and then immersed in the pure isopropanol for 30 s. The unexposed portion of the DCP washed away in water. During the exposure, hexavalent chromium ion Cr^{+6} is either directly or indirectly photoreduced to trivalent Cr^{+3} , which then forms a covalent cross link with pullulan molecules (the exposure mechanism of DCP was not studied in detail; the behavior is qualitatively the same as for DCG³ or DC-PVA⁶). It was found that the cross linking produced by light reduces the solubility of the exposed regions. This means that DCP could be used as a negative photoreist recording material.

3. Transmittance Properties of Dichromate-Sensitized Pullulan

Figure 1 shows the transmittance spectra of DCP film recorded with a spectrophotometer. The shape of the curve of unexposed DCP film reveals that the film is photosensitive in the blue–green region of the spectrum. The dotted curve shows the transmittance of the same DCP film after irradiation. It can be seen that the transmittance decreases with respect to the

curve of unexposed DCP film (i.e., absorption coefficient changes). Since DCP is primarily sensitive to ultraviolet light, it is expected that less exposure energy will be necessary to record a hologram with visible light of shorter wavelengths.

Real-time amplitude transmittance of the DCP film versus energy density is presented in Fig. 2. The experiment was carried out with an unexpanded laser beam at 488 nm (argon-ion laser), with a power density of 225 mW/cm².

During exposure, the material changes color from yellow to brown. For long exposure times (i.e., for high-energy density), the color partially bleaches in the exposed area. This can be seen from Fig. 2 where amplitude transmittance first decreases and then increases with prolonged exposure.

4. Diffraction Efficiency and Sensitivity in Real Time

To measure the holographic properties of DCP, we recorded simple holographic gratings formed by the interference of two coherent beams of equal power. The experimental setup is shown in Fig. 3. Both beams are incident on the recording material at the same angle, with respect to the normal to the material. The spatial frequency of the gratings was 1670 lines/mm. DCP was exposed at a wavelength of 488 nm with an argon-ion laser. Diffraction efficiency was measured (defined as the ratio of the diffracted first-order beam intensity to the intensity of the in-

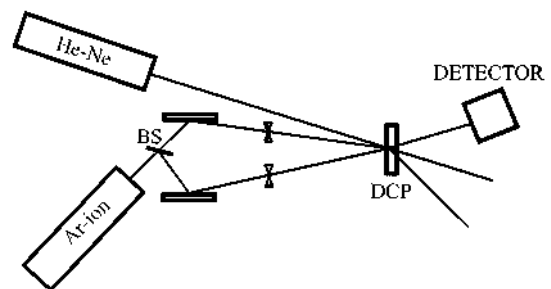


Fig. 3. Experimental setup for recording and reading diffraction grating.

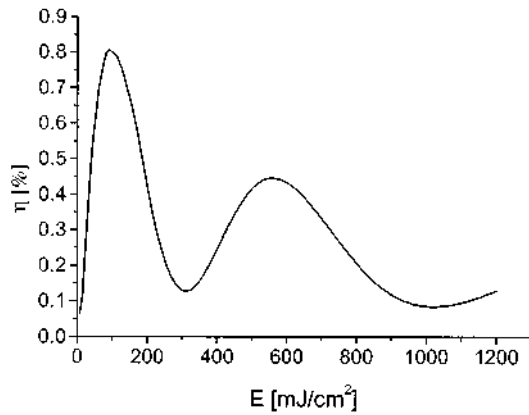


Fig. 4. Real-time diffraction efficiency versus energy density.

cident beam) as a function of the exposure, both in real-time and after processing. Reconstruction of gratings was made with a 10-mW He-Ne laser operating at 632.8 nm; the laser was adjusted near to the Bragg angle. From Fig. 1 it could be seen that DCP absorbs some light at the red part of the spectrum, so we tried to verify whether the He-Ne laser has any influence on the recording material. To do that, two diffraction gratings were recorded on the same DCP plate, the first while the He-Ne laser was on and the second while the He-Ne laser was off. Exposure time was the same for both. Diffraction efficiency after development was identical for both gratings. Therefore we concluded that the He-Ne laser does not produce significant photochemical reaction in the material.

During and after exposure we observed the diffraction without any processing both in transmission and in reflection, indicating that a surface-relief grating was formed in addition to an amplitude grating inside the material. To verify the existence of surface relief, we measured the surface shape directly by use of a Tally-step surface profiler.¹² In addition, we verified the existence of surface relief by means of gold plating the DCP grating. Diffraction efficiency in reflection was 8.5% (before gold-plating diffraction, efficiency in reflection was 3%). Diffraction efficiency was small as a result of inappropriate conditions for recording the reflection gratings; in any event, this was not our goal in the current research.

Figure 4 shows the real-time diffraction efficiency versus energy density. The power density of the recording beams was $P_0 = 0.25 \text{ mW/cm}^2$. From this figure it can be seen that the energy density necessary to obtain the maximum diffraction efficiency was 90 mJ/cm^2 .

The diffraction efficiency is not dependent only on exposure; the power density of the recording beams P_0 affects the recording characteristics as well. By comparing the dotted curve of Fig. 5 recorded at higher power density ($P_0 = 48 \text{ mW/cm}^2$) with the solid curve recorded at lower power density ($P_0 = 0.25 \text{ mW/cm}^2$), we found that as the power density is decreased, the sensitivity increased. The recording

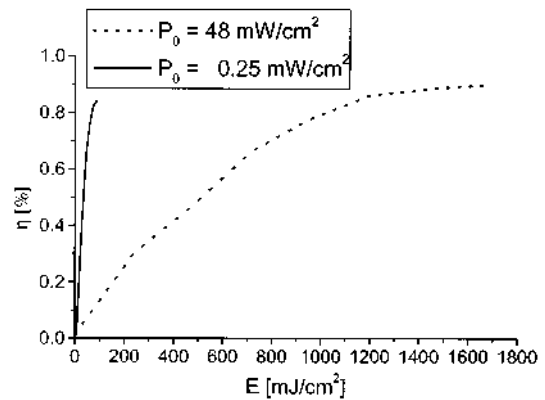
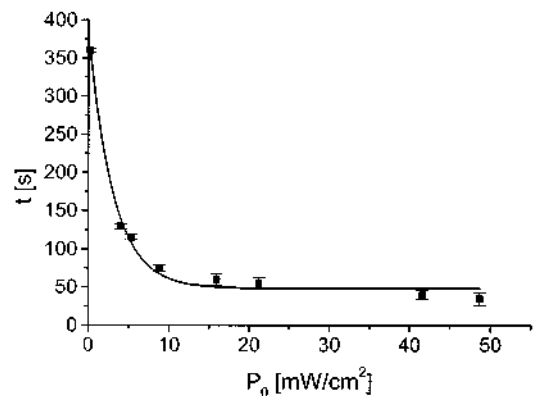


Fig. 5. Real-time diffraction efficiency versus energy density. The power density is a parameter.

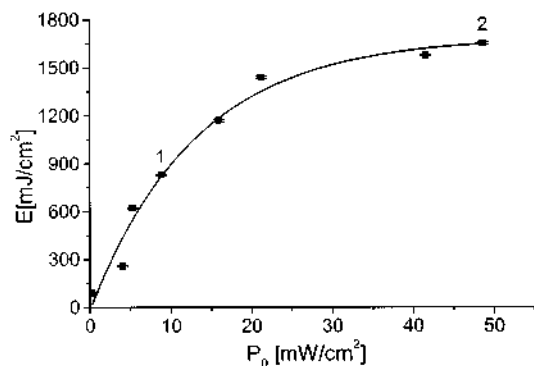
response is an exponential function of $P_0 t$, i.e., exposure [Fig. 6 (a)]. All points represent the average value of the five experimental measurements. The spatial frequency of the gratings was 1670 lines/mm.

Figure 6(b) illustrates energy density as a function of power density. Observe, for example, points (1) and (2). Power at (2) is five times larger than at (1), but energy is only two times smaller.

From these data it is apparent that there are two boundary-recording regimes: one at high recording power density and short recording time and another



(a)



(b)

Fig. 6. (a) Exposure time versus power density. (b) Energy density versus power density.

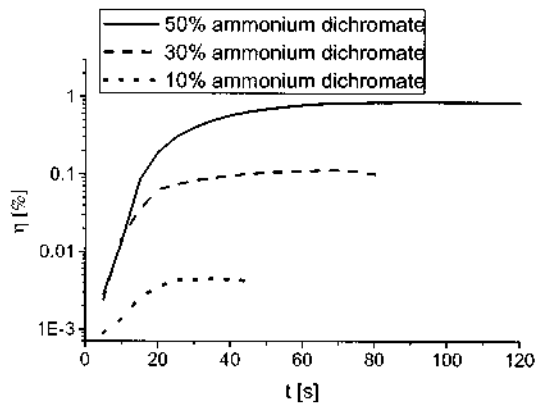


Fig. 7. Real-time diffraction efficiency versus exposure time. The dichromate concentration is a parameter.

at low recording power density and long recording times. For example, in the former region for $P_0 = 48 \text{ mW/cm}^2$ and $t = 35 \text{ s}$ the sensitivity is $0.06 \times 10^{-3} \text{ m}^2/\text{J}$, whereas in the latter region, for $P_0 = 0.25 \text{ mW/cm}^2$ and $t = 360 \text{ s}$, sensitivity is $1 \times 10^{-3} \text{ m}^2/\text{J}$.

We assume that the recording mechanism is nonlinear because the absorption is caused by a complex process of cross linking (among molecules of pullulan and ammonium dichromate) and probably chromium diffusion. In addition to amplitude modulation, the grating has phase modulation, too (resulting from surface relief and possibly refractive-index modulation). Also, nonlinearity of the phase holography recording process was observed in photoresist processing.¹⁵

5. Correspondence between Real-Time and Postprocessing Effects

We investigated the effect of dichromate concentration on the diffraction efficiency of gratings in DCP films. The real-time efficiency was measured versus exposure time, for varying concentrations of ammonium dichromate, from 10% to 50% by weight of pullulan (for concentrations greater than 50%, dichromate crystallized). Figure 7 illustrates the results. The power density of the recording beams was 6 mW/cm^2 .

The efficiency in real time increased with increasing concentrations of ammonium dichromate. The time necessary to achieve maximum diffraction efficiency is longer for higher concentrations (from Fig. 7, it is 90 s for 50%, 70 s for 30%, and 35 s for 10% of ammonium dichromate). This result indicates that sensitivity of the DCP material decreases with increasing concentration of ammonium dichromate. This behavior is unlike gelatin, for which sensitivity increases with increasing concentration of ammonium dichromate.¹⁶ Different behavior of DCP and DCG can be explained by the difference in the chemical structure of pullulan (saccharide structure) and gelatin (peptide structure). The main functional group of pullulan participating in cross linking is the carbonyl group. In contrast to pullulan, gelatin

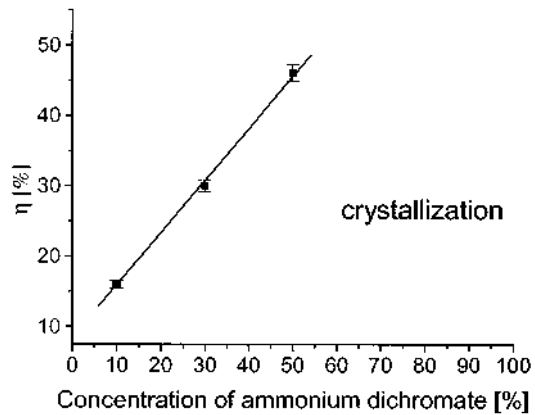


Fig. 8. Diffraction efficiency (after processing) versus concentration of ammonium dichromate.

forms cross links by amino and carboxyl groups.¹⁰ The exact chemical reactions are not clear.

After processing, maximum diffraction efficiency reached 46%, 30%, and 16% for concentrations of ammonium dichromate of 50%, 30%, and 10%, respectively (Fig. 8). In accordance with these results, pullulan was sensitized with 50% ammonium dichromate.

In comparison with gelatin¹⁷ sensitized from 10% to 20% ammonium dichromate, pullulan can be sensitized with the dichromate of appreciably higher concentration. In this way stronger real-time effects of DCP compared with those of DCG were achieved. We measured real-time diffraction efficiency of both DCP and DCG (7% aqueous solution of gelatin sensitized with 10% ammonium dichromate), under the same experimental conditions. We found that the real-time diffraction efficiency of DCP ($\sim 1\%$) is 2 orders of magnitude higher than that of DCG ($\sim 0.01\%$).

To obtain maximum diffraction efficiency, accurate exposure is essential. Measurement of the diffraction efficiency in real time is important for controlling the diffraction efficiency after processing. The purpose of our measurements was to predict accurate exposure and consistently obtain the maximum diffraction efficiency. It is shown that the effect of the variability in characteristics of the dichromate materials can be alleviated by monitoring of exposure in real-time. The relation between the real-time diffraction efficiency and diffraction efficiency after processing was investigated. We exposed the DCP film for a certain time and recorded its diffraction efficiency (before processing). After that, we developed the film and again measured diffraction efficiency. The process was repeated for a range of exposure times (those points, in fact, trace the real-time curve shown in Fig. 4). Corresponding pairs of points representing diffraction efficiency before and after processing are shown in Fig. 9.

Therefore it is possible to determine the right exposure energy in order to achieve the maximum diffraction efficiency after processing. In other words, grating with the maximum diffraction efficiency in

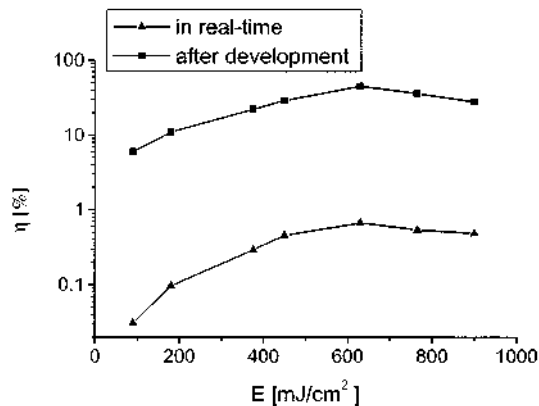


Fig. 9. Diffraction efficiency versus energy density in real time and postprocessing.

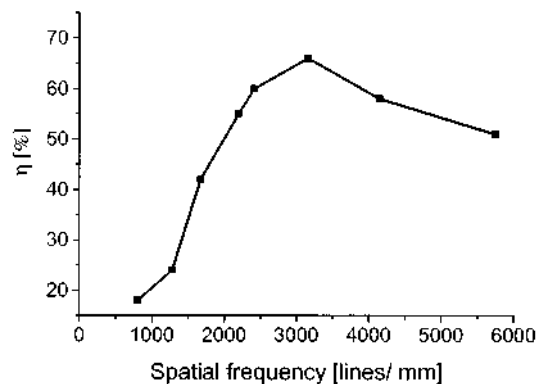


Fig. 10. Spatial-frequency response of DCP (after processing).

real time results in grating with the maximum efficiency after processing. The power density of the recording beams was 6 mW/cm^2 .

6. Spatial-Frequency Response

Information on the spatial-frequency response is important. By varying the recording angles in a holographic setup, we determined that the DCP has high resolving capabilities. The spatial-frequency response of DCP is shown in Fig. 10. During reconstruction, a He-Ne laser was adjusted to the Bragg angle. The spatial frequency was varied from 800 lines/mm up to nearly 6000 lines/mm.

For lower spatial frequencies we observed several diffracted orders (for 800 lines/mm, six orders are present). In this case diffraction efficiency is smaller because the light intensity goes into higher orders. Gratings with higher spatial frequencies have higher diffraction efficiency and smaller number of diffracted orders. For spatial frequencies above 5000 lines/mm only one diffracted order is present, and only for Bragg incidence. The fall in efficiency at spatial frequencies above 3200 lines/mm can be explained by the limited resolution of the material.

7. Conclusion

In our experiments we have investigated recording real-time gratings, using a new dichromate material, DCP. Because of variations in the characteristics of the dichromate materials, monitoring of the exposure in real time is important for controlling the diffraction efficiency. Real-time measurements show that it is possible to find the proper exposure resulting in the maximum diffraction efficiency after processing. Pullulan can be sensitized with a dichromate of appreciably higher concentration than gelatin. In this way, stronger real-time effects of DCP compared with those of DCG are achieved.

References

1. L. H. Lin, "Hologram formation in hardened dichromated gelatin films." *Appl. Opt.* **8**, 963–966 (1969).
2. R. K. Curran and T. A. Shankoff, "The mechanism of hologram formation in the dichromated gelatin," *Appl. Opt.* **9**, 1651–1657 (1970).
3. B. J. Chang and C. D. Leonard, "Dichromated gelatin for the fabrication of holographic optical elements," *Appl. Opt.* **18**, 2407–2417 (1979).
4. T. G. Georgekutty and H. K. Liu, "Simplified dichromated gelatin hologram recording process," *Appl. Opt.* **26**, 372–376 (1987).
5. G. M. Naik, A. Mathur, and S. V. Pappu, "Dichromated gelatin holograms: an investigation of their environmental stability," *Appl. Opt.* **29**, 5292–5297 (1990).
6. S. Lelièvre and J. J. A. Couture, "Dichromated polyvinyl alcohol films used as a novel polarization real time holographic recording material," *Appl. Opt.* **29**, 4384–4391 (1990).
7. M. Barikani, E. Simova, and M. Kavehard, "Dichromated polyvinyl alcohol as a real-time hologram recording material: some observations and discussions," *Appl. Opt.* **34**, 2172–2179 (1995).
8. R. Grzymala and T. Keinonen, "Self-enhancement of holographic gratings in dichromated gelatin and polyvinyl alcohol films," *Appl. Opt.* **37**, 6623–6626 (1998).
9. K. Wang, L. Guo, L. Zhou, and J. Zhu, "Imaging mechanism of the holographic recording material dichromated cellulose triacetate," *Appl. Opt.* **35**, 6369–6374 (1996).
10. K. Yokono and K. Nishide, "Hologram and method of production thereof from polysaccharide recording layer," U.S. patent 4,254,193 (3 March 1981).
11. T. Sano, Y. Uemura, and A. Furuta, "Photosensitive resin composition containing pullulan or esters thereof," U.S. patent 3,960,685 (1 June 1976).
12. D. Pantelić, S. Savić, and D. Jakovljević, "Dichromated pullulan as a novel photosensitive holographic material," *Opt. Lett.* **23**, 807–809 (1998).
13. J. C. Newell, L. Solymar, and A. A. Ward, "Holograms in dichromated gelatin: real-time effects," *Appl. Opt.* **24**, 4460–4466 (1985).
14. S. Calixto and R. A. Lessard, "Real-time holography with undeveloped dichromated gelatin films," *Appl. Opt.* **23**, 1989–1994 (1984).
15. R. A. Bartolini, "Characteristics of relief phase holograms recorded in photoresists," *Appl. Opt.* **13**, 129–139 (1974).
16. T. Kubota, "Recording of high quality color holograms," *Appl. Opt.* **25**, 4141–4145 (1986).
17. L. Xiong and B. Peng, "Effect of the content of ammonium dichromate in dichromated gelatin on $\text{Cr}2\text{P}_{3/2}$ x-ray photoelectron spectroscopy," *Appl. Opt.* **38**, 279–283 (1999).

Real-time measurement of internal stress of dental tissue using holography

Dejan Pantelić¹, Larisa Blažić², Svetlana Savić-Šević¹, Branka Murić¹,
Darko Vasiljević^{1,3}, Bratimir Panić¹, Ilija Belić¹

¹*Institute of Physics, Pregrevica 118, 11080 Zemun, Belgrade, Serbia*
pantelic@phy.bg.ac.yu

²*University of Novi Sad, Faculty of Medicine, Dental Clinic, Novi Sad, Serbia*

³*Faculty of Mechanical Engineering, Kraljice Marije 16, 11120 Belgrade 35, Serbia*

Abstract: We describe a real-time holographic technique used to observe dental contraction due to photo-polymerization of dental filling during LED lamp illumination. An off-axis setup was used, with wet in-situ processing of the holographic plate, and consequent recording of interference fringes using CCD camera. Finite elements method was used to calculate internal stress of dental tissue, corresponding to experimentally measured deformation. A technique enables selection of preferred illumination method with reduced polymerization contraction. As a consequence, durability of dental filling might be significantly improved.

©2007 Optical Society of America

OCIS codes: (090.2880) Holographic interferometry; (170.1850) Dentistry; (120.2650) Fringe analysis; (160.5470) Polymers.

References and links

1. K. F. Leinfelder, "Composite resin systems for posterior restorations," *Pract. Periodontics. Aesthet. Dent. Suppl.* **1**, 23-27 (1993).
2. C. J. Whitters, J. M. Girkin, and J. J. Carey, "Curing of dental composites by use of InGaN light-emitting diodes," *Opt. Lett.* **24**, 67-68 (1999).
3. R. W. Mills, A. Uhl, G. B. Blackwell and K. D. Jandt, "High power light emitting diode (LED) arrays versus halogen light polymerization of oral biomaterials: Barcol hardness, compressive strength and radiometric properties," *Biomaterials* **23**, 2955–2963 (2002).
4. G. A. Laughlin, J. L. Williams and J. D. Eick, "The Influence of System Compliance and Sample Geometry on Composite Polymerization Shrinkage Stress," *J. Biomed. Mater. Res. (Appl. Biomater.)* **63**, 671–678 (2002).
5. A. Versluis, D. Tantbirojn, M. R. Pintado, R. DeLong and W. H. Douglas, "Residual shrinkage stress distributions in molars after composite restoration," *Dent. Mater.* **6**, 554-564 (2004).
6. J. D. Eick and F. H. Welch, "Polymerization shrinkage of posterior composite resins and its possible influence on postoperative sensitivity," *Quintessence Int.* **17**, 103-111 (1986).
7. C. L. Davidson, A. J. de Gee and A. J. Feilzer, "The competition between the composite-dentin bond strength and the polymerization contraction stress," *J. Dent. Res.* **12**, 1396-1399 (1984).
8. E. A. Fogleman, M. T. Kelly and W. T. Grubbs, "Laser interferometric method for measuring linear polymerization shrinkage in light cured dental restoratives," *Dent. Mater.* **18**, 324 – 330 (2002).
9. H. Lang, R. Rampado, R. Mülleijans and W. H. M. Raab, "Determination of the dynamics of restored teeth by 3D electronic speckle pattern interferometry," *Lasers in Surg. Med.* **34**, 300-309 (2004).
10. T. G. Oberholzer, S. Grobler, C. H. Pameijer and R. J. Rossouw, "A modified dilatometer for determining volumetric polymerization shrinkage of dental materials," *Meas. Sci. Technol.* **13**, 78–83 (2002).
11. P. Ausiello, A. Apicella, C. L. Davidson and S. Rengo, "3D-finite element analyses of cusp movements in a human upper premolar, restored with adhesive resin-based composites," *J. Biomech.* **34**, 1269 – 1277 (2001).
12. H. Ensaff, D.M. O'Doherty and P.H. Jacobsen, "The influence of the restoration-tooth interface in light cured composite restorations: a finite element analysis," *Biomaterials* **22**, 3097-3103 (2001).

13. C.-L. Lin, C.-H. Chang, C.-S. Cheng, C.-H. Wang and H.-E. Lee, "Automatic finite element mesh generation for maxillary second premolar," *Comput. Methods Programs Biomed.* **59**, 187–195 (1999).
14. J. Gao, W. Xu and Z. Ding, "3D finite element mesh generation of complicated tooth model based on CT slices," *Comput. Methods Programs Biomed.* **82**, 97-105 (2006).
15. P.R. Wedendal and H.I. Bjelkhagen, "Dynamics of Human Teeth in Function by Means of Double Pulsed Holography: an Experimental Investigation," *Appl. Opt.* **13**, 2481-2485 (1974).
16. D. Pantelić, L. Blažić, S. Savić-Šević and B. Panić, "Holographic detection of a tooth structure deformation after dental filling polymerization," *J. Biomed. Opt.*, **12**, 024026, (2007)
17. N. Ilie, K. Felten, K. Trixner, R. Hickel and K. H. Kunzelmann, "Shrinkage behavior of a resin based composite irradiated with modern curing units," *Dent. Mater.* **21**, 483-489 (2005).
18. K. S. Vandewalle, J. L. Ferracane, T. J. Hilton, R. L. Erickson and R. L. Sakaguchi, "Effect of energy density on properties and marginal integrity of posterior resin composite restorations," *Dent. Mater.* **20**, 96-106 (2004).
19. H. Ensaff, D.M. O'Doherty and P.H. Jacobsen, "The influence of the restoration-tooth interface in light cured composite restorations: a finite element analysis," *Biomaterials* **22**, 3097-3103 (2001).
20. G. Couegnat, S.L. Fok, J.E. Cooper and A.J.E. Qualtrough, "Structural optimization of dental restorations using the principle of adaptive growth," *Dent. Mater.* **22**, 3–12 (2006).
21. D. Tantbiroj, A. Versluis, M. R. Pintado, R. DeLong, R. Douglas and W.H. Douglas, "Tooth deformation patterns in molars after composite restoration," *Dent. Mater.* **20**, 535-542 (2004).

1. Introduction

Dental tissues are under mechanical load for several reasons – due to mastication, external impact, surgery or other dental procedures. It is of utmost importance in dentistry to estimate internal mechanical pressures in order to find the most appropriate medical practices. The final goal is to heal teeth and prolong their life.

Mostly, mechanical loads are external, resulting from chewing, shock or dental appliances. On the other hand, modern dental techniques using implants and fillings can lead to forces acting from inside of a tooth. In any case, the resulting strain is small (in the micrometer range) but internal stress can be high enough to irreversibly damage dental tissues.

Placement of esthetic fillings is widespread in dentistry and photosensitive resin composites have become the most frequently used materials for this particular purpose [1]. During the clinical procedure caries lesion is removed with a diamond coated drill and a preparation is filled with a dental composite. Adhesion to pre-treated tooth tissues provides the necessary retention of a filling material. A resin composite is illuminated with actinic light (predominantly in the blue part of the spectrum [2]) until it is fully cured. The resulting polymerized layer is hard, closely matching the mechanical properties of enamel and dentin, enabling filling's permanence [1, 3].

It is well known that resin composites contract during setting reaction [4]. Contraction is transferred to dental tissues, inducing high level of mechanical stress [5], which may result in clinical symptoms associated with residual shrinkage stresses (micro-cracking, loss of marginal integrity, post-operative sensitivity and secondary caries) [6, 7]. As a consequence, lifetime of a dental filling may be considerably reduced.

This particular problem has been the subject of intense research, with an aim to find the most appropriate restorative procedure, which reduces or eliminates the residual contraction stresses. The problem is analyzed theoretically, numerically and experimentally. Various experimental techniques are used to monitor deformation, like classical and speckle interferometry [8, 9] or volumetric contraction measurement using dilatometer [10]. Theoretical and numerical methods are used to calculate stress, based on idealized models and to deduce mechanical stress from deformation measurements [11]. Mechanical models of a tooth are constructed, either based on simplified geometry [12], mechanical slicing [13] or tomographic measurements [14] of real teeth.

Holography [15] is an important method used to measure dental deformation, both in vivo and in vitro. While it gives certain insight in various medical procedures, internal stress

cannot be measured directly and this is what really matters in dentistry. The reason is simple, forces and pressures destroy teeth, not deformation by itself. This was the motivation to develop a method to measure dental deflection continuously and to calculate internal stress, based on experimental data.

In our previous research we observed tooth holographically only in its final state (after illumination) [16]. In this paper real-time off-axis holography was used to continuously measure (*in vitro*) deformation field of a human third molar during LED lamp illumination. A mechanical tooth model and Finite Elements Method (FEM) was used to calculate internal stress, based on measurements.

This particular technique enables observation of stress build-up, calculation of stress distribution, analysis of all stages of photo-polymerization, with special emphasis on initial stage and post illumination effects. Our research indicates that there is pronounced post-polymerization contraction, which further increases internal stress, even after illumination is over. Method can be used as a tool to analyze various illumination schemes (continuous, two step, ramp, impulse [17]) and various dental composites, with the aim to significantly reduce the internal polymerization stress. The most important consequence is improved durability of dental fillings.

2. Experimental technique

A Schematic view of the real-time holographic setup is shown in Fig. 1. Long coherence length, 532 nm second harmonic Nd-YAG, laser was used. A beam was split and one part was used to illuminate a tooth, while the second was utilized as a reference to irradiate the holographic plate (VRP-M green sensitive emulsion, produced by Slavich, Russia). A plate was placed in a liquid gate, so that the chemical processing could be performed in situ (without moving the holographic plate). Blue LED lamp (central wavelength approximately 480 nm) illuminated the tooth, while CCD camera and computer detected and recorded the interference pattern. It was necessary to use 532 nm interference filter, in order to reject 480 nm LED lamp light, and transmit 532 nm interference pattern. Variable density neutral filter was placed in the object beam, so that the intensity of light directly reflected from the tooth can be equalized with the light intensity reconstructed from hologram. By that means, the contrast of interference fringes is improved.

Specially constructed lamp with 42 LEDs produced 2 cm diameter spot with 80 mW/cm² irradiance. Construction is hemispherical as previously described in detail [16]. The lamp is placed directly above the tooth so that composite polymerization can be performed without contacting a tooth and with appropriate energy density (which should be 12 - 24 J/cm² according to [18]). In our case exposure time was 200 s and, consequently, energy density was 16 J/cm² - quite suitable for successful polymerization.

A tooth was analyzed in vitro, by fixing an extracted tooth with dental gypsum to an appropriate aluminum holder. Before procedure, teeth were kept in a saline solution in order to preserve their mechanical properties. They were prepared for measurement by drilling a class II MOD (Mesio-Ocluso-Distal) cavity (photographs of and intact tooth and the same tooth with MOD cavity are shown in Fig. 2(a) and 2(b)). An adhesive layer was applied and polymerized, according to manufacturer instruction. Finally, cavity was filled with dental composite and placed in the holographic setup.

Upon placing a tooth inside the experimental setup, a holographic plate is inserted in a liquid gate filled with distilled water. Plate is left for 2 minutes, to be soaked with water (letting emulsion to swell). An exposure is made, with the reference to object beam-ratio of 4:1. A plate is developed for 1 minute in fine grain developer (D-76) which is replaced with water, in order to wash the plate. Washing completed, fresh water is poured in the liquid gate again, and stays there throughout the whole real-time recording. This gives the same emulsion thickness before and after processing.

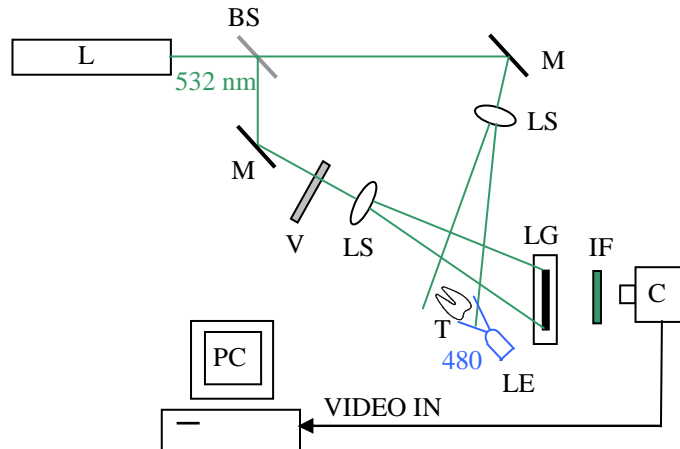


Fig. 1. Real time holographic setup: L - laser, BS - beam splitter, C - CCD camera, PC - computer, LE - LED lamp, LG - liquid gate for real time hologram processing, T - tooth, V - variable attenuator, M - mirror, LS - lens, IF- 532 nm interference filter.

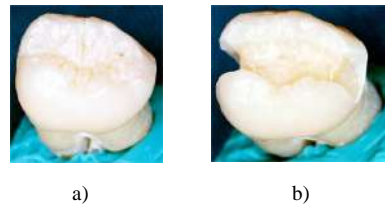


Fig. 2. Photograph of an extracted human tooth: a) intact, b) with mesio-occluso-distal (MOD) cavity.

There is no fixing, in order to avoid the emulsion shrinkage problem and possible change of the fringe localization plane. Our measurements lasted only a few minutes and we had no problems with hologram darkening, due to the omission of fixing step - even after several hours hologram was, bright and clearly visible.

When the hologram recording was finished, laser beam was turned-on so that the hologram and a tooth were simultaneously illuminated. Therefore, two wave-fronts were present: one emanating from hologram and another coming from a tooth itself. Before turning the LED lamp on, both wave-fronts were identical and there were no interference fringes.

By turning-on the LED lamp, polymerization process is initiated, resulting in dental filling polymerization and gradual shrinkage. Contraction forces are transferred to the tooth tissue and a tooth starts deforming. This can be seen as appearance of interference fringes which steadily increase their number and density across the tooth. A process is a dynamic one, recorded as a short film by CCD camera.

3. Experimental results

A series of 9 healthy teeth (extracted for medical reasons) was analyzed. Composite was illuminated without interruption for 200 seconds and films of holographic interferograms were recorded. Example of final interference pattern can be seen in Fig. 3, while a movie itself is a multimedia attachment to this paper. Movie is accelerated (so that the actual illumination duration of 200 s is reduced to 20 s) in order to make the resulting file more compact (2.16 MB, AVI film).

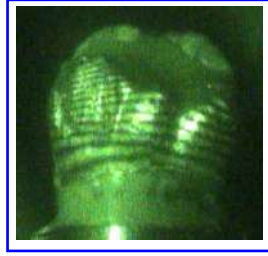


Fig. 3. Interference pattern seen on the tooth surface. This is the final frame from a film (AVI file, 2.16 MB large).

All teeth exhibited almost the same behavior, independent on variation of their shape, mechanical characteristics, and cavity size. In all instances, there is approximately 15 seconds period without any visible change in interference pattern. The first fringe appears at the tooth cusp and starts traveling down, towards a root. Other fringes follow with increasing speed up to a moment when the process starts slowing down.

We have analyzed teeth interferograms by counting fringes during illumination. Corresponding family of graphs is shown in Fig. 4. From the set of curves it can be seen that the maximum deformation is attained at the end of illumination process (after 200 s). On average, maximum deflection is $11.3 \mu\text{m}$.

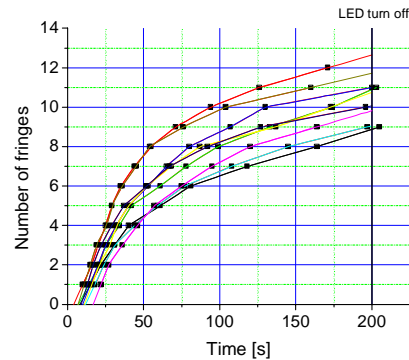


Fig. 4. Time dependence of fringe-count across the tooth. One fringe is equivalent to approximately 576 nm deformation.

4. Numerical calculation of internal stress

Based on holographic deformation measurements the internal stress of dental tissue is calculated. This is of utmost importance in dentistry, because too high pressure can lead to various adverse clinical effects.

It was impossible to measure individual characteristics of every tooth in our study (external shape, shape of dentino-enamel junction, shape of the pulpal region, cavity shape, mechanical properties – elasticity modulus and Poisson's ratio of dentin and enamel). Therefore, we made a mechanical model corresponding to average tooth dimensions and mechanical characteristics [19] (see table I). Geometry of the model is shown in Fig. 5(a) and 5(b) so that overall shape and internal structure (dentin and enamel) can be seen. The same model with MOD cavity is shown in Fig. 5(c).

In order to calculate internal stress based on resulting deformation, Finite Element Analysis (FEA) was used. A tooth model with MOD cavity was meshed with tetrahedral elements having 168786 nodes and, thus, prepared for FEA. It was assumed that the contraction forces exert uniform pressure on cavity sides. Dentin and enamel were modeled as linear and isotropic.

Table 1. Mechanical Characteristics of Dental Tissues.

	Elasticity modulus (GPa)	Poisson's ratio
Dentin	15	0.31
Enamel	60	0.3

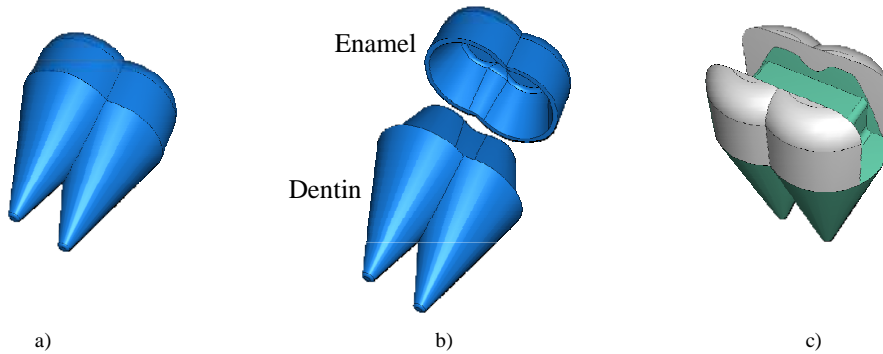


Fig. 5. a) Mechanical model of a third molar and b) its exploded view where dentin and enamel sections are shown. c) Tooth model with MOD cavity (enamel is shaded gray and dentin green).

We were able to calculate internal stress at any stage of composite contraction. First, deformation was determined from the holographic interferogram, taking into account experimental geometry (deformation direction is almost collinear with the line of sight, while the object beam deviates 45 degrees from the line of sight). Based on deformation measurement, internal stress was calculated [16]. The results, corresponding to the end of illumination, are presented in Fig. 6(a) (deformation) and 6(b) (von Mises stress). As can be seen, computed deformation pattern resembles the one recorded holographically (compare Fig. 6(a) and 3).

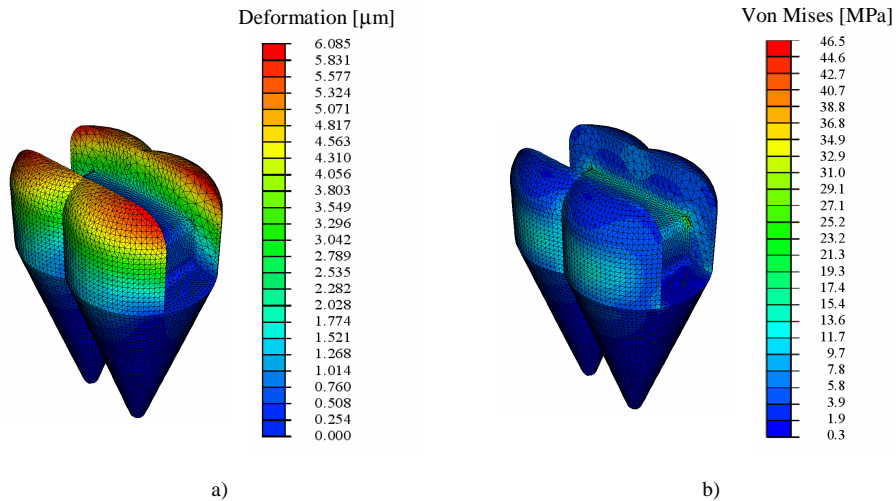


Fig. 6. a) Deformation distribution as a result of polymerization. Numerical values are color coded and expressed in μm . b) von Mises stress distribution during two-step polymerization. Numerical values are color coded and expressed in MPa.

While the stress is tensor, Von Mises stress is a scalar value calculated from three principal stresses and corresponds to mechanical deformation energy stored in particular area. We have found that its maximum is 46.5 MPa at the step-edge inside the cavity. While von Mises stress gives rough picture of stress distribution inside tooth cavity, maximum principal stress should be used as a measure of tooth susceptibility to mechanical damage (cracking). In our case it was 67.7 MPa.

5. Discussion

One peculiarity of the procedure was that teeth had to be painted with silver paint. The reason is that without paint interference fringes are barely visible or completely nonexistent. In a previous research [16], we attributed the disappearance of fringes to significant changes of internal structure of dentin and enamel, due to polymerization contraction. In short, dental tissues are highly translucent and scattering. Therefore, the beam reflected from a tooth is coming not only from its surface, but also from deeper internal layers. If internal structure changes significantly, reflected wave is considerably altered and interference fringes become extremely dense, beyond resolving power of a detection system.

Another important point is connected with the fact that only one side of a tooth could be observed holographically. Based on the fact that teeth are almost symmetrical with respect to MOD (mesio-occluso-distal) line and a cavity is drilled symmetrically, we assume that the deformation on both sides is almost the same.

Graphs in Fig. 4 are significantly inclined at the end of illumination, indicating that polymerization is not fully completed. Additionally, there is an indication that dark polymerization reaction takes place even after the illumination is over. In one case, accidentally, we continued recording of interference picture for more than one minute after LEDs were turned off. Later analysis has shown that one additional fringe appeared, meaning that dental composite contracts, even after it is no more illuminated. Medical effects of post-illumination contraction could be important and should be further investigated.

In order to understand the significance of dental stress found in our research, it should be compared to mechanical strength of dental tissues. According to [20] strength of enamel ranges from 10.3 to 384 MPa, while for dentin it is between 98.7 and 297 MPa, depending on whether stress is compressive, tensile or shear. Our results indicate that internal stress is below limiting values almost everywhere, except at the edge of a step-like feature of the cavity. This may lead to localized cracking or debonding of the composite filling.

The final remark is that results of finite element calculations should be taken with caution – more as an estimate rather than an exact value. This is due to a lot of approximations connected with variation in teeth geometry, variability in properties of dental tissues, a tooth model and computational method.

6. Conclusions

We present results of holographic real-time measurements of dental structure deformation, due to composite contraction. It is shown that dental tissue gradually deforms, with maximum deflection of around 11.3 μm on top of a tooth cusp. Based on experimental results and tooth model, internal stress was calculated. It is distributed inside the cavity, being concentrated on edges, reaching up to 40.3 MPa von Mises stress (67.7 maximum value of principal stress).

Technique enables testing of various dental procedures and photo-sensitive composites, with the aim to reduce polymerization contraction. Also, there is a strong indication that there is a noticeable post-exposure contraction, which deserves further research. This all could lead to more permanent and durable dental fillings.

Acknowledgments

This work is realized by the support of the Serbian Ministry of Science and Environmental Protection, through contract No. 141003. We thank 3M Representative Office in Belgrade, Serbia, for providing the dental adhesive system and the composite.

Relief hologram replication using a dental composite as an embossing tool

Svetlana Savić Šević and Dejan Pantelić

Institute of Physics, Pregrevica 118, 11070 Zemun, Belgrade, Serbia
savic@phy.bg.ac.yu

Abstract: A simplified method for holographic embossing tool production is presented. Surface relief diffraction gratings are holographically recorded in pullulan sensitized with ammonium dichromate (DCP). The surface structure is copied into dental photopolymer composite by direct contact and subsequent photo-polymerization. It was found that arbitrary surface micro-pattern can be replicated. Due to its excellent mechanical and thermal properties, micro-patterned dental composite can be further used as an embossing tool for mass production of holograms.

©2005 Optical Society of America

OCIS codes: (050.1950) Diffraction gratings, (090.2900) Holographic recording materials, (220.4000) Microstructure fabrication, (160.5470) Polymers

References and Links

1. Rudolf L. van Renesse, *Optical Document Security* (Artech House, Boston·London, 1998).
2. R. Bartolini, W. Hannan, D. Karlsons, and M. Lurie, "Embossed Hologram Motion Pictures for Television Playback," *Appl. Opt.* **9**, 2283-2290 (1970).
3. F. Iwata and Jumpei Tsujiuchi, "Characteristics of a Photoresist Hologram and Its Replica," *Appl. Opt.* **13**, 1327-1336 (1974).
4. A. D. Galperin, I. V. Kalinina, L. V. Selyavko, V. P. Smaev, "Obtaining relief-phase holograms on PE-2 photographic plates and their copying," *Opt. Spectrosc. (USSR)* **60**, 644-645 (1986).
5. S. N. Koreshev and S. V. Gil, "Profile of low frequency relief hologram structures obtained on thin layers of PE-2 photoemulsion," *Opt. Spectrosc. (USSR)* **68**, 247-249 (1990).
6. H. J. Bjelkhagen, *Silver Halide Recording Materials for Holography and Their Processing*, Springer Series in Optical Sciences **66** (Springer-Verlag, Berlin, 1993).
7. L. H. Lin and H. L. Beauchamp, "Write-read-erase in situ optical memory using thermoplastic holograms," *Appl. Opt.* **9**, 2088-20 (1970).
8. S. R. LaBelle, B. L. Bohn, "In Line Microembossing, Laminating, Printing and Diecutting," U.S. Patent 6,694,872 (2004).
9. M. W. Schaefer, T. L. Levandusky, S. Sheu, R. B. Larsen, N. C. Whittle, "Techniques for transferring holograms into metal surfaces," U.S. Patent 6,006,415 (1999).
10. L. J. Heyderman, H. Schift, C. David, J. Gobrecht, T. Schweiher, "Flow behavior of thin polymer films used for hot embossing lithography," *Microelectron. Eng.* **54**, 229-245 (2000).
11. U. S. Department of Health and Human Services, Food and Drug, Center for Devices and Radiological Health Administration, "Dental Composites – Premarket Notification," 1996, <http://www.fda.gov/cdrh/ode/642.pdf>.
12. N. Moszner, S. Klapdohr, "Nanotechnology for dental composites," *Int. J. Nanotechnology* **1**, 130-156 (2004).
13. Biomaterials properties database at the University of Michigan, www.lib.umich.edu/dentlib/Dental_tables/.
14. T. J. Trentler, J. E. Boyd, V. L. Colvin, "Epoxy resin-photopolymer composites for volume holography," *Chem. Mater.* **12**, 1431-1438 (2000).
15. S. Bartkiewicz, A. Januszko, A. Miniewicz, J. Parka, "Dye-doped liquid crystal composite for real time holography," *Pure. Appl. Opt.* **5**, 799-809 (1996).
16. M. D. Rahn, D. P. West, K. Khand, J. D. Shakos, R. M. Shelby, "Digital holographic data storage in a high-performance photorefractive polymer composites," *Appl. Opt.* **40**, 3395-3401 (2001).
17. Y. Tomita, H. Nishibiraki, "Improvement of holographic recording sensitivities in the green in SiO₂ nanoparticle-dispersed methacrylate photopolymers doped with pyrromethene dyes," *Appl. Phys. Lett.* **83**, 410-412 (2003).
18. N. Suzuki, Y. Tomita, T. Kojima, "Holographic recording in TiO₂ nanoparticle-dispersed methacrylate photopolymer films," *Appl. Phys. Lett.* **81**, 4121-4123 (2002).
19. N. Suzuki, Y. Tomita, "Silica-nanoparticle-dispersed methacrylate photopolymers with net diffraction efficiency near 100%," *Appl. Opt.* **43**, 2125-2129 (2004).

20. F. G. Robinson, F. A. Rueggeber, P. E. Lockwood, "Thermal stability of direct dental esthetic restorative materials at elevated temperatures," *J. Forensic Sci.* **43**, 1163-1167 (1998).
21. T. Sano, Y. Uemura, and A. Furuta, "Photosensitive resin composition containing pullulan or esters thereof," U. S. Patent 3,960,685 (1976).
22. Dejan Pantelić, Svetlana Savić, Dragica Jakovljević, "Dichromated pullulan as a novel photosensitive holographic material," *Opt. Lett.* **15**, 807-809 (1998).
23. Svetlana Savić, Dejan Pantelić and Dragica Jakovljević, "Real-time and postprocessing holographic effects in dichromated pullulan," *Appl. Opt.* **41**, 4484-4488 (2002).
24. Svetlana Savić, Dejan Pantelić, Dragica Jakovljević, "Dichromated Pullulan: Real-time Effects and Holographic Properties," presented at the International Conference "Optical Holography and its Applications", Ukraine, 26-29 Sept. 2000.
25. Y.W. Zhang, W.G. Zhu, F.T.S Yu, "Rainbow holographic aberrations and the bandwidth requirements," *Appl. Opt.* **22**, 164-169 (1983).
26. C-K. Lee, J.W-J. Wu, S-L. Yeh, C-W. Tu, Y-A. Han, E.H-Z. Liao, L.Y-Y. Chang, I-E. Tsai, H-H. Lin, J.C-T. Hsieh, J.T-W. Lee, "Optical configuration and color-representation range of a variable-pitch dot matrix holographic printer," *Appl. Opt.* **39**, 40-53 (2000).
27. V. Fano, I. Ortalli, S. Pizzi, M. Bonanini, "Polymerization shrinkage of microfilled composites determined by laser beam scanning," *Biomaterials* **18**, 467-470 (1997).
28. L. M. Averina, Yu. S. Milavskii, "Refractometric method of determining the shrinkage of polymers under UV hardening," *J. Opt. Technol.* **71**, (2), 115-116 (1997).

1. Introduction

The conventional method of hologram replication by embossing is a multi-step process [1]. In the first step, a surface relief hologram is generated on photoresist, silverhalide emulsion or thermoplastic film [2-7]. Relief micro-pattern is further copied (by sputtering and electroforming) into more durable material like nickel. Resulting shim is used as an embossing tool for mass replication of holograms by thermal stamping into plastic foils [8].

The stamping shim has a limited lifetime due to high pressure (1-15 MPa) and temperature (150-250 °C) during embossing [9, 10]. Therefore, it is of interest to find more durable materials, and simplified methods of holographic shim production. It seems that materials used in dentistry are good candidates, since they must imitate outstanding mechanical, chemical and thermal properties of hard dental tissues (dentin and enamel).

Photopolymer composites are extensively used in dental practice as filling material for cavities in tooth tissues. A typical dental composite consists of inorganic filler particles, embedded in a methacrylate based polymer matrix with camphorquinone added as a photoinitiator [11, 12]. Polymerization is done using blue light, corresponding to camphorquinone absorption maximum around 470 nm. Inorganic fillers (quartz, lithium aluminum silicate, glass) give the composite desired mechanical properties, comparable to dental tissues. Filler particles can measure from 0.04 microns up to several microns, depending on the manufacturer and the type of the composite. The resulting compressive strength ranges from 250 to 450 MPa [13].

It should be added that a range of composites were previously used as holographic recording materials [14-16]. They can be mixtures of various polymers (epoxy resin - photopolymer, dye doped LCD, chromophore - polymer matrix). Also, mixtures of inorganic hard particles (titania and silica) with polymers were used as holographic recording materials [17-19]. However, none of these materials was used as a hologram embossing tool.

We have simplified a process of embossing tool production, by direct copying of holographic surface relief grating into a layer of dental composite. Resulting copy is an almost exact replica of original grating (with respect to relief depth, profile and spatial frequency), as verified by atomic force microscopy (AFM). In addition, the composite shim is thermally stable, very hard, durable [20] and, thus, an excellent tool for further mass production of holograms.

Complete process of hologram embossing tool production is explained, starting with original, surface relief hologram, manufacturing and ending with contact copying and photopolymerization of the dental composite. We present the results concerning depth of profile, spatial frequency, thermal and mechanical properties of selected dental polymers.

2. Process of surface relief hologram replication in layers of dental composite

Pullulan, which is a natural linear polysaccharide [21], was sensitized with ammonium dichromate and used for surface relief hologram recording [22-24]. Dichromate sensitized pullulan (DCP) samples were prepared by mixing 8% aqueous solution of pullulan and 50% ammonium dichromate by weight of pullulan. The solution was coated onto clean glass slides in a horizontal position and the film was dried overnight under normal laboratory conditions. The thickness of the dried DCP layer was approximately 10 μm .

Surface-relief diffraction gratings were formed by the interference of two equal power coherent beams. DCP was exposed with single-frequency 400 mW diode pumped Nd-YAG laser, at 532 nm. He-Ne laser operating at 632.8 nm was used for real-time monitoring of diffraction efficiency. Exposure of DCP film was considered complete when the real-time maximum diffraction efficiency was achieved [23]. The exposed plates were developed with a mixture of 60% isopropanol and 40% water for 2 min and then immersed in the pure isopropanol for 30 s. Five DCP gratings, with spatial frequency ranging from 300 – 900 lines/mm, were produced in order to study diffraction efficiency and surface grating profile.

Uncured dental composites have a consistency of a thick cream or honey (depending on the type and the manufacturer), which makes them easy to smear on top of the surface relief pullulan grating. A small amount of the composite was placed between holographic grating and a glass slide. By applying pressure on the resulting “sandwich”, the composite was uniformly distributed and air bubbles were squeezed out. We did not take special measures to control the pressure since we experienced no problems with trapped bubbles at all. It is the consequence of the dental polymer structure, which is rather compact and keeps together well.

Polymerization was performed by an array of blue LEDs, with total irradiance of 80 mW/cm^2 . After 2 minutes exposure, composite was fully cured. It is our experience that dental composite does not stick to DCP, enabling simple mechanical separation. Also, composite does not bond to other materials that we tried – dichromated gelatin, nickel, gold, photoresist – and there were no need to use an anti-sticking coating. After separation, negative replica grating was obtained.

Three types of commercial dental composites were chosen for this study: “Helio Progress” (manufactured by Vivadent), “Herculite xrv”, (manufactured by Kerr) and “Degufill ultra” (manufactured by Degussa). Chemical composition details were not available, probably due to proprietary reasons. However, “Helio Progress” and “Degufill ultra” are classified as microfilled dental composites (with particle size 0.04 – 0.2 μm), while “Herculite xrv” is microhybrid material (with blend of particles ranging from 0.04 – 5 μm) [11]. Anyway, we found no differences in holographic properties between the three materials.

3. Comparison of holographic properties of the DCP original and the composite copy diffraction grating

Gratings with spatial frequencies of 315, 380, 470, 760 and 870 lines/mm were made and copied into dental composite. Spatial frequencies were chosen in the range corresponding to bandwidth of rainbow holograms [25] and dot image holograms [26], which are mostly used for embossing purposes. Profiles of the DCP original gratings depend on recording geometry and chemical processing. They varied from purely sinusoidal to saw-tooth profile. For the analysis, non-sinusoidal ones were chosen, since the faithfulness of the copying process can be verified.

The diffraction grating profiles of originals and copies were analyzed by AFM and average values of the grating period and its depth were calculated for each scan. For illustration purposes, two surface scans (20 x 20 μm area) of DCP original and copy (“Helio Progress”) are shown in Fig. 1(a) and 1(b). One dimensional scans are shown, too. The measured average relief depth of the DCP grating is 54 nm and its average period is 1.15 μm , correspondingly, the measured average relief depth of the dental composite grating is 52 nm and its average period is 1.14 μm .

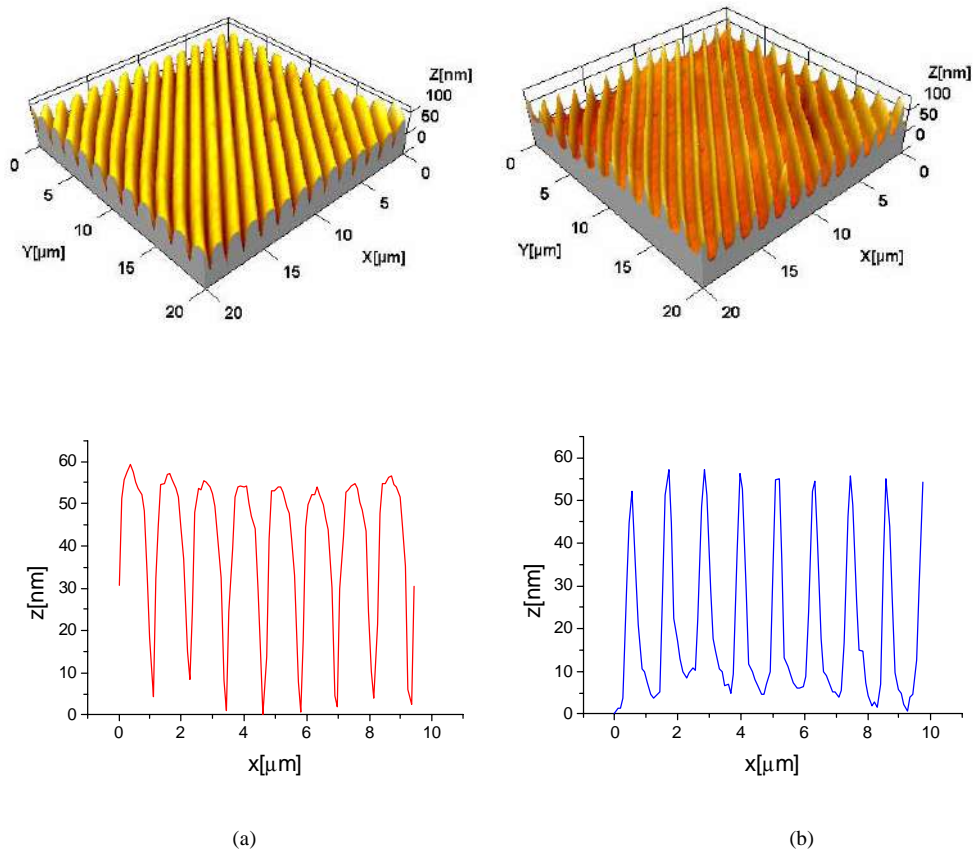


Fig. 1. (a) The AFM image of original DCP diffraction grating (top) with period of $1.15 \mu\text{m}$ and its line profile on a reduced scale (bottom) (b) The AFM image of dental composite ("Helio progress") diffraction grating copy (top) with period of $1.14 \mu\text{m}$ and its line profile on a reduced scale (bottom). In both cases the scan size is $20 \times 20 \mu\text{m}$.

Fast Fourier Transforms (FFT) of AFM scans of an original and a copy from Fig. 1 are shown in Fig. 2(a) and 2(b), respectively. Note that FFT of, both, original and a copy are almost identical, meaning that higher harmonics (up to the third) are well preserved. It can be estimated that dental polymer is capable of transferring spatial frequencies up to 2610 lines/mm (three times fundamental frequency of 870 line/mm).

Different surface profiles can be successfully replicated into dental composites. Figure 3 shows a saw-tooth shaped dental polymer grating and its line scan. The measured average relief depth of the dental composite copy ("Herculite xrv") is 167 nm (155 nm on the DCP original) and the average period is $3.10 \mu\text{m}$ ($3.17 \mu\text{m}$ on DCP original).

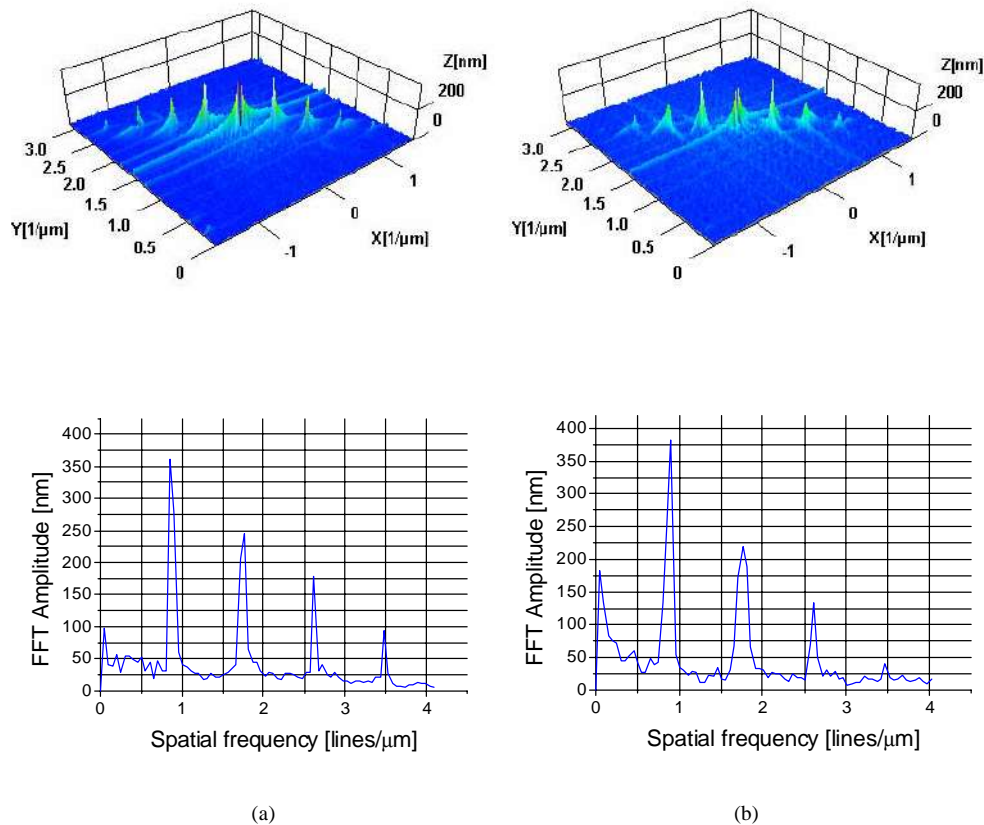


Fig. 2. (a) FFT of AFM image of original DCP grating (top) with period of $1.15\ \mu\text{m}$ and its line profile (bottom) (see Fig 1(a)). (b) FFT of AFM image of dental composite diffraction grating copy (top) with period of $1.14\ \mu\text{m}$ and its line profile (bottom) (see Fig 1(b)).

The relation between the surface profile depth and the spatial frequency is presented in Fig. 4. As expected, the depth decreases with increase of the spatial frequency. It is, however, interesting to note that the depth of the copy is somewhat larger than the original (for spatial frequencies up to $870\ \text{line/mm}$). Also, the spatial frequency of the copy differs from the original, within the statistical error. This disparity can be attributed to volume contraction of composite during polymerization, which is well known in polymer science and in dentistry [27, 28].

Our results show that contraction of the polymer is not isotropic (i.e., it contracts more in one direction compared to an orthogonal one). It can be argued that the speed of polymerization is not uniform and differs in the bulk material compared to ridges of the diffraction grating. Inside ridges, monomer can be polymerized more quickly because there is less monomer supply from the surrounding areas, like in the case of the bulk material. This may result in non-uniform shrinkage of the composite and increased depth of the grating.

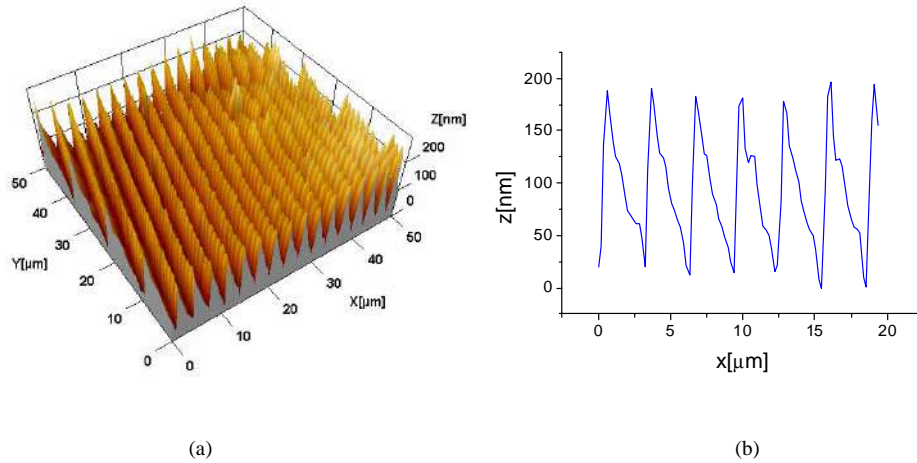


Fig. 3. (a) The AFM image of dental composite (“Herculite xrv”) diffraction grating with period of 3.10 μm and (b) its line profile on a reduced scale.

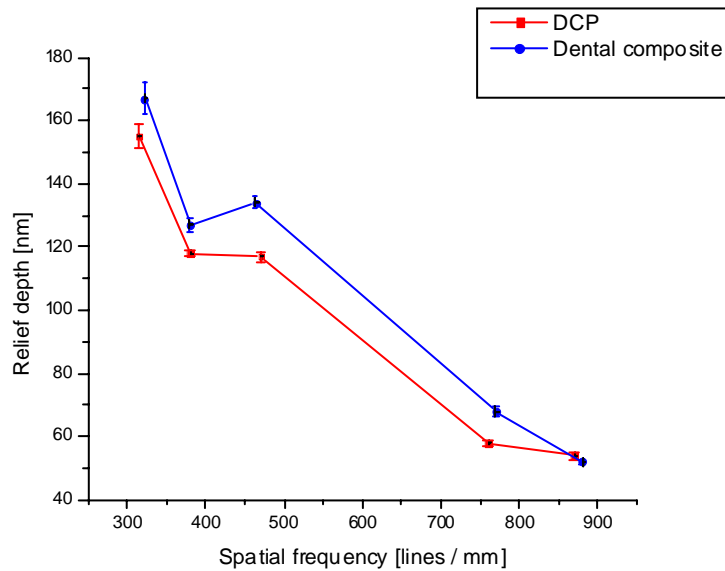


Fig. 4. Average relief depth versus spatial frequency.

Figure 5 shows the relationship between the diffraction efficiency (measured in reflection) and the spatial frequency, for both the original DCP gratings and the dental composite replica gratings. It can be seen that the maximum diffraction efficiency of the replica gratings are only a few percent less than the maximum diffraction efficiency of the original DCP gratings.

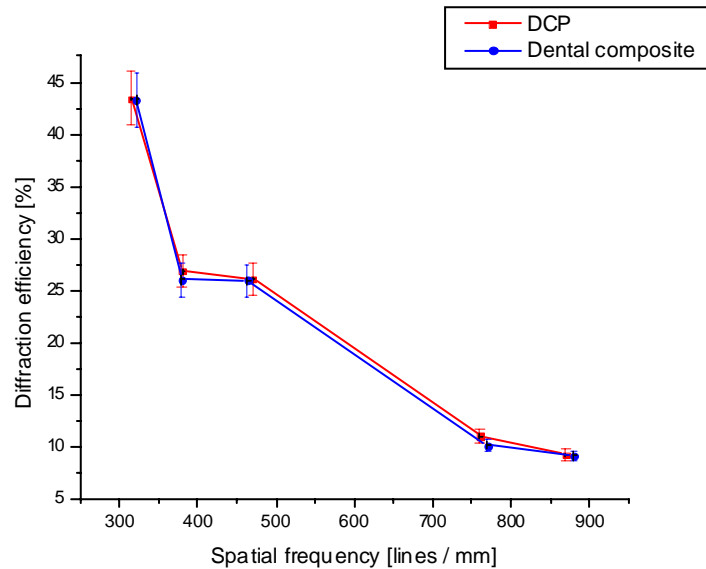


Fig. 5. Diffraction efficiency of DCP original and composite copy versus spatial frequency

In conclusion, obtained results are reproducible and do not vary from composite to composite and also for different AFM scans on the same composite.

4. Mechanical and thermal stability of the dental composite shim

We have performed some preliminary tests of mechanical and thermal stability of dental composites. After heating at 250° C, for one hour, no change of optical properties of dental embossing tool was observed. It was also found that exposing the dental composite embossing tool to ultrasonic waves had no adverse effect i.e. we observed no drop in diffraction efficiency.

Simple initial tests of dental polymer shim as a hot embossing tool were performed on 30 μm thickness metalized plastic foil. Hand press was used – therefore pressure could not be controlled. Also, composite shim was heated to approximately 150 °C. Diffraction gratings were successfully pressed into foil, although the quality was not very good, due to impossibility to tightly control the whole embossing procedure. Anyway, dental embossing shim survived the test without degradation.

To conclude, dental composite survived all the mentioned tests with no drop in diffraction efficiency.

5. Conclusions

The standard holographic shim production technique involves complicated and time consuming procedures like nickel sputtering and electroforming. Method presented in this paper is simpler and faster, while producing the resulting shim of excellent mechanical properties – comparable to ordinary nickel shims. Furthermore, nickel shims are thin, and susceptible to warp (which seems to be the main mechanism of failure), while dental polymer can be made several millimeters thick, making them tougher.

It was found that the original DCP grating and its copy are almost exact replicas of each other in all important aspects. The maximum diffraction efficiency is slightly lower for replica grating compared to the original. On the other hand, there is minor disparity between

frequency and relief depth of originals and copies. This result was attributed to polymerization contraction effect.

There is a vast range of dental polymers produced by many manufacturers. Composites vary in chemical polymer composition, photoinitiation system and inorganic filler particle type and size. It seems that any nanofilled dental composite can be used as holographic material. During our research, no significant differences in holographic replication properties between three types of composites were found.

Our future investigation includes copying of diffraction gratings and holograms using hot embossing. Initial tests were performed with promising results. Nevertheless, it was found that all process parameters must be controlled more tightly in order to obtain better replicas. The ultimate test of dental composite shims would be their incorporation into an embossing process on an industrial scale. However, this would require significant changes in existing embossing machines, taking into account the increased thickness of shim (several millimeters vs. several tenths of millimeter). It might be necessary to change commonly used rotary press to linear press. Finally, this will be the subject of our future research.

Holographic properties of dental polymers should be further tested, by copying from other surface relief materials like photoresists, to see if better relief depths and higher spatial frequencies could be transferred. Also, dental polymer should be tested as a direct holographic recording material, since this would enable production of shims without intermediate steps.

Acknowledgments

Research was performed under the contract 1443 funded by the Ministry of the Science and Environmental Protection of Serbia. Special thanks are given to Dana Vasiljević-Radović from the IHTM-Institute of Microelectronic Technologies and Single Crystals, Belgrade, Serbia for AFM scans of our samples.

Biopolymer holographic diffraction gratings

Svetlana Savić Šević *, Dejan Pantelić

Institute of Physics, Pregrevica 118, 11080 Zemun, Belgrade, Serbia

Available online 19 July 2007

Abstract

Surface-relief diffraction gratings are holographically recorded in dextran sensitized with ammonium dichromate (DCD). DCD was exposed with single-frequency 200 mW diode pumped ND-YAG laser, at 532 nm. The diffraction grating profiles were analyzed by atomic force microscopy (AFM). It was found that different surface profiles could be obtained. Gratings with 330 lines/mm spatial frequencies were made. Existence of higher harmonics in Fourier Transform of non-sinusoidal profiles shows that DCD is capable of recording spatial frequencies up to 1320 lines/mm (four times fundamental frequency). The measured maximum relief depth of the DCD grating is 402 nm.

© 2007 Elsevier B.V. All rights reserved.

PACS: 42.40.E; 42.70.L

Keywords: Holographic diffraction gratings; Holographic recording materials

1. Introduction

Surface-relief gratings are of particular interest due to their applications in the mass production of holographic optical elements. The usual method of hologram replication has been to create a surface-relief hologram in photoresist, produce a metal master (relief hologram is copied into nickel), and finally electrolytically create embossing shims. Shims impress the holographic ridges into plastics under heat and pressure [1]. We recently proposed a novel method of hologram replication by copying of holographic surface-relief grating into dental composite by direct contact and subsequent photo-polymerization [2]. Resulting shim is used as an embossing tool for mass replication of holograms by thermal stamping into plastic foils. Another method, reported recently, is to transfer the grating pattern onto a polydimethylsiloxane (PDMS) thin film using a typical micro-molding technique. This master was used as a stamp to transfer the grating pattern onto a UV cure epoxy [3].

Photoresists are the most widely used recording medium for relief hologram production [3,4]. Other materials are used too, such as chalcogenide glasses [5–7], thermoplastics [8], polymethyl methacrylate (PMMA) [9], and sol–gel glass [10,11].

In our case, surface-relief holograms are recorded in dextran sensitized with ammonium dichromate (DCD). Dextran is a biopolymer with branching polysaccharide structure. It has some useful properties: it is non-hydroscopic and not poisonous, it is easily soluble in water to make transparent solution which does not form gel.

In this paper, properties of surface-relief holograms recorded in dextran, sensitized with ammonium dichromate have been investigated. The diffraction grating profiles were analyzed by atomic force microscopy (AFM).

2. Grating production

Dichromate sensitized dextran (DCD) samples were prepared by mixing 8% aqueous solution of dextran and 50% ammonium dichromate by weight of dextran. The solution was subsequently coated onto clean glass slides in a horizontal position and the film was dried overnight under

* Corresponding author. Tel.: +381 113160793; fax: +381 113162190.
E-mail address: savic@phy.bg.ac.yu (S. Savić Šević).

normal laboratory conditions. The thickness of the dried DCD layer was approximately 10 μm .

Surface-relief diffraction gratings were formed by the interference of two equal power coherent beams. DCD was exposed with single-frequency 200 mW diode pumped Nd-YAG laser, at 532 nm. He-Ne laser operating at 632.8 nm was used for real-time monitoring of diffraction efficiency. It was found that the exposure of DCD film is complete when the real-time maximum diffraction efficiency is achieved [12]. Gratings with about 330 lines/mm spatial frequencies were made. It was found that profiles of the gratings depend on recording geometry and chemical processing.

During the exposure, hexavalent chromium ion Cr^{+6} is either directly or indirectly photo-reduced to trivalent Cr^{+3} , which then forms a covalent cross link with dextran molecules which accordingly changes the solubility of the material in a developer. It was found that the cross-linking produced by light reduces the solubility of the exposed regions and unexposed portion of DCD washed away in water.

The exposed plates were, first, chemically processed with a mixture of 80% isopropanol and 20% water for 90 s, and then immersed for 30 s in the pure isopropanol. After development in mixture of water and isopropanol an intensity light pattern is converted into a relief structure.

3. AFM analysis

The diffraction grating profiles were analyzed by atomic force microscopy (AFM). AutoProbe CP Research (from

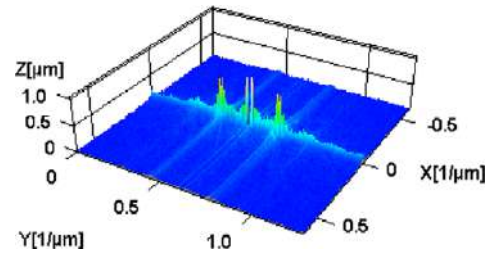


Fig. 2. 2D FFT of the AFM image from Fig. 1a.

ThermoMicroscopes) instrument was used. Measurements were performed in contact mode. The average values of the grating period and its depth were calculated for each scan.

Fig. 1a shows a sinusoidal shaped DCD grating. Surface is scanned on a $(20 \times 20) \mu\text{m}$ area. One-dimensional scan is shown, too, Fig. 1b. The measured average relief depth of the DCD grating is 402 nm and its average period is 2.99 μm .

Fast Fourier Transforms (FFT) of AFM scans of DCD diffraction gratings from Fig. 1 is shown in Fig. 2. Note that only first harmonics are present, diffraction grating has a sinusoidal profile.

Non-sinusoidal profile grating is shown in Fig. 3a. Surface scan is $(20 \times 20) \mu\text{m}$ area. Line scan is shown in Fig. 3b. The measured average relief depth of the DCD grating is 156 nm and its average period is 3.18 μm .

Fast Fourier Transforms (FFT) of AFM scans of DCD diffraction gratings from Fig. 3 is shown in Fig. 4. Higher harmonics are present. It can be estimated that DCD is capable of transferring spatial frequencies up to 1320 lines/mm (four times fundamental frequency of 330 lines/mm).

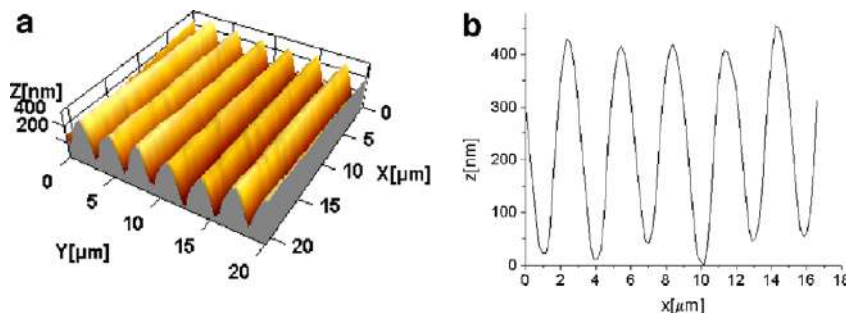


Fig. 1. (a) The AFM image of DCD surface-relief diffraction grating with sinusoidal profile and (b) its line profile.

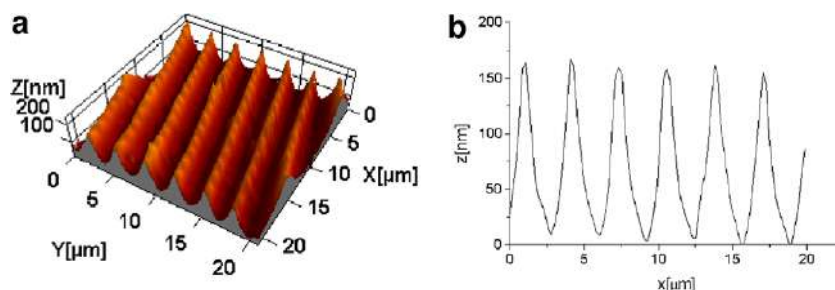


Fig. 3. (a) The AFM image of DCD surfaces-relief diffraction grating with non-sinusoidal profile and (b) its line profile.

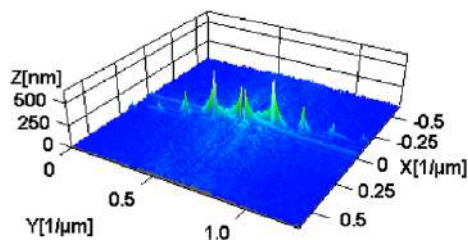


Fig. 4. 2D FFT of the AFM image from Fig. 3a.

3. Conclusion

Properties of relief phase holograms recorded in biopolymer, dextran, sensitized with ammonium dichromate have been investigated. It was shown that arbitrary surface-relief can be recorded in dichromated dextran, with relief depth up to 402 nm. Due to its properties, DCD is an excellent material for copying holograms by embossing.

Acknowledgments

Research was performed under the contract 141003 funded by the Ministry of the Science and Environmental

Protection of Serbia. Special thanks are given to Dana Vasiljević-Radović from the IHTM-Institute of Microelectronic Technologies and Single Crystals, Belgrade, Serbia for AFM scans of our samples.

References

- [1] R.L. van Renesse, *Optical Document Security*, Artech House, Boston, London, 1998.
- [2] S. Savić Šević, D. Pantelić, *Opt. Exp.* 13 (2005) 2747.
- [3] W.C. Chuang, C.T. Ho, W.C. Wang, *Opt. Exp.* 13 (2005) 6685.
- [4] F. Iwata, J. Tsujiuchi, *Appl. Opt.* 13 (1974) 1327.
- [5] A.D. Galperin, I.V. Kalinina, L.V. Selyavko, V.P. Smaev, *Opt. Spectrosc. (USSR)* 60 (1986) 644.
- [6] S.N. Koreshev, S.V. Gil, *Opt. Spectrosc. (USSR)* 68 (1990) 247.
- [7] H.J. Bjelkhagen, *Silver Halide Recording Materials for Holography and Their Processing*, Springer Series in Optical Sciences, 66, Springer Verlag, Berlin, 1993.
- [8] L.H. Lin, H.L. Beauchamp, *Appl. Opt.* 9 (1970) 2088.
- [9] Y. Li, K. Yamada, T. Ishizuka, W. Watanabe, K. Itoh, *Opt. Exp.* 10 (2002) 1173.
- [10] W. Yu, X.-C. Yuan, *Opt. Exp.* 11 (2003) 1925.
- [11] D.J. Kang, J.K. Kim, B.S. Bae, *Opt. Exp.* 12 (2004) 3947.
- [12] S. Savić, D. Pantelić, D. Jakovljević, *Appl. Opt.* 41 (2002) 4484.

Dichromated pullulan as a novel photosensitive holographic material

Dejan Pantelić and Svetlana Savić

Institute of Physics, Pregrevica 118, 11080 Zemun, Belgrade, Yugoslavia

Dragica Jakovljević

Institute of Chemistry, Technology and Metallurgy—Center for Chemistry, Njegoseva 12, 11000 Belgrade, Yugoslavia

Received December 15, 1997

We found that pullulan [an α -glucan with (1→4) and (1→6) linkages] doped with chromium ions possesses promising holographic properties. It is environmentally stable and is capable of registering high spatial frequencies (as many as 1500 lines/mm) and producing surface relief. At 1000 lines/mm pullulan's diffraction efficiency was 4%. Chemical treatment of pullulan with a mixture of water and isopropyl alcohol is simple. However, as expected from analogy with dichromated gelatin, pullulan is sensitive in only the blue-green region of the spectrum. © 1998 Optical Society of America

OCIS codes: 090.0090, 090.2900.

Photosensitive materials used in holography should possess a number of specific properties: high sensitivity, high resolution, environmental stability, broad spectral sensitivity (for color holography), and high diffraction efficiency. Many materials, including silver halide, photopolymers, photoresists, and thermoplastics, have been found to have useful holographic properties.

A significant class of holographic materials is based on the ability of chromium ions to induce photochemical reaction. Gelatin is one of the most widely used of these materials and has excellent holographic properties¹ but poor environmental stability and low sensitivity.² Dichromated poly(vinyl alcohol) solid films have shown high diffraction efficiency (68%) without any chemical or thermal postprocessing.^{3,4} Other materials, such as triacetate cellulose,⁵ pectin, and gum arabic,⁶ showed promising results. Even ordinary sugar was doped with dichromate⁷ but without much success. In photography, a number of dichromate processes were used; materials included albumen, gum, and gelatin.⁸

In this Letter we present the results of our research on the holographic properties of pullulan, an α -glucan with (1→4) and (1→6) linkages. Actually, this polymer has repetition units of maltotriose (whose structural chemical formula is shown in Fig. 1) with a molecular weight of 1000 to 4,000,000. Pullulan has some useful optical and mechanical properties: It is transparent, readily soluble in water, does not produce gel (as do gelatin and pectin, which require an elevated temperature during the coating process), is environmentally stable, and is not poisonous.

In Ref. 9 we found that photosensitization of pullulan is possible by the addition of photopolymerizable monomers such as acrylamide, acrylic acid, and methacrylic acid. However, keeping in mind that some polysaccharides can be rendered photosensitive by the addition of chromium ions,⁶ we doped pullu-

lan (which is also a polysaccharide) with ammonium dichromate. In a new material, which we call dichromated pullulan here, we observed photosensitivity in the blue-green region of the spectrum, together with high resolving power.

In our research 2–8% of pullulan by weight (molecular weight 200,000) was first dissolved in deionized water, yielding transparent and quite viscous liquid (with higher concentrations it is almost like honey). Afterward, ammonium dichromate was added (concentrations varied from 10% to 75% by weight of pullulan; however, for concentrations greater than 50% dichromate tended to crystallize). The prepared solution was coated upon a glass plate by thin-film applicators (used in chemistry for dye coating). We observed that the adhesion to the glass was not good unless the plate was thoroughly cleaned. We could improve adhesion by adding a small amount of some surfactant (such as saponin), but this would change the mechanical properties of the dried material. Subsequently, the films were dried and exposed.

In our experiments we irradiated the material with a 1-mW 543.5-nm green He–Ne laser (during exposure, the material changed color from yellow to brown). By analogy with the dichromated gelatin, we suspect that the sensitivity of pullulan at lower wavelengths is much higher (by an order or two), which we plan to verify in future experiments with an argon-ion laser. We could measure the holographic characteristics of the material but at the expense of long exposure times.

High-spatial-frequency holographic sinusoidal gratings were formed by simple two-wave interference, and the material was exposed. After exposure we could observe the diffraction picture without any postprocessing (see the magnified portion of a grating shown in Fig. 2). Diffraction was observed in both transmission and reflection, indicating that a surface-relief grating was formed in addition to an amplitude grating inside the material.

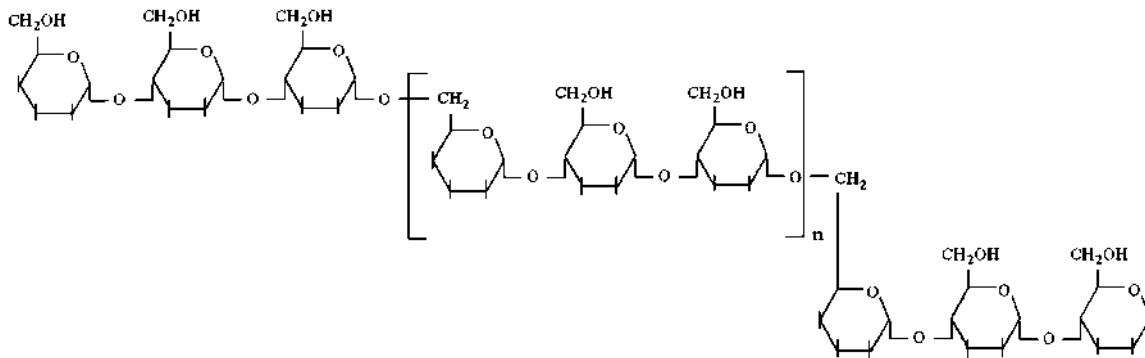
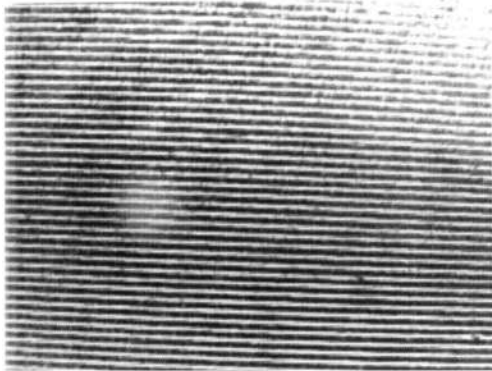


Fig. 1. Chemical structure of pullulan.

Fig. 2. Diffraction grating recorded in a thin pullulan layer (grating constant, 1 μm).

To verify the existence of surface relief, we produced a low-spatial-frequency picture with a defocused laser beam whose diffraction yielded a picture with varying spatial frequency, with a maximum of 200 lines/mm. Inside this range we could measure the surface shape directly by use of a Tallystep surface profiler (the trace is shown in Fig. 3). The relief height was a function of spatial frequency, as shown in Fig. 4. In the center of the diffraction picture we observed a rather complicated structure (owing to focusing-lens wave aberrations), and even-higher spatial frequencies were observed under an optical microscope (Fig. 5).

Dichromated photosensitive substances are usually postprocessed after exposure. Chromium ions, under the influence of light, induce cross-linking inside the base material, which consequently changes the solubility of the material in a suitable solvent. In our case postprocessing by pure water was not successful, since the pullulan layer tended to peel off from the glass quickly. Therefore we "diluted" water with isopropyl alcohol (pullulan does not dissolve in alcohol). The best results were obtained with a mixture of 40% water and 60% isopropyl. After we processed the film with this mixture, diffraction effects were somewhat improved, possibly owing to better surface relief.

As expected, many parameters influenced the characteristics of the recorded grating: exposure time, dichromate concentration, grating period, layer thickness, illuminance, chemical postprocessing, etc. Understandably, we could not vary all the parameters, and some of them were fixed. Through the rest of our research we used a 5% solution of pullulan in wa-

ter, with 50 g of ammonium dichromate per 100 g of pullulan.

It was found that the pullulan layer thickness (measured interferometrically) significantly influenced diffraction efficiency. From Fig. 6 we can see that diffraction efficiency (at 1000 lines/mm and exposure of 20 J/cm²) is very small for layer thicknesses lower than 10 μm and rises steeply for greater thicknesses. We were not able to produce thicker layers, so we could not verify whether the efficiency could be further improved.

Diffraction efficiency depends on exposure, too. We found that a maximum efficiency (4% at 1000 lines/mm) is obtained for an energy density of approximately 20 J/cm² and a layer thickness of 18 μm

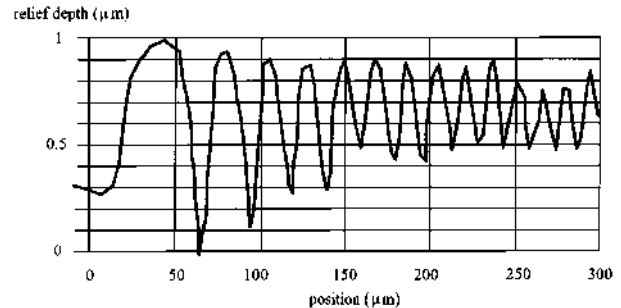


Fig. 3. Part of the surface-profile trace, as measured with a Tallystep surface profiler.

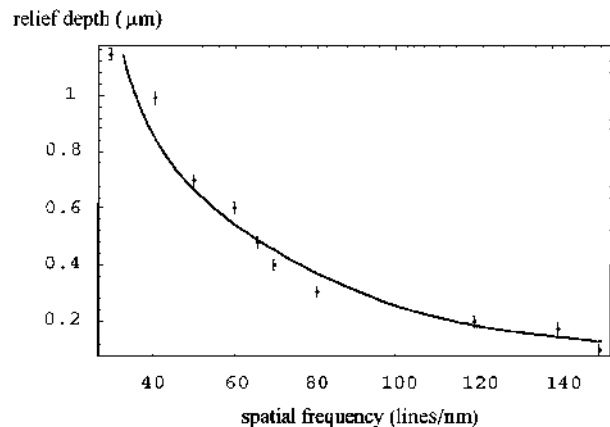


Fig. 4. Holographic grating relief depth as a function of spatial frequency.

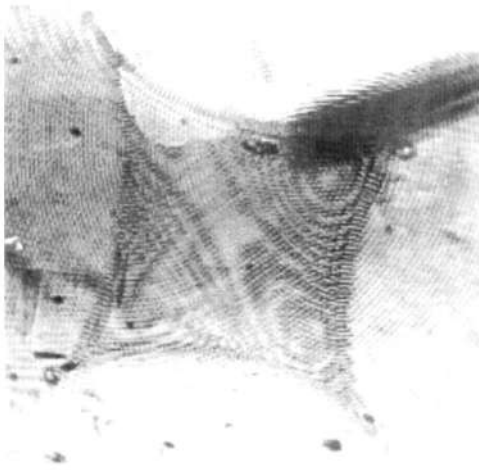


Fig. 5. Lens wave-aberration picture recorded upon a pullulan layer.

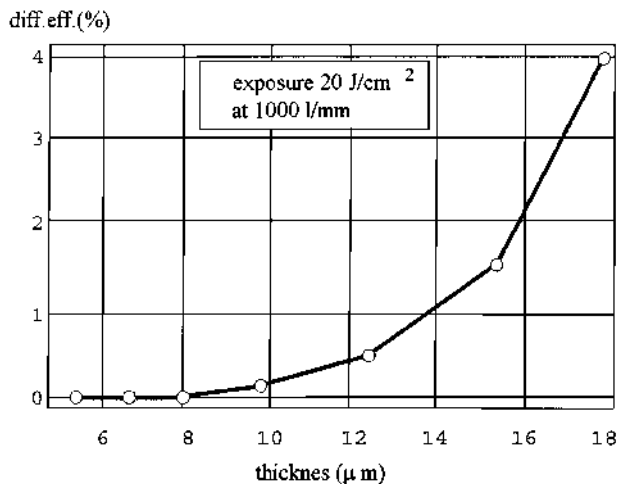


Fig. 6. Diffraction efficiency as a function of pullulan film thickness.

(the interfering beam ratio is 1:1). For lower and higher values of energy density the efficiency drops.

Maximum spatial frequency was obtained at an angle between the interfering beams of approximately 56° . A diffraction grating of 1500 lines/mm was made, yielding a diffraction efficiency of 1%.

In this Letter only the initial results are presented. Much more should be done to characterize dichromated pullulan fully. Its spectral sensitivity should be determined, its optimum dichromate concentration should be found, its modulation transfer function should be measured, optimum conditions or chemical processing should be found, a characteristic curve should be constructed, etc. However, we think that these initial results are good enough to justify further effort.

References

1. T. G. Georgekutty and H-K. Liu, *Appl. Opt.* **26**, 372 (1987).
2. G. M. Naik, A. Mathur, and S. V. Pappu, *Appl. Opt.* **29**, 5292 (1990).
3. S. Lelievre and J. J. A. Couture, *Appl. Opt.* **29**, 4383 (1990).
4. J. J. A. Couture, *Proc. SPIE* **2042**, 229 (1993).
5. K. Wang, L. Guo, L. Zhou, and J. Zhu, *Appl. Opt.* **35**, 6369 (1996).
6. K. Yokono and K. Nishide, "Hologram and method of production thereof from polysaccharide recording layer," U.S. patent 4,254,193 (March 3, 1981).
7. S. Calixto and V. Toal, *Appl. Opt.* **29**, 5315 (1990).
8. F. Purves, *Encyclopedia of Photography* (Focal Press, London, 1962).
9. T. Sano, Y. Uemura, and A. Furuta, "Photosensitive resin composition containing pullulan or esters thereof," U.S. patent 3,960,685 (June 1, 1976).

Dichromated pullulan diffraction gratings: influence of environmental conditions and storage time on their properties

Svetlana Savić Šević and Dejan Pantelić

Investigations of the environmental stability of diffraction gratings, recorded in dichromated pullulan (DCP), are reported. Profile changes of DCP surface relief gratings, under high humidity conditions, were analyzed using an atomic force microscope. It was found that the profile was not altered, while the diffraction efficiency was preserved. The influence of storage life on the diffraction efficiency and surface profile of DCP gratings were also investigated. It was concluded that DCP gratings offer much better stability compared with the dichromated gelatin. © 2007 Optical Society of America

OCIS codes: 050.0050, 090.2900, 160.2900.

1. Introduction

The dichromated gelatin (DCG) is one of the most useful holographic recording materials, due to its high diffraction efficiency (DE), high resolution, low noise, and reprocessibility.^{1–5} A critical disadvantage of the dichromated gelatin is its poor environmental stability. In particular, its humidity resistance is poor, so that the DE of DCG holograms, under humid conditions, is significantly reduced. The environmental stability of DCG holograms can be considerably improved either by use of ninhydrin,⁶ by coating with protective layers,^{7,8} or by doping DCG with synthetic vanilla.⁹

Pullulan (which is a natural linear polysaccharide¹⁰) sensitized with ammonium dichromate has good holographic properties. The material possesses desirable properties: high DE, high resolution, low noise, simple production, and, it can be used in real time.^{11–13} Existence of strong surface relief modulation is also established,¹¹ which makes DCP practical in hologram replication, using embossing techniques.¹⁴

Influence of environmental conditions and storage time on the DCP gratings was investigated. It was

found that the material is very stable (regarding the DE and surface relief), compared with DCG.

2. Preparation of the Dichromated Pullulan Photosensitive Layers and Recording of Holographic Diffraction Gratings

Pullulan was sensitized with ammonium dichromate and used for diffraction gratings recording.^{11–13} Dichromated pullulan (DCP) samples were prepared by mixing an 8% aqueous solution of pullulan and a 50% ammonium dichromate by weight of pullulan. The solution was coated onto clean glass slides in a horizontal position, and the film was dried under normal laboratory conditions. The thickness of the dried DCP layer was approximately 10 μm .

Diffraction gratings were produced by the interference of two coherent beams, of equal power. DCP was exposed at a 488 nm wavelength with an argon-ion laser. A He–Ne laser operating at 632.8 nm was used for real-time monitoring of the DE.

During real-time observation, we found that, initially, DE increases and, after approximately a few hundred seconds, reaches its maximum value. At that point, exposure of the DCP film was finished. Our previous investigations have shown that gratings with the maximum real-time DE have maximum efficiency after chemical processing, too.¹²

Chemical processing is quite simple and requires only two baths at room temperature (22 °C–25 °C). The exposed plates were first processed with a mixture of 60% isopropanol and 40% water for 2 min. The procedure was finished by immersing the plate for 30 s in pure isopropanol. For the purpose of this

The authors are with the Institute of Physics, Pregrevica 118, 11080 Zemun, Belgrade, Serbia. S. Savić Šević's e-mail address is savic@phy.bg.ac.yu.

Received 14 February 2006; revised 10 August 2006; accepted 11 September 2006; posted 28 September 2006 (Doc. ID 68050); published 4 January 2007.

0003-6935/07/030287-05\$15.00/0

© 2007 Optical Society of America

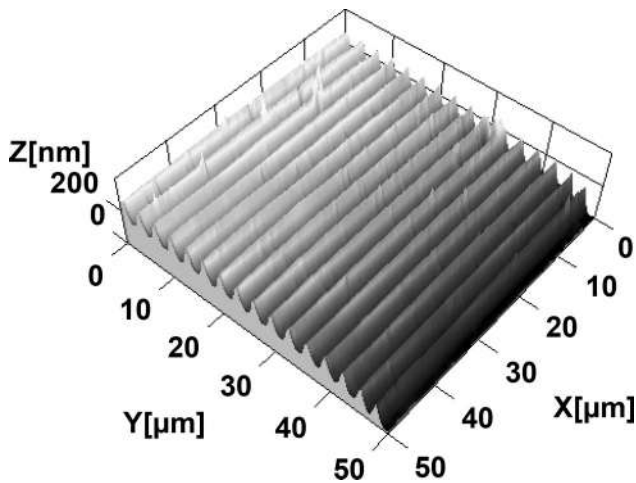


Fig. 1. AFM picture of a surface relief DCP diffraction grating before exposure to 87% RH (at 23.6 °C).

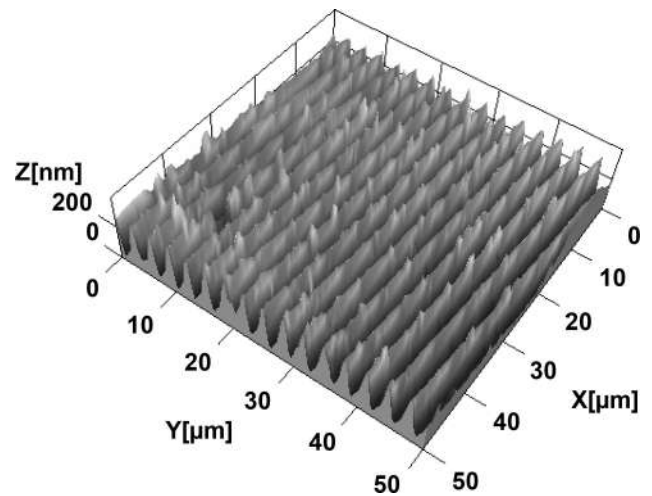


Fig. 3. AFM picture of a surface relief DCP diffraction grating after exposure to 87% RH (at 23.6 °C).

study, gratings with a spatial frequency ranging from 300 to 1000 lines/mm were produced (although spatial frequencies of more than 3000 lines/mm were manufactured).

3. Influence of High Humidity on the Profile of Surface Relief Dichromated Pullulan Gratings

DCP samples were analyzed by an atomic force microscope (AFM) before and after exposure to high humidity (87% at 23.6 °C). Three- (3D) and one-dimensional (1D) scans were recorded. A scan of a diffraction grating, before exposure to high humidity, is shown in Fig. 1 (covering a 50 × 50 μm area). The corresponding 1D scan is shown in Fig. 2.

After keeping the sample in a container with constant humidity (87% at 23.6 °C) for more than 10 h, a new AFM scan was recorded. Corresponding 3D and 1D patterns are shown in Figs. 3 and 4.

By comparing Figs. 1 and 3, it can be seen that diffraction grating relief is slightly degraded after ex-

posure to humidity. However, profile depth (230 nm, on average) and its average period (3.15 μm) remained unchanged (Figs. 2 and 4). DE is unaffected too, as will be shown in the next section.

4. Influence of Humidity on Diffraction Efficiency

As previously stated, humidity can adversely influence a number of holographic materials (such as DCG). Our goal was to compare the change of the DE of DCG and DCP gratings under humid conditions [87% relative humidity (RH) at 23.6 °C]. DE is defined as a ratio of the diffracted first-order beam intensity to the intensity of the incident beam.¹⁵

To study the effects of high humidity on the DE of both DCG and DCP gratings, samples were placed in a transparent box. This enabled us to monitor the change of the DE in real time using the He-Ne laser operating at 632.8 nm.

DCG and DCP behave quite differently under the same conditions, as can be seen in Fig. 5. Quite

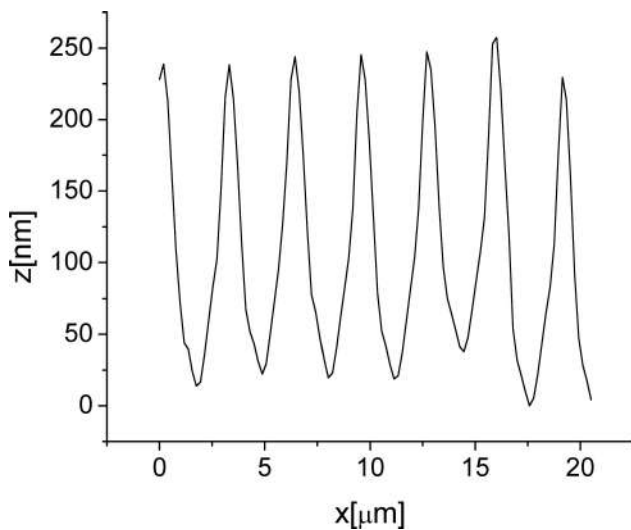


Fig. 2. Line profile (on a reduced scale) of the AFM picture from Fig. 1.

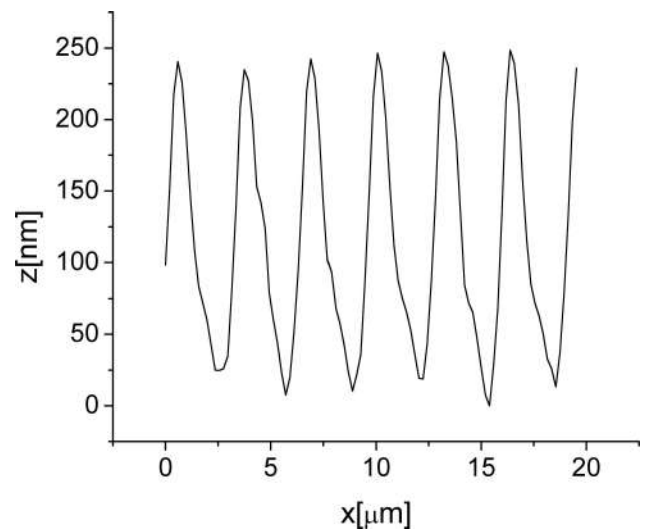


Fig. 4. Line profile (on a reduced scale) of the AFM picture from Fig. 3.

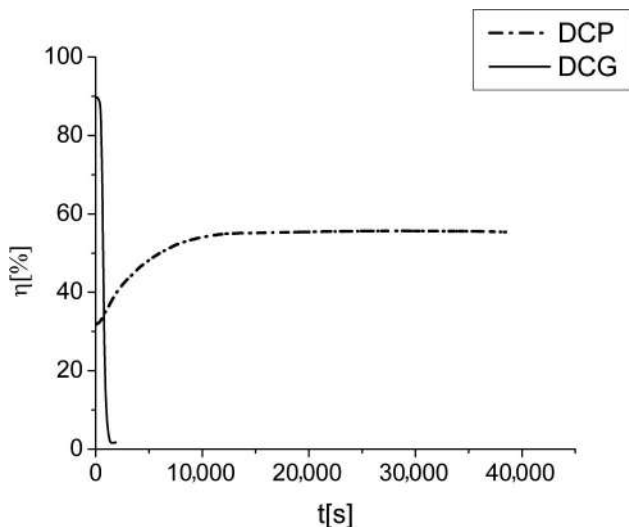


Fig. 5. Compared DE of DCP and DCG gratings versus time at 87% RH.

quickly (during several minutes) the DE of DCG is reduced close to zero—practically, the diffraction grating almost disappears. On the contrary, the DE of DCP increases during 10,000 s, and remains stable for the following 30,000 s (when the experiments were finished). In conclusion, it is evident that the stability of the DE of DCP gratings is superior to that of DCG gratings.

5. Thermal Stability and Resistance to Ultraviolet Radiation

Thermal stability is an important parameter of any holographic material. For the purpose of this study, DCP diffraction gratings were heated up to 150 °C in an oven for 1 h. Changes in the DE were not observed.

Resistance to UV radiation is also a significant parameter of holographic materials. UV stability of the diffraction gratings was tested using a 125 W mercury UV lamp (the well-known spectrum possesses several strong lines in UV—approximately from 260 to 400 nm). The grating specimens were positioned at a distance of 15 cm from the UV lamp. Following a 1 h exposure, there were no observable changes of the DE.

6. Influence of Storage Time on Diffraction Efficiency and Profile of Surface Grating

Influence of the storage time (this term is used to designate the time after the final chemical processing of the gratings) on the DE and grating profile was investigated. The DE of DCP gratings was measured immediately after chemical processing, during the following 5 days and, finally, after approximately 4 years.

DCP diffraction gratings reach their maximum DE very quickly (400 s), following the chemical processing. This was verified in real time, as can be seen in Fig. 6. Subsequently, the DE changes very slowly as found in this research.

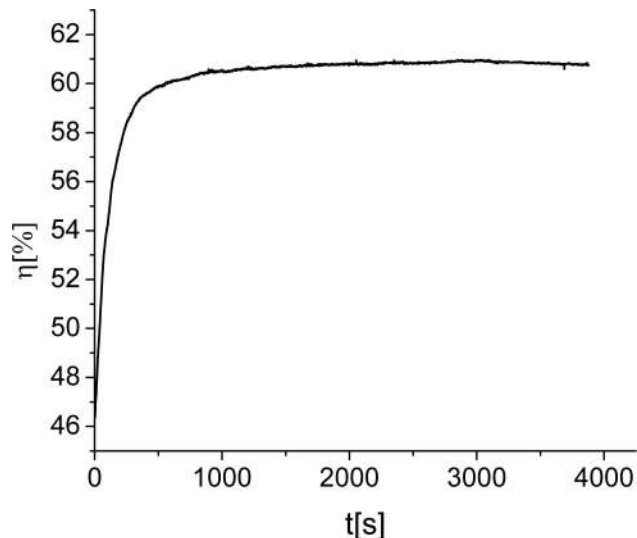


Fig. 6. DE of a DCP grating (immediately after development) versus drying time.

To investigate short-term effects (5 days), a number of diffraction gratings were recorded. The DE of each grating was, consequently, measured over a period of 5 days at 1 day intervals under normal laboratory conditions. Dependence of the DE on storage time is shown in Fig. 7 for a typical case. It can be seen that fluctuations of DE with storage time are small and have been stabilized after approximately 5 days.

Diffraction gratings generally lose their DE with time. For some materials like MBDCG (methylene-blue-sensitized DCG), the amount of the DE reduction depends on initial DE (first day DE). It was shown⁵ that gratings with high initial DE lose more of their efficiency, compared with gratings with low initial efficiency.

To better quantify this kind of process, a new quantity $D(\eta)$ (called the relative variation of DE) is de-

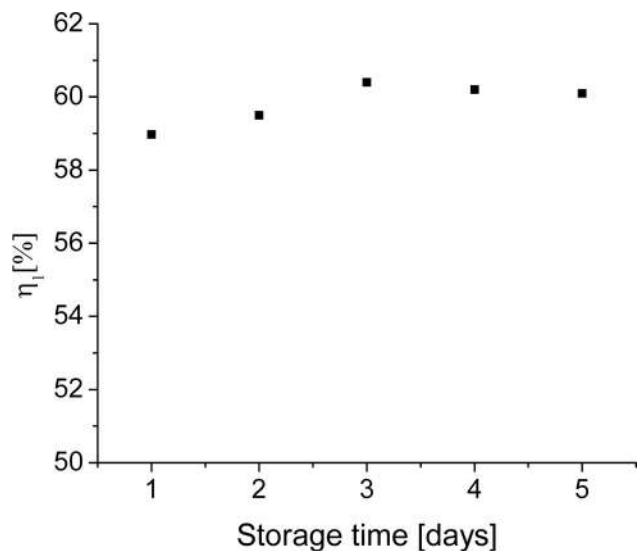


Fig. 7. DE of a DCP grating versus storage time.

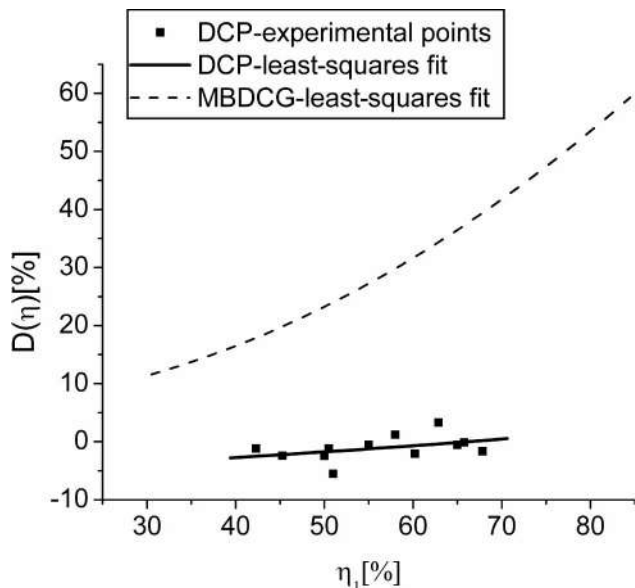


Fig. 8. Relative variation of DE $D(\eta)$ versus the initial DE η_1 of DCP (5 days of storage) and MBDCG gratings (4 days of storage).

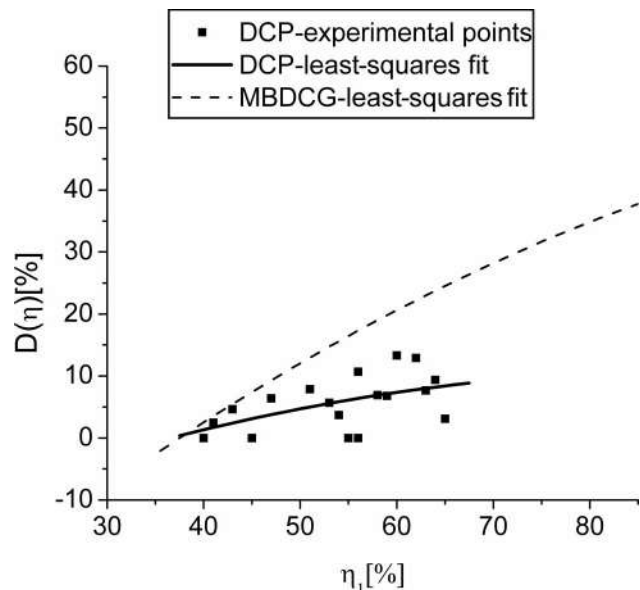


Fig. 9. Relative variation of DE $D(\eta)$ versus the initial DE η_1 of DCP (4 years storage time) and MBDCG gratings (2 years storage time).

finned (as applied to the case of MBDCG)⁵:

$$D(\eta) = \frac{\eta_1 - \eta_2}{\eta_1} 100, \quad (1)$$

where η_1 is a DE measured immediately after recording and developing; η_2 is a DE measured after a certain storage period. The same calculation method was used to analyze DCP gratings. Plots of $D(\eta)$ versus η_1 are shown in Fig. 8, compared with MBDCG data, published in Ref. 5. The solid line represents the least-squares fit of our experimental data, while the dashed curve represents the least-squares fit of the MBDCG DE variation.

As can be seen in Fig. 8, DCP DE fluctuations are small, ranging from -5.5% to $+3.3\%$ (in contrast to $+5\%$ to $+50\%$ fluctuations in the case of the MBDCG). In conclusion, the DE of the DCP gratings was quite stable after drying, unlike the MBDCG.⁵

To study the effects of long-term storage (4 years), the DE was measured immediately after recording and again after more than 4 years storage under unfavorable environmental conditions (temperature varied from 15°C to 30°C , and the RH was between 20% and 70%). A number of diffraction gratings were recorded during 2001, and their DE was measured again in December 2005. The relative variation of the DE $D(\eta)$ versus the initial DE η_1 is shown in Fig. 9. The solid curve represents the least-squares fit of our experimental data, while the fit of the MBDCG data was taken from Ref. 5.

Figure 9 indicates that the DE of the DCP gratings decreases after 4 years, the decrease being small [$D(\eta) < 13\%$] compared with the MBDCG.⁵ Profiles of diffraction gratings recorded in 2001 were analyzed in 2005 by an AFM and a regular profile, with no noise, was observed.

7. Conclusion

It was found that DCP diffraction gratings have excellent environmental stability, compared with the DCG. The profile of the DCP surface relief, after exposure to high humidity, was not changed, and the DE was preserved. The DE of the DCP gratings was almost constant shortly after drying, and it was possible to store gratings for long periods, without a noticeable decrease of the DE.

The research was performed under the contract 141003 funded by the Ministry of the Science and Environmental Protection of Serbia. Special thanks are given to Dana Vasiljević-Radović from the Institute of Microelectronic Technologies and Single Crystals, in the Institute of Chemistry, Technology, and Metallurgy, Belgrade, Serbia for AFM scans of our samples.

References

1. B. J. Chang and C. D. Leonard, "Dichromated gelatin for the fabrication of holographic optical elements," *Appl. Opt.* **18**, 2407–2417 (1979).
2. S. Calixto and R. A. Lessard, "Real-time holography with undeveloped dichromated gelatin films," *Appl. Opt.* **23**, 1989–1994 (1984).
3. J. C. Newell, L. Solymar, and A. A. Ward, "Holograms in dichromated gelatin: real-time effects," *Appl. Opt.* **24**, 4460–4466 (1985).
4. Y. L. Lee, C. H. Kwak, J. H. Kwon, and Y. S. Im, "Observation of a fast-formed absorption grating and a slowly formed phase grating in undeveloped dichromated gelatin," *Appl. Opt.* **40**, 3635–3639 (2001).
5. R. Changkakoti and S. V. Pappu, "Methylene blue sensitized dichromated gelatin holograms: a study of their storage life and reprocessibility," *Appl. Opt.* **28**, 340–344 (1989).
6. K. Wang, L. Guo, J. Zhu, W. Zhang, and B. Cheng, "Methylene blue dichromated-gelatin holograms: antihumidity method

- for taking off strongly adsorbing humidity groups," *Appl. Opt.* **37**, 326–328 (1998).
7. G. M. Naik, A. Mathur, and S. V. Pappu, "Dichromated gelatin holograms: an investigation of their environmental stability," *Appl. Opt.* **29**, 5292–5297 (1990).
 8. W. Ketai, G. Lurong, Z. Jianhua, Z. Weiping, T. Jiyauo, and P. Lin, "Methylene-blue-sensitized dichromated holograms with anti-humidity polymer coatings," *Appl. Opt.* **36**, 3116–3119 (1997).
 9. B. Pinto-Iguanero, A. Olivares-Perez, A. W. Mendez-Alvarado, I. Fuentes-Tapia, and C. G. Trevino-Palacois, "Non-hydroscopic vanilla doped dichromated gelatin holographic material," *Opt. Mater.* **22**, 397–404 (2003).
 10. T. Sano, Y. Uemura, and A. Furuta, "Photosensitive resin composition containing pullulan or esters thereof," U.S. patent 3,960,685 (1 June 1976).
 11. D. Pantelić, S. Savić, and D. Jakovljević, "Dichromated pullulan as a novel photosensitive holographic material," *Opt. Lett.* **23**, 807–809 (1998).
 12. S. Savić, D. Pantelić, and D. Jakovljević, "Real-time and post-processing holographic effects in dichromated pullulan," *Appl. Opt.* **41**, 4484–4488 (2002).
 13. S. Savić, D. Pantelić, and D. Jakovljević, "Dichromated pullulan: real-time effects and holographic properties," presented at the International Conference Optical Holography and its Applications, Ukraine, 26–29 September 2000.
 14. S. Savić Šević and D. Pantelić, "Relief hologram replication using a dental composite as an embossing tool," *Opt. Express* **13**, 2747–2754 (2005).
 15. R. J. Collier, C. B. Burckhardt, and L. H. Lin, *Optical Holography* (Academic, 1971).

High angular and spectral selectivity of purple emperor (*Lepidoptera: Apatura iris* and *A. ilia*) butterfly wings

Dejan Pantelić,^{1,*} Srećko Ćurčić,² Svetlana Savić-Šević,¹ Aleksandra Korać,^{2,3}
Aleksander Kovačević,¹ Božidar Ćurčić² and Bojana Bokić¹

¹Institute of Physics, University of Belgrade, Pregrevica 118, 11080 Zemun, Serbia

²Institute of Zoology, Faculty of Biology, University of Belgrade, Studentski Trg 16, 11000 Belgrade, Serbia

³Center for Electron Microscopy, Faculty of Biology, University of Belgrade, Studentski Trg 16, 11000 Belgrade, Serbia

*pantelic@ipb.ac.rs

Abstract: The iridescent features of the butterfly species *Apatura iris* (Linnaeus, 1758) and *A. ilia* (Denis & Schiffermüller, 1775) were studied. We recognized the structural color of scales only on the dorsal side of both the fore and hind wings of males of both of the aforementioned butterfly species. The scale dimensions and microstructure were analyzed by a scanning electron microscope (SEM) and transmission electron microscope (TEM). The optical properties were measured and it was found that the peak reflectivity is around 380 nm, with a spectral width (full width at half maximum) of approximately 50 nm in both species. The angular selectivity is high and a purple iridescent color is observed within the angular range of only 18 degrees in both species.

©2011 Optical Society of America

OCIS codes: (050.2770) Gratings; (050.52980) Photonic crystals; (050.6624) Subwavelength structures; (160.4760) Optical properties.

References and links

1. M. Srinivasarao, "Nano-optics in the biological world: beetles, butterflies, birds, and moths," *Chem. Rev.* **99**(7), 1935–1962 (1999).
2. P. Vukusic, J. R. Sambles, C. R. Lawrence, and R. J. Wootton, "Quantified interference and diffraction in single *Morpho* butterfly scales," *Proc. Biol. Sci.* **266**(1427), 1403–1411 (1999).
3. P. Vukusic, and J. R. Sambles, "Photonic structures in biology," *Nature* **424**(6950), 852–855 (2003).
4. R. O. Prum, T. Quinn, and R. H. Torres, "Anatomically diverse butterfly scales all produce structural colours by coherent scattering," *J. Exp. Biol.* **209**(4), 748–765 (2006).
5. P. Vukusic, "Structural colour in Lepidoptera," *Curr. Biol.* **16**(16), R621–R623 (2006).
6. N. L. Garrett, P. Vukusic, F. Ogrin, E. Sirotkin, C. P. Winlove, and J. Moger, "Spectroscopy on the wing: naturally inspired SERS substrates for biochemical analysis," *J Biophotonics* **2**(3), 157–166 (2009).
7. M. D. Shawkey, N. I. Morehouse, and P. Vukusic, "A protean palette: colour materials and mixing in birds and butterflies," *J. R. Soc. Interface* **6**(Suppl 2), S221–S231 (2009).
8. H. Ghiradella, "Light and color on the wing: structural colors in butterflies and moths," *Appl. Opt.* **30**(24), 3492–3500 (1991).
9. H. Ghiradella, "Hairs, bristles, and scales," in *Microscopic Anatomy of Invertebrates, Vol. 11A: Insecta*, F.W. Harrison and M. Locke eds. (Wiley, New York, 1988).
10. H. Ghiradella, D. Aneshansley, T. Eisner, R. E. Silberglied, and H. E. Hinton, "Ultraviolet reflection of a male butterfly: interference color caused by thin-layer elaboration of wing scales," *Science* **178**(4066), 1214–1217 (1972).
11. L. P. Biró, K. Kertész, Z. Vértesy, G. I. Márk, Z. Bálint, V. Lousse, and J.-P. Vigneron, "Living photonic crystals: butterfly scales – nanostructure and optical properties," *Mater. Sci. Eng. C* **27**(5-8), 941–946 (2007).
12. Z. Han, L. Wu, Z. Qiu, and L. Ren, "Microstructure and structural color in wing scales of butterfly *Thaumantis diores*," *Chin. Sci. Bull.* **54**(4), 535–540 (2009).
13. M. Imafuku, Y. Hirose, and T. Takeuchi, "Wing colors of *Chrysozephyrus* butterflies (Lepidoptera: Lycaenidae): ultraviolet reflection by males," *Zoolog. Sci.* **19**(2), 175–183 (2002).
14. P. Vukusic, J. R. Sambles, and C. R. Lawrence, "Structurally assisted blackness in butterfly scales," *Proc. Biol. Sci.* **271**(Suppl 4), S237–S239 (2004).
15. P. Vukusic, and I. Hooper, "Directionally controlled fluorescence emission in butterflies," *Science* **310**(5751), 1151 (2005).

16. S. M. Luke, P. Vukusic, and B. Hallam, "Measuring and modelling optical scattering and the colour quality of white pierid butterfly scales," *Opt. Express* **17**(17), 14729–14743 (2009).
17. K. Kertész, G. Molnár, Z. Vértésy, A. A. Koós, Z. E. Horváth, G. I. Márk, L. Tapasztó, Z. Bálint, I. Tamáska, O. Deparis, J. P. Vigneron, and L. P. Biró, "Photonic band gap materials in butterfly scales: a possible source of "blueprints"," *Mater. Sci. Eng. B* **149**(3), 259–265 (2008).
18. Z. Vértésy, K. Kertész, Z. Bálint, G. Molnár, M. Erős, and L. P. Biró, "SEM and TEM investigations in the scales of the European nymphalid butterfly *Apatura ilia* dark and light phenotypes," in *BioPhot Meeting Abstract Book*, Levente Tapasztó ed. (Reserach Institute for Technical Physics and Materials Science, Budapest, Hungary, 2007), pp. 14–15.
19. Z. Han, L. Wu, Z. Qiu, H. Guan, and L. Ren, "Structural colour in butterfly *Apatura ilia* scales and the microstructure simulation of photonic crystal," *J. Bionics Eng.* **5**(Supplement 1), 14–19 (2008).
20. R. E. Silberglied, "Visual communication and sexual selection among butterflies," In *The Biology of Butterflies. Symposium of the Royal Society of London, No. 11*, R. I. Vane-Wright, and P. E. Ackery eds. (Academic Press, London, 1984) pp. 207–223.
21. R. J. C. Page, "Perching and patrolling continuum at favoured hilltop sites on a ridge: a mate location strategy by the Purple Emperor butterfly *Apatura iris*," *The Entomologist's Record* **122**, 61–70 (2010).
22. S. Berthier, "Photonique des Morphos," (Springer-Verlag France, Paris, 2010).
23. G. A. Blackburn, "Hyperspectral remote sensing of plant pigments," *J. Exp. Bot.* **58**(4), 855–867 (2006).
24. M. A. Giraldo, S. Yoshioka, and D. G. Stavenga, "Far field scattering pattern of differently structured butterfly scales," *J. Comp. Physiol. A Neuroethol. Sens. Neural Behav. Physiol.* **194**(3), 201–207 (2008).
25. S. Yoshioka, and S. Kinoshita, "Wavelength-selective and anisotropic light-diffusing scale on the wing of the Morpho butterfly," *Proc. Biol. Sci.* **271**(1539), 581–587 (2004).

1. Introduction

The diurnal active members of the order Lepidoptera (butterflies) are considered to be the most attractive insects, together with representatives of the order Coleoptera (beetles). The delicate beauty of butterfly wings is a consequence of several phenomena: selective absorption by pigments, scattering, fluorescence and iridescence. The phenomenon of bright iridescence attracted much attention [1–7] and is observed in a great number of butterfly species, mostly tropical ones. Butterflies are known as the masters of mimicry (the type of camouflage which serves to avoid predators) and aposemy (warning coloration which is usually associated with an unpleasant taste to potential predators). In some species sexual dimorphism is observed, as in the two species analyzed in this paper.

Structural coloration investigations have been very popular in the last few decades and butterfly microstructure has been thoroughly investigated [8–10]. The following aspects have been studied as well: nanostructure and optical properties of wing scales [1, 11, 12], interference and diffraction in butterflies [2], ultraviolet reflection [13], structural blackness and whiteness in butterfly scales [14], fluorescence emission [15], and coherent scattering-induced structural color of scales [4]. The optical properties of butterfly scales have been thoroughly measured and modeled [16] and their nanoscale structures could encourage further developments in artificial material manufacturing [17].

The butterfly species *Apatura iris* (Linnaeus, 1758) and *A. ilia* (Denis & Schiffermüller, 1775) (Fig. 1a and b) are distributed from Europe to Eastern Asia (China). The most obvious difference between the two species is an extra eye spot on the fore wings of *A. ilia*. The males of *Apatura* spp. possess the iridescent color on the dorsal side of their wings [18, 19]. This is probably connected with intrasexual communication between males, rather than intersexual communication and attraction [20]. The structural color of males is visible in flight when the movements of the wings are noticeable within a certain range of angles. This kind of iridescent coloration represents an excellent contrast to forest canopy – a natural habitat of *Apatura* spp. Apart from structural coloration, pigment coloration is present as well.

The flight behavior of male *Apatura iris* was recently studied and it consisted mainly of perching and patrolling flights. The daily aggregation of males at favored landmark sites from approximately midday was observed as well [21].

Here we present a detailed study of two *Apatura* species with respect to their optical properties and the relationship of these properties to the microscopic structure of the wing scales.



Fig. 1. a) *Apatura iris*; b) *Apatura ilia*. Observe that *A. ilia* has an extra eye spot on fore wings.

2. Materials and methods

2.1 Collecting data

Specimens of the species *Apatura iris* and *A. ilia* were used for optical investigations (Fig. 1). Both species were collected from the Balkan Peninsula: *A. iris* – Mt. Stara Planina, Southeastern Serbia (July 2009, leg. D. Stojanović), and *Apatura ilia* – Mt. Fruška Gora, Northern Serbia (July 2009, leg. D. Stojanović). The specimens were kept in the collection of the Institute of Zoology, Faculty of Biology, University of Belgrade, Serbia.

2.2 SEM procedure

The specimens of *Apatura iris* and *A. ilia* were rinsed with diethyl-ether to obtain a clear surface of the wings. The wings of the males were cut into rectangular shape (surface area of several mm²). This was followed by dehydration in order to obtain dry samples, fixed on a test-bed and subsequently covered with gold. Prepared samples were analyzed by a scanning electron microscope (SEM) (JSM-6460LV, JEOL, Tokyo, Japan).

2.3 TEM procedure

Wings were cut into small pieces, fixed in 3% glutaraldehyde in 0.1M phosphate buffer (pH 7.2) and postfixed in 1% osmium tetroxide in the same buffer. The specimens were dehydrated with serial ethanol solutions of increasing concentration and embedded in Araldite (Fluka, Germany). For electron microscopic examination, the tissue blocks were trimmed and cut with diamond knives (Diatome, Switzerland) on an UC6 ultramicrotome (Leica, Austria). The thin sections were mounted on copper grids, stained with uranyl acetate and lead citrate (Ultrastain, Leica, Austria) and examined on a Philips CM 12 transmission electron microscope (TEM) (Eindhoven, the Netherlands) equipped with a Megaview III digital camera (Soft Imaging System, Münster, Germany).

2.4 Spectrometric measurements

A HR2000CG-UV-NIR Fiber spectrometer was used (Ocean Optics Inc., Dunedin, USA) to collect the reflection spectra of the investigated butterflies. Wing samples were positioned on a computer-controlled rotation platform and illuminated with a tungsten halogen lamp. Thus, we were able to record the reflection spectrum of the wings as a function of the angle of incidence. A MIRA titanium-sapphire laser with frequency doubler (Coherent Inc., USA) was used to investigate the spectral dependence of the wing scattering pattern in the blue and UV part of the spectrum. A diode-pumped Nd-YAG laser at 532 nm and diode laser at 630 nm were used as well. The wings were irradiated with a laser beam and the scattered radiation was photographed on the cylindrical screen by Canon EOS 50D camera. Rigorous coupled-wave analysis was used to calculate the spectral reflectivity.

3. Results

As in all butterfly species, the scales are positioned like roof tiles covering the entire dorsal and ventral sides of the wing (Fig. 2a). We recognized two types of scales on the dorsal side of both the fore and hind wings of *Apatura iris* and *A. ilia*. The cover scales are on top, while ground scales are situated below. We found that the cover scales are responsible for the blue iridescence of these two butterfly species (Fig. 2b) due to their much denser microscopic structure in comparison to the ground scales. We have found that iridescent scales are pigmented (see brownish scales in lower half of Fig. 2c).

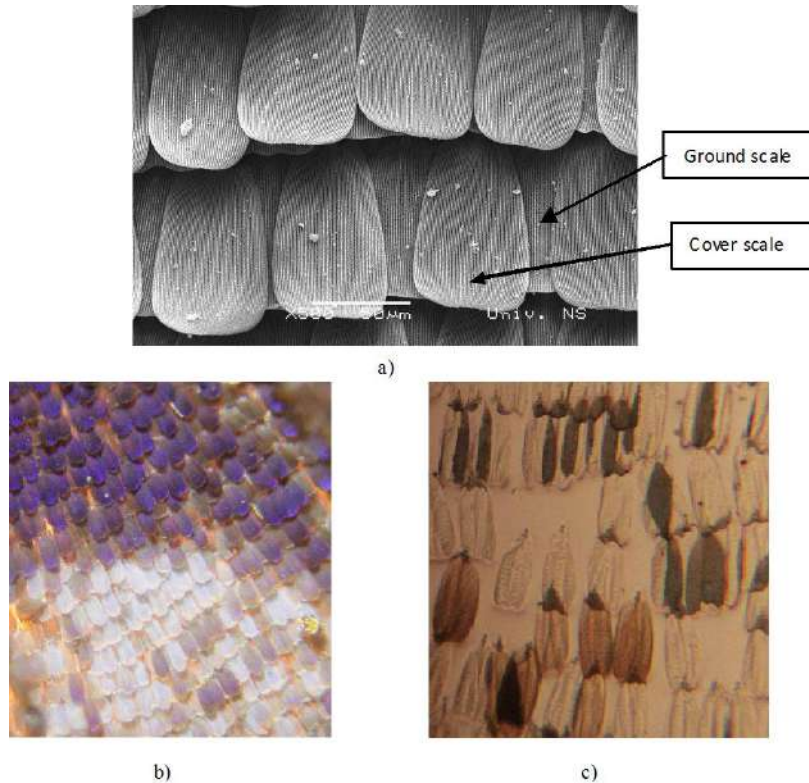


Fig. 2. *Apatura iris*: a) the cover scales on the dorsal wing side have a much denser structure in comparison to ground scales (SEM image); b) the blue iridescence of the cover scales positioned in regular rows. White scattering scales can be seen as well. The photograph is recorded in reflection; c) scattering scales have a glass-like appearance, while the iridescent scales are pigmented. Overlapping areas of glass-like scales are dark, indicating that the scattering is intensified. Microscope image is recorded in transmission.

The white areas of the dorsal wing side are also interesting. Examination of the reflective property revealed that the scales uniformly scatter light (Fig. 2b), while in transmission they look completely transparent (Fig. 2c). Scale overlapping increases the scattering, which can be seen as dark areas in upper half of Fig. 2c. We have found that there is a cumulative effect of overlapping. A single scale transmits around 90% and we measured the transmission of the overlapping scales to be about 60%.

By magnifying the iridescent butterfly scale surface of *Apatura iris* we observed long parallel ridges, each having a number of lamellas positioned one over another (see Fig. 3 for SEM images in two different views). The rows are mutually connected with orthogonally positioned cross ribs. TEM images were used to obtain the exact morphological and dimensional characteristics of each ridge and its lamellae (Fig. 4). The lamellae in cross section exhibit a multilayer structure, conifer-like, with six pairs of lateral projections which

are not widened distally and are triangularly pointed. The scale structure of *Apatura ilia* is similar, except that the ridge density is slightly higher.

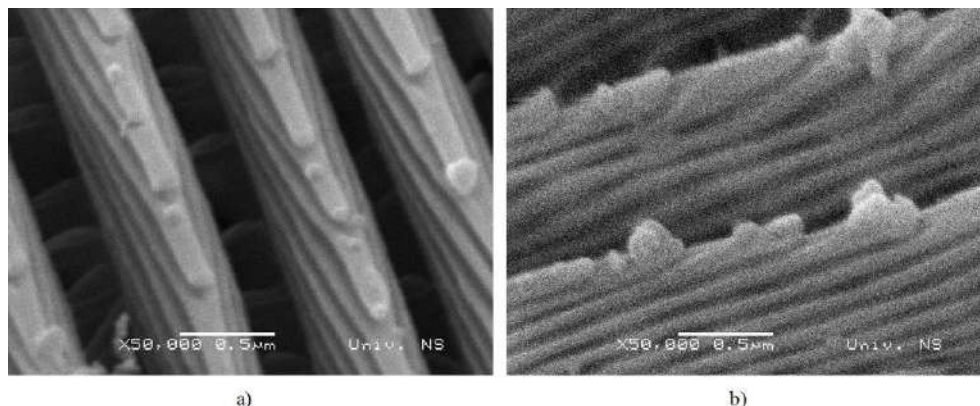


Fig. 3. SEM of the highly-magnified structure of a) *Apatura iris* cover scale in dorsal view; b) *A. iris* cover scale in dorso-lateral view. A stacked lamellar structure is apparent.



Fig. 4. TEM image of cover scale cross section of *Apatura iris*.

Electron microscope images were used to construct a geometrical model of the structure which was further utilized for theoretical analysis of the optical properties. Characteristic dimensions can be seen in Fig. 5. Ridges form a surface relief diffraction grating, with an 820 nm period and approximately the same depth (830 nm). On the other hand, the lamellae form a volume Bragg grating, with a roughly 75 nm period, with each lamella being 40 nm thick.

Butterfly wings were studied spectroscopically in relation to the illumination and observation angles. Several spectra were recorded for different angular orientations (Fig. 6a). Maximum reflectivity is observed in the UV part of the spectrum (380 nm) and does not depend on the observation angle. Spectral width is small (50 nm FWHM) compared with more visually spectacular species, such as *Morpho* butterflies [22]. There is a slight spectral shift (in the order of 10-20 nm) as a function of the angle of illumination. All of this apparently provides an evolutionary advantage when the butterfly reflectivity spectra (with UV maximum) are compared with the canopy spectra (with almost no reflectivity in UV region, a peak at 550 nm, and a plateau in the IR region) [23]. UV reflectivity makes the butterfly very visible to its own species and considerably less visible to all other animals, especially potential predators. The intensity of reflected light at visible and IR wavelengths is much lower, making the butterfly appear dull brown from almost all directions – an excellent camouflage in forest, where *Apatura* species is living.

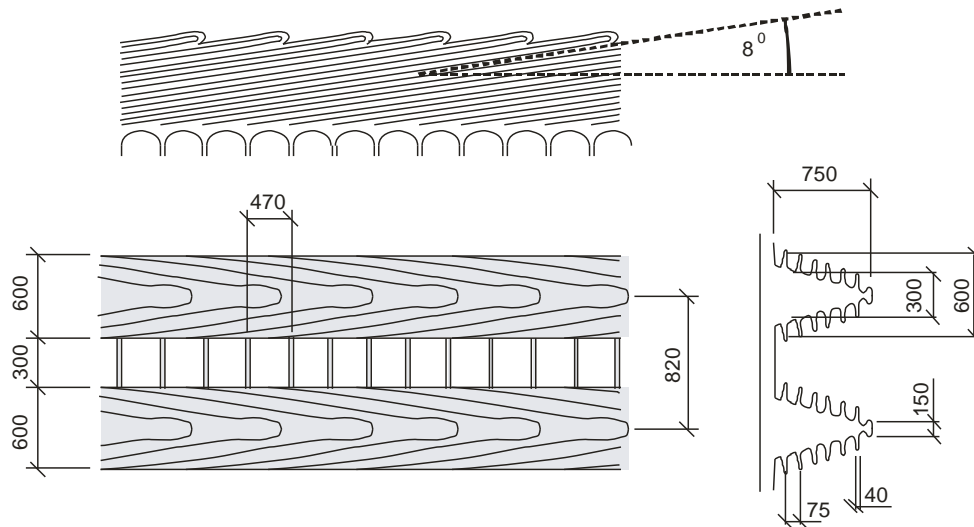


Fig. 5. Geometry of the microscopic structure of the *Apatura iris* wing scale (three orthogonal projections of the upper scale surface). All dimensions are in nanometers.

The iridescence of *Apatura iris* is observed in a rather narrow angular range (18 degrees); this is much narrower compared to other butterfly species [24]. Iridescence at 380 nm as a function of the angle of incidence is shown in Fig. 6b. Nearly identical spectral properties were observed in *Apatura ilia*.

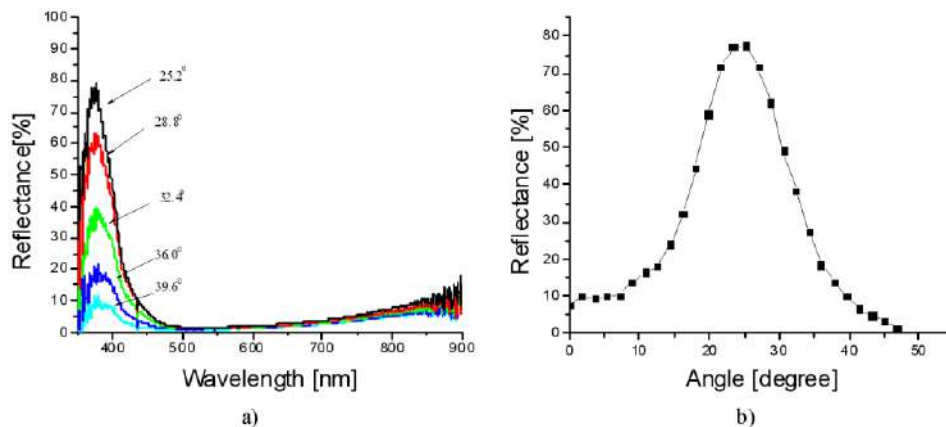


Fig. 6. a) Reflection spectra of the *Apatura iris* wing, with the angle of incidence as a parameter; b) iridescence at 380 nm as a function of the observation angle.

In order to observe the spatial distribution of iridescent light, we irradiated the butterfly wing with a laser beam from a tunable Ti-Sapphire laser coupled to frequency doubler. We were able to continuously tune the laser wavelength from 365 to 450 nm. A simple experimental setup is shown in Fig. 7a and 7b, and the typical spatial distribution of iridescence can be seen in Fig. 7c. It should be emphasized that the images were recorded by virtue of the natural fluorescence of the paper screen. In order to obtain an improved spatial distribution we applied pseudo-coloring of the recorded images.

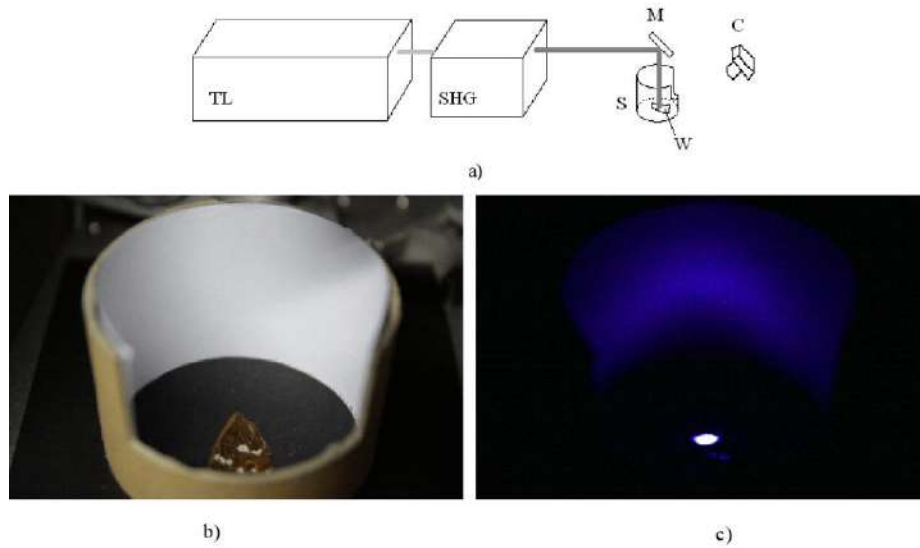


Fig. 7. a) Experimental setup used for the detection of the spatial distribution of *Apatura iris* wing iridescence (TL – titanium sapphire laser, SHG – frequency doubler, C – CCD camera, S – reflective cylinder, W – butterfly wing, M – mirror); b) a butterfly wing inside a reflective cylinder c) typical pattern of iridescence.

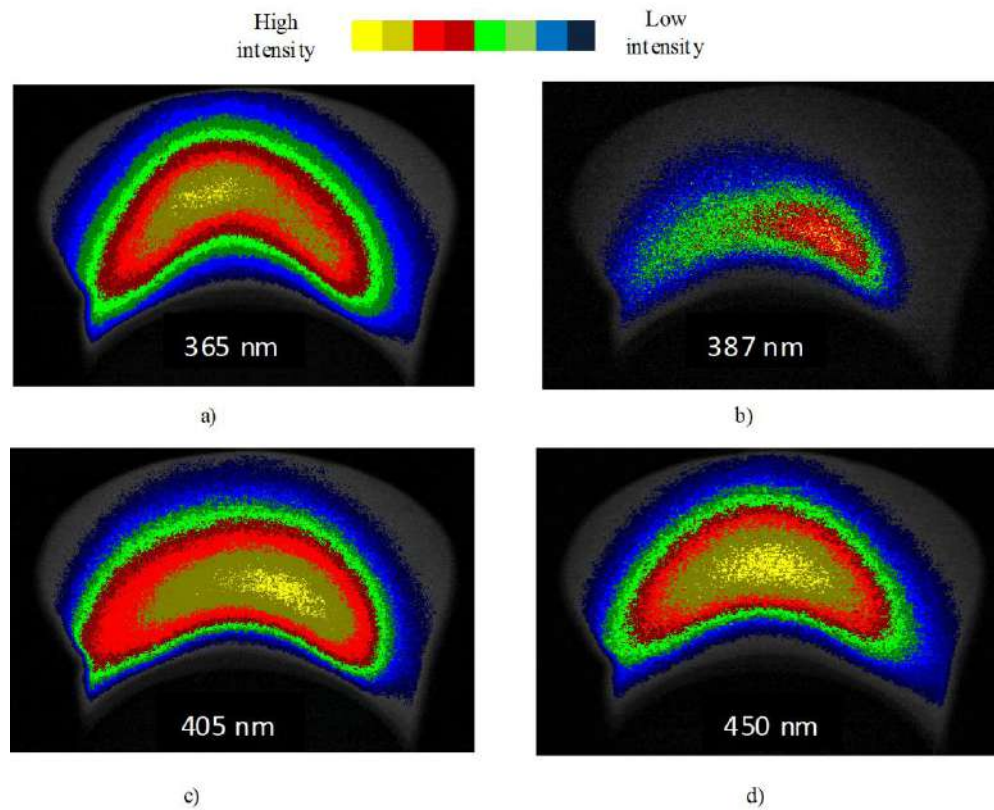


Fig. 8. Pseudo-colored images of iridescence recorded at: a) 365 nm; b) 387 nm; c) 405 nm; d) 450 nm. Patterns were recorded using a Ti-sapphire laser with frequency doubler. Light intensities are color coded according to the bar at the top of the figure.

Four images recorded at 365, 387, 405 and 450 nm are shown in Figs. 8a-8d. In comparison to other wavelengths, the spatial distribution at 387 nm is much narrower, indicating that at this particular wavelength the radiation is very directional. At 532 nm the directionality of scattered radiation is almost completely lost, as can be seen in Fig. 9, which was recorded by a diode-pumped Nd-YAG laser at 532 nm.

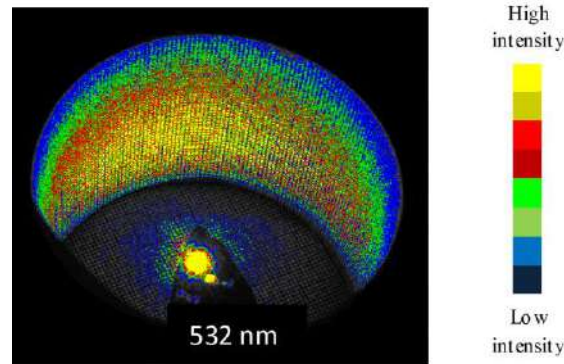


Fig. 9. Radiation at 532 nm is almost uniformly scattered at the wing of *Apatura iris*. The pattern was recorded by Nd-YAG laser. Light intensities are color coded – yellow representing the highest intensity, and blue the lowest.

4. Discussion

The results presented in this study show that the iridescence of *Apatura* spp. butterflies is spectrally and directionally constrained. With respect to the butterfly body, the radiation is directed as shown in Fig. 10 in three orthogonal projections. This particular feature is a consequence of the mutual orientations of lamellae with respect to the scale, and the scale with respect to the wing membrane (Fig. 11). There is a critical angle of incidence ($\gamma + 2\alpha + 2\beta = \pi/2$) when the radiation is Bragg-reflected along the wing surface. At a greater angle, the radiation cannot be further reflected (i.e., it is directed inside the material). In the case of *Apatura* butterflies, the angle α of the scale is large ($\sim 20^\circ$), as can be verified by the strong shadow cast by each scale in Figs. 2a and 2b.

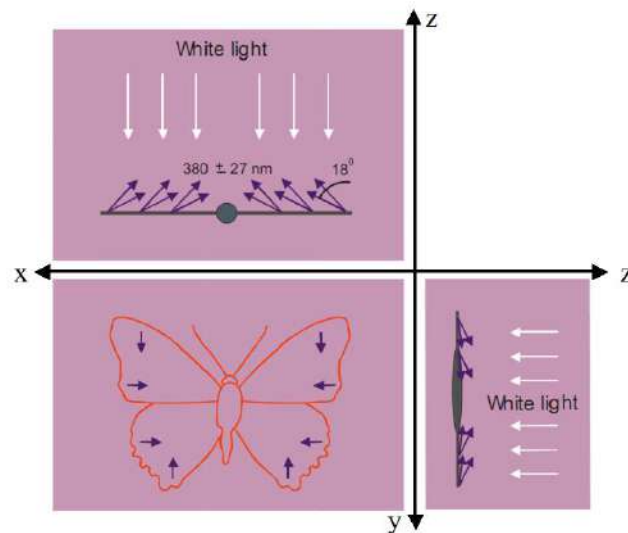


Fig. 10. Directions in which the blue iridescence can be observed (purple arrows). The butterfly is schematically presented in three orthogonal projections.

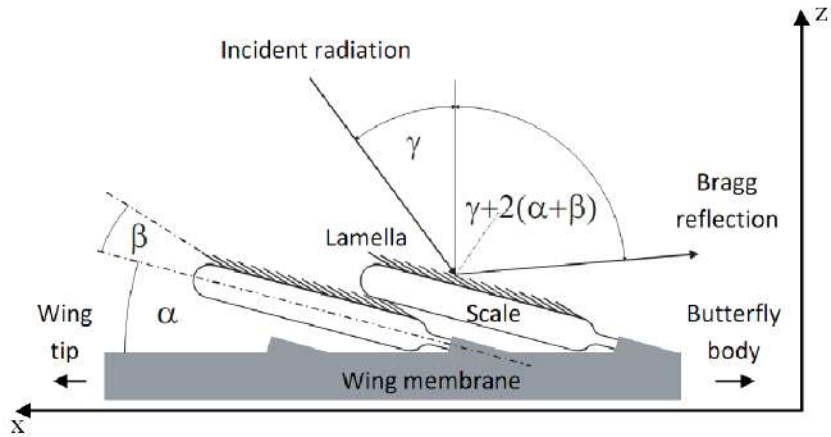


Fig. 11. Directionality of *Apatura* butterfly wing iridescence is a consequence of inclination of both lamellae (angle β) and the scale as a whole (angle α). γ is the angle of incidence of light with respect to the wing membrane. Axes x and z are in agreement with Fig. 10.

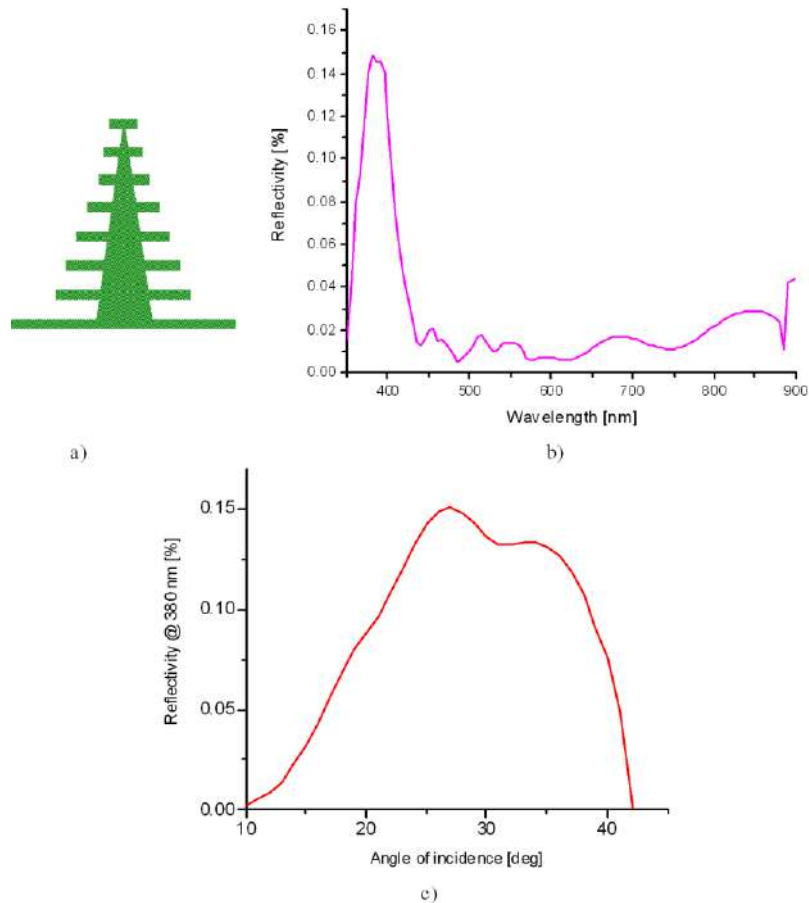


Fig. 12. a) Geometry of the butterfly cover scale in cross section, used for the calculation of the spectral reflectivity of *Apatura* spp.; b) spectral reflectivity as obtained by exact analysis using rigorous coupled-wave analysis; c) angular dependence of iridescence at 380 nm.

The spectral selectivity of the *Apatura* spp. scale was analyzed using rigorous coupled-wave analysis using simplified geometry as shown in Fig. 12a. We were able to correctly reproduce the spectral reflectivity (as shown in Fig. 12b) using dimensions presented in Fig. 5 and the refractive index of 1.56 for chitin [25]. Angular dependence of iridescence was calculated too and presented in Fig. 12c. Theoretical results slightly depart from experimental data, but this is due to idealized nature of calculation. In reality the butterfly grating is stochastically distorted, and the effect is averaged among many scales, inside illuminated wing area.

This phenomenon is in contrast with the reflection of *Morpho* butterfly wings, which direct radiation sideways and in a broad angular range. Also, the spectral maximum of iridescence shifts significantly with the angle of observation [22]. The difference between *Morpho* spp. and *Apatura* spp. is due to the different orientations of butterfly scales with respect to wing membrane. In *Morpho* butterflies the scales are almost parallel to the membrane (for example, *Morpho aega*), while in the *Apatura* species the scales are strongly inclined. On the nanoscopic level, ridges on the *Apatura* scale are not as dense as in *Morpho* butterflies. Even though the number of lamellas is almost the same in *Morpho helenor* [22] and *Apatura*, their cross sectional profile (as seen in TEM) is quite different. All these factors lead to radically different optical properties - *Apatura* iridescence is spectrally very pure, and the angular pattern is narrow.

5. Conclusions

Apatura ilia and *Apatura iris* are visually quite similar. *Apatura ilia* males have an iridescent purple color on the wings that dorsally arise from a fully ordered 3D structure, and a yellowish-brown color produced by pigments on the wings ventrally. On the other hand the males of *A. iris* have the same purple iridescent color on the dorsal side of the wings and a brownish color on the ventral side.

The photonic-type nanostructures consisting of chitin, occurring in the butterfly wing scales of the male individuals of the species *Apatura iris* and *A. ilia*, were investigated by both scanning and transmission electron microscopy and reflectance spectroscopy. A tunable laser was used to analyze the variation of spatial distribution of iridescence.

As in all butterfly species, the architecture of the scales is complex. They possess numerous alternating air and cuticle layers responsible for iridescence. From an optical point of view, both analyzed species behave similarly. Maximum reflectivity is observed in the UV region of the spectrum for both species and depends to a certain extent on the observation angle. We have found that the scale iridescence is remarkably narrow, both spectrally and angularly, in the studied butterfly species. This is the consequence of the interplay between scale structure and inclination with respect to the wing membrane. Iridescence is observed in a rather narrow angular range (18 degrees for both analyzed *Apatura* species while it is much greater in other butterfly species previously studied). The spectral width of the iridescence is small (around 50 nm FWHM for both analyzed *Apatura* species and is much greater in tropical *Morpho* butterflies).

Acknowledgments

We are grateful to Mr. Miloš Bokorov (Faculty of Science, University of Novi Sad, Novi Sad, Serbia) for helping prepare the SEM photographs. Mrs. Anita Lazarević (Center for Electron Microscopy, Faculty of Biology, University of Belgrade, Belgrade, Serbia) assisted in the production of TEM micrographs. Finally, Dejan Stojanović, M.Sc. (Fruška Gora National Park, Sremska Kamenica, Serbia) provided some butterfly specimens for the investigations. The study was financially supported by the Serbian Ministry of Science and Technological Development (projects 141003, 143053, 143050, 45016, 171038, 173038, and 173055).

HOLOGRAPHIC MEASUREMENT OF A TOOTH MODEL AND DENTAL COMPOSITE CONTRACTION

DEJAN PANTELIĆ¹, SVETLANA SAVIĆ-ŠEVIĆ¹, DARKO VASILJEVIĆ¹, BRANKA MURIĆ¹, LARISA BLAŽIĆ², MARKO NIKOLIĆ¹, AND BRATIMIR PANIĆ¹

QUERY SHEET

This page lists questions we have about your paper. The numbers displayed at left can be found in the text of the paper for reference. In addition, please review your paper as a whole for corrections.

AQ1: Au: Please clarify page range.

AQ2: Au: Please provide publisher location.

TABLE OF CONTENTS LISTING

The table of contents for the journal will list your paper exactly as it appears below:

Holographic Measurement of a Tooth Model and Dental Composite Contraction

Dejan Pantelić¹, Svetlana Savić-Šević¹, Darko Vasiljević¹, Branka Murić¹, Larisa Blažić², Marko Nikolić¹, and Bratimir Panić¹

Holographic Measurement of a Tooth Model and Dental Composite Contraction

DEJAN PANTELIĆ¹, SVETLANA SAVIĆ-ŠEVIĆ¹, DARKO VASILJEVIĆ¹, BRANKA MURIĆ¹, LARISA BLAŽIĆ²,
MARKO NIKOLIĆ¹, AND BRATIMIR PANIĆ¹

¹*Institute of Physics, Zemun, Belgrade, Serbia*

²*University of Novi Sad, Faculty of Medicine, Dental Clinic, Novi Sad, Serbia*

We have developed a real-time holographic technique to observe deformation induced by dental composite contraction. The standard split beam method was used, in conjunction with in situ holographic plate processing. Experiments were performed on a mechanical model of a human tooth with cavity. A silicone mold was used to manufacture a number of identical casts, using photoactivated composite. A LED lamp was used to induce photo-polymerization reaction in a composite. We have shown that the proposed method is ideal to analyze various polymerization strategies, with the purpose of recommending one which minimizes the polymerization contraction.

Keywords Composites; Holographic interferometry; Polymerization contraction.

INTRODUCTION

Photo-activated composites are widely used during dental restorative procedures. In that respect they have almost replaced amalgam fillings. Composites are composed of a polymer matrix (resin) and photo-initiator (mostly camphorquinone) filled with powder of a hard solid substance [1]. Before polymerization, they are viscous (in some cases thixotropic) fluids which solidify upon irradiation with blue light (around 470nm wavelength). The resulting solid is hard and, if properly applied, it forms impermeable bond with healthy dental tissues. It mimics tooth in mechanical and optical properties, satisfying both medical and esthetic requirements [2, 3].

There is a problem of contraction, connected with the polymerization process. Contraction induces certain amount of stress, which is transferred to surrounding dental structures. Great effort is undertaken to find new materials with reduced polymerization shrinkage [4]. Also, different polymerization methods are devised in order to relieve and reduce the associated stress [5, 6].

It is common to study the contraction both theoretically (using finite elements method or FEM) and experimentally. There is a great body of literature dealing with many aspects of composite polymerization. Composites are studied inside dental cavities or separately. Contraction was investigated experimentally by using mechanical (using pressure or deformation transducers) or optical methods (interferometry, photo-elasticity) [7, 8].

We have previously proposed using holographic interferometry as a tool to observe effects of polymerization contraction on dental tissues [9, 10]. We have found

that deformation induced by composite contraction can be effectively measured, giving the information about deformation field. Stress was calculated using FEM, and an appropriate digital tooth model.

During our previous experiments we faced two problems. The first is connected with natural variability of real human tooth samples. It is, therefore, necessary to use a large number of teeth, to test the effectiveness of particular polymerization scheme. Apart from the problem of obtaining the required number of teeth, there is always a large statistical variability of results. We have decided to use a mechanical model of a tooth in order to eliminate the problem of variability of tooth samples, and to simplify calculations in FEM.

The second problem is connected with the classical holographic setup, which enables observation of one tooth side only. The other surface remains completely hidden. Therefore, we have modified our holographic setup, by placing a tooth in front of a spherical mirror. It produced real, inverted image of the other tooth surface. If positioned appropriately, both an object and its (unit magnification) image can be observed simultaneously, side by side.

Previously described modifications enabled us to observe the effects of polymerization contraction in more details.

MECHANICAL TOOTH MODEL

Mechanical analysis of dental tissues was previously performed in three main ways: using real human teeth, animal teeth or mechanical models made of appropriate artificial material (like epoxy resins and methacrylates in photo-elasticity). We have decided to use a dental composite, since it mimics (to a certain extent) tooth tissue in its mechanical and optical properties. An Mesio-Ocluso-Distal (MOD) cavity was drilled in an intact, real, human third molar. The crown part of this particular tooth was used to produce a silicone mold. We decided not to produce a model of the whole tooth, since our previous

Received September 8, 2008; Accepted January 23, 2009

Address correspondence to Dejan Pantelić, Institute of Physics, Pregrevica 118, Zemun, Belgrade 11080, Serbia; E-mail: pantelic@atom.phy.bg.ac.yu

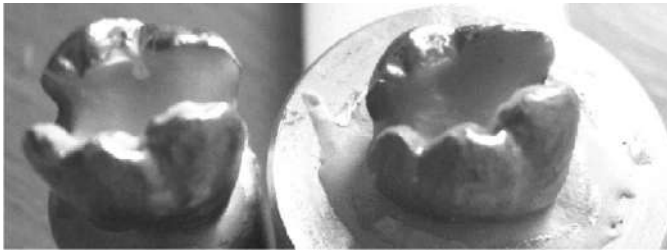


FIGURE 1.—Human molar with MOD cavity (left) and its mechanical model made of dental composite (right). They are both painted with silver paint, as required in holography.

research has shown that the polymerization contraction is localized only within the tooth cusp. A silicone mold was filled with a commercial dental composite (Gradia direct anterior, manufactured by GC America Inc.). According to manufacturer (GRADIA DIRECT Technical Manual version 1.12, March 2006), 27% by weight is composed of methacrylate monomers, 38% silica particles ($0.38\ \mu\text{m}$), and 35% prepolymerized filler. Composite was polymerized using commercial blue polymerization light source (LEDition, manufactured by Ivoclar Vivadent). A real tooth and its model are shown in Fig. 1.

Due to the stability requirements of holographic setup, a tooth model was placed in an aluminum holder and kept in place by dental plaster. Also, outside surface of a model had to be painted with silver paint in order to reflect the light only from the surface.

Dental composites have somewhat different properties compared to dentine and enamel. Elasticity modulus of various composites is within the range of 4–15 GPa [11]. Modulus of dentine ranges from 20–30 GPa [12] and enamel from 32–95 GPa [13].

EXPERIMENTAL SETUP AND PROCEDURE

We decided to use a real time holographic setup, in order to observe the dynamics of polymerization contraction, and its influence on a tooth model (Fig. 2). Long coherence length, 100 mW output power, 532 nm wavelength, laser was used as a light source. Its beam was split into two parts. One was used to illuminate the holographic plate, after passing through the diverging lens (reference beam). The other beam illuminated the object (a tooth model in our case).

A model was placed at the centre of curvature ($2f$ position, where f is a focal distance) of a spherical mirror. One part of the object beam illuminated the front surface of a model. The light missing the object reflected from the spherical mirror and illuminated back side of the model. Scattered radiation produced a mirror image placed at the same distance as the object. By slightly offsetting the model from the optical axis, both object and its spherical mirror image could be observed simultaneously (Fig. 3).

A model had to be painted with silver paint (UniPaint silver marker PX-20, manufactured by Mitsubishi Pencil Co., Ltd.). If left unpainted, the radiation would penetrate the model and scatter from inner layers of dental composite. During polymerization contraction, scattered beam would

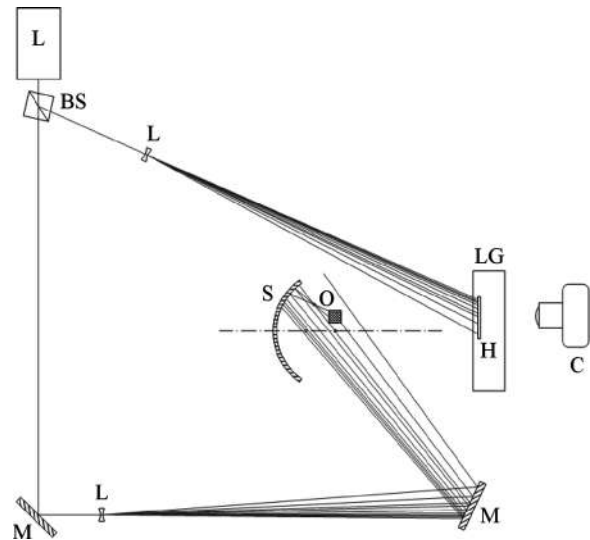


FIGURE 2.—A real time holographic setup: L = laser, BS = beam splitter, L = diverging lens, M = folding mirror, S = spherical mirror, O = object, LG = liquid gate, H = holographic plate, C = CCD camera. k_1 is illumination vector, while k_2 is observation vector.

significantly change its local speckle structure, compared to the beam scattered from the model before the contraction. This would make interference fringes almost invisible. Therefore, it is necessary to use the paint which prohibits light penetrating beneath the surface.

Real time holography is based on producing hologram of an undisturbed object, and observing the object through the hologram when mechanical loads are applied. The resulting picture is a result of interference of the wave-front reflected from the object itself, and the beam reconstructed from the hologram. In this way, hologram represents a “frozen” picture of an object in its initial state. Any further mechanical change of the object is seen as a series of fringes on its surface.

The consequence of these requirements is that the holographic plate must be fixed in space to the fraction of a micrometer during the whole experiment. This problem is



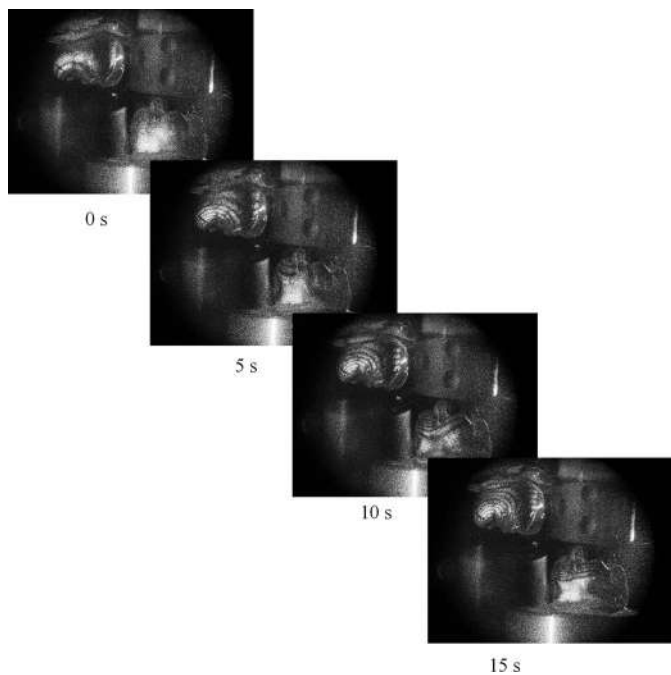
FIGURE 3.—An object (a dice on the right side) and its image in a spherical mirror (on the left). Observe that both front and back side of the same object are seen.

123 solved by making the complete holographic film processing
 124 in place, by using so-called liquid gate. This is a container
 125 with transparent, glass, walls where the holographic plate is
 126 placed, exposed, and chemically processed, without moving.

127 We used home-made liquid gate, where holographic
 128 plates (VRP-M, green sensitive, manufactured by Slavich,
 129 Russia) were processed using a simple procedure.
 130 A holographic plate is placed in a liquid gate, and soaked
 131 in darkness for 4 minutes in distilled water. This is done in
 132 order to leave the gelatin photosensitive layer enough time
 133 to swell, so that the layer thickness before and after the
 134 processing is the same. This is important, since the gelatin
 135 swelling results in the change of the recorded interference
 136 fringe period. As a consequence, the recorded wave-front is
 137 no longer identical to the object. In that case, two interfering
 138 waves in holographic interferometry might be so different
 139 that interference pattern cannot be observed.

140 Further, the film is exposed through the water filled, liquid
 141 gate and consequently developed in Ilford ID-11 developer
 142 (equivalent to Kodak D-76) for 30 s. The film is washed in
 143 distilled water twice, and left in the final water rinse. The
 144 fixing step is omitted since it can affect the holographic
 145 emulsion thickness. Even without fixing, we could observe
 146 the high quality holographic image for several days, with
 147 room lighting fully lit.

148 As a final result, we could observe both the object and
 149 its holographically reconstructed image. If a load is
 150 applied, interference fringes appear on the object, and can
 151 be recorded using a CCD camera. In our case a tooth
 152 model is observed. Its MOD cavity is filled with dental
 153 composite (the same one used in model manufacture), and
 154



155
156
157
158
159
160
161
162
163
164
165
166
167
168
169
170
171
172
173
174
175
176
177
178
179
180
181
182
183
FIGURE 4.—Temporal sequence of the interference pattern produced by dental filling polymerization. A tooth model is on the right left corner, while its inverted image is in the upper left corner. The tip of the polymerization lamp is in the upper right corner, and its image is in the lower left.



FIGURE 5.—The final interference pattern observed on a tooth model, after 120 s of polymerization. As in previous figure, a tooth model is on the right bottom part of a photograph, while its image is on the upper left. Polymerization LED light source is on the upper right corner, while its image is on the lower left.

154
155
156
157
158
159
160
161
162
163
164
165
166
167
168
169
170
171
172
173
174
175
176
177
178
179
180
181
182
183
polymerized with LED lamp. Polymerization contraction applies the load from inside the cavity. As a consequence, interference fringes start appearing at the tooth model cusp and propagate downwards. Temporal sequence during the first 15 s of polymerization is shown in Fig. 4, and the final fringe pattern, after 120 s of polymerization, is shown in Fig. 5.

The distance between two consecutive fringes corresponds to a certain deformation, which is determined by the angle between illumination (\vec{k}_1) and observation (\vec{k}_2) direction, as well as the object displacement vector (\vec{L}) [14, 15]. The displacement ($|\vec{L}|$) corresponding to one wavelength (λ) fringe shift, can be found from a scalar product equation:

$$\lambda = (\vec{k}_1 - \vec{k}_2) \cdot \vec{L}.$$

If applied to our case (532 nm wavelength, angle between the observation and illumination direction is 47 degrees, and displacement vector is collinear with the observation), two consecutive fringes correspond to deformation of 722 nm.

RESULTS AND DISCUSSION

Based on the sequence of photographs recorded during the course of experiment, we were able to observe the deformation of each point on the model surface. Graph in Fig. 6 shows how many fringes appeared at the

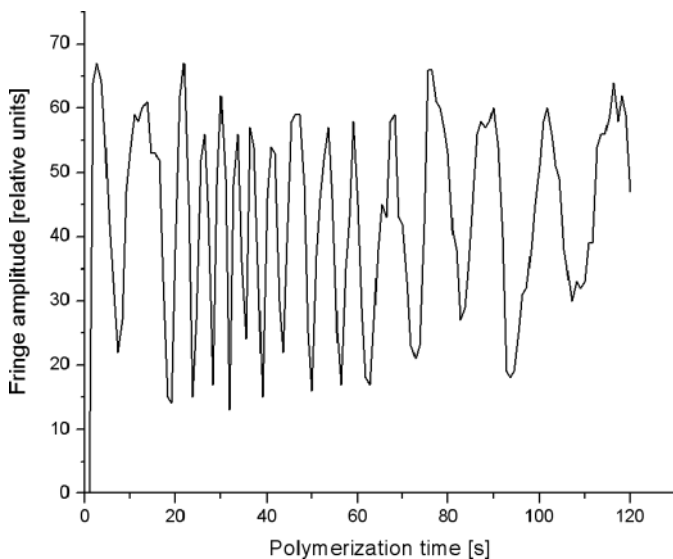


FIGURE 6.—Dynamics of fringe appearance at a tooth cusp. There are 16 fringes at the end of 120s period. Each peak in the graph corresponds to additional deformation of 722 nm. The final deformation after 120s is 11.6 μm .

model cusp. By multiplying the number of maxima in a graph with 722 nm (a distance corresponding to two consecutive fringes), a total deformation can be calculated (11.552 μm).

Results obtained using mechanical model of a tooth are of the same order as in previous research [9, 10]. Real human teeth were used and it was found that cuspal deformation lies within the 5–7 μm range. Difference between model and real tooth deformation can be attributed to difference in mechanical properties of human dentine and dental composite. Anyway, fringe shape and orientation is almost the same irrespective whether we study a tooth or its composite model. This signifies that the stress distributions are almost the same, except for the scaling factor, resulting from difference in elastic modulus.

The dynamics of the polymerization process was observed, too. For the first ~ 20 s fringes appear slowly, corresponding to initialization of photochemical reactions. During that period, composite is still viscous and capable of flowing under the action of contraction forces. The contraction accelerates during the next 40–50 s, as the composite solidifies. The process slows down towards the end of illumination, which is the sign of completion of polymerization.

We made particular attention to two different methods of polymerization. One is quick, using high irradiance (500 mW/cm^2) light source. The other is slow—using 80 mW/cm^2 polymerization lamp. Both light sources are based on blue LED lamps. Irradiation times were adjusted so that energy density transmitted to composite was the same ($\sim 15000 \text{ mJ}/\text{cm}^2$) for both lamps.

Both polymerization methods were analyzed by the method previously described in this article. An interesting result is that, slower method, with low power density source is preferable. The resulting deformation (and consequent stress) is 50% lower, compared to quick, high intensity, irradiation.

Explanation for the observed fact is that during slow polymerization, composite can flow for the first 5–10 seconds (before solidification). This relieves the stress inside the composite, without transferring it to cavity walls. On the contrary, if power density is too large, polymer is solidified too quickly, without having chance to flow. We can conclude that slower methods should be preferred in dental practice.

CONCLUSIONS

We have found that dental composites can be effectively used to manufacture mechanical model of a tooth. The model mimics tooth geometry as well as its mechanical and optical properties. The manufacturing process is fast and a number of identical copies can be manufactured. Composite models are ideal for the study of various dental procedures, since the effects of human tooth variability are excluded. Also, there are no ethical questions arising. In our case, a model was used to analyze the effect of polymerization contraction on dental structures. We have shown that holographic interferometry can be used to observe the deformation of a tooth model in real-time. The deformation field can be recorded, from both sides of an object, thus fully characterizing the deformation field. Also, the dynamical effects can be easily recorded and analyzed. Based on experimental results, preferred irradiation strategies can be suggested. Current developments of digital holographic techniques as described in [16, 17] could provide further access to additional quantitative data and parameters.

ACKNOWLEDGMENT

This research was funded by the Serbian Ministry of Science and Technological Development, under the contract No. 141003.

REFERENCES

1. Ferracane, J.L. Current trends in dental composites. *Crit. Rev. Oral. Biol. Med.* **1995**, *6*, 302–318.
2. Manhartl, J.; Kunzelmann, K.-H.; Chen, H.Y.; Hickel, R. Mechanical properties and wear behavior of light-cured composite resins. *Dental Materials* **2000**, *16*, 33–40.
3. Lee, Y.-K.; Lim, B.-S.; Kim, C.-W. Difference in the colour and colour change of dental resin composites by the background. *Journal of Oral Rehabilitation* **2005**, *32*, 227–233.
4. Condon, J.R.; Ferracane, J.L. Reduced polymerization stress through non-bonded nanofiller particles. *Biomaterials* **2002**, *23*, 3807–3815.
5. Kuijs, R.H.; Fennis, W.M.M.; Kreulen, C.M.; Barink, M.; Verdonchot, N. Does layering minimize shrinkage stresses in composite restorations? *J. Dent. Res.* **2003**, *82*, 967–971.
6. Lim, B.-S.; Ferracane, J.L.; Sakaguchi, R.L.; Condon, J.R. Reduction of polymerization contraction stress for dental composites by two-step light-activation. *Dental Materials* **2002**, *18*, 436–444.
7. Braga, R.R.; Ferracane, J.L. Alternatives in polymerization contraction stress management. *Crit. Rev. Oral. Biol. Med.* **2004**, *15*, 76–184.
8. Sato, T.; Miyazaki, M.; Rikuta, A. Real-time dimensional change in light-cured composites at various depths using laser speckle contrast analysis. *Eur. J. Oral. Sci.* **2004**, *112*, 538–544.

- 245 9. Pantelić, D.; Blažić, L.; Savić-Sević, S.; Panić, B. Holographic
246 detection of a tooth structure deformation after dental
247AQ1 polymerization. *J. Biomed. Opt.* **2007**, *12*, 024026.
- 248 10. Pantelić, D.; Blažić, L.; Savić-Sević, S.; Murić, B.; Vasiljević, D.;
249 Panić, B.; Belić, I. Real-time measurement of internal stress of
250 dental tissue using holography. *Opt. Express*, **2007**, *15*, 6823–6830.
- 251 11. Chung, S.M.; Yap, A.U.J.; Tsai, K.T.; Yap, F.L. Elastic modulus
252 of resin-based dental restorative materials: a microindentation
253 approach. *J. Biomed. Mater. Res. Part B: Appl. Biomater.* **2005**,
254 *72B*, 246–253.
- 255 12. Senawongse, P.; Otsuki, M.; Tagami, J.; Mjor, I. Age-related
256 changes in hardness and modulus of elasticity of dentine.
257 *Archives of Oral Biology.* **2006**, *51*, 457–463.
- 258
- 259
- 260
- 261
- 262
- 263
- 264
- 265
- 266
- 267
- 268
- 269
- 270
- 271
- 272
- 273
- 274
- 275
- 276
- 277
- 278
- 279
- 280
- 281
- 282
- 283
- 284
- 285
- 286
- 287
- 288
- 289
- 290
- 291
- 292
- 293
- 294
- 295
- 296
- 297
- 298
- 299
- 300
- 301
- 302
- 303
- 304
- 305
13. Hea, L.H.; Fujisawab, N.; Swain, M.V. Elastic modulus and
stress–strain response of human enamel by nano-indentation.
Biomaterials. **2006**, *27*, 4388–4398.
14. Hariharan, P.; Oreb, B.F.; Brown, N. Real-time holographic
interferometry: a microcomputer system for the measurement of
vector displacements. *Appl. Opt.* **1983**, *22*, 876–880.
15. Vest, C.M. *Holographic Interferometry*; Wiley-Interscience, AQ2
1979.
16. Schnars, U.; Jueptner, W. *Digital Holography, Digital Hologram
Recording, Numeric Construction, and Related Techniques*;
Springer-Publishing, 2005. AQ2
17. Kreis, T. *Handbook of Holographic Interferometry, Optical and
Digital Methods*; Wiley-VCH, 2006. AQ2

Micro- and Nanostructures of Iridescent Wing Scales in Purple Emperor Butterflies (Lepidoptera: *Apatura ilia* and *A. iris*)

SREĆKO B. ĆURČIĆ,^{1*} DEJAN V. PANTELIĆ,² BOŽIDAR P.M. ĆURČIĆ,¹ SVETLANA N. SAVIĆ-ŠEVIĆ,² SLOBODAN E. MAKAROV,¹ VESNA B. LAČKOVIĆ,³ MILICA M. LABUDOVIĆ-BOROVIĆ,³ NINA B. ĆURČIĆ,⁴ AND DEJAN V. STOJANOVIĆ⁵

¹Institute of Zoology, Faculty of Biology, University of Belgrade, Studentski Trg 16, 11000 Belgrade, Serbia

²Institute of Physics, University of Belgrade, Pregrevica 118, 11080 Zemun, Serbia

³Institute of Histology and Embryology, Faculty of Medicine, University of Belgrade, Višegradska 26, 11000 Belgrade, Serbia

⁴Geographical Institute “Jovan Cvijić”, Serbian Academy of Sciences and Arts, Đure Jakšića 9, 11000 Belgrade, Serbia

⁵Fruška Gora National Park, Zmajev Trg 1, 21208 Sremska Kamenica, Serbia

KEY WORDS *Apatura ilia* and *A. iris*; Purple Emperor butterflies; SEM; TEM; wing scale morphology

ABSTRACT *Apatura ilia* (Denis and Schiffermüller, 1775) and *A. iris* (Linnaeus, 1758) are fascinating butterflies found in the Palaearctic ecozone (excepting the north of Africa). The wings of these insects are covered with a great number of two types of scales positioned like roof tiles. Type I scales are on the surface, while type II scales are situated below them. The structural color of the type I scales is recognized only on the dorsal side of both the fore and hind wings of the males of the aforementioned species. Both types of scales are responsible for pigment color of the wings, but iridescence is observed only in the type I scales. The brilliant structural color is due to a multi-layer structure. The features of the scales, their dimensions and fine structure were obtained using scanning electron microscopy. Cross sections of the scales were then analyzed by transmission electron microscopy. The scales of the “normal” and *clytie* forms of *A. ilia* have a different nanostructure, but are of the same type. A similar type of structure, but with a different morphology, was also noticed in *A. iris*. The scales of the analyzed species resemble the scales of tropical *Morpho* butterflies. *Microsc. Res. Tech.* 75:968–976, 2012. © 2012 Wiley Periodicals, Inc.

INTRODUCTION

The diurnal representatives of the order Lepidoptera (butterflies) are thought to be very attractive insects. Iridescence features are present in numerous butterfly species, and in particular those inhabiting the tropics (Garrett et al., 2009; Matejková-Plšková et al., 2009; Prum et al., 2006; Shawkey et al., 2009; Srinivasarao, 1999; Vukusic, 2006; Vukusic and Sambles, 2003; Vukusic et al., 1999). Some butterflies are mimetic, camouflaged, and therefore unattractive and invisible to potential predators. Others have visible aposemy and therefore have warning coloration. Sexual dimorphism is present in some taxa, like in the *Apatura* species.

Apart from structural coloration, pigment coloration is also present in the butterfly species. Coloration in butterflies is due to several physical effects. Selective absorption and fluorescence are the consequence of the chemical properties of chitin and various pigments. On the other hand, interference, diffraction, and scattering produce coloration due to the micro- and nanostructure of the cuticle. Structural color investigations in butterflies have been intensive and diverse in the last period (Ghiradella, 1989, 1991, 1998; Ghiradella et al., 1972). The following features are the most interesting in these studies: the optical properties of scales and their nanostructure (Birø et al., 2007; Han et al., 2009; Srinivasarao, 1999; Vártesy et al., 2006), diffraction

and interference in butterflies (Vukusic et al., 1999), ultraviolet reflection (Imafuku et al., 2002), brightness (Stavenga et al., 2004) and blackness of butterfly scales (Vukusic et al., 2004), fluorescence (Vukusic and Hooper, 2005), coherent scattering-induced structural color of scales (Prum et al., 2006), light scattering and absorption of scales (Morehouse et al., 2007), possible role of scales in artificial material manufacturing (Kertész et al., 2008), measuring and modeling of the optical properties of scales (Luke et al., 2009), and optical reflectors in butterflies (Vukusic et al., 2009). The coloration of the ventral side of the wings originated from pigments and is not structural.

The species *Apatura ilia* (Denis and Schiffermüller, 1775) includes a total of six subspecies and is represented by two phenotype forms: *ilia* or “normal” form (the darker one) and *clytie* (the lighter one) (Higgins and Riley, 1970). The presence of these forms depends on the type of habitat and climate (Lafranchis, 2004;

*Correspondence to: Srećko Ćurčić, Institute of Zoology, Faculty of Biology, University of Belgrade, Studentski Trg 16, 11000 Belgrade, Serbia. E-mail: srecko@bio.bg.ac.rs

Received 2 December 2011; accepted in revised form 13 January 2012

Contract grant sponsor: Serbian Ministry of Education and Science; Contract grant numbers: ON173038, ON171038, III45016, III41002, III47007, III43002.

DOI 10.1002/jemt.22021

Published online 6 March 2012 in Wiley Online Library (wileyonlinelibrary.com).

Tolman and Lewington, 1997). It was proven that the “normal” form of the species is present in cooler regions, where larval development is generally longer. On the other hand, the form *clytie* is found in warmer habitats, where the larvae develop faster. These forms are treated as two distinctive subspecies by some authors (Jakšić, 2003). The so-called “normal” form of the Lesser Purple Emperor (*Apatura ilia*) is very similar to the Purple Emperor (*A. iris*). These are distinguishable by the underside wing pattern and by the extra eye spot on the dorsal side of the fore wing. The form *clytie* of *Apatura ilia* is generally common as well. This form has more extensive pale markings on the upper side of the wings that are yellow or buff, not white. It is very similar to the Freyer’s Purple Emperor (*Apatura metis* Freyer, 1829).

The species *Apatura iris* (Linnaeus, 1758) comprises four subspecies. The dorsal side of the wings in males has violet reflection.

The occurrence of iridescence in *Apatura* spp. is known, but insufficiently studied (Han et al., 2008; Vértsey et al., 2007). The authors analyzed the phenomenon in *Apatura ilia* f. *clytie* (Han et al., 2008), but very rarely in the “normal” form of the species (Vértsey et al., 2007). Until very recently, *Apatura iris* has not been studied at all. In our previous article, we started a study of its optical properties and this article is an in-depth analysis of biological significance of submicron structures of *Apatura* spp. (Pantelić et al., 2011).

Apatura species are characterized by the basic pigment color and intensive iridescence in the UV region of the spectrum. The males of *Apatura* spp. have iridescent color on the dorsal side of the wings. The role of this characteristic is probably in the intrasexual communication between males (i.e., territorial behavior of the butterflies), rather than intersexual communication and attraction (Silberglied, 1984). The male individuals of *Apatura* species can be easily noticed by the wing iridescence in their habitats. The flight behavior of the male *Apatura iris* was recently studied, and it consisted mainly of conspecific and patrol flights within the continuum from perching to patrolling (Page, 2010). The daily aggregation of males at favored landmark sites from around midday was observed as well (Page, 2010). The structural color of the wings in males is visible in their flight. The iridescence of the wings is noticeable at certain angles during wing movements. During flight, the color of the dorsal side of the wings changes from violet-blue to brownish.

Two types of scales are present on the dorsal side of the wings of the *Apatura ilia* form *clytie* (Han et al., 2008). These scales cover the wing surface like tiles on a roof. Each of the scales possesses parallel ridges. About 1,200 ridges per millimeter are situated on the surface of the first type of scale. On the second type, there are about 700 ridges per millimeter. Cross ribs connect adjacent ridges. Type I scales are iridescent, while type II are not. The ventral side of the wings is without iridescence. The second type of scale is mostly situated ventrally, but is also present dorsally on the wings, below type I scales. The iridescent effect of the scales is caused by the presence of the first type of scale (Han et al., 2008). From the transverse section of the first type of scale, we can see that they are composed of multilayer-structured ridges. Each ridge comprises

about 10 cuticle layers mutually separated by an air layer. The cuticle layers are thicker than the air layers. The mentioned structures enable the structural coloration of the wings due to Bragg diffraction.

The article presents full information on wing scale micro- and nanostructures related to wing color in the given species, as well as in both forms of *Apatura ilia* observed by high resolution scanning electron microscopy (SEM) and transmission electron microscopy (TEM).

Analyzed Species

The species considered herein belong to the subfamily Apaturinae, family Nymphalidae, of butterflies. These butterflies are of medium to large dimensions (wingspan 50–70 mm). The thorax is massive and the wings are strong. The genus *Apatura* Fabricius, 1807 comprises a total of four species, among which three are present in Europe: *Apatura ilia*, *A. iris*, and *A. metis*. Sexual dimorphism is clearly noticeable. The dorsal side of the male wings of *Apatura* butterflies is of violet-blue iridescent hue. This hue is caused by optical interference (Pantelić et al., 2011). Additional difference between the sexes is found in the structure of their fore legs that are larger in females, with five tarsomeres, while in males there are three tarsomeres.

***Apatura ilia* (Denis and Schiffermüller, 1775) (Fig. 1a).**

Total Distribution. Inhabits the areas of Central and Southern Europe, the Caucasus Mountains, the southern part of the Urals, south-western Kazakhstan, and north-eastern China.

Short Description. Wingspan: 50–60 mm. “Normal” form: the dorsal side of the fore wings has a well-defined eye-shaped spot. Both dorsal and ventral sides of the hind wings have a slightly curved white strip each. Ventral side of the fore wings: the cell has two two-point shaped black spots. Form *clytie*: the dorsal side of the fore wings: orange postdiscal strip not prolonged to the apex. Dorsal side of the hind wings: postdiscal row of points well developed, without pale points. Ventral side of the hind wings: postdiscal points well distinguished, the lower one being eye-shaped, blue. Females are usually bigger, with elongated white spots. Their iridescence was not observed.

Flight Period. Two generations per year exist in southern regions—May–June and August–September, but only one in northern areas—July (Higgins and Riley, 1970; Lafranchis, 2004; Tolman and Lewington, 1997).

***Apatura iris* (Linnaeus, 1758) (Fig. 1b).**

Total Distribution. Lives in Central Europe, north-western Kazakhstan, southern Urals, Amur region, north-eastern China, and Korea.

Short Description. Wingspan: 58–70 mm. The dorsal side of the fore wings is without eye-shaped spots. Both dorsal and ventral sides of the hind wings have a straight white strip each. Ventral side of the fore wings: the cell has two compact black spots. The female is usually bigger, without iridescence, with extended white spots on dorsal side of the wings.

Flight Period. May–June and August–September. Two generations per year in southern and one in northern parts of Europe (Higgins and Riley, 1970; Lafranchis, 2004; Tolman and Lewington, 1997).

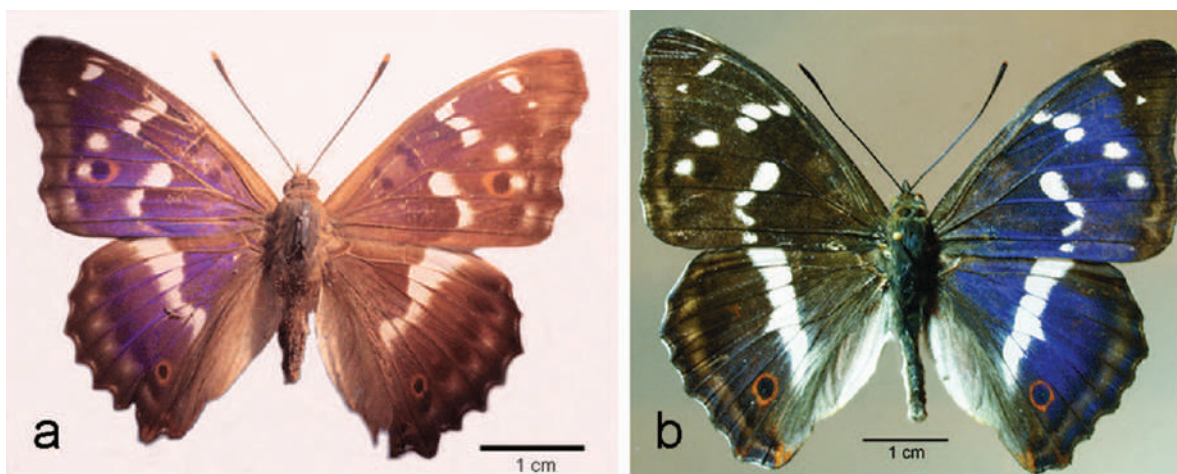


Fig. 1. The Purple Emperor butterfly species analyzed. Optical microscopy images of body habitus of "normal" form of *Apatura ilia* (Denis and Schiffermüller, 1775) (a) and of *A. iris* (Linnaeus, 1758) (dorsal views) (b). [Color figure can be viewed in the online issue, which is available at wileyonlinelibrary.com.]

MATERIALS AND METHODS

Data Collection

Specimens of the species *Apatura ilia* and *A. iris* were used for fine morphological investigations of the wings. Both species were collected from the Balkan Peninsula: *Apatura ilia* ("normal" form)—Mt. Fruška Gora, northern Serbia (July 2009, leg. D. Stojanović), and *A. iris*—Mt. Stara Planina, south-eastern Serbia (July 2009, leg. D. Stojanović). The butterflies were killed by pressing their thorax between the fingertips. The specimens were kept in entomological boxes belonging to the collection of the Institute of Zoology, Faculty of Biology, University of Belgrade (Figs. 1a and 1b).

SEM Procedure

Two specimens of *Apatura ilia* and two specimens of *A. iris* were rinsed by diethyl ether to obtain a clear surface of the wings. The wings of the males were cut to form squares with a surface of 1 mm². This was followed by dehydration to get dry samples. These were fixed on test-beds and subsequently covered with gold. The prepared samples were analyzed using a tungsten-filament scanning electron microscope (JSM-6460LV, JEOL, Tokyo, Japan). During the microscopy, a 20-kV voltage was used.

TEM Procedure

The wings were cut into small pieces. The tissue was fixed by immersion in 3% solution of glutaraldehyde in 0.1 mol/dm³ cacodylic buffer (pH = 7.4) over night at +4°C. The cacodylic buffer was prepared as an aqueous solution of cacodylic acid sodium salt trihydrate (C₂H₆AsO₂Na × 3 H₂O). Thereafter, the tissue samples were carefully rinsed with cacodylic buffer and postfixated in 1% solution of osmium tetroxide (OsO₄) in 0.1 mol/dm³ cacodylic buffer for 1 h at +4°C. The tissue was then rinsed in cacodylic buffer and incubated over night at +4°C in a 4.8% aqueous solution of uranyl acetate.

The tissues were dehydrated in graded ethanol aqueous solutions. First, 50% ethanol was used for 5 min at room temperature. Thereafter, the tissues were treated

with 70% ethanol for 30 min at +4°C, and with 96% ethanol (Gram, Belgrade, Serbia) for 30 min at +4°C. Afterward, 100% ethanol (Zorka Pharma, Sabac, Serbia) was applied three times for 10 min at room temperature. The tissues were then cleared by propylene oxide (C₃H₆O; SERVA 33715, Heidelberg, Germany) twice for 10 min at room temperature. During the procedure, the tissues were continuously and completely immersed into the described chemicals. Potential air drying of tissues was avoided with special caution. Ethyl alcohol solutions of 50% and 70% were made from 100% ethanol.

After the dehydration procedure, the samples were embedded in a four-component embedding medium made of: (i) epoxy embedding medium (Fluka Chemika 45345, Buchs, Germany), (ii) dodecyl succinic anhydride (C₁₆H₂₆O₃; Fluka Chemika 45346), (iii) Epon hardener methyl nadic anhydride (C₁₀H₁₀O₃; Fluka Chemika 45347), and (iv) Epon hardener accelerator *n*-benzyl dimethylamine [C₆H₅-CH₂-N(CH₃)₂; Agar Scientific R1062b, Stansted, United Kingdom]. Embedding of the tissue through polymerization of the medium was done at +60°C for 36–48 h.

The blocks of embedded tissue were sectioned by an ultramicrotome (Leica Ultracut UCT, Vienna, Austria). First, semithin 1-μm-thick sections were cut, stained with toluidine blue, and analyzed by an Olympus BX41 microscope (Olympus GmbH, Hamburg, Germany). All the slides were photo-documented by an Olympus C—5060 ADU wide zoom camera and the Olympus DP-soft Image Analyzer programme (Olympus GmbH).

Thereafter, the ultrathin sections were sampled from chosen representative areas. The ultrathin sections were treated with uranyl acetate [(CH₃COO)₂UO₂ × 2 H₂O] and lead citrate [Pb₃(C₆H₅O₇)₂ × 3 H₂O], and were analyzed by TEM (Fei Morgagni 268D transmission electron microscope, Eindhoven, The Netherlands). The transmission electron microscope was equipped with a MegaViewIII Soft Imaging System digital camera (Olympus Soft Imaging Solutions GmbH, Münster, Germany).

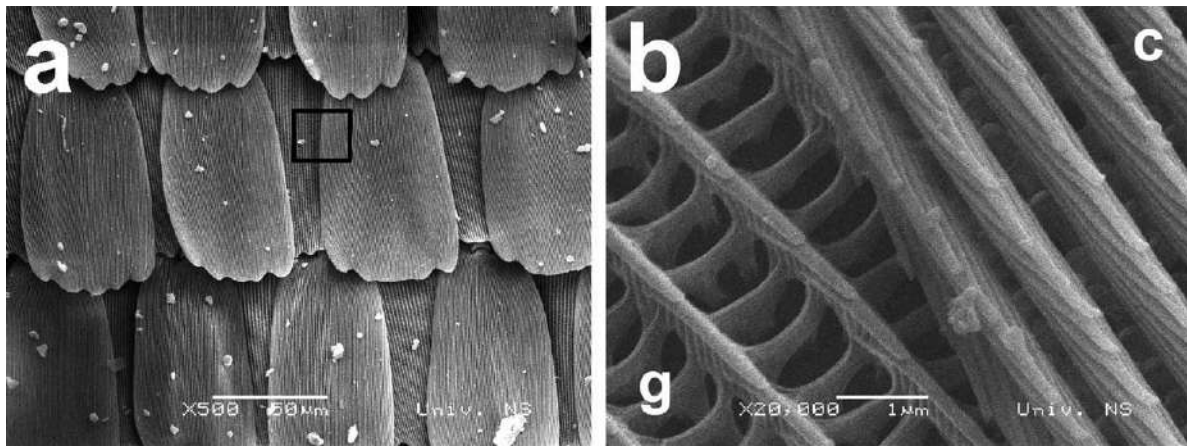


Fig. 2. SEM images of scales of upper surface of wing of *Apatura ilia* (dorsal view) at lower (a) and higher magnifications (b). The parts of cover (c) and ground scales (g) are marked by a rectangle and enlarged (b).

RESULTS

Location, General and Fine Structure, and Morphometric Measurements of Scales in *Apatura ilia*

We recognized two types of scales on the dorsal side of both the fore and hind wings of the “normal” form of *Apatura ilia*. All the scales are positioned like roof tiles and possess parallel ridges covering the entire dorsal side. Type I scales (cover scales) are on the surface, and type II scales (ground scales) are situated below them. The type I scales are $\sim 104\text{--}112\ \mu\text{m}$ long and $53\text{--}58\ \mu\text{m}$ wide (Fig. 2a). Han et al. (2008) reported that the type I scales in the *clytie* form of *Apatura ilia* are larger— $150\ \mu\text{m}$ long and $60\ \mu\text{m}$ wide. The type I scales are responsible for the violet-blue iridescence of *Apatura ilia* (Pantelić et al., 2011). Iridescent violet-blue can be seen on the whole dorsal wing surface in males and is observed in narrow angular range. These scales are pale brown, with melanin, reflecting violet-blue iridescence on their surfaces. The ones in white spots of the wings are almost the same in shape and structure except the color, which is transparent and lustrous white due to lack of pigment. The type II scales are pigmented, but without reflective effects. Their apical border mostly has five projections.

The ridges on the type I scales are mutually closer (about $680\ \text{nm}$) than the same structures on the scales of type II (distance $1.23\text{--}1.35\ \mu\text{m}$). The ridges of the type I scales are $0.50\ \mu\text{m}$ wide, while the ridges situated on the type II scales are $0.27\ \mu\text{m}$ wide. About 1,500 ridges are present per millimeter on the surface of the type I scales (vs. about 1,200 ridges per millimeter in the form *clytie*), while there are about 700 ridges per millimeter on the surface of the type II scales (like in the form *clytie*; Han et al., 2008). Each pair of ridges from the type II scale is connected by cross ribs (Fig. 2b). Lamellae on the ridges of the type I scales are dorsally subtriangular, overlap, and form the multilayer structure responsible for iridescence (Fig. 2b; Pantelić et al., 2011). Lamellae exist dorsally on the ridges of the type II scales as well, but these are subcylindrical, slightly widened basally, only partly

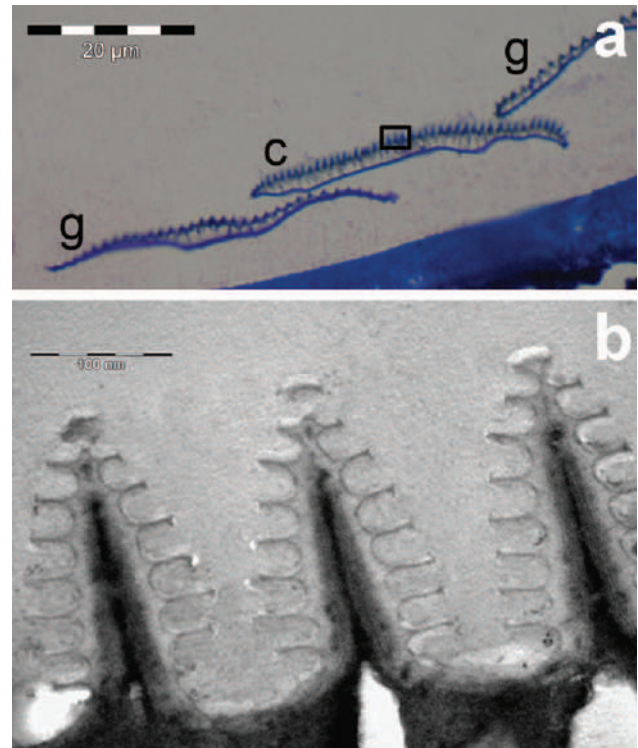


Fig. 3. Images of cross sections through wing scales in *Apatura ilia*. Optical microscopy image of semithin cross section through cover (c) and ground scales (g) (a). The lamellae are marked by a rectangle. TEM image of ultrathin cross section through longitudinal ridges of the cover scale, showing lamellae on the ridges (b). One-fifth of the whole scale line = $100\ \text{nm}$. [Color figure can be viewed in the online issue, which is available at wileyonlinelibrary.com.]

overlap, and do not produce structural coloration. The lamellae on the ridges of the type I scales of the “normal” form of *Apatura ilia* in lateral view have a visible multilayer structure, are conifer-like in cross section, with six-seven pairs of straight lateral projections widened distally, and are triangularly pointed (Figs. 3a and 3b). The whole interior of the ridges of

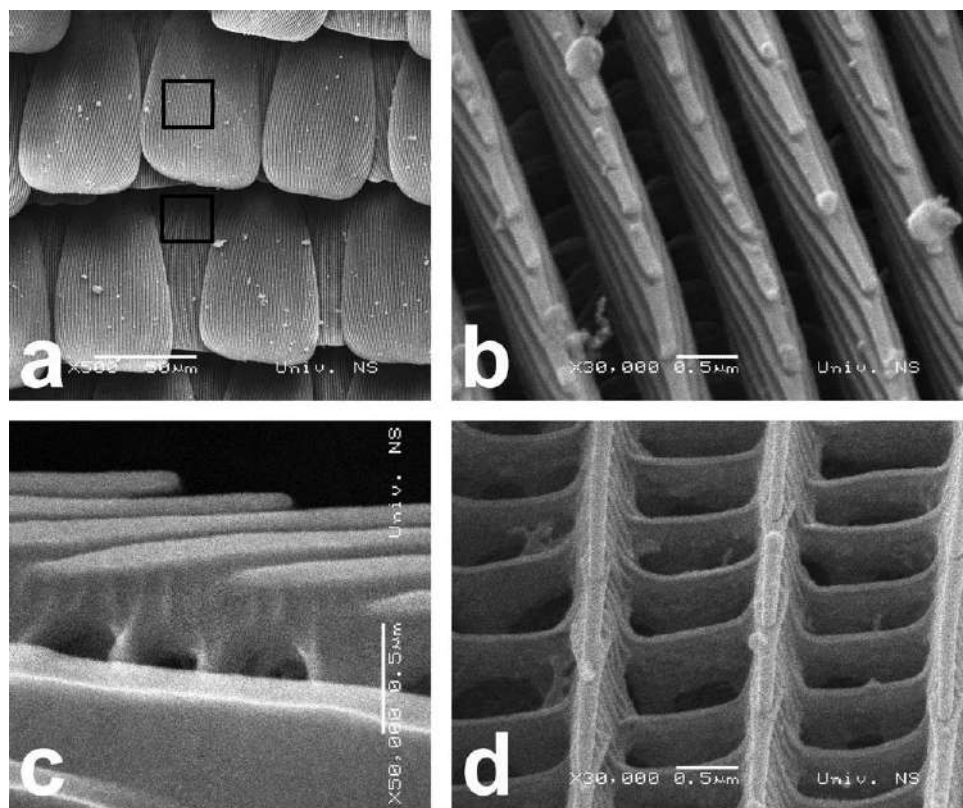


Fig. 4. SEM images of scales of upper surface of wing of *Apatura iris*. SEM image of scales of the upper surface of wing (dorsal view) (a). The parts of cover and ground scales are marked by rectangles. SEM images of lamellae of the cover scale in dorsal (b) and lateral views (c). SEM image of surface of ground scale (dorsal view) (d).

the type I scales is with a dark pigment and strongly melanized (Fig. 3b). The ventral wing surface is virtually flat, but small ridges are apparent on the lower surface, as seen in its cross section.

The micrographs of the TEM-photographed cross sections of the “normal” and *clytie* forms of *Apatura ilia* show clear distinctions between them: the lamellae of the “normal” form are higher, widening basally, with six/seven pairs of lateral projections; the lamellae of form *clytie* are lower, almost subparallel, with five/six pairs of lateral projections (Han et al., 2008; present study). The abovementioned morphological differences supported by the ecological preferences, other existing morphological differences, and our data provide additional support to the view that these forms may even be two distinct subspecies.

The type I scales of both forms of *Apatura ilia* have a role in iridescence due to their denser microscopic structure in comparison to the type II scales (Pantelić et al., 2011). The type I scales are numerous in the iridescent areas of the wings. There are no such scales on the pairs of female wings and on the non-iridescent areas of male wings, so that the color of these wings does not change when viewed from different angles. Type II scales are present both on the dorsal (below the type I scales) and ventral sides of the wings. They do not have iridescent features, but possess pigments.

Location, General and Fine Structure, and Morphometric Measurements of Scales in *Apatura iris*

Two types of scales are situated on the dorsal side of both the fore and hind wings in *Apatura iris* males. The scales here also look like roof tiles. They have parallel ridges situated dorsally. Analyzing the dorsal side of both wings in males, we registered type I scales (cover scales) on the surface with type II scales (ground scales) below them. The type I scales have a role in the violet-blue iridescence effects of *Apatura iris* (Pantelić et al., 2011). Iridescent violet-blue can be seen on the whole dorsal wing surface in males and is observed in narrow angular range. These scales are brown, with melanin, reflecting violet-blue iridescence on their surfaces. The ones in white spots of the wings are almost the same in shape and structure except the color, which is transparent and lustrous white due to lack of pigment. The type II scales are pigmented, but do not produce iridescence. The type I scales are ~ 95–100 μm long and 55–61 μm wide, somewhat shorter than in *Apatura ilia* (Fig. 4a). Their apical border is mostly straight or with three projections. The ridges on the scales are mutually closer (distance of about 820 nm vs. 680 nm in *A. ilia*) than the ridges on the scales of type II (distance 1.23–1.46 μm). The ridges of the type I scales are 0.53 μm broad (vs. 0.50 μm in *Apatura ilia*), while the ridges on type II scales are 0.18 μm



Fig. 5. TEM image of ultrathin cross section through longitudinal ridges of the cover scale in *Apatura iris*, showing lamellae on the ridges. One-fifth of the whole scale line = 100 nm.

TABLE 1. Character differences between the scales of the analyzed Purple Emperor and Morpho butterfly species

Morphological character	<i>Apatura ilia</i>	<i>A. iris</i>	<i>Morpho</i> spp.
Type I scale length (μm)	104–150	95–100	200–220
Type I scale width (μm)	53–60	55–61	85–108
Shape of apical border of the scale I	Mostly with five projections	Straight/with three projections	Straight/rounded
Distance between ridges on the type I of scale (nm)	680	820	450–1,000
Distance between ridges on the type II of scale (μm)	1.23–1.35	1.23–1.46	—
Width of a ridge on the type I of scale (μm)	0.50	0.53	0.45–0.78
Width of a ridge on the type II of scale (μm)	0.27	0.18	—
Type I scale ridge period	1,200–1,500/mm	1,200/mm	1,400–2,000/mm
Type II scale ridge period	700/mm	630/mm	—
Shape of lamellae of the type I of scale	Higher/of the same height, triangular/almost subparallel, somewhat narrowed sub-basally	Lower, triangular, not narrowing basally	Much higher, gradually narrowing distally, almost subparallel, not narrowing basally
Number of lateral lamellar projections of the type I of scale	Six/seven pairs	Five/six pairs	Five-twelve pairs
Shape of lateral lamellar projections of the type I of scale	Widened distally, straight	Not widened distally, bent	Not widened distally, straight
Degree of melanization of interior of the ridge of the type I of scale	More expressed	Less expressed	More expressed

The ranges of single measurements are presented (Berthier, 2010; Prum et al., 2006; Srinivasarao, 1999; Vukusic et al., 1999; present study).

wide (vs. 0.27 μm in *A. ilia*). About 1,200 ridges are present per millimeter on the surface of the type I scales (vs. 1,200–1,500 ridges per millimeter in *A. ilia*), while about 630 ridges per millimeter exist on the surface of the type II scales (vs. 700 ridges per millimeter in *A. ilia*). The lamellae on the ridges of the type I scales are subtriangular (dorsal view), overlap, and form the multilayer structure responsible for the iridescent color (Figs. 4b and 4c; Pantelić et al., 2011). Each pair of ridges from the type II scales is connected by cross ribs (Fig. 4d). The lamellae on the ridges of the

type II scales are subcylindrical (dorsal view), widened only basally, just partly lying one on another. They are not iridescent. The lamellae on the ridges in cross section exhibit a multilayer structure (lateral view), conifer-like, with five/six pairs of bent lateral projections that are not dilated distally, triangularly pointed (Fig. 5). Only basal part of the ridge interior of the type I scales is with a dark pigment. The ridges are therefore less melanized (Fig. 5). The ventral wing surface is virtually flat, but small ridges are apparent on the lower surface, as seen in its cross section. The geometry of

the microscopic structure of the *A. iris* wing scale resembles that in *A. ilia*.

Presence, number, color, and position of both types of scales in *Apatura iris* are similar to ones in *Apatura ilia*, as listed in the last paragraph of the previous heading.

DISCUSSION

Apart from the differences between *Apatura ilia* and *A. iris* observed by SEM that are listed in the previous chapter, the following differences between the mentioned species were additionally registered in the structures visible in micrographs done by TEM. The lamellae of *Apatura ilia* are higher/of the same height, triangular/almost subparallel, somewhat narrowed sub-basally, with

six/seven pairs of straight lateral projections widened distally; the lamellae of *Apatura iris* are lower, triangular, not narrowed basally, with five/six pairs of bent lateral projections that are not widened distally. Furthermore, the type I scales of both species look somewhat different in the degree of melanization (occurrence of a dark pigment in the ridge interiors; Table 1). Additionally, character differences between the scales of the analyzed Purple Emperor butterfly species and tropical *Morpho* species (where scale iridescence is noticeable as well) are listed in Table 1 (Berthier, 2010; Prum et al., 2006; Srinivasarao, 1999; Vukusic et al., 1999; present study).

The type I scales in both analyzed butterfly species show iridescent effects due to their denser microscopic structure in comparison to the type II scales (Pantelić et al., 2011). The type I scales have a superficial position on the dorsal side of both the fore and hind wings in males, and they are present there in great abundance. The result of this is the occurrence of violet-blue brilliance in the areas of the wings. Females lack such scales and these are not registered on the ventral side of both wing pairs in males. Therefore, no optical effects are present in females and on the ventral surface of male wings. Type II scales totally cover the ventral side of the wings, and lie below the type I scales on the dorsal side of the wings. The color of the type II scales has pigment origin.

Additionally, lamellae are not present along the whole type I scale length in either species. The proximal-most part of the scale I has ridges, but lamellae are missing and appear subproximally. Therefore, we can say that iridescent effects may be produced by most of the surface of the dorsal scales, but not by the whole scales. Furthermore, the cross ribs with pigment granules are absent in this area as well. The proximal-most parts of the type I scales are covered by distal-most parts of the scales of the same type, and are not responsible for the color of the wings. On the other hand, both lamellae and cross ribs exist in the distal-most parts of the scales (Fig. 6). These parts are not covered by other scales and their color is both of structural and pigment origin.

Additional differences were registered between two analyzed *Apatura* species. The greater part of the sur-

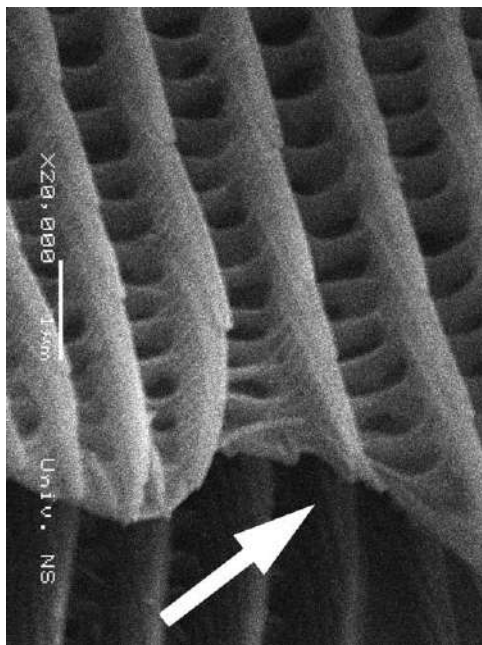


Fig. 6. SEM image of distal-most part of cover scale in *Apatura ilia* (dorsal view), as indicated by an arrowhead.

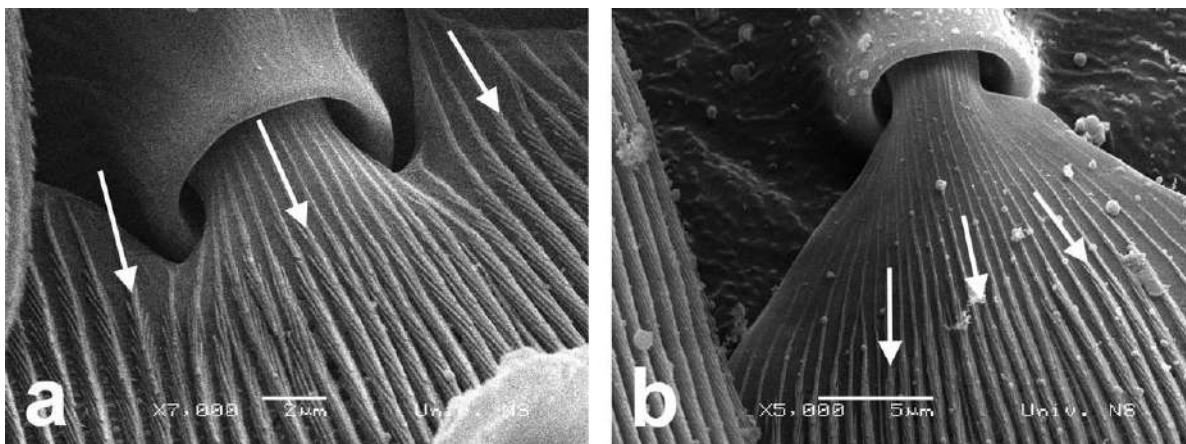


Fig. 7. SEM images of proximal parts of cover scales in *Apatura ilia* (a) and *A. iris* (dorsal views) (b). Places of lamellar appearance are indicated by arrowheads.

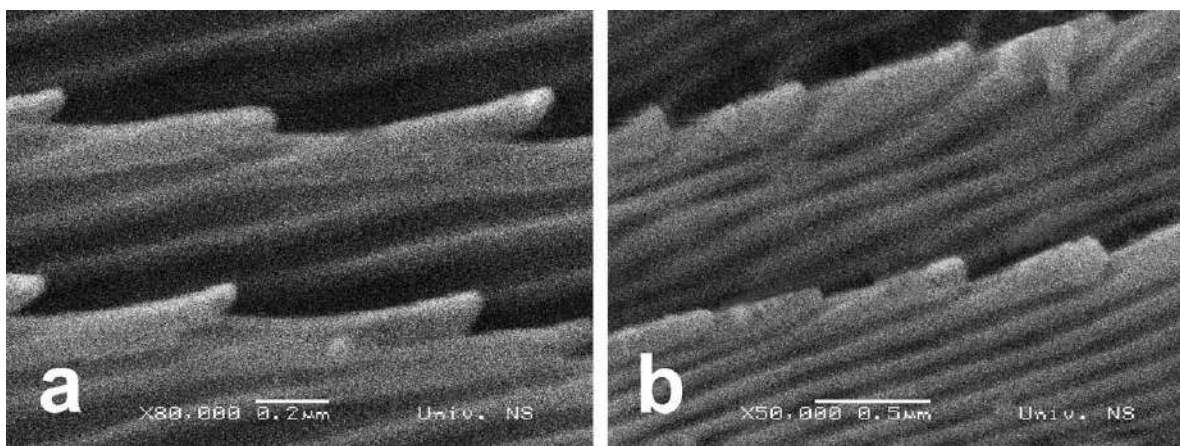


Fig. 8. SEM images of lamellae of cover scales in *Apatura ilia* (a) and *A. iris* (dorsolateral views) (b).

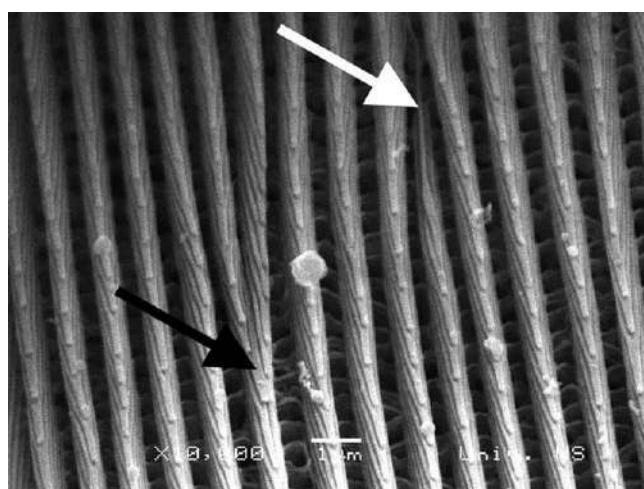


Fig. 9. SEM image of fusion (black arrowhead) and appearance of lamellae (white arrowhead) in cover scale of *Apatura iris* (dorsal view).

face of the type I scale is covered with lamellae in *Apatura ilia* (starting closer to the proximal edge of the scale; Fig. 7a) in comparison to *A. iris* (appearing somewhat distally from the mentioned point; Fig. 7b). Iridescence effects of *Apatura ilia* may be produced by the greater surface of the type I scales as compared with *A. iris*. Lamellae are somewhat elevated distally in *Apatura ilia*, while almost straight distally in *A. iris* (Figs. 8a and 8b). Both lamellae and cross ribs exist on the ventral wing side and they are like those in the type II scale. They cover the whole upper surface of the scales.

Some lamellar rows may be fused in some cases in both analyzed species, looking like dislocation in a crystal (Fig. 9). This may be a developmental defect. Additionally, certain lamellar rows appear distant from the subproximal part of the scale toward its distal end (Fig. 9). These features could be manifestations of intraspecific polymorphism.

The ventral side of the scales is mostly smooth in both species, but distally with ridges and weakly expressed cross ribs (Fig. 10). Sometimes the mentioned structures are visible laterally on the ventral side of the scales as well.

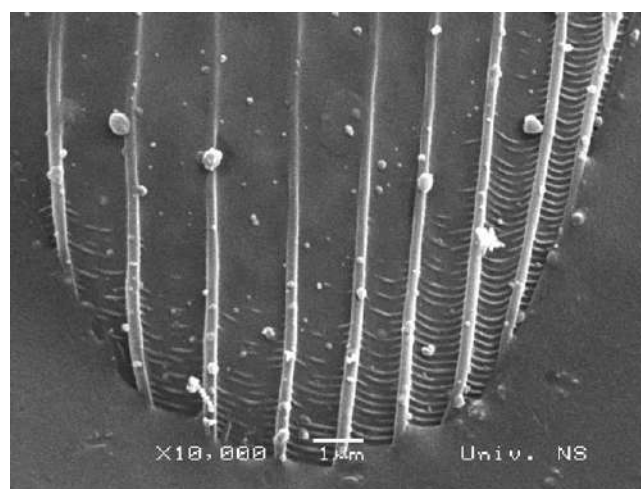


Fig. 10. SEM image of apical part of cover scale in wing of *Apatura iris* (ventral view).

The difference between the *Apatura* and *Morpho* species is partly due to different orientations of butterfly scales with respect to wing membrane. In *Apatura* butterflies, the scales are strongly inclined, while in *Morpho* butterflies the scales are parallel to the membrane.

CONCLUSIONS

The brilliant iridescent color in some male butterflies enables long-range communication between members of the species. Micro- and nanostructures are presumably responsible for this coloration and it is to a lesser extent of pigment origin. It seems that intrasexual communication between males is the reason for the brilliant coloration in male butterflies (Silberglied, 1984). The wing iridescence in the two analyzed butterfly species serves for both threat and movement of rival males from locations (Page, 2010). This phenomenon is visible in flight or at rest with opened wings.

The photonic type nanostructures consisted of chitin, occurring in the butterfly wing scales of the male

individuals of the species *Apatura ilia* and *A. iris*, were investigated by both SEM and TEM.

Although males of *Apatura ilia* have an iridescent violet-blue color of wings dorsally arising from the both micro- and nanostructures and a yellowish-brown color produced by pigments on the wings ventrally, the males of *A. iris* have a similar iridescent color on the dorsal side of the wings and a brownish color on the ventral side.

The system producing structural color comprises ridges of the type I scales bearing lamellae. The architecture of the scales is complex—they possess numerous alternating lucent (air) and dense (cuticle) layers.

The SEM micrographs show that there are two types of scales on the dorsal side of the wings in males in both species, while only type I scales are responsible for the structural color of the wings. The type II scales play a role in the creation of the pigment-originated brownish color.

Iridescence is observed in a quite narrow angular range in both analyzed Purple Emperor species (18 degrees for both species), while it is much greater in other previously studied butterfly species. The spectral width of iridescence is small (around 50 nm FWHM for both analyzed *Apatura* species), but it is much greater in *Morpho* butterflies inhabiting the tropics (Pantelić et al., 2011).

ACKNOWLEDGMENTS

The authors owe their gratitude to Mr. Miloš Bokorov (Faculty of Science, University of Novi Sad, Novi Sad, Serbia) for help in preparing SEM photographs. The study was financially supported by the Serbian Ministry of Education and Science (Projects Nos. ON173038, ON171038, III45016, III41002, III47007, and III43002).

REFERENCES

- Berthier S. 2010. *Photonique des morphos*. Paris: Springer-Verlag France. 214 p.
- Biró LP, Kertész K, Vértésy Z, Márk GI, Bálint Z, Lousse V, Vigneron J-P. 2007. Living photonic crystals: Butterfly scales—Nanostructure and optical properties. *Mater Sci Eng C* 27:941–946.
- Garrett NL, Vukusic P, Ogrin F, Sirotkin E, Winlove CP, Moger J. 2009. Spectroscopy on the wing: Naturally inspired SERS substrates for biochemical analysis. *J Biophotonics* 2:157–166.
- Ghiradella H. 1989. Structure and development of iridescent butterfly scales: Lattices and laminae. *J Morphol* 202:69–88.
- Ghiradella H. 1991. Light and colour on the wing: Structural colours in butterflies and moths. *Appl Opt* 30:3492–3500.
- Ghiradella H. 1998. Hairs, bristles, and scales. In: Locke M, editor. *Microscopic anatomy of invertebrates*, Vol. 11A: Insecta. New York: Wiley-Liss. pp. 257–287.
- Ghiradella H, Aneshansley D, Eisner T, Silberglied RE, Hinton HE. 1972. UV reflection of male butterfly: Interference colour caused by thin-layer elaboration of wing scales. *Science* 178:1214–1217.
- Han Z, Wu L, Qiu Z, Guan H, Ren L. 2008. Structural colour in butterfly *Apatura ilia* scales and the microstructure simulation of photonic crystal. *J Bionic Eng Suppl* 5:14–19.
- Han Z, Wu L, Qiu Z, Ren L. 2009. Microstructure and structural colour in wing scales of butterfly *Thaumantis diores*. *Chin Sci Bull* 54:535–540.
- Higgins LG, Riley ND. 1970. *A field guide to the butterflies of Britain and Europe*. London: Collins. 380 p.
- Imafuku M, Hirose Y, Takeuchi T. 2002. Wing colours of *Chrysozephyrus* butterflies (Lepidoptera; Lycaenidae): Ultraviolet reflection by males. *Zool Sci* 19:175–183.
- Jakšić P. 2003. *Red data book of Serbian butterflies*. Lepidoptera: Hesperioidea and Papilionoidea. Belgrade: Institute for Nature Conservation of Serbia. 198 p.
- Kertész K, Molnár G, Vértésy Z, Koós AA, Horváth ZE, Márk GI, Tapasztó L, Bálint Z, Tamáska I, Deparis O, Vigneron J-P, Biró LP. 2008. Photonic band gap materials in butterfly scales: A possible source of “blueprints”. *Mater Sci Eng B* 149:259–265.
- Lafranchis T. 2004. *Butterflies of Europe*. New field guide and key. Paris: Diatheo. 350 p.
- Luke SM, Vukusic P, Hallam B. 2009. Measuring and modelling optical scattering and the colour quality of white pierid butterfly scales. *Opt Express* 17:14729–14743.
- Matejková-Plšková J, Shiojiri S, Shiojiri M. 2009. Fine structures of wing scales in *Sasakia charonda* butterflies as photonic crystals. *J Microsc* 236:88–93.
- Morehouse NI, Vukusic P, Rutowski R. 2007. Pterin pigment granules are responsible for both broadband light scattering and wavelength selective absorption in the wing scales of pierid butterflies. *Proc R Soc Lond B Biol Sci* 274:359–366.
- Page RJC. 2010. Perching and patrolling continuum at favoured hill-top sites on a ridge: A mate location strategy by the Purple Emperor butterfly *Apatura iris*. *Entomol Rec J Var* 122:61–70.
- Pantelić D, Čurčić S, Savić-Sević S, Korać A, Kovačević A, Čurčić B, Bokić B. 2011. High angular and spectral selectivity of Purple Emperor (Lepidoptera: *Apatura iris* and *A. ilia*) butterfly wings. *Opt Express* 19:5817–5826.
- Prum RO, Quinn T, Torres RH. 2006. Anatomically diverse butterfly scales all produce structural colours by coherent scattering. *J Exp Biol* 209:748–765.
- Shawkey MD, Morehouse NI, Vukusic P. 2009. A protean palette: Colour materials and mixing in birds and butterflies. *J R Soc Interface* 6:S221–S231.
- Silberglied RE. 1984. Visual communication and sexual selection among butterflies. In: Vane-Wright RI, Ackery PE, editors. *The biology of butterflies*. Symposium of the Royal Society of London, No. 11. London: Academic Press. pp. 207–223.
- Srinivasarao M. 1999. Nano-optics in the biological world: Beetles, butterflies, birds, and moths. *Chem Rev* 99:1935–1961.
- Stavenga DG, Stowe S, Siebke K, Zeil J, Arikawa K. 2004. Butterfly wing colours: Scale beads make white pierid wings brighter. *Proc R Soc Lond B Biol Sci* 271:1577–1584.
- Tolman T, Lewington R. 1997. *Collins field guide. Butterflies of Britain and Europe*. London: HarperCollins Publishers. 320 p.
- Vértésy Z, Bálint Z, Kertész K, Vigneron J-P, Lousse V, Biró LP. 2006. Wing scale microstructures and nanostructures in butterflies—Natural photonic crystals. *J Microsc* 224:108–110.
- Vértésy Z, Kertész K, Bálint Z, Molnár G, Eros M, Biró LP. 2007. SEM and TEM investigations in the scales of the European nymphalid butterfly *Apatura ilia* dark and light phenotypes. In: Tapasztó L, editor. *BioPhot Workshop 2007. Complexity and Evolution of Photonic Nanostructures in Bioorganisms: Templates for Materials Science (BioPhot)*, Workshop 6, Budapest, Hungary, 24–25 September 2007. Abstract Book. Budapest: Research Institute for Technical Physics and Materials Science. pp. 14–15.
- Vukusic P, Hooper I. 2005. Directionally controlled fluorescence emission in butterflies. *Science* 310:1151.
- Vukusic P. 2006. Structural colour in Lepidoptera. *Curr Biol* 16:R621–R622.
- Vukusic P, Kelly R, Hooper I. 2009. A biological sub-micron thickness optical broadband reflector characterized using both light and microwaves. *J R Soc Interface* 6:S193–S201.
- Vukusic P, Sambles JR. 2003. Photonic structures in biology. *Nature* 424:852–855.
- Vukusic P, Sambles JR, Lawrence CR. 2004. Structurally assisted blackness in butterfly scales. *Proc R Soc Lond B Biol Sci Suppl* 271:S237–S239.
- Vukusic P, Sambles JR, Lawrence CR, Wootton RJ. 1999. Quantified interference and diffraction in single *Morpho* butterfly scales. *Proc R Soc Lond B Biol Sci* 266:1403–1411.

Band-Gap Photonic Structures in Dichromate Pullulan

SVETLANA SAVIĆ-ŠEVIĆ, DEJAN PANTELIĆ, MARKO NIKOLIĆ, AND BRANISLAV JELENKOVIĆ

Institute of Physics, Zemun, Belgrade, Serbia

One-dimensional photonic crystals are fabricated in a dichromate-sensitized pullulan as volume holograms. A single-frequency, diode pumped Nd-YAG laser, at 532 nm, is used for exposure. Band gaps in the visible range are observed. The spectral measurements show that band-gap position can be tuned by varying the concentration of ammonium dichromate.

Keywords Band gap; Photonic structures.

1. INTRODUCTION

The holographic method has been recently used to fabricate photonic crystals [1]. Several photonic band-gap materials such as dichromated gelatin [2, 3], polymers with TiO₂ [4], photoresists [5, 6], sol-gel materials [7], and silver halide emulsions [8, 9] have been used for fabrication of photonic structures using holographic techniques.

In this article, fabrication of photonic crystals as volume holograms is reported. We used the pullulan sensitized with ammonium dichromate (DCP) as recording material [10–12]. Pullulan is a natural linear polysaccharide, produced from starch by *Aureobasidium pullulans* [13]. It is nonpoisonous, and easily soluble in water to make clear and viscous solution. Due to its high adhesion, a thin film is easily formed.

In this study, we have investigated the effects of ammonium dichromate concentration on the one-dimension photonic band gap structure inside DCP.

2. PULLULAN AS A HOLOGRAPHIC RECORDING MATERIAL

An aqueous solution of pullulan, sensitized with ammonium dichromate, was prepared. Pullulan (Sigma, average molecular weight 200,000) dissolved in 8% solution of distilled water. Ammonium dichromate was added, and the mixture was stirred at 50°C to achieve homogeneity. Three concentrations of ammonium dichromate were used in our experiments: 10, 35, and 50%, by weight of pullulan. Solutions are coated onto clean glass slides in a horizontal position. Films were dried under normal laboratory conditions. The dried DCP layers were around 10 μm thick.

3. EXPERIMENTAL SETUP AND PROCEDURE

The laser beam at 532 nm (second harmonic of Nd-YAG laser) is used to fabricate one-dimensional photonic

structure in dichromate pullulan. Expanded laser beam illuminates the DCP film and the mirror placed directly behind it. At normal incidence angle, the standing wave was produced, and recorded as the Bragg grating inside the DCP. The energy density of the incident beam was 24 J/cm².

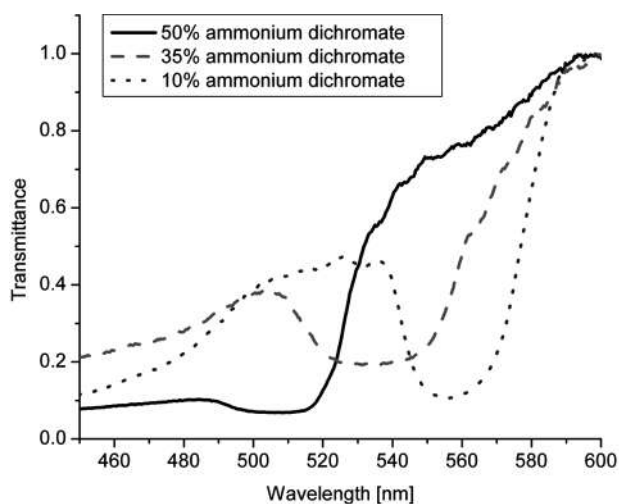
After exposure, the plate was developed in the mixture of water and isopropyl alcohol for 120 seconds, and then dried for 60 seconds in pure isopropyl alcohol. Underexposed regions were washed away and exposed regions remained. The refractive index of the DCP is $n = 1.44$, and the space between the two adjacent constructive planes (i.e., planes which happen to cause constructive interferences, according to Bragg theory) was about 184 nm.

To confirm the existence of band gaps in DCP photonic structures, diffraction spectra were measured. The transmission (and reflection) spectra of light impinging on photonic crystals show directly their band structure. To obtain such spectra, light from the 50 W halogen lamp was collimated and directed onto the DCP plate from the substrate side. Spectra of our photonic structures (gratings) were measured by the fiber-type spectrometer (from Ocean Optics). Figures 1(a) and (b) show, for normal beam incidence transmission and reflection spectra for gratings with 10, 35, and 50% concentrations of ammonium dichromate. The transmission (reflection) gaps were centered at around 507, 535, and 556 nm for samples with 50, 35, and 10% ammonium dichromate, respectively. The bandwidths of gaps were between 30–40 nm. It can be seen from Fig. 1, that the position of the band gap can be tuned by changing the concentration of ammonium dichromate. The tuning is possible because of the influence of ammonium dichromate on the shrinking of photosensitive material. Our results show that, by increasing the concentration of the ammonium dichromate, the band gap is shifted towards the shorter wavelengths.

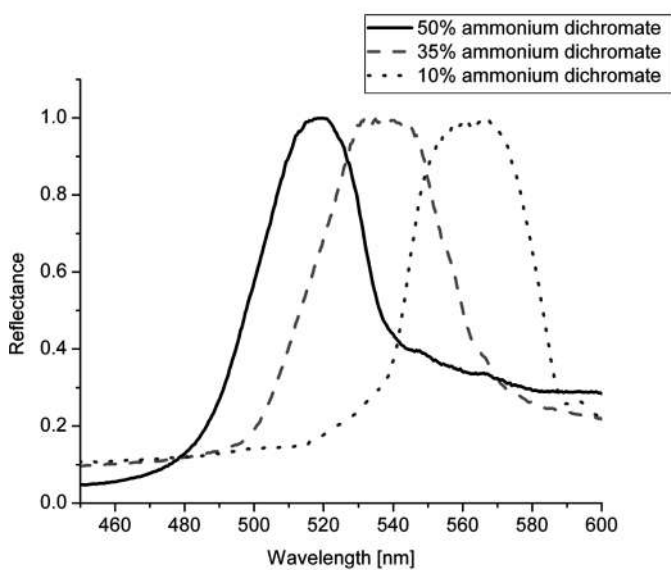
We have shown that the position of the central wavelength of the band gap also varies with the incident angle of the reconstruction beam. Figure 2 shows that, when the incident angle increases (from 0° to ±45°), the band gap center shifts towards the shorter wavelengths. Fits using Bragg formula are included in Fig. 2. Discrepancies between

Received September 8, 2008; Accepted January 12, 2009

Address correspondence to Svetlana Savić-Šević, Institute of Physics, Pregrevica 118, Zemun, Belgrade 11080, Serbia; E-mail: savic@uranus.phy.bg.ac.yu



(a)



(b)

FIGURE 1.—Normal transmittance (a) and reflectance (b) for the DCP samples with 50% (solid line), 35% (dashed line), and 10% (dotted line) concentration of ammonium dichromate.

experimentally obtained curves and fits are due to imperfect experimental setup.

4. CONCLUSIONS

We have produced band-gap photonic structure in dichromate pullulan, using holographic recording method. It has been shown that the band gap position can be tuned by varying the concentration of sensitizer (ammonium dichromate) and by varying the incident angle of the reconstruction beam. In this article, we report our early experimental results, and in our next study we will perform numerical analysis.

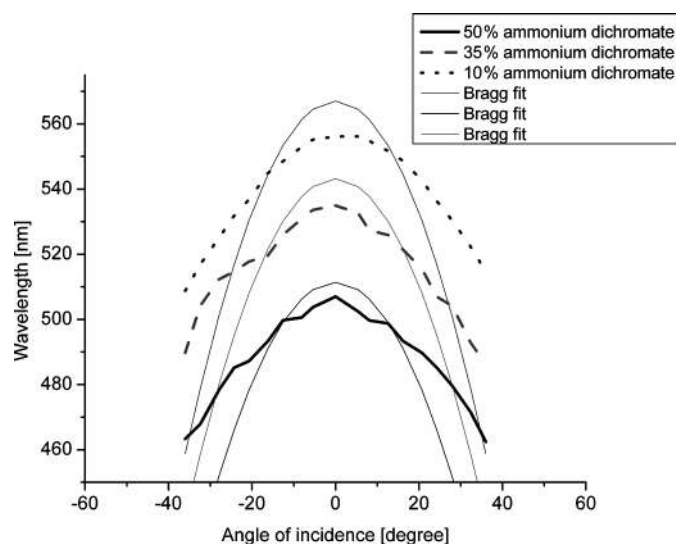


FIGURE 2.—Position of the band gap center as a function of the incident angle of the reconstruction beam.

ACKNOWLEDGMENTS

This research was funded by the Serbian Ministry of Science and Technological Development, under the contract No. 141003.

REFERENCES

1. Busch, K.; Lolkes, S.; Wehrspohn, R.B.; Foll, F. Photonic crystals. *Advance in Design, Fabrication and Characterization*; Wiley-VCH Verlag GmbH & Co. KGaA: Weinheim, 2003.
2. Ma, R.; Xu, J.; Tam, W.Y. Wide band gap photonic structures in dichromated gelatin emulsions. *Applied Physics Letters* **2006**, *89*, 081116/1–081116/3.
3. Ye, Z.; Zheng, J.; Liu, D.; Pei, S. Structures of photonic crystals and band gaps in volume hologram. *Physics Letters A* **2002**, *299*, 313–317.
4. Sharp, D.T.; Campbell, M.; Dedman, E.; Harrison, M.; Denning, R.G.; Tuberfield, A.J. Photonic crystals for the visible spectrum by holographic lithography. *Opt. and Quantum Electronics* **2002**, *34*, 3–12.
5. Ohira, T.; Segawa, T.; Nagai, K.; Utaka, K.; Nakao, M. Large area InP submicron two-dimensional (2D) periodic structures fabricated by two-time laser holography. *Jpn. J. Appl. Phys.* **2002**, *41*, 1085–1089.
6. Miklyaev, Y.; Meisel, D.; Blanco, A.; Freymann, G. Three-dimensional face-centered-cubic photonic crystal templates by laser holography: Fabrication, optical characterization, and band-structure calculations. *Appl. Phys. Lett.* **2003**, *82*, 1284–1286.
7. Saravanamuttu, K.; Blanford, C.; Sharp, C.; Dedman, E.; Tuberfield, A.; Denning, R. Sol-Gel organic-inorganic composites for 3-D holographic lithography of photonic crystals with submicron periodicity. *Chem. Mater.* **2003**, *15*, 2301–2304.
8. Ulibarrena, M.; Carretero, L.; Madrigal, R.; Blaya, S.; Fimia, A. Multiple band holographic reflection gratings recorded in new ultra-fine grain emulsion BBVPan. *Opt. Express* **2003**, *11*, 3385–3392.
9. Ulibarrena, M.; Carretero, L.; Madrigal, R.; Blaya, S.; Fimia, A. Nonlinear effects on holographic reflection gratings recorded with BB640 emulsions. *Opt. Express* **2003**, *11*, 1906–1917.

10. Pantelić, D.; Savić-Šević, S.; Jakovljević, D. Dichromated pullulan as a novel photosensitive holographic material. *Opt. Lett.* **1998**, *23*, 807–809.
11. Savić-Šević, S.; Pantelić, D.; Jakovljević, D. Real-time and postprocessing holographic effects in dichromated pullulan. *Appl. Opt.* **2002**, *41*, 4484–4488.
12. Savić-Šević, S.; Pantelić, D. Dichromated pullulan diffraction gratings: influence of environmental conditions and storage time on their properties. *Appl. Opt.* **2007**, *46*, 287–291.
13. Sano, T.; Uemura, Y.; Furuta, A. Photosensitive resin composition containing pullulan or esters thereof. U.S. Patent 3,960,685; 1976.

Copyright of *Materials & Manufacturing Processes* is the property of Taylor & Francis Ltd and its content may not be copied or emailed to multiple sites or posted to a listserv without the copyright holder's express written permission. However, users may print, download, or email articles for individual use.

Flexible design of band gaps in the biopolymer photonic crystals

This article has been downloaded from IOPscience. Please scroll down to see the full text article.

2012 Phys. Scr. 2012 014073

(<http://iopscience.iop.org/1402-4896/2012/T149/014073>)

View [the table of contents for this issue](#), or go to the [journal homepage](#) for more

Download details:

IP Address: 147.91.1.45

The article was downloaded on 12/06/2012 at 12:38

Please note that [terms and conditions apply](#).

Flexible design of band gaps in the biopolymer photonic crystals

S Savić-Šević

Institute of Physics, University of Belgrade, Pregrevica 118, 11080 Zemun, Serbia

E-mail: savic@ipb.ac.rs

Received 31 August 2011

Accepted for publication 23 November 2011

Published 27 April 2012

Online at stacks.iop.org/PhysScr/T149/014073

Abstract

One-dimensional photonic crystals (PC) are fabricated in dichromate-sensitized biopolymer as volume holograms. The flexibility of the PC band gap (BG) parameters was investigated. The spectral position of a BG can be varied by changing the exposure for two concentrations of sensitizer during the fabrication process. The spectral measurements show that the BG centre shifts towards longer wavelengths with decreasing exposure and concentration of the sensitizer. A tuning of the position of the BG for about 120 nm was obtained.

PACS numbers: 42.70.Qs, 42.40.Eq, 42.70.Ln

(Some figures may appear in colour only in the online journal)

1. Introduction

Photonic crystals are dielectric materials that exhibit band gaps (BGs) in which electromagnetic wave propagation is forbidden [1]. Several photonic BG materials, such as dichromated gelatin [2, 3], polymers with TiO₂ [4] and photoresists [5, 6] have been used for the fabrication of photonic structures using holographic techniques. Here, we report the fabrication of photonic crystals using optical holography. One-dimensional (1D) periodic structures, i.e. holographic volume gratings, were fabricated by using a single-beam method. Volume gratings have been created by standing waves formed in holographic material by two-beam interference of an incident laser beam.

Tunability of the photonic crystals (PC) BG during the fabrication of the 1D PC in dichromate biopolymer was investigated. We used pullulan sensitized with ammonium dichromated pullulan (DCP) as recording material [7–9]. Pullulan is a natural linear polysaccharide, produced by a fungus *Aureobasidium pullulans*. It is non-poisonous and easily soluble in water making a clear and viscous solution [10].

We found that the position of the BG can be tuned by changing the exposure and concentration of the dichromate. Spectral measurements show that the BG centre shifts towards longer wavelengths with decreasing exposure and concentration of dichromate. The tuning is a consequence of the different amounts of swelling of photosensitive material.

An efficient tuning of the position of the BG for about 120 nm is obtained. These results are important as they present a convenient way to move the centre wavelength of the BG of the photonic crystal, thus making holographic filters for different spectral ranges.

2. The sample preparation

Holographic photosensitive material was prepared by an 8% aqueous solution of pullulan (Sigma). Ammonium dichromate was added and the mixture was stirred at 50 °C to achieve homogeneity. Two concentrations of ammonium dichromate were used in our experiments: 5 and 30% by weight of pullulan. Solutions are coated onto clean glass slides in the horizontal position. Films were dried under normal laboratory conditions. The dried DCP layers were about 15 μm thick.

3. Fabrication of biopolymer photonic crystals

1D periodic structures, i.e. Bragg gratings, in a DCP, were fabricated using a single-beam method. To minimize vibrations, the experimental setup for the recording of holograms was assembled on an optical table placed on the large concrete block, suspended on vibration-damping supports. Hologram recording was achieved by exposing DCP by a single-frequency, diode-pumped Nd-YAG laser, at 532 nm. The radius of the laser beam was expanded

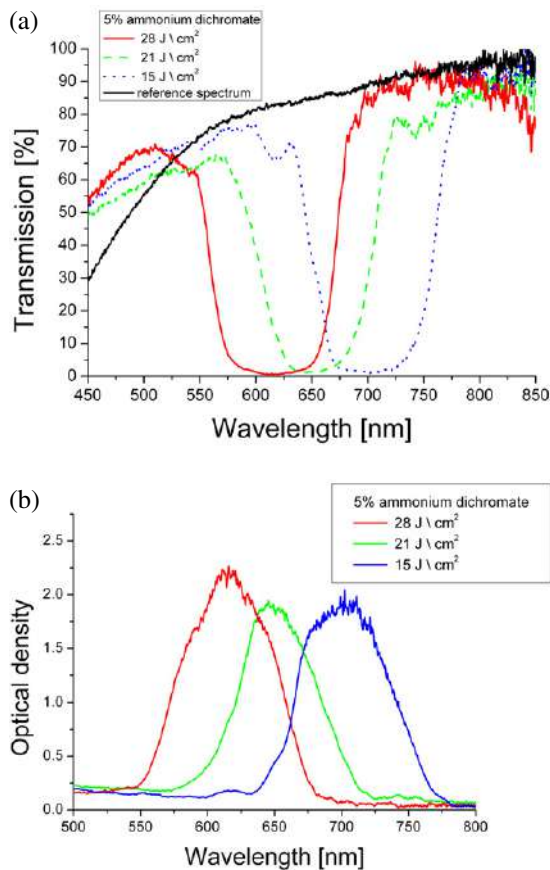


Figure 1. Transmission (a) and optical density (b) for the DCP sample with 5% concentration of ammonium dichromate for three different energy densities of the recording beam: 15, 21 and 28 J cm^{-2} .

and the pullulan layer was exposed at normal incidence. After propagation through the emulsion, the laser beam was reflected back from the mirror behind the holographic plate. The two counter-propagating beams interference creates a standing wave pattern and the hologram within an emulsion. The interference pattern consists of planes parallel to the substrate surface with the spacing $d = \lambda/2n$, where λ is the wavelength of the laser source and n is the refractive index. For DCP, $n = 1.44$, and the space between the two adjacent constructive planes was calculated to be 184 nm.

After exposure, the plates were chemically processed. Processing involves washing the plates in a mixture of water and isopropyl alcohol (in the ratio 3 : 1) for 120 s, and drying for 60 s in pure isopropyl alcohol.

4. Tunability of the band gaps during grating fabrication

The transmission (reflection) spectra of PC directly show their band structures. Spectra were measured using a microscope attached to a spectrometer. The spectral position of a BG was varied by changing the exposure for two concentrations of dichromate during the fabrication process.

Figure 1 shows the transmission spectra and optical densities of DCP PC with 5% ammonium dichromate for three different energy densities of the recording beam: 15, 21 and 28 J cm^{-2} .

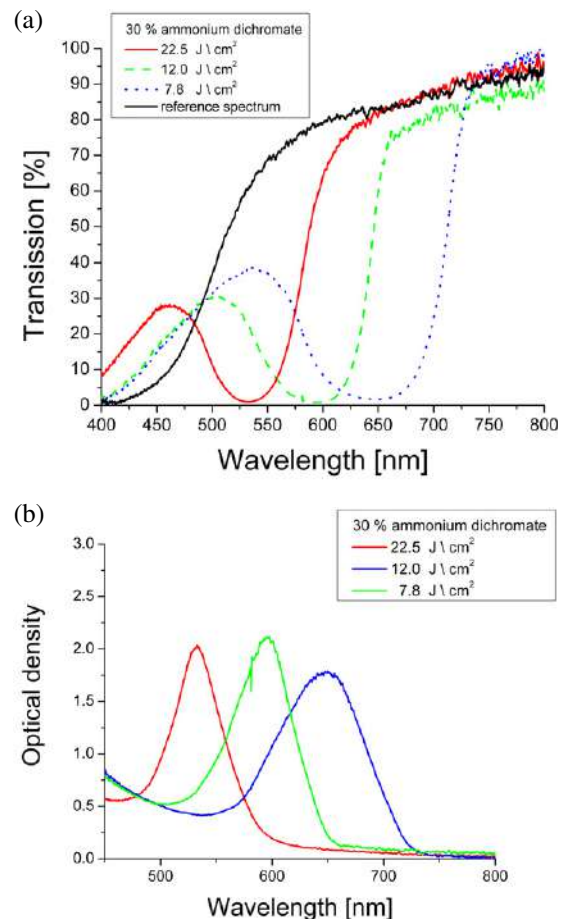


Figure 2. Transmission (a) and optical density (b) for the DCP sample with 30% concentration of ammonium dichromate for three different energy densities of the recording beam: 7.8, 12 and 22.5 J cm^{-2} .

The transmission gaps for 5% ammonium dichromate were centred at about 615, 650 and 700 nm for different energy densities of the recording beam: 15, 21 and 28 J cm^{-2} , respectively. The bandwidths of gaps were about 110 nm. The centre wavelength of the PC BG was shifted by about 85 nm towards the shorter wavelengths by raising the exposure from 15 to 28 J cm^{-2} .

Figure 2 shows the transmission spectra and optical densities of DCP PC with 30% ammonium dichromate for three different energy densities of the recording beam: 7.8, 12 and 22.5 J cm^{-2} .

The transmission gaps for 30% ammonium dichromate were centred at about 530, 600 and 650 nm, for energy density of the recording beam: 7.8, 12 and 22.5 J cm^{-2} , respectively. The bandwidths of gaps were between 70 and 115 nm. The centre of the wavelength of the PC was shifted by about 120 nm towards the shorter wavelength by raising the exposure from 7.8 to 22.5 J cm^{-2} .

It can be seen from figures 1 and 2 that the position of the BG can be tuned by changing the exposure and concentration of ammonium dichromate. The tuning is a consequence of the different amounts of swelling of photosensitive material for different exposures and concentrations of ammonium dichromate. Our results show that by increasing the exposure and concentration of ammonium dichromate, the BG is shifted towards shorter wavelengths.

5. Conclusion

We have produced BG photonic structure in dichromate-sensitized biopolymer using the holographic recording method. It has been shown that the BG position can be tuned by varying the exposure and concentration of ammonium dichromate during the fabrication. These results are important since they present a convenient way to move the centre wavelength of the BG of the photonic crystal, thus making holographic filters for different spectral ranges.

Acknowledgment

This work was supported by the Ministry of Education and Science of the Republic of Serbia under project grant numbers ON171038 and III45016.

References

- [1] Busch K, Lolkes S, Wehrspohn R B and Foll F 2003 *Photonic Crystals: Advance in Design, Fabrication and Characterization* (Weinheim: Wiley)
- [2] Ma R, Xu J and Tam W Y 2006 *Appl. Phys. Lett.* **89** 081116
- [3] Ye Z, Zheng J, Liu D and Pei S 2002 *Phys. Lett. A* **299** 313
- [4] Sharp D T, Campbell M, Dedman E, Harrison M, Denning R G and Tuberfield A J 2002 *Opt. Quantum Electron.* **34** 3
- [5] Ohira T, Segawa T, Nagai K, Utaka K and Nakao M 2002 *Japan. J. Appl. Phys.* **41** 1085
- [6] Miklyaev Y, Meisel D, Blanco A and Freymann G 2003 *Appl. Phys. Lett.* **82** 1284
- [7] Pantelić D, Savić S and Jakovljević D 1998 *Opt. Lett.* **23** 807
- [8] Savić S, Pantelić D and Jakovljević D 2002 *Appl. Opt.* **41** 4484
- [9] Savić-Šević S and Pantelić D 2007 *Appl. Opt.* **46** 287
- [10] Sano T, Uemura Y and Furuta A 1976 *US Patent Specification* 3960685

Holographic Measurement of a Tooth Model and Dental Composite Contraction

DEJAN PANTELIĆ¹, SVETLANA SAVIĆ-ŠEVIĆ¹, DARKO VASILJEVIĆ¹, BRANKA MURIĆ¹,
LARISA BLAŽIĆ², MARKO NIKOLIĆ¹, AND BRATIMIR PANIĆ¹

¹*Institute of Physics, Zemun, Belgrade, Serbia*

²*University of Novi Sad, Faculty of Medicine, Dental Clinic, Novi Sad, Serbia*

We have developed a real-time holographic technique to observe deformation induced by dental composite contraction. The standard split beam method was used, in conjunction with in situ holographic plate processing. Experiments were performed on a mechanical model of a human tooth with cavity. A silicone mold was used to manufacture a number of identical casts, using photoactivated composite. A LED lamp was used to induce photo-polymerization reaction in a composite. We have shown that the proposed method is ideal to analyze various polymerization strategies, with the purpose of recommending one which minimizes the polymerization contraction.

Keywords Composites; Holographic interferometry; Polymerization contraction.

1. INTRODUCTION

Photo-activated composites are widely used during dental restorative procedures. In that respect they have almost replaced amalgam fillings. Composites are composed of a polymer matrix (resin) and photo-initiator (mostly camphorquinone) filled with powder of a hard solid substance [1]. Before polymerization, they are viscous (in some cases thixotropic) fluids which solidify upon irradiation with blue light (around 470nm wavelength). The resulting solid is hard and, if properly applied, it forms impermeable bond with healthy dental tissues. It mimics tooth in mechanical and optical properties, satisfying both medical and esthetic requirements [2, 3].

There is a problem of contraction, connected with the polymerization process. Contraction induces certain amount of stress, which is transferred to surrounding dental structures. Great effort is undertaken to find new materials with reduced polymerization shrinkage [4]. Also, different polymerization methods are devised in order to relieve and reduce the associated stress [5, 6].

It is common to study the contraction both theoretically (using finite elements method or FEM) and experimentally. There is a great body of literature dealing with many aspects of composite polymerization. Composites are studied inside dental cavities or separately. Contraction was investigated experimentally by using mechanical (using pressure or deformation transducers) or optical methods (interferometry, photo-elasticity) [7, 8].

We have previously proposed using holographic interferometry as a tool to observe effects of polymerization contraction on dental tissues [9, 10]. We have found

that deformation induced by composite contraction can be effectively measured, giving the information about deformation field. Stress was calculated using FEM, and an appropriate digital tooth model.

During our previous experiments we faced two problems. The first is connected with natural variability of real human tooth samples. It is, therefore, necessary to use a large number of teeth, to test the effectiveness of particular polymerization scheme. Apart from the problem of obtaining the required number of teeth, there is always a large statistical variability of results. We have decided to use a mechanical model of a tooth in order to eliminate the problem of variability of tooth samples, and to simplify calculations in FEM.

The second problem is connected with the classical holographic setup, which enables observation of one tooth side only. The other surface remains completely hidden. Therefore, we have modified our holographic setup, by placing a tooth in front of a spherical mirror. It produced real, inverted image of the other tooth surface. If positioned appropriately, both an object and its (unit magnification) image can be observed simultaneously, side by side.

Previously described modifications enabled us to observe the effects of polymerization contraction in more details.

2. MECHANICAL TOOTH MODEL

Mechanical analysis of dental tissues was previously performed in three main ways: using real human teeth, animal teeth or mechanical models made of appropriate artificial material (like epoxy resins and methacrylates in photo-elasticity). We have decided to use a dental composite, since it mimics (to a certain extent) tooth tissue in its mechanical and optical properties. An Mesio-Ocluso-Distal (MOD) cavity was drilled in an intact, real, human third molar. The crown part of this particular tooth was used to produce a silicone mold. We decided not to produce a model of the whole tooth, since our previous

Received September 8, 2008; Accepted January 23, 2009

Address correspondence to Dejan Pantelić, Institute of Physics, Pregrevice 118, Zemun, Belgrade 11080, Serbia; E-mail: pantelic@atom.phy.bg.ac.yu



FIGURE 1.—Human molar with MOD cavity (left) and its mechanical model made of dental composite (right). They are both painted with silver paint, as required in holography.

research has shown that the polymerization contraction is localized only within the tooth cusp. A silicone mold was filled with a commercial dental composite (Gradia direct anterior, manufactured by GC America Inc.). According to manufacturer (GRADIA DIRECT Technical Manual version 1.12, March 2006), 27% by weight is composed of methacrylate monomers, 38% silica particles ($0.38\ \mu\text{m}$), and 35% prepolymerized filler. Composite was polymerized using commercial blue polymerization light source (LEDition, manufactured by Ivoclar Vivadent). A real tooth and its model are shown in Fig. 1.

Due to the stability requirements of holographic setup, a tooth model was placed in an aluminum holder and kept in place by dental plaster. Also, outside surface of a model had to be painted with silver paint in order to reflect the light only from the surface.

Dental composites have somewhat different properties compared to dentine and enamel. Elasticity modulus of various composites is within the range of 4–15 GPa [11]. Modulus of dentine ranges from 20–30 GPa [12] and enamel from 32–95 GPa [13].

3. EXPERIMENTAL SETUP AND PROCEDURE

We decided to use a real time holographic setup, in order to observe the dynamics of polymerization contraction, and its influence on a tooth model (Fig. 2). Long coherence length, 100 mW output power, 532 nm wavelength, laser was used as a light source. Its beam was split into two parts. One was used to illuminate the holographic plate, after passing through the diverging lens (reference beam). The other beam illuminated the object (a tooth model in our case).

A model was placed at the centre of curvature ($2f$ position, where f is a focal distance) of a spherical mirror. One part of the object beam illuminated the front surface of a model. The light missing the object reflected from the spherical mirror and illuminated back side of the model. Scattered radiation produced a mirror image placed at the same distance as the object. By slightly offsetting the model from the optical axis, both object and its spherical mirror image could be observed simultaneously (Fig. 3).

A model had to be painted with silver paint (UniPaint silver marker PX-20, manufactured by Mitsubishi Pencil Co., Ltd.). If left unpainted, the radiation would penetrate the model and scatter from inner layers of dental composite. During polymerization contraction, scattered beam would

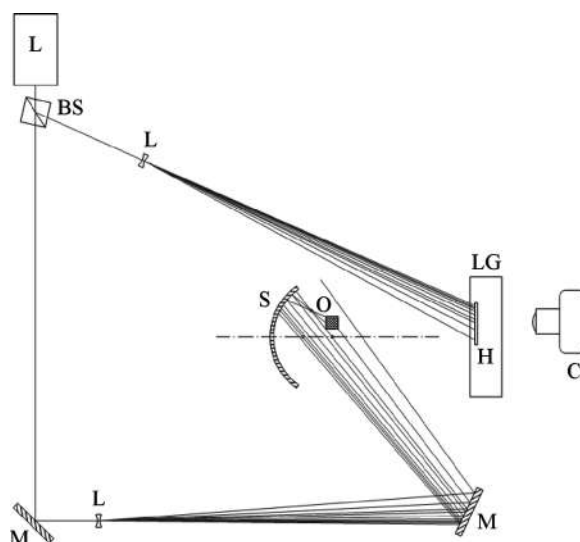


FIGURE 2.—A real time holographic setup: L = laser, BS = beam splitter, L = diverging lens, M = folding mirror, S = spherical mirror, O = object, LG = liquid gate, H = holographic plate, C = CCD camera. k_1 is illumination vector, while k_2 is observation vector.

significantly change its local speckle structure, compared to the beam scattered from the model before the contraction. This would make interference fringes almost invisible. Therefore, it is necessary to use the paint which prohibits light penetrating beneath the surface.

Real time holography is based on producing hologram of an undisturbed object, and observing the object through the hologram when mechanical loads are applied. The resulting picture is a result of interference of the wave-front reflected from the object itself, and the beam reconstructed from the hologram. In this way, hologram represents a “frozen” picture of an object in its initial state. Any further mechanical change of the object is seen as a series of fringes on its surface.

The consequence of these requirements is that the holographic plate must be fixed in space to the fraction of a micrometer during the whole experiment. This problem is



FIGURE 3.—An object (a dice on the right side) and its image in a spherical mirror (on the left). Observe that both front and back side of the same object are seen.

solved by making the complete holographic film processing in place, by using so-called liquid gate. This is a container with transparent, glass, walls where the holographic plate is placed, exposed, and chemically processed, without moving.

We used home-made liquid gate, where holographic plates (VRP-M, green sensitive, manufactured by Slavich, Russia) were processed using a simple procedure. A holographic plate is placed in a liquid gate, and soaked in darkness for 4 minutes in distilled water. This is done in order to leave the gelatin photosensitive layer enough time to swell, so that the layer thickness before and after the processing is the same. This is important, since the gelatin swelling results in the change of the recorded interference fringe period. As a consequence, the recorded wave-front is no longer identical to the object. In that case, two interfering waves in holographic interferometry might be so different that interference pattern cannot be observed.

Further, the film is exposed through the water filled, liquid gate and consequently developed in Ilford ID-11 developer (equivalent to Kodak D-76) for 30 s. The film is washed in distilled water twice, and left in the final water rinse. The fixing step is omitted since it can affect the holographic emulsion thickness. Even without fixing, we could observe the high quality holographic image for several days, with room lighting fully lit.

As a final result, we could observe both the object and its holographically reconstructed image. If a load is applied, interference fringes appear on the object, and can be recorded using a CCD camera. In our case a tooth model is observed. Its MOD cavity is filled with dental composite (the same one used in model manufacture), and



FIGURE 5.—The final interference pattern observed on a tooth model, after 120 s of polymerization. As in previous figure, a tooth model is on the right bottom part of a photograph, while its image is on the upper left. Polymerization LED light source is on the upper right corner, while its image is on the lower left.

polymerized with LED lamp. Polymerization contraction applies the load from inside the cavity. As a consequence, interference fringes start appearing at the tooth model cusp and propagate downwards. Temporal sequence during the first 15 s of polymerization is shown in Fig. 4, and the final fringe pattern, after 120 s of polymerization, is shown in Fig. 5.

The distance between two consecutive fringes corresponds to a certain deformation, which is determined by the angle between illumination (\vec{k}_1) and observation (\vec{k}_2) direction, as well as the object displacement vector (L) [14, 15]. The displacement ($|L|$) corresponding to one wavelength (λ) fringe shift, can be found from a scalar product equation:

$$\lambda = (\vec{k}_1 - \vec{k}_2) \cdot \vec{L}.$$

If applied to our case (532 nm wavelength, angle between the observation and illumination direction is 47 degrees, and displacement vector is collinear with the observation), two consecutive fringes correspond to deformation of 722 nm.

4. RESULTS AND DISCUSSION

Based on the sequence of photographs recorded during the course of experiment, we were able to observe the deformation of each point on the model surface. Graph in Fig. 6 shows how many fringes appeared at the

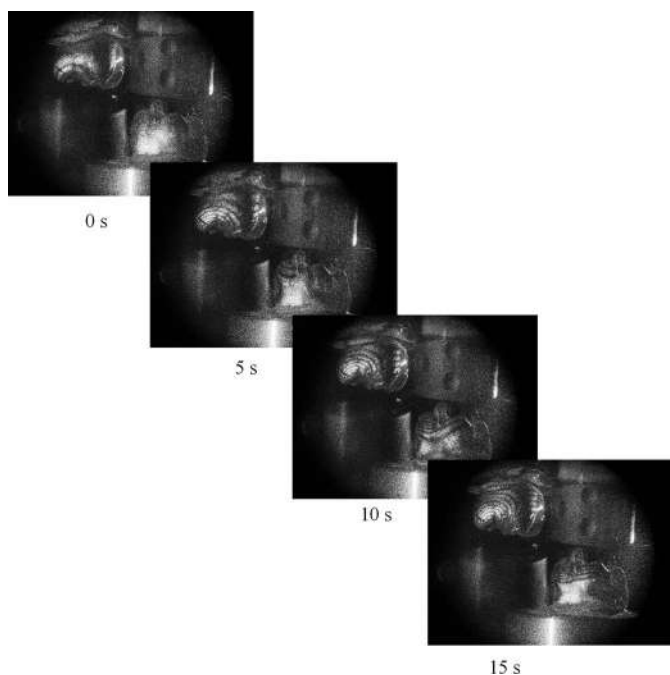


FIGURE 4.—Temporal sequence of the interference pattern produced by dental filling polymerization. A tooth model is on the right bottom corner, while its inverted image is in the upper left corner. The tip of the polymerization lamp is in the upper right corner, and its image is in the lower left.

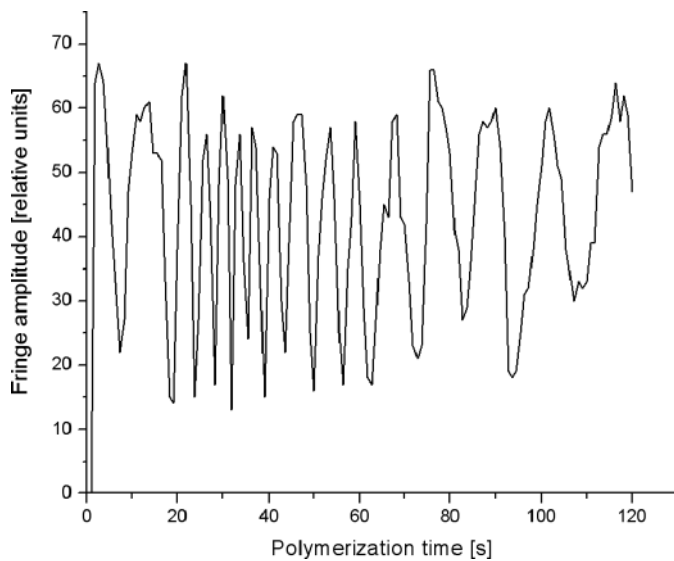


FIGURE 6.—Dynamics of fringe appearance at a tooth cusp. There are 16 fringes at the end of 120 s period. Each peak in the graph corresponds to additional deformation of 722 nm. The final deformation after 120 s is 11.6 μm .

model cusp. By multiplying the number of maxima in a graph with 722 nm (a distance corresponding to two consecutive fringes), a total deformation can be calculated (11.552 μm).

Results obtained using mechanical model of a tooth are of the same order as in previous research [9, 10]. Real human teeth were used and it was found that cuspal deformation lies within the 5–7 μm range. Difference between model and real tooth deformation can be attributed to difference in mechanical properties of human dentine and dental composite. Anyway, fringe shape and orientation is almost the same irrespective whether we study a tooth or its composite model. This signifies that the stress distributions are almost the same, except for the scaling factor, resulting from difference in elastic modulus.

The dynamics of the polymerization process was observed, too. For the first ~ 20 s fringes appear slowly, corresponding to initialization of photochemical reactions. During that period, composite is still viscous and capable of flowing under the action of contraction forces. The contraction accelerates during the next 40–50 s, as the composite solidifies. The process slows down towards the end of illumination, which is the sign of completion of polymerization.

We made particular attention to two different methods of polymerization. One is quick, using high irradiance (500 mW/cm^2) light source. The other is slow—using 80 mW/cm^2 polymerization lamp. Both light sources are based on blue LED lamps. Irradiation times were adjusted so that energy density transmitted to composite was the same ($\sim 15000 \text{ mJ}/\text{cm}^2$) for both lamps.

Both polymerization methods were analyzed by the method previously described in this article. An interesting result is that, slower method, with low power density source is preferable. The resulting deformation (and consequent stress) is 50% lower, compared to quick, high intensity, irradiation.

Explanation for the observed fact is that during slow polymerization, composite can flow for the first 5–10 seconds (before solidification). This relieves the stress inside the composite, without transferring it to cavity walls. On the contrary, if power density is too large, polymer is solidified too quickly, without having chance to flow. We can conclude that slower methods should be preferred in dental practice.

5. CONCLUSIONS

We have found that dental composites can be effectively used to manufacture mechanical model of a tooth. The model mimics tooth geometry as well as its mechanical and optical properties. The manufacturing process is fast and a number of identical copies can be manufactured. Composite models are ideal for the study of various dental procedures, since the effects of human tooth variability are excluded. Also, there are no ethical questions arising. In our case, a model was used to analyze the effect of polymerization contraction on dental structures. We have shown that holographic interferometry can be used to observe the deformation of a tooth model in real-time. The deformation field can be recorded, from both sides of an object, thus fully characterizing the deformation field. Also, the dynamical effects can be easily recorded and analyzed. Based on experimental results, preferred irradiation strategies can be suggested. Current developments of digital holographic techniques as described in [16, 17] could provide further access to additional quantitative data and parameters.

ACKNOWLEDGMENT

This research was funded by the Serbian Ministry of Science and Technological Development, under the contract No. 141003.

REFERENCES

1. Ferracane, J.L. Current trends in dental composites. *Crit. Rev. Oral. Biol. Med.* **1995**, *6*, 302–318.
2. Manhartl, J.; Kunzelmann, K.-H.; Chen, H.Y.; Hickel, R. Mechanical properties and wear behavior of light-cured composite resins. *Dental Materials* **2000**, *16*, 33–40.
3. Lee, Y.-K.; Lim, B.-S.; Kim, C.-W. Difference in the colour and colour change of dental resin composites by the background. *Journal of Oral Rehabilitation* **2005**, *32*, 227–233.
4. Condon, J.R.; Ferracane, J.L. Reduced polymerization stress through non-bonded nanofiller particles. *Biomaterials* **2002**, *23*, 3807–3815.
5. Kuijjs, R.H.; Fennis, W.M.M.; Kreulen, C.M.; Barink, M.; Verdonschot, N. Does layering minimize shrinkage stresses in composite restorations? *J. Dent. Res.* **2003**, *82*, 967–971.
6. Lim, B.-S.; Ferracane, J.L.; Sakaguchi, R.L.; Condon, J.R. Reduction of polymerization contraction stress for dental composites by two-step light-activation. *Dental Materials* **2002**, *18*, 436–444.
7. Braga, R.R.; Ferracane, J.L. Alternatives in polymerization contraction stress management. *Crit. Rev. Oral. Biol. Med.* **2004**, *15*, 76–184.
8. Sato, T.; Miyazaki, M.; Rikuta, A. Real-time dimensional change in light-cured composites at various depths using laser speckle contrast analysis. *Eur. J. Oral. Sci.* **2004**, *112*, 538–544.

9. Pantelić, D.; Blažić, L.; Savić-Sević, S.; Panić, B. Holographic detection of a tooth structure deformation after dental filling polymerization. *J. Biomed. Opt.* **2007**, *12*, 024026/1-7.
10. Pantelić, D.; Blažić, L.; Savić-Sević, S.; Murić, B.; Vasiljević, D.; Panić, B.; Belić, I. Real-time measurement of internal stress of dental tissue using holography. *Opt. Express*, **2007**, *15*, 6823–6830.
11. Chung, S.M.; Yap, A.U.J.; Tsai, K.T.; Yap, F.L. Elastic modulus of resin-based dental restorative materials: a microindentation approach. *J. Biomed. Mater. Res. Part B: Appl. Biomater.* **2005**, *72B*, 246–253.
12. Senawongse, P.; Otsuki, M.; Tagami, J.; Mjor, I. Age-related changes in hardness and modulus of elasticity of dentine. *Archives of Oral Biology*. **2006**, *51*, 457–463.
13. Hea, L.H.; Fujisawab, N.; Swain, M.V. Elastic modulus and stress–strain response of human enamel by nano-indentation. *Biomaterials*. **2006**, *27*, 4388–4398.
14. Hariharan, P.; Oreb, B.F.; Brown, N. Real-time holographic interferometry: a microcomputer system for the measurement of vector displacements. *Appl. Opt.* **1983**, *22*, 876–880.
15. Vest, C.M. *Holographic Interferometry*; Willey-Interscience: New York, 1979.
16. Schnars, U.; Jueptner, W. *Digital Holography, Digital Hologram Recording, Numerical Reconstruction, and Related Techniques*; Springer-Publishing: Berlin, Heidelberg, 2005.
17. Kreis, T. *Handbook of Holographic Interferometry, Optical and Digital Methods*; Wiley-VCH: Weinheim, 2006.

Copyright of *Materials & Manufacturing Processes* is the property of Taylor & Francis Ltd and its content may not be copied or emailed to multiple sites or posted to a listserv without the copyright holder's express written permission. However, users may print, download, or email articles for individual use.

Influence of the Heat Treatment on the Band Gaps in the Biopolymer Photonic Crystals

S. SAVIC-SEVIC*, D. PANTELIC AND B. JELENKOVIC

Institute of Physics, Belgrade, Serbia

1D photonic crystal was fabricated in a dichromate-sensitized biopolymer using holography method. The effects of the temperature of the photonic crystal layer on the center of photonic band gaps were studied. We showed that the central wavelength of the band gap can be tuned by heating the photonic crystal layer. By applying such heat treatment, tuning of the position of the band gap for about 80 nm was obtained.

PACS numbers: 42.70.Qs, 42.40Pa, 82.35.Pq, 87.15.rp

1. Introduction

Photonic crystals are dielectric materials that exhibit band gaps (BG) in which electromagnetic wave propagation is forbidden [1]. Photonic crystals find various applications in single-mode waveguides [2], super-prisms [3], perfect lenses [4], and biosensors [5]. These applications would be significantly improved if the band structure of the crystal could be tuned.

In our laboratory we fabricate a one-dimensional dichromate biopolymer PC having a tunable photonic band gap. The biopolymer used in this study is pullulan. Pullulan is a natural linear polysaccharide, produced from starch by *Aureobasidium pullulans*. Upon heating the photonic crystal from the room temperature to 105 °C we observed a wavelength shift of 80 nm for the wavelength band.

2. Experimental

Holographic photosensitive material was prepared by mixing 8% aqueous solution of biopolymer and 10% ammonium dichromate by weight of biopolymer. The solution was coated onto clean glass slides in a horizontal position. Film was dried overnight under normal laboratory conditions. The thickness of the dried layer was only $\approx 10 \mu\text{m}$. The thin layer ensures the narrower band gaps.

A single-frequency, diode pumped Nd-YAG laser, at 532 nm, was used to generate PC in the holographic material. The laser beam was expanded and exposed biopolymer layer at normal incidence. Mirror was set behind the holographic plate. The hologram was obtained by interference of two oppositely directed beams inside the emulsion. The interference pattern consists of planes parallel to the substrate.

After exposure, plates were chemically processed. Processing involves washing the plates in mixture of water

and isopropyl alcohol (the ratio of water and alcohol in the bath was 1:1) for 120 seconds, and drying for 60 seconds in pure isopropyl alcohol.

The influence of temperature of the PC, and duration of the heat treatment on the position of the band gap were investigated. Transmission spectra of the white light from the halogen lamp, through biopolymer films were measured by the fiber-based spectrometer.

3. Results

Figure 1 shows the shifting of the transmission spectra of biopolymer photonic crystal during the process of heating the PC. The sample was heated from 25 °C to 105 °C, in steps of 20 °C. Increasing the temperature of the sample we were able to shift the band gap position towards shorter wavelengths, from 561 to 481 nm.

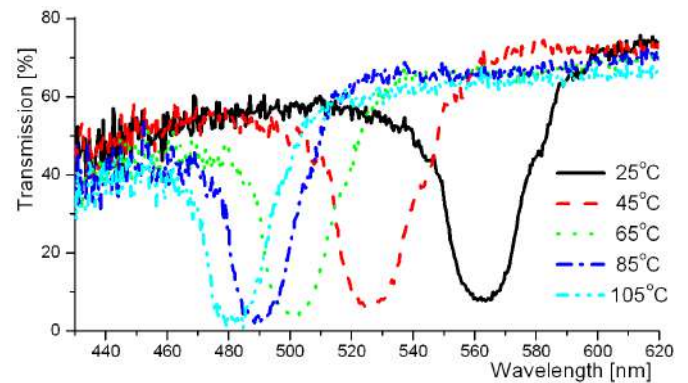


Fig. 1. Transmission spectra of the PC as a function of temperature. For measurements the halogen lamp and the fiber based spectrometer were used.

The total shift of the wavelength band gap as the temperature increases from 25 to 105 °C degrees was about 80 nm. We believe that the shift of the band gap position is due to temperature dependent refractive index of a biopolymer [6].

* corresponding author; e-mail: savic@ipb.ac.rs

The changes of transmission spectra with prolonged heating at elevated temperature are shown in Fig. 2. The sample PC was placed on the plate held at 100 °C and transmission spectra are recorded in intervals of 15 min. The band gap of the biopolymer PC at room temperature (25 °C) is centered at 561 nm (solid line in Fig. 2). After first 15 minutes at 100 °C the shift of the center of the wavelength band gap was from 561 nm to 481 nm, i.e. about 80 nm. It can be seen from Fig. 2 that there are no further significant changes of the band gap position, with prolonged heat treatment.

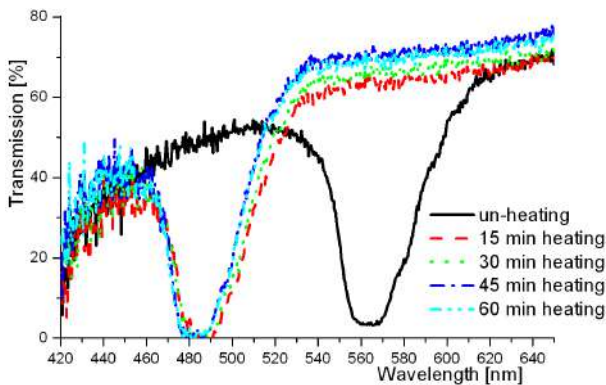


Fig. 2. Transmission spectra as a function of heat treatment duration.

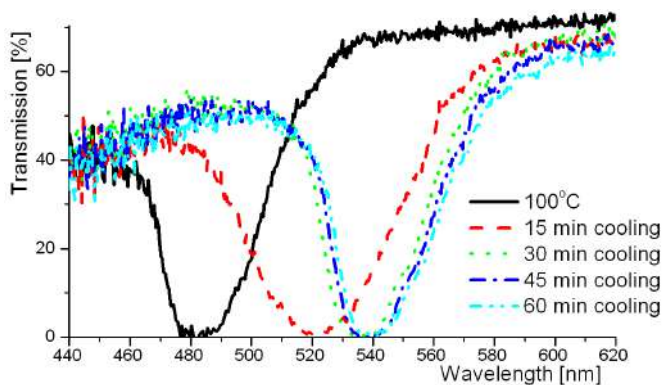


Fig. 3. Transmission spectra as a function of cooling duration.

Next, the sample was left to cool down to room temperature and transmission spectra were measured for a period of one hour, in intervals of 15 min. Figure 3 shows the transmission spectra of biopolymer photonic crystal measured during the cooling process. With temperature decreasing from 100 °C to a room temperature, the band gap position shifts back towards longer wavelengths from 481 to 540 nm.

4. Conclusion

In conclusion, we have developed PC, using dichromate biopolymer, with tunable photonic band gap. The center of the wavelength of the PC was shifted over 80 nm towards the lower wavelength by raising the temperature from room temperature to 105 °C. The changes of the location of the band gap occur fairly quickly after the PC is heated to the new temperature. Cooling the PC shifts the center of the band gap back to the longer wavelength which shows reversibility of the tuning process. These results are important as they present an easy way to move the center wavelength of band gap of the PC, thus making a tunable filter at optical frequencies.

Acknowledgments

The work has been done within the project OI 141003 financed by the Ministry of Science and Technological Development, Republic of Serbia.

References

- [1] K. Busch, S. Lolkes, R.B. Wehrspohn, F. Foll, *Photonic Crystals. Advance in Design, Fabrication and Characterization*, Wiley-VCH, Weinheim 2003.
- [2] A. Mekis, J.C. Chen, I. Kurland, F. Shanhui, R. Pierre, Villeneuve, J.D. Joannopoulos, *Phys. Rev. Lett.* **77**, 3787 (1996).
- [3] T. Prasad, V. Colvin, D. Mittleman, *Phys. Rev. B* **67**, 165103 (2003).
- [4] P.V. Parimi, T.L. Wentao, V. Plarenta, S. Sridhar, *Nature* **426**, 404 (2003).
- [5] W. Zhang, N. Ganesh, I.D. Block, B.T. Cunningham, *Sensors Actuators B* **131**, 279 (2008).
- [6] W. Belhadj, O. Boukari, D. Gamra, F. AbdelMalek, H. Bouchriha, *Synthetic Metals* **151**, 6 (2005).

Measurement of Beet Root Extract Fluorescence Using TR-LIF Technique

M.S. RABASOVIC^a, D. SEVIC^{a,*}, M. TERZIC^b, S. SAVIC-SEVIC^a, B. MURIC^a, D. PANTELIC^a
AND B.P. MARINKOVIC^a

^aInstitute of Physics, Belgrade, Serbia

^bFaculty of Science, University of Novi Sad, Serbia

Laser induced fluorescence is a powerful spectroscopic technique commonly used to study the structure and internal state distributions in molecules of biological interest. Betanin (C₂₄H₂₆N₂O₁₃) is a specific violet betacyanin and the most prominent pigment in the red beet root where it contributes to 75–95% of the total visible color. Our method of excitation of the beet root extract is based on the tunable (320 nm to 475 nm) Nd:YAG laser system. Fluorescence images of beet root extract excited at 320, 340, 360 and 400 nm were obtained. The fluorescence is observed in range from 580 nm to 660 nm. The influence of the solution concentrations on the fluorescence intensity is also analyzed.

PACS numbers: 42.62.Be, 32.50.+d, 33.50.Dq

1. Introduction

A variety of different pigments are produced by nature. The main food pigments found in the common red beet (*Beta vulgaris*) are the betalains, water soluble pigments. Two main groups of betalains are red-violet betacyanins and the yellow betaxanthins. Betaxanthins are relatively stable and do not have antioxidant properties. The most important betacyanin in red beet is betanin, which is a betanidin 5-O- β -glucoside.

Betanin (C₂₄H₂₇N₂O₁₃) makes up 75–95% of the total colouring matter found in the beet root, therefore it is used as a natural food coloring agent [1]. This pigment, like other betacyanins, is highly susceptible to changes induced by both pH and temperature [2]. As a powerful antioxidant pigment, betanin may provide protection and reduce risk of cardiovascular disease and cancer [3]. Bioassays in the mouse skin and lung clearly revealed betanin to be a potent cancer chemopreventive agent [4, 5]. High antioxidant activity of betanin is associated with phenolic and cyclic amine groups. Both of which are very good electron donors, acting as antioxidants [6]. Some compounds in beet root juice emit a strong fluorescence suitable for direct measurements [7, 8]. The growing interest in betalains is demonstrated by the floral fluorescence effect that is crucial for pollination. In flower of *Mirabilis jalapa* there is observed that visible fluorescence is emitted by yellow pigment betaxanthin and is absorbed by another, violet betacyanin [9, 10]. Investi-

gation of natural corrosion inhibitors is attracted because they are not toxic, biodegradable and not expensive. An aqueous extract of beet root in presence of Zn²⁺ is used to control and inhibit the corrosion of carbon steel [11].

In the present study, beet root juice was investigated in relation to its fluorescent properties. Also, we study the changes of the fluorescence wavelength range and intensity, with the different laser excitation wavelengths and different solution concentrations.

2. Experimental setup

The experimental time resolved laser-induced fluorescence (TR-LIF) setup is shown in Fig. 1. Sample in quartz cuvette was illuminated using a tunable Nd:YAG laser system (Vibrant models 266-I made by Opotek, Inc.). This system incorporates the optical parametric oscillator (OPO) that is pumped by the fourth harmonics of the Nd:YAG Brilliant laser at 266 nm and control electronics. The output of the OPO can be continuously tuned over a spectral range from 320 nm to 475 nm. The samples were illuminated by 5.4 ns pulses with energy up to \approx 50 mJ at 266 nm at repetition rate of 10 Hz.

The laser induced fluorescence in the samples was recorded using streakscope (Hamamatsu model C4334-01) with integrated video streak camera. The streak camera allows detection sensitivities in the photon counting region and enables a wide range of fluorescence lifetime measurements from ps to ms with high accuracy. For all spectra measurements, the emission was collected at 90° from the excitation and dispersed by a 0.3 m focal length triple grating imaging spectrograph (SpectraPro-2300i). The spectrograph is added to

* corresponding author; e-mail: sevic@ipb.ac.rs

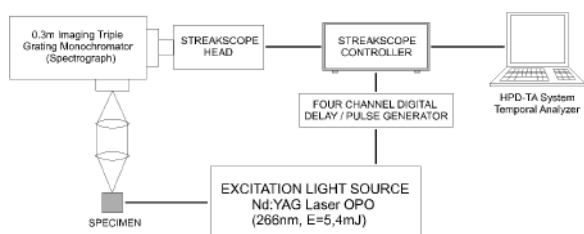


Fig. 1. Schematic illustration of experimental setup for TR-LIF spectroscopy.

the system for simultaneous wavelength and time measurements ($I_f(\lambda, t)$). The fluorescence data have been acquired in photon counting mode using HPD-TA software. All the measurements were made at room temperature.

The juices of fresh beet-root were prepared by separation of the juice in a juice maker. After that, juice was filtered to remove impurities. The 0.25 ml native beet root juice extract was diluted with 2 ml distilled water (solution volume proportion 1:8). Such obtained solution was diluted 2 times, 4 times and 8 times and we measured the fluorescence of these solutions.

As shown in literature [8, 9], betanin, the main pigment of the beet root extract, shows no fluorescence, it absorbs light and weakens measured fluorescence. Fluorescence is due to the presence of other beet-roots pigments.

3. Results and discussion

Streak images of the fluorescence spectrum at 360 nm tunable laser excitation of beet root water solution are shown in Fig. 2. We measured $I_f(\lambda, t)$ using a high MCP gain and a 500 s accumulation time in photon counting mode. We varied the solution concentration, seeking the

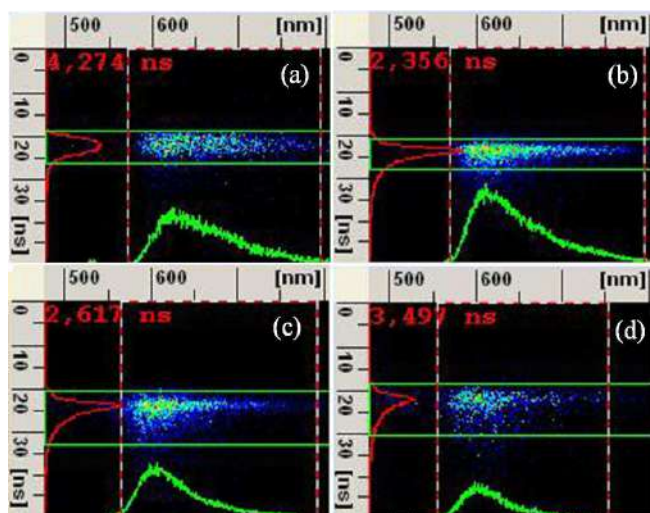


Fig. 2. Streak images of the fluorescence spectrum at 360 nm tunable laser excitation of beet root water solution: (a) 0.25 ml beet-root juice + 2 ml distilled water, (b) 2 times diluted, (c) 4 times diluted, (d) 8 times diluted.

maximum intensity of fluorescence. Maximum intensity of fluorescence is observed in Fig. 2b, so this concentration is regarded as optimal. We did not determine the concentration of pigments in solution, but comparing our results with results presented in [10], concentration of about $6 \mu\text{M}$ should be a good guess.

We also compare characteristics of fluorescence as a function of excitation wavelength. Instead of showing all streak images, fluorescence intensity of beet-root juice (optimal concentration) as a function of OPO tuned excitation wavelength is shown in Fig. 3a, and as a function of time in Fig. 3b. As can be seen from Fig. 3a, b, the intensity of fluorescence is the most prominent at the 340 nm laser excitation. The intensity decreases gradually as the excitation wavelength increases up to 400 nm excitation. However, the result obtained at the 320 nm excitation showed the least intensity of the fluorescence spectra.

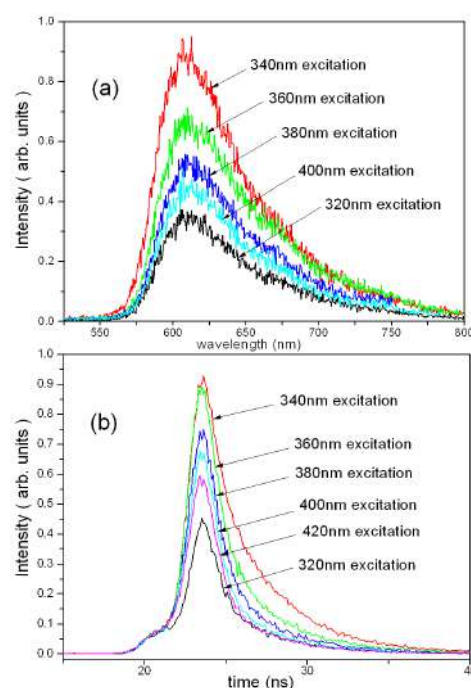


Fig. 3. (a) Fluorescence spectra of beet-root juice (optimal concentration) as a function of OPO tuned excitation wavelength. (b) Fluorescence spectra as a function of time.

4. Conclusion

We presented the beet root extract fluorescence images obtained by the TR-LIF detection system. The dependence of fluorescence intensity on the solution concentrations was analyzed. The fluorescence spectra of beet root water solution were acquired at different excitation wavelengths.

Acknowledgment

The work has been done within the projects OI 141011 and OI 141003 financed by the Ministry of Science and Technological Development, Republic of Serbia.

References

- [1] H.M.C. Azeredo, A.N. Santos, A.C.R. Souza, Kenya C.B. Mendes, M.I.R. Andrade, *Am. J. Food Technol.* **2**, 307 (2007).
- [2] Ma Pedreno, J. Escribano, *J. Sci. Food Agric.* **81**, 627 (online:2001).
- [3] M. Rakin, M. Vukasinovic, S. Markovic, M. Maksimovic, *Food Chem.* **100**, 599 (2007).
- [4] G.J. Kapaida, H. Tokuda, T. Konoshima, H. Nishino, *Cancer Lett.* **100**, 211 (1996).
- [5] G.J. Kapaida, M.A. Azuine, R. Sridhar, Y. Okuda, A. Tsuruta, E. Ichiishi, T. Mukainake, M. Takasaki, T. Konoshima, H. Nishino, H. Tokuda, *Pharmacol. Res.* **47**, 141 (2003).
- [6] A. Gliszczyńska-Świąło, H. Szymusiak, P. Malinowska, *Food Additives Contaminants* **23**, 1079 (2006).
- [7] F. Gandia-Herrero, F. Garcia-Carmona, J. Escribano, *J. Chromatogr. A* **1078**, 83 (2005).
- [8] F. Gandia-Herrero, F. Garcia-Carmona, J. Escribano, *Food Res. Int.* **38**, 879 (2005).
- [9] F. Gandia-Herrero, F. Garcia-Carmona, J. Escribano, *Nature* **437**, 7057 334 (2005).
- [10] F. Gandia-Herrero, J. Escribano, F. Garcia-Carmona, *Planta* **222**, 586 (2005).
- [11] J. Arockia Selvi, Susai Rajendran, V. Ganga Sri, A.J. Amalraj, B. Narayanasamy, *Portugaliae Electrochim. Acta* **27**, 1 (2009).

Proceedings of the International School and Conference on Optics and Optical Materials, ISCOM07, Belgrade, Serbia, September 3–7, 2007

Holographic Measurement of Dental Tissue Contraction and Stress, due to Postpolymerization Reaction

D. PANTELIC^{a,*}, L. BLAŽIĆ^b, S. SAVIĆ-ŠEVIĆ^a, B. MURIĆ^a,
D. VASILJEVIĆ^a, B. PANIĆ^a AND I. BELIĆ^a

^aInstitute of Physics, Pregrevica 118, 11080 Zemun, Belgrade, Serbia

^bUniversity of Novi Sad, Faculty of Medicine, Dental Clinic, Novi Sad, Serbia

Polymerization contraction of dental photo-polymer composites induces internal stress, in a tooth cavity. This stress is measured indirectly by, first, holographic determination of tooth deformation, with consequent calculation of stress using finite element method. Real time holographic technique enabled observation of dental deformation in all stages of polymerization. Specially constructed blue-LED light source was used to polymerize photopolymer composite. We have found that polymerization continues even after illumination is over. Consequently, stress is increased, too.

PACS numbers: 42.40.Kw, 87.85.G-, 87.15.rp, 87.10.Kn

1. Introduction

Contraction of dental polymers during polymerization is a long standing problem in dentistry [1]. When placed inside tooth cavity, polymer contraction is transferred to surrounding hard tissues (dentine, enamel). This, in turn, induces internal stress, possibly resulting in pain, dental filling debonding or dental microcracking. It is therefore important to observe tooth deformation during dental filling placement. This makes possible to choose the most appropriate placement and polymerization techniques. The aim of this research was to investigate the postpolymerization process and additional stress build-up inside the tooth.

Human third molar with mesio-occluso-distal (MOD) cavity were used in this study. Cavity was filled with dental composite photopolymer and polymerized using blue-light LED lamp. A real-time holography was used to measure deformation of dental tissue due to dental filling contraction.

*corresponding author; e-mail: pantelic@phy.bg.ac.yu

Finite element method (FEM) was used to calculate stress inside a tooth, based on deformation measurement. A simplified model of a human third molar was constructed and used to calculate von Mises and principal stresses.

2. Experimental procedure and results

Split-beam holographic setup with liquid gate was used to *in situ* expose and chemically process holographic plate [2]. 532 nm Nd:YAG laser was utilized as a coherent light source. SLAVICH green sensitive holographic plates were used to record holographic information. Plates were developed in D76 developer and fixing step was omitted, in order to suppress emulsion shrinkage.

Human tooth was mounted in a holder using dental gypsum. A cavity (mesio-occluso-distal) was drilled and filled with composite, using a procedure recommended by a composite manufacturer. Prepared tooth is placed in a holographic setup and a hologram is recorded and chemically processed. LED lamp is turned on for a period necessary to fully polymerize the composite.

If a tooth is observed through the hologram, interference between holographically recorded and directly reflected wave fronts can be observed. A system of interference fringes is seen on the tooth surface. Number of fringes gradually increases until the illumination is over. Interference pattern was observed and recorded by a CCD camera from the very beginning of polymerization.

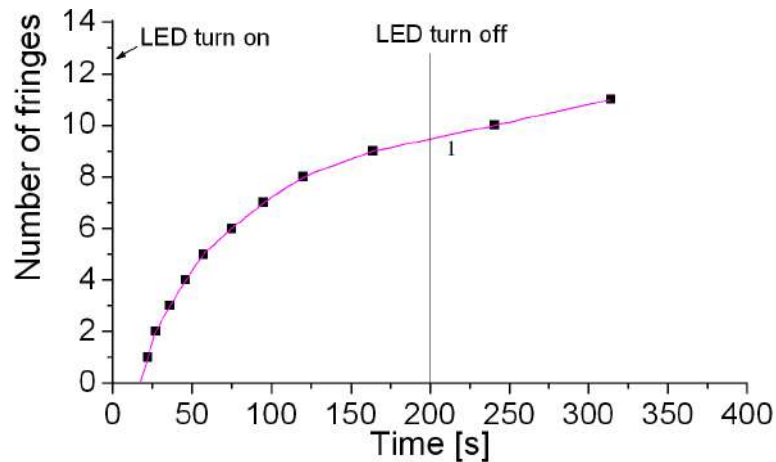


Fig. 1. Number of interference fringes observed on a tooth as a function of time.

Three phases were distinctly observed: initial stage, when the polymer is still viscous and contraction is compensated through polymer flow; contraction stage, where contraction forces gradually build up inside a tooth, and finally, postpolymerization occurs after the termination of polymer illumination and continues contraction for some time. All three phases can be easily identified in Fig. 1. We

have found that the number of fringes as a function of time closely follows a simple exponential relation:

$$y = A - e^{-B(x-C)}, \quad (1)$$

where A , B , and C are constants.

Internal dental tissue stress was calculated using finite element method applied to a mechanical tooth model (see Fig. 2, and compare it to real tooth, shown in Fig. 3). Uniform pressure was applied to cavity sides. Pressure value was chosen so that the calculated deformation of a tooth cusp was identical to experimentally measured.

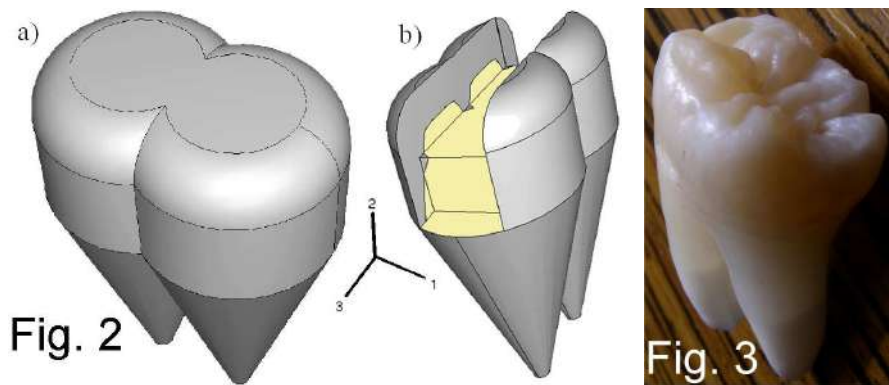


Fig. 2. (a) Intact tooth model, (b) tooth model with MOD cavity.

Fig. 3. Photograph of a human third molar (compare to Fig. 2a).

We have found that postpolymerization reaction continues for several minutes, following illumination. During that period, contraction is further increased for approximately 10%, and maximal principal stress reaches up to 70 MPa. It should be noted that tooth may crack under pressures ranging from 50 to 150 MPa, depending whether forces are tensile, contraction or shear.

3. Conclusions

Our results have shown that there is a dark, postpolymerization reaction, lasting several minutes after the illumination period has ended. During that period deformation is increased for additional 10%. Consequently, internal stress is increased, too. Therefore, when analyzing various polymerization strategies, postpolymerization reaction should be taken into account.

Acknowledgments

This work is realized with the support of the Serbian Ministry of Science and Environmental Protection, through contract No. 141003.

References

- [1] A. Versluis, D. Tantbiroj, M.R. Pintado, R. DeLong, W.H. Douglas, *Dent. Mater.* **6**, 554 (2004).
- [2] D. Pantelić, L. Blažić, S. Šavić-Šević, B. Murić, D. Vasiljević, B. Panić, I. Belić, *Opt. Express* **15**, 6823 (2007).

Application of Fourier–Padé Approximation in Analysis of Holographic Photonic Crystal Structures

D. SEVIC*, S. SAVIC-SEVIC, D. PANTELIC, B. JELENKOVIC AND B.P. MARINKOVIC

Institute of Physics, Belgrade, Serbia

In this paper a method based on the Fourier transform and Padé approximants is investigated for analysis of holographic photonic crystal structures fabricated in Laboratory for Photonics, Institute of Physics, Belgrade. Padé approximants are numerical tool that can be used to accelerate the convergence of a slowly converging sequence.

PACS numbers: 42.40.Eq, 42.70.Qs, 02.30.Nw

1. Introduction

Photonic crystal structures are fabricated in Laboratory for Photonics, Institute of Physics, Belgrade, by the holographic technique [1]. Fast Padé approximation is used as a numerical aid in studies of photonic crystals, see recent publication [2] and some of references therein.

In this paper a method based on the Fourier transform and Padé approximants is investigated for analysis of holographic photonic crystal structures. The Padé approximants are numerical tool that can be used to accelerate the convergence of a slowly converging sequence. For a power series defined as:

$$F_n(z) = \sum_{k=0}^N c_k z^k \quad (1)$$

of order N in the variable z (real or complex) with coefficients c_k , Padé approximant is a rational fraction $P_m(z)/Q_n(z)$, which approximates the fully converged values of the function $F_n(z)$. If we let $z = e^{-jkn}$, then Eq. (1) corresponds to discrete Fourier transform (DFT), so the Padé method is used to improve spectral resolution of fast Fourier transform (FFT), the most popular tool in spectral analysis. This method is usually called Fourier–Padé (FP) approximation.

We applied Fourier–Padé approximation to analyze photonic crystal structures fabricated in our laboratory, enhancing the FFT analysis of the investigated samples. Our FP is implemented as a C code.

2. Analyzed samples

One-dimensional photonic crystals (PC) are fabricated in a dichromate-sensitized pullulan (DCP) by holography. Photonic crystals are created as volume reflection holograms [3, 4]. A single-frequency, diode pumped

Nd-YAG laser, at 532 nm, is used for exposure. Band gaps in the visible range are observed. In addition to the volume grating, a surface relief grating is also formed. In this paper we will analyze this surface relief structure of one dimensional PC. Surface relief of one of the samples measured by the profilometer is shown in Fig. 1. Digital image of a DCP hologram obtained by the optical microscope is shown in Fig. 2.

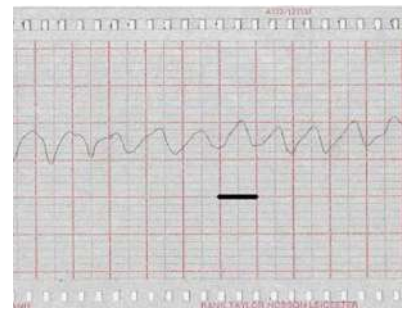


Fig. 1. Surface relief of one of the DCP holograms measured by the profilometer. Bar corresponds to 50 μm .

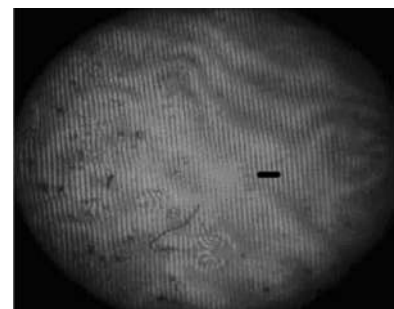


Fig. 2. Digital image of a DCP hologram obtained by optical microscope. Bar corresponds to 20 μm .

* corresponding author; e-mail: sevic@ipb.ac.rs

3. Analysis of photonic crystal DCP structures using FP

The Fourier transform of the surface relief shown in Fig. 1 is calculated and presented in Fig. 3. FP of the same data is calculated and presented in Fig. 4. Spatial frequency is in the range 0 to π and is scaled to 1024 points. Spectral component, easily visible in Fig. 4, is indiscernible on the Fourier transform spectrum, Fig. 3, masked by spectral leaking. FP provides enhanced insight into spatial frequency characteristics of PC structures.

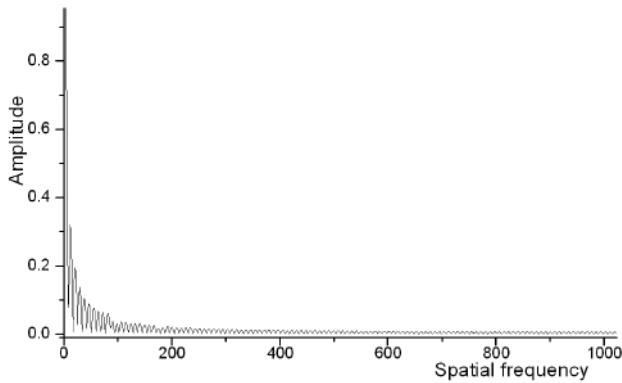


Fig. 3. Fourier transform of surface relief shown in Fig. 1.

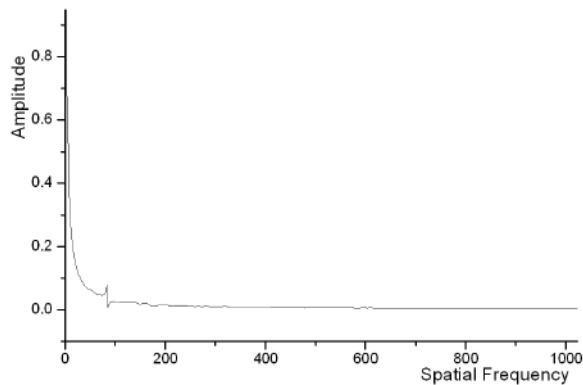


Fig. 4. Fourier-Padé approximation of surface relief shown in Fig. 1.

Unlike the 2D Fourier transform, 2D Padé approximation is not separable, so calculating the 2D FP is very demanding task [5, 6]. Fortunately, PC structures which are of interest here have very directional structure, so we will use Padé approximation to enhance FFT analysis only in the direction of interest, which is horizontal for the grating shown in Fig. 2.

Region of interest for analysis of the digital image of a DCP hologram obtained by optical microscope is shown in Fig. 5a.

The Fourier transform of the image (a) is shown in Fig. 5b, and Fourier Padé approximation of the same image is shown in Fig. 5c. Output is reordered so the

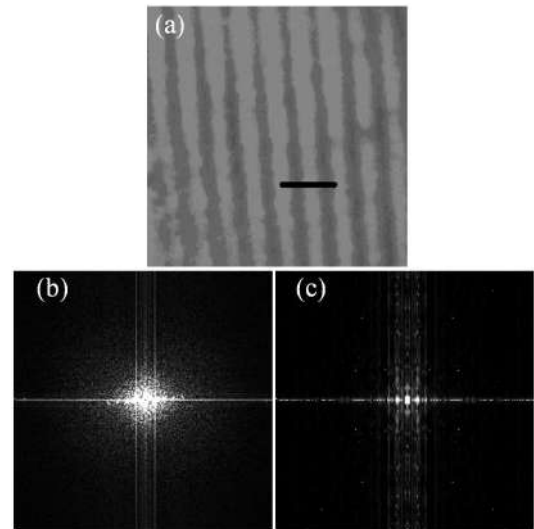


Fig. 5. (a) Analyzed part of the image shown in Fig. 2 (bar corresponds to 100 μm). (b) Fourier transform of the (a), (c) Fourier-Padé approximation of the (a), enhanced in the horizontal direction.

DC component is in the centre. Similar to the 1D case shown in Fig. 3, blurring of the Fourier transform spectrum is obvious in Fig. 5b, better spectral component localization is easy to notice in the Fig. 5c.

4. Conclusion

In this paper a method based on Fourier transform and Padé approximants is investigated for analysis of holographic photonic crystal structures fabricated in our laboratory. Compared to usual use of the Fourier transform, structural analysis of fabricated samples is enhanced by better spatial frequency resolution provided by Fourier-Padé approximation.

Acknowledgments

The work has been done within the projects OI 141011 and OI 141003 financed by the Ministry of Science and Technological Development, Republic of Serbia.

References

- [1] S. Savic-Sevic, D. Pantelic, R. Gajic, G. Isic, *Acta Phys. Pol. A* **112**, 1079 (2007).
- [2] Y. Zhang, W. Zheng, M. Xing, G. Ren, H. Wang, L. Chen, *Opt. Commun.* **281**, 2774 (2008).
- [3] Z. Ye, J. Zheng, D. Liu, S. Pei, *Phys. Lett. A* **299**, 313 (2002).
- [4] R. Ma, J. Xu, W.Y. Tam, *Appl. Phys. Lett.* **89**, 081116 (2006).
- [5] M.F. Calaghan, D.J. Larkman, J.V. Hajnal, *Magn. Res. Med.* **54**, 1490 (2005).
- [6] Dz. Belkic, *Nucl. Instrum. Methods Phys. Res. A* **471**, 165 (2001).

Формирање тродимензионалног математичког модела зуба методом коначних елемената

Татјана Пушкар¹, Дарко Васиљевић², Дубравка Марковић¹, Данимир Јевремовић³,
Дејан Пантелић², Светлана Савић-Шевић², Бранка Мурић²

¹Клиника за стоматологију Војводине, Медицински факултет, Универзитет у Новом Саду,
Нови Сад, Србија;

²Лабораторија за оптоелектронику и ласере, Институт за физику, Универзитет у Београду,
Земун, Србија;

³Клиника за стоматолошку протетику, Стоматолошки факултет, Универзитет у Београду,
Београд, Србија

КРАТАК САДРЖАЈ

Увод Математички модел зубног патрљка намењен је испитивању интензитета и расподеле напона у зубним структурама применом методе коначних елемената. Он подразумева формирање тродимензионалних модела коришћењем стандардних геометријских тела у рачунарским програмима за параметарско пројектовање. Најједноставнији и најприступачнији начин стварања модела зуба је коришћење података из литературе о димензијама и морфолошким одликама зуба.

Циљ рада Циљ рада је био да се формира математички модел брушеног горњег другог премолара за анализу деформација и напона у тврдим зубним структурама изазваних различитим протетичким клиничким поступцима.

Методе рада Брушени зуб има облик сложеног геометријског тела и због тога је погодан за моделовање у рачунарском програму за параметарско пројектовање *SolidWorks*. Након прикупљања података о димензијама и облику зуба, приступило се изради модела разлагањем зуба (сложеног геометријског тела) на основна геометријска тела (ваљак, купу, пирамиду). Модел је затим пребачен у програм за прорачун методом коначних елемената (*Abaqus, SIMULIA, USA*). Пренос података између два програма урађен је преко *ACIS SAT*, стандардне датотеке за пренос података о тродимензионалним моделима.

Резултати Коришћењем рачунарског програма за параметарско пројектовање развијена су три модела брушеног горњег другог премолара: модел брушеног горњег другог премолара с очуваном пулпом, модел ендодонтски леченог горњег другог премолара са два очувана зида кавитета и модел ендодонтски леченог горњег другог премолара са два очувана зида кавитета и постављеним пулпарним кочићем.

Закључак Математички модел брушеног зуба добијен на основу података из литературе веома је близак морфолошким одликама стварног зуба, односно упрошћавање је урађено у најмањој могућој мери. Модел омогућава прорачун деформација и напона у зубним структурама који се јављају током њиховог лечења и функционисања стоматогнатог система.

Кључне речи: зубни патрљак; метода коначних елемената; биомеханика; напон; деформација

УВОД

Метода коначних елемената (енгл. *Finite Element Analysis – FEA*) је истраживачка метода која се данас широко примењује у испитивањима биомеханичког понашања сложених биолошких структура. За разлику од експерименталних метода, као што су оптерећење испитиване структуре помоћу универзалних тест-машина [1], метода с тензометром [2] и метода с мерним плочицама као мерачима напона [3], *FEA* омогућава мерење и сагледавање напона и деформација који су изазвани различитим терапијским поступцима и њихов распоред у читавом испитиваном објекту. За разлику од осталих истраживачких техника, *FEA* пружа могућност симулације клиничких процедура до микрометарских детаља у физиолошким и нефизиолошким условима, те сагледавање утицаја појединих, изолованих фактора на биолошке системе [4, 5]. Због сложености клиничких истраживања, где на испити-

вани биолошки систем делује веома велик број фактора, као и због дужине клиничког опсервационог периода, резултати добијени помоћу *FEA* представљају корисну смерницу за разумевање биомеханичких проблема биолошких структура и прецизирање и усмеравање клиничких истраживања [6, 7].

FEA се примењује у стоматолошким истраживањима још од 1973. године, када су Фара (*Farah*) и сарадници објавили истраживања на аксисиметричном моделу реставрираног првог молара [7]. Највећи број радова у којима је коришћена ова методологија објављен је из области стоматолошке протетике и имплантологије; следе реставративна стоматологија, ортопедија вилица, ендодонција и орална хирургија [4].

FEA је коришћен и у стоматолошкој протетици за испитивање и дизајнирање различитих фиксних и мобилних зубних надокнада. Циљ свих истраживања је био да се утврди како, на пример, димензије надокнаде, дебелина метала, керамике и цементног слоја,

Correspondence to:

Tatjana PUŠKAR
Klinika za stomatologiju,
Hajduk Veljkova 12,
21000 Novi Sad, Srbija
tatjanapuskar@yahoo.com

врста материјала од којих је израђена надокнада, упадни угао, површина оклузивног оптерећења и температурне промене у оралној средини утичу на напонска стања у оралним структурама и зубним надокнадама [4, 8-11]. У области имплантологије *FEA* се примењује у различитим испитивањима као што су: решавање проблема везаних за дизајн имплантата и протетичке супраструктуре, испитивање материјала за израду имплантата, испитивање одговора имплантата и биолошког система на оптерећење и испитивање проблема везе имплантата и кости [4, 12].

У области рестауративне стоматологије *FEA* је веома погодан за испитивање различитих рестауративних материјала и техника рада, као и утицаја дизајна кавитета на напрезања тврдих зубних ткива током адхезивних поступака рестаурације [13]. *FEA* омогућава сагледавање расподеле напона у зубним структурама који се јављају током рестауративних захвата, а који су изазвани полимеризационом контракцијом композитних материјала на бази смола [14, 15, 16]. Исто тако се и расподеле напона који се јављају као последица оптерећења зуба рестаурираних различитим материјалима и техникама могу анализирати помоћу *FEA* [6, 7, 17-21]. Механичке особине препарисаних канала корена, анализа напона током њиховог пуњења и фактори који утичу на пуцање (оштећење) ендодонтски лечених зуба само су неки од проблема који се истражују коришћењем *FEA* у области ендодонције [4, 22].

У ортодонцији, оралној и максилофацијалној хирургији *FEA* се користи за испитивање механичких одлика вилица, темпоромандибуларних зглобова и пародонталног лигамента за време жвакања, односно бруксизма, при дејству физиолошких и нефизиолошких сила [4].

Први корак у истраживању биомеханичког понашања сложених биолошких структура је формирање математичког модела који се користи за прорачуне применом *FEA*. У зависности од циља истраживања, математички модел одређене биолошке структуре, у овом случају зуба, може бити дводимензионалан или тродимензионалан. За формирање модела користе се специфични програми за параметарско пројектовање. Током деведесетих година двадесетог века рачунари нису били довољно брзи, па су се за моделовање углавном користили специјално пројектовани рачунари (графичке радне станице), а модели су се углавном радили у две димензије. Данас су рачунари довољно брзи, па се углавном формирају тродимензионални модели.

Неопходне информације о величини и облику зуба за формирање модела могу се добити на неколико начина: на основу података из литературе о димензијама и морфолошким обележјима појединих група зуба [11, 20-24], сечењем зуба и дигитализацијом добијеног низа пресека зуба, компјутеризованом томографијом (*CT*) или нуклеарном магнетном резонанцијом (*NMR*) [5, 6, 17, 18, 25].

Неопходни подаци за формирање модела зуба могу се добити његовим сечењем са одговарајућим кораком (размаком између пресека). Добијени пресеци се на од-

говарајући начин дигитализују било путем скенирања или фотографисањем помоћу дигиталног фотоапарата [5, 7, 8]. У оба случаја добијају се графичке датотеке у формату *.jpg* које служе као основа за формирање модела у програмима за параметарско пројектовање.

Веома прецизни пресеци могу се добити помоћу *CT* или *NMR* [17, 18, 25]. Обе технике су савремене и прецизне методе за формирање модела, али су већини истраживача недоступне због високе цене опреме и самог снимања. Додатну тешкоћу у раду са микро *CT* и *NMR* представља специфичан формат података, те је, да би се они могли увести у стандардне програме за параметарско пројектовање, потребан наменски развијен програм који ће добијене податке прилагодити захтевима програма за параметарско пројектовање. Поменути програми се посебно набављају и веома су скупи.

Скенирањем површине извађеног зуба *3D* скенером може се добити модел зуба који не садржи податке о унутрашњој грађи зуба, граници између глеђи, дентина и коморе пулпе. Такви модели се у научним радовима користе за испитивање мобилности зуба под утицајем различитих оптерећења [9].

Најједноставнији начин за формирање модела зуба је коришћење података из литературе о димензијама и морфолошким одликама зуба. Овај начин се заснива на формирању тродимензионалних модела коришћењем стандардних геометријских тела (ваљак, купа, пирамида, квадар,...) у програмима за параметарско пројектовање. Један од таквих програма је и *SolidWorks (SolidWorks Corporation, USA)*. Предност овог начина формирања модела је у томе што не захтева скупу и, за наше услове, врло често недостижну рачунарску опрему.

ЦИЉ РАДА

Циљ рада је био да се применом *FEA* формира математички модел брушеног горњег другог премолара. Модел се може користити за анализу напона и деформација тврдих зубних структура изазваних различитим протетичким клиничким поступцима.

МЕТОДЕ РАДА

Формирању математичког модела брушеног зуба претходило је прикупљање података из литературе о морфолошким одликама и димензијама горњег другог премолара (Табела 1).

Димензије и облик круне брушеног зуба добијају се на основу општеприхваћених принципа струке у вези са брушењем зуба за керамичке круне [26]. Брушени зуб има облик сложеног геометријског тела и због тога је погодан да се моделује у програму за параметарско пројектовање. Ови програми раде на следећем принципу: тело, односно предмет произвољне сложености треба разложити на основна геометријска тела (ваљак, купу, пирамиду, квадар,...) и њиховим додавањем једно на друго (сабирањем) и одузимањем фор-

Табела 1. Димензије горњег другог премолара
Table 1. Dimensions of maxillary second premolar

Параметар Parameter	Димензија (mm) Dimensions (mm)
Висина круне Coronal length	7.5±0.6 [27]
МД ширина у пределу екватора зуба MD width in the dental equator	7.0 [27]
БЛ ширина у пределу екватора зуба BL width in the dental equator	9.0 [26]
МД ширина у пределу ГЦ споја MD width level of CE junction	4.9±0.3 [26]
БЛ ширина у пределу ГЦ споја BL width level of CE junction	7.9±0.5 [26]
МД пречник корена 4 mm од апекса MD root radius 4 mm from apex	3.2±0.6 [26]
БЛ пречник корена 4 mm од апекса BL root radius 4 mm from apex	5.0±0.7 [26]
МД пречник корена на половини дужине корена MD root radius in the midpoint	3.8±0.4 [26]
БЛ пречник корена на половини дужине корена BL root radius in the midpoint	7.0±0.7 [26]
Дужина корена Root length	13.5±1.4 [27]

МД – мезиодистални; БЛ – буколингвални; ГЦ – глеђно-цементни
 MD – mesiodistal; BL – buccolingual; CE – cementoenamel

мира се сложено геометријско тело. Процес формирања геометријског тела почиње цртањем скице која представља основу тог тела. Да би се формирало сложено геометријско тело, неопходно је формирати велики број основних геометријских тела и њих уклапати као да су то „лего“ коцкице. Неки пут је потребно спојити два основна геометријска тела или више њих, а неки пут од сложеног одузети једно основно геометријско тело или више тела. Зато сва сложена геометријска тела која су формирана на овакав начин имају велики број површина, ивица које их раздвајају и темена у којима се те ивице сусрећу.

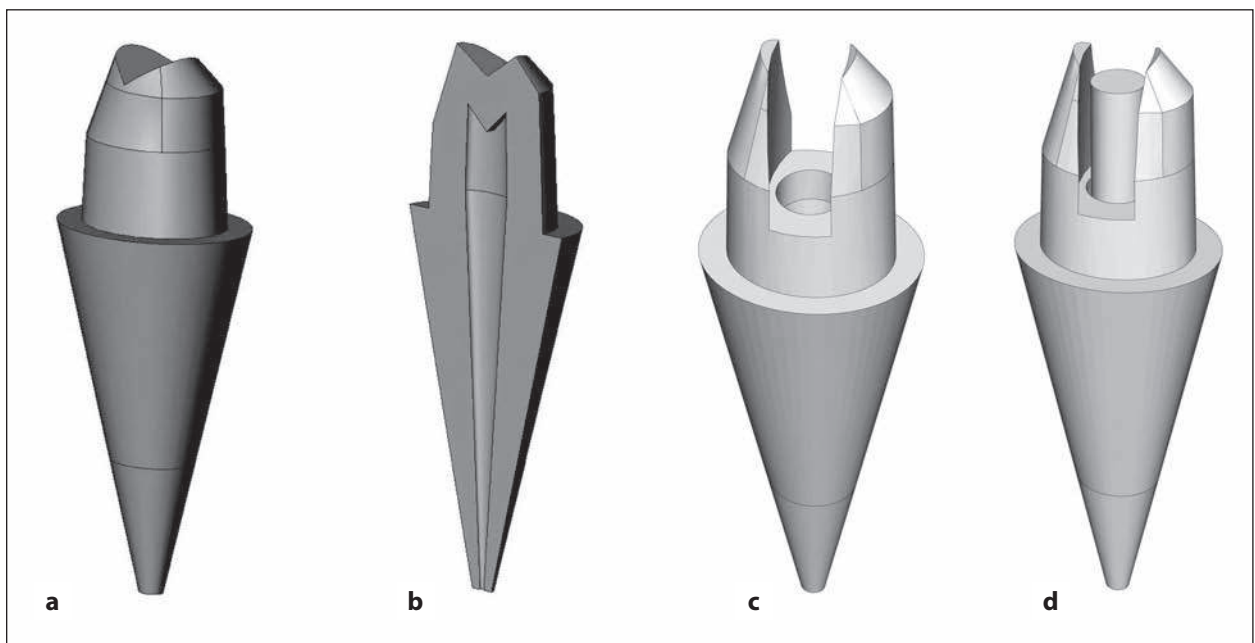
Када су модели брушеног горњег другог премолара направљени у програму *SolidWorks*, они су пребачени у програм за прорачун помоћу *FEA* (*Abaqus*, *SIMULIA*, *Dassault Systems S.A.*, USA). Пренос података између два програма урађен је преко *ACIS SAT*, стандардне датотеке за пренос података о тродимензионалним моделима.

На моделу је изведено дизајнирање кавитета уз постављање претходно измоделованог паралелно-коничног пулпарног кочића.

РЕЗУЛТАТИ

Коришћењем програма за параметарско пројектовање развијена су три модела брушеног горњег другог премолара. На слици 1a приказан је модел брушеног горњег другог премолара с очуваном пулпом, а на слици 1b уздужни пресек модела. Зубни патрљак је формиран на основу савремених принципа за препарацију зуба за керамичку круну [26]. Након тога је формиран модел ендодонтски леченог горњег другог премолара са два очувана зида кавитета (Слика 1c). На слици 1d приказан је модел ендодонтски леченог горњег другог премолара са два очувана зида кавитета и постављеним пулпарним кочићем. За моделажију је одабран паралелно-конични пулпарни кочић. Коничност коренског дела омогућава уклањање минималне количине зубне супстанце при препарацији канала корена и несметано отицање вишка цемента при цементирању кочића. У табели 2 су дати подаци о броју површина, ивица и темена на моделима.

Да би програм за прорачун помоћу *FEA* уопште могао да функционише, тј. да прорачуна напоне и деформације на приказаном моделу, било је неопходно да се модел подели на велики број коначних елемена



Слика 1. Модел брушеног горњег другог премолара (a), у пресеку (b), с кавитетом (c), с кавитетом и постављеним кочићем (d)
Figure 1. Model of abutment of maxillary second premolar (a), vertical section (b), with cavity (c), with cavity and post (d)

Табела 2. Број површина, ивица и темена на моделу брушеног горњег другог премолара (A), ендодонтски леченог зубног патрљка с очувана два зида кавитета (B) и ендодонтски леченог зубног патрљка с кавитетом и постављеним кочићем (C)

Table 2. Number of solid faces, edges and vertices on the model of maxillary second premolar (A), endodontically treated abutment with two remaining walls of the cavity (B), endodontically treated abutment with cavity and post (C)

Број Number	Модел / Model		
	A	B	C
Површине Solid faces	23	30	30
Ивице Edges	179	179	180
Темена Vertices	160	150	154

Табела 3. Број чворова и елемената на моделу брушеног горњег другог премолара (A), ендодонтски леченог зубног патрљка с очувана два зида кавитета (B) и ендодонтски леченог зубног патрљка с кавитетом и постављеним кочићем (C)

Table 3. Number of nodes and elements on the model of maxillary second premolar (A), endodontically treated abutment with two remaining walls of the cavity (B), endodontically treated abutment with cavity and post (C)

Број Number	Модел / Model		
	A	B	C
Чворови Nodes	40348	25790	29176
Елементи Elements	207870	124524	144101

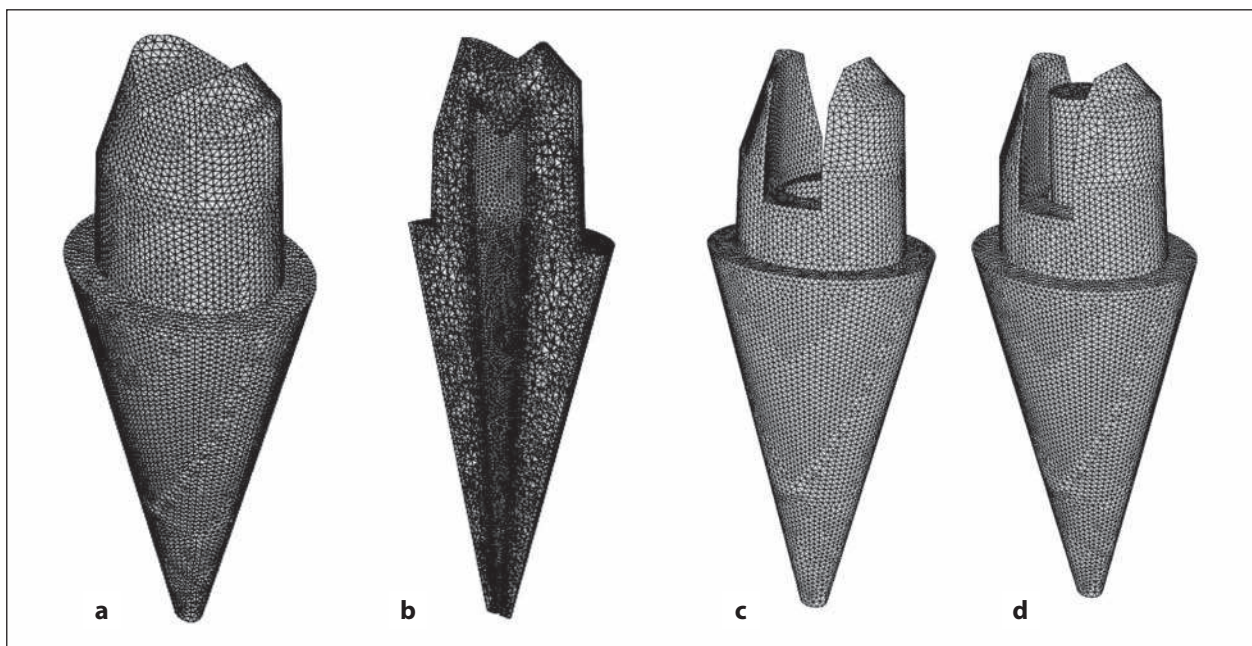
та. Због сложености модела брушеног горњег другог премолара, изабрани су линеарни тетраедри (њихова ознака у програму *Abaqus* је *C3D4*) као основа за формирање мреже коначних елемената. У табели 3 дати су подаци о броју елемената (линеарних тетраедара) и броју чворова у којима се спајају елементи за сваки од развијена три модела.

На слици 2a-d приказани су модели брушеног горњег другог премолара с формираном мрежом коначних елемената.

ДИСКУСИЈА

Савремена истраживања у области медицине, стоматологије и различитих биоматеријала су у великој мери мултидисциплинарна. Без обзира на то што је формирање математичких модела инжењерски посао, сваки члан тима који користи *FEA* у области биомедицинских истраживања мора имати потпуна сазнања о истраживачком поступку и могућностима које ова методологија пружа. Након дефинисања проблема који се истражује, медицински део тима инжењерима мора поставити захтеве у вези с формирањем математичког модела, пружити теоријске основе за дефинисање граничних услова и податке о особинама материјала који се истражује. Истраживач мора имати јасну слику о томе у којој мери упрошћавање модела и прецизност унетих података утичу на валидност истраживања. Без познавања методологије рада у области *FEA* све претходно наведено просто није могуће.

За разлику од израде модела на основу података из литературе, приликом израде математичког модела зуба на основу анализе и мерења пресека зуба, што је често коришћена метода [5, 6, 7], постоји низ потешкоћа и проблема. Да би се од информација добијених на основу мерења или скенирања пресека зуба добио модел у дигиталном облику, потребно је применити неки од софтверских пакета за обраду и формирање дигиталног записа. Ови пакети се користе за ускоспецифичне проблеме, тако да су обично врло скупи. При анализи пресека, граница између различитих зубних ткива је тешко уочљива, а проблем ствара и материјал којим се фиксира зуб у носач приликом сечења. Он мора бити таквих особина да чврсто држи исечени слој зуба, а да се не деформише приликом сечења. Поред тога, проблем представља и објекат којим се врши сечење, јер може деформисати сам пресек.



Слика 2. Мешан модел брушеног горњег другог премолара (a), у пресеку (b), с кавитетом (c), с кавитетом и постављеним кочићем (d)
Figure 2. Meshed model of abutment of maxillary second premolar (a), vertical section (b), with cavity (c), with cavity and post (d)

СТ и NMR су савремене и прецизне методе за формирање модела [17, 18, 25], али већини истраживача нису доступне како због високе цене њихове опреме и самог снимања, тако и због потребе за постојањем међупрограма који би омогућио да програм за дискретизацију и формирање мреже коначних елемената прихвати на тај начин добијене информације.

Формирањем модела зуба у неком од програма за параметарско пројектовање урађен је само први неопходан корак у целокупном процесу формирања модела за анализу напона и деформација. Неопходно је формирани модел увести у рачунарски програм за прорачун помоћу FEA. Овај пренос се обично врши преко стандардних типова датотека за пренос тродимензионалних модела, као што су: ACIS SAT, IGES или STEP. Када се модел зуба унесе у програм, да би се могли прорачунати напони и деформације зуба, неопходно је најпре модел зуба поделити на велики број основних геометријских елемената, који се овде називају „коначни елементи”. Процес дефинисања мреже коначних елемената или „меширања” (енгл. mesh – мрежа) налази се у основи свих прорачуна напона и деформација. FEA се заснива на простој чињеници да није могуће срачунати напоне и деформације тела сложене структуре, али је то зато могуће урадити за једноставна геометријска тела. Сама метода се заснива на подели тела сложене структуре на велики број једноставних геометријских тела и прорачуну напона и деформација за свако геометријско тело понаособ. Користећи адекватне математичке прорачуне и брзе рачунаре могуће је утврдити напоне и деформације тела произвољне сложености.

У приказаном раду коришћени су подаци из литературе о морфолошким обележјима и димензијама зуба за формирање упрошћеног математичког модела брушеног горњег другог премолара, као једноставан, доступан и релативно брз начин формирања модела [26, 27]. Формирани модел омогућава дизајнирање кавитета и постављање претходно измоделованих пулпарних кочића различитих облика, у зависности од потреба истраживања.

Математички модел зубног патрљка начињен у овом истраживању намењен је испитивању интензитета и расподеле напона помоћу FEA. Напони и деформације јављају се на зубном патрљку при терапијским поступцима, физиолошким и нефизиолошким оптерећењима у току функције стоматогнатог система. Ова методологија пружа могућност веома прецизне симулације клиничких процедура уз могућност сагледавања утицаја појединачних фактора на биолошки систем. Иако је интензитет напона различит, у случају да анализирамо оптерећени зубни патрљак без протетичке круне, расподела напона се не разликује значајно [28]. Поред тога, модел зубног патрљка (модел сложеног геометријског тела) чини основни модел, који се даље може модификовати, што је предност програма за параметарско пројектовање у односу на остале програме за пројектовање. То значи да, када је пројектован модел брушеног горњег другог премолара, на веома лак

начин је омогућено формирање кавитета, пласирање пулпарних кочића различитог облика или моделација протетичке круне, као и слоја цемента постављеног на патрљак, у зависности од потреба истраживања. Модел се може даље развијати и моделацијом пародонталног лигамента и околне кости. Коришћењем различитих параметара који одговарају механичким особинама рестауративних материјала који се истражују, на овом моделу се применом FEA могу испитати напонска стања при оптерећењу зубног патрљка рестаурiranог различитим врстама материјала или различитим врстама и облицима пулпарних кочића. Интензитет и расподела напона који настају као последица полимеризационе контракције композитних материјала на бази смола приликом припреме зуба за керамичке круне такође се могу на врло једноставан начин испитати на овом моделу.

Математички модел брушеног зуба добијен на основу података из литературе о морфолошким особинама зуба веома је близак изгледу стварног зуба, а морфолошко упрошћавање је изведено у најмањој могућој мери. Димензије коморе пулпе зависе од старости пацијента, претходних терапијских захвата и патолошких промена каријесне и некаријесне етиологије који су евентуално деловали на зуб [29]. Стога формирање коморе пулпе на основу података из литературе – који су, када су димензије коморе пулпе у питању, заиста штурти и веома ретки – не доводи до значајног упрошћавања модела с морфолошког аспекта. Приликом моделације брушених зуба постоји неколико специфичности и олакшавајућих околности у односу на моделовање интактних зуба. Облик брушених зуба је задата форма која у великој мери личи на геометријско тело, тако да се уз мало упрошћавање модела, коришћењем података из литературе о морфолошким обележјима и принципима препарације зуба, може добити прецизан модел. Приликом брушења зуба скоро се потпуно уклања слој глеђи, тако да се при моделацији не јавља потреба за разграничавањем глеђног слоја од дентинског.

Приликом истраживања помоћу FEA потребно је потврдити математички модел и коришћене параметре неком од експерименталних метода, а коначан и свеобухватан одговор за већину истраживаних проблема у области стоматологије дају клиничка истраживања којима FEA омогућава прецизније, лакше и брже постављање експеримента и долажење до резултата и усавршавање терапијских поступака.

С математичког аспекта, брушени зуб има облик сложеног геометријског тела. Стога је потпуно адекватно и рационално формирати математички модел брушеног зуба на основу података из литературе о морфолошким особинама зуба и просечним димензијама круне и корена. Једноставним додавањем или одузимањем геометријских тела од основног модела лако се могу дизајнирати кавитети различитог облика и пласирати пулпарни кочићи. Убацивањем података за механичке одлике различитих рестауративних материјала у програм за FEA могу се прорачуна-

ти напони и деформације при различитим протетичким процедурама.

ЗАКЉУЧАК

Приказани математички модел брушеног зуба, формиран на основу података о морфолошким одликама зуба добијеним из литературе, веома је близак стварном зубу, јер је изведено веома мало морфолошко упрошћавање. Прорачунавањем методом коначних елемената деформација и напона зубних структура које се јавља-

ју током лечења зуба и функције стоматогнатог система могу се добити корисне информације за разумевање биомеханичких проблема и усмеравање и прецизирање клиничких истраживања, као и за усавршавање терапијских поступака.

НАПОМЕНА

Рад је реализован у оквиру пројекта „Квантна и оптичка интерферометрија” (број 141003) Министарства за науку и технолошки развој Републике Србије.

ЛИТЕРАТУРА

- Soares P, Santos-Filho P, Cavalcanti-Queiroz E, Araujo TC, Campos RE, Araujo CA, et al. Fracture resistance and stress distribution in endodontically treated maxillary premolars restored with composite resin. *J Prosthodont*. 2008; 17:114-9.
- Feilzer AJ, De Gee AJ, Davidson CL. Setting stress in composite resin in relation to configuration of the restoration. *J Dent Res*. 1987; 66:1636-9.
- Sakaguchi RL, Farracane JL. Stress transfer from polymerization shrinkage of a chemical-cured composite bonded to a pre-cast composite substrate. *Dent Mater*. 1998; 14:106-11.
- Mackerle J. Finite element modelling and simulations in dentistry: A bibliography 1990-2003. *Comput Methods Biomech Biomed Engin*. 2004; 7(5):277-303.
- Lin CL, Chang CH, Cheng CS, Wang CH, Lee HE. Automatic finite element mesh generation for maxillary second premolar. *Comput Methods Programs Biomed*. 1999; 59(3):187-95.
- Palamara JEA, Palamara D, Messer HH, Tyas MJ. Tooth morphology and characteristics of non-carious cervical lesions. *J Dent*. 2006; 34:185-94.
- Miletić V. Analiza kontaktnih opterećenja na trodimenzionalnom modelu zuba metodom konačnih elemenata [magistarska teza]. Beograd: Stomatološki fakultet Univerziteta u Beogradu; 2005.
- Pegoretti A, Fambri L, Zappini G, Bianchetti M. FEA of a glass fiber reinforced composite endodontic post. *Biomaterials*. 2002; 23:2667-82.
- Muraki H, Wakabayashi N, Park I, Ohya T. FE contact stress analysis of the RPD abutment tooth and periodontal ligament. *J Dent*. 2004; 32:659-65.
- Magne P, Parakis N, Belser UC, Krejci I. Stress distribution of inlay-anchored adhesive fixed partial dentures: a FEA of the influence of restorative materials and abutment preparation design. *J Prosthet Dent*. 2002; 87:516-27.
- Kamposhiora P, Papavasiliou G, Bayne S, Felton D. Predictions of cement microfracture under crowns using 3D-FEA. *J Prosthodont*. 2000; 9:201-9.
- Stamenković D. Biomehanika oralnih implantata i nadoknada. *Srp Arh Celok Lek*. 2008; 136:73-83.
- Blažić L. Primena svetlosnih izvora sa plavim svetlosno-emitujućim diodama (LED) u polimerizaciji direktnih kompozitnih restauracija. Beograd: Građevinska knjiga; 2007.
- Pantelić D, Blažić L, Savić-Šević S, Panić B. Holographic detection of tooth structure deformation after dental filling polymerisation. *J Biomed Opt*. 2007; 12:24-6.
- Pantelić D, Blažić L, Savić-Šević S, Murić B, Vasiljević D, Panić B, et al. Real-time measurement of internal stress of dental tissue using holography. *Optics Express*. 2007; 15:6823-30.
- Pantelić D, Blažić L, Savić-Šević S, Murić B, Vasiljević D, Panić B, et al. Holographic measurement of dental tissue contraction and stress due to postpolymerisation reaction. *Acta Physica Polonica A*. 2007; 112:1155-7.
- Lin CL, Yen-Hsiang C, Perng-Ru L. Multi-factorial analysis of a cusp-replacing adhesive premolar restoration: A finite element study. *J Dent*. 2008; 36:194-203.
- Fennis W, Kuijss R, Barink M, Kreulen C, Verdonchot N, Creugers N. Can internal stresses explain the fracture resistance of cusp-replacing composite restorations? *Eur J Oral Sci*. 2005; 113:443-8.
- Lin CH, Chang CH, Wang CH, Ko CC, Lee HE. Numerical investigation of the factors affecting interfacial stresses in a MOD restored tooth by auto-meshed FE method. *J Oral Rehabil*. 2001; 28:517-25.
- Arola D, Galles LA, Sarubin MF. A comparison of the mechanical behavior of posterior teeth with amalgam and composite MOD restorations. *J Dent*. 2001; 29:63-73.
- Aykol H, Toparli M. A comparison of the stress analysis of an unrestored and restored tooth with amalgam and composite resin. *Mathematical and Computational Applications*. 2005; 10:89-98.
- Lertchirakarn V, Palamara JEA, Messer HH. Finite element analysis and strain gauge studies of vertical root fracture. *J Endod*. 2003; 29:529-34.
- Toparli M, Gokay N, Aksoy T. Analysis of a restored maxillary second premolar tooth by using 3D FEA method. *J Oral Rehabil*. 1999; 26:157-64.
- Yu WJ, Kwon TY, Kyung HM, Kim KH. An evaluation of localized debonding between fiber post and root canal wall by FE simulation. *Int Endodontic J*. 2006; 39:959-67.
- Dorow C, Sander FC. Investigation of the stress and strain profiles during intrusion and torque of a premolar. *Appl Math Mech*. 2003; 3:268-9.
- Rosenstiel S, Land M, Fujimoto J. *Contemporary Fixed Prosthodontics*. St. Louis: Mosby; 2006.
- Martinović Ž. Osnovi dentalne morfologije. Beograd: Službeni glasnik; 2000. p.106-125.
- Joshi S, Mukherjee A, Kheur M, Mehta A. Mechanical performance of endodontically treated teeth. *Finite Element in Analysis and Design*. 2001; 37:587-601.
- Ash M. *Wheeler's Dental Anatomy, Physiology and Occlusion*. Philadelphia: WB Saunders Company; 1993.

Three Dimensional Mathematical Model of Tooth for Finite Element Analysis

Tatjana Puškar¹, Darko Vasiljević², Dubravka Marković¹, Danimir Jevremović³, Dejan Pantelić², Svetlana Savić-Šević², Branka Murić²

¹Dental Clinic of Vojvodina, School of Medicine, University of Novi Sad, Novi Sad, Serbia;

²Laboratory for Optoelectronics and Lasers, Institute of Physics, Zemun, Belgrade, Serbia;

³Clinic for Prosthodontics, School of Dentistry, University of Belgrade, Belgrade, Serbia

SUMMARY

Introduction The mathematical model of the abutment tooth is the starting point of the finite element analysis of stress and deformation of dental structures. The simplest and easiest way is to form a model according to the literature data of dimensions and morphological characteristics of teeth. Our method is based on forming 3D models using standard geometrical forms (objects) in programmes for solid modeling.

Objective Forming the mathematical model of abutment of the second upper premolar for finite element analysis of stress and deformation of dental structures.

Methods The abutment tooth has a form of a complex geometric object. It is suitable for modeling in programs for solid modeling *SolidWorks*. After analysing the literature data about the morphological characteristics of teeth, we started the modeling dividing the tooth (complex geometric body) into simple geometric bodies (cylinder, cone, pyramid,...). Connecting simple geometric bodies together or subtracting bodies from the basic body, we formed complex geometric body, tooth.

The model is then transferred into Abaqus, a computational programme for finite element analysis. Transferring the data was done by standard file format for transferring 3D models ACIS SAT.

Results Using the programme for solid modeling *SolidWorks*, we developed three models of abutment of the second maxillary premolar: the model of the intact abutment, the model of the endodontically treated tooth with two remaining cavity walls and the model of the endodontically treated tooth with two remaining walls and inserted post.

Conclusion Mathematical models of the abutment made according to the literature data are very similar with the real abutment and the simplifications are minimal. These models enable calculations of stress and deformation of the dental structures. The finite element analysis provides useful information in understanding biomechanical problems and gives guidance for clinical research.

Keywords: abutment; finite element analysis; biomechanics; stress; deformation

Примљен • Received: 23/01/2009

Прихваћен • Accepted: 23/02/2009

Proceedings of the International School and Conference on Optics and Optical Materials, ISCOM07, Belgrade, Serbia, September 3–7, 2007

Holographic Fabrication of Periodic Microstructures in Dichromated Pullulan

S. SAVIĆ-ŠEVIĆ*, D. PANTELIĆ, R. GAJIĆ AND G. ISIĆ

Institute of Physics, Pregrevica 118, 11080 Belgrade, Serbia

Photonic crystal structures are fabricated in dichromated pullulan by the holographic technique. Relief structures of photonic lattices with rectangular, rhombic, and hexagonal arrays of peaks and holes are obtained. The structures have periodicities of the order $1.1 \mu\text{m}$ and depth of about 50 nm .

PACS numbers: 42.40.-i, 42.70.Ln, 42.70.Qs

1. Introduction

One way to create photonic crystal structures is realized by holography [1–4]. In this study dual-beam multiple exposure technique is used to generate various lattice structures. In the dual-beam process, the photonic crystal structure is obtained by rotating the holographic recording material between exposures. A range of lattice structures can be obtained by varying the angle between two beams, and the rotation angle of holographic material.

Previously, photonic structures have been recorded also in low-refractive index materials such as photoresists [4]. The holographic material used in this study is pullulan, doped with dichromate [5, 6]. Pullulan is a biopolymer with linear polysaccharide structure.

2. Periodic microstructures fabrication

Dichromate-sensitized pullulan samples were prepared by mixing 8% aqueous solution of pullulan and 50% ammonium dichromate by weight of pullulan. The solution was subsequently coated onto clean glass slides in a horizontal position and the film was dried under normal laboratory conditions. The thickness of the dried layer was approximately $10 \mu\text{m}$.

A single-frequency, diode pumped Nd:YAG laser, at 532 nm , is used for exposure (200 mW laser power). Linearly polarized, laser beam is split into two

*corresponding author; e-mail: savic@phy.bg.ac.yu

equal power beams (to obtain the highest contrast in fringe intensity) and the beam interference pattern is recorded. He-Ne laser operating at 632.8 nm was used for real-time monitoring of diffraction efficiency. By proper choice of rotation angles different structures can be generated [7]. Double and triple exposures, to the same interference pattern of dichromated pullulan, were used.

The exposed plates were, first, chemically processed with a mixture of 60% isopropanol and 40% water for 120 seconds, and then immersed for 30 seconds in the pure isopropanol. After development in mixture of water and isopropanol unexposed regions are washed out, and an intensity light pattern is converted into a relief structure.

The structures were characterized by atomic force microscope (AFM) needle sensor on the TwinSnom system.

Relief structure of photonic lattice with rectangular array of peaks and holes was obtained by rotating the material for 90° , between exposures. Figure 1 shows an AFM image of the lattice structure.

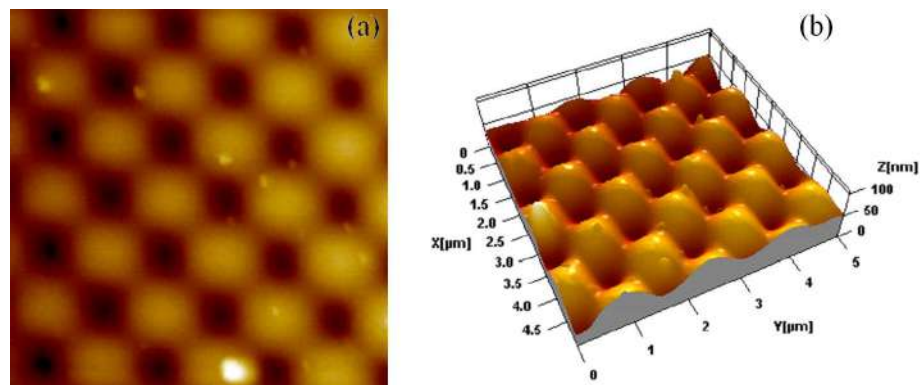


Fig. 1. AFM images of a rectangular photonic crystal structure. (a) Top view, (b) 3D view of the same sample.

A rhombic photonic crystal lattice was similarly produced by rotating the material for 45° , Fig. 2.

A hexagonal photonic crystal structure was produced using three exposures with holographic material rotated by 60° and 120° , Fig. 3.

The structures have periodicities of the order $1.1 \mu\text{m}$ and depth about 50 nm.

It could be seen that the structure from Fig. 3 has smaller depth contrast, compared to structures shown in Figs. 1 and 2. While structures from Figs. 1 and 2 were produced with two exposures (only one intermediate rotation), the structure shown in Fig. 3 was obtained with three exposures, so the depth contrast was decreased because of cumulative angle errors of two intermediate rotations. However, by more precise control of rotation angle of the holographic recording material between exposures the depth contrast could be improved.

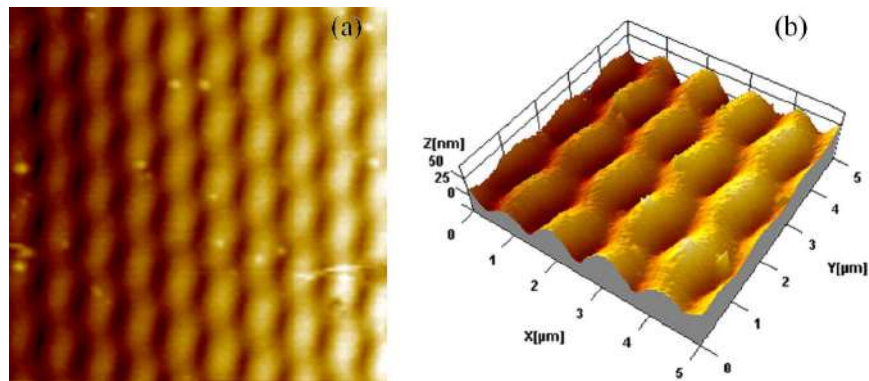


Fig. 2. AFM images of a rhombic photonic crystal structure. (a) Top view, (b) 3D view of the same sample.

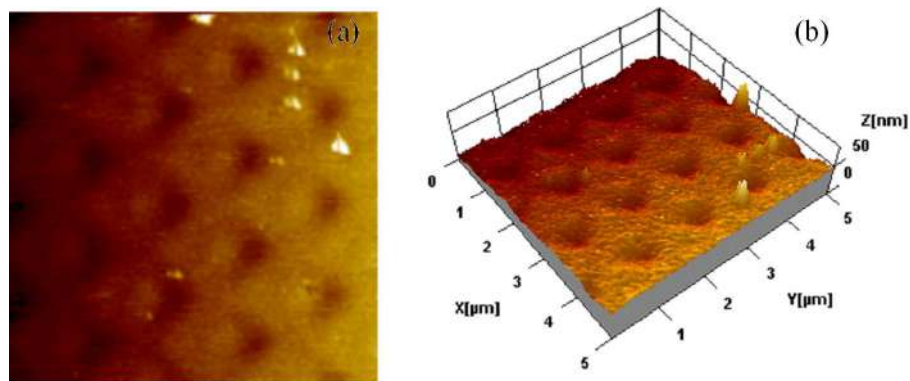


Fig. 3. AFM images of a hexagonal photonic crystal structure. (a) Top view, (b) 3D view of the same sample.

3. Conclusion

We have fabricated photonic crystal structures in a dichromate-sensitized pullulan by holography. Dual-beam multiple exposure technique is used. Our microstructures, although with low refractive index, may be used as templates for the construction (development) of photonic crystal with higher refractive index contrast for complete band gaps.

Acknowledgments

Research was performed under the contract 141003 funded by the Ministry of the Science and Environmental Protection of Serbia.

References

- [1] M. Campbell, D.N. Sharp, M. Harrison, R.G. Denning, A.J. Turberfield, *Nature* **404**, 53 (2000).
- [2] Y.K. Pang, J.C.W. Lee, C.T. Ho, W.Y. Tam, *Opt. Express* **14**, 9013 (2006).
- [3] S. Pissadakis, C. Pappas, *Opt. Express* **15**, 4296 (2007).
- [4] T. Kondo, S. Matsuo, S. Juodkazis, V. Mizeikis, *Appl. Phys. Lett.* **82**, 2758 (2003).
- [5] D. Pantelić, S. Savić, D. Jakovljević, *Opt. Lett.* **23**, 807 (1998).
- [6] S. Savić-Šević, D. Pantelić, *Opt. Express* **13**, 2747 (2005).
- [7] R.C. Gauthier, K.W. Mnyamneh, *Opt. Laser Technol.* **36**, 625 (2004).